OFFICE OF CIVILIAN RADIOACTIVE WASTE MANAGEMENT
SPECIAL INSTRUCTION SHEET

1 QA QA
Page 1 of 1

Complete Only Applicable Items

This is a placeholder page for records that cannot be scanned or microfilmed

2 Record Date	3 Accession Number
10/22/1999	MOL.20000104.0306
4 Author Name(s)	**5 Author Organization**
J B CHO	N/A

6 Title
SINGLE HEATER TEST FINAL REPORT

7 Document Number(s)	8 Version
BAB000000-01717-5700-00005	REV 00 ICN #1
9 Document Type	**10 Medium**
REPORT	Optic / Paper

11 Access Control Code
PUB

12 Traceability Designator
BAB000000-01717-5700-00005, 1 2 21 3 N, SP3120M3

13 Comments
This is a one-of-a-kind due to the color graphs enclosed, and can be located through the Records Processing Center (RPC)

QA QA

TRW

TRW Environmental
Safety Systems Inc

MOL.20000104.0306

Single Heater Test Final Report

Revision 00 ICN 1

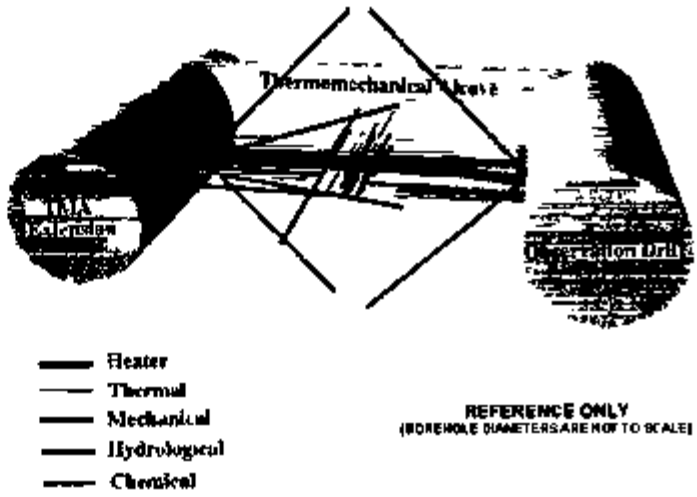

May 1999

Civilian Radioactive Waste Management System

Management & Operating Contractor

B&W Federal Services
Duke Engineering & Services, Inc
Fluor Daniel, Inc
Framatome Cogema Fuels
Integrated Resources Group
JAI Corporation
JK Research Associates, Inc
Lawrence Berkeley National Laboratory
Lawrence Livermore National Laboratory
Los Alamos National Laboratory
Morrison-Knudsen Corporation
Sandia National Laboratories
Science Applications International Corp.
TRW Environmental Safety Systems Inc.
Winston & Strawn
URSG-Woodward-Clyde Federal Services
Cooperating Federal Agency:
U S Geological Survey

Prepared by:
TRW Environmental Safety Systems Inc.

Prepared for:
U.S. Department of Energy
Office of Civilian Radioactive Waste Management
1000 Independence Avenue, S W
Washington, D.C 20565

SP3120M3
WBS: 1.2.21.3.N
QA: QA

Civilian Radioactive Waste Management System
Management & Operating Contractor

Single Heater Test Final Report

BAB000000-01717-5700-00005 REV 00 ICN1

October 1999

Prepared for:

U.S. Department of Energy
Yucca Mountain Site Characterization Office
P.O. Box 30307
North Las Vegas, NV 89036-0307

Prepared by:

TRW Environmental Safety Systems Inc.
1261 Town Center Drive
Las Vegas, Nevada 89134-6352

Under Contract Number
DE-AC08-91RW00134

DISCLAIMER

Civilian Radioactive Waste Management System
Management & Operating Contractor

Single Heater Test Final Report

BAB000000-01717-5700-00005 REV 00 ICN 1

October 1999

Author:

J.B. Cho — Date: 10/22/99

Checker:

R.A. Wagner
Product Quality Checker — Date: 22 Oct 99

Responsible Manager:

M.T. Peters — Date: 10/22/99

CHANGE HISTORY

Revision Number	Interim Change No.	Effective Date	Description of Change
0	0	05/25/1999	Initial issue
0	1	10/25/1999	Minor editorial changes. Page viii Clarified the preference for dual permeability model. Page 2-3 Changed TBV nmbers from 1181 to 1154 for Ramirez and Daily 1998. Page 5-1 Clarified capabilities of TOUGH and NUFT code. Page 6-1 Clarified absence of post-cooling mapping. Page 6-3 Added description of 100° isotherm. Page 6-10 Corrected equation 6-8b. Page 6-27 Referenced LBNL Procedure. Page 6-35 Clarified status of POWD10 Version 10 software. Page 8-1 Referenced LBNL Procedure. Page 8-13 Referenced LBNL Procedure. Page 8-15 Referenced LBNL Procedure. Page 8-26 Referenced LLNL Procedure. Page 8-40 (41) Referenced LBNL Procedure. Clarified status of TOUGH/TOUGH2 software. Page 8-42 (43) Clarified version of TOUGH2 software.

Revision Number	Interim Change No.	Effective Date	Description of Change
			Page 8-43, 44 (44) Clarified status of TOUGH2 software. Page 8-62 (63) Clarified status of NUFT Version 6-17-98 software. Page 8-63 (64) Clarified version of NUFT software. Page 9-23 Clarified version and status of FLAC Version 3.22 software. Page 9-27 Added Chapter Summary. Page 10-2 Clarified status of TOUGHREACT Version 1.0 software. Page 10-3 Clarified status of SUPRCRT2 Version 1.0 software. Page 10-6 Referenced USGS procedure used for uranium and strontium analyses. Page 10-10 Clarified status of TOUGHREACT Version 1.0 software. Page 10-14 Clarified status of EQ3/6 Version 7.2b software. Page 10-15 Clarified information regarding zeolites. Page 12-3 Clarified the preference for dual permeability model. Section 13 Added references for additional procedures and added TBV numbers to several software references. Figures 8-20 to 8-22, 8-28, and 8-33 Added up arrows to figures.

Revision Number	Interim Change No.	Effective Date	Description of Change
			Appendix I now includes appropriate TDIFs. Appendix I page numbers 17, 18, 21, 27, 28, 29, 30, 31, 32, 33, 34, 37, 38, 39, 40, 41, 42, 53, and 54 of ICN0 were removed and new pages 40 through 58 have been added to ICN1.

INTENTIONALLY LEFT BLANK

EXECUTIVE SUMMARY

The Single Heater Test is the first of the in-situ thermal tests conducted by the U.S. Department of Energy as part of its program of characterizing Yucca Mountain in Nevada as the potential site for a proposed deep geologic repository for the disposal of spent nuclear fuel and high-level nuclear waste. The Site Characterization Plan (DOE 1988) contained an extensive plan of in-situ thermal tests aimed at understanding specific aspects of the response of the local rock-mass around the potential repository to the heat from the radioactive decay of the emplaced waste. With the refocusing of the Site Characterization Plan by the *Civilian Radioactive Waste Management Program Plan* (DOE 1994), a consolidated thermal testing program emerged by 1995 as documented in the reports *In-Situ Thermal Testing Program Strategy* (DOE 1995) and *Updated In-Situ Thermal Testing Program Strategy* (CRWMS M&O 1997a). The concept of the Single Heater Test took shape in the summer of 1995 and detailed planning and design of the test started with the beginning fiscal year 1996.

The overall objective of the Single Heater Test was to gain an understanding of the coupled thermal, mechanical, hydrological, and chemical processes that are anticipated to occur in the local rock-mass in the potential repository as a result of heat from radioactive decay of the emplaced waste. This included making a priori predictions of the test results using existing models and subsequently refining or modifying the models, on the basis of comparative and interpretive analyses of the measurements and predictions. A second, no less important, objective was to try out, in a full-scale field setting, the various instruments and equipment to be employed in the future on a much larger, more complex, thermal test of longer duration, such as the Drift Scale Test. This "shake down" or trial aspect of the Single Heater Test applied not just to the hardware, but also to the teamwork and cooperation between multiple organizations performing their part in the test.

Planning for the test started in the summer of 1995 and the heating and cooling of the test block was carried out between August 1996 and January 1998. Post cooling characterization, laboratory testing, modeling, analysis, and documentation continued, culminating in this *Single Heater Test Final Report*.

Section 3 of this report provides a description of the test in terms of its objectives, configuration, and measurements, as well as overview chronology and a listing of reports associated with the test. Preheating and post-cooling characterizations of the test block are discussed in Sections 4 and 6 respectively, while pretest predictive analyses are covered in Section 5. Thermal, thermal-hydrological, thermal-mechanical, and thermal-chemical data are discussed and analyzed in Sections 7, 8, 9, and 10 respectively. The performance of various measuring systems and equipment are discussed in Section 11. Section 2 lists the data tracking numbers for the various Single Heater Test measurements, including their Quality Assurance status and whether they are in the technical data base.

The outcomes of the Single Heater Test are described in Section 12 and are recapitulated below.

- Conduction is the dominant heat transfer mechanism in the Single Heater Test block, although the pore water in the rock plays a role via the convection mode, both in the

liquid and gas phases. It is important to take this into account in modeling, to correctly predict the effects of heating the rock, such as the distribution of temperature increase and movement of water.

- Based on locations of increased and decreased saturations as monitored in the test by electrical resistivity tomography, neutron logging, and ground penetrating radar, and such locations predicted by the models, as well as comparisons of the predicted and measured temperatures, the dual permeability model is considered to be more effective than the equivalent continuum model in simulating the thermal-hydrological processes in the Single Heater Test block.

- Electrical resistivity tomography and ground penetrating radar measurements in the Single Heater Test tend to suggest, as does dual permeability modeling, that rock moisture mobilized by heating drains (on condensation) by gravity via fractures to below the heated region rather than stay perched above it. This is an important finding with respect to a hot repository, and various observations in the Drift Scale Test so far are bearing this out.

- Pneumatic measurements in the Single Heater Test indicate that air-permeability in certain regions of the test block some distance away from the heater, decreased by a factor of 2 to 5 during the heating phase due to filling of fractures by the condensation of mobilized moisture. Permeability recovered when the heating stopped, as the supply of mobilized moisture ended and liquid water drained down the fractures by gravity.

- Electrical resistivity tomography and neutron logging measurements show good agreement with each other in tracking the growth of the drying regions as shown in Figure 12-1, which compiles these two sets of measurements near the end of the heating phase (day 270). The transition from drying to wetting regions observed by neutron logs in boreholes 22 and 23 matches well with the drying/wetting transition derived from electrical resistivity tomography measurements.

- Temperature measurements in the neutron boreholes indicate that drying of the rock begins to occur well before reaching the boiling temperature which is 96°C at Yucca Mountain because of the altitude. Figure 12-2 shows the electrical resistivity tomography tomographs of day 270 overlaid on temperature contours calculated for day 275. This figure shows drying in regions where the temperature is 60°C or more.

- The coefficient of thermal expansion of the rockmass below 200°C, as derived from measured displacements and temperatures in the Single Heater Test, is as much as 50 percent less than that measured in the laboratory using small hand samples. This lowering of the coefficient of thermal expansion in the larger scale is considered to be caused by fractures which tend to accommodate a large part of the expansion of the rock due to heating.

- Based on comparative analyses of various sets of predicted temperatures and the measured temperatures, the Single Heater Test indicates that the thermal conductivity of

the in situ rock is substantially higher than that of dried rock, because the moisture in the rock has a higher thermal conductivity. This difference needs to be taken into account in simulating the thermal-hydrological process to yield more accurate temperature predictions.

- Chemical analysis of samples of water mobilized by heat in the Single Heater Test and subsequent modeling to recreate the characteristics of this water demonstrated that gas-phase reactions play an important role in the thermal-chemical response of the rock. The slightly depressed pH of the water samples indicates that CO_2 partial pressure in the Single Heater Test have been as much as two orders of magnitude higher than that in ambient atmosphere.

- Interpretive analysis of the chemical compositions of the samples of water from borehole 16 in the context of reaction-transport simulations of the chemical processes in the Single Heater Test, leads to the conclusion that the borehole 16 water resulted from steam condensation in fractures. The mildly acidic character of the water reflects the dissolution of gaseous CO_2 at the time of condensation. The simulations indicate that dissolved carbonate species in matrix water is a sufficient source of CO_2 gas to drive the pH down to a mildly acidic range.

- Calcium, gypsum and amorphous silica were found in the posttest mineralogic analyses of the samples from the overcoring of borehole 16. The distribution and textural attribute of these minerals suggest that they formed through evaporation of residual water during the post-heating (cooling phase) of the test.

- Strontium and uranium analyses of the borehole 16 water samples indicate that the concentrations of these cations are not unreasonable compared to that of pore water from these strata, although data on the uranium content of pore water are limited. The $^{87}Sr/^{86}Sr$ ratio of all the borehole 16 water samples remain essentially constant at ~ 4.5 which is well within the range measured on pore water from these strata.

- Post-cooling air-permeability measurements show an increase in permeability ranging from 20 percent to a factor of 3.5 compared to the pre-heating values. Since air-permeability measurements are made over meters of length of borehole and the fluid always seeks the path of least resistance, this increase in permeability is considered to be resulting from the opening of fractures due to heating and/or cooling.

- All the test specimens or coupons of carbon steel left in the two hydrology boreholes before the start of heating underwent various degrees of corrosion. The corrosion products were generally goethite (α-$Fe^{+3}O(OH)$) and magnetite (Fe_3O_4). The chloride containing mineral akaganeite (β-$Fe^{+3}O(OH,Cl)$) was identified in one coupon.

- The copper tubing protecting the heating elements was found to be covered with oxidation products upon withdrawal after heating and cooling. The oxidation mineralization included tenorite, cuprite, paratacamite and atacomite.

- The performance of the temperature sensors was within expectation; approximately 5 percent of them failed. A small fraction of both thermocouples and resistance temperature detectors failed. None of the thermistors failed.

- The chemical sensors installed in SEAMIST liners and designed to measure various chemical parameters did not function at all because of the unsaturated environment they were in.

- The performance of multiple-point borehole extensometers with high temperature linear variable displacement transducers was superior to the ones with vibrating wire gages; posttest examination and calibration checks indicated that all the high temperature linear variable-displacement transducers were within calibration standards.

- The optical multiple-point borehole extensometers performed as expected; however, the measurements were inferior, in terms of resolution and precision, to those from other systems such as mechanical multiple-point borehole extensometers.

- The ground penetrating radar technique of monitoring the saturation of the rock was found to work as expected. The ability of ground penetrating radar to identify areas of drying was good, while the ability to identify areas of increased saturation was qualitative. The results of ground penetrating radar and electrical resistivity tomography measurements generally coincided, thereby lending credence to each other.

- The infrared imaging conducted next to the Single Heater Test block failed to detect any heat-mobilized moisture escaping via fractures.

- Last, but not the least, the experiment of having numerous organizational entities work together in a short period of time and in limited space in fielding the Single Heater Test proved to be successful. The experience made the fielding of the much larger and more complex Drift Scale Test to be completed smoothly the following year.

A number of the findings of the Single Heater Test listed above are also borne by the other thermal tests, namely, the Large Block Test and the early results of the Drift Scale Test. The following recommendations are, therefore, appropriate for taking into account in future total system performance assessments and the various analyses supporting them:

- The dual permeability model should be the preferred conceptual model over the equivalent continuum model for simulating the thermal-hydrological responses of the near-field rock mass in the drift scale. The dual permeability model should also be the preferred model for simulating the thermal-hydrological-mechanical responses.

- All three thermal tests indicate that the rock porewater mobilized by the heat tends to drain by gravity, via the fractures, to below the heated region rather than stay perched above it. This means that condensate refluxing or episodic seepage into the emplacement drifts are unlikely to occur during the postclosure period.

CONTENTS

Page

CONTENTS (Continued)

CONTENTS (Continued)

Page

CONTENTS (Continued)

CONTENTS (Continued)

Page

CONTENTS (Continued)

Page

APPENDICES

FIGURES

FIGURES (Continued)

FIGURES (Continued)

FIGURES (Continued)

FIGURES (Continued)

FIGURES (Continued)

FIGURES (Continued)

FIGURES (Continued)

FIGURES (Continued)

FIGURES (Continued)

FIGURES (Continued)

FIGURES (Continued)

FIGURES (Continued)

FIGURES (Continued)

FIGURES (Continued)

FIGURES (Continued)

TABLES

TABLES (Continued)

Page

TABLES (Continued)

INTENTIONALLY LEFT BLANK

ACRONYMS

2D	two-dimensional
3D	three-dimensional
ASTM	American Society for Testing and Materials
CRWMS	Civilian Radioactive Waste Management System
DCS	Data Collection System
DKM	dual-permeability model
DOE	U.S. Department of Energy
DST	Drift Scale Test
DTN	data tracking number
ECM	equivalent continuum model
EDX	energy-dispersive X-ray spectroscopy
ERT	electrical resistivity tomography
ESF	Exploratory Studies Facility
FLAC	Fast Lagrangian Analysis of Continua
FMX	fracture-matrix interaction
FY	fiscal year
GHFM	guarded heat flow meter
GPR	ground penetrating radar
ICTE	instantaneous coefficient of thermal expansion
IR	infrared
LANL	Los Alamos National Laboratory
LBNL	Lawrence Berkeley National Laboratory
LLNL	Lawrence Livermore National Laboratory
LVDT	linear variable displacement transducer
M&O	Management and Operating Contractor
MCTE	mean coefficient of thermal expansion
ME	Mean Error
MINC	multiple interacting continua
MOP	Multiple Offset Profile
MPBX	multiple-point borehole extensometer
NIST	National Institute of Standards and Technology
NUFT	Nonisothermal Unsaturated-Saturated Flow and Transport
QA	quality assurance

RBLC	rock bolt load cell
RMSE	Root Mean Square Error
RTD	resistance temperature detector
SEM	scanning electron microscopy
SHT	Single Heater Test
SNL	Sandia National Laboratories
SRM	Standard Reference Material
TDIF	Technical Data Information Form
TDMS	Technical Data Management System
Tptpmn	Tertiary Miocene (Age), Paintbrush (Group), Topopah Spring Tuff (Formation), Crystal-Poor (Member), Middle Nonlithophysal (Zone)
TSPA-VA	Total System Performance Assessment-Viability Assessment
TSw2	Topopah Spring welded unit 2
UV	ultraviolet
XRD	X-ray diffraction
YMP	Yucca Mountain Site Characterization Project
ZOP	Zero Offset Profile

1. INTRODUCTION

The Single Heater Test (SHT) is the first of the in-situ thermal tests conducted by the U.S. Department of Energy (DOE) as part of its program of characterizing Yucca Mountain in Nevada as the potential site for a proposed deep geologic repository for the disposal of spent nuclear fuel and high-level nuclear waste. The *Site Characterization Plan: Yucca Mountain Site Nevada Research and Development Area* (DOE 1988) contained an extensive plan of in-situ thermal tests aimed at understanding specific aspects of the response of the local rock mass around the potential repository to the heat from the radioactive decay of the emplaced waste. With the refocusing of the Site Characterization Plan by the *Civilian Radioactive Waste Management Program Plan* (DOE 1994), a consolidated thermal testing program emerged by 1995 as documented in the reports *In-Situ Thermal Testing Program Strategy* (DOE 1995) and *Updated In-Situ Thermal Testing Program Strategy* (CRWMS M&O 1997a). The concept of the SHT took shape in the summer of 1995 and detailed planning and design of the test started with the beginning of fiscal year (FY) 1996. The test and its objectives are described in Section 3, while the overall schedule of activities is covered in Section 3.4.

The reports associated with the SHT are listed in Section 3.5. This, the *Single Heater Test Final Report*, documents all known aspects of the test in an integrated, comprehensive manner either between its covers or by reference to other previous reports.

Testing and analyses for the SHT were performed under a quality assurance (QA) program. However, data and analyses presented in this report do not meet all QA requirements at this time, necessitating the initiation of TBVs for data and software, as appropriate. The SHT and this report are carried out by the Natural Environment Program Operation of the Civilian Radioactive Waste Management Contractor Management and Operating Contractor. All Natural Environment Program Operation work is determined to be quality affecting work in accordance with QAP-2-0, *Conduct of Activities*.

This report supercedes two prior reports, *Single Heater Test Status Report* (CRWMS M&O 1997b), and *Single Heater Test Interim Report* (CRWMS M&O 1997c).

INTENTIONALLY LEFT BLANK

2. ORGANIZATION OF THE REPORT

After the Executive Summary, Contents Listings, and the Introduction preceding this section, the remainder of this report is organized to present, first, a description of the test and all associated activities in Section 3. This is followed by pre-heating or ambient characterization of the test block in Section 4 and pre-heating or predictive analyses of the test to forecast the test results in Section 5. Post-cooling characterizations are covered in Section 6, followed by discussion and analyses of results in Sections 7 through 10. Discussion of results is presented according to the heat-driven coupled processes in the near-field. Thermal, thermal-hydrological, thermal-mechanical and thermal-chemical processes are, thus, covered in Sections 7, 8, 9, and 10, respectively. Performance of the various measuring systems is discussed in Section 11 followed by the conclusions in Section 12. Appendices follow the References in Section 13.

2.1 ACCEPTANCE CRITERIA

Table 2-1 enumerates the acceptance criteria for this report and specifies the sections of this report satisfying each criterion.

Table 2-1. Acceptance Criteria and Location of Compliance

Acceptance Criteria	Report Location
The report will document measurements, numerical analyses, and corresponding interpretations of the four processes under consideration in the SHT	Sections 7, 8, 9 and 10
This deliverable shall be prepared in accordance with Office of Civilian Radioactive Waste Management-approved QA procedures implementing requirements of the *Quality Assurance Requirements and Description* (DOE 1998).	All Sections
The product shall be developed on the basis of the best technical data, including both qualifed and non-qualified data.	Section 2
The QA status of data used and cited in the report shall be appropriately noted	Section 2
Stratigraphic nomenclature used shall be consistent with the Reference Information Base (YMP 1997) Section 1.12(a): Stratigraphy-Geology Lithologic Stratigraphy.	Section 6.4.2
Within the report's reference section, references to data used in the report shall include record Accession Numbers or Data Tracking Numbers when available.	Section 13
Technical data contained within the deliverable and not already incorporated in the Technical Data Management System (TDMS) shall be submitted, if appropriate for incorporation into the TDMS in accordance with YAP-SIII 3Q.	Section 2.4, Table 2-4
Verification of technical data submittal compliance shall be demonstrated by including as part of the deliverable: 1) a copy of the Technical Data Information Form (TDIF) generated identifying the data in the Automated Technical Data Tracking system, and 2) a copy of the transmittal letter attached to the technical data transmittal to the TDMS Administrator.	Appendix I
This deliverable will be developed, reviewed, and submitted in accordance with Yucca Mountain Site Characterization Office's "Policy on Development of Documents that will be Available to the License Proceeding "	All Sections

2.2 DATA SOURCES AND QA STATUS

Testing and analyses for the SHT were performed under a QA program. However, data and analyses presented in this report do not meet all QA requirements at this time, necessitating the initiation of TBVs for data and software, as appropriate. The SHT and this report are carried out by the Natural Environment Program Operation of the Civilian Radioactive Waste Management Contractor Management and Operating Contractor. All Natural Environment Program Operation work is determined to be quality affecting work in accordance with QAP-2-0.

Tables 2-2 and 2-3 identify by accession numbers and data tracking numbers (DTNs) the source of results data of the SHT, and the qualification status of that data, used in this report in figures and tables, respectively.

Table 2-2. Source and QA Status of Data in Figures

Figure No.	Data Source	Q Status of the Data
6-5 through 6-7	DTN: SNL22080196001.003, Table S98409_001 DTN: SNL22080196001.001, Table S99095_001	TBV-1149 TBV-1191
6-8	DTN: SNL22080196001.003, Table S98409_002	TBV-1149
6-9 through 6-10	DTN: SNL22080196001.003, Table S98409_002 DTN: SNL22080196001.001, Table S99095_002	TBV-1149 TBV-1191
6-11 through 6-13	DTN: SNL22080196001.003, Table S98409_003 Boyd et al. 1996, Table 2	TBV-1149 TBV-1148
6-14	DTN: LB980901123142.006, Table S98282_001	TBV-1176
6-23	DTN: LASL831151AQ98.001, Table S98284_006	TBV-1168
6-25	DTN: LASL831151AQ98.001, Table S98284_005	TBV-1168
6-28	DTN: LASL831151AQ98.001, Table S98284_005	TBV-1168
7-1a and 7-1b	DTN: SNF35110695001.008, Table S98080_001	TBV-1161
7-2 through 7-21, 7-23, 7-24, and 7-35 through 7-44	DTN: SNF35110695001.008, Table S98080_002	TBV-1161
7-22, 7-25, 7-26, and 7-28 through 7-33	DTN: SNF35110695001.008, Table S98080_002 DTN: SNF35110695001.009, Table S98417_002	TBV-1161 TBV-1163
8-2	DTN: LB960500834244.001, Table S97535_001	TBV-1141
8-4 and 8-5	Freifeld and Tsang 1997a, Table 2 and Table 3 Freifeld and Tsang 1997b, Table 2 and Table 3 Freifeld and Tsang 1997c, Table 2 and Table 3 Freifeld 1997, Table 2 and Table 3 Freifeld 1998a, Table 2 and Table 3	TBV-1192 TBV-1193 TBV-1164 TBV-1194 TBV-1190
8-9	DTN: LB980901123142.001, Table S98264_001	TBV-1173
8-10	DTN: LB980901123142.002, Table S98265_003	TBV-1174
8-11	DTN: LB980901123142.002, Table S98265_001	TBV-1174
8-12 and 8-13	DTN: LB980901123142.002, Table S98265_002	TBV-1174
8-17 through 8-22	DTN: LB980901123142.003, Table S98263_001	TBV-1175
8-23	DTN: SNF35110695001.008, Table S98080_002	TBV-1161
8-25	DTN: LL981109904242.072, Table S99003_003	TBV-1181
8-35	Cook 1997, Plate 2	TBV-1195
8-36	Cook 1998, Plate 4 and Plate 5	TBV-1183
8-37	Cook 1998, Plate 4	TBV-1183
8-38	Cook 1998, Figure 2	TBV-1183
8-39	Cook 1998, Figure 3	TBV-1183

Table 2-2 Source and QA Status of Data in Figures (Continued)

Figure No.	Data Source	Q Status of the Data
8-41	Ramirez 1997, Figure 2 and Figure 2b	TBV-1147
8-42	Ramirez and Daily 1998, Figure 2	TBV-1154
8-44	Ramirez 1997, Figure 2 and Figure 2b	TBV-1147
8-45	Ramirez and Daily 1998, Figure 2	TBV-1154
8-47 through 8-53	DTN: LL971004604244.045, Table S98110_001	TBV-1153
8-54 through 8-67	DTN: LL980106904244.051, Table S98109_001	TBV-1182
8-68 through 8-73	DTN: LL971004604244.045, Table S98110_001	TBV-1153
8-74 through 8-86	DTN: LL980106904244.051, Table S98109_001	TBV-1182
8-89	DTN: SNF35110695001.008, Table S98080_001	TBV-1161
8-107 through 8-114 and 8-119	DTN: SNF35110695001.008, Table S98080_002	TBV-1161
9-3, 9-5, 9-7 and 9-9	DTN: SNF35110695001.008, Table S98080_003 DTN: SNF35110695001.009, Table S98417_004	TBV-1161 TBV-1163
9-11 through 9-16	DTN: SNF35110695001.008, Table S98080_003 DTN: SNF35110695001.009, Table S98417_003	TBV-1161 TBV-1163
9-17 through 9-21	Finley et al. 1998, Figures 4-17 through 4-21	TBV-1163
9-22 through 9-27	Finley et al. 1998, Table 4-6	TBV-1163
9-28 through 9-35	DTN: SNF35110695001.008, Table S98080_004 DTN: SNF35110695001.009, Table S98417_001	TBV-1161 TBV-1163
9-46	Ramirez 1997, Figure 2 and Figure 2b Ramirez and Daily 1998, Figure 2	TBV-1147 TBV-1154
10-1	DTN: GS980908312272.003, Table S99221_001 DTN: GS980908312322.009, Tables S99222_001 and S99222_002	TBV-1176 TBV-1177
10-38 and 10-39	Glassley 1997a, Table 1 Glassley 1997b, Table 1	TBV-1185 TBV-1184
12-1 and 12-2	Ramirez and Daily 1998, Figure 3	TBV-1154
A-1 through A-28,	DTN: SNL22080196001.003, Table S98409_002	TBV-1149
B-1 through B-8	DTN: SNL22080196001.003, Table S98409_001	TBV-1149
C-1 through C-14 D-1 through D-9	DTN: SNL22080196001.003, Table S98409_002	TBV-1149
E-1 through E-14	DTN: SNL22080196001.003, Table S98409_003	TBV-1149
G-1 through G-16	DTN: SNF35110695001.008, Table S98080_002	TBV-1161
H-1 through H-13	Finley et al. 1998, Appendix D	TBV-1163

Table 2-3. Source and QA Status of Data in Tables

Table No.	Data Source	Q Status of the Data
4-1	Wang and Suarez-Rivera 1997, Table 3, pp. 17 and 18	TBV-1150
4-2	Wang and Suarez-Rivera 1997, Table 4, p. 18	TBV-1150
6-9	DTN: SNL22080196001.003, Table S98409_001	TBV-1149
6-10 through 6-13	DTN: SNL22080196001.003, Table S98409_002	TBV-1149
6-14 and 6-15	DTN: SNL22080196001.003, Table S98409_003	TBV-1149
6-16	Boyd et al. 1996, Table 2 DTN: SNL22080196001.003, Table S98409_003	TBV-1148 TBV-1149
6-17	SNL 1997a, Table 5	TBV-1148
6-18	DTN: LB980901123142.006, Tables S98282_001 to S98282_005	TBV-1178
6-19	DTN: LASL831151AQ98.001, Tables S98284_001 and S98284_002	TBV-1168

Table 2-3. Source and QA Status of Data in Tables (Continued)

Table No.	Data Source	Q Status of the Data
6-21	DTN: LASL831151AQ98.001, Tables S98284_003 through S98284_011, and S98284_020	TBV-1168
6-22	DTN: LASL831151AQ98.001, Tables S98284_012 through S98284_019	TBV-1168
8-1	DTN: LB960500834244.001, Table S97535_001	TBV-1141
8-2	DTN: LB960500834244.001, Table S97535_001	TBV-1141
8-3	Freifeld and Tsang 1997c. Table 3, p. 14 DTN: LB971000123142.001, Table S97590_001 DTN: LB980120123142.002, Table S98118_001	TBV-1164 TBV-1186 TBV-1187
8-4	DTN: LB980901123142.001, Table S98264_001	TBV-1173
8-5 and 8-6	DTN: LB960500834244.001, Table S97535_001 DTN: LB980901123142.001, Table S98264_001	TBV-1141 TBV-1173
8-7	DTN: LB980901123142.001. Table S98264_001	TBV-1173
8-8	DTN: LB980901123142.001. Table S98264_002	TBV-1173
8-15	DTN: LL980810804242.050	TBV-1188
9-1	DTN: SNF35110695001.008, Table S98080_003 DTN: SNF35110695001.009, Table S98417_004	TBV-1161 TBV-1163
9-2	Brodsky 1997, Table 1 p. 3	TBV-1189
9-3	DTN: SNF35110695001.008, Table S98080_003	TBV-1161
9-4	DTN: SNF35110695001.008, Table S98080_003 DTN: SNF35110695001.009, Table S98417_003	TBV-1161 TBV-1163
9-5	DTN: SNF35110695001.008, Table S98080_005	TBV-1161
9-6	Finley et al. 1996, Table 4-6 p. 90	TBV-1163
9-7	DTN: SNF35110695001.008, Table S98080_004 DTN: SNF35110695001.009, Table S98417_001	TBV-1161 TBV-1163
9-8	DTN: SNF35110695001.008, Table S98080_004	TBV-1161
10-2	DTN: LL970703904244.034, Tables S97593_001 to S97593_024 DTN: GS980908312322.009, Tables S99222_001 and S99222_002	TBV-1151 TBV-1177
10-3	DTN: GS980908312272.003, Table S99221_001 DTN: GS980908312322.009, Tables S99222_001 and S99222_002	TBV-1176 TBV-1177
10-4	DTN: GS970208312271.002, Tables S97236_001 through S97236_020	TBV-1143
10-5	DTN: LL980106404244.050, Tables S98056_001 through S98056_007	TBV-1188
10-9 and 10-10	DTN: LL970703904244.034, Tables S97593_001 through S97593_024	TBV-1151
G-1	DTN: SNF35110695001.008, Table S98080_001	TBV-1161
G-2	DTN: SNF35110695001.008, Table S98080_002	TBV-1161
G-3	DTN: SNF35110695001.008, Table S98080_003 DTN: SNF35110695001.009, Table S98417_004	TBV-1161 TBV-1163
G-4	DTN: SNF35110695001.008, Table S98080_004 DTN: SNF35110695001.009, Table S98417_001	TBV-1161 TBV-1163
G-5	DTN: SNF35110695001.008, Table S98080_003 DTN: SNF35110695001.009, Table S98417_003	TBV-1161 TBV-1163
G-6	DTN: SNF35110695001.008, Table S98080_005	TBV-1161

3. TEST DESCRIPTION

The SHT is an integral part of the DOE program of characterizing Yucca Mountain to evaluate its suitability as the potential site for a geologic repository for the permanent disposal of spent nuclear fuel and high-level nuclear waste. Located in the Thermal Testing Facility, or Alcove 5, of the Exploratory Studies Facility (ESF) in Yucca Mountain, the SHT is the first of the in situ thermal testing program to investigate the coupled processes that would occur in the local rock mass around the potential repository, because of the decay heat from the emplaced waste. In the SHT, a block of rock, approximately 13 m wide, 10 m deep and 5 m high, is heated by one electric rod heater placed inside the block, and various types of responses in the rock are monitored or measured by sensors placed in or on the rock.

The heating phase of the SHT spanned over nine months, followed by a cooling phase of similar duration.

Characterization of the test block under ambient conditions prior to heating was carried out after it was defined by the excavation of the drifts on its three sides. Such characterization included testing in the laboratory for thermal, mechanical, and hydrological properties, mineralogic-petrologic characteristics, as well as field measurements of permeabilities and fracture characteristics. Pretest predictive analyses were done to forecast the various measurements to be made during the entire duration of heating and cooling. Comparative and interpretive analyses of the measurements and the predictions led to a number of conclusions as the outcome of the test.

3.1 TEST OBJECTIVE

The overall objective of the SHT, coinciding with that of the in situ thermal testing program, is gaining greater understanding of the coupled thermal, mechanical, hydrological, and chemical processes that would occur in the local rock mass around the potential repository as a result of the heat from the radioactive decay of the emplaced waste. Within that context, the emphasis in the SHT was to investigate thermal-mechanical processes, especially to measure rock mass thermal and mechanical properties.

The other, no less important, objective of the SHT was to try out in a full scale field setting, the various instruments and equipment to be employed in the future on a much larger, more complex, thermal test of longer duration, such as the Drift Scale Test (DST). For this reason, the SHT has often been referred to as the "shake-down" test. This "shake-down" or trial aspect of the SHT applies not just to the hardware in the test, but also to the teamwork and cooperation between multiple organizational entities performing their part in the test. Additionally, the process of making *a priori* predictions of the test results using existing models and subsequently refining or modifying the models, on the basis of comparative and interpretive analyses of the measurements and predictions, received a first trial in the SHT.

The discrete elements contributing to the overall objectives of the test are to:

- Measure the temporal and spatial distributions of temperature in the rock during heating and cooling
- Measure the saturation of the rock before, during, and after heating and during cooling
- Measure displacements in the rock during heating and cooling
- Measure rock mass thermal and mechanical properties at ambient and elevated temperatures
- Measure the rock mass pneumatic bulk permeability before, during, and after heating and cooling
- Measure rockbolt anchorage response before and after heating
- Monitor the propagation of a drying front in the rock during heating and subsequent re-wetting, if any, during cooling and afterwards
- Determine the mineralogic-petrologic characteristics of the rock before and after the test
- Analyze the chemical characteristics of water samples, if any, collected during the test.

3.2 TEST CONFIGURATION

The SHT is located in Alcove 5 in the ESF as shown in Figure 3-1. A plan and cross-section of the SHT are shown in Figure 3-2. The SHT block is nominally 12.9 m wide, 9.5 m deep and 5.5 m high. Forty-one boreholes with total length of approximately 230 m are drilled into the block. One of these boreholes, borehole 1, houses the single 5 m long heater capable of generating nominal 4 kW of heat. A detailed description of the boreholes reflecting the as-built conditions in the SHT is given in Table 3-1. The numbers of the boreholes given in Figure 3-2 correspond to those in Table 3-1. Table 3-1 gives the sensor type or type of measurement for which any particular borehole is used. A total of 530 sensors are housed in the boreholes to monitor the thermal, mechanical, hydrological, and chemical responses of the rock as it is heated and cooled.

Most of the measurements made by the sensors are scanned and recorded by an automated Data Collection System (DCS). The central component of the DCS is a Geomation Model 2380 MCUs in NEMA-12 enclosure with a capacity of 640 channels. The DCS records the heater power and the readings of the thermocouples mounted on the heater itself every fifteen minutes. The readings of the other sensors are recorded on an hourly basis. There are certain measurements made which are not recorded by the DCS. These non-DCS measurements are electrical resistivity tomography (ERT), neutron logging, ground penetrating radar (GPR), Goodman Jack, pneumatic permeability, and infrared (IR) imaging.

Table 3-1 Borehole and Sensor Information for the Single Heater Test

Borehole Number	Borehole Identification	Primary Purpose	Collar Coordinates (meter)[1]			Bottom Coordinates (meter)[1]			Orientation Degree	Diameter cm	Length Meters	Volume Meters[2]	Types and Number of Sensors											Comments
			x	y	z	x	y	z					Thermocouples	RTD	Thermistors	Load Cell	Anchors in MPBX	Tape/Wire Extensometer	Humidity Sensor	Pressure Transducer	Electrode Sensor (ERT)	Chemistry Absorbing Pads	
1	ESF-TMA-H-1	Heater	0.01	0.04	-0.03	0.00	6.97	-0.01	0.5	9.60	7.00	0.05	27										5 m Long Heater w/ Metallic Spring Centralizers
2	ESF-TMA-MPBX-1	MPBX - Rock Mass Displacement	0.18	0.06	0.27	0.14	6.99	0.29	0.5	7.57	7.00	0.03	9		1		6						Thermocouple Sensors Between and at Anchors in MPBX
3	ESF-TMA-MPBX-2	MPBX - Rock Mass Displacement	-0.62	0.23	0.21	-0.62	7.25	0.26	0.5	7.57	7.00	0.09	13				7						Thermocouple Sensors Between and at Anchors in MPBX
4	ESF-TMA-MPBX-3	MPBX - Rock Mass Displacement	0.75	0.10	1.24	0.78	7.00	1.29	0.5	7.57	7.00	0.03	9		1		6						Thermocouple Sensors Between and at Anchors in MPBX
5	ESF-TMA-MPBX-4	MPBX - Rock Mass Displacement	6.43	3.50	-0.11	0.40	3.50	-0.21	0.5	7.57	6.20	0.03	12		1		8						Thermocouple Sensors Between and at Anchors in MPBX
6	ESF-TMA-OMPBX-1	Optical MPBX	1.19	-0.05	0.29	1.21	11.99	0.13	-0.5	7.57	12.00	0.05					-						Laser Reflection MPBX System
7	ESF-TMA-OMPBX-2	Optical MPBX	6.20	6.49	-0.17	0.30	6.45	0.27	-0.5	7.57	6.20	0.03					-						Laser Reflection MPBX System
8	ESF-TMA-TC-1	Thermocouple	-0.18	0.15	0.28	-0.27	7.85	0.34	0.0	4.80	8.00	0.01	15										Thermocouple Probes Grouted in Hole
9	ESF-TMA-TC-2	Thermocouple	0.63	0.05	0.21	0.62	8.15	0.26	0.0	4.80	8.00	0.01	15										Thermocouple Probes Grouted in Hole
10	ESF-TMA-TC-3	Thermocouple	-0.75	0.23	1.26	-0.71	8.05	1.31	0.0	4.80	8.00	0.01	15										Thermocouple Probes Grouted in Hole
11	ESF-TMA-TC-4	Thermocouple	-0.02	0.03	-0.69	-0.09	5.49	-0.77	0.0	4.80	8.00	0.01	15										Thermocouple Probes Grouted in Hole
12	ESF-TMA-TC-5	Thermocouple	0.00	0.16	0.65	-0.04	8.84	0.66	0.0	4.80	8.00	0.01	16										Thermocouple Probes Grouted in Hole
13	ESF-TMA-TC-6	Thermocouple	6.26	5.49	-0.01	1.67	5.46	-0.04	0.0	4.80	6.20	0.01	10										Thermocouple Probes Grouted in Hole
14	ESF-TMA-TC-7	Thermocouple	-5.59	3.46	-0.01	-0.34	3.43	-0.02	0.0	6.00	6.20	0.02	10										Thermocouple Probes Grouted in Hole
15	ESF-TMA-NEU-1	Neutron Probe & Temp	6.10	4.29	0.33	-1.60	4.28	2.74	17.0	7.57	8.50	0.04		27									RTDs Grouted Between Hole and Teflon Tube
16	ESF-TMA-NEU-2	Hydrology	6.19	4.30	0.04	1.14	4.32	0.71	7.5	7.57	5.50	0.02		4					4	4			Pressure RTD & Humidity Sensors in Packer Systems
17	ESF-TMA-NEU-3	Neutron Probe & Temp	6.16	4.30	-0.45	-1.78	4.31	-1.47	-7.0	7.57	8.50	0.04		29									RTDs Grouted Between Hole and Teflon Tube
18	ESF-TMA-NEU-4	Hydrology	6.17	4.29	-0.22	1.51	4.28	-0.28	-0.5	7.57	6.00	0.02		4					4	4			Pressure RTD & Humidity Sensors in Packer Systems
19	ESF-TMA-BJ-1	Borehole Jack	-6.55	5.52	-0.14	-0.34	5.51	-0.07	0.5	7.57	6.20	0.03											Open Hole for Borehole Jack
20	ESF-TMA-CHE-1	Chemistry - SEAMIST	-5.54	4.91	-0.66	-1.61	4.90	-0.77	-0.5	7.57	5.00	0.02										50	SEAMIST System with Chemical Sensors 45 Sensors Failed
21	ESF-TMA-CHE-2	Chemistry - SEAMIST	-5.59	5.01	-0.01	-1.05	5.10	0.63	7.5	7.57	5.50	0.02										50	SEAMIST System with Chemical Sensors 45 Sensors Failed
22	ESF-TMA-HYD-1	Neutron Probe & Temp	-5.60	4.43	-0.65	-1.56	4.39	-0.74	-0.5	7.57	6.00	0.02		20									RTDs Grouted Between Hole and Teflon Tube
23	ESF-TMA-HYD-2	Neutron Probe & Temp	-5.57	4.43	0.00	-1.31	4.42	0.65	7.5	7.57	8.50	0.02		19									RTDs Grouted Between Hole and Teflon Tube
24	ESF-TMA-ERT-1	Electrical Resistivity Tomography	-5.56	3.89	0.12	-0.41	3.82	6.28	45.0	7.57	8.70	0.04									9		Electrical Resistivity Tomography Electrode Sensor on 1 m Intervals

INTENTIONALLY LEFT BLANK

Table 3-1. Borehole and Sensor Information for the Single Heater Test (Continued)

Borehole Number	Borehole Identification	Primary Purpose	Collar Coordinates (meter)[1]			Bottom Coordinates (meter)[1]			Orientation Degree	Diameter cm	Length Meters	Volume Meters[3]	Types and Number of Sensors										Comments
			x	y	z	x	y	z					Thermocouples	RTD	Thermistors	Load Cell	Anchors in MPBX	Tape/Wire Extensometer	Humidity Sensor	Pressure Transducer	Electrode Sensor (ERT)	Chemistry Absorbing Pads	
25	ESF-TMA-ERT-2	Electrical Resistivity Tomography	-6 57	3 91	-0 13	-0 29	4 07	-6 22	-45 0	7 57	6 70	0 04									9		Electrical Resistivity Tomography Electrode Sensor on 1 m Intervals
26	ESF-TMA-ERT-3	Electrical Resistivity Tomography	6 25	3 89	-0 36	1 15	3 85	-5 71	-45 0	7 57	6 70	0 04									9		Electrical Resistivity Tomography Electrode Sensor on 1 m Intervals
27	ESF-TMA-ERT-4	Electrical Resistivity Tomography	6 26	3 90	0 38	0 38	3 97	5 29	45 0	7 57	6 70	0 04									9		Electrical Resistivity Tomography Electrode Sensor on 1 m Intervals
28	ESF-TMA-RB-1	Rock Bolt w/ Load Cell	0 14	0 05	-0 36	0 26	4 21	-0 38	0 0	5 72	4 00	0 01			1	1							Vibrating Wire Load Cell on Head of Rock Bolt
29	ESF-TMA-RB-2	Rock Bolt w/ Load Cell	-0 23	0 00	-0 35	-0 18	4 22	-0 42	0 0	5 72	4 00	0 01			1	1							Vibrating Wire Load Cell on Head of Rock Bolt
30	ESF-TMA-RB-3	Rock Bolt w/ Load Cell	0 59	0 10	-0 31	0 60	4 03	-0 35	0 0	5 72	4 00	0 01			1	1							Vibrating Wire Load Cell on Head of Rock Bolt
31	ESF-TMA-RB-4	Rock Bolt w/ Load Cell	-0 58	0 13	-0 29	-0 59	4 19	-0 23	0 0	5 72	4 00	0 01			1	1							Vibrating Wire Load Cell on Head of Rock Bolt
32	ESF-TMA-RB-5	Rock Bolt w/ Load Cell	0 14	-5 37	-0 39	0 08	-9 47	-0 41	0 0	5 72	4 00	0 01			1	1							Vibrating Wire Load Cell on Head of Rock Bolt
33	ESF-TMA-RB-6	Rock Bolt w/ Load Cell	-0 20	-5 45	-0 42	-0 21	-9 45	-0 42	0 0	5 72	4 00	0 01			1	1							Vibrating Wire Load Cell on Head of Rock Bolt
34	ESF-TMA-RB-7	Rock Bolt w/ Load Cell	0 59	5 49	-0 30	0 64	-9 60	-0 36	0 0	5 72	4 00	0 01			1	1							Vibrating Wire Load Cell on Head of Rock Bolt
35	ESF-TMA-RB-8	Rock Bolt w/ Load Cell	-0 64	-5 38	-0 31	-0 73	-9 43	-0 45	0 0	5 72	4 00	0 01			1	1							Vibrating Wire Load Cell on Head of Rock Bolt
36	ESF-TMA-TE-1	Tape Extensometer Array 3	-2	0	Multiple				0 0	2 54	Up to 0 5							1					4 - Pin Tape Extensometer Array
37	ESF-TMA-TE-2	Tape Extensometer Array 3	2	0	Multiple				0 0	2 54	Up to 0 5							1					4 - Pin Tape Extensometer Array
38	ESF-TMA-TE-3	Tape Extensometer Array 3	4 5	3	Multiple				0 0	2 54	Up to 0 5							1					4 - Pin Tape Extensometer Array
39	ESF-TMA TE-4	Tape Extensometer Array 3	-8 5	5 1	Multiple				0 0	2 54	Up to 0 5							1					4 - Pin Tape Extensometer Array
40	ESF-TMA-TE-5	Tape Extensometer Array 3	6 5	3	Multiple				0 0	2 54	Up to 0 5							1					4 - Pin Tape Extensometer Array
41	ESF-TMA-TE-6	Tape Extensometer Array 3	6 5	6	Multiple				0 0	2 54	Up to 0 5							1					4 - Pin Tape Extensometer Array
	ESF-TMA-IN-THRM-1 thru 15	Thermistors													15								5 Thermistors in the Insulation of Each Rib
	ESF-TMA-STC-1 thru 36	Thermocouple											36										Surface Thermocouples Located on Each Rib
	ESF-ATC-1 thru 3	Thermocouple											3										Surface Thermocouples Located on Each Rib
	ESF-TMA-WX-1 thru 6	Wire Extensometer																6					6 Sets of Strain Measurements on Rib
										Total	226 30	0 84	204	103	26	8	25	12	8	8	36	100	
												Total Number of Sensors (All Types) 530											

NOTE Borehole Coordinates are Referenced to a 0,0,0 Coordinate Located at the Center of the Collar for the Heater Borehole.

INTENTIONALLY LEFT BLANK

3.3 MEASUREMENTS

The SHT measurements can be divided into two broad groups. In the first group are the measurements associated with the characterization of the test block. These, carried out both before the heating and after the cooling, are described in Sections 4 and 6. The second group of measurements, made during the heating and cooling phases, are described herein.

Note that no measurements were made in the SHT block before the boreholes were drilled; therefore, the effects of drilling (if any) on the characteristics of the block are not known. However, such effects are not considered to be significant.

In addition, infrared images of exposed rock next to the SHT block were collected periodically beginning before the start of heating. If any moisture, mobilized by heating, escapes via fractures, such phenomena may be detected by infrared images, since there is bound to be a difference in temperature between any escaping moisture and the rock surface in the vicinity.

3.3.1 Thermal

The thermal measurements include the heater power and the temperatures at various locations in the test block. The heater power, measured by a Magtrol Power Monitor, is scanned and recorded by the DCS every 15 minutes.

Type-K thermocouples in 0.64 cm stainless steel sheaths were the primary temperature sensors. The sheathed thermocouples were grouted into boreholes with the sensor at various predetermined locations. Thermocouples were also used to measure the temperatures at various locations on the heater itself, on the anchors and the connecting rods of the multiple point borehole extensometers (MPBXs), and on the three surfaces of the SHT block. In addition, resistance temperature detectors (RTDs) were used to measure temperatures in the four neutron logging boreholes (boreholes 15, 17, 22, and 23) and the two hydrology boreholes (boreholes 16 and 18). Finally, thermistors were used to measure the temperatures in the layers of fiberglass insulation on the three surfaces of the block.

The temperature sensors were scanned and the temperature recorded by the DCS on an hourly basis starting from before the start of heating and during the entire heating and cooling phases. A detailed description of the thermal measurements can be found in Subsections 5.1.1 and 5.1.2 of the *Single Heater Test Status Report* (CRWMS M&O 1997b).

3.3.2 Mechanical

The mechanical measurements included displacements in the rock and the modulus of deformation of the rock. In addition, measurements from load cells installed on rockbolts on both the heated side and the ambient side can be considered to be mechanical measurements. MPBXs as well as tape and wire extensometers are used to measure displacements in the rock. The modulus of deformation of the rock was measured using a Goodman Jack at various locations in a borehole drilled into the test block.

A prototype Optical MPBX based on the use of a modulated laser beam and reflecting targets was installed in boreholes 6 and 7 to investigate its effectiveness and efficiency in monitoring the displacements in the rock. The outcome of this trial is discussed in Section 11.

The mechanical measurements are fully described in Section 5.2 of the *Single Heater Test Status Report* (CRWMS M&O 1997b).

3.3.3 Hydrological

The hydrological measurements made during the heating and cooling phases of the SHT can be divided into two groups. In the first group are the periodic geophysical measurements to monitor the moisture saturation of the rock. These are ERT, neutron logging, and GPR. Four boreholes (boreholes 24, 25, 26, and 27) were dedicated to ERT measurements. As shown in Figure 3-2, these four boreholes form an approximate diamond transverse to the heater at about its midlength.

Four boreholes (numbers 15, 17, 22, and 23) were used for neutron logging. A teflon tube was grouted in these boreholes and the neutron probe was run in the teflon tube. As mentioned in Subsection 3.3.1, temperatures were also measured in the neutron boreholes by RTDs which were attached to the teflon tubes. The four neutron boreholes were also used to make GPR measurements to monitor the changes in the moisture saturation. GPR measurements in the SHT were for trial purposes only, to demonstrate the proof of principle of the technique. Only a limited number of GPR measurements were made in the SHT.

The second group of hydrology measurements were made in boreholes 16 and 18 (see Figure 3-2). Short sections in these two boreholes were isolated by inflatable packers and sensors were placed in these sections to measure the air pressure, relative humidity, and temperature. These are continuously monitored by the DCS and the readings recorded on an hourly basis. In addition, boreholes 16 and 18 were used to make pneumatic permeability measurements periodically by injecting a known quantity of air into one of the isolated sections and monitoring the response in the other sections. The purpose of these pneumatic measurements was to monitor the changes in the bulk permeability of the rock. As described in Sections 4 and 5, such pneumatic measurements involved most of the boreholes before the start of heating and many of the boreholes after cooling.

The hydrological measurements are fully described in Section 5.3 of the *Single Heater Test Status Report* (CRWMS M&O 1997b).

3.3.4 Chemical

Boreholes 20 and 21, designated as the chemistry boreholes, had SEAMIST liners installed in them. The SEAMIST system for the SHT consisted of two flexible liners which were everted into the borehole and kept pressurized by gas supplied by a cylinder. One of the paired SEAMIST liners carried sensors designed to measure specific chemical characteristics of the water they contacted. These chemical sensors were connected to the DCS. The SEAMIST liners are pressurized all the time, so the sensors mounted on them would be in contact with the rockwall of the borehole. Thus, if any water of the rock, mobilized by heating, finds its way into the borehole

and comes in contact with a chemical sensor, the specific chemical characteristics of the water will be measured and recorded. Unfortunately, as described in Section 11, the chemical sensors did not function as designed, primarily because they were in an unsaturated or dry environment most of the time. Water absorbing pads were attached on the other SEAMIST liners in the chemistry boreholes. Water absorbed by these pads could be squeezed out and analyzed in the laboratory for various chemical properties.

The SEAMIST system is described in Subsection 6.5.1 of *Test Design, Plans and Layout Report for the ESF Thermal Test* (CRWMS M&O 1996a).

Water mobilized by heat collected in one of the isolated chambers in borehole 16, section 16-4. The water was sampled from time to time and various types of analyses were performed on the samples in the laboratory. This aspect of chemical measurements in the SHT is described fully in Section 5.4 of the *Single Heater Test Status Report* (CRWMS M&O 1997b).

Additionally, small coupons or test specimens of carbon steel were placed in the two hydrology boreholes, 16 and 18, before the start of heating. The coupons were placed in those sections of these boreholes which were created and isolated by inflatable packers, as described in Section 3.3.3. Some of the coupons stood alone, while some were sandwiched between pieces of concrete used for making the tunnel invert. The purpose was to observe the effects on the metal coupons after the heating and cooling of the SHT.

3.4 OVERVIEW CHRONOLOGY OF ACTIVITIES

The overall schedule of the SHT is shown in Figure 3-3. The idea of a single heater test evolved with the consolidation of the thermal testing program in the summer of 1995 as documented in *In-Situ Thermal Testing Program Strategy* (DOE 1995). Detailed planning for the test started with the beginning of FY1996, and the excavation of Alcove 5, or Thermal Testing Facility, in the ESF began on January 22, 1996. Construction, installation, ambient characterization, and predictive analyses continued through the rest of FY1996 until the start of the heating phase of the test on August 26, 1996. The heating phase of the test ended with the switching off of the heater on May 28, 1997. Data collection associated with the cooling phase of the test was terminated on January 5, 1998. Posttest characterization activities analyses of results, and documentation continued until this final report to the DOE, Yucca Mountain Site Characterization Office in April 1999.

3.5 REPORTS

The reports and documents associated with the SHT can be divided into two groups. In the first group are those prepared before the start of heating, covering such subjects as test design, pretest predictive analyses, ambient characterization of the test block, etc. In the second group are the reports presenting and discussing test results and the analyses thereof. The reports are listed below.

3.5.1 Pretest Reports

Forecast of Thermal-Hydrological Conditions and Air Injection Test Results of the Single Heater Test at Yucca Mountain (Birkholzer and Tsang 1996)

Unconfined Compression Tests on Specimens from the Single Heater Test Area in the Thermal Testing Facility at Yucca Mountain, Nevada (Boyd et al. 1996)

Thermal Properties of Test Specimens from the Single Heater Test Area in the Thermal Testing Facility at Yucca Mountain, Nevada (Brodsky 1996)

Analysis of Thermal-Hydrological Behavior During the Heating Phase of the Single-Heater Test at Yucca Mountain (Buscheck, Shaffer, Lee, and Nitao 1997)

Test Design, Plans and Layout Report for the ESF Thermal Test (CRWMS M&O 1996a)

Characterization of the ESF Thermal Test Area (CRWMS M&O 1996b)

Laboratory Measurements of Thermal Expansion and Thermal Conductivity for Specimens from Alcoves 5 and 7 of the Exploratory Studies Facility and from SD Drillholes at Yucca Mountain, Nevada (SNL 1997b)

Pre-Experiment Thermo-Hydrological-Mechanical Analyses for the ESF Single Heater Test (Sobolik, Francis, and Pott 1996)

Pre-Experiment Thermal-Hydrological-Mechanical Analyses for the ESF Single Heater Test - Phase 2 (Sobolik, Francis, and Finley 1996)

Letter Report on Hydrological Characterization of the Single Heater Test Area in the ESF (Tsang et al. 1996).

3.5.2 Reports Presenting Results and Analyses

Numerical Analysis of Thermo-Hydrological Conditions in the Single Heater Test at Yucca Mountain (Birkholzer and Tsang 1998)

Thermal Expansion of Carbon Fiber and Invar Rods (Brodsky 1997)

Fourth Quarter FY1997 Results of Infrared Mapping in the Single Heater Test Area (Cook 1997)

First Quarter FY1998 Results of Infrared Mapping in the Single Heater Test Area (Cook 1998)

Infrared Imaging in the Single Heater Test Area (Cook and Wang 1997a)

Infrared Imaging in the Single Heater Test Area (Cook and Wang 1997b)

Third Quarter Results of Infrared Mapping of the Single Heater Test Block (Cook and Wang 1997c)

Single Heater Test Status Report (CRWMS M&O 1997b)

Single Heater Test Interim Report (CRWMS M&O 1997c)

Letter Report on Fourth Quarter Results of Measurements in the Hydrology Holes in the Single Heater Test Area in the ESF (Freifeld 1997)

Letter Report on First Quarter Results of Measurements in the Hydrology Holes in the Single Heater Test Area in the ESF Area, 1998 (Freifeld 1998a)

Letter Report on First Quarter Results of Measurements in Hydrology Holes in the Single Heater Test Area in the ESF (Freifeld and Tsang 1997a)

Letter Report on Second Quarter Results of Measurements in Hydrology Holes in the Single Heater Test Area (Freifeld and Tsang 1997b)

Letter Report on Third Quarter Results of Measurements in the Hydrology Holes in the Single Heater Test Area (Freifeld and Tsang 1997c)

Thermochemical Analysis of the Single Heater Test (Glassley 1997a)

Third Quarter Report, Chemical Analyses of Waters Collected from the Single Heater Test (Glassley 1997b)

Second Quarter Results of Chemical Measurements in the Single Heater Test (Glassley and DeLoach 1997)

To Assess the Effectiveness of the Ground Penetrating Radar Method in Measuring Moisture Content in the Single Heater Test (Peterson and Williams 1997)

Determination of Mineral Abundances in Core Samples from the Exploratory Studies Facility Using X-ray Diffraction (Roberts and Viani 1996)

Single Heater Test: SNL As-Built Gage Table (SNL 1996)

Evaluation of Single Heater Test Thermal and Thermomechanical Data: Second Quarter Results (8/26/96 through 2/28/97) (SNL 1997c)

Evaluation and Comparative Analysis of Single Heater Test Thermal and Thermomechanical Data: Third Quarter Results (SNL 1997d)

Laboratory Measurements of Thermal Conductivity as a Function of Saturation State for Welded and Nonwelded Tuff Specimens (SNL 1998)

Interpreting the Thermal-Hydrological Response of the ESF Single Heater Test (Tsang and Birkholzer 1997).

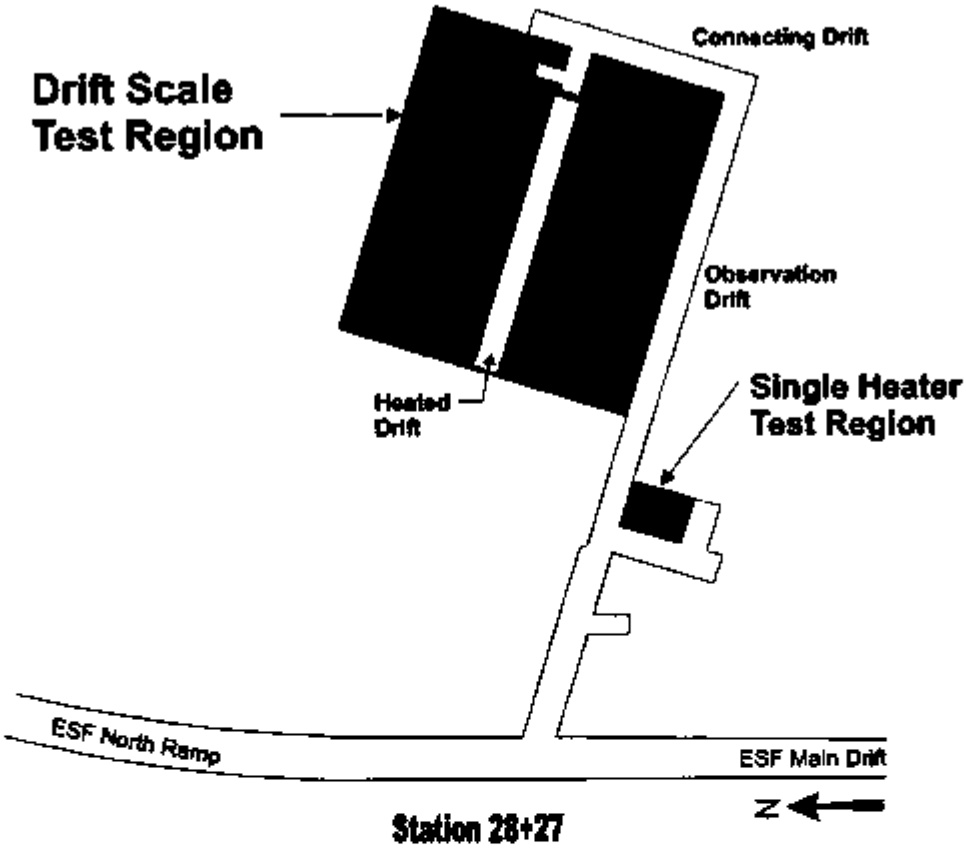

NOTE. Not to scale Reference only.

Figure 3-1. Plan View of ESF Thermal Test Facility

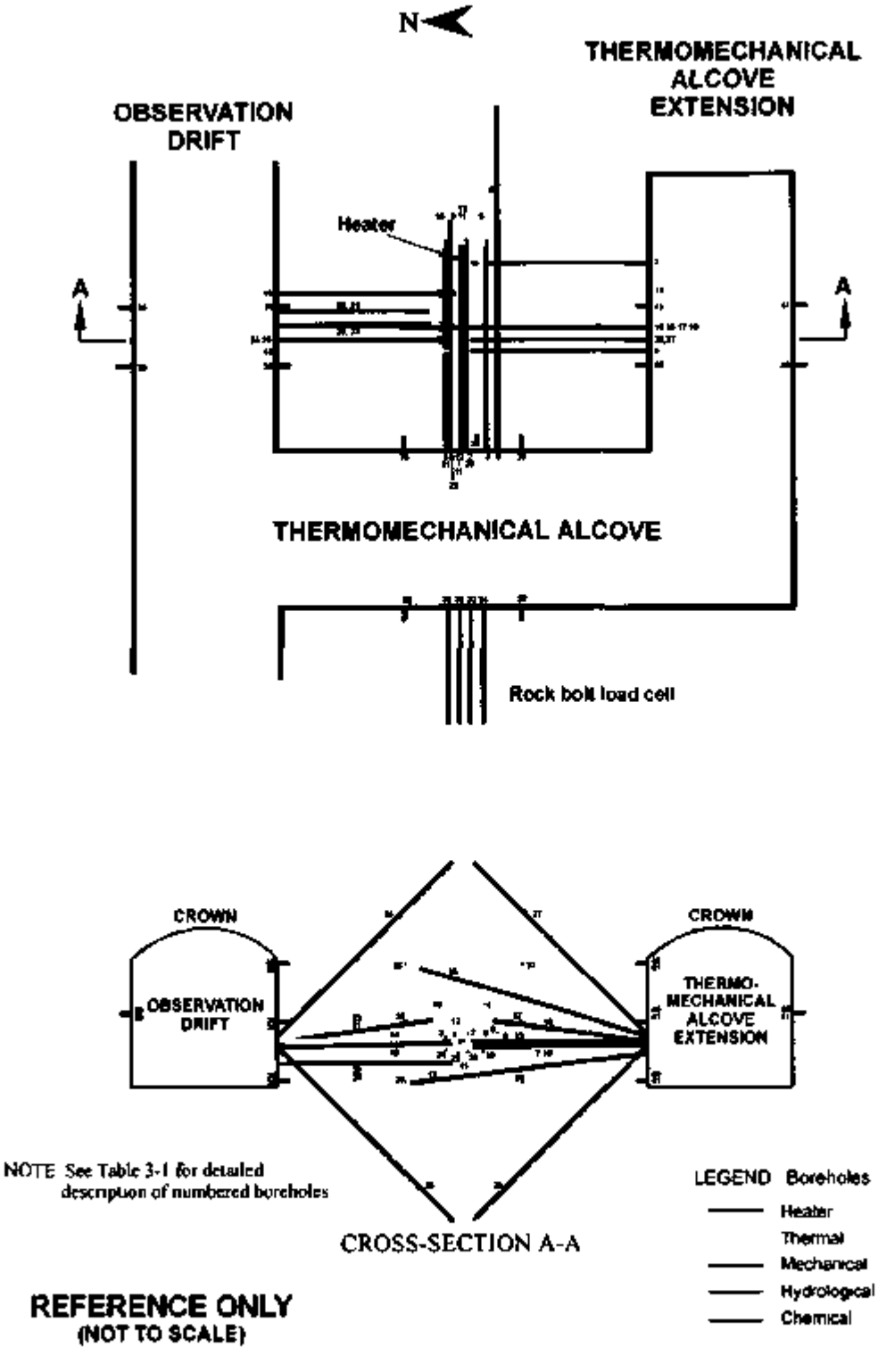

Figure 3-2. Layout of the Single Heater Test

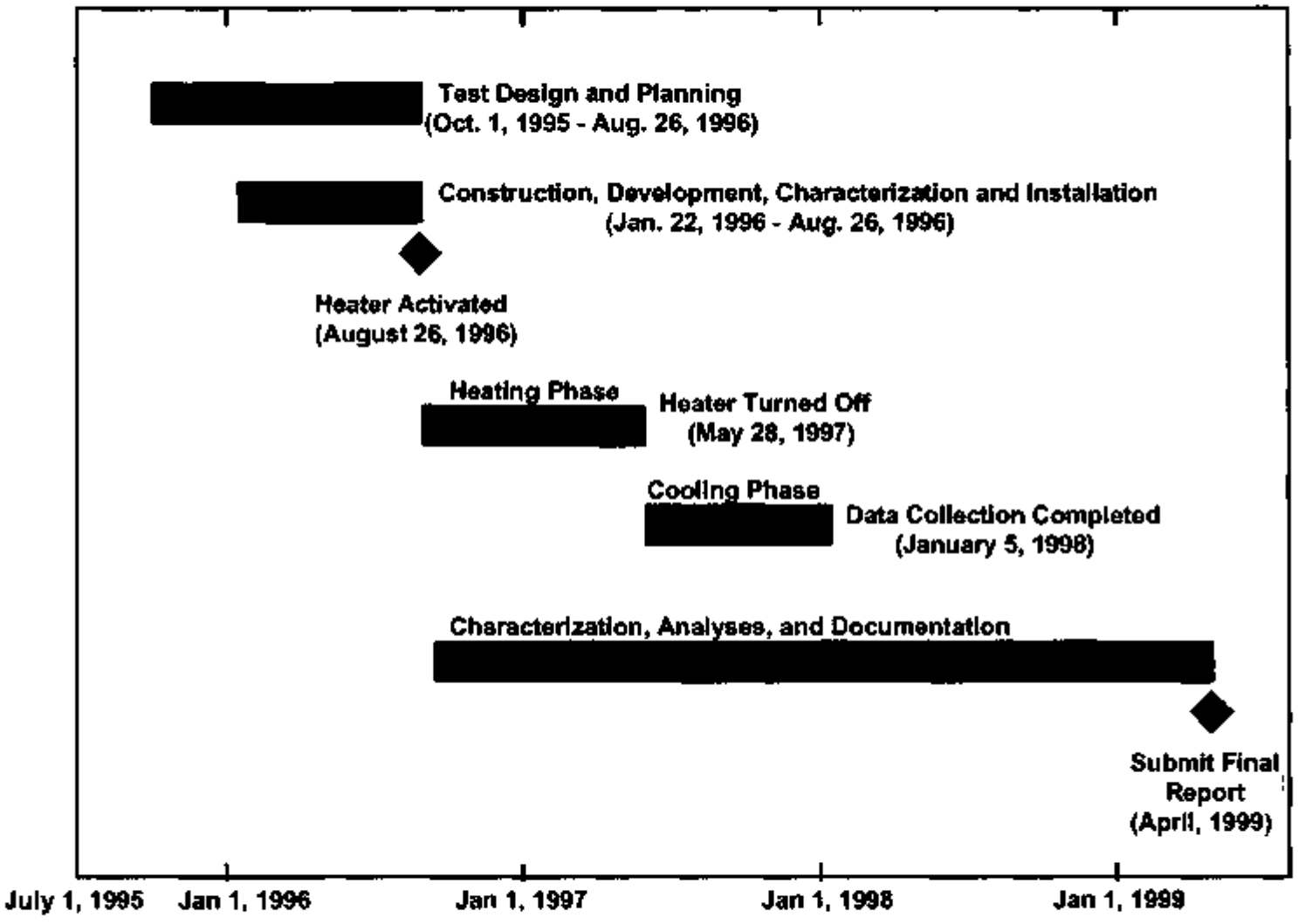

Figure 3-3. Summary Schedule for the Single Heater Test

INTENTIONALLY LEFT BLANK

4. PRE-HEATING CHARACTERIZATION

The pre-heating analyses to predict various results or measurements of the SHT in a time-bound sequence, are central to the subsequent exercises of examining the conceptual process models used to make these analyses in the context of the actual results. Such examinations yield new insights into the processes and eventually lead to modifications and refinements to the models representing them. For this effort to be effective, it is imperative that the predictive analyses are as specific to the test block as possible. One of the steps to this end is to characterize the test block in its ambient state, so that various rock properties and other parameters to be used as input to the pre-heating predictive analyses are specific to the test block.

The ambient characterization activities can be divided into two groups. In the first group are tests or activities performed in the field. These are mapping of the exposed rock surfaces, video logging of holes drilled into the SHT block, and measuring its pneumatic bulk permeability by the air-K method. The other group consists of tests performed in the laboratory to various properties of the rock including its mineralogic-petrologic characteristics.

4.1 FIELD MEASUREMENTS

Field measurements included: a) full periphery mapping of the excavations around the SHT block; b) line surveys and Schmidt Hammer Rebound Index Testing in the excavations for rock mass classification by the Q (Barton, N.R. et al. 1974) and RMR (Bieniawski 1974) systems; c) pneumatic permeability measurements in the SHT block; d) infrared imaging of rock surfaces; and e) video logging of boreholes. These components of pre-heating characterization and the results are fully described in Sections 7 through 9 in *Characterization of ESF Thermal Test Area* (CRWMS M&O 1996b).

4.2 LABORATORY MEASUREMENTS

Tests were performed in the laboratory on core samples collected in connection with the drilling of the heater and instrument holes in the SHT block. Samples of rock were also collected during the excavation of the openings around the SHT block. Laboratory tests were done to measure thermal, mechanical, hydrological properties of the rock and to describe its mineralogic petrologic characteristics. These tests and the results are described in Sections 3 through 6 of *Characterization of ESF Thermal Test Area* (CRWMS M&O 1996b).

Additional laboratory measurements of saturation, porosity, bulk density, particle density, and gravimetric water content for cores from the SHT area were conducted. These studies constitute a component of the hydrological characterization study, and aim to determine the amount of pore water available for evaporation and boiling during the heating phase. Core data from both the DST and the SHT boreholes in the Thermal Testing Facility at the ESF were reported in a previous project milestone (Wang and Suarez-Rivera 1997). The information specific to the SHT area shall be summarized here.

4.2.1 Methodology

Core samples previously stored in sealed packets were placed in containers with tight-fitting lids and immediately weighed. The samples were subsequently oven-dried at a temperature between 100°C to 110°C, until they reached a constant weight (from several weighings). They were then placed in a desiccator, cooled, and weighed to determine the gravimetric water content. This procedure ensures that the samples are dried at a specified temperature to a constant weight, and that only water is lost.

The samples were then water-saturated in a vacuum chamber, after which they were weighed following the Archimedes method (i.e., immersed in air and water) to determine the weight under conditions of full saturation and the sample bulk volume. Knowledge of the dry-weight, saturated weight, and sample bulk volume were used to calculate bulk density, porosity, and particle density.

4.2.2 Results

The data from two grab samples from the wet-excavation of the Observation Drift near the SHT block are shown in Table 4-1. Five subsamples were tested. One of the subsamples had an 81 percent saturation, while the saturation of the other four subsamples exceeded 94 percent. These measurements provide the only site-specific data for the liquid saturation at the time of the initiation of the SHT, forming the basis of the choice of parameter value (92 percent) in modeling of the SHT (see Table 8-11, Section 8.7). In Wang and Suarez-Rivera (1997), liquid saturation for 39 cores from the DST (12 dry-drilled and 27 wet-drilled), and 17 wet-drilled cores from the SHT were reported. The measurements from the cores from boreholes 1, 5, and 6 of the SHT are shown in Table 4-2. Note that the liquid saturation is in the 95 percent range. Wang and Suarez-Rivera (1997, p. 6) also reported that the average liquid saturation for the dry-drilled DST samples was 84 percent, while that for the wet-drilled samples was 93 percent. They attributed the 9 percent discrepancy partly to spatial heterogeneity, and partly to the different drilling methods.

Table 4-1. Pre-Heat Laboratory Measurement of Grab Samples from Wet Excavation of the Observation Drift

Observation Drift Grab Samples					
Sample location (m)	Saturation (%)	Porosity (%)	Bulk Density (g/cc)	Particle Density (g/cc)	Gravimetric Water Content (g/g)
30.0	99.00	8.60	2.26	2.47	0.038
Sub-sample	94.90	8.30	2.27	2.47	0.035
40.0	95.40	9.30	2.27	2.50	0.039
Sub-sample	93.80	10.10	2.24	2.49	0.042
Sub-sample	80.50	10.40	2.24	2.50	0.037

Table 4-1. Pre-Heat Laboratory Measurement of Grab Samples from Wet Excavation of the Observation Drift (Continued)

Observation Drift Grab Sample Summary					
	Saturation (%)	Porosity (%)	Bulk Density (g/cc)	Particle Density (g/cc)	Gravimetric Water Content (g/g)
Observation Drift average:	92.72	9.34	2.26	2.49	0.038
Standard deviation:	7.10	0.91	0.02	0.02	0.003

Table 4-2. Pre-Heat Laboratory Measurement of Wet Drilled Cores from the SHT

Borehole 1, ESF-TMA-H1					
Sample location (m)	Saturation (%)	Porosity (%)	Bulk density (g/cc)	Particle density (g/cc)	Gravimetric water content (g/g)
1.0	89.46	10.86	2.25	2.51	0.043
2.5*	88.04	13.30	2.18	2.52	0.054
3.7	93.60	8.87	2.29	2.52	0.036
4.7	97.27	11.83	2.22	2.51	0.051
5.7	93.97	13.83	2.16	2.51	0.061
6.7	96.03	11.89	2.21	2.51	0.052
* contains small voids					
Borehole 6, ESF-TMA-CMPBX-1					
Sample location (m)	Saturation (%)	Porosity (%)	Bulk density (g/cc)	Particle density (g/cc)	Gravimetric water content (g/g)
0.2	94.82	11.00	2.24	2.51	0.047
2.4	94.75	10.43	2.25	2.51	0.044
4.4	93.58	10.18	2.26	2.51	0.042
7.5*	96.87	23.62	1.96	2.57	0.104
Subcore		20.44	2.02	2.53	
9.3	96.17	11.55	2.22	2.52	0.050
11.3	93.07	9.74	2.27	2.51	0.040
* split along axis during oven drying					
Borehole 5, ESF-TMA-MPBX-4					
Sample location (m)	Saturation (%)	Porosity (%)	Bulk density (g/cc)	Particle density (g/cc)	Gravimetric water content (g/g)
0.7*	95.85	17.03	2.05	2.48	0.079
2.1*	101.61	9.69	2.25	2.49	0.044
2.6#	102.17	13.33	2.17	2.50	0.063
3.8#	96.74	10.58	2.24	2.50	0.046
Subcore		10.44	2.24	2.50	
5.4	97.65	9.60	2.27	2.51	0.040
* contains open fractures and large vugs # received in fragments					

Table 4-2. Pre-Heat Laboratory Measurement of Wet Drilled Cores from the SHT (Continued)

SHT Borehole Summary					
	Saturation (%)	Porosity (%)	Bulk density (g/cc)	Particle density (g/cc)	Gravimetric water content (g/g)
SHT average:	95.39	12.53	2.20	2.51	0.053
standard deviation	3.56	3.89	0.09	0.02	0.017

5. PRETEST PREDICTIVE ANALYSES

The predictive analyses performed in connection with the SHT can be divided into two groups. In the first group are the analyses done early on in the process of planning and designing of the test. These are sometimes referred to as scoping analyses. The purpose of the scoping analyses is to help decide specifics of the configuration of the test. These analyses were carried out before the characterization of the test block using best available data for rock properties at the time.

The other group of predictive analyses were done using results of the initial test block characterization. These are central to the subsequent interpretation of the test results, in that comparative analyses of the predicted and measured results are made to gain insight into the processes caused by the heat. These analyses were performed separately to study the various coupled processes being investigated, namely, the thermal-hydrological, thermal-mechanical, and thermal-chemical processes. Generally, thermal-hydrological analyses are done first to yield time-bound temperature distributions in the test block. These temperature distributions are then used as input for the thermal-mechanical and thermal-chemical analyses.

The thermal-hydrological predictive analysis of the SHT is fully described in Birkholzer and Tsang (1996) and Buscheck, Shaffer, and Nitao (1997). The thermal-mechanical predictive analysis is described in Sobolik, Francis, and Finley (1996), and Sobolik, Francis, and Pott (1996), and the thermal-chemical analysis is described in Glassley (1997a).

When rock is heated, porewater in the rock plays a role in the heat transfer process. The thermal-hydrological process is thus the primal coupled process. For this reason, thermal-mechanical and thermal-chemical analyses are performed on the basis of the temperature fields predicted by a thermal-hydrological analysis. Sandia National Laboratories (SNL), Lawrence Berkeley National Laboratory (LBNL), and Lawrence Livermore National Laboraotry (LLNL) performed the thermal-mechanical, thermal-hydrological, and thermal-chemical predictive analyses, respectively. Both SNL and LBNL employed the TOUGH code for the thermal-hydrological analysis, while LLNL used the NUFT code. This is why both TOUGH and NUFT codes have been employed to simulate the thermal-hydrological response of the SHT in the predictive phase as well as the subsequent test results analysis phase. The TOUGH code and the NUFT code differ from each other in computational technique only. Either code is capable of implementing the ECM and DKM conceptual models.

5.1 THERMAL-HYDROLOGICAL PREDICTIONS

Thermal-hydrological numerical calculations predict temperature and moisture distributions in the SHT block during heating and cooling. The thermal-hydrological response of the fractured rock mass of the SHT test block was simulated using an equivalent continuum model (ECM). In the ECM model a single value is used for the permeability of the rock mass containing fractures and rock matrix. Both two-dimensional (2D) and three-dimensional (3D) models were employed in the predictive analyses. Responses that are important as the temperature rises and falls include boiling, vaporization, drying, condensation, and rewetting. Bulk permeability values were obtained from air injection measurements before heating was initiated. Unlike the ECM, the dual

permeability model (DKM) allows different permeability values for the fractures and matrix of the rock mass. Both the ECM and DKM were used in making subsequent analyses of test results.

One model predicted temperatures as high as 350°C at the heater borehole after one year of heating, with the boiling zone at 96°C located at a radius of about 1.5 m from the heater. The model showed that temperature predictions are sensitive to permeability values. Both models show a distinct dryout zone around the heater. Once the heater is turned off the block was predicted to cool quickly. Birkholzer and Tsang (1996) and Buscheck, Shaffer, and Nitao (1997) describe the thermal-hydrological predictions by the TOUGH code and the NUFT code, respectively.

5.2 THERMAL-MECHANICAL PREDICTIONS

Thermal-mechanical numerical calculations predict displacements and changes of stress in the rock mass during the heating and cooling. A finite element nonlinear structural mechanics model was used by SNL to analyze the thermal-mechanical response. Displacements of less than 3 mm were predicted due to heating within the zones of measurements in the test block. Potential opening and closing of fracture apertures were predicted to account for displacements of a similar magnitude. Sobolik, Frances, and Finley (1996) and Sobolik, Francis, and Pott (1996) describe the thermal-mechanical predictions.

5.3 THERMAL-CHEMICAL PREDICTIONS

The thermal-hydrological analysis predicts that vaporized water will move from areas of high heat to cooler areas and condense, although the actual pathway is not known. Thermal-chemical simulations were conducted in which condensate was modeled to flow through the test block for a period of approximately five months under isothermal conditions of 96°C. The chemistry of the test block was simulated using a relatively coarse-grained calcite-opal lined fracture in relatively finer-grained Topopah Spring Tuff with pumice fragments. Calculated results suggest that the solutions may be saturated with respect to quartz and may precipitate quartz particularly as the solutions cool. The predictions show that other secondary phases may develop, but they would account for less than 0.2 percent of the rock volume. Glassley (1997a) describes the thermal-chemical predictive analysis.

6. POST-COOLING CHARACTERIZATION

The purpose of post-cooling characterization is to study the permanent effects of heating and cooling on the rock. The results of post-cooling characterization may provide important clues toward understanding the processes that took place during heating and cooling. As listed in Table 6-1, a total of ten boreholes were drilled into the SHT block for post-cooling characterization. The locations of these boreholes are given in Table 6-1 and are illustrated in Figure 6-1. Of the ten boreholes, four are overcores on existing boreholes. The other six are new boreholes. All ten boreholes were cored and samples were collected for various testing in the laboratory.

Video logging was performed on the ten boreholes mentioned above. In addition, post-cooling activities included field measurement of pneumatic bulk permeability, laboratory testing for thermal, mechanical, and hydrological properties, and examination/analyses of rock samples for mineralogic-petrologic characteristics.

No mapping was done for post-cooling characterization because little mappable changes were expected to occur on the exposed surfaces of the block and none were observed on a visual inspection.

6.1 FIELD MEASUREMENT OF BULK PERMEABILITY

Post-cooling permeability measurements were made before the drilling of the ten boreholes mentioned above. The idea was to measure the permeability before any further disturbance that might be caused by drilling. In the pre-heating permeability measurements, 31 of the 41 boreholes drilled in the SHT block were used. However, only seven of these 31 boreholes were available for post-cooling permeability measurements because various instruments were grouted in the others. Post-cooling bulk permeability measurements are fully described in Subsection 8.1.3 of this report including the results and the analyses thereof.

6.2 LABORATORY TESTS FOR THERMAL AND MECHANICAL PROPERTIES

Core from the boreholes described above was used for laboratory measurements of thermal expansion, thermal conductivity, and unconfined compressive strength. Thermal expansion measurements were made on 14 specimens at temperatures from 25° to 325°C. Each specimen was subjected to two thermal cycles and thermal expansion/contraction data were obtained during heating and cooling for both cycles. Thermal conductivity measurements were made on 16 specimens between 30° and 200°C and measurements were made at discrete points during both the heating and cooling segments. Unconfined compression tests were performed on 14 specimens at room temperature. Measurements of Young's modulus, Poisson's ratio, and unconfined compressive strength were obtained.

Table 6-1. Single Heater Test Posttest Characterization - Administration Borehole Layout Table

Borehole No.	Borehole ID	Primary Purpose	Collar Coordinates (Cartesian)[1]			Orientation[2]	Direction[3]	Borehole Diameter	Borehole Length[3]	Borehole Criteria	Orig. Core Bit	Orig. Borehole No.
			x (meters)	y (meters)	z (meters)	(azim/ decline)		(cm)	(meters)			
194	ESF-TMA-PTC-N-1	Overcore Heater Borehole	0.00	0.00	0.00	az -288/ 0 5 deg	W-E (TMA)	25.40	7.00	up to 0 5 deg - Dry Cored	HQ	1
196	ESF-TMA-PTC-MPBX-1	Overcore MPBX Borehole	0.18	0.00	0.29	az -288/ 0 5 deg	W-E (TMA)	15.24	7.00	Dry Cored	NQ	2
197	ESF-TMA-PTC-NEU-2	Overcore Hydrology Borehole	6 50	4.30	0 00	az 18/ 75 deg	S-N (TMAE)	15.24	6.00	7.5 degrees up - Dry Cored	NA	16
198	ESF-TMA-PTC-TC-6	Overcore Thermo-couple Borehole	6.50	5.50	0.00	az 18/ 0 00 deg	S-N (TMAE)	15.24	6.50	Horizontal Dry Cored	AQ	13
199	ESF-TMA-PTC-1	Observation Borehole	6.50	4.70	0.53	az 18/ 0.00 deg	S-N (TMAE)	7.57	7.50	NQ - Dry Cored - Horizontal	N/A	N/A
200	ESF-TMA-PTC-2	Observation Borehole	6 50	4.70	0.26	az 18/ -7 94 deg	S-N (TMAE)	7.57	8.10	NQ - Dry Cored - Decline 7 94 deg	N/A	N/A
201	ESF-TMA-PTC-3	Observation Borehole	6.50	4.70	-0.28	az 18/ -22.68 deg	S-N (TMAE)	7 57	8.10	NQ - Dry Cored - Decline 22.68 deg	N/A	N/A
202	ESF-TMA-PTC-4	Observation Borehole	-0.31	0 00	0.16	az -288/ 0.0 deg	W-E (TMA)	7.57	8.00	NQ - Dry Cored - Horizontal	N/A	N/A
203	ESF-TMA-PTC-5	Observation Borehole	0.40	0.00	0.25	az -288/ 0 0 deg	W-E (TMA)	7 57	8.00	NQ - Dry Cored - Horizontal	N/A	N/A
204	ESF-TMA-PTC-6	Observation Borehole	1.14	0 00	0 50	az -288/ 9.6 deg	W-E (TMA)	7 57	8.00	NQ - Dry Cored - Inclined to 9.6 deg	N/A	N/A

NOTE: [1] +X-direction azimuth = 18 degrees (N); Z-direction azimuth = vertical (up); Y-direction azimuth = 288 degrees (W). [2] Direction refers to direction of borehole with collar bottom borehole (e g , W-E). [3] Based on the designed 13-m wide Thermomechanical Alcove test block. Actual as-built width may vary. TMA = Drilled from the Thermomechanical Alcove; TMAE = Drilled from the Thermomechanical Alcove Extension

The laboratory data are used to compare properties of rocks that were inside and outside of the estimated 100°C isotherm at the end of heating. The 100°C isotherm is a surface on which the temperatures are 100°C at all locations. These test results are also compared with values obtained during pretest characterization activities and other characterization data obtained for Alcove 5. Before the SHT was conducted, boreholes were drilled into the test area to accommodate placement of the heater and additional instrumentation. Pretest characterization of the SHT block included taking material from these boreholes for both thermal and mechanical properties laboratory testing. The pretest characterization data are given in Brodsky (1996) and Boyd et al. (1996) for thermal and mechanical properties, respectively. These pretest thermal properties characterization tests were performed by Holometrix, Inc., and the pretest mechanical tests were performed by New England Research. Additional Alcove 5 characterization data that will be used for comparisons were obtained in preparation for the DST (SNL 1997e) and for general Alcove 5 characterization (SNL 1997b).

6.2.1 Samples Acquisition and Specimen Preparation

All specimens are from the Tptpmn (Tertiary Miocene, Paintbrush Group, Topopah Spring Tuff, crystal poor, middle nonlithophysal) lithostratigraphic unit and from the TSw2 (Topopah Springs welded unit 2) thermal-mechanical unit. The locations of the boreholes used to provide laboratory sample material were given in Table 6-1 and illustrated in Figures 6-1 through 6-4. Table 6-2 shows the correlation between borehole identification numbers (given in Table 6-1) and the abbreviated form of the number incorporated into the specimen identification number.

Core from the boreholes was viewed and samples were selected in an effort to (1) obtain equal numbers of specimens oriented parallel and perpendicular to the heater, (2) obtain a reasonable sampling of material from within the approximate maximum extent of the 100°C isotherm at the end of heating, and (3) obtain core from evenly spaced intervals. The availability of sufficient lengths of intact core limited core selection. The approximate original locations of the thermal expansion, thermal conductivity, and mechanical properties specimens are shown in Figures 6-2, 6-3, and 6-4, respectively.

Table 6-2. Borehole Nomenclature

Borehole Identification	Borehole Number	Abbreviated Borehole Identification used in Specimen Identification Numbers
ESF-TMA-PTC-H1	194	PTC H1
ESF-TMA-PTC-MPBX-1	196	PTC MPBX1
ESF-TMA-PTC-1	199	PTC1
ESF-TMA-PTC-2	200	PTC2
ESF-TMA-PTC-4	202	PTC4
ESF-TMA-PTC-5	203	PTC5

Thermal expansion and mechanical test specimens were prepared according to SNL Technical Procedure SNL TP-51, *Preparing Cylindrical Samples Including Inspection of Dimensional and Shape Tolerances*. Six thermal expansion specimens did not meet the measurement requirements in that procedure; however, they did meet the requirements given in SNL TP-200, *Inspection of Samples Used in Thermal Properties Measurements*. This procedure was used to inspect specimens used for pretest SHT characterization and so the additional 6 specimens were tested.

Thermal conductivity specimens were prepared using SNL TP-200. All specimens were ground, right circular cylinders with nominal specimen dimensions as given in Table 6-3.

Table 6-3. Nominal Dimensions of Test Specimens

Test Specimen Dimensions	Thermal Expansion Test Specimens	Thermal Conductivity Test Specimens	Mechanical Test Specimens
Length (mm)	50.8	12.7	95.3
Diameter (mm)	25.4	38.1	38.1

The thermal expansion specimens are the same dimensions as the pretest characterization specimens. The pretest thermal conductivity specimens were 50.8 mm in diameter whereas the posttest specimens are 38.1 mm. During pretest activities, the thermal conductivity apparatus had not yet been modified to accept smaller diameter specimens and so pretest sampling was limited to the heater borehole because it was larger in diameter than the other sampling boreholes. The pretest characterization mechanical test specimens were 41.9 mm in diameter and 101.6 mm in length. These specimens are very close in dimension and in length-to-diameter ratio to those used in the posttest study.

Specimens were assigned identification numbers according to SNL QAIP 20-3, *Sample Control*. The specimen identification numbers begin with the designation of the borehole, and include the depth (distance from the collar of the borehole, in feet) of the top of the piece of core from which the specimen was prepared. If multiple test specimens were prepared from a single piece of core, then the specimens were sequentially labeled A through Z.

All specimens were tested in the air dried state (i.e., in the as-received condition with no effort made to preserve or alter the moisture content). The moisture content during testing was substantially different than in situ. After recovery from the ESF, the cores may have dried out at the Sample Management Facility at the Nevada Test Site. They were then machined into specimens using water as a coolant, and then they were allowed to dry out again in the laboratory until testing. During thermal conductivity and thermal expansion tests, specimens dried out in response to the elevated temperatures. Mass changes are reported in Tables 6-4 and 6-5 for thermal conductivity and thermal expansion, respectively. For thermal expansion specimens, which were subjected to two thermal cycles, specimens were drier during the second cycle. Previous work (Brodsky et al. 1997, p. 73) has shown that for welded tuff moisture content has no appreciable effect on thermal expansion. An increase in moisture increases thermal conductivity values. For all specimens but one, there was a net decrease in thermal conductivity during testing that may be related to specimen drying. Moisture contents for mechanical specimens were measured after testing was completed. Immediately after testing, specimen fragments were collected and weighed. They were subsequently dried using SNL TP-065, *Drying Geologic Samples to Constant Weight*, to determine moisture contents during testing. The results are given later in this report.

Table 6-4. Changes in Mass (Moisture Content) for Thermal Conductivity Test Specimens

Specimen ID*	Pretest Mass (g)	Posttest Mass (g)	Change (g)
PTC1–A 15.7	32.506	32.180	-0.326
PTC1–A 19.0	33.065	32.773	-0.292
PTC2–A 4.1	32.501	32.292	-0.209
PTC2–A 10.8	32.415	32.083	-0.332
PTC2–A 14.1	31.821	31.475	-0.346
PTC4–A 4.3	32.222	31.840	-0.382
PTC4–A 6.6	32.462	32.106	-0.356
PTC4–A 9.2	32.584	32.184	-0.400
PTC4–A 14.8	32.806	32.459	-0.347
PTC4–A 19.8	33.439	33.122	-0.317
PTC4–A 26.0	32.910	32.529	-0.381
PTC5–A 4.1	31.843	31.532	-0.311
PTC5–A 14.9	32.804	32.485	-0.319
PTC5–A 25.4	32.320	31.800	-0.520
PTCH1–A 8.6	33.089	32.931	-0.158
PTC MPBX1–A 14.4	33.071	32.750	-0.321

*The distance from the borehole collar is given (in feet) as part of the specimen identification number.

Table 6-5. Changes in Mass (Moisture Content) for Thermal Expansion Test Specimens

	Cycle 1			Cycle 2		
Specimen ID*	Pretest Mass (g)	Posttest Mass (g)	Change (g)	Pretest Mass (g)	Posttest Mass (g)	Change (g)
PTC 1–A 2.9 - B	55.572	55.030	-0.542	55.170	54.975	-0.195
PTC 1–A 16.8 - B	58.087	57.343	-0.744	57.493	57.363	-0.130
PTC 1–B 19.0 - B	59.009	58.181	-0.828	58.242	58.154	-0.088
PTC 2–B 4.1	57.615	57.109	-0.506	57.232	57.098	-0.134
PTC 4–A 4.6 - B	56.468	55.710	-0.758	55.835	55.686	-0.149
PTC 4–A 19.0	57.985	57.305	-0.680	57.380	57.305	-0.075
PTC 4–B 6.8 - B	57.915	57.309	-0.606	57.392	57.293	-0.099
PTC 4–B 14.8 - B	57.604	56.850	-0.754	56.955	56.827	-0.128
PTC 4–B 19.8 - B	59.107	58.276	-0.831	58.276	58.265	-0.11
PTC 5–B 4.1 - B	57.386	56.779	-0.607	56.880	56.755	-0.125
PTC 5–B 24.4 - B	58.853	58.029	-0.824	58.200	58.027	-0.173
PTC5–B 24.4 - C	56.029	55.065	-0.964	55.065	55.049	-0.016
PTC H1–A 15.6 - B	57.576	57.182	-0.394	57.182	57.113	-0.069
PTC MPBX1 14.2 - B	57.820	57.242	-0.578	57.242	57.166	-0.076

*The distance from the borehole collar is given (in feet) as part of the specimen identification number.

6.2.2 Test Methods

6.2.2.1 Thermal Conductivity

The flow of heat across a material per unit time is proportional to the temperature gradient. The constant of proportionality, k, is the thermal conductivity and is a property of the material. This proportionality can be written as follows (Feynman et al. 1964, p. 12-3):

$$\vec{h} = -k\vec{\nabla}T \qquad (6\text{-}1)$$

where $\vec{h}$ is a vector and represents the flow of heat across a material of unit cross sectional area per unit time, and ∇T is the temperature gradient. For one-dimensional flow this equation can be written:

$$\frac{Q}{A} = \frac{k\Delta T}{\Delta x} \qquad (6\text{-}2)$$

where:

Q	=	rate of heat flow (W),
k	=	thermal conductivity (W/(m·K)),
ΔT	=	temperature difference across material (K),
Δx	=	thickness of material (m), and
A	=	cross sectional area (m^2).

Thermal conductivity measurements were made using the guarded heat flow meter (GHFM). The test specimen was located between two heater plates controlled at different temperatures, producing heat flow through the specimen. The heat flow was measured by a heat flux transducer located between the specimen and one heater plate. Radial heat flow losses were minimized in two ways: first, a cylindrical guard heater surrounded the specimen and was maintained near the mean specimen temperature; second, specimens with lengths less than 20 mm were used.

The GHFM is calibrated by comparing theoretical values to results obtained using specimens of known thermal conductivity. A single calibration is performed to determine both the contact resistance between the specimen and heater plates and the proportionality constant relating the output of the heat flux transducer to the actual heat flux.

The total thermal resistance of the specimen and contact area is given by:

$$R_t = \frac{N\Delta T}{q} \qquad (6\text{-}3)$$

where:

R_t	=	total thermal resistance (m^2K/W),
N	=	sensitivity of the heat flux transducer (m^2V/W),
ΔT	=	measured temperature difference between thermocouples (K), and
q	=	heat flow transducer output (V).

The total thermal resistance comprises the thermal resistance of the specimen and the residual value associated with the interfaces:

$$R_t = R_S + R_O \qquad (6\text{-}4)$$

where:

R_s	=	thermal resistance of the specimen (m^2K/W), and
R_o	=	residual thermal resistance (m^2K/W).

Substituting Equation 6-3 into Equation 6-4 gives

$$R_S = \frac{N\Delta T}{q} - R_O \qquad (6\text{-}5)$$

Calibrations, discussed later in this section, are performed to determine N and R_o. This equation is then used to determine R_s from measured values of q and ΔT.

The following equations relate R_s to thermal conductivity. The thermal resistance of the specimen is given by:

$$R_S = \frac{\Delta T}{(Q/A)} \qquad (6\text{-}6)$$

Substituting Equation 6-2 into Equation 6-6 gives

$$k = \frac{-\Delta x}{R_s} \tag{6-7}$$

This final equation is used to calculate thermal conductivity from R_s.

Calibrations were performed on reference samples of Pyrex 7740. A range of thermal resistance values was obtained using specimens of different thicknesses (6, 9, 12, 15, and 18 mm). Thermal resistance measurements were made at five temperatures (30°, 70°, 110°, 150°, and 200°C) spanning the operating range. Values of ΔT and q were obtained from the thermocouples and the heat flux transducer, respectively. A straight line fit to Equation 6-5 was used to determine the calibration constants N and R_0.

Calibrations were verified by performing measurements on reference specimens of high-purity (99.99 percent) fused quartz. Verifications were obtained using three specimen sizes spanning the operating range and testing at each of the five temperatures. Verifications were performed periodically (at least every 31 days) throughout the testing program.

Recommended thermal conductivity values for Pyrex 7740 and high purity fused quartz are published by the National Institute of Standards and Technology (NIST). These were chosen as reference materials because no additional NIST Standard Reference Materials of suitable conductivity were available. In some recent work on the thermal conductivity apparatus (SNL 1998) fused quartz was used as the calibration standard and Pyrex as the verification standard. That report showed that fused quartz is most likely a better calibration standard than Pyrex. In this study, however, Pyrex was used as the calibration standard to more accurately simulate the procedure used for pretest characterization work by Holometrix Inc.

Verifications were performed periodically throughout the testing program and results are summarized in Table 6-6 and 6-7 for the minimum and maximum test temperatures, respectively. The verification errors obtained immediately after a calibration but before testing (pretest values) show the agreement between results obtained on two types of standards, Pyrex and fused quartz. The NIST-recommended values for each standard are accurate to only ±5 percent and so a disparity of up to ±10 percent or approximately 0.13 W/(m·K) may only reflect inaccuracies in published values for the standards. The pretest errors given in Tables 6-6 and 6-7 are well within these bounds. These tables show that the pretest verifications gave errors no greater than 6.5 percent or 0.1 W/(m·K). The difference between pretest and subsequent verifications is an indication of apparatus reproducibility and drift over time at a specific thermal resistance. Tables 6-6 and 6-7 show that apparatus output was reproducible and drift was not significant (less than 0.04 W/(m·K)).

Table 6-6 Results of Calibration Verifications of Thermal Conductivity Apparatus at Approximately 30°C

Date	Pretest/ Posttest	Calibration File Name	Deviation from Expected for 9mm Standard		Deviation from Expected for 15mm Standard		Deviation from Expected for 18mm Standard	
			%	W/(m·K)	%	W/(m·K)	%	W/(m·K)
06-18-98 to 06-25-98	Pretest	TC980615.LTC-Heat	-5 91	-0 08	-6.70	-0 09	-6.44	-0.09
		TC980615.LTC-Cool					-5.71	-0.08
07-15-98 to 07-20-98	Posttest	TC980615.LTC-Heat	-5 38	-0 07	-7.05	-0.10	-3.90	-0.05
		TC980615.LTC-Cool	-5 79	-0.08	-6 88	-0 10	-6.58	-0.09
08-05-98 to 08-07-98	Posttest	TC980615.LTC-Heat	-5.62	-0 08	-6.62	-0 09	-6.87	-010
		TC980615.LTC-Cool	-6.06	-0.08	-6.59	-0.09	-6.73	-0.09

Table 6-7. Results of Calibration Verifications of Thermal Conductivity Apparatus at 200°C

Date	Pretest/ Posttest	Calibration File Name	Deviation from Expected for 9mm Standard		Deviation from Expected for 15mm Standard		Deviation from Expected for 18mm Standard	
			%	W/(m·K)	%	W/(m·K)	%	W/(m·K)
06-18-98 to 06-25-98	Pretest	TC980615.LTC	-5.13	-.08	-5.46	-.09	-6.50	-.10
07-15-98 to 07-20-98	Posttest	TC980615.LTC	-6.96	-.11	-7.15	-.12	-8.65	-.14
08-05-98 to 08-07-98	Posttest	TC980615.LTC	-6.98	-.11	-6.77	-.11	-7.79	-0.13

Additional system components requiring calibration included thermocouples and an analog-to-digital converter. The thermocouple cold junction electronic ice reference was calibrated with a thermocouple calibrator, and the analog-to-digital converter was calibrated with a NIST-traceable precision voltage source. These calibrations were performed using SNL TP-215, *Calibration of Lawson Board Systems*. Thermocouples were calibrated by the SNL Primary Standards Laboratory.

After the instrument was calibrated, the specimens were tested in the same manner as the reference materials. This procedure, described in SNL TP-202, *Measurement of Thermal Conductivity of Geologic Samples Using the Guarded-Heat-Flow-Meter Method*, is summarized here. Specimens were placed in the apparatus and temperature was increased at 1°C/min. to each measurement temperature. Data were obtained after the instrument had reached steady-state thermal equilibrium as determined by taking readings of the thermocouples and heat flux transducers as a function of time until the readings were constant. Five readings were taken per minute and were considered to be at steady state when they were constant to within ±0.2 percent for 10 minutes, which is within the stability criteria given in ASTM F433-77, *Standard Practice for Evaluating Thermal Conductivity of Gasket Materials*, an American Society for Testing and Materials (ASTM) standard based on use of the GHFM. The measured ratio, DT/q, was then used

to determine the thermal resistance of the specimen. Thermal conductivity was calculated from R_s and specimen thickness. SNL TP-202 is fully in compliance with ASTM F433-77.

6.2.2.2 Thermal Expansion

The coefficient of linear thermal expansion, α, is the ratio of change in specimen length per degree centigrade to the length at 0°C and is given by Weast (1985, p. F-104):

$$l_t = l_0(1+\alpha T) \tag{6-8a}$$

where:

l_0 = length at 0°C, and
l_t = length at T °C.

Thermal expansion is temperature sensitive, and the more general equation is

$$l_t = l_0\left(1+\alpha T+\beta T^2+\gamma T^3+\ldots\right) \tag{6-8b}$$

where α, β, and γ are empirically determined constants.

All the thermal expansion data were obtained from experiments using one of two identical push-rod dilatometer instruments manufactured by Harrop Industries. The push-rod dilatometer is one of several instruments for measuring the linear coefficient of thermal expansion of materials. The specimen is placed in a receptacle at the end of a tube made of fused silica. The tube, or specimen holder, containing the specimen and push rod slides into a cylindrical furnace so that the specimen is positioned near the center of the furnace. As the temperature of the specimen changes, its length changes; this motion is transmitted to the push rod. The change in length is continuously measured by a linear variable displacement transformer (LVDT) located outside the heated area of the specimen. A type K thermocouple near the surface of the specimen measures specimen temperature.

The dilatometer system expansion was calibrated and then verified by running Standard Reference Materials (SRMs) traceable to NIST and comparing data with expected results. Calibrations were performed using a specimen of fused silica (SRM 739), and verifications were provided by measuring the expansion of SRM 731 (borosilicate glass) and SRM 738 (stainless steel). The LVDT and associated electronics were calibrated with a micrometer using an 11-point calibration. The reverification error is calculated for the dilatometer system as the difference between the expected and measured displacement versus temperature curves. The area between the two curves is divided by the area under the expected curve and then expressed as a percentage. The system calibration was reverified twice during the testing program and also after completion of all tests. The largest reverification error was approximately 3 percent.

The thermal expansion data were corrected for system expansion using calibration data obtained as previously described. These data were then used to calculate thermal strain (ε_T), starting at 25°C, during the heating and cooling phases as follows:

$$\varepsilon_T = \frac{L_{Tn} - L_o}{L_o} \tag{6-9}$$

where:

L_{Tn} = specimen length (m) at a particular temperature (Tn),
(i.e., Tn = 25°C, 50°C, 75°C, ... 300°C, 275°C, 250°C, ... 35°C)
L_0 = specimen length (m) at the reference temperature.

The mean coefficient of thermal expansion ($\bar{\alpha}$ or MCTE) is the linear thermal expansion per unit change in temperature. It was calculated in 25°C intervals where possible, starting at 25°C, during heating and cooling (i.e., 25°–50°C, 50°–75°C, 75°–100°C, ... 300°–325°C, 325°–300°C, ... 50°–30°C). Note that the last interval is over a smaller temperature window because the tests were terminated before complete cooling. For tests that did not reach 325°C, the high temperature intervals were also smaller. The MCTE must be accompanied by the values of the two temperatures used in the calculation. The MCTE is defined as follows:

$$\bar{\alpha} = \frac{1}{L_o}\left\{\frac{L_{T2} - L_{T1}}{(T_2 - T_1)}\right\} \tag{6-10a}$$

or

$$\bar{\alpha} = \frac{\Delta\varepsilon_T}{\Delta T} \tag{6-10b}$$

where:

L_{T1} = specimen length (m) at temperature T_1,
L_{T2} = specimen length (m) at temperature T_2,
L_0 = specimen length (m) at reference temperature,
Δ = change in specimen strain over temperature range T_1 - T_2, and
$T_2 - T_1$ = temperature increment.

The strain-versus-temperature data were fit over each temperature interval using a linear least squares regression, and the slope of the linear fit provided values of α.

The instantaneous coefficient of thermal expansion (ICTE) is calculated in a manner identical to the MCTE. The only difference is that the ICTE is calculated over a 5°C window. Values of ICTE and plots of ICTE-versus-temperature are given in Appendix A.

The test procedure is given in SNL TP-203, *Measurement of Thermal Expansion of Geologic Samples Using a Push Rod Dilatometer*. The test specimen was placed in the notched end of a fused silica tube and the test apparatus was set up as described. The furnace temperature was ramped up and down at a constant rate of 1°C per minute. Displacement and temperature data were acquired continuously throughout the heating and cooling phases of the test and recorded by the automated DCS. Each test specimen was subjected to two complete heating cycles.

SNL TP-203 differs from ASTM E228-85, *Standard Test Method for Linear Thermal Expansion of Solid Materials with a Vitreous Silica Dilatometer,* in the following ways:

- The temperature was incremented at a constant rate (as per ASTM D-4535-85, *Standard Test Methods for Measurement of Thermal Expansion of Rock Using a Dilatometer* p. 4) rather than held constant at a series of temperatures.

- If the length of a specimen changes by more than 20×10^{-6}, the ASTM standard calls for a retest or requires that the deformation be taken into account when reporting expansion values. All specimens were tested twice regardless of the permanent strain. Permanent length changes are given in Appendix A.

SNL TP-203 differs from ASTM D4535-85 as follows:

- The ASTM standard specifies 3 calibration runs, reproducible to within 5 percent, on one type of standard material; it does not call for performing verifications. Instead of the ASTM method, a single calibration on fused quartz was used to calibrate the apparatus. Verifications were then performed on two different standard materials (borosilicate glass and stainless steel). The method used here is considered an improvement over the ASTM method for the following reasons:

  1. The system is verified using a variety of materials with thermal expansion coefficients closer to those expected for rock. The system performance is therefore shown to be consistent over a range of thermal expansions.

  2. The system performance can be verified both before and after testing.

  3. With the exception of one verification on borosilicate glass, the verification errors were always below 5 percent as shown in Table 6-8.

Table 6-8. Results of Calibration Verifications of Thermal Expansion Apparatus

Date	Pretest/ Posttest	Calibration File Name	Reference Standard	Deviation from Expected During Heating (%)	Deviation from Expected During Cooling (%)	Average Deviation from Expected (%)
06-25-98	Pretest	DT980624.TXC	Stainless Steel	2.5	3.8	3.1
06-26-98	Pretest	DT980624.TXC	Borosilicate Glass	3.0	3.8	3.4
07-07-98	Pretest	TD980706.TXC	Borosilicate Glass	2.3	0.8	1.6

Table 6-8. Results of Calibration Verifications of Thermal Expansion Apparatus (Continued)

Date	Pretest/ Posttest	Calibration File Name	Reference Standard	Deviation from Expected During Heating (%)	Deviation from Expected During Cooling (%)	Average Deviation from Expected (%)
07-08-98	Pretest	TD980706.TXC	Stainless Steel	1.4	1.7	1.6
07-22-98	Posttest	DT980624.TXC	Borosilicate Glass	4.7	5.9	5.3
07-22-98	Posttest	TD980706.TXC	Stainless Steel	2.7	0.5	1.6
07-23-98	Posttest	DT980624.TXC	Stainless Steel	2.4	2.0	2.2
07-23-98	Posttest	TD980706.TXC	Borosilicate Glass	1.6	1.6	1.6
08-04-98	Posttest	TD980706.TXC	Borosilicate Glass	4.2	4.1	4.2
08-05-98	Posttest	TD980706.TXC	Stainless Steel	0.9	1.0	0.9
08-06-98	Posttest	DT980624.TXC	Borosilicate Glass	4.1	4.2	4.1
08-07-98	Posttest	DT980624.TXC	Stainless Steel	2.3	2.3	2.3

6.2.2.3 Mechanical Properties

Mechanical test specimens were used in unconfined compression tests. Specimens were monitonically loaded to failure while axial force, and axial and lateral deformations were monitored. These measurements were used to determine ultimate strength, Young's modulus, and Poisson's ratio.

Each specimen was placed in a flexible jacket to maintain constant moisture content during testing and contain the specimen fragments during failure. Ports were cut out of the jacket at the requisite locations to accommodate axial and lateral deformation gages. The axial displacement gage consisted of two LVDTs, located on opposite sides of the specimen. The LVDT barrels were located in a ring which was attached approximately one specimen radius above the specimen midheight. The cores were on extended rods that rested in cups located on a lower ring placed approximately one specimen radius below specimen midheight. The axial displacement gage therefore measured displacements occurring over the central section of the specimen. Radial strains were measured across one diameter of the specimen at midheight using the radial displacement gage developed by Holcomb and McNamee (1984). This gage consists of an LVDT mounted in a ring which is spring-loaded against the specimen. The barrel of the LVDT is mounted in the ring, and the core of the LVDT is attached to a leaf spring that directly contacted the specimen surface. Changes in specimen diameter directly displaced the LVDT core relative to the barrel. The accuracies of calibrations for both the axial and lateral displacement gages were within ±2 percent of reading over the verified range of 10–100 percent of full scale.

Tests were conducted in a servo-controlled hydraulic loading frame. The servo-controller was operated in strain-control feedback mode and force was applied such that a constant axial strain rate of 10^{-5} s^{-1} was imposed. The axial force was measured with a load cell calibrated in place by the manufacturer. The calibration constant for the load cell has a standard deviation of 0.02 percent.

Specimens were inspected for surface irregularities, vugs, and preexisting fractures. After being jacketed and instrumented, specimens were loaded at a constant strain rate of 10^{-5} s^{-1} until peak stress was reached. Data on all channels were collected whenever the output of one channel increased by a preset amount. Data were stored if time incremented by 60 seconds, if axial stress incremented by 0.9 MPa, if axial strain incremented by 5×10^{-5}, or if lateral strain incremented by 3×10^{-5}. Specimens were unloaded after passing the peak in axial force.

Strains were calculated by dividing the measured axial and lateral displacements by the current gage separations. The axial gage consisted of two LVDTs and the average axial strain is reported. Peak stress is the peak force divided by the current cross-sectional area of the specimen. The static elastic constants were calculated by performing linear least squares fits to the data collected between 10 and 50 percent of the stress difference at failure. Young's modulus is the slope of the linear fit to the axial strain versus axial stress data, and Poisson's ratio is the slope of the linear fit to the axial strain versus lateral strain data.

Before testing tuff specimens, validation tests were performed on 6061 aluminum to validate the test method. Tests were also performed after 10 of the 14 specimens were tested and again after completion of the test suite. For the pretest validation, measurements of Young's modulus and Poisson's ratio differed from the expected values by 3.4 percent and 4.8 percent, respectively. Measurements of Young's modulus and Poisson's ratio differed from the expected values by -1.5 percent and -2.6 percent, respectively, for the midtest validation, and by 1.2 percent and 0 percent, respectively, for the posttest validations.

6.2.3 Results

6.2.3.1 Summary of Thermal Conductivity Data and Comparison with Relevant Data Sets

The posttest specimens of thermal conductivity data for posttest specimens are summarized in Table 6-9. Data are grouped according to orientation and location with respect to the approximate maximum extent of the 100°C isotherm at the end of SHT heating. The mean thermal conductivities and standard deviations about the mean are given at each temperature. Mean values of thermal conductivities ranged from 1.6 to 1.8 W/(m·K) with an average thermal conductivity of 1.7 ±0.1 W/(m·K). Thermal conductivities are plotted for each specimen as a function of temperature in Appendix B.

Figure 6-5 shows thermal conductivities measured during heating in this study and also for the pretest characterization data (Brodsky 1996) The posttest data generally fall within the scatter of the pretest results. The large scatter in the pretest data should be noted and may indicate that there was some problem with these specimens or data set. The overlap of pretest and posttest values would indicate that conducting the SHT did not affect conductivities; however, there appear to be differences between posttest specimens that were inside and outside the approximate maximum extent of the 100°C isotherm. Figure 6-6 shows the posttest conductivities measured during heating and grouped by specimen orientation and location with respect to the approximate maximum extent of the 100°C isotherm. The data for a given temperature are plotted slightly offset from one another on the temperature axis so that the error bars can be viewed easily.

Although the error bars overlap (error bars represent ± one standard deviation), the specimens from outside the isotherm generally have lower conductivities than those from within the isotherm, because of the absence of any water in the latter. For reference, the thermal conductivities measured during characterization of Alcove 5 are also shown in Figure 6-6. These specimens were oven-dried before testing and so the conductivity values are expected to be below those measured in this study. At the higher test temperatures, after the posttest specimens have dried somewhat in the thermal conductivity apparatus, the Alcove 5 characterization values and values for posttest specimens from outside the approximate maximum extent of the 100°C isotherm overlap. The differences between specimens that appear to be related to their location relative to the approximate maximum extent of the 100°C isotherm are maintained during cooling as shown in Figure 6-7.

Table 6-9. Thermal Conductivities for SHT Posttest Specimens

	Thermal Conductivity for SHT Posttest W/(m·K)								
Sample ID*	Heating					Cooling			
	30°C	70°C	110°C	150°C	200°C	150°C	110°C	70°C	30°C
Outside 100°C Isotherm, Perpendicular to Heater									
PTC 1-A 15.7	1.79	1.78	1.79	1.77	1.74	1.70	1.69	1.71	1.75
PTC 2-A 4.1	1.70	1.70	1.73	1.73	1.72	1.68	1.66	1.66	1.70
PTC 2-A 10.8	1.83	1.80	1.72	1.72	1.70	1.67	1.66	1.66	1.70
PTC 2-A 14.1	1.65	1.66	1.65	1.62	1.61	1.57	1.56	1.56	1.59
N=	4	4	4	4	4	4	4	4	4
Mean=	1.74	1.73	1.72	1.71	1.69	1.65	1.64	1.65	1.69
Standard Deviation=	0.08	0.06	0.06	0.06	0.06	0.06	0.06	0.07	0.07
Outside 100°C Isotherm, Parallel to Heater									
PTC 4-A 4.3	1.73	1.73	1.73	1.69	1.67	1.63	1.62	1.63	1.67
PTC 5-A 4.1	1.56	1.56	1.56	1.53	1.52	1.48	1.47	1.47	1.50
PTC 5-A 25.4	1.77	1.76	1.76	1.71	1.68	1.64	1.63	1.64	1.68
PTC4-A 26.0	1.81	1.82	1.80	1.75	1.73	1.70	1.69	1.70	1.75
N=	4	4	4	4	4	4	4	4	4
Mean=	1.72	1.72	1.71	1.67	1.65	1.61	1.60	1.61	1.65
Standard Deviation=	0.11	0.11	0.10	0.10	0.09	0.09	0.10	0.10	0.11
Inside 100°C Isotherm, Perpendicular to Heater									
PTC 1-A 19.0	1.83	1.82	1.83	1.81	1.79	1.77	1.75	1.76	1.82
Inside 100°C Isotherm, Parallel to Heater									
PTC 4-A 6.6	1.71	1.73	1.72	1.69	1.68	1.64	1.62	1.63	1.67
PTC 4-A 9.2	1.84	1.82	1.75	1.74	1.71	—	—	—	—
PTC 4-A 14.8	1.78	1.78	1.77	1.75	1.74	1.70	1.69	1.70	1.75
PTC 4-A 19.8	1.86	1.85	1.79	1.78	1.78	1.73	1.72	1.73	1.77
PTC 5-A 14.9	1.79	1.79	1.72	1.71	1.71	1.66	1.65	1.66	1.71
PTC H1-A 8.6	1.81	1.82	1.82	1.78	1.75	1.72	1.71	1.72	1.76
PTC MPBX1-A 14.4	1.86	1.85	1.82	1.79	1.77	1.75	1.73	1.75	1.81
N=	7	7	7	7	7	6	6	6	6
Mean=	1.81	1.80	1.77	1.75	1.73	1.70	1.69	1.70	1.75
Standard Deviation=	0.05	0.04	0.04	0.04	0.04	0.04	0.04	0.05	0.05
All Data									
N=	16	16	16	16	16	15	15	15	15
Mean=	1.77	1.77	1.75	1.72	1.71	1.67	1.66	1.67	1.71
Standard Deviation=	0.08	0.08	0.07	0.07	0.07	0.07	0.07	0.08	0.08

Table 6-9. Thermal Conductivities for SHT Posttest Specimens (Continued)

	Thermal Conductivity for SHT Posttest W/(m•K)								
Sample ID*	Heating					Cooling			
	30°C	70°C	110°C	150°C	200°C	150°C	110°C	70°C	30°C
All Data, All Temperatures									
N=	140								
Mean=	1.71								
Standard Deviation=	0.08								

*The distance from the borehole collar is given (in feet) as part of the specimen identification number.

The data obtained in this study cannot be directly compared with data obtained during characterization of the DST area. The SHT specimens were all tested with "as is" moisture contents whereas the DST specimens were saturated. Saturation causes a large change in conductivity values.

6.2.3.2 Coefficient of Thermal Expansion

6.2.3.2.1 Summary of Data

The MCTEs are summarized in Tables 6-10 and 6-11 for heating and cooling, respectively, during the first thermal cycle. MCTEs are summarized in Tables 6-12 and 6-13 for heating and cooling, respectively, during the second thermal cycle. Data are categorized as being either from within or outside the maximum extent of the 100°C isotherm, and either perpendicular or parallel to the heater. The mean MCTEs and standard deviations about each mean are given at each temperature for each category. Summary data for the entire test suite are given with standard deviations and 95 percent confidence limits at the bottom of each table.

Appendix A provides a summary data sheet for each thermal cycle on each specimen. Each summary sheet includes plots of strain versus temperature, MCTE versus temperature, and ICTE versus temperature. Values of MCTE and ICTE are also tabulated. Specimen lengths and masses are also given.

Table 6-10. Mean Coefficients of Thermal Expansion During First Cycle Heating of Posttest SHT Characterization Specimens

Specimen ID	Distance from collar (ft)	Max. Temp. (°C)	MCTE on Heat-up (10^{-6}/°C)											
			25-50	50-75	75-100	100-125	125-150	150-175	175-200	200-225	225-250	250-275	275-300	300-325
Perpendicular to Heater, Outside 100°C Isotherm														
PTC1-A 2 9-B	2 9	322	8 7	9 6	9 8	11 2	12 3	13 1	14 6	19 4	32 7	58 3	75 0	52 3
PTC1-A 16 8-B	16 8	321	9 1	11 0	9 6	10 4	11 3	12 5	12 3	15 8	20 3	33 2	62 1	49 8
PTC2-B 4 1-B	4 1	321	9 2	10 5	9 9	10 3	11 1	12 3	12 8	16 4	23 8	43 1	81 4	45 6
Completion without cooling outlier		N[a] =	3	3	3	3	3	3	3	3	3	3	3	3
		Mean =	9 0	10 4	9 8	10 7	11 8	12 8	13 2	17 2	25 8	44 2	88 2	49 2
PTC1-A 2 9-B		STD[a] =	0 3	0 7	0 1	0 5	0 7	0 4	1 2	1 9	6 4	11 8	7 7	3 4
Perpendicular to Heater, Inside 100°C Isotherm														
PTC1-B19 0-B	19 0	322	9 0	10 1	8 9	9 4	10 8	12 9	13 5	16 0	20 4	30 6	51 4	54 0
Parallel to Heater, Outside 100°C Isotherm														
PTC4-A 4 6-B	4 6	321	8 8	10 0	8 3	9 5	10 5	11 9	11 2	13 9	20 1	34 1	61 4	69 0
PTC5-B 4 1-B	4 6	321	8 7	10 4	8 8	9 6	10 6	11 6	11 7	14 5	34 2	38 5	57 0	63 1
PTC5-B 24 4-B	4 6	321	8 9	10 5	8 6	9 4	10 2	11 2	11 1	14 1	17 9	26 7	47 5	52 9
PTC5-B 24 4-C	4 6	331	8 8	9 9	8 5	9 3	10 2	11 4	12 6	17 2	21 5	34 5	59 9	45 1
		N[a] =	4	4	4	4	4	4	4	4	4	4	4	4
		Mean =	8 8	10 2	8 6	9 5	10 4	11 5	11 7	14 9	23 4	33 5	61 5	57 5
		STD[a] =	0 1	0 3	0 3	0 1	0 2	0 3	0 7	1 5	7 3	4 9	14 3	10 6
Parallel to Heater, Inside 100°C Isotherm														
PTC4-A 6 8-B	6 8	318	7 9	8 8	9 1	9 4	10 5	11 1	12 4	15 4	24 3	39 0	70 2	73 0
PTC4-B 14 8-B	14 8	321	9 0	10 3	8 6	9 3	10 4	12 0	12 4	15 0	19 2	28 1	45 8	52 2
PTC4-A 19 0-B	19 0	319	8 1	8 9	8 9	9 2	10 1	11 1	12 4	14 5	17 5	28 0	51 0	56 9
PTC4-B 19 8-B	19 8	318	8 4	9 1	9 4	9 8	10 6	11 5	12 8	15 4	19 2	27 8	44 2	44 4
PTC H1-A 15 6-B	15 6	322	7 68	9 48	8 24	9 11	10 19	10 65	11 05	12 33	14 83	22 02	41 38	54 172
PTC MPBX1 14 2-B	14 2	322	8 51	9 64	8 49	9 04	9 86	11 50	11 62	15 29	20 75	28 98	60 49	55 85
		N[a] =	6	6	6	6	6	6	6	6	6	6	6	6
		Mean =	8 2	9 4	8 8	9 3	10 3	11 3	12 2	14 7	19 3	28 8	50 5	56 1
		STD[a] =	0 5	0 6	0 4	0 3	0 3	0 5	0 6	1 2	3 2	5 1	10 3	9 4
All Data Outside 100°C Isotherm														
		N[a] =	7	7	7	7	7	7	7	7	7	7	7	7
		Mean =	8 9	10 3	9 1	10 0	10 9	12 0	12 3	15 9	23 4	38 1	63 5	54 0
		STD[a] =	0 2	0 4	0 7	0 7	0 8	0 7	1 2	2 0	6 5	9 5	11 3	8 9
All Data Inside 100°C Isotherm														
		N[a] =	7	7	7	7	7	7	7	7	7	7	7	7
		Mean =	8 3	9 5	8 8	9 3	10 4	11 5	12 3	14 9	19 4	29 1	50 6	55 6
		STD[a] =	0 5	0 6	0 4	0 2	0 3	0 8	0 8	1 2	3 0	4 7	9 4	8 6
All Data														
		N[a] =	14	14	14	14	14	14	14	14	14	14	14	14
		Mean =	8 6	9 9	9 0	9 6	10 6	11 8	12 3	15 4	21 9	33 6	57 1	54 9
		STD[a] =	0 5	0 7	0 6	0 6	0 6	0 7	1 0	1 7	5 5	8 6	12 0	8 5
		95% [a]	0 2	0 3	0 3	0 3	0 3	0 4	0 5	0 9	2 9	4 5	6 3	4 5

[a] N = Number of samples, STD = Standard deviation, 95% = 95 Percent Confidence Limit Lithostratigraphic Unit Tptpmn, Thermal-mechanical Unit TSw2, Air dried

Table 6-11 Mean Coefficients of Thermal Expansion During First Cycle Cooling of Posttest SHT Characterization Specimens

Specimen ID	Distance from collar (ft)	Max Temp (°C)	MCTE on Cool-down (10^{-6}/°C)											
			325-300	300-275	275-250	250-225	225-200	200-175	175-150	150-125	125-100	100-75	75-50	50-30
Perpendicular to Heater, Outside 100°C Isotherm														
PTC1-A 2 9-B	2 9	322	12 2	16 5	31 8	21 6	67 2	35 4	22 1	15 2	13 2	15 0	11 6	11 4
PTC1-A 16 8-B	16 8	321	16 1	30 2	42 1	39 5	28 3	19 2	15 1	12 9	12 1	10 7	10 2	9 7
PTC2-B 4 1-B	4 1	321	14 9	27 8	43 6	48 0	30 1	20 4	15 6	13 3	12 3	10 8	10 2	9 6
Completion without		N[1] =	2	2	2	2	2	2	2	2	2	2	2	2
cooling outlier		Mean =	15 5	29 0	42 9	43 7	28 2	19 8	15 4	13 1	12 2	10 7	10 2	9 6
PTC1-A 2 9-B		STD[1] =	0 9	1 7	1 2	6 0	2 7	0 8	0 4	0 3	0 1	0 1	0 0	0 1
Perpendicular to Heater, Inside 100°C Isotherm														
PTC1-B19 0-B	19 0	322	18 6	32 2	36 3	32 9	22 9	18 0	15 0	12 7	12 3	10 3	10 2	9 1
Parallel to Heater, Outside 100°C Isotherm														
PTC4-A 4 8-B	4 8	321	14 2	29 3	50 7	53 6	29 5	20 7	15 6	13 7	12 6	11 5	10 4	10 4
PTC5-B 4 1-B	4 6	321	15 1	31 6	43 4	40 4	29 2	31 2	17 1	13 5	12 7	11 2	10 4	9 9
PTC5-B 24 4-B	4 6	321	19 1	29 9	36 9	32 0	21 9	16 8	14 0	11 9	11 5	10 2	9 7	9 1
PTC5-B 24 4-C	4 6	331	18 6	28 1	40 9	41 1	27 8	22 1	15 6	12 9	11 9	10 5	9 8	9 2
		N[1] =	4	4	4	4	4	4	4	4	4	4	4	4
		Mean =	16 6	29 8	42 7	41 8	27 1	22 7	16 7	13 0	12 2	10 8	10 1	9 7
		STD[1] =	2 5	1 5	6 1	9 0	3 6	6 2	1 3	0 8	0 6	0 6	0 4	0 6
Parallel to Heater, Inside 100°C Isotherm														
PTC4-A 5 8-B	5 8	318	12 2	26 6	39 0	46 8	33 5	26 0	17 5	14 0	12 2	11 9	10 4	9 6
PTC4-B 14 8-B	14 8	321	16 6	29 5	36 5	33 1	23 7	18 1	14 6	12 5	11 8	10 4	9 9	9 3
PTC4-A 19 0-B	19 0	319	16 9	29 2	38 3	34 8	23 4	17 5	13 7	12 3	11 2	9 7	9 7	10 0
PTC4-B 19 8-B	19 8	318	19 8	28 8	31 2	29 8	22 5	18 2	14 0	12 3	11 4	10 6	10 0	9 4
PTC H1-A 15 6-B	15 6	322	19 33	30 87	32 25	24 14	18 09	14 42	12 59	11 20	10 55	10 03	9 29	20 154
PTC MPBX1 14 2-B	14 2	322	17 89	30 67	39 41	33 88	23 31	18 80	15 12	12 42	11 60	10 27	9 79	8 99
		N[1] =	6	6	6	6	6	6	6	6	6	6	6	6
		Mean =	17 1	28 8	36 1	33 6	24 1	18 9	14 6	12 5	11 5	10 5	9 9	11 3
		STD[1] =	2 7	1 9	3 8	7 1	5 1	3 8	1 7	0 9	0 6	0 8	0 4	4 4
All Data Outside 100°C Isotherm (Without cooling outlier PTC1-A 2 9-B)														
		N[1] =	6	6	6	6	6	6	6	6	6	6	6	6
		Mean =	16 3	29 5	42 6	42 4	27 6	21 7	15 6	13 0	12 2	10 6	10 1	9 7
		STD[1] =	2 1	1 4	4 8	7 6	3 1	5 0	1 0	0 6	0 4	0 5	0 3	0 5
All Data Inside 100°C Isotherm														
		N[1] =	7	7	7	7	7	7	7	7	7	7	7	7
		Mean =	17 4	29 4	36 4	33 5	23 9	18 7	14 7	12 5	11 6	10 5	9 8	11 0
		STD[1] =	2 5	2 1	3 4	6 5	4 7	3 5	1 5	0 8	0 6	0 7	0 4	4 1
All Data (Without cooling outlier PTC1-A 2.9-B)														
		N[1] =	13	13	13	13	13	13	13	13	13	13	13	13
		Mean =	16 9	29 4	39 4	37 6	25 8	20 1	15 1	12 7	11 8	10 6	10 0	10 4
		STD[1] =	2 3	1 8	5 1	8 2	4 3	4 4	1 4	0 8	0 6	0 8	0 3	3 0
		95%[1]	1 3	1 0	2 8	4 4	2 3	2 4	0 7	0 4	0 3	0 3	0 2	1 6

[1] N = Number of samples STD = Standard deviation 95% = 95 Percent Confidence Limit Lithostratigraphic Unit Tptpmn Thermal-mechanical Unit TSw2, Air dried

Table 6-12 Mean Coefficients of Thermal Expansion During Second Cycle Heating of Posttest SHT Characterization Specimens

Specimen ID	Distance from collar (ft)	Max Temp. (°C)	MCTE on Heat-up (10^{-6}/°C)										
			25-50	50-75	75-100	100-125	125-150	150-175	175-200	200-225	225-250	250-275	275-300	300-325
Perpendicular to Heater, Outside 100°C Isotherm														
PTC1-A 2 9-B	2 9	323	8 2	9 4	9 6	10 5	11 7	13 3	20 5	28 1	35 0	56 2	51 1	31 2
PTC1-A 16 8-B	16 8	321	8 8	10 3	9 0	10 3	11 1	12 4	13 4	19 2	23 2	43 4	55 0	33 5
PTC2-B 4 1-B	4 1	323	8 7	10 4	9 3	10 8	11 4	12 4	13 9	19 3	29 5	54 8	49 4	27 7
Compilation without		N[a] =	3	3	3	3	3	3	3	3	3	3	3	3
cooling outlier		Mean =	8 6	10 0	9 3	10 5	11 4	12 7	15 9	22 2	29 2	51 5	51 8	30 8
PTC1-A 2 9-B		STD[b] =	0 3	0 5	0 3	0 1	0 3	0 5	4 0	5 1	5 9	7 0	2 9	3 0
Perpendicular to Heater, Inside 100°C Isotherm														
PTC1-B19 0-B	19 0	322	9 0	10 0	9 5	10 7	11 5	13 1	14 2	18 0	23 9	39 2	47 9	32 5
Parallel to Heater, Outside 100°C Isotherm														
PTC4-A 4 8-B	4 8	323	8 7	9 9	9 0	9 9	11 0	12 6	13 0	18 6	24 7	57 9	67 7	33 8
PTC5-B 4 1-B	4 8	322	8 4	9 9	9 0	10 2	10 7	11 9	13 5	20 0	25 3	41 2	60 3	35 6
PTC5-B 24 4-B	4 6	322	8 9	10 0	8 9	10 1	10 9	11 9	12 9	16 5	22 1	35 5	42 2	30 8
PTC5-B 24 4-C	4 6	322	9 1	10 0	9 4	10 5	11 6	12 5	15 8	21 1	27 5	51 1	47 9	27 6
		N[a] =	4	4	4	4	4	4	4	4	4	4	4	4
		Mean =	8 8	9 9	9 1	10 2	11 0	12 2	13 6	19 1	24 9	46 4	54 5	31 9
		STD[b] =	0 3	0 1	0 2	0 2	0 4	0 4	1 4	2 0	2 2	10 0	11 6	3 5
Parallel to Heater, Inside 100°C Isotherm														
PTC4-A 6 8-B	6 8	318	8 0	9 0	8 3	10 0	11 1	12 1	14 5	21 5	29 9	52 8	55 3	36 0
PTC4-B 14 8-B	14 8	323	8 7	9 9	9 3	10 2	11 1	12 1	13 4	17 2	22 7	36 1	45 2	32 2
PTC4-A 19 0-B	19 0	318	8 4	8 9	9 1	9 8	10 9	11 6	13 0	16 7	22 4	39 1	48 5	33 1
PTC4-B 19 8-B	19 8	318	7 9	9 2	7 4	10 3	11 5	12 2	14 0	17 4	24 0	33 8	35 0	27 2
PTC H1-A 15 6-B	15 6	320	7 85	8 58	8 87	9 47	10 27	10 83	11 33	14 10	18 00	28 52	41 91	33 655
PTC MPBX1 14 2-B	14 2	322	8 82	9 88	8 43	10 33	11 06	12 37	13 98	19 40	24 20	40 15	47 56	30 31
		N[a] =	6	6	6	6	6	6	6	6	6	6	6	6
		Mean =	8 3	9 2	8 7	10 0	11 0	11 9	13 4	17 7	23 5	38 4	45 8	32 1
		STD[b] =	0 4	0 6	0 7	0 3	0 4	0 6	1 1	2 5	3 8	8 2	6 8	3 0
All Data Outside 100°C Isotherm														
		N[a] =	7	7	7	7	7	7	7	7	7	7	7	7
		Mean =	8 7	10 0	9 2	10 3	11 2	12 4	14 7	20 4	26 7	48 8	53 4	31 5
		STD[b] =	0 3	0 3	0 2	0 2	0 4	0 5	2 7	3 7	4 4	8 6	8 5	3 1
All Data Inside 100°C Isotherm														
		N[a] =	7	7	7	7	7	7	7	7	7	7	7	7
		Mean =	8 4	9 3	8 8	10 1	11 0	12 0	13 5	17 8	23 6	38 5	45 9	32 1
		STD[b] =	0 5	0 6	0 7	0 4	0 4	0 7	1 1	2 3	3 6	7 6	6 3	2 6
All Data														
		N[a] =	14	14	14	14	14	14	14	14	14	14	14	14
		Mean =	8 5	9 7	9 0	10 2	11 1	12 2	14 1	19 1	25 2	43 6	49 7	31 8
		STD[b] =	0 4	0 6	0 6	0 3	0 4	0 6	2 1	3 3	4 2	9 3	8 2	2 6
		95% [c]	0 2	0 3	0 3	0 2	0 2	0 3	1 1	1 7	2 2	4 9	4 3	1 5

[a] N = Number of samples STD = Standard deviation 95% = 95 Percent Confidence Limit Lithostratigraphic Unit Tptpmn Thermal-mechanical Unit TSw2 Air dried

Table 6-13 Mean Coefficients of Thermal Expansion During Second Cycle Cooling of Posttest SHT Characterization Specimens

Specimen ID	Distance from collar (ft)	Max Temp. (°C)	MCTE on Cool-down (10^{-6}/°C)											
			325-300	300-275	275-250	250-225	225-200	200-175	175-150	150-125	125-100	100-75	75-50	50-30
Perpendicular to Heater, Outside 100°C Isotherm														
PTC1-A 2 9-B	2 9	323	10 8	17 1	36 2	38 1	25 5	30 7	21 6	32 0	16 2	21 0	14 8	29 8
PTC1-A 16 8-B	16 8	321	18 9	30 7	42 8	39 6	28 3	18 9	14 7	12 5	11 8	10 6	10 0	9 7
PTC2-B 4 1-B	4 1	323	15 6	27 6	43 5	47 9	29 9	20 6	15 4	13 1	12 1	10 8	9 9	9 6
Compilation without cooling outlier		N[a] =	2	2	2	2	2	2	2	2	2	2	2	2
		Mean =	17 2	29 3	43 2	43 8	28 1	19 8	15 1	12 8	11 9	10 7	10 0	9 7
PTC1-A 2 9-B		STD[a] =	2 4	2 1	0 5	5 9	2 5	1 3	0 5	0 4	0 2	0 2	0 0	0 1
Perpendicular to Heater, Inside 100°C Isotherm														
PTC1-B19 0-B	19 0	322	19 5	32 1	40 2	35 0	23 6	18 0	14 7	12 6	11 9	10 4	10 1	9 6
Parallel to Heater, Outside 100°C Isotherm														
PTC4-A 4 6-B	4 6	323	16 4	29 9	50 1	53 1	29 7	20 6	15 4	13 4	12 2	11 0	10 5	10 1
PTC5-B 4 1-B	4 6	322	17 3	29 6	43 8	42 5	29 2	20 3	15 3	13 0	12 2	10 6	10 3	10 1
PTC5-B 24 4-B	4 6	322	19 1	30 4	36 4	31 3	21 6	16 6	13 9	11 9	11 3	10 ?	9 6	9 ?
PTC5-B 24 4-C	4 6	322	17 9	28 7	43 3	41 3	28 6	21 5	15 7	12 5	11 5	10 8	9 7	9 1
		N[a] =	4	4	4	4	4	4	4	4	4	4	4	4
		Mean =	17 7	29 6	43 4	42 1	28 8	19 8	15 1	12 7	11 9	10 6	10 0	9 8
		STD[a] =	1 1	0 7	5 6	8 9	3 7	2 1	0 8	0 6	0 4	0 4	0 4	0 6
Parallel to Heater, Inside 100°C Isotherm														
PTC4-A 6 8-B	6 8	316	14 7	28 5	40 3	47 3	33 1	24 8	18 3	13 4	11 8	10 8	10 0	9 7
PTC4-B 14 8-B	14 8	323	18 5	29 7	37 1	32 8	23 5	18 0	14 7	12 4	11 6	10 4	9 8	9 2
PTC4-A 19 0-B	19 0	316	16 4	29 3	38 8	35 6	23 5	17 7	13 6	12 1	11 0	10 1	9 4	9 3
PTC4-B 19 8-B	19 8	316	19 3	27 4	31 3	28 6	22 1	18 0	13 6	12 1	10 8	9 9	9 4	8 9
PTC H1-A 15 6-B	15 6	320	20 82	31 09	35 79	31 13	25 54	15 09	12 48	8 27	9 14	9 38	8 63	8 406
PTC MPBX1 14 2-B	14 2	322	19 26	30 62	40 43	34 82	24 11	19 06	14 58	12 41	11 65	10 01	9 72	9 30
		N[a] =	6	6	6	6	6	6	6	6	6	6	6	6
		Mean =	18 0	29 1	37 2	35 0	25 3	18 8	14 3	11 8	11 0	10 1	9 5	9 1
		STD[a] =	2 2	1 8	3 4	6 5	4 0	3 3	1 3	1 8	1 0	0 5	0 5	0 4
All Data Outside 100°C Isotherm (Without cooling outlier PTC1-A 2 9-B)														
		N[a] =	6	6	6	6	6	6	6	6	6	6	6	6
		Mean =	17 5	29 5	43 3	42 6	27 2	19 8	15 1	12 7	11 9	10 7	10 0	9 6
		STD[a] =	1 4	1 1	4 4	7 5	3 1	1 8	0 7	0 5	0 4	0 3	0 3	0 4
All Data Inside 100°C Isotherm														
		N[a] =	7	7	7	7	7	7	7	7	7	7	7	7
		Mean =	18 2	29 5	37 7	35 0	25 1	18 7	14 3	11 9	11 1	10 1	9 6	9 2
		STD[a] =	2 1	2 0	3 3	5 9	3 7	3 0	1 2	1 7	1 0	0 5	0 5	0 4
All Data (Without cooling outlier PTC1-A 2 9-B)														
		N[a] =	13	13	13	13	13	13	13	13	13	13	13	13
		Mean =	17 9	29 5	40 3	38 5	26 1	19 2	14 7	12 3	11 5	10 4	9 8	9 4
		STD[a] =	1 7	1 6	4 7	7 5	3 5	2 5	1 0	1 3	0 8	0 5	0 5	0 5
		95% [a]	0 9	0 9	2 6	4 1	1 9	1 3	0 6	0 7	0 4	0 2	0 3	0 3

[a] N = Number of samples, STD = Standard deviation, 95% = 95 Percent Confidence Limit Lithostratographic Unit Tptpmn, Thermal-mechanical Unit TSw2, Air dried

6.2.3.2.2 First Heating

The data obtained during the first heating are plotted in Figure 6-8, which shows MCTE as a function of temperature for all specimens. All specimens show steep increases in MCTE beginning at approximately 150°–200°C and continuing until approximately 300°C. The steepest increases are between 250° and 300°C. This steep increase is attributed to phase changes in the silica mineral phases. The MCTEs calculated over the temperature interval of 300°–325°C decrease as the phase change is completed. The specimens with lower MCTEs are primarily from within the approximate maximum extent of the 100°C isotherm.

Specimens from different orientations and original locations are compared in Figure 6-9. The mean MCTEs and standard deviations for each data grouping are plotted along with data obtained during the pretest characterization of the SHT block. The data for a given temperature interval are plotted slightly offset from one another on the temperature axis so that the error bars can be viewed easily. This figure shows that specimens from outside the approximate maximum extent of the 100°C isotherm (both parallel and perpendicular to the heater) have similar values and plot above MCTEs from inside the maximum extent of the 100°C isotherm. The SHT pretest characterization data are closely matched to the posttest data from within the approximate maximum extent of the 100°C isotherm.

6.2.3.2.3 Subsequent Thermal Cycles

Appendix C provides a comparison of data obtained during the two heating cycles for each test. Each specimen is represented by two plots. The first plot shows strain-versus-temperature where the strain measured during the second cycle is offset by the permanent strain that accumulated during the first cycle. The second plot shows ICTE-versus-temperature for the two cycles. With the exception of the development of permanent strains during the first cycle, the data are generally reproducible from cycle to cycle. The ICTE-versus-temperature curves and strain-versus-temperature curves obtained during cooling almost overlay one another for many specimens.

6.2.3.2.4 Comparison of Thermal Expansion Data with Relevant Data Sets

Figure 6-10 is a summary of MCTE versus temperature data obtained from different parts of Alcove 5. Only data collected during the first heating are shown. The SHT posttest data from parallel and perpendicular specimens have been combined. The SHT data are shown in comparison to data obtained during Alcove 5 and DST pretest characterizations. In general, the SHT pretest characterization data and data from within the approximate maximum extent of the 100°C isotherm continue to track one another and fall below the remaining data sets.

Appendix D includes figures analogous to Figures 6-8, 6-9, and 6-10 for the first cooling, the second heating, and the second cooling. Specimen PTC1-A 2.9-B provided anomalous cooling data for both cycles that may be related to dilatometer performance. These data were therefore omitted from the calculations of mean and standard deviation. These figures show that the differences observed between specimens from inside and outside the approximate maximum extent of the 100°C isotherm are maintained during subsequent heating cycles.

6.2.3.2.5 ASTM Reporting Requirements

The ASTM procedures relevant to these tests are ASTM D4535-85, *Standard Test Methods for Measurement of Thermal Expansion of Rock Using a Dilatometer*, and ASTM E228-85, *Standard Test Method for Linear Thermal Expansion of Solid Materials With a Vitreous Silica Dilatometer*. ASTM D4535 gives two test methods: one method for unconfined tests, which is very similar to that described in ASTM E228, and one method for confined tests. The method for unconfined tests was used here.

6.2.3.3 Elastic Moduli and Unconfined Compressive Strengths

6.2.3.3.1 Summary of Data

Fourteen specimens were tested in unconfined compression and the experimental data are summarized in Table 6-14. Mean values, standard deviations, and 95 percent confidence limits are given for Young's modulus, Poisson's ratio, peak stress, and axial strain at peak stress. Young's moduli ranged from 20.1 GPa to 37.0 GPa with a mean value of 31.6 GPa. The standard deviation was ±4.8 GPa and the 95 percent confidence limit was ±2.5 GPa. Poisson's ratio ranged from 0.12 to 0.39 with a mean value of 0.20. The standard deviation was ±0.07 and the 95 percent confidence limit was ±0.03. Peak stress ranged from 34 MPa to 246 MPa with a mean value of 134 MPa. The standard deviation was ±70 MPa and the 95 percent confidence limit was ±37 MPa. Axial strain at peak stress ranged from 0.11 percent to 0.89 percent with a mean value of 0.47 percent. The standard deviation was ±0.25 percent and the 95 percent confidence limit was ±0.13 percent. Stress-strain curves for all tests are given in Appendix E.

Table 6-14. Summary Data: SHT Posttest Characterization Unconfined Compression Tests

Test ID	SHTUC02	SHTUC03	SHTUC04	SHTUC05	SHTUC06	SHTUC07	SHTUC08	SHTUC09	SHTUC10	SHTUC11	SHTUC13	SHTUC14	SHTUC15	SHTUC16
Specimen ID[a]	PTC4-B 9.2	PTC4-B 4.3	PTC4-B 6.6	PTC4 11.8	PTC4 17.4	PTC4 20.9	PTC4-B 26.0	PTC2-B 10.8	PTCH1 8.6	PTCH1 15.6	PTCH1 18.7	PTC1 12.5	PTC MPBX1-B 14.4	PTC1-B 15.7
Date Tested	21-07-98	22-07-98	22-07-98	23-07-98	23-07-98	23-07-98	24-07-98	24-07-98	24-07-98	27-07-98	28-07-98	29-07-98	29-07-98	30-07-98
Thermal-Mechanical Unit	TSw2	TSw2	TSw2	TSw2	TSw2	TSw2	TSw2	TSw2	TSw2	TSw2	TSw2	TSw2	TSw2	TSw2
Lithostratigraphic Unit	Tptpmn	Tptpmn	Tptpmn	Tptpmn	Tptpmn	Tptpmn	Tptpmn	Tptpmn	Tptpmn	Tptpmn	Tptpmn	Tptpmn	Tptpmn	Tptpmn
Dry Bulk Density	2.25	2.27	2.26	2.32	2.30	2.32	2.31	2.21	2.30	2.23	2.28	2.29	2.31	2.21
Moisture Content (%)	1.1	1.0	0.8	0.9	1.1	1.1	1.1	1.0	1.0	1.3	0.9	1.1	0.9	0.9
Confining Pressure	0	0	0	0	0	0	0	0	0	0	0	0	0	0
Static Young's Modulus (GPa)	34.4	33.4	32.3	37.0	34.0	34.4	32.9	20.1	34.3	24.2	34.2	26.6	35.4	28.9
Static Poisson's Ratio	0.185	0.168	0.166	0.259	0.182	0.187	0.178	0.251	0.159	0.123	0.173	0.393	0.168	0.183
Peak Stress	175.4	34.3	113.9	144.9	240.5	245.7	191.4	51.8	80.5	38.7	137.0	78.7	183.5	159.2
Axial Strain at Peak Stress	0.005274	0.001138	0.003637	0.008941	0.007924	0.007909	0.006003	0.00213	0.002629	0.002316	0.004349	0.001641	0.005806	0.005614

Statistical Summary[b]

	Mean	Standard Deviation	Count	95% Confidence Limit
Static Young's Modulus (GPa)	31.6	4.8	14	2.5
Static Poisson's Ratio	0.198	0.066	14	0.034
Peak Stress	134.0	70.2	14	36.8
Axial Strain at Peak Stress	0.004665	0.002521	14	0.001321

[a] The distance from the borehole collar is given (in feet) as part of the specimen identification number.

[b] Tests SHTUC01, SHTUC12, and SHTUC17 were conducted on an aluminum specimen.

Specimens from inside and outside the approximate maximum extent of the 100°C isotherm are compared in Table 6-15. Young's moduli and peak stress values are lower outside the isotherm than inside the isotherm. Poisson's ratios also appear to differ; however, if one outlier (PTC1-12.5 with a Poisson's ratio of 0.39) is omitted, then Poisson's ratios are almost the same for the two groups of data.

Table 6-15 Posttest Mechanical Data from Single Heater Test Area

Test Region	Young's Modulus (GPa)			Poisson's Ratio			Unconfined Compressive Strength (MPa)		
	Mean	Standard Deviation	No. of Tests	Mean	Standard Deviation	No. of Tests	Mean	Standard Deviation	No. of Tests
Specimens from inside 100°C Isotherm	33 3	3 6	9	0 18	0 04	9	151 1	68 7	9
Specimens from outside 100°C Isotherm	28 4	5 4	5	0 23	0 09	5	103 1	68 7	5

6.2.3.3.2 Comparison of Unconfined Compression Data with Other Data Sets

Table 6-16 compares elastic moduli and peak stress values obtained during the pretest and posttest characterizations. Mean values of Young's modulus and peak stress are both lower for the posttest characterization data; however, the differences between the mean values are well within one standard deviation. Mean Poisson's ratio is higher for the posttest characterization. In this case, the difference between mean values is greater than the standard deviation obtained for the pretest suite but within one standard deviation of the posttest values. The posttest mean Poisson's ratio is heavily influenced by one outlier (PTC1-12.5) with a ratio of 0.39.

Table 6-16 Comparison of Mechanical Data from Pretest and Posttest Characterizations

Test Region	Young's Modulus (GPa)			Poisson's Ratio			Unconfined Compressive Strength (MPa)		
	Mean	Standard Deviation	No. of Tests	Mean	Standard Deviation	No. of Tests	Mean	Standard Deviation	No. of Tests
SHT Pretest	32 4	2 9	22	0 17	0 02	22	143 2	50 3	22
SHT Posttest	31 6	4 8	14	0 20	0 07	14	134 0	70 2	14
Difference	-2 5%			16%			-6 6%		

Elastic moduli and peak stresses for the SHT are compared with data from the DST pretest characterization (SNL 1997a, p. 14) and from borehole characterizations (CRWMS M&O 1996c, pp. 5-87, 5-95, and 5-108) in Table 6-17. There were minor differences in the testing programs that should be discussed. The SHT test specimens (both pretest and posttest) had a length to diameter (L:D) ratio of 2.5 whereas the DST and surface drillhole specimens had an L:D ratio of 2.0. Work reported in Paterson (1978, p. 36) indicates that decreasing the L:D from 2.5 to 2.0 would result in a 2 percent (approximately 3 MPa) increase in strength. The increase in observed strengths is generally tens of MPa and so the effect of different L:D ratios is considered minor. Moisture contents were also different for different test suites and increasing moisture content decreases the strength. Moisture contents for the DST and SHT posttest specimens were approximately 1 percent or less, whereas the surface drillhole specimens were tested in the

saturated state. Two of the SHT pretest characterization specimens were tested saturated and the remainder were tested "as is," similar to the DST pretest and the SHT posttest specimens. The SHT specimens were drier than the surface drillhole specimens, and probably of equal moisture content to the DST specimens, yet their strengths were lower. The lower strengths observed for the SHT specimens therefore cannot be attributed to moisture content.

Table 6-17. Summary of Drillhole Mechanical Properties Data for Tptpmn

Drillhole	Young's Modulus (GPa)			Poisson's Ratio			Unconfined Compressive Strength (MPa)		
	Mean	Standard Deviation	No. of Tests	Mean	Standard Deviation	No. of Tests	Mean	Standard Deviation	No. of Tests
SHT Pretest	32.4	2.9	22	0.17	0.02	22	143.2	50.3	22
SHT Posttest	31.6	4.8	14	0.20	0.07	14	134.0	70.2	14
DST Pretest	36.8	3.5	16	0.20	0.04	16	176.4	65.8	16
NRG-5	32.5	10.8	8	0.20	0.06	8	173.3	99.4	8
NRG-6	32.1	3.0	8	0.19	0.03	8	193.0	55.7	8
NRG-7/7A	33.2	4.2	19	0.22	0.03	19	192.1	51.1	9
SD-9	32.8	5.1	15	0.21	0.02	15	189.1	64.8	7
SD-12	34.3	2.0	4	0.20	0.01	4	195.8	3.5	2

The data distributions for Young's modulus, Poisson's ratio, and peak stress are given in Figures 6-11, 6-12, and 6-13, respectively. Each figure shows data from the pretest and posttest SHT characterizations. Figure 6-11 shows that the Young's moduli are evenly distributed about the mean (32.4 GPa) for the pretest specimens; however, only four posttest specimens have Young's moduli below the posttest mean (31.6 GPa) whereas 10 posttest specimens have values above the mean. Figure 6-12 shows that the distribution of Poisson's ratio values is very skewed for the posttest specimens. Were it not for one specimen with a Poisson's ratio of 0.39 (PTC1-12.5), the mean ratio would be 0.18 ±0.02 instead of 0.20 ±0.034. The pretest and posttest peak strength values are both approximately evenly distributed about their respective means (Figure 6-13).

6.2.3.3.3 Failure Mode

Photographs were taken of each failed specimen. There was no apparent correlation between failure mode (shear failure or axial splitting) and strength or specimen location. For the pretest suite of unconfined compressive tests (Boyd et al. 1996, p. 14) and for the DST pretest characterization (SNL 1997a, p. 20) it was also reported that there was no correlation between strength and the mode of failure.

6.2.4 Discussion of Results

The SHT posttest thermal and mechanical properties data were compared with pretest SHT data in Subsection 6.2.3. The comparisons are summarized as follows:

- Thermal expansion coefficients for posttest specimens from within the approximate maximum extent of the 100°C isotherm were below those of specimens from outside the

isotherm. Values for pretest specimens were approximately coincident with those for posttest specimens from within the approximate maximum extent of the 100°C isotherm.

- Thermal conductivities fell within the range defined by the pretest measurements. Conductivities for specimens outside the approximate maximum extent of the 100°C isotherm were below those of specimens from inside the isotherm.

- Unconfined compression tests provided a mean peak stress value that was 9 MPa below the pretest values. The standard deviations for mean peak stresses were 50–70 MPa and so this decrease is not significant. Young's moduli and peak stresses were lower for specimens outside the approximate maximum extent of the 100°C isotherm than inside the isotherm.

- No anisotropy was evident, consistent with conclusions reported by SNL (1997b).

A consistent explanation for the differences between pretest and posttest results and the differences between values inside and outside of the approximate maximum extent of the 100°C isotherm was not found. It was expected that within the approximate maximum extent of the 100°C isotherm, cracking might occur due to higher thermal gradients, differential thermal expansion of minerals, or due to steam pressure resulting from the vaporization of non-surface-connected water. Greater damage would be indicated by lower strengths, lower measured values of Young's moduli, lower thermal conductivities, and lower thermal expansion coefficients. (Thermal expansion coefficients would be lowered if thermal expansion during laboratory tests were taken up by volume expansion into newly formed cracks.)

The data do not show consistent evidence that damage was greater inside the approximate maximum extent of the 100°C isotherm. Specimens from inside the isotherm exhibited lower thermal expansion coefficients than those from outside of the isotherm, consistent with the hypothesis that specimens from inside the approximate maximum extent of the 100°C isotherm were more damaged than those from outside the isotherm. In addition, coefficients of thermal expansion from other locations in Alcove 5 most closely matched results obtained outside the isotherm. However, additional data do not indicate greater damage within the 100°C isotherm. The thermal expansion data from inside the isotherm closely match the pretest thermal expansion values. Also, lower Young's moduli, strengths, and thermal conductivities were obtained outside the approximate maximum extent of the 100°C isotherm than inside. These data indicate that for the intact sections of rock tested here, rocks inside the isotherm were not more damaged than those outside.

The role of moisture content was also evaluated. It might be expected that specimens from inside the approximate maximum extent of the 100°C isotherm would be drier than those from outside. All specimens were cored and ground under water and then allowed to dry in the laboratory at room temperature until testing. The specimens were then tested "as is." If the specimens from inside the approximate maximum extent of the 100°C isotherm remained drier than those from outside, it would be expected that those from inside the isotherm would have higher strengths and lower thermal conductivities. Thermal expansion and elastic moduli should be relatively unaffected by moisture content. The data did show that strengths were higher for specimens from

inside the isotherm, consistent with the idea that these specimens were drier; however, thermal conductivities showed the opposite. Conductivities from inside the isotherm were higher than those from outside, reflecting that if moisture content were relevant, specimens from the interior were not drier than those from outside the isotherm. These data indicate that differences in moisture content that may have existed in situ were not sufficiently preserved to affect the laboratory properties data.

6.2.5 Conclusions

The objectives of this study were to characterize the posttest SHT area and to evaluate changes in rock properties that might have resulted from conducting the SHT. Sixteen specimens were tested for thermal conductivity, 14 specimens were measured for thermal expansion, and 14 specimen were tested in unconfined compression. All specimens had horizontal or subhorizontal orientations and no anisotropy was observed. Thermal conductivity values fell within the range defined by pretest characterization activities. Specimens from outside the approximate maximum extent of the 100°C isotherm generally had lower thermal conductivities than those from the interior. Thermal expansion coefficients for specimens from within the approximate maximum extent of the 100°C isotherm were well matched to those obtained during pretest characterization tests. Those from outside the isotherm were higher and more closely matched to existing data collected on specimens from other parts of Alcove 5. Unconfined compressive strengths and Young's moduli were slightly, but not significantly, reduced as compared with pretest values. Strengths and Young's moduli from inside the approximate maximum extent of the 100°C isotherm were higher than values obtained outside the isotherm.

The data were evaluated and found to be not completely consistent with the hypothesis that there was increased damage within the approximate maximum extent of the 100°C isotherm. Similarly, the data showed no indication that differences in moisture content were retained through the specimen preparation process. No consistent explanation for the differences between pretest and posttest results and the differences between values inside and outside of the approximate maximum extent of the 100°C isotherm was found. The major conclusion for repository design and performance assessment is that the thermal cycle imposed by the SHT has no significant impact on long-term thermal-mechanical intact rock properties.

6.3 LABORATORY TESTING FOR HYDROLOGICAL PROPERTIES

The following investigations were documented in accordance with LBNL procedure YMP-LBNL-QIP-SIII.0 (c), *Scientific Investigation.*

A number of boreholes were dry-drilled following the termination of the cooling phase of the SHT for posttest characterization. In particular, protected (wrapped and sealed) cores from three dry-drilled boreholes (boreholes 199, 200, 201) were tested for porosity, density, and water content or liquid saturation. The locations of these protected cores were designed to pass through both the anticipated "dry-out" and "condensing" regions developing in the SHT block as a result of the heating. Figure 6-14 shows a x-z view of the boreholes and the locations of the protected core samples. Locations of the cores along the borehole are identified by the last two digits of their Sample Management Facility identification number, shown in the legend of Figure 6-14. The two dashed circles, with radii of 1 m and 3 m, respectively, from the heater, delineate the anticipated drying zone (approximately within the inner circle), and the wetting region (between the two circles). The radial symmetry does not account for gravity drainage of the condensate,

hence borehole 201 was drilled at a steep angle in order to access rock at depth over 3 m below the heater horizon, with the intention that the importance of drainage of condensate via the fractures may be investigated.

While the quantities measured and the methodology of these post-cooling laboratory measurements remain the same as their pre-heat counterparts described in Section 4, the focus here in the post-cooling effort is substantially different. In the pre-heat results, the intent is to estimate an average initial liquid saturation of the matrix cores; in the post-cooling results, the focus is on the change from their initial values, and more importantly, the spatial location of the cores (with respect to the heater) where changes have occurred.

Table 6-18 presents the laboratory-determined saturation, porosity, and particle density. Average porosity and particle density values are given at the end of the table. An average value for liquid saturation is not a meaningful parameter in these post-cooling cores because liquid saturation of the cores reflect the thermal-hydrological processes that have taken place in the SHT, and their importance lies in their spatial variability. Rather, Figure 6-14 plots the liquid saturation of all cores tested, in their respective locations. Note (Table 6-18) that the porosity of three core samples LBNL identification number H-1, H-22, H-27) is exceptionally high, and is attributed to visible evidence of fractures. In turn, the liquid saturation of these samples would be less reliable, and this should be kept in mind while studying the saturation results in Figure 6-14.

Saturation for cores along borehole 201 is relatively uniform. Excluding the two samples with large porosity, liquid saturation for all cores along borehole 201 is within 2 percent of their average 86 percent. For the cores along boreholes 199 and 200, we note the following: (a) drying due to heat has occurred near the heater, as evidenced by the lower liquid saturation of cores within the 1-m radius from the heater; (b) the liquid saturations in the anticipated "condensing" zone between two circles are generally lower than those values in borehole 201; and (c) the liquid saturation seems to be higher below the heater horizon than above the heater horizon. These observations are consistent with a scenario stipulating that condensate is not held in the matrix (thus elevating its liquid saturation) but is drained through fractures of hierarchical scales. Drainage through the microscopic fractures account for the slightly drier cores above the heater horizon in borehole 199 than below the heater horizon in borehole 200. Drainage through larger fractures extending a few meters account for the overall wetter cores in borehole 201 than those in the "condensing" zones in boreholes 199 and 200.

Table 6-18. Laboratory Measurement of Post-Cooling Dry Drilled Cores from the SHT

Sample Identifier	LBNL Identifier	Saturation	Porosity	Bulk Density	Particle Density	Gravimetric Water Content
				(g/cc)	(g/cc)	(g/g)
SPC01009880	H-1	0.50	0.169	1.96	2.38	0.043
SPC01009882	H-2	0.79	0.105	2.19	2.44	0.038
SPC01009884	H-3	0.75	0.115	2.16	2.44	0.040
SPC01009885	H-4	0.44	0.099	2.20	2.44	0.020
SPC01009887	H-5	0.19	0.101	2.18	2.42	0.009
SPC01009888	H-6	0.32	0.110	2.17	2.43	0.016
SPC01009889	H-7	0.80	0.104	2.19	2.45	0.038
SPC01009806	H-8	0.80	0.098	2.19	2.43	0.035

Table 6-18. Laboratory Measurement of Post-Cooling Dry Drilled Cores from the SHT (Continued)

Sample Identifier	LBNL Identifier	Saturation	Porosity	Bulk Density (g/cc)	Particle Density (g/cc)	Gravimetric Water Content (g/g)
SPC01009807	H-9	0.61	0.099	2.19	2.43	0.027
SPC01009808	H-10	0.82	0.090	2.21	2.43	0.033
SPC01009809	H-11	0.78	0.092	2.20	2.42	0.033
SPC01009810	H-12	0.53	0.105	2.16	2.41	0.026
SPC01009811	H-13	0.38	0.097	2.19	2.43	0.017
SPC01009812	H-14	0.41	0.089	2.21	2.43	0.016
SPC01009890	H-15	0.76	0.090	2.21	2.43	0.031
SPC01009891	H-16	0.87	0.102	2.17	2.42	0.041
SPC01009892	H-17	0.89	0.101	2.18	2.42	0.041
SPC01009893	H-18	0.94	0.093	2.20	2.43	0.040
SPC01009894	H-19	0.83	0.106	2.17	2.43	0.041
SPC01009895	H-20	0.85	0.087	2.24	2.45	0.033
SPC01009896	H-21	0.89	0.082	2.22	2.42	0.033
SPC01009897	H-22	0.73	0.131	2.12	2.44	0.044
SPC01009898	H-23	0.86	0.104	2.17	2.42	0.041
SPC01009899	H-24	0.86	0.099	2.20	2.44	0.039
SPC01009900	H-25	0.82	0.117	2.15	2.44	0.045
SPC01009901	H-26	0.86	0.103	2.20	2.45	0.040
SPC01009902	H-27	0.77	0.143	2.09	2.44	0.053
SPC01009903	H-28	0.88	0.087	2.23	2.44	0.034
Average			0.104	2.18	2.43	
Standard Deviation			0.018	0.05	0.02	

6.4 MINERALOGIC-PETROLOGIC CHARACTERISTICS

The purpose of posttest mineralogic characterization is to support current and ongoing geochemical modeling efforts and measurements of thermal and mechanical rock properties in the thermal test alcove. Geochemical models of the thermal tests are process models that simulate mineral dissolution and precipitation and the evolution of water and gas chemistry within the environment of heating, dryout, condensation, and reflux. Mineralogic data from the SHT will be very useful as interim input for the geochemical model refinement in support of two other in situ thermal tests—the DST and the proposed cross-drift thermal test. The DST, currently in the heating phase, is located within the same alcove and in the same rock subunit as the SHT. Research reported here supports the development of characterization techniques and a background database for the DST and other thermal tests.

Mineralogic characterization of the test block, to be accomplished within the limits of available resources, must be a combination of appropriate macroscopic, low-magnification microscopic, and high-magnification microscopic study. High-magnification studies yield very precise information about very small sample areas. The representativeness of small-sample data is difficult to assess unless the data can be related to rock attributes that are measurable at a larger scale. Observations made at a larger scale, with the aid of low-magnification microscopy, have large associated uncertainties. The combination of small-scale and large-scale observations may

yield results with only order-of-magnitude significance, but such data may be sufficient for current modeling requirements.

6.4.1 Methods

The rock materials available for examination and characterization include core from boreholes that were drilled before the beginning of the SHT, 6- to 10-inch diameter overcore from boreholes that were drilled along the trajectories of original pretest boreholes, and core from new posttest boreholes. Pretest drill boreholes and cores in the SHT block are identified by the prefix ESF (Exploratory Studies Facility)–TMA (Thermal-Mechanical Alcove)–, followed by an abbreviation for the purpose of the borehole (e.g., H for heater, NEU for neutron-logging, MPBX for multi-point borehole extensometers) and a numeric designator. New posttest boreholes have prefixes ESF-TMA-PTC (posttest characterization) followed by a numeric designator. Posttest overcores of pre-test boreholes have the prefix ESF-TMA-PTC- followed by the original borehole designator. For brevity, the ESF-TMA- prefix is omitted in the reporting of results. Distances along wellbores or in cores are measured in feet inward from the collar location on the surface of the test block.

The first challenge in characterizing test-induced alteration is to locate the mostly minute quantities of alteration products by visual inspection and stereomicroscopic examination (up to 500x magnification). An important advantage of the overcores is that they include the original borehole itself, allowing examination of effects of the test on fresh rock surfaces without the complicating presence of natural rock-alteration products. Textural modifications of the rock surface and the presence of new mineral deposits are easier to document and sample on the artificial borehole wall.

The search for mineralogic effects of the SHT concentrated on overcores PTC-MPBX-1, PTC-NEU-2, and PTC-H-1 because the original boreholes were not filled with grout. Wherever grout is present, it is essentially impossible to identify mineralogic products of rock/water interaction. The presence of mineral deposits and stains derived from dripping and ponded water in the PTC-MPBX-1 and PTC-NEU-2 boreholes provided a fortuitous means of orienting the overcores even though the cores were not collected as oriented samples.

At the time posttest characterization began, a comprehensive pretest inventory of test-block mineralogy did not exist. In particular, the fracture mineralogy was not documented. A small set of X-ray diffraction data, collected from pre-test core samples, provided useful guidance for mineral identification (CRWMS M&O 1998a, pp. 12-2 to 12-5). Within the scope of this study, it was not possible to generate a comprehensive database of pre-test mineralogic and textural data. As a consequence, the search for evidence of mineral dissolution and deposition of reaction products on natural fracture surfaces could not be conducted with high confidence in the results. This limitation also dictated that the characterization of test products concentrate on examination of pretest borehole surfaces.

6.4.1.1 Ultraviolet-Light Survey

All of the pre- and posttest core available for study was examined by short-wavelength ultraviolet (UV) illumination. This technique is effective for detecting macroscopically observable calcite, fluorite, opal, some quartz, some microcrystalline silica, and some primary and secondary feldspar at Yucca Mountain. Most natural calcite in the Topopah Spring Tuff fluoresces weakly purple to strong blue. Natural opal commonly fluoresces strongly green; quartz and microcrystalline silica in fractures and cavities (but not in the rock matrix) may fluoresce weakly green (Fabryka-Martin et al. 1997, Table 1). The UV properties of SHT mineralogic products were also investigated for comparison with the natural minerals.

6.4.1.2 Estimation of Fracture Mineral Abundance

A quantitative inventory of natural minerals in the fracture network of the test block addresses a number of data needs. Continuous characterization over meter-scale distances is essential to provide estimated mineral abundances of general validity as input to numerical geochemical models of thermal tests. Collection of data on this scale also documents the existence of variability in the mineral content of the fracture network. Spatial variability in mineral content may reflect hydrological variability that could influence mineral deposition during a thermal test.

A survey of stellerite abundance in macroscopically visible fractures was undertaken for pre-test drill core MPBX-1. Stellerite, a zeolite, was chosen because it can be identified with a high level of confidence based on stereomicroscopic examination; visual-recognition criteria of crystal morphology, luster, and hardness were verified by X-ray diffraction analysis of typical deposits. Zeolites other than stellerite have been identified only in trace quantities in the SHT block (CRWMS M&O 1998a, p. 12-2), also simplifying the task of visual identification. Because stellerite is a major fracture-coating mineral in the SHT test block, quantification of its abundance would be useful input for geochemical modeling.

The survey was conducted piece-by-piece for the MPBX-1 1.75-inch diameter core. For each fracture, the following information was recorded: 1) estimated fracture orientation with respect to the core axis, classified as longitudinal (subparallel to core axis), vertical (perpendicular to axis), or 30°, 45°, or 60° to axis; and 2) whether the fracture lies within the core piece (a complete fracture) or is at an end of the core piece (a half fracture). The percent coverage by stellerite as the outermost fracture coating was estimated by comparison with standard abundance diagrams such as Compton (1962, pp. 332-333). The "fracture area" is conceived of as a space shaped like the fracture but that doesn't correspond either to aperture or to fracture surface area. The observed or calculated coverage of a fracture by stellerite is defined for this estimation as an attribute shared by the opposing surfaces of an intact fracture; the coverage is not equivalent to either the volume or surface area of the stellerite fracture coatings but could be used to help estimate values for these parameters.

Based on the recorded observations, the percent of the fracture area covered by stellerite was calculated in two different ways. In the first formulation, the zeolite content of each fracture was calculated as a percent of the total area of that fracture intersected by the core. Many fractures have other fillings such as crystalline silica beneath the stellerite. The silica completely filled and

sealed the fracture in some places, leaving no room for later stellerite deposition. In such a case, the amount of zeolite coverage observed in the more open portions of the fracture is expressed as a percentage of the total fracture area including the sealed portions. Fracture faces at the ends of core pieces are counted as half fractures and allocated half the surface area they would have if they were located within the core pieces. This accounting convention accommodates the observation that in many cases stellerite coatings on high-angle fractures (i.e., fractures other than vapor-phase partings and stringers) tend to break away cleanly from one fracture surface and adhere to the other surface when a fracture is broken open, either by natural deformation or during a drilling operation. Adjacent millimeter- or centimeter-scale domains of stellerite coatings may alternately adhere to one or the other face of a fracture. If the zeolite coatings split in half parallel to the fracture trace, there would be a problem with double-counting of zeolite coverage. By estimating the stellerite coverage on the matching half-fracture surfaces at the ends of adjacent core pieces, the approximate stellerite content of the original, undisturbed fracture is reconstructed. In cases where the end-fracture surfaces of adjacent core pieces do not match because a small amount of core has been lost, the half-fracture measurement is less than or equal to the original zeolite coverage.

In the second formulation, the same dataset of basic information was evaluated in a way that allocates more importance to the nonsealed, more permeable portions of fractures. For each fracture, the estimated percent stellerite coverage of nonsealed fracture area was treated as an attribute of the entire fracture. Matching fracture faces at the ends of adjacent core pieces count as a single fracture with percent zeolite coverage equal to the higher of the values estimated for each face. This accounting convention accommodates the observation that, especially where zeolite coatings are thin, the zeolite coatings on opposing fracture faces may not be connected to each other. In such a case, choosing the higher value for coverage has the effect of merging the two coatings into one equivalent coating.

The results of this exercise for both formulations of stellerite coverage are presented in Table 6-19 and discussed in Subsection 6.4.2. A formal error analysis was not performed for this exploratory research technique. The principal sources of error lie in estimating the angle of intersection between the fracture and the core axis, in measuring the length of a core piece (applicable only to longitudinal fractures), in estimating the percent zeolite coverage of a fracture, and in estimating the portion of a fracture that is sealed by vapor-phase minerals. The loss of small amounts of core described above is an additional source of uncertainty not related to errors of measurement.

Table 6-19. Stellerite Inventory Estimates, MPBX-1 Fractures

Drill hole and core characteristics:	7 m long, 0.5° dip toward bottom of hole (eastward), core diameter 4.45 cm (1.75 in.)	
Core interval examined:	0 to 4.33 m, minus 0.49 m unrecovered or removed for thermal-mechanical measurements	
	Fracture area or coverage by stellerite	**Percent coverage by stellerite**
Total fracture area examined:	**1572.9 cm² (243.8 sq. in.)**	
Total fracture coverage by stellerite	**355.5 cm² (55.1 sq. in.)**	**23%**
Total longitudinal fracture examined[1]	896.1 cm² (138.9 sq. in.)	
Longitudinal fracture coverage by stellerite	251.6 cm² (39.0 sq. in.)	28%
Total vertical fracture examined[1]	463.2 cm² (71.8 sq. in.)	
Vertical fracture coverage by stellerite	50.3 cm² (7.8 sq. in.)	11%
Core-end vertical fracture	353.3 cm² (54.8 sq. in.)	
Core-end vertical fracture coverage by stellerite	44.4 cm² (6.9 sq. in.)	13%
Intact vertical fracture	110.2 cm² (17.1 sq. in.)	
Intact vertical fracture coverage by stellerite	6.0 cm² (0.9 sq. in.)	6%
Total 45° and 30° fracture examined[1]	212.9 cm² (33.0 sq. in.)	
45° and 30° fracture coverage by stellerite	53.5 cm² (8.3 sq. in.)	25%
Core-end 45° and 30° fracture	125.3 cm² (19.4 sq. in.)	
Core-end 45° and 30° fracture coverage by stellerite	33.7 cm² (5.2 sq. in.)	27%
Intact 45° and 30° fracture	87.8 cm² (13.6 sq. in.)	
Intact 45° and 30° fracture coverage by stellerite	20.0 cm² (3.1 sq. in.)	23%
	Number of fractures	**Average percent coverage by stellerite**
Total number of fractures examined	**75**	
Number of fractures with stellerite	**58**	
Overall average coverage of fractures with stellerite		**31%**
Total number of longitudinal fractures examined[1]	21	34%
Total vertical fractures examined[1]	39	
Total core-end vertical fractures examined	30	15%
Total intact vertical fractures examined	9	82%
Total 45° and 30° fractures examined[1]	15	27%
Total core-end 45° and 30° fractures examined	10	26%
Total intact 45° and 30° fractures examined	5	28%

[1] Longitudinal fractures are subparallel to the core axis, vertical fractures are perpendicular to the axis, and 45° and 30° fractures intersect the axis approximately at the given angles. Some 45° and 30° fractures may be vertical but would have different orientations than "vertical fractures," which are oriented approximately N-S.

6.4.1.3 Scanning-Electron Microscopy

The morphology and semi-quantitative chemistry of reaction products and natural secondary minerals were investigated by scanning-electron microscopy (SEM) and energy-dispersive X-ray spectroscopy (EDX). All samples examined by SEM-EDX were coated with carbon to reduce the buildup of electric charge on the sample surface. The Tracor Northern scanning-electron microscope, model ADEM, equipped with an integrated EDX analytical system, was operated at 20 KeV for imaging and most spectral analysis. The operating voltage was dropped to 15 KeV

for analysis of the smallest mineral deposits to reduce the penetration of the electron beam into underlying materials.

Mineralogic identification by SEM-EDX study employs a combination of morphological and chemical criteria, aided by professional judgment based on mineralogic study of Yucca Mountain. Extremely small crystals of calcite ($CaCO_3$) without well-developed crystal morphology may be difficult to identify because Ca is the only major chemical component of the mineral that can be detected by EDX. The carbonate component consists of elements that are too light for EDX detection. Similarly, fluorine is undetectable, so that calcite of anhedral morphology could not be positively distinguished from fluorite (CaF_2) on the basis of SEM-EDX alone. Other Ca-rich minerals such as gypsum ($CaSO_4$ H_2O) or zeolites, if closely intergrown with calcite, would contribute to a composite EDX spectrum masking that portion of the Ca signal from calcite alone. The provisional criteria for optimal identification of minute calcite crystals by SEM-EDX are an EDX spectrum heavily dominated by the Ca peak and rhombohedral, flat, or elongate crystal morphology (unlike fluorite). Alkali feldspar is identified by the presence of Si, Al, and K as the dominant components of the EDX spectrum, supported if possible by X-ray diffraction analysis.

SEM examination was an important screening technique to select materials for X-ray diffraction analysis because diffraction alone does not necessarily distinguish between natural minerals and reaction products of the heater test. High-magnification images document the locations of mineral deposits in places where no natural deposits would be expected, such as wellbore surfaces. In conjunction with optical examination, SEM-EDX also helped detect the presence of impurities such as physical inclusions of pretest rock or mineral fragments and layers or coatings of fine particulates whose contribution to an X-ray diffraction pattern must be taken into account in the identification of test products.

6.4.1.4 X-Ray Powder Diffraction Analysis

X-ray powder diffraction analysis was routinely used to provide the definitive identification of mineral species. Quantitative analyses utilized the reference-intensity or Chung method (Chung 1974a; 1974b). Although quantitative X-ray diffraction (XRD) methods exist that, with further development, could potentially provide more accurate and precise results, for example, Rietveld analysis (Hill and Howard 1987; Bish and Howard 1988) and full-pattern fitting routines (Smith, Johnson et al. 1987), the Chung method is widely used because it provides reliable results with minimal effort for all sample types. The following descriptions provide background information on the use of this method in the SHT experiment.

Whenever sufficient sample (>400 mg) was available, the internal standard or "matrix-flushing" method of Chung (1974a, pp. 519 to 525) was employed using 1.0-μm corundum as the internal standard. To prepare the samples, a small portion of each sample (~0.8 g) was mixed with 1.0-μm corundum (Al_2O_3) internal standard in the ratio 80 percent sample to 20 percent corundum by weight. This method requires that reference-intensity ratios be determined before quantitative analysis. The reference-intensity ratio is defined as the intensity of the peak of interest for a given phase divided by the intensity of a peak from a standard (usually the 113 reflection of corundum) in a 50:50 mixture (weight ratio) of phase-to-standard (e.g., see Hubbard et al. 1976). The 1:1 ratio of standard to sample was chosen for convenience. Reference-intensity ratios for most

phases found in Yucca Mountain tuffs have been experimentally determined. In the absence of sufficient pure material, reference-intensity ratios for some phases were calculated using the program POWD10 Version 10 (Smith, Nichols et al, 1983). The POWD10 Version 10 is not a qualified software. The QA status of the calculation performed by the software POWD10 Version 10 is to be verified (TBV-3569). Reference-intensity ratio standard mixtures were prepared by mixing 1.0-μm metallurgical grade α-alumina powder (corundum) to each mineral standard, usually in a 50:50 ratio by weight. However, several minerals that exhibit significant preferred orientation effects (for example, mica, chlorite, feldspars) were prepared in a mixture of 20:80 with the resultant reference-intensity ratio values normalized to represent 50:50 mixtures. The increased corundum matrix helps to support the individual mineral particles, thereby producing a more randomly oriented sample mount. Each sample and/or standard was then ground under acetone in an automatic Brinkmann Micro-Rapid mill (fitted with an agate mortar and pestle) for a time greater than 10 minutes. This produced a sample with an average particle size of less than 5 μm and ensured thorough mixing of sample/standard and the Al_2O_3 internal standard. The fine particle size is necessary to ensure adequate particle statistics and to reduce primary extinction and other sample-related effects (Klug and Alexander 1974, pp. 364-376; Bish and Reynolds 1989, p. 78-82). The adequacy of grinding times and techniques has been confirmed utilizing a Horiba CAPA-500 automatic particle-size-distribution analyzer calibrated with Duke Scientific glass microspheres.

Several factors were considered in choosing the peaks for quantitative XRD by the reference-intensity ratio method, including peak intensity (greater intensity provides greater sensitivity), orientation of crystallographic planes, and whether the peaks exhibit overlap with peaks from other phases with which they are likely to coexist. To determine reference-intensity ratio values for each mineral phase, at least six replicate XRD scans were measured on each reference-intensity ratio standard. Mean, standard deviation, and percent relative error were then calculated for each reference-intensity ratio standard. For phases with chemical or preferred-orientation variability (such as feldspar and clinoptilolite), numerous reference-intensity ratio standards were prepared with six replicate runs conducted on each as outlined above. Mean, standard deviation, and percent relative error were then calculated using all data from all reference-intensity ratio standards (Chipera and Bish 1995).

The mineralogy of reaction products from the single-heater test was determined by qualitative or semi-quantitative XRD. Many reaction products could be collected only in milligram quantities, and much of the collected material is irreplaceable because so little was recovered in the posttest coring. Sample-preparation steps, such as the use of internal standards, were minimized or eliminated to prevent loss of material. Water was not used for sample purification or any other purpose to minimize the potential loss of soluble phases. Samples were ground under acetone in a miniature corundum mortar and pestle and deposited onto an off-axis-cut "zero background" quartz plate. All diffraction patterns were obtained on a Siemens D500 X-ray powder diffractometer using CuKα radiation, incident- and diffracted-beam Soller slits, and a Kevex Si(Li) solid-state detector. XRD runs were conducted from 2 to 70° 2θ, with 0.02° steps and counting times of 14 seconds per step, a nominal overnight run. One sample was run for 72 hours to improve counting statistics and detection limits. Mineral identification was accomplished by comparing observed patterns with patterns of pure standards, published patterns from the Joint Committee on Powder Diffraction Standards (JCPDS 1986, pp. 16 to 20, 28, 122, 172, 241, 269, 455, 456, 481, 491, 492, 535 to 537, 770, 771, 787 to 789, 792, 843, 861, 862, 966, 1025 to 1027, 1030 to 1032, 1038, 1039, 1107, 1193, 1194), or calculated mineral patterns obtained from the

program POWD10 (Smith, Nichols et al. 1983). The materials analyzed by XRD are described in Table 6-20, and semiquantitative XRD results are presented in Table 6-21.

6.4.1.5 Detection of Bulk Mineralogic Changes

Bulk mineralogic changes in the rock matrix could be especially important for their effect on rock mechanical and thermal-mechanical properties as well as for their geochemical significance. The detection of mineralogic changes within the matrix requires a different approach than the documentation of new mineral deposition on borehole surfaces. Changes such as the transformation of tridymite to quartz or cristobalite may be effected within the original tridymite crystals, unaccompanied by any precipitation of new quartz or cristobalite deposits (Carlos, Chipera, and Bish 1995, p. 17). The textural and chemical nature of mineralogic change may be investigated by microbeam analysis, whereas the mineralogic-phase changes may be quantified by XRD analysis. Comparisons of before-and-after quantitative mineralogy must be made between populations of analyses. This is necessary because natural variability exists in the mineralogy of the rock matrix and because before-and-after analyses are not made on exactly the same material. A statistically significant and useful determination of differences or similarities between populations can be made only if the XRD analytical errors are known and are smaller than the detected differences. The magnitudes of analytical errors can be reduced by increasing the count times for each step of the XRD analysis.

A statistically defensible study of mineralogic change in the rock matrix will have to be deferred to the DST and cross-drift test, because pretest data for the SHT contained in project documents (CRWMS M&O 1998a, p. 12-2) do not meet the criterion of known analytical error. In addition, resources are not available for quantitative XRD analysis of the posttest rock matrix other than the thermal-mechanical samples. These quantitative XRD data for the thermal-mechanical samples will be the first entries into a mineralogic database that can be used to test hypotheses about variability and changes in the rock matrix.

Quantitative chemical analysis of reactants or alteration products was not feasible within the resource constraints of this study. The minute grain sizes and intimately intergrown textures of both reactants and alteration products also compromise attempts to obtain interpretable results. Some of the mineral phases, both natural and test-induced, would be suitable for microbeam chemical analysis, and the collection of quantitative data should be a goal for ongoing characterization activities associated with the DST.

Table 6-20. Summary Descriptions of Natural-Fracture-Mineral and Test-Product XRD Samples

Sample Identifier	Borehole	Depth (ft)	Description of sample
LANL 3052,p1	H-1	2.3-2.4	Centimeter-scale vapor-phase pocket with zeolite-cemented breccia. Sample is mostly zeolite, with some brecciated tuff.
LANL 3054,p1	H-1	13.0-13.2	Fracture coating, 0.1 mm thick, of microcrystalline zeolite, deposited directly on smooth, planar cooling-joint surface.
LANL 3006,p1	PTC-NEU-2	16.5-17.0	Small white mounds on original borehole surface with minor bedrock impurities, orientation of sample site unknown.
LANL 3004, SSL08p1	PTC-NEU-2	15.5-16.5	Outermost 0.5 mm of original borehole surface, orientation of sample site unknown.
LANL 3003	PTC-NEU-2	12.0-12.1	Cohesive brownish particulate layer peeled from bottom of original pretest borehole.
LANL 3000, SSL02	PTC-MPBX-1	2.9-3.4	Silica scale, maximum thickness 0.2 mm, on bottom of original borehole surface. Impurities of bedrock and brownish particulates.

Table 6-21. Semiquantitative XRD Identification of Natural Fracture Minerals and Test Products*

Sample Identifier	Borehole	Depth (ft)	Smectite	Zeolite	Amorphous	Calcite	Gypsum	Feldspar	Tridymite	Cristobalite	Quartz	Hematite	Other
Natural Fracture Minerals													
LANL 3052,p1	H-1	2.3-2.4	minor	major[1]				minor			major		
LANL 3054,p1	H-1	13.0-13.2	trace	major[1]									
Test Products													
LANL 3006,p1	PTC-NEU-2	16.5-17.0		minor	major[2]	major	minor	minor			trace		minor[3]
LANL 3004, SSL08p1	PTC-NEU-2	15.5-16.5	minor	minor		minor	minor	major		major	major	trace	major al metal
LANL 3003	PTC-NEU-2	12.0-12.1	trace	trace		minor		major	minor	major	major		
LANL 3000, SSL02	PTC-MPBX-1	2.9-3.4	minor		minor?[2]	minor		major	minor	major	major	minor	minor mica

NOTE: *Approximate limits of semiquantitative descriptors, all in weight %: major = >20%, minor = <20%, trace = <1%, "–" = not detected.
[1]Stellerite.
[2]Identified on the basis of XRD and SEM-EDX as opal-A.
[3]Unidentified mineral, possibly a sulfate-bearing phase.

6.4.2 Natural Mineralogy of the Pretest Block

Characterization of pretest mineralogy and mineral textural relations provides the basis for documenting mineralogic changes that resulted from the thermal-chemical-hydrological regime of the SHT. The pre-test mineralogy, including the chemical compositions of the mineral phases, also helps determine the input parameters for numerical simulations of geochemical evolution during the test. This section summarizes the data collected for this study as well as existing Yucca Mountain data that help fill the gaps in pretest mineralogic characterization.

The rock matrix and the fractures and other voids represent distinctly different mineralogic assemblages in terms of both mineral species and mineral abundances. The relative importance of matrix and fracture mineral assemblages with respect to fluid/rock interaction probably varied within the test block. In the dryout zone surrounding the heater, the fluid had to move through the rock matrix before migrating away through the fracture system. Beyond the dryout zone, condensation, fluid accumulation, and reflux would have occurred largely within the fractures during the short period of the heating test.

6.4.2.1 Alkali Feldspar

Alkali feldspar in the tuff of the test block occurs as primary volcanic phenocrysts, as devitrification products in the rock matrix, and as deposits in fractures and other voids. The plagioclase and sanidine phenocryst contents of the Tptpmn and immediately overlying lithophysal rock in drill boreholes Ue25a#1, USW G-1, USW GU-3, and USW G-4 vary from 0.2 to 0.8 and 0.1 to 0.6 volume percent, respectively (Byers 1985, pp. 28-29; Byers and Moore 1987, pp. 52 to 55 and 58 to 59). Secondary feldspar, however, is a major component of the devitrified matrix. The average normalized abundance of feldspar from XRD of five pretest drill cores is 67 wt. percent, almost all of which is in the matrix (CRWMS M&O 1998a, p. 12-2).

The overall abundance of feldspar in fractures and voids is estimated to be much less than that of matrix feldspar. Fracture feldspars in the test block are not well characterized. Based on texture alone, there are several distinct generations of feldspar within the fractures. Vapor-phase feldspar crystals in lithophysal cavities typically are ≤1 mm long. Corroded forms, encrusted by irregular, mostly ≤10-μm K-rich feldspar crystals, are common (Figure 6-15).

Given the importance of fractures as fluid pathways, the void-filling feldspars may play a larger role in fluid/rock interaction than do the feldspars of the rock matrix. Characterization of the fracture feldspars would improve basic understanding of the natural alteration processes that produced the starting material for in situ tests. Information about the compositions, structural states, and crystal sizes and surface areas of the natural fracture feldspars is required to specify the starting conditions for geochemical simulations of the heating tests. In addition, documenting the prevalence of pre-existing natural dissolution textures in feldspars and other phases improves the ability to detect evidence of fluid/rock interaction resulting from a heater test.

6.4.2.2 Zeolites

Stellerite ($CaAl_2Si_7O_{18}$ $7H_2O$) is the predominant zeolite in the test block cores. It is a common fracture-lining mineral and is also present within some areas of highly porous rock matrix adjacent to lithophysae. In open fractures that contain secondary minerals in addition to the zeolite, stellerite typically lies on top of the other minerals. However, secondary-electron images reveal examples in which stellerite is intergrown with and/or overgrown by K-rich alkali feldspar crystals mostly ≤10 μm across (Figure 6-16), accompanied by smectite and silica (sample LANL 3052, Table 6-21).

Estimates of stellerite coverage on the fractures, as described in Subsection 6.4.1.2, suggest that stellerite commonly coats fractures of all observed orientations. Results from the two alternative estimating formulations are very similar for longitudinal fractures (corresponding largely to vapor-phase partings and stringers) and 45° (plus 30°) fractures, but large differences exist for the vertical fractures (Table 6-19). The core-end and intact (within-core) vertical fractures have similar calculated areal coverage by stellerite. The calculated coverage emphasizing unsealed portions of fractures yielded values for core-end fractures that are comparable to the calculated areal coverage of vertical fractures, but the values for intact fractures are much higher. Intact fractures probably owe their survival during the coring operation to fillings of dense vapor-phase crystalline silica that strengthen the fractures, whereas fractures that lack such fillings break open and become the ends of core pieces. Deposition of vapor-phase silica reduced the amount of open fracture so that stellerite could only precipitate in areas with surviving porosity. As a result, the stellerite is highly concentrated in such areas. The calculated difference in stellerite content between separated and intact fractures is a matter of distribution rather than overall percent coverage. This difference could be detected and accounted for because two formulations were used to calculate zeolite coverage. To the extent that stellerite deposition is related to fluid flow, these results suggest that vertical fractures variably sealed by crystalline silica may have received about the same amount of flow at the time of zeolite deposition.

6.4.2.3 Smectite

Smectite clay is a common fracture coating in the test-block cores. Layers of translucent white clay ≤0.1 mm thick are especially common on fracture surfaces without vapor-phase coatings. Clay of unknown purity, removed from a fracture surface of H-1 core, is calcium-rich, with lesser potassium, magnesium, and sodium. Possible clay coatings on K-feldspar crystals (e.g., Figure 6-15) are also Ca-rich. The Yucca Mountain literature contains no chemical analyses of clays from the stratigraphic interval of the SHT; however, smectite from the Tptpln/Tptrv3 boundary (top of the Topopah Spring lower vitrophyre) below the test alcove contains Ca as the dominant exchangeable cation with much smaller proportions of Na and K (Levy 1984, p. 74).

6.4.2.4 Calcite

The presence of calcite in the Topopah Spring Tuff is attributed to at least two distinct processes operating at different times and on different time scales. Early-stage calcite, with distinctive $\delta^{13}C$ and $\delta^{18}O$ values, was deposited at least in part from thermal waters, along with quartz and chalcedony (Paces et al. 1996, p. 29). This deposition probably took place either late in the

cooling of the host tuff or in association with later nearby magmatic events. Early-stage calcite is most prevalent in the nonlithophysal units of the Topopah Spring Tuff, including the middle nonlithophysal zone where the thermal test alcove is located. The remainder of the calcite was deposited incrementally during the last ~12 million years by downward-percolating water of meteoric origin. A large proportion of the calcite present in the ESF near the test alcove, especially the readily observable millimeter- to centimeter-scale crystals, probably was deposited in this way (Paces et al. 1996, pp. 8 and 11).

Microscopic crystals of calcite are also present. Vapor-phase deposits from PTC-NEU-2, 15.5 to 16.5 ft, include a few 20-μm elongate, irregular calcite crystals intergrown with stellerite. Although this material is from posttest core, the textural setting suggests a natural origin of the calcite that is most likely akin to the calcites deposited from thermal waters, described above. These microscopic crystals have not been chemically characterized except as very minor contributors to whole-rock chemical values.

Examination of both pre-test and posttest cores by UV light confirmed that macroscopically observable calcite is rare in an absolute sense and also in comparison with other fracture fillings such as crystalline silica, stellerite, and feldspar. This observation is comparable to the measured abundance of zero for calcite+opal in fractures, combined with some notable occurrences in lithophysal cavities, in the ESF main drift for tens of meters either direction from the entrance to the thermal test alcove (Paces et al. 1997, Figure F3).

6.4.2.5 Crystalline Silica Phases

Crystalline silica phases in the tuff matrix are predominantly cristobalite and lesser quartz (CRWMS M&O 1998a, p. 12-2). The crystalline silica mineralogy of fracture fillings has not been determined for the SHT block. Based on the fracture mineralogy of this stratigraphic interval as determined for a few samples from the DST (CRWMS M&O 1998a, p. 12-13), cristobalite, quartz, and tridymite are all present. Crystalline silica is especially common in, though not restricted to, the low-angle vapor-phase partings and stringers.

6.4.2.6 Opaline Silica

The term "opal-CT" denotes opaline silica with short-range cristobalite and tridymite ordering. The term "amorphous silica," following the usage noted earlier in this report, refers only to opal-A. Because the fracture mineralogy of the SHT has not been systematically characterized, no XRD identification of either opal-CT or opal-A exists for the test block. However, the physical properties and associations of both materials at Yucca Mountain are sufficiently distinctive, as described below, that visual identifications can be made with confidence.

One example of opal-CT was observed in a vapor-phase parting at 12.2 ft. (3.7 m) along the PTC-MPBX-1 overcore. The vapor-phase minerals are coated by stellerite, which is separated by a small gap from overlying calcite and minor opal-CT. The opal-CT is present as ≤1-mm frosty-textured botryoidal aggregates of translucent white silica. The opal fluoresces strongly green in short-wave UV light. Overlying the calcite and opal-CT are coarser calcite crystals, as much as 1 cm across, with included flourescent opaline silica of no discernible form. Although

this is posttest overcore, the calcite and opal are typical of natural deposits (Fabryka-Martin et al. 1997 Table 1; Levy and Chipera 1997, pp. 31-32). The calcite and opal-CT adjacent to the vapor-phase and stellerite layers may have been deposited by thermal waters shortly after the host tuff was emplaced.

Within the Tptpmn, opal-A is a common but not abundant fracture coating associated with calcite deposited by percolating water (Paces et al. 1996, pp. 9 and 38; Paces et al. 1997, pp. D-1 and D-2). No definitive identification of opal-A has been made in the rocks of the SHT block, but trace quantities are likely to be present. Opal-A is typically colorless and transparent, with a globular morphology.

6.4.2.7 Fracture Pathways

The fracture framework of the single-heater test block consists predominantly of vapor-phase partings and cooling joints, both of which are genetically related to the cooling of the host pyroclastic flow. Vapor-phase partings were the earliest fractures formed during the cooling of the Topopah Spring Tuff. Typically, the partings share the low-angle eastward inclination of the welding fabric or flattening foliation. The lateral continuity of the partings can be as much as tens of meters. Less well developed partings of only cm-scale continuity and with slightly steeper inclinations are referred to as vapor-phase stringers, following the terminology of Buesch and Spengler (1998, p. 20). The approximately known orientations of the vapor-phase partings and stringers were used to infer orientations of the drill core and of other fractures in the core. Cooling joints are more steeply inclined than the vapor-phase partings and stringers. The cooling joints and vapor-phase partings together form a three-dimensional network of fracture pathways for fluid migration.

6.4.3 Heater-Test Alteration Products

6.4.3.1 General Description

All available posttest cores and overcores were examined for alteration products of the test. To date, alteration products of the SHT resulting from fluid/rock interaction have been identified in the overcores PTC-NEU-2 and PTC-MPBX-1. The new mineral deposits are of three general varieties, all of which are present in the NEU-2 borehole. This borehole was inclined upward from the surface of the test block, so that the "bottom" of the borehole was above the heater and water that entered the borehole near the bottom flowed downslope along the wellbore. Small white mounds and patches, ≤1 mm across, of gypsum ± calcite ± opal-A are present on natural fracture surfaces and pre-test NEU-2 borehole surfaces near the bottom of the PTC-NEU-2 overcore (Figures 6-17, 6-18, and 6-19). Some of the mounds are concentrated along the traces of very tight fractures intersecting the borehole or fracture surfaces on which the mounds were deposited (Figure 6-17). Glassy scale deposits, mostly silica, are especially abundant on the bottom of the pre-test MPBX-1 borehole (Figure 6-20). Some scale deposits have the form of dried drip marks on the sides of the borehole (Figure 6-21).

Both the mound deposits and the scale fluoresce in short-wavelength UV light. The white mounds and patches generally fluoresce pale purple to white, whereas the scale fluoresces white

to very pale yellow white. The fluorescing minerals most likely are calcite (pale purple) and opal-A (pale yellow white). Fluorescence is the primary basis for recognition of the third variety of alteration product, borehole and fracture coatings that are nearly or completely invisible in ordinary light, even under moderate magnification. Centimeter-scale portions of the pre-test borehole surface from 9.35 ft to the bottom of NEU-2 fluoresce purple white. Under moderate magnification (≤400 x) and ordinary incandescent illumination, these areas have faint whitish crusts or a slightly glazed appearance. Areas of similar fluorescence were observed on the surface of a probably vertical fracture intersecting the horizontal H-1 heater borehole at the 21.3- to 21.9-ft depth. On this fracture surface, the areas of fluorescence are mostly superimposed on clay skins that coat parts of the surface.

Several unusual examples of fluorescence were observed in the PTC-MPBX-1 overcore, in which centimeter-scale pale purple fluorescent haloes surround patches of loose, pearly particulates and brassy metal fragments. The particulates, ≤0.1 mm across, are located on an approximately horizontal natural fracture surface. This material is not natural and probably was introduced during the drilling of the original borehole. The particulates apparently created a local geochemical environment conducive to mineral precipitation, probably of calcite.

6.4.4 Gypsum

The identification of gypsum is based on X-ray diffraction analysis of white deposits from pre-test borehole surface and adjoining fractures in the 15.5- to 16.5-ft interval of PTC-NEU-2. Only one core fragment contained enough material to collect about a milligram for XRD analysis. Smaller deposits on other core pieces are identified as gypsum on the basis of similar crystal morphology observed in SEM images and the Ca+S peaks in the energy-dispersive x-ray spectrum (Figures 6-22 and 6-23).

Although the gypsum deposits in PTC-NEU-2 are definitely products of the thermal test, it is not certain that the chemical constituents were derived from the natural water/rock system. The constituents could have been acquired during fluid interactions with cementitious materials introduced during construction of the test bed or simply present due to general ESF operations. A dust sample collected in the ESF near the entrance of the thermal test alcove in 1996 contained probable trace amounts of gypsum (Bish 1996). If gypsum is encountered as a product of the DST, it would be sensible to perform sulfur isotopic analyses of the gypsum and of cementitious products used in the test facility. Such analyses might show whether introduced materials contributed to the geochemistry of the mineral products.

6.4.5 Opal-A and Other Silica

Opal-A in the white deposits from PTC-NEU-2 was identified by a combination of XRD and SEM-EDX. A broad peak, characteristic of structurally amorphous material, was observed in the XRD pattern from the white deposits. SEM-EDX examination of the deposits revealed the presence of nearly pure silica (Si peak on the EDX spectrum) in portions of the deposits with no discernible crystal form.

Some opal-rich areas of the white mounds contain masses of minute silica tubules projecting up to about 5 μm from the surface of the deposit (Figures 6-24 and 6-25). A few tubules are straight, but most have variably tortuous shapes. Outside diameters of the tubules range from about 0.3 to 0.7 μm, whereas inside diameters vary from less than 0.1 to about 0.3 μm.

Deposits of glassy silica scale ≤0.2 mm thick were observed on the pre-test wellbore surface of PTC-MPBX-1, a horizontal borehole close to the heater borehole. There is a 2- to 3-cm-wide zone of silica deposition along what is inferred to be the bottom of the wellbore surface. In addition, silica scale deposits define elongate drip marks on the inferred lower half of the wellbore surface. The silica scale generally consists of two texturally distinct components. At the base of the deposits are aggregates of platy silica particles about 1 to 5 μm across, silica rods 1 to 2 μm across and up to about 15 μm long, and a few round particles 1 to 2 μm across. Overlying the silica particles are cracked silica sheets about 2 μm thick (Figures 6-26 and 6-27). The siliceous composition of the scale was documented by EDX (Figure 6-28).

Sampling the silica scale for mineralogic analysis was complicated by the small quantities of material and the difficulty in removing the scale from the wellbore surface while minimizing the incorporation of bedrock. Some of the thickest scale deposits were laid down on top of 0.1-mm-thick fine particulate layers, to which the scale adheres. The milligram sample collected for XRD was estimated by visual examination to contain about 20 percent silica scale. Because of the high impurity content, identification of the scale mineralogy on the basis of XRD is very uncertain. Of the silica phases identified in the sample–cristobalite, quartz, tridymite, and opal-A–the opal-A (queried in Table 6-21 because its presence is uncertain) is most likely to be solely a test product. The presence of platy morphology within the silica scale suggests that some of the silica may be crystalline. There are slight similarities between the forms observed in the scale and those of natural quartz and cristobalite in some fractures at Yucca Mountain (Carlos 1985, p. 32; Carlos 1987, p. 22). Resampling and reanalysis of the scale will be necessary to make a more definitive mineralogic identification. The MPBX-1 borehole, where this material was deposited, was heated to more than 150°C during the test. In comparison, the maximum temperature was slightly less than 80°C in the NEU-2 borehole where opal-A without platy morphology was deposited (CRWMS M&O 1997b, pp. 3-3 and I-1). Further mineralogic study would establish whether structural differences exist between the silicas from the two boreholes and whether those differences might be related to the different thermal histories.

6.4.6 Calcite

Calcite has been documented by XRD as a constituent of the white mounds deposited on natural fracture surfaces and on the pre-test borehole surface of overcore PTC-NEU-2 in the 15.5- to 17.0-ft interval. The mineral is also part of the thin, nearly invisible coatings present on the pre-test wellbore surface in the same interval. A thin, brown particulate deposit on the bottom of the wellbore also contains calcite. In overcore PTC-MPBX-1, calcite occurs with silica scale, fine particulate deposits, or other deposits on the pre-test wellbore. Discrete calcite crystals have not been documented by SEM-EDX studies of these deposits, due perhaps to spectroscopic interference from other calcium-rich phases such as gypsum and stellerite, or to overgrowths of other minerals, as well as to time and resource constraints on the number of samples examined.

6.4.7 Other Alteration Products

The small mound-like deposits on the borehole surface of PTC-NEU-2 16.5-17.0 ft contain an unidentified mineral, possibly a hydrous sulfate phase in addition to gypsum. This mineral is a minor component of the tiny sample collected for analysis and could not be uniquely identified even on the basis of a 72-hour X-ray diffraction run. Possible mineral identifications include loweite, $Na_{12}Mg_7(SO_4)_{13}\ 15H_2O$, or other sulfate minerals.

6.4.8 XRD Results for Posttest Thermal-Mechanical Samples

Portions of thirteen posttest core samples collected for laboratory measurements of thermal-mechanical properties were analyzed by quantitative XRD (Table 6-22). The thermal-mechanical testing was performed at SNL, Albuquerque, New Mexico. All of the samples are densely welded, devitrified Topopah Spring Tuff from the middle nonlithophysal zone. The majority of samples contain natural fractures with fillings of vapor-phase minerals (predominantly crystalline silica), stellerite, manganese minerals, and clay.

6.4.9 Discussion

The identities of mineralogic alteration products may be the most important data for geochemical modeling of the SHT and subsequent tests. However, studies of the distribution and textures of the mineral deposits may help address questions about the nature of fluid behavior at the fracture-borehole intersection, the evolution of more concentrated fluids, and the timing of mineral deposition.

6.4.9.1 Concentrations of Evaporite Minerals around Fracture/Borehole Intersections

The observed concentrations of gypsum-calcite-silica along some tight fracture traces intersected by the NEU-2 wellbore are prominent macroscopic attributes of the mineral deposits. The mineral deposits exist at the fracture-borehole intersections presumably because these sites were loci for many episodes of fluid accumulation and evaporation. At least one of these fractures, shown in Figure 6-17, is so tight that it seems unlikely to have acted as a pathway for fluid entering the borehole.

Table 6-22. Quantitative XRD Mineralogy of Posttest Thermal-Mechanical Samples
(weight percent)

Sample Identifier[1]	Smectite	Stellerite	Tridymite	Cristobalite	Quartz	Feldspar	Mica	Hematite	Total
PTC1-A 2.9-A	6±2[2]	1±1	4±1	34±2	2±1	50±7	TRACE[3]	1±1	98±8
PTC1-A 16.8 A	9±3	1±1	3±1	29±2	8±1	48±7	TRACE	TRACE	98±8
PTC1-B 19.0 A	8±2	1±1	3±1	29±2	9±1	50±7	TRACE	---[5]	100±8
PTC2-B 4.1A	6±2	4±1	3±1	32±2	3±1	49±7	TRACE	1±1	98±8
PTC4-A 4.6A	7±2	2±1	1±1	31±2	6±1	51±7	TRACE	TRACE	98±8
PTC4-B 6.8-A	6±2	2±1	3±1	29±2	7±1	49±7	TRACE	TRACE	96±8
PTC4-B 14.8A	7±2	TRACE	3±1	27±2	9±1	50±7	TRACE	TRACE	96±8
PTC4-B 19.8-A	8±2	---	4±1	26±2	11±1	51±7	TRACE	—	100±8
PTC5-B 4.1-A	5±2	TRACE	2±1	29±2	8±1	51±7	TRACE	1±1	96±8
PTC5-B 24.4-A	10±3	---	4±1	30±2	7±1	48±7	TRACE	---	99±8
PTCH1-A 15.6A	8±2	???[4]	3±1	31±2	6±1	49±7	TRACE	---	97±8
PTCMPBX1 14 2-A	5±2	4±1	3±1	30±2	7±1	48±7	TRACE	TRACE	97±8

1 Sample Identifiers are presented exactly as they appear on the sample containers received from Nancy Brodsky, SNL.
2 Errors are conservative 2-σ values.
3 "TRACE" signifies a phase present at a level below 0.5 weight percent.
4 "???" signifies a phase believed to be present
5 "—" signifies that a phase was not detected

A basic conceptual model of fluid migration during a heating experiment (e.g., Sonnenthal, Spycher, Apps, and Simmons 1998, pp. 9-22) postulates the formation of a dryout zone surrounding the heat source, with the boiling front moving outward from the heater as the experiment progresses. A condensation zone forms beyond the boiling front, and a portion of the condensate flows downward back to the boiling front to rejoin the cycle of evaporation, transport, and reflux. In this scenario, the boiling zone is the preferred location for evaporite deposition because it continues to receive reflux water containing sulfate derived from rock surfaces and from mixing with ambient pore fluids. Mineral deposition would also occur in the vicinity of the boiling zone during the cool-down phase of a test as the boiling front recedes while reflux water is still migrating downward and possibly redissolving previously deposited salts. Although research has been unable to document such deposition, there is no basis to suppose that it has *not* occurred; however, the observed deposition of gypsum and other salts well into the condensation zone was not an expected outcome. Evaporated water driven away from the heater and into the condensation zone should be essentially devoid of solutes and would not acquire a high concentration of dissolved sulfate from interaction with rock or pore fluids unless evaporation could occur. Evaporation in the vicinity of NEU-2 would seem to have been an unlikely event during the heating phase, considering that about 20 liters of liquid water were cumulatively recovered from the packed-off portion of this borehole over the course of the test (Buesch and Spengler 1998, p. 22). The water collected from the packed-off borehole is much more dilute than J-13 water (saturated-zone water from the Topopah Spring Tuff east of Yucca Mountain), consistent with the interpretation that the water is condensate which had interacted for a relatively short period of time with rock-matrix and fracture minerals (CRWMS M&O 1997b, p. 5-51). Even if some evaporative deposition did occur during the test, the water flowing down the borehole would likely have dissolved previously deposited salts.

The most likely period for deposition might have been during the cool-down phase when boreholes began to equilibrate with drier air entering the test block from the rest of the tunnel and alcove system. Preferential deposition along the traces of tight fractures may have occurred because water was slightly drawn into the fracture and adjacent rock matrix, where it evaporated and deposited its solutes.

6.4.9.2 Origin of Silica Tubules

The silica tubules in opal-A deposits are distinctive structures that have not been observed in natural opal-A at Yucca Mountain. Tubular structures of macroscopic dimensions in mineral deposits are widely recognized even in popular literature on caves, springs, and deep-ocean hydrothermal sites. The submicrometer-scale tubules from the SHT are unlikely to have formed from dripping water or fluids streaming through an orifice. The potential roles of water vapor or condensed steam are difficult to assess. Maximum bottom-hole temperatures in NEU-2 were slightly below 80°C, although the bottom was only about half a meter away from the boiling front at the end of the heating phase (CRWMS M&O 1997b, pp. 3-3 and I-1). Vapor or steam could have entered the borehole carrying entrained fine mineral particulates to be deposited eventually on the borehole surface. There is no textural evidence, however, that vapor or steam were discharging into the borehole through minute pores at the locations where opal tubules were formed. It is therefore difficult to envision that vapor or steam played a direct role in the formation of the tubules.

A mechanism to form the tubules from liquid water may have involved capillary imbibition. The tubules may have formed by capillary suction of silica-bearing water into microscopic pores within the masses of amorphous silica deposited on the borehole surface. Some pores, without appended tubules, are visible in the opal mass of Figure 6-24. Evaporation at the pore openings may have led to the gradual deposition of new silica outward from the original opening, with more water being drawn into the developing tubule. As described above, evaporative mineral deposition may have occurred mostly during the cool-down phase of the experiment.

6.4.10 Conclusions

Calcite, gypsum, and opal-A were identified as the principal alteration products of the SHT. These minerals were observed on pretest borehole surfaces and in natural fractures adjacent to the boreholes. The distribution and textural attributes of the mineral deposits in a borehole within the condensation zone may be most compatible with mineral precipitation during the posttest cool-down period. The amounts of secondary minerals available from posttest overcores were minimally adequate to identify the mineralogic test products. Given the combined limitations of time constraints on posttest analysis and availability of suitable core, a three-dimensional distribution of mineral deposition could not be established. If a database on the three-dimensional distribution of secondary minerals were constructed, it would be possible to test whether attributes of mineralogy or mineral textures correlate with the geometries of the dryout and condensation zones. Evidence of reflux might also be detectable with a more complete investigation of mineral deposition in fractures.

There are indications that the mineralogic products of the SHT may reflect an influence of materials introduced during drilling operations. Introduced materials such as gypsum could alter the sulfate budget of the water/rock system. The magnitude of this influence is probably small, but additional documentation would be required to increase confidence in this assessment. Existing geochemical models of the test do not account for introduced materials that may participate as reactants or catalysts.

Based on the experience gained from mineralogic studies of the SHT, several recommendations can be made to improve the mineralogic characterization of the DST and cross-drift thermal test. Above all, it is imperative that all available pre-test drill core be archived for future study because there is no way to predict which boreholes will become centers of unusually abundant geochemical activity. Characterization of fracture mineralogy is especially important because most of the water/rock interaction that results in mineral deposition probably occurs in the fractures. Because of the unpredictable distribution of hydrogeochemical activity during the course of a test, characterization of pretest core should be regarded as an ongoing process. The bulk of pre-test mineralogic study may be performed during the early stages of a test, but additional, more specific characterization should always be performed during the posttest analysis stage. The full value of posttest analysis will not be realized unless this is done.

UV study of fracture and borehole surfaces in both pre- and posttest core shows considerable promise as a quick tool for mapping the distribution of alteration products. The present study established that deposits containing calcite and opal fluoresce in a variety of colors. For the full

value of this tool to be realized, additional characterization of fluorescing mineral deposits will be required so that fluorescent behavior can be correlated with specific minerals.

6.4.11 Status of data

The relevant notebook for this work is LA-EES-1-NBK-98-001. The records package containing traceability information is LA-EES-1-TIP-98-007. Data acquired as part of this activity and presented in this report were developed under YMP (Yucca Mountain Site Characterization Project) QA procedures. All data presented in this report are to be considered unqualified at this time, because of a Corrective Action Report (CAR #2).

The YMP quality assurance procedures governing work presented here are LANL-YMP-QP-03.5, R8 (*Documenting Scientific Investigations*), LANL-EES-DP-03, R5 (*Petrography Procedure*), LANL-EES-DP-16, R5 (*Siemens X-Ray Diffraction Procedure*), LANL-EES-DP-56, R4 (*Brinkman Automated Grinder Procedure*), and LANL-EES-DP-101, R3 (*Sample/Specimen Collection, Identification, and Control for Mineralogy-Petrology Studies*).

XRD data were obtained on the Los Alamos National Laboratory (LANL) EES-1 Siemens D500 X-ray powder diffractometers using the commercial software package DIFFRAC5000, LANL YMP release label is DIFFRAC5000-01-00-00. Integrated peak intensities were obtained using the program GRAPHINT, LANL YMP release label is GRAPHINT-01-00-00. QUANT (version 5.04) had been qualified under the software QA requirements of the earlier QA program which included auxiliary software. The LANL YMP release label is QUANT-01-00-00. The latest modifications to QUANT (producing version 5.05) were conducted in accordance with the QA program emplaced January 31, 1994 and are documented in notebook TWS-ESS-1-1-92-03, pages 54 to 70.

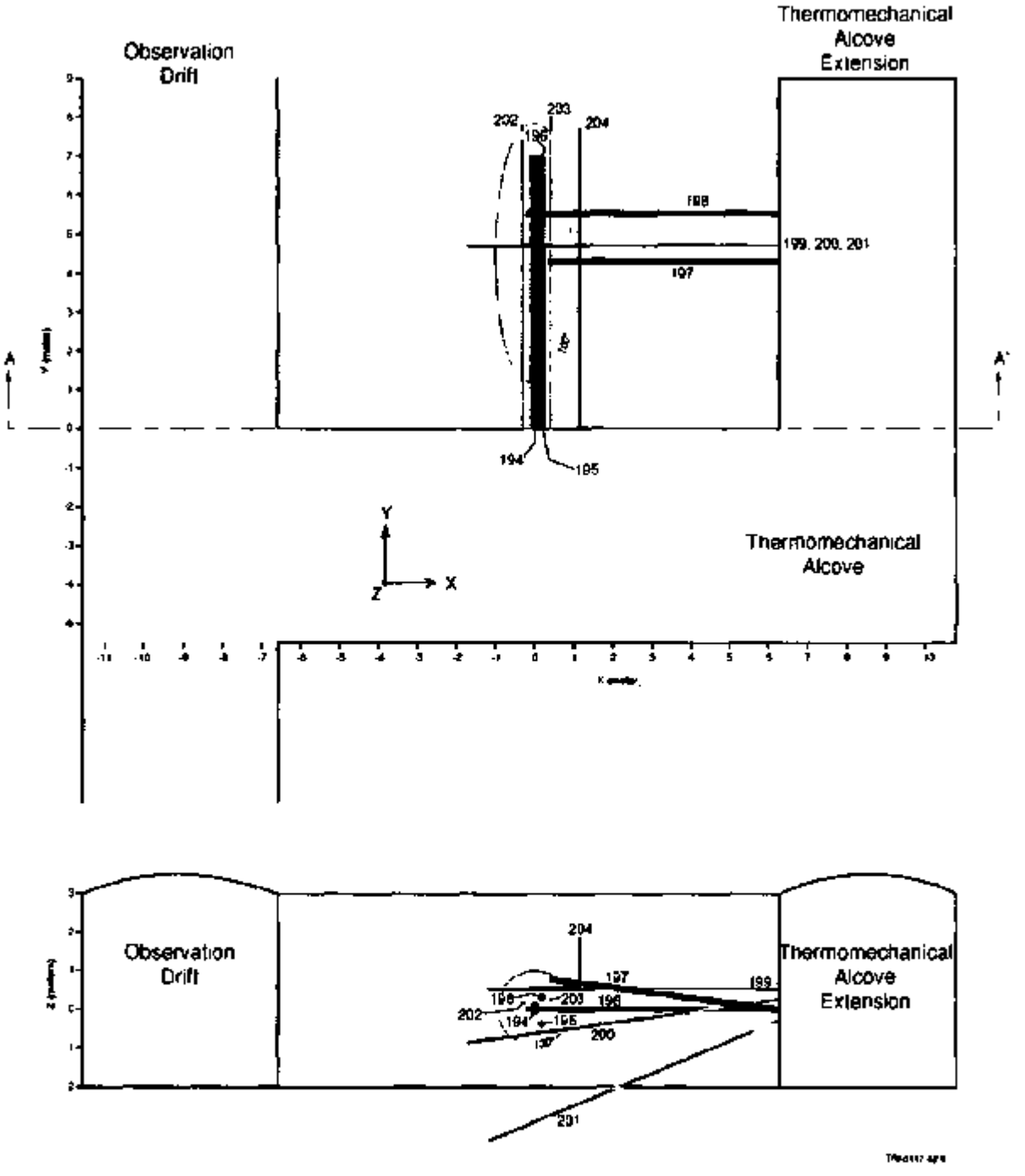

NOTE: 100°C Isotherm Estimated from Thermal Data at the End of the Heating Cycle.

Figure 6-1. Posttest Overcores and New Boreholes in SHT Block, (Top) Plan View and (Bottom) Elevation A-A'

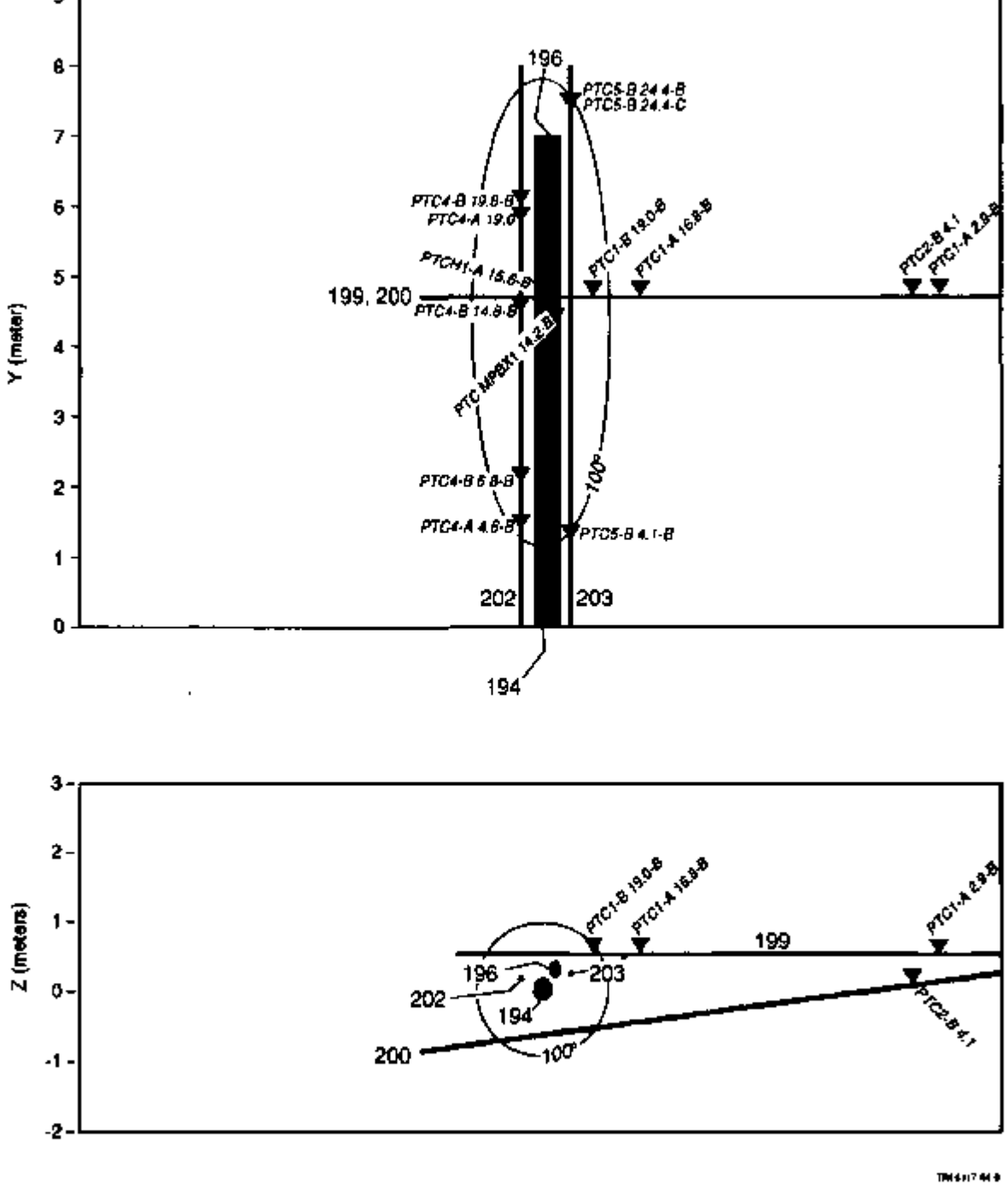

NOTE: 100°C isotherm estimated from thermal data at the end of the heating cycle.

Figure 6-2. Approximate Original Locations of Thermal Expansion Test Specimens

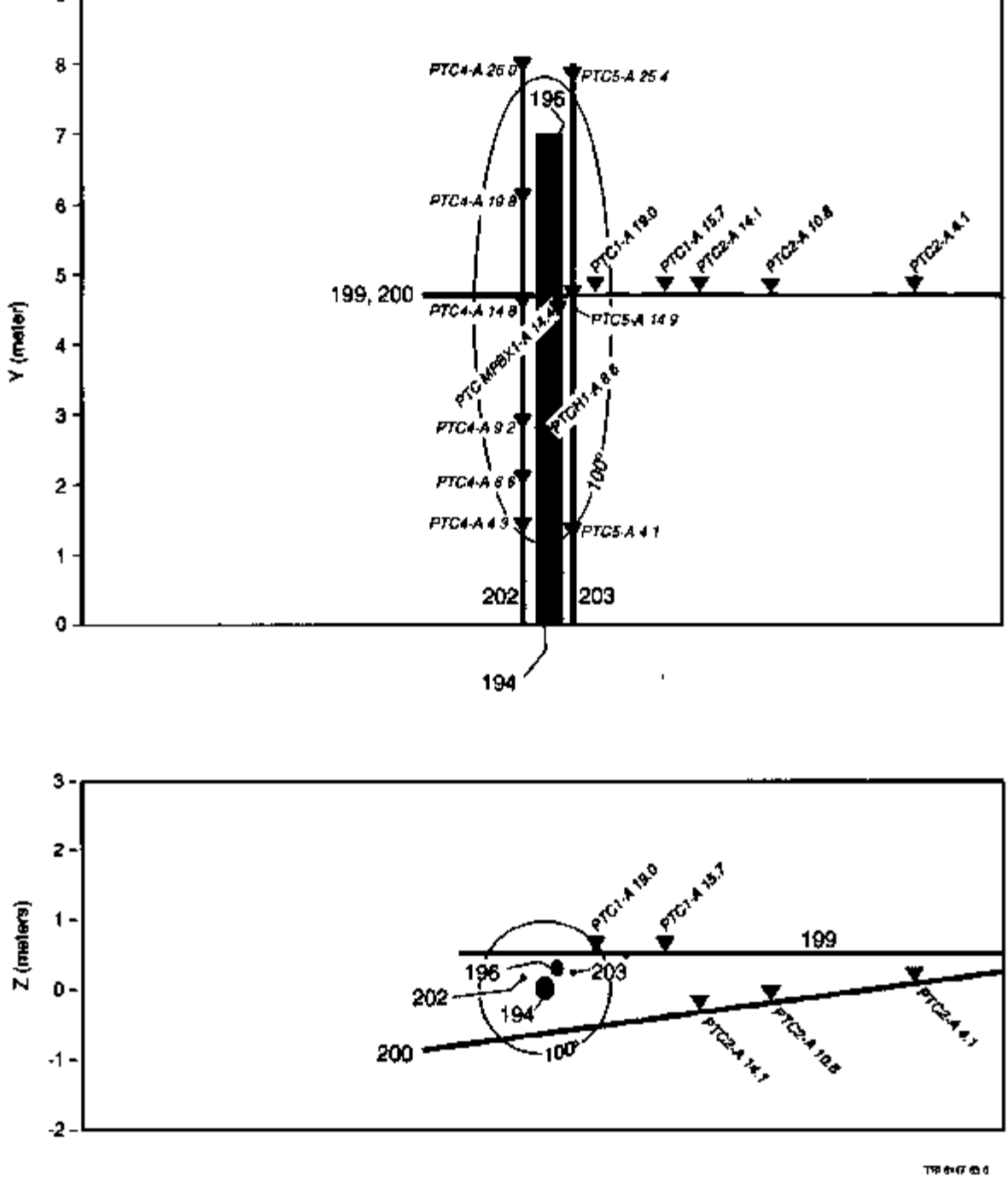

NOTE: 100°C isotherm estimated from thermal data at the end of the heating cycle.

Figure 6-3. Approximate Original Locations of Thermal Conductivity Test Specimens

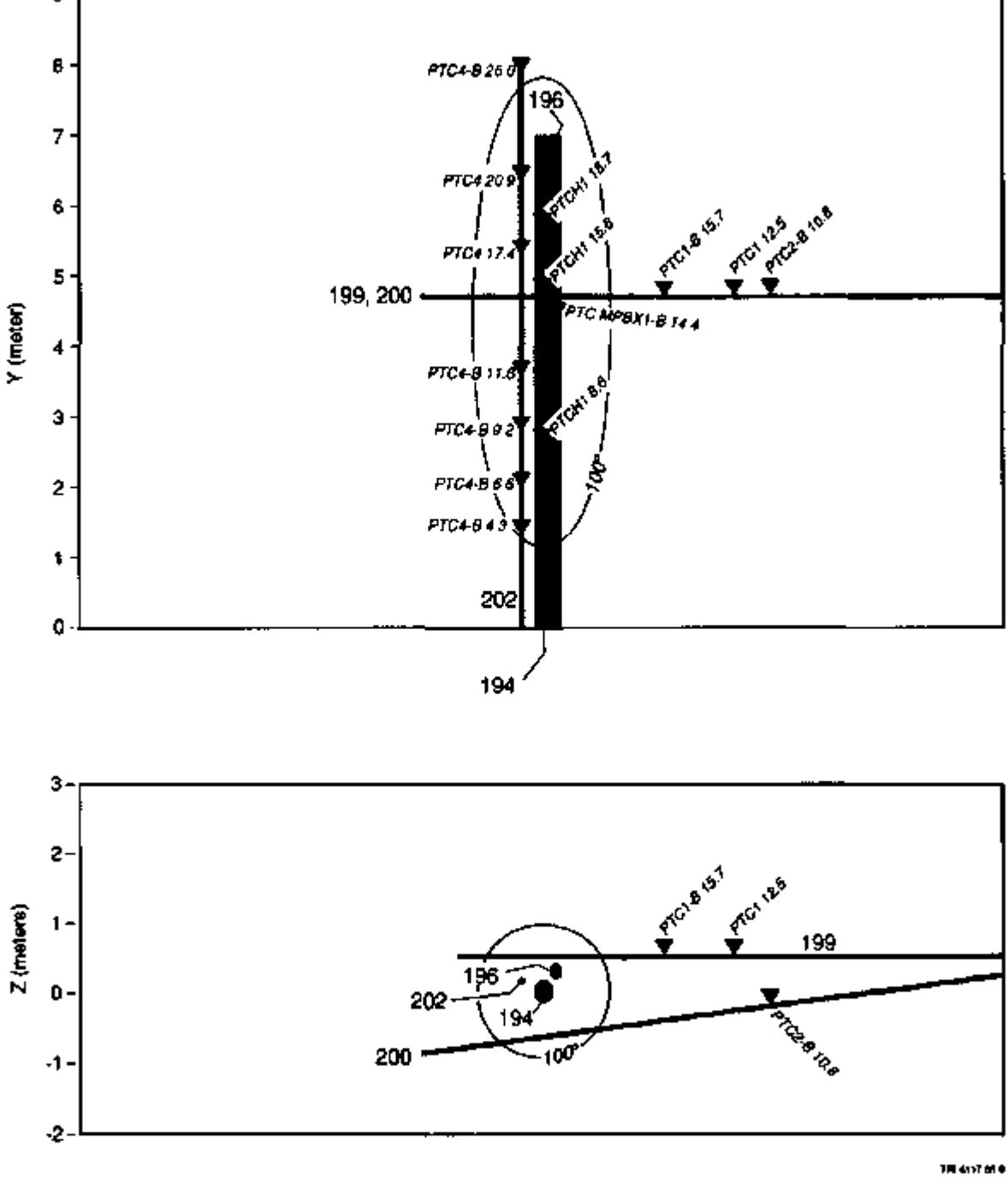

NOTE: 100°C isotherm estimated from thermal data at the end of the heating cycle.

Figure 6-4. Approximate Original Locations of Mechanical Test Specimens

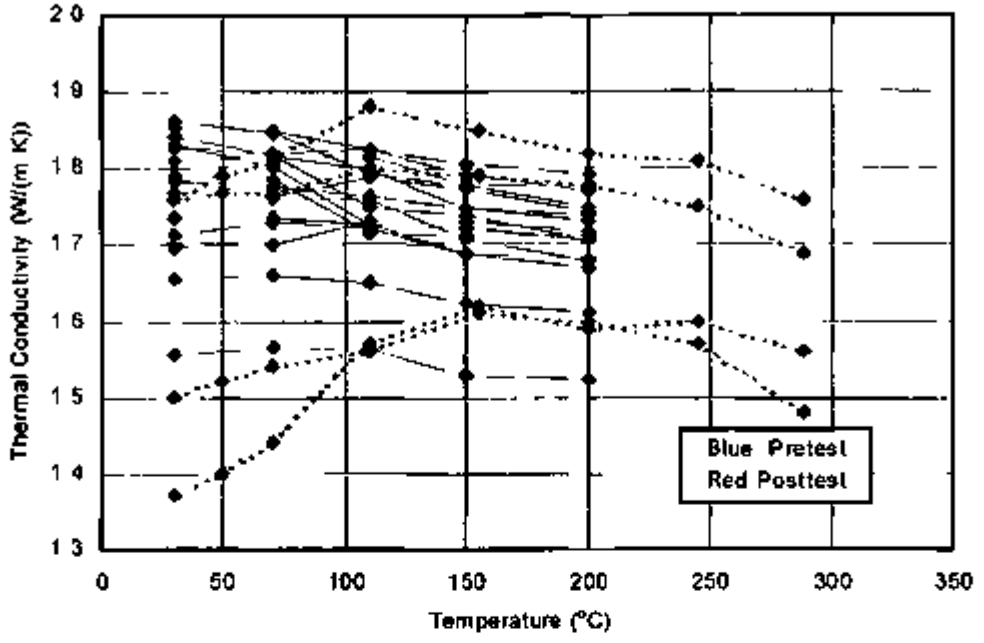

Figure 6-5 Thermal Conductivities Measured during Heating for Pretest and Posttest SHT Characterizations

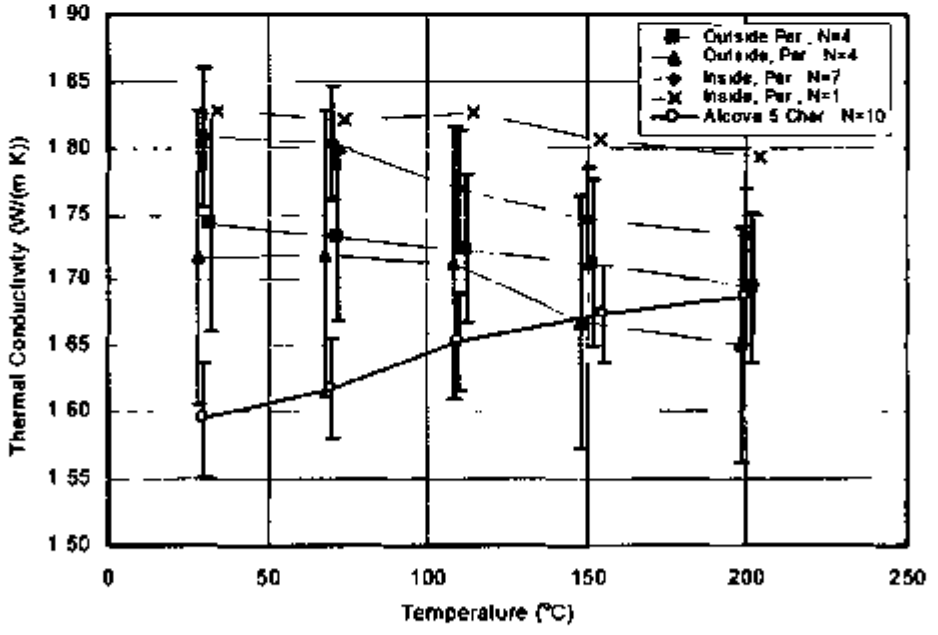

NOTE "Per" implies specimen orientation was perpendicular to heater, "Par" implies specimen was parallel to heater Additional relevant Alcove 5 data are shown for comparison N = number of specimens tested

Figure 6-6. Thermal Conductivities Measured during Heating of Posttest SHT Specimens Categorized by Orientation and Location Relative to Approximate Maximum Extent of the 100°C Isotherm

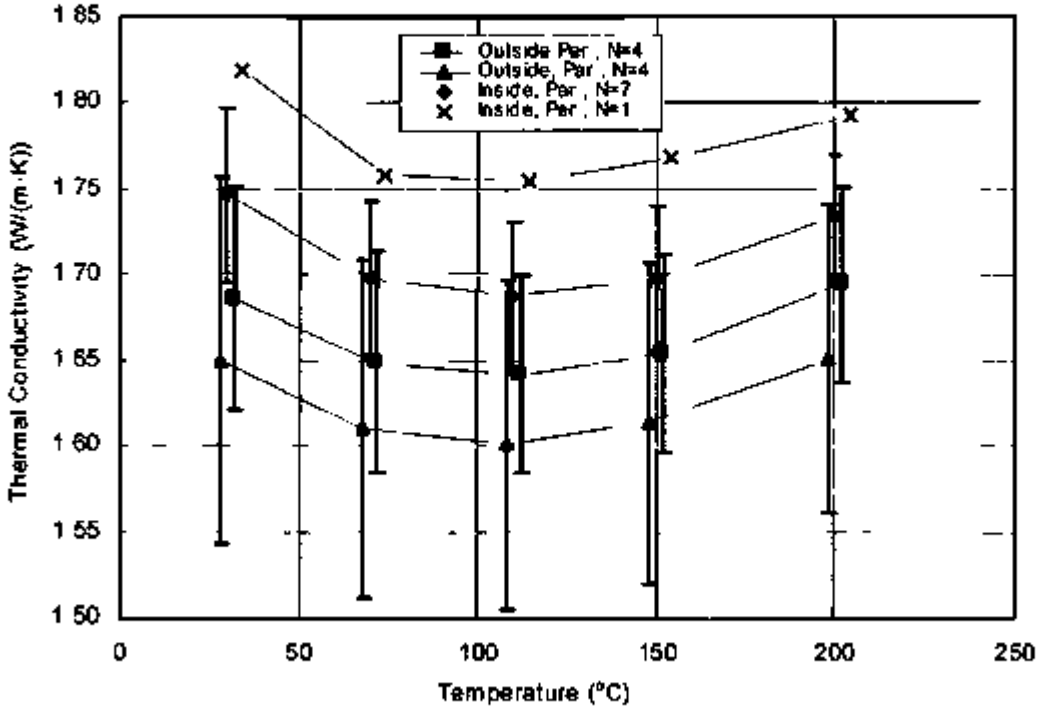

NOTE N = number of specimens tested "Per" implies specimen orientation was perpendicular to heater. "Par" implies specimen was parallel to heater

Figure 6-7 Thermal Conductivities Measured during Cooling for Postlest SHT Specimens Categorized by Orientation and Location Relative to Approximate Maximum Extent of the 100°C Isotherm

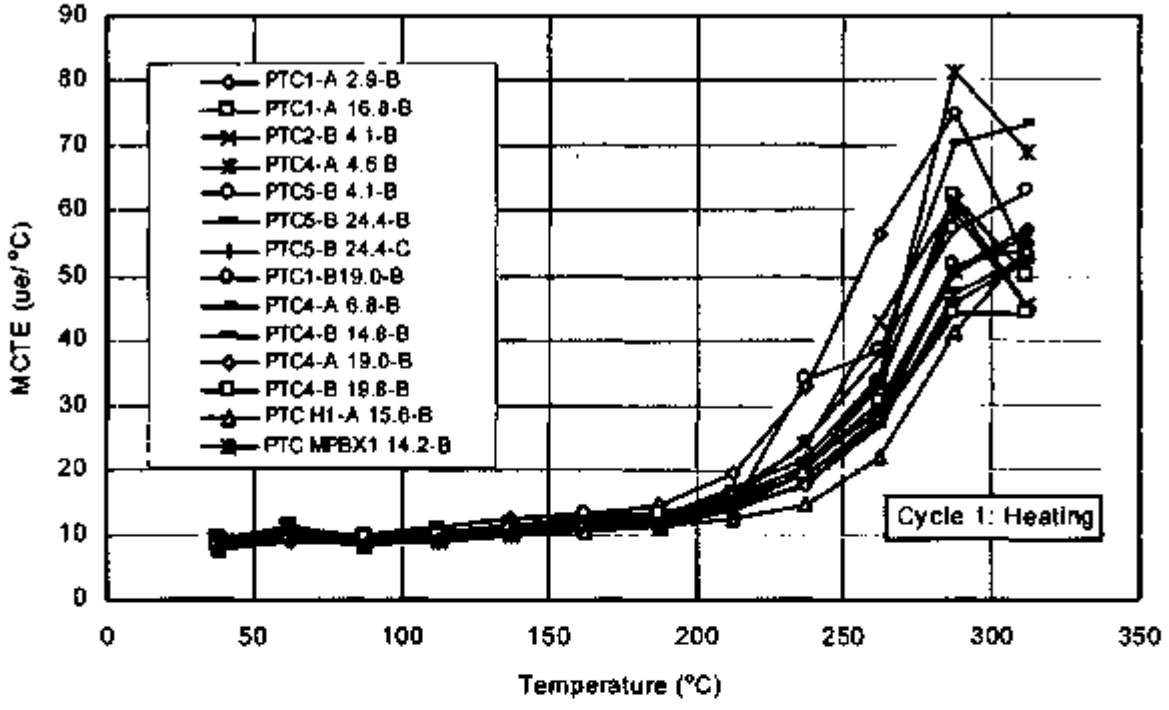

NOTE: Each specimen is plotted individually. Specimens from within the approximate maximum extent of the 100°C isotherm are plotted in red; the remaining specimens are plotted in blue.

Figure 6-8. MCTE vs. Temperature during First Heating for SHT Posttest Characterization

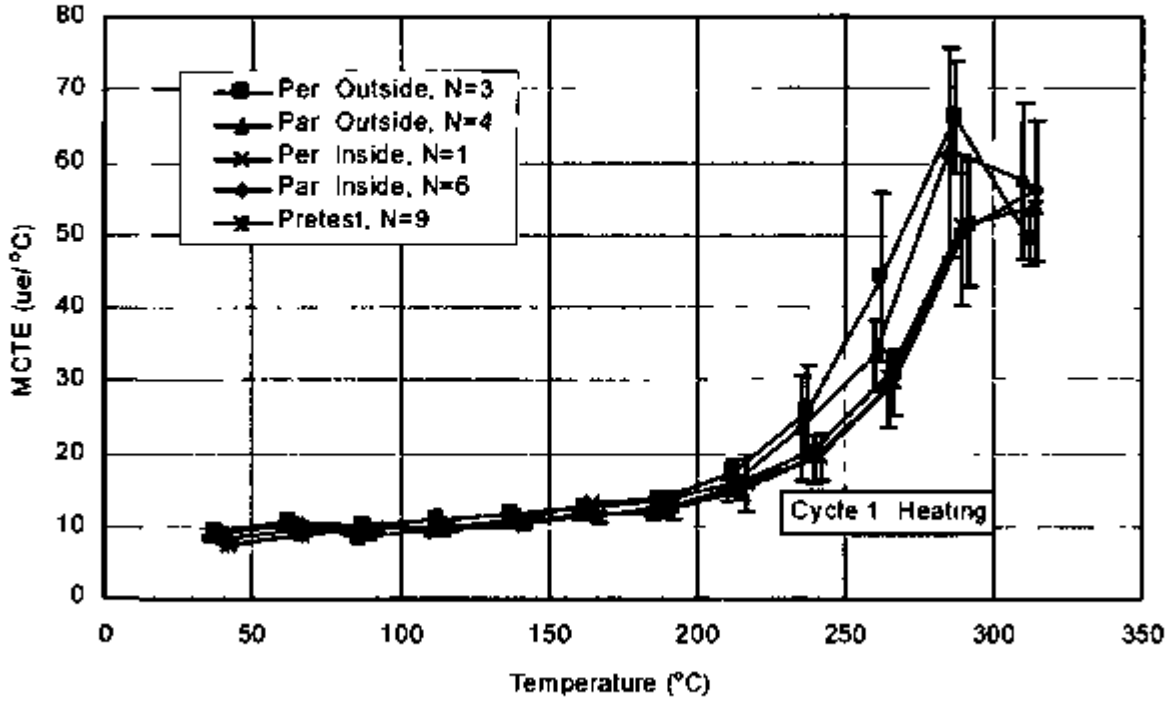

NOTE Data are grouped according to orientation and location (inside or outside) with respect to the approximate maximum extent of the 100°C isotherm "Per" implies specimen orientation was perpendicular to heater, "Par" implies specimen was parallel to heater Pretest characterization data are also given The legend provides the number of specimens tested Error bars represent ± one standard deviation

Figure 6-9 MCTE vs. Temperature during First Heating for SHT Posttest Characterization, Grouped According to Orientation and Location

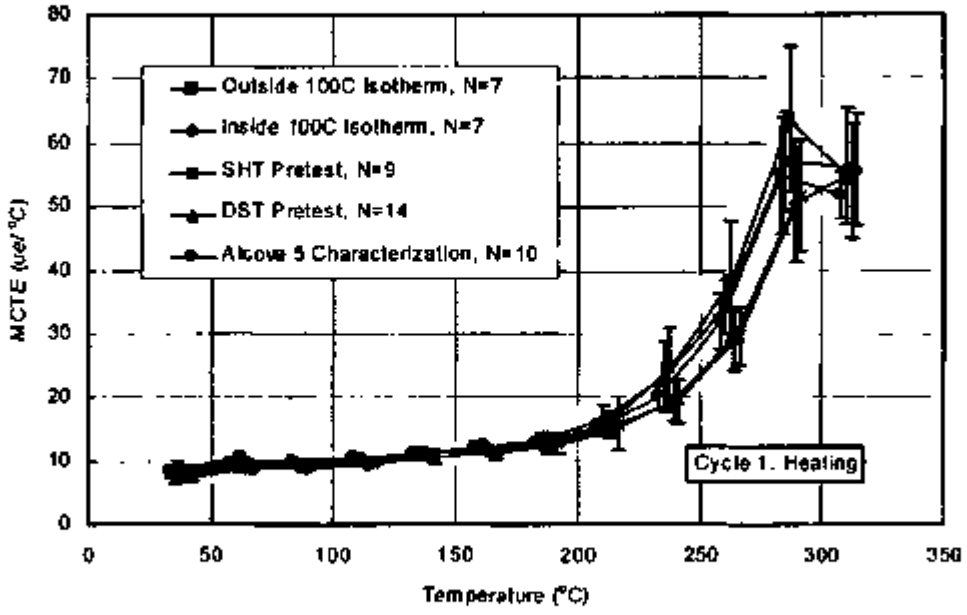

NOTE: The legend provides the number of specimens tested. Error bars represent ± one standard deviation.

Figure 6-10. MCTE vs. Temperature during First Heating for All Alcove 5 Data Sets

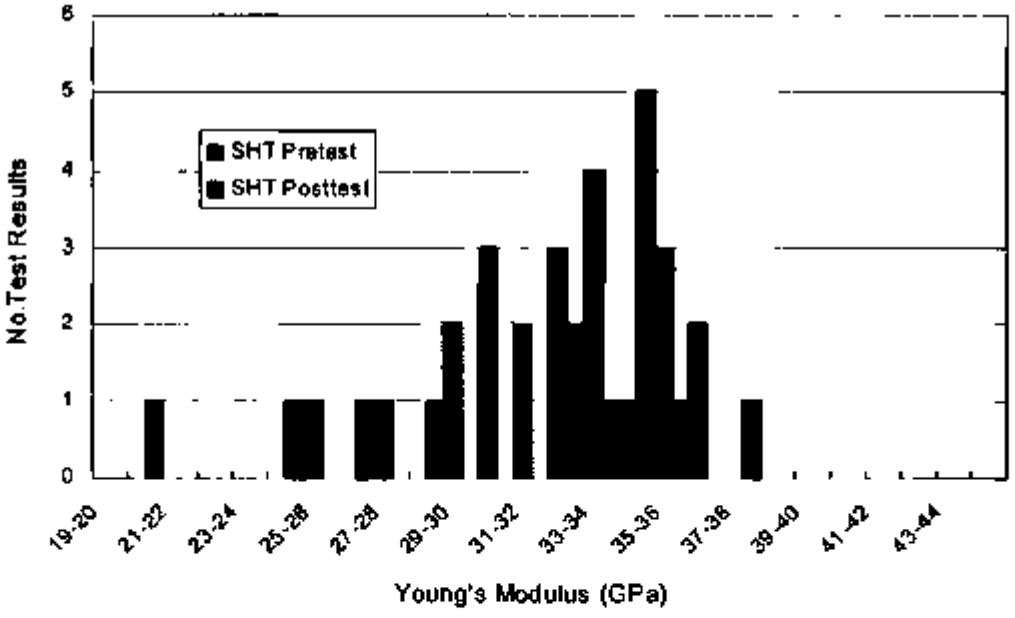

Figure 6-11. Distribution of Young's Modulus Values Obtained for Pretest and Posttest Specimens from the SHT Block

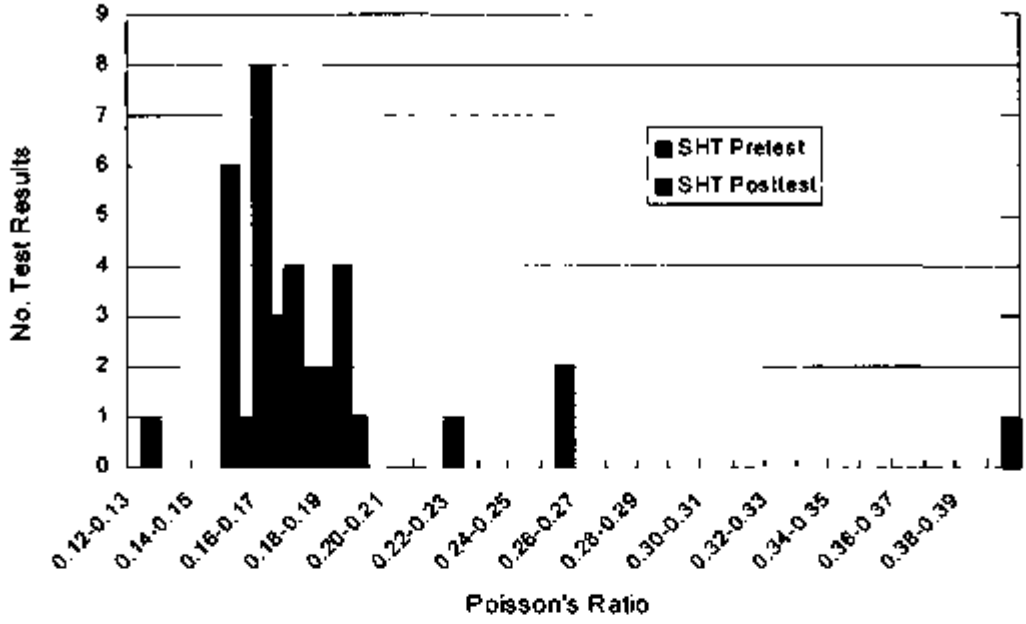

Figure 6-12. Distribution of Poisson's Ratio Values Obtained for Pretest and Posttest Specimens from the SHT Block

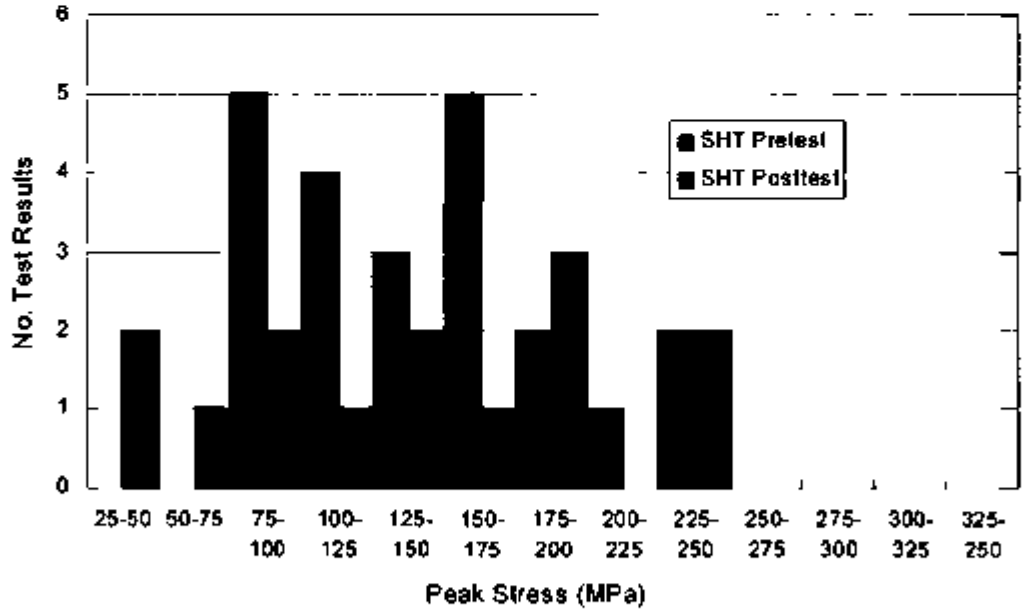

Figure 6-13. Distribution of Peak Stress Values Obtained for Pretest and Posttest Specimens from the SHT Block

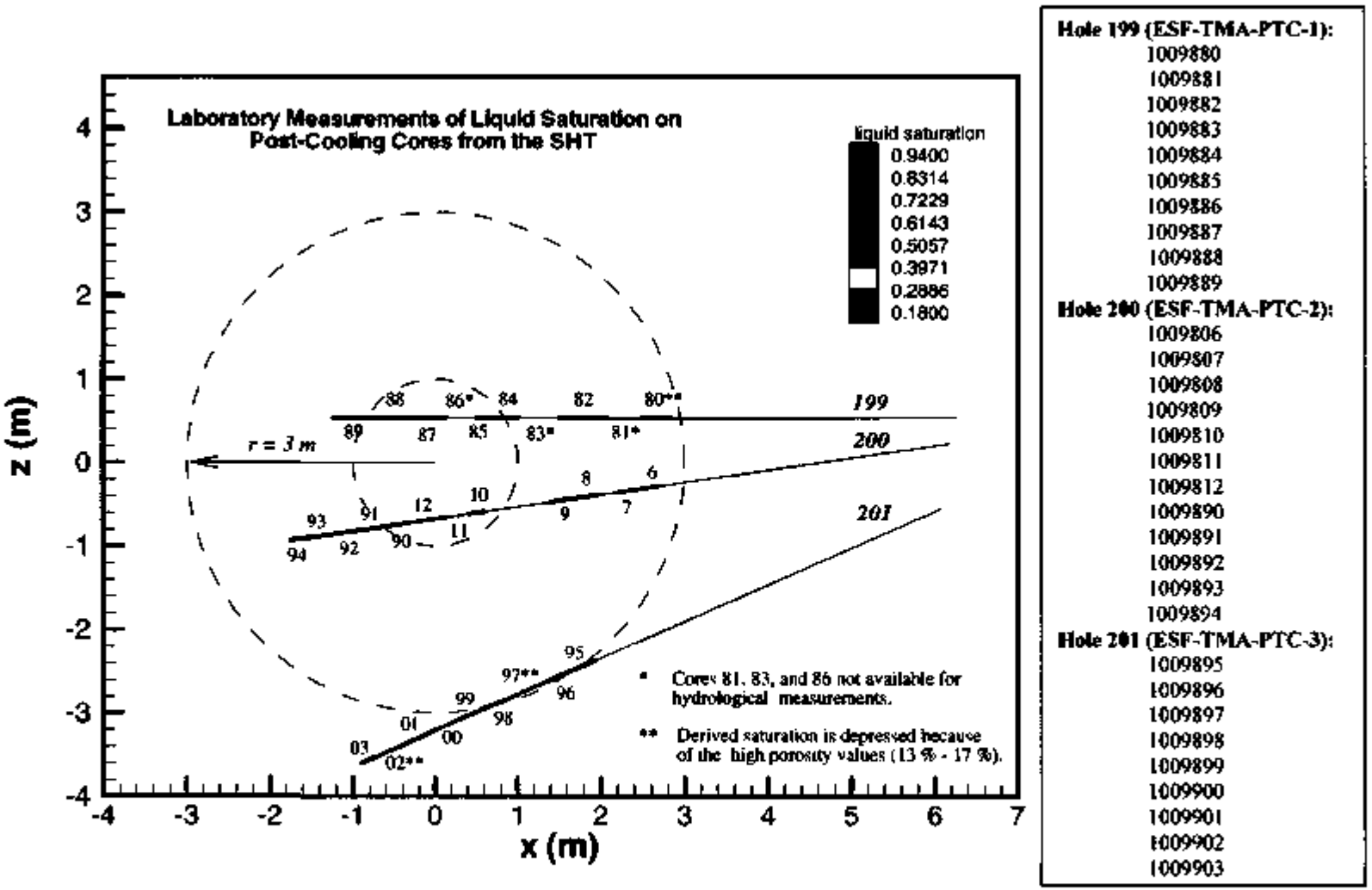

Hole 199 (ESF-TMA-PTC-1):
1009880
1009881
1009882
1009883
1009884
1009885
1009886
1009887
1009888
1009889

Hole 200 (ESF-TMA-PTC-2):
1009806
1009807
1009808
1009809
1009810
1009811
1009812
1009890
1009891
1009892
1009893
1009894

Hole 201 (ESF-TMA-PTC-3):
1009895
1009896
1009897
1009898
1009899
1009900
1009901
1009902
1009903

NOTE: The inner dashed circle indicates the extent of the dryout zone, the annulus defines the wetting region. The two dashed circles, with radii of 1 m and 3 m, respectively, from the heater, delineate the anticipated drying zone (approximately within the inner circle), and the wetting region (between the two circles).

Figure 6-14. Liquid Saturation of Cores from Boreholes 199, 200, 201, Dry-Drilled After the Cooling Phase of the SHT

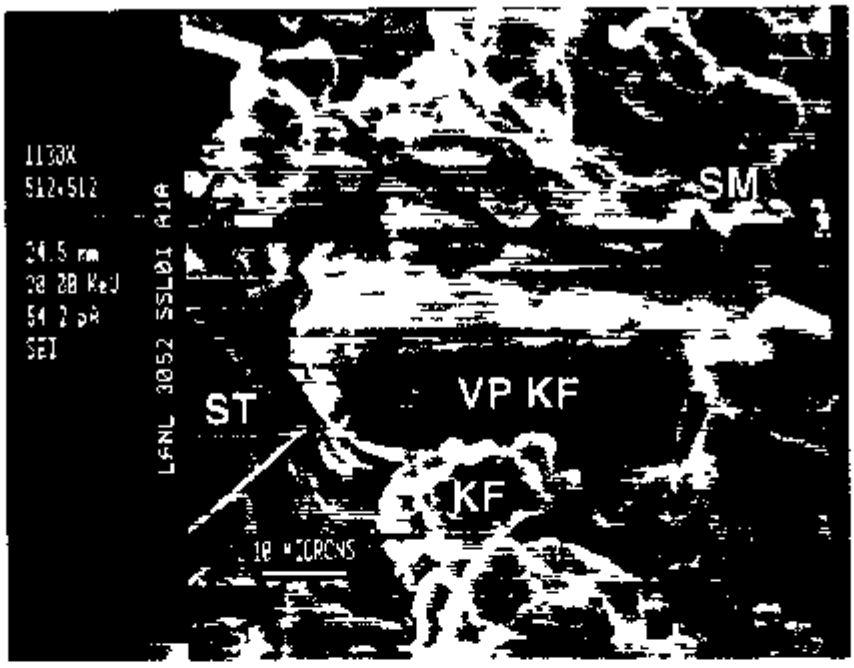

NOTE Secondary-electron image, ESF-TMA-H-1 2 3-2 4 ft

Figure 6-15 Corroded Vapor-Phase Feldpsar (VP KF), Overgrown by Younger Alkali Feldspar (KF), with Smectite Overgrowths (SM) and Stellerite (ST)

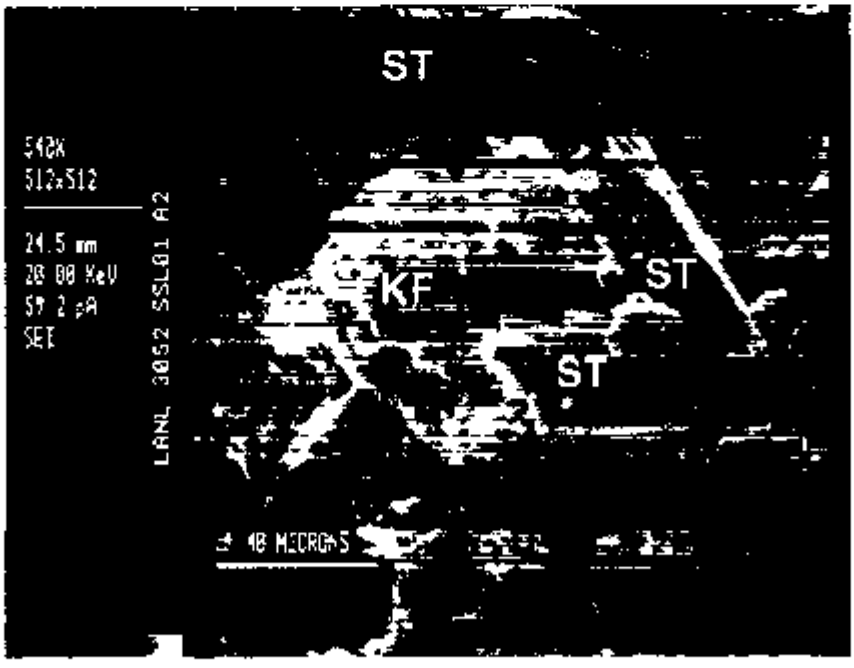

NOTE Secondary-electron image, ESF-TMA-H-1 2 3-2 4 ft

Figure 6-16 Stellerite (ST) with Intergrowths and Overgrowths of Alkali Feldspar (KF)

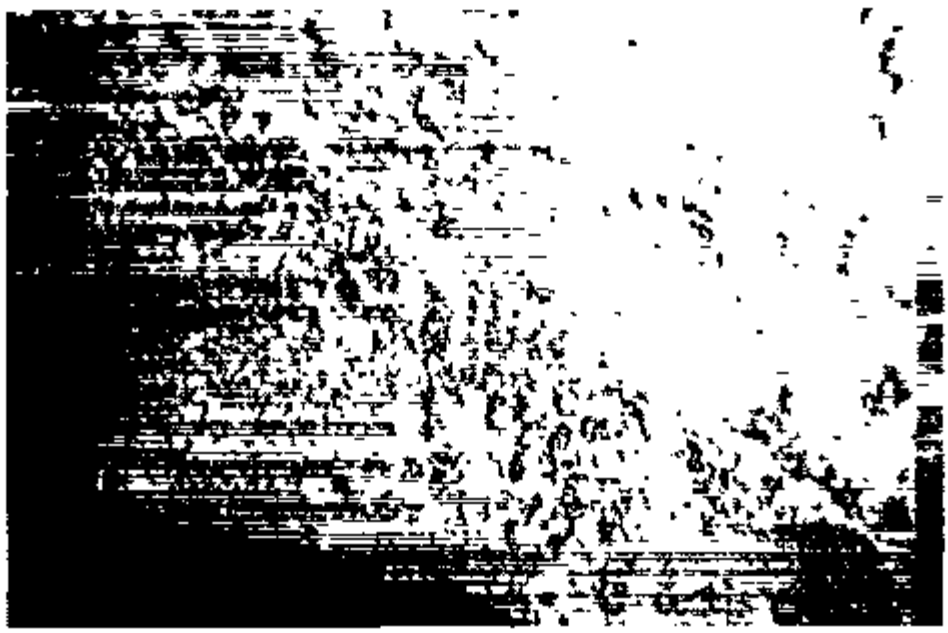

NOTE ESF-TMA-PTC-NEU-2, 15 5-16 5 ft Note the concentration of deposits in a line along the intersection with a tight fracture Long dimension of image is 1 7 cm

Figure 6-17 White Mound Deposits on Fracture Surface

NOTE ESF-TMA-PTC-NEU-2, 15 5-16 5 ft

Figure 6-18 Secondary-Electron Image of White Mound Deposits on Fracture Surface

NOTE ESF-TMA-PTC-NEU-2, 15 5 to 16 5 ft Long dimension of image is 1 7 cm

Figure 6-19 White Patchy Deposits on Pretest Borehole Surface

NOTE ESF-TMA-PTC-MPBX-1, 2 9 to 3 4 ft Long dimension of image is 1 7 cm

Figure 6-20. Silica Scale on Pretest Borehole Surface

NOTE ESF-TMA-PTC-MPBX-1, 2 9 to 3 4 ft Long dimension of image is 1 7 cm

Figure 6-21 Drip Mark of Silica Scale on Side of Pretest Borehole

NOTE: ESF-TMA-PTC-NEU-2, 15.5 to 16.5 ft.

Figure 6-22. Secondary-Electron Image of Gypsum-Rich Portion of White Mound Deposits

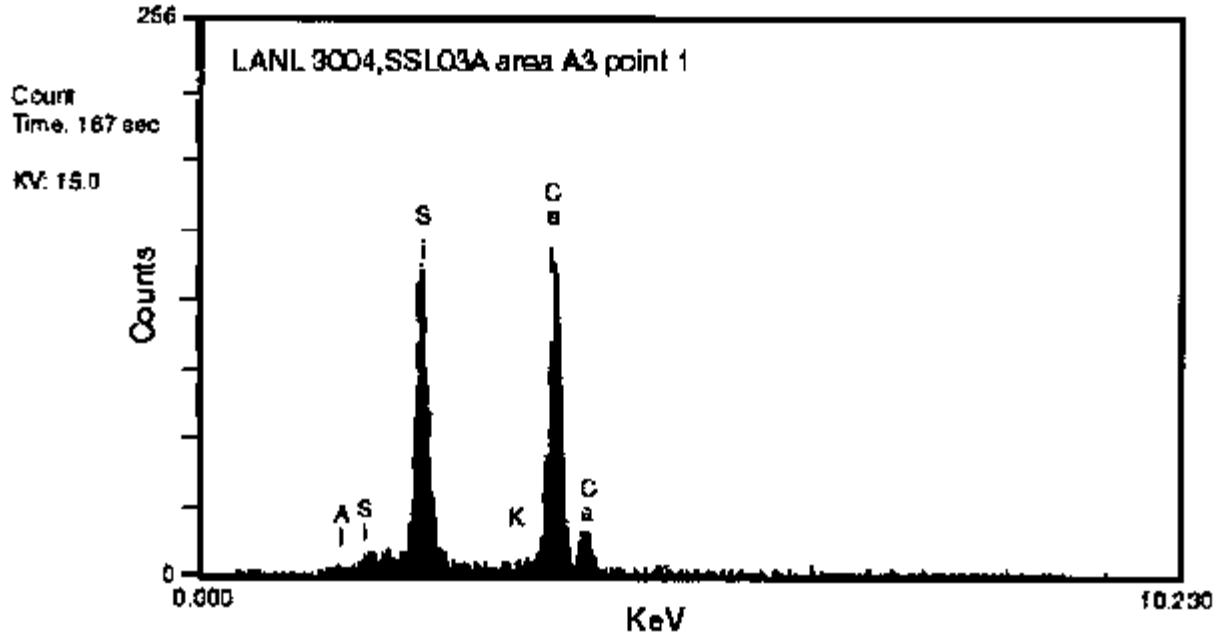

NOTE: ESF-TMA-PTC-NEU-2, 15.5-16.5 ft.

Figure 6-23. Energy-Dispersive X-Ray Spectrum of Gypsum-Rich Portion of White Mound Deposits

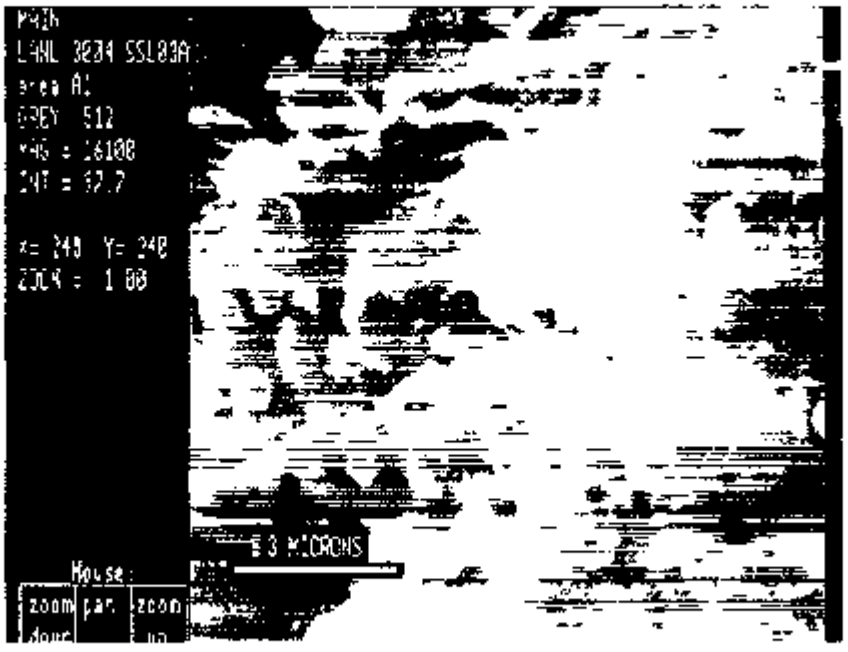

NOTE ESF-TMA-PTC-NEU-2, 15 5-16 5 ft

Figure 6-24 Opal-A Tubules in Silica-Rich Portion of White Mound Deposits

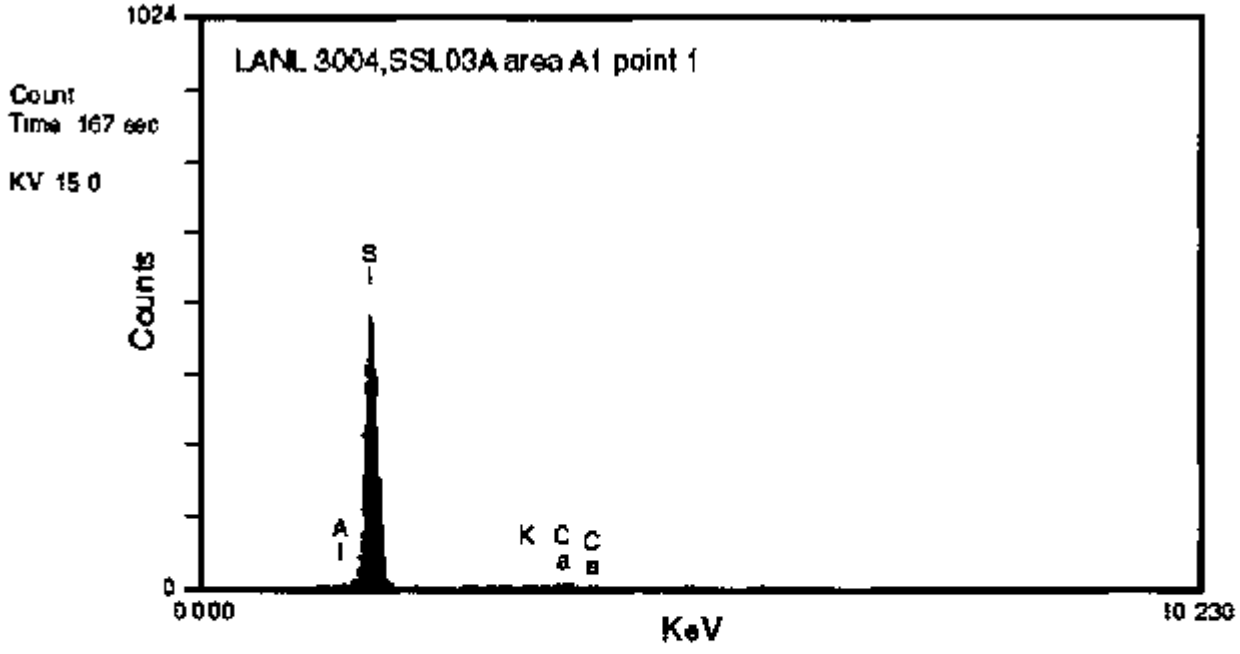

NOTE ESF-TMA-PTC-NEU-2, 15 5-16 5 ft

Figure 6-25 Energy-Dispersive X-Ray Spectrum of Silica Tubule

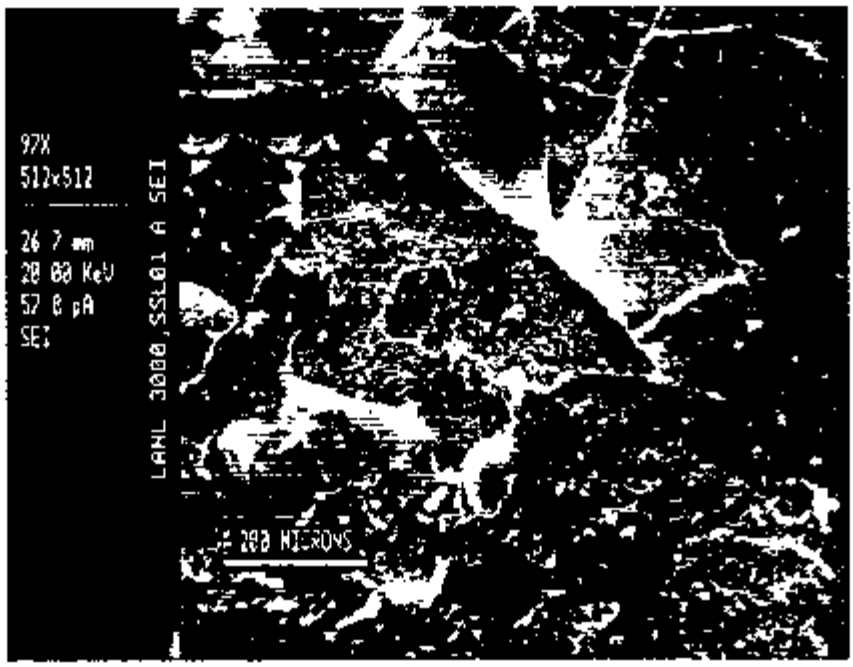

NOTE: ESF-TMA-PTC-MPBX-1, 2.9 to 3.4 ft.

Figure 6-26. Secondary-Electron Image of Silica Scale

NOTE: ESF-TMA-PTC-MPBX-1, 2.9 to 3.4 ft. This image shows the details of the rods and platy particles overlain by silica sheets.

Figure 6-27. Secondary-Electron Image of Silica Scale

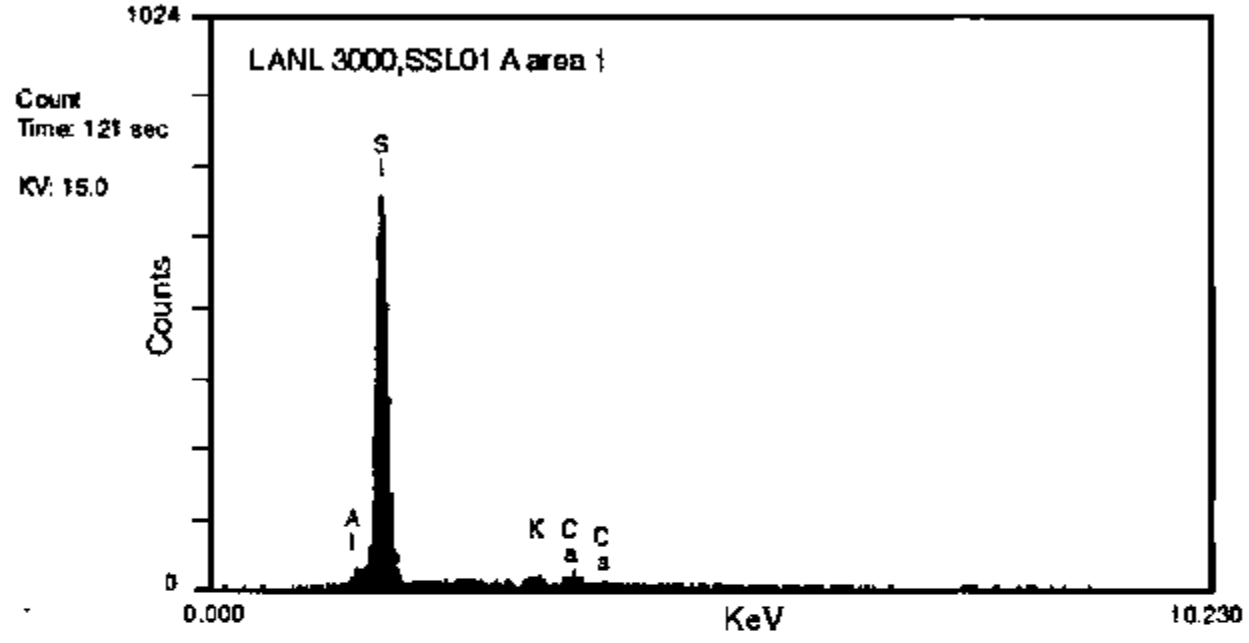

NOTE: ESF-TMA-PTC-MPBX-1, 2.9 to 3.4 ft.

Figure 6-28. Energy-Dispersive X-Ray Spectrum of Silica Scale

INTENTIONALLY LEFT BLANK

7. THERMAL MEASUREMENTS

This section describes measurements of heater power and temperature. These measurements primarily represent SNL-installed gages and activities; however, temperature data from RTDs installed by LLNL are also included. Figures summarizing plan and SHT block surface views of gage locations are presented for each type of measurement. Data are presented through January 31, 1998. A brief description of instruments and equipment is given in Appendix F.

7.1 HEATER POWER

The heater assembly for the SHT consisted of two single-ended 4,000-watt heating elements centered in a 5.4-cm (2.125-in.) diameter copper tube with a copper end cap at the bottom end. The two heating elements were contained in a nominally 2.5-cm (1-in.) diameter carbon steel inner casing. The heating elements were made of nicrome and were each 5-m long with a 180° bend at the bottom end. The design of the SHT heater allowed for one of the heating elements to act as a secondary heating source in the event that the other failed, or if additional heat needed to be added to the rock. The heater included a control loop that allowed for automatic switching from the primary element to the secondary element if the heater power dropped below a prescribed set point. Throughout the test only one of the heating elements was operated at a time.

The heater assembly also included four 1.3-cm (0.5-in.) diameter copper sheaths brazed onto the outer surface of the copper canister at 90° intervals around the circumference. These small tubes served as guides for 0.6-cm (0.25-in.) diameter thermocouple probes intended to measure the temperature of the surface of the heater canister. Three such probes were installed in three of the four guide tubes. One thermocouple probe was inserted on the top of the heater canister (ESF-TMA-TCT), one was located on the left side (north) of the heater assembly (ESF-TMA-TCS), and one was located on the bottom of the heater canister (ESF-TMA-TCB). Each of these probes included nine Type-K thermocouples. The intent of placing the thermocouple probes on the heater canister as described was to evaluate potential temperature anomalies and temperature distribution lengthwise along the heater assembly.

The heater power, voltage, and current were monitored using a Magtrol power monitor. The SHT called for the heater power to be nominally 4,000 watts for a period of 9 to 12 months, followed by a cooldown period with the heater off completely.

The heater power data are illustrated in Figure 7-1a. Power was applied to the heater starting on August 26, 1996 at 18:30:30 Universal Coordinated Time. Time zero in Figure 7-1a corresponds to the time of activation of the heater. During the few hours immediately prior to powering up the heater, the heater power readings averaged about -4.5 watts, reflecting zero power. Between the time of activation and May 28, 1997, but omitting the anomalous data intervals and heater down times discussed below, the heater power output averaged about 3,795 watts. The heater power was not perfectly stable over the course of the test, however, as can be seen in Figure 7-1b, which illustrates the average weekly power output of the heater, omitting heater down time and anomalous data.

The data indicate that the power output of the heater under normal operation declined by about 130 watts (3 percent) over the 9 months that it was in operation. The heater was deactivated on May 28, 1997 at 20:31 Universal Coordinated Time, 275 days and 2 hours after initially being activated.

During the roughly nine months that the heater was in operation, there were a few time intervals during which anomalous data were observed or when the power to the heater was temporarily interrupted. During the first two hours of heater operation, the heater was turned on and off a few times, primarily to test the switching mechanism for heating elements #1 and #2. The heater power data collected during this interval appear to be accurate because the temperatures measured by the thermocouples on the heater tracked the heater power in a predictable manner. On day 9, the heater power data suggest that the heater power jumped abruptly from about 3900 watts to 6000 watts, then quickly decayed to about 4500 watts in a few hours. Then a gap of approximately 24 hours appeared in the heater power data. This power fluctuation was caused by a power outage, and when data collection resumed late on day ten, the heater power had returned to about 3850 watts. These anomalous readings do not appear accurate because the temperatures measured by the thermocouples on the heater did not record the degree of temperature change that would be expected for heater power variations of this magnitude.

Following this event, the heater power remained quite steady, varying with high frequency between about 3700 and 3950 watts for about 40 days. Late on day 51 one heater power reading is missing and the next reading is near zero, suggesting that the power was off for a period up to 45 minutes. This outage is also reflected in the thermocouple data from the heater, which dropped about 100°C but quickly recovered when heater power was restored. Early on day 59 the power went off for about 2.5 hours. This outage resulted in a significant temperature drop, recorded on the thermocouples mounted on the heater. A small drop was observed on the thermocouples on probe ESF-TMA-TC-1, located some 40 cm away from the heater. The temperatures recovered quickly after power was restored. Similar events occurred on days 81 and 93. In both these cases the heater power was off for 15 to 45 minutes and the thermocouples on the heater showed modest temperature drops but quickly recovered when heater power was restored. A 15.8-hour power outage occurred on day 112, followed by a 12-minute interruption on day 116. Longer heater down times were experienced on day 118 (23.1 hours), day 139 (24.6 hours), and day 202 (13.6 hours). The four longest power outages were sufficiently severe as to noticeably influence the temperatures recorded by the temperature gages in nearby boreholes.

7.2 TEMPERATURE

The thermocouple probes used in the SHT consist of Type-K thermocouples enclosed within 304 stainless steel, 0.64-cm (0.25-in.) diameter sheaths that were manufactured by STI in Houston, Texas. The thermocouples within the sheaths were insulated from each other with magnesium oxide. The thermocouple probes were installed in seven boreholes in the rock mass around the heater to monitor temperature changes away from the heater. Three additional thermocouple probes were installed on the top, side, and bottom of the heater canister to monitor heater surface temperatures. Five of the boreholes were drilled roughly parallel to the heater axis to a depth slightly exceeding the planned heater installation depth. Within these five boreholes, probes TMA-TC-1, TMA-TC-2, TMA-TC-3, TMA-TC-4, and TMA-TC-5 were located at

nominal radial distances from the heater borehole of 0.33 m, 0.66 m, and 1.48 m, roughly corresponding with the numerically predicted temperature isotherms of 200°C, 150°C, and 100°C, respectively (CRWMS M&O 1996a, p. 5-8). Within each of these five boreholes, two thermocouple probes were installed. Two probes were required during test planning because it was thought that the drift width was too narrow (about 5.5 m) to allow installation of 8-m long thermocouple probes. Therefore, for each of these boreholes, two probes were used: one about 6 m long with ten Type-K thermocouple junctions spaced along its length (designated probe "A" for each borehole), and one about 2 m long with five Type-K thermocouple junctions spaced along its length (designated probe "B" for each borehole). The other two thermocouple probes (TMA-TC-6 and TMA-TC-7) were drilled perpendicular to the heater borehole from the Observation Drift and the Thermomechanical Alcove Extension. Each of these two boreholes included a single thermocouple probe with ten Type-K thermocouple junctions spaced along its length. The locations of the individual thermocouple junctions within each borehole were determined from (1) the survey and corrected borehole collar coordinates, (2) the field notes for installation (e.g., installed depth to various points on the probes), and (3) manufacturer and SNL specifications for the probes. Throughout the remainder of this document, the "A" and "B" designations have been dropped.

Temperatures were also measured on each of the free surfaces of the SHT block using individual Type-K thermocouple junctions. Twelve individual thermocouples were installed on each face of the SHT block. The locations for each of these thermocouples were measured manually in the field using a metric tape measure.

Temperatures were also measured between the two layers of insulation on each of the three free surfaces of the SHT block using individual thermistors. Five individual thermistors were installed between the layers of insulation on each face of the SHT block. The locations for each of these thermistors were measured manually in the field using a metric tape measure.

The locations of the 319 temperature gages and the median daily reading before heater activation (day 0), at the conclusion of heating (day 275), and after 215 days of cooling (day 490) are listed in Appendix G. The locations of gages situated in the interior of the SHT are illustrated in Figure 7-2. The median daily temperature is reported instead of the mean daily temperature because the median value is less affected by isolated anomalous values such as temperature spikes caused by electrical glitches, etc. Note that time is measured relative to the time of heater activation (August 26, 1996 at 18:31 Universal Coordinated Time). In Table G-2, day 0.5 refers to the twenty-four-hour period that ended when the heater was activated, day 13.5 refers to the 14th twenty-four-hour period after heater activation, etc.

Although all temperature gages are included in Appendix G, Table G-2, seventeen of the 319 temperature gages (~5 percent) were judged to be unreliable. These gages are listed in Table 7-1, and plots of the data obtained from sixteen of them are presented in Appendix G. Although in most cases the reasons for these gage failures are not known, it is possible that the failures represent either fabrication or installation errors. For gage TMA-MPBX-4-TC-3, the thermocouple extension wire was broken during installation of the probe, so the gage was never connected to the automated DCS and no data were ever collected. For TMA-H-1-TCB-4,

something happened when the power was applied to the heater and no temperature data are available for that gage after heater activation.

Table 7-1. Unreliable Temperature Gages from the SHT Block

Gage	Reason For Omission
TMA-H-1-TCB-4	No data after heater activation
TMA-TC-2A-4	Erratic temperature readings
TMA-TC-4A-1	Erratic temperature readings
TMA-TC-6-4	Erratic temperature readings
TMA-MPBX-1-TC-9	Erratic or missing temperature readings starting on day 210
TMA-MPBX-3-TC-1	Erratic temperature readings starting on day 122
TMA-MPBX-3-TC-2	Erratic temperature readings starting on approximately day 210
TMA-MPBX-3-TC-7	Erratic temperature readings starting on day 140
TMA-MPBX-3-TC-9	Erratic temperature readings; no data after day 90
TMA-MPBX-4-TC-3	Thermocouple extension wire broken during installation
TMA-MPBX-4-TC-8	Erratic or missing temperature readings starting on day 289
TMA-MPBX-4-TC-10	Missing data after day 120
TMA-RTD-15-20	Erratic temperature readings
TMA-RTD-15-23	Erratic temperature readings
TMA-RTD-17-26	Erratic temperature readings
TMA-RTD-23-11	Erratic temperature readings
TMA-RTD-23-19	Erratic temperature readings

The remaining fifteen unreliable temperature gages are deemed unreliable because either they ceased to function altogether (no data recorded in the DCS) or they exhibited erratic behavior, which is defined as very abrupt changes in temperature that are not recorded by other nearby temperature gages. In most, but not all, cases the temperatures recorded are also clearly implausible, for example, yielding impossibly hot or cold temperatures.

Because of the small percentage of gages that yielded unreliable data, a conservative approach has been adopted for dealing with suspect data: if a gage exhibited any erratic behavior, it is excluded from all analyses, even if prior or later data from that gage appear to be reliable. The data from gage TMA-TEMP-16-4, discussed later in this section, are the only exceptions to this rule.

It is important that good judgment be applied in the determination of the reliability of suspect gages because anomalous behavior may also be evidence of important phenomena that should not be ignored. For the seventeen unreliable gages identified above, it is quite clear that the data are unreliable and that—even if some "good" data are available—it is unlikely that any anomalous data would be missed by ignoring all the data from these gages.

In addition to the unreliable gages identified in Table 7-1, temperature data from gages TMA-RTD-15-11, TMA-RTD-15-12 and TMA-RTD-15-13 were not recorded between June 11, and October 18, 1997. This appears to have been due to a DCS software problem. Resistance data from these RTDs were recorded but the temperature data was not. It would likely be possible to convert the recorded resistance data to temperatures but this has not been done. Because there appears to be nothing wrong with the available data from the these gages, they have not been omitted from the analyses.

For the purpose of creating summary data plots, the 302 gages considered reliable were divided into 27 different sets. Each set contains the gages from a single probe, a single borehole, or, in the case of the surface thermocouples and the thermistors in the surface insulation, data from a particular rock face. Figures 7-3 through 7-22 illustrate the data from the data sets within the interior of the SHT block. The curves in Figures 7-3 through 7-22 illustrate (a) the median daily temperature as a function of spatial position along one of the coordinate directions every fourteen days during the heating phase of the SHT; (b) the median daily temperature as a function of spatial position along one of the coordinate directions every fourteen days during the cooling phase of the SHT; and (c) for each data set, the median daily temperature as a function of time, with one curve for each temperature gage in the set. Time zero refers to the time of heater activation. The median temperature of the data collected during the first 24-hour period following heater activation is plotted at time 0.5 days, and so forth. The dots along the bottom of the spatial plots indicate the location of each gage in the borehole.

Figures 7-3 through 7-5 illustrate the temperatures recorded by the three thermocouple probes mounted on the outside of the copper canister in which the heater element is located. They indicate that the temperature of the heater reached 350°C within a day or two of power application to the heater and then increased to around 375°C approximately one week after heater activation. Note that during times when power was being applied to the heater these readings represent the temperatures in the heater borehole and not the temperature of the rock at the surface of the heater borehole. This latter quantity is not accurately determined by these measurements, but the rock temperature was certainly somewhat less than the temperature in the heater borehole. Note that the temperatures recorded in the heater borehole 6.0 to 6.5 m from the borehole collar were warmer than the rest of the locations in the heater borehole by approximately 50°C. This condition is believed to have resulted from the coincidental juxtaposition of the thermocouples in these locations with one of the centralizers that maintained the heater element in the center of the heater canister, and is not a result of anomalous rock thermal properties. Note also the temperature profiles on the spatial temperature distribution plots, which are at an intermediate temperature of 100 to 170°C. These are the median daily temperature profiles observed on the 112th and 140th days of heating when the heater power was temporarily interrupted. When the power to the heater was turned off after 275.08 days of heating, the temperatures recorded on the surface of the heater dropped by roughly 100°C in the first half hour, dropped to about 100°C after about 3 days, and cooled to about 45°C after 50 days. The heater, along with the thermocouples on its surface, was removed from the SHT block on July 17, 1997 (day 325), so no data are available from TMA-H-1-TCT, TMA-H-1-TCS or TMA-H-1-TCB after this time.

Figures 7-6 and 7-7 illustrate the temperatures recorded by probes TMA-TC-1 and TMA-MPBX-1, which are nominally parallel to the heater and located at radial distances of 42 cm and 34 cm from the heater, respectively. These two probes are located on either side of a presumed plane of symmetry that is vertical and contains the axis of the heater, therefore they should respond similarly. The temperature sensors in TMA-TC-1 exhibit relatively smooth temperature increases with time and a spatial temperature distribution that is reasonably symmetric about the position Y=4.5 m, which corresponds to the center of the heater. A minor anomaly exists at Y=2.5 m; its origin is not known as of this writing. There are also significant dips in the temperature data on days 112, 118, 139, and 202, which result from interruptions to the heater power that occurred on those days.

The interruptions to heater power were of sufficient duration that the temperature of the rock is probably several degrees centigrade cooler several days after the interruptions than it would have been had the interruptions not occurred. When the heater was turned off 275 days after it was turned on, the temperatures of the gages dropped precipitously. The temperatures recorded by gages closest to the center of the heater, which recorded the warmest temperatures, dropped more rapidly than the gages further from the center of the heater, which recorded lower temperatures. By 523 days after heater activation (after 248 days of cooling) the temperature recorded by the sensors in TMA-TC-1 had cooled to between 23.4° and 32.1°C.

At early times the response of TMA-MPBX-1 (Figure 7-7) is quite different from that of TMA-TC-1 (Figure 7-6). The most significant differences occur during the time interval from about day 9 to day 18, during which time the temperatures in the borehole were warming through the boiling point of water (at atmospheric pressure). During this time, and particularly on day 10, the spatial temperature distribution between Y=2 m and Y=6 m was virtually isothermal at about 96°C. It is likely that this resulted because TMA-MPBX-1 is installed in an open borehole. As the temperatures in the surrounding rock passed through the boiling point, vapor phase heat transport within the borehole created the observed isothermal conditions, which likely did not accurately reflect the temperature in the adjacent rock in detail. TMA-TC-1 did not respond in this way because the temperature sensors were grouted in the borehole and there is no open borehole in which vapor phase transport could occur. After the readily accessible water in the rock adjacent to borehole TMA-MPBX-1 had evaporated, the convective heat transfer in the borehole was reduced in importance and the temperature response returned to a conduction-dominated regime.

Another noteworthy feature about TMA-MPBX-1 is that the spatial temperature distribution was somewhat asymmetric about the center of the heater during the heating phase of the test (Figures 7-23 and 7-24 illustrate the asymmetry for probes oriented parallel to the heater on day 275). Most dramatic for TMA-MPBX-1 was the gage at Y=6.9 m (2.4 m from the center of the heater), which had only warmed to about 48°C by day 275, whereas the sensor at the other end of the heater (Y=2.0 m; 2.5 m from the center of the heater) had warmed to 126°C. The temperature sensors closer to the center of the heater were asymmetric as well. The two sensors at Y=3 m and 6 m, which were also symmetrically positioned with respect to the center of the heater, differ in temperature by about 7°C.

It is interesting to note that approximately 12 days after the heater was turned off, the temperature recorded by the gage at Y=6.9 m actually increased by about 12°C over a nine-hour period. This change took place when the warmest gage in the remainder of the borehole was at about 75°C. The possibility that this gage should be considered a failed gage should not be dismissed. If this is the case, the data derived from it between the time of heater activation and the time when the temperature jumped 12°C (twelve days after turning off the heater) is the most suspect because it is inconsistent with other data from the probe. After the temperature jump, the data are much more consistent with other data from the probe, perhaps indicating that whatever caused the gage to yield unreliable data prior to the temperature jump was remedied at the time of the temperature jump. If the data obtained from this temperature sensor are reliable, then the temperature gage was maintained at an anomalously low temperature by some unknown mechanism throughout the

heating phase of the test. Whatever the nature of this mechanism, it ceased to influence the temperature gage after the borehole had cooled through the boiling point.

A third notable feature in TMA-MPBX-1 is a brief reduction in temperature recorded by the sensors at Y=6.0, 1.5, 1.0, and 0.6 m during the time intervals from 20 to 24 days and from 31 to 32 days. The fact that these anomalies were observed by several sensors within the borehole makes it unlikely that they result from unreliable sensors. The cause of these anomalies is unknown but likely reflects complex vapor phase heat transport phenomena within the open borehole. Also, no major power fluctuations occurred during that time period. The dips in temperature recorded on days 112, 118, 139, and 202 resulted from heater power outages.

Finally, the warmest temperatures recorded in TMA-TC-1 and TMA-MPBX-1-TC are about 160°C and 166°C, respectively. The fact that TMA-MPBX-1-TC reached somewhat warmer temperatures than TMA-TC-1 likely reflects the fact that it was approximately 8 cm closer to the heater than was TMA-TC-1, and the radial temperature gradient this close to the heater was substantial.

Figures 7-8 and 7-9 illustrate the temperatures recorded by probes TMA-TC-2 and TMA-MPBX-2-TC, which were located 67 cm and 68 cm from the heater, respectively. By day 275, the central portions of both probes had warmed through the boiling point and reached maximum temperatures of 125°C and 122°C. TMA-TC-2 is grouted into its borehole while TMA-MPBX-2-TC is installed in an open borehole and was therefore subject to convection effects as it warmed through the boiling point. These effects were not as severe as in TMA-MPBX-1-TC because TMA-MPBX-2-TC is located twice the distance from the heater as TMA-MPBX-1-TC, but they are evident nonetheless. The temperature sensor at Y=4.9 m warmed smoothly up to the boiling point but then remained at a temperature near the boiling point for several weeks. As the liquid water boiled away from that vicinity, the temperature started to increase again and by day 275 the spatial temperature profile indicates that the anomalously low temperatures observed earlier near Y=4.9 m had disappeared. The temperature gage near Y=6 m rose smoothly up to the 100°C mark, then remained isothermal after that. After the heater was turned off and the warmest temperature in the borehole had cooled to below the boiling point of water, all anomalous temperature readings disappeared. The dips in temperature on days 112, 118, 139, and 202 resulted from heater power outages on those days.

TMA-TC-4 and TMA-TC-5 (Figures 7-10 and 7-11) are an important pair of probes because they are located directly below and above the heater, respectively. If convective heat transport through the rock mass was important, TMA-TC-4 should have been slightly cooler than TMA-TC-5 because heat from the heater would be carried convectively upward by buoyancy effects. As of day 275, these probes had reached maximum temperatures of 116°C and 123°C, respectively. Note that near Y=4.5 m, TMA-TC-5 was about 7°C warmer than TMA-TC-4 on day 275. It was also located about 3 cm closer to the heater than was TMA-TC-4, so it is not clear that this difference in temperature is an indication of convective heat transfer. Given that the radial temperature gradient at the radial distances of these boreholes was substantial, the observed difference in temperature can be explained by conduction effects alone. After the heater was turned off, all the gages on both probes cooled smoothly. The cooling data from the gages in TMA-TC-5 located beyond the ends of the heater indicate that the front part of the block cooled

more rapidly than the back part of the block, presumably because of heat loss from the front face of the block. Because there are no gages located past the back end of the heater in TMA-TC-4, it is not possible to reach that conclusion from the TMA-TC-4 data.

Probes TMA-TC-3 and TMA-MPBX-3-TC (Figures 7-12 and 7-13) are located approximately 1.48 m from the heater and hence had only warmed to a maximum of about 79°C by day 275. Some anomalous behavior is evident in TMA-TC-3 in the distal parts of the block. At 5.8 and 6.3 m into the block, the temperatures seem a bit warmer than the trends of other gages would lead one to expect. Because TMA-MPBX-3-TC, which is an open borehole similar to TMA-MPBX-1-TC and TMA-MPBX-2-TC, never reached the boiling point, it never exhibited any of the temperature signatures associated with intra-borehole vapor phase heat transport. Four of the thermocouples in TMA-MPBX-3-TC failed or ceased to provide data during the course of the SHT, more than any other borehole. The reasons for this are not clear. The gages from both probes cooled smoothly after the heater was turned off.

Probes TMA-TC-6 and TMA-MPBX-4-TC (Figures 7-14 and 7-15) are both oriented parallel to the X-direction and hence are perpendicular to the axis of the heater. TMA-TC-6 is located approximately 1 m past the midpoint of the heater in the Y-direction, while TMA-MPBX-4-TC is located 1 m on the near side of the midpoint of the heater. The data from TMA-TC-6 are very smooth, both in their spatial and temporal distributions. Note in particular that near the boiling point neither the temporal nor the spatial temperature profiles show any evidence of inflections or other anomalies that would indicate significant vapor phase convection. Note also that the temperature drops associated with the heater power outage were observed in the data out to a radial distance from the heater of about 2 m. After the heater was turned off, the temperatures recorded by TMA-TC-6 cooled smoothly.

TMA-MPBX-4-TC exhibits more erratic behavior than TMA-TC-6 because it is deployed in an open borehole. Because the end of the borehole closest to the heater exceeded the boiling point, intra-borehole vapor phase heat transport was significant and was the likely cause of the erratic behavior apparent in the temperature plots. When the heater was turned off, note that the temperature of the gage closest to the heater initially increased a few degrees before beginning to cool. This observation supports the hypothesis that the gages in this borehole do not accurately reflect the rock temperature adjacent to the borehole. The temperatures recorded by the gage closest to the heater were probably maintained at a temperature significantly below the adjacent rock temperature during the heating phase of the SHT by intra-borehole convection. When the heater was turned off, steam flux into the borehole ceased, thereby allowing the temperature gage to equilibrate with the rock mass adjacent to the borehole.

Probe TMA-TC-7 (Figure 7-16) is also parallel to the X-direction but approaches the heater from the opposite side (from the negative X-direction). This probe, like all the other thermocouple-series probes, is grouted into its borehole and hence was not subject to the effects of intra-borehole convective heat transport, which accounts for the relatively smooth spatial and temporal temperature distributions obtained from this probe.

Temperature data from TMA-RTD-15 are illustrated in Figure 7-17. As indicated in Figure 7-2, this borehole is parallel to the X-direction. It starts from the Thermomechanical Alcove

Extension and angles upward, over and beyond the heater. Several notable temperature anomalies are evident in this borehole. In Figure 7-25, data from TMA-RTD-15-1 are compared to data collected from its nearest neighbor, gage TMA-RTD-15-2, about 30 cm away. Up until about day 90, the data from these two gages tracked each other nicely, but after day 90 the temperature of TMA-RTD-15-1 started to increase more rapidly than the temperature of TMA-RTD-15-2. On day 120 the temperature of TMA-RTD-15-1 actually exceeded that of TMA-RTD-15-2, even though TMA-RTD-15-2 is approximately 13 cm closer to the heater.

Between day 160 and day 275 TMA-RTD-15-1 warmed significantly less than expected, such that by the end of the heating phase of the SHT it was once again cooler than TMA-RTD-15-2. After the heater was turned off on day 275, TMA-RTD-15-1 cooled smoothly until about day 380, when the readings became significantly erratic. TMA-RTD-15-2, which appeared stable throughout the heating phase of the SHT, began exhibiting erratic behavior a few weeks after the end of the heating phase. Temperature readings from TMA-RTD-15-2 became more erratic at the same time as TMA-RTD-15-1, about day 390. It should also be noted that TMA-RTD-15-1 exhibited several sudden, brief temperature reductions on days when the heater power was interrupted. There are at least two plausible explanations for these observations. The first is that TMA-RTD-15-1 and TMA-RTD-15-2 experienced some sort of electrical malfunction that rendered their behavior erratic. Another plausible explanation is that a rock fracture exists near the location of gage TMA-RTD-15-1 and that relatively warm fluid was being transported from near the heater into the vicinity of gage TMA-RTD-15-1. The abrupt reductions in temperature observed when the heater power was temporarily interrupted would be consistent with this scenario because during these times the flow of warm fluid in the fracture would also be interrupted. Given the apparent failure of the gages near the end of the test, the erratic readings are likely the result of gage failure.

Another gage exhibiting anomalous behavior is TMA-RTD-15-9, located approximately 2.17 m from the heater. In Figure 7-26 the temperature data recorded by this gage are compared with the data from TMA-RTD-15-10, its nearest neighbor. The two tracked each other nicely up until about day 103, when TMA-RTD-15-9 experienced a slight inflection. Then between days 112 and 117, TMA-RTD-15-9 experienced an approximately 2°C temperature drop. It may be significant that the timing of this drop coincides with a 15-hour interruption in the heater power. Although TMA-RTD-15-9 had been slightly warmer than TMA-RTD-15-10 before the start of the anomalous behavior, its temperature remained about 1°C cooler than that of TMA-RTD-15-10 up until day 253, at which time it once again started to diverge from TMA-RTD-15-10. Because the data from TMA-RTD-15-10 and from other nearby neighbors of TMA-RTD-15-9 exhibit qualitatively similar but more subdued anomalies at the same time, these data are believed to be valid and not the result of a gage malfunction. This type of behavior is suggestive of fluid flow in a fracture near TMA-RTD-15-9, which is bringing cooler fluid into the vicinity of TMA-RTD-15-9 from greater radial distances from the heater.

The temperature data from TMA-RTD-17 are illustrated in Figure 7-18. Like TMA-RTD-15, this suite of gages starts from the Thermomechanical Alcove Extension but is angled downward so as to pass below and beyond the heater. There are no significant thermal anomalies evident in this borehole.

The temperature data from TMA-RTD-22 and TMA-RTD-23 are illustrated in Figures 7-19 and 7-20. The only noticeable anomalies in these boreholes occurred on days 130 and 140. Because these anomalies are evident on the temporal temperature distribution plots from all the gages, independent of radial distance from the heater, these anomalies are likely the result of field personnel working in the vicinity of the boreholes.

Figures 7-21 and 7-22 illustrate the spatial and temporal temperature distributions measured in boreholes TMA-TEMP-16 and TMA-TEMP-18. The temperature gages in these boreholes are all located at least 3 m from the heater and hence have warmed only slightly during the test. The only anomalous data are from TMA-TEMP-16-4, located about 3.2 m from the heater, which recorded impossible data (less than 30°C) from about day 75 to day 80 as well as negative spikes at several other points in time. Because the remaining data from this gage appear to be reliable, and because the gage exhibits other interesting behavior, its data have not been omitted from the analysis. Water was removed from this borehole during the course of the SHT and the unreliable data obtained from TMA-TEMP-16-4 may have resulted from water contacting the temperature gage. Other than the unreliable data, there are several times during the test when temperature drops of a few degrees have been recorded. These may coincide with field operations in the borehole. At the end of the cooling phase, the data suggest that TMA-TEMP-16-4 increased in temperature, which seems implausible. It is likely that either this gage failed or water accumulation in the borehole compromised the data.

The probes that were oriented parallel to the long axis of the heater (the y-axis) lend themselves well to an evaluation of the symmetry of the temperature distribution about a vertical plane perpendicular to the heater and intersecting the heater at its midpoint. In Figures 7-23 and 7-24, the temperature of each gage observed after 275 days of heating is plotted as a function of the distance from the gage to the vertical plane at Y=4.5 m. Caution must be exercised when interpreting the data because the boreholes in which the temperature gages are deployed were not perfectly parallel to the axis of the heater (see Figure 7-2). For probes near the heater, where the radial temperature gradient was high, this imparted a significant asymmetry to the borehole spatial temperature profile that does not accurately reflect rock conditions. The data indicate that, in general, the observed temperature distributions were quite symmetric about the vertical plane that intersected the heater at its midpoint.

The locations of the temperature gages on the three rock faces and in the insulation material are illustrated in Figure 7-27.

The temperatures of the thermocouples mounted on the front face of the SHT block are illustrated in Figure 7-28. Several of the thermocouples started warming above ambient only a few days after activation of the heater. By day 275 the temperature gage located 1.25 m vertically above the heater borehole collar had reached a temperature of about 48°C. After the heater was turned off, the temperatures of all the gages began to cool.

Figures 7-29 and 7-30 illustrate the temperatures measured by the thermocouples on the side faces of the SHT block. These faces are parallel to the Y-Z planes at approximately X = -6.6 m and X = 6.3 m, respectively. Several of the thermocouples on the face at X = -6.6 m are relatively constant and are behaving independently of the remaining gages, but these are located near the top

of the face near some lights and/or electrical conduits that are warming and thus corrupting the temperature readings. In general, the data indicate that the temperatures of the side faces of the block rose about 8°C above their starting point as a result of the SHT. After the heater was turned off on day 275, the surface thermocouples started to cool slowly.

Figures 7-31 through 7-33 illustrate the temperatures measured by the thermistors deployed in the insulation covering the surface of the SHT block. Although several of the gages on the front face rose as much as 13°C above ambient, those on the sides of the block increased by only about 5°C after 275 days of heating. After the heater was turned off, the insulation on the front face of the block cooled at first and then remained essentially isothermal for the last 150 days. The insulation on the side faces of the block, which was warming very slowly during the heating phase of the SHT, became either essentially isothermal or continued to warm very slowly after the heater was turned off.

The fact that the temperature gages on the SHT block surfaces and in the surface insulation did not cool back down to their pretest values likely reflects warmer air temperatures in the ESF drift at the end of the SHT.

Figure 7-34 illustrates the temperatures of the surface and insulation temperature gages on the front face of the SHT block as a function of radial distance from the heater borehole collar after 275 days of heating. These data indicate that although the temperatures of the surface of the block were generally higher near the heater borehole collar, the correlation between surface temperature and radial distance from the heater borehole collar is far from perfect.

On each of the three insulated surfaces of the SHT block, temperature sensors were installed to estimate the thermal flux. Twelve thermocouples were installed on each of the three rock surfaces, and five thermistors were installed between the layers of insulation. With the exception of two pairs of gages, the locations of the thermocouples and thermistors were coincident. Figure 7-35 illustrates the temperature drop across the insulation at the four locations on the front face of the SHT where the surface and insulation temperature gages were located at similar X-Z locations. The temperature drop is proportional to the heat flux through the insulation. During the heating phase of the SHT the measured temperature drops were quite small and, based on only four pairs of data points, do not appear to have been strongly correlated with radial distance from the heater borehole collar. Ninety-five days after the heater was turned off, the temperature drop across the insulation had decreased to less than the accuracy of the thermocouples used to make the measurements (±2.2°C).

Figures 7-36 through 7-42 illustrate isotherms on seven different planes through the SHT block after 275 days of heating. These temperature contour plots were generated by hand, using engineering judgment. The isotherms do not violate any of the temperature data from the TMA-TC, TMA-RTD, or TMA-TEMP probes. Some of the data from the TMA-MPBX probes are violated. This is justified because these probes are deployed in open boreholes and intra-borehole vapor-phase heat transport has influenced the data from the gages so that they do not accurately reflect the rock temperature near the borehole. On slices parallel to the X-Z face (i.e., planes perpendicular to the long axis of the heater), temperature contours are almost perfectly circular and centered on the heater location. There is a slight asymmetry, with the 50

and 75°C contours in the upper left part of the block being bowed out slightly. This is the result of slightly elevated temperatures observed by probe TMA-RTD-23. The contour plot parallel to the Y-Z plane, which is the vertical plane containing the heater, illustrates the symmetry of the temperature distribution in the Y-direction. The contour plots parallel to the X-Y plane indicate that the temperature distribution is relatively symmetric about the vertical plane through and parallel to the heater.

Figure 7-43 is a plot of temperature as a function of radial distance from the heater for all gages from sealed boreholes near the vertical plane that intersects the heater near its midpoint. The data indicate that the temperature distribution around the heater is radially symmetric. The only exceptions are the temperature data from borehole TMA-RTD-23, which are illustrated by the triangle symbols in Figure 7-43. In the radial distance range from about 1.4 to 2.8 m, they appear to be as much as 5°C warmer than other gages at similar distances from the heater.

Figure 7-44 illustrates the amount by which the gages used to generate Figure 7-43 increased in temperature during the time interval from 186 to 275 days. For radial distances from the heater greater than 1 m, where temperatures were less than 100°C, the amount of warming is well correlated with radial distance from the heater, ranging from about 3.5°C at 1 m to about 2.5°C at 6 m from the heater. The gages located less than 1 m from the heater, however, where the temperatures exceeded 100°C, all warmed by almost twice that much. This can be taken as evidence for the formation of a dryout zone around the heater. As the water in the rock evaporated, two thermal properties of the rock changed. Drying the rock reduced its heat capacity, with the result that after drying the same rate of heat input to the rock resulted in faster warming of the rock. Evaporation of the water in the rock also reduced its thermal conductivity. As the drying front propagated radially outward, the temperature of the relatively low thermal conductivity rocks in the dryout zone increased more rapidly than the temperature of rocks outside the dryout zone. The data in Figure 7-44 suggest that by the end of the heating phase of the SHT, the dryout zone extended out to about the 100°C isotherm, located approximately 1 m from the heater.

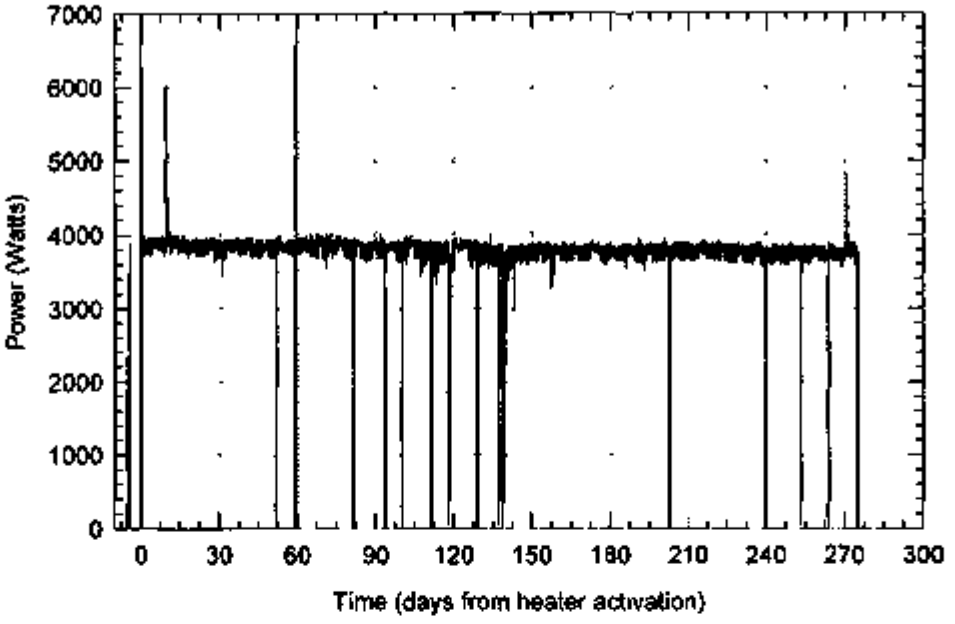

Figure 7-1a. Heater Power Summary through May 28, 1997

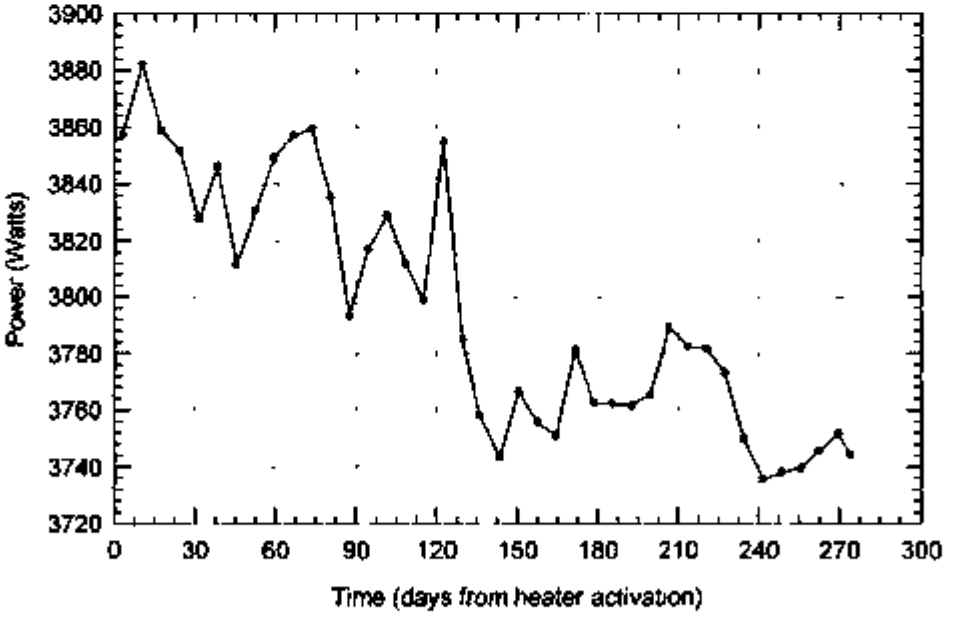

Figure 7-1b. Average Weekly Power Output of Heater through May 28, 1997

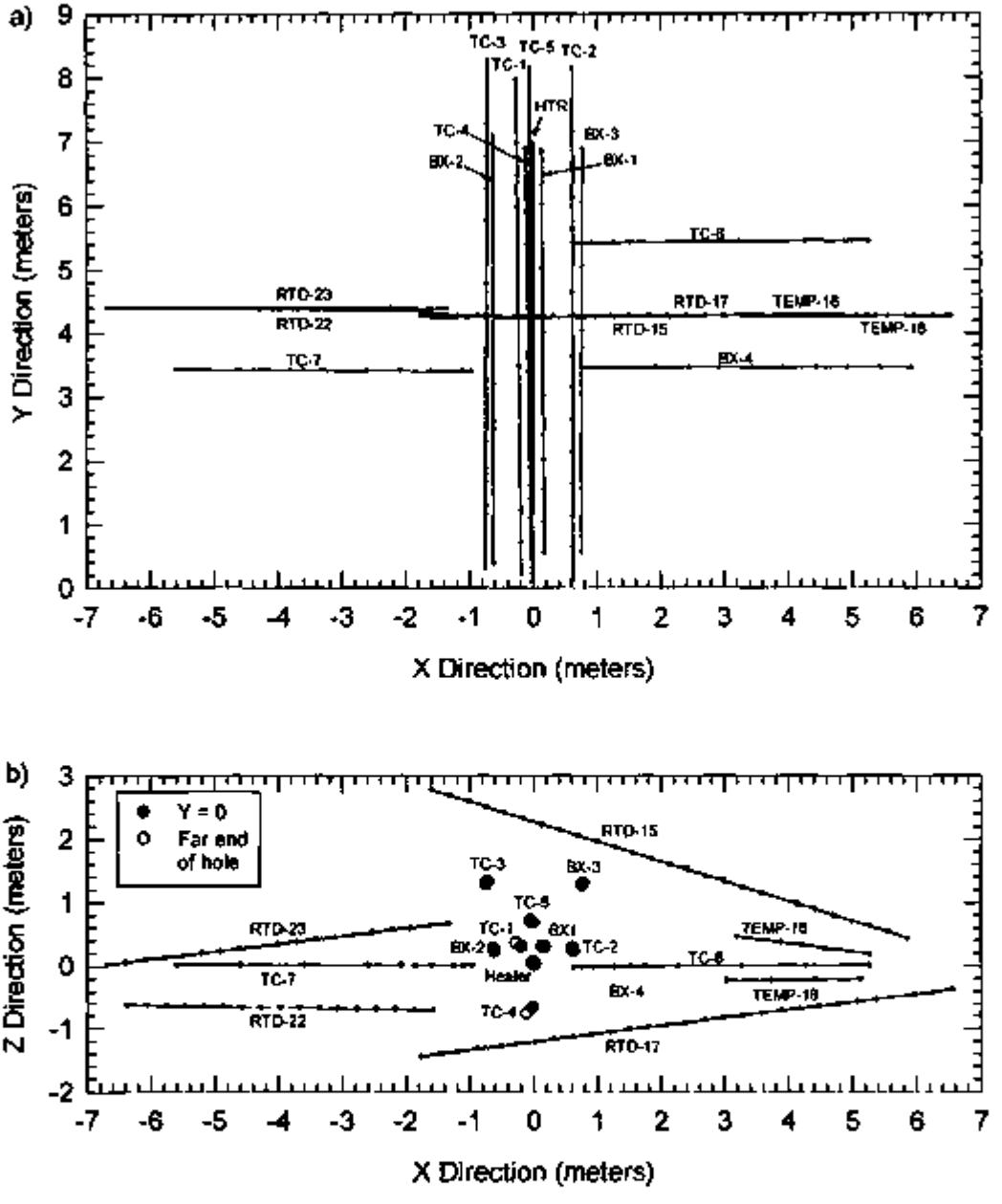

Figure 7-2. Map (a) and Cross-Section (b) Views of the SHT Block Showing the Locations of Interior Temperature Gages

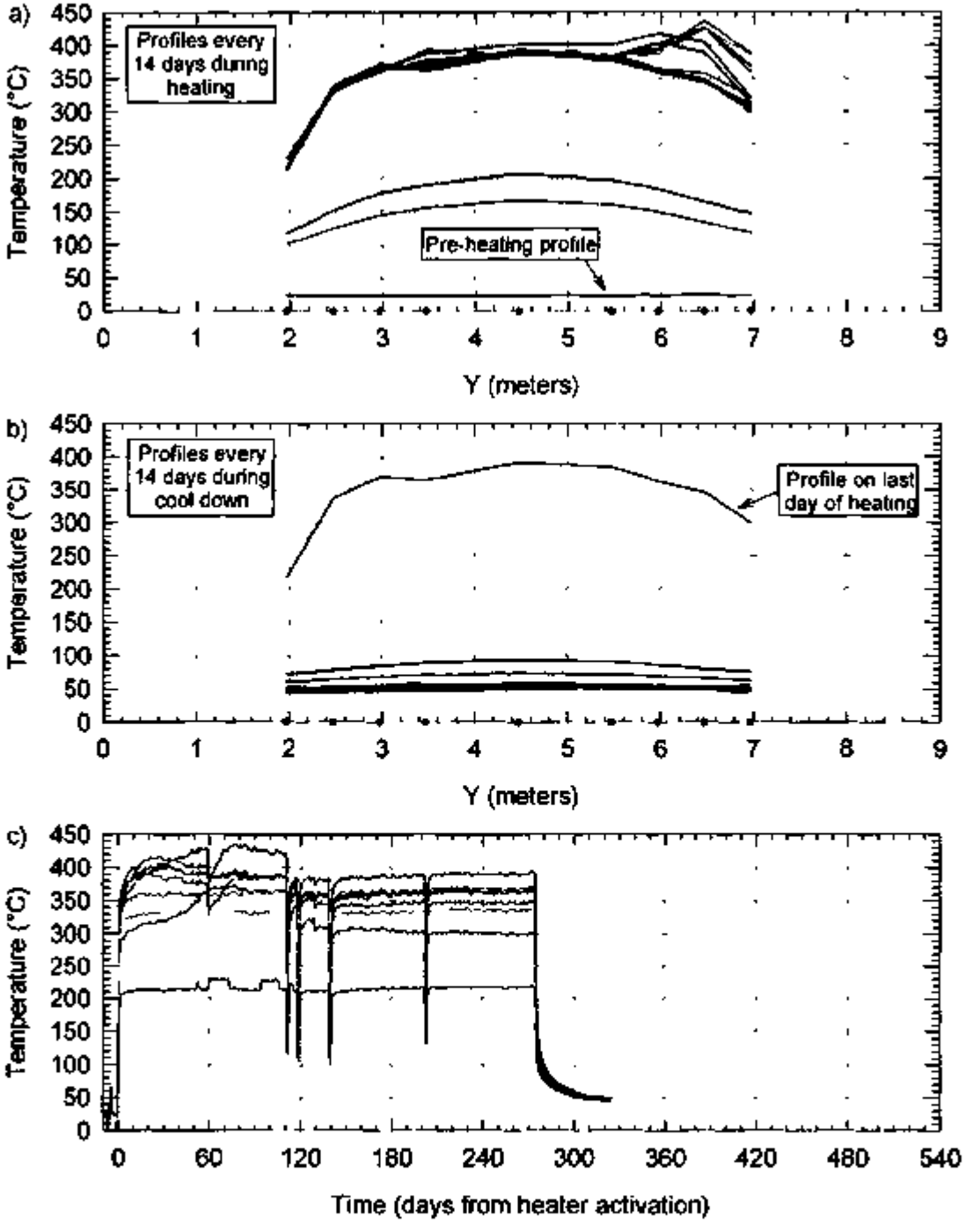

NOTE Temperatures reflect measurements taken by thermocouples evenly spaced along the heater.
Temperature shown: (a) as a function of Y every 14 days during the heating phase of the SHT
(b) as a function of Y every 14 days during the cooling phase of the SHT
(c) as a function of time.

Figure 7-3. Median Daily Temperature of the Gages in Probe TMA-H-1-TCT (x=-0.005 m, z=0 04 m)

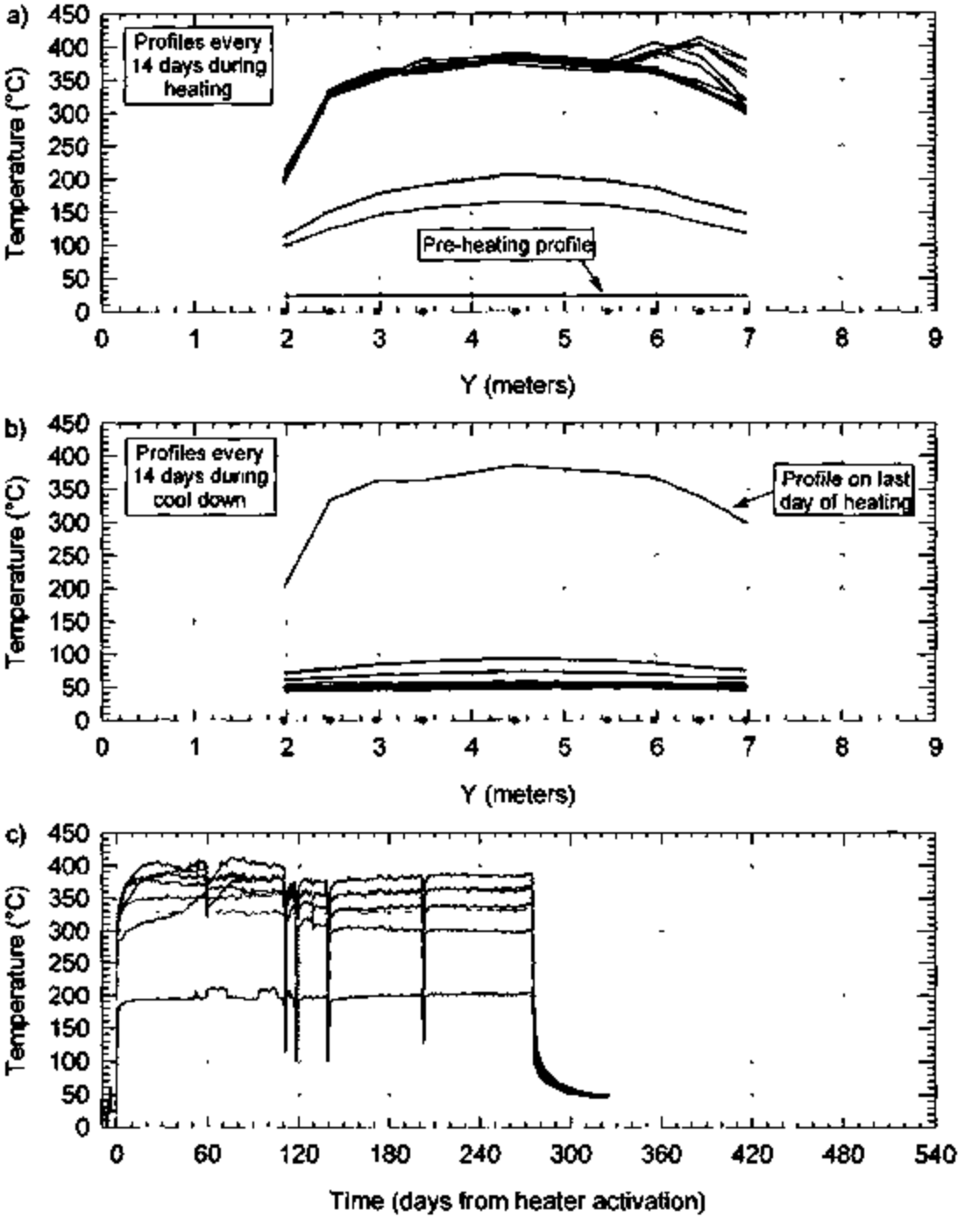

NOTE Temperatures reflect measurements taken by thermocouples evenly spaced along the heater
Temperature shown: (a) as a function of Y every 14 days during the heating phase of the SHT
(b) as a function of Y every 14 days during the cooling phase of the SHT
(c) as a function of time

Figure 7-4. Median Daily Temperature of the Gages in Probe TMA-H-1-TCS (x=-0 038 m, z=-0.006 m)

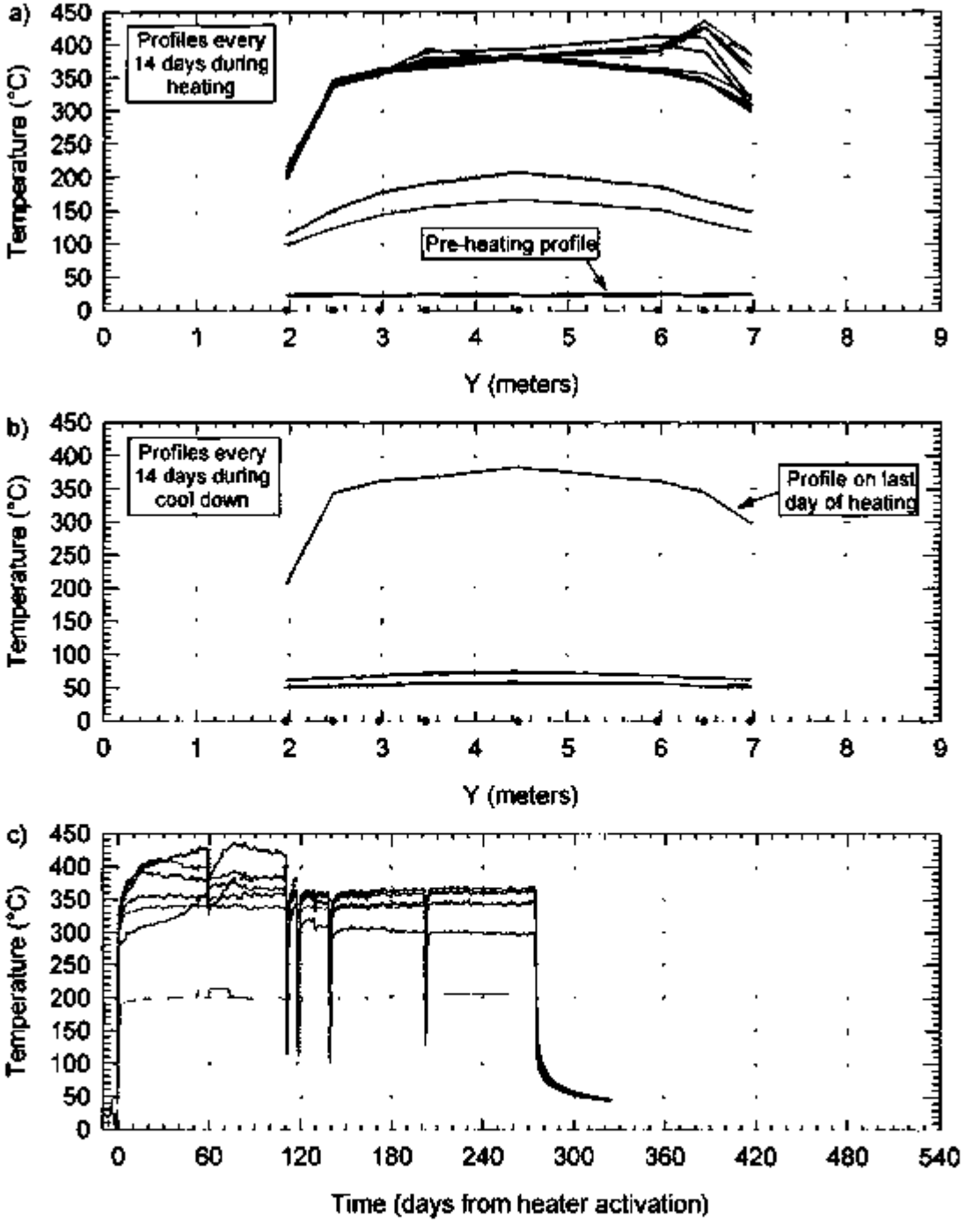

NOTE: Temperatures reflect measurements taken by thermocouples evenly spaced along the heater
Temperature shown: (a) as a function of Y every 14 days during the heating phase of the SHT
(b) as a function of Y every 14 days during the cooling phase of the SHT
(c) as a function of time.

Figure 7-5 Median Daily Temperature of the Gages in Probe TMA-H-1-TCB (x=-0.005 m, z=-0.027 m)

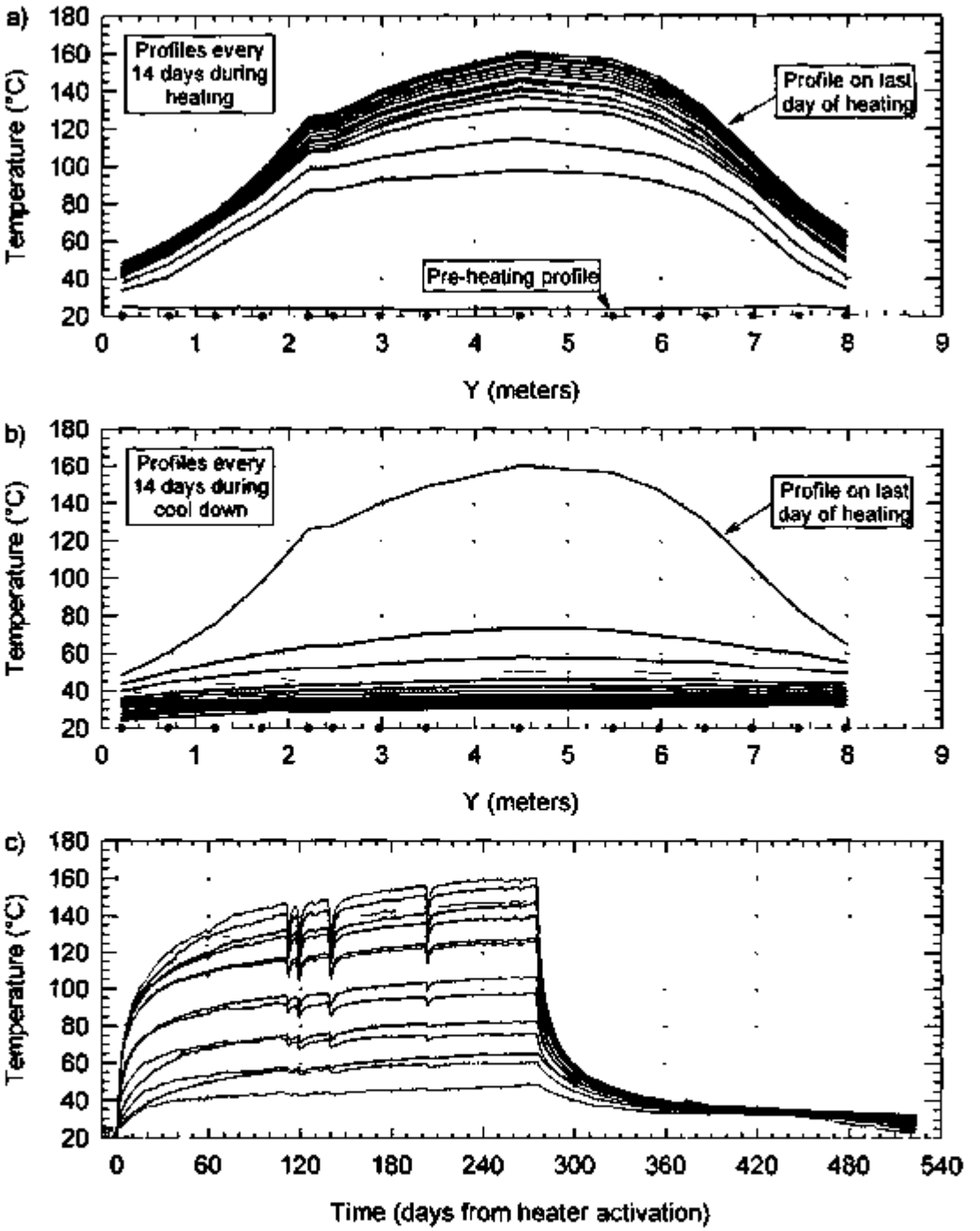

NOTE: Temperatures reflect measurements taken by thermocouples evenly spaced in a borehole parallel to and 0.42 m away from the heater.
Temperature shown: (a) as a function of Y every 14 days during the heating phase of the SHT
(b) as a function of Y every 14 days during the cooling phase of the SHT
(c) as a function of time

Figure 7-6 Median Daily Temperature of the Gages in Probe TMA-TC-1 (x=-0.237 m, z=0.342 m)

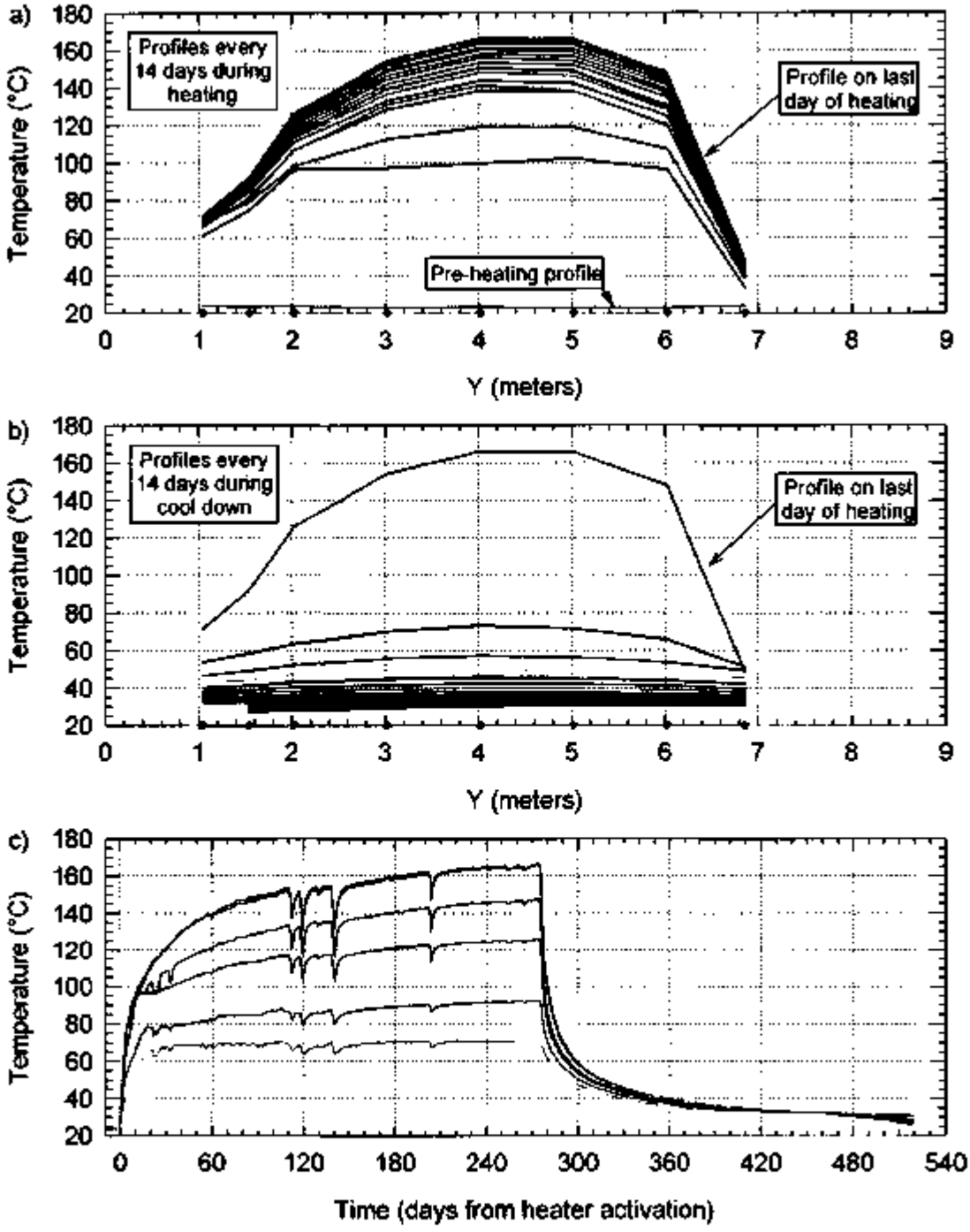

NOTE: Temperature shown: (a) as a function of Y every 14 days during the heating phase of the SHT
(b) as a function of Y every 14 days during the cooling phase of the SHT
(c) as a function of time.

Figure 7-7. Median Daily Temperature of the Gages in Probe TMA-MPBX-1 (x=0.148 m, z=0.306 m)

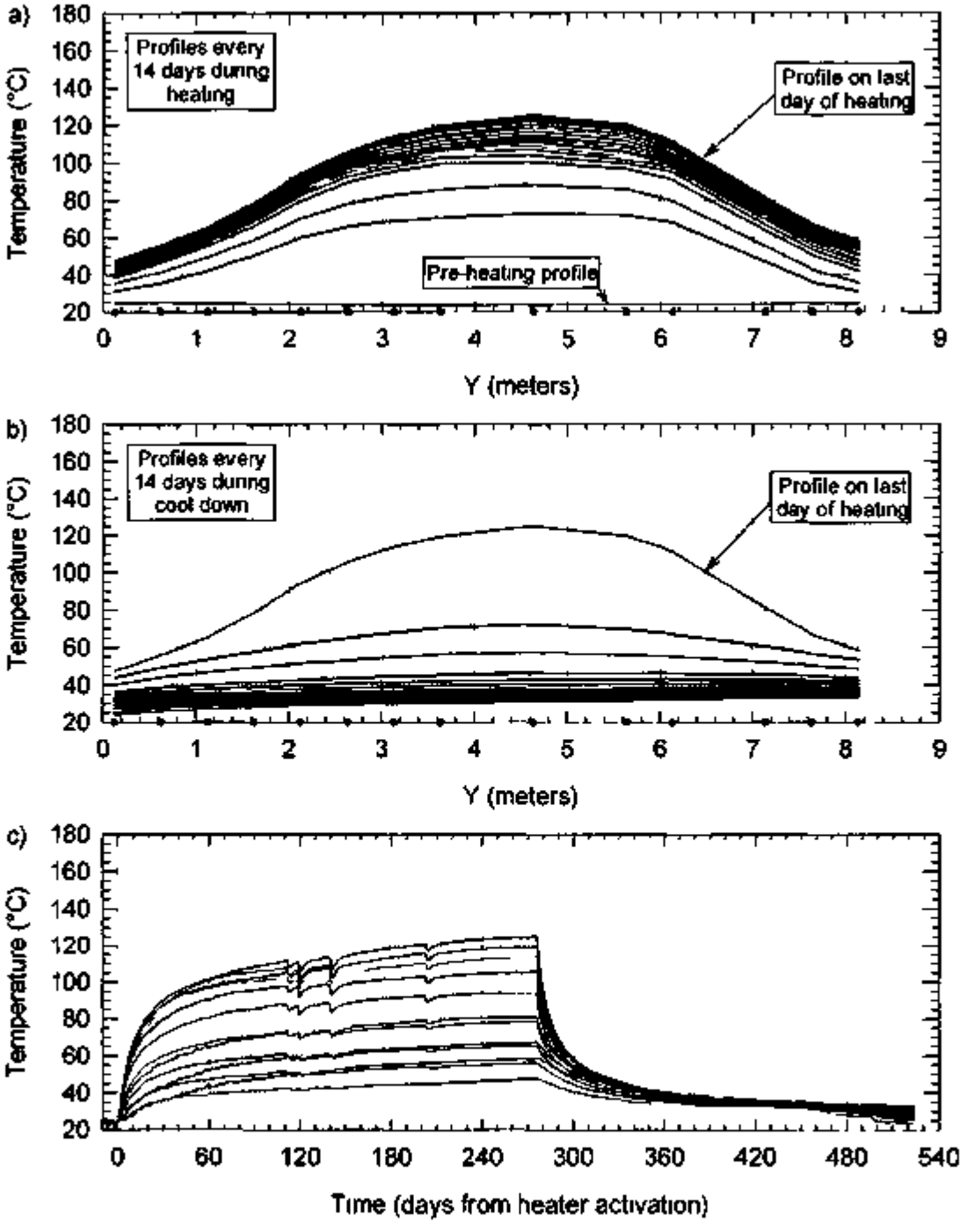

NOTE Temperatures reflect measurements taken by thermocouples evenly spaced in a borehole parallel to and 0 66 m away from the heater
Temperature shown (a) as a function of Y every 14 days during the heating phase of the SHT
(b) as a function of Y every 14 days during the cooling phase of the SHT
(c) as a function of time

Figure 7-8 Median Daily Temperature of the Gages in Probe TMA-TC-2 (x=0 613 m, z=0 263 m)

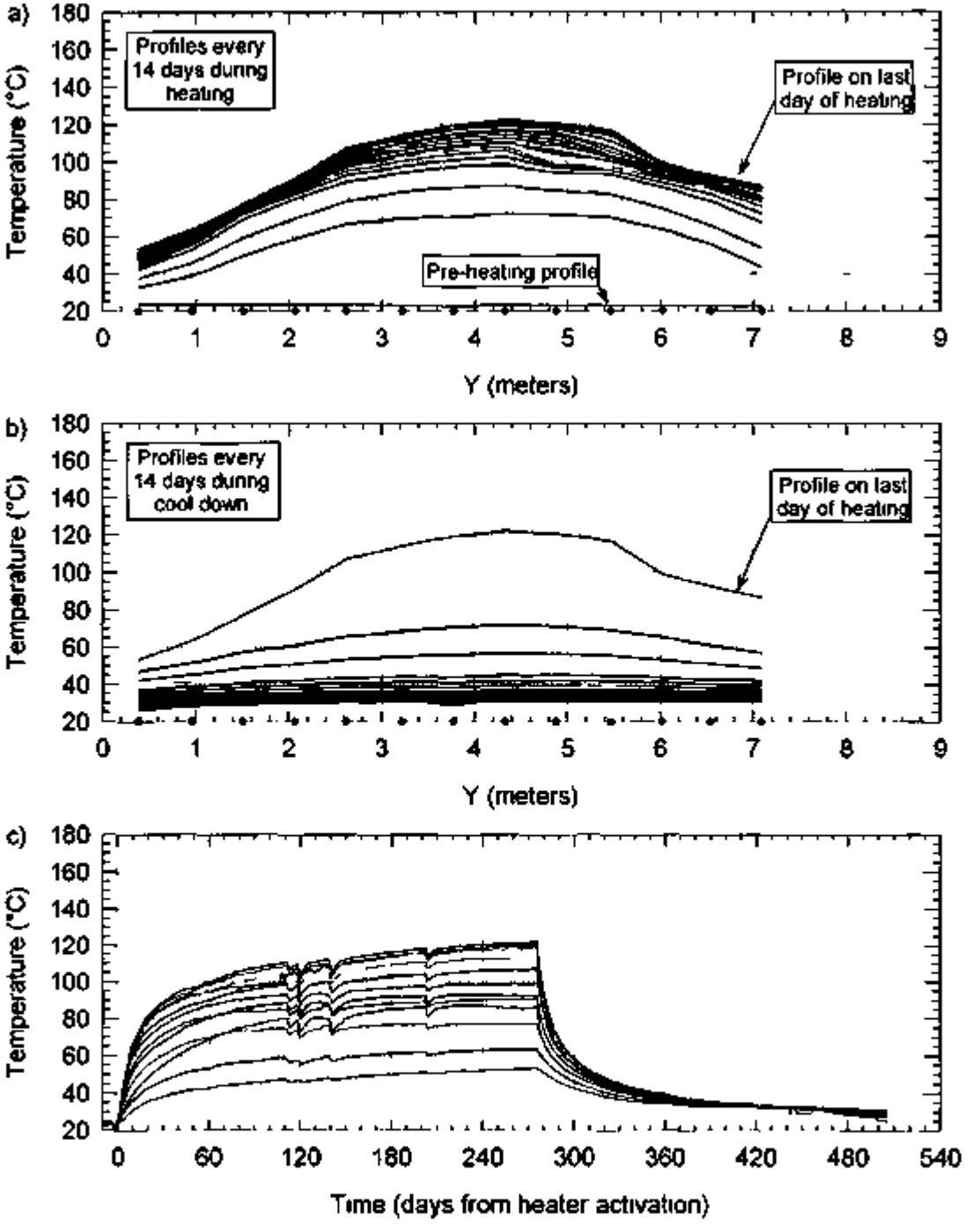

NOTE Temperature shown (a) as a function of Y every 14 days during the heating phase of the SHT
(b) as a function of Y every 14 days during the cooling phase of the SHT
(c) as a function of time

Figure 7-9 Median Daily Temperature of the Gages in Probe TMA-MPBX-2 (x=-0 628 m, z=0 263 m)

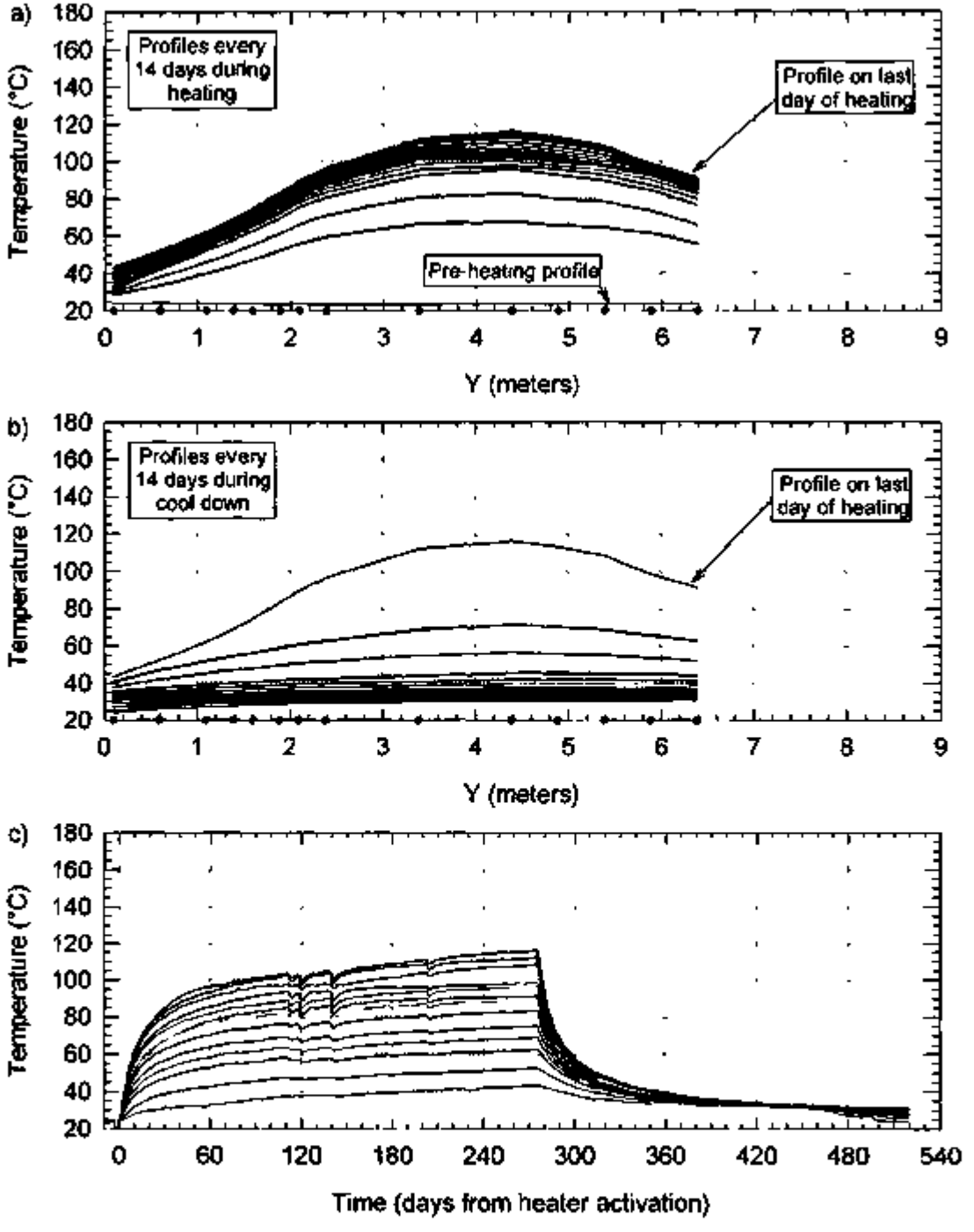

NOTE Temperature shown: (a) as a function of Y every 14 days during the heating phase of the SHT
(b) as a function of Y every 14 days during the cooling phase of the SHT
(c) as a function of time.

Figure 7-10. Median Daily Temperature of the Gages in Probe TMA-TC-4 (x=-0.083 m, z=-0.724 m)

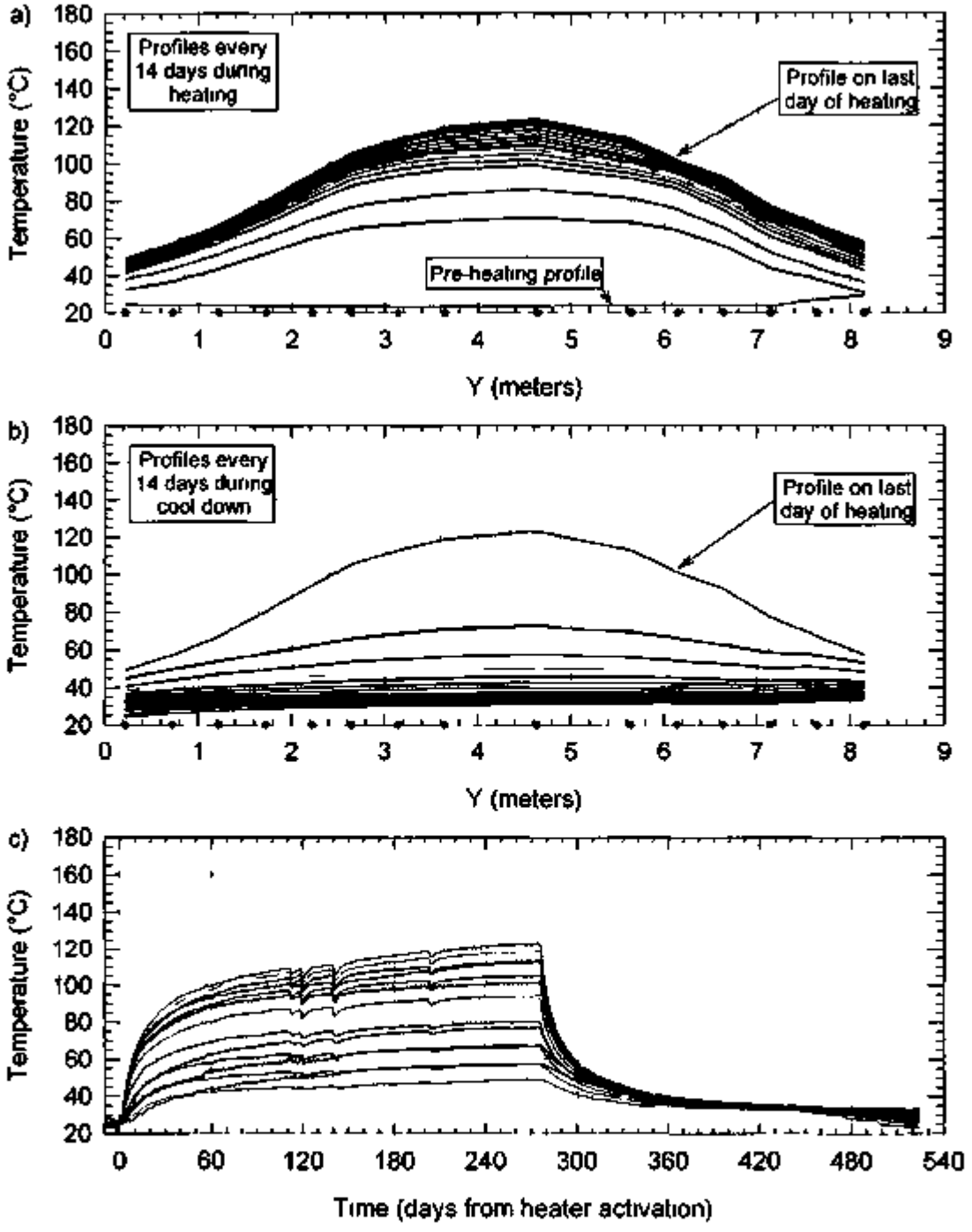

NOTE Temperature shown (a) as a function of Y every 14 days during the heating phase of the SHT
(b) as a function of Y every 14 days during the cooling phase of the SHT
(c) as a function of time

Figure 7-11 Median Daily Temperature of the Gages in Probe TMA-TC-5 (x=-0 038 m, z=0 699 m)

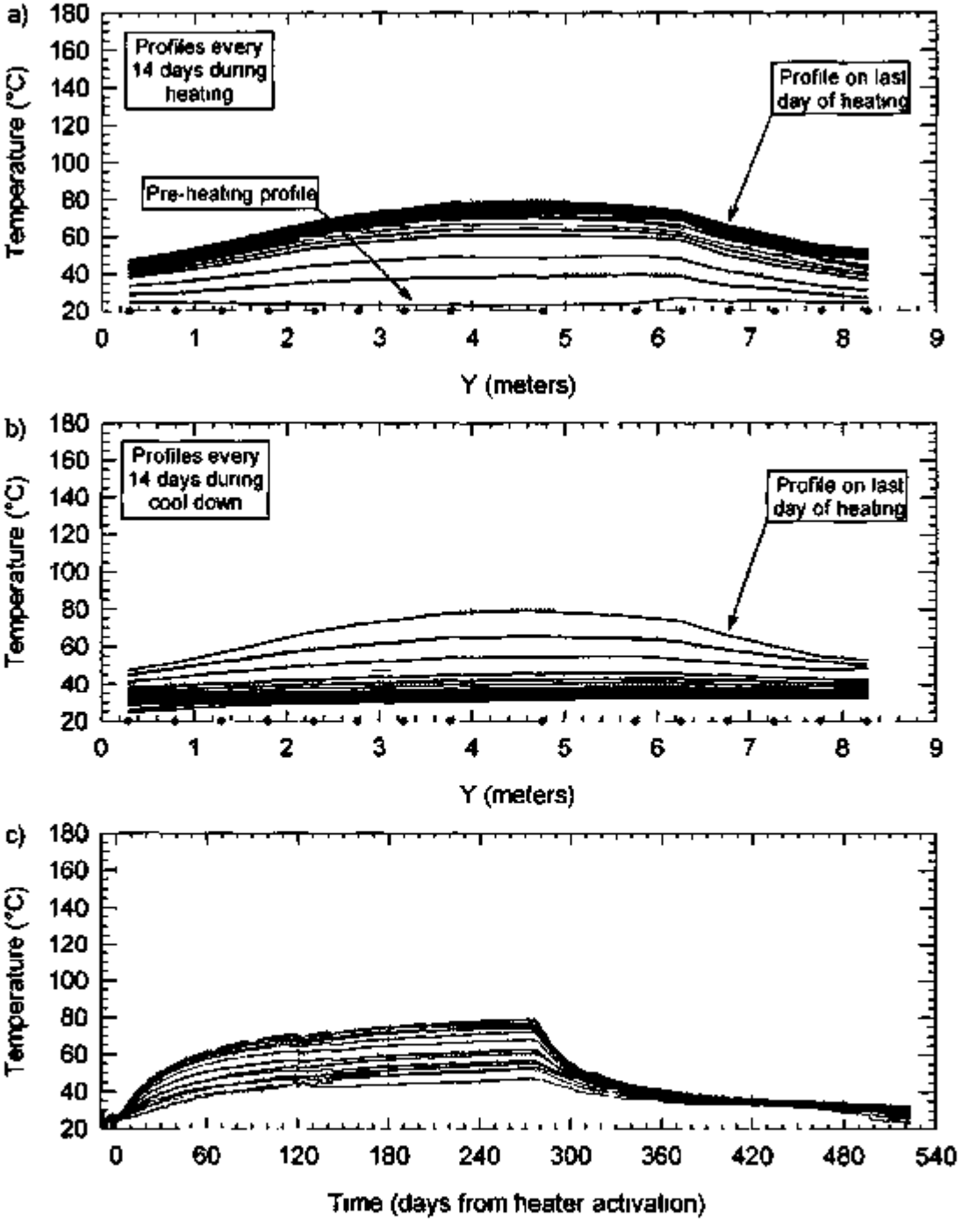

NOTE Temperatures reflect measurements taken by thermocouples evenly spaced in a borehole parallel to and 1 47 m away from the heater
Temperature shown (a) as a function of Y every 14 days during the heating phase of the SHT
(b) as a function of Y every 14 days during the cooling phase of the SHT
(c) as a function of time

Figure 7-12 Median Daily Temperature of the Gages in Probe TMA-TC-3 (x=-0 734 m, z=1 138 m)

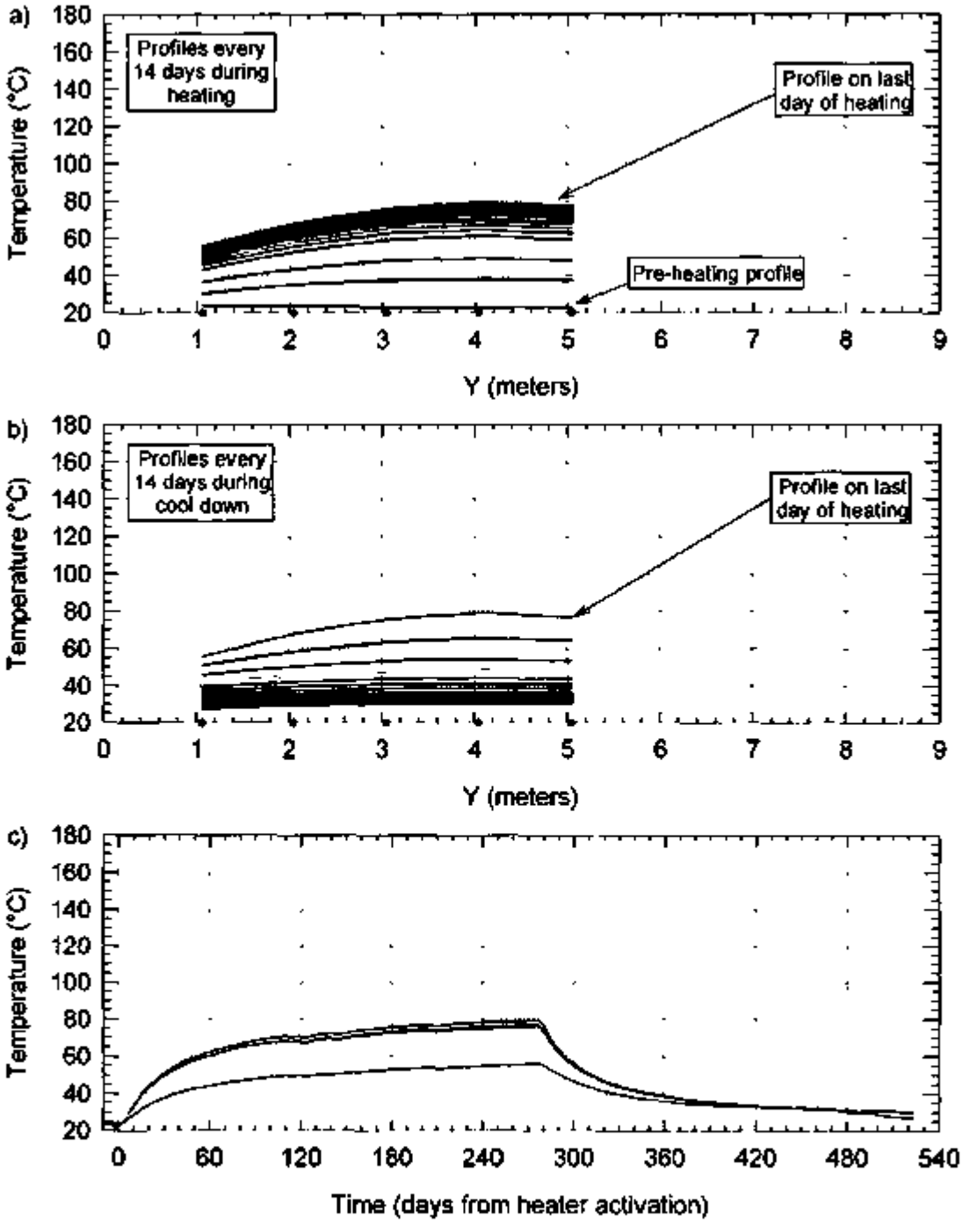

NOTE: Temperature shown: (a) as a function of Y every 14 days during the heating phase of the SHT
(b) as a function of Y every 14 days during the cooling phase of the SHT
(c) as a function of time

Figure 7-13. Median Daily Temperature of the Gages in Probe TMA-MPBX-3 (x=0.759 m, z=1.295 m)

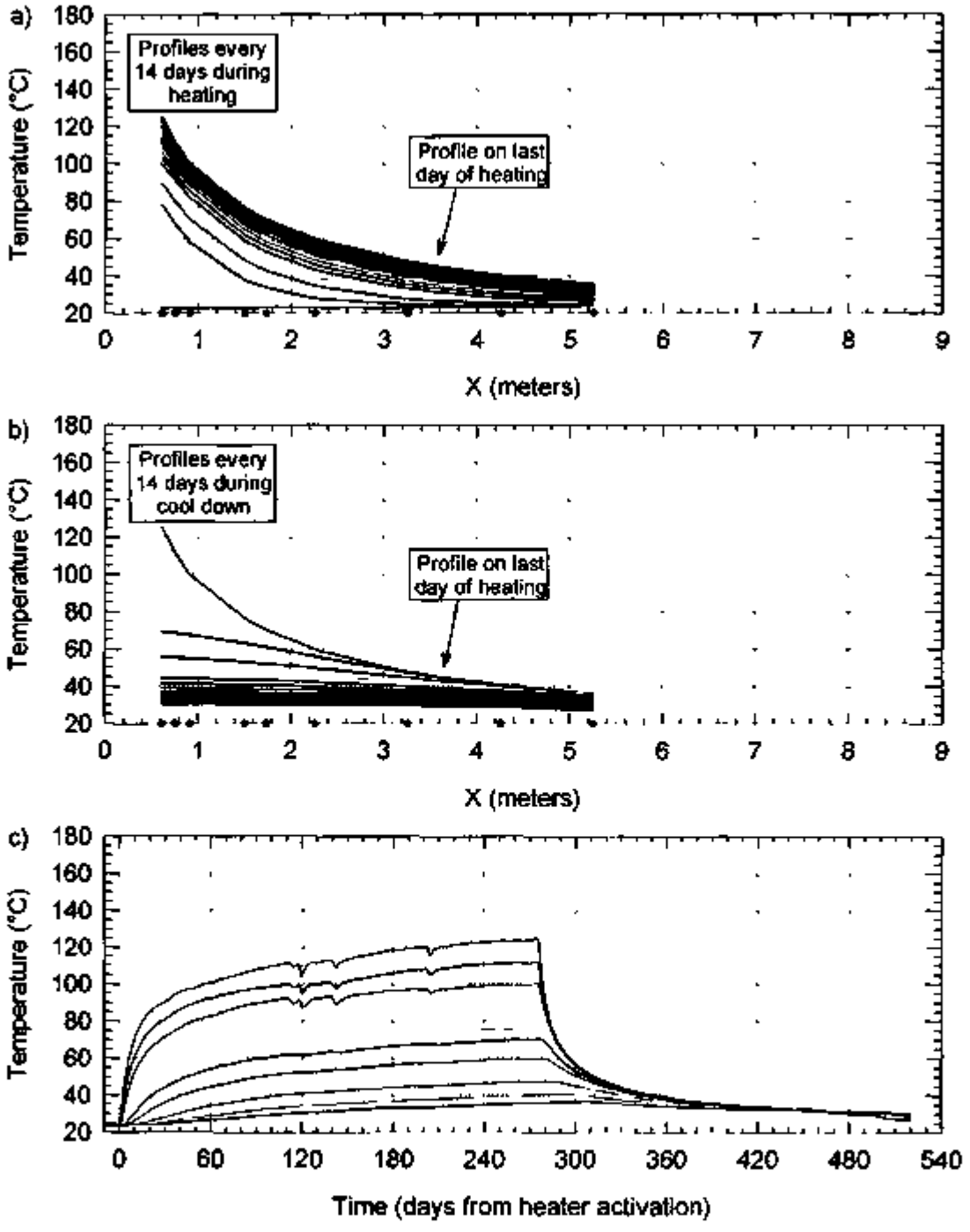

NOTE Temperature shown (a) as a function of Y every 14 days during the heating phase of the SHT
(b) as a function of Y every 14 days during the cooling phase of the SHT
(c) as a function of time.

Figure 7-14. Median Daily Temperature of the Gages in Probe TMA-TC-6 (y=5.434 m, z=-0 001 m)

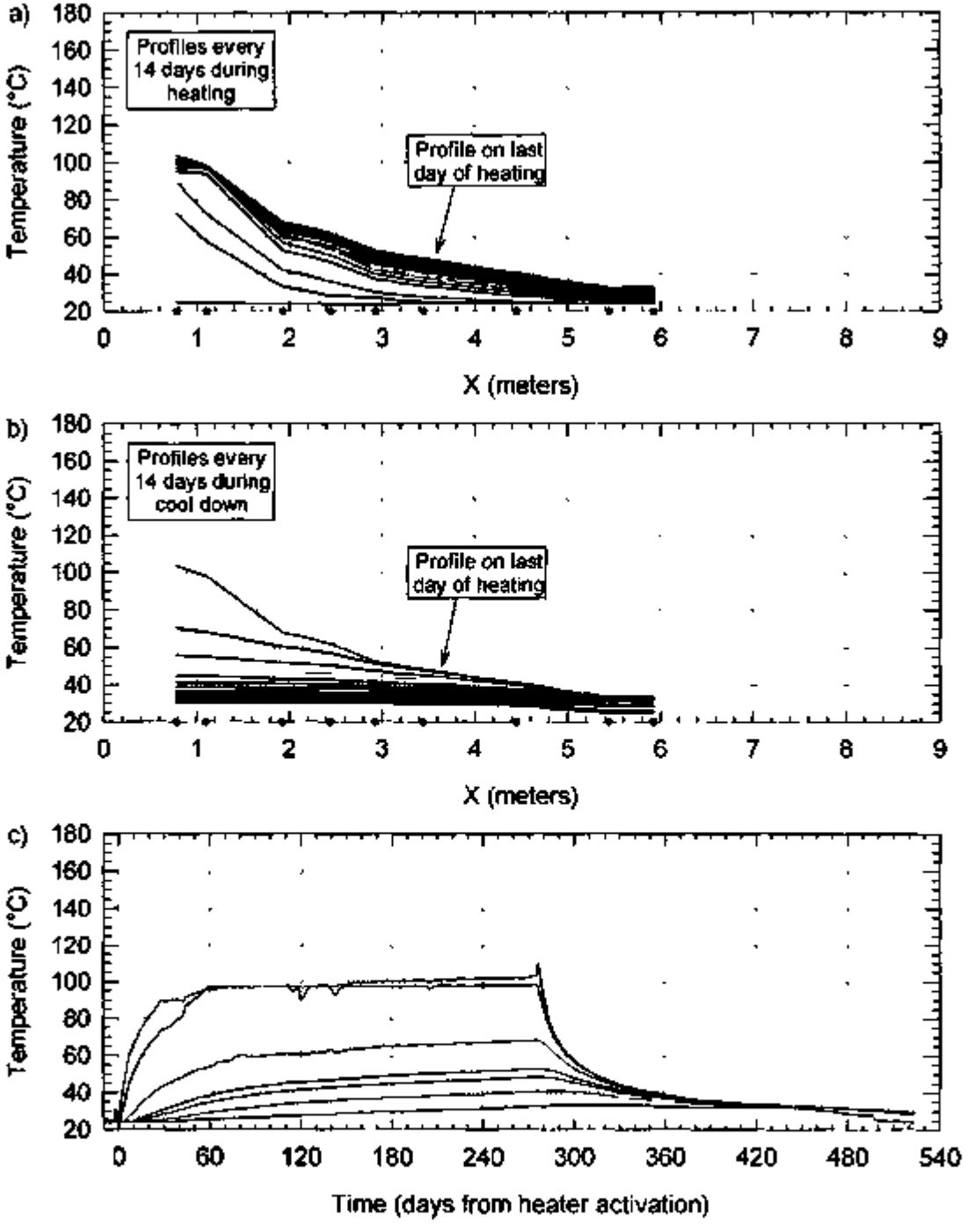

NOTE: Temperature shown (a) as a function of Y every 14 days during the heating phase of the SHT
(b) as a function of Y every 14 days during the cooling phase of the SHT
(c) as a function of time.

Figure 7-15. Median Daily Temperature of the Gages in Probe TMA-MPBX-4 (y=3.461 m, z=-0.139 m)

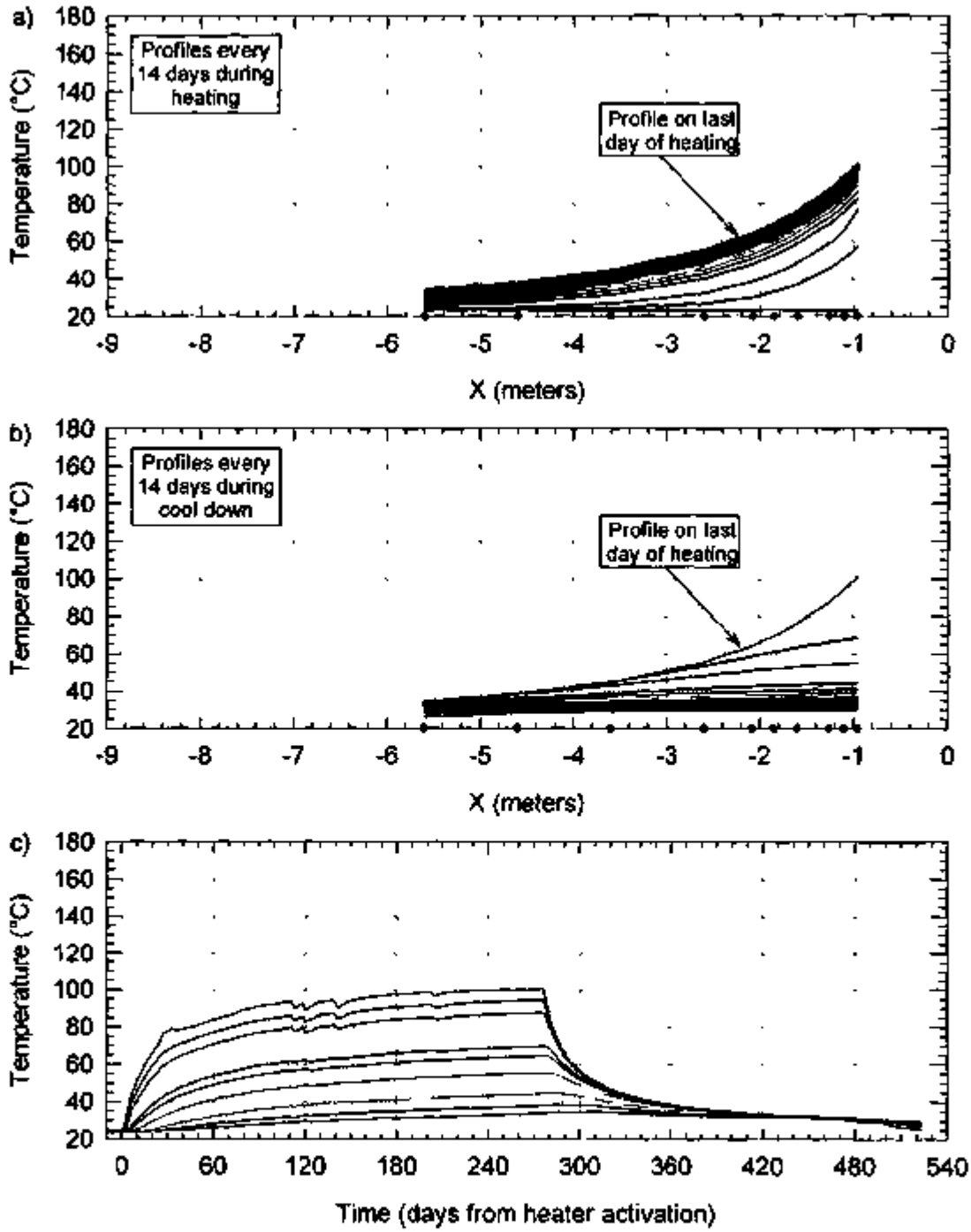

NOTE: Temperature shown: (a) as a function of Y every 14 days during the heating phase of the SHT
(b) as a function of Y every 14 days during the cooling phase of the SHT
(c) as a function of time.

Figure 7-16. Median Daily Temperature of the Gages in Probe TMA-TC-7 (y=3.408 m, z=0.011 m)

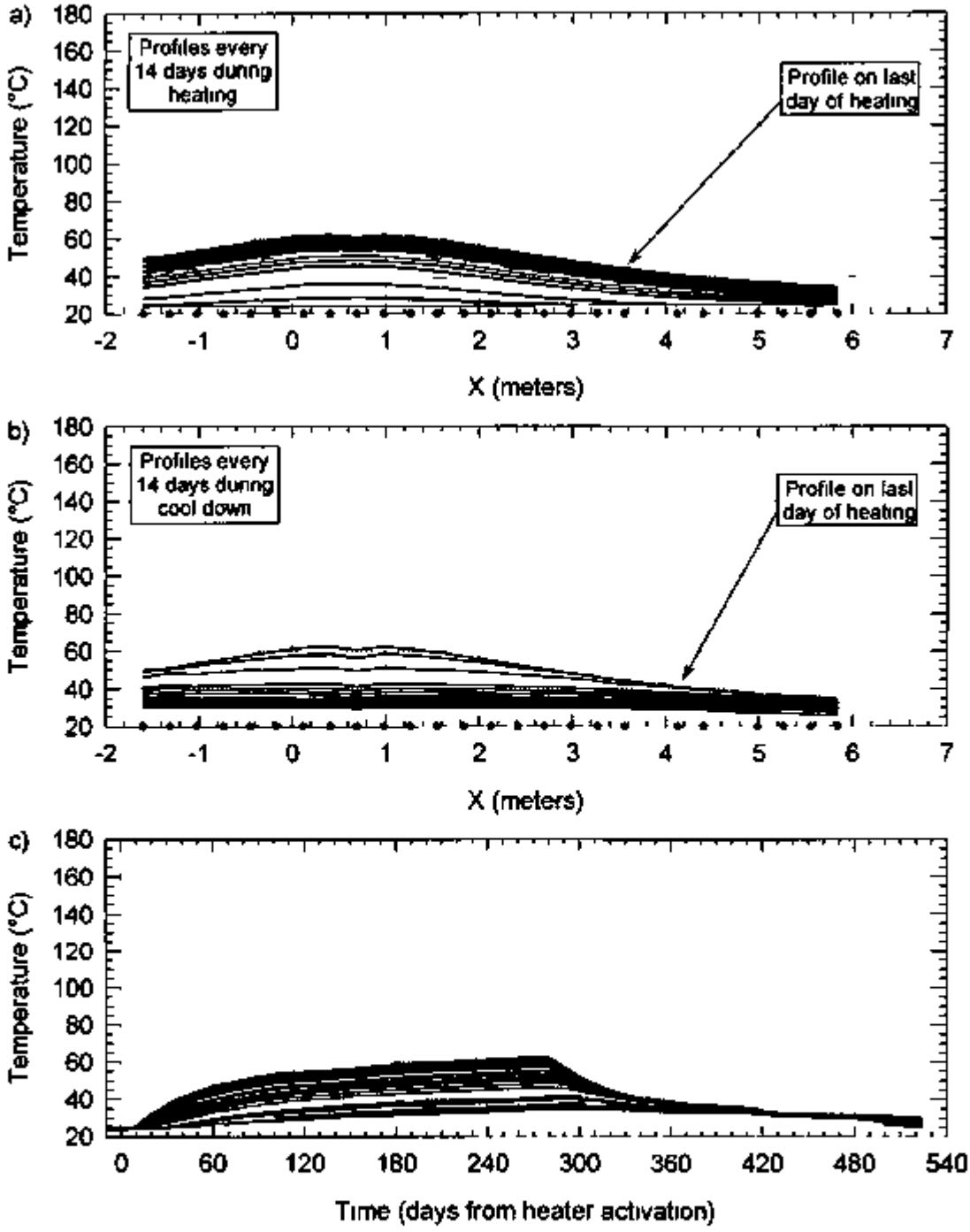

NOTE Temperature shown (a) as a function of Y every 14 days during the heating phase of the SHT
(b) as a function of Y every 14 days during the cooling phase of the SHT
(c) as a function of time

Figure 7-17 Median Daily Temperature of the Gages in Probe TMA-RTD-15 (y=4 25 m)

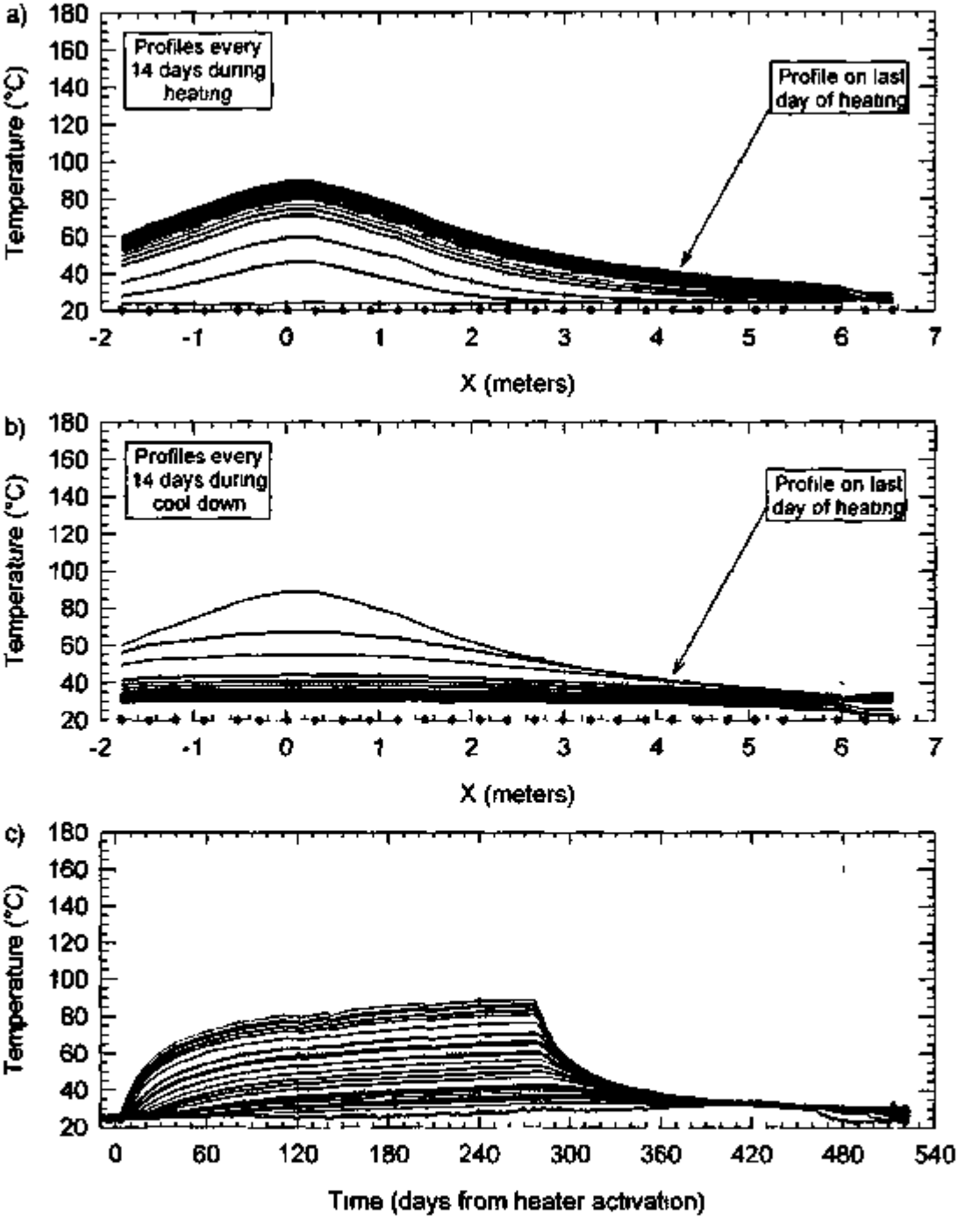

NOTE Temperature shown (a) as a function of Y every 14 days during the heating phase of the SHT
(b) as a function of Y every 14 days during the cooling phase of the SHT
(c) as a function of time

Figure 7-18 Median Daily Temperature of the Gages in Probe TMA-RTD-17 (y=4 27 m)

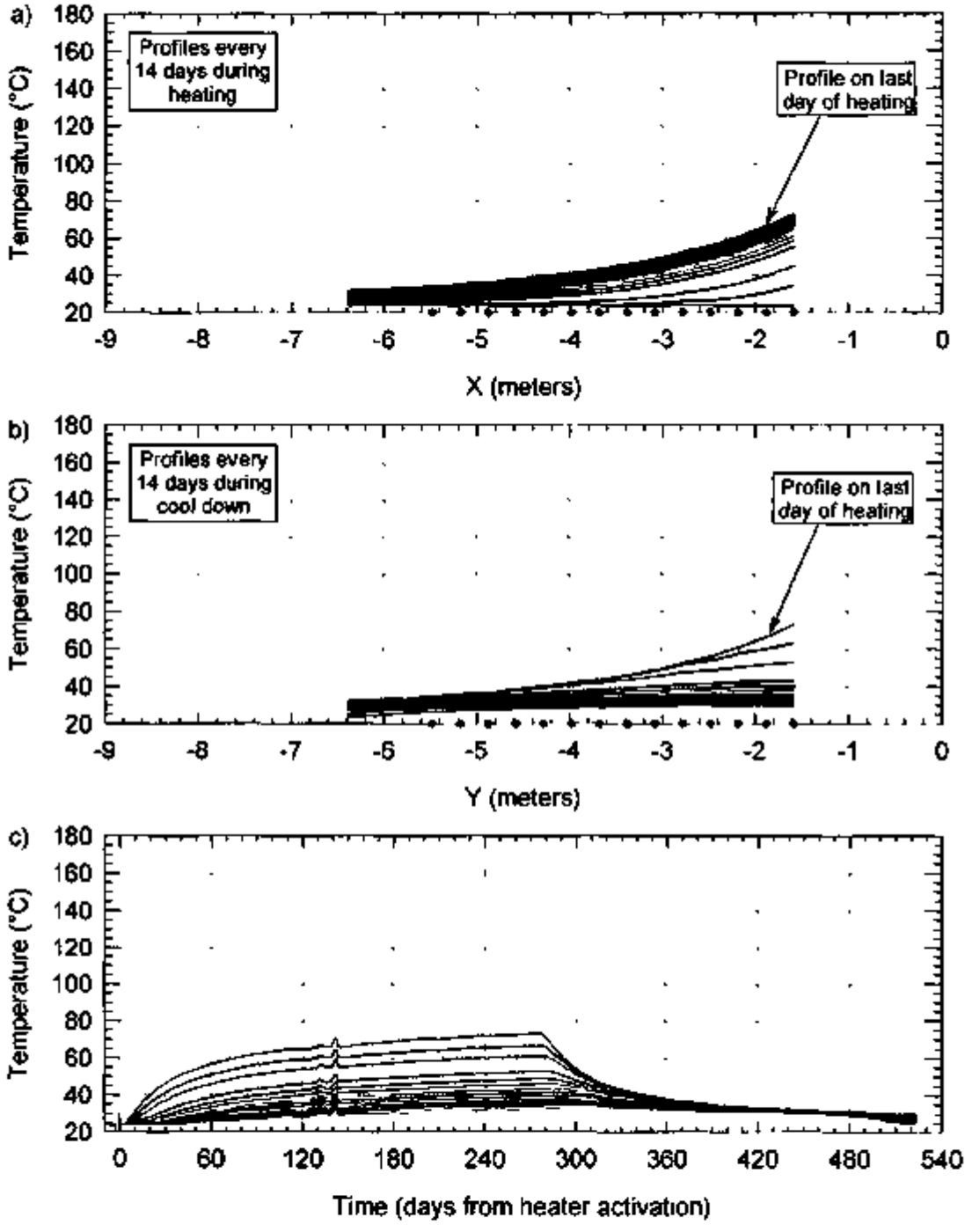

NOTE Temperature shown: (a) as a function of Y every 14 days during the heating phase of the SHT
(b) as a function of Y every 14 days during the cooling phase of the SHT
(c) as a function of time

Figure 7-19. Median Daily Temperature of the Gages in Probe TMA-RTD-22 (y=4.38 *m*, z=-0.66 *m*)

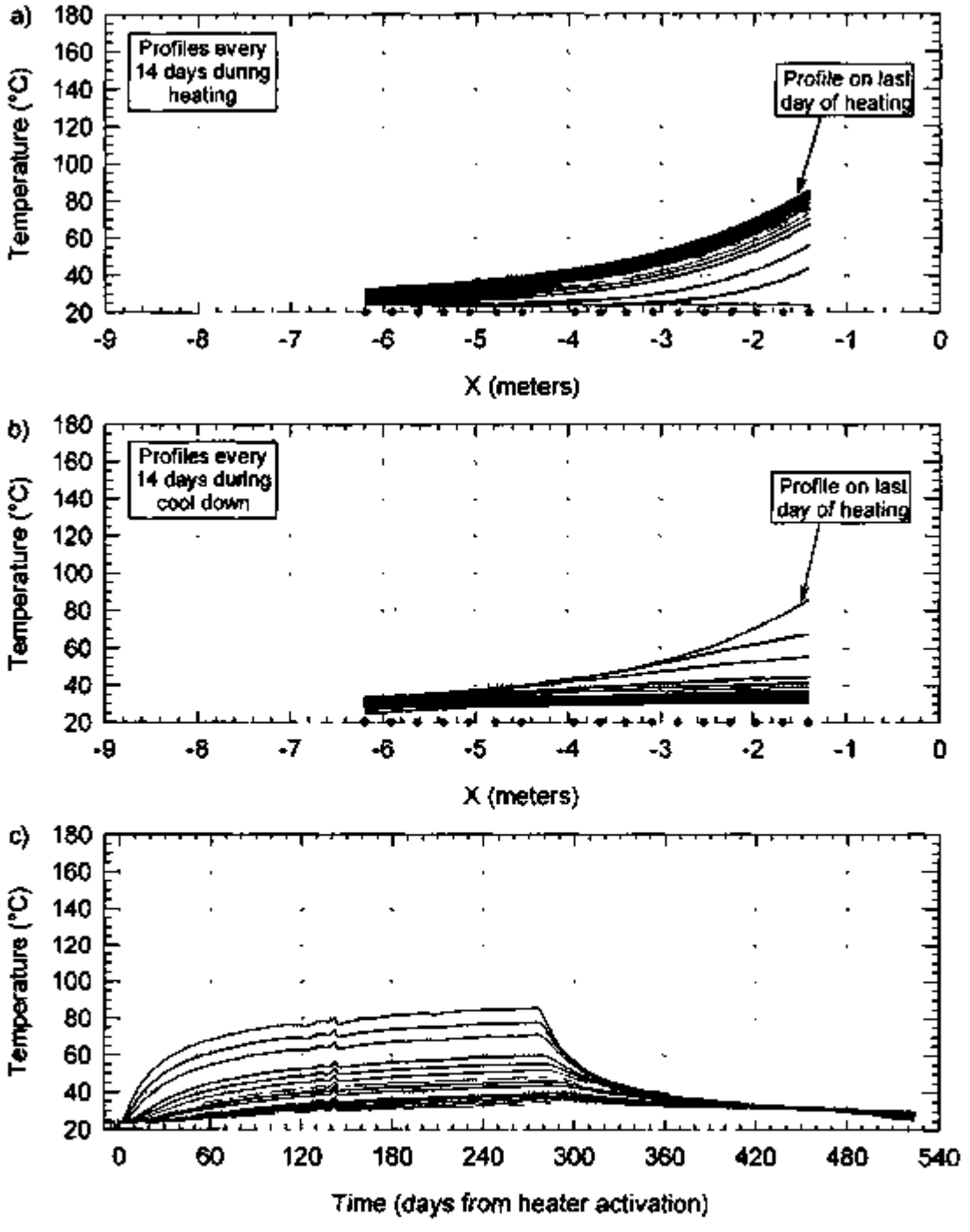

NOTE Temperature shown: (a) as a function of Y every 14 days during the heating phase of the SHT
(b) as a function of Y every 14 days during the cooling phase of the SHT
(c) as a function of time

Figure 7-20. Median Daily Temperature of the Gages in Probe TMA-RTD-23 (y=4.39 m)

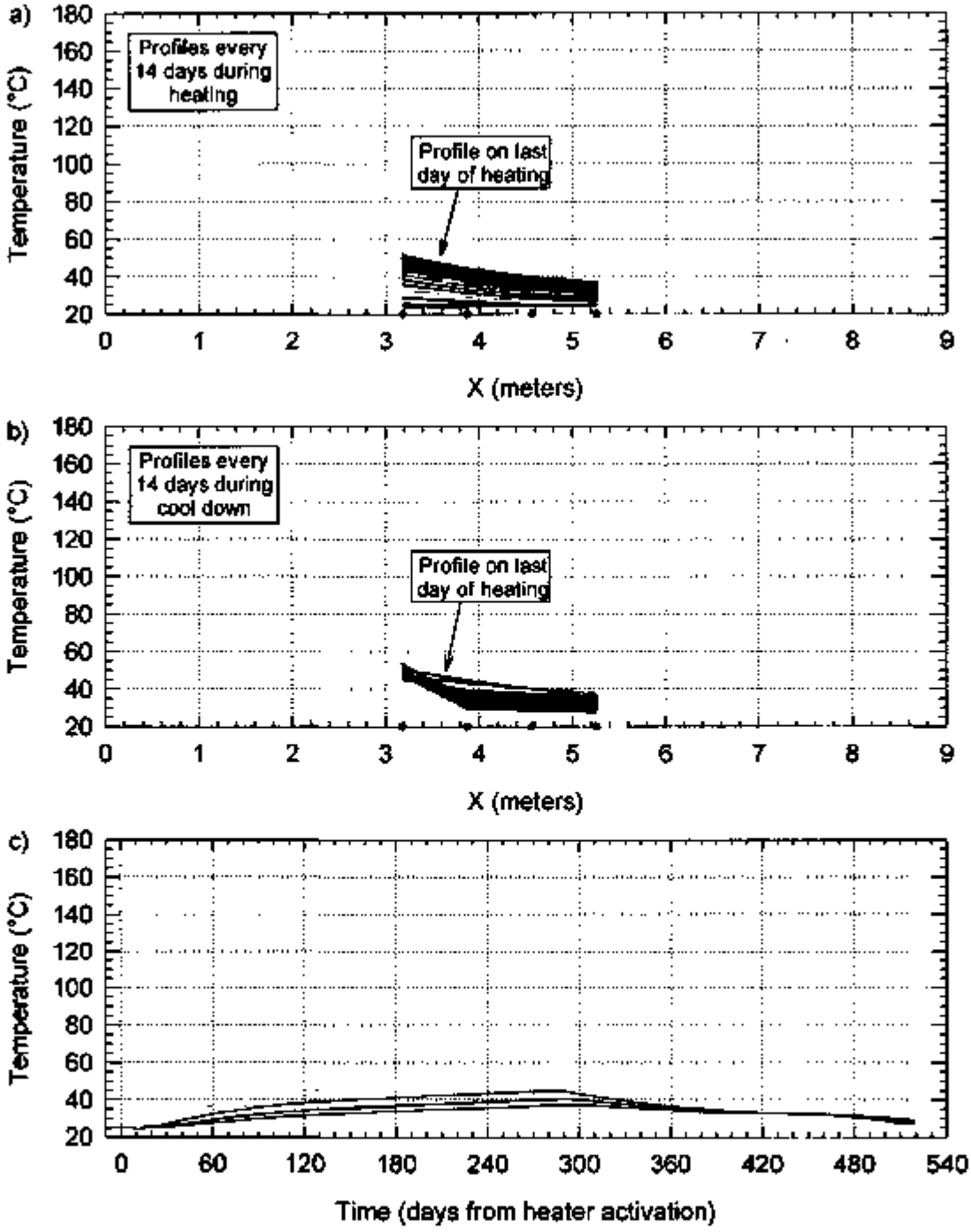

NOTE: Temperature shown: (a) as a function of Y every 14 days during the heating phase of the SHT
(b) as a function of Y every 14 days during the cooling phase of the SHT
(c) as a function of time.

Figure 7-21. Median Daily Temperature of the Gages in Probe TMA-TEMP-16 (y=4.275 m)

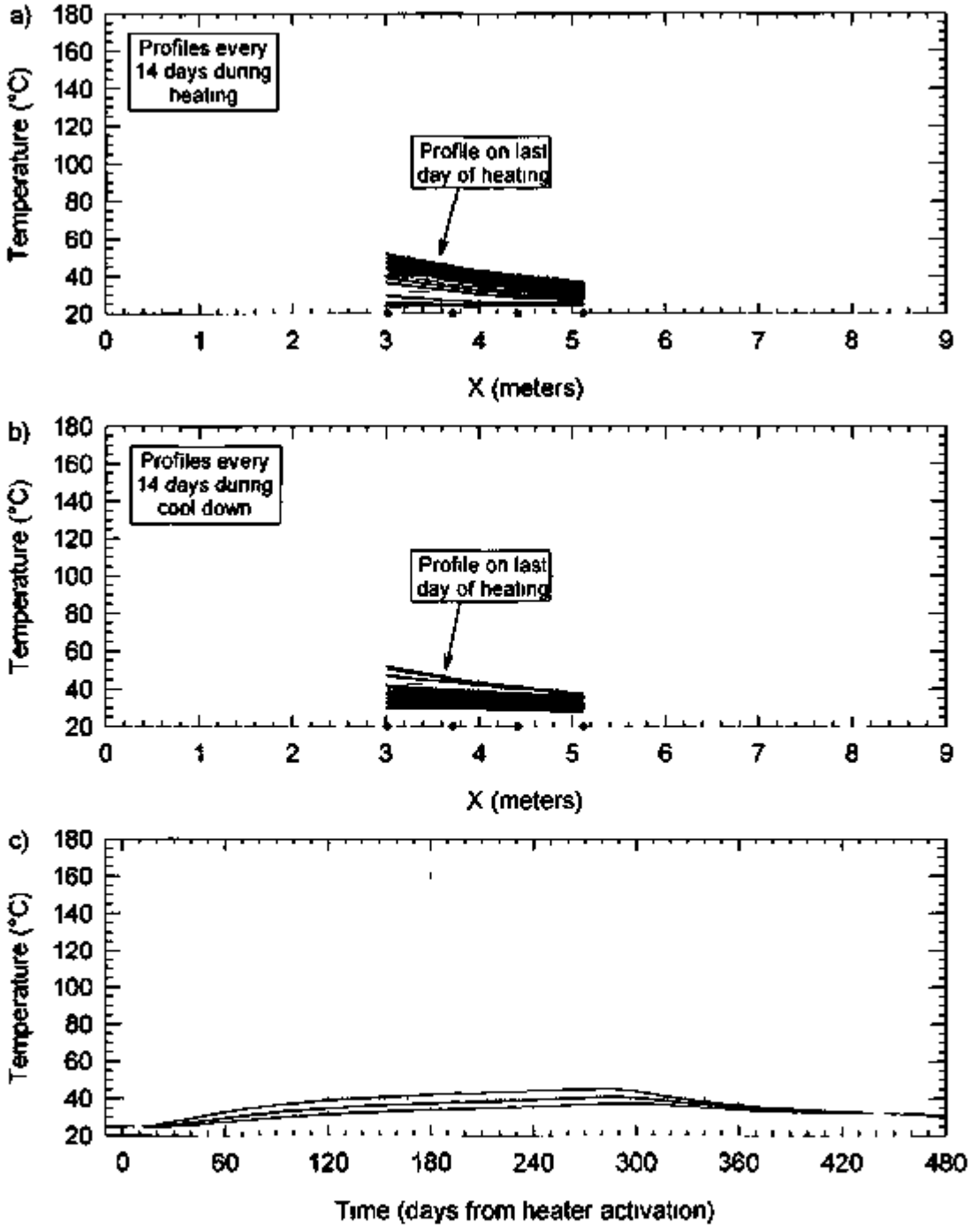

NOTE Temperature shown (a) as a function of Y every 14 days during the heating phase of the SHT
(b) as a function of Y every 14 days during the cooling phase of the SHT
(c) as a function of time

Figure 7-22 Median Daily Temperature of the Gages in Probe TMA-TEMP-18 (y=4 25 m, z=0 22 m)

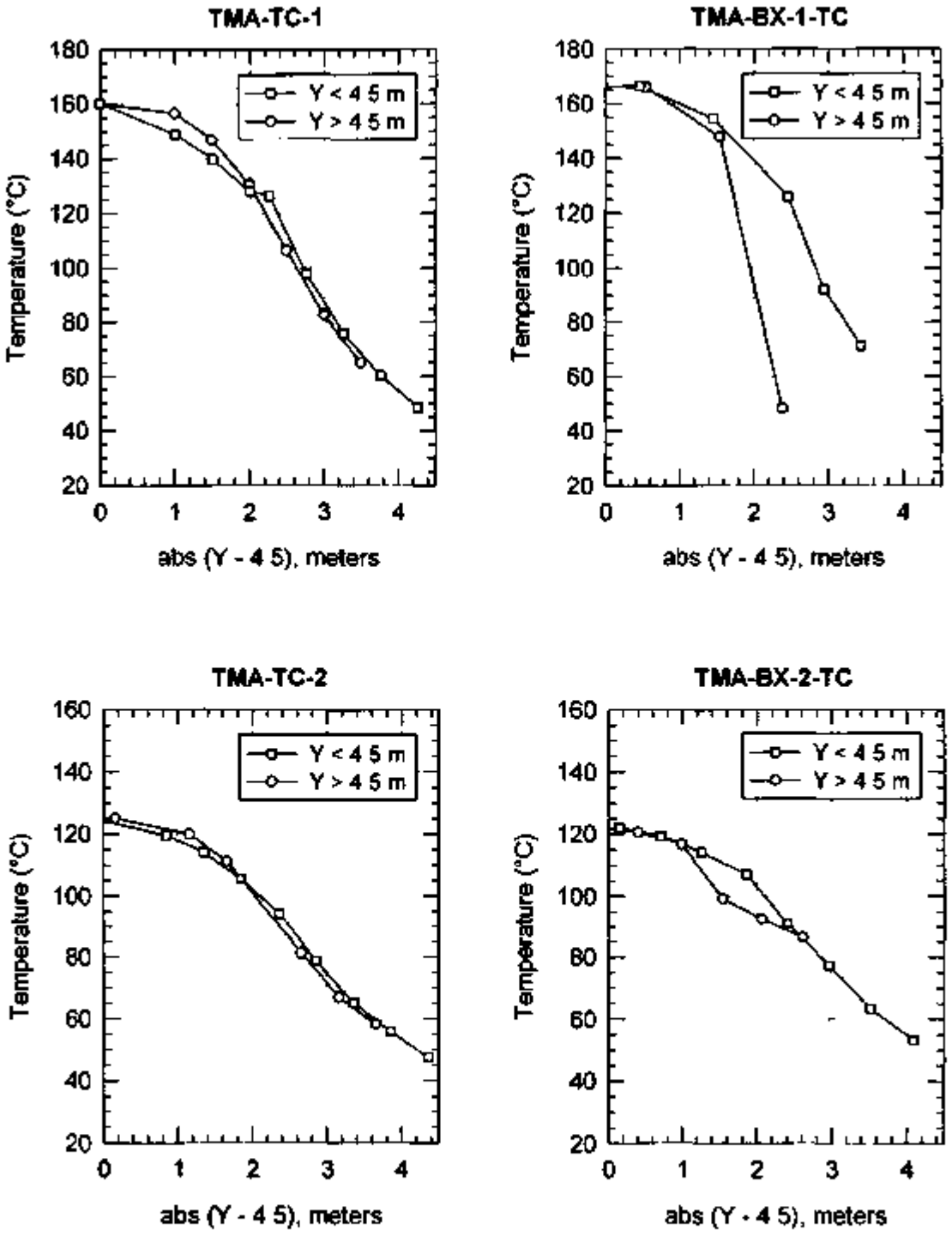

NOTE abs = absolute

Figure 7-23 Temperatures at the End of the Heating Phase Plotted as a Function of Distance from the Center Point of the Heater

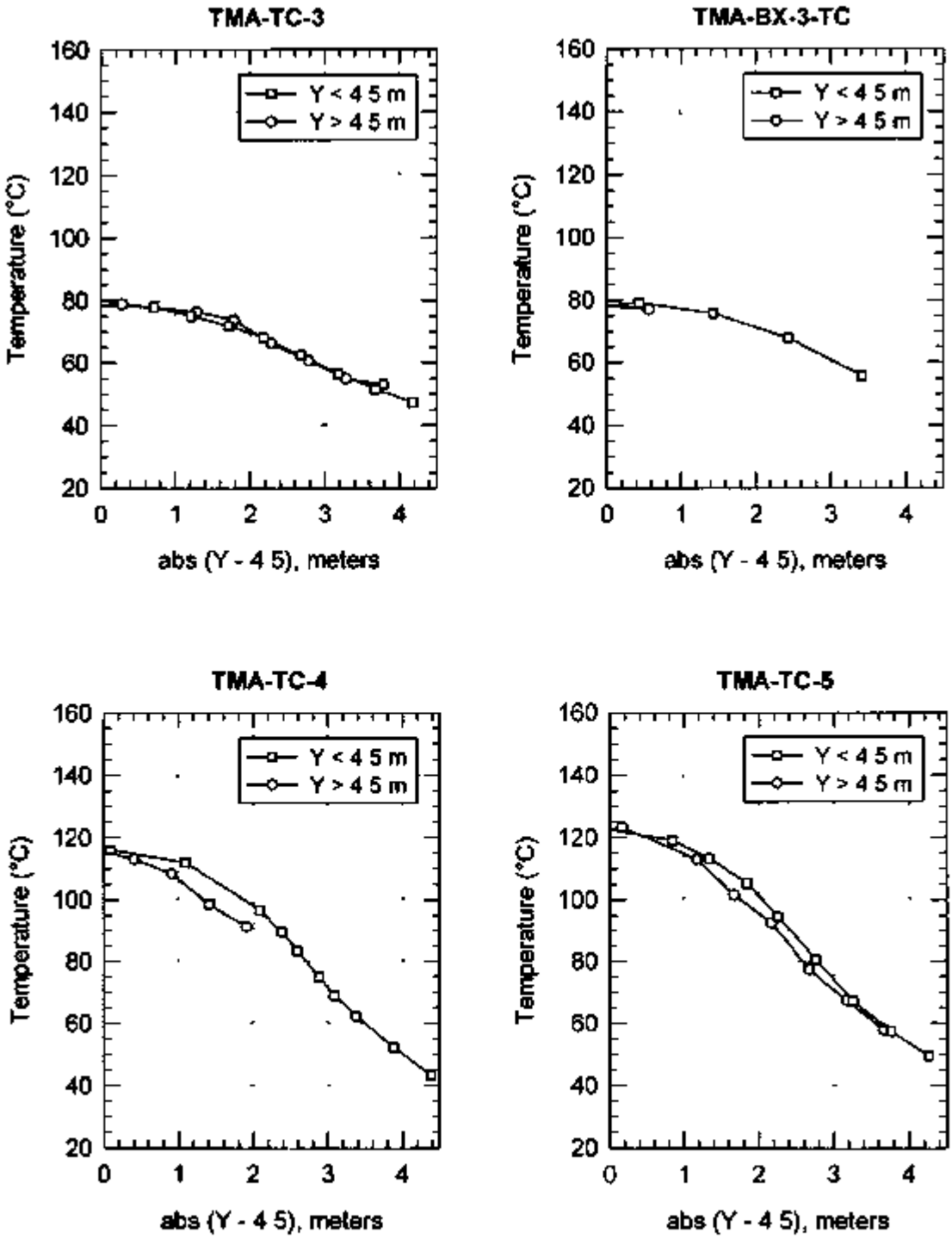

NOTE abs = absolute

Figure 7-24 Temperatures at the End of the Heating Phase Plotted as a Function of Distance from the Center Point of the Heater

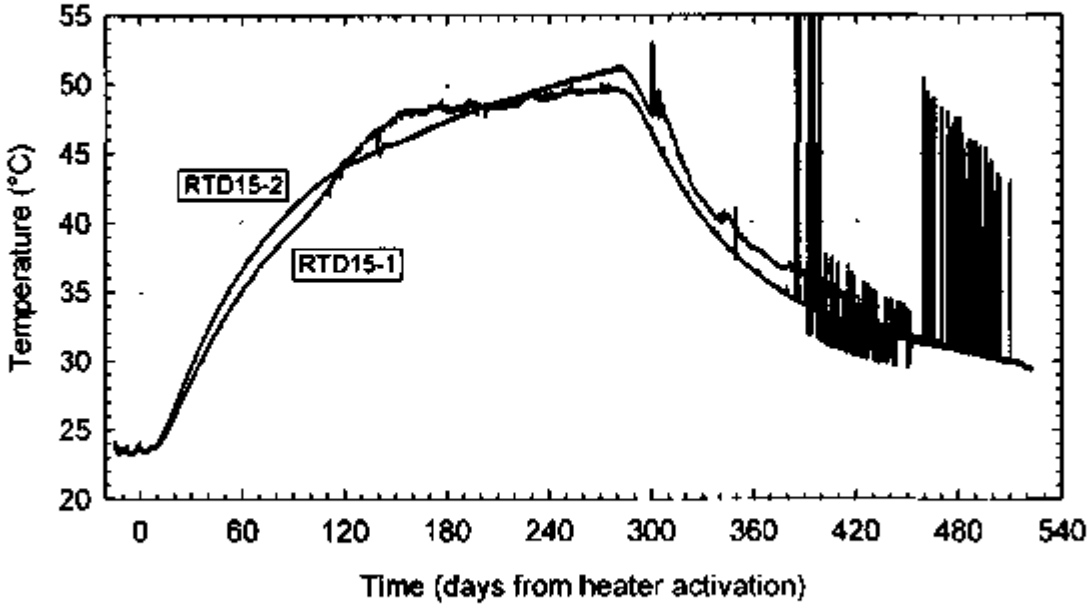

Figure 7-25. Comparison of Data from TMA-RTD-15-1 and TMA-RTD-15-2

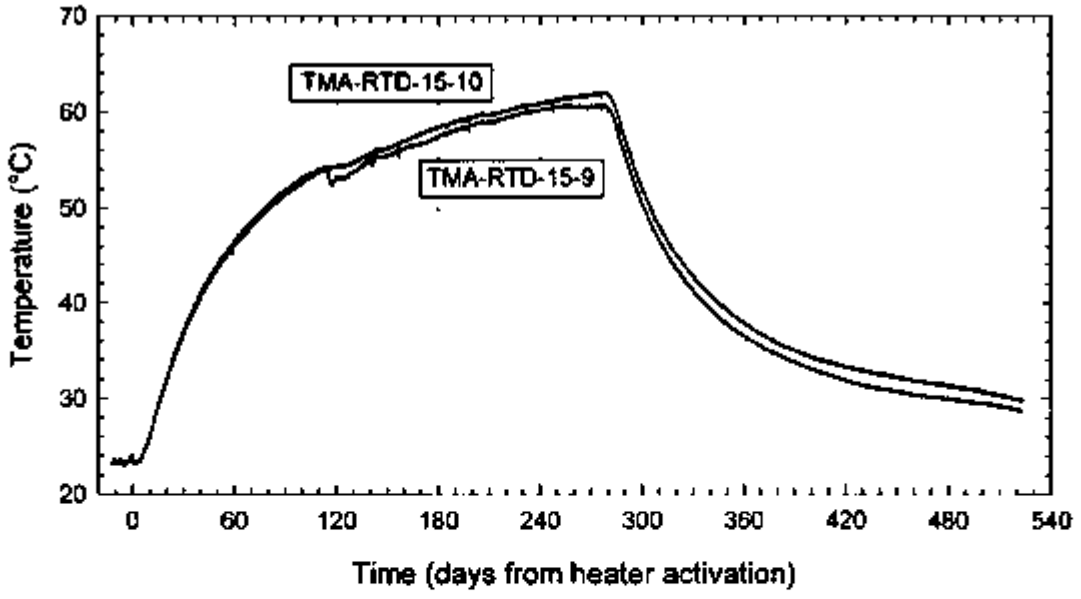

Figure 7-26. Comparison of Data from TMA-RTD-15-9 and TMA-RTD-15-10

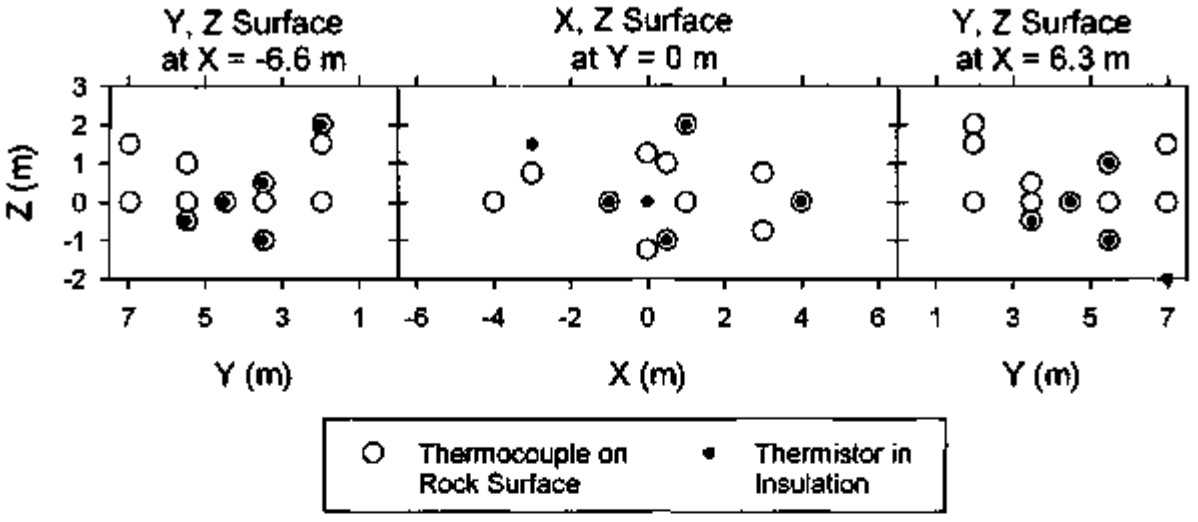

Figure 7-27. Locations of Temperature Gages on the Three Rock Faces and in the Insulation Material

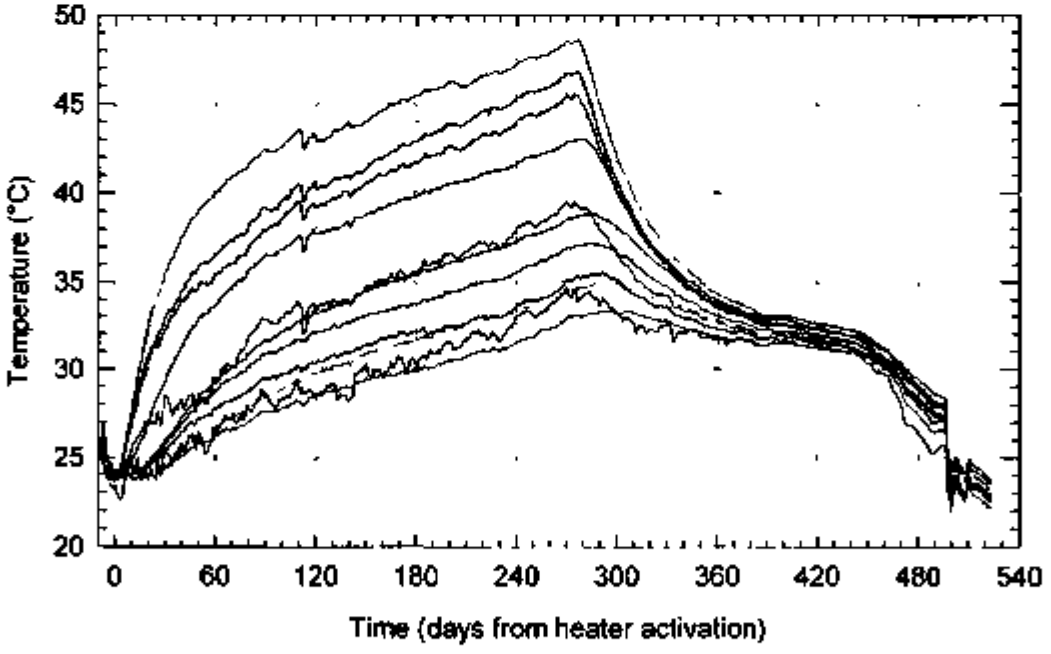

Figure 7-28. Temperature vs. Time for the Thermocouples Mounted on the Thermomechanical Alcove Face of the SHT Block

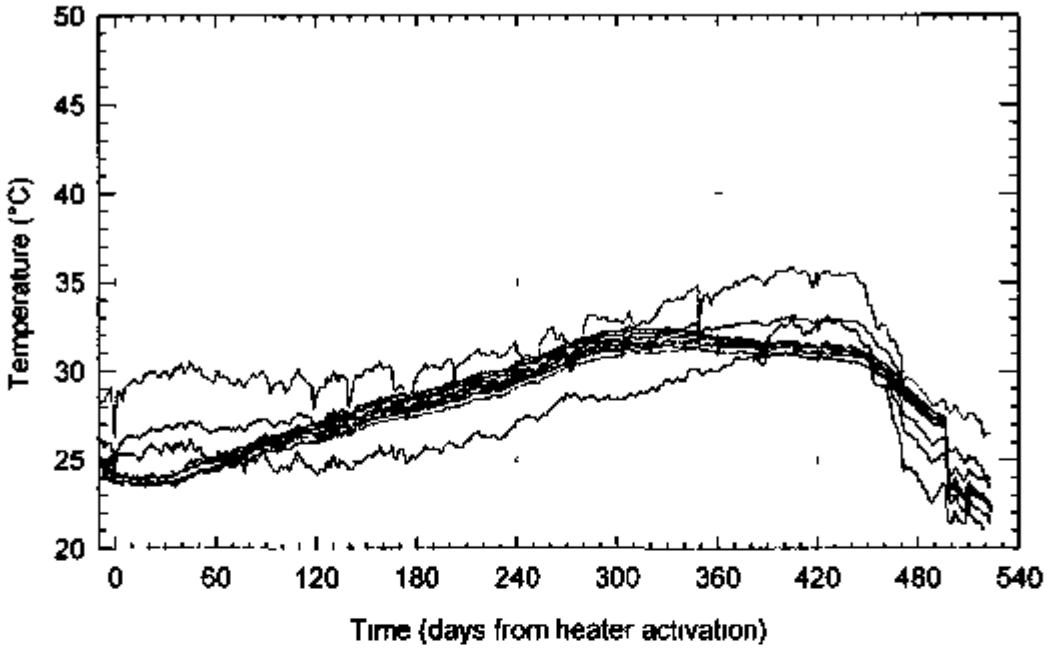

Figure 7-29 Temperature vs Time for the Thermocouples Mounted on the Observation Drift Face of the SHT Block

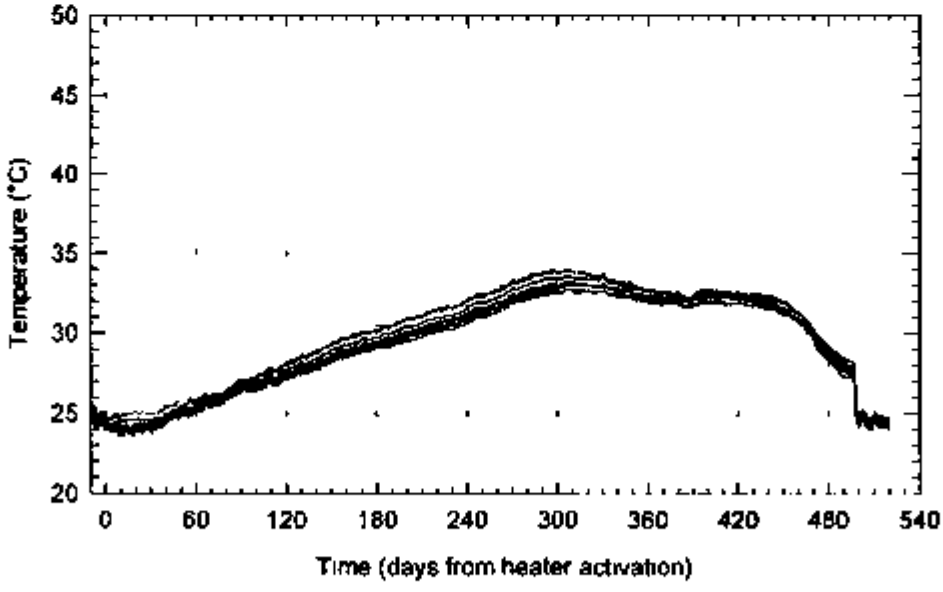

Figure 7-30 Temperature vs Time for the Thermocouples Mounted on the Thermomechanical Alcove Extension Face of the SHT Block

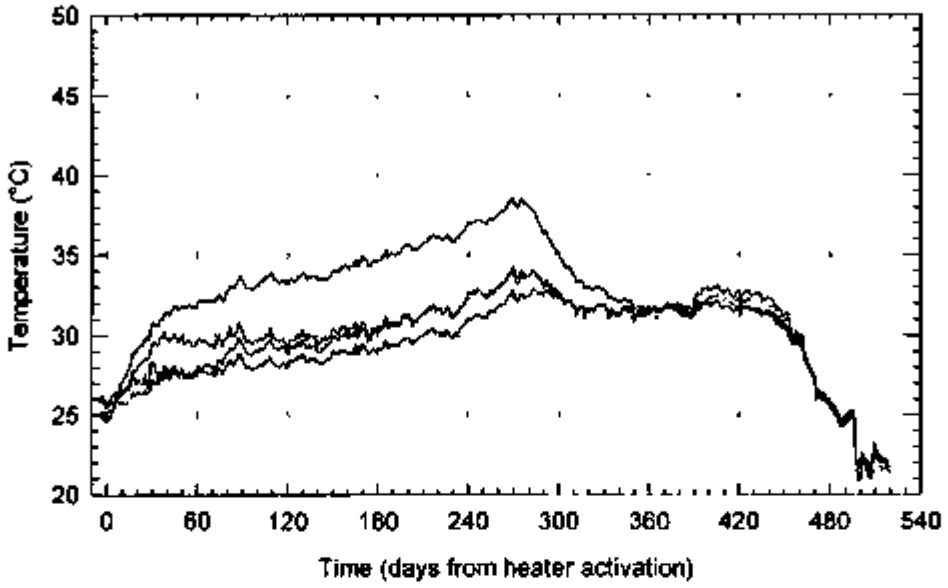

Figure 7-31. Temperature vs. Time for the Thermistors Installed in the Insulation Covering the Thermomechanical Alcove Face of the SHT Block

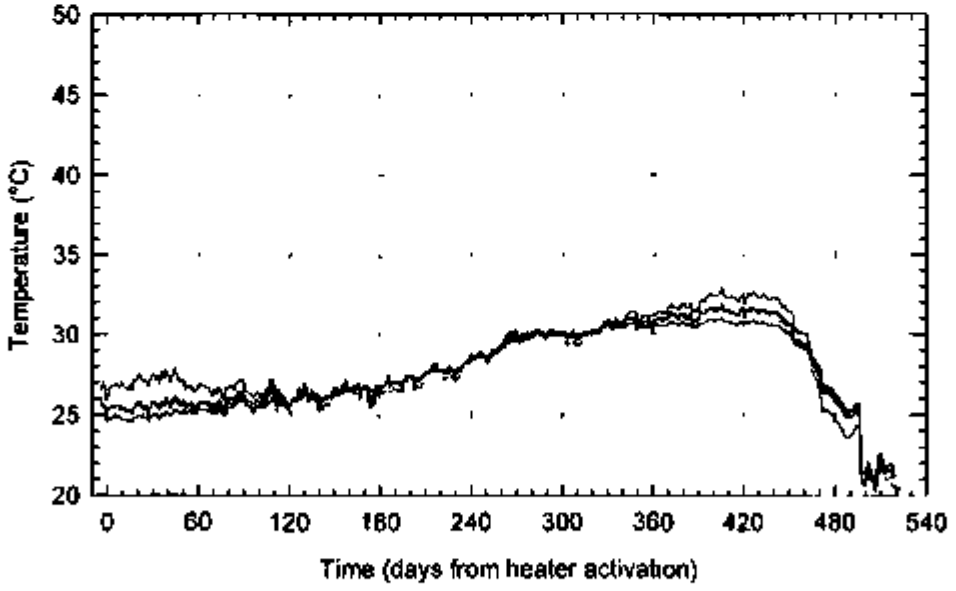

Figure 7-32. Temperature vs. Time for the Thermistors Installed in the Insulation Covering the Observation Drift Face of the SHT Block.

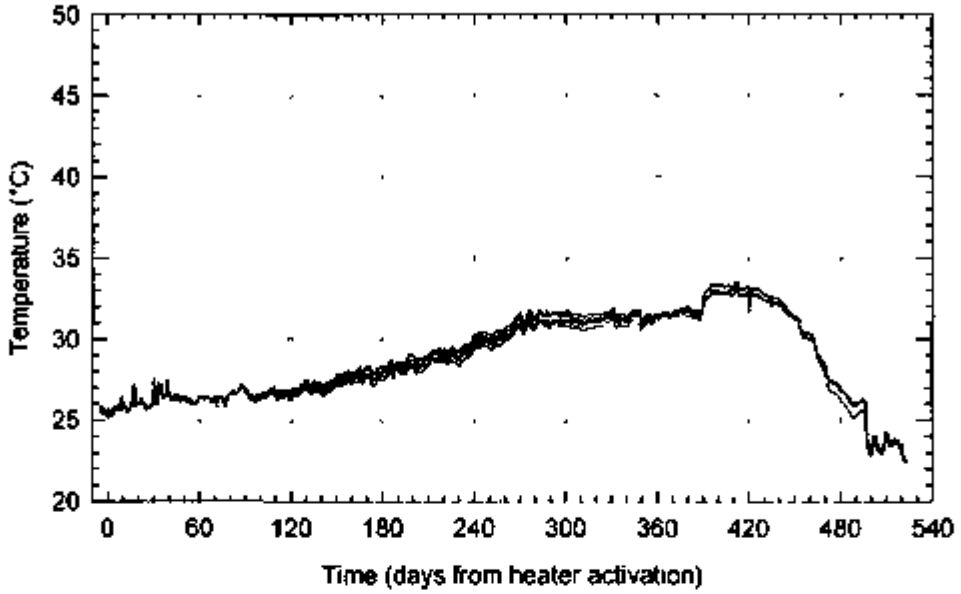

Figure 7-33. Temperature vs. Time for the Thermistors Installed in the Insulation Covering the Thermomechanical Alcove Extension Face of the SHT Block

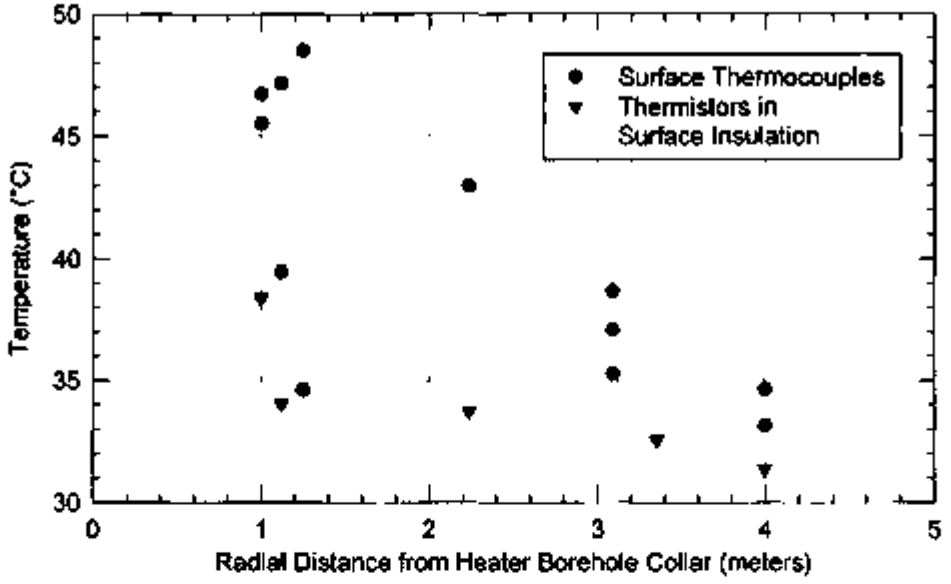

Figure 7-34. Temperature as a Function of Radial Distance from the Heater Borehole Collar for the Surface and Insulation Temperature Gages on the Thermomechanical Alcove Face of the SHT Block, after 275 Days of Heating

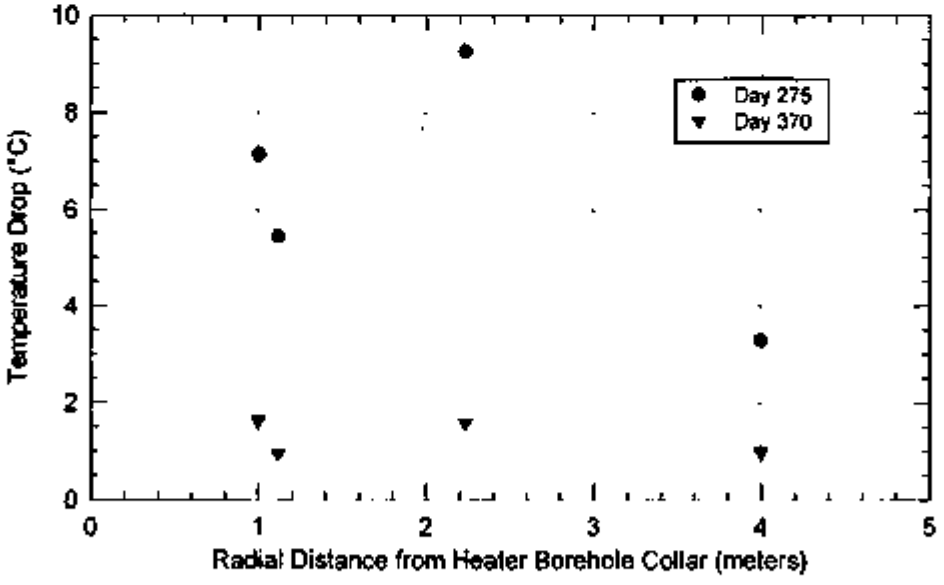

Figure 7-35. Temperature Drop Across the Insulation for Surface-Insulation Temperature Gage Pairs at Four Locations on the Thermomechanical Alcove Face of the SHT, as a Function of Radial Distance from the Heater Borehole Collar, after 275 Days of Heating and after 95 Days of Cooling

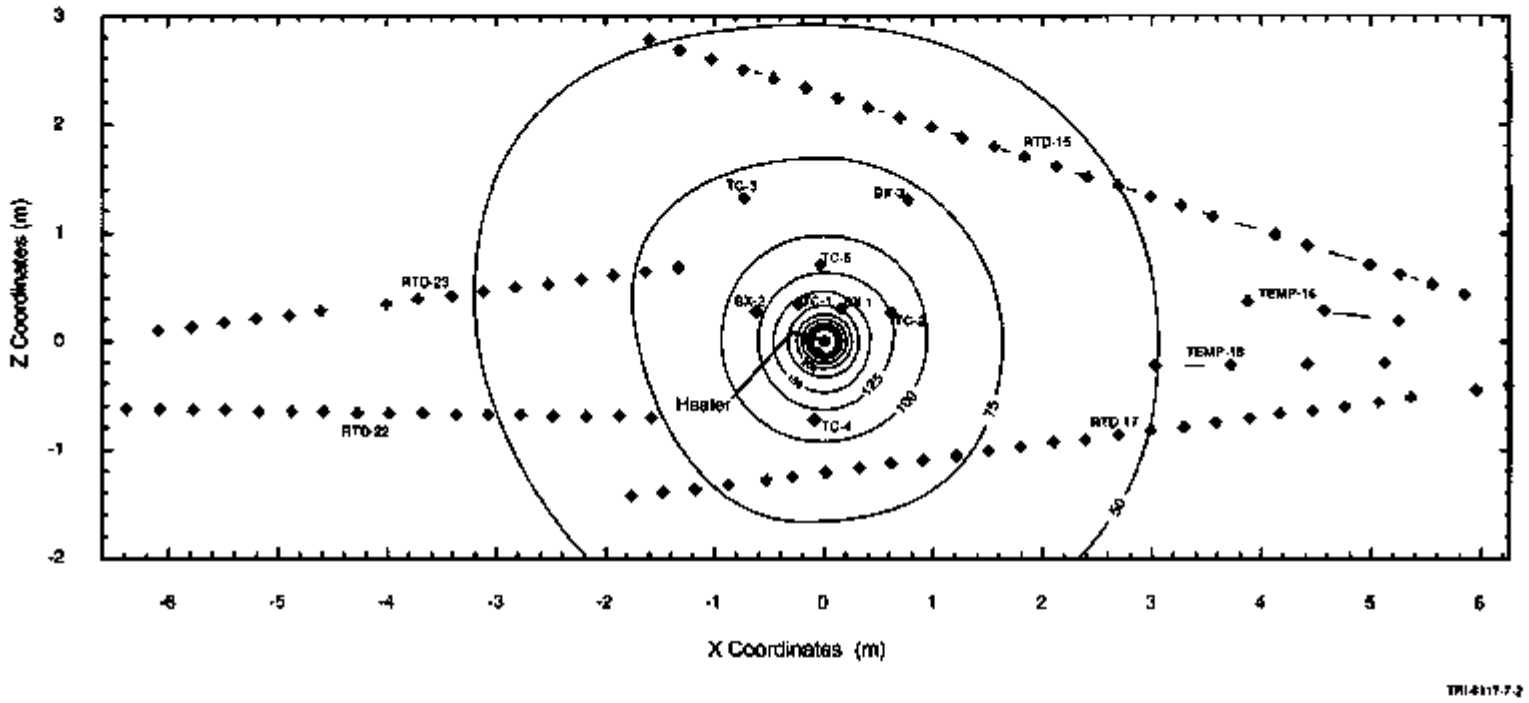

NOTE: Gages in close proximity to the plane of the slice are shown for reference. Contour interval = 25°C.

Figure 7-36. Temperature Contours, after 275 Days of Heating, on a Plane Perpendicular to the Heater Axis at Y=4.5 m

NOTE: Gages in close proximity to the plane of the slice are shown for reference. Contour interval = 25°C.

Figure 7-37. Temperature Contours, after 275 Days of Heating, on a Plane Perpendicular to the Heater Axis at Y=3.5 m

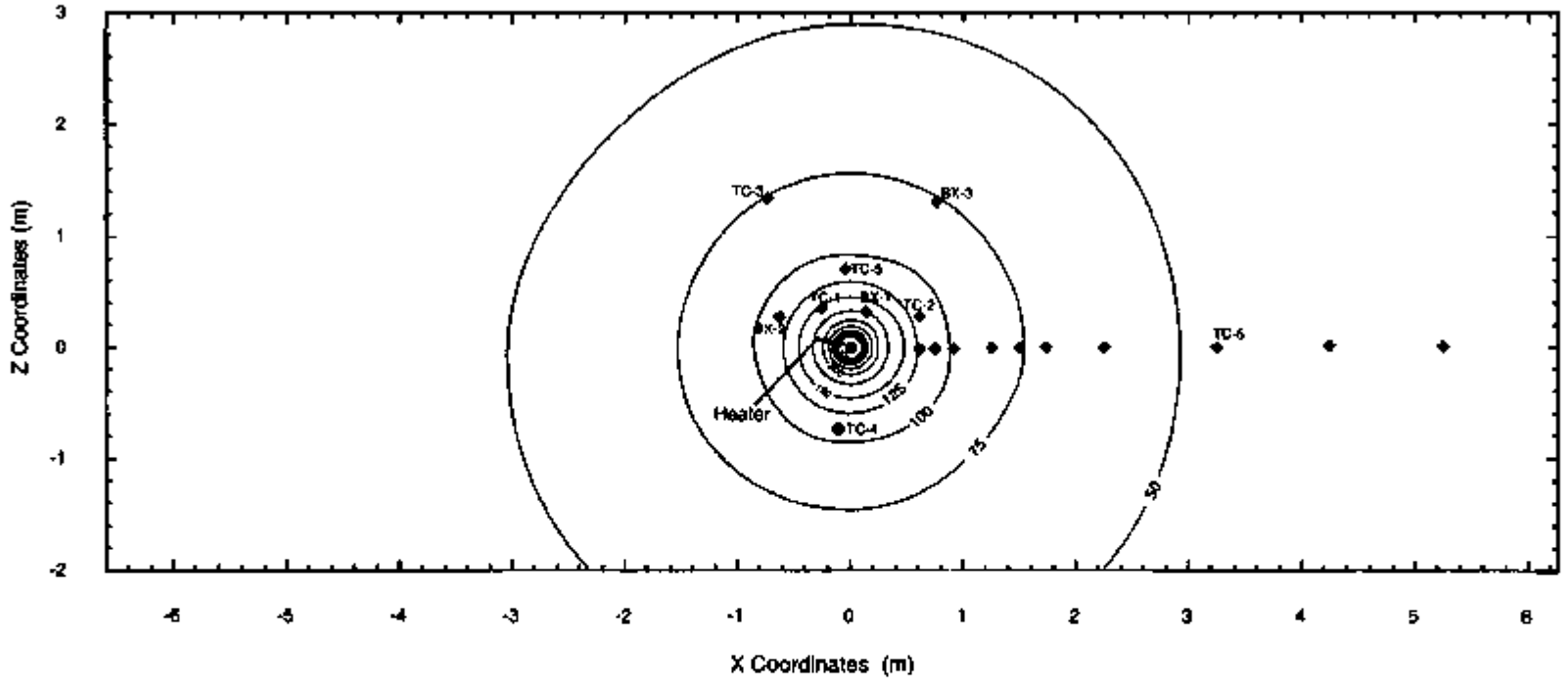

NOTE: Gages in close proximity to the plane of the slice are shown for reference. Contour interval = 25°C.

Figure 7-38. Temperature Contours, after 275 Days of Heating, on a Plane Perpendicular to the Heater Axis at Y=5.5 m

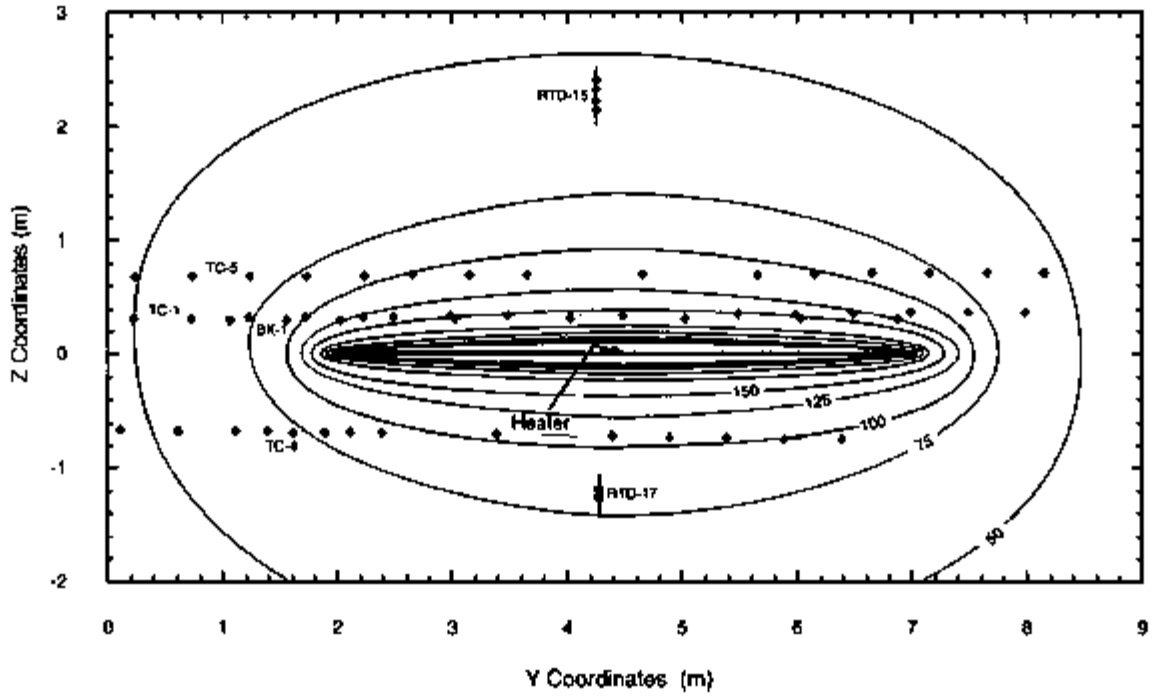

TRH-6117-19-2

NOTE: Gages in close proximity to the plane of the slice are shown for reference. Contour = 25°C.

Figure 7-39. Temperature Contours on a Vertical Plane Parallel to the Heater Axis at X=0 m after 275 Days of Heating

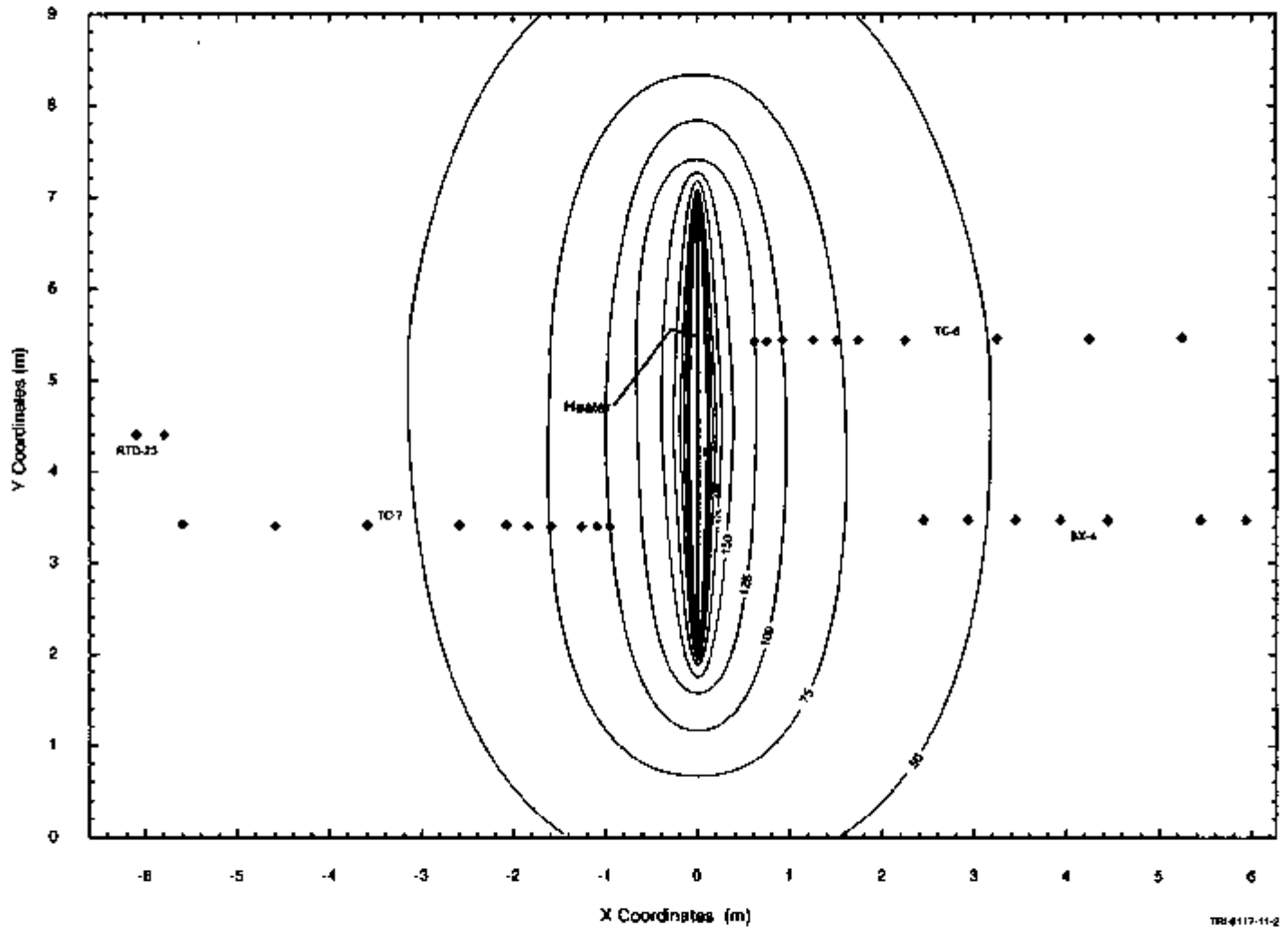

NOTE: Gages in close proximity to the plane of the slice are shown for reference. Contour interval = 25°C.

Figure 7-40. Temperature Contours on a Horizontal Plane Parallel to the Heater Axis at Z=0 m after 275 Days of Heating

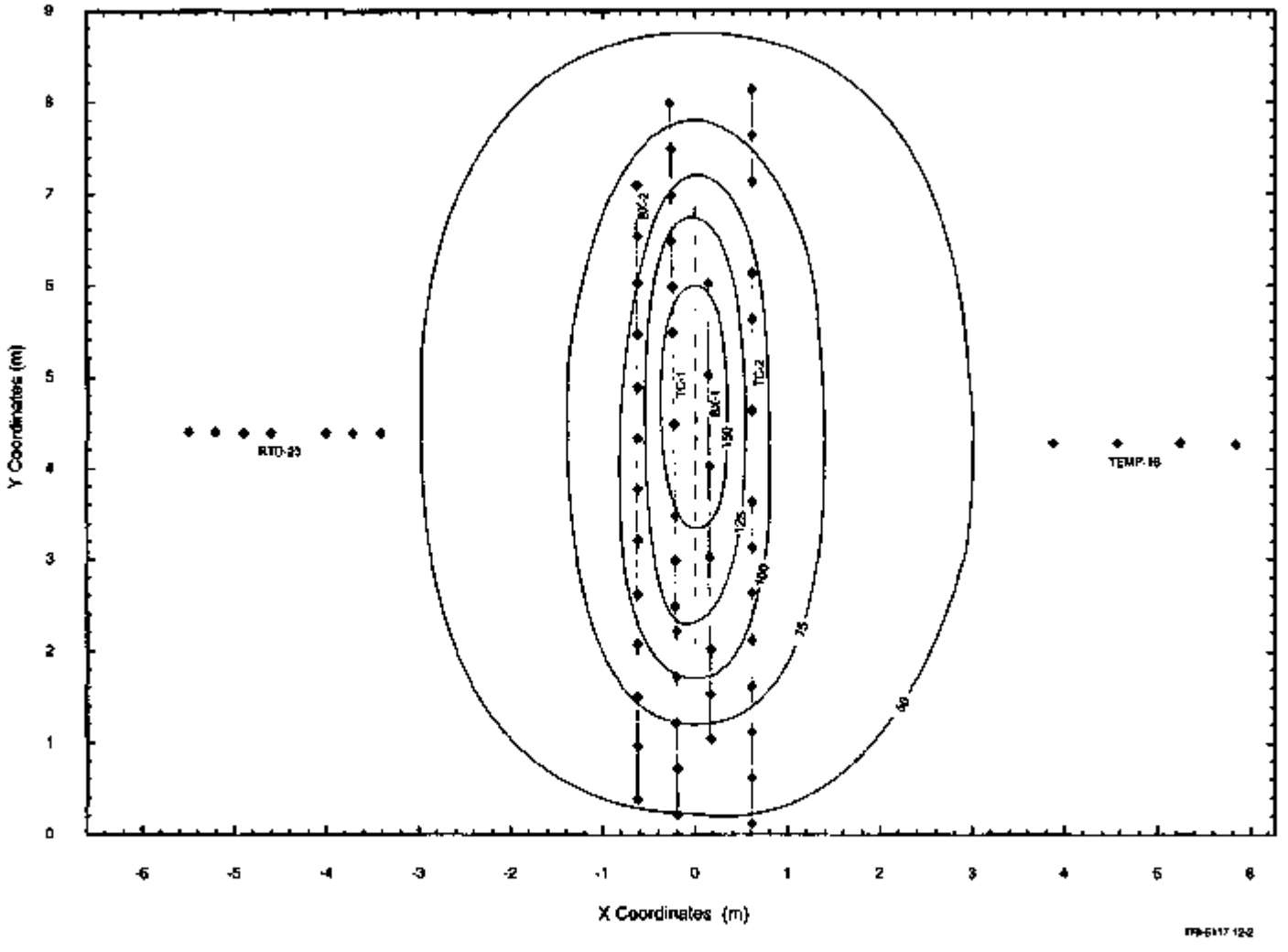

NOTE: Gages in close proximity to the plane of the slice are shown for reference. Contour interval = 25°C.

Figure 7-41. Temperature Contours on a Horizontal Plane Parallel to the Heater Axis at Z=0.3 m after 275 Days of Heating

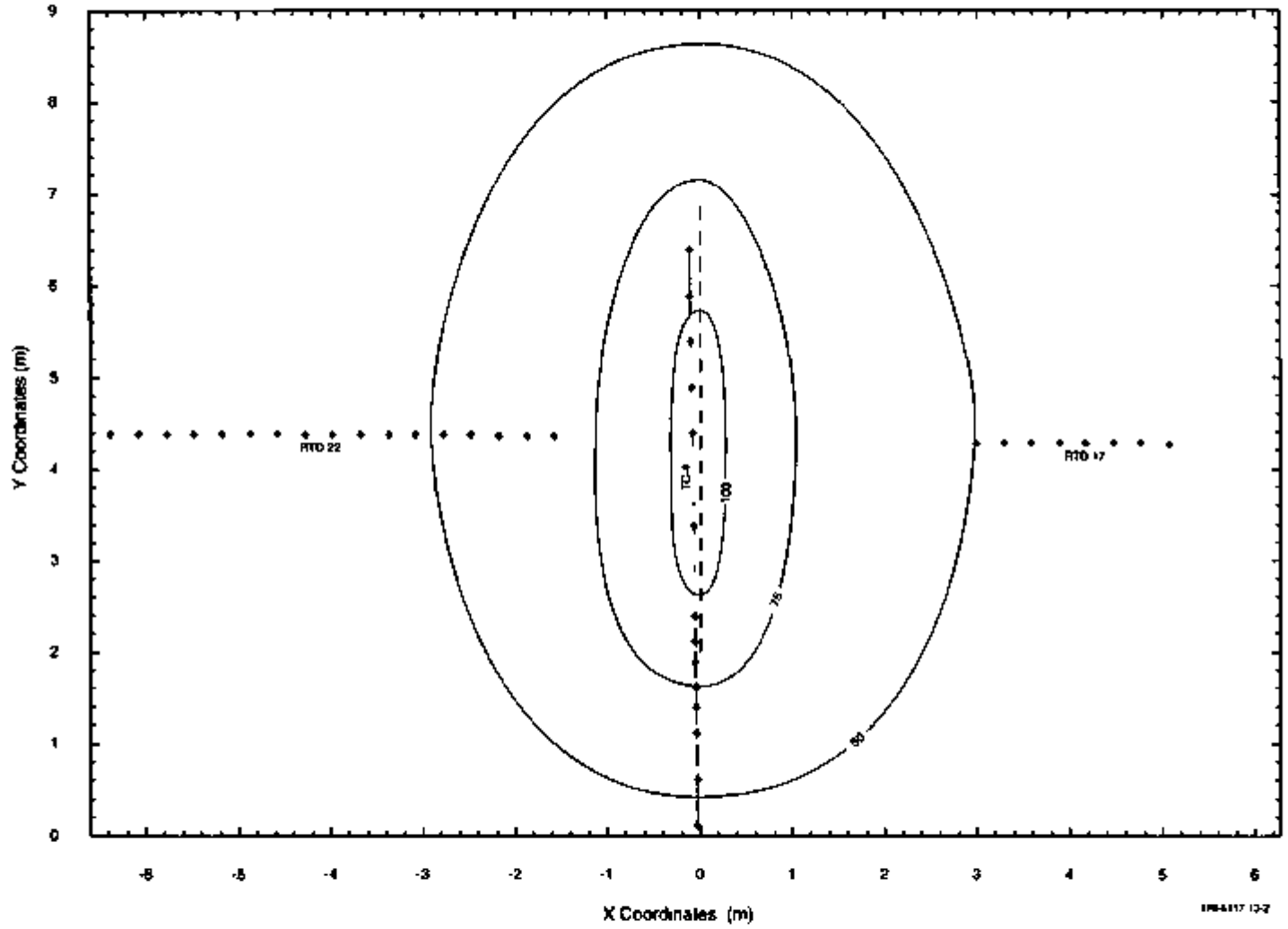

NOTE Gages in close proximity to the plane of the slice are shown for reference Contour interval = 25°C

Figure 7-42 Temperature Contours on a Horizontal Plane Parallel to the Heater Axis at Z=0 7 m after 275 Days of Heating

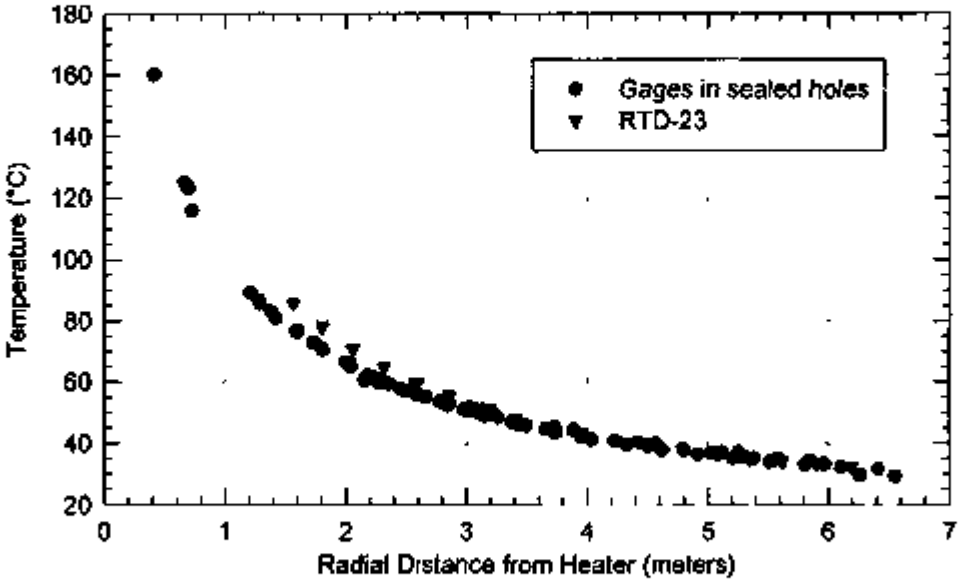

Figure 7-43. Temperature as a Function of Radial Distance from the Heater after 275 Days of Heating

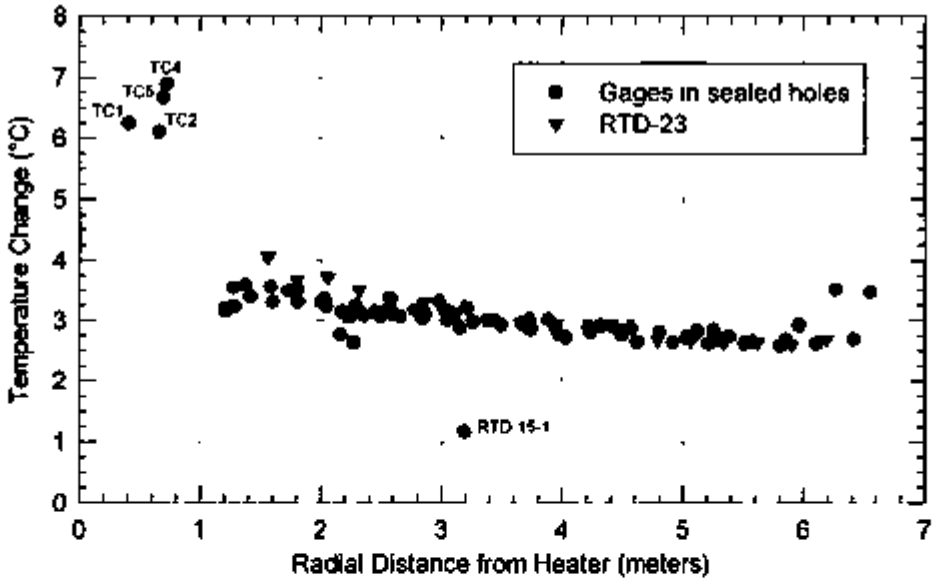

Figure 7-44. Increase in Temperature during the Time Interval from 186 to 275 Days

8. THERMAL-HYDROLOGICAL MEASUREMENTS AND ANALYSIS

While the complete set of SHT data is shared by all members of the Thermal Test Team for interpretation and analysis, the responsibility of conducting specific measurements in the SHT was assigned to respective laboratories. This section summarizes the SHT measurements obtained by LBNL, which concern the thermal-hydrological aspects of the test. They include periodic air-permeability measurements, ERT, GPR, and neutron logging (1) before the onset of heating, (2) periodically during the heating and cooling phases, and (3) during the post-cooling phase of the SHT. Passive monitoring data such as temperature, humidity, and pressure in boreholes 16 and 18 will also be discussed in this section. Infrared imaging of the SHT test block surfaces was conducted prior to heating, and periodically during the heating and cooling phases of the test. The imaging results are summarized in Section 8.4. Additionally, the laboratory measurements of the hydrological properties of rock cores from the SHT, both pretest and posttest, were presented in Sections 4.2 and 6.3, respectively.

8.1 ACTIVE PNEUMATIC TESTING

The following investigations were documented in accordance with LBNL procedure YMP-LBNL-QIP-SIII.0(c), *Scientific Investigation*.

Active pneumatic testing was conducted in boreholes 16 and 18 during both the heating and cooling phases. Air-permeability measurements before the heating period and after the cooling period involved other boreholes.

8.1.1 Pre-Heat Field Characterization by Air-Injection

A detailed discussion of the pre-heat characterization by means of air permeability tests in the SHT block has been presented in previous milestone reports (Tsang et al. 1996; CRWMS M&O 1996b). A summary of the key findings is presented here.

Characterization by means of air-permeability tests, prior to the onset of heating, provides an understanding of the initial conditions in the SHT block, specifically the potential pathways for gas flow. As the rock mass is heated during testing, water in the rock vaporizes, and the majority of fluid movement presumably occurs in this gas phase. Results of air-permeability tests provide an estimate of the three-dimensional heterogeneous permeability structure and fracture connectivity in the block. This information can provide input to a conceptual model, and allow estimates of liquid, heat, and gas flow in the SHT region. The pre-heat characterization data also serve as a basis for post-cooling comparison by observing where changes in permeability have occurred due to heating and possible thermal-mechanical-hydrological-chemical coupling.

In May 1996, air injection tests were conducted in the SHT area after all the boreholes had been drilled and logged by video, and prior to the boreholes being installed with instrumentation for monitoring the heater test proper. To prevent the boreholes from pneumatically communicating with the drifts, inflatable packers were fabricated and installed near the collar in every borehole numbered from 1 through 31 (see Figure 3-2 for the borehole layout). A typical test consisted of air injection in one chosen borehole at constant mass flux maintained by mass flow controllers. Pressure responses in this and all other boreholes were monitored continuously for about 20 to 30 minutes after steady state had been reached, which was typically within minutes. Air injection was then terminated. The pressure response in the injection borehole itself was used to calculate

the local permeability, averaged over the packed-off zone, L. Interference pressure responses in all other boreholes provided information on the connectivity of pneumatic pathways between the observation and the injection boreholes.

8.1.1.1 Local Air Permeability Estimation

Local permeability in the injection borehole was estimated from the steady state pressure response to the air injection test. An analytical solution for the steady state pressure response of a constant flow rate injection in a finite line source has been used by both LeCain (1995, p. 10) and Guzman et al. (1996, p. 10) for the analysis of single hole injection tests in fractured tuff at Apache Leap Research Site, Arizona. It was adapted from the steady state analytical solution for ellipsoidal flow of incompressible fluid from a finite line source (Hvorslev 1951) in an infinite medium ($L/r_w >> 1$) and is as follows:

$$k = \frac{P_{SC} Q_{SC} \mu \ln \frac{L}{r_w} T_f}{\pi L \left(P_2^2 - P_1^2\right) T_{SC}} \qquad (8\text{-}1)$$

where

k = permeability (m^2)
P_{SC} = pressure at standard conditions (1.013×10^5 Pa)
Q_{SC} = flowrate at standard conditions (m^3/s)
μ = dynamic viscosity of air (Pa-s 1.81×10^{-5} at 20°C)
L = length of air injection zone (m)
r_w = radius of borehole (m)
T_f = temperature of formation (°K)
P_2 = steady state pressure (Pa)
P_1 = ambient pressure (Pa)
T_{SC} = temperature at standard conditions (293.16°K)

The derivation of Equation 8-1 requires the assumption that air is the only mobile phase within the rock near the test interval, and that it obeys the ideal gas law so that its compressibility is inversely proportional to pressure. Equation 8-1 has its origin in well test analysis for a homogeneous porous medium. The welded tuff of the SHT block is a fractured medium and is most likely not well represented conceptually by a homogeneous porous medium. Furthermore, the proximity of the drifts implies that the finite line source is not in an infinite medium. Nevertheless, Equation 8-1 is valuable as a simple tool of choice to obtain an order-of-magnitude estimate of the average permeability values around each borehole, thus providing an initial idea of the spatial variability of fracture permeability in the test block.

The permeability values estimated from Equation 8-1 for injection tests performed in 21 boreholes in the SHT block are tabulated in Table 8-1. These values range over three orders of magnitude, from 5.0×10^{-15} m^2 to 5.2×10^{-12} m^2, and correspond to borehole packed-off zones of lengths, L, typically from 1.7 m to 11 m. The large range of local permeability values is consistent with the geological formation of the SHT (i.e., the densely fractured Topopah Spring middle

nonlithophysal stratigraphic unit). One complete set of estimated permeability values for the 21 boreholes is also shown in 3D in Figure 8-1. The logarithm of permeability is color-coded using a rainbow color palette, with the highest value in red and the lowest value in blue.

Table 8-1. Parameters for the Estimation of Pre-Heat Permeability, k, around Injection Zones for Different Boreholes Based on Equation 8-1

Borehole and datafile ID	Borehole length (m)	Borehole radius (cm)	Packed zone, L (m)	Constant flowrate, Q(SLPM)	P2-P1 (kPa)	Estimated permeability k(m^2)
Borehole 1 (5/24-03)	7.00	4.8*	1.73	53.	35.0	1.5E-13
Borehole 1 (5/28-08)	7.00	4.8*	1.73	50.	32.5	1.5E-13**
Borehole 1 (5/30-14)	7.00	4.8*	2.70	22.	9.5	1.8E-13**
Borehole 2 (5/28-06)	6.91	3.79	6.00	22.	13.4	7.2E-14
Borehole 3 (5/28-02)	7.02	3.79	6.11	100.	22.3	1.8E-13
Borehole 4 (5/28-03)	6.89	3.79	5.98	22.	77.0	9.2E-15
Borehole 6 (5/30-07)	11.99	3.79	11.07	40.	20.0	5.1E-14
Borehole 7 (5/31-01)	5.91	3.79	5.00	360.	10.7	1.7E-12
Borehole 7 (5/31-07)	5.91	3.79	2.26	500.	16.0	2.9E-12
Borehole 10 (5/24-02)	8.00	2.4	7.09	3.	10.6	1.2E-14
Borehole 11 (5/28-04)	6.80	2.4	5.89	300	3.0	5.2E-12
Borehole 12 (5/28-05)	7.67	2.4	6.76	200.	37.0	2.1E-13
Borehole 13 (5/30-08)	5.95	3.79	5.04	22.	16.5	6.6E-14
Borehole 15 (5/29-14)	8.18	3.79	7.09	20.	48.0	1.4E-14
Borehole 16 (5/30-09)	5.18	3.79	3.94	11.	64.0	8.3E-15
Borehole 17 (5/26-07)	8.00	3.79	6.91	100.	1.5	2.8E-12
Borehole 18 (5/30-10)	4.86	3.79	3.59	21.	15.5	8.8E-14
Borehole 19 (5/31-04)	5.79	3.79	4.88	20.	6.6	1.6E-13
Borehole 22 (5/29-02)	5.00	3.79	4.09	1.	6.4	9.9E-15
Borehole 23 (5/29-01)	5.50	3.79	4.59	1.	11.0	5.0E-15
Borehole 24 (5/31-03)	8.71	3.79	7.44	5.	15.7	1.2E-14
Borehole 25 (5/31-02)	8.74	3.79	7.62	100.	7.8	4.6E-13
Borehole 26 (5/31-05)	8.70	3.79	7.73	200.	6.8	1.1E-12
Borehole 27 (5/30-13)	8.70	3.79	7.43	4.5	30.0	5.1E-15

NOTE: T_i =24.6°C, P_i=89.1 kPa

* The radius of 4.8 cm is applicable only to the last 5 m of heater borehole 1.
** Revised from values reported in Tsang et al. (1996, p. 11) due to miscalculation of packed zone length

Permeability values in Table 8-1 are applicable to the entire borehole. However, since borehole videos indicate differing degrees of fracturing in localized zones within each borehole, one would expect the permeability within each borehole to vary from one localized zone to another. This is confirmed by results of air-injection tests performed in consecutive intervals of 0.69 m separated by a movable straddle packer string in borehole 6. The estimated permeability values of the 16 consecutive 0.69-m sections in the same borehole is tabulated in Table 8-2, and ranging from less than 10^{-15} m^2 to 6.2 x 10^{-13} m^2. The first 5 m of the borehole (measured from the collar) are rather impermeable, having values of 10^{-15} m^2 and less. The two most permeable zones, with permeability values that range from 1.1 to 6.6 x 10^{-13} m^2, are (1) from ~7. to 8.3 m from the

borehole collar, and (2) a 0.69-m section centered about 10.36 m from the borehole collar. A comparison of the range of permeability values in Table 8-2 for 0.69-m sections to that averaged over the packed length of 11 m for the entire borehole 6, 5.1×10^{-14} m^2 (Table 8-1) lends support to the belief that fluid flow seeks the least resistive path in a heterogeneous fractured system. Due to a time constraint requiring all characterization effort to be completed within a two-week period before permanent installation of the SHT, the detailed small-scale characterization by straddle packer was not duplicated for other boreholes, in which similar level of heterogeneity can be expected.

Table 8-2 Input Parameters and Estimated Pre-Heat Permeability, k(m^2), based on Equation 8-1 for Consecutive 0.69-m Zones from Injection Tests between Straddle Packers in Borehole 6

Borehole 6 data file and straddle zone ID	Mid-zone location from collar (m)	Constant flowrate, Q(SLPM)	P_2-P_1 (kPa)	Permeability k(m^2)
(5/29-03) 3'-5'	1.22	1.03	47.00[1]	4.0E-15[1]
(5/29-04) 5'-7'	1.83	0.39	65.00	1.0E-15
(5/29-05) 7'-9'	2.44	0.62	57.20	1.9E-15
(5/29-06) 9'-11'	3.05	0.62	58.00	1.9E-15
(5/29-07) 11'-13'	3.66	0.62	*	*
(5/29-08) 13'-15'	4.27	2.04	*	*
(5/29-09) 15'-17'	4.88	2.01	58.00	6.1E-15
(5/29-10) 17'-19'	5.49	2.01	24.50	1.7E-14
(5/29-11) 19'-21'	6.10	2.01	28.00	1.4E-14
(5/29-12) 21'-23'	6.71	4.00	17.20	5.0E-14
(5/30-06) 23'-25'	7.32	4.02	8.00	1.1E-13
(5/29-13) 25'-27'	7.92	42.00	25.00	3.4E-13
(5/30-01) 25'-27'	7.92	40.50	25.20	3.3E-13
(5/31-06) 25'-27'	7.92	41.00	27.00	3.1E-13
(5/30-02) 27'-29'	8.53	2.00	6.20	7.3E-14
(5/30-03) 29'-31'	9.14	2.03	13.00[1]	3.4E-14
(5/30-04) 31'-33'	9.75	2.03	14.00[1]	3.1E-14
(5/30-05) 33'-35'	10.36	2.00	0.75	6.2E-13

[1] Modified slightly from previously reported in Tsang et al. (1996, p. 14) based on data review.

* The pressure response to the constant injection flowrate is linear with time, which is that of injection into a nearly closed system, indicating very low permeability.

8.1.1.2 Interference Pressure Response to Air Injection

A typical set of air-injection test data is shown in Figure 8-2 for air injection into a 5-m zone in borehole 7. The horizontal axis denotes time, the right vertical axis denotes injection flow rate in standard liters per minute (SLPM = 1.67×10^{-5} m^3/s), and the left axis denotes the pressure increase from ambient, ΔP, P_2-P_1, in kPa. The legend on the graph denotes all boreholes in which pressure response is registered. The figure shows that, as expected, the maximum pressure increase occurs in the injection hole. The pressures in the majority of the 31 boreholes in the SHT block rise and fall in response to the constant-flow air injection in borehole 7, though the magnitude of pressure response is smaller in boreholes other than the injection hole. The

behavior displayed in Figure 8-2 is typical of that in all the boreholes tested. The almost universal cross-hole pressure response demonstrates that on the scale of 1 to 10 m, the fractures are well connected, and that the gas flow in the fractures resembles more that of flow through a heterogeneous continuum than flow through a discrete fracture network, in which case interference pressure response will be limited to very few monitoring zones.

Further study of the cross-hole interference pressure responses of the air injection tests uncovers the presence of a high-permeability direct flow path from borehole 11 to borehole 7 (Birkholzer and Tsang 1996, p. 7). For the injection test performed in borehole 1, the magnitudes of pressure rise in the distant monitoring borehole 7 is almost identical to that in the injection borehole 11, while the pressure response in boreholes 28, 29, 30, 31 (which are in close proximity to injection borehole 11) is much less pronounced. An examination of the borehole video logs show discrete zones of open, unfilled fractures in boreholes 1, 7, 11, 12 lying in a common vertical plane oriented N22°E. Fracture mapping in the Alcove 5 (CRWMS M&O 1996b, p. 7-2) shows that there is indeed one subvertical joint set with that value of strike azimuth and having a length of 3 to 4 m. The combined data of fracture mapping in the SHT block, borehole video logs, and air-injection interference tests therefore confirm the presence of a high-permeability subvertical fracture zone which is intersected by those horizontal boreholes (boreholes 1, 7, 11, and 12) that give relatively high permeability values. This subvertical fracture lies beyond the mid-plane of the heater, since it apparently is missed by boreholes 28, 29, 30, and 31, all parallel to heater borehole 1 and 5 m in length from the drift wall.

While a high permeability value can be correlated to a zone of fractures observed in the video log, the air injection data also show that visual observations of densely fractured or rubbled zones (from the video log or mapping data) do not necessarily indicate high permeability in fluid flow. This observation is consistent with common knowledge of fluid flow in saturated fractured formation, where only a very small fraction of the mapped (or visually observed) fractures are hydrologically significant (Tsang and Tsang 1987, p. 469).

8.1.1.3 Summary

Pre-heat characterization by air-injection tests on boreholes with isolated zone lengths, L, ranging from 2 to 11 m show that the permeability values range from 5.0×10^{-15} m^2 to 5.2×10^{-12} m^2. The three-orders-of-magnitude difference in permeability values can be attributed to flow through fractures of hierarchical scales, with the microfractures accounting for the lower values, and fracture zones (a few meters in extent) responsible for the highest values. The range of measured permeability values of the boreholes in the SHT is similar to those obtained from surface-based vertical boreholes at the SHT stratigraphic unit over zones 2-3 m long (LeCain 1997, pp. 11-14).

The spatial distribution of the permeability values from steady state pressure response of the injection boreholes (Figure 8-1) indicates that on the scale of the SHT block (~13m x 8m x 4.5m), there seems to be an overall segregation of the permeability values: lower to the north of the single heater borehole 1 (on the side of the Observation Drift) than to the south (the Thermomechanical Alcove Extension); lower above the single heater borehole 1 horizon than below; and lower permeability toward the front of the heater borehole 1 (west) than in the back (east). Higher permeability toward the back of the heater borehole 1 may be associated with a

discrete, high-permeability fracture zone, whose presence was corroborated by the combined data of fracture mapping in the SHT block, borehole video logs, and air-injection interference tests. The subvertical fracture zone is about 4 m in extent, beyond the mid-plane of the heater, and is intersected by several horizontal boreholes parallel to the heater borehole 1.

The interference pressure responses in the SHT test block show that the fractures are well connected and may be conceptualized as a continuum. However, on a finer scale the estimated permeability can vary by an order of magnitude between adjacent boreholes. Within the same borehole, permeability estimates of different 0.69-m isolated sections can again vary over three orders of magnitude. The data in Table 8-2 confirm that in the SHT block there are fractures of hierarchical scales forming a heterogeneous continuum, and that gas flow does not occur uniformly in the continuum; rather, flow seeks out preferential, least resistive paths (Tsang and Tsang 1987, p. 469). Therefore, the pre-heat air-permeability characterization, though providing useful information and valuable insight on the "average" fracture permeability and large-scale connectivity in the SHT block, cannot possibly identify all the preferential gaseous pathways in the SHT block. The presence of these preferential pathways linked to fractures were supported by the thermal-hydrological data during the heating and cooling phases of the SHT, and confirmed by post-cooling hydrological characterization.

8.1.2 Air-Permeability Measurements During Heating and Cooling Phases of the SHT

While pre-heat air-permeability measurements provide a description of the potential flow paths in the test block, periodic air-permeability measurements during the SHT provide information on the changes of flow path during the heating (i.e., on the coupled thermal-hydrological behavior). Constant mass flux air-injection tests, in addition to continuous monitoring of relative humidity, temperature, and pressure, were conducted periodically in the SHT block in the two hydrology boreholes 18. These data have been presented in a series of Level 4 Milestone reports (Freifeld and Tsang 1997a, 1997b, and 1997c; Freifeld 1997 and 1998a). Key insight into the hydrological response of the host rock based on results of the active testing will be reiterated here. A discussion of the passive monitoring data will be presented in Section 8.2.

8.1.2.1 Testing Procedure

Boreholes 16 and 18 are instrumented with relative humidity, temperature, and pressure transducers. Each borehole contains four pneumatically inflated packers, labeled P_1, P_2, P_3, and P_4 on Figure 8-3. Instrumented intervals are numbered from the closest to the collar of the borehole, 1, to the deepest zone, behind the last packer in the string, 4. The eight instrumented intervals are referred to by borehole number followed by the instrument interval number (e.g., 18-3 is the third instrument cluster from the collar in borehole 18). The pressure, temperature, and relative humidity sensors are all located just below the packer (deeper in the borehole) and are assigned the same numeric identifier as the packer just above them.

Each interval between packers and one interval past the end of the last packer are fitted with a 1/4" Teflon injection tube. Dry, clean, compressed air is regulated using mass flow controllers and injected into the designated zone. By selectively deflating different packers, various injection zones for each hydrology borehole are formed. Illustrated in Figure 8-3 are three possible test

configurations: (1) deflate packer P_2, and use air injection line for P_1; (2) deflate packer P_3 and use air injection line for P_2; (3) inflate all four packers and inject behind packer P_4. These three configurations are denoted as injection zones 1, 2, and 3 respectively in Figure 8-3. All four packers in the monitoring borehole are always inflated so that pressure response can be monitored in each of the four sensors.

8.1.2.2 Test Results

The local permeabilities specific to each of the zones were estimated from Equation 8-1, and are shown in Table 8-3. Only sensor 4 in injection zone 3 in boreholes 16 and 18 shows a significant decrease of permeability values from its pre-heat level during the heating phase. This reduction in the local air permeability is attributed to the fact that a larger portion of the fracture pore space is occupied by water condensed from vapor transported from the boiling zones near the heater. Note that after heating was terminated, during the cooling phase, the permeability returned to the pre-heating values of August 1996 in the same zones. This is clearly seen in Figure 8-4. The slight increase in permeability values post-heat may be due to fracture opening during heating and/or the presence of drilling water from wellbore construction. The effect of thermal-mechanical coupling—either opening of existing fractures or generation of new fractures—on air-permeability will be discussed in more detail in the following section. These results focus on effects from thermal-hydrological coupling. Based on the permeability values in Table 8-3, it is clear that the increase in liquid saturation in the fractures during the heating phase of the SHT was limited only to injection zone 3 (behind packer P_4) of boreholes 16 and 18 (which spans a radial distance of about 1.5 m to 3 m from the heater). No apparent change of liquid saturation is noted at radial distance larger than 3 m from the heater.

Table 8-3. Comparison of Air Permeability (in m^2) Measured at Different Phases in Hydrology Boreholes 16 and 18

Location	Measurement Dates						
	Pre-Heat	Heating				Cooling	
	7,8-Aug-96	25-Nov-96	4,5-Feb-97	8-Mar-97	22,23-May-97	8-Oct-97	18,19-Nov-97
Inj Behind 16-4	1.10E-14	2.58E-15	2.67E-15	N/A	2.61E-15	2.72E-14	2.67E-14
Inj Behind 18-4	2.30E-13	1.00E-13	1.01E-13	9.86E-14	9.86E-14	2.69 E-13	2.57E-13
Inj Between 16-2, 16-4	5.27E-15	2.83E-15	3.81E-15	4.14E-15	2.76E-15	4.05E-15	4.44E-15
Inj Between 16-1, 16-3	8.85E-14	9.03E-14	9.56E-14	8.76E-14	8.76E-14	8.67E-14	1.34E-13
Inj Between 18-1, 18-3	1.12E-14	1.08E-14	1.12E-14	1.29E-14	9.73E-15	1.27E-14	1.30E-14

The increase of liquid saturation in the fractures surrounding boreholes 16 and 18, behind packer P_4, during the heating phase of SHT, is also evidenced by the transient air pressure response. Figure 8-5 shows a comparison of the before, during, and after heating pressure increases for borehole 18, zone 3, in response to air injection into this zone. The pressure responses before and after heating show that the pressure remains constant during the test. On the other hand, in the air injection tests during the heating phase of the SHT, the pressure reaches a maximum immediately after the beginning of injection, from which it slowly declines during the test. This indicates that there is a slight increase in air permeability during the two-hour air-injection test. This behavior is attributed to the evaporation of some of the water in the fractures by the dry injected air, and its transport away from the boreholes under the pressure

gradient created by injection (Freifeld 1998a, pp. 3 and 4). The different behavior during injection for the pre-heat and post-heat phases of the SHT indicates that increase in the water saturation of the fractures surrounding boreholes 18 (behind P_4) occurs only during heating, while condensation of vapors is continuous. In the absence of vapor transport when the heater is turned off, thermodynamic equilibrium between fractures and matrix resumes, and the disparity of the capillary suction between matrix and fractures ensures that the majority of water is being held in the matrix pores.

The summary above on air-permeability tests in the hydrology boreholes shows that the pressure response data to air injection can be used to delineate the redistribution of moisture in the fractures in the SHT, and to confirm understanding of strongly heat-driven two-phase flow and transport processes in fractured rocks.

8.1.3 Post-Cooling Characterization by Air-Permeability and Gas-Tracer Tests

8.1.3.1 Air Permeability Tests

Posttest activities at the SHT began in the first week of January 1998 with the removal of insulation material from the test block. Most of the 31 boreholes involved in the pre-heat air injection tests in the SHT (see Section 8.1.1) had since been grouted for installation of instruments for the heater test and were therefore not suitable for air permeability tests. The exceptions are boreholes 1, 3, 6, 7, and 19. Therefore, instrumentation was removed from these boreholes, immediately following the removal of insulation material, to make them available for post-cooling characterization. Instrumentation in all other boreholes which were grouted were left in place; their removal was scheduled to follow the completion of air permeability tests. Figure 8-6 shows the subset of ungrouted boreholes in which post-cooling pneumatic tests were performed. This is in contrast to the pre-heat characterization, where all 31 boreholes of the SHT (as shown in Figure 3-2) were involved.

The post-cooling characterization by means of pneumatic field tests took place in the third and fourth weeks of January 1998. The posttest characterization strategy was to duplicate the pretest characterization test conditions when feasible. Therefore, inflatable packers were installed near the collar of boreholes 3, 6, 7, and 19 to depths identical to those of their pretest characterization positions. The hydrology boreholes 16 and 18 were already equipped with packer strings for the duration of the SHT (see Section 8.1.2 and Figure 8-3). They were left "as is" for the post-cooling air permeability measurements (i.e., pressure response would be monitored in four isolated zones in boreholes 16 and 18). For injection, test was conducted in injection zone 3, behind the fourth packer P_4, as discussed earlier (Section 8.1.2).

The pneumatic connection between the heater borehole 1 and the two hydrology boreholes 16 and 18 is of particular interest. Pressure response to air-injection tests during the heating phase of the SHT (Section 8.1.2.2) indicated the presence of condensed water in the fractured rock mass surrounding boreholes 16 and 18 behind the fourth packer. On the other hand, accumulation of water in the borehole itself was observed and collected (Section 8.2.3) only in borehole 16 behind P_4. Since a borehole is a capillary barrier, seepage into a borehole occurs only if the capillary barrier is overcome by presence of fully saturated rock mass at the borehole wall. Localized zones

of fully saturated rock mass at the borehole wall are more likely if there is a fast path for vapor transport (i.e., if there is a fracture connection between the heater borehole 1, where vaporization takes place, and borehole 16, between P_4 and the bottom of borehole, where condensation takes place). The fact that water is found in borehole 16, and not in borehole 18, suggests that a fast path for vapor transport exists between heater borehole 1 and the former, but not the latter. Post-cooling pneumatic characterization allows testing of this hypothesis, and the determination of fast pathway(s). With this in mind, air-permeability tests were carried out in a multi-zone configuration for boreholes 1, 16, and 18. Specifically, injection was conducted in six consecutive zones in the heater borehole 1, and the pressure response in sensors 16-4 and 18-4 were measured to identify plausible fast path connections. Upon conclusion of air permeability tests, gas tracer tests were also performed between the heater borehole 1 and boreholes 16 and 18 to investigate the possible presence of fast paths for vapor transport. The multi-zone configuration for injection in borehole 1 and monitoring in boreholes 16 and 18 is shown in Figure 8-7.

The air-permeability values of the various injection zone were estimated from Equation 8-1. Table 8-4 includes all the post-cooling results. Table 8-5 shows a comparison of permeability estimates from pre-heat and post-cooling measurements using data from injection into boreholes 3, 6, 7, 16, 18, and 19. Direct comparison is possible in these boreholes because of the identical pretest and posttest packer configurations. The post-cooling and pre-heat permeability values in these boreholes are on the same order of magnitude. Furthermore, a study of the cross-hole steady state pressure responses show that they are also comparable under pretest and posttest conditions (i.e., the data do not reveal that the pneumatic connectivity between the boreholes tested had been significantly altered by the heating and cooling of the SHT). The ratios of post to pretest permeability values, however, show that there is a consistent upward trend in the permeability values from pre-heat to post-cooling (Table 8-5). This increase in the permeability ranges from about 20 percent to a factor of 3.5. The magnitude of the increase is not as significant as the fact that the change is positive for every zone tested. One may speculate that the consistent increase in post-heat permeability values in the SHT test block arises from the fact that wet-drilling of the boreholes increased the moisture content in the fractures and suppressed the pre-heat air permeability. A more likely scenario, though, is that the overall larger posttest permeabilities in the SHT block may be attributed to microfracturing and expansion of fracture apertures. Heating may cause some fractures to close and others to open. However, since (1) the air-permeability tests are conducted over length scales of meters, and (2) fluid flow always seeks the least resistive path and avoids low permeability zones, air-permeability field tests preferentially register the effect of fracture opening. This is consistent with the interpretation in Section 8.1.2.2 that the reduction of air-permeability in injection zone 3 of boreholes 16 and 18 (Table 8-3, Figure 8-4) during heating should be attributed to thermal-hydrological coupling, that is, to water condensation that occupies a large, continuous zone, and thus prevents their being circumvented by the air flow. On the other hand, the post-heat increase in permeability in zone 3 of boreholes 16 and 18 is most likely due to thermal-mechanical coupling effects, which may have been present, but masked by the thermal-hydrological effects during heating. These mechanisms are supported by the observation that, as soon as the heating ceased, measurements

during the cooling phase of the SHT show air permeability in zone 3 of boreholes 16 and 18 exceeding their pre-heat values (Table 8-3 and Figure 8-4).

Table 8-4. Post-Cooling Air Permeability, [(km^2) Based on Equation 8-1], for Boreholes 1, 3, 6, 7, 16, 18, and 19

Injection zone and datafile ID	Packed zone L (m)	Constant flowrate. Q(SLPM)	P_2-P_1 (kPA)	k(m^2) assuming T_f=24.6° C	k(m^2) assuming T_f=30.6°C
Borehole 1-Zone 1 (Jan21-08)	0.59	1	1.62	1.4E-13	1.5E-13
Borehole 1-Zone 2 (Jan21-09)	0.59	10	3.48	6.7E-13	6.8E-13
Borehole 1-Zone 3 (Jan21-10)	0.59	10	2.3	1.0E-12	1.0E-12
Borehole 1-Zone 4 (Jan21-11)	0.59	10	2.36	9.8E-13	1.0E-12
Borehole 1-Zone 5 (Jan21-13)	0.59	10	0.46	5.1E-12	5.2E-12
Borehole 1-Zone 6 (Jan21-12)	1.34	10	0.972	1.4E-12	1.4E-12
Borehole 3 (21Jan03)	6.11	40	3.22	5.6E-13	5.7E-13
Borehole 6 (21Jan04)	11.07	40	14.8	7.1E-14	7.2E-14
Borehole 7 (21Jan05)	5.00	100	2.17	2.5E-12	2.5E-12
Borehole 7-back zone (22Jan01)	2.43	100	2.15	4.4E-12	4.5E-12
Borehole 16 Zone 3 (Jan2106)	2.10	1	2.71	3.9E-14	3.9E-14
Borehole 18 Zone 3 (Jan2107)	1.55	10	4.9	2.6E-13	2.7E-13
Borehole 19 (21Jan02)	4.88	20	3.37	3.2E-13	3.3E-13

Table 8-5. Comparison of Pre-Heat and Post-Cooling Air Permeability Measurements for Boreholes 3, 6, 7, 16, 18, and 19

Pretest air permeability (assume T_f=24.6°C)			Posttest air permeability (assume T_f=30.6°C)			Comparison
Borehole and datafiles ID	L (m)	k(m^2)	Borehole and datafiles ID	L (m)	k(m^2)	Posttest ÷ Pretest
Borehole 3 (5/28-02)	6.11	1.8E-13	3 (21Jan-03)	6.11	5.7E-13	3.1
Borehole 6 (5/30-07)	11.07	5.1E-14	6 (21Jan-04)	11.07	7.2E-14	1.4
Borehole 7 (5/31-01)	5.00	1.7E-12	7 (21Jan-05)	5.00	2.5E-12	1.5
Borehole 7 (5/31-07)	2.26	2.9E-12	7 (22Jan-01)	2.43	4.5E-12	1.6
16 Zone 3 (Aug 7,8, 1996)	2.10	1.1E-14	16-Zone 3 (Jan21-06)	2.10	3.9E-14	3.5
18 Zone 3 (Aug7,8, 1996)	1.55	2.3E-13	18-Zone 3 (Jan21-07)	1.55	2.7E-13	1.2
Borehole 19 (5/31-04)	4.88	1.6E-13	19 (21Jan-02)	4.88	3.3E-13	2.0

To further investigate the connectivity of flow paths from the heater borehole I to the two hydrology boreholes 16 and 18, post-cooling air-injection tests were performed in consecutive zones (intervals isolated by straddle packers) in borehole 1. Table 8-6 shows a comparison of the pretest and posttest air-permeability measurements. Note that the heater occupies the borehole length from 2 m to 7 m from the collar, and for pretest characterization, two packed-off zones were tested, 1.73 m and 2.70 m from the bottom of the borehole (at ~ 7 m from the collar). In the post-cooling characterization, pressure data from injection into borehole 1 revealed that zone 5, a 0.59-m section centered at 5.36 m from the collar, was the most permeable. This is consistent with observations from the pre-heat characterization of the SHT test block, which indicated the presence of a high permeability fracture zone intersecting heater borehole I somewhere beyond y=5.0 m. That conclusion was drawn mainly from the interference pressure

responses to injection in borehole 11, which suggest that the fracture zones are intersected by boreholes 1, 7, 11, and 12. Detailed post-cooling testing of borehole 1 confirmed the location of its intersection with that hypothesized fracture. The post-cooling results also afford an opportunity to investigate further the conclusion from the pre-heat permeability measurements that this fracture zone provides the large-permeability pathway between several boreholes: 1, 7, 11, and 12 (Birkholzer and Tsang 1996, p. 7).

Table 8-6. Comparison of Pre-Heat and Post-Cooling Air Permeability Measurements for Borehole 1

Pretest air permeability (assume T_f=24.6°C)			Posttest air permeability (assume T_f=30.6°C)			
Borehole injection zone and datafiles ID	L (m)	Permeability k(m^2)	Borehole injection zone and datafiles ID	L (m)	Permeability k(m^2)	Zone center wrt collar (m)
			1-Zone 1 (Jan21-08)	0.59	1.5E-13	2.92
			1-Zone 2 (Jan21-09)	0.59	6.8E-13	3.53
Borehole 1 (5/24-03)	1.73	1.5E-13	1-Zone 3 (Jan21-10)	0.59	1.0E-12	4.14
Borehole 1 (5/28-08)	1.73	1.5E-13	1-Zone 4 (Jan21-11)	0.59	1.0E-12	4.75
Borehole 1 (5/30-14)	2.70	1.8E-13	1-Zone 5 (Jan21-13)	0.59	5.2E-12	5.36
			1-Zone 6 (Jan21-12)	1.34	1.4E-12	6.33

To investigate this connectivity issue, the pressure response in the monitoring zones were examined during air injection in the six consecutive zones in borehole 1. Table 8-7 shows the cross-hole steady-state pressure response to the constant flux injection in isolated sections of borehole 1. The steady-state pressure change in the monitoring zones—borehole 7, and zone 3 of boreholes 16 and 18—are expressed as a fraction of the pressure response in the injection zone of borehole 1. The magnitude of the response in borehole 7 clearly identifies the preferred pneumatic connection to be between borehole 1, zone 5, and borehole 7, thus confirming the pretest assumption of the presence and location of the large permeability fracture zone.

Table 8-7. Ratio of Pressure Increases in Monitoring Boreholes 7 and Zone 3 of Borehole 16 and 18 to that in the Six Injection Zones in Borehole 1

	1-Zone1*	1-Zone2	1-Zone3	1-Zone4	1-Zone5	1-Zone6
ΔP for injection in Borehole 1	1.62	3.48	2.3	2.36	0.46	0.97
ΔP(Borehole 7)/ΔP(injection in 1)	6.79E-03	8.62E-04	1.74E-02	1.23E-02	3.70E-02	2.16E-02
ΔP(16-Zone 3)/ΔP(injection in 1)	1.54E-03	1.32E-02	3.54E-01	7.63E-02	1.02E-01	1.75E-02
ΔP(18-Zone 3)/ΔP(injection in 1)	1.54E-03	8.19E-03	2.39E-02	2.12E-02	2.35E-01	2.89E-02

* Injection flowrate is 1 SLPM for zone 1, 10 SLPM for zones 2 through 6.

8.1.3.2 Gas Tracer Tests

Following the cooling phase of the SHT, gas tracer tests were conducted between borehole 1, the heater hole, and boreholes 16 and 18. The purpose of the tracer tests was to gain a better understanding on the hydrological conditions that permitted rapid transport from the heated region into borehole 16. The zones behind the 4th packer (referred to as zone 3 in previous sections) in boreholes 16 and 18 were chosen as the tracer withdrawal interval, and borehole 1

was chosen as the tracer injection borehole. A schematic drawing of the equipment used for conducting the tracer tests is shown in Figure 8-8.

Based on the results of the post-cooling air-permeability tests, two intervals in borehole 1 were selected for gas injections. The first interval extended from 3.83 m to 4.42 m (denoted as 1-zone 3 in Tables 8-4, 8-6, and 8-7) from the collar of the borehole, produced a strong response in zone 3 of borehole 16, and a much weaker response in zone 3 of borehole 18. The second interval extended from between 5.05 m to 5.64 m (denoted as 1-zone 5 in Tables 8-4, 8-6, and 8-7) from the collar of the borehole produced a stronger response in zone 3 of borehole 18 than in zone 3 of borehole 16. Four other intervals in borehole 1 were tested (see Table 8-7), but because of weaker cross-hole responses were not selected for conducting tracer testing. Figure 8-9 shows the pressure response in sensors 16-4 and 18-4 in response to air injection in the six different intervals isolated of borehole 1. It is clear that the strongest cross-hole response is between zone 3 of borehole 1, and 16-4, and secondly, from zone 5 of borehole 1 to 18-4. Very weak cross-hole responses are obtained from injection in any other zones.

Several factors complicate the analysis of the tracer data. First, the perpendicular layout between borehole 1 and boreholes 16 and 18 (Figure 8-6), which significantly complicates transport geometry, made the test results less amenable to more detailed analysis. Analyses such as the effective porosity calculations that were performed on DST gas tracer data (Freifeld 1998b, p. 2-8) were not applied to the SHT tracer data. Second, the use of SF_6 as a gas tracer during air-permeability testing in pre-heat characterization had elevated the background concentration of SF_6 in the SHT area. Due to elevated background SF_6 concentration, a determination of the mean transport time t_{50}, at which 50 percent of total tracer mass injected was recovered, was problematic, and, therefore, was not attempted. Since the purpose of the tracer testing was to gain an understanding of the rapid flux of water (condensate) into the back of borehole 16, as opposed to borehole 18, which saw no influx of condensate, it was determined that study would focus on the first arrival of tracer and only qualitatively examine the rate at which cumulative mass recovery occurred.

The results of five gas tracer tests are shown in Table 8-8. Tracer transport from zone 3 of borehole 1 to zone 3 of borehole 16 was extremely rapid, with 100 percent tracer recovery occurring within 30 minutes from injection. First arrival of tracer to zone 3 of borehole 18 took more than twice as long and 100 percent tracer recovery took approximately 15 hours. The differences in the transport times and recovery efficiencies suggests that the path between zone 3 of borehole 18 and borehole 1 is much more tortuous and indirect than the path between zone 3 of borehole 16 and borehole 1. The air-permeability tests, which indicate high permeability between the 3.83 m to 4.42 m interval in borehole 1 and zone 3 of borehole 16 support the hypothesis that there exists a direct fracture connection between borehole 1 and zone 3 of borehole 16, behind the 4th packer. This high permeability feature does not exist in zone 3 of borehole 18, even though single-hole permeability analysis (see Tables 8-4) shows that zone 3 of borehole 18 has a higher air-permeability than zone 3 of borehole 16. The orientation of fractures and the location of the fractures' intersection with the borehole may also lead to a condition in borehole 18 in which any flux of water moving through the packed off interval does not lead to an accumulation of condensate. The complexity of the system precludes the detailed description of the system

behavior and serves to highlight the difficulty in monitoring transport in heterogeneous fractured rock.

Table 8-8. Gas Tracer Results.

Tracer Injection (borehole 1, location w.r.t collar)	Withdrawal Location Borehole # - Zone	First Arrival Time	Mass Recovery (qualitative analysis)
3.93m – 4.42m	16-Zone 3	3 minutes	100% within 30 minutes
3.93m – 4.42m	16-Zone 3	3 minutes	100% within 30 minutes
3.93m – 4.42m	18-Zone 3	7 minutes	100% within 15 hours
5.05m – 5.64m	16-Zone 3	12 minutes	50% within 1 hour
5.05m – 5.64m	18-Zone 3	8 minutes	No analysis made

NOTE: Only a qualitative analysis was performed on the cumulative tracer mass recovery data, due to high background concentrations of tracer.

8.2 PASSIVE MONITORING DATA IN HYDROLOGY BOREHOLES 16 AND 18

The following investigations were documented in accordance with LBNL procedure YMP-LBNL-QIP-SII.0 (c), *Scientific Investigation*.

As discussed earlier in Section 8.1.1.2 and illustrated in Figure 8-3, borehole 16 and borehole 18 each contain four pneumatically inflated packers, labeled as P_1, P_2, P_3, and P_4. Relative humidity, temperature, and pressure sensors are located just below (deeper in the borehole) the packer, and are assigned the same numeric identifier as the packer immediately above them. The eight instrumented intervals are referred to by borehole number followed by the instrument interval number (i.e., 18-3 is the third instrument cluster from the collar in borehole 18). Temperature, relative humidity, and gauge pressure are monitored continuously, at hourly intervals, for the duration of the SHT. Figures 8-10 through 8-13 display the temperature, relative humidity, and pressure measurements from August 1996 through December 1997.

8.2.1 Temperature Measurements

Temperature monitoring data are shown in Figure 8-10. Because of their relative distance from the heater, sensors in boreholes 16 and 18 registered modest temperature rise. The highest temperature attained is about 52°C in sensor 18-4. Temperature data for 16-4 are not represented in Figure 8-10 because the sensor failed to function normally after November 8, 1996 (Freifeld and Tsang 1997b, p. 2). As expected, the sensors located closest to the heater borehole 1 show the quickest response to heater turn-on and turn-off. Temperatures began declining in 18-4 within a few days from the heater turn-off (May 28, 1997), but it took several weeks before cooling become apparent in the more distant sensors (16-1 and 18-1). At the termination of the SHT in January 1998, the temperature in the sensors closest to the borehole collar had fallen below 30°C, but were still a few degrees above the pretest values. The match between temperature data and numerical modeling will be discussed in Section 8.7.

8.2.2 Relative Humidity Measurements

Relative humidity measurements for the duration of the SHT are shown in Figure 8-11. These measurements have an accuracy of ± 2 percent below 90 percent relative humidity and an accuracy of ± 3 percent above that point. The relative humidity sensor is effective in monitoring

very dry rock mass with strong capillary suction, but is not sensitive to "normal" liquid saturation—that is, unless the rock mass is very dry, the relative humidity sensor is expected to register 100 percent (Freifeld and Tsang 1997b, p. 6). Laboratory measurements (Sections 4.2 and 6.3) show that the pretest matrix liquid saturation at the SHT is of the order of 90 percent, it was therefore expected that all the sensors in boreholes 16 and 18 should register effectively 100 (±3) percent before the initiation of heating. Moreover, since even the sensors closest to the heater (16-4 and 18-4) are about 3 m from the heat source and lie outside the drying zone developed after one year of heating, based on thermal-hydrological predictive simulations (Birkholzer and Tsang 1996, p. 18), the readings of humidity sensors are expected to continue registering 100 percent during the heating phase of the SHT.

The relative humidity monitoring data in Figure 8-11 show that by the first week of September, 1996, the vapor phase in the monitoring zones in boreholes 16 and 18 have come into equilibrium with the liquid in the rock mass, and the readings in 16-4 and 18-4 stabilize to 100 percent (and for 18-4, remain at 100 percent for the duration of the test). Sensor 16-4 ceased to function properly beginning November 8, 1997, possibly because of being submerged in condensate in borehole 16 (Freifeld and Tsang 1997b, p. 2). Data in all the humidity sensors were expected to be similar to those of 18-4; in fact, the humidity measurements of the three sensors that are closest to the collar for each borehole remain below 96 percent for the duration of the SHT. These observed low values of relative humidity are attributed to drying from the ventilation in the Thermomechanical Alcove Extension. At the locations of the first three humidity sensors, boreholes 16 and 18 appear to be in communication with the drift through the fractures in the rock mass.

The small discontinuities in the humidity readings are due to perturbation from injection of dry air during active air permeability testing which took place on November 25, 1996; February 4 and 5, 1997; March 8, 1997; May 22 and 23, 1997; October 8, 1998; and November 18 and 19, 1997. The large dip in sensor 18-2 from March through July of 1997 indicate drying of the zone, and subsequent recovery to its former value; the exact cause for the drying is not understood.

8.2.3 Pressure Measurements

Gauge pressure monitoring data are presented in Figure 8-12. It is expected that no significant pressure buildup would occur due to heating, because all monitoring zones in boreholes 16 and 18 are too far removed from the boiling zone near the heater, and because the heater borehole is in direct communication with the Thermomechanical Alcove. All pressure transients, except the ones from 16-4, show no significant pressure variation from ambient. The pressure response in 16-4 has been replotted in Figure 8-13. The pressure buildup shown in Figure 8-13 corresponds to the buildup of condensate in zone 3 of borehole 16. The four pressure drop events (prior to the termination of heat) correspond to the four times that water was drained from zone 3 (i.e., on November 25, 1996; February 4, 1997; February 27, 1997; and May 22, 1997). Note that within one week from August 26, 1996 (the heater turn-on date), the pressure of condensate resulted in an increase of the pressure in zone 3. The very rapid transport of vapor to zone 3 is confirmed by the post-cooling tracer test results described earlier (Section 8.1.3.2).

An explanation for water accumulation in zone 3 of borehole 16 is as follows: vapor from the boiling of water near the heater flows outward and condenses around zone 3 of borehole 16. The liquid saturation in the rock mass reaches unity in some areas adjacent to the borehole, thus overcoming the capillary barrier at the borehole wall and enabling water to drip freely into the borehole. Within days from the heater turn-off date (May 28, 1998), the pressure in zone 3 of borehole 16 started to decrease. This indicated that the condensate was being imbibed by the rock formation. This imbibition process may very well have occurred during heating, but could have been masked by the continuous supply of vapor transported through fractures from the heater borehole to zone 3.

8.2.4 Summary

Many of the observed responses of the passive monitoring data of temperature, relative humidity, and pressure are understood and predictable. Observations such as the drying of rock formation adjacent to the drifts and the seepage of condensate into borehole 16, all add to knowledge of the important role of fractures in the performance of the SHT. In the former, drying is caused by communication of the rock formation with ventilated alcoves and drifts through fracture network. In the latter, a discrete fast path for vapor transport accounts for the fact that seepage of condensate occur in borehole 16, and not in borehole 18.

8.3 GROUND PENETRATING RADAR

8.3.1 Overview

The following investigations were documented in accordance with LBNL procedure YMP-LBNL-QIP-SIII.0 (c), *Scientific Investigations.*

This section presents a discussion of the borehole radar tomography experiment conducted within the Thermomechanical Alcove centered around the SHT. The intent of the experiment was to perform high resolution, cross-hole radar data to estimate the spatial distribution of the moisture content within the rock mass. The application of heat over time to the subsurface rock mass was expected to progressively drive moisture away from the heater. The extreme sensitivity of radar measurements to even very slight changes in water saturation suggested the suitability of this data collection methodology. Borehole radar tomography data are useful for delineating the geometry of the condensation front and for studying moisture migration that occurs as a result of the dramatic increase in rock temperature during the heater test. The effect of temperature on radar measurements and its impact on the estimation of moisture content estimation is included in the processing methodology.

The borehole radar field effort in the ESF for FY96-97 consisted of data collection exclusively within the Thermomechanical Alcove. The boreholes available for survey consisted of those neutron log access boreholes left open during the entire duration of the SHT. These boreholes are numbered as follows: boreholes 22 and 23 (boreholes collared on the Observation Drift) and boreholes 15 and 17 (boreholes collared on the Thermochemical Alcove Extension wall). The boreholes themselves are drilled several degrees off horizontally into the drift, cased with a Teflon liner and grouted into place. Each pair of boreholes defines a two-dimensional plane perpendicular to the heater assembly and trending towards this assembly (Figure 8-14, where the collar of the heater borehole is at (0, 0, and 0)). In the case of boreholes 15 and 17, this plane actually extends across the strike of the heater. This is not the case with boreholes 22 and 23,

which stop just short of this boundary. Deviation records specifying azimuth angle and declination for locations along the length of each borehole (derived from ESF survey of as-built boreholes in the Thermomechanical Test Block) were used for the data processing.

8.3.2 Data Acquisition

A pulseEKKO 100 radar system was used for data acquisition at the Thermomechanical Alcove. A full description of the instrumentation and acquisition is given in Peterson and Williams (1997, pp. 2 to 5). The borehole radar technique utilized at the Thermomechanical Alcove during the SHT experiment was a cross-hole radar profiling method in which the transmitter and receiver antennas were located in separate boreholes and data were collected with the antennas at various vertical offsets. The data collection was performed using two acquisition modes. The first was a Zero Offset Profile (ZOP) in which the transmitter and receiver antennas were positioned within the boreholes at equal depths such that there was no vertical offset. The second was a Multiple Offset Profile (MOP) in which the receiving antenna remained at a fixed depth while the transmitter antenna was moved incrementally in the second borehole. Each MOP constitutes a "receiver gather," and a series of these gathers are used to construct tomographic images.

Over the course of the heater experiment, the radar system was operated by using identical acquisition parameters for each of the five field surveys: one before the heater was turned on, and four during the heater test. No adjustments, filters, or gains are applied to the stored raw data. Therefore, data acquisition and data repeatability are the same regardless of who operates the system and when—provided that the antenna configuration is the same. Data repeatability is tantamount to successful tomographic differencing and interpretation. Small deviations in experimental methodology at such close spacing can result in large discrepancies in data processing.

The most important information to be obtained from radar data is the travel times, which are inverted for the velocity structure between boreholes. It is important to know the precise time when the transmitter fires (known as time-zero), to determine accurate travel times between the transmitter and receiver antennas. Direct air wave measurements (the signal from transmitter antenna to receiver antenna in air) with the antennas held together in air and at the borehole collars in air were taken to help determine the zero-time. After these measurements were taken, the antennas were immediately moved into the boreholes and a ZOP dataset was collected, concluding with another set of measurements in air at the borehole collars and together in air. Following this procedure, the MOP datasets were then collected with the locations determined before the start of the survey. In the case of the Thermomechanical Alcove surveys, the transmitter and receiver intervals were every 0.25 m. As in all MOP gathers, the receiver antenna remained at a fixed location (1 m, 1.25 m, 1.5 m, etc.) while the transmitter antenna occupied each of its possible locations down the borehole (e.g., 0-19 m at 0.25-m spacing). Each of the necessary raypaths was collected and recorded for the subsequent tomographic processing. Following MOP acquisition, a final ZOP data set is collected as described above. This is done in an attempt to estimate the time-zero drift that unavoidably occurs.

Five separate surveys were performed using the two well pairs 22 to 23 and 15 to 17. The first data set was acquired on August 22, 1996 before the heater was turned on (time = t_0). Three data

sets were acquired during the heater test: on January 15, 1997, 5 months after heating began (t_2); on March 12, 1997, 7 months after heating began (t_3); and on May 29, 1997, the day after the heater was turned off (t_4). Another data set was acquired on January 7, 1998, after the termination of the cooling phase of SHT (t_5).

8.3.3 Processing

8.3.3.1 Determining the Zero Time

The zero time is defined as that instant the source emits a signal. The determination of this time is essential for the inversion of travel times for velocity and any differencing of times between data sets. The determination of the zero time proved far more difficult than anticipated. It was hoped that taking a measurement with the source and receiver antennas together before each surveyed well pair would give an adequate value for the zero time. It was not anticipated that the zero time would shift after some time, or when the battery was recharged, or for various other reasons. Therefore, a different methodology had to be found to determine the zero time accurately. The zero time, as measured with the antennae together, was subtracted from the ZOP data to find the absolute time for this data. An equivalent ZOP profile was extracted from the MOP data set that could be compared to the ZOP profile acquired from the field. The zero time was subtracted from this pseudo-ZOP profile and if the travel times match, then this is taken to be the zero time. When the times were offset, the average offset time was calculated and the MOP zero times were corrected for this value. This proved to provide an accurate measure of zero time throughout the surveys.

8.3.3.2 Boreholes 22 and 23

Boreholes 22 and 23 are 0.656 m apart at their collars at the alcove wall and deviate to approximately 1.4 m at their endpoints while remaining in the same plane. Accurate coordinates must be calculated for each source and receiver point before any processing can begin. This is done using the surveyed borehole coordinates. The source and receiver coordinates, which are at 0.25-m intervals, must be determined by interpolating between the given coordinates. The casing sticks out of the wall about 0.3 m for borehole 22 and 0.6 m for borehole 23. Since boreholes 22 and 23 are virtually in-plane, the x and z coordinates can be used as coordinates for the 2D tomographic inversions.

Figure 8-15 shows three typical receiver gathers for the 22-23 well pair. The time scale along each trace is in nanoseconds, and each gather contains one receiver depth and many source depths. The frequency content of a trace at near zero offset shows the peak energy occurring at 100 MHz with a slow roll-off for higher and lower frequencies (Figure 8-16). The travel times were picked for the three surveys: t_0, t_1, and t_2. Since this well pair has only three surveys and the results were consistent with the 15-17 well pair, the results will not be shown.

8.3.3.3 Boreholes 15 and 17

Boreholes 15 and 17 are separated by 0.785 m at their collars at the alcove wall and deviate to approximately 4.0 m at their endpoints while remaining in the same plane. The source and

receiver coordinates are determined from the deviation coordinates as in the 22-23 well pair. The casing stick-up was 0.50 m for both borehole 15 and borehole 17 so the zero point was more easily and accurately determined for this well pair.

Figure 8-17 shows a typical receiver gather for the 15-17 well pair. The variation in amplitude as a function of source/receiver antenna separation distances indicates that the threshold distance for using radar in this material is about 4.5 m. This is more easily observed in the plot of the log of the root mean square of the amplitude as determined by the first 20 samples after the first arrival time (Figure 8-18). Given the system and acquisition parameters, the lower limit of detection was a log amplitude of 5.9 which was detected at a source/receiver separation distance of 4.5 m. The spectrum of a typical trace shows that the peak amplitude remains at about 100 MHz, so no loss in frequency content of the signal is observed (Figure 8-19).

Despite the low signal amplitudes, a sufficient number of travel times could be picked to perform a velocity inversion for each of the five surveys. The Algebraic Reconstruction Technique, as described by Peterson (1986), was used for the inversion. All travel time inversion techniques invert for the slowness, which is equal to 1/v, where v is velocity. A 4.25 m x 8.5 m field in the plane of boreholes 15 and 17 was divided into a grid of 16x32 pixels producing a pixel dimension of 0.265x0.265 m, which approximately corresponds to the station spacing of 0.25 m. The multiplicity of source and receivers resulted in a dense sampling of the interwell area; 400 arrival times were available for each tomographic inversion.

The inverted times produce the velocity fields surveys shown in Figures 8-20 and 8-21. The velocity field changes significantly between each survey, with the greatest changes occurring between the t_0 and t_1 surveys (baseline tomogram in Figure 8-20 and tomogram at five months in Figure 8-21, respectively). There are some common features such as a diagonal high velocity zone, a high velocity zone around the heater, and a low velocity zone a meter away from the heater. The differences can be highlighted by subtracting the velocity values between two tomograms. The baseline velocity tomogram is subtracted from the four post-heating velocity tomograms producing four velocity difference tomograms. The difference tomograms are shown in Figure 8-22. The average absolute velocity value is about 0.1 m/ns, so a difference value of 0.01 m/ns is about a 10 percent change in velocity. The tomograms all show significant velocity increases and decreases. The increases in velocity occur in two zones: one around the heater (black dot at (0,0)), the other near the alcove wall (top of figures). There is one decrease in velocity and it occurs near the center of the tomogram, about 1 m toward the alcove wall from the heater. Another decrease in velocity may occur 1 m on the other side of the heater, but the resolution at this area of the tomogram is quite poor.

8.3.4 Interpretation

For low electrical conductivity environments and at the frequencies used for GPR imaging, the relationship between electromagnetic wave velocity and dielectric constant is $v = c/\sqrt{\kappa}$, where v is velocity, c is the velocity of light and κ is dielectric constant. Temperature and saturation are two parameters which affect the dielectric constant and thus the velocity change in this experiment. The dielectric constant of dry rocks is 3 to 6 and of water is 80; the dielectric constant of a material increases and thus the velocity decreases with increasing saturation. If the temperature

dependence of dielectric constant was ignored, then the difference tomograms (Figure 8-22) would suggest that saturation decreases near the heater and increases about a meter away, consistent with the thermal hydrological condition of a drying zone around the heater, and a condensation zone commencing at about 1 m from the heater. However, temperature dependence of the dielectric constant is not negligible and must be compensated for in the estimation of saturation from dielectric constant estimates.

Saturation estimates can be obtained from ground penetrating radar data using two different methods. The first method involves obtaining relationships between temperature, saturation and dielectric constant under laboratory conditions. These relationships can then be used together with field measurements of dielectric constants from radar and field measurements of temperature to predict the interwellbore saturation. An alternative method of relating the dielectric constant to saturation and temperature is to determine a relationship between dielectric constants obtained at the wellbore from cross-hole radar, borehole measurements of saturation obtained from neutron logs, and borehole temperature measurements. This method will also produce a dielectric constant-saturation-temperature relationship that can be used in a predictive manner to estimate interwellbore saturation. A drawback of this method is that the inverted radar velocities are less reliable near the wellbore, and the neutron logs must be of good quality. Both methods require the temperature field between boreholes. The temperature can be interpolated from the values from the temperature probes down the boreholes. A relationship between temperature and distance from the heater is estimated using regression analysis on all temperature measurements in the plane of the two well pairs (Figure 8-23). A fifth order polynomial equation was used to fit these data values and to then estimate the temperature at each pixel as a function of distance to the heater.

Linear regression and neural network methods were used with both the borehole and laboratory data to develop relationships between dielectric constant, temperature, frequency, and saturation. Linear regression techniques for relating geophysical and hydrological measurements have been used extensively to aid reservoir studies; these techniques assume a linear relationship between some parameterization of the geophysical and hydrological variables. Neural networks are being used to solve a variety of scientific and engineering problems concerned with unknown and varied functional relationships among measured variables. Neural networks attempt to emulate the brain process by adopting simple rules that govern interactions between input and output information; this technique is particularly advantageous when searching for nonlinear relationships. Typical neural network systems have an input layer, where data are presented to the network, and an output layer, which holds the response of the network to a given input, and at least one hidden layer, which connects the input layer to the output layer (Figure 8-24). Each layer is fully connected to the succeeding layer with corresponding weights. The values of the weights represent the current state of knowledge of the network, and the weights are adjusted during training to improve the network performances. The number of hidden layers and nodes in each layer are chosen by the user. Training is complete when convergence has been achieved, or when the mean squared error at the output is less than a designated tolerable error. The recent success of neural networks is in part due to advances in computer technology which have made it possible to bring together a large number of nodes and massive connections of simple neurons. However, developing a proper neural network model that is an accurate representation of the process of interest is still a combination of art, science, and technology.

8.3.4.1 Saturation Dependence of Dielectric Constant Based on Laboratory Measurements

Laboratory measurements of dielectric constant as a function of saturation and temperature were obtained from Topopah Spring Tuff cores and made available for analysis in Roberts and Carlberg (1998). An example of similar laboratory measurements using a 1 MHz signal is shown in Figure 8-25 where it is observed that dielectric constant increases with both temperature and saturation. Regression analysis was used to obtain a relationship between the logarithm of saturation and the explanatory variables of temperature and dielectric constant; this relationship was linear and valid for saturations greater than 15 percent. The original intent was to use dielectric constant values obtained from radar velocity data together with field temperature measurements, both collected prior to and during the heater experiment, to predict saturation states at different times. The difference in these two saturation states would then delineate the change in saturation due to the influence of the heater. However, upon application, it was observed that the range of dielectric constant measurements obtained from the cross-hole radar (using a frequency of 100 MHz) differed dramatically from those collected under laboratory conditions (with frequency ranging from 400 Hz to 1 MHz). The difference is attributed to the dispersive nature of the dielectric constant, or to the fact that the dielectric constant measurement is a function of measurement frequency.

The effect of frequency on the results can be seen in Figure 8-26 where a large variation of the affects of saturation on dielectric constant due to frequency of the signal is observed. The data in this figure are preliminary and confirmatory only. The saturation versus dielectric constant curves level off at dielectric constants above 25 in Figure 8-25. The dielectric constants determined from the velocity inversions at the Thermomechanical Alcove site are between 5 and 12, which are similar in range to dielectric constants estimated by Daily and Ramirez (1989, p. 1084) using cross-hole radar techniques in the Topopah Spring Tuff. This suggests that to adequately determine a relationship between temperature, saturation, and dielectric constant using the above methodology, laboratory measurements must be made at a frequency similar to the field measurements (100 MHz). At this time these laboratory measurements have not been made. Therefore, frequency must be used as one of the variables when determining a relationship to estimate saturation. The saturations may be estimated by obtaining a relationship between the logarithm of saturation (S) and the explanatory variables of temperature (T), dielectric constant (κ), and frequency (f). Linear regression was used to obtain the following relationship:

$$\ln(S) = 0.1083 \ln(\kappa) - 0.4523 \ln(T) + 0.112 \ln(\kappa f) \qquad (8\text{-}2)$$

with a correlation coefficient of 0.88. The fit is shown in Figure 8-27. Using this relationship, the saturation field at each survey time was estimated by using a frequency of 100 MHz in Equation 8-2 (Figure 8-28). The saturation values indicate an increase in drying near the heater with time while the heater was on, with the saturation returning toward baseline after the heater was turned off. There is also a small decrease in saturation near the drift wall (located at bottom of each tomogram) which may be due to effects from ventilation of the drifts. A very small increase in saturation occurs a meter or two away from the heater.

The relationship between the saturation and dielectric constant and temperature can also be obtained using a neural network approach (Boadu 1997). The input data to the neural network consisted of laboratory values of dielectric constant and temperature, and the output data consist of laboratory saturation measurements. Hence, for this application, there are only two input variables to the neural net system (Figure 8-24). Because no laboratory measurements were made at the frequency of the cross-hole radar data (100 MHz), and because neural networks have a difficult time interpolating outside of the training range, only the highest frequency laboratory data of 1 MHz was used to train the neural network. It is assumed that the change in dielectric constant values due to the difference in frequencies between the field radar and laboratory measurements (1 MHz to 100 MHz) will be a linear shift. The tomographic radar data were scaled prior to saturation estimation so that the dielectric constant values would fall in the range of the 1 MHz laboratory data (see Figure 8-25); this was accomplished by multiplying the dielectric constants obtained from the field tomographic radar data by 2.3. Also, the laboratory maximum temperature value of 95°C was used when the field temperatures exceeded this value. The observed versus predicted values obtained from the neural network model are shown in Figure 8-29. The change in saturation predicted using the neural network model (Figure 8-30) is quite similar to the results from linear regression (Figure 8-28). Because of the scaling that was performed to compensate for the frequency discrepancies, the absolute values shown in Figure 8-30 may not be precise, but the relative position between areas of drying and wetting should be reasonable.

8.3.4.2 Comparison to Borehole Neutron Probe Measurements

An alternative method to using laboratory data is to compare the change in dielectric constant obtained from cross-hole radar data at the wellbore to the change in moisture content and temperature measurements obtained along the borehole using neutron and temperature probes, respectively. The nonlinearity revealed by the neutron borehole measurements (Figure 8-31) suggested that these data are good candidates for the neural network, but not the linear regression. However, for this technique to work, it must be assumed that the neutron data is most sensitive to a change in water content. Neutron logs were acquired every two to four weeks at 0.1 m intervals down each well. The neutron data were calibrated to give the difference in moisture content from the baseline measurement taken before the heat initiation. An average moisture content was calculated using the value plus the two values adjacent in time. This value was again averaged using the value plus the two adjacent values in space. Since the neutron data is in change in water content from one survey time to another, change in dielectric constant and change in temperature values must also be used. The average change in dielectric constant associated with this neutron value was calculated by averaging all dielectric constant values within a radius of 0.4 m of the neutron log point. Such a large radius was taken since the size of each dielectric pixel is 0.25 x 0.25 and the center of the pixel must be within the chosen radius of the neutron acquisition point to be included. As in the laboratory data neural net analysis, the temperature data are limited by the maximum borehole temperatures; much higher temperatures exist in the interior where there is no neutron log data. Therefore, the results would not be valid in this region of higher temperatures, so a maximum change in temperature value was assigned in this region.

These averaged field dielectric constant differences and change in temperature values were used as input to the neural network model (Figure 8-24), and the change in moisture content was used

as the desired output. The observed versus predicted values as calculated by the neural network model is shown in Figure 8-32. The model obtained from the neural network was used together with the tomographic dielectric constant field and interwellbore temperature field to predict the change in moisture content for three time intervals (borehole neutron data were not collected at 17 months as shown in Figure 8-33). The change in water content predicted by this model appear to correlate more with the temperature field than with the models estimated by the laboratory data (Figures 8-28 and 8-30). This may indicate that the neutron probe may be more sensitive to change in temperature than change in water content.

8.3.4.3 Discussion of Saturation Estimates

Saturation changes were estimated from dielectric constant tomograms as converted from the velocity tomograms using various methods. In order to compare the estimates obtained using linear regression and neural network approaches on both laboratory and borehole data, the correlation between the different estimated change in saturation or moisture content at the time interval t_i-t_0 was obtained as shown in Table 8-9.

Table 8-9. Correlation of Different Methods for Estimates of Change in Saturation

	Laboratory Data Regression	Laboratory Data Neural Net	Borehole Data Neural Net
Laboratory Data Regression	1.00	0.86	0.54
Laboratory Data Neural Net	0.86	1.00	0.52
Borehole Data Neural Net	0.54	0.52	1.00

Table 8-9 indicates that the neural network and linear methods produce similar results if the data used to develop the petrophysical relationship are the same (i.e., laboratory data), and that correlation decreases when different data sets (borehole data) are used to develop the petrophysical model. In spite of the differences suggested by the correlation table for the absolute values of the change in saturation or moisture content, the estimated fields shown by Figures 8-28, 8-30, and 8-33 all reveal similar patterns in the condensation front that moves away from the heater upon heat application. Comparison of these estimates with those obtained using petrophysical relationships developed with laboratory data suggests that the borehole data are more influenced by the temperature than the laboratory measurements. Two-dimensional time-lapse high resolution information about the saturation patterns such as that given by these figures is necessary for understanding and predicting the influence of the stored radioactive waste in the Topopah Spring Tuff; this information is unattainable with conventional one-dimensional borehole measurement techniques.

8.3.5 Conclusion

The radar velocity tomograms taken before heating and after heating show significant differences. These tomograms and the differenced tomograms were quite effective in mapping changes in moisture content due to the heating. Saturation changes were estimated from dielectric constant tomograms as converted from the velocity tomograms using various methods (Figures 8-28, 8-30,

and 8-33). The saturation changes indicate a region of extreme drying to about a radius of 1 m from the heater, where the saturation drops to about 20 to 40 percent. Beyond this region of drying is a region of no saturation change or an increase in wetting. It is difficult to detect small changes in saturation in highly saturated material using radar. This region is about 2 m thick. It is not symmetric, possibly due to a zone of anomalous velocities (Figure 8-20). There is also another region of drying near the drift walls, most likely due to ventilation in the drift.

8.4 INFRARED IMAGING

During the SHT, the noninsulated surfaces of the SHT block were periodically examined using an IR camera. The purpose of this study was to assess whether the temperature distribution observed on the block surface can be related to any physical features in the block, and perhaps to discover features, including surface outlets for pathways of fluids or gases that undergo thermally induced changes. The results of the IR mapping study have been discussed in quarterly progress reports (Cook and Wang 1997a, 1997b, 1997c; Cook 1997; and Cook 1998). A sample of the results reported previously (Cook 1998) shall be presented below.

Because the insulated material on all three exposed surface of the SHT block extends almost to the top of the drift walls, surfaces available for IR imaging were several meters removed from the collar of the heater. That was sufficiently removed from the heat source to limit the maximum temperature rise to only about 10°C above ambient, in the region above the heater collar. Otherwise, the IR data have revealed no discernible discrete thermal features of the rock.

8.4.1 Data and Discussion

The IR camera (Inframetrics PM 200 Thermacam SN 8954) was used to take pictures of the region above the heater collar, along the right side of the heater block and at the end of the extension drift (Figure 8-34). The same areas were mapped at approximately three-month intervals, starting in August 1996 before the onset of heating. Frames in a given data set were taken from approximately the same distance and perpendicular to the surface of interest. Each frame covers an area approximately 1 m square. The 2D gray scale IR montages and line plots (Figures 8-35 through 8-39) illustrate the evolution of IR data over time.

Montages from the area above the heater are shown on Figures 8-35 through 8-37. The image from August 1996 is included in Figure 8-35 as baseline data. Figure 8-36 shows the montages from February and July of 1997, and the image for December 1997 is shown in Figure 8-37. All montages except that of December 1997 have the same temperature scale. The scale for the December 1997 data was adjusted to maintain contrast at the lower temperature levels, which followed the conclusion of heating on May 28, 1997. May 1997 data are not shown on the montages due to partial data file corruption (Cook and Wang 1997c, pp. 2 and 3); sufficient data, however, were salvaged for line plots. The main features in the montages of Figures 8-35 through 8-37 are the presence of two warm regions directly above the heater borehole collar, which are discernible in the data of December 1996 (three months after heating), and which become more prominent in February 1997. The temperature distribution of the warm areas had become spatially diffused in July 1997 mapping (i.e., six weeks after termination of heat).

Figure 8-38 shows line plots of August and December 1996, and February, May, July, and December 1997 temperatures obtained from the montages of the SHT front face just above the insulation. Line plots give better quantitative detail than montages and are able to highlight actual changes in temperature over time better than a montage. The location of data collection corresponds to the red line overlaid across the February image in Figure 8-36. Temperature is plotted against distance. The scale of the bottom of the plot represents the distance between the extensometer pins TMA-WX-2 and TMA-WX-1, left to right. This distance is roughly 4 m, centered on the single heater itself. The magnitude and variation with position of the temperatures on the face are consistent with the heating and cooling schedule of the SHT. The trough in the values in the center of the line plots corresponds to the image of a cable tray that radiates at ambient temperature. The trough is of different widths because the tray is an item not flush with the wall, and its image is subject to parallax changes in the images. The highest temperature seen is in the May 1997 data set just prior to termination of heat, at about 35°C.

Figure 8-39 contains line plots of the December 1996, and February, May, July, and December 1997 temperatures taken immediately above the insulation on the right side of the SHT block (see Figure 8-34). Here also, the temperature variation and magnitude increases with time while the heating in SHT is in progress. The left side of the plot, which corresponds to the corner, shows lower temperatures than the rest of the plot due to the higher exposed area of the corner section. It is uncertain why there are two temperature peaks along the top of the insulation in the May data. A possible explanation for the first peak on the left could be a heat leak from the insulating blanket.

The plots from July 1997 in Figures 8-38 and 8-39 both show a temperature decline after six weeks of heater shutoff. In addition, the peaks in the July 1997 data have flattened as the heat redistributes on the rock surface. The data from December 1997 (six months after cooling), show that the temperatures have decreased to approximately the February 1997 levels, for both the side and front faces of the SHT block.

8.4.2 Summary

The data from the IR camera show that the heat distribution followed the expected pattern, initially emanating from regions closer to the single heater and then dissipated towards the corners of the SHT block. The maximum temperature recorded on the images was about 35°C on the front face. No discernible discrete thermal features were detected.

8.5 ELECTRIC RESISTIVITY TOMOGRAPHY

This section describes ERT surveys made during the SHT to map the changes in moisture content caused by heating. Of particular interest is the formation and movement of condensate within the fractured rock mass. Figure 8-40 shows the relative position of the ERT boreholes in the SHT. Four inclined boreholes, forming a plane perpendicular to the heater axis, were used to position electrodes around the region of interest; this plane intersects the heater near its midpoint. Twenty-eight electrodes, equally spaced within the four boreholes, were used to conduct ERT surveys around the heater.

8.5.1 ERT Measurements

ERT is a geophysical imaging technique that can be used to map subsurface resistivity. Rock mass heating creates temperature and liquid saturation changes that result in readily measured electrical resistivity changes. The ERT measurements are made with an automated data collection system and consist of a series of voltage and current measurements from buried electrodes. The data are then processed to produce electrical resistivity tomographs using state-of-the-art data-inversion algorithms. These measurements are used to calculate tomographs that show changes in electrical resistivity as a function of space and time.

Following are brief descriptions of some of the important features of the 2D algorithm. For additional details, the reader is referred to Morelli and LaBrecque (1996, pp. 629 to 631). The algorithm solves both the forward and inverse problems. The forward problem is solved using a finite element technique in two dimensions. The inverse problem implements a regularized solution that minimizes an objective function. The goal of the inverse routine is to minimize the misfit between the forward modeling data and the field data. The resistivity model's roughness is used as a function to stabilize the solution. This means that the inverse procedure tries to find the smoothest resistivity model that fits the field data to a prescribed tolerance. Resistivity values assigned in this way to the finite element mesh constitute the ERT image. Although the mesh is of a large region around the electrode arrays, only the region inside the ERT electrode array is shown in the results because the region outside the array is poorly constrained by the data.

To calculate the changes in the rock's electrical resistivity, a data set obtained after heating started was compared to a corresponding data set obtained prior to heating. One may consider subtracting, pixel by pixel, images from two different conditions. However, this approach could not be used because the resistivity structure was 3D (i.e., several boreholes containing metallic instruments were located orthogonal and parallel to the plane of interest; see Figure 8-40). These metallic instruments caused large conductive anomalies and made the resistivity structure 3D. The finite-element forward solver cannot generate a model that will fit the data; thus, the code chooses a solution with a poor fit. Experience shows that these effects can be reduced by inverting the quantity:

$$\frac{R_a}{R_b} * R_h \qquad (8\text{-}3)$$

where R_a is the measured transfer resistance after heating started, R_b is the transfer resistance before heating and R_h is the calculated transfer resistance for a model of uniform resistivity. This approach tends to reduce the effects of anomalies that do not match the 2D assumptions of the resistivity model because the 3D effects cancel in the ratio (because they are contained in both terms R_a and R_b).

The data used for the tomographs in this section were the average of three consecutive data sets (the time intervals between data sets was approximately 40 minutes). That is, each reading used for the tomographs was the average value of the reading measured in three consecutive field

surveys. This was done to improve the signal-to-noise ratio of the measurements made at low voltages.

The ERT measurements in the SHT were performed under procedure LLNL QP 3.4, *Scientific Notebooks*.

8.5.2 Changes in Resistivity

To get an estimate of the effects of measurement noise on the tomographs, data sets collected a few hours apart on August 22, 1996, were used to calculate resistivity-change tomographs. No changes were expected at this time because the heater was off (heating started on August 26, 1996). Therefore, any changes observed in this image would be indicative of the effects of measurement error on the inversion process; thus, this image can be used to determine the significance of resistivity changes shown in subsequent images. On average, these "noise" images showed the resistivity ratio to deviate from 1.0 (i.e., perfect result when no changes occur) by ±0.05, so changes of about 5 percent can be expected on the basis of measurement error. Therefore, to be considered reliable, the changes observed during heating need to be substantially larger than 5 percent.

Figure 8-41 shows tomographs of electrical resistivity change during the course of the heating phase; these tomographs are shown in the left hand column of the figure. The images labeled 9/03/96 in Figure 8-41 show changes 8 days after heating started on August 26, 1996. After just 8 days, there is a weak conductive anomaly showing significant changes (i.e., changes significantly larger that those expected to be caused by measurement error; up to 20 percent change) with a circular region of enhanced conductivity forming—not centered on the heater, but shifted about 1 m upward.

The rest of the images in Figure 8-41 show a clear trend of overall increase in electrical conductivity in the rock mass (i.e., decreasing resistivity or a ratio less than 1.0). However, the first 59 days of heating show a pattern that is different from the pattern observed in subsequent images. Prior to the December data, the conductive anomaly is mostly circular in section (although not centered on the heater). However, after a 41-day data gap between October and December 1996, the pattern is much more irregular, and there is no clear pattern or symmetry from which one could locate the heater. This is due to the fact that rock heterogeneities such as fractures are influencing the changes in saturation and temperature, which in turn drive the resistivity changes observed; the relationships among saturation, temperature, and resistivity ratio are discussed in detail in Section 8.5.3.

The complex and irregular pattern in the images (after day 59) is interpreted as changes in moisture content due to drying and wetting along fracture systems having a complex, 3D geometry. As the temperature increases above ambient, the vapor pressure in the pores increases. Fractures connected pneumatically to the drift will provide a pressure gradient so that moisture will leave the rock through fracture openings and move along the fractures in response to buoyancy or thermally driven pressure gradients. The result will be dryer zones along fractures near the heater but wetter zones along fractures further away, where temperature and pressure allow condensation below the local dew point.

Between heating days 100 and 270 (middle to late portions of the heating phase), the rock zones showing the largest conductivity increases (i.e., zones showing the smallest resistivity ratios)

appear to gradually migrate downward below the heater borehole. The image collected on May 23, 1997 (heating day 270) shows the resistivity changes observed near the end of the heating phase (the heater was turned off on May 28, 1997). Note that an inverted-L-shaped resistivity decrease region (indicated by resistivity ratios less than 1.0) is located near the heater location.

Figure 8-42 shows tomographs of electrical resistivity change during the course of the cooling phase; these tomographs are shown in the left-hand column of the figure. Twelve days into the cooling phase, the upper tip of the inverted-L-shaped resistivity decrease region had disappeared; a region of resistivity increase (ratios greater than 1.0) began to develop near the heater. After 29 days of cooling, the zone of resistivity increases near the heater grew in size and continued growing, as seen in subsequent images. Note that this resistive anomaly was not centered on the heater, possibly because of heterogeneities in the rock mass (notably fractures). Also, the regions of decreased resistivity observed below the heater became smaller in size as cooling progressed.

During heating, there were competing effects at work (i.e., temperature increases caused resistivity decreases while drying caused resistivity increases). Just before the end of the heating phase, the dominant effect was the resistivity decrease due to temperature. This changed by June 26, 1997 (cooling phase day 29) when the local region at the nine-o'clock position from the heater was more resistive than initial conditions. Note that the temperatures at this time had already dropped to near 50°C at the heater borehole. As the temperature decreased to near 40°C (cooling phase day 57), the water resistivity returned to these tomographs higher values. The effects of drying on the resistivity (which made the resistivity increase) were now beginning to dominate over the effects of temperature (which made the resistivity decrease); as result, the resistivity was increasing. The net effect was that, up to day 57 during cooling, the resistivity increased. However, once the pattern on day 57 was established, it remained fairly stable until the last survey (taken cooling day 270); there were minor changes, but the basic pattern was the same.

Interpretation of moisture content based on resistivity changes is complicated by several factors. One of these is related to the dependency of the resistivity on temperature and saturation. Fortunately, a measure of temperature exists so that it is possible, in principle, to separate the two effects; an attempt to do this is made in the section that follows.

8.5.3 Inferences of Moisture Changes

Background-The resistivity changes in Figure 8-41 and Figure 8-42 are influenced by changes in moisture content and temperature (e.g., an increase in temperature or moisture causes a resistivity decrease, while drying will cause the resistivity to increase). Near the heater, there are regions where the resistivity decrease caused by increasing temperatures is counterbalanced by the effect of drying, which increases the resistivity; the resistivity ratio may be higher than 1.0 (resistivity is higher than the preheat case) or lower than 1.0 depending on the temperature. Farther away from the heater, where steam condenses and temperatures are above ambient, the resistivity will go down because of the increasing saturation and temperature. The goal is to use the images of resistivity change, along with the measured temperature field (shown in the second column of Figure 8-41 and Figure 8-42) and what is known of initial conditions in the rock mass, to estimate moisture during the test (shown in the third and fourth columns of Figure 8-41 and Figure 8-42).

To estimate moisture content changes, one needs to make use of temperature, measured at many points by temperature sensors, and resistivity changes, measured by ERT. The saturation estimates can be made by using empirically derived relations based on laboratory data or by using a suitable model of electrical conduction in porous media. Roberts and Lin (1997, pp. 579-580) published data on the resistivity of Topopah Spring Tuff as a function of moisture content and temperature. There is, however, only limited data on temperature dependence (up to 95°C), and the samples were not from the SHT alcove, so direct use of this data is not straightforward.

A second approach is to use an electrical conduction model. Waxman and Thomas (1974, pp. 213-214) describe the Waxman-Smits model (intended for oil field data) for electrical conduction in partially saturated shale sands that accounts for conduction through the bulk porewater as well as conduction through the electrical double layer near the pore surface. This model can predict temperature dependence of the resistivity (Waxman and Thomas 1974, pp. 218-220), but several of the model parameters are empirically determined and not available for tuff. Roberts and Lin (1997, p. 585) suggest that the Waxman-Smits conceptual model provides reasonably good estimates of resistivity for saturations greater than 20 percent. For saturations less than 20 percent, their data show that the Waxman-Smits conceptual model substantially underpredicts the resistivity. The capacity of this model to account for the temperature-dependent behavior of welded tuff was not investigated by Roberts and Lin (1997). This model will be used to account for the temperature effects on the resistivity because, as far as is known, it is the only approach that provides the means to cover the temperature range of interest and that has been used successfully in other field applications.

Waxman and Thomas (1974, p. 213) begin with a parallel circuit model for conductance for saturated rock:

$$C = \frac{1}{F^*}\left(C_w + BQ_v\right) \tag{8-4}$$

where

C is the conductivity or $1/R$ where R is the resistivity,
F^* is the formation factor or ϕ^{-m} where ϕ is the porosity and m the porosity exponent,
C_w is the porewater conductivity,
B is the equivalent conductance of counter-ions on the double layer, and
Q_v is the effective concentration of exchange cations.

The first term within parentheses represents conductance through the bulk porewater; the second term is the conductance along the double layer. This expression can be modified for partially saturated media by realizing that the first term is just Archie's equation and $Q/S = Q_v$, where S is

the fractional saturation, and Q is the cation-exchange capacity of the rock. In terms of resistivity, Equation 8-4 can be rewritten as

$$R = \frac{R_w \phi^{-m} S^{1-n}}{S + R_w BQ} \tag{8-5}$$

where the exponent n is approximately 2, the saturation index in Archie's modified equation, and R_w is the water resistivity. Waxman and Thomas (1974, p. 217) reported results that suggest that m is approximately equal to n. When $R_w BQ >> S$, the electrical double layer is the primary conduction pathway. When $R_w BQ << S$, the primary conduction pathway is through the pore space. For rocks and soils having low cation-exchange capacities (e.g., clean sands and granite), the primary conduction pathway is through the pore space. For rocks and soils with high cation-exchange capacities (e.g., clays and rocks with zeolite minerals), the primary conduction pathway is the electrical double layer.

Equation 8-5 can be used in ratio form to calculate resistivity changes in the form of resistivity ratios. The analysis that follows assumes that the porosity and cation-exchange capacity remain constant during the test; thus, these terms will cancel when Equation 8-5 is used to calculate resistivity ratios. When the primary conduction pathway is through water in the open pore space, one can assume that the term $(S+ R_w BQ)$ in the denominator of Equation 8-5 is approximately equal to S. In this case, the resistivity ratio can be calculated as

$$\frac{R_a}{R_b} = \frac{R_{w,a}}{R_{w,b}} \left(\frac{S_b}{S_a} \right)^2 \tag{8-6}$$

where R_b and R_a are the resistivities before and after heating started, $R_{w,b}$ and $R_{w,a}$ are the water resistivities before and after heating. S_b and S_a are the saturations before and after heating started; this case will be referred to as model 1. This equation implies that the temperature dependence of the resistivity change is proportional to the change in water resistivity caused by temperature increases.

When the primary conduction pathway is through the electrical double layer, one can assume that the term $(S+ R_w BQ)$ in the denominator of Equation 8-5 is approximately equal to $R_w BQ$. In this case, the ratio form of Equation 8-5 simplifies to

$$\frac{R_a}{R_b} = \frac{S_b}{S_a} \frac{B_b}{B_a} \tag{8-7}$$

where B_b and B_a are the equivalent conductances of counter-ions in the electrical double layer; this case will be referred to as model 2. This equation implies that the temperature dependence of the resistivity ratio is caused by changes in counter-ion conductance due to temperature changes. Also note that this model is independent of R_w. Comparing Equations 8-6 and 8-7, one can see that the resistivity changes caused by saturation changes are largest for model 1, where the

primary conduction pathway is through the pore space. One notes that neither of these models accounts for changes in water resistivity caused by rock-water chemical interactions. If chemical reactions cause large changes in the concentration or types of ions in the water, the estimated saturation changes will be in error.

Inferences–The dependence of resistivity ratios on temperature and saturation for models 1 and 2 is illustrated in Figure 8-43. Both models show qualitatively similar behavior. The resistivity ratio curves assume that the starting conditions are 25°C and a saturation of 92 percent. The following observations are based on model 2. Note that the 25°C curve indicates a resistivity ratio of 1.0 (no change condition) for a 92 percent saturation. If temperature remains constant at 25°C and saturation decreases, the resistivity ratio reaches values greater than 1.0 (i.e., the resistivity is higher than the preheat case, and drying makes the resistivity increase). On the other hand, if the saturation remains constant at 92 percent and the temperature increases to 150°C, the resistivity ratio becomes approximately 0.3 (this means that the resistivity during heating is 0.3 times as high as the preheat resistivity and that heating makes the resistivity go down).

The bottom set of curves in Figure 8-43 shows the trajectory that the resistivity ratio would follow for two different regions near the heater. The trajectory curves assume that the initial conditions were 25°C and 92 percent initial saturation. The trajectories shown are approximate. For rock very near the heater, temperatures increased to approximately 300°C, and saturations decreased to 10 percent or less. In this case, the temperature and saturation changes have opposing effects: the temperature increases would make the resistivity ratio decrease to less than 1.0, while the saturation decreases tend to increase the resistivity ratio more than 1.0. The approximate trajectory for this case is shown by the red curve near the bottom of Figure 8-43. Note that the resistivity ratio drops below 1.0 as the temperature increases and saturation decreases.

During the early stages of heating, the rock heated up, but relatively little drying had occurred; this causes the temperature effect to dominate over the drying effect. and the resistivity ratio drops to less than 1.0. As heating progresses, the resistivity ratio reaches a minimum near saturation of 40 percent and then begins to increase as the temperatures continue to increase and saturation continues to decrease. The resistivity ratio reaches a maximum of about 1.3 when the temperatures have reached approximately 300°C and the saturation is 10 percent. Note that there is a rapid increase in resistivity ratio when the saturation drops to less than 25 percent; at low saturation the film of water along which conduction occurs becomes discontinuous, thereby forcing the resistivity to increase rapidly. Thus, when the saturation gets low enough, the effect of drying (which makes the resistivity increase) dominates over the effect of heating (which makes the resistivity decrease).

A second trajectory curve is shown in blue to illustrate the behavior for rock that reaches a maximum temperature of 100°C while its saturation increases to 100 percent. In this case, the increasing temperature and saturation both make the resistivity decrease. Thus, in this case, the resistivity decreases faster than for the previous case.

In the SHT, saturation and temperature were both changing at the same time. For the case of rock near the heater borehole during the heating phase (large increase in temperature and large decrease in saturation), the model 2 curves show that, for temperatures greater than 150°C, the

resistivity ratio will be less than 1.0 if the saturation remains at 20 percent or more. This means that the effect of temperature tends to dominate over the effect of saturation because the net effect is one of decreasing resistivity. In other words, the drying effects near the heater make the resistivity decreases created by the rising temperatures less pronounced (closer to a ratio of 1.0). For saturations less than 20 percent, the drying effect on the resistivity more than makes up for the heating effect, and the net effect is for the resistivity to increase. For the case of rock farther from the heater (smaller increases in temperature and increases in saturation due to condensate imbibition), model 2 indicates that the resistivity ratio will be less than 1.0 in all cases. In other words, saturation increases coupled with rising temperatures make the resistivity decreases more pronounced (the resistivity ratio is smaller than it would be if only one of the effects were present).

The available temperature data were used to construct temperature maps along the ERT image plane. It is necessary to have a reliable temperature measurement for each area (each tomograph pixel) if one wishes to calculate the saturation change. At the SHT, there are many temperatures sensors located along roughly horizontal boreholes. However, the temperature coverage in the vertical direction is sparse, extending only ± 1.7 m from the heater. To construct temperature maps, it was necessary to extrapolate vertically out to ± 6.3 m from the heater. It was also necessary to assume that the vertical temperature gradient equaled the horizontal gradient to obtain physically reasonable temperature values for regions beyond 1.7 m vertically. Thus, the accuracy of the temperature maps is expected to be good along the horizontal direction but may be in error along the vertical direction for regions farther than 1.7 m from the heater.

The ERT images provide a measure of change in R from baseline (through the resistivity ratio). Equations 8-6 and 8-7 can be used to relate electrical resistivity changes to changes in saturation when the temperatures are known and the temperature dependence of R_w and B can be calculated. Because the magnitude of R_wBQ is changing in space and time, it was decided to estimate the changes in saturation by using both model 1 and model 2. This approach should provide bounds to the domain of possible saturations that may be present. Available data suggests that the welded tuff at the SHT should show behavior closer to model 2 than to model 1. Assuming average values of cation-exchange capacity for welded tuff of about 3 meq/100 g, porosity of 0.10 (porosity is used to calculate Q), and R_w=39 ohm-m at 25°C (resistivity of J-13 water), it can be shown that R_wBQ is about 23 at 25°C and that it increases as the temperature increases. Given that S ranges from 0.0 to 1.0 this result suggests that R_wBQ is >>S and thus that the primary pathway for conduction at the SHT is the electrical double layer. Therefore, it is believed that the results of model 2 are probably closer to reality. However, if the cation-exchange capacity, porosity, or water resistivity varied significantly across the ERT image plane, it is possible that model 1 results may be closer to reality.

Figure 8-41 and Figure 8-42 show estimates of saturation (third and fourth columns) based on the resistivity ratios and interpolated/extrapolated maps of temperature. The temperature maps were used to calculate the temperature-dependent properties on models 1 and 2 (R_w, B). It was assumed that initial saturation (S_i) of the rock unit was 92 percent; this is the average saturation from grab samples collected along the Observation Drift and reported in *Ambient Characterization of the Drift Scale Test Block* (CRWMS M&O 1997d, p. 5-8). Both models indicate that the saturation around the heater decreased as heating time increased. Model 2 generally predicts substantially

drier saturations near the heater than does model 1; model 2 saturations near the heater are closer to *a priori* expectations than those from model 1. The discussions that follow will be based on the model 2 results.

The saturation estimates produced by model 2 have been used to produce cartoons that highlight the drying and wetting zones interpreted from the moisture estimates. It is hoped that these cartoons facilitate the interpretation of the saturation estimates previously shown in Figure 8-41 and Figure 8-42. The cartoons can be found in Figure 8-44 (heating phase) and Figure 8-45 (cooling phase). The outline of the drying and wetting regions roughly coincide with saturations equal to 70 percent or less for the drying zone and 98 percent or more for the wetting zone.

A significant region of drying is present around the heater. The dry zone is not centered on the heater and certainly is not symmetric about the heater. The pattern suggests a distribution of moisture that is strongly controlled by fractures. As time increased, the drying zone appeared to propagate upward, especially after 219 days of heating; also, the minimum saturation estimate was near 10 percent (model 2). During the cooling phase, the dry zone around the heater appeared to remain relatively stable; an exception to this observation is the result from September 25, 1997, which showed a change in the dry zone near the heater's location.

Drying appears strongest in regions at the heater elevation and above. The lowest imaged moisture content is on May 23, 1997, the last ERT data before the heater was turned off; the saturation estimates indicated that the driest rock had a saturation of about 10 percent. As the temperature field collapsed during the first 29 days of cool down, that extremely dry region remains relatively stable. The rest of the dry zone also appeared stable except for minor changes that imply water is still moving in the rock mass.

Moisture accumulation appears prevalent in regions below and to the sides of the heater, where some rock zones show saturations near or greater than 100 percent. (In some regions, the saturation is calculated to be greater than 100 percent—clearly a nonphysical condition because the rock can be no more than fully saturated. It is possible that those regions began as dryer than the 92 percent saturation level assumed to be the initial condition for the calculation or that the water resistivity changed because of changes in the concentration or types of ions.) The largest zones near full saturation are mostly located below the heater at the four- and five-o'clock positions and the seven- and eight-o'clock positions. Smaller zones are visible above the heater elevation at the ten-o'clock and two-o'clock positions. On April 2, 1997 (late heating phase), these regions cover a significant portion of the area below the heater.

The results of June 26, 1997 show the moisture content estimates after 29 days of cooling. The fully saturated regions below the heater appear somewhat smaller, suggesting that some of the water was leaving this area. Between the June 26, 1997, and August 27, 1997, images, the wet regions below and above the heater appeared to be stable. The data from September 25, 1997, indicate a change from the trend above the heater (i.e., above the heater, at the two-o'clock position, a couple of small regions show increased moisture content). It is interesting that wet regions at the two- and eight-o'clock positions on the September 25 data are aligned with a region near the heater that did not dry as much during the course of the heating phase. This pattern suggests the possibility that a fracture or fracture zone was bringing moisture to dry regions near

the heater. The final cool-down phase result shown in Figure 8-45 (December 17, 1997) still shows a clear dry zone around the heater and significant wetting regions on the lower, left flank of the heater. The wetting regions on the lower right flank of the heater are substantially diminished in size relative to the sequence observed during heating.

The behavior of the wetting zones on the right flank of the heater borehole is different from that of those on the left flank. Note that the wetting zones on the left flank remain relatively large and stable during the course of the cool-down phase. Those on the right flank of the heater appear to break into smaller zones during the cool-down phase. This behavioral difference may indicate differences in rock hydraulic conductivity between the left and right flanks. This may be associated with fractures.

The saturation estimates presented here are impacted by one or more of the following factors:

- The accuracy of the temperature maps in the vertical direction is limited by the sparse vertical coverage of the temperature sensors. Errors in the interpolated/extrapolated temperature maps will result in erroneous saturation estimates.

- The effects of rock-water chemical interactions on electrical resistivity are not accounted for by the Waxman-Smits conceptual model. This means that, if significant changes develop in the number or types of ions in solution, such changes will cause resistivity changes that the model would treat as saturation changes.

- Laboratory measurements of the electrical resistivity of welded tuff (Roberts and Lin 1997, p. 585) indicate that the Waxman-Smits conceptual model underpredicts resistivity for saturations less than 20 percent. The estimates of saturation less than 20 percent in Figure 8-41 and Figure 8-42 are affected by this limitation.

- The inversion algorithm used to reconstruct the tomographs finds the smoothed model that fits the data. This means that the structures observed are "smeared" versions of the true target. Thus, the size of the anomalies is larger than that of the true target.

- Work by Llera et al. (1990, p. 576) suggests that growth of microcracks at high temperature can affect electrical resistivity of welded tuff; this effect, if present at the SHT, is not accounted for by the Waxman-Smits conceptual model.

- The resistivity ratios were calculated using a 2D algorithm; natural heterogeneities such as fractures are likely 3D. Changes in resistivity occurring along fractures may be distorted by use of the 2D algorithm.

- Several boreholes containing metallic instruments are located near the plane of interest. These metallic instruments caused large conductive anomalies that may reduce sensitivity to resistivity changes occurring in the rock, thereby resulting in resistivity-change tomographs that show smaller change than those changes present in the rock.

- The Waxman-Smits conceptual model was developed for the case of shale sands. The validity of this model for welded tuff has been only partially investigated by the laboratory work of Roberts and Lin (1997); the temperature dependence implied by the Waxman-Smits conceptual model has not been tested in the laboratory with welded tuff samples.

- The thermal expansion of the water and the bulk rock is assumed to have negligible effects on the saturation.

8.5.4 Summary and Conclusions

To calculate the changes in the rock's electrical resistivity, a data set obtained after heating started was compared to a corresponding data set obtained prior to heating. Resistivity-change tomographs were calculated based on these data. Saturation estimates have been presented. These estimates were calculated using two models derived from the Waxman-Smits equation, the resistivity ratio tomographs, and maps of interpolated temperatures. It is believed that, of the two models considered, the model that assumes dominant surface conductance (model 2) may provide the most accurate estimates.

During the heating phase, the resistivity-change tomographs show a region of decreasing resistivity approximately centered around the heater. The size of this region grew with time, and the resistivity decreases became stronger. The resistivity decreases migrated downward as heating progressed. The resistivity-ratio tomographs show that heterogeneities in the rock (e.g., fractures) are probably affecting drying and wetting in the rock mass. The complex and irregular pattern in the images was interpreted as changes in moisture content due to drying and wetting along fracture systems having a complex 3-D geometry. As the temperature increased above ambient, the vapor pressure in the pores increased. Fractures connected pneumatically to the drift will provide a pressure gradient so that moisture will leave the rock through fracture openings and move along the fractures in response to buoyancy or thermally driven pressure gradients. The result will be dryer zones along fractures near the heater, but wetter zones along fractures further away, where temperature and pressure allow condensation below the local dew point.

During the cooling phase, the resistivity around the heater increased relative to the preheat case, and the saturation estimates showed a region of drying around the heater. The dry region shape appeared to be controlled by heterogeneities in the formation (fractures).

The dry region appeared to remain stable throughout most of this time; by September 25, 1997, small increases in moisture content could be seen for regions above the heater at the two-o'clock position. These increases disappeared by the time of the December 27, 1997 tomographs. Wetter rock regions observed below the heater slowly became smaller early in the cooling phase, up to the September 25, 1997 results. The wetting zones on the lower left flank appeared to grow in size, as shown on the December 17, 1997 tomographs. The reasons for the apparent enlargement are unknown; perhaps they are due to activities, unrelated to the test, that may have spilled water along the Observation Drift.

The saturation estimates presented can be used as the basis for a conceptual model of thermal-hydrological behavior (shown in Figure 8-46). The model shows a hot boiling zone in which a large fraction of the steam produced during heating moves away from the hot boiling region and condenses. Some of this condensate slowly imbibes into the cooler surrounding rock and causes the saturation to increase. The rest of the condensate drains along fractures to lower-elevation regions. The zones of saturation increase located above the heater elevation are smaller in size than those below the heater because condensate drains quickly from the zones above the heater elevation. Zones below the heater elevation receive condensate generated locally as well as condensate draining from regions above; this allows larger amounts of water to be imbibed below the heater.

8.6 NEUTRON-LOGGING

Thermal neutron-logging is used to determine moisture content in rocks and soils and was used to monitor moisture content in boreholes 15, 17, 22, and 23 (see Figure 3-2) during the SHT. The neutron probe contains a source of high-energy neutrons and a detector for slow (thermal) neutrons. The hydrogen in the water in the rocks slows down the neutrons, making them detectable. Thus, higher counts (or a positive difference in counts relative to background or pre-heat levels) indicate higher water content (or increased water content over background).

The neutron probe used in this test is a Campbell Pacific Nuclear model 503DR. A 3.81-cm (1.5-in.) diameter probe (serial number H37067677) was used for the SHT. Under ambient conditions, the sampling volume surrounding the probe has a diameter of approximately 15-cm; this volume diameter increases as moisture content decreases. Measurements are sensitive to the presence of elements, such as chlorine and boron, that have large neutron-capture cross sections. The uncertainty of the neutron logging is about 3 to 5 percent in water content.

For the SHT, a Teflon™ tube, with an RTD bundle mounted on its outside, was inserted into the boreholes and grouted into place. The Teflon™ tube permits easy insertion, placement, and removal of the tool. Calibrations of the neutron tool in a liner-RTD-grout assembly identical to that used in the boreholes were conducted by Richard Carlson and Dan Neubauer, as described subsequently in this section. Relative change in water content is calculated from the neutron counts using the calibration results.

As mentioned previously, the heating phase of the SHT was from August 23, 1996 to May 28, 1997; the cooling phase was from May 28, 1997 to January 15, 1998.

8.6.1 Measurement Procedures

The following procedure describes the method of collecting neutron data during the SHT. The 3.81-cm diameter probe and a counting time of 16 sec were used. Standard counts, which are the neutron counts when the tool is in the tool holder away from any influence of the rock mass to be measured, were measured and recorded immediately prior to and subsequent to performing measurements. The neutron probe was placed in a borehole at a specific location, and the neutron count was recorded in a scientific notebook as well as electronically in the device memory. Upon completion of the test, data were downloaded to a computer, and the data values were checked

against the hand-recorded values. Data were recorded at depth intervals of 10 cm in each borehole.

Eighteen neutron loggings were conducted during the heating and cooling phases of the SHT. The data were smoothed in both the space and time domains using a three-point smoothing algorithm, which weights the middle point by 0.6 and the two side points by 0.2 each. The smoothing made the data look smoother but did not significantly change the amplitude of the differences in the fraction volume water. All of the in-heat and cool-down data up to December 17, 1997 are presented in this section.

The test of the coupled thermal-hydrological-chemical-mechanical processes focuses on the change in effect of heat on the behavior of the rock mass. Therefore, presented is the difference of the water content in the rock mass between the pre-heat background (measured on August 21, 1996) and that on the dates of measurement listed on the figures. The heaters were turned on at 1:30 p.m. on August 26, 1996. The heater was turned off on May 28, 1997, which was 275 days after the heater was energized. Two neutron logs were conducted during the first month of the in-heat and cool-down phases.

8.6.2 Calibration of the Neutron Tool

The neutron measurement boreholes at the SHT are lined with Teflon™ tubing, and the annulus is sealed with grout. The liner inside diameter is 4.04 cm to just past the 3.81 cm tool, and the liner has a 0.381-cm thick wall. The boreholes were drilled at 7.62 cm to provide space for RTD wires to measure temperature in the same borehole. The 1.41-cm annulus of water-rich grout was expected to affect the response of the probe, thus a special calibration for this geometry was required.

To calibrate the neutron probe in terms of volume fraction of water, a 7.62-cm walled aluminum tubing was installed along the centerline of each of five 55-gal. drums; each annular space was filled with a mix of sandlike material to achieve a known density and hydrogen content (water content equivalent). Grout was then poured around a piece of the Teflon™ liner inside a slightly undersized piece of the aluminum tubing, so the grout/liner assembly would slide snugly inside the tubes in the drums. Counts were then taken with both the probe and the grout/liner assembly at various heights in each drum to check for homogeneity and edge effects in the vertical direction; long counts were taken in the central regions to improve statistics on the values actually used for calibration. Because RTDs were installed in the annular space between the Teflon™ liner and the borehole wall, the calibration procedures were also repeated in a grout-liner-RTD assembly. To check for neutron loss from the finite-sized drums, additional counts were taken with a 100-lb bag of tabular alumina, one of the mix constituents, placed against the side of the drum; that increased the radius by 15 cm. The raw counts were then adjusted for the loss as described subsequently.

It is clear that the density of the rock will change over the course of the SHT. However, it is not expected that the solid parts of the rock will change appreciably; only the amount of water in the pores will change. Thus, if the calibration is constructed in terms of water and dry density, the density effects can be absorbed into constants. Initial information indicated the porosity at the SHT was approximately 13 percent, and the density was about 2.2 gm/cc. It was decided to build

three drums with dry density 2.2 gm/cc and with 0, 5, and 10 vol percent water (drums a, b, and c in Table 8-10). To control for density variations, two additional drums were built; they had dry density 1.8 gm/cc and 0 and 10 vol percent water (drums d and e in Table 8-10). The weight fraction water was precisely controlled by digital scales. Density, however, was determined (after the mix was vibrated in place) by how high a given weight of mix increased the fill height in the drum. The recipe for the mix was determined by trial and error on small samples, and the entire drum was filled in approximately 12.7 cm lifts of that recipe. For each lift, the mix was vibrated, leveled, and packed, and the fill height was measured to within 0.16 cm. The total fill height was about 81.28 cm; thus, density and volume fraction water are known to about 2 percent of value in each lift and to about 1 percent of value overall.

Table 8-10. Probe Calibration Data

		Drum				
	Drum	a	b	c	d	e
1.	raw count	3358	6453	9078	2512	7774
2.	total density (gm/cc)	2.165	2.195	2.201	1.789	1.839
3.	H_2O (vol. %)	0	0.0486	0.096	0	0.0967
4.	dry density (gm/cc)	2.155	2.1464	2.105	1.789	1.7423
5.	100 lb TA	3414	6622	9227	2575	7955
6.	dcnt/dTA	56	169	149	63	161
7.	dw/d6"	418.7	426.4	427.6	347.5	357.3
8.	loss	234.4	720.7	637.1	219.0	646.6
9.	fraction loss	0.06526	0.10046	0.06558	0.08018	0.07679
10.	fraction loss*density	0.14064	0.22051	0.14434	0.14343	0.14122
11.	count	3580	6872	9665	2712	8376
12.	adj den (gm/cc)	2.146	2.195	2.242	1.789	1.886
13.	adj count	3560	6872	9813	2712	8542

The five drums are represented as a, b, c, d, and e in Table 8-10. The first four rows of the table show the raw counts, the total density in gm/cc, the volume percent water (H_2O), and the dry density in gm/cc obtained for the drums. The fifth row (100lb TA) is the count obtained with the extra 100 lb of material against the side of the drum, and the sixth row (dcnt/dTA) gives the change in count between row 1 and row 5. The seventh row (dw/d6") is the weight of that drum's mix needed to add 6 in. (15 cm) to the drum radius (about the thickness of the 100-lb bag), and the

eighth row (loss) gives the expected count change if that were done; this equals dcnt/dTA times dw/d6" divided by 100. The "loss" is shown in terms of the fraction of the total count in the ninth row. The values in row 9 multiplied by the densities in row 2 are shown in row 10. The values in row 10 are nearly equal, except for drum b which is very different. Eliminating the drum b value and averaging the rest gives a value of 0.1424, which is used to calculate the count on row 11: Count (row 11) = raw count (row 1)•[1 + 0.1424/density (row 2)]. The count in row 11 is the expected count for an infinite drum of that density and water content. To make plots, one needs dry densities that do not change with water content. Appropriate density values are shown on row 12 (adj den); these are calculated using a dry density of 2.1464 gm/cc and the associated water content. The counts in row 13 (adj count) were then calculated by taking into account the effect of density. The effect of density on the count was determined from the raw count (row 1) and density (row 2) data in columns a and d. The "adj count" (row 13) are used to calculate volume water content from measured counts.

There are a number of ways to fit equations to these calibration data. Water values given in this section are generated from count data using the equation for the line through the upper two water-content points for dry density 2.1464 gm/cc. These are the values closest to SHT conditions. Further calibration work is planned to better define the linearity of the probe response, especially in the region above 10 percent water where one currently must extrapolate.

8.6.3 Data and Discussion

All the moisture content data determined by neutron logging is included in this section. The fraction volume water calculated from the neutron counts at every 10 cm in each borehole is presented in this section. The fraction volume water content as a function of time at some locations in each borehole is also presented. The neutron results are presented as the difference in water content between the in-heat measurements, which were conducted after the heater was energized on August 26, 1996, and the pre-heat background data, which were obtained on August 21, 1996. Therefore, in the following figures, the positive difference fraction volume water means gaining moisture content, and negative difference fraction volume water means drying. The fraction volume water results depicted in the following figures are presented on the same scale so that comparisons can be easily made. Saturation level in the rock mass can be calculated by dividing the fraction volume water by the fraction porosity of the rock mass. For example, if the porosity of the rock is 0.1, a difference fraction volume water of 0.01 equals a change of 10 percent in saturation level.

Figure 8-47 through Figure 8-55 show the difference fraction volume water in borehole 15 as a function of depth from the collar on various dates of in-heat and cool-down phase measurements. Figure 8-56 shows the water content in this borehole at various depths from collar as a function of time. The 0 day in Figure 8-56 is the date the heater was turned on. Borehole 15 is above the heater and has an inclination of about 17 degrees (CRWMS M&O 1997b, Table 3-1). The shortest distance between the borehole and the heater is about 2.07 m, at approximately 5.75 m from the collar of the borehole. The peak temperature in this borehole before the heater was de-energized was approximately 62°C. A slight decrease in fraction volume water content began to develop at the closest point between the heater and the borehole in October 1996. This decrease in the water content reached approximately 0.004 on May 21, 1997. If one assumes a porosity of 0.13

(CRWMS M&O 1997d, Table 5-3), the maximum saturation level decrease was about 3 percent. A similar decrease in the moisture content was also observed at about 1.5 m from the collar of the borehole. During the cooling phase, the neutron results show a slight rewetting, especially at the closest point between the heater and the borehole, as shown by Figure 8-52 through Figure 8-56.

The neutron logging results in borehole 17 as a function of depth from the collar on various dates of the in-heat and cool-down phase measurements are shown in Figure 8-57 through Figure 8-65. Figure 8-66 shows the water content in this borehole at various depths from collar as a function of time. The 0 day in Figure 8-66 is the day the heater was turned on. Borehole 17 is below the heater and has a decline angle of about 7 degrees (CRWMS M&O 1997b, Table 3-1). The shortest distance between the heater and this borehole is about 1.2 m, at approximately 6.48 m from the collar of the borehole. The peak temperature in this borehole before the heater was turned off was approximately 90°C. A well-defined trend of drying was observed on November 26, 1996, at just below the closest point to the heater. The maximum decrease in the fraction volume water content in this borehole was approximately 0.010, which equals a decrease in saturation level of about 8 percent, again assuming a porosity of 0.13. This region of decrease in the water content later extended to the bottom of the borehole. The width of the drying region in this borehole is greater than that in other boreholes. An increase in the water content was also observed near the collar of the borehole. The amplitude of that increase in the water content was approximately 0.01. The abnormally low fraction volume water on January 16, 1997, at about 5.5 m from the collar (Figure 8-59) is probably due to a measurement error, not to the water content in the rock. Figures 8-62 to 8-66 show that no change in the moisture content was observed during the cool-down phase, except at 4.46 m from the collar, where the decrease in the water content was slightly recovered after the cool-down phase started (Figure 8-66).

Figures 8-67 through 8-75 show the difference fraction volume water content in borehole 22 as a function of depth from the collar on various dates of the in-heat and cool-down phase measurements. Figure 8-76 shows the water content in this borehole at various depths from collar as a function of time. The 0 day in Figure 8-76 is the day the heater was turned on. Borehole 22 is almost horizontal and is approximately 0.65 m below the heater horizon. The end of this borehole is about 1.56 m from the heater (CRWMS M&O 1997b, Table 3-1). The peak temperature in this borehole before the heater was turned off was approximately 74°C. A slight drying region near the bottom of the borehole was observed near the end of the heating phase (Figure 8-71). The decrease in the fraction volume water content in that region was approximately 0.006, slightly greater than that in borehole 15. The cause of the two single-point anomalies on September 6, 1996 (Figure 8-67) was not clear, but they seemed to be isolated events and, therefore, not related to the thermal-hydrological conditions in the rock.

Again, Figures 8-74 through 8-76 show some changes in the moisture content during the cool-down phase. The cause of the spike at about 1.2 m depth from the collar on June 24, 1997, and July 23, 1997 (Figure 8-72 and Figure 8-73) is not clear. Because it is a localized phenomenon, it probably has no significant implication on the moisture distribution in the rock mass. Figure 8-75 and Figure 8-76 show that, during the last three measurements, the outer half (the portion closest to the collar) of the borehole showed rewetting, but the inner half showed further drying. The cause for these changes is still not clear. Because the SHT was terminated shortly after the December 1997 measurements, it is difficult to determine its cause.

The difference fraction volume water content in borehole 23 as a function of depth from the collar on various dates during the heating and cool-down phases are shown in Figure 8-77 through Figure 8-85. Figure 8-86 shows the water content in this borehole at various depths from the collar as a function of time. The 0 day in Figure 8-86 is the day the heater was turned on. Borehole 23 reaches the upper left side of the heater with an incline angle of about 7.5 degrees. The end of this borehole is approximately 1.31 m from the heater (CRWMS M&O 1997b, Table 3-1). The peak temperature in this borehole was approximately 88°C. A drying region near the bottom of this borehole began to develop about two months into the heating phase. The maximum decrease in the fraction volume water content in this borehole was approximately 0.016, which equals about 13 percent in saturation level for a porosity of 0.13. The spike at 1.2 m from the collar on May 21, 1997 (Figure 8-81) is an isolated occurrence and probably has no significant implication on the moisture distribution in the rock mass. However, the region near the collar (at about 2 m from the collar) showed a slight increase in water content during the heating phase. Figures 8-82 through 8-86 show no significant changes in the water content during the cool-down phase (May 28, 1997 through February 28, 1998), except in the region deeper than 4.7 m, where rewetting has been observed (Figure 8-86).

8.6.4 Other Observations

Vapor condensation was observed in boreholes 22 and 23 during the later part of the heating phase (April and May 1997). The inner surfaces of the liners in those boreholes were wiped dry before each logging. Some condensed water was collected from the liner of borehole 23. Chemical analyses on the water samples are being conducted. During the first month of the cool-down phase, vapor condensation was still observed in boreholes 22 and 23, but no condensed water was in borehole 23 to be collected. Later, after the third month of the cooling phase, no condensation was observed in boreholes 22 and 23. During both the heating and cool-down phases, no vapor condensation was observed in boreholes 15 and 17.

8.6.5 Summary

Neutron logging in the SHT region observed changes in the moisture content in the heated rock mass. The degree of drying seemed in good correlation with the temperatures in the rock. The decreases of the water content in the drying regions were small because the neutron logging boreholes are not close to the heater. The results indicate that the drying seems to be more widespread in the vicinity of the heater than in other regions. Rewetting was observed at a few localized regions during the cooling phase. The amplitude of the rewetting was small.

8.7 THERMAL-HYDROLOGICAL ANALYSIS OF THE SHT BY TOUGH CODE

The following investigations were documented in accordance with LBNL procedure YMP-LBNL-QIP.SII1.0 (c), *Scientific Investigation*.

Thermal-hydrological analysis of the SHT was carried out by both the TOUGH and NUFT codes. An explanation of why the analysis was performed by both codes can be found in the introductory material of Section 5.

The numerical model used in this report is based on the 3D predictive model of the SHT developed by LBNL in 1996 (Birkholzer and Tsang 1996). Since then, some improvements and refinements have been made to the predictive model to better represent the actual test conditions (Tsang and Birkholzer 1997). Also, a few parameter adjustments were made, based on more recent results from site characterization measurements. The refined numerical model represents the best understanding to date of the SHT; it describes the SHT realistically with respect to test configuration, rock properties, initial and boundary conditions, etc. The predicted results based on

this refined model compare favorably with measured data from the SHT, thus adding confidence in the understanding of the complex processes involved with the heating of unsaturated fractured tuff, and in the ability to predict the performance of the potential waste repository.

8.7.1 Thermal-Hydrology in the SHT and Model Conceptualization

8.7.1.1 Pre-Heat Conditions in the SHT Block

An extensive pre-heating characterization program was carried out to obtain site-specific thermal, mechanical, and hydrological rock properties (see Sections 8.1 through 8.3). These site-specific data include laboratory measurements of hydrological properties such as grain density, matrix porosity, and liquid saturation; and thermal parameters such as thermal conductivity, heat capacity, and thermal expansion coefficients. In addition to these site-specific data, numerous laboratory measurements of matrix properties are also available from borehole cores taken from the same geological unit as the SHT. A detailed field characterization by means of air permeability tests was conducted in the SHT block to determine the in situ fracture permeability prior to turning on the heater. Additional fracture information was available from fracture mapping and borehole video logs.

The welded tuff in the SHT block has very low matrix permeability. However, the rock is intensely fractured, with the fracture permeability several orders of magnitude higher than the matrix permeability. The interference pressure data from air-injection tests indicate that the fractures are well connected, because pressure response to injection is obtained in most monitoring boreholes. This is consistent with the borehole videos, showing that all the boreholes are intersected by numerous fractures. A fracture zone with particularly high permeability was identified in the back of the SHT block, connecting the end of the heater borehole with some of the monitoring boreholes.

Due to the low precipitation at Yucca Mountain, the percolation flux in the unsaturated flow regime is very small. At ambient state, the fractures are essentially dry and not very conductive. In contrast, strong capillary forces hold a significant amount of water in the matrix pores, with a liquid saturation of about 80 percent to 99 percent at the SHT location (Tsang et al. 1996, p. 23, Table 3; Wang and Suarez-Rivera 1997, pp. 17and 18, Tables 3 and 4). This water is hardly mobile at ambient state, but can be mobilized when the rock mass is heated above boiling. This can give rise to significant heat-induced moisture redistribution processes in the SHT block.

8.7.1.2 Potential Thermal-Hydrological Processes in the SHT

Emplacement of a heat source into the unsaturated fractured tuff at Yucca Mountain can initiate very complex thermal-hydrological processes, which depend on the hydrological properties of the fractures and the rock matrix. Most of the key processes potentially involved are reviewed in Figure 8-87. As the formation temperatures rise to 100°C around the heater, matrix porewater boils and vaporizes. Most of the vapor generated moves into the fractures, where it becomes highly mobile, and is driven by the gas pressure gradient away from the heat source. When the vapor encounters cooler rock, it condenses at the fracture walls, and the local fracture saturation builds up. Part of the condensate may then imbibe into the matrix, where it is subject to a very

strong capillary gradient towards the heat source, giving rise to a reflux of liquid to the dry-out areas. If matrix imbibition is relatively slow, the condensate may also remain in the fractures and eventually become mobile. Because capillary forces are relatively weak in the fractures, a substantial amount of liquid may drain from the heater by gravity. Occurrence of gravity drainage depends on the strength of vaporization-condensation and fracture-matrix interaction. The stronger the vapor flux away from the heater and the condensate reflux towards the heater, the more obvious will be a "heat pipe" signature in the temperature data, namely, a small temperature gradient at the nominal boiling point. In fact, certain matrix and fracture hydrological properties may give rise to such strong condensate reflux that a stable heat-pipe extends all the way to the heater, preventing the drying of rock and keeping the temperatures near or below 100°C.

The results of vaporization, drying, condensation and rewetting processes in the SHT are reflected in the spatial variation and temporal evolution of the liquid saturation in the rock mass. Changes in the rock mass moisture content have been evaluated by active testing such as neutron logging, electrical resistivity tomography, cross-hole radar tomography, and interference air permeability tests (Sections 8.1 through 8.3). In addition, passive monitoring was performed with a multitude of sensors to measure the temperature, humidity, gas pressure, mechanical displacement, and stresses of the rock mass. Both the passive monitoring and active testing data are considered in the analysis and interpretation of SHT (see Subsection 8.7.3).

8.7.1.3 Conceptual Model of the SHT

A model for the SHT must be capable of representing all the important thermal-hydrological processes taking place in the unsaturated fractured rock. The 3-D modeling study uses the numerical simulator TOUGH2, Version 1.3, Module EOS4 V 1.0 (TBD-412) (Pruess 1991; Pruess, Simmons et al. 1996; Wu et al. 1996), which simulates multi-dimensional coupled transport of water, vapor, air, and heat in heterogeneous porous and fractured media. TOUGH2 accounts for the movement of gaseous and liquid phases (under pressure, viscous, and gravity forces according to Darcy's Law, with interference between the phases represented by relative permeability functions); transport of latent and sensible heat; and phase transitions between liquid and vapor. Mass- and energy-balance equations are written in integral form for an irregular flow domain in one-, two-, or three-dimensions. The physical processes of capillary suction and adsorption in the liquid phase, binary diffusion in the gas phase, thermal conduction, and the effect of vapor pressure lowering due to capillary and phase adsorption effects are all accounted for in the model.

A key issue in simulating flow processes in fractured tuffs at Yucca Mountain is the numerical representation of fractures and matrix, and the interaction between them, under multi-phase, nonisothermal conditions. Available concepts representing fracture-matrix systems with numerical models include (1) an explicit discrete fracture and matrix model, (2) the equivalent continuum model (ECM), (3) the dual-permeability model (DKM), and (4) the more general multiple interacting continua (MINC) method. One question arising from the choice of model concept is whether the fractured system in the SHT block may be considered as a continuum at the scale of interest; a second question deals with the complexity of describing flow of fluid, gas, and heat between fractures and matrix. Because the combined data from fracture mapping, borehole video logs, and air-injection interference tests indicate that the numerous fractures in the SHT block form a well-connected network, it seems appropriate to represent the SHT block with

a continuum approach rather than a discrete model. (Furthermore, a discrete-fracture modeling approach would hardly be feasible because of the computational intensity involved and the lack of detailed data describing the discrete fractures.)

The continuum model used for the SHT block must be capable of accurately describing the heat-induced flow processes in fractures and matrix (e.g., the rock must be conceptualized as composed of the matrix continuum with very low permeability, and the fracture continuum with permeability orders of magnitude higher). Also, the model must account for the significant differences in capillarity and storativity in fractures and matrix. All the above-mentioned continuum models—ECM, DKM, and MINC—capture the different characteristics of unsaturated flow in fractures and matrix; however, they differ in the way the fracture-matrix interaction is treated (Figure 8-88). The ECM is the most simplified method; it assumes that a local thermaldynamic equilibrium is maintained between the fractures and the matrix at all times, thus implying infinitely fast mass and energy exchange between fractures and matrix (Pruess, Wang et al. 1990). As a result, gravity-driven liquid flow in the fractures tends to be underestimated, because heat-generated vapor condensing on the fracture walls is readily imbibed into the matrix pores. The DKM conceptualizes the fractured rock as two interacting continua, one representing the matrix, the other representing the fractures, with the fracture-matrix exchange explicitly calculated from the local pressure and temperature difference. Thus, the DKM can account for different transient behavior in fractures and matrix. However, it may sometimes overestimate gravity-driven liquid flow in the fractures, as the rate of condensate imbibing into the matrix can be underestimated for early times when steep gradients occur at the fracture-matrix interfaces. Such steep gradients cannot be appropriately modeled with the DKM, because a linear pressure/temperature distribution is assumed within the matrix blocks. The more rigorous MINC method solves this steep-gradient problem by subdividing the matrix continuum into a number of nested continua defined at different distances from the surface (Pruess and Narasimhan 1985). This concept allows for representing a nonlinear distribution of pressure or temperature in the matrix; therefore, the MINC method should be best suited for simulating a localized intense perturbation such as that encountered in the SHT. In terms of computational efficiency, however, the MINC method is less suitable to a complex 3D model, because it requires definition of multiple additional inner grid elements.

As a good compromise between accuracy and feasibility, the DKM is chosen to be the baseline method in this study. It is assumed that the entire geometric matrix-fracture interface, estimated from fracture mapping along the ESF tunnel walls (Sonnenthal, Ahlers et al. 1997, p. 7-9, Table 7.7), participates in the matrix-fracture coupling. A possible reduction of the matrix-fracture interaction—arising from fracture coating, flow channeling in fractures, and other factors—is not accounted for. For comparison with the DKM simulations, the ECM concept is also investigated in a sensitivity analysis (Subsection 8.7.3.3).

8.7.2 Numerical Model of the SHT

8.7.2.1 Basic Model Assumptions

The thermal-hydrological simulations of the SHT are performed with Version 1.3 Module EOS4 V 1.0 of the Integrated Finite Difference Code TOUGH2 (Pruess 1991; Pruess, Simmons et al.

1996; Wu et al. 1996). The software tracking number of this version of TOUGH2 is 10062-1.3MEOS4V1.0-00, and it is a qualified code. The TOUGH2-EOS4 module is used which simulates the nonisothermal two-phase flow of water and air, and accounts for vapor pressure lowering effects. Fracture and matrix characteristic curves for liquid flow are described by the commonly used van Genuchten model (van Genuchten 1980, p. 893 to 897), while the relative permeability to gas is calculated from the Brooks-Corey formulation. Thermal conductivity is assumed to be a square-root function of liquid saturation, using a measured conductivity value at high saturation ("wet" conductivity) and a measured conductivity value at low saturation ("dry" conductivity) to define the relationship. Binary vapor-air diffusion rather than enhanced vapor diffusion is implemented.

The dual permeability method is applied to account for the combined effect of matrix and fracture flow. All hydrological properties and initial conditions are assumed to be homogeneous, except for the fracture permeability. The simulations use an average permeability value for the major part of the SHT block, but also represent a local high-permeability feature that was identified from air-injection tests and borehole video logs during pre-heat characterization. The majority of the matrix and fracture property values are directly based on laboratory or field measurements, which are referred to as the base-case properties (see Subsection 8.7.2.5). No calibration to measured data from the SHT was performed. The simulation results presented in Subsection 8.7.3.1 and Subsection 8.7.5.2 of this report are obtained using the base-case model setup. In addition, Subsection 8.7.3.3 presents results from a sensitivity study where the conceptual model of fracture-matrix interaction is changed or key hydrological properties of the fractured rock are varied.

The simulation runs cover a 9-month period of heating the rock, and a 12-month period of natural rock cooling, after the heater is turned off. The heater is assumed to operate at a constant 3758 W, which was the average power during the operation of the SHT. A closer look at the time evolution of heater power reveals small fluctuations and a slightly declining trend (Figure 8-89); however, none of these is sufficiently significant to account for in the numerical model.

8.7.2.2 Model Domain

The computational domain for the thermal-hydrological simulations includes the actual test block plus significant rock volumes added in all directions to guarantee a proper definition of boundary conditions (Figures 8-90 and 8-91). The top and bottom boundaries of the model area are 14 m each from the heater axis; they are sufficiently far from the heater that they can safely represent infinity conditions (i.e., constant primary variables). The north and south boundaries extend to the outer wall of the bounding drifts (i.e., the Observation Drift on the north side and the Thermomechanical Alcove Extension on the south side). The distance from the heater centerline to the south boundary is 10.76 m, which is defined by the 6.26-m distance from the heater to the alcove inner wall plus the 4.5-m alcove width. The north boundary is at 11.59 m, defined by the 6.59-m distance to the Observation Drift wall and the 5.0-m drift width. The eastern boundary extends to the outer wall of the Thermomechanical Alcove; the western boundary is 17 m from the inner wall of the Thermomechanical Alcove, sufficiently far from the heater to represent a no-flow boundary for fluid, gas and heat.

8.7.2.3 Computational Grid Design

Grid generation is an important part of developing a complex 3D model. The aim of grid generation is to achieve a proper balance between desired numerical accuracy and computational effort, both of which are controlled by the total number of gridblocks. In the SHT, the grid must be compatible with sharp gradients of temperature, saturation, and pressure that may occur at different distances from the heat source as time progresses. At the same time, geological features must be captured, and the special geometry of the test must be realistically represented.

Several automatic grid-generation modules have been developed to allow for accurate and efficient generation of 2D and 3D grids. In a first step, a 2D vertical mesh is designed within the local XZ-plane (i.e., orthogonal to the heater centerline). Local mesh refinement is particularly important in this plane, because most of the heat produced is released transverse to the heater axis. In a second step, the complete 3D SHT grid is created by appropriately extending several vertical 2D planes into the third dimension and merging them.

Figure 8-92 shows an XZ-cross section of the grid. The origin of the coordinate system is at the collar of the heater borehole. Fine gridding and radial symmetry is maintained around the heater borehole up to a radius of 2.9 m, at which distance the grid is converted gradually to cartesian in order to better represent the boundaries of the drift and alcove walls. The size of the gridblocks increases with distance to minimize the number of computational elements. The radial increments start as small as 2.2 cm at the heater borehole and increase to 50 cm at a distance of 5 m. This discretization is very fine close to the heat source in order to guarantee a proper representation of the physical processes, but rather coarse away from the heater in order to avoid excessive computational load. The Observation Drift and the Thermomechanical Alcove Extension are cut out from the model area, and their walls are treated as inner model boundaries.

Nineteen 2D element planes are merged in the Y-direction to generate the entire 3D mesh. (The Y-direction extends along the heater axis, perpendicular to the XZ-cross section shown above.) Figure 8-93 shows a horizontal cross section (i.e., XY-plane) of the grid at Z = 0.0. Starting from the Thermomechanical Alcove wall at Y = -5.5 m, the first two element planes represent the rock volume above and below the alcove (-5.5 m < Y < 0.0 m). The next five planes represent the 2-m standoff between the west wall and the heater (0.0 m < Y < 2.0 m). The following six planes represent the 5-m heater length (2.0 m < Y < 7.0 m). The last six planes extend from the heater to a no-flow boundary at Y = 17.0 m. The entire 3D grid consists of about 30,000 gridblocks and more than 100,000 connections between them. Figure 8-93 also indicates the location of the fractured zone with higher permeability, which had been identified in the pre-heat characterization effort. The 40° strike azimuth feature is represented by extending the fracture zone over three different element layers in the XY-plane. In the Z-direction, the high-permeability zone extends from -2.8 m to 1.2 m. (Note that the displayed grid in Figure 8-93 does not show the actual interfaces between gridblocks in the finite difference discretization. The post-processing software automatically designs a mesh by connecting the center nodes of each finite difference grid. These post-processed meshes are depicted here.)

About 30 boreholes were drilled into the SHT block for passive monitoring and active testing. Several boreholes, in particular those specifically designed for temperature measurements, were

grouted after instrumentation. Others, however, were left open for testing, for example those boreholes designed for displacement measurements. These open boreholes may act as conduits for vapor flux, and may possibly allow for significant gas-driven convective heat flow in axial direction. This phenomenon cannot be accounted for in the model, because boreholes are not explicitly represented in the numerical grid.

8.7.2.4 Boundary and Initial Conditions

The top and the bottom of the model domain are modeled using a constant primary variable boundary condition (i.e., pressure, saturation, and temperature in fractures and matrix are fixed at given values throughout the simulation period). All lateral boundaries are modeled as no-flow boundaries for heat, liquid, and gas. These definitions imply that the outer boundaries of the model domain are not affected by the heat source, which is a valid assumption because they are far enough away from the heater.

All the drifts included in the model domain—Observation Drift, Thermomechanical Alcove, and Thermomechanical Alcove Extension—are modeled by constant pressure, temperature, and saturation conditions, assuming that they are ventilated and the heating of the rock does not affect the parameters in the open drifts. No attempt was made to model the initial drying of the rock adjacent to tunnel walls due to ventilation. The relative humidity of the drifts is fixed so that the open void is in equilibrium with the adjacent rock at initial state. The drift walls are open for liquid and gas to escape from the model domain; however, no liquid or gas can enter the model domain from the alcoves.

The test block is insulated from the alcove walls with a low thermal conductivity material to minimize heat losses from the rock. This insulation is explicitly represented in the model, with a thickness of 15.2 cm, a thermal conductivity of 0.0447 W/(m^2•K), a density of 32 kg/m^3, and a heat capacity of 835 J/(kg•K) (Birkholzer and Tsang 1996, p. 15). Note that in this model the insulation material allows moisture to escape from the test block in the form of both liquid water and vapor. A similar insulation material is used as a backfill in the heater borehole for the 2-m standoff between the borehole collar and the heater element. The floor and the ceiling of the alcoves are not insulated; thus, they represent boundaries with constant primary variables.

Heater power is applied in the model at a constant rate throughout the entire heating period, starting from August 26, 1996, to May 28, 1997. The assumed power of 3758 W is the average for the heating period of 275 days and 2 hours. During the operation of the SHT, anomalous data were occasionally observed when the power to the heater was temporarily interrupted (Figure 8-89). Longer heater down times were observed on day 112 (15.8 hours), day 118 (23.1 hours), day 139 (24.6 hours, and day 202 (13.6 hours). The four long power outages were sufficiently strong as to temporarily influence the temperature data in nearby gages (SNL 1997d, p. 15). Also, there was a slight trend of declining heater power over the 275 days of heating, probably due to the aging of heaters. However, none of the anomalies and trends observed was too severe, so that the constant heater power assumed in the model is a fair approximation.

The heater simulation runs start from a fully equilibrated initial situation in the test block. The initial conditions are a gas pressure of 87.0 kPa, a temperature of 25°C, a matrix liquid saturation

of 0.92, and a fracture liquid saturation of 0.046. No geothermal and gas pressure gradients are assigned because of the small vertical extension of the model. A typical geothermal gradient of 0.02°C/m would only give a temperature difference of 0.56° between the top and the bottom boundary, which is negligibly small compared to the perturbation enforced by the heater. This is similarly true for the potential gas pressure variation between the top and bottom of the model area. Also note that the ventilated alcoves surrounding the test block provide a constant barometric pressure boundary to the rock, so that the natural gas pressure field has already been altered at ambient state.

The initial matrix liquid saturation of 0.92 is the average value for the Tptpmn measured in cores from surface borehole SD9, which is in close proximity to the heater alcove (Flint 1998, p. 50, Table 9). This relatively high saturation is consistent with the laboratory data from grab samples obtained directly from the SHT block (Tsang et al. 1996, p. 23, Table 3; Wang and Suarez-Rivera 1997, pp. 17and 18, Tables 3 and 4; also Section 4 of this report, Tables 4-1 and 4-2) where values ranging from 0.805 to 0.99 have been reported. The chosen fracture liquid saturation is not a measured value; it is derived from the assumption of thermodynamic equilibrium between the matrix and fracture continua at initial state. Applying the van Genuchten characteristic relationships and using the chosen characteristic properties for matrix and fractures (see Subsection 8.7.2.5), the matrix saturation of 0.92 results in a fracture saturation of 0.046 at equilibrated capillary pressure.

The initial values of gas pressure, saturation and temperature are also used to define the constant primary variable boundaries at the top/bottom of the model domain, and at the alcove walls. In prescribing saturation at the upper boundary, a gravity-driven percolation flux entering the model area from above is implicitly defined. For the saturation values chosen to represent the initial state—0.92 in the matrix, 0.046 in the fractures—the percolation flux is quite small, on the order of 1 mm/yr or less, because the fractures are almost dry and nonconductive. This is somewhat smaller than current estimates of percolation at Yucca Mountain, which range from about 1 mm/yr up to 10 mm/yr. Sensitivity studies indicate, however, that the thermal-hydrological situation in the SHT is only slightly affected by the actual amount of percolation, because the heat-induced fluxes are much larger than any reasonable estimate of percolation flux at Yucca Mountain.

8.7.2.5 Model Parameters

The hydrological and thermal input parameters used in the numerical simulations for the SHT are based mainly on laboratory or field measurements. All values are qualified if not otherwise indicated. Table 8-11 lists all the hydrological and thermal input values used for the SHT analyses. Table 8-12 gives the sources for these values and lists the QA status of the data.

Table 8-11. Hydrological and Thermal Input Values

Parameter	Value	Comments
Matrix Porosity	0.11	Tptpmn-average
Matrix Permeability	4.0×10^{-18} m^2	Tptpmn-average
Matrix van Genuchten parameter α	6.4×10^{-7} Pa^{-1}	Tptpmn-average
Matrix van Genuchten parameter	1.47	Tptpmn-average

Table 8-11. Hydrological and Thermal Input Values

Matrix Residual Liquid Saturation	0.18	Tptpmn-average
Matrix Grain Density	2530.0 kg/m^3	Tptpmn-average
Initial Matrix Liquid Saturation	0.92	SHT lab measurements, SD9 Tptpmn-average
Fracture Porosity	0.000124	UZ site scale model
Fracture Permeability (low permeability background)	5.85 x 10^{-14} m^2	SHT air-injection tests
Fracture Permeability (high-permeability feature)	5.2 x 10^{-12} m^2	SHT air-injection tests
Fracture van Genuchten α	1.0 x 10^{-3} Pa^{-1}	UZ site scale model
Fracture van Genuchten β	1.47	UZ site scale model
Fracture Residual Liquid Saturation	0.01	UZ site scale model
Initial Fracture Saturation	0.046	Equilibrium with matrix
Fracture Frequency	1.88 1/m	UZ site scale model
Rock Mass Thermal Conductivity $C(S_l) = C_{dry} + (C_{wet} - C_{dry})\sqrt{S_l}$	C_{dry} = 1.67 W/(m•K) C_{wet} = 2.0 W/(m•K)	Alcove 5 lab measurements*
Rock Mass Heat Capacity	953.0 J/(kg•K)	Tptpmn-average
Vapor Diffusion Coefficient D^o_{va} Temperature dependence θ Tortuosity Factor	2.14 x 10^{-5} m^2/s 2.334 0.2	Standard values after Pruess and Tsang (1994, p. 10)

*The analyses performed at SNL give a "dry" conductivity of 1.71 W/(m•K) and a "wet" conductivity of 2.14 W/(m•K) (SNL 1998, p. 16, Table 5). Due to a change in calibration procedure, these values are slightly higher than earlier estimates, approximately by 0.1 W/(m•K). The LBNL model, reported here, uses earlier estimates (i.e., a "dry" conductivity of 1.67 W/(m•K) and a "wet" conductivity of 2.0 W/(m•K)).

Table 8-12. Data Sources

Data Type	DTN/AN
Core measurements from surface boreholes, in Flint (1998); matrix porosity, permeability, van Genuchten properties, grain density, initial saturation	TIC: 236515
Core measurements from SHT block, in Tsang et al. 1996; matrix initial saturation, porosity, grain density	DTN: LB960500834244.001
Core measurements from SHT block, in Wang and Suarez-Riviera 1997; matrix initial saturation, porosity, grain density	DTN: LB970500123142.003
Pre-heat air-injection tests for the SHT block, in Tsang et al. 1996; fracture permeability	DTN: LB960500834244.001
Calibrated properties for UZ site scale model layers, in Bodvarsson et al. 1997; fracture van Genuchten properties	DTN: LB970601233129.001
Analysis of ESF fracture mapping data, in Sonnenthal, Ahlers et al. 1997; fracture van Genuchten, fracture frequency and spacing, porosity	DTN: LB970601233129.001
Core measurements on Alcove 5 rock specimens, in SNL 1998; thermal conductivity	ACC: MOL.19971125.0845
Core measurements from surface boreholes, in Brodsky et al. 1997; heat capacity	DTN: SNL01A05059301.005
Vapor diffusion parameters, in Pruess and Tsang 1994; vapor diffusion coefficient, factor for temperature dependence	ACC: NNA.19940427.0248

For the base-case property set, site-specific measurements from the SHT block are used whenever possible; otherwise, data measured at other locations in the Tptpmn unit are incorporated. In some cases, properties are estimated from the current calibration efforts for the unsaturated zone site-scale model (Bodvarsson et al. 1997, Chapter 6). With the exception of fracture permeability, all model parameters are assumed to be homogeneous. Note that most of the model parameters remain unchanged from the predictive modeling effort performed in 1996 (Birkholzer and Tsang 1996, p. 12, Table 3.3-1). No calibration to measured data from the SHT was performed; no parameter adjustment of measured property values was needed to arrive at a good agreement between measured and predicted temperature data. In addition to the base-case parameter set, sensitivity studies were performed by perturbing certain key parameters of the fractured rock.

Here the model parameters for the base-case property set are discussed item by item. Most matrix properties are measured on core samples from surface-based boreholes, representing an average over the different locations in the Tptpmn unit. The matrix grain density of 2530 kg/m^3 is the particle density given in Flint (1998, p. 44, Table 7). This value is consistent with laboratory measurements of cores from the SHT area (Tsang et al. 1996, p. 23, Table 3; Wang and Suarez-Rivera 1997, pp. 17and 18, Tables 3 and 4; also Section 4 of this report, Tables 4-1 and 4-2). The average matrix porosity of all core measurements in the Tptpmn is reported to be 0.11 (Flint 1998, p. 44, Table 7). Permeability data are available for surface boreholes SD9 and UZ16. The geometric mean of saturated hydraulic conductivity of Tptpmn is given in Flint (1998, p. 44, Table 7) as 4.0×10^{-11} m/s. This is equivalent to matrix permeability of 4.0×10^{-18} m^2. Matrix van Genuchten parameters have been measured in three samples from surface borehole UZ16. The values given in Flint (1998, p. 45, Table 8) are 6.4×10^{-7} Pa^{-1} for α, 1.47 for β, and 0.18

for residual liquid saturation. The measured residual saturation value is used only for the relative permeability function. In the capillary pressure function, a zero residual saturation is applied to avoid the extremely strong increase of capillary pressure at small saturations levels.

Fracture porosity and frequency were estimated by Sonnenthal, Ahlers et al. (1997, pp. 7-9, 7-19 and 7-20) based on ESF fracture mapping. A fracture porosity of 0.000124 and a fracture frequency of 1.88 1/m is used in the LBNL simulation. The fracture permeability values are estimated from air-injection tests performed in the SHT block prior to heating, as previously discussed in Subsection 8.7.1.3. The median of all measured air permeability values (i.e., 5.8×10^{-14} m^2) is assigned to most of the SHT block (Tsang et al. 1996, p. 11, Table 1). In addition, a zone of higher permeability (i.e., 5.2×10^{-12} m^2) has been accounted for at the southeast end of the heater element. No measurements of the van Genuchten properties of fractures are available. The values used in this study are based on average values for the Tptpmn estimated from calibration efforts for the Yucca Mountain Site Scale Model (Bodvarsson et al. 1997, pp. 6.32 to 6-34, A-22 to A-30). Van Genuchten α-values calibrated with the UZ site scale model typically range from 10^{-5} Pa^{-1} to 10^{-3} Pa^{-1}. This model, uses a value at the high end of this range (i.e., $\alpha = 10^{-3}$ Pa^{-1}) which represents a rather small capillarity in the fractures. This value is consistent with estimates derived in Sonnenthal, Ahlers et al. (1997, p. 7-16, Table 7.13). The van Genuchten β is chosen to be 1.47, a value similar to the respective matrix parameter. Residual liquid saturation for the fracture continuum is chosen to be 0.01 in the relative permeability function, and zero in the capillary pressure function. Obviously, as the characteristic properties of the fractures have not been measured, the uncertainty associated with these parameters is significant. Therefore, analysis of the sensitivity of the predicted temperatures to some key hydrological properties, including van Genuchten properties for the fractures is provided in Subsection 8.7.3.3.

The thermal properties required to model the thermal-hydrological situation in the SHT are thermal conductivity (which may be temperature and saturation dependent) and heat capacity. Thermal conductivity is assumed to be a square-root function of liquid saturation, using two coefficients, a thermal conductivity value at low saturation ("dry") and at high saturation ("wet"). Site-specific conductivity measurements are available from six rock specimens taken from the thermal test domain in Alcove 5. Recent analyses of these data give a dry conductivity of 1.71 W/(m•K) and a wet conductivity of 2.14 W/(m•K) (SNL 1998, p. 16, Table 5). Due to a change in calibration procedure, however, these values are slightly higher than earlier estimates, approximately by 0.1 W/(m•K). The model uses earlier reported values (i.e., a dry conductivity of 1.67 W/(m•K) and a wet conductivity of 2.0 W/(m•K)). These values are identical to the Tptpmn-properties chosen for the DST model (Birkholzer and Tsang 1997, p. 20, Table 4.3-2). Note that the predictive model for the SHT (Birkholzer and Tsang 1996, p. 12, Table 3.3-1) did not distinguish between dry and wet thermal conductivity values; a constant 1.67 W/(m•K) was applied to all saturation conditions (Sobolik, Francis, and Pott 1996, p. 17, Table 5). This approximation, however, proved to be unsatisfactory. The heat capacity of 953.0/(kg•K) was calculated based on experimentally determined values of thermal capacitance, given in Brodsky et al. (1997, p. 48, Table 4-8) for different temperature ranges. The heat capacity of 953.0 J/(kg•K) used in the SHT model is very similar to the heat capacity of 948.0 J/(kg•K), calculated and reported in two memoranda (Francis 1997; Ho and Francis 1997). Those calculations used

slightly different assumptions for the sample liquid saturation when deriving heat capacity from the experimentally determined thermal capacitance values.

Reasonable numbers for the vapor diffusion parameters are $D^{o}_{\tau,g} = 2.14 \times 10^{-5}$ m^2/s and $\theta = 2.334$, after Pruess and Tsang (1994, p. 10, Table 1). A reasonable number for the tortuosity factor of the path followed during the gas diffusion process is $\tau = 0.2$. These parameters are non-qualified, as no measurements exist; however, the effect of binary vapor-air diffusion is very small compared to other thermal-hydrological processes.

Note that the parameter distribution is assumed to be isotropic. Rock properties are assigned for all boreholes except for the heater borehole, thus making the implicit assumption that wiring, grouting, and instrumentation in the test block do not affect the thermal-hydrological behavior. Possible chemical or mechanical alterations in response to the heating are not included in this study. However, thermal-mechanical coupled processes have been considered and analyzed by other SHT Thermal Testing Team members (Sobolik, Francis, and Pott 1996; Finley 1997). Chemical processes are studied and discussed in detail in Section 10 of this report.

8.7.3 Simulation Results and Comparison to Measured Data

Introducing a heat source into the unsaturated fractured tuff at Yucca Mountain may give rise to strong two-phase flow effects, typically characterized by the following:

1. drying of the rock and vaporization of porewater close to the heater;
2. vapor transport away from the heated area due to gas pressure build-up;
3. condensation of the vapor in cooler regions outside of the drying zone;
4. reflux of condensate to the vicinity of the heating due to capillary suction; and
5. drainage of water away from the heated area due to gravity.

These processes are reflected in the spatial variation and temporal evolution of the liquid saturation in the rock mass. They also contribute to heat transfer in the near-field environment, as heat-induced gas and liquid fluxes may give rise to significant convective heat transport. For example, strong vapor-liquid counterflow may be reflected in a distinct "heat pipe" temperature signal (i.e., the temperature values remain at the nominal boiling point for some time before they continue to increase). The relative importance of convective heat transfer compared to heat conduction is related to the respective hydrological properties of the rock, as well as to the temporal and spatial scale of the heat perturbation. Careful analysis of SHT data from both active tests and passive monitoring can help constrain hydrological properties of the fractured rock mass, and can serve to evaluate the applicability of different conceptual modeling approaches.

This section presents both a qualitative and quantitative discussion of SHT model results in comparison to field measurements from the heating and cooling phase of SHT. The predicted data are calculated with the base-case model described in Section 8.7.2. The results described below are obtained using a three-dimensional representation of the SHT, applying the dual-continuum model for fracture-matrix interaction, and assigning the rock properties given in Subsection 8.7.2.5. Subsection 8.7.3.1 presents contour plots and profiles of predicted temperature, fracture, and matrix saturation in the rock at different stages during the test. This is

intended to provide a basic understanding of the important processes related to the heating of the formation. The predicted results in a qualitative comparison with active and passive testing results. Subsection 8.7.3.2 provides a more detailed quantitative comparison of model results to measured data, specifically the temperature measurements in several instrumented boreholes. Statistical measures are applied to evaluate the "goodness-of-fit" between predicted and measured temperature. The impact of alternative fracture-matrix interaction concepts and different hydrological property sets is discussed in Subsection 8.7.3.3.

8.7.3.1 Qualitative Discussion of Simulation Results

Predicted temperature results for the SHT are presented in Figures 8-94 and 8-95 at 3 months and 9 months from the onset of heating, respectively. The figures include two graphs. The first graph is a contour plot on the YZ–plane showing a vertical cross section oriented orthogonal to the heater axis in the center of the 5-m-long heater element (i.e., at Y = 4.5 m in the plane of boreholes 16 and 18). The locations of boreholes 16 and 18, used for active and passive hydrological testing, are also indicated. The symbols along the borehole axis mark the positions of sensors for temperature, pressure, and relative humidity measurements. The second graph describes the temperature profile along the vertical axis at X = 0.0 m. The z-axes of both graphs are identical. All temperature values correspond to the matrix continuum; the fracture temperature distribution is almost identical.

Figures 8-94 and 8-95 show that rock temperature close to the heat source increases very rapidly after turning on the heat, resulting in strong localized perturbations. The maximum temperature has already reached about 275°C after 3 months of heating. At later stages, the temperature buildup is slower, reaching the maximum of about 300°C at the end of the nine-month heating period. The temperature distribution shows an almost perfect radial symmetry around the heater centerline, indicating that the heat transport is conduction-dominated. The 50°C-isotherm is at a radial distance of about 2.0 m at 3 months of heating, and moves out to about 3.3 m at 9 months from the onset of heating. The zone of temperature above the nominal boiling point, however, is much smaller, extending to approximately 1.2 m from the heater at the end of the heating period. A sufficiently large zone of boiling is an important feature of the test, because it gives rise to significant moisture redistribution. The very good match between the predicted and measured temperature data in the SHT block is discussed in Subsection 8.7.3.2.

Figures 8-96 through 8-99 show predicted liquid saturation contours after 3 months and 9 months of heating in the fracture and matrix continuum, at the same vertical cross section. Vertical saturation profiles are also presented. During heating, moisture is driven by the gas pressure gradient away from the boiling zone in the form of vapor, mainly through the fractures because of the low matrix conductivity. As a result, the rock close to the heater is dry, with saturation values below residual. At the end of the heating period, drying has extended to a radial distance of about 1.2 m from the heater. In cooler regions, the vapor condenses at the fracture walls, resulting in an increase of liquid saturation in both fractures and matrix. Fracture saturation increases to values of about 0.6 at 3 months of heating, from an initial saturation of only 0.046. Strong downward drainage flux is noticeable below the heater, indicating that the capillary pressure gradient in the fractures is overcome by gravity. In the matrix, the predicted saturation build-up in the condensation zone is less apparent and less extended than in the fractures. Apparently, the vapor

condenses and flows in the fractures faster than it is drawn into the matrix, so that only a small fraction of condensate imbibes into the rock pores. This leads to a condition of disequilibrium between fractures and matrix. The rock matrix is drier above the heater than below, not because of gravity-driven liquid flux in the matrix, but because of the downward drainage in the fractures and subsequent imbibition into the matrix pores. The thermally induced liquid fluxes are orders of magnitude higher than the ambient percolation flux at Yucca Mountain. Comparison of the 3-month with the 9-month results indicates that most of the moisture redistribution occurs during the first months of heating; the heat-driven processes are slower in the later stages of the test.

Figure 8-100 presents the predicted rock temperature after about 1 year into the test (3 months from the onset of the cooling phase). The rock mass has cooled off substantially; the maximum temperature in the test block is slightly above 40°C. Figures 8-101 and 8-102 show the saturation distribution in fractures and matrix after 3 months of the cooling. Because the rock temperature drops below nominal boiling almost immediately after the heating stops, vaporization and condensation processes have disappeared. The strongly dynamic nature of flow during heating becomes less pronounced, and the pressure and saturation gradients tend to equilibrate. This equilibration process is very slow in the matrix so that the moisture redistribution established during heating is still apparent after 3 months of cooling. The dominant mode of fluid movement during cooling is capillary-driven flux in the matrix, mainly directed toward the heater, and slowly rewetting the dry-out region. Gravity drainage in the fractures and matrix imbibition probably occurs only during the early stages of cooling, when fractures and matrix are not in equilibrium.

The redistribution of the moisture content described by the numerical model is consistent with the results of active and passive hydrological testing (see Sections 8.1 and 8.3). Active tests, such as cross-hole radar tomography and air injection, had been conducted prior to and periodically during the SHT. Radar tomography was performed in boreholes 15, 17, 22, 23; air-injection tests were performed in boreholes 16 and 18. All these boreholes are orthogonal to the heater axis and located in the mid-plane of the heater element at approximately Y = 4.5 m. Radar tomography data probes the change in water content in the matrix (which is strongly related to the porosity), while air permeability tests give information about liquid saturation changes in the fractures. Continuous passive hydrological monitoring of pressure and relative humidity was performed throughout the entire test period at four locations in boreholes 16 and 18, respectively.

Cross-hole radar surveys were carried out before the onset of heating, and then after about 5 months, 7 months, and 9 months of heating (Section 8.3). The radar velocity fields produced from tomographic inversion at 5 months show an increase of velocity close to the heater and a decrease about 1 m away from the heater toward the alcove walls. A radar velocity increase is indicative of liquid saturation decrease in the matrix, while velocity decrease the opposite. Thus the survey is consistent with the thermal-hydrological conditions of a drying zone around the heat source and a condensation zone commencing about 1 m away, as obtained by the simulations (Figures 8-96 through 8-99). The tomograms at 7 and 9 months show a further velocity increase near the heater compared to the 5-month results, but no significant changes in the areas beyond the 1-m radius. This indicates a more extended drying zone, a rather constant spatial extent of the condensation zone, and is in agreement with predicted results that show most of the liquid saturation build-up occurring in the first 3 months of heating. Another survey was performed in

January 1998, about 7 months into the cooling phase of the test. The test results still show a drying zone, not too different from that delineated by the 7- and 9-month velocity fields, indicating less dynamic thermal-hydrological processes after the heat is turned off.

The formation of a zone with increased saturation during the first few months of heating is also corroborated by the air permeability data obtained during heating and cooling in boreholes 16 and 18 (Subsection 8.1.2). To demonstrate the qualitative agreement between simulation and test results, the predicted thermal-hydrological situation in the vicinity of borehole 16 is analyzed in more detail. Figures 8-103 through 8-106 present temperature and saturation measured along this borehole at 3 and 9 months of heating, and at 3 and 9 months of cooling. Air-injection tests were carried out in three different zones approximately extending from sensor 16-1 to 16-2 (zone 1), from 16-2 to 16-3 (zone 2), and from 16-4 (zone 3) all the way to the end of the borehole. The location of the sensors (pressure transducers and humidity sensors) is given in the figures to provide better orientation. The simulation results show a significant increase in fracture liquid saturation in zone 3 of borehole 16 at 3 and 9 months of heating. During cooling, however, this situation changes; the fracture saturation drops almost instantly to pretest values as soon as the heater is turned off. These simulation results are in good agreement with the measured data from air injection tests, shown in Figure 8-4. As fracture liquid saturation increases in the condensation zone during heating, one would expect that air permeability should decrease. Indeed, after 3 months of heating, the measured air permeability values in zone 3 have decreased by a factor of 4 in borehole 16 and a factor of 2 in borehole 18, compared to the pre-heat values. For the rest of the heating period, the measured permeabilities remain essentially constant. Then, as soon as the heat-induced vaporization and condensation processes disappear during the cooling phase, the air permeabilities increase to values equal to or higher than the pre-heat measurements. Little change in air permeability is observed in the other injection zones in boreholes 16 and 18 during the entire test, because the distance to the heater is too large for it to be significantly affected.

Additional air permeability measurements were performed in January 1998, seven months after turning off the heat (Subsection 8.1.3). The measured permeabilities exhibited a consistent, yet small increase compared to the pre-heat values. This increase cannot be attributed to thermal-hydrological effects, because the fracture saturation before and after heating is fairly similar. It can be possibly attributed to mechanical processes resulting in microfracturing or fracture opening during the test. Such effects are not accounted for in the numerical model.

Simulation results show that all sensors in boreholes 16 and 18 remain in an environment of high matrix saturation during the entire heating period, as the dry-out zone does not extend to the sensor locations (Figure 8-103 through 8-106). Therefore, the relative humidity readings from passive monitoring should effectively register 100 percent. However, as pointed out in Subsection 8.2.2, this is only the case for sensor 18-4. Sensor 16-4 ceased to function properly beginning November 8, 1997; the other sensors in boreholes 16 and 18 exhibit relative humidity readings below 96 percent. This is probably related to drying from ventilation in the Thermomechanical Alcove Extension, which is not accounted for in the model.

Because gas pressure buildup occurs only in the boiling area close to the heater, which is not intersected by boreholes 16 and 18, the predicted pressure sensors in boreholes 16 and 18 do not register readings much different from the ambient value. This again is consistent with the

measured data, except for sensor 4 in borehole 16, where pressure buildup was observed during the heating phase of the test (Figure 8-13). This, however, was not a result of elevated gas pressure, but related to the influx of condensate into the bottom zone of borehole 16, resulting in a hydrostatic pressure buildup. The model results suggest an area of high fracture saturation and significant liquid flow processes in the vicinity of zone 3, indicating that water seepage into the packed-off borehole interval is indeed a possibility. No water was collected in borehole 16 during the cooling phase of the test, as the vaporization-condensation processes had ceased and the fracture saturation had significantly dropped.

Rock samples taken from dry-drilled boreholes at about 7 months into the cooling phase were analyzed for porosity, density, and moisture content (Section 6.3, Figure 6-14). Some of these samples were located in the dry-out zone close to the heater; others were taken from the condensation zone. The matrix saturation data derived from these measurements give values for the dry-out zone in the range of 10 percent to 30 percent, consistent with the very slow rewetting process predicted by the model. The model matrix saturation in the dry-out zone is about 4 percent at the end of heating period, about 7 percent after 3 months of cooling and about 10 percent after 9 months of cooling. In the condensation zone, the measured matrix liquid saturation is approximately in the range of the pre-heat data (taking into account that the liquid saturation can differ by 9 percent between dry-drilled and wet-drilled cores, as discussed in Subsection 4.2.2), in some cases slightly lower. Overall, matrix cores taken from below the heater horizon have higher saturation than cores taken from above the heater horizon (Figure 6-14). These findings again are in good agreement with the model results: during heating, most of the condensate is predicted to drain through the fractures, limiting the effect of matrix imbibition. Therefore, matrix saturation increases only slightly from the initial value of 0.92 to a maximum value of about 0.95, with higher saturation obtained below the heater than above it (Figures 8-98 and 8-99). During cooling, the predicted liquid and gas flow processes are very slow; thus, the moisture redistribution established during heating remains almost unchanged through several months of cooling (Figure 8-102). However, porewater from the condensation zone is slowly driven back towards the dry-out zone, so that matrix saturation in the vicinity of the dry areas can decrease below the pre-heat value. This effect can clearly be seen from the predicted results in Figures 8-105 and 8-106, where the entire bottom section of borehole 16 features matrix saturation values smaller than the pre-heat value of 0.92.

8.7.3.2 Quantitative Comparison of Measured and Predicted Temperature

Hourly temperature data are available at multiple locations within the SHT block, providing a unique opportunity to analyze the spatial and temporal evolution of the thermal-hydrological processes in fractured tuff. Although heat conduction is the dominant heat transfer process, heat transport due to gas or liquid flow can also influence the temperature field, as evidenced by subtle, sometimes strong temperature "plateaus" near the nominal boiling point. Detailed analysis of the numerous temperature measurements in the SHT can help identify and constrain moisture redistribution processes, and comparison between measured and modeled temperature data can serve to determine the accuracy of the thermal-hydrological model and the adequacy of the simulation input parameters.

8.7.3.2.1 Discussion of Temperature Profiles

The continuous temperature measurements from the SHT allow the display of data either as temperature profiles at a given time or as temperature evolution at a particular spatial location. Figures 8-107 and 8-108 present snapshots after 3 months and 9 months of heating, for the subset of temperature data measured close to the mid-plane of the heater, at Y = 4.5 m. Measured data points are indicated by symbols. The figures also show predicted results, which are extracted from the 3D grid for a horizontal sampling line at Y = 4.5 m. The predicted results have separate curves for matrix (solid line) and fracture (dashed line) temperature. The measured data are compared to the matrix simulation results, as most of the sensors are placed in grouted boreholes and would thus represent the temperature response of nonfractured rock. Temperature is displayed as a function of radial distance from the heater borehole.

The predicted matrix and fracture temperature are similar except near the nominal boiling point, where the fracture curve shows a narrow plateau, indicative of substantial heat transfer contributions from vapor-liquid counterflow. This two-phase heat pipe region centers around 0.8 m radial distance from the heater at 3 months of heating, and moves out to about 1.2 m at the end of 9 months of heating. Little of this behavior can be seen in the predicted matrix temperatures. Obviously, the assumed thermal and hydrological properties in the matrix do not promote heat pipe effects. It is unfortunate that there is a lack of measured data at these distances. Nevertheless, the predicted temperatures compare favorably with the measured data.

Figure 8-109 gives a similar comparison of measured and predicted data for the cooling phase, at 3 months after heater turn-off. The drastic temperature drop from the heating phase temperatures is well represented, but the predicted results exhibit a slight overprediction compared to the measured data. Possible reasons are discussed in Subsection 8.7.3.3.

8.7.3.2.2 Discussion of Temperature Evolution

Figure 8-110 through 8-1113 present the time evolution of temperatures over a 15-month period (9 months of heating and 6 months of cooling), for sensors close to the center-plane of the heater in boreholes parallel to the heater axis. Radial distances between the heater and the sensors are 0.34 m for borehole 2, 0.68 m for borehole 3, 1.5 m for borehole 4, 0.42 m for borehole 8, 0.67 m for borehole 9, 1.51 m for borehole 10, 0.73 m for borehole 11, and 0.70 m for borehole 12. The majority of these boreholes are grouted, with the exception of boreholes 2, 3, and 4, which are open boreholes to allow for mechanical displacement measurements. The temperature in the open boreholes may be somewhat affected by convective heat transfer within the boreholes. Generally, the temperature data show very subtle, if any, heat pipe effects, indicating that the dominant heat transfer mechanism operating in the SHT is thermal conduction. In borehole 9, for example, the temperature increases to nominal boiling within about 50 days, but then continues to increase without the evidence of a significant temperature plateau. The other sensors registering temperatures above 100°C show similar behavior; it seems that the rock properties in the SHT do not allow for appreciable liquid reflux from the condensation zone back to the heater. The curves also exhibit a drastic drop of temperature as soon as the heater is turned off. The down spikes in the measured data register incidences of power outage, which have not been accounted for in the model.

Comparison between the measured and the predicted temperature evolution shows very good overall agreement for the heating phase. The observed behavior of only minor heat pipe effects is well captured in the predicted data, and there is no general trend of over- or underpredicting the measurements. Some of the observed discrepancies are probably related to the model assumption of homogeneous properties. In borehole 11, for example, the simulation overpredicts the measured temperature, possibly because the assumed fracture continuum permeability of 5.85×10^{-14} m^2 is two orders of magnitude smaller than the measured air-permeability value at this borehole. A local increase of fracture permeability in the model would promote heat transfer by convection and result in a lower temperature close to the borehole. During the cooling phase, the agreement between model results and data is generally good, but the numerical results show a small but consistent temperature overprediction compared to the measured data.

8.7.3.2.3 Discussion of Model Accuracy

The accuracy of the thermal-hydrological model is evaluated both visually and by statistically analyzing temperature differences between simulation and measured data. This analysis is performed for all SHT sensors, except for a few gages that exhibit obviously erroneous behavior. Figure 8-114 visualizes possible systematic errors in the model results by presenting the temperature residuals as a function of the measured temperature. This procedure is performed at 3 months and 9 months from the onset of heating, and at 3 months from heater turn-off. It is seen that, for the heating period, (1) most of the temperature residuals are within a ±10°C, (2) the scatter of data is larger for the high-temperature range, and (3) there is no general trend of over- or underpredicting data. In evaluating the simulation results, one should keep in mind that the model uses homogeneous properties for the entire block, so that local heterogeneity is not accounted for. These and other simplifying assumptions, such as neglecting the presence of boreholes or relatively coarse gridding in the Y-direction, give rise to such temperature discrepancies. It is the general trends that have to be accurately predicted by a model, not the temperature at each individual location. Thus, it may be concluded that the overall model accuracy is very good for the heating phase. During cooling, most of the residuals have positive values, indicating a systematic problem where the predicted values are consistently too high.

Two statistical measures for model evaluation have been proposed by the Thermal Testing Teams in participating laboratories: the Mean-Error (ME) and the Root-Mean-Square-Error (RMSE). The ME is simply the average of the temperature residuals for all gages; a model would not feature a systematic error of consistently over- or underestimating data if the ME's were close to zero. Positive and negative values would indicate model overprediction and underprediction, respectively, of the measured data. The RMSE is similar to a standard deviation; the smaller the RMSE, the better the overall model fit. It was suggested to apply these measures at discrete times throughout the test, and to use a weighting scheme based on the frequency of temperature measurements in given temperature subranges. A detailed description of ME, RMSE, and the weighing scheme follows.

The temperature gages in the SHT block are associated with a measured temperature value, $T_{mea,i}$, and a modeled temperature, $T_{sim,i}$, the latter obtained by spatial interpolation from the model grid nodes. At a given instant in time, the ME can be evaluated from

$$ME = \frac{\sum_{i=1}^{N} w_i (T_{sim,i} - T_{mea,i})}{\sum_{i=1}^{N} w_i} \qquad (8\text{-}8)$$

where N is the number of temperature gages used in the analysis, and w_i is the weighting factor given to the i^{th} temperature gage. On average over a given temperature range, a model would *not* feature a systematic error of consistently over- or underestimating data, if the ME is equal to zero for that temperature range. The RMSE is given by

$$RMSE = \left(\frac{\sum_{i=1}^{N} w_i (T_{sim,i} - T_{mea,i})^2}{\sum_{i=1}^{N} w_i} \right)^{1/2} \qquad (8\text{-}9)$$

The smaller RMSE, the better is the model fit to the data in a given temperature range.

The weighting factors, w_i, used in Equations 8-8 and 8-9, are based on a frequency analysis of the temperature measurements, acknowledging that the sensors are not uniformly distributed throughout the test block. It is desired to give equal importance to all temperature sub-ranges in the total range of temperatures observed. For example, in case only a few temperature gages are located in the "hot" zone close to the heater compared to numerous sensors located in "colder" areas, data in the "hot" temperature sub-range should get a larger weighting factor than data in the "colder" sub-range. The total range of temperature measurements are divided into 20 equally sized temperature sub-ranges. The number of measurements falling into each sub-range are calculated. Finally, the weighting factors for each sub-range are defined as the inverse of the number of occurrences in that sub-range, namely,

$$w_j = 1/N_o \qquad (8\text{-}10)$$

where j denotes the temperature sub-range considered, and N_o gives the number of occurrences within this sub-range. Note that Equation 8-10 cannot be applied if there is no occurrence in a certain sub-range; however, no weighting factor is needed in this case.

The statistical procedures were applied at three times: after 3 and 9 months of heating, and after 3 months of cooling. Results are given in Table 8-13. MEs and the RMSEs are presented for the

entire temperature range, and for two temperature windows below and above nominal boiling. Considering all sensors, the RMSE is 4.7°C at 3 months and 4.6°C at 9 months, which is fairly small compared to the large range of temperatures obtained in the SHT. The ME calculated for all sensors suggests a very modest underestimation of temperature data by the model; on average, the model results are 1.7°C too low at 3 months and 0.3°C too low at 9 months. Separate analysis for the two temperature windows above and below boiling indicates a similarly good agreement between measured and model data. It may be concluded the model represents the important thermal-hydrological processes in the SHT quite well, because possible systematic problems would become clearly evident in the above-boiling temperature range (a range where heat-convection processes are very important). The model is less accurate during the first several months of cooling. At 3 months after heater turn-off, the RMSE is 2.5°C. The ME indicates a consistent trend of overestimating the measured data, by 1.9°C on average.

Table 8-13. Error Analysis

Criterion	Range	3 months	9 months	12 months (cooling)
Root-Mean-Square-Error (°C)	All Temp.	4.7	4.6	2.5
Mean-Error (°C)	All Temp.	-1.7	-0.3	1.9
Root-Mean-Square-Error (°C)	Temp. < 97°C	4.5	3.0	2.5
Mean-Error (°C)	Temp. < 97°C	-1.5	0.9	1.9
Root-Mean-Square-Error (°C)	Temp. > 97°C	5.0	5.0	N/A
Mean-Error (°C)	Temp. > 97°C	-2.0	-1.7	N/A

8.7.3.3 Sensitivity Analysis

The good agreement between the measured data and the predicted results shown in the previous sections indicates that the thermal-hydrological response of the SHT is well represented by the numerical model. While heat conduction accounts for most of the temperature rise, effects of thermal-hydrological coupling cannot be ignored in the interpretation of the measured data. In particular, the choice of different parameter values of the hydrological properties can play a significant role in affecting the simulation results. The spatial heterogeneity and uncertainty of the hydrological properties is large, particularly in the fractures. This section presents an investigation of the sensitivity of the predicted temperatures to some key properties of the rock. Insight from these studies can serve to constrain these hydrological properties. In addition, the importance of percolation flux, the effect of initial saturation in the rock, and the impact of different conceptual models for fracture-matrix interaction is examined.

One must keep in mind that findings from this sensitivity study are specific to a small-scale experiment, and cannot readily be applied to larger problems, such as the DST or the entire repository. In the SHT, the impact of the thermal perturbation is very localized and intense. The strong perturbation of the thermal-hydrological system may accentuate the differences in model prediction from alternative conceptual models and different hydrological properties.

8.7.3.3.1 Thermal-Hydrological Parameters

The sensitivity study is performed in two dimensions for a vertical plane orthogonal to the heater axis at Y = 4.5 m. Results from a 2D model cannot exactly represent the actual 3D behavior of the

rock mass; the 2D temperature response overestimates the 3D system behavior. However, 2D simulations have considerable merit in a sensitivity study. They are instructive in uncovering the relative importance of parameters and processes, while allowing for more efficient computation and data handling compared to a fully 3D study. From the base-case properties used before, only one parameter at a time is varied, while all other parameters are kept constant. Sensitivity is evaluated by analyzing the temperature history in the rock matrix measured at a radial distance of 0.67 m from the heater, representing the location of borehole 9 in relation to the heater.

Figure 8-115 shows simulation results for the base-case matrix permeability and for cases where the matrix permeability is increased and decreased by one order of magnitude. The increase of matrix permeability results in a large suppression of temperature, arising from (1) increased imbibition of condensate from the fractures into the matrix, and (2) increased liquid flow back to the heater area through the matrix continuum. Lowering the matrix has negligible effect because the base-case value is already small enough such that only minor imbibition and liquid reflux is present. Figure 8-116 presents sensitivity of temperature to fracture permeability. Higher fracture permeability promotes increased convective heat transport by removal of vapor from the heater area, giving rise to lower temperatures. Lower permeability in the fractures does the reverse, resulting in higher temperature. Overall, the temperature evolution is less sensitive to an increase by one order of magnitude in the fracture permeability than in the matrix permeability.

Figure 8-117 shows the predicted temperature response when the matrix α-values are varied by one order of magnitude compared to the base case. The α-value is a fitting parameter for the van Genuchten characteristic function, inversely corresponding to the potential strength of capillary suction. A smaller α-value implies a stronger capillary suction in the matrix, which promotes imbibition of condensate from the fracture walls into the matrix. Thus, more water is available in the matrix to flow toward the heater area, resulting in increased convective heat transfer and lowering of the temperature. A larger α-value has the opposite effect; however, a one-order-of-magnitude increase has rather small impact on the temperatures. As discussed earlier, the base-case matrix properties allow for little matrix imbibition and small liquid reflux due to the small matrix permeability, so that the effect of a reduction in capillarity is negligible. Sensitivity to the fracture α-value is shown in Figure 8-118. The effect on temperature is similar in trend, but smaller in magnitude compared to that of changing the matrix α-value.

The examples shown above demonstrate that one order of magnitude variation in some of the key properties of the rock can significantly alter the predicted temperature of the SHT. One-order-of-magnitude variation is well within the limit of the spatial heterogeneity and uncertainty of the hydrological properties within the fractured welded tuff. In particular, one can conclude from the above analysis that property sets with high matrix permeability and strong capillarity in fractures and matrix are not likely to represent the SHT thermal-hydrological situation. All these cases tend to overestimate vapor-liquid counterflow and to underestimate the observed temperatures.

Further analysis was conducted to study the sensitivity of the temperature evolution to the characteristic curve parameter β, to the ambient percolation flux at Yucca Mountain, and to initial matrix saturation in the SHT block. Changes in van Genuchten β, a fitting parameter related to the aperture distribution of fractures, hardly affect the predicted temperature. Similar results were

obtained for percolation flux, as varying the flux range from 0.1 mm/yr to about 20 mm/yr would change the initial fracture saturation in the SHT block, but not affect the temperature response. This is because all reasonable values of percolation at Yucca Mountain are negligibly small compared to the thermally induced fluxes in the SHT. In contrast, the initial matrix saturation of the SHT block does have an impact on temperature. Smaller initial matrix saturation results in higher temperature, because less liquid is available in the matrix pores for vaporization and subsequent condensation.

8.7.3.3.2 Fracture-Matrix Interaction

For comparison with the DKM modeling results presented so far, the ECM concept is an alternative conceptual model for fracture-matrix interaction. ECM is a simplified approach where thermal-hydrological equilibrium is assumed at all times between fractures and matrix. It allows for fast, computationally efficient simulation of thermal-hydrological processes in fractured rock. The simulation runs are performed using a 3D representation of the SHT.

Figure 8-119 compares measurements to numerical simulation results analyzing the time evolution of temperature for the different conceptual models, using the center gage in borehole 9 as an example. Note that the ECM results display only one temperature curve due to the local equilibrium assumption, while DKM has separate curves for fracture and matrix temperatures. For both models, the general agreement between the measured and predicted data is good, indicating that the thermal-hydrological response of the SHT is well represented. However, the ECM results display a subtle heat pipe signal, which retards the temperature increase at nominal boiling for a certain time and gives rise to an underestimation of temperature for the remaining heating period. In contrast, the matrix temperature curves obtained with the DKM match the measured data curve almost exactly.

Analysis of the predicted moisture redistribution processes demonstrates more substantial differences between the model concepts. Figure 8-120 shows matrix saturation contours in a vertical plane at Y = 4.5 m after 3 months of heating, predicted using ECM. This is to be compared to Figure 8-98 for the DKM results. In both cases, drying occurs up to a radial distance of about 1 to 1.5 m from the heater; beyond that is the condensation zone where liquid saturation is higher than at ambient conditions. However, while strong gravity drainage in the fractures is obtained using DKM, indicated by the saturation build-up below the heater, no gravity drainage is observed using the ECM. The ECM concept involves the crucial assumption that pressure equilibrium between the fractures and matrix is maintained at all times. As a result, gravity driven liquid flow in the fractures tends to be underestimated, because vapor condensing on the fracture walls is readily imbibed into the matrix pores and driven back towards the heater. Because no water drains through the fractures, the condensate accumulates in matrix pores and gives rise to matrix saturation values close to 1. However, hydrological data suggest that most of the condensate indeed drains away from the test area so that matrix saturation cannot significantly build up in the condensation zone, evidenced for example in the geophysical data or in the posttest core sample analysis. It may be concluded that the DKM seems to be much better suited in realistically representing thermal-hydrological processes in the SHT than the ECM. However, the DKM has a tendency to underestimate fracture-matrix interaction particularly at early times, due to the assumption of a linear gradient between fractures and matrix. This could be improved by

analysis using the more rigorous, yet computationally exhaustive MINC method (Birkholzer and Tsang 1998).

8.7.3.3.3 Discussion of Cooling Phase Results

As mentioned earlier, the modeled temperatures show a consistent trend of overpredicting the measured data during the first several months of cooling. Because heat-conduction processes are less significant after the heater has been turned off, the discrepancy between predicted and measured data is probably not attributed to hydrological processes being misrepresented by the model, but more likely related to model assumptions and parameters of the thermal processes. For example, insulation of the test block may be less effective than assumed in the model, "wet" thermal conductivity of the rock may be underestimated, or heat capacity of the rock may be overestimated. In the first two cases, thermal energy would more efficiently be driven away from the test block, resulting in faster cooling. The third possibility suggests that the amount of heat stored in the test block is smaller than assumed; therefore, temperature would decrease more rapidly after turning off the heat. Scoping simulations indicate that all these possibilities contribute to improving the model results. Although possible reasons for the discrepancy between modeled and measured data may be suggested, there are currently no data to support or refute any of the above hypotheses.

8.8 THERMAL-HYDROLOGICAL ANALYSIS OF THE SHT BY THE NUFT CODE

Non-isothermal Unsaturated-saturated Flow and Transport (NUFT) code was used to perform the thermal-hydrological model calculations for the SHT. Version 6-17-98 of the NUFT code was used which is a modification of NUFT Version 2.0 (Nitao 1998a; Nitao 1998b). This version of the code is not qualified. The QA status of the calculations performed using NUFT Version 6-17-98 is to be verified. (TBV-3571). The SHT was conducted in the Tptpmn unit, which is one of the three major host-rock units for the potential repository at Yucca Mountain, Nevada. A primary purpose of the thermal-hydrological model calculations described in this chapter is to compare the predicted temperatures with the temperatures measured in the field during the heat-up and cool-down periods of the SHT. The thermal-hydrological model calculations assume the December 1997 base-case hydrological parameter set used in Total System Performance Assessment-Viability Assessment (TSPA-VA); thus, this comparison between predicted and measured temperatures is a useful way of assessing the applicability of that property set to predicting thermal-hydrological behavior in one of the three major host-rock units. In the process of comparing the predicted and measured temperatures, it is necessary to analyze the relationship between temperature change and (gas-and liquid-phase) moisture movement in the SHT. Another purpose of the thermal-hydrological model calculations is to investigate differences in predicted thermal-hydrological behavior between two different approaches to representing fracture-matrix interaction: ECM and DKM.

The thermal-hydrological models of the SHT described in this chapter are similar to the 3D thermal-hydrological models used in previous studies (Buscheck, Shaffer, and Nitao 1997). Several significant improvements and changes have been incorporated in the current thermal-hydrological models of the SHT, including the following:

- The model assumes the TSPA-VA (December 1997) base-case hydrologic parameter set for I x I $\alpha_{f,mean}$, where I stands for the nominal infiltration-flux map and α_f is the van Genuchten alpha parameter for the fractures. In the TSPA-VA analysis, this set is assumed to be the most likely hydrological parameter set. Previous thermal-hydrological model calculations (Buscheck, Shaffer, and Nitao 1997) considered the TSPA-VA (July 1997) preliminary base-case hydrological parameter set.

- The model includes the influence of vapor and heat flow along the axis of the heater borehole. The previous thermal-hydrological model neglected this effect.

- The model domain is extended (westward) to include the entire Thermomechanical Alcove as well as 33 m of rock to the west of the Thermomechanical Alcove. The western boundary of the previous thermal-hydrological model domain was at the eastern face of the Thermomechanical Alcove.

- Fracture-matrix interaction is represented with DKM. Two alternatives for representing the degree of fracture-matrix disequilibrium are considered: (1) using a static fracture-matrix interaction (FMX) term and (2) using a dynamic fracture-matrix coupling term that is a function of the liquid-phase relative permeability in the fractures.

The first two features are included in all thermal-hydrological model calculations. The third feature is included in all but one of the thermal-hydrological model calculations. The fourth feature (DKM) is included in two of the thermal-hydrological model calculations; the other calculations use ECM to represent fracture-matrix interaction.

8.8.1 NUFT Numerical Simulation Code

All of the thermal-hydrological model calculations in this study used the NUFT code. NUFT uses the integrated-finite-difference method and simulates the transport of air, water, energy, and other species such as radionuclides. NUFT determines the spatial and temporal distribution of gas- and liquid-phase pressure, gas- and liquid-phase saturation, air-mass fraction in gas and liquid phases, water-mass fraction in gas and liquid phases, and temperature. NUFT can treat the mechanical dispersion of components. NUFT was successfully benchmarked against the VTOUGH code (Nitao 1989), which has been qualified for quality-affecting work, and was recently qualified for quality-affecting work, according to the individual software plan for NUFT.

8.8.2 Representing Fracture-Matrix Interaction

There are three principal classes of the mathematical treatment of fracture-matrix interaction that are used in thermal-hydrological models: the ECM, the DKM, and the discrete fracture method (Chapter 3 of Hardin 1998). Because of the computational demands of the DKM and the discrete fracture method, past thermal-hydrological model calculations have used the ECM. Both the

ECM and the DKM are used in the thermal-hydrological models described in this chapter. Cases 1 and 2 use ECM; Cases 3 and 4 use the DKM (Table 8-14).

Table 8-14. Summary of Four Cases Considered in this Study

	Case 1	Case 2	Case 3	Case 4
Hydrological parameter set	12/97 TSPA-VA base case*	12/97 TSPA-VA base case*	12/97 TSPA-VA base case*	12/97 TSPA-VA base case*
Conceptual model for fracture-matrix interaction	ECM	ECM	DKM	DKM
Fracture-matrix connectivity factor (FMX)	NA	NA	Fixed FMX	Dynamic FMX
Model domain	Western boundary 33 m to the west of the Thermomechanical Alcove	Western boundary at the eastern wall of the Thermomechanical Alcove	Western boundary 33 m to the west of the Thermomechanical Alcove	Western boundary 33 m to the west of the Thermomechanical Alcove

* All hydrological parameters except for the bulk permeability, fracture-continuum permeability, and fracture porosity values were taken from this set.

8.8.2.1 Equivalent-Continuum Method

The ECM assumes that the local matric potential (water potential plus osmotic potential) is equal in the fractures and the adjacent matrix. Local thermodynamic equilibrium is assumed between the fractures and matrix. Composite functions are derived to describe the equivalent behavior of a single continuum and to define the relations between unsaturated hydraulic conductivity and liquid-phase saturation and between matric potential and liquid-phase saturation (Klavetter and Peters 1986, pp. 385 through 402). The ECM does not treat fractures as discrete features; instead, fracture-flow effects are averaged over the whole spatial domain. The ECM involves less computational effort than do the DKM and the discrete fracture method because it uses a single continuum to represent the fractures and matrix.

The assumption of local equilibrium between fractures and matrix is appropriate if the liquid-phase flux in the fractures is sufficiently small (Buscheck, Nitao and Chesnut 1991; Nitao et al. 1993). Thus, the ECM is appropriate for modeling condensate drainage during periods of quasi-steady moisture movement in thermally driven models, but may be less well suited for modeling the early stages of repository heating, when the rate of thermally driven moisture reflux will be near its peak and when condensate shedding between emplacement drifts is greatest. Because of the large liquid-phase fluxes that were expected to occur during the heat-up period of the SHT, the ECM is probably not well suited for representing the influence of condensate shedding around the dry-out zone in the SHT.

8.8.2.2 Dual-Permeability Method

The DKM treats the matrix and the fractures as two distinct porous continua, with transfer terms to represent the mass and heat flux between them. Because the DKM does not assume capillary-pressure equilibrium between fracture and matrix continua, it can handle much larger liquid-phase fluxes than can the ECM without producing conditions near 100 percent liquid saturation in the matrix. The DKM also allows thermodynamic disequilibrium between matrix blocks and the adjoining fractures because of its capability to represent heat flow between these two continua.

The DKM approach has been applied in drift-scale thermal-hydrological models supporting TSPA-VA, with direct bearing on prediction of conditions in the near-field and altered zone. The DKM is applied to all the line-averaged-heat-source drift-scale thermal-hydrological model calculations used in the multiscale thermal-hydrological modeling approach to predict near-field environment conditions for performance assessment (CRWMS M&O 1998b, Chapter 3, Volume 2). In this family of models, the fracture-to-matrix liquid flow is strongly influenced by the FMX parameter, which is specified as a model input for each hydrostratigraphic unit. This parameter varies between 0 and 1 and quantifies the fraction of the fracture surfaces that is wetted by the liquid phase. This fraction, together with a specified value for the fracture spacing, quantifies the interfacial flow area per unit volume of the rock matrix available for fracture-to-matrix liquid-phase mass transfer.

The FMX parameter for liquid-phase interaction accounts for channeling of flow as the liquid phase "fingers" through the fracture network. However, this factor probably underrepresents the wetted surface area of fractures that occurs during condensate drainage in thermal-hydrological models. Other approaches (Ho 1997) attempt to account dynamically for changes in the influence of condensate drainage on the FMX parameter. In such approaches, the parameter that is analogous to FMX increases with the magnitude of liquid flux in the fracture continuum. Because repository decay heat will generally produce greater liquid flux than that which occurs at ambient conditions, and because condensate flow may be more ubiquitous than ambient percolation in fractures, this dynamic approach results in a larger value of the interaction factor where there is development of condensate flow. As the repository heat output declines, thermally driven reflux decreases asymptotically toward the ambient percolation, and the interaction factor decreases to its previous value. The drift-scale thermal-hydrological calculations supporting TSPA-VA assume a constant value for FMX rather than taking the dynamic-FMX approach. In this study, the constant-FMX approach is compared with the dynamic-FMX approach.

The dynamic-FMX approach used in this study assumes that FMX is equal to the square of the liquid-phase relative permeability, $k_{r,liq,f}$, in the fractures. The basis for this dynamic-FMX approach is that the fraction of the fracture surfaces that are wetted by the liquid phase increases strongly with increasing q_{liq}. The value of the dynamic FMX was chosen to be the square of $k_{r,liq,f}$ because this relationship was judged to be much stronger than a simple linear relationship. Because $k_{r,liq,f}$ increases with liquid-phase flux q_{liq}, FMX increases with q_{liq}. For the relatively small q_{liq} that occur under ambient percolation conditions, FMX is small. For the much larger q_{liq} that occur as a result of radioactive decay heat, FMX is much larger—representing how condensate flux is more ubiquitously distributed over the fracture surfaces. During the heat-up

period of the SHT, q_{liq} predicted by the thermal-hydrological model is relatively large, resulting in a much larger value of FMX than occurred prior to heating.

8.8.3 Model Geometry, Boundary Conditions, and Numerical Mesh

A conceptual plan and overview of the SHT is described in the *Test Design, Plans, and Layout Report* (CRWMS M&O 1996a). The test layout is shown in Figure 8-121. An electrical-resistance heater placed in a small-diameter horizontal borehole was used to heat the rock. The thermal-hydrological-chemical-mechanical response of the rock was monitored by instrumentation placed in boreholes at various locations within the rock. The heated block was 12.86 m wide, bounded to the north by the Observation Drift, to the south by the Thermomechanical Alcove Extension, and to the west by the Thermomechanical Alcove. The horizontal heater borehole was 9.6 cm in diameter, collared 6.59 m from the Observation Drift and 1.52 m above the floor of the Thermomechanical Alcove, and drilled parallel to the Observation Drift. The heater was 5.0 m long, installed with its front (closest) end 1.99 m from the borehole collar. The walls of the Observation Drift and alcoves that faced the block were covered by a 15-cm-thick layer of fiberglass insulation with a thermal conductivity of 0.044 W/m•K. The nominal electrical power supplied to the heater was 3.86 kW. The actual deviations of power from 3.86 kW, because of fluctuations and outages, is accounted for in all the model calculations.

The 3D SHT model takes into account the geometric details of the SHT area, including the heater borehole, the Observation Drift, the Thermomechanical Alcove, and the Thermomechanical Alcove Extension. The model uses a Cartesian (x, y, z or i, j, k) coordinate system. The x direction is transverse to the heater borehole, with x or i increasing to the right (south). The y direction is parallel to the heater borehole, with y or j increasing with distance from the borehole collar into the rock mass. The z direction is vertical, with z or k increasing with distance above the heater borehole axis. The overall grid-block dimensions of the model are $i = 54$, $j = 32$, and $k = 44$. For the ECM models there are 2484 null blocks in the model, which results in a total of 73,548 active grid blocks. For the DKM models there are 147,096 active grid blocks and 4968 inactive blocks.

The lateral model boundaries are adiabatic/no-mass flow boundaries. The northern and southern boundaries are 52.5 m from the heater axis, while the eastern boundary is 62.7 m to the east of the eastern end of the heater (Figure 8-121). The ground surface is far enough above the SHT horizon (250 m) that fluctuations in surface conditions do not influence thermal-hydrological conditions at the SHT horizon. Thus, the ground surface can be accurately represented as a constant-temperature, constant-pressure, and constant-relative-humidity boundary. The water table, which is 572.3 m below the ground surface, is a constant-temperature, constant-pressure, and constant-liquid-saturation boundary. The models are initialized to account for the geothermal temperature gradient and static air-pressure gradient in the SHT area. The initial temperature at the heater horizon is 24.4°C.

In previous thermal-hydrological calculations (Hardin 1998, Chapter 3), the western boundary was the inside surface of the insulation on the eastern wall of the Thermomechanical Alcove (at $y = 0$ in Figure 8-121); one of the ECM thermal-hydrological calculations in this study (Case 2) uses the same western boundary. For all of the other thermal-hydrological calculations reported

here (Cases 1, 3, and 4), the western boundary is 33 m to the west of the western side of the Thermomechanical Alcove, which places this boundary 40.64 m to the west of the western end of the heater. For the model, the Observation Drift and the Thermomechanical Alcove Extension are maintained at a constant temperature (24.4°C), relative humidity (82.5 percent) and a constant gas-phase pressure (8.91×10^4 Pa). These values were chosen to account approximately for the influence of ventilation in the SHT area.

8.8.4 Thermal/Hydrological Properties and Percolation-Flux Assumptions

The thermal properties used in the thermal-hydrological models are similar to those used in previous SHT modeling studies (Buscheck, Shaffer, Lee et al. 1997, Table 2-1). The only difference in thermal properties is that the wet value of thermal conductivity $K_{th,wet}$ used in this study ($K_{th,wet} = 2.1$ W/m•K) is slightly higher than that used in previous studies ($K_{th,wet} = 2.0$ W/m•K). The measured in situ value of K_{th} is 2.0 W/m•K (CRWMS M&O 1996b; CRWMS M&O 1997c, Table 9-1). The in situ liquid-phase saturation S_{liq} is 0.92; thus, ambient saturation conditions are less than fully saturated. Extrapolating to full saturation (i.e., wet) conditions results in $K_{th,wet} = 2.1$ W/m•K.

With the exception of the values of bulk permeability k_b, fracture-continuum permeability k_f, and fracture porosity ϕ_f, the hydrological properties used in this study are taken from the December 1997 TSPA-VA base-case hydrological parameter set (Table 8-15). The value of k_b (122 millidarcy) used in this study is the log center mean of the values measured in the SHT area (CRWMS M&O 1996b; CRWMS M&O 1997c, Table 9-1) and is the same as that used in a previous study (Case 2 in Section 3.4 of Hardin 1998). Because k_b is equal to $k_f \phi_f + km(1 - \phi_f)$, where k_m is equal to the matrix permeability, and $k_b >> k_m$, k_b is essentially equal to $k_f \phi_f$ (where k_b, k_f, and k_m are expressed in m^2). Note that the ECM and DKM model calculations use the same matrix and fracture properties.

Table 8-15. Thermal and Hydrological Properties Summarized for the Host Rock of the SHT Area

Thermal-Hydrological Property	Cases 1 and 2	Case 3	Case 4
Percolation Flux q_{perc} (mm/yr)	0.23	0.22	11.52
Bulk Permeability k_b (millidarcy)	122	122	122
Bulk Permeability k_b (m^2)	1.22×10^{-13}	1.22×10^{-13}	1.22×10^{-13}
Matrix Permeability (m^2)	4.07×10^{-18}	4.07×10^{-18}	4.07×10^{-18}
Fracture-Continuum Permeability	9.84×10^{-10}	9.84×10^{-10}	9.84×10^{-10}
Matrix Porosity	0.089	0.089	0.089
Fracture Porosity	1.46×10^{-4}	1.46×10^{-4}	1.46×10^{-4}
Matrix van Genuchten α_m (1/Pa)	1.02×10^{-6}	1.02×10^{-6}	1.02×10^{-6}

Table 8-15. Thermal and Hydrological Properties Summarized for the Host Rock of the SHT Area (Continued)

Thermal-Hydrological Property	Cases 1 and 2	Case 3	Case 4
Matrix van Genuchten m	0.322	0.322	0.322
Matrix Residual Saturation	0.18	0.18	0.18
Fracture van Genuchten α_f (1/Pa)	8.36×10^{-4}	8.36×10^{-4}	8.36×10^{-4}
Fracture van Genuchten m	0.492	0.492	0.492
Fracture Residual Saturation	1.00×10^{-2}	1.00×10^{-2}	1.00×10^{-2}
Initial Liquid Saturation	0.92	0.92	0.92
Dry Thermal Conductivity (W/m•K)	1.67	1.67	1.67
Wet Thermal Conductivity (W/m•K)	2.10	2.10	2.10
Specific Heat (J/kg•K)	865	865	865
Grain Density (kg/m^3)	2560	2560	2560
Conceptual Model for Fracture-Matrix Interaction	ECM	DKM with fixed FMX (=1)	DKM with dynamic FMX

NOTE: With the exception of the bulk permeability and fracture-continuum permeability, these property values are the same as in the December 1997 TSPA-VA base-case hydrological property set. TSw34.

The percolation flux, q_{perc}, values in Table 8-15 are those required to obtain a liquid-phase saturation $S_{liq} = 0.92$ in the rock at the heater horizon. The ECM cases and the DKM case with a fixed FMX of unity (Case 3) require nearly the same value of q_{perc} to obtain $S_{liq} = 0.92$. The dynamic-FMX case assumes that FMX is equal to the square of the relative liquid-phase permeability $k_{r,liq,f}$ in the fracture. Because $k_{r,liq,f}$ is almost always less than one (and usually much less than one), FMX is usually much smaller than one. Thus, under ambient conditions, Case 4 has an FMX that greatly restricts fracture-to-matrix flow, which effectively allows much of the percolation flux to bypass the rock matrix. Therefore, q_{perc} must be much larger in Case 4 (than it is in the cases that do not restrict fracture-to-matrix flow) to achieve a given level of liquid-phase saturation (such as $S_{liq} = 0.92$). In other words, when fracture-to-matrix flow is restricted (as it is in Case 4) a larger value of q_{perc} is required to wet the rock matrix to $S_{liq} = 0.92$. Note that the value of q_{perc} (11.52 mm/yr) for Case 4 is closer to the repository-area-average value of q_{perc} (7.8 mm/yr) than are Cases 1-3 (Section 3.2 of Hardin 1998). However, as will be discussed later in this chapter, predicted thermal-hydrological behavior in the SHT is insensitive to the value of q_{perc}.

8.8.5 Modeling Results

8.8.5.1 Equivalent-Continuum-Method Calculations

The predicted temperature, T, and liquid-phase saturation, S_{liq}, distributions at the end of the heating phase (275 days) of the SHT are given in Figure 8-122 and Figure 8-123 for Case 1 (see Table 6-1). The predicted T and S_{liq} distributions for Case 2 are essentially identical to those of Case 1 at the end of heating—thus, Figure 8-122 and Figure 8-123 are also representative of Case 2.

Because the 5-m-long heater effectively functions as a point heat source, the temperature T and liquid-phase saturation S_{liq} distributions attain nearly steady-state profiles within 9 months. Because of the relatively short distance between the western end of the heater and the Thermomechanical Alcove (1.99 m), the temperature field is influenced by heat loss to the Thermomechanical Alcove, which is clearly indicated by the flattening of the 40°C contour (Figure 8-123, a). The model assumes the drifts and alcoves bounding three sides of the SHT area are maintained at a constant temperature (24.4°C) to represent the influence of ventilation. Figure 8-123 (a) shows that there is no flattening of the 40°C contour in the vicinity of the drifts bounding the northern and southern sides of the SHT area, which indicates that the Observation Drift and Thermomechanical Alcove Extension exert little influence on the temperature distribution around the heater, including the boiling and superheated zones. Because the heater axis is 6.59 m from the Observation Drift and 6.26 m from the Thermomechanical Alcove Extension—distances which are relatively large compared to the radius of the boiling zone—these rooms are too far from the heater to exert a noticeable influence on the temperature distribution.

The liquid-phase saturation S_{liq} distribution (Figure 8-122, b and Figure 8-123, b) has the same overall shape as does the temperature distribution; both distributions are essentially symmetric with respect to the heater axis. Dry-out is seen to occur for temperatures in excess of 96°C. The 96°C contour almost exactly coincides with the $S_{liq} = 0.9$ contour, which is close to the initial (ambient) value $S_{liq} = 0.92$ in the SHT area. Notice that the 150°C isotherm approximately coincides with the $S_{liq} = 0.2$ contour; therefore, it is necessary to drive temperatures well above the nominal boiling point to significantly dry out the rock.

Figure 8-122 (b) and Figure 8-123 (b) indicate the formation of a pronounced condensation zone, which is the area where $S_{liq} > 0.92$. This zone is nearly symmetric about the heater axis. The ECM-model calculations indicate that the condensate zone is pronounced (and, therefore, should be readily observable) and is vertically symmetrical about the heater axis. The ECM-model calculations also imply that the effects of gravity-driven condensate drainage are negligible for the SHT. However, the field measurements by ERT, described in Section 8.5 of this report, show that the condensation zone primarily forms below the heater, indicating the importance of gravity-driven condensate drainage for the SHT. Therefore, the ECM model does not adequately capture the influence of gravity on condensate drainage. As will be discussed in Subsection 8.8.6, the ECM model also predicts temperatures that are lower than the measured temperatures in the superheated/dry-out zone.

The potential importance of gravity on condensate drainage has been demonstrated in previous calculations of field-scale thermal tests. When a model is used that represents fracture-matrix disequilibrium (e.g., the DKM model or the discrete fracture method model), the influence of gravity-driven drainage is readily apparent. Calculations of the G-Tunnel (single-heater) test (Nitao and Buscheck 1995, Figures 3 and 4, p. 751), which used the discrete fracture method model and hydrological properties that did not result in strongly capillary-driven liquid-phase flow, predicted significant gravity-driven drainage around the dry-out zone. The DKM-model calculations conducted for this report (see Subsection 8.8.5.2) also clearly show the importance of gravity-driven condensate drainage.

In previous thermal-hydrological model studies of the SHT (Buscheck, Shaffer, Lee et al. 1997; Hardin 1998, Section 3.4), the heater borehole was assumed to be impermeable; thus, the influence of vapor and heat flow along the heater borehole were neglected. In this study, the entire length of the heater borehole, including unheated interval, is assumed to be permeable, which allows vapor and heat flow along the borehole axis. Figure 8-123 (b) shows the influence of vapor flow and condensation effects along the axis of the heater borehole, which results in a highly efficient mass- and heat-transport mechanism called the "cold-trap" effect. Vapor is driven from the heated interval to the cold end of the borehole adjacent to the borehole collar on the Thermomechanical Alcove wall; there the vapor condenses and imbibes into the rock, resulting in a local increase in S_{liq}. The cold-trap effect efficiently transports heat toward the borehole collar, which is manifested by the elongated T contours (Figure 8-123, a). It is important to note that moisture was observed near the wall of the Thermomechanical Alcove. This moisture can be explained by the cold-trap effect. This effect is a potentially important mechanism influencing thermal-mechanical behavior in emplacement drifts (Buscheck, Nitao, and Ramspott 1997, p. 1029).

8.8.5.2 Dual-Permeability-Method Calculations

The predicted temperature, T, and liquid-phase saturation, S_{liq}, distributions at the end of the heating phase (275 days) of the SHT are given in Figure 8-124 through Figure 8-127 for Case 3 (see Table 8-14). Because the DKM readily distinguishes between thermal-hydrological conditions in the matrix and fracture continua, the predicted T and S_{liq} distributions are given for the matrix continuum (Figure 8-124 and Figure 8-126) as well as for the fracture continuum (Figure 8-125 and Figure 8-127). As indicated by Figure 8-128, the predicted T distribution for Case 4 is essentially identical to that of Case 3 at the end of heating; thus, Figure 8-124 (a), Figure 8-125 (a), Figure 8-126 (a), and Figure 8-127 (a) are also representative of Case 4. Because the predicted matrix S_{liq} distribution for Case 3 is similar to that of Case 4 at the end of heating, Figure 8-124 (b) and Figure 8-126 (b) are also representative of Case 4. Qualitatively, the fracture S_{liq} distribution for Case 3 is similar to that of Case 4; thus, Figure 8-125 (b) and Figure 8-127 (b) are qualitatively representative of Case 4.

The negligible differences in predicted T between Cases 3 and 4 indicate that the SHT cannot distinguish between alternative conceptual models of the FMX factor. The much higher ambient percolation flux in Case 4 (q_{perc} = 11.52 mm/yr) than in Case 3 (q_{perc} = 0.22 mm/yr), along with the negligible difference in predicted T for these two cases, indicates that thermal-hydrological behavior in the SHT is insensitive to the magnitude of q_{perc}. The lack of sensitivity of the SHT to

q_{perc} arises from the heat-driven condensate fluxes being much greater than any of the values of q_{perc} that were considered. Therefore, the SHT is not a useful test for diagnosing the magnitude of percolation flux. In general, any in situ thermal test that is relevant to thermal-hydrological behavior in the repository, such as the DST, generates heat-driven condensate fluxes that are much greater than q_{perc} during the heating phase. However, during the cool-down phase, the condensate fluxes will quickly decline to the point that they are less than q_{perc}. If percolation flux (rather than imbibition flux in the matrix) is found to be the rate-limiting process controlling rewetting of the dry-out zone in the DST, the DST may turn out to be a very useful test for diagnosing the magnitude of the local percolation flux.

The T distributions in the matrix and fractures are quite similar; T in the fractures is slightly cooler than T in the matrix (compare Figure 8-124, a and Figure 8-125, a). The T distributions in both the matrix and fractures are symmetrical about the heater axis. The S_{liq} distribution in the matrix has a similar shape to that of the T distribution; thus, the S_{liq} distribution in the matrix is symmetrical about the heater axis. The S_{liq} distribution in the fracture is horizontally symmetrical about the heater axis; however, there is strong vertical asymmetry in the S_{liq} distribution in the fractures. The vertical asymmetry results from gravity-driven condensate drainage. Because the DKM represents nonequilibrium fracture-matrix interaction, condensate is able to readily shed around the dry-out zone. The increase in S_{liq} in the fractures is much greater below the heater than above the heater. This agrees qualitatively with the field ERT measurements of S_{liq} change (Section 8.5 of this report) that indicate that the condensation zone primarily forms below the heater; this indicates the importance of gravity-driven condensate drainage for the SHT.

The DKM-model calculations indicate that the cold-trap effect strongly influences the distribution of condensate flux and the formation of the condensate zone. The greatest increase in S_{liq} occurs adjacent to the borehole collar (Figure 8-126, b and Figure 8-132, b). The increase in S_{liq} in the fractures is nearly twice as great next to the borehole collar than it is in the condensate-shedding zone lying immediately below the heater (Figure 8-127, b); the greater S_{liq} increase next to the borehole collar indicates that condensate drainage flux is heavily concentrated in that area. In the matrix, a discernible increase in S_{liq} is seen only in the area adjacent to the borehole collar. The cold-trap effect is also manifested by the strongly elongated T contours between the heater and the borehole collar. These DKM calculations indicate that the cold-trap effect is an important mechanism because it may result in strongly focusing decay-heat-driven seepage flux into cooler intervals of the emplacement drifts and thereby cause condensate to drip onto cooler waste packages.

The DKM model predicts less intensive matrix dry-out (for the region where S_{liq} <0.8) than does the ECM model (compare Figure 8-126, b with Figure 8-122, b, and compare Figure 8-126, b with Figure 8-123, b). Because the ECM assumes equilibrium between the fractures and matrix blocks, there is essentially no resistance to the flow of vapor out of the matrix blocks; thus, there is no gas-phase pressure, P_{gas}, buildup in the matrix blocks (relative to the fractures) that can lead to any throttling of dry-out. Because the DKM represents the disequilibrium between the fractures and matrix blocks, there is P_{gas} buildup in the matrix blocks that tends to throttle dry-out in the matrix blocks. For rock dry-out around emplacement drifts, this throttling behavior is only likely to be significant during the heat-up period, which lasts approximately 30 years for the repository (Buscheck 1996, Section 1.8).

For $S_{liq} > 0.8$, the DKM model predicts a larger spatial extent of rock dry-out than does the ECM model. Thus, the dry-out front extends farther away from the heater in the DKM-model calculations. For DKM-model calculation, the $S_{liq} = 0.9$ contour occurs at a radial distance of 1.45 m from the heater axis (Figure 8-124, b); for the ECM-model calculation, the $S_{liq} = 0.9$ contour occurs at a radial distance of only 1.1 m (Figure 8-124, b). The radial extent of dry-out predicted by the DKM model agrees qualitatively with the neutron-probe measurements of S_{liq} change (see Section 8.6 of this report). The greater spatial extent of rock dry-out (for $S_{liq} > 0.8$) results from the DKM model predicting more effective condensate shedding than that predicted by the ECM model. More effective condensate shedding causes less S_{liq} increase in the matrix, which reduces the rate of rewetting resulting from matrix imbibition. Greater condensate shedding also causes less S_{liq} increase in the fractures, which reduces the rate of rewetting resulting from capillary wicking in the fractures.

8.8.6 Comparison of Predicted and Measured Temperatures

The temporal and spatial evolution of temperatures in the SHT area is a useful indicator of thermal-hydrological behavior during the test. Of particular importance is the ability to use the temperature distribution as an indicator of the extent of rock dry-out. Figure 8-128 compares the predicted temperatures for the four cases with temperatures observed in the field. During the heating stage, the two ECM cases (Cases 1 and 2) predict nearly identical temperatures. During both the heating and cooling stages, the two DKM cases (Cases 3 and 4) predict nearly identical temperatures.

During heating, there are differences in the predicted temperatures between the ECM and DKM cases. In spite of the fact that the ECM model predicts more intense matrix dry-out for the lower liquid-phase saturation S_{liq} range ($S_{liq} < 0.8$) than does the DKM model, the ECM model predicts lower temperatures (compared to the DKM model) in the superheated/dry-out zone. The differences in predicted temperatures arise from two causes. First, the spatial extent of matrix dry-out for the higher liquid-phase saturation range ($S_{liq} > 0.8$) is greater for the DKM model cases, causing superheated/dry-out conditions to extend over a slightly larger region than in the ECM model cases. The second (and probably more significant) cause is the manner in which fracture-matrix interaction is represented in the respective models. Because the DKM model allows P_{gas} in the matrix to increase well above ambient conditions, the saturation temperature (which is the boiling temperature at the local pressure) can increase well above the nominal boiling point (96°C). Thus, the larger temperature increase predicted by the DKM model is primarily facilitated by the elevated P_{gas} in the matrix (whereas the ECM predicts no increase in P_{gas} in the matrix) and is partly facilitated by the greater extent of dry-out in the matrix (for $S_{liq} > 0.8$) predicted by the DKM model.

At thermocouple TMA-TC-1A-9 (Figure 8-128, a), the ECM model underpredicts temperatures by as much as 5° to 10°C during the heating stage, while the DKM model predicts temperatures that are only as much as 1° to 4°C higher than the observed temperatures. At the end of the heating stage (275 days), the DKM-model predicted temperatures are within less than 1°C of most of the measured temperatures along borehole TMA-TC-5 (Figure 8-128, b), while the ECM-model predicted temperatures are as much as 10°C lower than the observed temperatures.

During the cool-down period (Figure 8-128, c), the three cases with the extended western boundary (Cases 1, 3, and 4) predict similar temperatures—all of which are in slightly better agreement with the measured temperatures than are those predicted in Case 2 (which has the western boundary located at the eastern wall of the Thermomechanical Alcove). As discussed in a previous study (Hardin 1998, Section 3.4), placing the western boundary (which is adiabatic above and below the Thermomechanical Alcove) too close to the heated interval tends to underpredict the heat loss to the Thermomechanical Alcove. Because fracture-matrix disequilibrium processes are less important during the cool-down period, the ECM model is nearly as good as the DKM model in predicting temperatures during the cool-down period.

Although Cases 1, 3, and 4 are in somewhat better agreement, than is Case 2, with the observed temperatures during the cool-down period, all of the cases overpredict temperatures in the vicinity of the Thermomechanical Alcove; this overprediction increases as the distance to the Thermomechanical Alcove decreases. The likely cause for this overprediction is the manner in which heat flow is treated in the Thermomechanical Alcove. The contribution of thermal radiation is neglected in the Thermomechanical Alcove. Because thermal-radiative heat transfer is proportional to the difference in T^4 it is a highly efficient mechanism for transferring heat from warmer to cooler surfaces. If thermal radiation from the warmer to cooler wall surfaces in the Thermomechanical Alcove had been accounted for in the SHT models, it is likely that the cooling rate on the eastern Thermomechanical Alcove wall would have been substantially greater. The enhanced cooling rate would lower the temperatures in the rock mass close to the Thermomechanical Alcove. Explicitly incorporating thermal radiation into the thermal-mechanical models would substantially add to the computational requirements of these models, probably making it impossible for them to run on the SUN ULTRA2 workstations that were used in this study.

8.8.7 Summary

The heating and cooling stages of the SHT were modeled with the NUFT code, using the December 1997 TSPA-VA base-case hydrological parameter set, which was modified to include the field measurements of bulk permeability in the SHT area. Two different conceptual models for fracture-matrix interaction were considered: the ECM, which assumes equilibrium between the fracture and matrix continua, and the DKM that accounts for disequilibrium processes between the fracture and matrix continua. For the DKM calculations, two different approaches for representing the FMX were considered: a fixed-FMX approach and a dynamic-FMX approach. For the ECM calculations, two different western boundaries were considered: one that placed the western boundary at the eastern wall of the Thermomechanical Alcove and one that placed the western boundary 33 m to the west of the western wall of the thermal-mechanical boundary. Unlike earlier thermal-mechanical models of the SHT, all of the models in this study included the influence of vapor and heat flow along the heater borehole. This modeling study resulted in the following observations and conclusions:

- The DKM predicts higher temperatures in the dry-out zone close to the heater, which underwent the greater rise in temperature, than does the ECM model, primarily because the DKM model predicts a substantial gas-phase pressure, P_{gas}, increase in the matrix blocks, whereas the ECM model assumes P_{gas} equilibrium between the matrix and

adjoining fractures. The P_{gas} increase predicted by the DKM model causes the saturated temperature T_{sat} (which is the boiling temperature at the local pressure) to increase well above the nominal boiling point (96°C).

- The DKM model predicts temperatures that are in outstanding agreement with the observed temperatures throughout the heating stage of the SHT.

- The ECM model predicts temperatures that are in good agreement with the observed temperatures in the sub-boiling region of the SHT during the heating stage. In the superheated dry-out zone, the ECM model predicts temperatures that are lower than the observed temperatures during the heating stage.

- For the DKM model, the predicted radial extent of the dry-out zone is in good, qualitative agreement with the neutron-probe measurements of liquid-phase saturation change. For the ECM model, the radial extent of the dry-out zone is less than that predicted by the DKM model (and is somewhat less than that indicated by the neutron-probe measurements).

- The DKM model predicts a condensate-shedding zone that is to the sides and below the dry-out zone, which is qualitatively consistent with the measurements of liquid-phase saturation change made with ERT.

- The ECM model predicts a pronounced condensation zone that is vertically symmetrical about the heater axis; this is inconsistent with the measurements of liquid-phase saturation change made with ERT.

- For the lower liquid-phase saturation S_{liq} range ($S_{liq} < 0.8$), the DKM model predicts less dry-out in the matrix than is predicted by the ECM model. The DKM model accounts for flow resistance in the matrix blocks (as vapor is driven out of the matrix into the adjoining fractures), thereby throttling dry-out in the matrix. The ECM model neglects this flow resistance; thus, the ECM model does not throttle matrix dry-out.

- For the higher S_{liq} range ($S_{liq} > 0.8$), the DKM model predicts greater dry-out in the matrix than is predicted by the ECM model. The DKM model accounts for how nonequilibrium, fracture-matrix interaction facilitates more effective condensate shedding around the dry-out zone than does the ECM model. More effective condensate shedding causes less S_{liq} increase in the matrix, which reduces the rate of rewetting arising from matrix imbibition, and less S_{liq} increase in the fractures, which reduces the rate of rewetting arising from capillary wicking in the fractures.

- The SHT is not a useful test for diagnosing the magnitude of percolation flux q_{perc}. The lack of sensitivity of the SHT to q_{perc} arises from the heat-driven condensate fluxes being much greater than any of the values of q_{perc} that were considered.

- The SHT cannot distinguish between alternative conceptual models of the FMX factor. Both approaches result in the same outstanding agreement with observed temperatures, and both approaches predict the same distribution of S_{liq} in the matrix continua.

- Both the ECM and DKM models predict a pronounced cold-trap effect in the heater borehole. Vapor and latent-heat flow from the heated interval of the heater borehole to the cool end of the heater borehole adjacent to its collar, where the vapor condenses, resulting in focused condensate drainage and a local increase in S_{liq} in the matrix. The cold-trap effect efficiently transfers heat along the heater borehole toward the Thermomechanical Alcove. The cold-trap effect is a potentially important mechanism influencing thermal-hydrological behavior in emplacement drifts.

- The models with an extended western boundary predict temperatures that are in better agreement with the observed temperatures than are those predicted by the model with the western boundary located at the eastern wall of the Thermomechanical Alcove.

- All of the models underrepresent the heat loss to the Thermomechanical Alcove, resulting in predicted temperatures being greater than the observed temperatures in the vicinity of the Thermomechanical Alcove; this overprediction increases as the distance to the Thermomechanical Alcove decreases. The cause for this overprediction is the manner in which heat flow in the Thermomechanical Alcove is treated. Had thermal radiation from the warmer to cooler wall surfaces in the Thermomechanical Alcove been accounted for in the SHT models, the cooling rate on the eastern Thermomechanical Alcove wall would have been much greater, resulting in lower predicted temperatures in the vicinity of the Thermomechanical Alcove.

8.9 SUMMARY

The SHT is the first of two in situ thermal tests included in the site characterization program for the potential underground nuclear waste repository at Yucca Mountain. The extensive data available from this test provide a unique opportunity to improve understanding of the thermal-hydrological processes in the natural setting of the repository rocks and validate conceptual and numerical model. The SHT was predicted using a three-dimensional numerical model of the fractured tuff in the heater vicinity, and compared the simulation results were compared to field data. The fractured rock is modeled by the dual-permeability scheme, assuming a continuum behavior in fractures and rock matrix. As much as possible, site-specific thermal and hydrological data have been used as input parameters. The model has not been calibrated to measured SHT data in order to derive a "best-fit" property set.

A very good agreement was obtained between the measured and predicted temperature data, showing that the thermal-hydrological response in the SHT is well represented by the numerical model. Both the measured and predicted temperatures suggest that while heat is mainly transported by conduction, the contribution from thermal-hydrological coupling is also important. Overall, the signature of convective transport due to heat-induced vapor and liquid fluxes is very subtle, indicating that the hydrological properties of the matrix and fractures in the SHT are such that they do not promote significant vapor-liquid counterflow during the heating phase. Detailed

analysis of the measured and modeled temperature data indicates that the average model error over all gages is in the range of a few degrees centigrade. If conduction-only calculations were used, the discrepancies between modeled and measured temperatures are of the order of 10°C (CRWMS M&O 1997b, Figures 6-16 and 6-18; Tsang and Birkholzer 1997, Figures 3-10 and 3-11). Slight discrepancies occurring at certain temperature gages may be in part attributed to local heterogeneity, which is not accounted for in the model. Conduction only modeling predicts temperatures adequately, but not moisture saturation.

Qualitatively, the model results show good agreement with field measurements of moisture redistribution in the rock mass. In the heating phase, the model predicts a dry-out zone of about 1.2 m extent close to the heater, and a condensation zone further away with strong increase in fracture saturation, which gives rise to significant gravity drainage through the fractures. The predicted matrix saturation increases only slightly in the condensation zone, since most of the condensate drains away before it is imbibed into matrix pores. During cooling, the dynamic nature of moisture redistribution becomes less pronounced, and very slow rewetting of the dry-out regions occurs. Field data from air injection tests, radar tomography, and post-heating core analyses are consistent with these model findings: during heating, the increase of fracture saturation due to condensation is evidenced by a significant reduction in air permeability. Radar tomography data, supported by analysis on rock samples, show a dry-out zone developing close to the heater and a zone of slightly increased matrix liquid saturation further away. They also show that the moisture content in the matrix is larger below the heater than above, suggesting that gravity drainage through the fractures is present during the heating phase. Measurements of core moisture content conducted after 7 months of cooling give saturation values of 10 percent to 30 percent in the dry-out zone, supporting the model results of a very slow rewetting after the heater has been turned off.

A sensitivity study was carried out to gain a better understanding of how the coupled thermal-hydrological processes in the repository formation are affected by rock properties and model conceptualization. Results of the sensitivity study provide constraints on key hydrological parameters of the fractured rock mass, namely on permeability and capillarity values in the fractured rock. In particular, property sets with high matrix permeability, and strong capillarity in the fractures and the matrix, cannot realistically represent the SHT thermal-hydrological situation. Other parameters, such as the ambient percolation flux, have only limited impact on measured temperature, and thus cannot be constrained by comparing model results with the measured data. Studies performed using the ECM conceptualization of the fractured rock show that this simple fracture-matrix interaction concept does not accurately represent the thermal-hydrological situation in the SHT. The ECM scheme underestimates gravity drainage in the fractures and overpredicts effects of vapor-liquid counterflow, giving rise to a less accurate simulation of the temperature field.

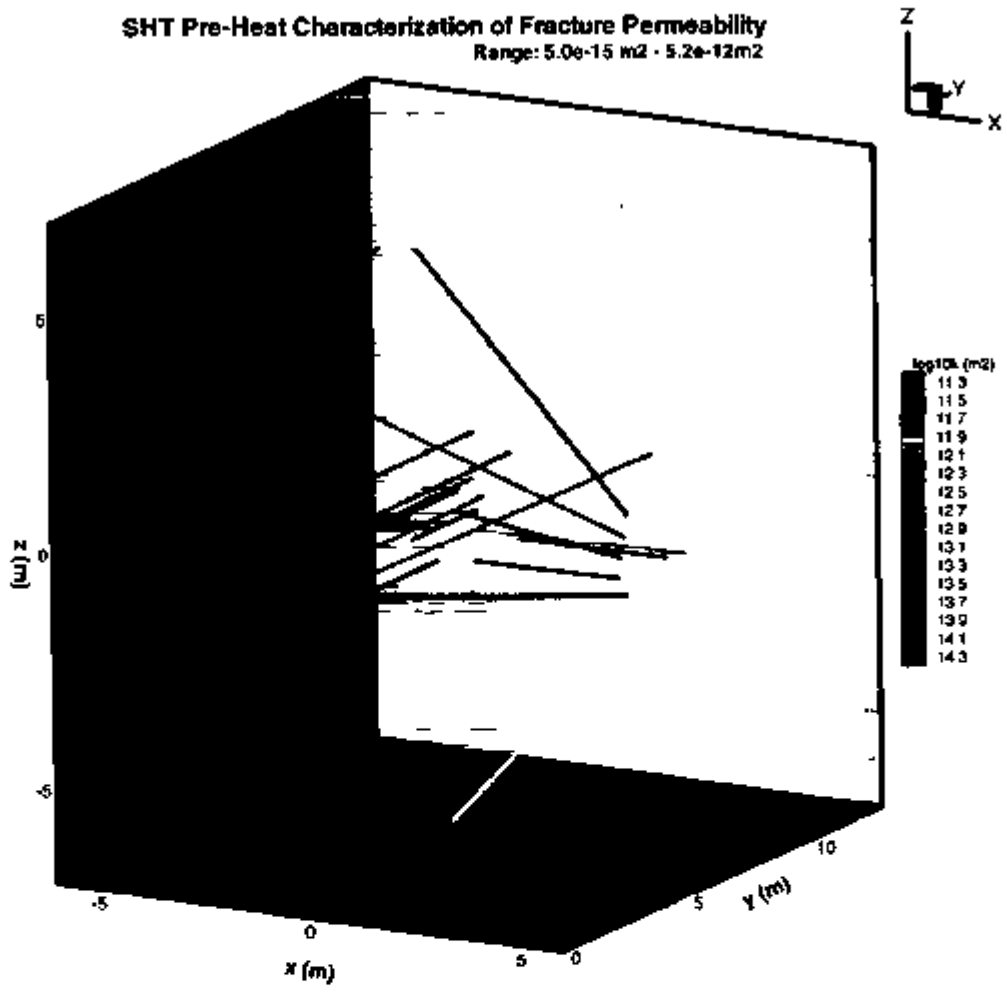

Figure 8-1. Pretest Estimated Air Permeability Values Associated with the 21 Boreholes in the SHT

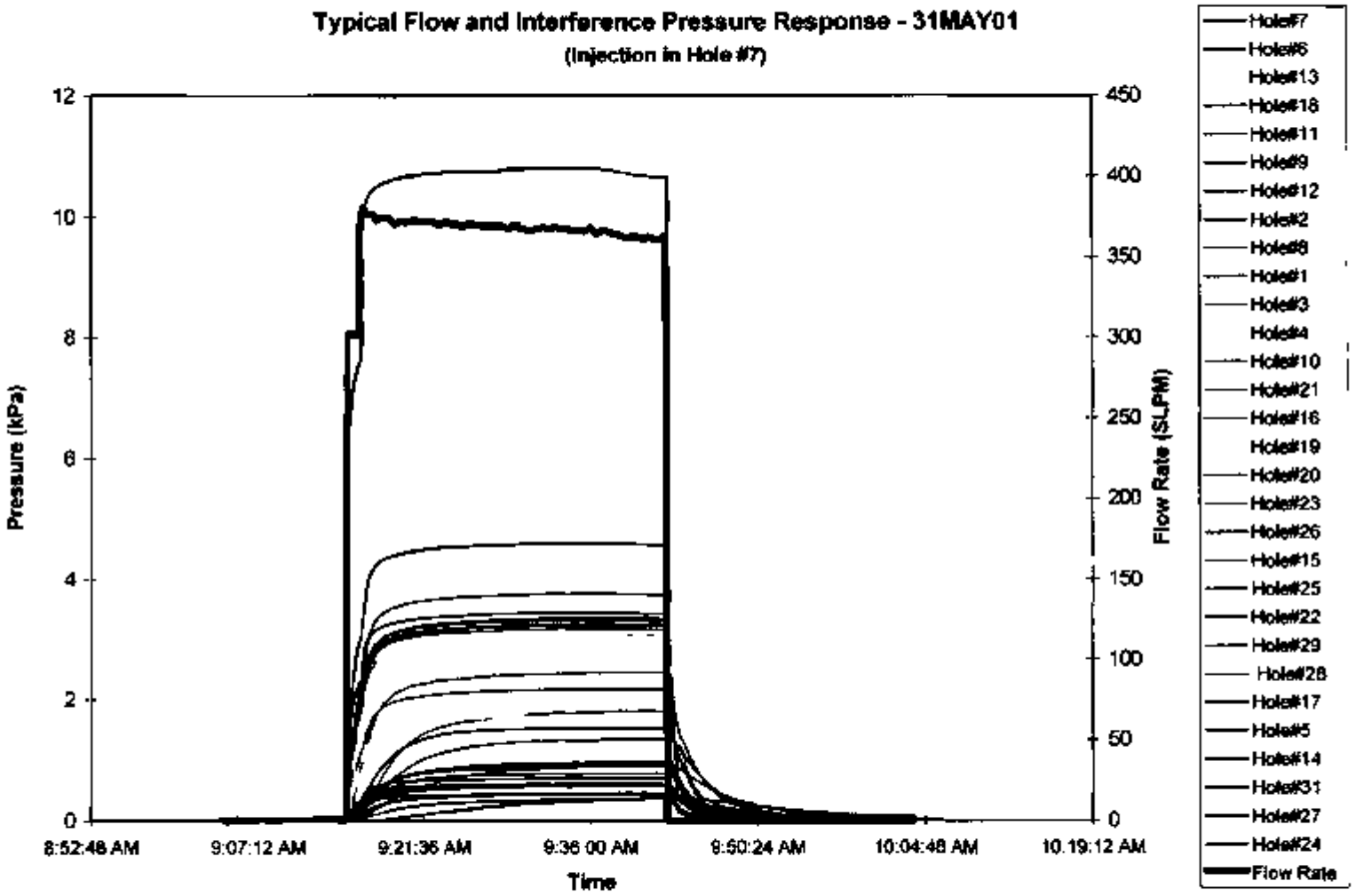

Figure 8-2. Flow and Interference Pressure Responses of a Typical Air Injection Test Performed in the Pretest Characterization

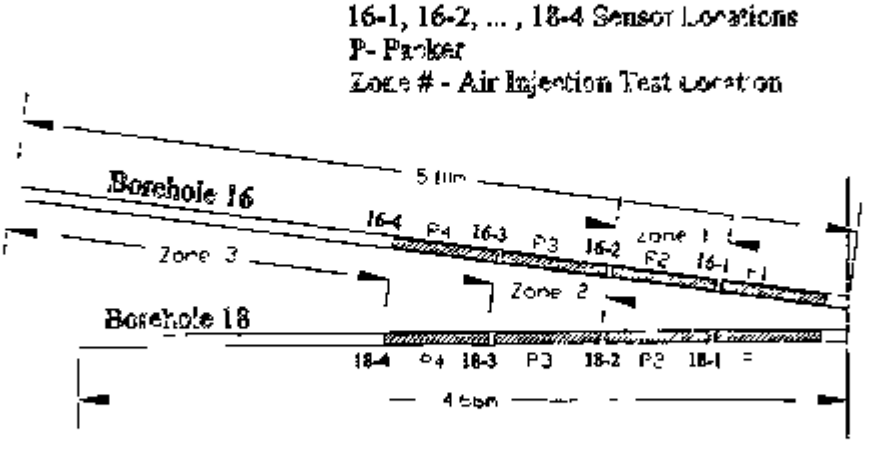

Figure 8-3 Geometry of the Instrumentation and Air Injection Zones in Boreholes 16 and 18

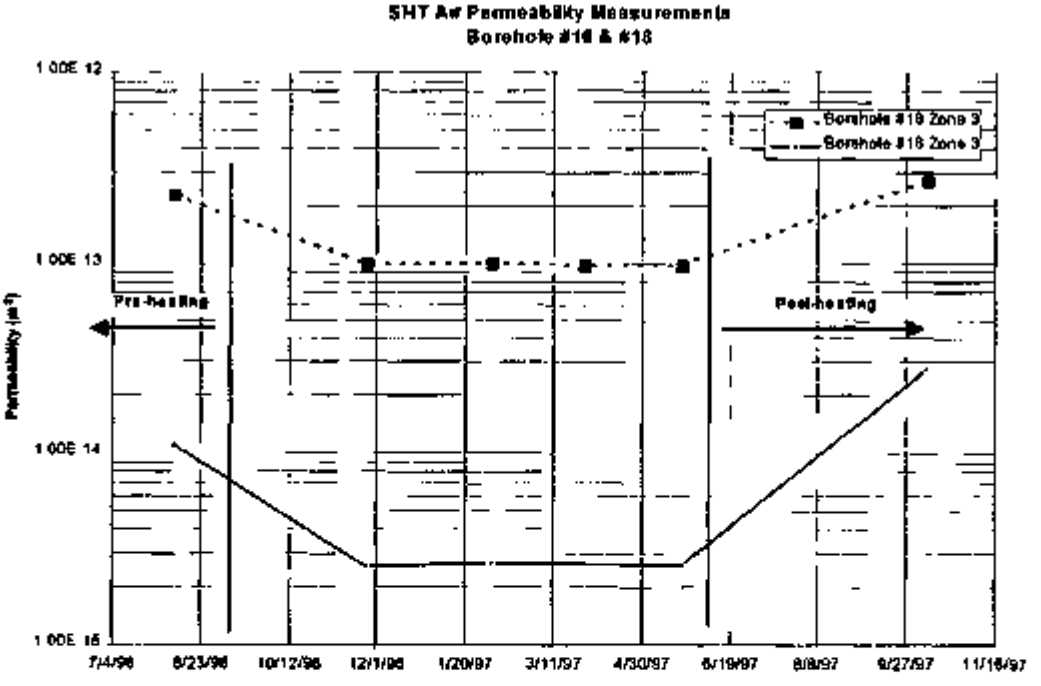

Figure 8-4 Changes in Air Permeability Values for Injection Zone 3 in Boreholes 16 and 18

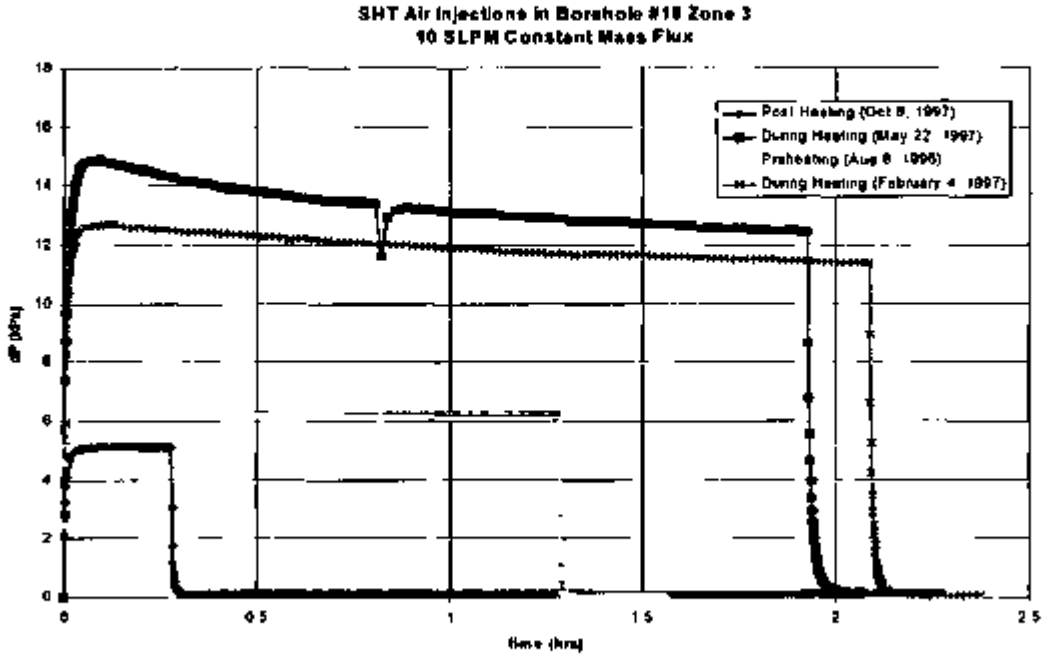

NOTE Before and after the heating phase of the SHT, air injection quickly reaches a steady state pressure. During heating, the large amount of condensate present creates a transient, two-phase system which reduces permeability

Figure 8-5. Pressure Transients for the Air Injection Tests Conducted in Borehole 18, Injection Zone 3

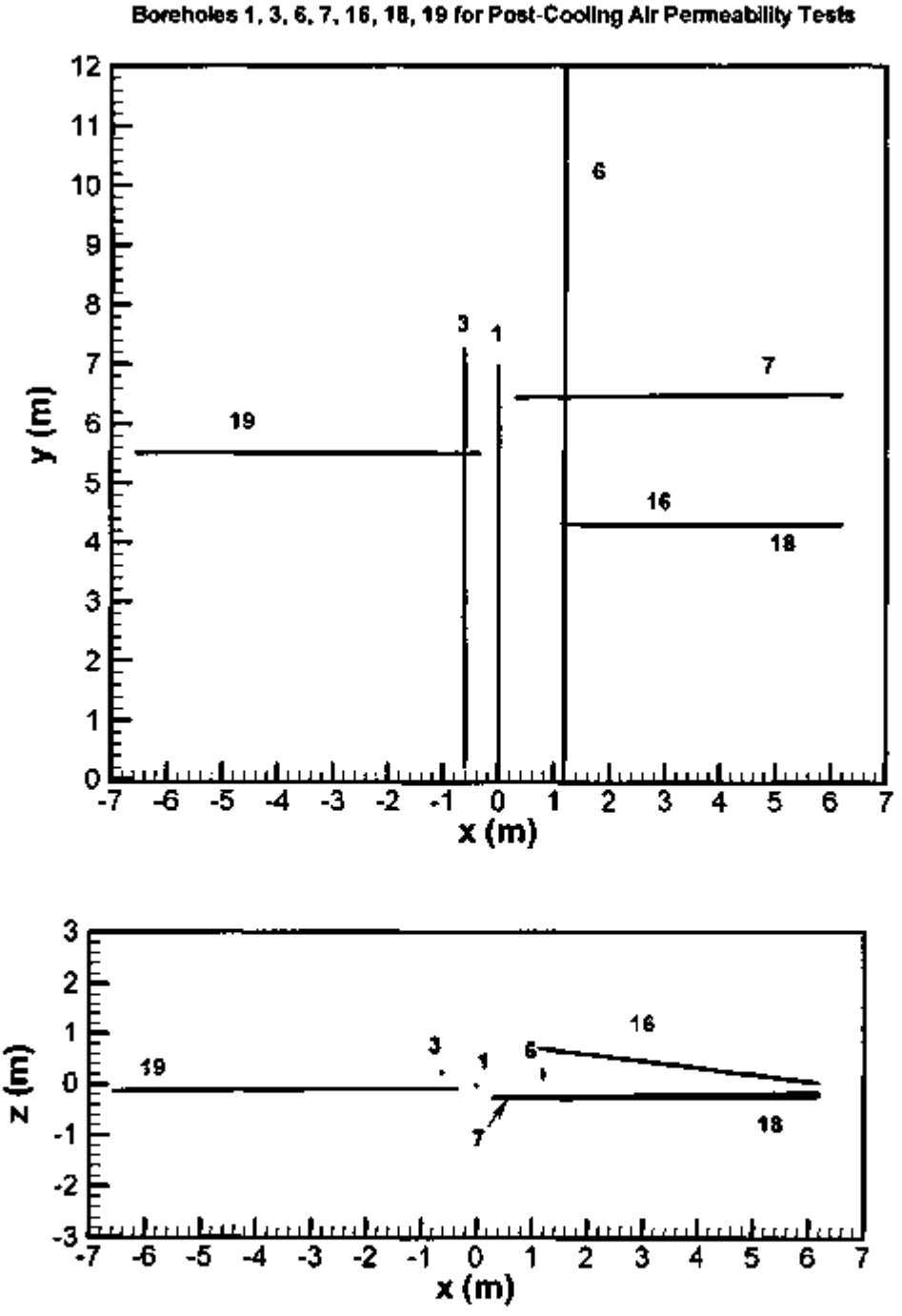

Figure 8-6. Subset of SHT Boreholes Available for Post-Cooling Air Permeability Measurements

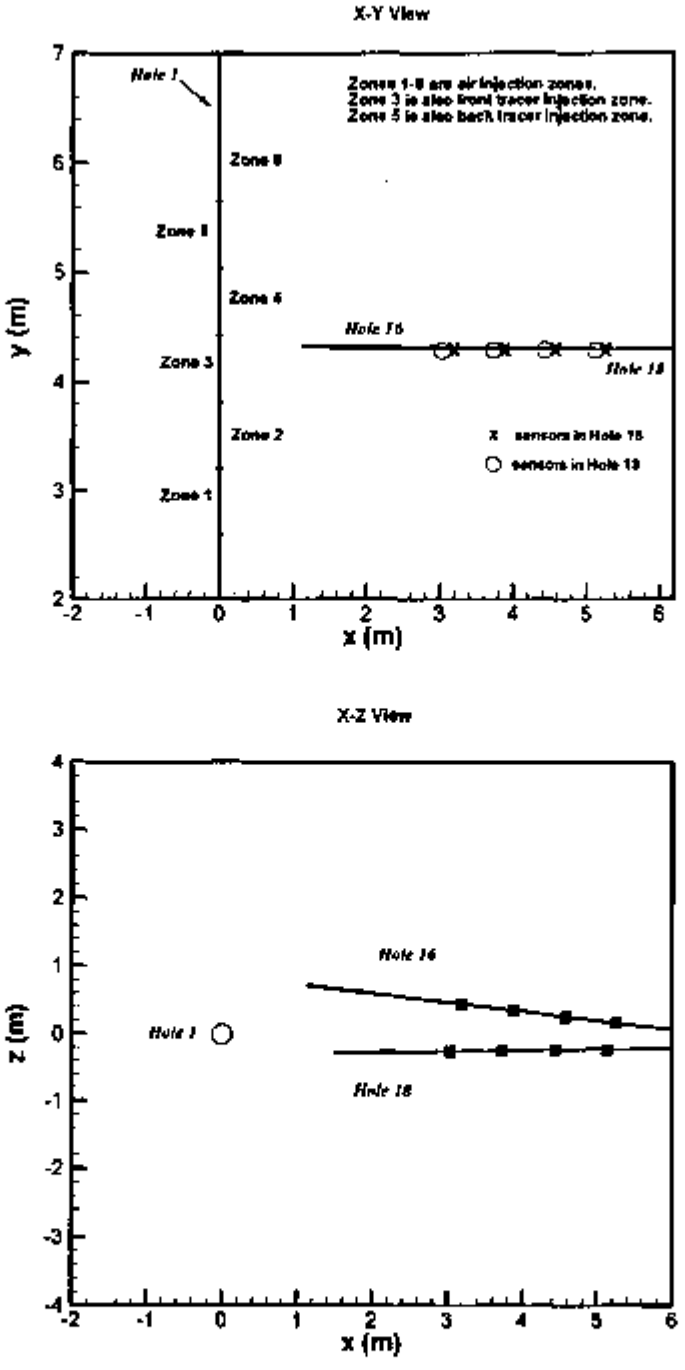

Figure 8-7. Multi-Zone Configuration of Borehole 1, and Boreholes 16 and 18 for Post-Cooling Air Injection Tests

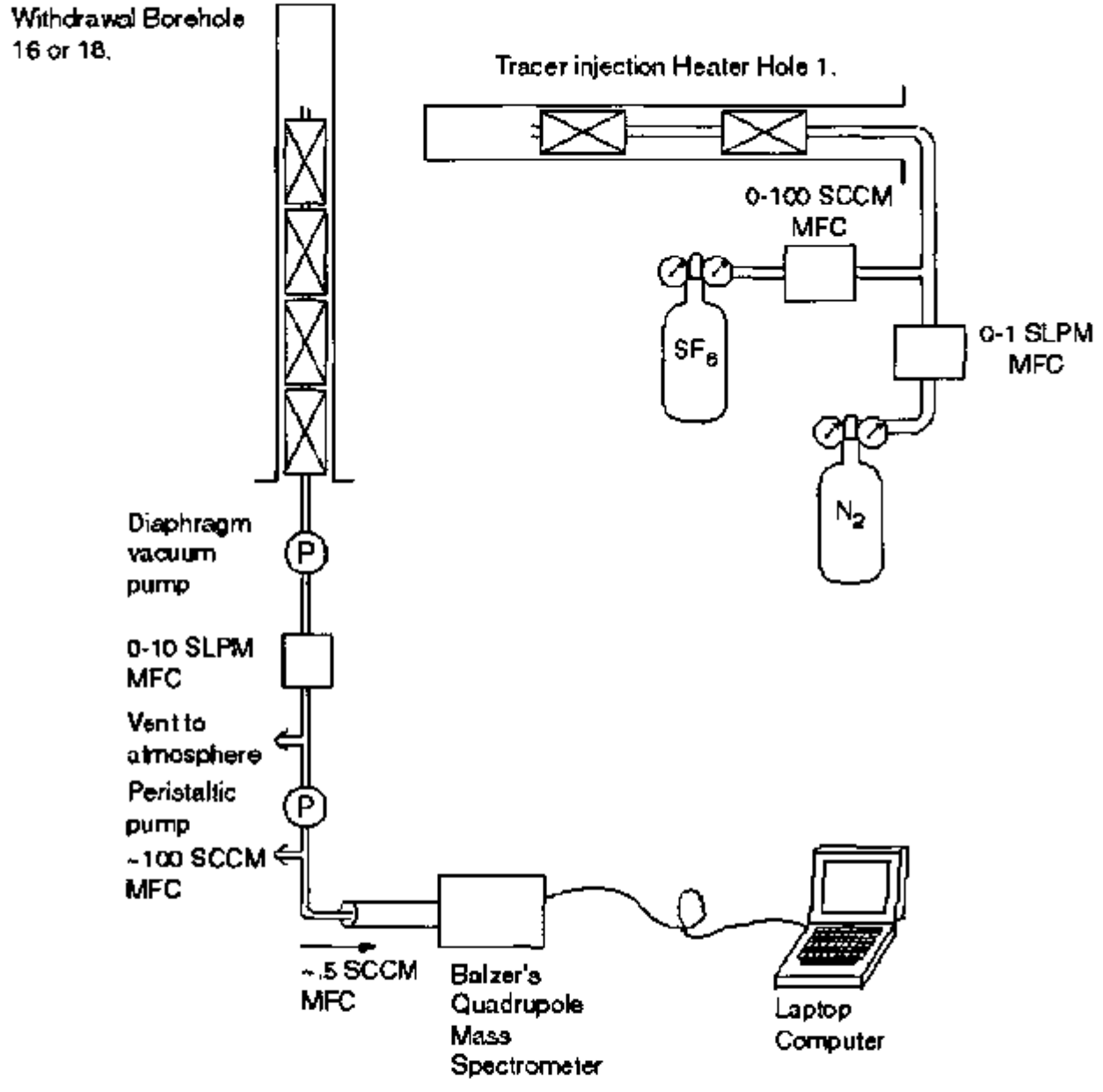

Figure 8-8. A Schematic Drawing of the Equipment Used for Conducting Tracer Tests in Boreholes 1, 16, and 18

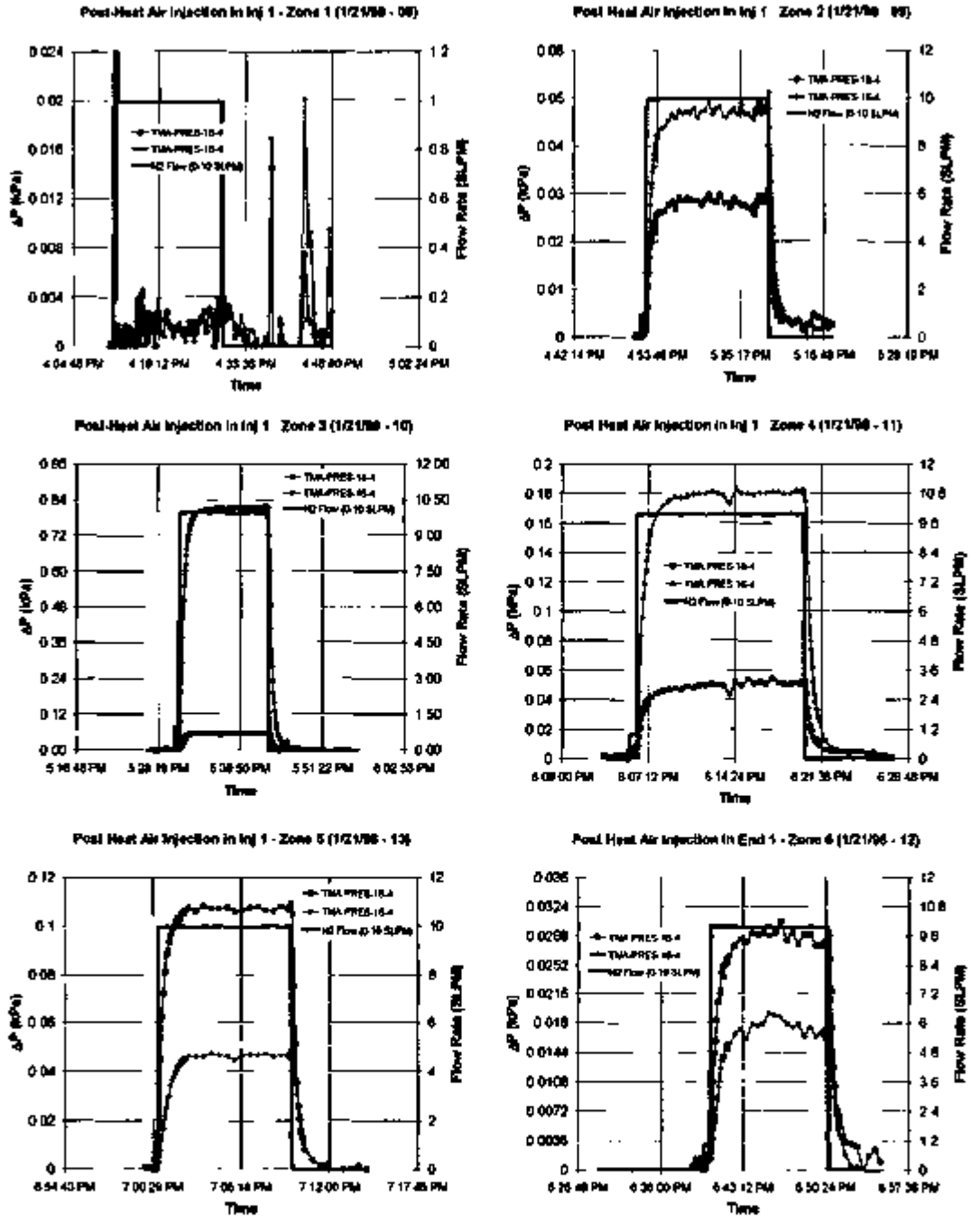

Figure 8-9. Response in Pressure Sensor 4 in Zone 3 of Boreholes 16 and 18 to Injection in Consecutive Isolated Sections in Borehole 1

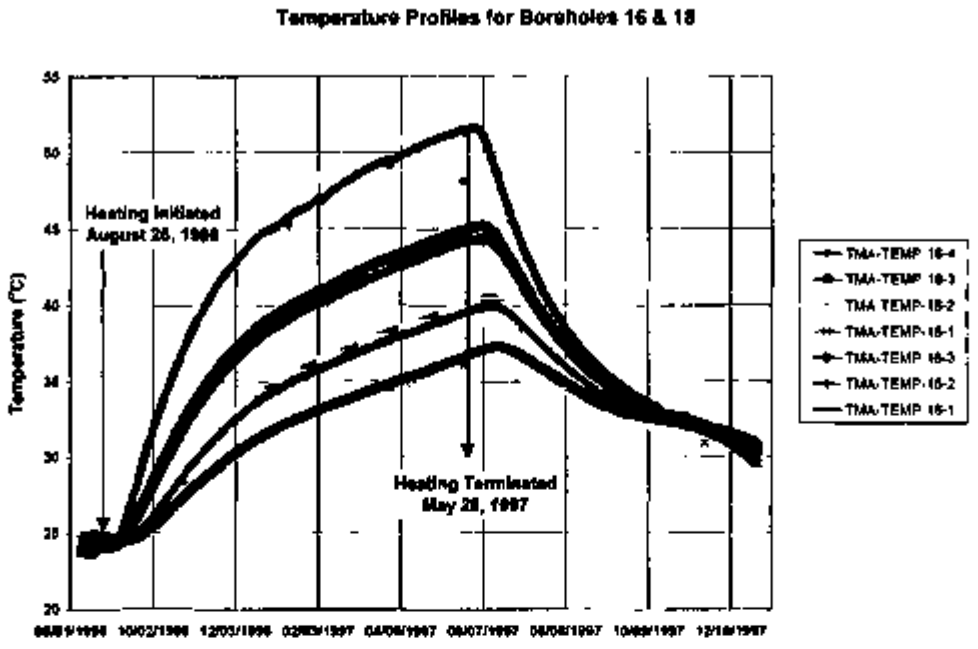

Figure 8-10. Passive Monitoring Temperature Data in Boreholes 16 and 18

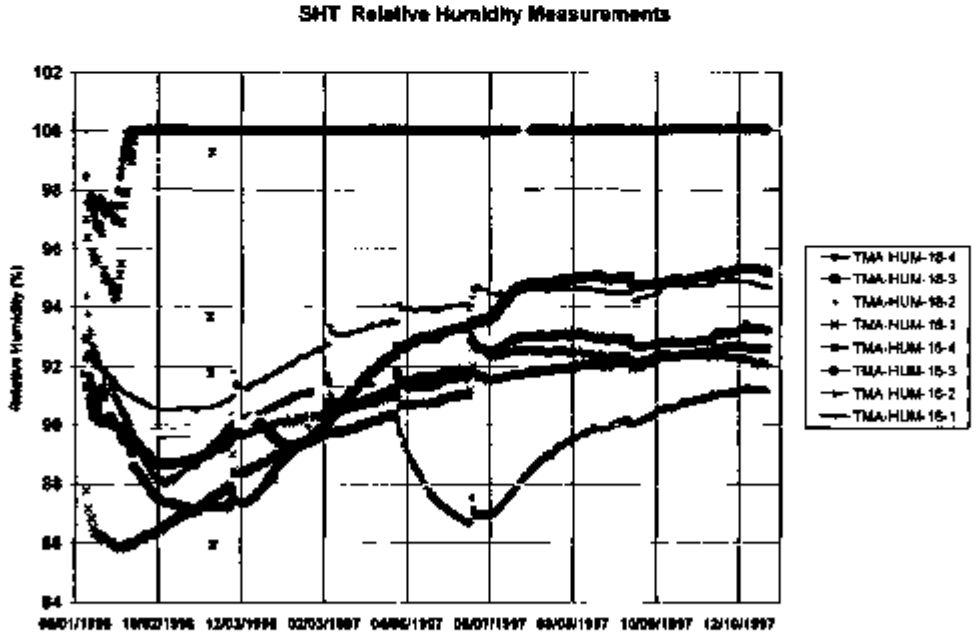

Figure 8-11. Passive Monitoring Relative Humidity Data in Boreholes 16 and 18

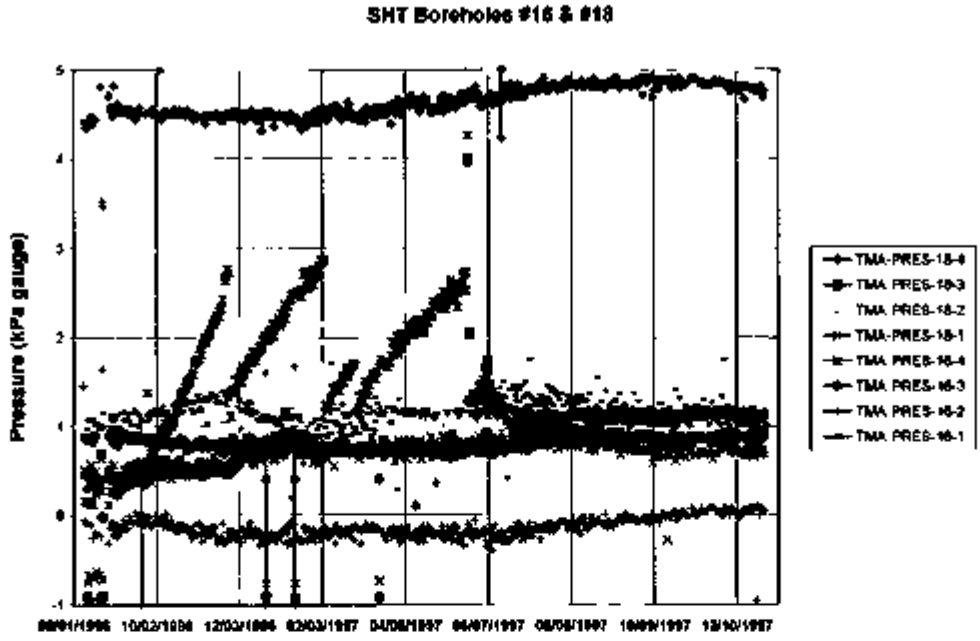

Figure 8-12. Passive Monitoring Pressure Data in Boreholes 16 and 18

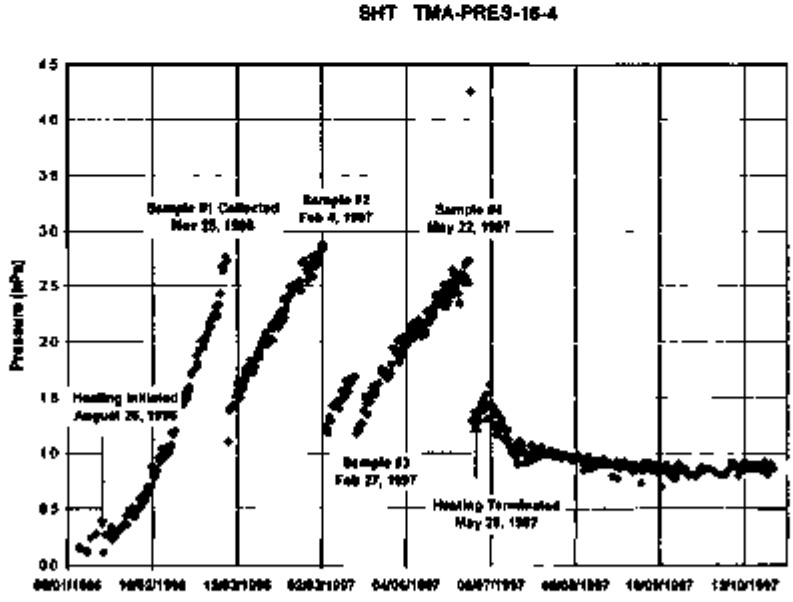

Figure 8-13. Passive Monitoring Pressure Data from Sensor 16-4 in Borehole 16

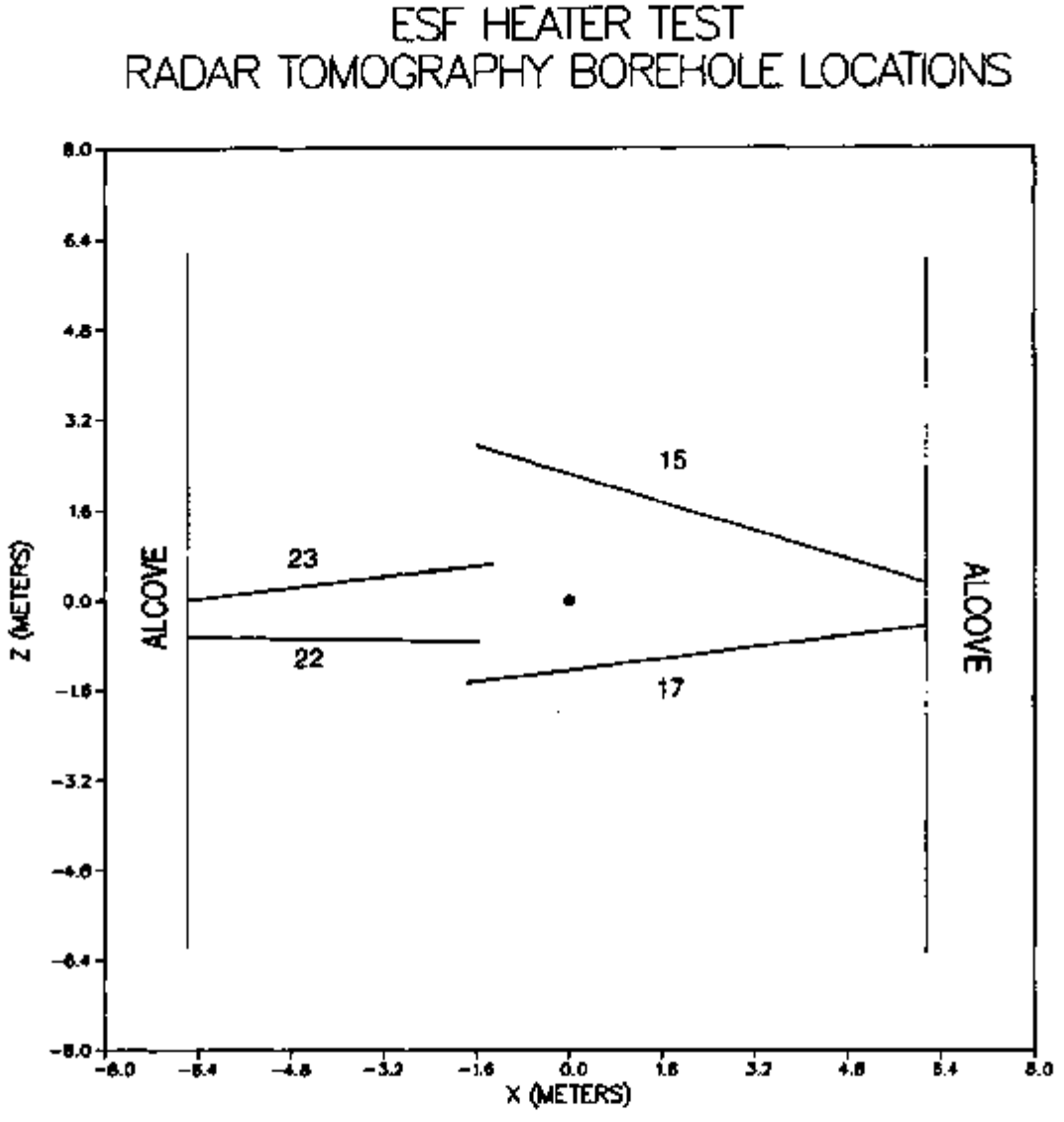

NOTE: The heater well is located at (0,0,0)

Figure 8-14. The Geometry of the Boreholes Used for Crosswell Radar

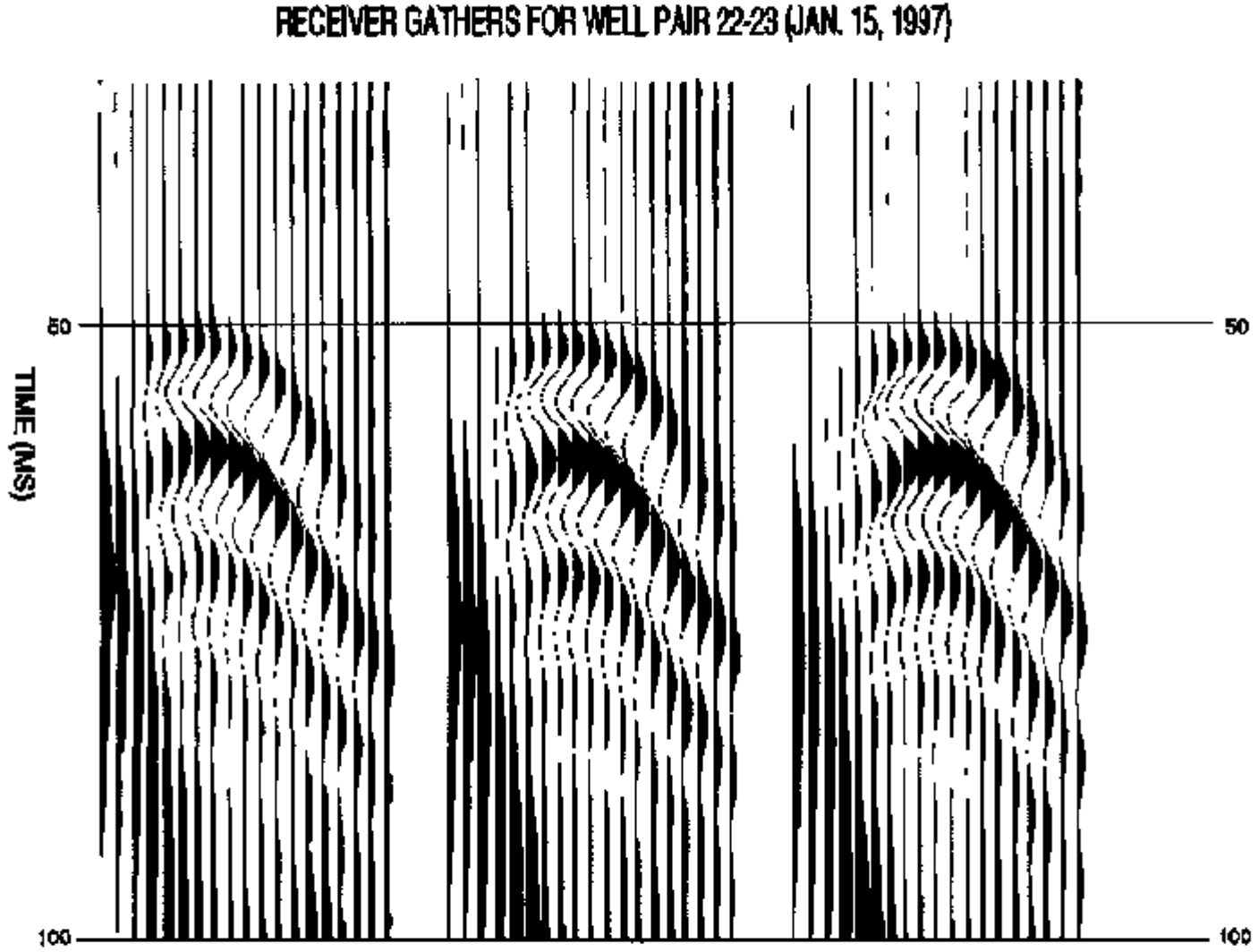

NOTE Shown are gathers for receivers at 1 49 m, 1 74 m, and 1 98 m down borehole 23

Figure 8-15 Three Typical Receiver Gathers for Borehole Pair 22-23

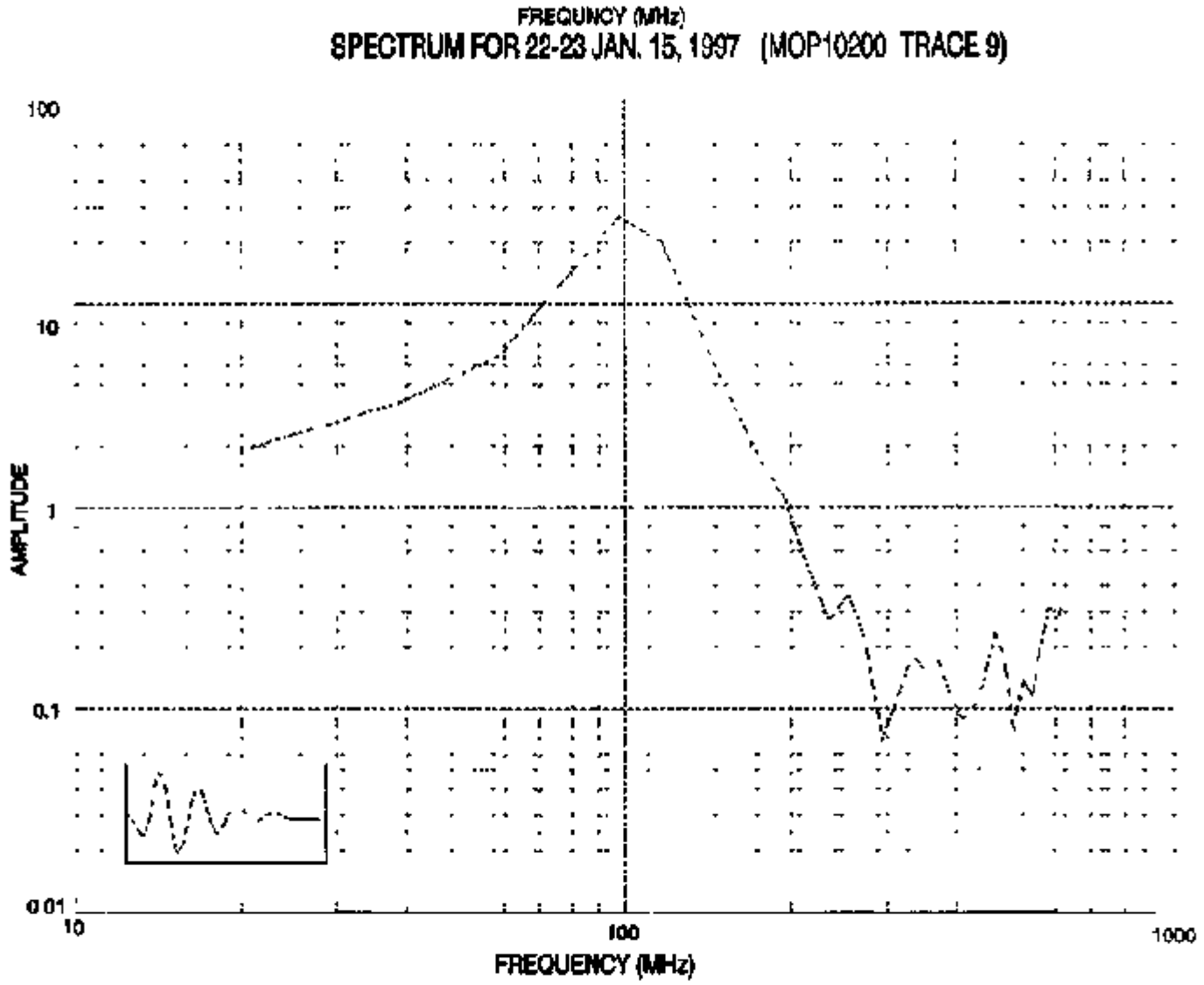

Figure 8-16 Frequency Spectrum for Trace Number 9 in MOP10200, when the Receiver is 2 0 m Down Borehole 23

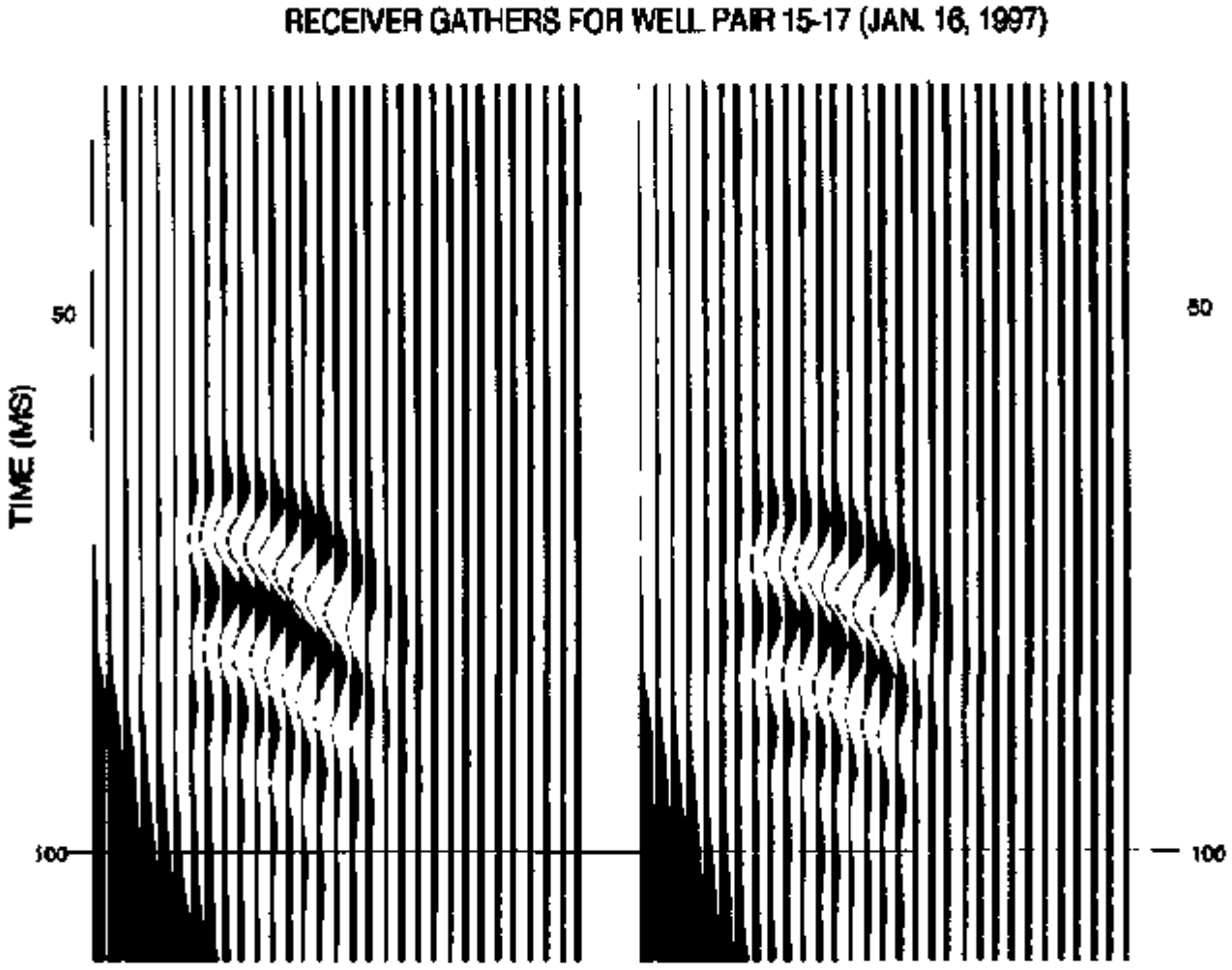

NOTE: Shown are gathers for receivers 2.37 m and 2.61 m down borehole 15.

Figure 8-17. Two Typical Receiver Gathers for the 17-15 Borehole Pair

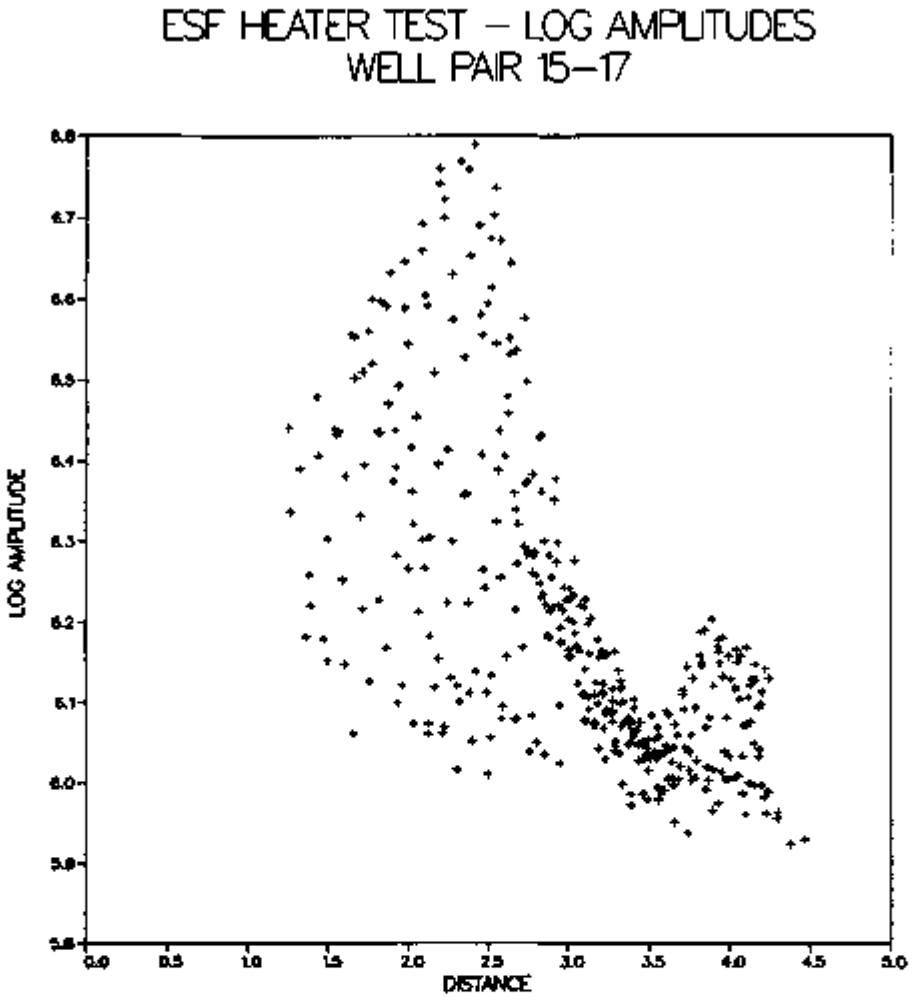

NOTE: The amplitudes are RMS values of the first 20 samples after the picked sample.

Figure 8-18. The Log Amplitudes of All Traces with Picked Travel Time for Borehole Pair 17-15

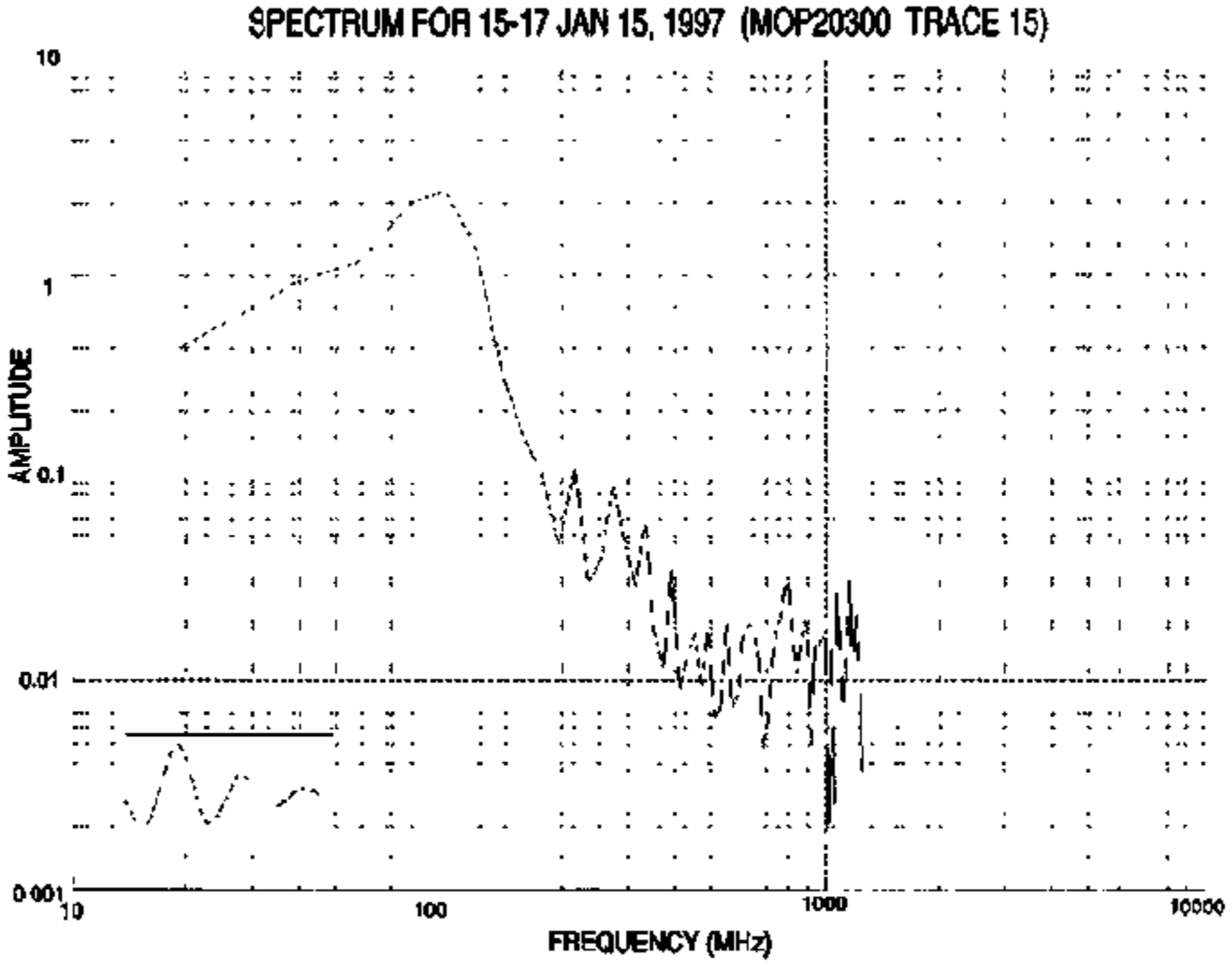

Figure 8-19 Frequency Spectrum for Trace Number 15 in MOP20300, when the Receiver is 3 0 m Down Borehole 15

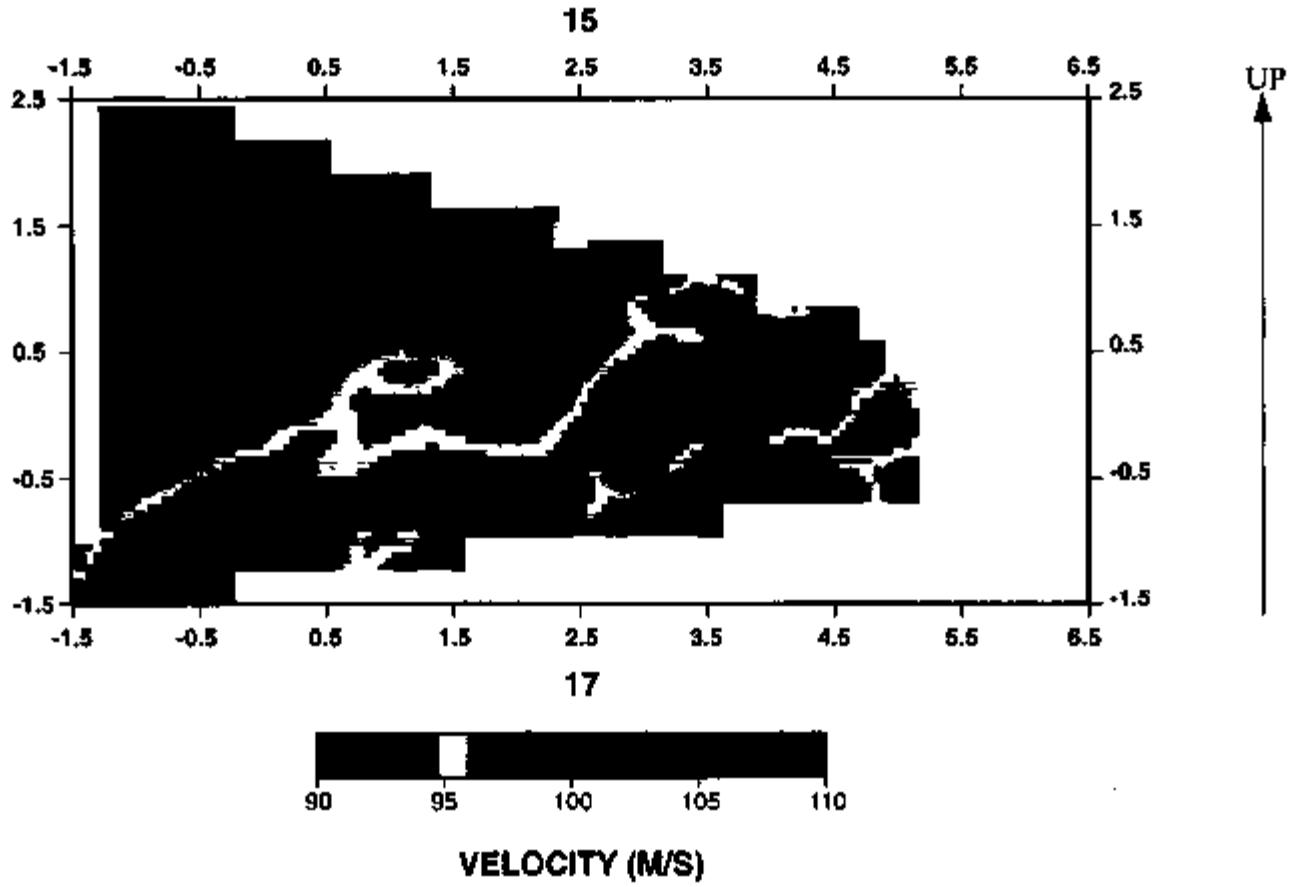

NOTE: See Figure 7-2 Cross Section (b) (p. 7F-2) for locations of boreholes 15 and 17. The black dot indicates the heater borehole (0,0). Axes indicate distance from the heater borehole in meters.

Figure 8-20. Baseline Radar Velocity Tomogram for Borehole Pair 17-15

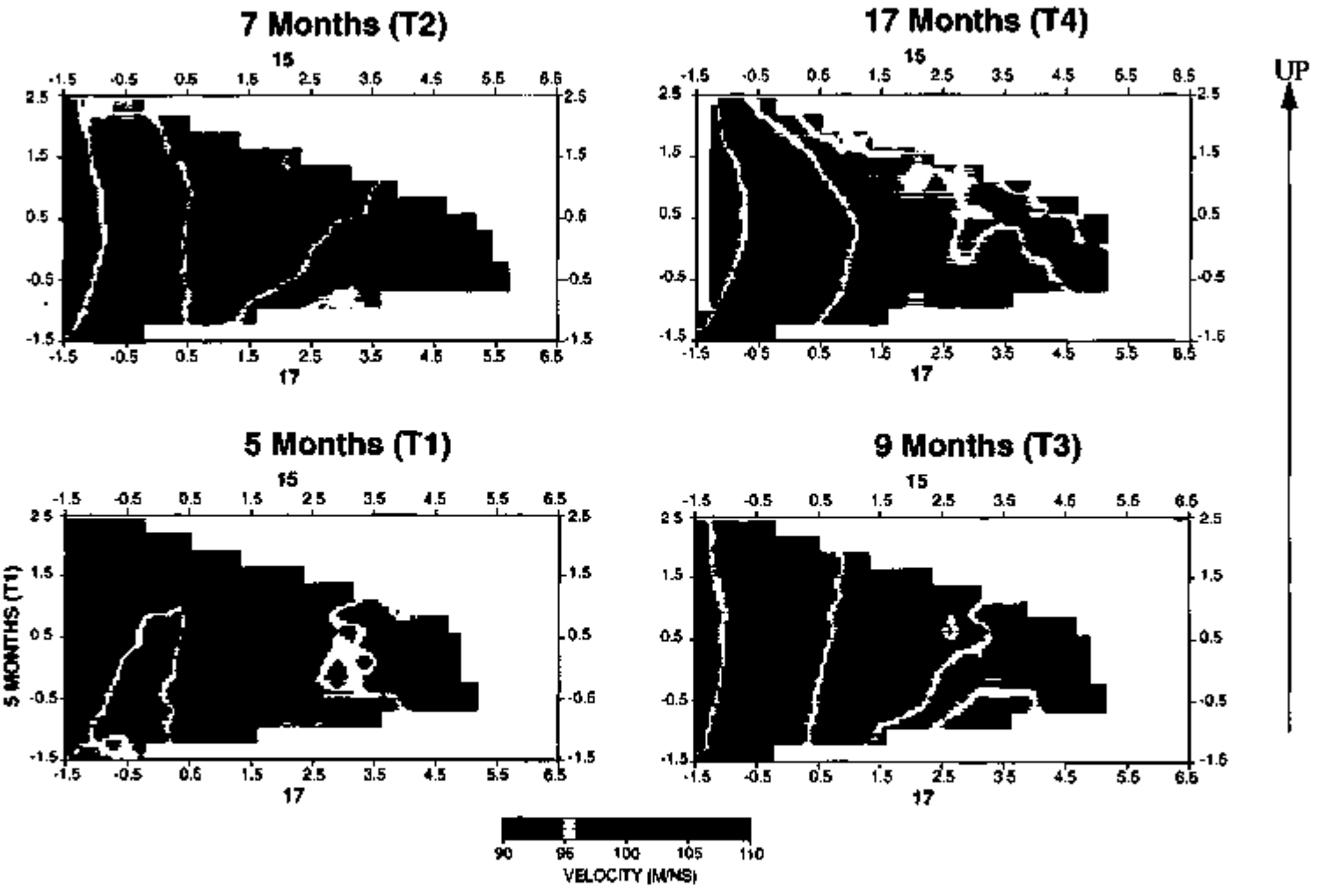

NOTE: See Figure 7-2 Cross Section (b) (p. 7F-2) for locations of boreholes 15 and 17. The black dot indicates the heater borehole (0,0). Axes indicate distance from the heater borehole in meters.

Figure 8-21. Velocity Tomograms for Borehole Pair 17-15 during (at 5, 7, and 9 months) and after (at 17 months) Heating

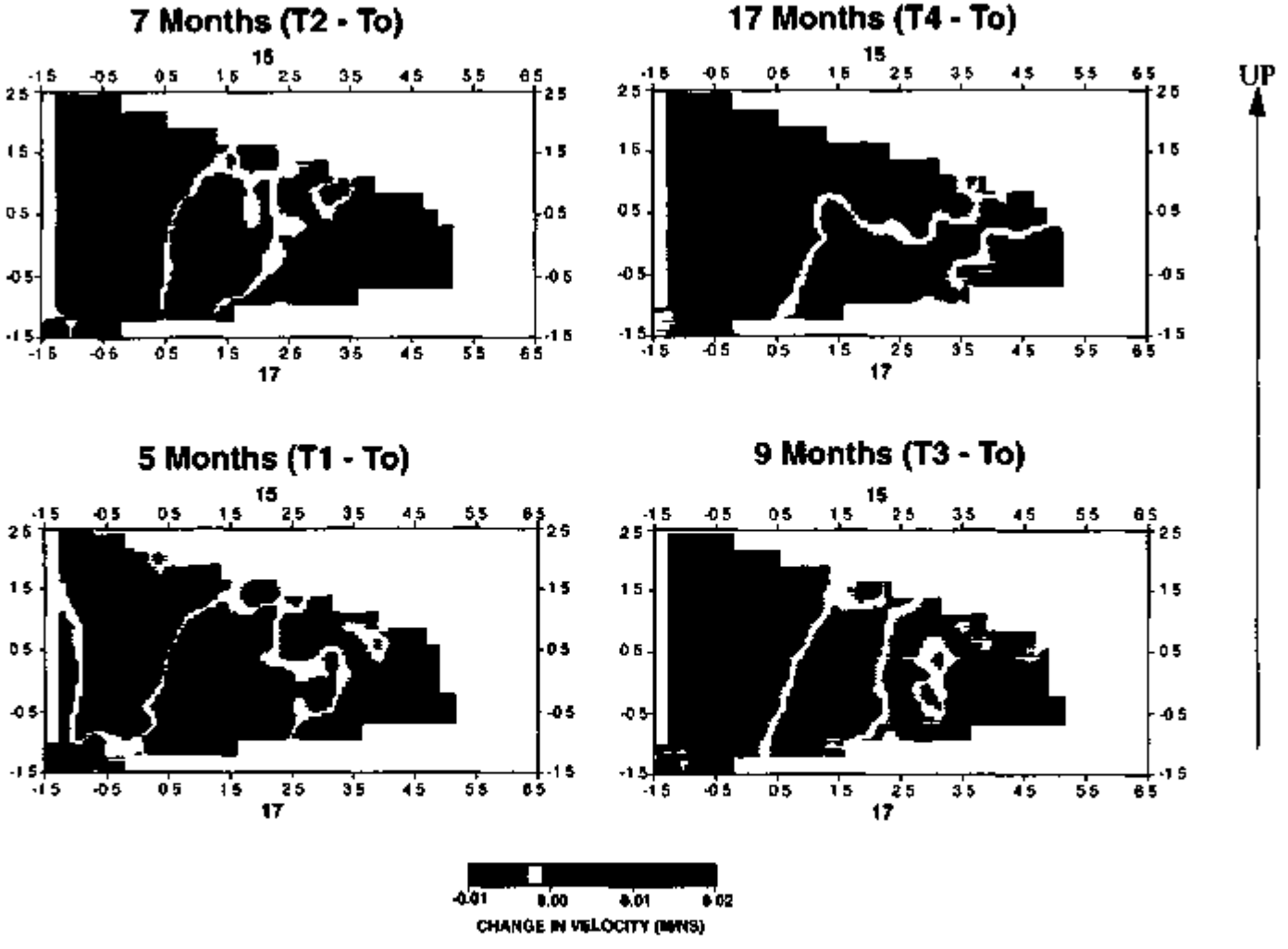

NOTE See Figure 7-2 Cross Section (b) (p 7F-2) for locations of boreholes 15 and 17 The black dot indicates the heater borehole (0,0) Axes indicate distance from the heater borehole in meters

Figure 8-22. Change in Velocity during the Heater Test for Borehole Pair 17-15

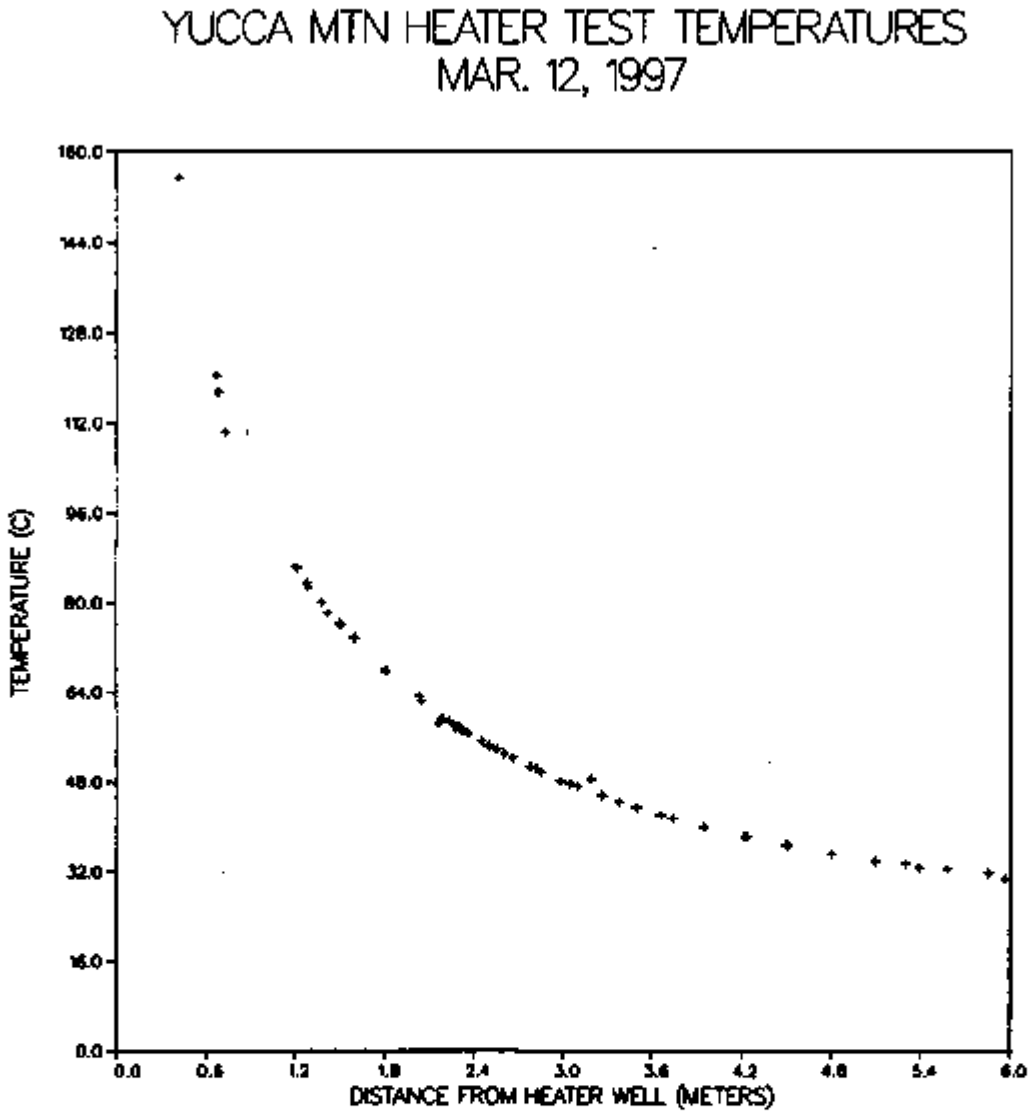

Figure 8-23. Temperature Measurements with respect to Distance from Heater in the Plane of the Tomograms, Used to Estimate Temperature Profile

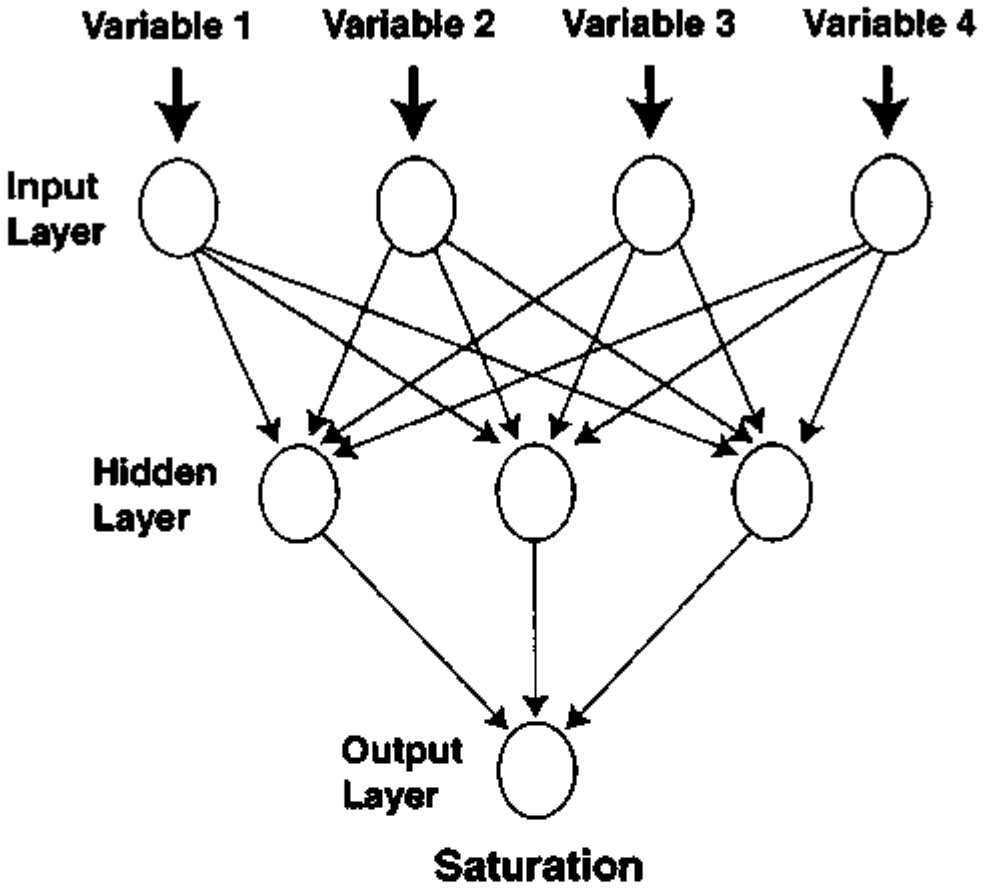

Figure 8-24. Neural Net Methodology Flowchart

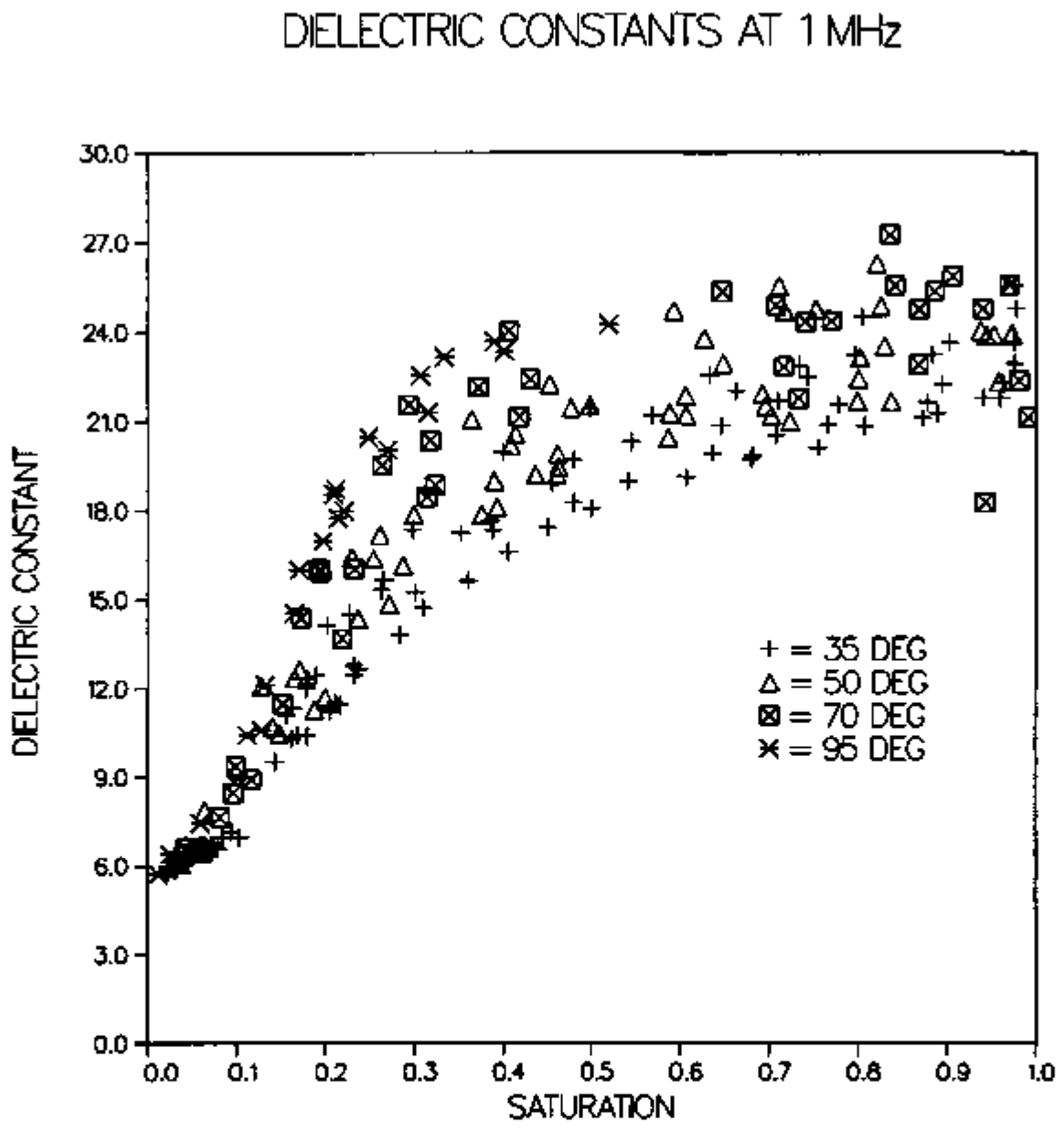

Figure 8-25. Laboratory Measurements of Dielectric Constant at Various Saturations and Temperatures at a Frequency of 1 MHz

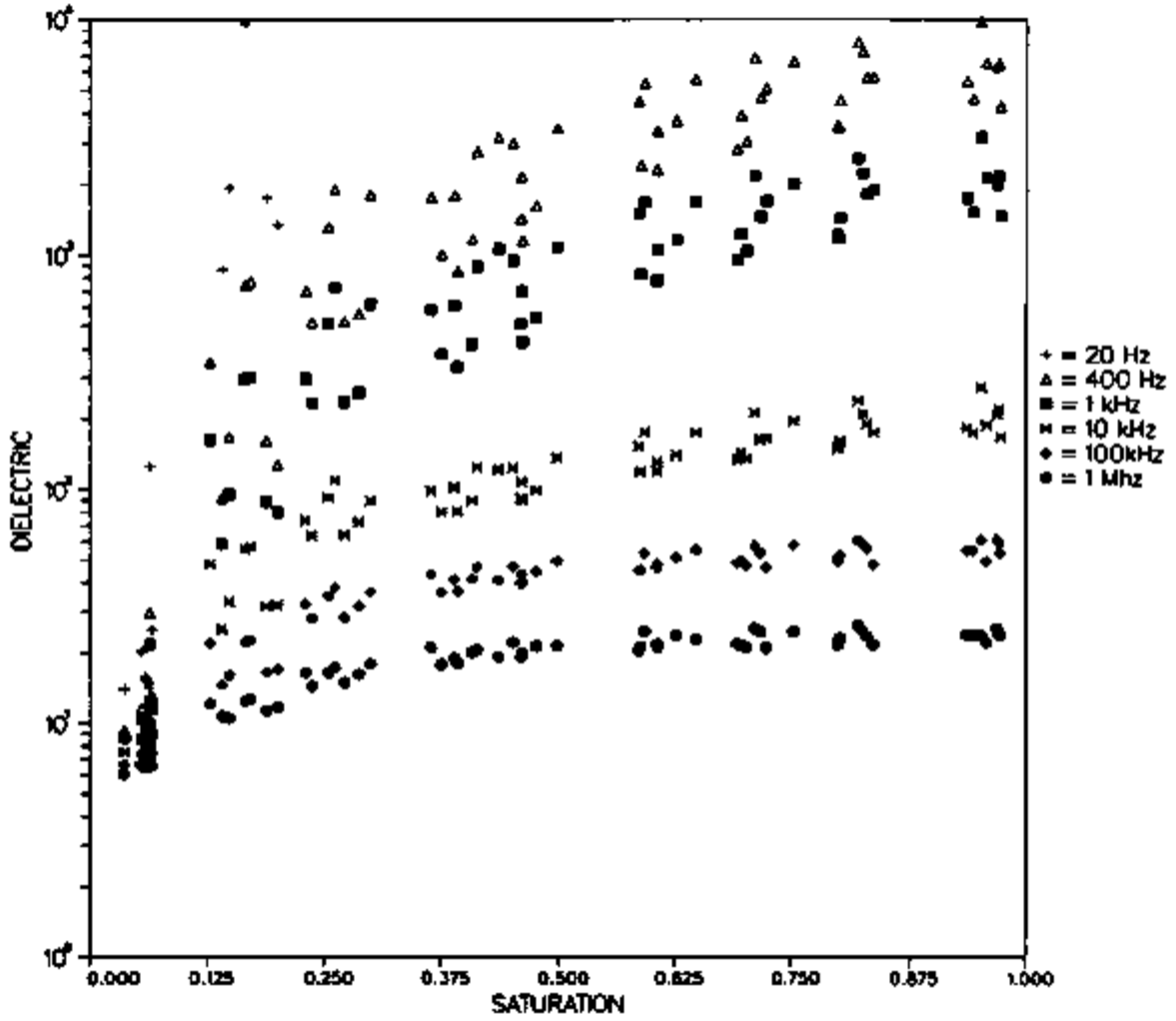

NOTE: The data in this figure are preliminary and confirmatory only.

Figure 8-26. Laboratory Measurements of Dielectric Constant at Various Saturations and Frequencies and a Temperature of 50°C

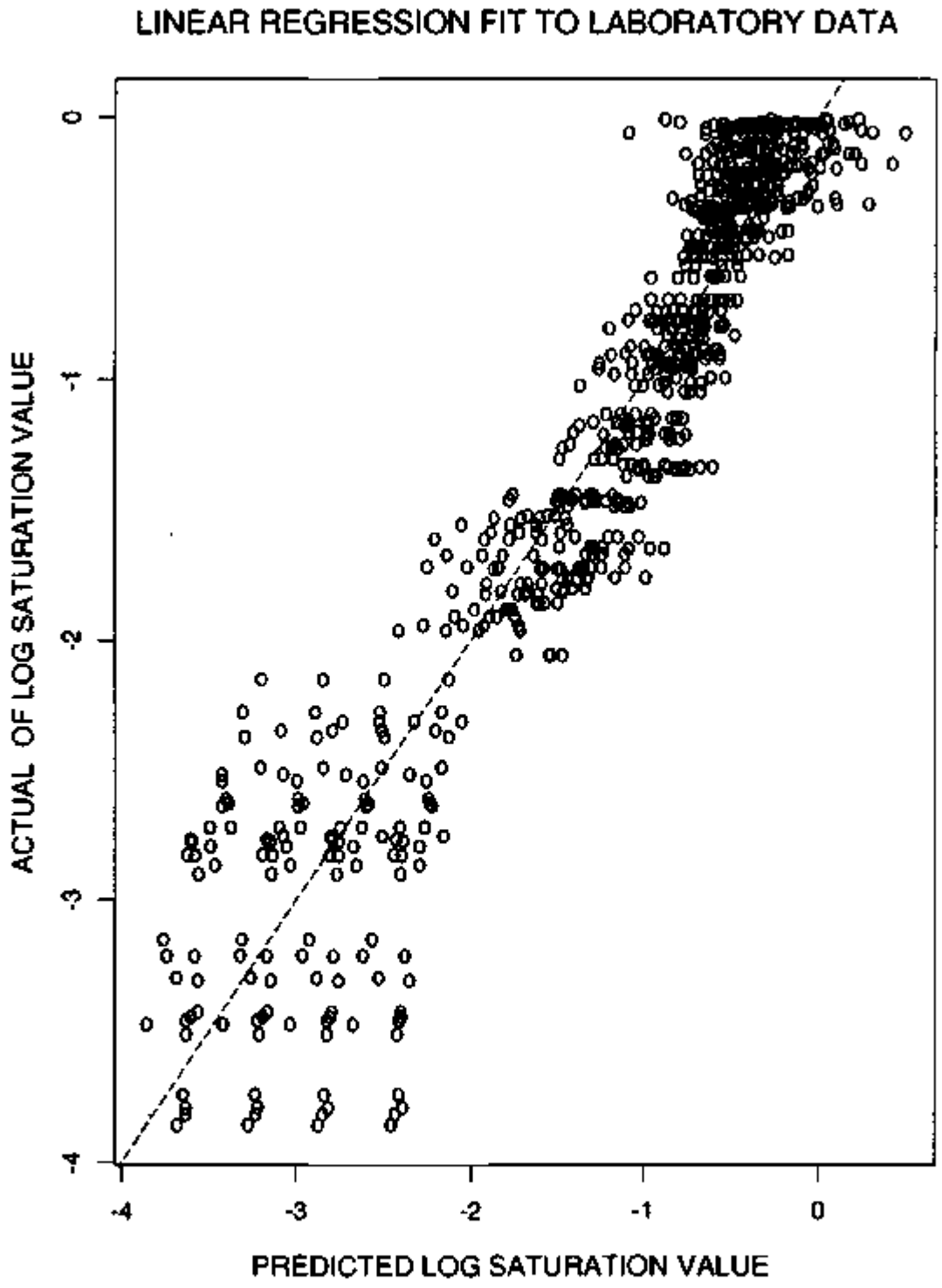

NOTE: Calibrated using the relationship in Equation 8-2.

Figure 8-27. The Estimated Fit to the Laboratory Data

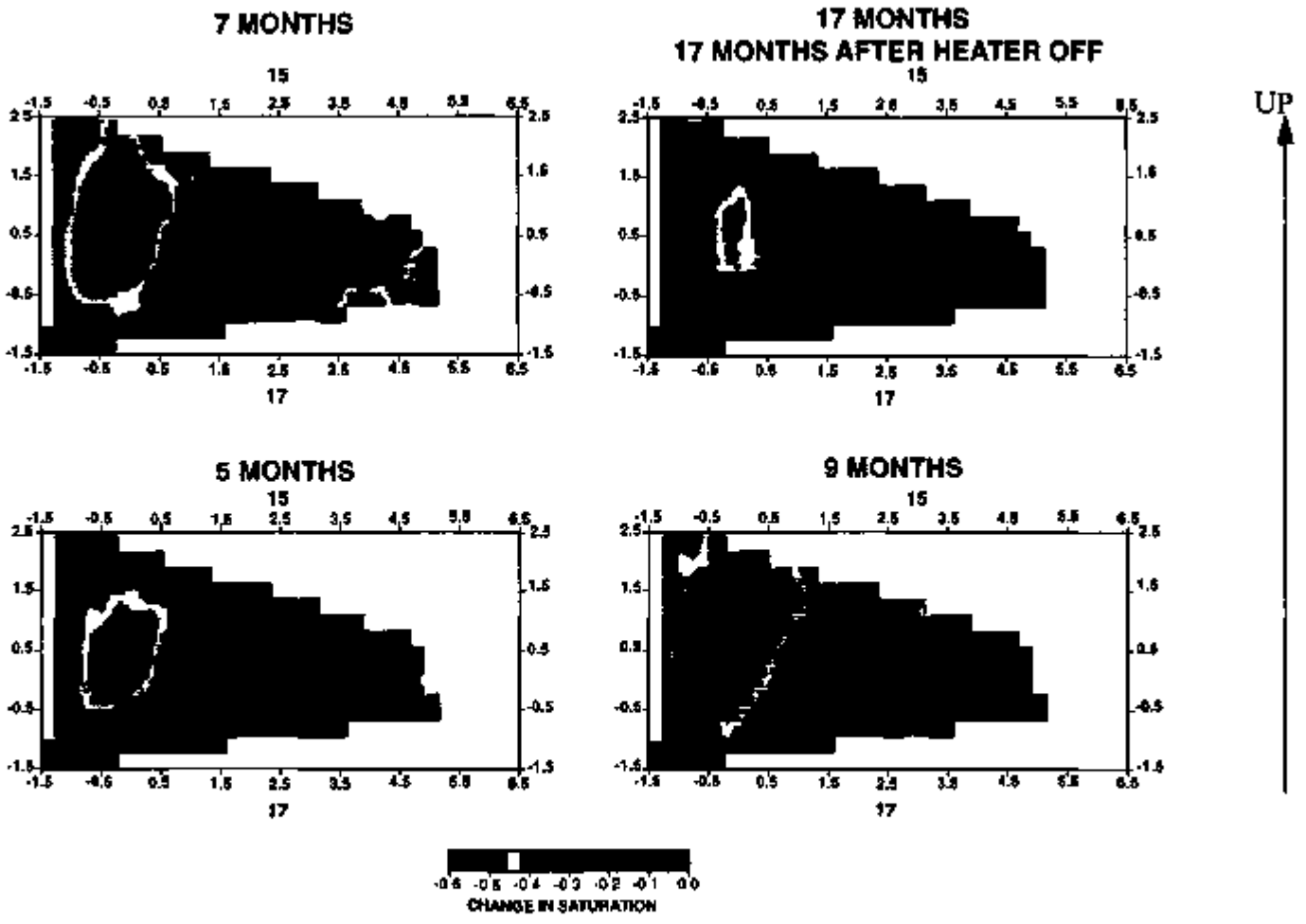

NOTE: See Figure 7-2 Cross Section (b) (p. 7F-2) for locations of boreholes 15 and 17. The black dot indicates the heater borehole (0,0). Distances along both axis are in meters.

Figure 8-28. Saturations for Borehole Pair 17-15 Estimated from the Linear Fit to the Laboratory Data

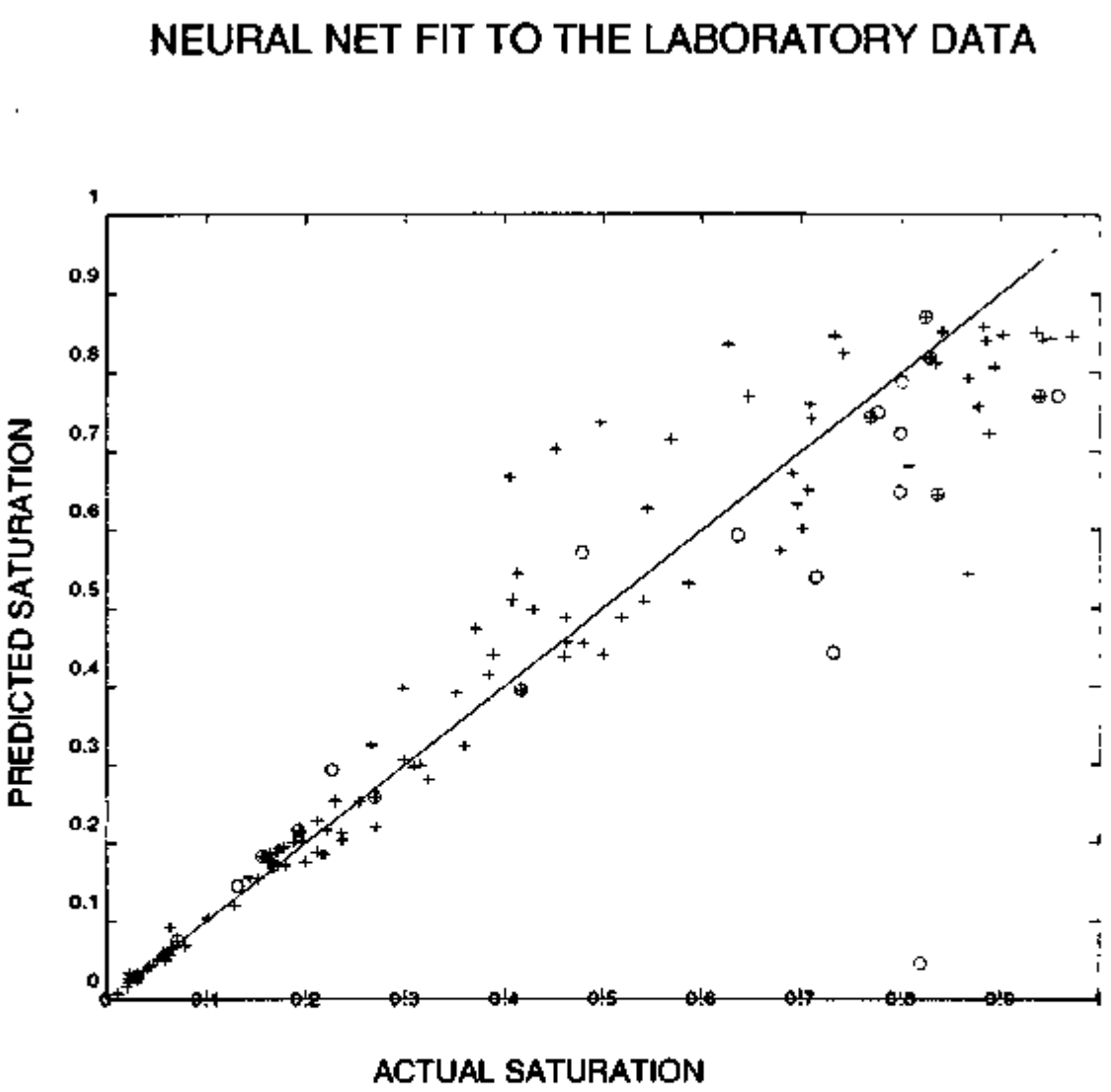

Figure 8-29. The Observed vs. Predicted Values Obtained from the Neural Fit to the Laboratory Data

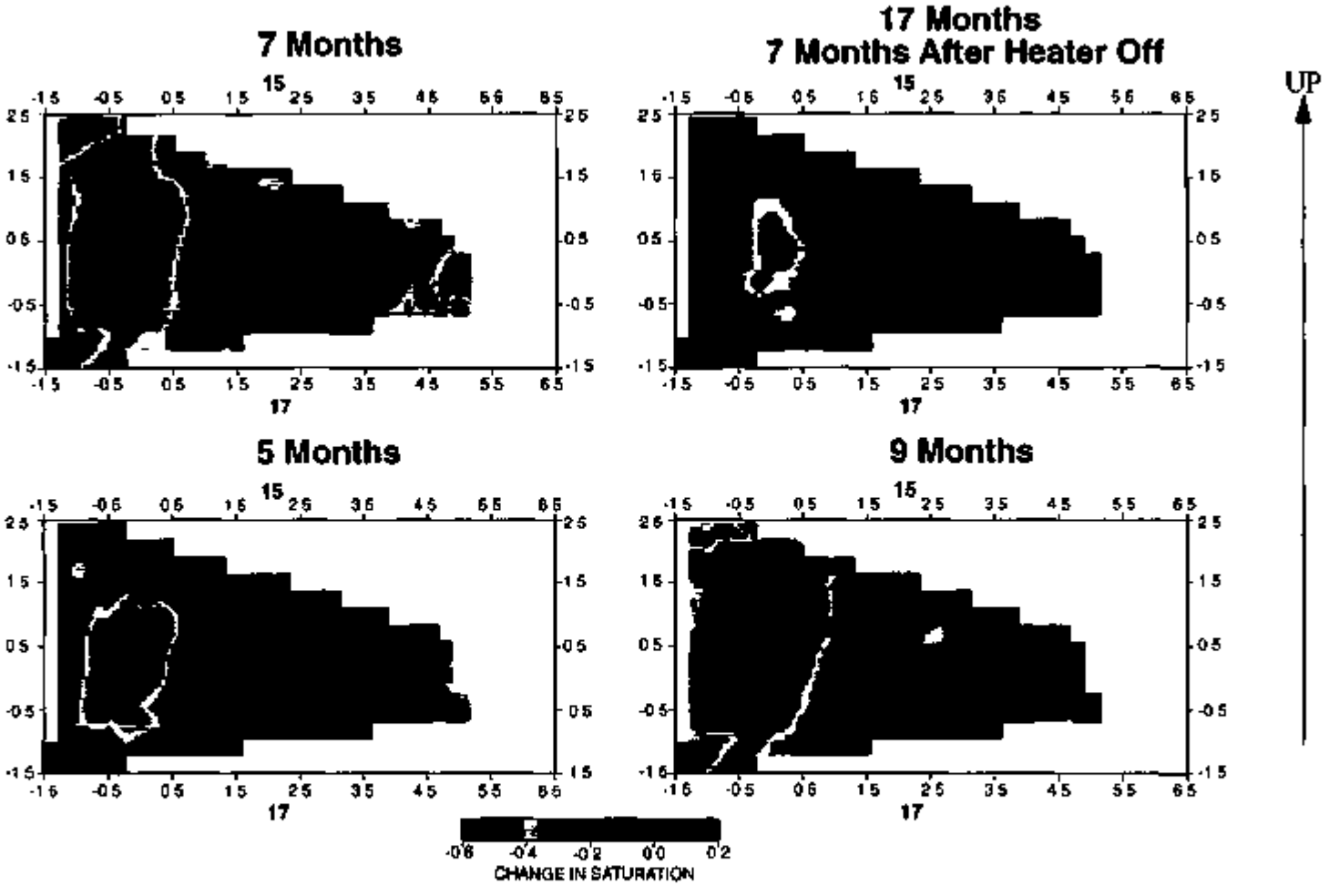

NOTE See Figure 7-2 Cross Section (b) (p 7F-2) for locations of boreholes 15 and 17 The black dot indicates the heater borehole (0,0) Distance along both axis are in meters

Figure 8-30. Estimated Saturations for Borehole Pair 17-15 from the Neural Network Analysis Using Laboratory Data

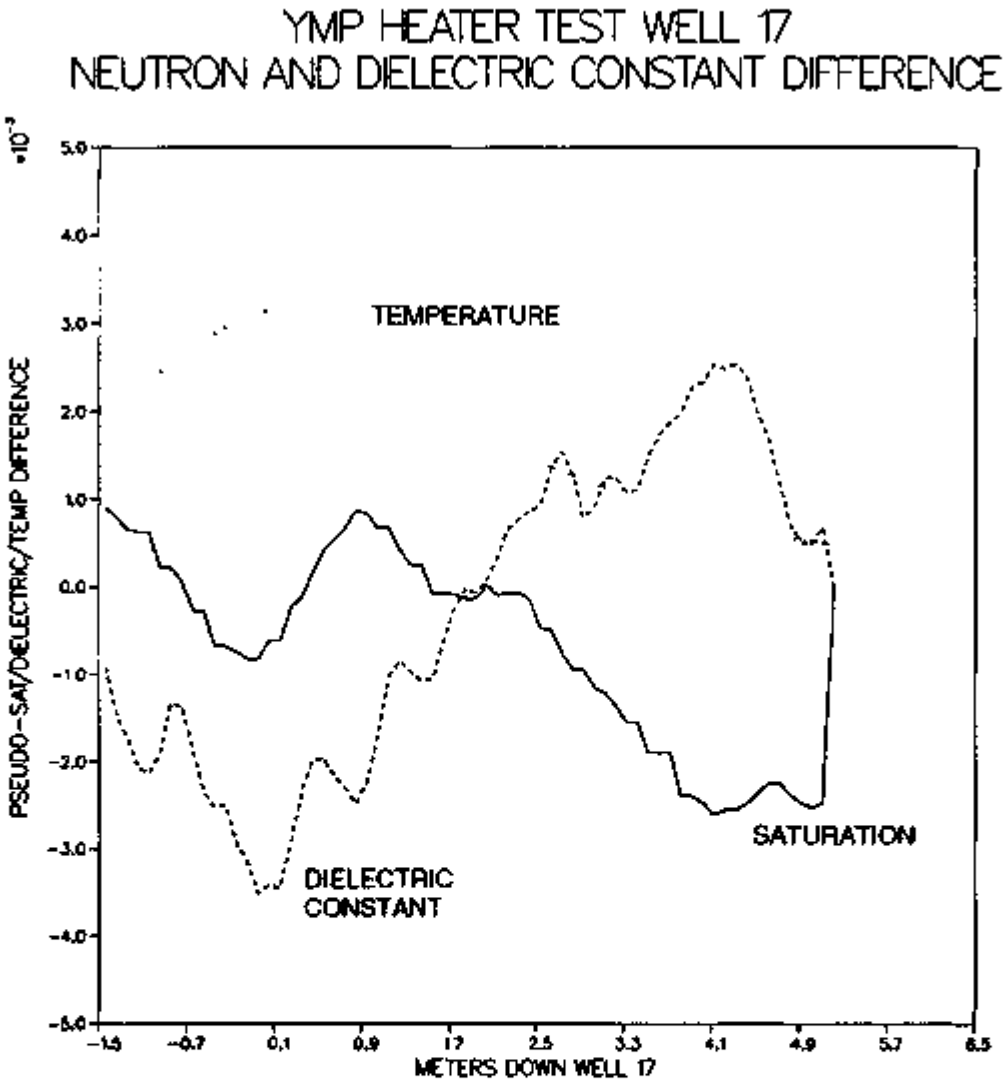

NOTE: The values have been normalized to fit on the same plot

Figure 8-31. Normalized Change in Saturation, Temperature, and Dielectric Constant Values Down Borehole 17

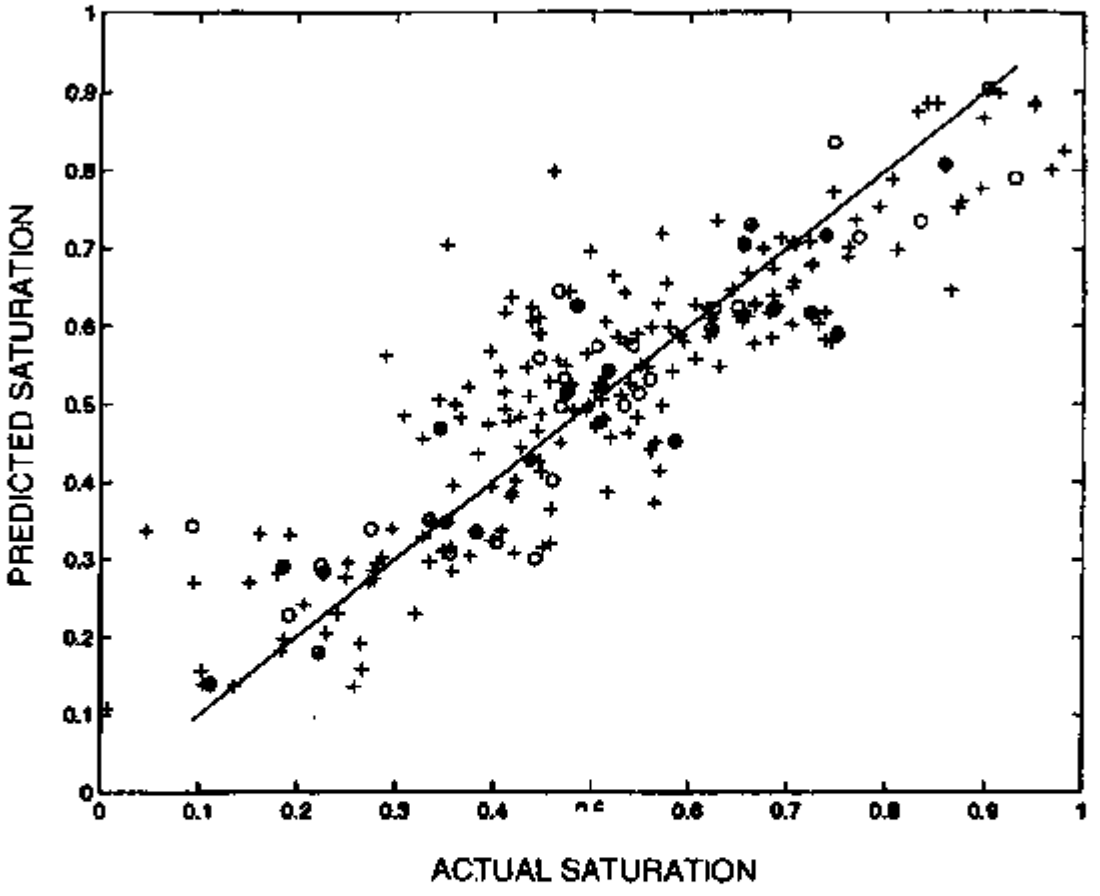

Figure 8-32. The Observed vs. Predicted Values Obtained from the Neural Net Fit to the Neutron Log Data

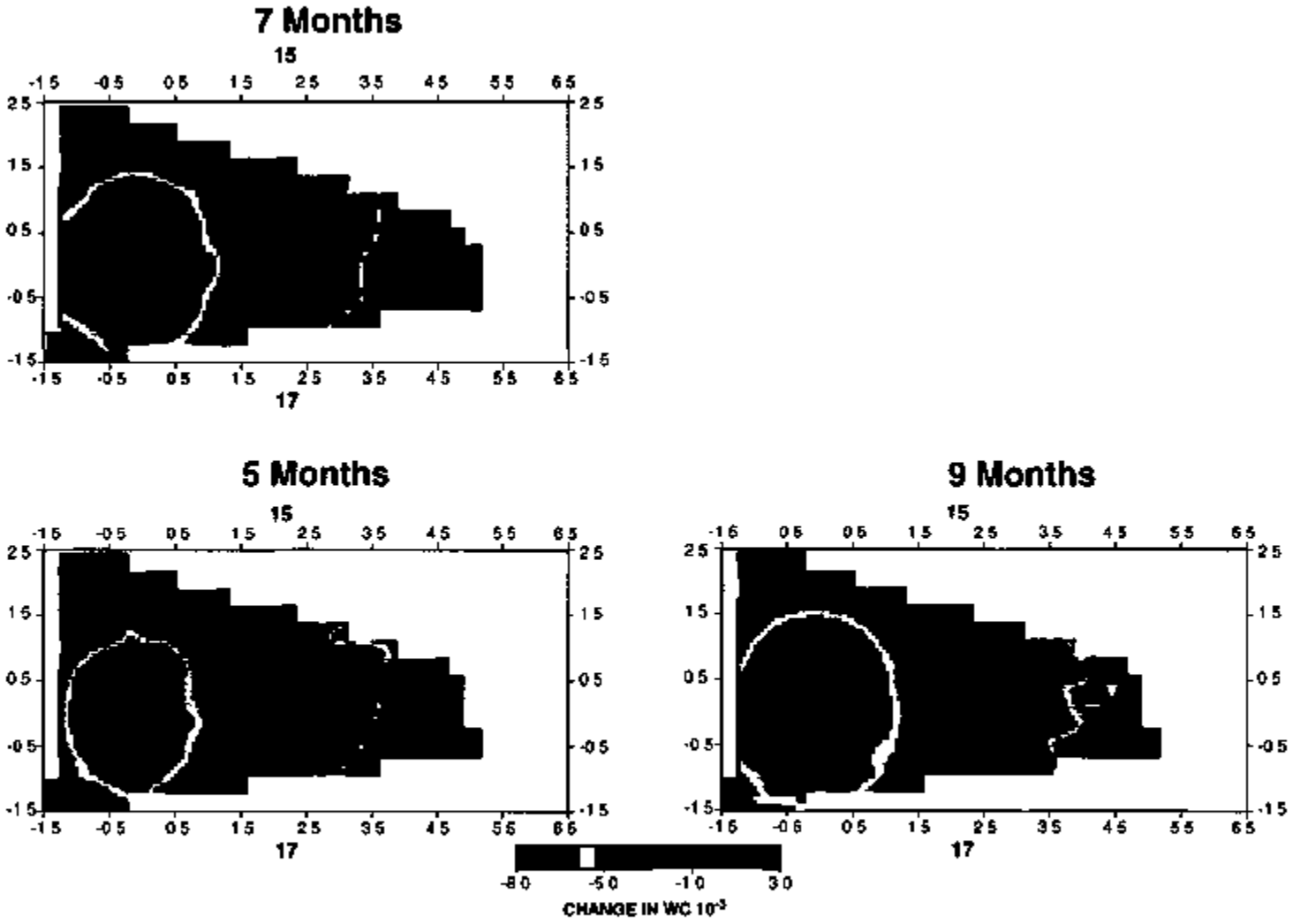

NOTE See Figure 7-2 Cross Section (b) (p 7F-2) for locations of boreholes 15 and 17 The black dot indicates the heater borehole (0,0)

Figure 8-33 Estimated Saturations for Borehole Pair 15-17 from the Neural Network Analysis Using Neutron Log Data

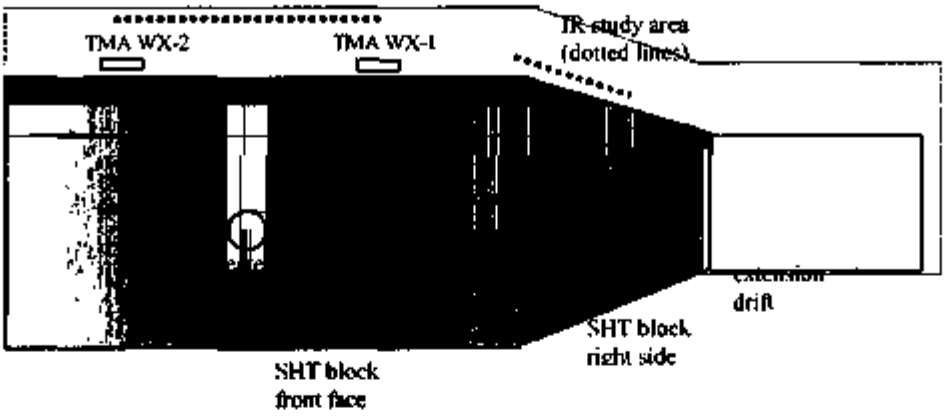

NOTE: Heavy dashed lines show location of temperature plot lines shown in Figures 8-38 and 8-39.

Figure 8-34. Diagram of IR Study Area at the SHT Area

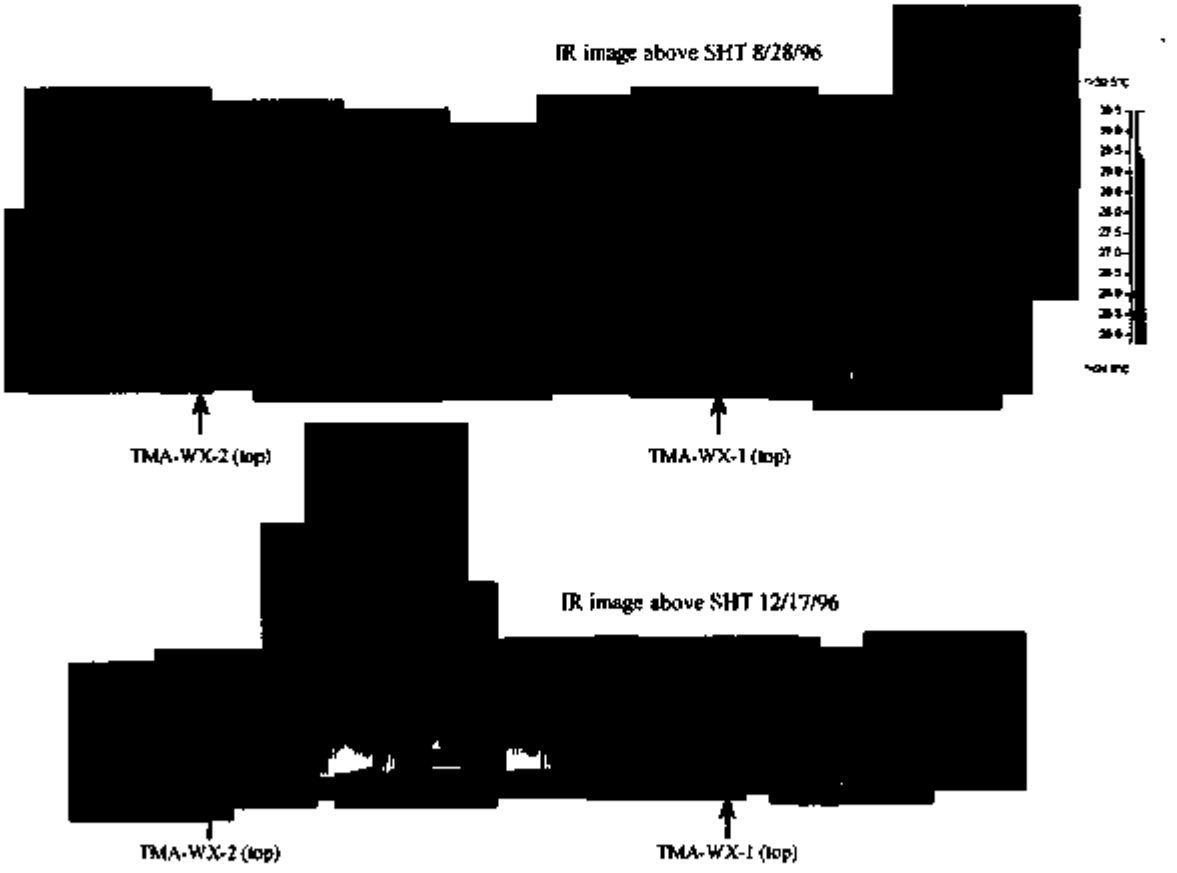

Figure 8-35. IR Images from the Front Face of the SHT, August and December 1996

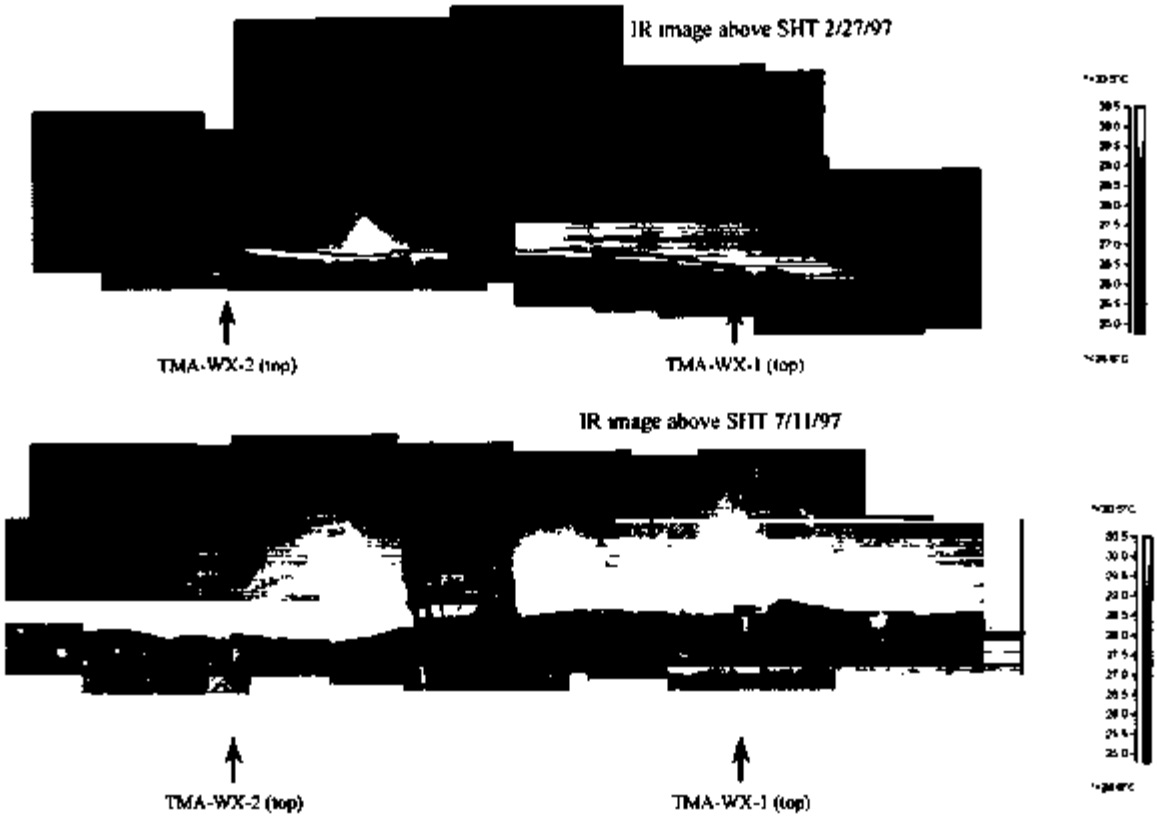

Figure 8-36. IR Images from the Front Face of the SHT, February and July 1997

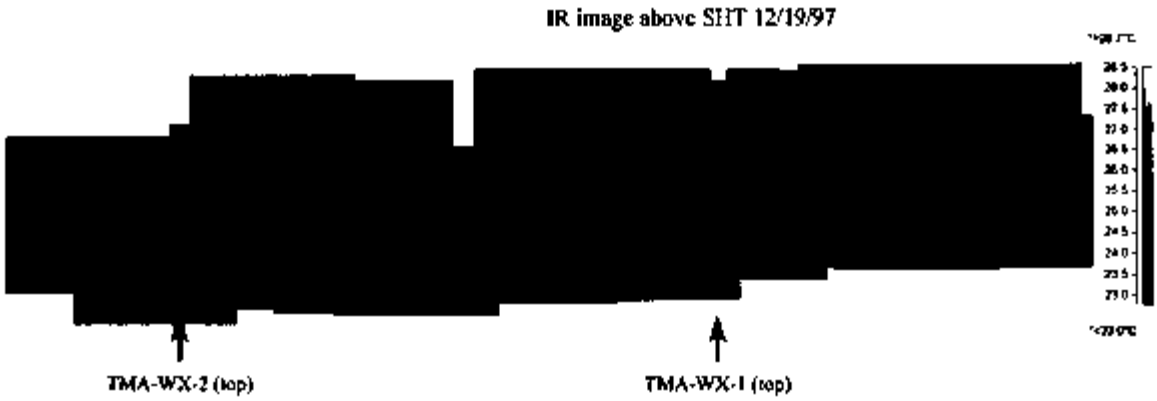

Figure 8-37. IR Images from the Front Face of the SHT, December 1997

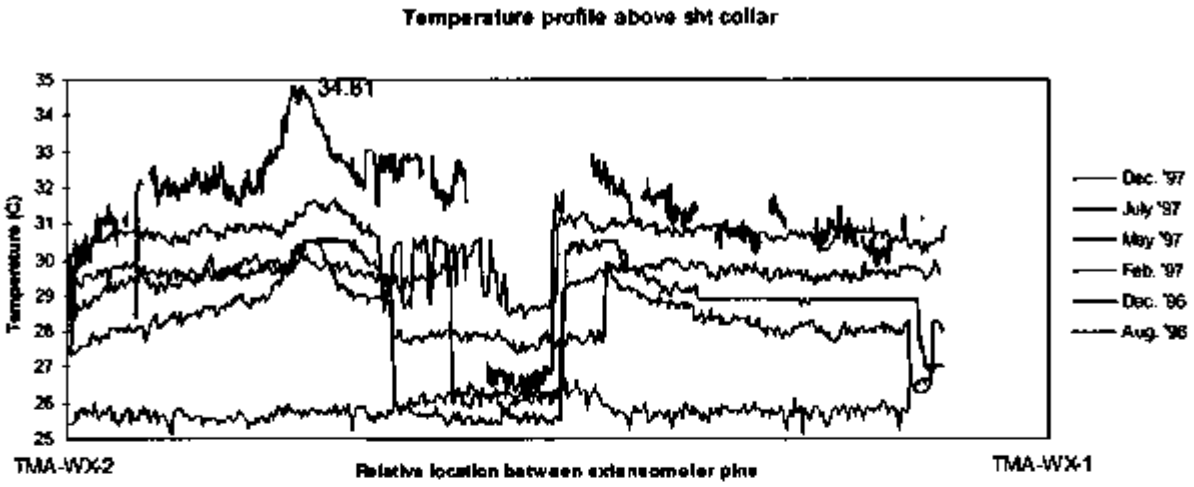

NOTE: See illustration in Figure 8-34 and Figure 8-36, February 1997 montage, for line location.

Figure 8-38. Line Plots of the Front Face above the Insulation

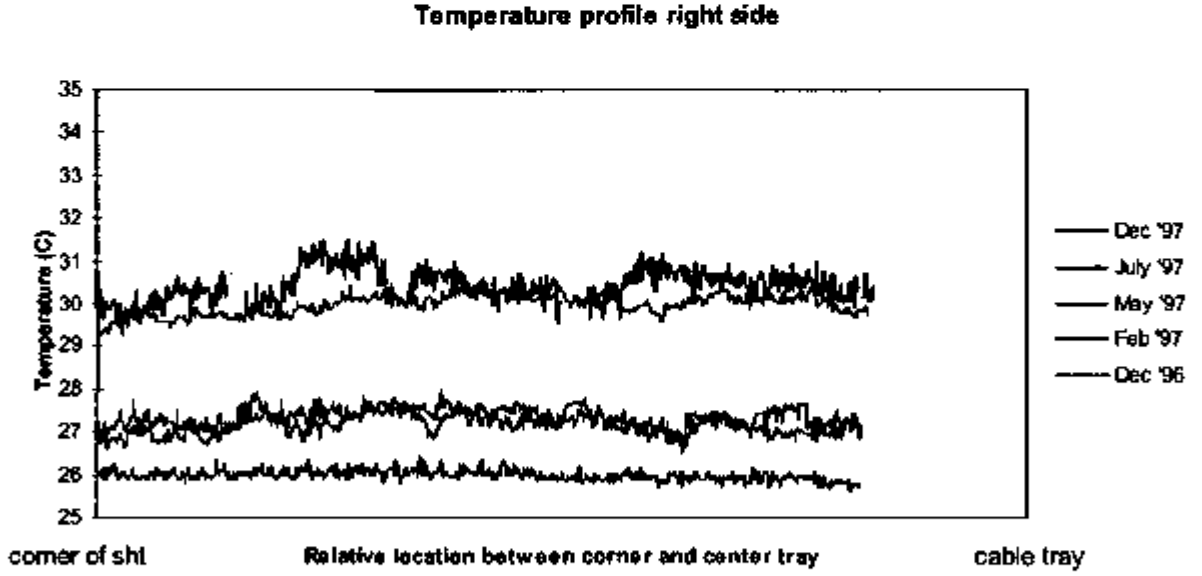

NOTE: See illustration in Figure 8-34 for line location.

Figure 8-39. Line Plots on Right Side above Insulation from Corner to Center of Block

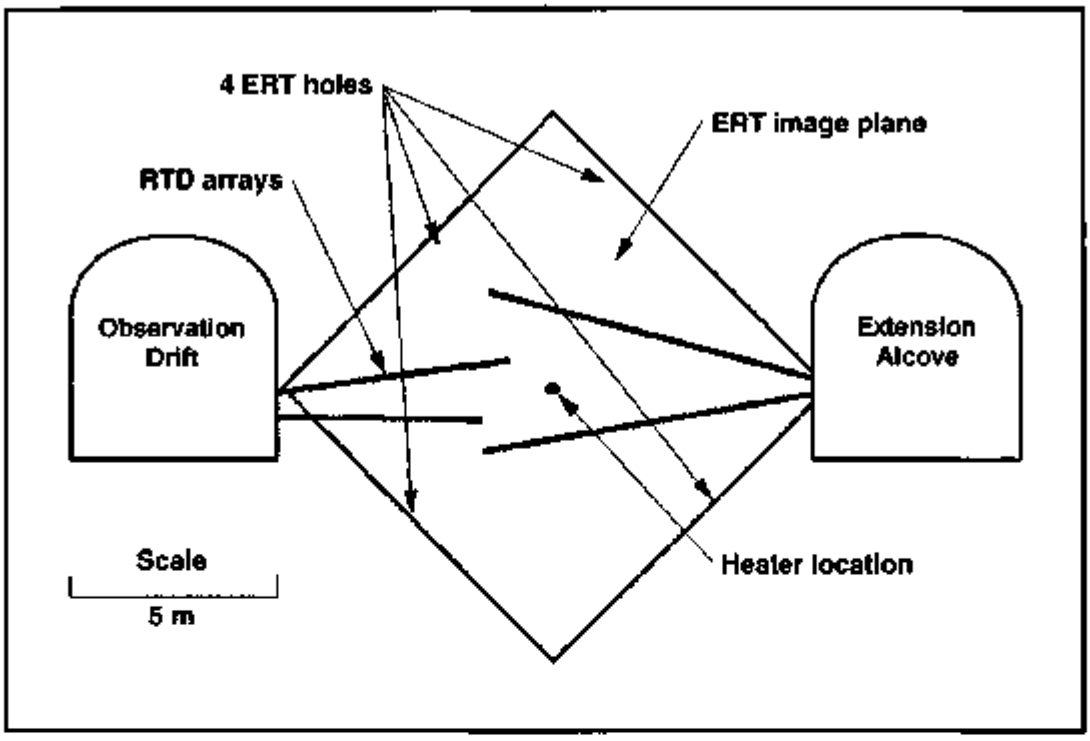

NOTE: Twenty-eight electrodes distributed among the four boreholes were used to conduct ERT surveys around the heater

Figure 8-40. The Borehole Layout Relative to the Drifts and the RTD Boreholes

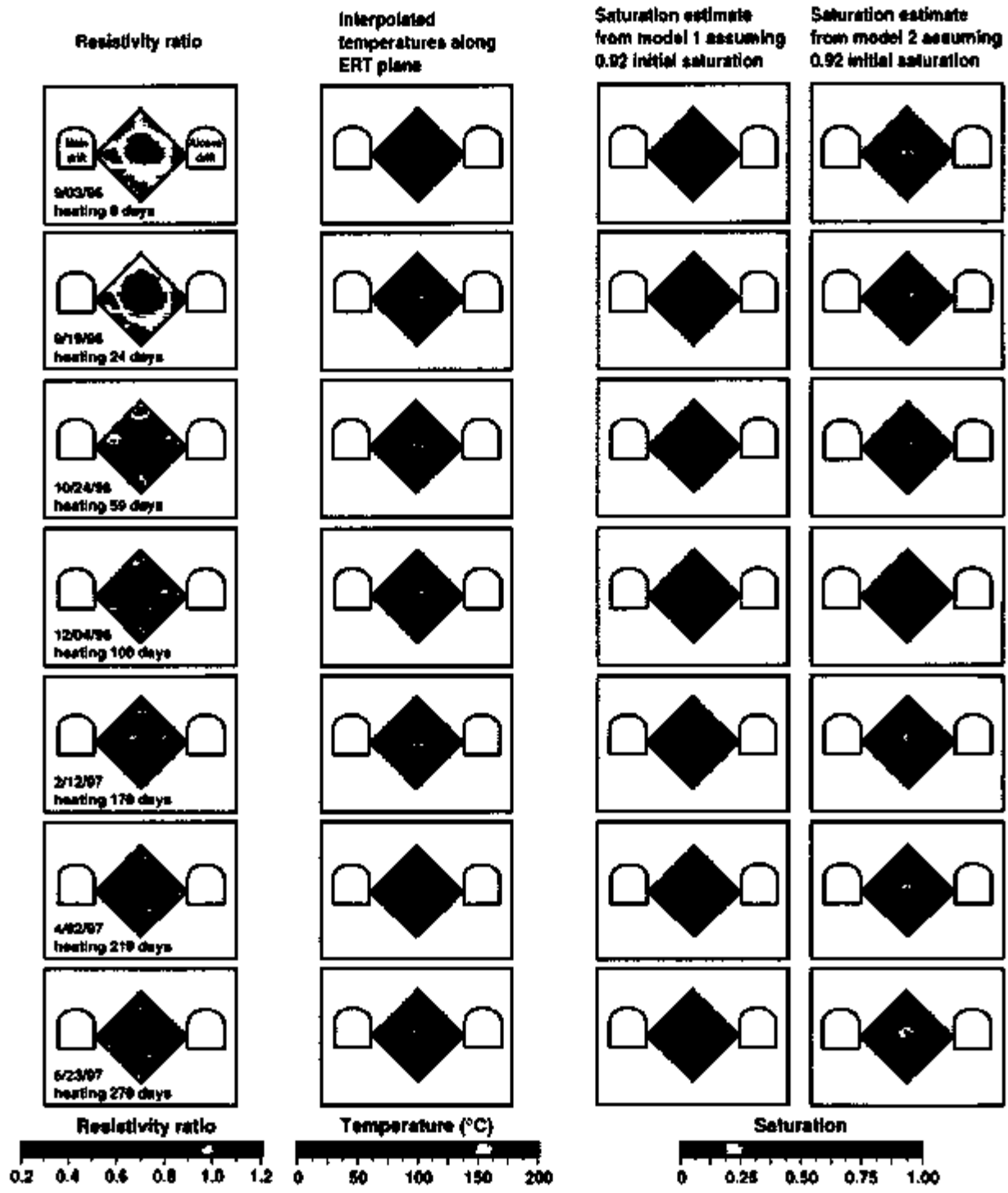

NOTE: Resistivity-ratio tomographs during the heating phase (left column of images). Also shown are corresponding temperature maps (second column from the left). The results of the saturation calculations are shown by the images in the third and fourth columns. The estimates of saturation assume that the initial saturation is 92% and are based on two models (described in the text) relating moisture content to resistivity.

Figure 8-41. Resistivity-Ratio Tomographs, Temperature Maps, and Estimates of Saturation during the Heating Phase

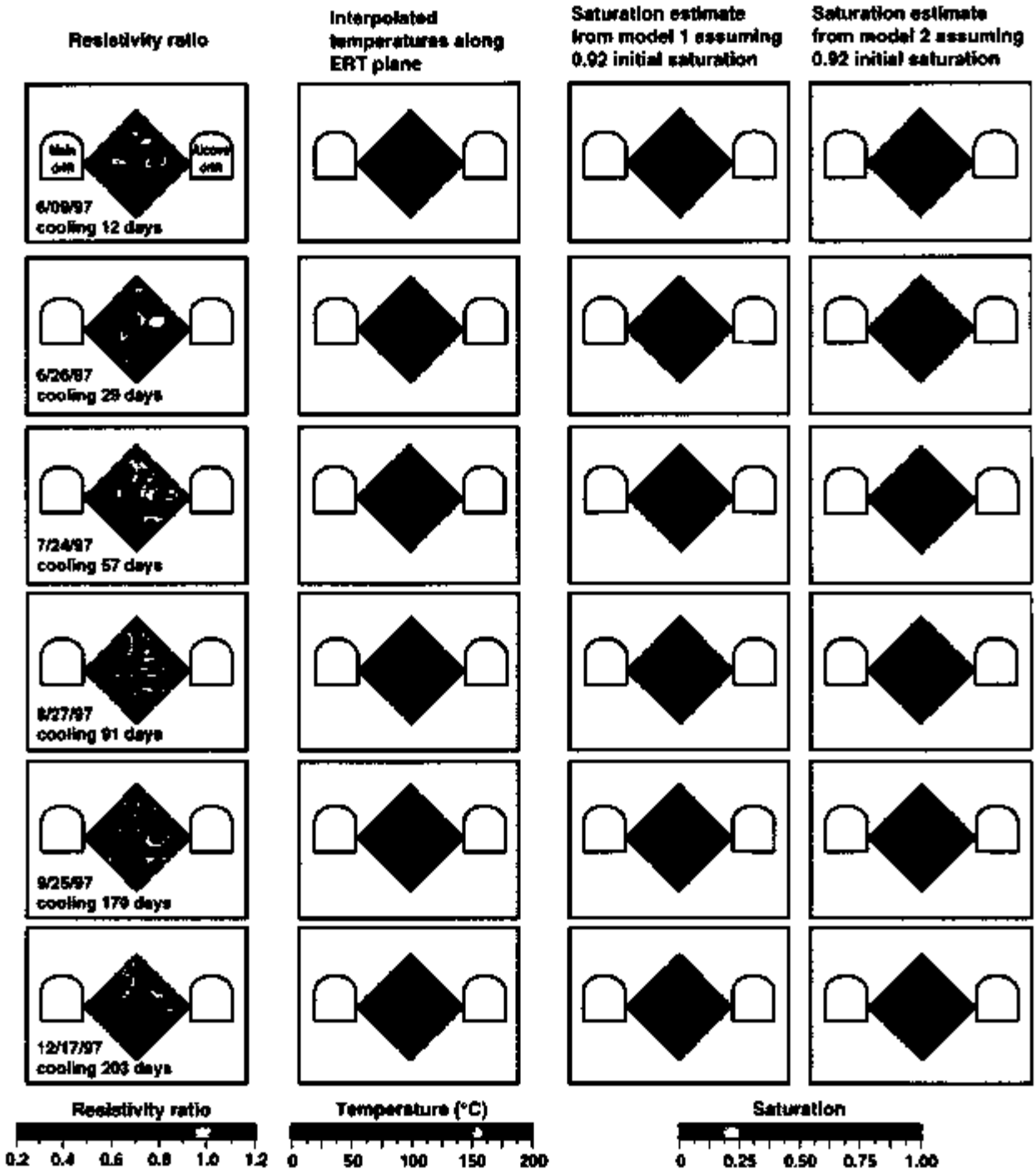

NOTE: Resistivity-ratio tomographs during the cooling phase (left column of images). Also shown are corresponding temperature maps (second column from the left). The results of the saturation calculations are shown by the images in the third and fourth columns. The estimates of saturation assume that the initial saturation is 92% and are based on two models (described in the text) relating moisture content to resistivity.

Figure 8-42. Resistivity-Ratio Tomographs, Temperature Maps, and Estimates of Saturation during the Cooling Phase

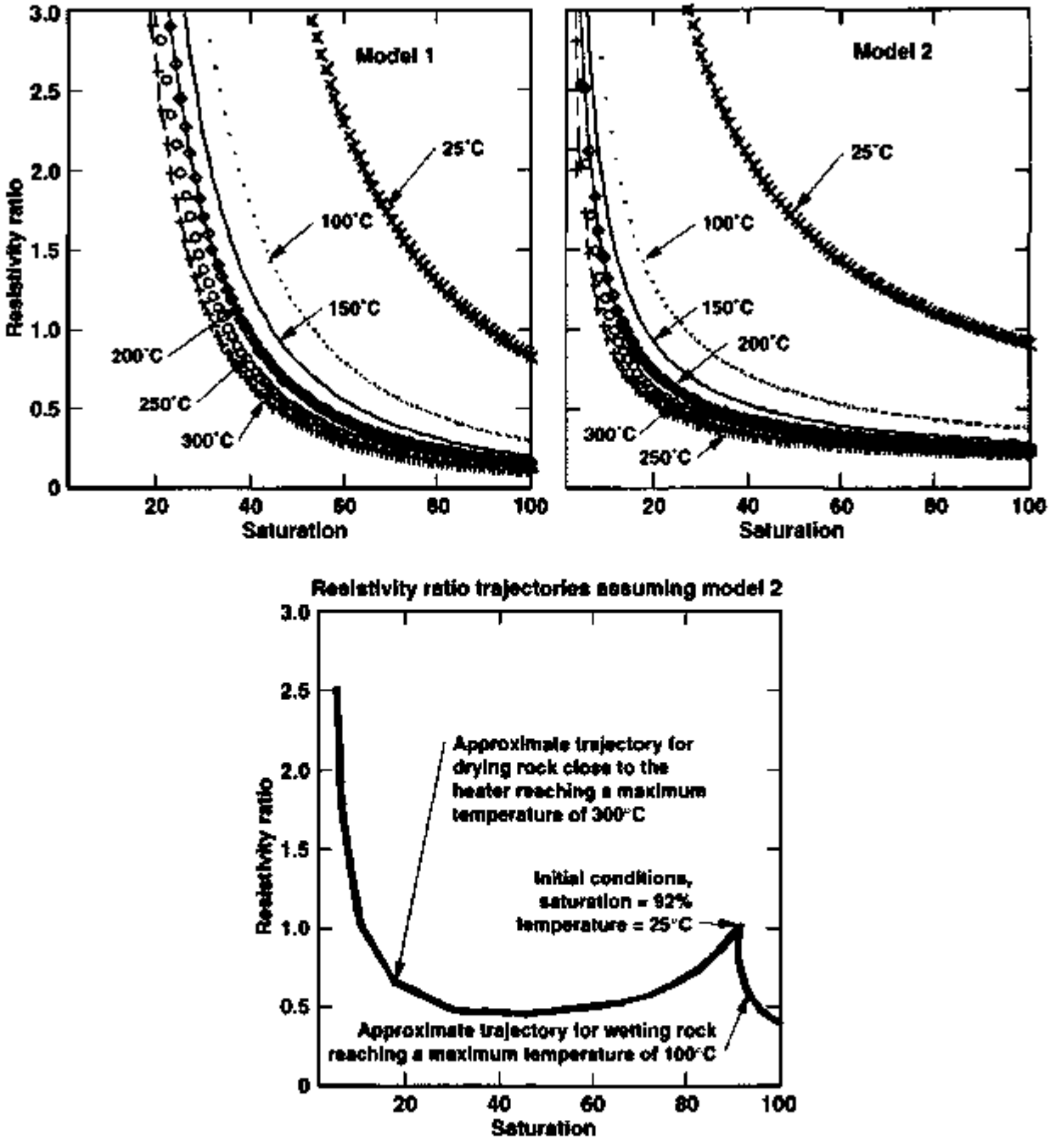

NOTE: Curves representing the temperature range of 25° to 300°C are shown to illustrate the temperature and saturation dependence of the resistivity ratios. The bottom part of the figure shows resistivity-ratio trajectories for two different rock environments.

Figure 8-43. Resistivity Ratios as a Function of Saturation and Temperature for Models 1 and 2

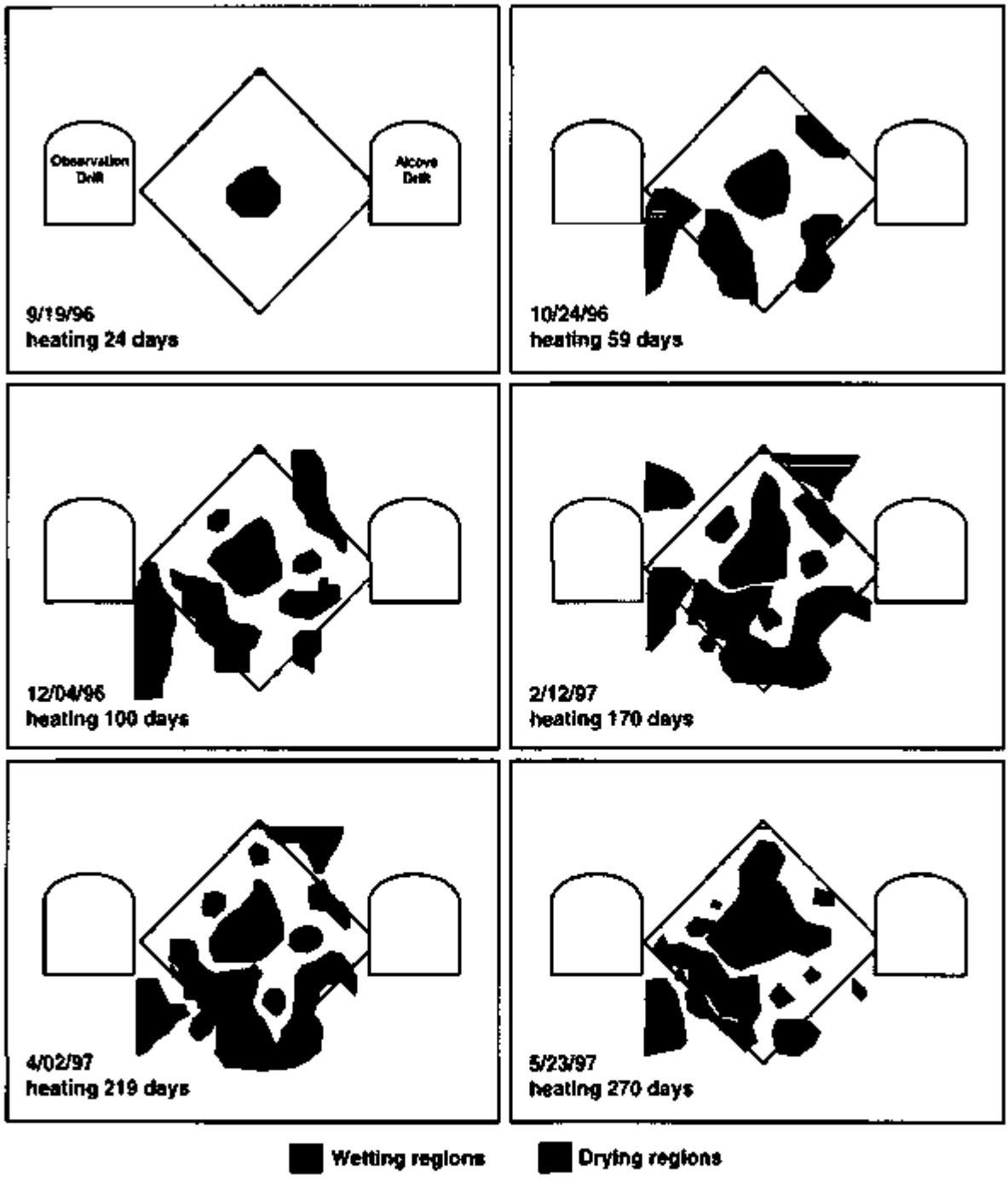

NOTE: The drying and wetting regions in this figure are based on hand tracings made over the model 2 saturation estimates shown in Figure 8-41.

Figure 8-44. Interpretation of Where the Rock Lost or Gained Moisture during the Heating Phase

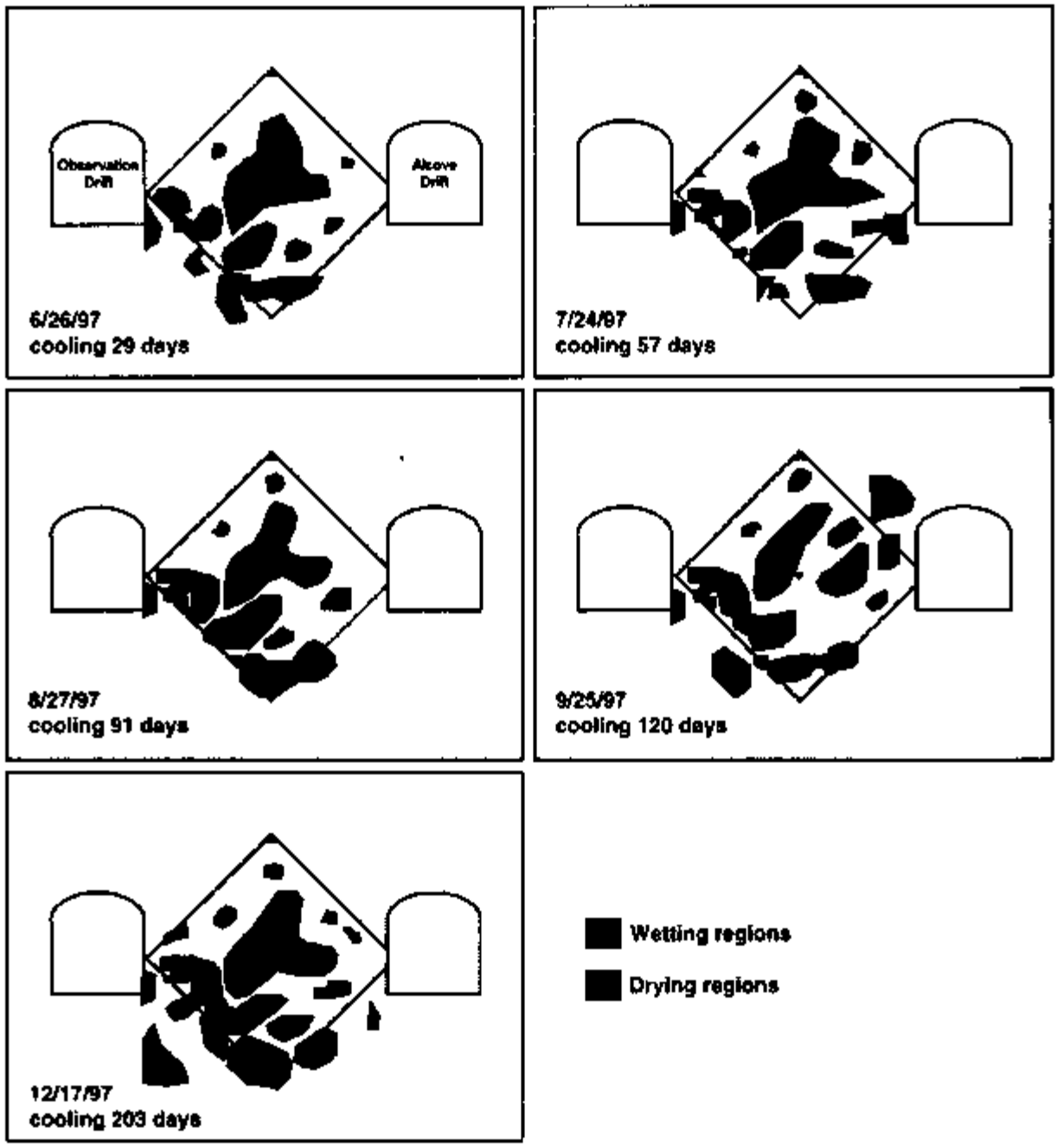

NOTE: The drying and wetting regions in this figure are based on hand tracings made over the model 2 saturation estimates shown in Figure 8-42.

Figure 8-45. Interpretation of Where the Rock Lost or Gained Moisture during the Cooling Phase

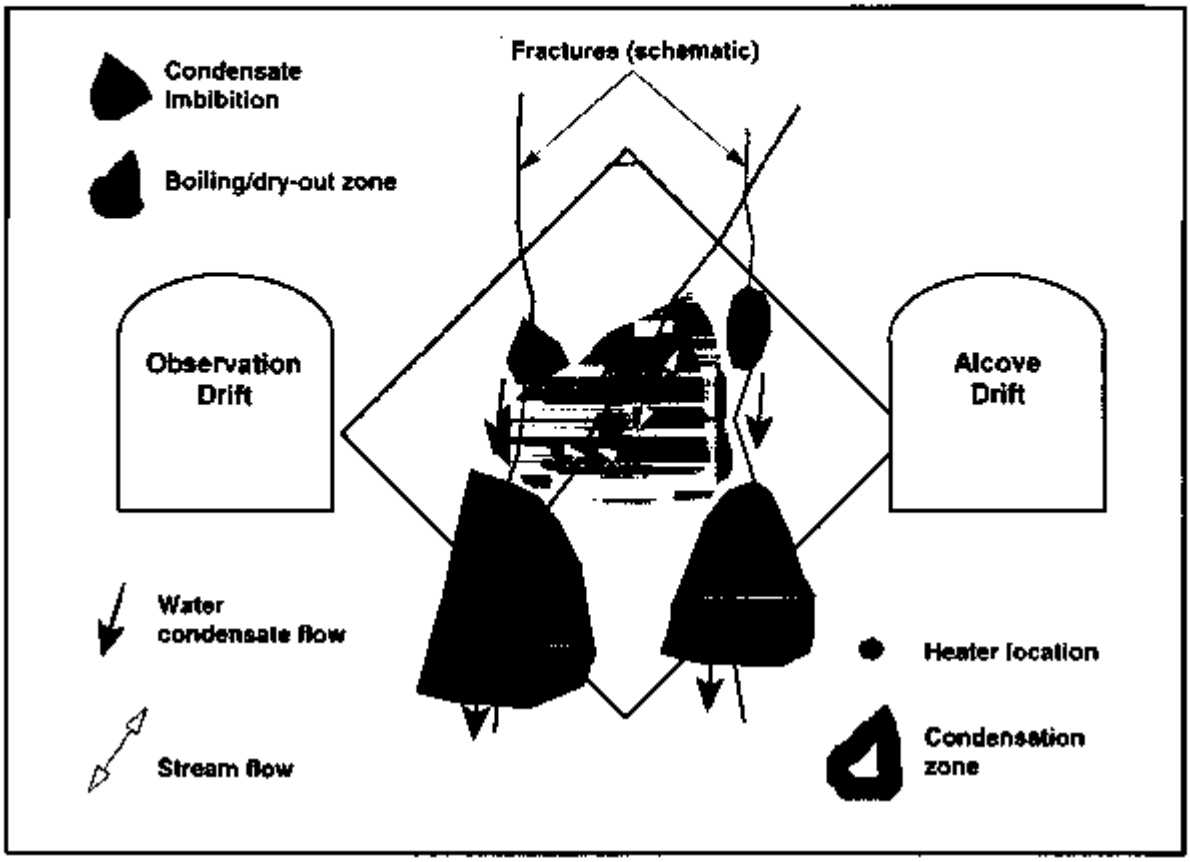

Figure 8-46. Conceptual Model of Thermal-Hydrological Behavior during the SHT, Consistent with the Saturation Estimates Presented in Figures 8-42 and 8-43

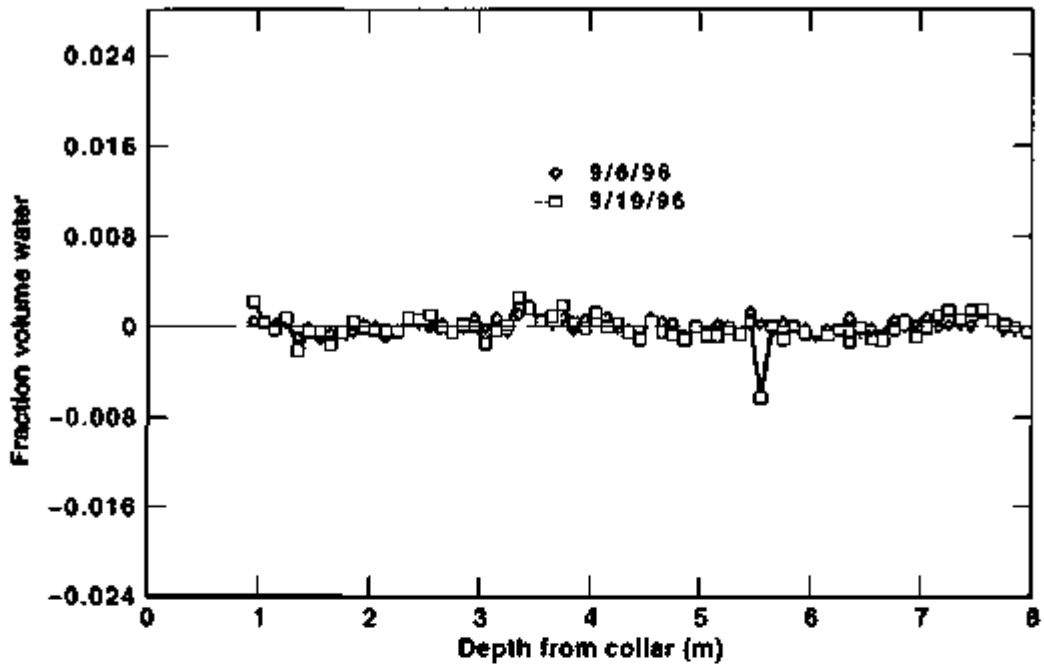

Figure 8-47. Smoothed Difference Fraction Volume Water Content in Borehole 15 as a Function of Depth from Collar on September 6 and September 19, 1996

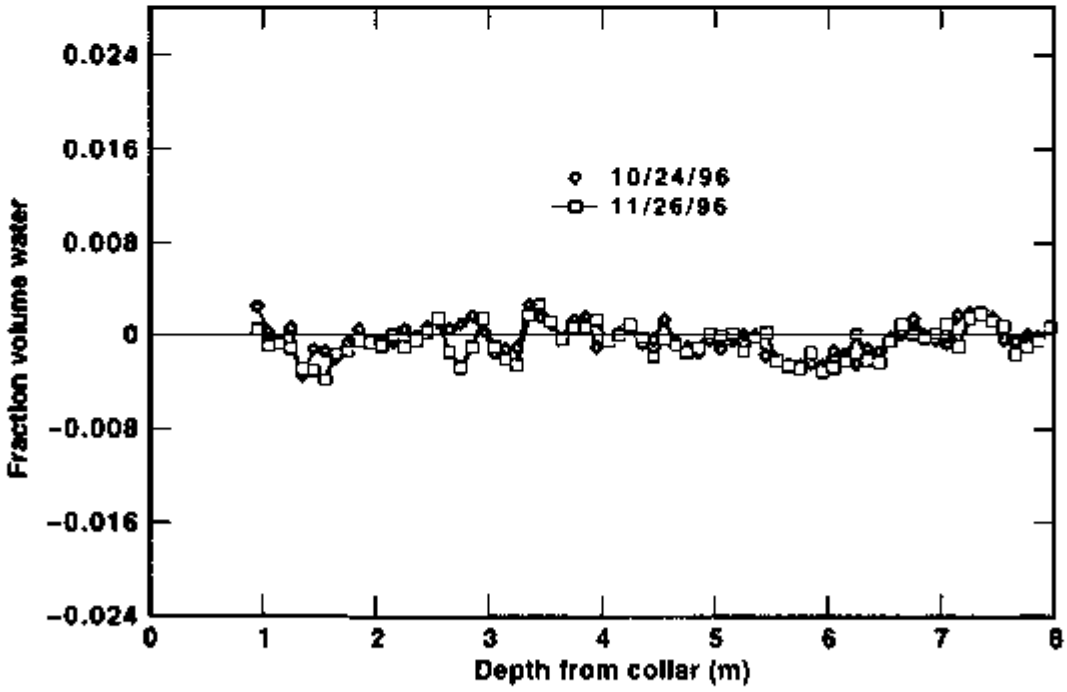

Figure 8-48. Smoothed Difference Fraction Volume Water Content in Borehole 15 as a Function of Depth from Collar on October 24 and November 26, 1996

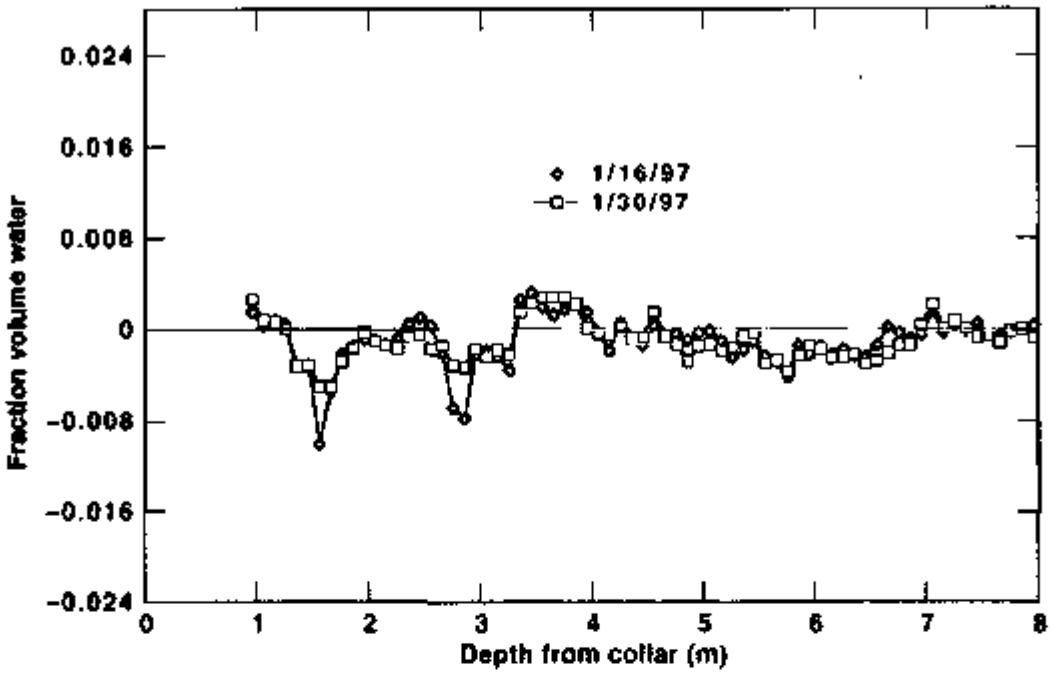

Figure 8-49. Smoothed Difference Fraction Volume Water Content in Borehole 15 as a Function of Depth from Collar on January 16 and January 30, 1997

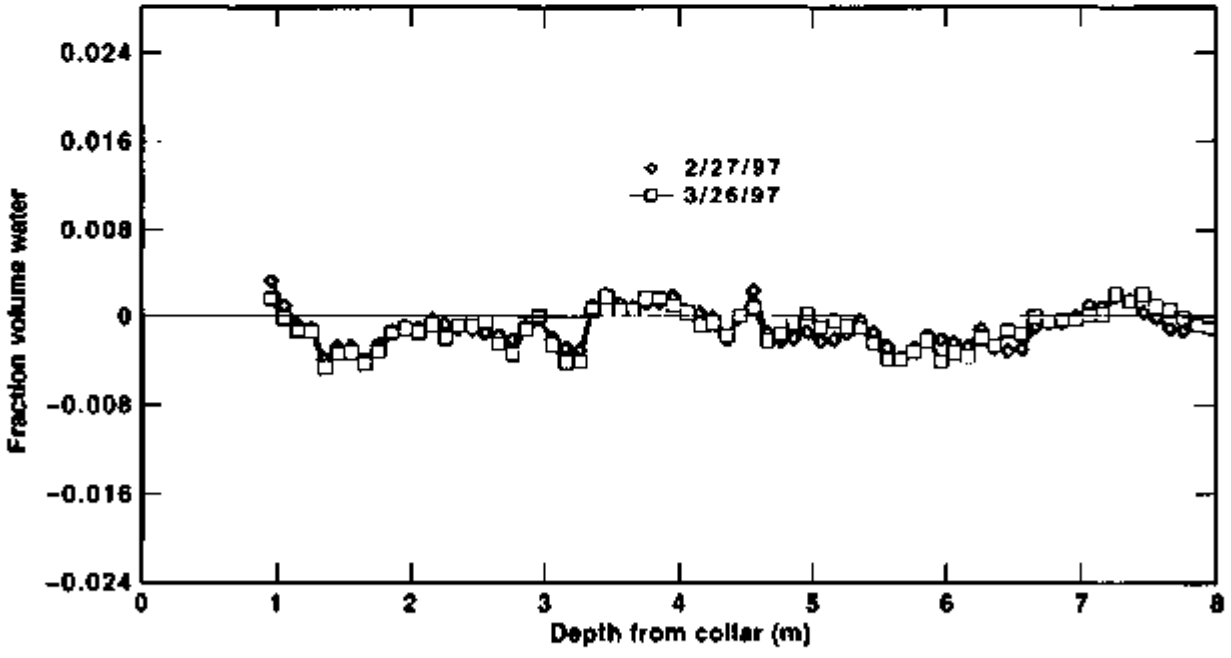

Figure 8-50. Smoothed Difference Fraction Volume Water Content in Borehole 15 as a Function of Depth from Collar on February 27 and March 26, 1997

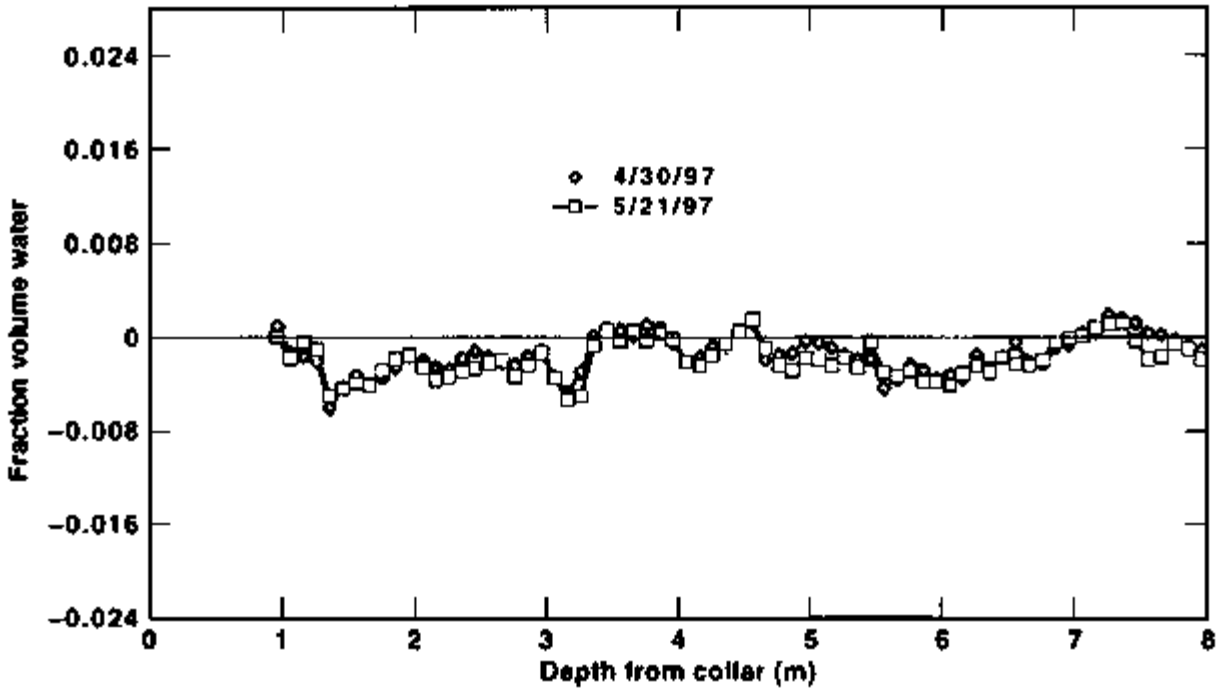

Figure 8-51. Smoothed Difference Fraction Volume Water Content in Borehole 15 as a Function of Depth from Collar on April 30 and May 21, 1997

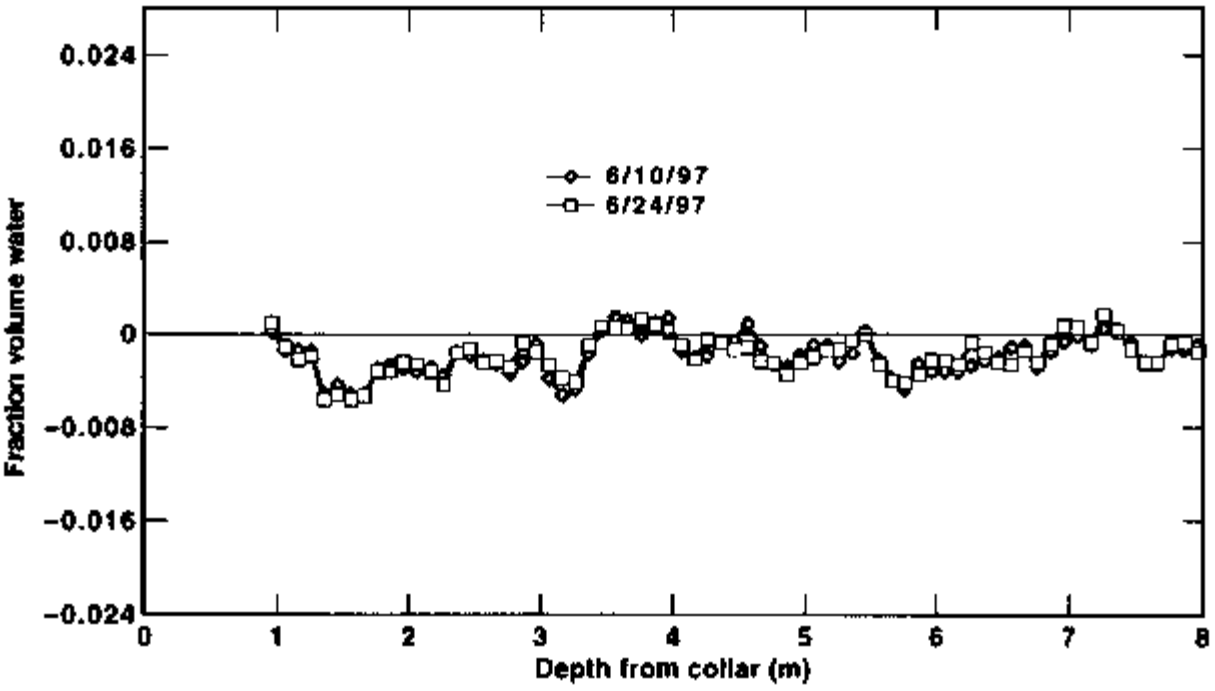

Figure 8-52. Smoothed Difference Fraction Volume Water Content in Borehole 15 as a Function of Depth from Collar on June 10 and June 24, 1997

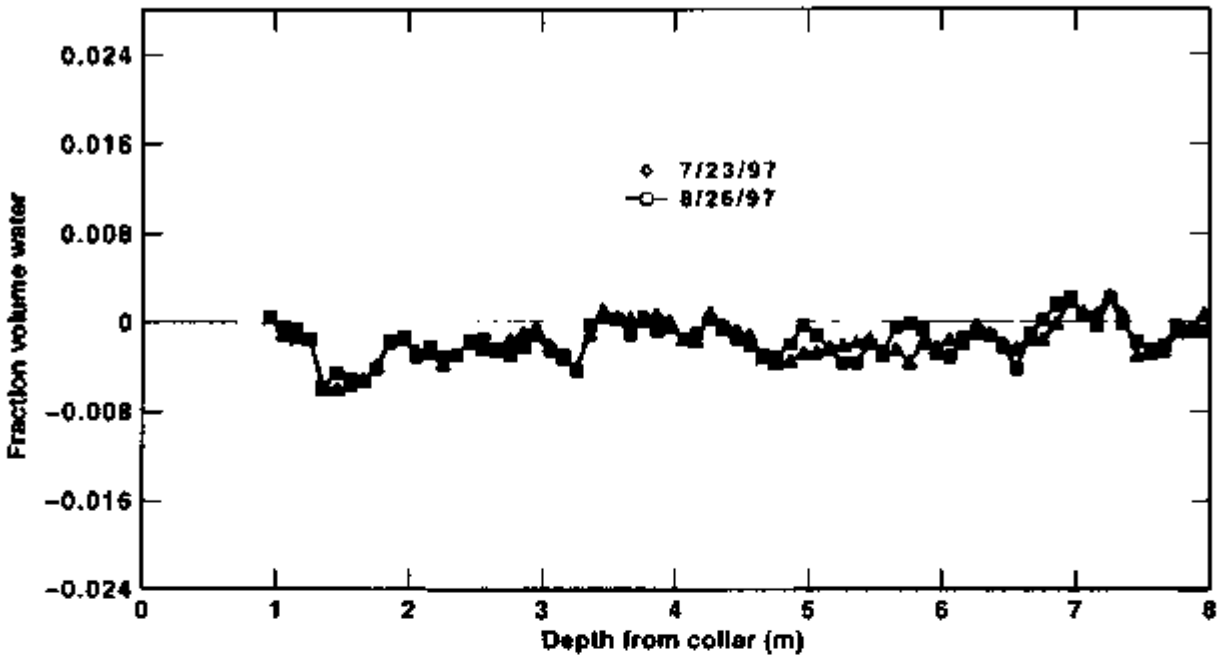

Figure 8-53. Smoothed Difference Fraction Volume Water Content in Borehole 15 as a Function of Depth from Collar on July 23 and August 26, 1997

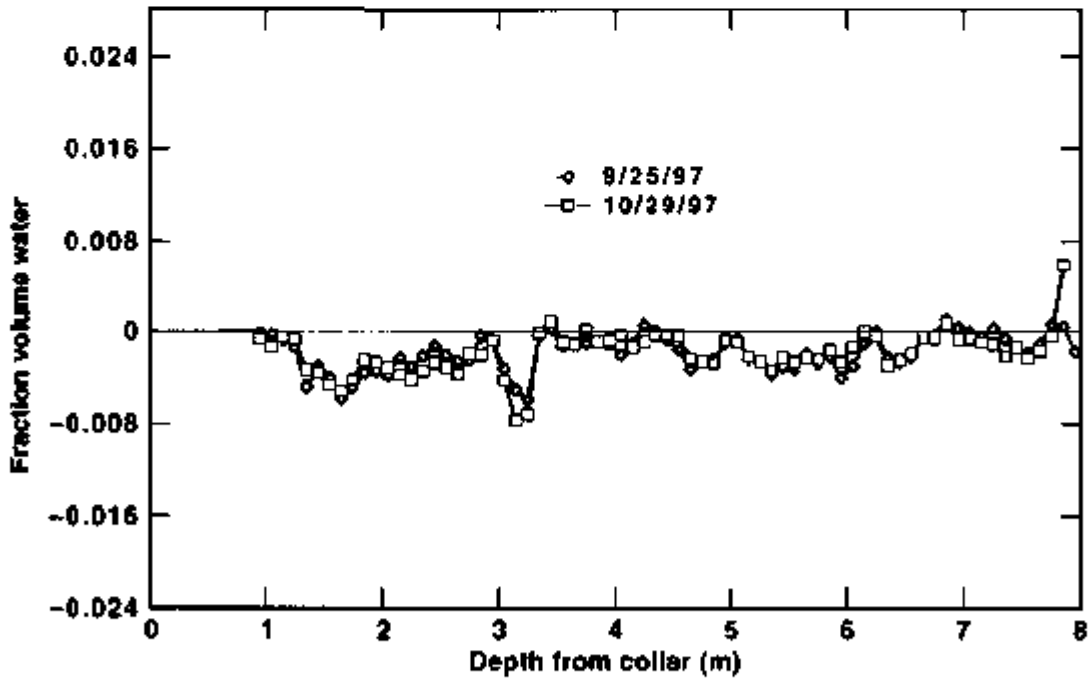

Figure 8-54. Smoothed Difference Fraction Volume Water Content in Borehole 15 as a Function of Depth from Collar on September 25 and October 29, 1997

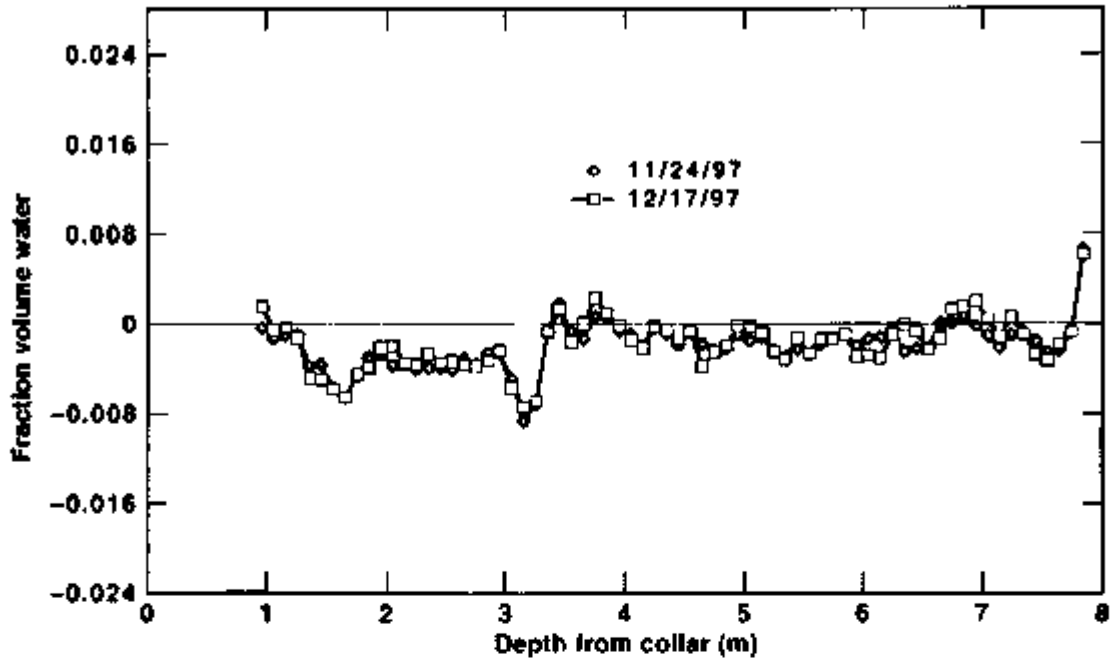

Figure 8-55. Smoothed Difference Fraction Volume Water Content in Borehole 15 as a Function of Depth from Collar on November 24 and December 17, 1997

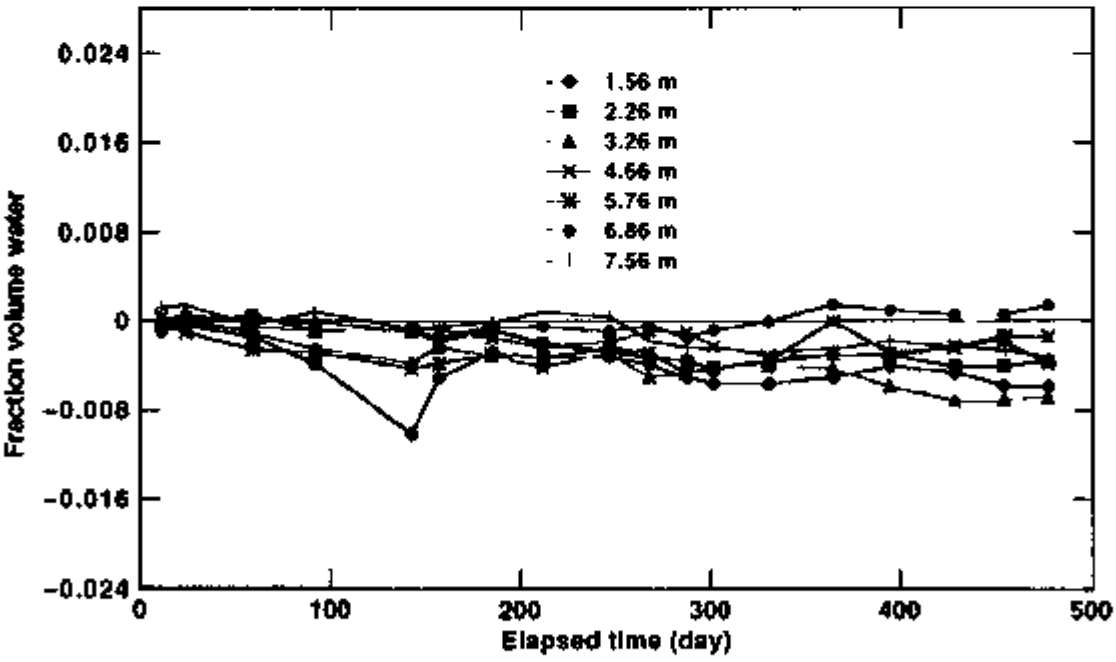

Figure 8-56. Smoothed Difference Fraction Volume Content at Various Depths in Borehole 15 as a Function of Time

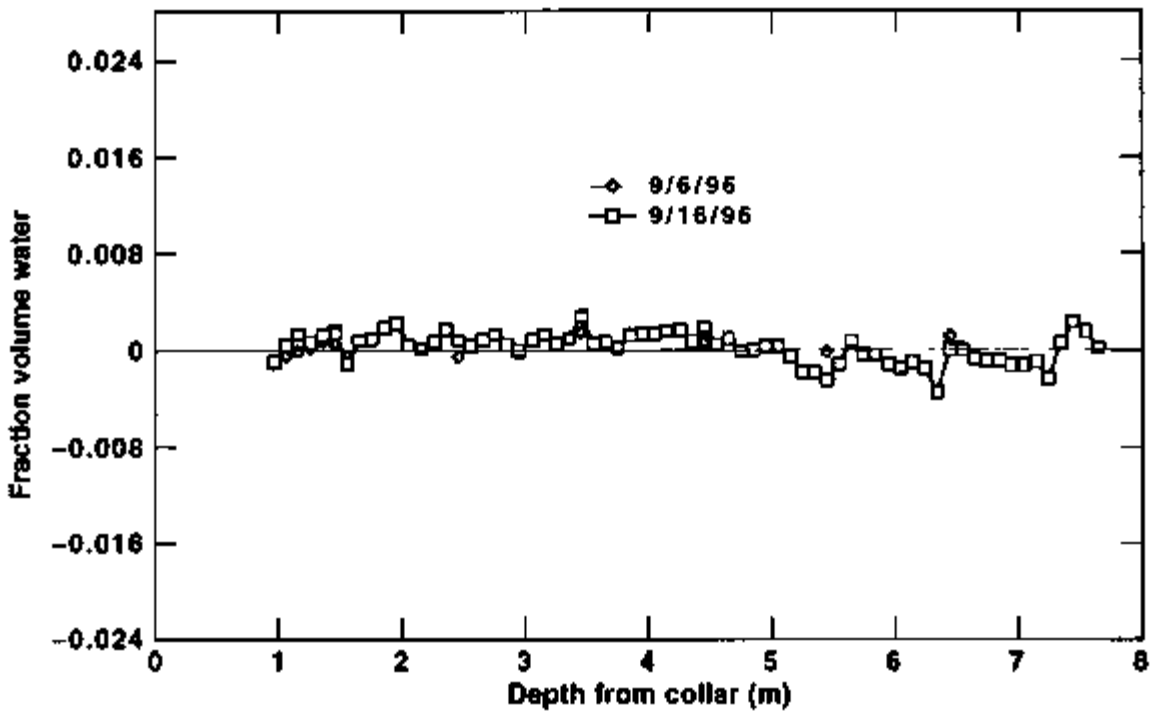

Figure 8-57. Smoothed Difference Fraction Volume Water Content in Borehole 17 as a Function of Depth from Collar on September 6 and September 19, 1996

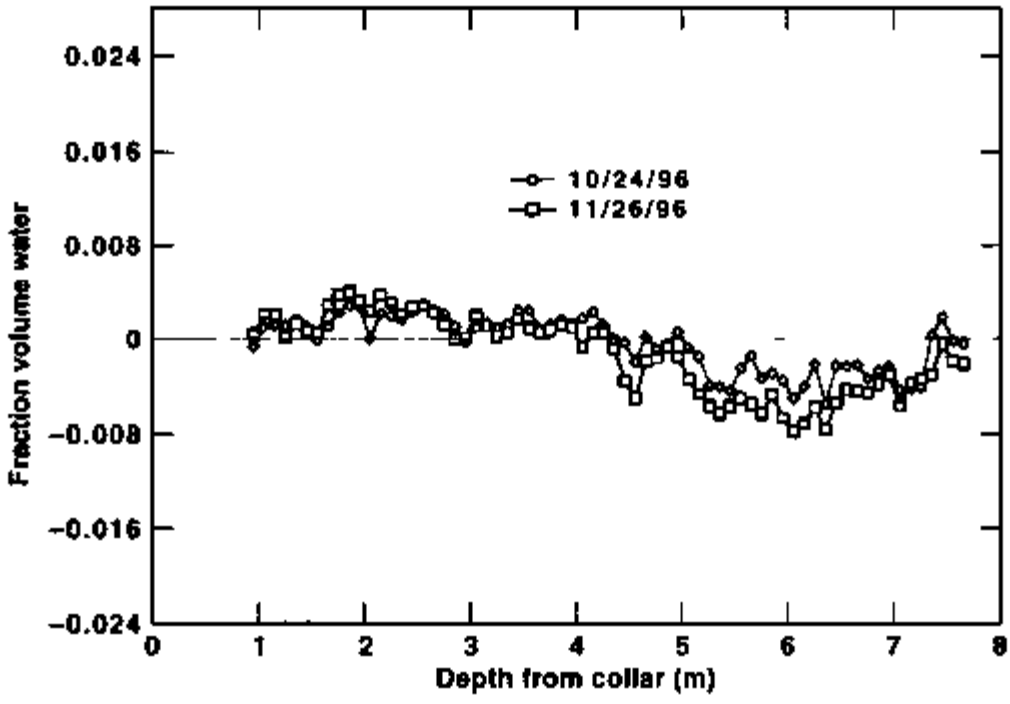

Figure 8-58. Smoothed Difference Fraction Volume Water Content in Borehole 17 as a Function of Depth from Collar on October 24 and November 26, 1996

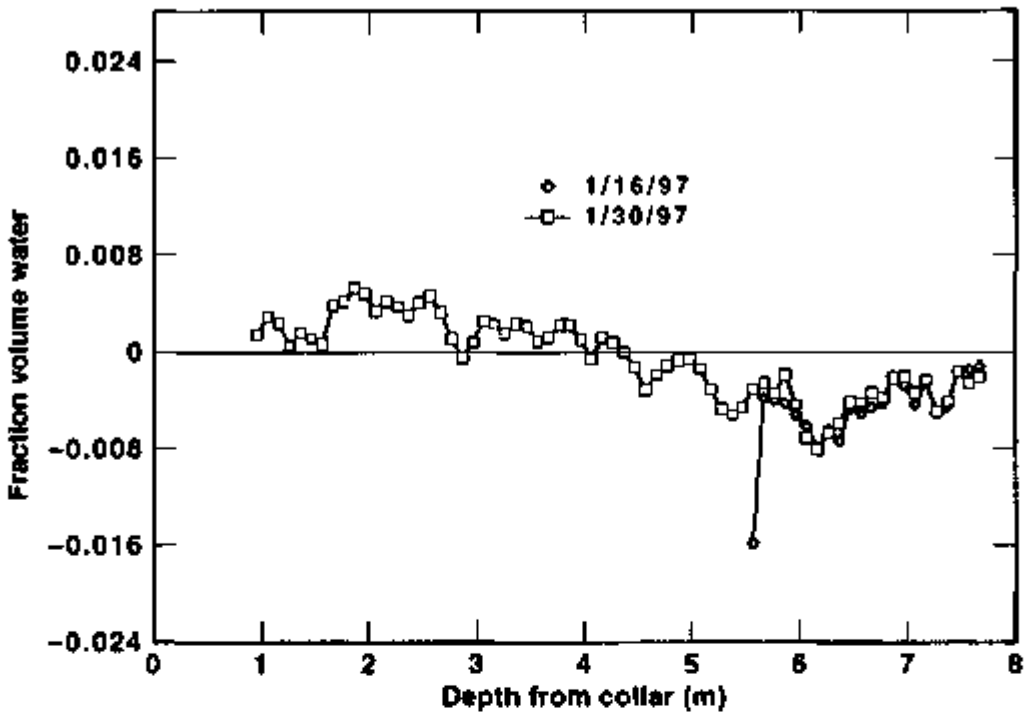

Figure 8-59. Smoothed Difference Fraction Volume Water Content in Borehole 17 as a Function of Depth from Collar on January 16 and January 30, 1997

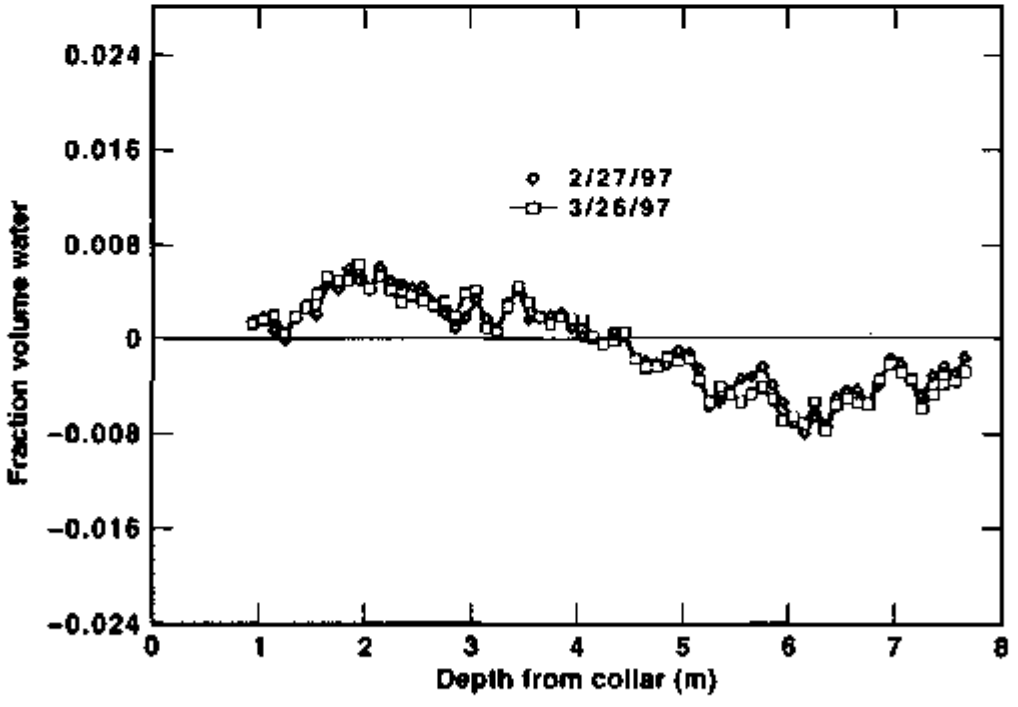

Figure 8-60. Smoothed Difference Fraction Volume Water Content in Borehole 17 as a Function of Depth from Collar on February 27 and March 26, 1997

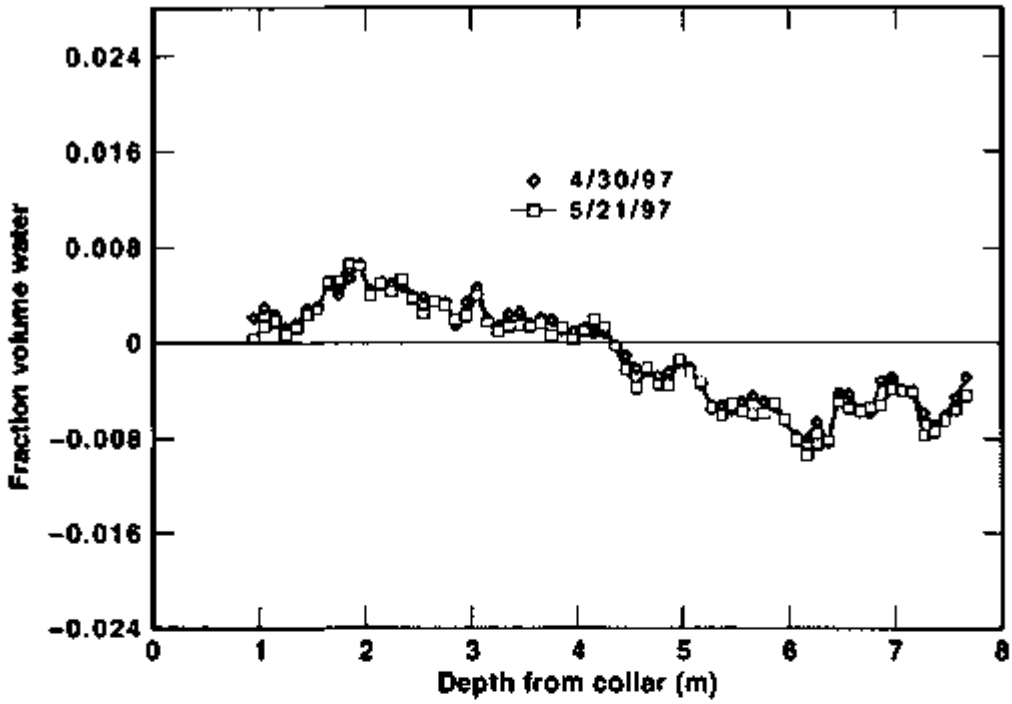

Figure 8-61. Smoothed Difference Fraction Volume Water Content in Borehole 17 as a Function of Depth from Collar on April 30 and May 21, 1997

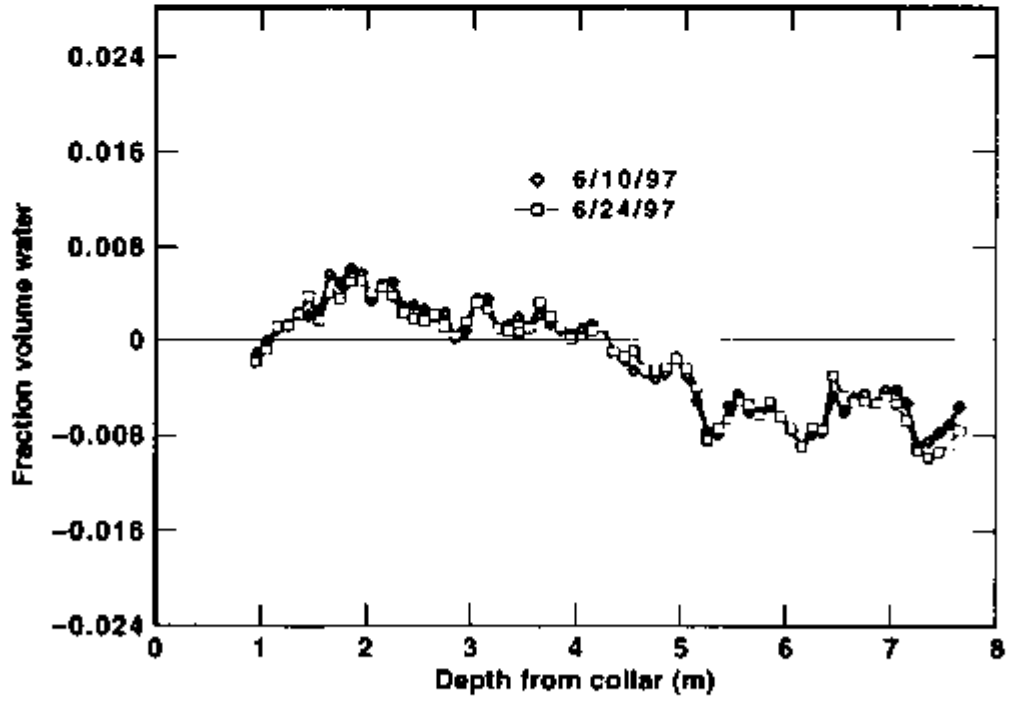

Figure 8-62. Smoothed Difference Fraction Volume Water Content in Borehole 17 as a Function of Depth from Collar on June 10 and June 24, 1997

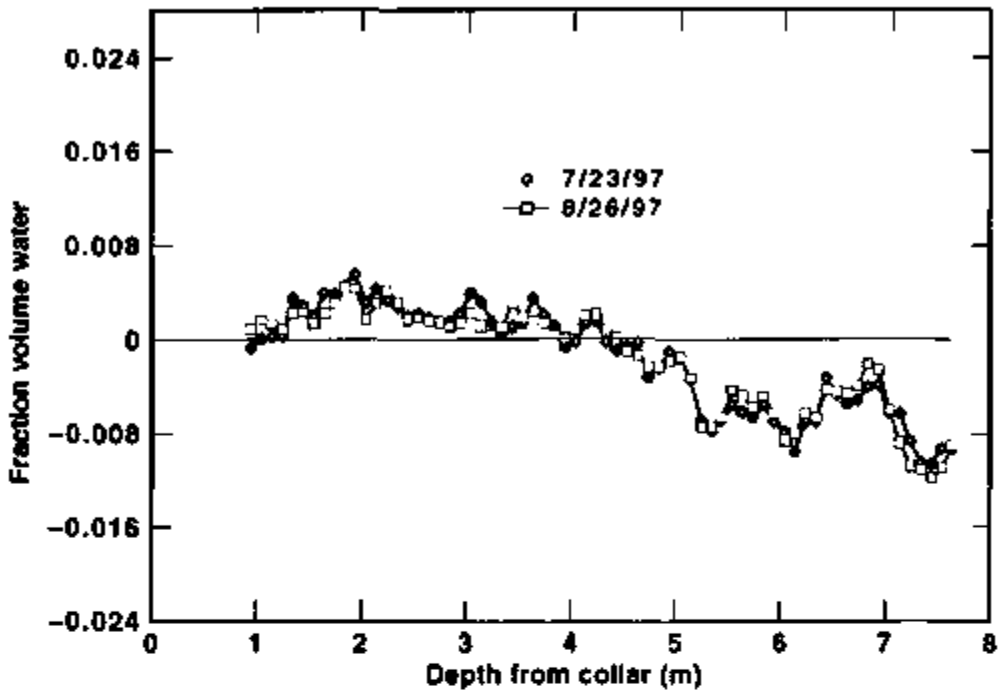

Figure 8-63. Smoothed Difference Fraction Volume Water Content in Borehole 17 as a Function of Depth from Collar on July 23 and August 26, 1997

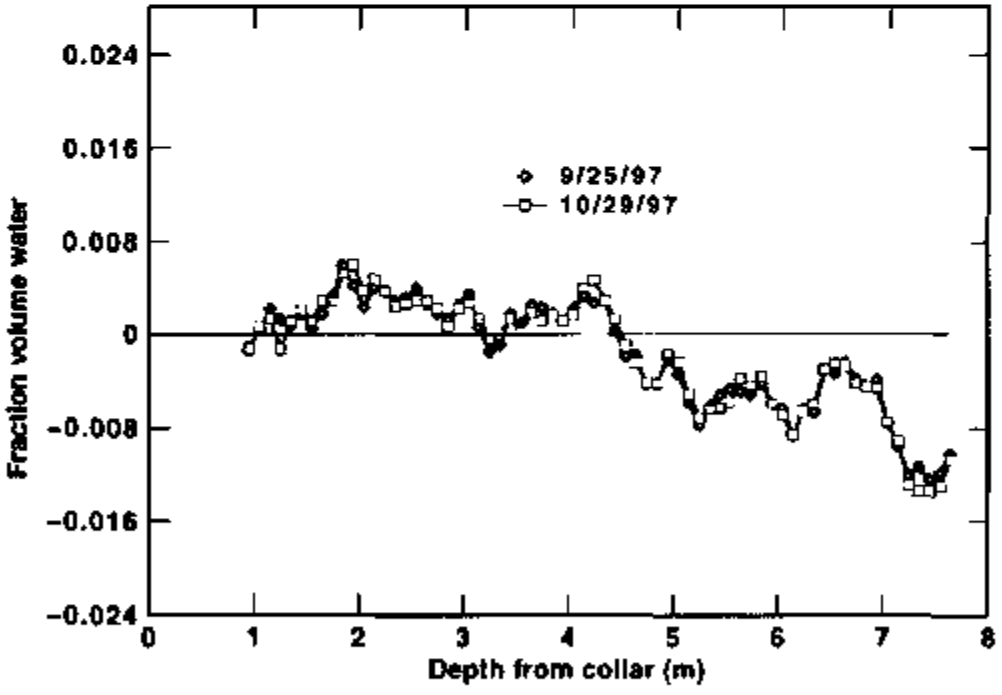

Figure 8-64. Smoothed Difference Fraction Volume Water Content in Borehole 17 as a Function of Depth from Collar on September 25 and October 29, 1997

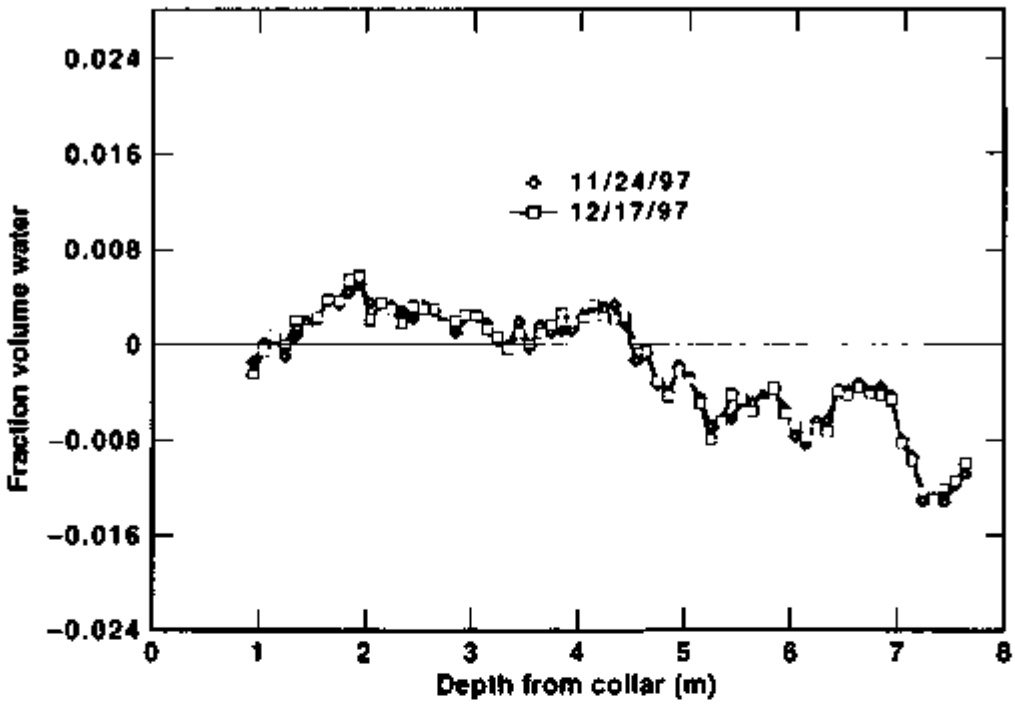

Figure 8-65. Smoothed Difference Fraction Volume Water Content in Borehole 17 as a Function of Depth from Collar on November 24 and December 17, 1997

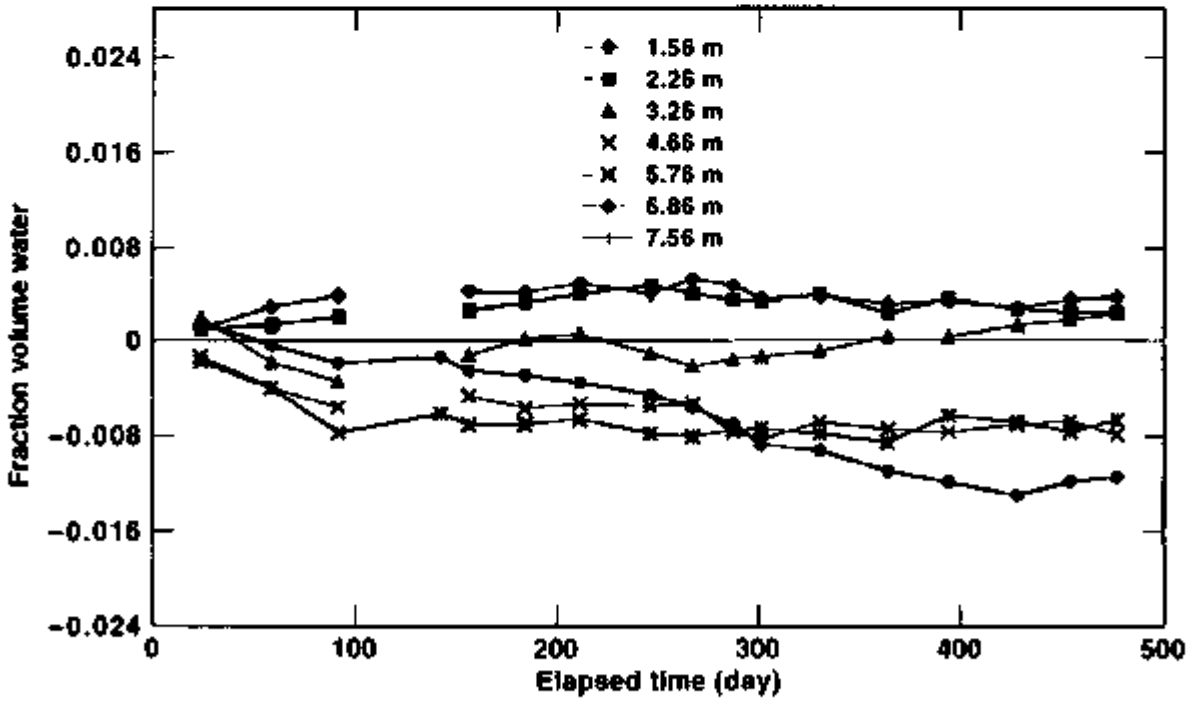

Figure 8-66. Smoothed Difference Fraction Volume Water Content at Various Depths in Borehole 17 as a Function of Time

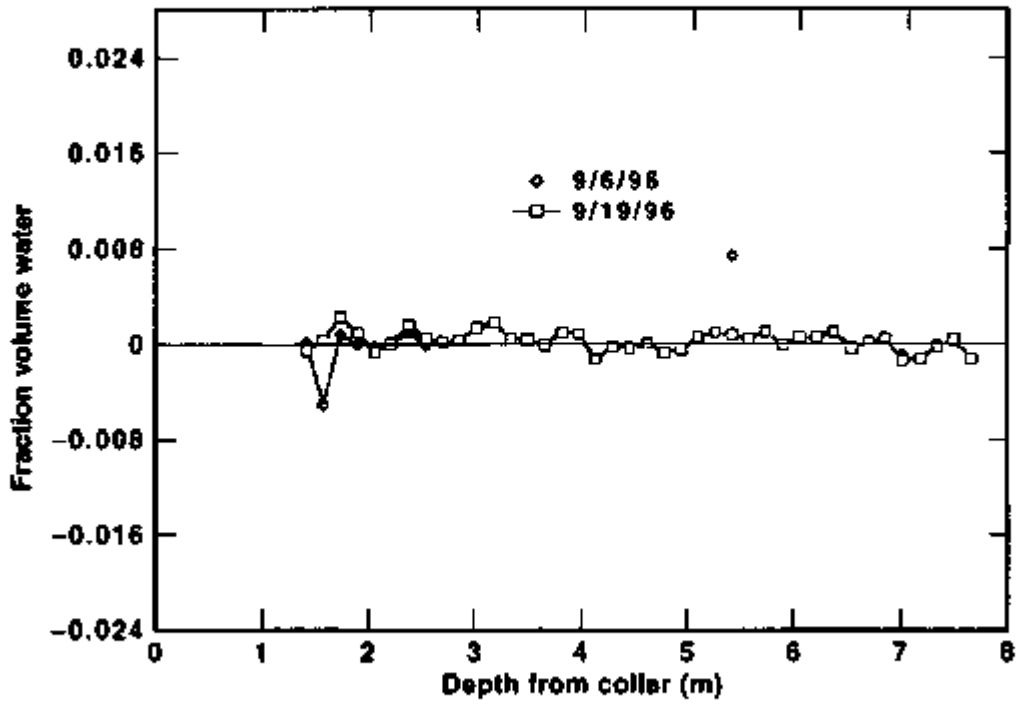

Figure 8-67. Smoothed Difference Fraction Volume Water Content in Borehole 22 as a Function of Depth from Collar on September 6 and September 19, 1996

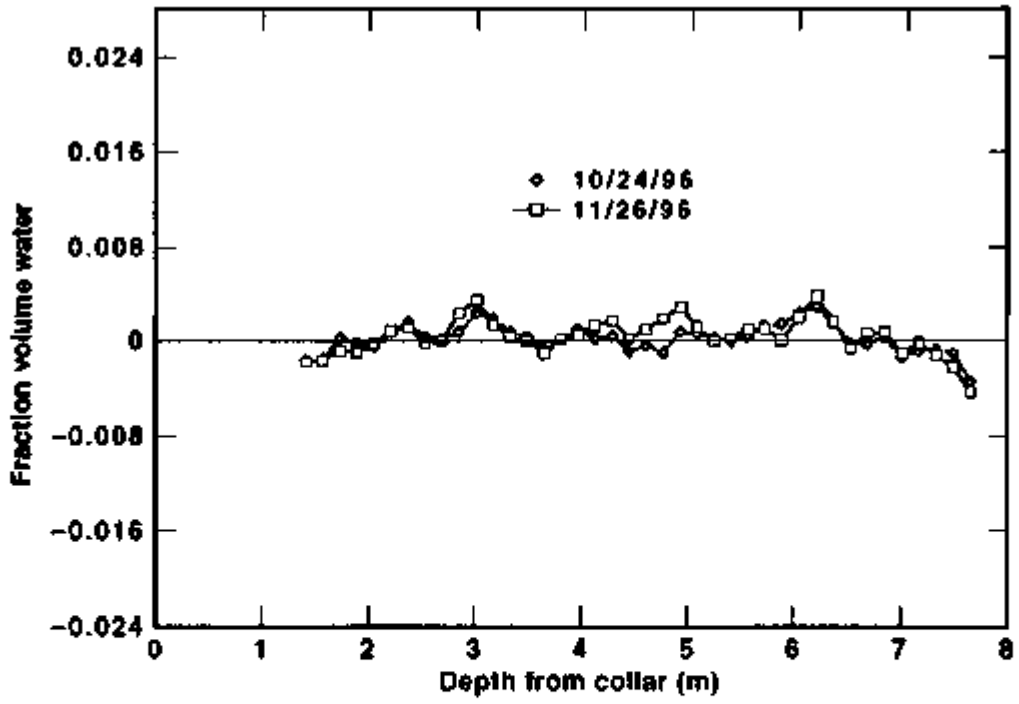

Figure 8-68. Smoothed Difference Fraction Volume Water Content in Borehole 22 as a Function of Depth from Collar on October 24 and November 26, 1996

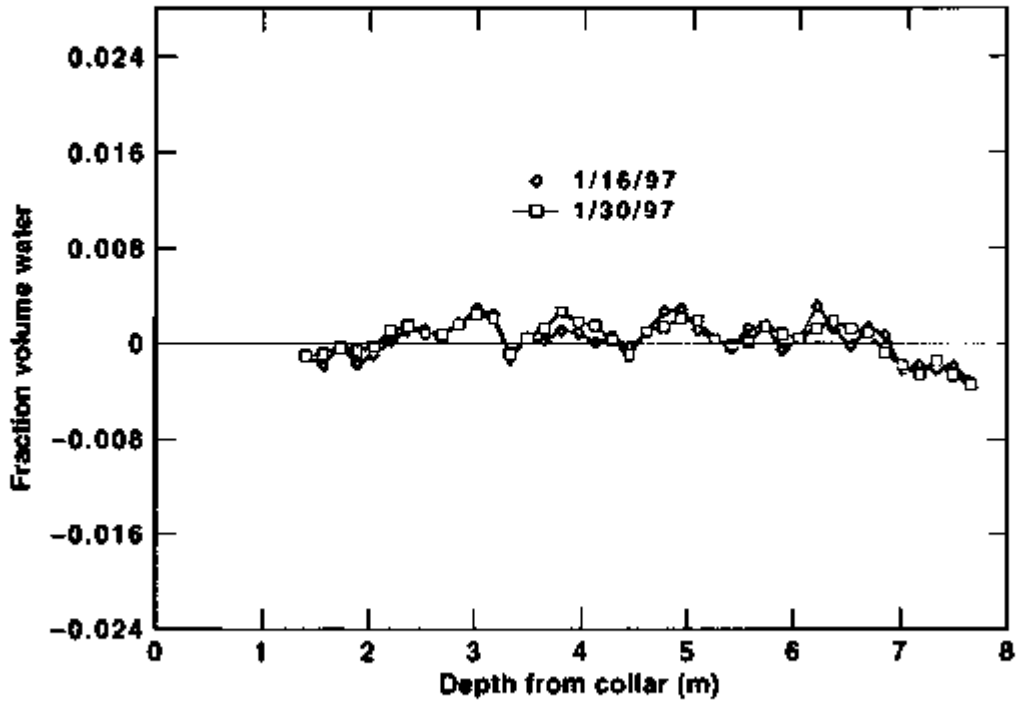

Figure 8-69. Smoothed Difference Fraction Volume Water Content in Borehole 22 as a Function of Depth from Collar on January 16 and January 30, 1997

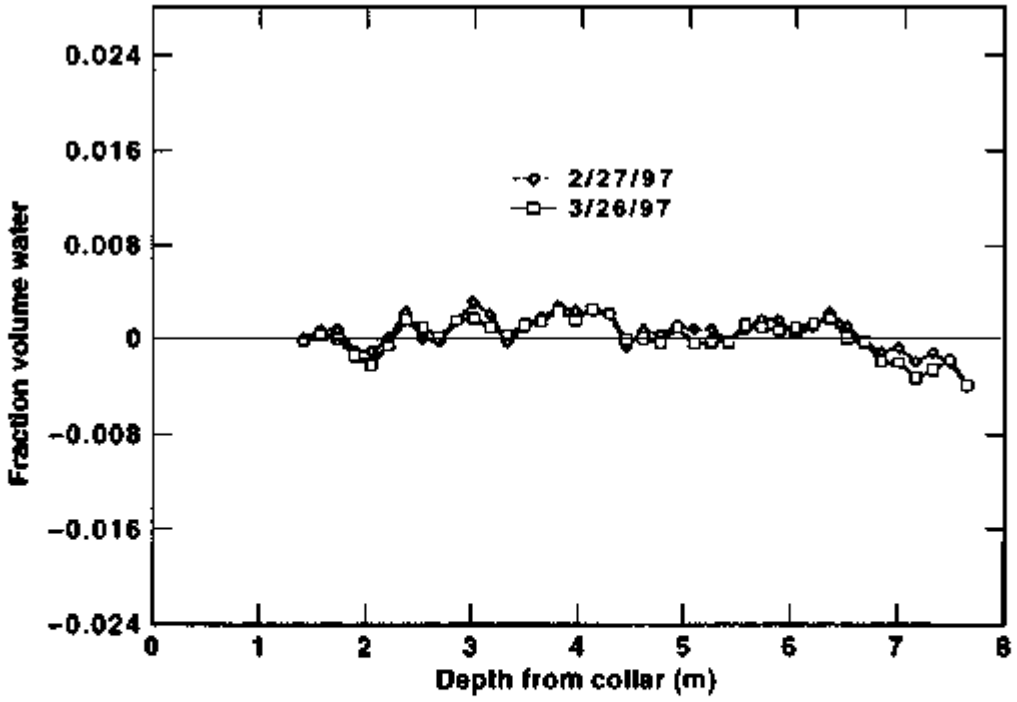

Figure 8-70. Smoothed Difference Fraction Volume Water Content in Borehole 22 as a Function of Depth from Collar on February 27 and March 26, 1997

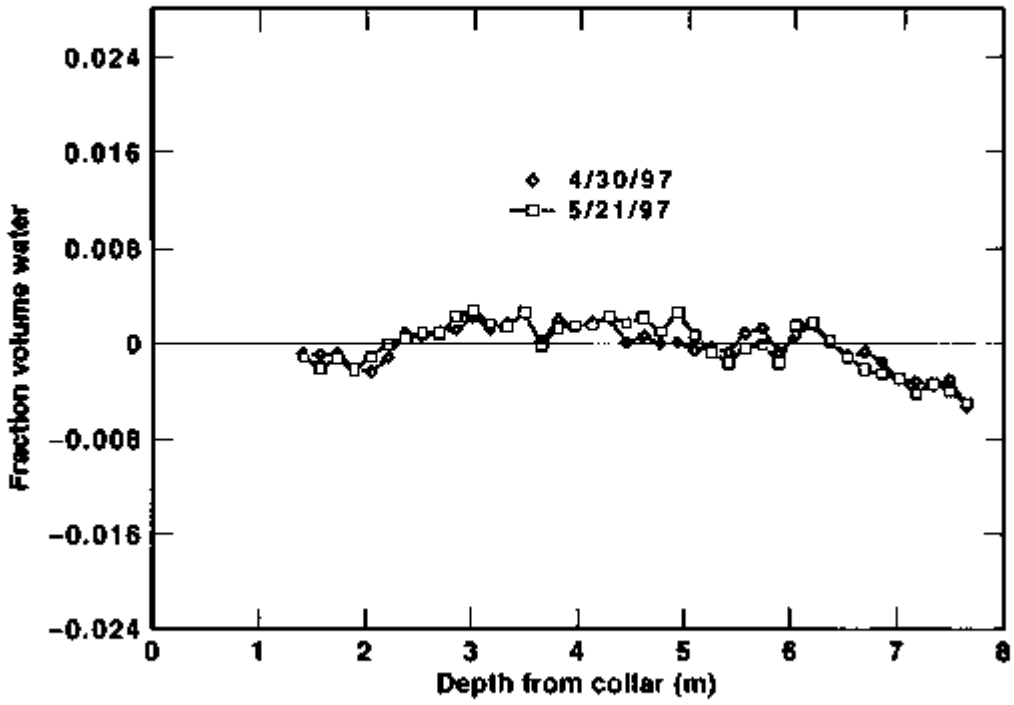

Figure 8-71. Smoothed Difference Fraction Volume Water Content in Borehole 22 as a Function of Depth from Collar on April 30 and May 21, 1997

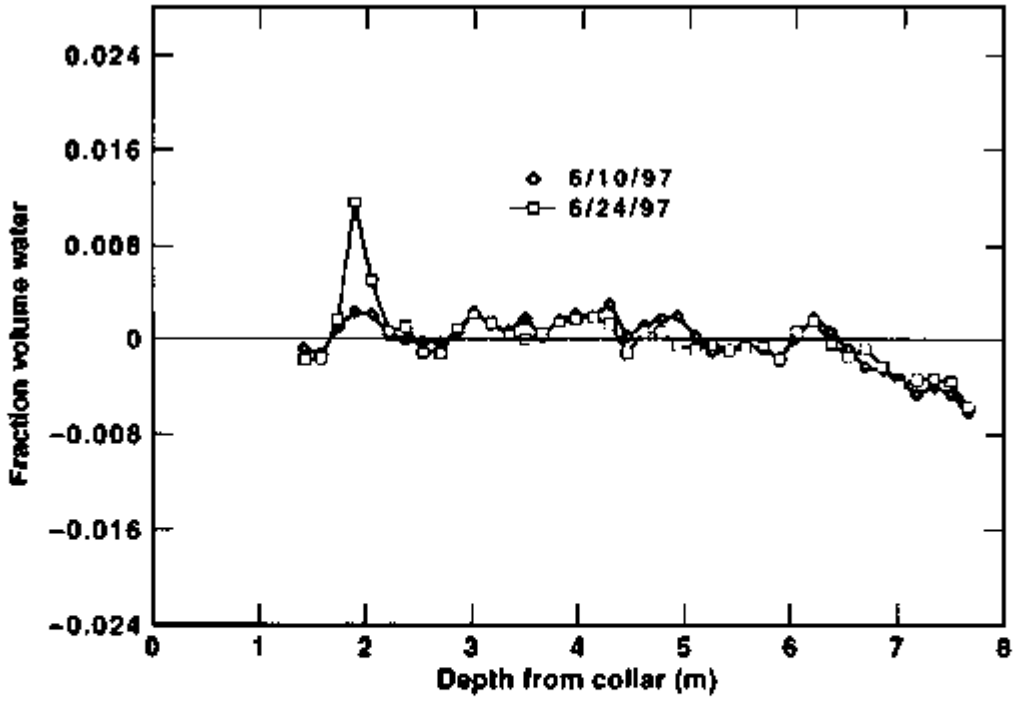

Figure 8-72. Smoothed Difference Fraction Volume Water Content in Borehole 22 as a Function of Depth from Collar on June 10 and June 24, 1997

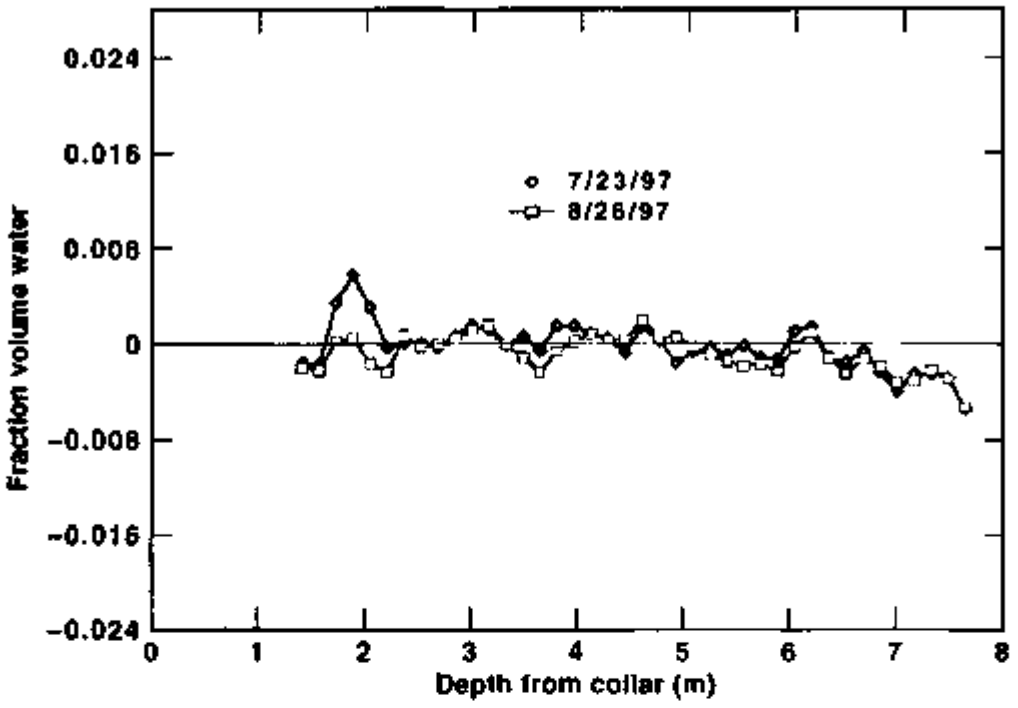

Figure 8-73. Smoothed Difference Fraction Volume Water Content in Borehole 22 as a Function of Depth from Collar on July 23 and August 26, 1997

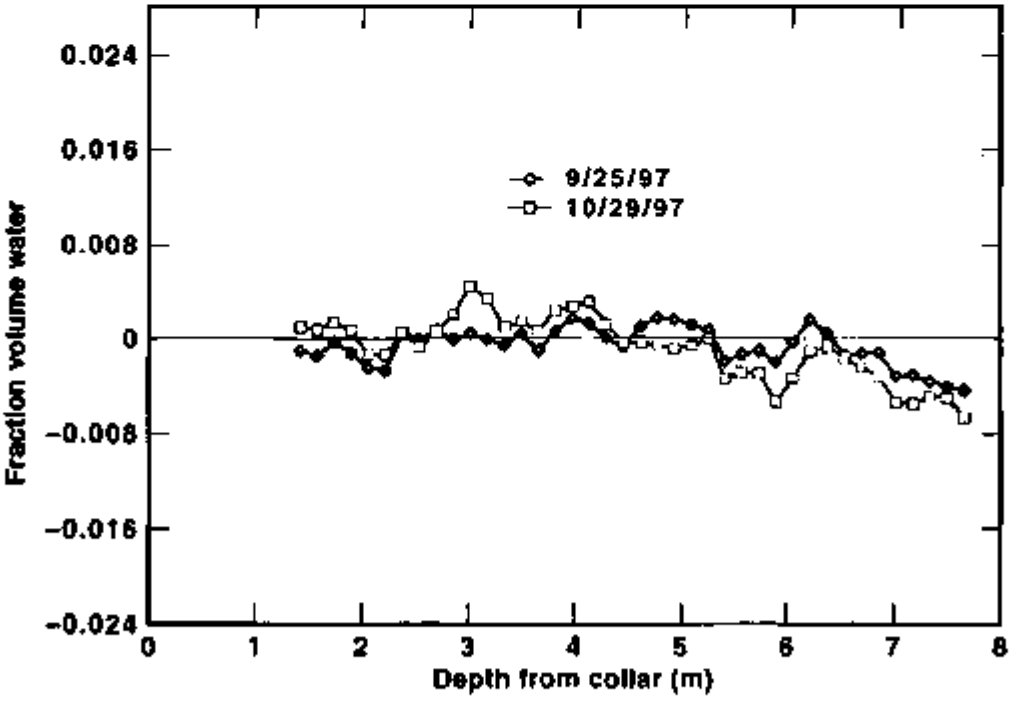

Figure 8-74. Smoothed Difference Fraction Volume Water Content in Borehole 22 as a Function of Depth from Collar on September 25 and October 29, 1997

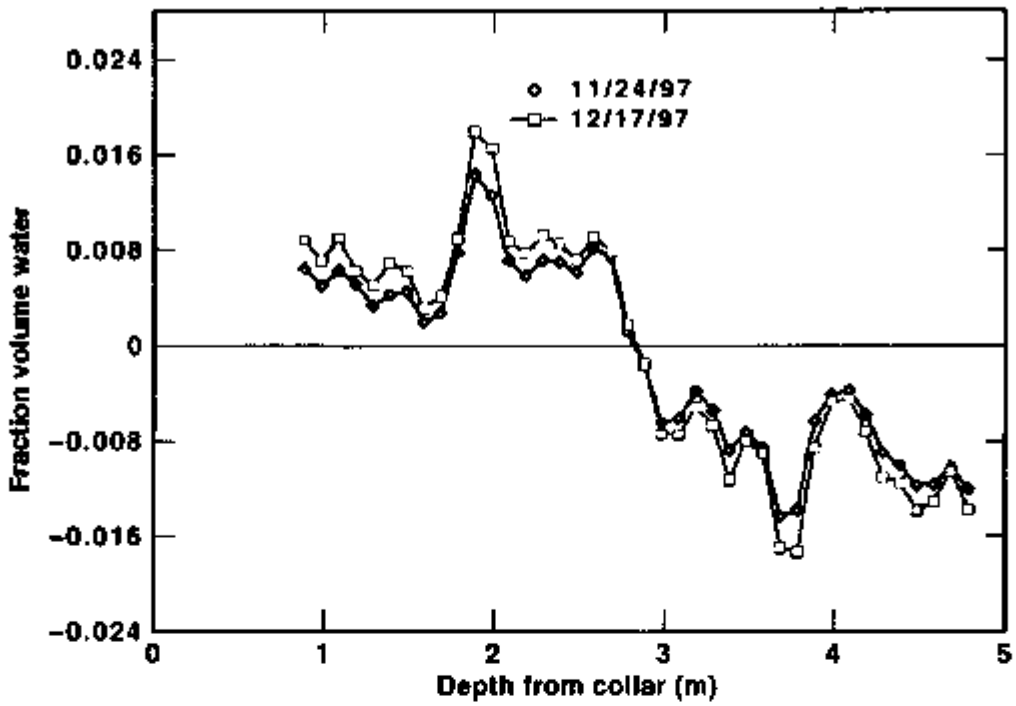

Figure 8-75. Smoothed Difference Fraction Volume Water Content in Borehole 22 as a Function of Depth from Collar on November 24 and December 17, 1997

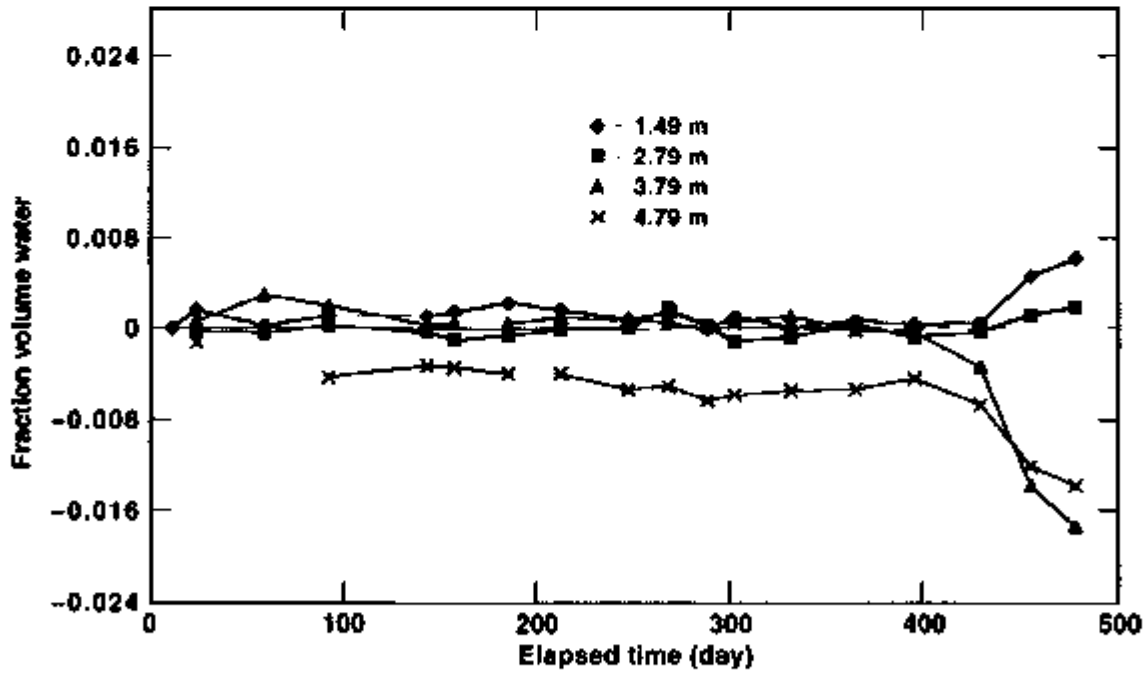

Figure 8-76. Smoothed Difference Fraction Volume Water Content at Various Depths in Borehole 22 as a Function of Time

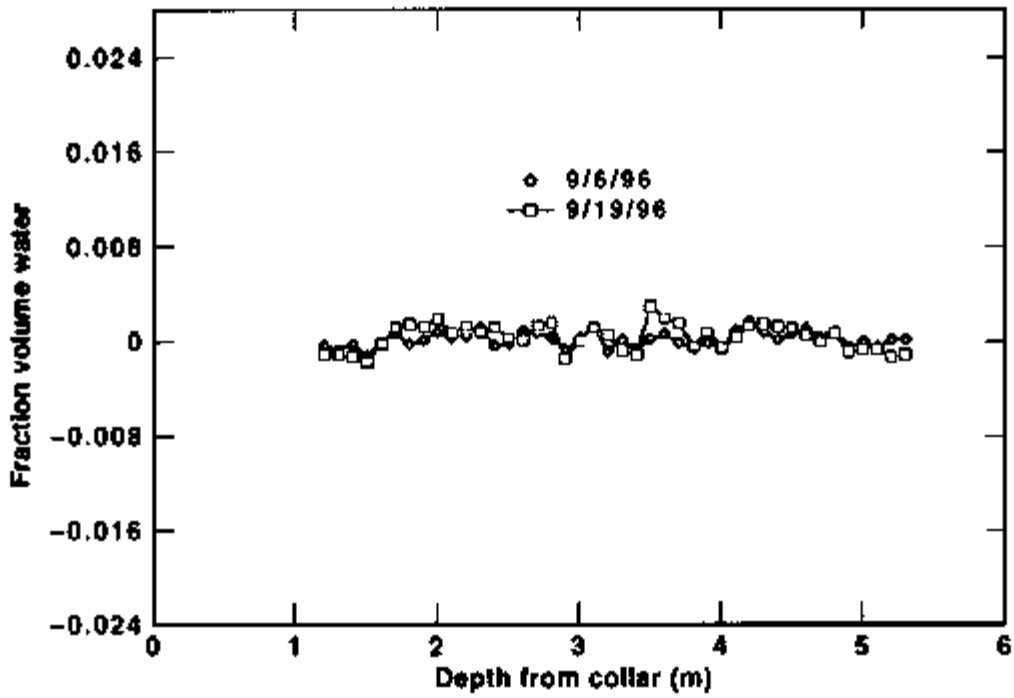

Figure 8-77. Smoothed Difference Fraction Volume Water Content in Borehole 23 as a Function of Depth from Collar on September 6 and September 19, 1996

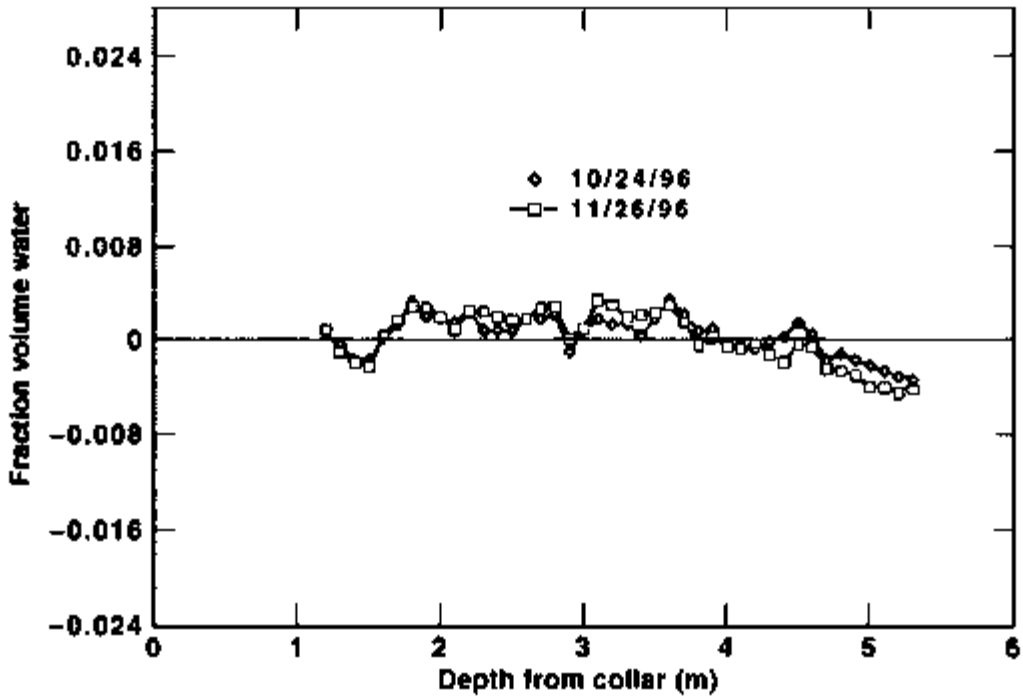

Figure 8-78. Smoothed Difference Fraction Volume Water Content in Borehole 23 as a Function of Depth from Collar on October 24 and November 26, 1996

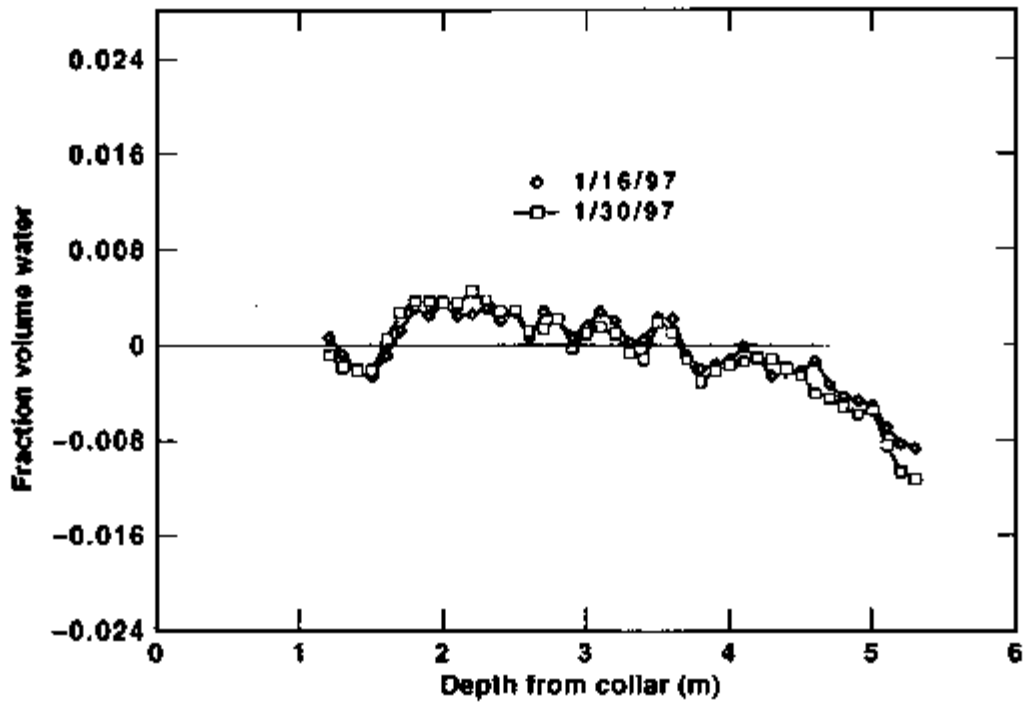

Figure 8-79. Smoothed Difference Fraction Volume Water Content in Borehole 23 as a Function of Depth from Collar on January 16 and January 30, 1997

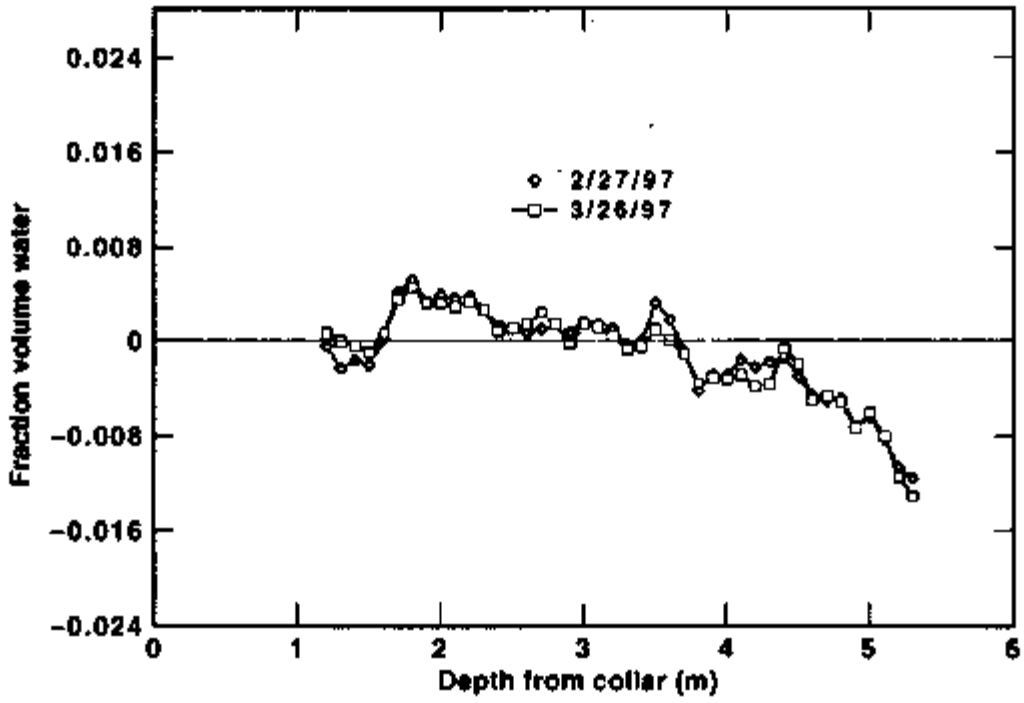

Figure 8-80. Smoothed Difference Fraction Volume Water Content in Borehole 23 as a Function of Depth from Collar on February 27 and March 26, 1997

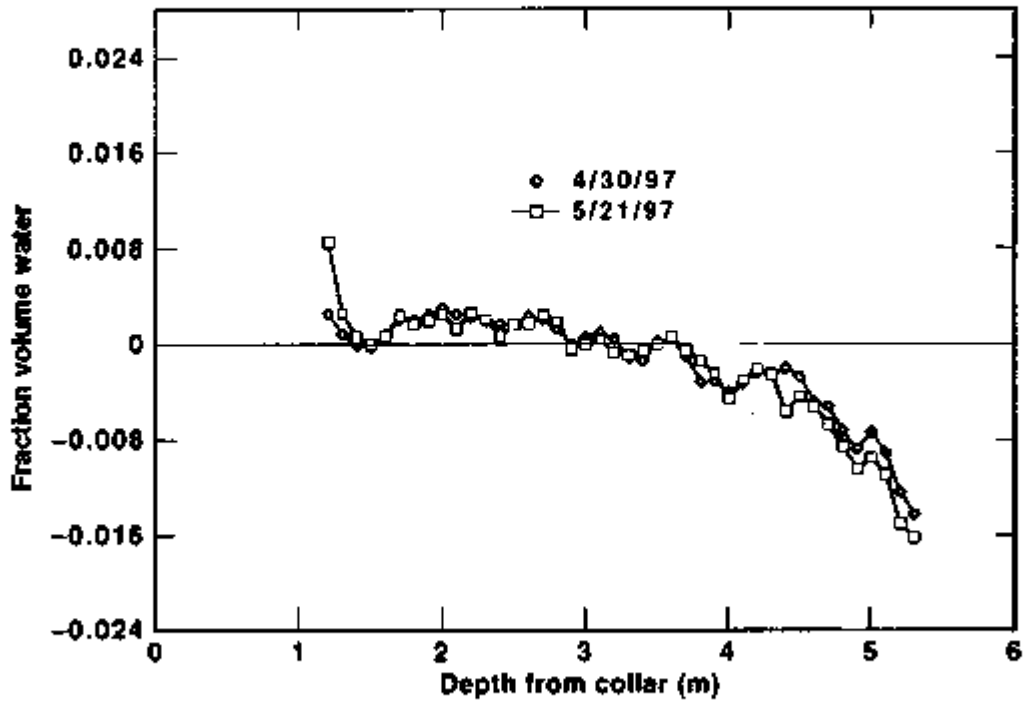

Figure 8-81. Smoothed Difference Fraction Volume Water Content in Borehole 23 as a Function of Depth from Collar on April 30 and May 21, 1997

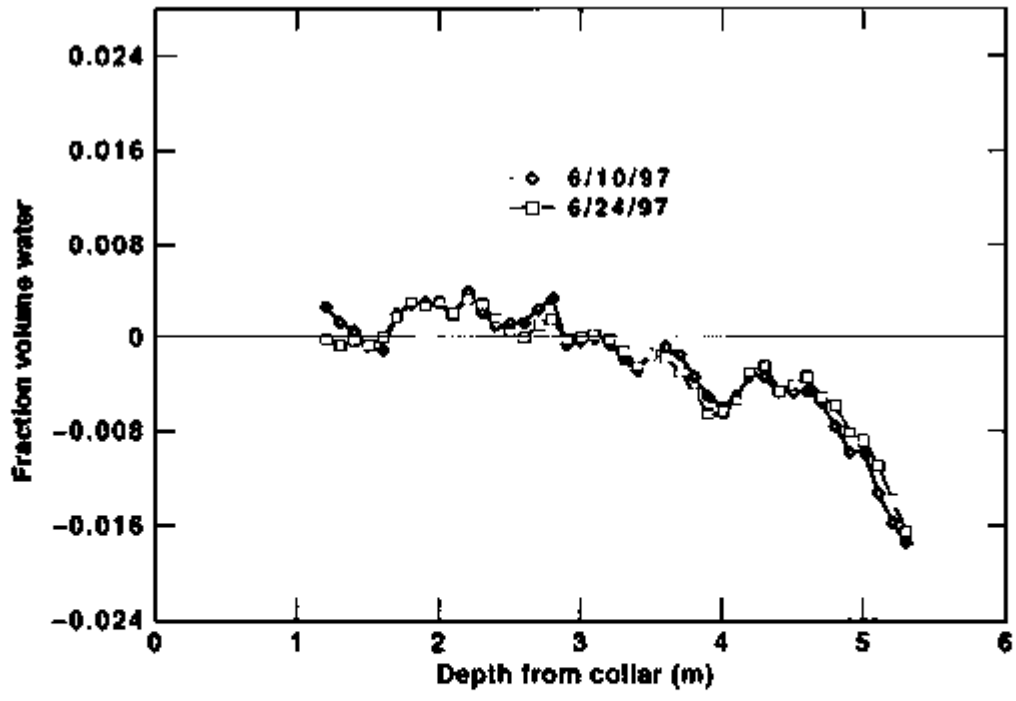

Figure 8-82. Smoothed Difference Fraction Volume Water Content in Borehole 23 as a Function of Depth from Collar on June 10 and June 24, 1997

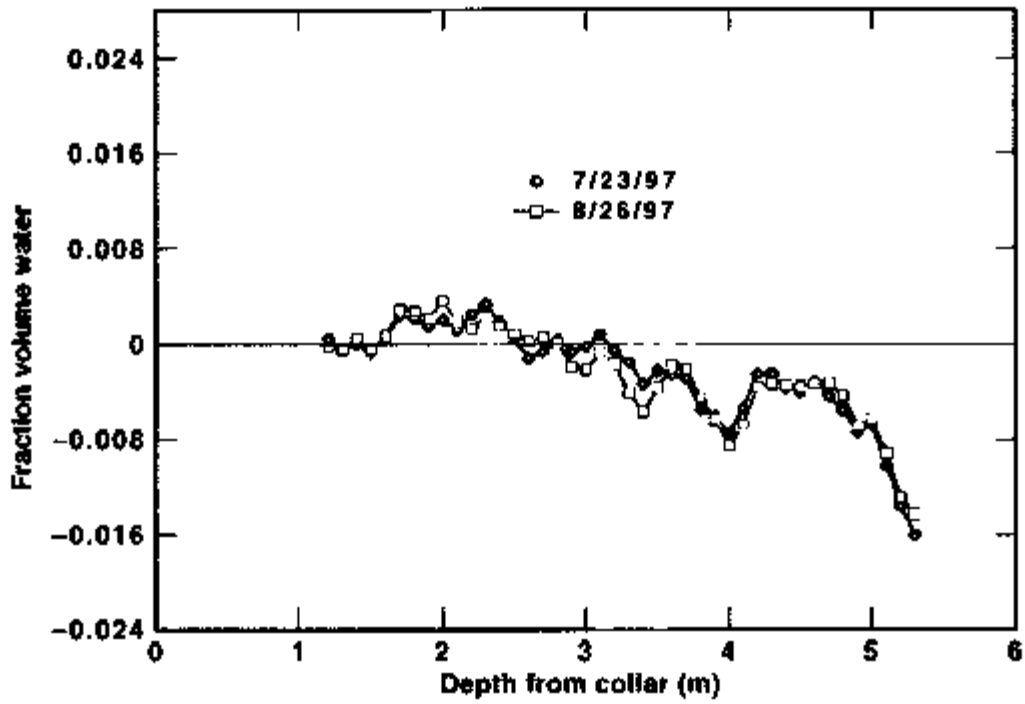

Figure 8-83. Smoothed Difference Fraction Volume Water Content in Borehole 23 as a Function of Depth from Collar on July 23 and August 26, 1997

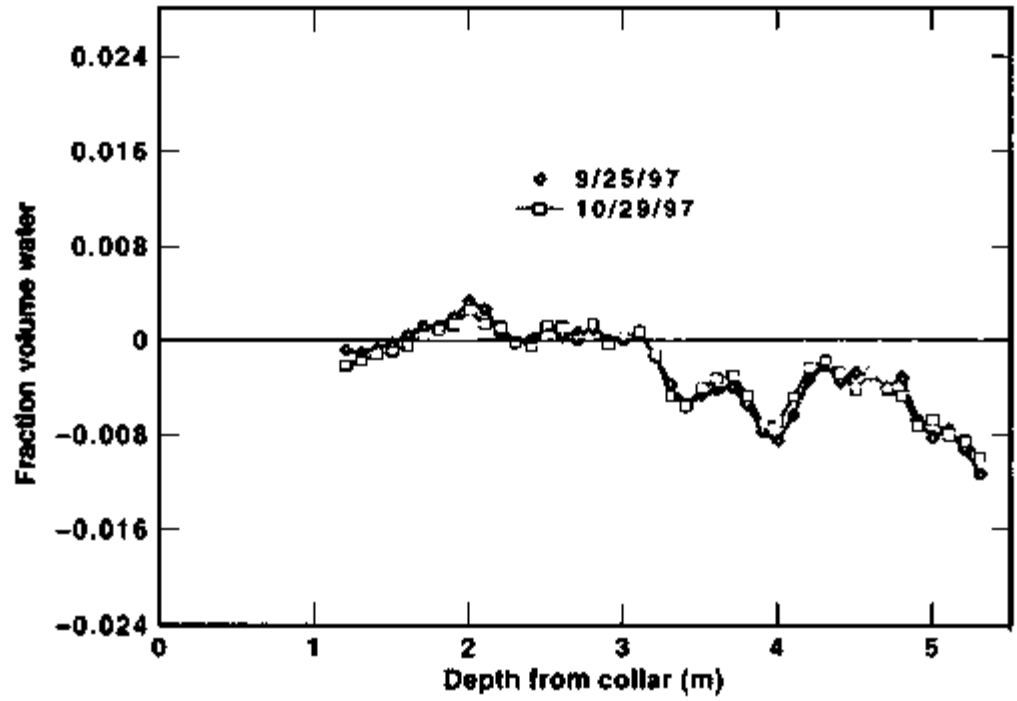

Figure 8-84. Smoothed Difference Fraction Volume Water Content in Borehole 23 as a Function of Depth from Collar on September 25 and October 29, 1997

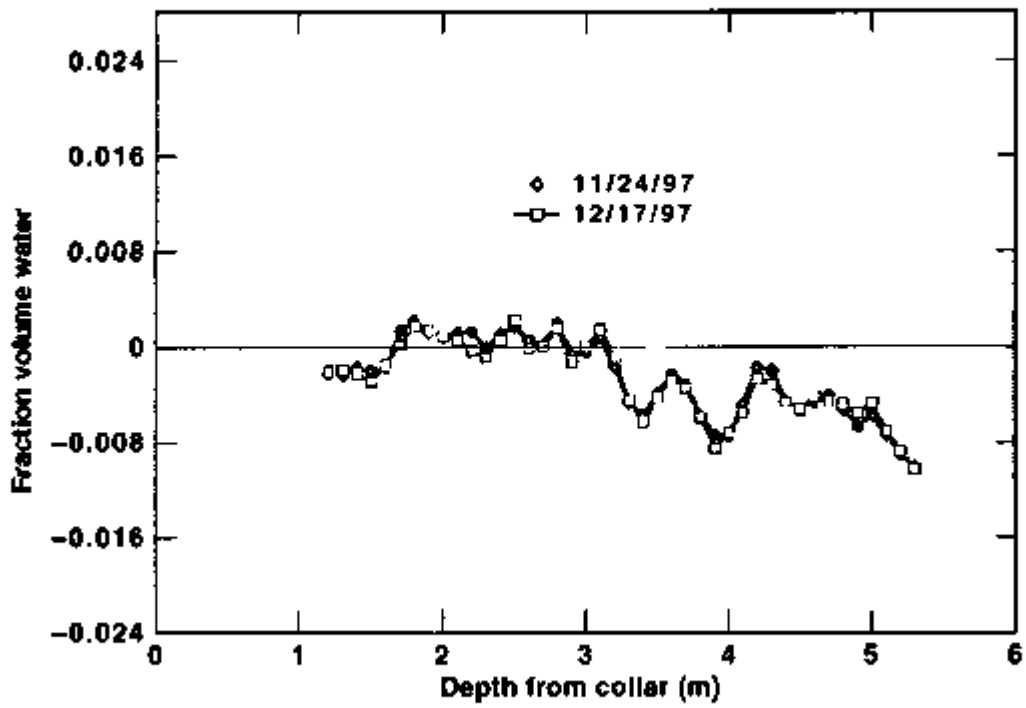

Figure 8-85. Smoothed Difference Fraction Volume Water Content in Borehole 23 as a Function of Depth from Collar on November 24 and December 17, 1997

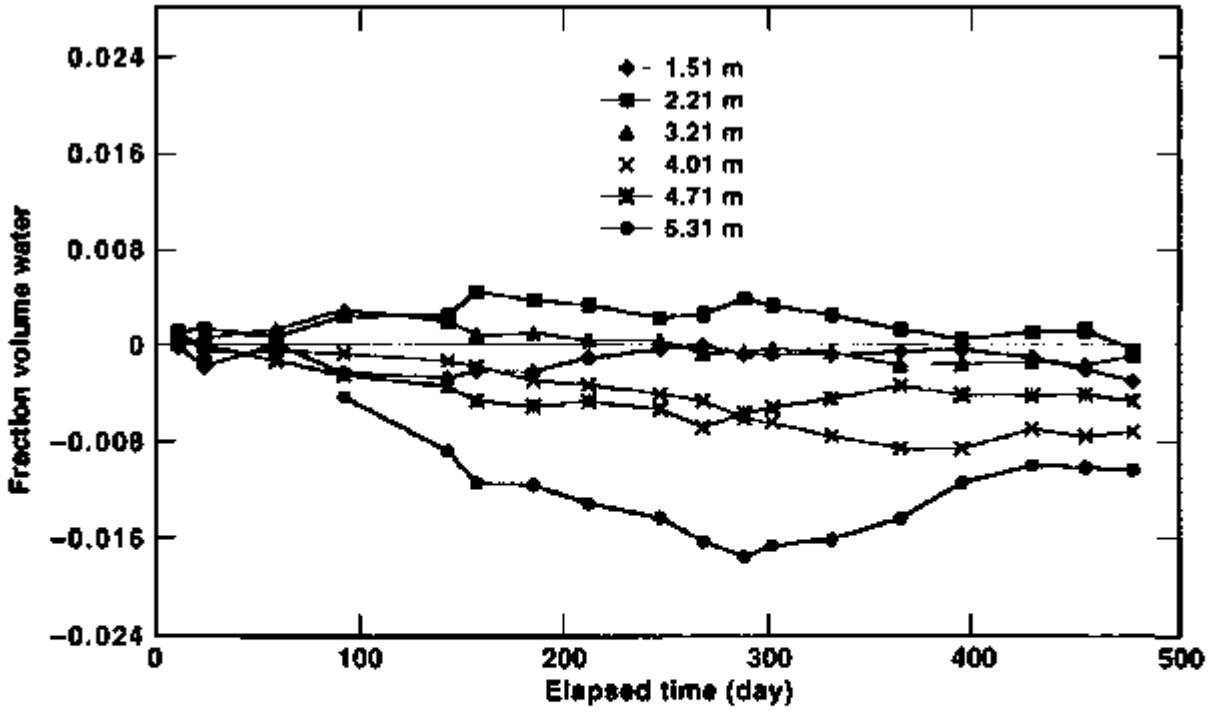

Figure 8-86. Smoothed Difference Fraction Volume Water Content at Various Depths in Borehole 23 as a Function of Time

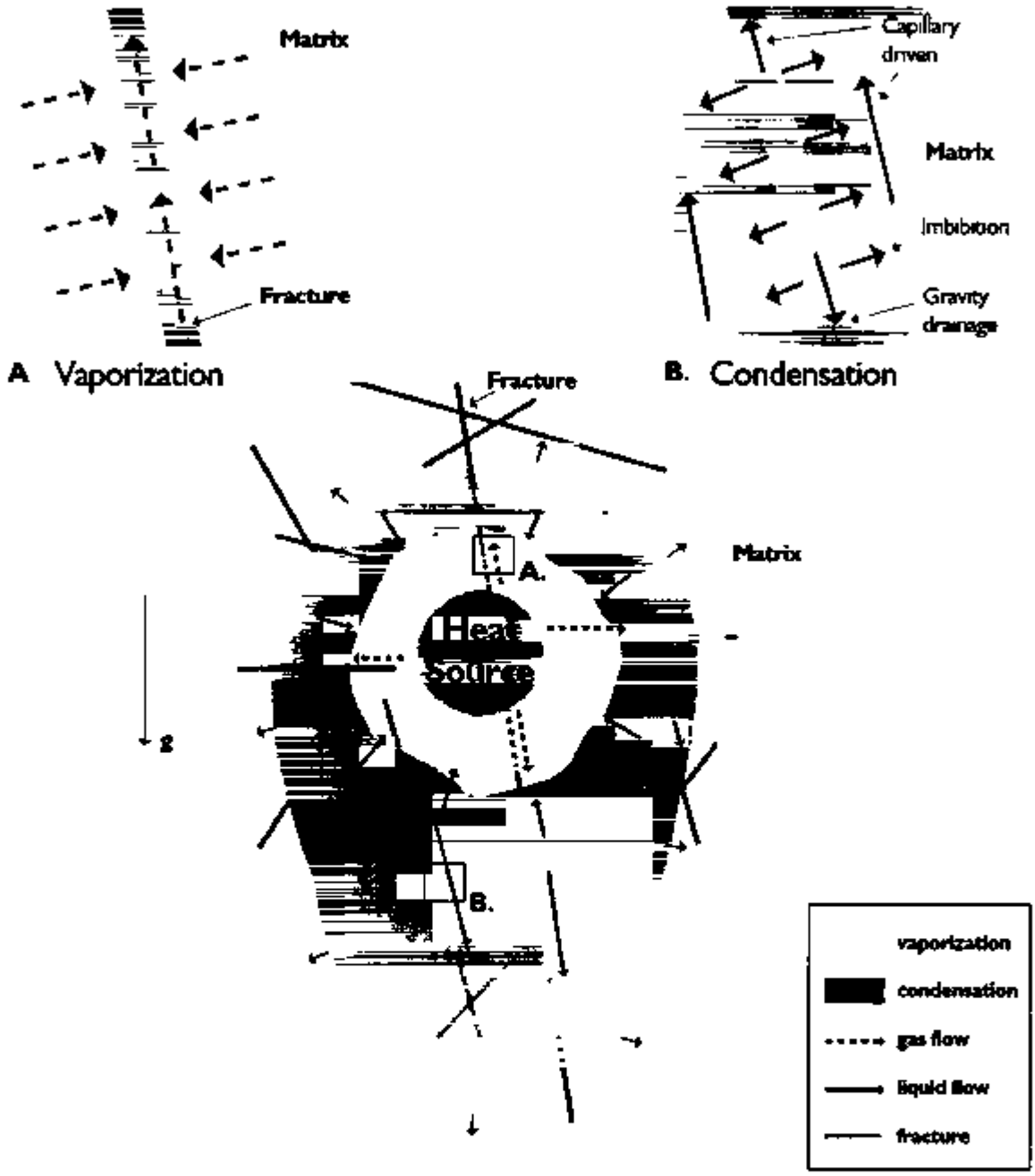

Figure 8-87 Potential Thermal-Hydrological Processes in Fractured Tuff after Emplacement of a Heat Source

Conceptual Models for Fracture-Matrix Interaction

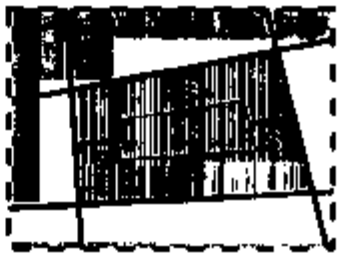

Concept	Capillary Pressure	Interflow
ECM (1 Continuum)	Equilibrium ($P_f = P_m$)	Infinitely Fast
DKM (2 Continua)	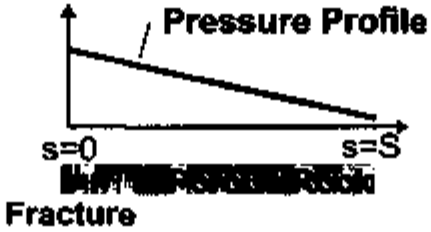	proportional to pressure difference
MINC (Multiple Continua)	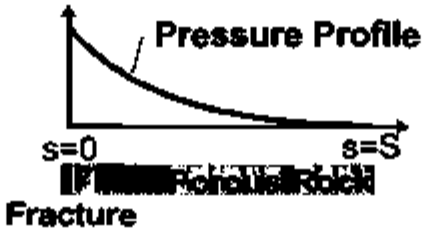	proportional to interface gradient

Figure 8-88. Conceptual Models for Fracture-Matrix Interaction (ECM, DKM and MINC)

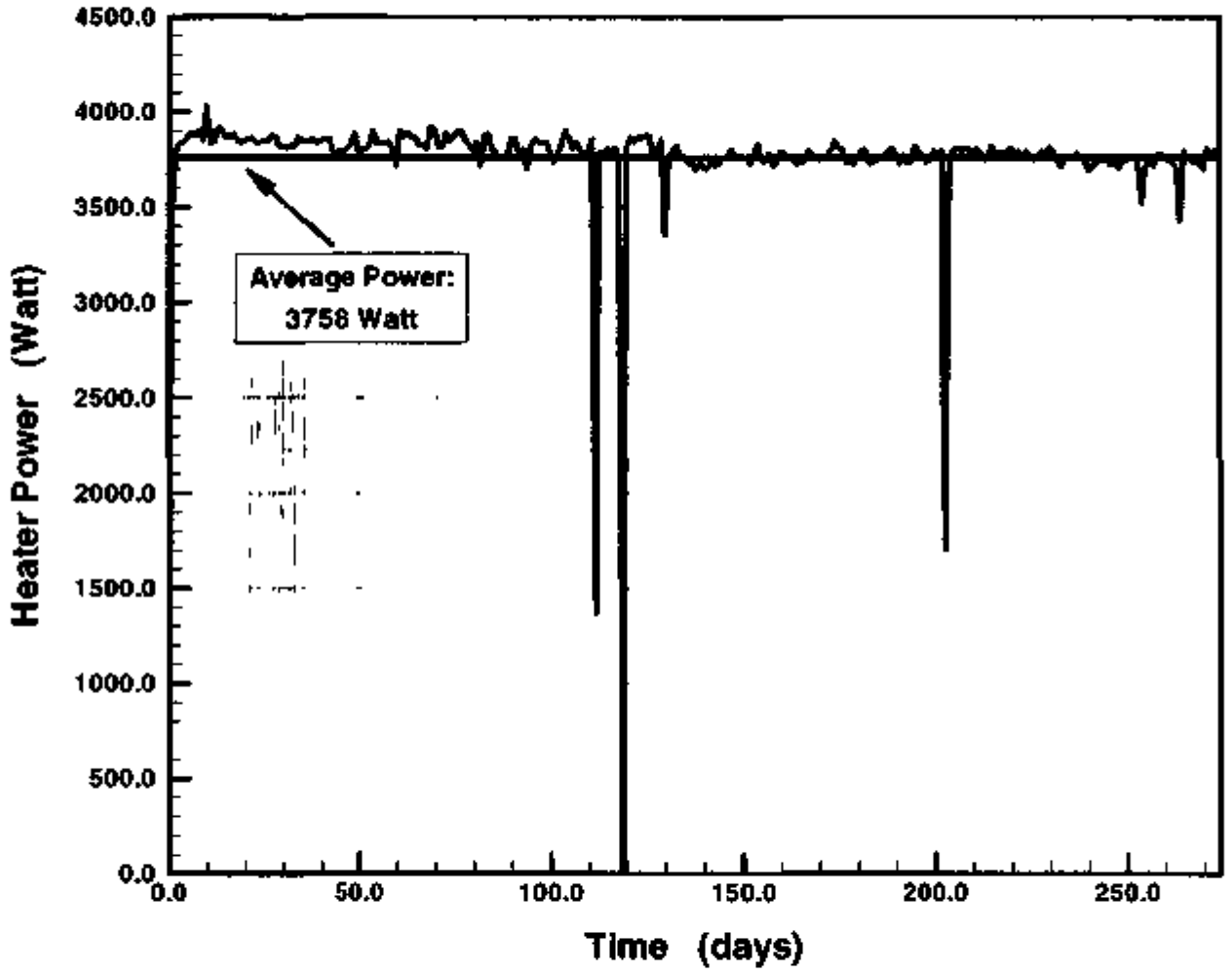

Figure 8-89. Heater Power during Operation of the Test

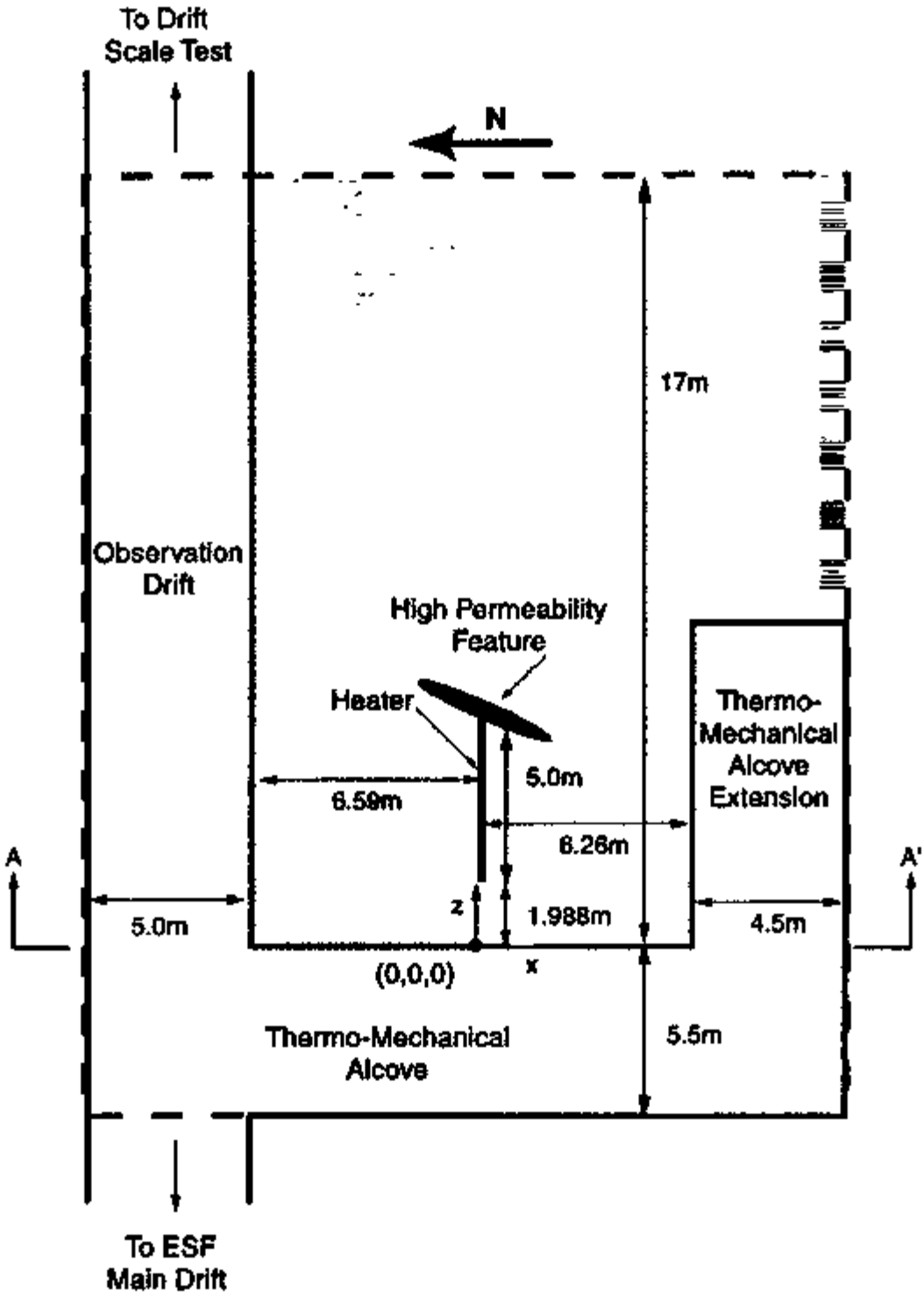

NOTE The shaded areas indicate the model domain extension

Figure 8-90 Boundaries of SHT Model Domain in a Plan View

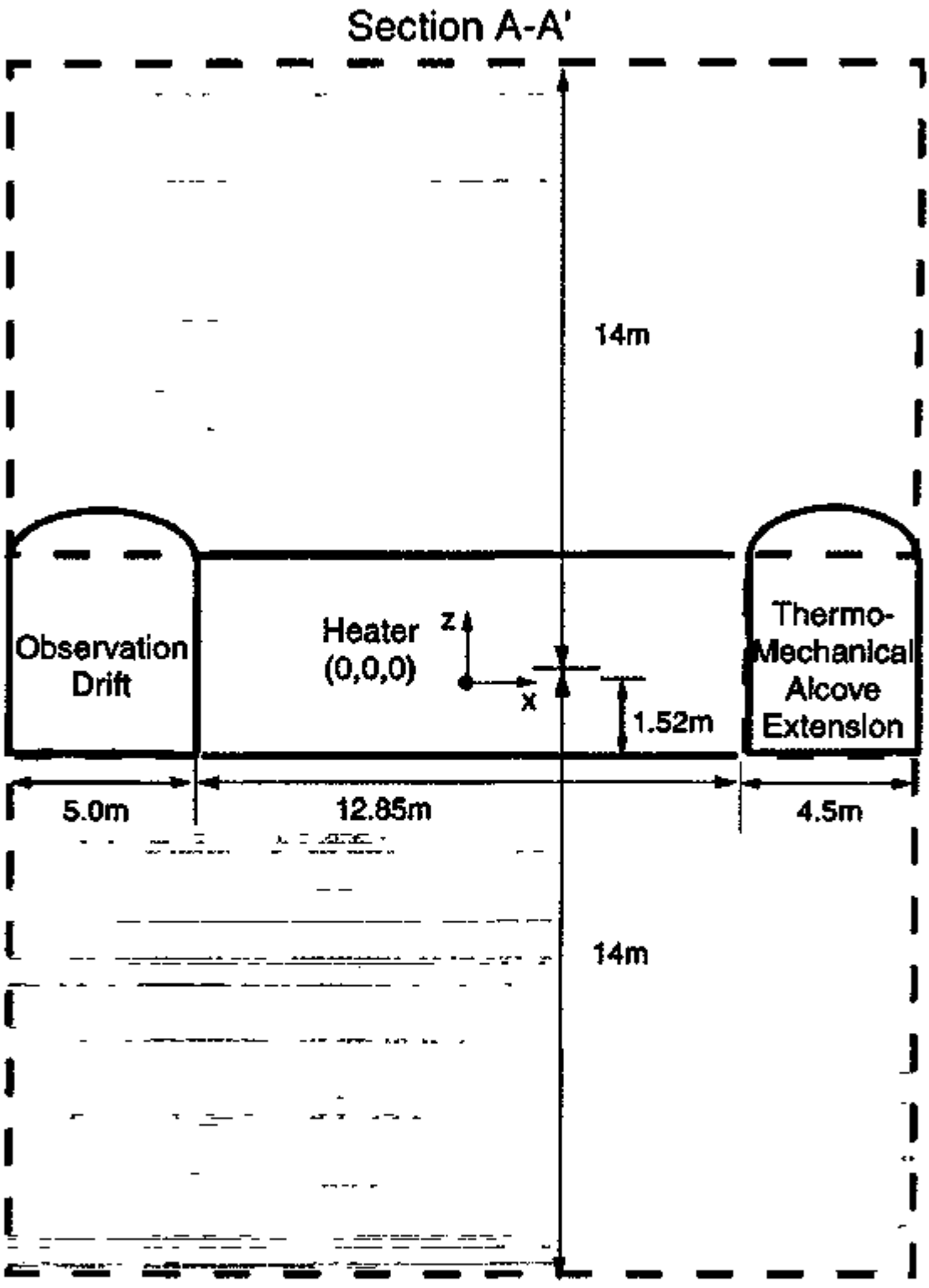

NOTE The shaded area indicates the model domain extension

Figure 8-91 Boundaries of SHT Model Domain in a Vertical Cross-Section

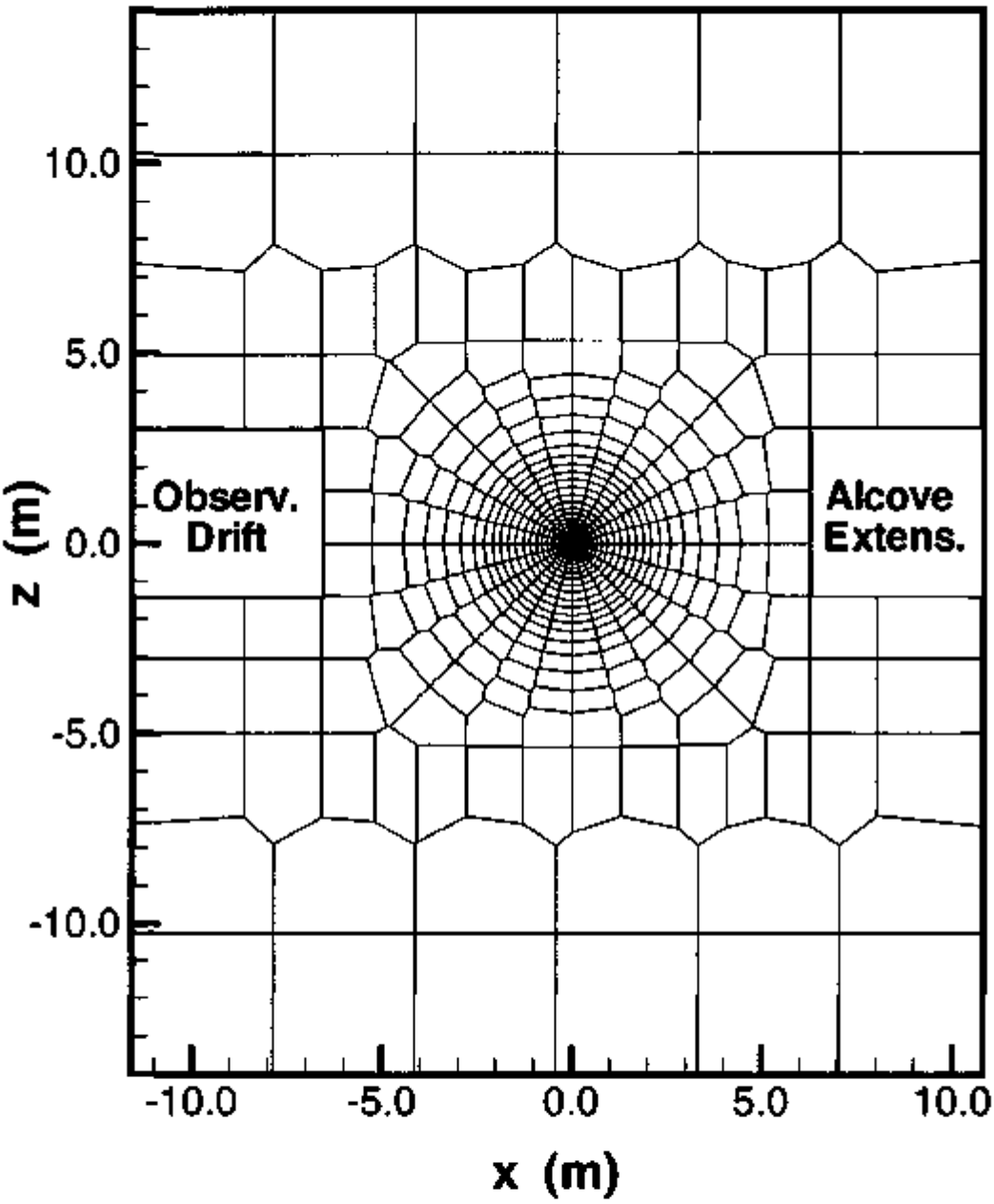

Figure 8-92. Discretization of SHT Model in a Vertical Cross-Section

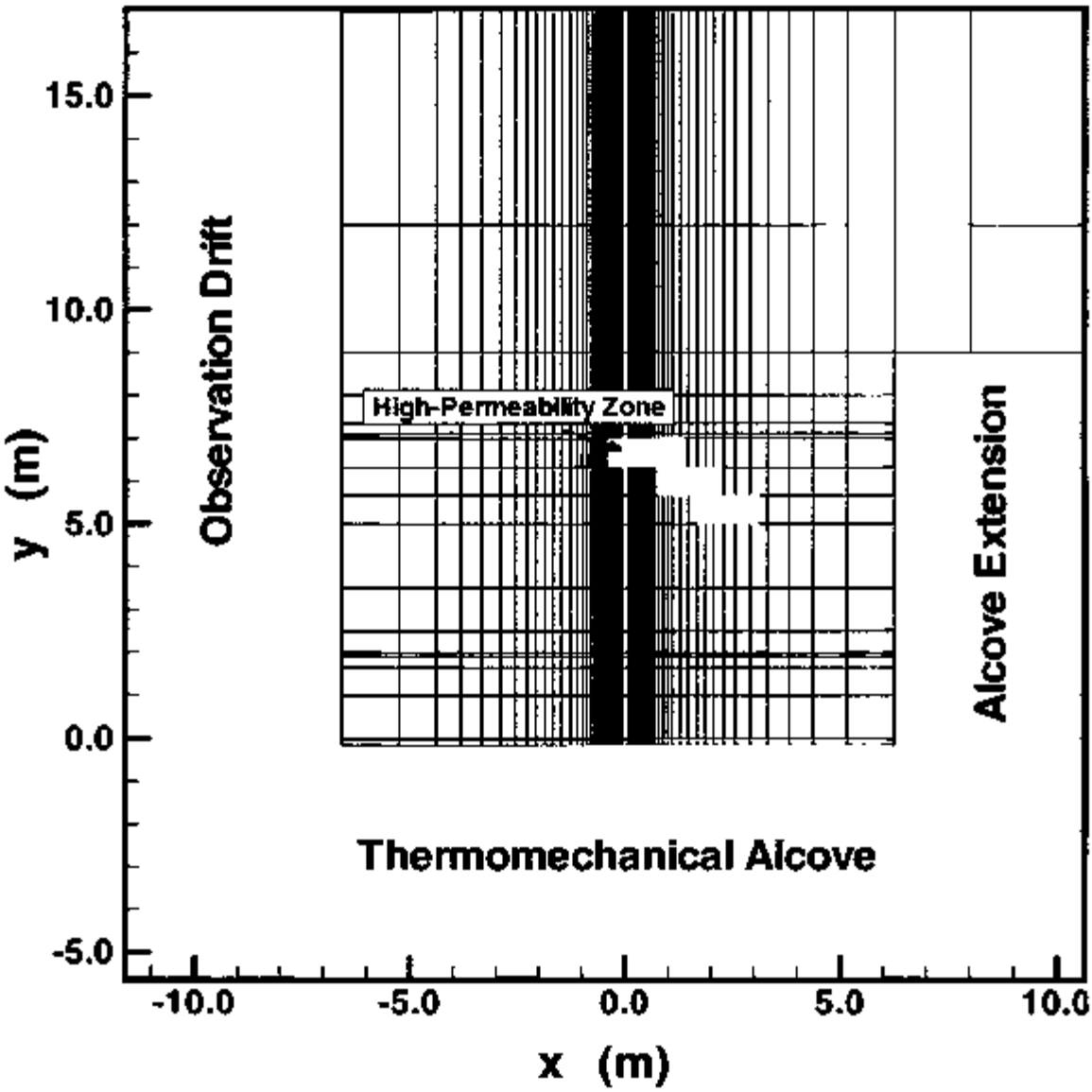

Figure 8-93. Discretization of SHT Model in a Plan View

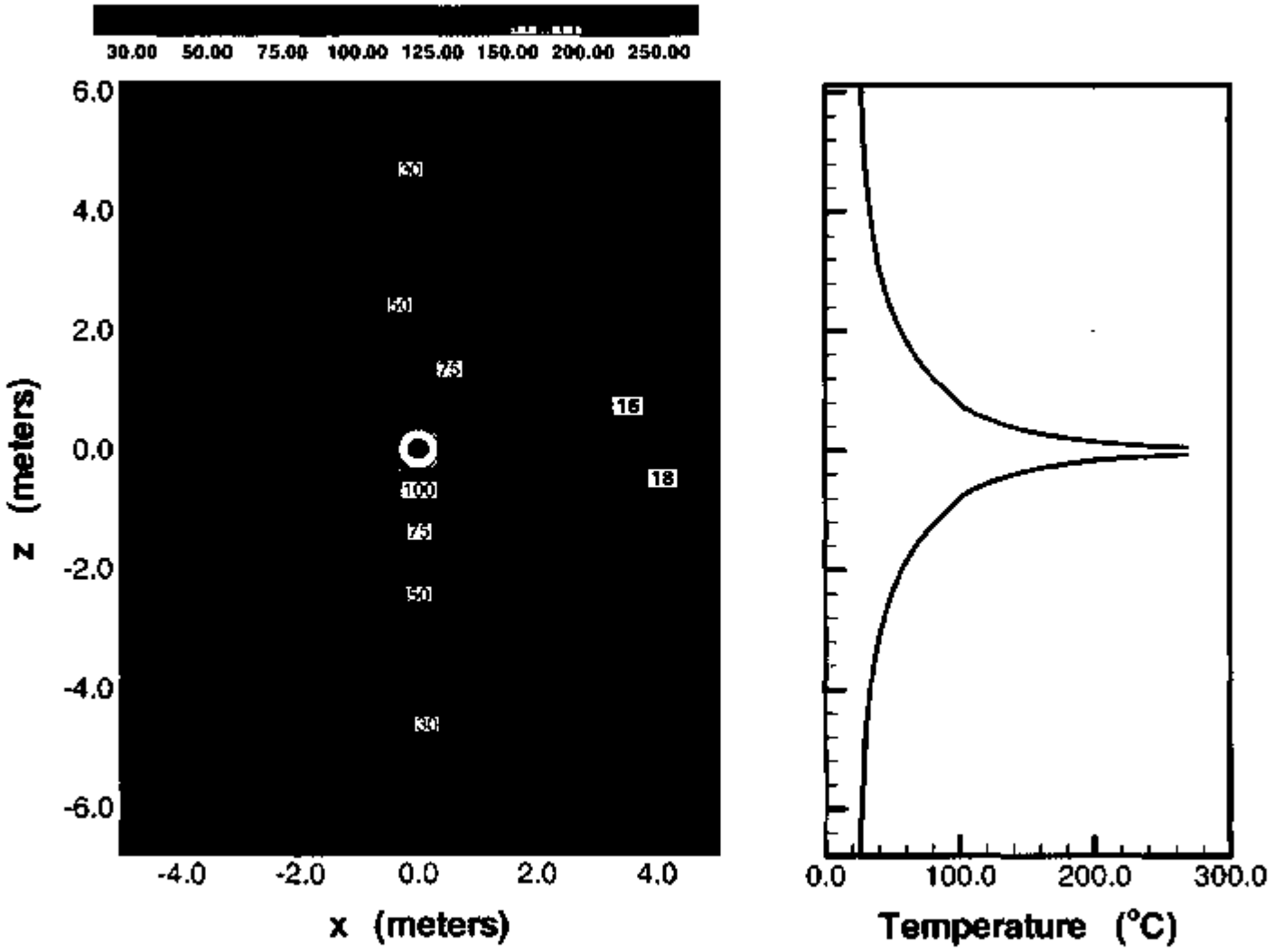

Figure 8-94. Simulated Matrix Temperature after 3 Months of Heating in XZ–Cross Section at Y = 4.5 m

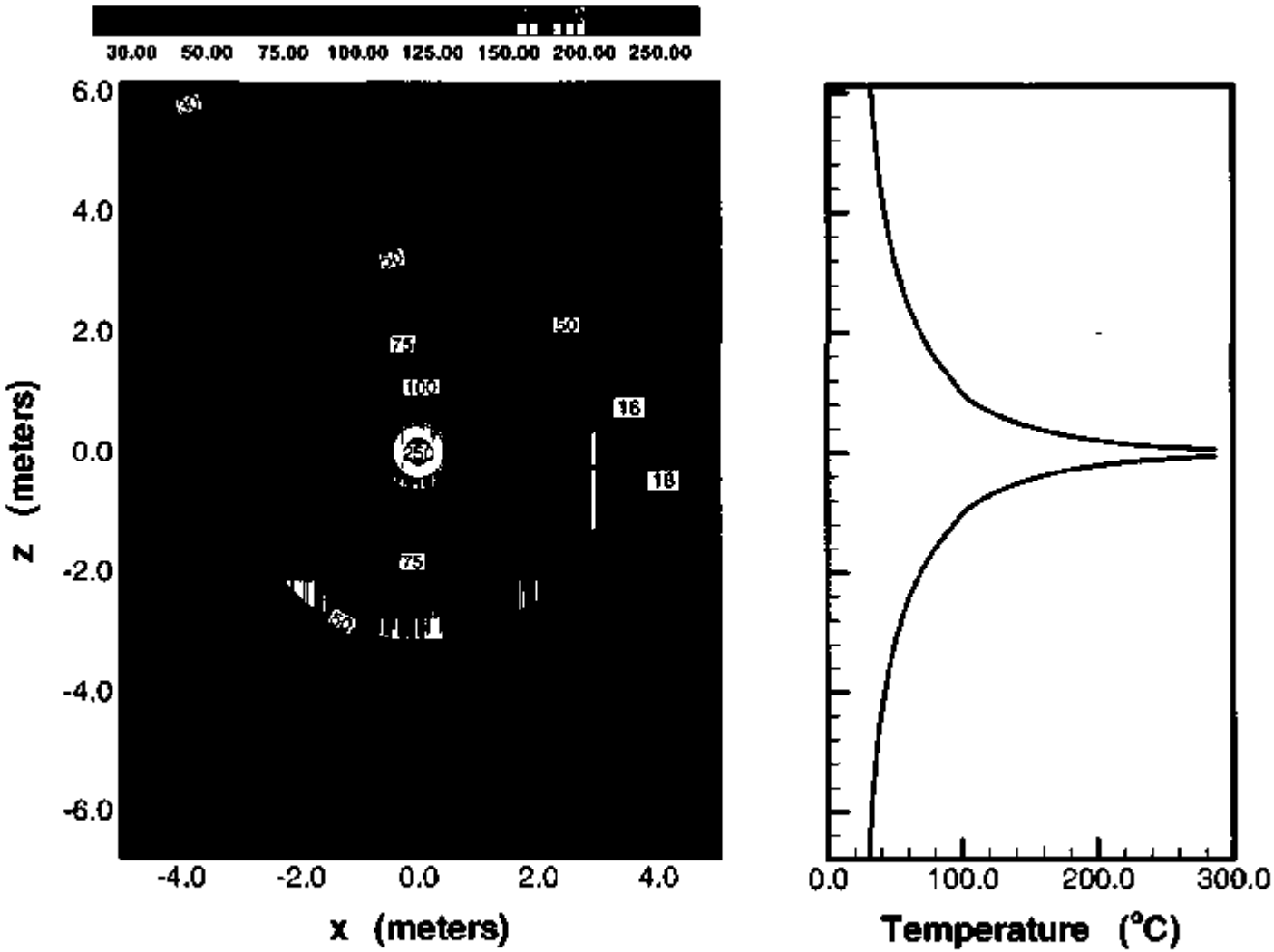

Figure 8-95. Simulated Matrix Temperature after 9 Months of Heating in XZ-Cross Section at Y = 4.5 m

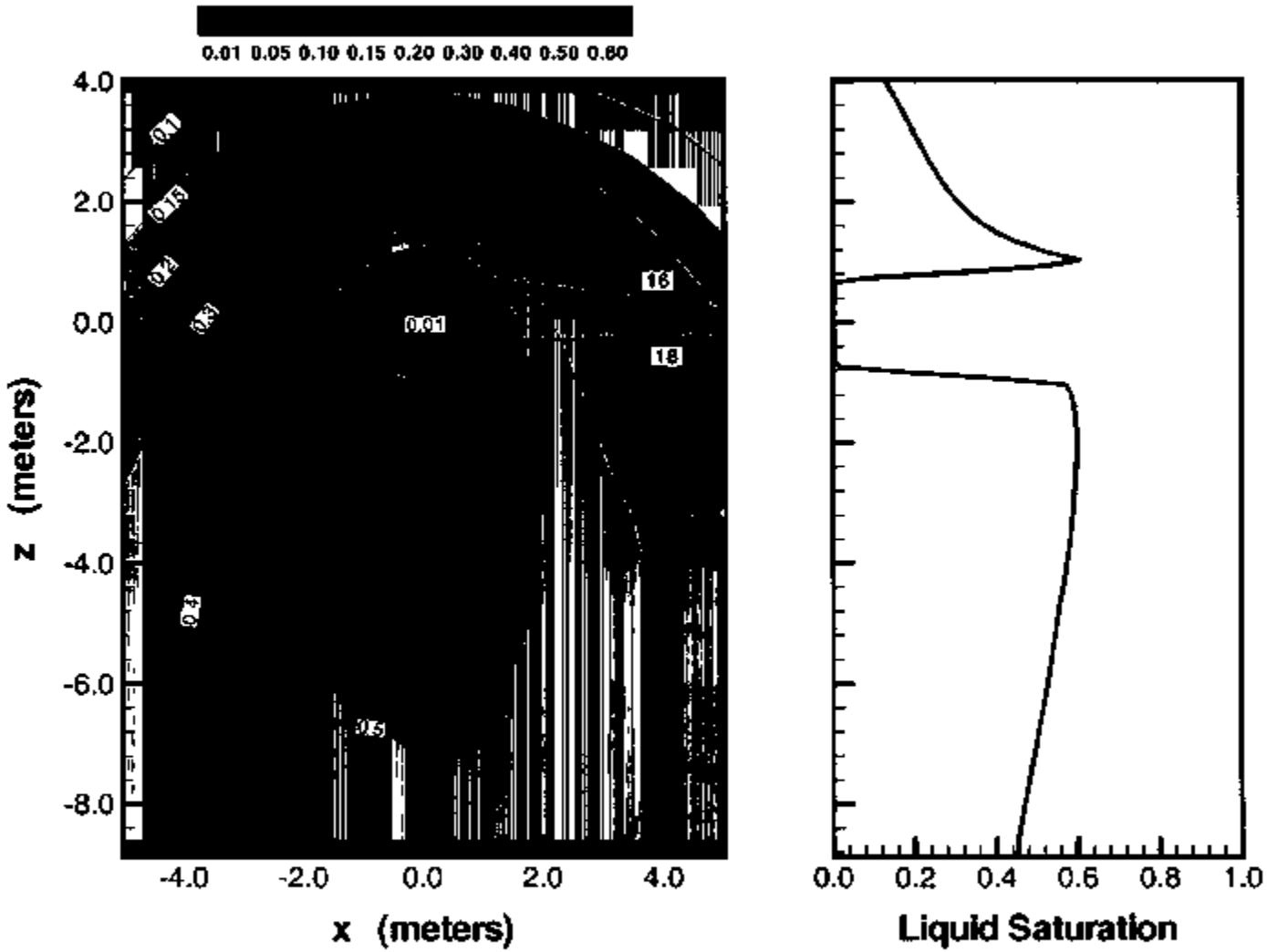

Figure 8-96. Simulated Fracture Liquid Saturation after 3 Months of Heating in XZ–Cross Section at Y = 4.5 m

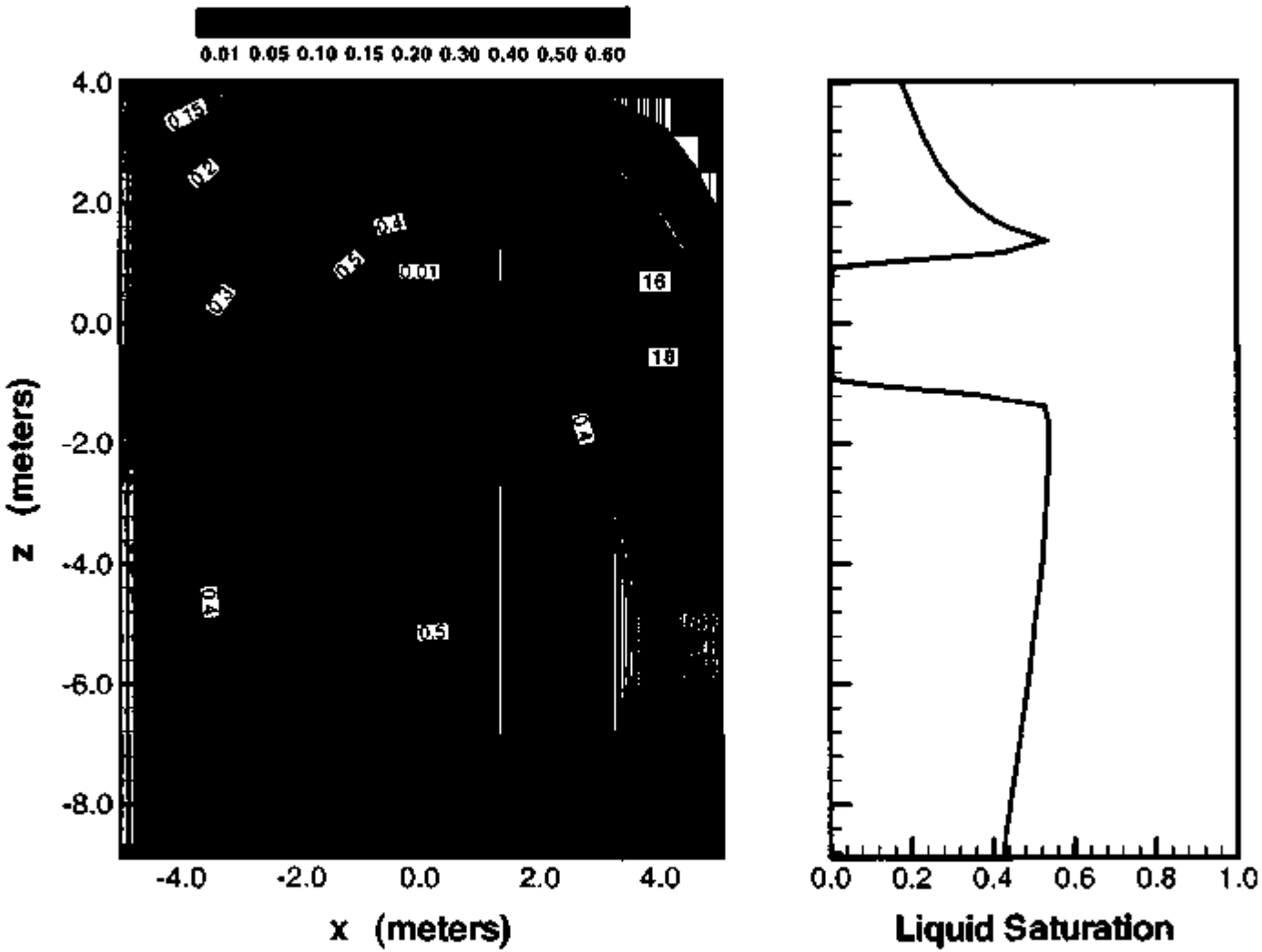

Figure 8-97. Simulated Fracture Liquid Saturation after 9 Months of Heating in XZ–Cross Section at Y = 4 5 m

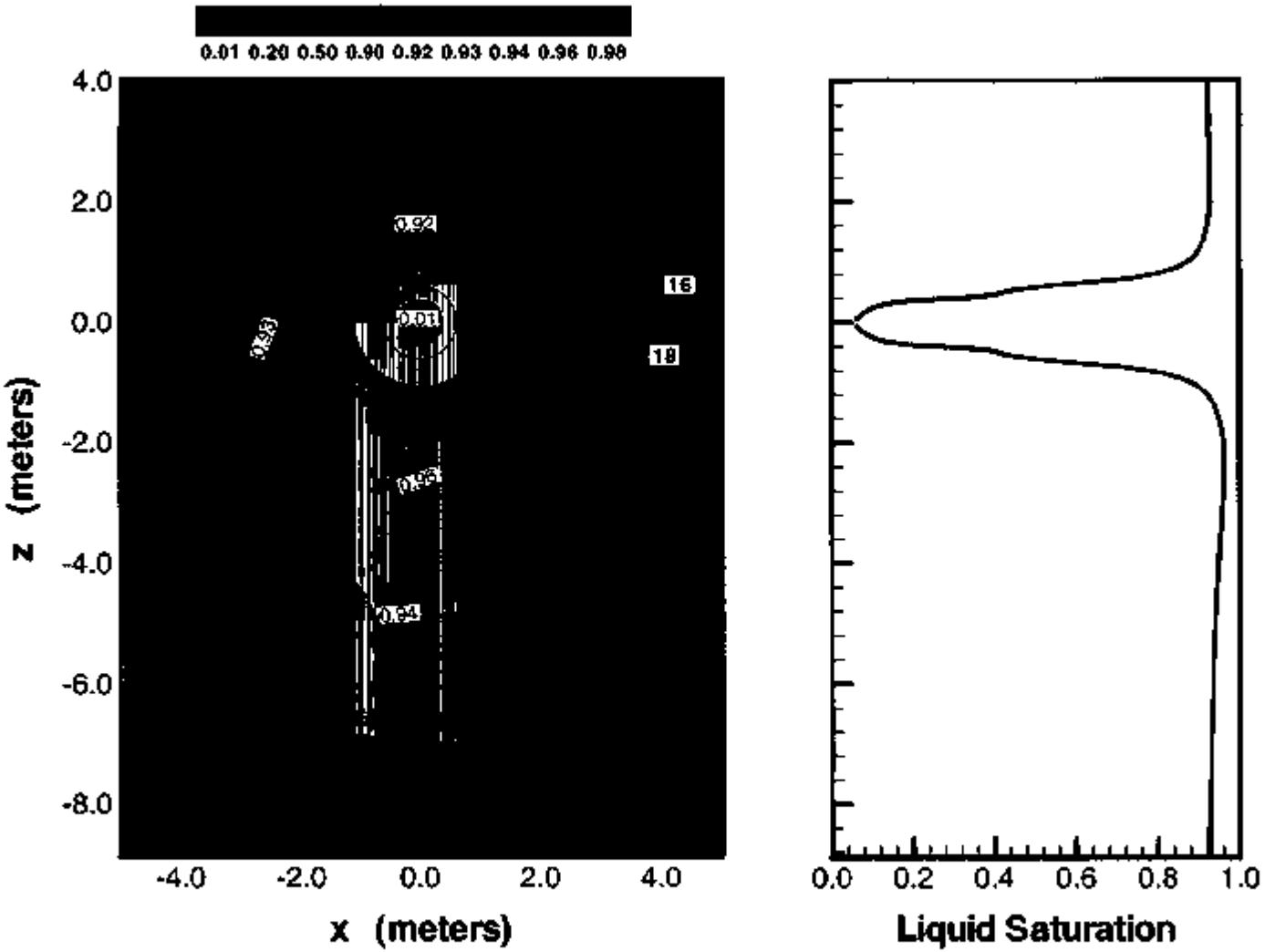

Figure 8-98. Simulated Matrix Liquid Saturation after 3 Months of Heating in XZ–Cross Section at Y = 4.5 m

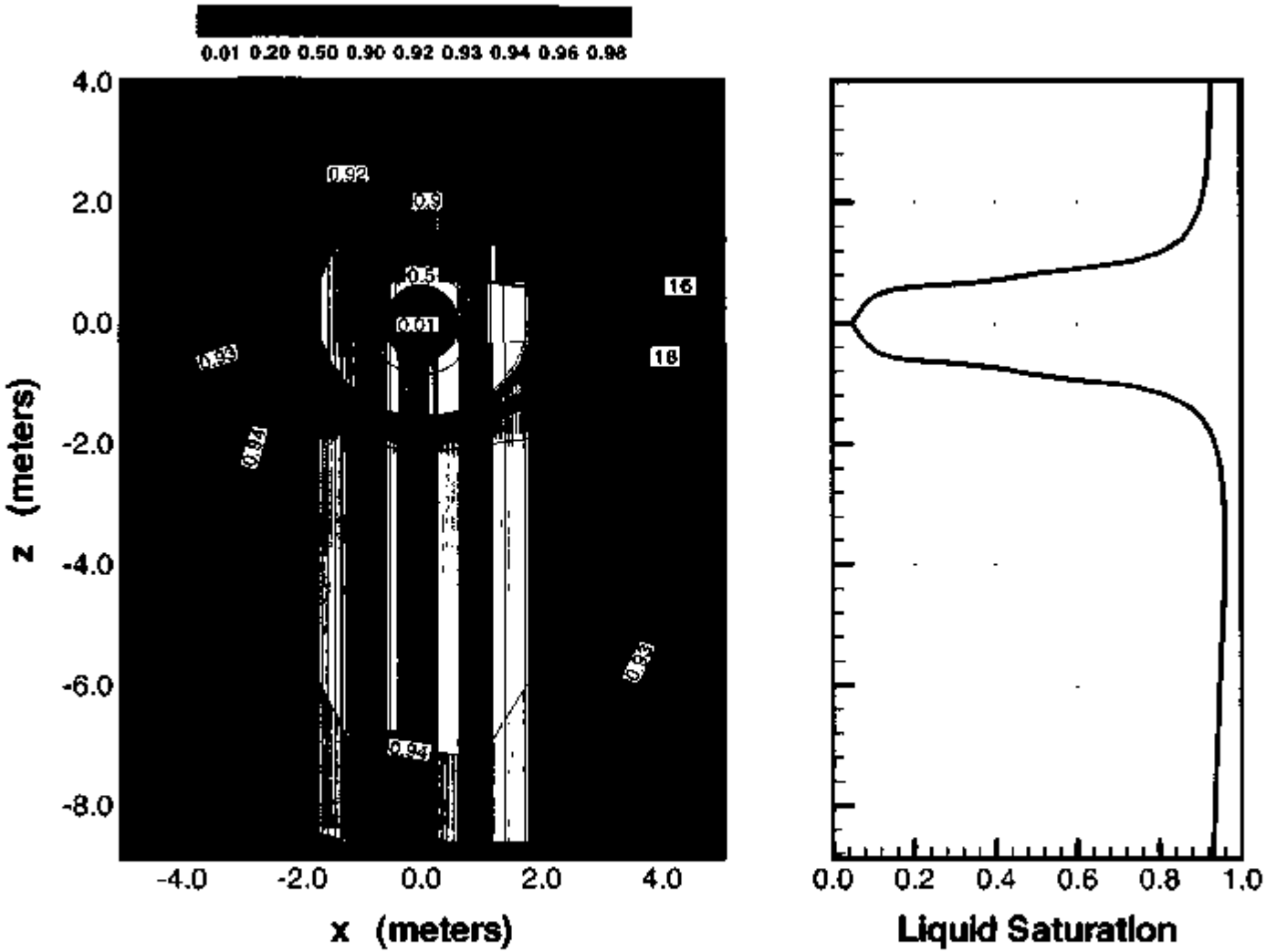

Figure 8-99. Simulated Matrix Liquid Saturation after 9 Months of Heating in XZ–Cross Section at Y = 4.5 m

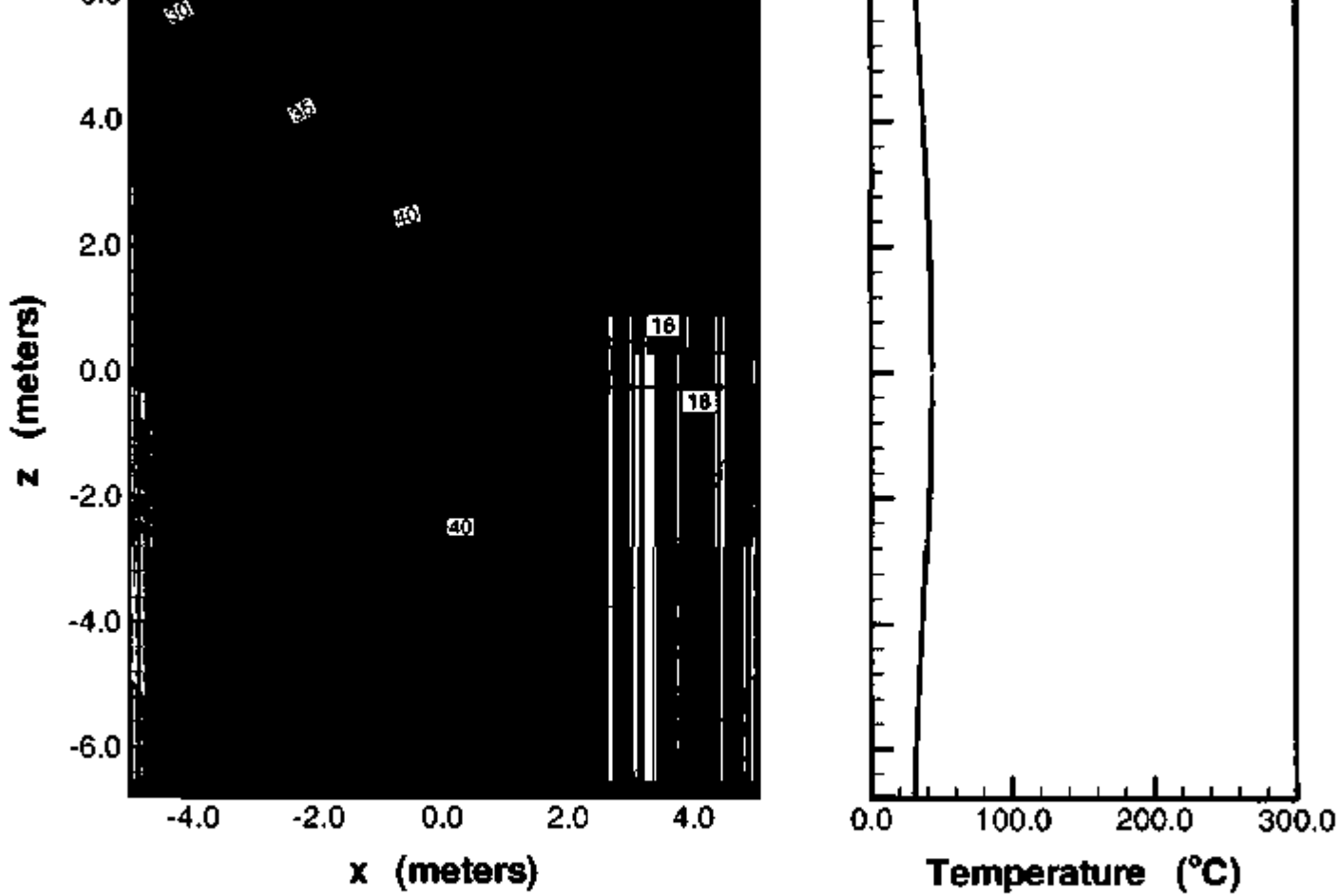

Figure 8-100. Simulated Matrix Temperature after 3 Months of Cooling in XZ–Cross Section at Y = 4.5 m

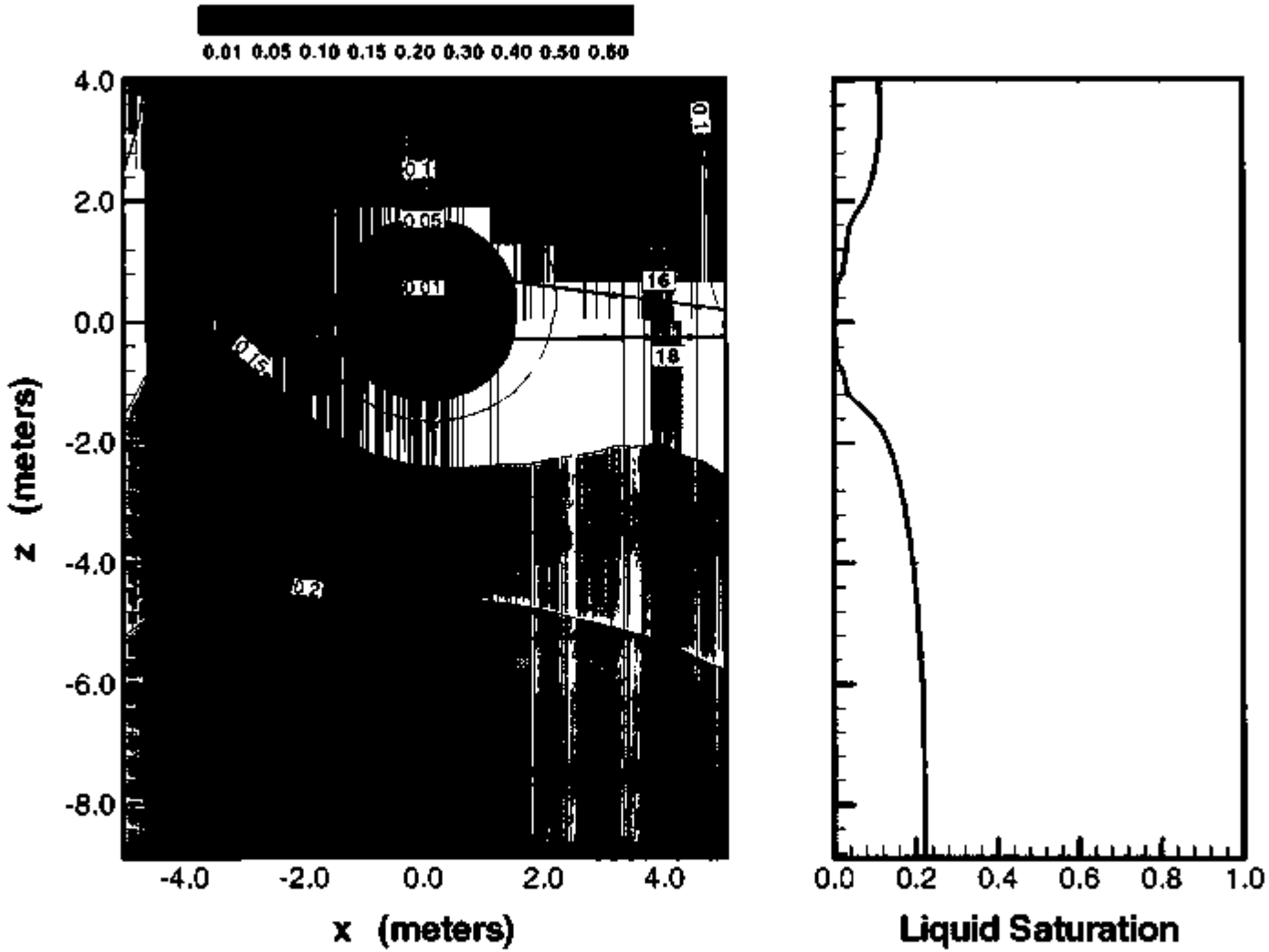

Figure 8-101 Simulated Fracture Liquid Saturation after 3 Months of Cooling in XZ–Cross Section at Y = 4.5 m

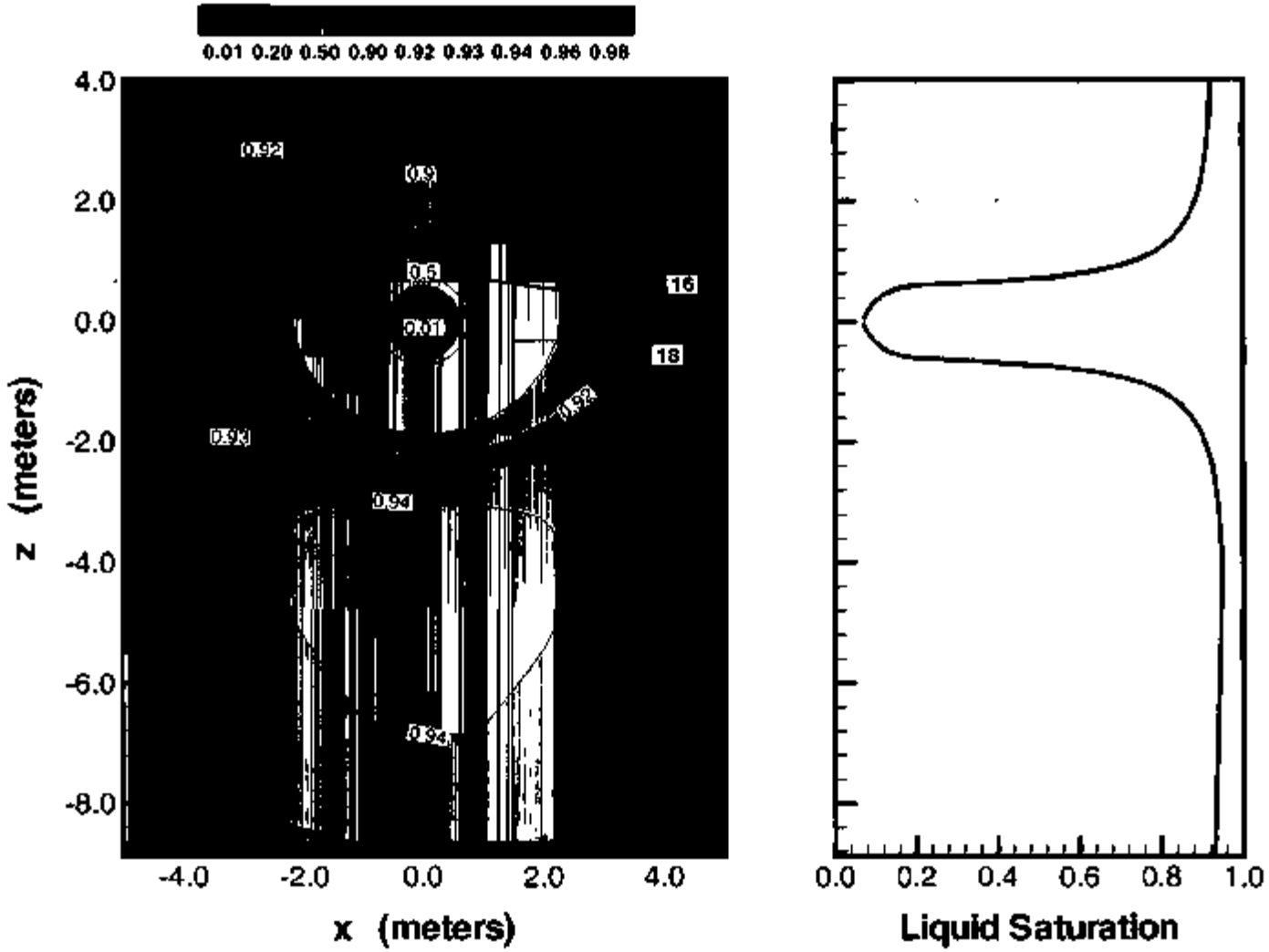

Figure 8-102. Simulated Matrix Liquid Saturation after 3 Months of Cooling in XZ–Cross Section at Y = 4.5 m

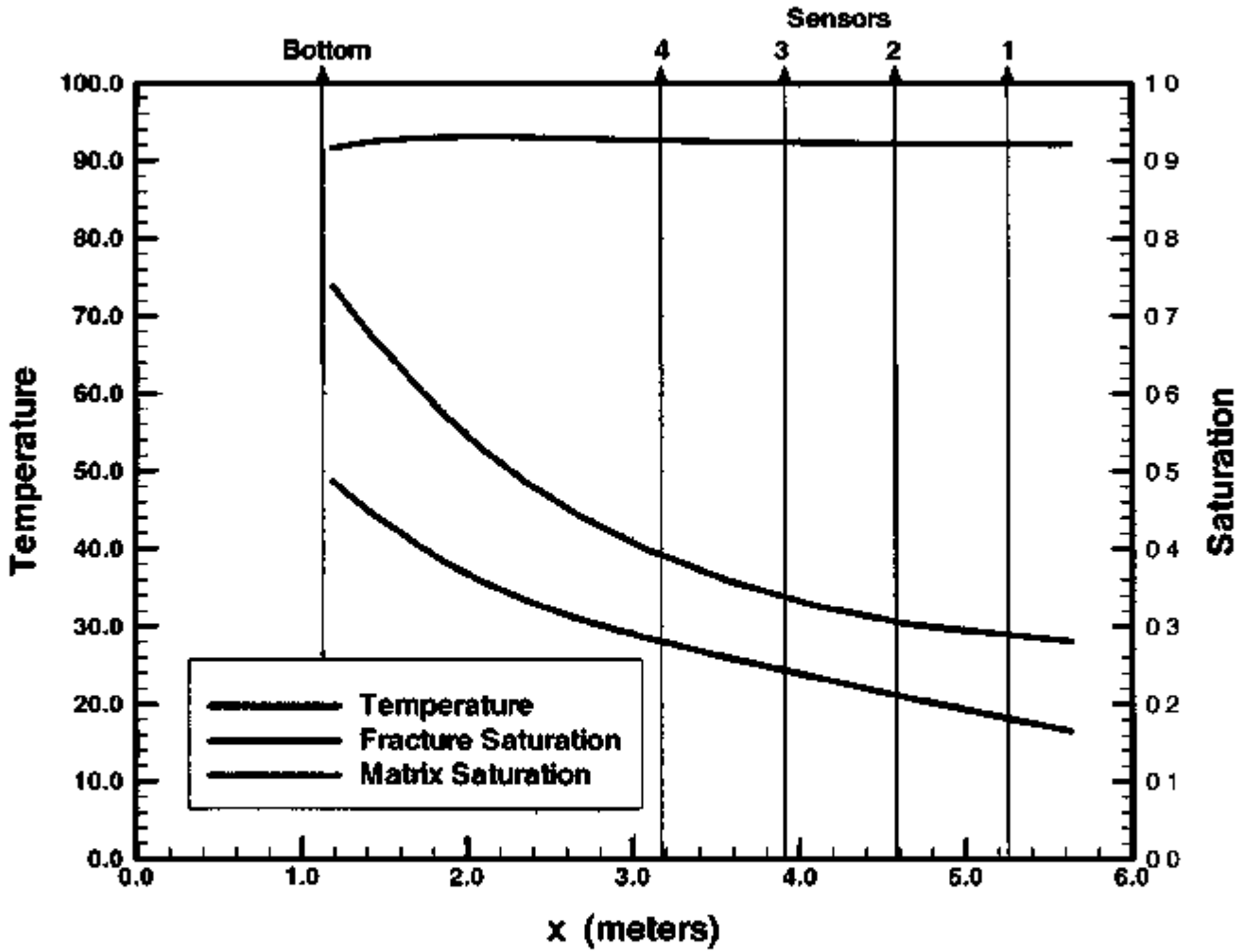

Figure 8-103 Simulated Temperature and Saturation along Borehole 16 after 3 Months of Heating

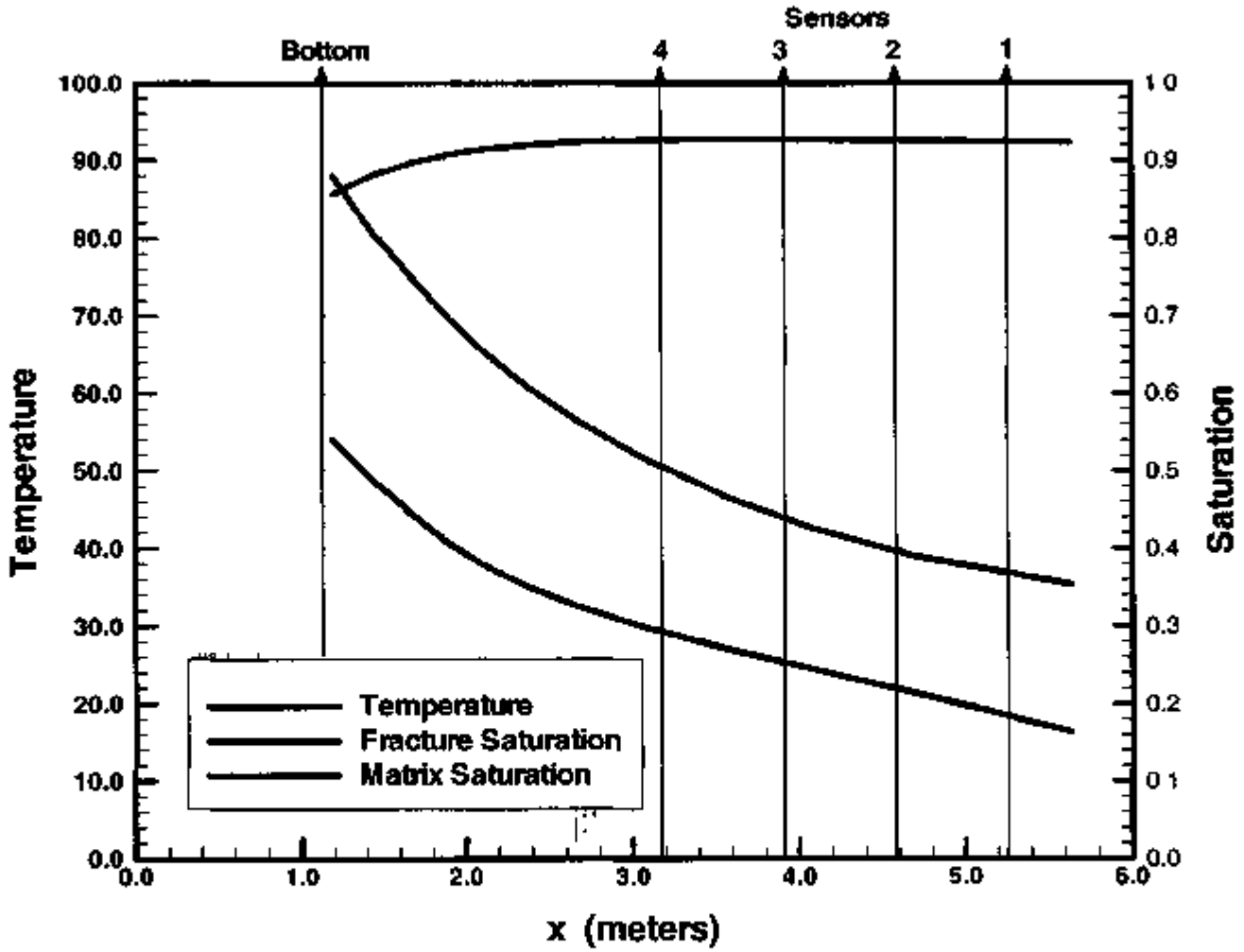

Figure 8-104. Simulated Temperature and Saturation along Borehole 16 after 9 Months of Heating

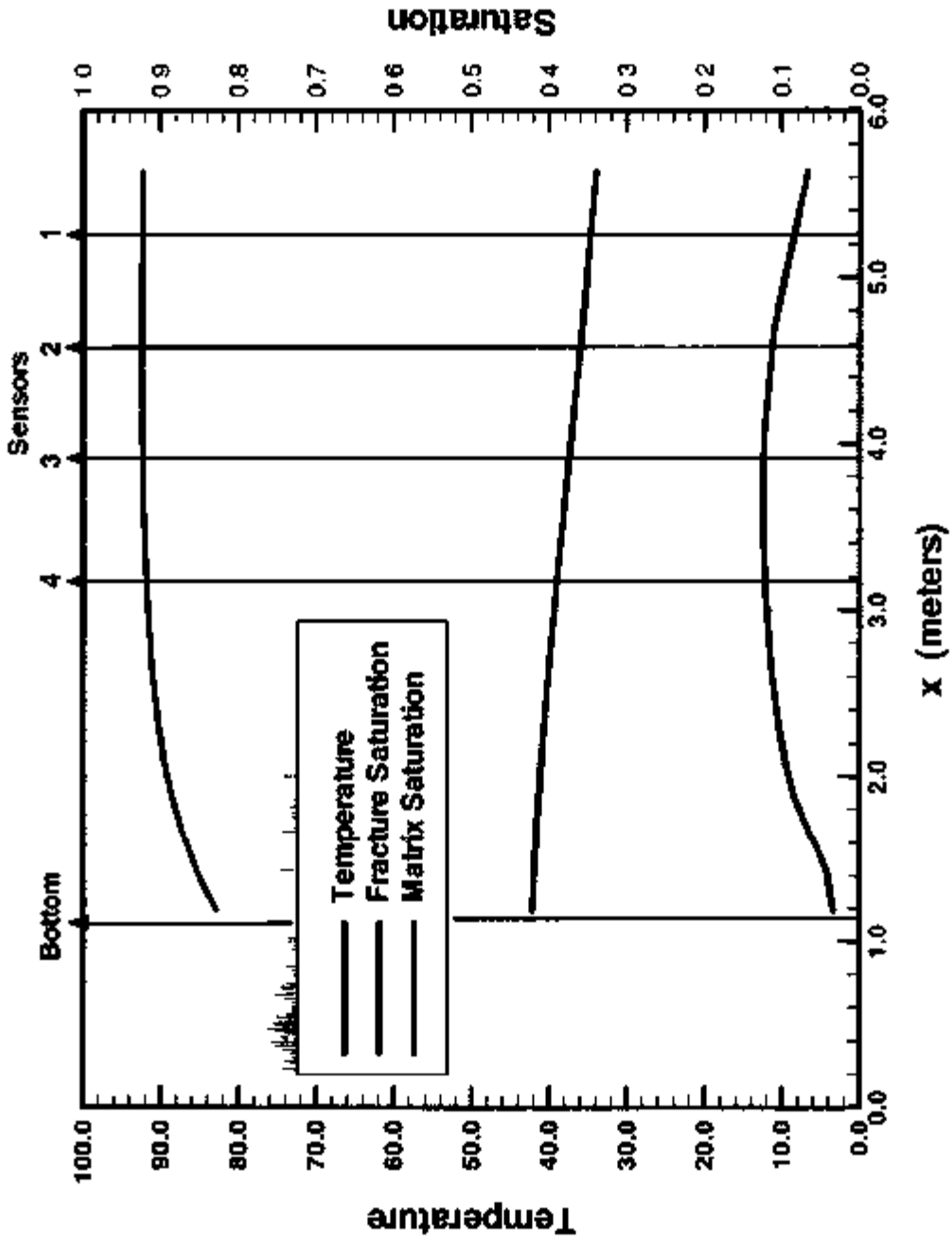

Figure 8-105 Simulated Temperature and Saturation along Borehole 16 after 3 Months of Cooling

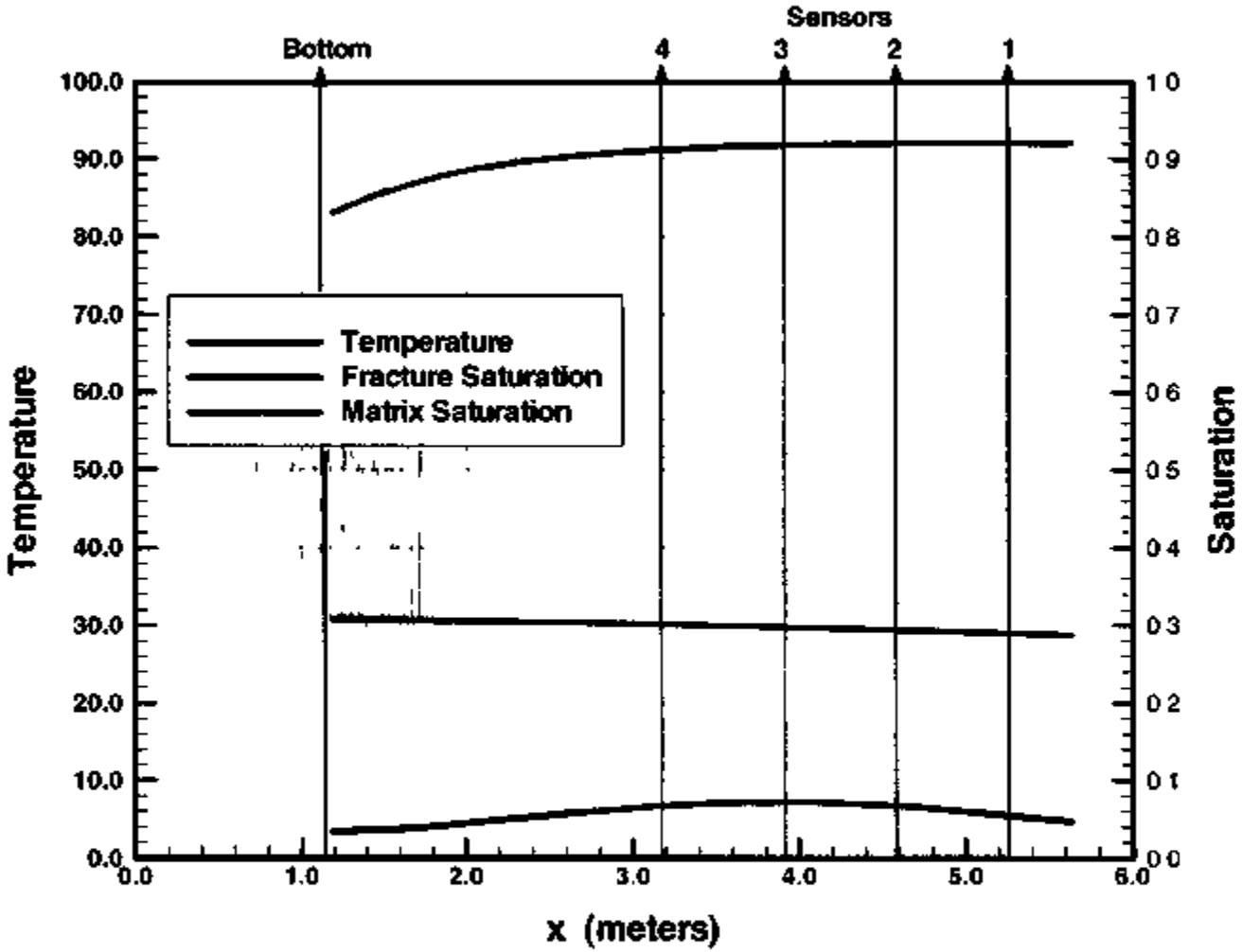

Figure 8-106 Simulated Temperature and Saturation along Borehole 16 after 9 Months of Cooling

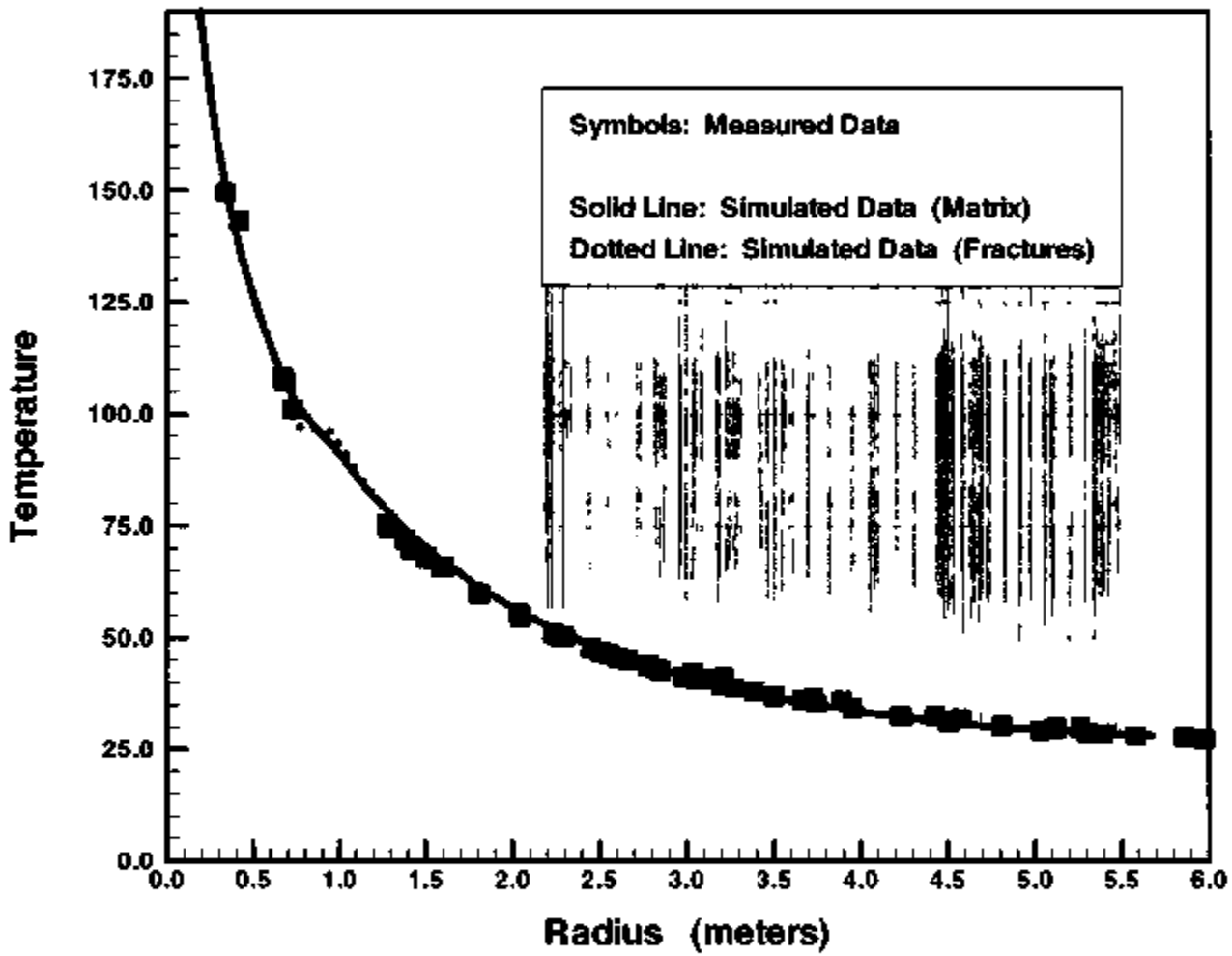

NOTE Temperature for sensors in the center-plane of the SHT block at Y=4 5 m

Figure 8-107 Measured and Simulated Temperature after 3 Months of Heating

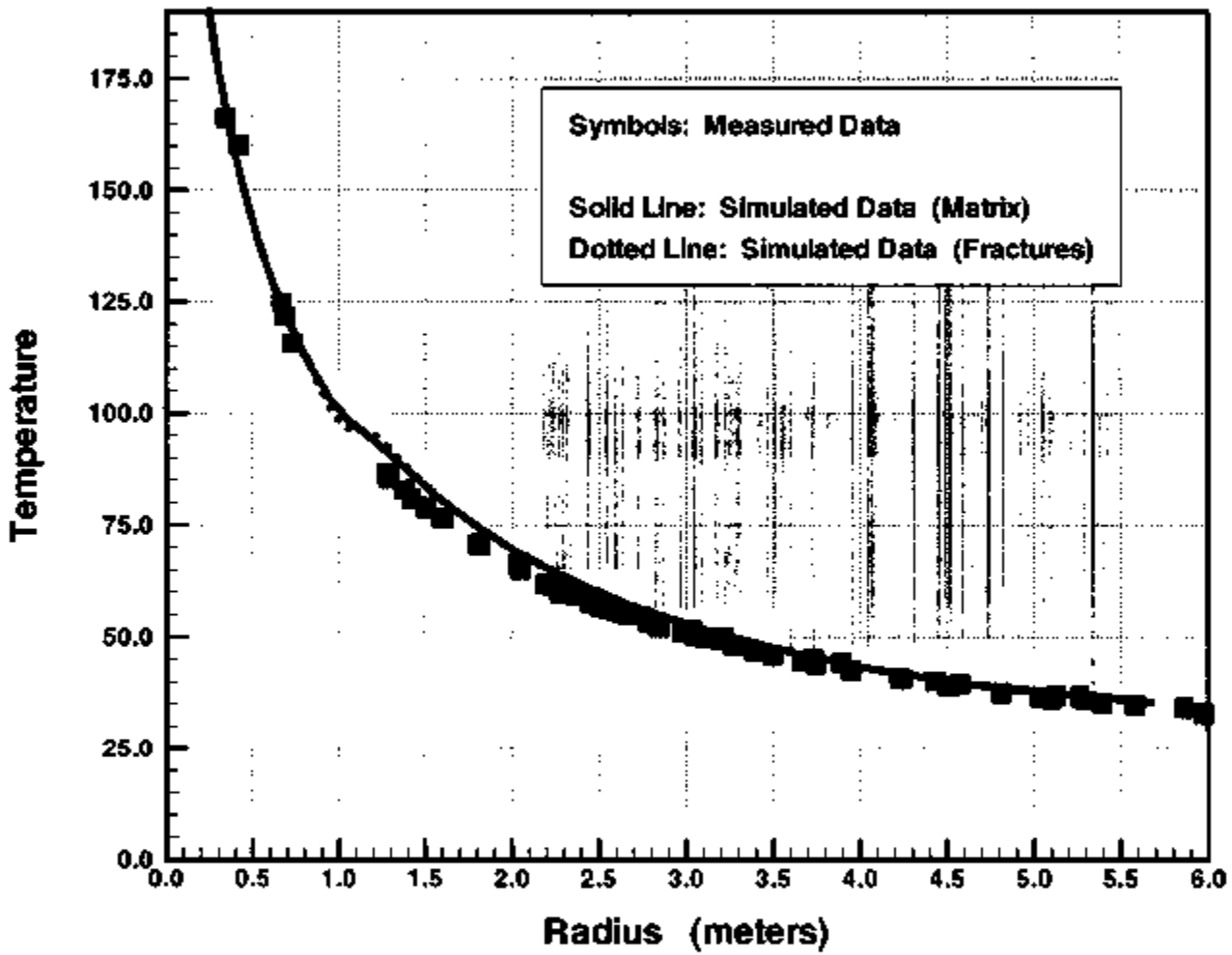

NOTE: Temperatures for sensors in the center-plane of the SHT block at Y=4.5 m.

Figure 8-108. Measured and Simulated Temperature after 9 Months of Heating

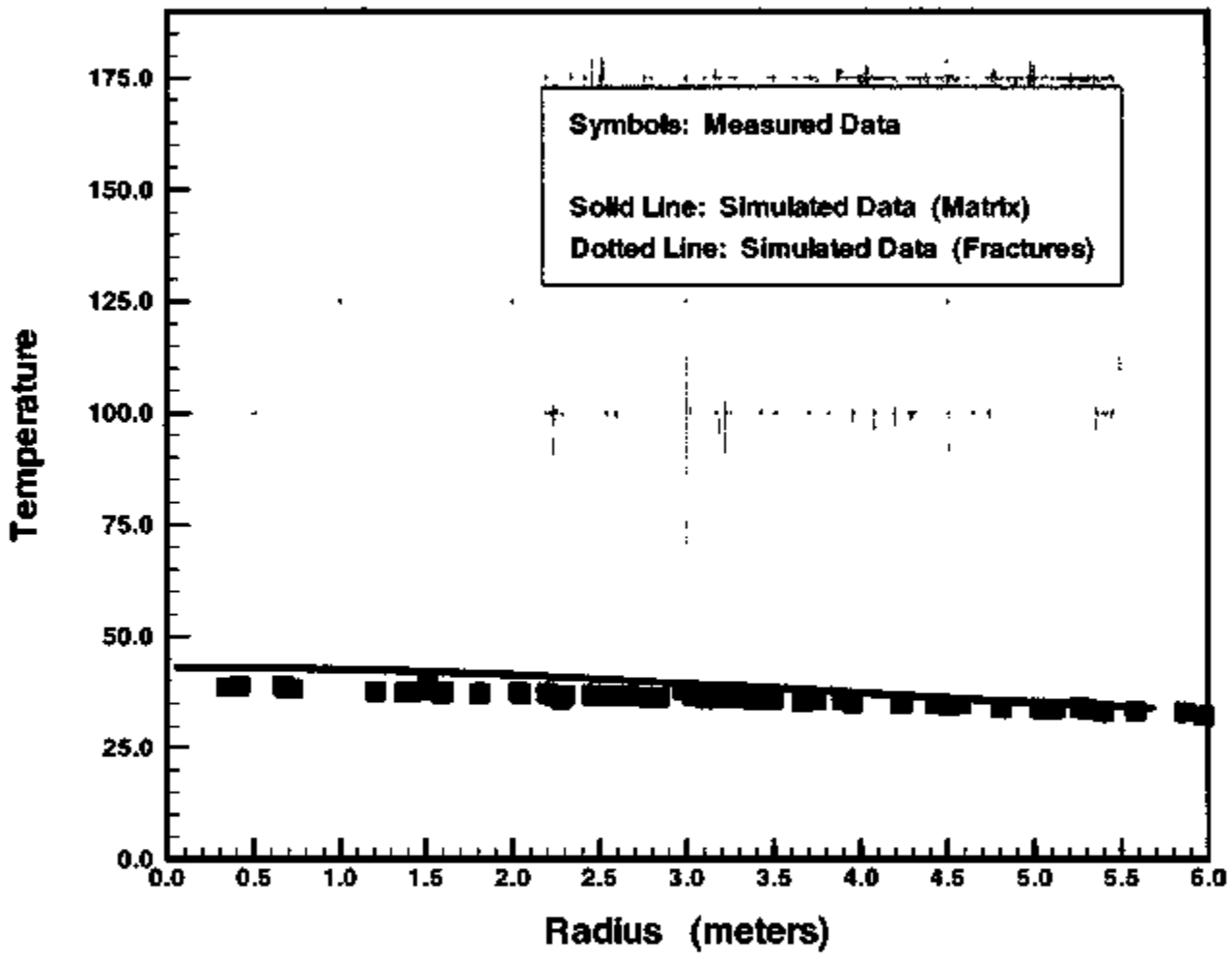

NOTE Temperatures for sensors in the center-plane of the SHT block at Y=4 5 m

Figure 8-109 Measured and Simulated Temperature after 3 Months of Cooling

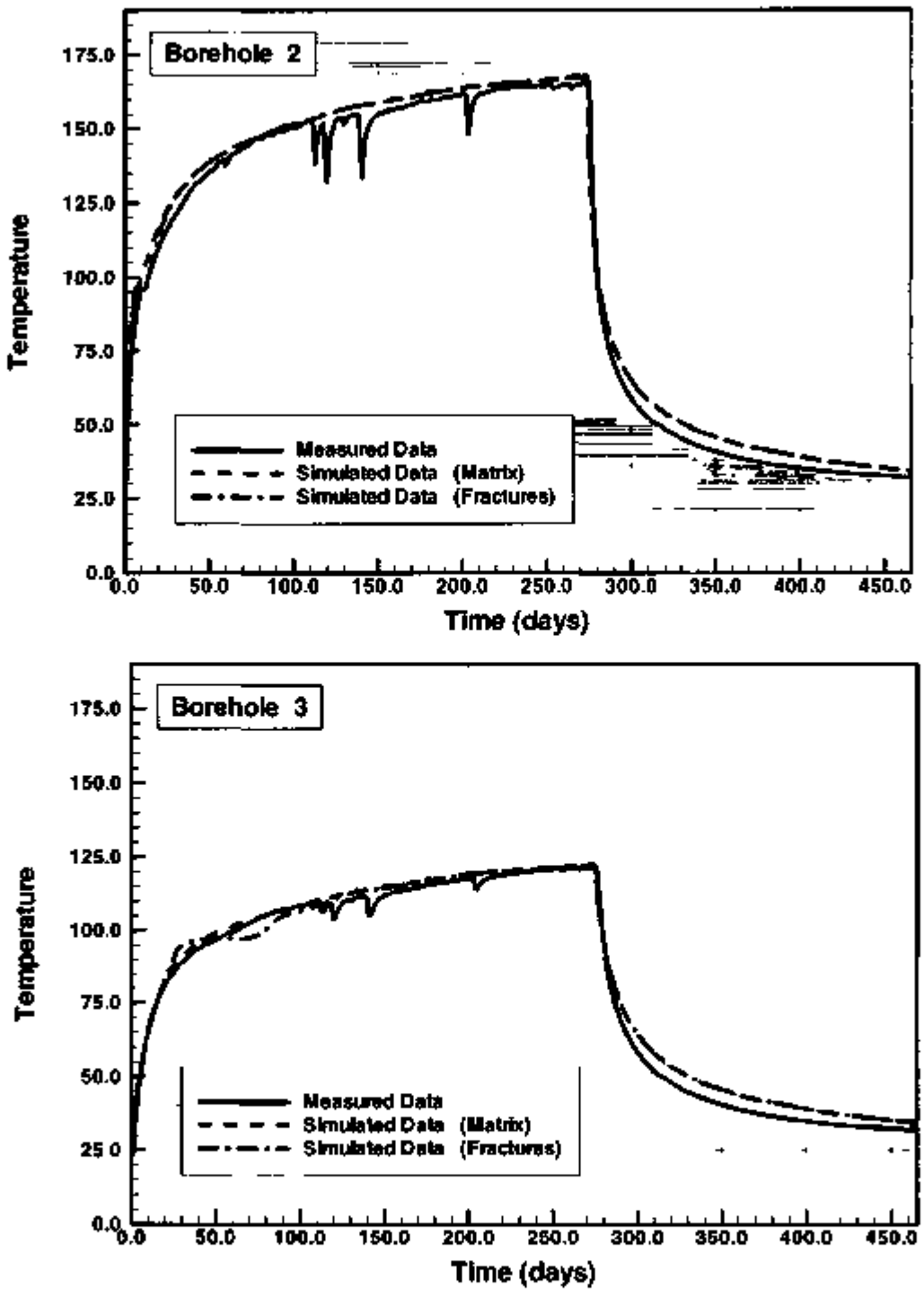

NOTE Temperatures for sensors in the center-plane of the SHT block at Y=4 5 m

Figure 8-110 Measured and Simulated Temperature History in Boreholes 2 and 3,

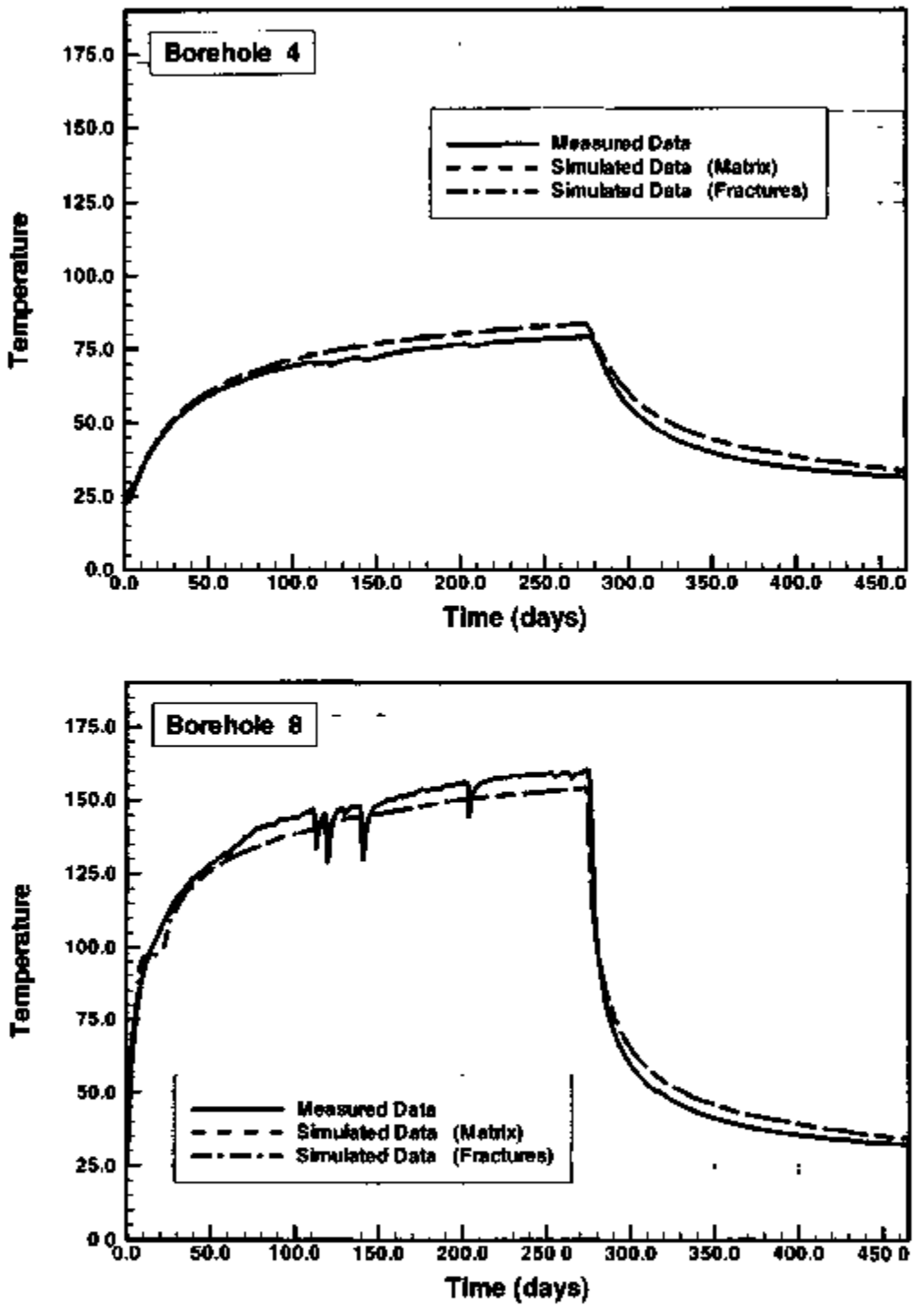

NOTE Temperatures for sensors in the center-plane of the SHT block at Y=4 5 m

Figure 8-111 Measured and Simulated Temperature History in Boreholes 4 and 8

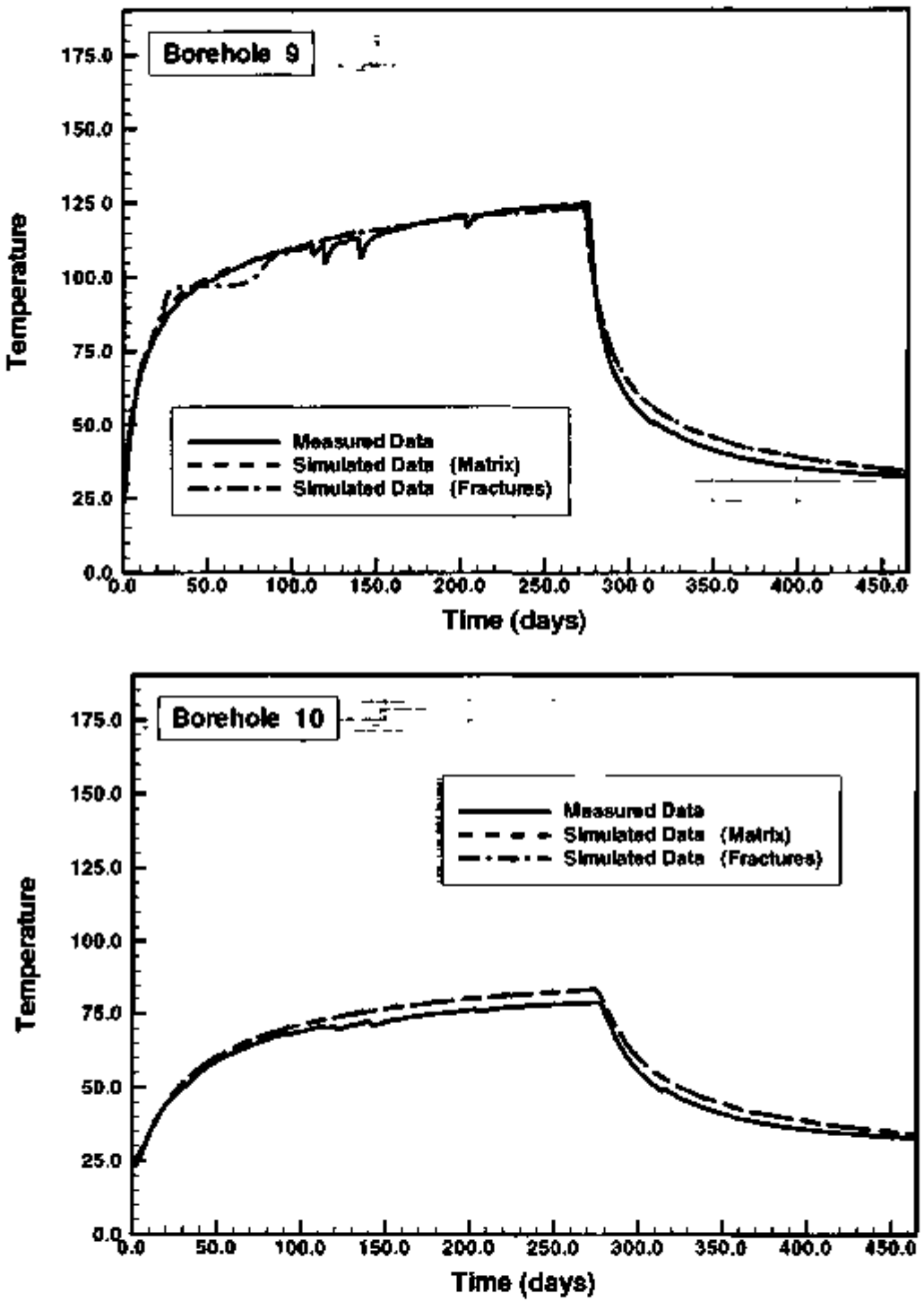

NOTE Temperatures for sensors in the center-plane of the SHT block at Y=4 5 m

Figure 8-112 Measured and Simulated Temperature History in Boreholes 9 and 10

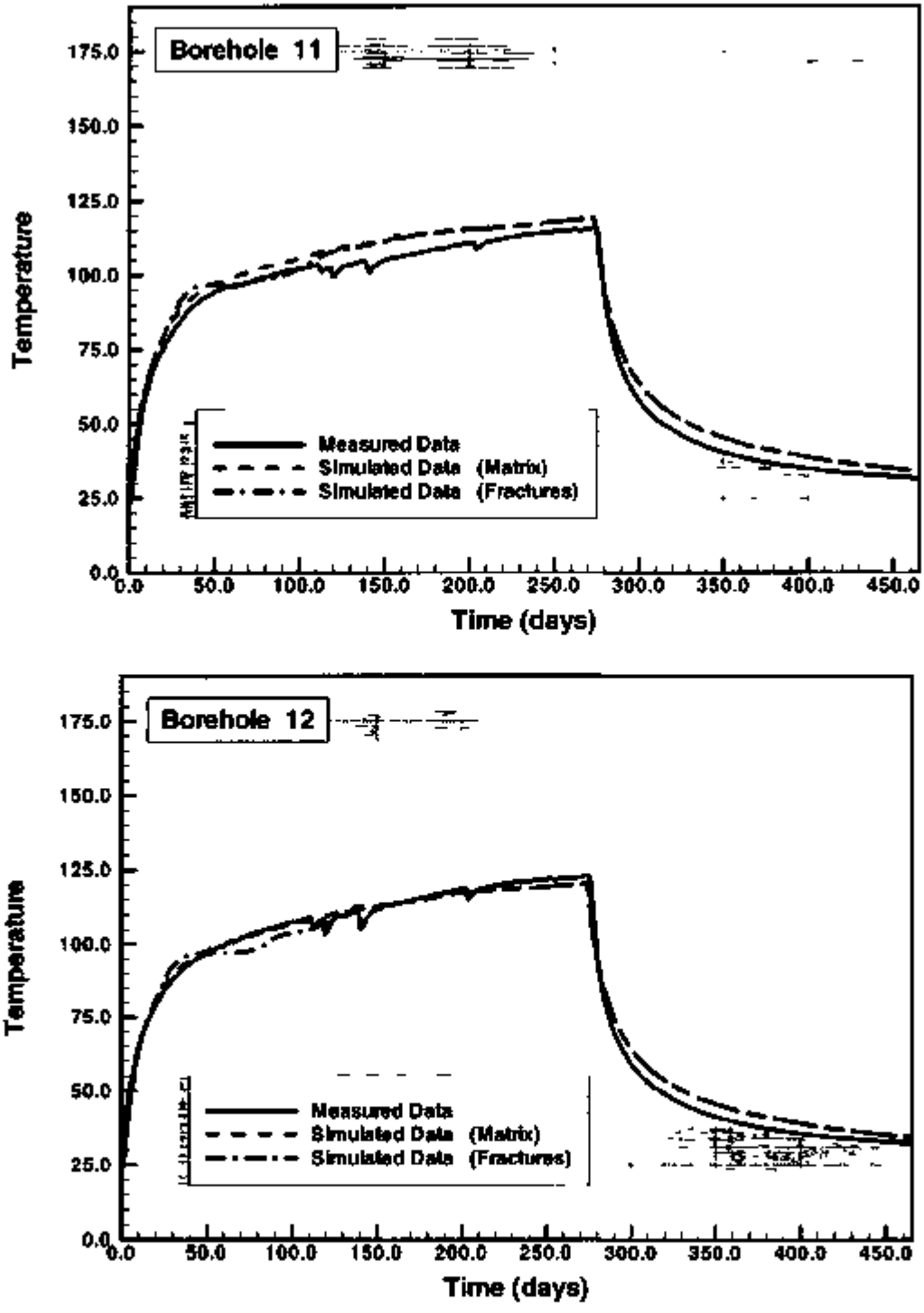

NOTE Temperatures for sensors in the center-plane of the SHT block at Y=4 5 m

Figure 8-113 Measured and Simulated Temperature History in Boreholes 11 and 12

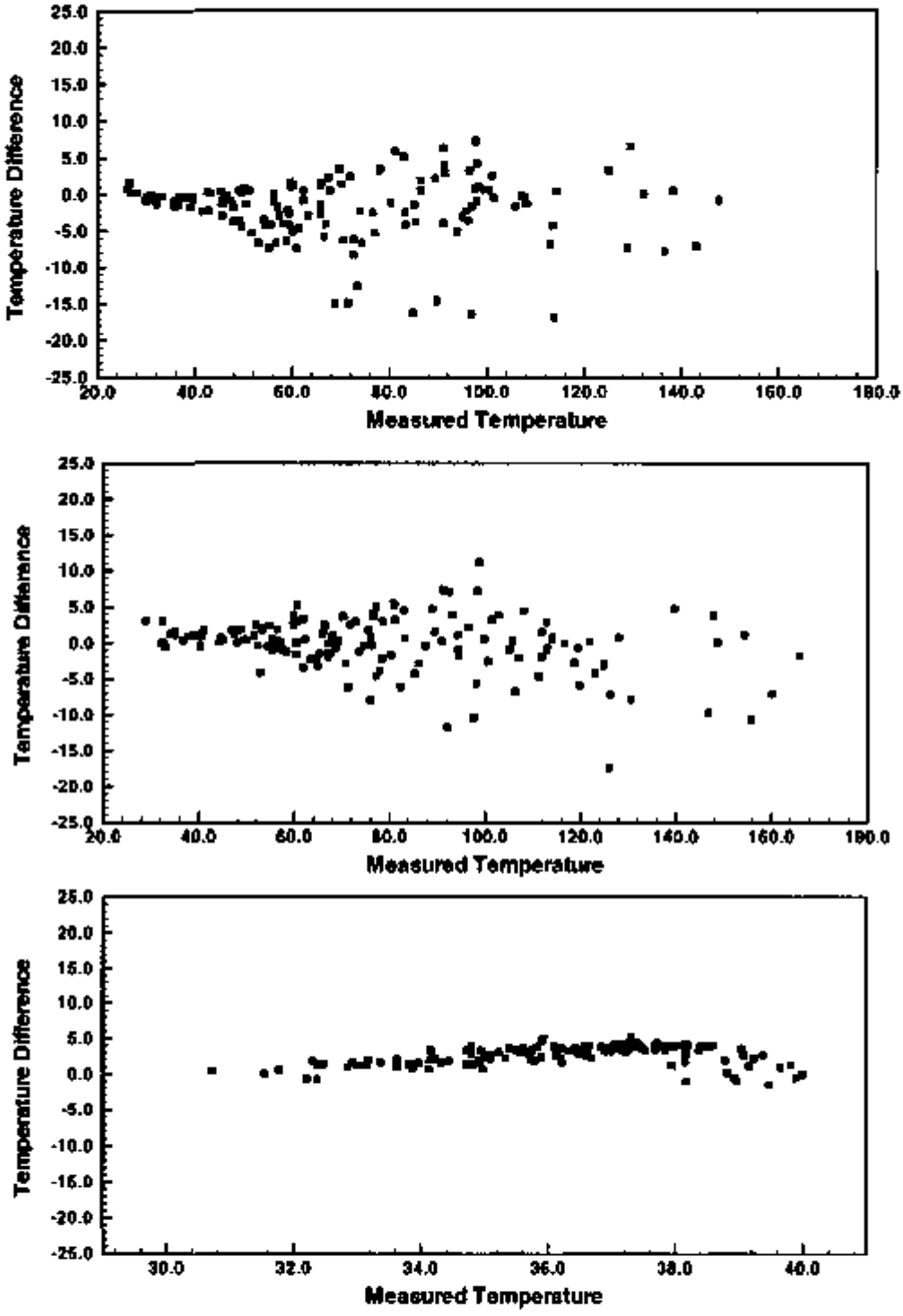

NOTE The top graph, center graph and bottom graph show results at 3 months, 9 months of heating, and 3 months into cooling, respectively

Figure 8-114. Difference Between the Simulated and the Measured Temperature as a Function of Measured Temperature

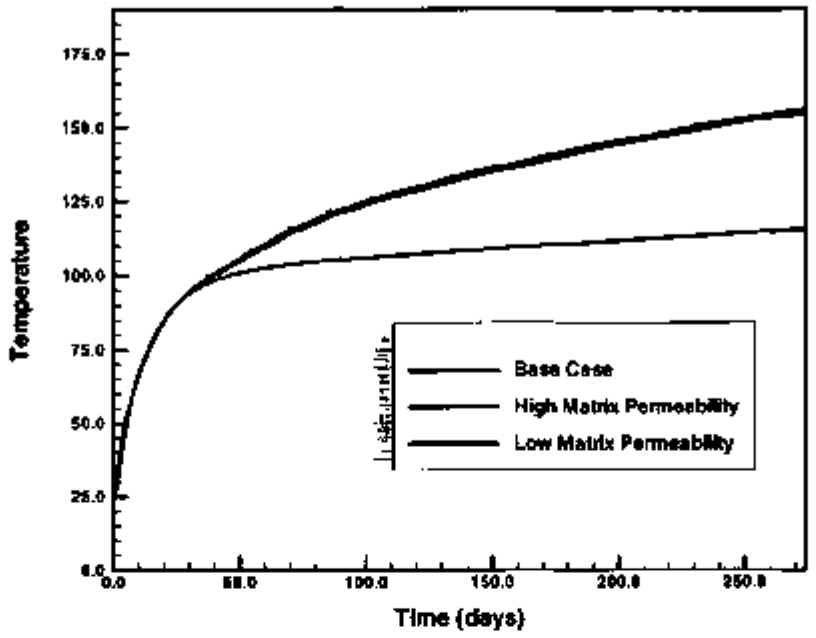

Figure 8-115. Sensitivity of Temperature to a One-Order-of-Magnitude Change in Matrix Permeability

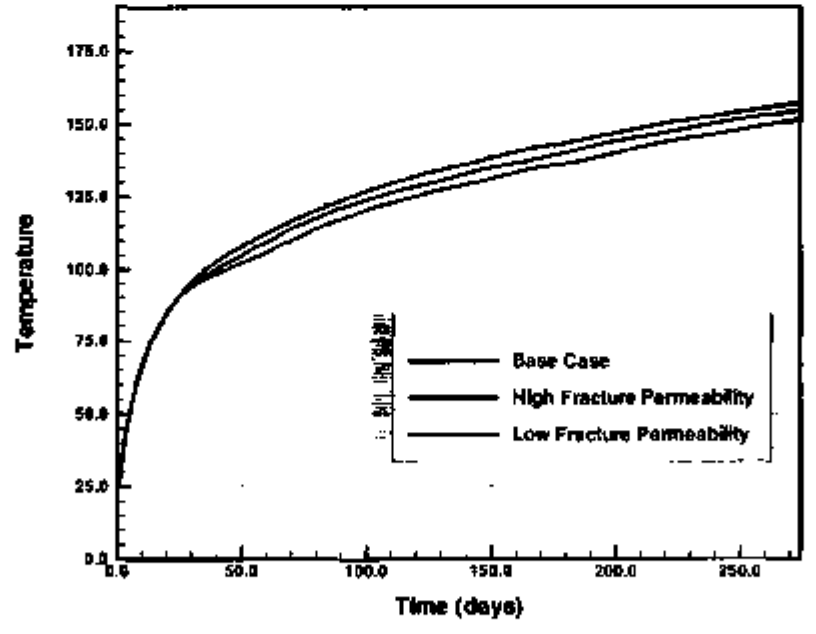

Figure 8-116. Sensitivity of Temperature to a One-Order-of-Magnitude Change in Fracture Permeability

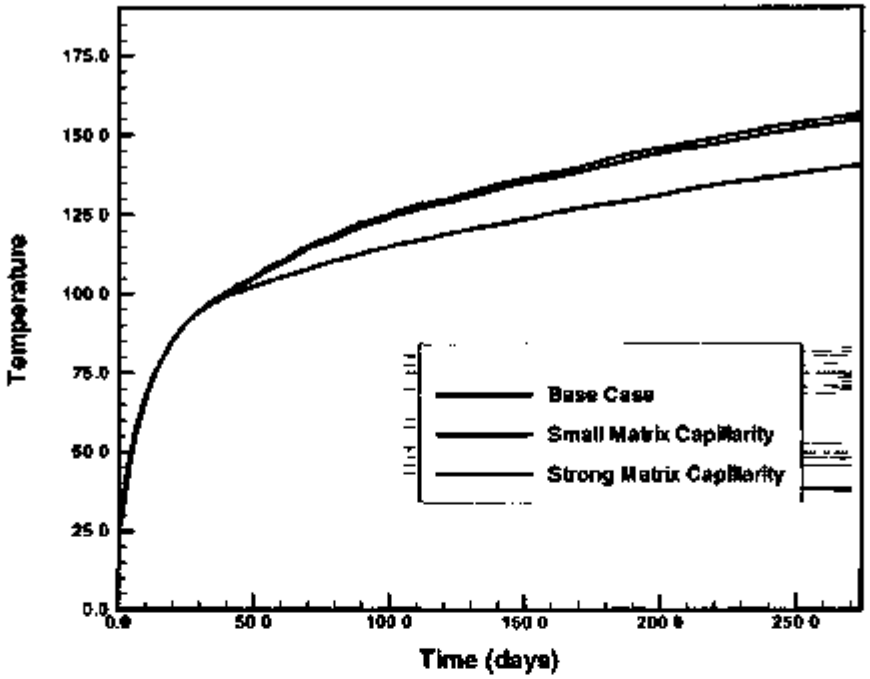

Figure 8-117 Sensitivity of Temperature to a One-Order-of-Magnitude Change in Matrix α - Parameter

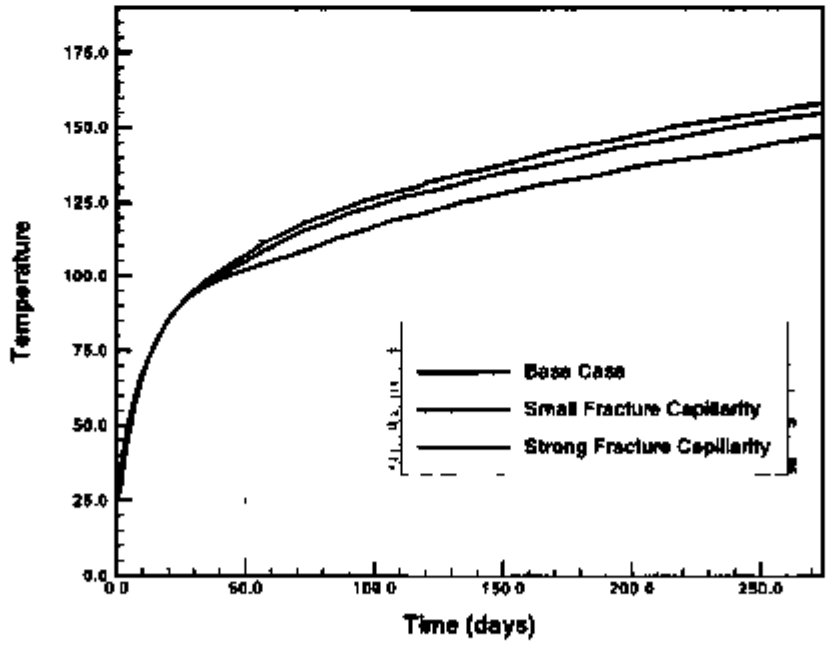

Figure 8-118. Sensitivity of Temperature to a One-Order-of-Magnitude Change in Fracture α - Parameter

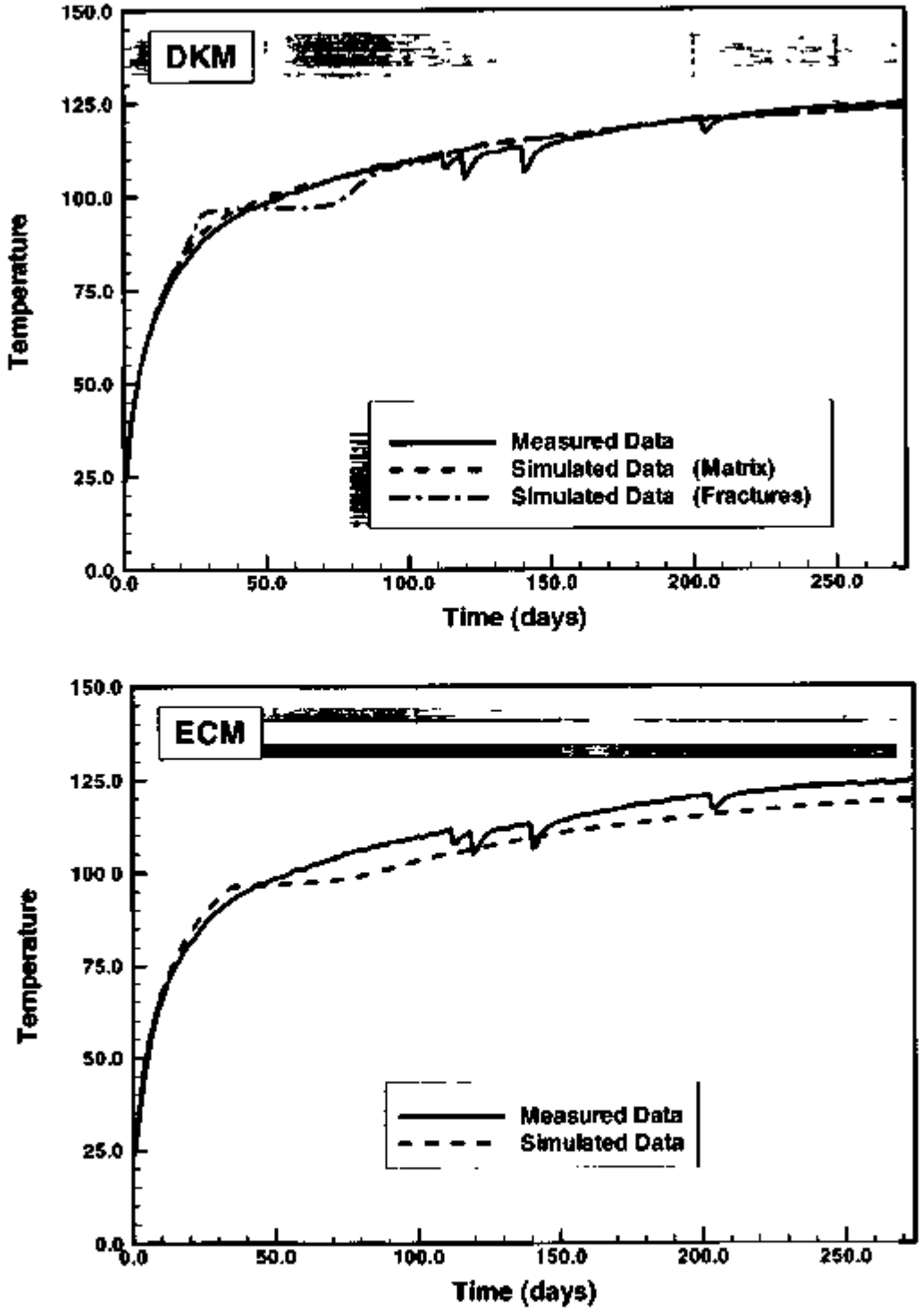

Figure 8-119 Measured vs Simulated Temperature History for DKM and ECM

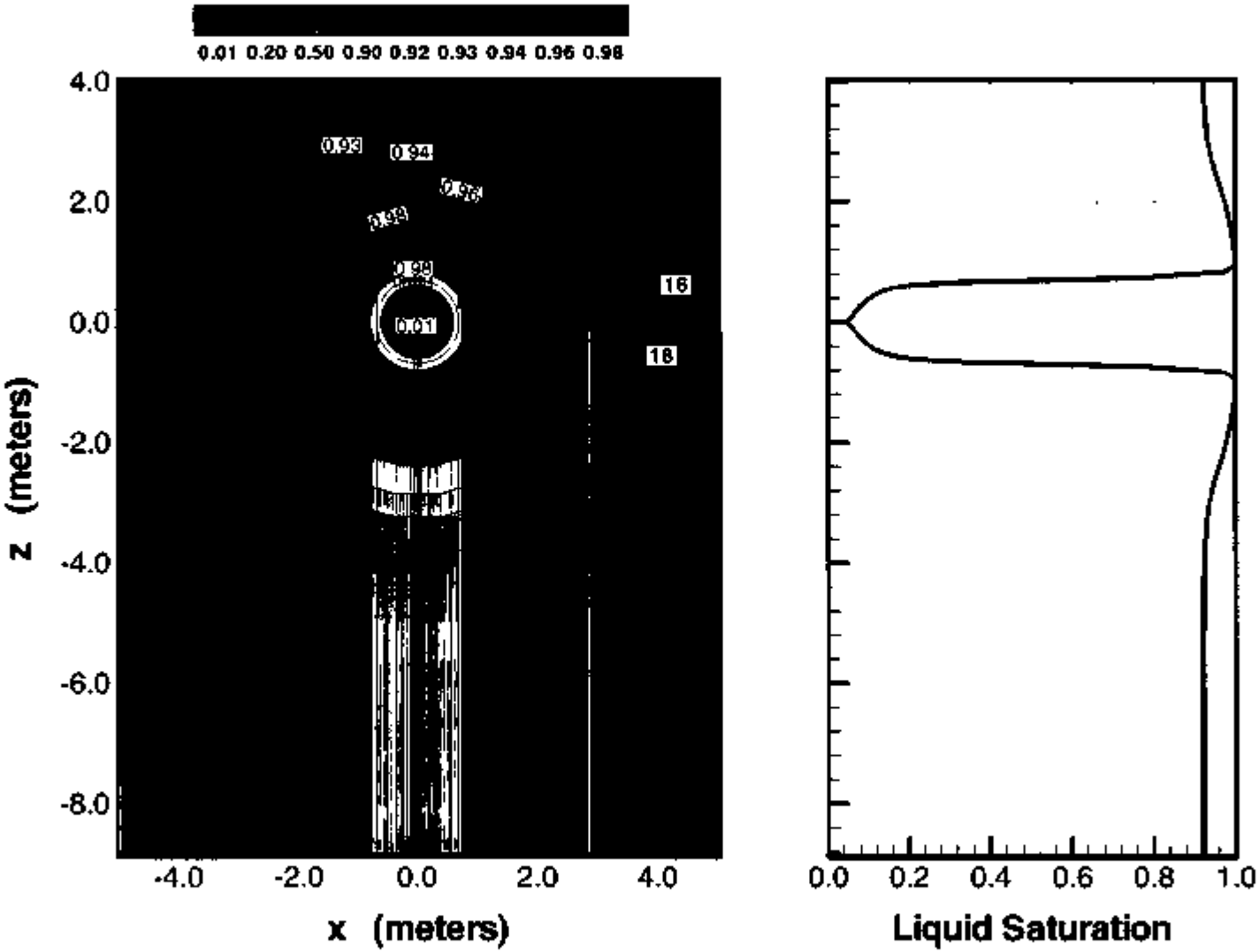

Figure 8-120. Simulated Matrix Liquid Saturation at 3 Months of Heating In XZ–Cross Section at Y = 4 5 m, using ECM

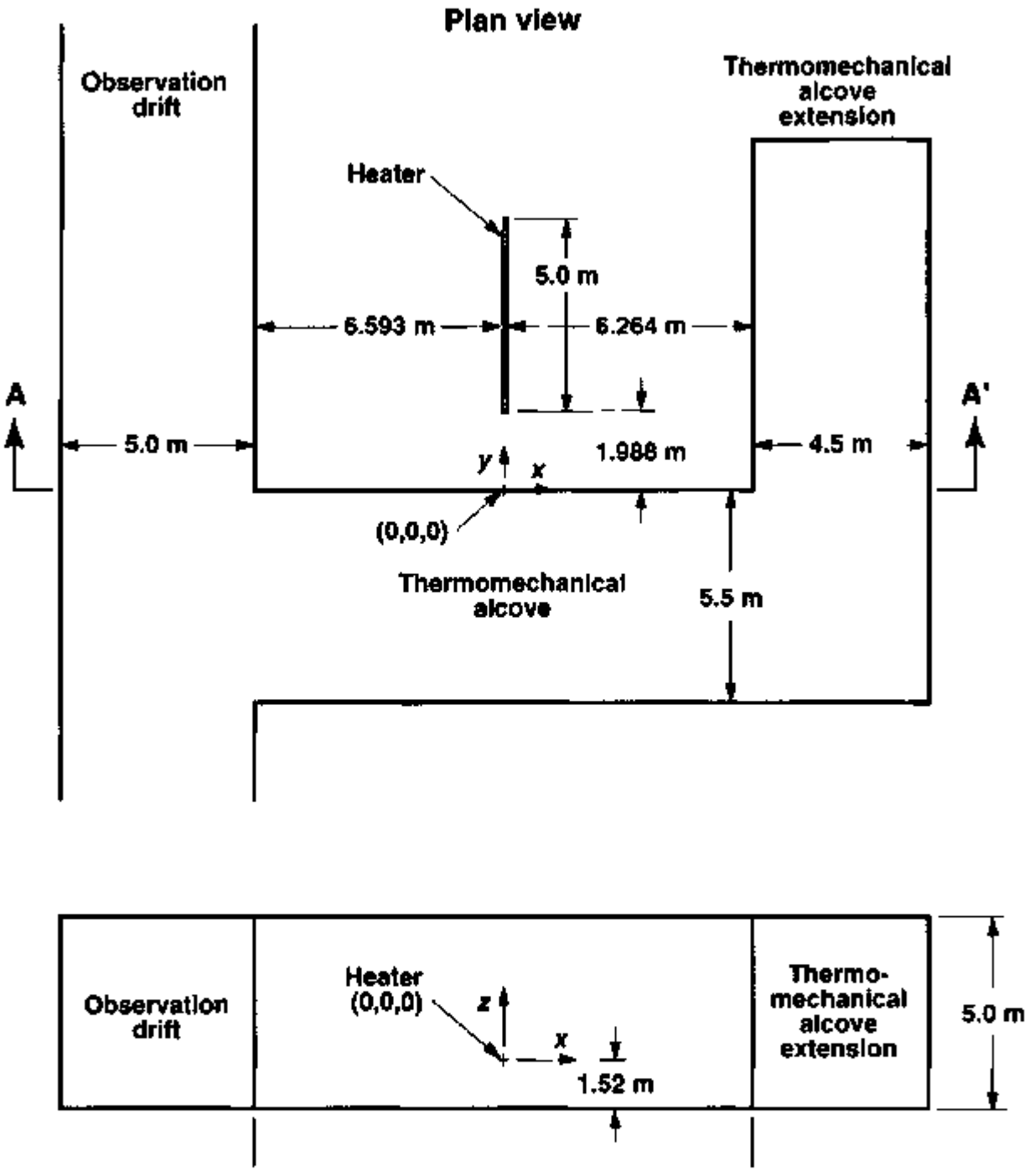

Figure 8-121. SHT Layout, Including Dimensions and SHT Model Coordinate System, in Plan View and Vertical Section A-A'

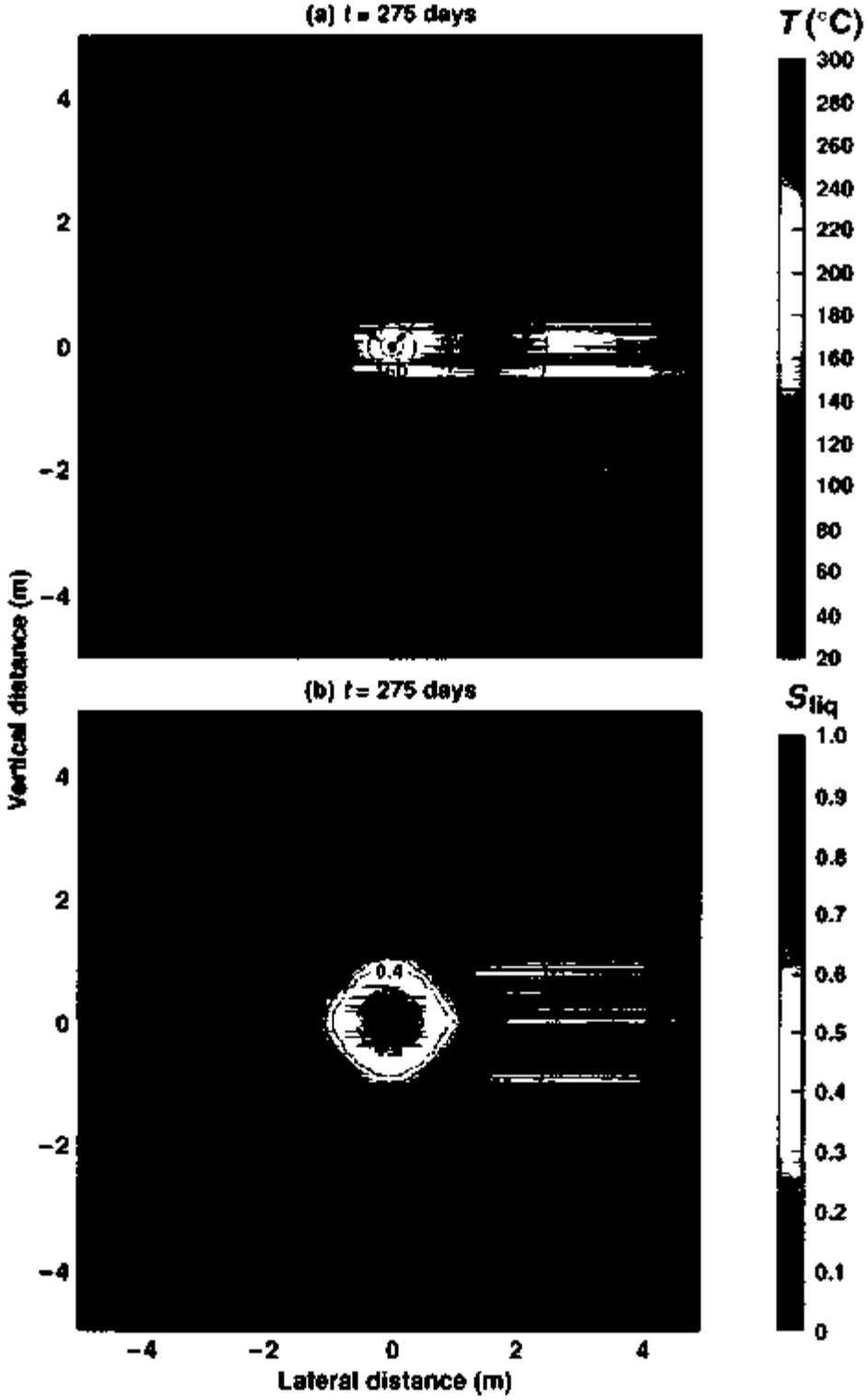

NOTE Case f uses the ECM model

Figure 8-122. Case 1: (a) Temperature Distribution and (b) Liquid-Phase Saturation Distribution at the End of Heating, Plotted on a Vertical Plane Transverse to the Midpoint of the Heater

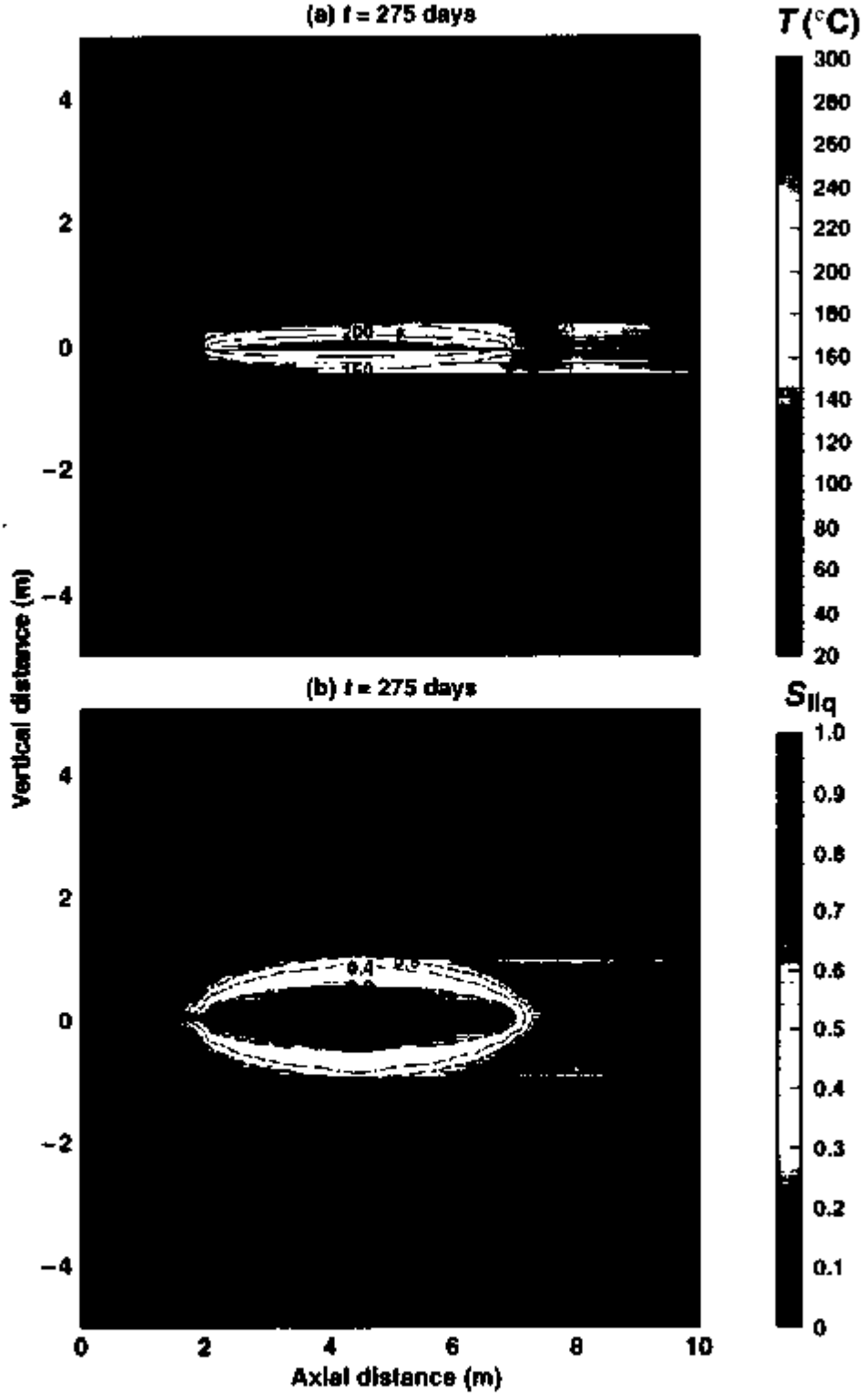

NOTE: Case 1 uses the ECM model. Zero axial distance corresponds to the collar of the heater borehole.

Figure 8-123. Case 1: (a) Temperature Distribution and (b) Liquid-Phase Saturation Distribution at the End of the Heating Phase, Plotted on a Vertical Plane along the Axis of the Heater

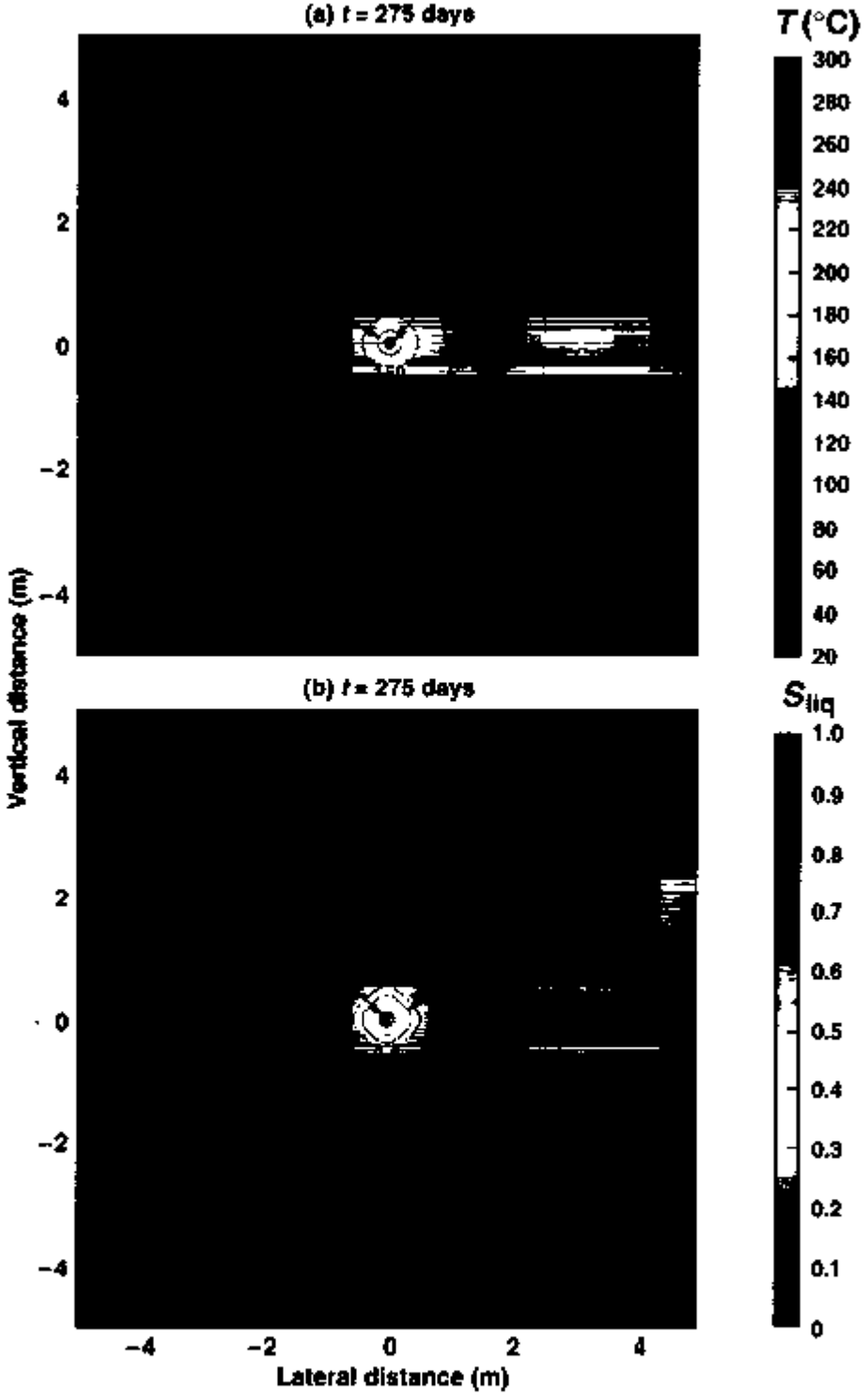

NOTE: Case 3 uses the DKM model.

Figure 8-124. Case 3: (a) Temperature Distribution and (b) Liquid-Phase Saturation Distribution in the Matrix Continuum at the End of Heating, Plotted on a Vertical Plane Transverse to the Midpoint of the Heater

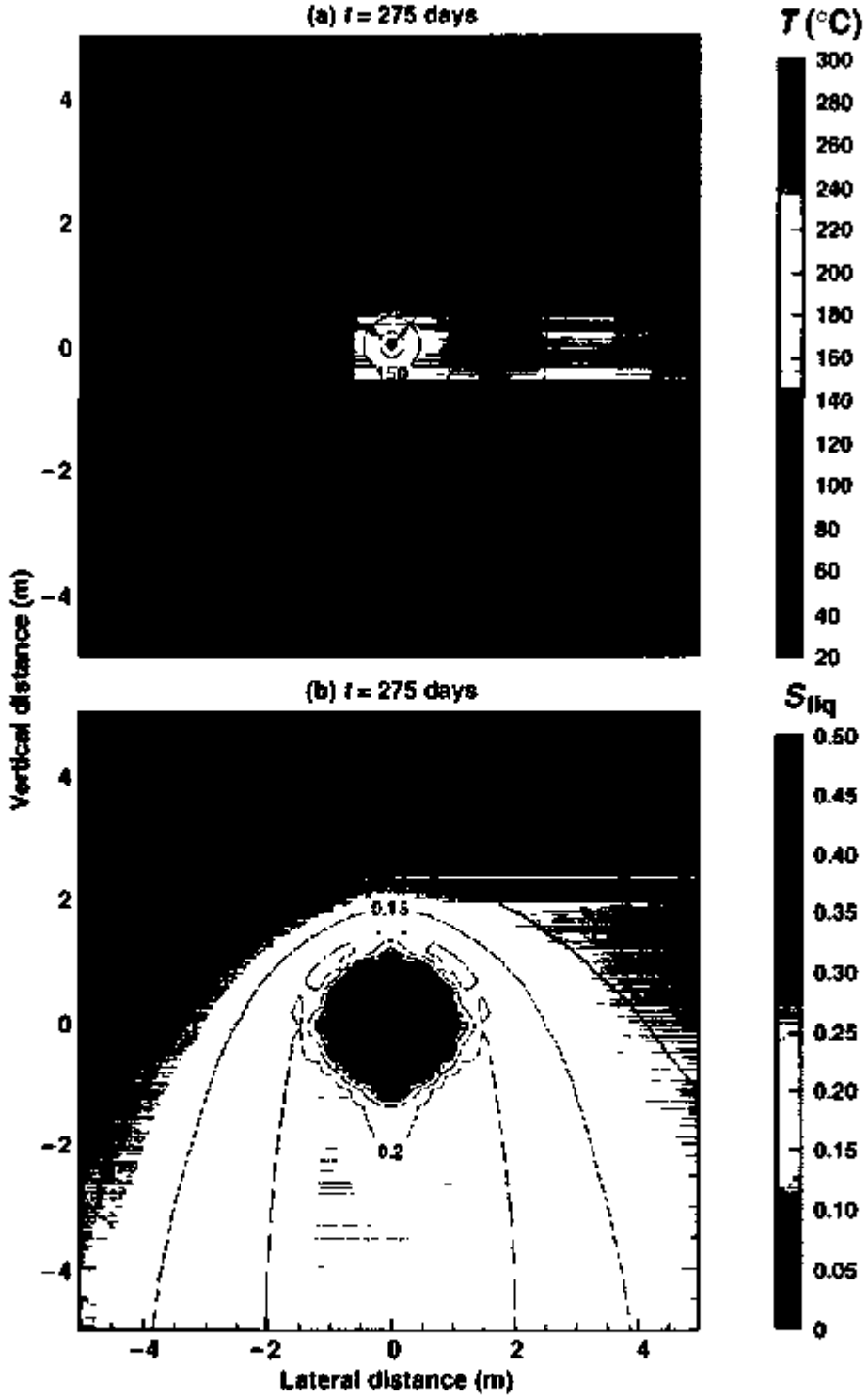

NOTE Case 3 uses the DKM model. The color scale for S_{liq} is different from the one used in Figure 8-120.

Figure 8-125. Case 3: (a) Temperature Distribution and (b) Liquid-Phase Saturation Distribution in the Fracture Continuum at the End of Heating, Plotted on a Vertical Plane Transverse to the Midpoint of the Heater

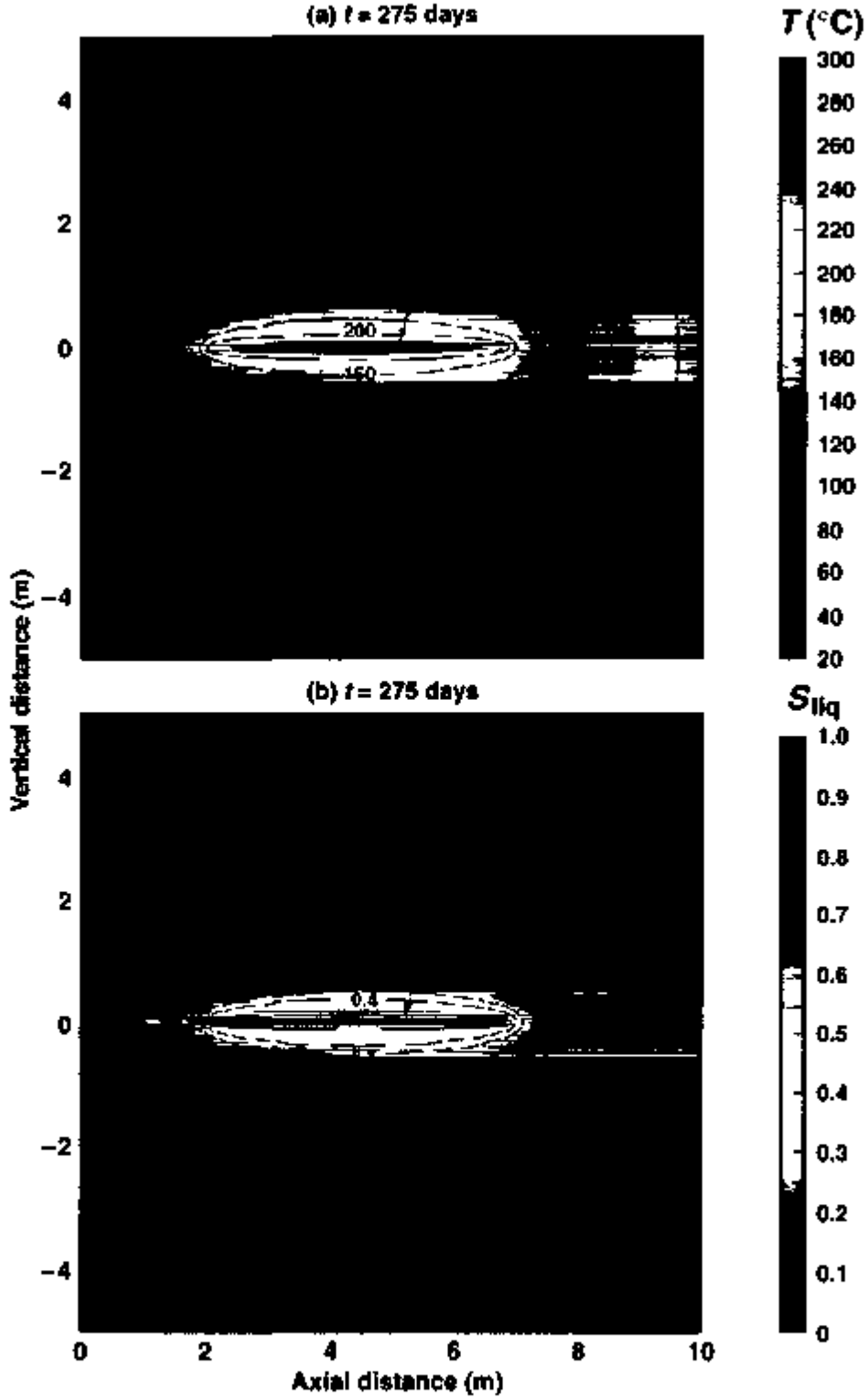

NOTE: Case 1 uses the DKM model. Zero axial distance corresponds to the collar of the heater borehole.

Figure 8-126. Case 3: (a) Temperature Distribution and (b) Liquid-Phase Saturation Distribution in the Matrix Continuum at the End of the Heating Phase, Plotted on a Vertical Plane along the Axis of the Heater

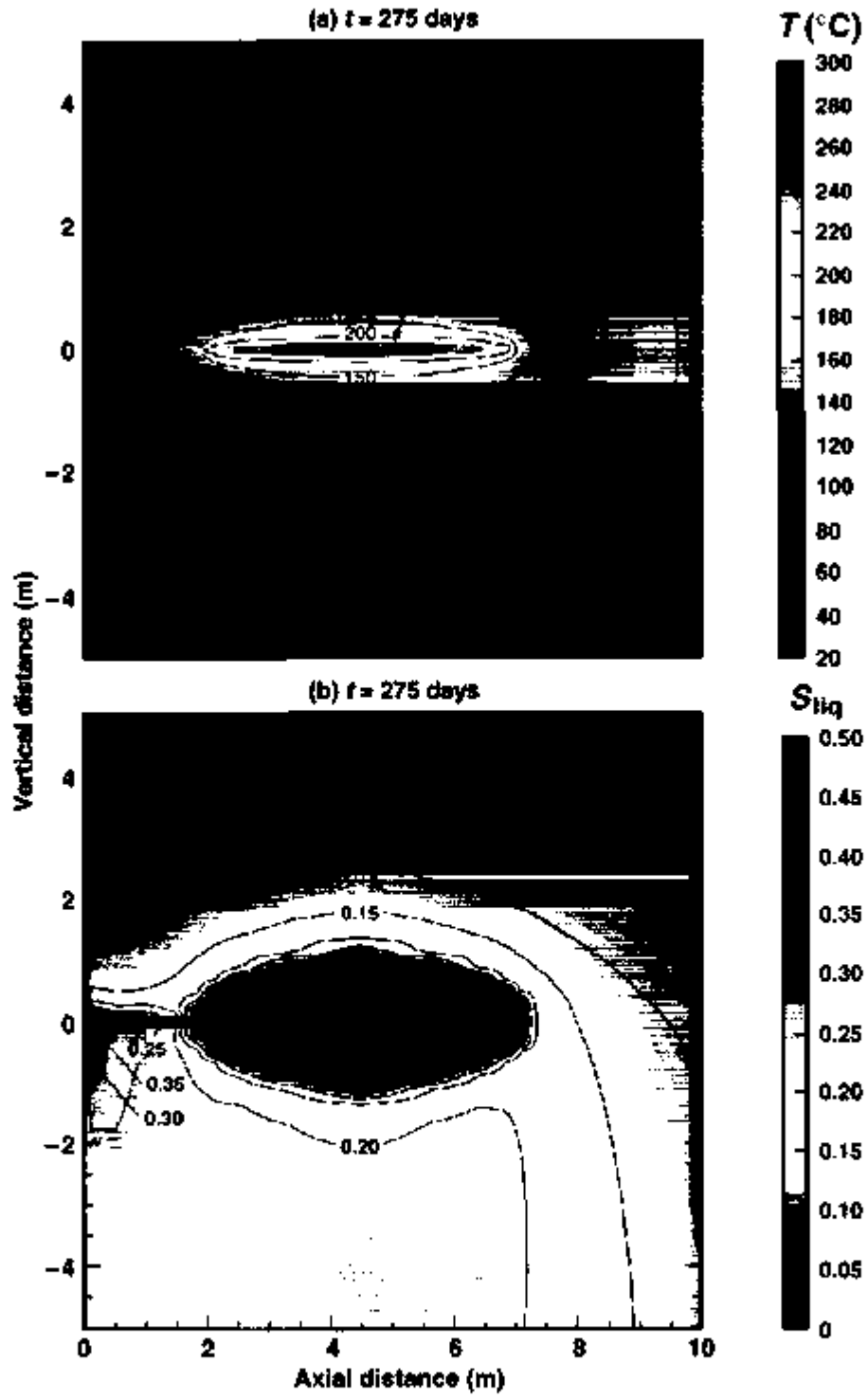

NOTE: Case 3 uses the DKM model. The color scale for S_{liq} is different from the one used in Figure 8-124. The color scale for S_{liq} is different from the one used in Figure 8-126.

Figure 8-127. Case 3: (a) Temperature Distribution and (b) Liquid-Phase Saturation Distribution in the Fracture Continuum at the End of the Heating Phase, Plotted on a Vertical Plane along the Axis of the Heater

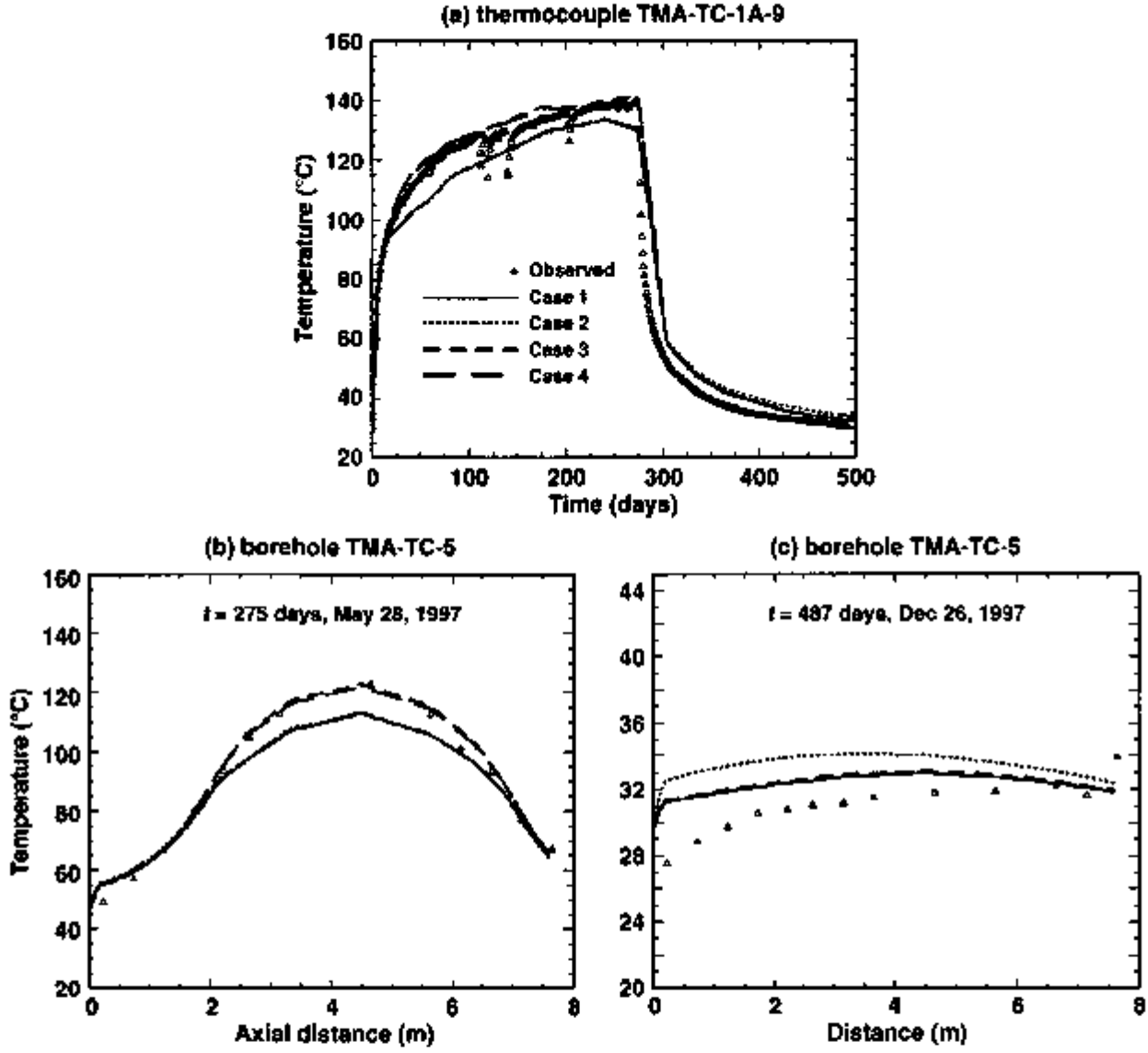

NOTE: (a) Thermocouple TMA-TC-1A-9 is located at x = -0.221, y = 2.978, and z = 0.331.
(b) Measured and simulated temperature distributions shown at the end of heating (t = 275 days).
(c) Measured and simulated temperature distributions shown at 213 days after the end of heating (t = 487 days).

Figure 8-128. Simulated and Measured Temperature Histories Compared at TMA-TC-1A-19 and Simulated and Measured Temperature Distributions along Borehole TMA-TC-5

9. THERMAL-MECHANICAL MEASUREMENTS AND ANALYSIS

This section presents measurements of rock displacement, rock mass modulus, and rock bolt loads for the duration of the SHT. A brief description of instruments and equipment is given in Appendix F.

Displacements were measured both within and on the surfaces of the SHT block. These measurements support numerical model evaluations related to thermal-mechanical-hydrological coupling as well as provide data for determination of rock mass thermal expansion. All displacements reported in this document follow the convention of extension positive.

9.1 EXTENSOMETERS

Four of the original boreholes were instrumented with MPBXs: three boreholes drilled parallel to the heater axis and one borehole drilled perpendicular to the heater axis. The MPBXs include six or seven anchors spaced along the length of the borehole. Displacements were measured using high temperature LVDTs and vibrating wire displacement transducers. For three of the boreholes, Geokon C-ring six-anchor MPBXs were used with carbon fiber extension rods transmitting displacements of each of the six anchors to the head, which was fixed and sealed into the borehole collar using cement grout. The displacements measured for each of the anchors is expressed as the relative displacement between the anchor and the borehole collar (head). The other MPBX that was installed was a seven-anchor Roctest Bof-Ex extensometer that used screw-type mechanical anchors, between each of which was installed a high temperature LVDT. Extension rods between the LVDTs and adjacent anchors were constructed from Invar tubing. The displacements measured for each of the LVDTs represent the discrete displacements between each set of adjacent anchors. Total displacement along the Bof-Ex borehole is the sum of the displacements measured between each set of adjacent anchors. Temperature measurements using Type K thermocouples were made along the length of each MPBX to provide temperature compensation for rod thermal expansion effects. The locations of the anchors and individual thermocouple junctions were determined from the survey and corrected borehole collar coordinates, from the field notes for installation (e.g., installed depth to various anchors and points on the MPBXs), and from the manufacturers' and SNL specifications for the MPBXs. Information on the MPBX gages is included in Appendix F.

Wire extensometers and tape extensometer pins were installed on the three free surfaces of the SHT block. The wire extensometers consist of spring-loaded linear potentiometers mounted on brackets welded to steel rebar segments. These segments are grouted into the rock near the top of the SHT block at six locations (two on each of the three free surfaces of the SHT block). The wires are then stretched roughly vertically downward to another anchor located near the base of the SHT block. Tape extensometer pins are also located roughly along the midpoints of each of the six vertical lines defined by the wire extensometers. These six tape extensometer stations include six pins on the SHT block and six pins on the opposite ribs. As-built locations for each of these gages were determined from tape and level measurements referred to known points of reference. Also, the rock surfaces represented by each of the three free surfaces were simplified to be represented by planar surfaces for numerical modeling efforts. Because the pins are mounted in shallow holes, they can be strongly influenced by movement of discrete blocks near

the surface. All the wire extensometer stations show displacement changes of over several millimeters, with the exception of WX-4, which experienced displacements of less than 1 mm throughout the test. The data from these measurements should be used only for qualitative purposes.

Figures 9-1 and 9-2 show the locations of the MPBX boreholes and anchor locations. The figures also show wire and tape extensometer pin locations on the SHT block. MPBX-1, MPBX-2, and MPBX-3 are located in boreholes drilled parallel to the heater from the Thermomechanical Alcove (Figure 9-2, west face of the SHT block). Two wire and tape extensometer stations are located on each of the three free surfaces of the SHT block. On the west face (Thermomechanical Alcove side), station locations are WX-1, WX-2, WXM-1, and WXM-2 (Figure 9-2). The designator "M" in WXM denotes manual (tape extensometer) pin locations. On the south face of the SHT block (Thermomechanical Extension), MPBX-4 is located in a borehole drilled perpendicular to the heater (Figure 9-2). WX-3, WX-4, WXM-3, and WXM-4 wire and tape extensometer stations are located on the south face. Wire and tape extensometer stations WX-5, WX-6, WXM-5, and WXM-6 are located on the north face of the SHT block along the Observation Drift (Figure 9-2).

The displacement measurements and pretest elastic predictions (Sobolik, Francis, and Finley 1996, Appendix F) for the MPBXs are presented in Figures 9-3 through 9-10. The MPBX data are also given in tabular form in Table 9-1.

Table 9-1. MPBX Displacement (millimeter) History

Gage	Days After Start of Heating												
	0	14	28	42	56	70	84	98	112	126	140	154	168
TMA-BX-1-1*	-0.0903	0.8491	1.2904	1.5386	1.7070	1.7723	1.7967	1.7414	1.7478	1.8076	1.8731	1.8790	1.9726
TMA-BX-1-2*	-0.0797	0.9609	1.3925	1.6606	1.5712	0.9974	0.6131	0.3272	0.1345	0.1877	0.2518	0.2566	0.2726
TMA-BX-1-3	-0.0808	0.8471	1.3092	1.5377	1.6929	1.8491	1.9417	2.0075	2.0275	2.0914	2.1798	2.1819	2.2459
TMA-BX-1-4	-0.0582	0.6777	1.0119	1.2224	1.2910	1.2626	1.2471	1.2077	0.9563	0.8047	0.6376	0.5601	0.3681
TMA-BX-1-5*	-0.0373	0.4603	0.7178	0.8613	0.8949	0.8592	0.7615	0.7694	0.6772	0.4892	0.3710	NA	NA
TMA-BX-1-6*	-0.0176	0.2194	0.3621	0.4187	0.3690	-0.0035	-0.3849	-0.7106	-1.0241	-1.3237	-1.5200	-1.7773	-1.8235
TMA-BX-2-1	-0.0003	0.0049	-0.0013	0.0013	0.0148	0.0193	0.0227	0.0250	0.0721	NA	NA	0.0349	0.0392
TMA-BX-2-2	0.0013	0.1294	0.0945	0.1148	0.1306	0.1385	0.1426	0.1462	0.2013	NA	NA	0.1952	0.1985
TMA-BX-2-3	-0.0009	0.0603	0.0850	0.0919	0.0984	0.1428	0.1506	0.1561	0.1816	NA	NA	0.1733	0.1820
TMA-BX-2-4	0.0023	0.2514	0.1512	0.1678	0.1775	0.1807	0.1854	0.2285	0.3735	NA	NA	0.2358	0.3071
TMA-BX-2-5	-0.0013	-0.0158	0.0423	0.0679	0.0762	0.0819	0.0881	0.0872	0.0452	NA	NA	0.0856	0.0873
TMA-BX-2-6	0.0006	-0.0363	0.0329	0.0474	0.0530	0.0592	0.0611	0.0649	0.0016	NA	NA	0.0014	0.0733
TMA-BX-3-1	0.0006	0.6725	1.1419	1.4522	1.6686	1.8499	1.9501	1.9921	1.8026	1.4568	1.3378	1.3199	1.2558
TMA-BX-3-2	-0.0248	0.6602	1.1455	1.4494	1.6866	1.8644	1.9107	1.8489	1.8607	1.8332	1.8212	1.8784	1.8889
TMA-BX-3-3	-0.0250	0.6663	1.1372	1.4323	1.6633	1.7348	1.6754	1.4331	1.3920	1.3902	1.4264	1.5078	1.5670
TMA-BX-3-4*	-0.0250	0.5430	0.9215	1.1611	1.3545	1.4465	1.4083	1.4171	1.4754	1.4742	-0.5758	1.4864	1.4926
TMA-BX-3-5*	-2.4889	0.4198	0.7824	0.9812	1.1223	1.2094	1.2433	1.2240	1.2039	1.2286	1.2589	NA	NA
TMA-BX-3-6	-0.0252	0.3247	0.5973	0.7617	0.8715	1.0047	1.1112	1.0895	1.0166	0.9909	1.0447	1.0724	1.1258
TMA-BX-4-1	0.0256	-0.1472	-0.1107	-0.0329	0.0727	0.1417	0.2313	0.2881	0.3986	0.4000	0.5081	0.5141	0.5447
TMA-BX-4-2	0.0006	-0.1772	-0.1796	-0.1073	-0.0813	0.0049	0.0936	0.1503	0.2092	0.2111	0.2425	0.1970	0.2017
TMA-BX-4-3	0.0259	-0.0965	-0.1139	-0.1017	-0.0655	-0.0300	0.0041	0.0607	0.0924	0.1202	0.1495	0.1544	0.0816
TMA-BX-4-4	0.0005	-0.0499	-0.0734	-0.0675	-0.0364	-0.0306	-0.0001	0.0293	0.0589	0.0660	0.1138	0.1175	0.1196
TMA-BX-4-5	0.0004	-0.0252	-0.0255	-0.0231	-0.0207	-0.0178	0.0102	0.0121	0.0389	0.0660	0.0674	0.0696	-0.0055
TMA-BX-4-6	0.0003	0.0000	-0.0004	0.0004	0.0011	0.0274	0.0283	0.0289	0.0299	0.0304	0.0564	-0.0574	0.0833

Table 9-1. MPBX Displacement (millimeter) History (Continued)

Gage	Days After Start of Heating												
	182	196	210	224	238	252	266	280	294	308	322	336	350
TMA-BX-1-1*	2 0128	2.0494	2.4287	2 4180	2.4503	2 4292	2 4020	NA	NA	NA	NA	NA	NA
TMA-BX-1-2*	0 3112	0.2959	0.2565	NA	NA	NA	NA	NA	NA	NA	NA	NA	NA
TMA-BX-1-3	2 2815	2.2891	2.3125	2 3228	2.3275	2.3302	2 3285	1.9027	1.4687	1 4038	1 1168	1.0917	1.0744
TMA-BX-1-4	0 3500	0.2027	0.2768	0 2839	0.2111	0 2130	0.1613	-0 0686	-0 4499	-0 4979	-0.7767	-0.7957	-1 0629
TMA-BX-1-5*	NA	NA	NA	NA	NA	NA	NA	NA	NA	NA	NA	NA	NA
TMA-BX-1-6*	-1 8471	-1.8461	-1.8495	NA	NA	NA	NA	NA	NA	NA	NA	NA	NA
TMA-BX-2-1	0 0409	0 0431	0.0455	0.0480	0.0499	0.0518	0.0524	0 0458	0.0271	0.0191	0.0136	0 0192	-0 0229
TMA-BX-2-2	0.2006	0.2032	0.2061	0 2095	0.2129	0.2147	0.2140	0.1527	0 1088	0 0982	0.0876	0 0840	0.0760
TMA-BX-2-3	0.1870	0.1891	0 1861	0.1877	0.1887	0.2015	0.1963	0.1131	0.0778	0 0690	0.0538	0 0579	0.0050
TMA-BX-2-4	0 2436	0.2462	0.2406	0.2470	0.2486	0.2500	0 2488	-0 1442	0.0588	0 0308	0.0157	0 0099	-0.1970
TMA-BX-2-5	0 0859	0.0869	0.0851	0.0874	0.0884	0.0879	0.0876	0 0760	0.0507	0 0315	0.0351	0.0304	-0.0519
TMA-BX-2-6	0.0744	0.0760	0.0753	0.0780	0.0785	0.0800	0.0792	0.0794	0 0760	0 0785	0 0734	0 0699	-0.0414
TMA-BX-3-1	1.4447	1.4780	1.5079	1.5446	1.6006	1.6811	1.7097	1 4418	1 3345	1.0194	0 9788	0.9513	0.6774
TMA-BX-3-2	1.9232	1.9805	2.0079	2 0700	2.1006	2.0541	2.0828	1 7894	1.6821	1.3671	1 3264	1.2989	1.0250
TMA-BX-3-3	1.6246	1.6552	1.7065	1.7386	1.7682	1.7972	1.7999	1.7131	1.3743	1.3253	1.0383	1.0160	0 9998
TMA-BX-3-4*	1.5231	1.4255	1.2483	1.2533	1.2560	NA	NA	NA	NA	NA	NA	NA	NA
TMA-BX-3-5*	NA	NA	NA	NA	NA	NA	NA	NA	NA	NA	NA	NA	NA
TMA-BX-3-6	1.1534	1.1805	1.1810	1.2084	1.2352	1.2388	1 2634	1 0589	1.2930	1.0253	1.0152	1.0082	1.0032
TMA-BX-4-1	0 5489	0.5788	0.6067	0.6107	0.6399	0.6433	0.6718	0 7110	1.3551	1.3287	1 0546	1.0397	1.0283
TMA-BX-4-2	0 2309	0.2605	0.2885	0.2920	0.3209	0.3495	0.3780	0 4766	0.8877	0 8700	0.8553	0.8440	0.8352
TMA-BX-4-3	0.0337	0.0117	0.0397	0.0423	0.0452	0.0733	0.1015	0.1291	0.5588	0 5517	0.5440	0.5377	0 5324
TMA-BX-4-4	0.1214	0.1237	0.1258	0.1530	0.1550	0.1571	0.1847	0.1359	0.5710	0.5696	0.5668	0.5641	0.5617
TMA-BX-4-5	-0.0553	-0 0792	-0.0779	-0.0767	-0.0755	-0.0487	-0 0725	-0 1726	-0 1717	-0.1718	-0.1732	-0.1746	-0.1760
TMA-BX-4-6	0.0838	0.0844	0.0850	0.0856	0.0862	0.0870	0 0878	-0 0131	-0 0125	-0.0122	-0.0125	-0.0127	-0.0131

Gage	Days After Start of Heating											
	364	378	392	406	420	434	448	462	476	490	504	518
TMA-BX-1-1*	NA	NA	NA	NA	NA	NA	NA	NA	NA	NA	NA	NA
TMA-BX-1-2*	NA	NA	NA	NA	NA	NA	NA	NA	NA	NA	NA	NA
TMA-BX-1-3	1.0616	1.0258	0.9929	0.7842	0.7791	0.9529	0 9238	0.8942	0.8632	0 8576	0.8009	1.0697
TMA-BX-1-4	-1 0725	-0.9534	-1.0098	-1.0900	-1.0938	-1.0460	-1 0996	-1.2554	-7.8610	-1.2908	-1.2961	-1.0266
TMA-BX-1-5*	NA	NA	NA	NA	NA	NA	NA	NA	NA	NA	NA	NA
TMA-BX-1-6*	NA	NA	NA	NA	NA	NA	NA	NA	NA	NA	NA	NA
TMA-BX-2-1	0.0137	0.0187	0.0181	0.0089	0.0178	0.0160	0.0172	0 0176	0.0191	0 0166	0.0130	0.8480
TMA-BX-2-2	0.0760	0.0735	0.0718	0.0692	0 0690	0.0680	0 0681	0 0674	0 0678	0.0673	0.0619	-0.5751
TMA-BX-2-3	0 0509	0.0504	0.0485	0.0451	0 0438	0.0488	0.0472	0.0494	0 0480	0.0484	0.0425	0.0505
TMA-BX-2-4	0.0029	-0.0045	-0.0073	-0.0027	-0.0039	-0.0110	-0.0124	-0 0092	-0.0068	-0.0085	-0.0114	0.2636
TMA-BX-2-5	0 0246	0.0306	0.0302	0.0302	0.0193	0.0306	0 0289	0 0293	0 0284	0.0283	0.0242	-0 0248
TMA-BX-2-6	0.0657	0.0714	0.0713	0.0628	0.0621	0.0726	0 0729	0 0740	0.0742	0.0725	0.0678	0.0028
TMA-BX-3-1	0 6620	0 7771	0.7425	0.6342	0.6285	0.6280	0 6280	NA	NA	NA	NA	NA
TMA-BX-3-2	1.0096	1.1755	1 1409	0.9818	0.9761	1.0986	1 0688	NA	NA	NA	NA	NA
TMA-BX-3-3	0 9873	1.0032	0 9703	0.7111	0.7066	0.9061	0 9280	NA	NA	NA	NA	NA
TMA-BX-3-4*	NA	NA	NA	NA	NA	NA	NA	NA	NA	NA	NA	NA
TMA-BX-3-5*	NA	NA	NA	NA	NA	NA	NA	NA	NA	NA	NA	NA
TMA-BX-3-6	0.9992	1 1488	1 1468	0.9930	0.9916	1.1684	1 1671	NA	NA	NA	NA	NA
TMA-BX-4-1	1.0192	0 6472	0.5904	0.3067	0.5571	0.6297	0 6007	0.5964	0.5645	0 5325	0.4739	0.4137
TMA-BX-4-2	0.8280	0 4575	0.4527	0.3731	0.3703	0.3926	0 3896	0 3603	0.3288	0 2973	0.2646	0.2052
TMA-BX-4-3	0.5280	0.2104	0.1819	0.0783	0.0765	0.1505	0.1481	0 1449	0.1140	0 0833	0.0261	-0.0059
TMA-BX-4-4	0.5595	0 2692	0.2422	0.1143	0.1134	0.2389	0 2371	0 2345	0.2043	0.1743	0.1434	0.1117
TMA-BX-4-5	-0.1773	-0.0259	-0.0264	-0.1789	-0.1792	-0.0277	-0 0290	-0 0310	-0.0605	-0.0895	-0.1191	-0.1240
TMA-BX-4-6	-0.0135	0.1386	0.1388	-0.0135	-0.0136	0.1384	0.1377	0 1111	0.1086	0 0812	0.0534	0.0508

Corrected for rod thermal expansion. Extension positive. Displacement data given in mm.
NA = Not available *Suspected failed gages.

The data presented in Figures 9-3 through 9-10 are corrected for thermal expansion of the MPBX rods. These rods connect each anchor individually with the borehole collar where the displacement gages are located. The rods are constructed of either carbon fiber, with a linear thermal expansion coefficient (as reported by the manufacturer, Geokon) of 1.48×10^{-6}/°C, or Invar, with a variable thermal expansion coefficient. The linear thermal expansion of the rods connecting each anchor is calculated using temperature data from the thermocouples located along their length and integrated for each incremental length between individual thermocouples.

The thermal expansion of the rods that are used to connect MPBX anchors to the displacement sensors located in the MPBX head (collar) must be determined. The rod thermal expansion must be added to the measured displacements to obtain the actual rock mass displacements. Because the rods expand due to heating, the displacements measured at the head or by the gages downhole appear to be smaller than the actual displacements. The actual rock mass displacements are therefore the measured displacements plus the rod expansion. The rod thermal expansion is calculated from temperatures measured on the rods, measured rod lengths, and known Invar (SNL laboratory determined; Brodsky 1997) or carbon fiber thermal expansion coefficients (from the manufacturer, Geokon). The calculated rod thermal expansion is:

$$\delta = \alpha \Delta T \lambda \qquad (9\text{-}1)$$

where:

δ	=	MPBX connecting rod thermal expansion (m)
α	=	thermal expansion coefficient for the connecting rods (10^{-6}/°C)
ΔT	=	change in temperature above ambient (°C)
λ	=	rod segment length (m)

For the MPBXs with carbon fiber connecting rods (MPBX-1, MPBX-3, MPBX-4), the cumulative thermal expansion for each successive anchor is the sum of the previous anchors' thermal expansions. This cumulative calculation is used because a temperature gradient is expected along the length of the MPBXs. For this calculation, the "average" temperature change over each rod segment length is used. For MPBX-2, which uses Invar connecting rods and downhole high-temperature LVDTs between anchors, the rod thermal expansion correction is applied to the rod length between each adjacent set of anchors.

Because the carbon fiber thermal expansion is practically stable over the range of temperatures experienced in the SHT, the manufacturer's suggested thermal expansion coefficient of 1.48 ppm/°C was used for thermal expansion corrections for MPBX-1, MPBX-3, and MPBX-4. The displacements measured by MPBX-1, MPBX-3, and MPBX-4 are the relative displacements between each anchor and the MPBX head located at the borehole collar. The temperatures are measured using thermocouples attached to the connecting rods and anchors downhole. There are typically at least two thermocouples located within each rod segment length. The locations of the anchors and thermocouples are identified in Appendix G, and these locations are used in the rod expansion calculation for the rod segment length and temperature change terms in Equation 9-1 above.

The Invar thermal expansion coefficient has been measured in the laboratory at SNL and been found to be temperature dependent (Brodsky 1997). Table 9-2 presents measured Invar thermal expansion coefficients over a range of temperatures that are to be used in the MPBX rod thermal expansion correction calculation.

Table 9-2. Invar Thermal Expansion Coefficients

Temperature Range (°C)	Thermal Expansion Coefficient (10^{-6}/°C)
25-50	1.62
50-75	1.89
75-100	2.17
100-125	2.71
125-150	3.44
150-175	4.51
175-200	5.62
200-225	7.17

The Invar rod thermal expansion correction for MPBX-2 is applied for each rod segment between adjacent anchors. The total displacement for any anchor relative to the collar of the borehole is the sum of the corrected collar-side displacements measured between all sets of adjacent anchors.

Figure 9-3 shows the displacements measured by TMA-MPBX-1 (located parallel and approximately 0.33 m from the heater, above and to the south). The anchor locations in x, y, z coordinates for MPBX-1 are given in Appendix G. The displacements given in Figure 9-3 are expressed relative to the borehole collar, with MPBX-1-1 deepest in the borehole and MPBX-1-6 nearest the borehole collar. The y-coordinates for each of the TMA-MPBX-1 anchors are spaced approximately 1 m apart from the bottom of the borehole (anchor MPBX-1-1 at 6.883 m to anchor MPBX-1-6 at 2.043 m along the y-coordinate axis).

The data for MPBX-1 show general extension for all anchor locations through about day 50. After day 50, the displacements for anchors TMA-MPBX-1-6 and TMA-MPBX-1-2 change directions and become more compressive. Note that only anchor TMA-MPBX-1-6 is truly compressive; anchor TMA-MPBX-1-2 merely becomes less extensional. About day 80, anchors TMA-MPBX-1-4 and TMA-MPBX-1-5 become less extensional. Anchors TMA-MPBX-1-1 and TMA-MPBX-1-3 remain extensional through about day 150 and stabilize at 2 mm of net extension. Anchor TMA-MPBX-1-1 experienced a slight change in displacement sign about day 90, but thereafter continued in an extensional mode. At about day 210, anchor TMA-MPBX-1-1 experienced a sudden increase in displacement. This is possibly due to discrete fracture movement between anchors 1 and 2, as none of the other MPBX-1 anchors show such movement. Anchor TMA-MPBX-1-4 continues a subtle relative compression from about day 90 through about day 200. Several of the MPBX-1 gages appear to have failed. The gage for anchor TMA-MPBX-1-3 failed around day 140. The gages for anchors TMA-MPBX-1-2 and TMA-MPBX-1-6 failed around day 205. The gage for anchor TMA-MPBX-1-1 failed around day 265. Following the completion of the cooldown phase, the MPBX-1 head was removed, the gages were examined, and the borehole was overcored and the anchors and rods removed. The results of these posttest investigations are discussed in Section 6 of this report.

The cooldown data for TMA-MPBX-1 are presented in Figure 9-3 from day 274 through the end of testing. Only two gages were operating after day 275 of the test for MPBX-1: TMA-MPBX-1-3 and TMA-MPBX-1-4. These two gages exhibit the expected type of response as a result of deenergizing the heater. Both operating gages show a marked decrease in the measured displacements. In addition, the decreases are "step-wise," which is suggestive of "stick-slip" type behavior probably occurring along joints. Anchor TMA-MPBX-1-4, which exhibited a marked decrease in measured displacement from about day 100 through the end of heating, actually crosses into the compressive regime immediately after heater turnoff with a maximum compression of about 1 mm through the end of testing. The compressive regime suggests that, if the gage is operating properly, there was a net decrease in gage length between anchor TMA-MPBX-1-4 and the collar from the beginning of the SHT to the present.

The data for MPBX-1 presented in Figure 9-3 give a somewhat confusing picture of the displacements along the length of the borehole. Although all anchors but one exhibit net extension during the heating period, the magnitudes and order of anchor displacements differ from the linear elastic pretest predictions presented in Sobolik, Francis, and Finley (1996, p. F-2) after approximately 50 days of heating (see Figure 9-4). These predictions suggested that the deepest anchor (MPBX-1-1) should exhibit the greatest extension and the shallowest (MPBX-1-6) the least, with the other anchors between dependent on their locations. Because the rock surrounding the SHT is fractured, and the thermal expansion of the rock blocks is volumetric, it could be expected that some regions surrounding the heater can experience net compression due to closing or shear along fractures. However, it should be emphasized that the analyses presented in Sobolik, Francis, and Finley (1996) are simplified linear elastic predictions using laboratory-derived intact rock values for modulus and thermal expansion coefficient. Therefore, the analyses do not account for normal or shear displacements on fractures nor discontinuum effects. The maximum measured displacements exhibited in MPBX-1 (by MPBX-1-1 and MPBX-1-3 of about 2.4 mm) are not inconsistent with the predicted displacements. However, only anchor MPBX-1-3 exhibits the predicted displacement history throughout both heating and cooling, although the decrease during cooldown is less than the predicted amount. It is also interesting to note that anchor MPBX-1-2 ceases compression about day 110 and exhibits slight extension through day 205, when the gage apparently failed. The trend of MPBX-1-2 parallels those of MPBX-1-1 and MPBX-1-3 for this time period. This type of behavior may be evidence of closing or slip along fractures between anchors MPBX-1-1 and MPBX-1-2 from day 50 through about day 110. After day 140, the trends of MPBX-1-1 and MPBX-1-2 parallel each other, suggesting that fracture slip in this region has occurred. It is also important to note that the displacement trends for MPBX-1-4 roughly parallel those of MPBX-1-1 and MPBX-1-3 after about day 200. Again, this is suggestive of a mechanically closed fracture system. The temperatures measured along the length of MPBX-1 are presented graphically in Section 7. The maximum temperatures measured on MPBX-1 are about 160°C and occur near the midpoint with significantly lower temperatures near the bottom anchor (MPBX-1-1).

Figure 9-5 and Table 9-1 show the corrected displacements measured by TMA-MPBX-2, which is located approximately 0.69 m from the heater, above and to the left (north). The anchor locations in x, y, z coordinates for MPBX-2 are given in Appendix G. The y-coordinates for each of the TMA-MPBX-2 anchors are spaced approximately 1 m apart from the bottom of the borehole (anchor MPBX-2-1 at 7.093 m, anchor MPBX-2-6 at 2.073 m, and anchor MPBX-2-7

at 0.39 m along the y-coordinate axis). As previously discussed, TMA-MPBX-2 differs from the other MPBXs installed in the SHT by having the gages (high temperature LVDTs) installed in the borehole between each pair of anchors connected via Invar extension rods. Therefore, the relative displacement between anchors is measured and plotted in Figure 9-5. As such, the individual measured displacements should be and are much smaller than those measured from the other MPBX anchors, particularly the deep anchors. Also, because of the discreet nature of the LVDT measurements, it is possible that adjacent sets of anchors can record displacements of opposite sign (extension versus compression). This is possible because of the variability of fracturing within the SHT block and the possibility of fracture closure or shear resulting from rock matrix thermal expansion.

One of the primary purposes of TMA-MPBX-2 is to evaluate the reliability of the high temperature LVDTs to severe thermal-hydrological environments. This type of LVDT was used for MPBXs installed in the DST, where similar environments are expected to exist. Figure 9-5 exhibits small displacements between all sets of adjacent anchors (less than 0.2 mm). The data also show gaps at various time intervals. These gaps result from power outages that blew the fuse in the signal conditioner for the LVDTs. The LVDT readings are quite stable. None of the high-temperature LVDT gages failed during the SHT.

For TMA-MPBX-2 the temperature distribution along the length of the borehole is given in Section 3. For TMA-MPBX-2, thirteen temperature measurements were made (MPBX-2-TC-1 through MPBX-2-TC-13), one on each of the seven anchors and one on the extension rods between anchors. The temperatures measured along the length of MPBX-2 are similar to those in MPBX-1 in that the maximum recorded temperatures (about 120°C) are located near the midpoint of MPBX-2, with significantly lower temperatures at the end anchors (MPBX-2-1 and MPBX-2-7). MPBX-2 exhibits general extension between all pairs of anchors through the heating period, with the exception of anchors 4 and 5, which show minor compression near the end of heating. Absolute maximum relative displacements during heating are low, with maximum adjacent anchor displacements of about 0.15 mm (for gage TMA-MPBX-2-4) between anchors 4 and 5. The thermal expansion coefficient for Invar tubing, a low-thermal-expansion nickel alloy, is reported by the supplier, Geokon, to be about 1.48×10^{-6}/°C. SNL performed linear thermal expansion tests on Invar tube samples and obtained larger thermal expansion coefficients ranging from 1.62×10^{-6}/°C at ambient temperatures to about 2.71×10^{-6}/°C for temperatures between 100° and 125°C (Brodsky 1997, p. 3). These upper temperatures are consistent with the maximum temperatures seen in MPBX-2. The data presented in Figure 9-5 incorporate the SNL-derived thermal expansion coefficients for Invar.

The MPBX-2 measurements shown in Figure 9-5 are consistent in form with the predicted values (Figure 9-6) from Sobolik, Francis, and Finley (1996, p. F-11). The measured values are consistently lower than the predicted values but are much more stable than the other MPBX responses. The largest displacements are seen in TMA-MPBX-2-4, and the smallest are in TMA-MPBX-1-2, which is consistent with the model predictions. Also, the cooldown data shown in the measurements are reasonably stable with some minor "jumps." These jumps may be suggestive of "stick-slip" behavior associated with shear or compression/extension of fractures in the heated volume of rock. Comparison of the measured and predicted displacements present an image of the actual rock mass as less stiff and less thermally expansive than conceived of in the

predictions. Also note that MPBX-2 is installed on the left side of the SHT heater, and the region between anchors MPBX-2-2 and MPBX-2-3 (see Figures 9-1 and 9-2) was interrogated using the NX borehole jack intermittently during the SHT. As will be presented in Section 9.2, the borehole jack testing yielded rock mass moduli between 8.3 GPa and 22.8 GPa during the SHT. The high borehole jack value occurred near the end of heating and could be the result of fracture closing and resultant rock mass stiffening, although such a possibility does not appear to be supported by the MPBX-2 data, which show no displacement trend changes during heating. However, the stability of the MPBX-2 readings through time and the small cumulative measured displacements do indeed suggest that either the thermal expansion of the rock mass in the region surrounding the borehole is lower than expected, or that the thermal expansion is being accommodated in a systematic way by the fracture system in that area. The data also suggest that some mechanical hysteresis exists in the rock mass surrounding MPBX-2, as the data show excess extension at day 448 when compared to the initial model predictions.

Figure 9-7, Figure 9-8, and Table 9-1 show displacement data and model predictions for TMA-MPBX-3, which is located approximately 1.5 m from the heater, above and to the right (south). The anchor locations in x, y, z coordinates for TMA-MPBX-3 are given in Appendix G. The y-coordinates for each of the anchors are spaced approximately 1 m apart from the bottom of the borehole (anchor MPBX-3-1 at 6.887 m to anchor MPBX-3-6 at 2.047 m along the y-coordinate axis). The data from TMA-MPBX-3 exhibit results consistent with those of MPBX-1. The data presented in Figure 9-7 show an increase in gage length (extension) for all anchor positions through about the first 70 days. From 70 to about 100 days, all anchors exhibit a gradual decrease in gage length. After about 100 days, all anchors except MPBX-3-1 reverse trend and increase extension through the second quarter of heating. Anchor MPBX-3-1 continues the relative compression from day 100 through about day 180, when it experiences a sudden extensional jump followed by continued extension throughout the fourth quarter of heating. The extensional jump at about day 180 is seen only in anchor MPBX-3-1; therefore, it is likely that it results from discrete movement along a fracture or system of fractures located between anchors MPBX-3-2 and MPBX-3-1. This region corresponds with similar presumed behavior near anchor MPBX-1-1 (MPBX-1) near day 210. Also, pretest characterization suggested that a fracture zone extends through this region (CRWMS M&O 1996b, p. 7-3). The change in slope of most of the anchor responses after about 70 days may be the result of matrix thermal expansion closing existing fractures, thus limiting additional thermally-driven displacements until a greater volume of rock is heated. Thus three-dimensional confinement effects may influence the response of some anchors.

For TMA-MPBX-3, the temperature distribution along the length of the borehole is given graphically in Section 3. MPBX-3 temperatures are similar to those measured in MPBX-1 and MPBX-2 in that the maximum temperatures up to about 80°C are located near the midpoint of the borehole, with lower temperatures at the end anchors (MPBX-3-1 and MPBX-3-6).

As stated, the general trends presented for MPBX-3 in Figure 9-7 are somewhat consistent with data for MPBX-1. Figure 9-7 suggests that volumetric expansion of the rock mass may have resulted in mechanically closing fractures beginning after about 60 days for anchor MPBX-3-3 through about 125 days. It is of interest to note that all anchors except MPBX-3-1 and MPBX-3-4 exhibit roughly parallel displacement histories after day 100 and including MPBX-3-1 after

day 180. Additional discussion of all MPBX displacements is given in Section 6. For TMA-MPBX-3, originally nine temperature measurements were made, one on each of the six anchors (MPBX-3-TC-1 through MPBX-3-TC-6) and three on the extension rods near the collar (MPBX-3-TC-7 through MPBX-3-TC-9). The thermal expansion coefficient for carbon fiber is 1.48 ppm/°C, as noted above. For each anchor, the thermal expansion of the extension rod is determined by integrating the measured temperatures from the anchor to the collar, as previously discussed. Naturally, the largest thermal correction is for anchor MPBX-3-1 because it includes the greatest length of extension rod.

The cooldown data for TMA-MPBX-3 are presented in Figure 9-7 from day 274 through the end of testing. Four gages in MPBX-3 are operational; gages MPBX-3-4 and MPBX-3-5 are suspected to have failed from unknown causes during heating. The operational gages in MPBX-3 exhibit behavior similar to the MPBX-1 gages during cooldown. MPBX-3 exhibits step-wise decreases in all operational gages during cooldown. As with MPBX-1, this type of behavior may be suggestive of "stick-slip" type behavior resulting from normal and/or shear extension/compression of fractures in the cooling rock mass. This type of behavior should not be unexpected in a fractured rock mass.

Figure 9-9, Figure 9-10, and Table 9-1 show displacement data and model predictions for TMA-MPBX-4 (relative to the borehole collar), which is located in a borehole drilled roughly horizontal and perpendicular to the heater. TMA-MPBX-4 is about 3.5 m from the heater collar in the y-coordinate direction (about 1.5 m from the collar end of the heater). The anchor locations in x, y, z coordinates for MPBX-4 are given in Appendix G. The x-coordinates for each of the MPBX-4 anchors are spaced at the bottom of the borehole (MPBX-4-1 at 0.768 m and MPBX-4-2 at about 1.428 m) and then at 1-m intervals to MPBX-4-6 at X=5.427 m. The data from TMA-MPBX-4 exhibit fairly consistent response, with the deepest anchor (MPBX-4-1) displacing the most. The data presented in Figure 9-9 show all gages experiencing decreasing gage length (compression) through about the first 30 days. After 30 days the anchors, one by one, reverse the sign of the displacement and become extensional. Total corrected displacements for all anchors are small, less than 1.5 mm. However, a smaller length of MPBX-4-1 has been heated beyond the 100°C isotherm, resulting in a smaller displacement.

The change in slope of most of the anchor responses after about 30 days is likely the result of rock mass thermal expansion. The anchors, particularly those nearest the heater at early times, are directly affected by near-heater thermal expansion, whereas at distances farther from the heater no such expansion has yet occurred. The cooldown data for MPBX-4 show a quick extensional response for the deepest four anchors and compressional response for the two anchors nearest the collar immediately after the heater is turned off. The extensional response for the deeper anchors can be explained by the quick decrease in temperature in the near field after the heater is turned off. The thermal pulse in the rock mass continues to thermally expand the rock mass toward the MPBX-4 collar while a cooling pulse tends to cause relative thermal contraction near the heater. Therefore the deepest anchors will move in a relative sense toward the heater due to the thermal contraction, while the borehole collar moves in the opposite direction due to the expanding thermal pulse. The net result is a sharp increase in measured relative expansion for the deepest anchors of MPBX-4.

For TMA-MPBX-4 the temperature distribution along the length of the borehole is given in Section 3. For TMA-MPBX-4, twelve temperature measurements originally were made (MPBX-4-TC-1 through MPBX-4-TC-12), one on each of the six anchors and at intermediate points on the extension rods. The thermal expansion coefficient for carbon fiber is 1.48 ppm/°C, as noted above. For each anchor, the thermal expansion for the extension rod is determined by integrating the thermal expansion for the measured temperatures and rod lengths from the collar to the anchor. Naturally, the maximum thermal correction is for anchor MPBX-4-1 because it includes the greatest length of extension rod as well as the highest temperatures. Comparison of the MPBX-4 data and model predictions (Figures 9-9 and 9-10) shows extremely good correspondence during the test, although the measured displacements tend to be larger than the pretest model predictions by about 20 percent for the heating cycle. The general trends—from the initial compression, followed by general extension, and ending with the sharp extension after the heater is deenergized—are consistent between both data and model predictions. The initial cooldown increase in extension exhibited in the data corresponds well with the pretest thermoelastic predictions in Sobolik, Francis, and Finley (1996). This increase is likely due to quick cooldown of the rock mass near the heater. This rock will tend to move due to thermal compression toward the heater. The thermal pulse continues to expand the majority of the rock mass toward the borehole collar. The net effect of this complex thermal behavior during cooldown is for anchors near the heater to experience increase in extension immediately during cooldown due to these thermal changes.

Thermal-mechanical data obtained during the SHT include preliminary estimates of rock mass thermal expansion, rock mass modulus, and rock bolt load. The rock mass thermal expansion coefficient (α) is determined from selected MPBX displacements and temperatures for the heating cycle.

The responses of MPBX-1 and MPBX-3 are complex and generally conform well with the magnitude linear-elastic pretest predictions; however, the shapes of the measured displacement curves differ from the predicted ones. MPBX-2, which is aligned parallel to MPBX-1 and MPBX-3, exhibits fairly stable displacement response, which is consistent, although smaller, than the displacement response predicted by the pretest analyses. The response of MPBX-4, which is perpendicular to the heater, is also complex, but remarkably consistent with the pretest predictions although the magnitudes of displacement differ somewhat from the predictions.

Rock mass thermal expansion was estimated for the pretest numerical analyses (see Sobolik, Francis, and Finley 1996, p. 25) based on unconstrained laboratory tests on welded tuff samples obtained from the SHT block. These laboratory values ranged from 7.47×10^{-6}/°C for temperatures of 25° to 50°C, to 51.7×10^{-6}/°C for temperatures of 275° to 300°C. The very high thermal expansions reported for the intact laboratory specimens represent the effect of the silica phase transition. It is unlikely that a significant volume of rock surrounding the heater reached these temperatures. The maximum temperatures at thermal-mechanical instrumentation locations did not exceed 170°C during SHT testing. The intact thermal expansion reported for temperatures between 200° and 225°C is 15.86×10^{-6}/°C. It is likely that the rock mass thermal expansion calculated from the in situ data would be lower than the laboratory values because of the presence of fractures. The fractures would tend to accommodate some of the thermal expansion in the joint stiffness, particularly during early heating, because the thermal displacement would be

insufficient to mechanically close fractures (i.e., low stresses). Also, the 3D effects of heated rock bounded by lower temperature rock would decrease the net effect of thermal expansion by resisting the thermal displacements in adjacent volumes of rock.

Rock mass thermal expansion is calculated from the in situ heating cycle data, including temperature change for a given axial length from ambient, gage length, and measured thermal displacement over the gage length. The rock mass thermal expansion coefficient was calculated for the SHT using selected data from MPBX-1, MPBX-3, and MPBX-2. Only the data from these MPBXs with relatively uniform temperature were used.

The characterization of Invar conducted by SNL (Brodsky 1997) shows the thermal expansion coefficient of Invar to be almost twice as large as reported by the supplier (Geokon) for temperatures above 100°C. Because the MPBX-2 data are quite smooth compared to the other MPBXs, the rock mass thermal expansion coefficient was calculated from MPBX-2 gage lengths as well as from MPBX-1 and MPBX-3.

The data presented in Table 9-3 are consistently lower than laboratory intact values regardless of temperature and gage length. The data are averaged values for each MPBX over the gage lengths shown. For MPBX-1, the values ranged from $4.26 - 5.73\times10^{-6}$/°C; for MPBX-3, they ranged from $3.91 - 6.32\times10^{-6}$/°C; and for MPBX-2, a value of 2.36×10^{-6}/°C was estimated. The calculated values for rock mass thermal expansion are, as expected, lower than the values from intact laboratory specimens and less than the values used in the pretest thermal-mechanical analyses. Also, the values presented in Table 9-3 are for the single orientation parallel to the heater (N72° W). It is possible that there could be some significant anisotropy in the rock mass thermal expansion coefficient due to differences in fracturing along different orientations. Following the time periods of relative compression seen in the data for MPBX-1, MPBX-2, and MPBX-3, the anchor responses again become extensional. It is possible to estimate rock mass linear thermal expansion at the conclusion of the SHT heating period by evaluating the relative differences in displacement and between anchors of a given MPBX. For anchors (gages) that have failed, the displacements for the last reliable data can be used. The thermal expansion at each time is simply the relative displacement difference divided by the respective gage length and the change in temperature from ambient. Using the anchors for MPBX-3 and MPBX-1, an estimate of the rock mass thermal expansion at the end of the heating period (or at gage failure) can be made. Simple analytical calculation of the thermal expansion coefficients for the longest gage lengths available near the end of the heating cycle yield the results presented in Table 9-3.

Table 9-3. Thermal Expansion Coefficients for Longest Available Gage Lengths Near Heating Cycle Culmination

MPBX Number	Anchor Numbers	Average α 10^{-6}/°C	Average Temperature (°C)	Gage Length (m)
TMA-MPBX-1	1 to 4	5.88	160.3	2.84
TMA-MPBX-3	2 to 6	4.14	70.07	4.0
TMA-MPBX-2	2 to 5	2.36	116.6	3.4

The linear rock mass thermal expansion in its simplest perspective is the relative displacement change between anchors (gage length) for a given measured temperature (temperature change

from ambient). Because temperature gradients exist in the SHT, the approach is to use "average" temperatures over a given gage length (between anchors).

The rock mass thermal expansion values presented in Table 9-3 are consistent, though slightly lower than expected values. Previous in situ thermal tests in G-Tunnel (in a welded tuff similar to TSw2, the Grouse Canyon welded tuff) measured thermal expansion coefficients of similar magnitude (8.0×10^{-6}/°C), although the intact values reported were lower than the intact values from samples taken from the SHT (Zimmerman and Finley 1987, p. 7-8).

The primary concern regarding the thermal-mechanical measurements reported here is the reliability of the MPBX measurements. As stated previously, the MPBXs employing the long carbon fiber extension rods with vibrating wire displacement transducers in the MPBX head at the borehole collar exhibit somewhat consistent displacement data, with all three showing changes in displacement for at least some of their anchors. These results are not expected based on the simplistic linear elastic analyses conducted prior to testing (Sobolik, Francis, and Finley 1996). These analyses predicted only extension for MPBX-1 and MPBX-3. The analyses did predict initial compression for MPBX-4 and are remarkably consistent with the in situ data presented in this report. The analyses did not predict relative compression between the anchors of MPBX-1 and MPBX-3.

One possible explanation for the anomalous MPBX responses is that there was a catastrophic failure of some part of these MPBX components. For these MPBXs, the possible contributors to this behavior include gage failure, rod failure, anchor failure, or actual rock mass response. Although one of the vibrating wire gages is known to have failed, it is questionable whether these gages are not responding properly because the vibrating wire and activator are sealed against the effects of moisture and the temperatures at the head are within the operating range of these instruments. The instantaneous "jumps" seen in the bottom anchors for both MPBX-1 and MPBX-3 also support the validity of the data. These type of gages have been used throughout the ESF without gage failure and are used extensively in the mining industry, often in harsh moisture environments. As a check of the vibrating wire response, SNL checked several of the gage counts using a portable readout box and found the vibration frequency consistent with the DCS output. To assure that the vibrating wire gage response from these MPBXs is correct, the gages should be recalibrated after cooldown of the SHT to provide assurance that they remained in calibration.

It is also unlikely that the MPBX anchors have slipped. These are C-ring anchors that are relatively heavy (about 1 to 2 lb). If the C-ring has failed, there is little impetus to "slip," particularly in horizontal boreholes. Finally, the carbon fiber extension rods are connected using stainless steel male/female screw end pieces. SNL conducted some simple heated tension tests to evaluate the possibility that these rods could slip themselves. The tests showed no evidence of slipping or failing at temperatures up to 200°C. To evaluate possible component failure, MPBX-1 was overcored during the SHT posttest evaluations. The results of this show no deterioration of the MPBX components. The posttest investigation is further discussed in Section 5. Therefore, without additional information suggesting MPBX component failure, the data presented in this report must be considered valid.

Wire and tape extensometer pins were placed on the three free surfaces of the SHT block (see Figures 9-1 and 9-2). These surface displacements are intended to augment the displacement data collected from the MPBXs and to provide qualitative "control" of the SHT free surfaces to support future modeling efforts. Because the measurements are made from short pins installed near the rock surface, they can be influenced by discrete block movement. All the wire extensometer stations show displacement changes of over several millimeters, with the exception of WX-4, which experienced displacements of less than 1 mm throughout the test. The data from the wire extensometers are provided in tabular form in Table 9-4 and shown graphically in Figures 9-11 through 9-16.

Table 9-4. Wire Extensometer Data, Movement in Millimeters

	Days after Start of Heating									
Gage	0	14	28	42	56	70	84	98	112	126
TMA-WX-1	0	-0.1	0.08	0.02	0.03	0.27	0.2	0.33	0.49	0.47
TMA-WX-2	0	-0.14	-0.15	-0.12	3.16	3.21	3.26	3.27	3.29	3.27
TMA-WX-3	0	-0.03	-0.09	0.01	0.01	0.2	0.25	0.31	0.33	0.41
TMA-WX-4	0	-0.83	-0.78	-0.78	-0.78	-0.58	-0.49	-0.66	-0.63	-0.31
TMA-WX-5	0	-0.61	-0.66	-0.58	-0.52	-0.5	-0.44	-0.67	-0.4	-0.58
TMA-WX-6	0	-2.45	-2.46	-1.98	-1.88	-1.89	-1.83	-2.95	-2.97	-2.97
	Days after Start of Heating									
Gage	140	154	168	182	196	210	224	238	252	266
TMA-WX-1	0.39	0.66	0.66	0.55	0.55	0.55	0.55	0.55	0.44	0.59
TMA-WX-2	3.17	3.52	3.51	3.51	3.51	3.5	3.5	3.5	3.41	3.38
TMA-WX-3	0.28	0.69	-23.92	-23.92	-23.84	-23.99	-24.08	-24.08	-24	-24.03
TMA-WX-4	-0.59	-0.2	-0.21	-0.04	-0.04	-0.09	-0.09	-0.1	-0.1	-0.12
TMA-WX-5	-0.89	-0.48	-0.59	-0.65	-0.78	-0.82	-0.82	-0.83	-0.81	-0.82
TMA-WX-6	-3.21	-2.75	-2.91	-2.74	-2.74	-3.06	-3.06	-3.06	-2.96	-2.92
	Days after Start of Heating									
Gage		280	294	308	322	336	350	364	378	392
TMA-WX-1		0.46	0.22	0.01	-0.05	-5.89	-5.89	-6.4	-6.56	-6.63
TMA-WX-2		4.49	4.49	4.22	4.22	3.99	4.11	4.04	4.04	3.93
TMA-WX-3		-23.91	-24.16	-24.16	-23.91	-24.42	-24.42	-24.42	-24.68	-24.66
TMA-WX-4		-0.17	-0.17	-0.17	-0.17	-0.58	-0.42	-0.68	-0.90	-0.91
TMA-WX-5		-0.69	-0.69	-0.95	-0.95	-0.95	-1.2	-38.29	-38.61	-38.65
TMA-WX-6		-2.99	-3.25	-3.5	-3.5	-3.75	-3.75	-3.5	-3.77	-3.83
	Days after Start of Heating									
Gage		406	420	434	448	462	476	490	504	518
TMA-WX-1		-6.40	-6.65	-3.93	-5.52	-5.54	-4.11	-2.31	-2.01	-2.39
TMA-WX-2		2.97	2.97	2.85	0.37	0.67	0.22	-21.04	-20.51	-20.89
TMA-WX-3		-24.67	-24.67	-24.72	-24.71	-24.65	-24.65	1.19	1.92	1.46
TMA-WX-4		-0.68	-0.68	-0.91	-0.91	-0.89	-0.87	-53.45	-53.42	-53.48
TMA-WX-5		-38.54	-38.54	-38.72	-38.76	-38.98	-38.99	1.72	1.55	-3.99
TMA-WX-6		-3.75	-3.50	-3.80	-3.79	-3.74	-3.71	-3.6	-3.42	-3.66

NOTE: Extension is positive

The wire extensometer data presented in Figures 9-11 through 9-16 exhibit closure by the end of heating, with the exception of WX-2 (located on the west face of the SHT block, about 2 m to the left of the heater) which exhibits a small extension of less than 1 mm through the end of heating.

Other wire extensometer stations (such as WX-3 and WX-5, which are located on the south and north face of the block 3.7 mm from the Thermomechanical Alcove) show over 20 mm of closure at the end of the fourth quarter. Such large displacements can reasonably be attributed to block loosening on the surface of the SHT.

The vertical displacements measured using the wire extensometers exhibit erratic behavior. Naturally, the predicted displacements from Sobolik, Francis, and Pott (1996, p. 28) exhibit relatively smooth displacements, with all wire extensometers exhibiting net extension and the greatest extension measured by WX-1 and WX-2, which are located on the "front" face of the SHT block. The actual wire extensometer measurements are not nearly so smooth. The measurements are typical of wire extensometer data, with displacement jumps that likely result from discrete block movement near the surface. In fact, five of the six wire extensometers exhibit net compression, which is not seen in the model results. As was stated previously, the wire extensometers are influenced by the competing processes of thermal expansion-driven extension and gravity-driven compression of the SHT block. Also, the wire extensometers are mounted on shallow pins, which can be highly influenced by block rotation and other surface mechanical processes.

Tape extensometer pins for measuring the roughly horizontal displacements of the SHT block are associated with each of the six wire extensometer stations. The x, y, z coordinate locations of the tape extensometer pins (denoted by WXM) on the SHT block are given in Appendix G. Tape extensometer measurements were made periodically during the course of the SHT.

Tape extensometer WXM-1 is located near the WX-1 station about 0.3 m below the heater borehole collar level. A mating pin is located on the ambient side across the Thermomechanical Alcove. Tape extensometer WXM-2 is located near the WX-2 station about 0.1 m above the level of the heater borehole collar. A mating pin is located on the ambient side across the Thermomechanical Alcove. Tape extensometer WXM-3 is located near the WX-3 station just above the level of the heater borehole collar. A mating pin is located on the ambient side across the Thermomechanical Alcove Extension. Tape extensometer WXM-4 is located near the WX-4 station just below the level of the heater borehole collar. A mating pin is located on the ambient side across the Thermomechanical Alcove Extension. Tape extensometer WXM-5 is located near the WX-5 station just above the level of the heater borehole collar. A mating pin is located on the ambient side across the Observation Drift. Tape extensometer WXM-6 is located near the WX-6 station just below the level of the heater borehole collar. A mating pin is located on the ambient side across the Observation Drift.

The data from the manual tape extensometer measurements are given in Table 9-5. The data show that the horizontal cross-drift measurements are largest for WXM-1, WXM-2, and WXM-3, with all measurements compressive (i.e., shortening of the gage length). In other words, the surface pins are moving away from the SHT block in all cases. These displacements are consistent with the gross displacements measured using the MPBXs. In addition, the tape extensometer results for WXM-2 are consistent with the large displacements measured by the wire extensometer station WX-2. This is suggestive of gross surface displacements near the surface of the SHT block to the left of the heater. It is likely that either or both of the WXM-2 pins are located in a loose block of rock, which appears to have loosened almost immediately during the SHT. The

subsequent data suggest that the block(s) stabilized somewhat with only minor additional displacement after September 24, 1996.

Table 9-5. Tape Extensometer Measurements for the SHT (Extension Positive)

Gage No.	Initial Reading (m)	Δ Displ. 9/24/96 (mm)	Δ Displ. 10/21/96 (mm)	Δ Displ. 12/19/96 (mm)	Δ Displ. 1/7/97 (mm)	Δ Displ. 2/11/97 (mm)	Δ Displ. 3/10/97 (mm)
WXM-1	5.40439	-0.48	-0.78	-0.86	-0.76	-1.14	-1.19
WXM-2	5.08585	-3.20	-3.20	-1.17	-3.71	-3.71	-3.71
WXM-3*	*	4.67249*	0.33	erroneous	0.08	-1.93	2.24
WXM-4	4.33635	-0.46	-0.21	-0.56	-0.64	-0.84	erroneous
WXM-5	5.87639	-0.04	-0.32	-0.49	-0.57	-0.37	-0.82
WXM-6	5.83158	-0.29	-0.129	-0.17	-0.39	-0.72	-0.80
Gage No.		**Δ Displ. 4/21/97 (mm)**	**Δ Displ. 5/6/97 (mm)**	**Δ Displ. 6/25/97 (mm)**	**Δ Displ. 7/24/97 (mm)**	**Δ Displ. 8/20/97 (mm)**	**Δ Displ. 7/15/97 (mm)**
WXM-1		-1.27	-0.86	-1.39	-1.52	-1.34	-1.16
WXM-2		erroneous	-4.39	-4.21	-4.21	-4.21	-3.71
WXM-3*		0.26	0.31	-0.17	2.29	-0.07	0.26
WXM-4		-0.36	-0.18	-1.17	-1.22	-1.20	-1.50
WXM-5		-0.72	-0.79	-0.88	-0.95	-0.62	-0.60
WXM-6		-0.64	-0.31	-1.15	-0.95	-0.21	-0.64

NOTE: This table includes corrected data not included in previous reports.
*WXM-3 initial reading suspect. Change in displacement from 9/24/96.

It should be noted, however, that the tape extensometer measurements represent contributions from both sides of each drift, although the contribution from the heated side is expected to be larger.

9.2 BOREHOLE JACK

An additional suite of borehole jack tests was performed in ESF-TMA-BJ-1 on January 29, 1998. The discussion presented in previous SHT reports is included here for completeness. Because the rock mass modulus measured using the borehole jack is directional (perpendicular to the borehole), no estimate of horizontal modulus anisotropy was possible during conduct of the SHT. It is likely that some anisotropy in modulus exists locally due to differences in fracture stiffness for each set of fractures present in the SHT block. Also, it is likely that the rock mass modulus varies across the repository block. Additional sets (orthogonal boreholes) of borehole jack measurements at various locations throughout the repository block would serve to provide critical information on the spatial variability and potential anisotropy of rock mass modulus. These borehole tests could be conducted in conjunction with additional single heater tests to evaluate the thermal dependence of rock mass modulus seen in the SHT testing. Bounding knowledge of the rock mass modulus is important for interpretation of ESF heater tests as well as predictions of long-term stability of repository openings.

A single borehole (ESF-TMA-BJ-1) was drilled roughly horizontal and perpendicular to the SHT heater borehole for operation of the NX borehole jack (Goodman Jack) (see Figures 9-1 and 9-2). This nonpermanent borehole instrument is periodically inserted into the borehole and pressurized

at various distances along the borehole. Jack pressure and loading platen displacements are monitored, and rock mass modulus is determined from the pressure/displacement curve. For the SHT, borehole jack tests were run before heater startup (August 26, 1996), again on October 10, 1996, on November 26, 1996, on March 18, 1997, on October 23, 1997, and on January 29, 1998. Temperatures were measured, or estimated as "ambient" for tests on October 23, 1997 and January 29, 1998 in the borehole for each set of tests prior to insertion of the jack using a portable Type-K thermocouple probe at various points, and by manually taking temperature readings using a hand-held thermocouple reader. Jacking tests were run along the borehole at depths (from the collar) of 2.0 m, 3.0 m, 4.0 m, 4.51 m, and 6.2 m, although not all locations were tested on each of the dates. All borehole jack testing followed ASTM 4971-89 reapproved 1994 with minor exceptions. These exceptions include performing multiple loadings on only 50 percent of the ambient (preheating) runs. No multiple loadings were conducted during the October 10, 1996, the November 26, 1996, or the March 18, 1997 tests to limit thermal effects on the jack. Multiple tests were conducted at the 6.2 m depth during the January 29, 1998 testing.

Borehole ESF-TMA-BJ-1, located about 5.5 m from the front (west) face of the SHT block, is collared in the Observation Drift and is oriented toward the heater. As such, the borehole is expected to exhibit a temperature gradient from the bottom to the collar as the test is conducted. This allows for evaluation of the effect (if any) of increased temperature on the measured rock mass modulus. Figures 9-1 and 9-2 show the general location of borehole ESF-TMA-BJ-1 and its location relative to the heater.

The NX borehole jack consists of two hydraulically activated steel loading platens approximately 20.3 cm long, which apply a unidirectional load to a nominal 7.62-cm diameter borehole wall. The maximum jack pressure is 69 MPa, and the maximum platen displacement is 0.63 cm. The total displacement of both platens is 1.27 cm, with total jack diameter at 8.25 cm. Platen displacement is measured using LVDTs (one for each platen). The platens pressurize 90° of the borehole wall on each side. Jack pressure is applied using an Enerpak hand pump. Typically the jack is pressurized in 3.44 MPa (500 psi) increments to 55.2 MPa (8000 psi), then back to zero, with LVDT readings recorded during both loading and unloading.

The historical use of the borehole jack has shown that corrections must be taken into consideration for the mismatch between borehole and platen radii, longitudinal bending of the platens, and tensile cracking of the intact rock or opening of existing fractures. The use and interpretation of the borehole jack is discussed at length in ASTM D4971-89 and Heuze and Amadei (1985). The jack is inserted into the borehole and platens are slowly expanded until the pressure just begins to rise. The resulting LVDT readings represent the initial borehole diameter and are used for calculations of borehole wall displacement under pressure. The jack pressure is increased in increments to the desired maximum pressure and then decreased in similar increments. Because of the necessary data corrections, as described in ASTM D4971-89 (p. 4), the calculated minimum pressure to achieve "full platen contact" based on the approximate borehole diameter (7.57 to 7.90 cm) was about 21 MPa (3000 psi). For the tests conducted on August 26, 1996, the maximum pressure applied to the rock by the jack was limited to about 34.5 MPa. For all subsequent tests, the maximum pressure was limited to about 55.2 MPa. Also, it should be noted that Equation 1 in ASTM D4971-89 (p. 4) is incorrect. Equation 6 from Heuze and Amadei (1985, p. 109) was used to determine the calculated modulus.

According to ASTM-D4971-89 and Heuze and Amadei (1985), the Goodman jack data must be evaluated to estimate the jack pressure required to achieve full platen contact with the borehole wall. This is necessary because the analyses described in ASTM D4971-89 and Heuze and Amadei (1985) assume full contact of the two platens with the borehole wall. In reality, there is initially some mismatch because of different radii of curvature between the borehole (in the DST plate loading test, nominally NQ sized) and the jack platens. As the jack is pressurized, the mismatch decreases until a pressure Q_{hmin} is reached where "full" contact is achieved. ASTM D4971-89 recommends that only the displacement/pressure data that exceed this minimum pressure (Q_{hmin}) be used to calculate the rock mass modulus. According to ASTM D4971-89 (p. 4) and Heuze and Amadei (1985, p. 109) the "minimum pressure" to achieve full platen contact for oversized holes (initial diameter > 3.0 in.) is:

$$Q_{hmin} = \frac{0.2\alpha(30\times10^6)E_{Theoretical}}{(30\times10^6)(1-\nu^2)0.91E_{Theoretical}} \qquad (9\text{-}2)$$

where:

Q_{hmin}	=	jack pressure for full platen contact
α	=	deviation of hole diameter in excess of 3.0 in.
$E_{Theoretical}$	=	E_{True} = actual rock mass modulus
ν	=	Poisson's ratio (can be assumed to be 0.25)

For this analysis, $E_{Theoretical}$ must be estimated to determine Q_{hmin} a priori.

For the data for jack pressures > Q_{hmin}, the rock mass modulus can be calculated using Equation 9-3 (from Heuze and Amadei 1985. p. 109):

$$E_{calc} = (0.86)(0.93)D\frac{\Delta Q_h}{\Delta D}T^* \qquad (9\text{-}3)$$

where:

D	=	initial borehole diameter (in.)
ΔQ_h	=	jack pressure change (psi)
ΔD	=	borehole diameter change (in.)
T^*	=	coefficient dependent on Poisson's ratio

It should be noted that Equation 9-3 for E_{calc} differs from Equation 1 in ASTM D4971-89 (p. 4) which contains at least two errors. This can be seen from review of the previous and subsequent borehole jack literature and comparison to Equation 2 in ASTM D4971-89.

Finally, the true modulus (theoretical modulus), $E_{Theoretical}$, can be determined from Figure 3 of ASTM D4971-89 (p. 4). The E_{True} versus E_{calc} correction in Figure 3 ASTM D4971-89 is necessary to correct for platen bending, particularly at higher moduli (> (7 GPa).

For practical purposes, the Q_{hmin} calculation for modulus values between 400,000 psi (2.75 GPa) and 1,000,000 psi (6.9 GPa) varies between 3000 and 6500 psi. As noted in ASTM D4971-89

(p. 24), the procedure "may result in rejections of too many data with consequent degradation of the corpus of the data." An alternative to using the Q_{hmin} equation, ASTM D4971-89 suggests that there is full platen contact if the loading curve is approximately linear. Therefore, Q_{hmin} can be estimated by simple evaluation of the pressure-displacement curves for each test, although for simplicity a minimum value of 3000 psi has been used for Q_{hmin} in all calculations.

The data from the January 29, 1998 testing are presented graphically in Figures 9-17 through 9-21. The complete suite of data from the borehole jack testing conducted during the SHT is presented graphically in Appendix H for completeness. Selected data from the 6.2 m depth are presented and discussed here. The data shown in the figures have been analyzed using the procedure outlined in ASTM D4971-89 (p. 3). Only the data above a jack pressure of about 21 MPa were used to calculate the rock mass modulus. For most of the pressure/displacement curves, this also corresponds to the most linear portions of each loading curve. The calculated rock mass moduli are given in Table 9-6 along with the rock temperature at the time of the test.

Table 9-6. Estimated Rock Mass Modulus in Borehole ESF-TMA-BJ-1 Using the Borehole Jack

Date	Distance from Collar				
	2.0 m	3.0 m	4.0 m	4.51 m	6.2 m
	Rock Mass Modulus GPa (Temp °C)				
8/26/96	6.9 (25)	3.71 (25)	No test	No test	No test
10/10/96	10.3 (27.5)	10.3 (27.7)	8.3 (30.2)	6.0 (34)	No test
11/26/96	*Results discarded (31.1)*	10.2 (35.9)	*5.71 (46.4)*	*5.01 (55.4)*	8.4 (141.8)
3/18/97	*Results discarded (35)*	6.3 (41)	*10.3 (52)*	*5.7 (58.7)*	22.8 (143.1)
10/23/97 1st run	No test	No test	6.28 (Ambient)	Discarded	8.28 (Ambient)
10/23/97 2nd run	No test	No test	8.97 (Ambient)	7.1 (Ambient)	10.0 (Ambient)
1/29/98 1st run	5.47 (Ambient)	9.67 (Ambient)	6.28 (Ambient)	7.60 (Ambient)	Not calculated
1/29/98 2nd run	No test	No test	No test	No test	11.72 (Ambient)
1/29/98 3rd run	No test	No test	No test	No test	11.72 (Ambient)

Note: Italicized calculated moduli are based on field data in which the difference between the two borehole jack LVDT readings slightly exceeded the limits set in ASTM D4971-89. The fractured nature of the rock made setting the jack difficult. Discarded results were for data that far exceeded ASTM D4971-89 limits.

The results from the borehole jack testing show that the measured rock mass modulus ranges from about 3 to 23 GPa. The highest value is for the deepest measurement location in the borehole (~6.2 m from the collar). This location corresponds to roughly 0.33 m from the heater borehole located about 1.5 m from the end of the heater. The previous measurement at this location on November 26, 1996 showed a modulus of only 8.46 GPa, and the results from October 23, 1997 give an average modulus of 9.14 GPa. The large increase and decrease in modulus after cooling may be consistent with the closing of fractures due to thermal expansion in this region, or it may simply be due to measurement error, with the exception of the tests conducted at the 6.2 m depth. The data are also consistent with some of the MPBX data and numerical modeling discussed in Section 6, which may suggest fracture closure as well. All the other borehole jack data are relatively low, less than about 10 GPa.

These values are considerably less than the intact modulus of about 32.4 GPa measured on intact samples of the Topopah Spring welded tuff and from the rock mass value estimated using the RMR technique outlined in Serafim and Periera (1983). The data presented in Table 9-6 include italicized results in which the two LVDT readings (far and near) differ by slightly greater than 0.02 in. at the maximum test pressure. According to ASTM D4971-89 (p. 3) these data should be discarded because of uneven loading. The fractured nature of the rock surrounding the borehole made it difficult in some cases to "set" the borehole jack at those locations. However, the data presented represent only slight deviation from the ASTM D4971-89 (p. 3) criteria and are presented to qualitatively assess modulus difference along borehole BJ-1. The italicized data should not be used in calculations requiring rock mass modulus.

For the pretest analyses, the rock mass modulus was estimated from laboratory tests on intact specimens from the SHT and by estimating the modulus from rock mass quality data using the RMR technique described in Serafim and Periera (1983). The rock mass modulus value suggested from these sources (upper bound value of 32.4 GPa) was used in the pretest numerical analyses. The results of the Goodman Jack testing in the SHT suggest rock mass modulus values ranged from about 3 GPa to 23 GPa. The SHT borehole jack testing shows significant change due to heating at the deepest testing location in the borehole (about 6.2 m from the collar or about 0.33 m from the heater) from one test. Initial readings at that location (8.4 GPa) increased to 22.8 GPa after seven months of heating, followed by a marked decrease to about 9 GPa after cooldown. Other testing locations in the borehole do not show any thermal effects. The lower modulus values measured throughout ESF-TMA-BJ-1 would result in the development of significantly lower stresses in the SHT block than the pretest analyses predicted. However, the SHT displacements would not change in the elastic analyses with a reduced modulus. The low ambient measured modulus is certainly not unexpected. It is known from previous in situ experiments conducted in welded tuff in G-Tunnel that the modulus values measured for various in situ tests were about half the intact value of about 23 to 35 GPa (Zimmerman and Finley 1987, p. 5-3). Zimmerman and Finley (1987, p. 5-11) also report results of Goodman Jack measurements in welded tuff from the G-Tunnel facility. Over forty Goodman Jack tests were conducted, and the recommended rock mass modulus from these tests ranged from 14.7 GPa to 17.6 GPa, roughly half the intact value from laboratory tests.

Figures 9-22 through 9-27 present the results of the borehole jack in graphical form showing the test locations and measured moduli with respect to the heater borehole and Observation Drift wall locations. The rock mass modulus information presented in Table 9-6 and Appendix H does not exhibit identifiable trends either spatially, temporally, or thermally, with the exception of the bottomhole measurements. The reported low values of modulus could be the result of the relatively small volume of rock energized (~0.15 m^3) and as such could be overly influenced by nearby fractures.

Rock mass modulus of deformation measured over large scale is expected to be lower than the modulus of deformation measured in the laboratory because of the presence of fractures and other inhomogeneities. The Goodman Jack applies the pressure over approximately 20 cm length of a 7.6 cm diameter hole. This compares with approximately 5 cm diameter and 10 cm long samples used in measuring the modulus of deformation in the laboratory. The scale of measurements by the Goodman Jack is thus larger than the laboratory measurements by substantially less than an

order of magnitude. These measurements cannot, thus, be considered a representative measure of the rock mass modulus of deformation. Yet these measurements were lower than the laboratory measured values by a factor of four or so. It is possible that the Goodman Jack measurements were influenced by localized features such as fractures or other voids at the spot of measurement. The Goodman Jack measurements give lower values of modulus of deformation compared to the Plate Loading Test Measurements in the Drift Scale Test (CRWMS M&O 1998c).

9.3 ROCK BOLT LOAD CELLS

Eight rock bolt load cells were installed on Williams B7X Hollow Core rock bolts as part of the SHT. The objective is to evaluate qualitatively the effects of elevated temperature on bolt performance by (1) monitoring load changes during the test, (2) posttest evaluations of the bolt/grout/rock interface, and (3) pull testing selected bolts to failure after heating and subsequent cooling. Each rock bolt included one vibrating wire load cell (load washer) that was installed between cover plates and adjustable angled washers. This entire assembly was bolted to the Williams bolt on the cold side of the insulation.

Four of the rock bolts were installed on the heated side of the Thermomechanical Alcove below the level of the heater. Another four rock bolts were installed on the opposite cold side of the Thermomechanical Alcove. The rock bolts and load cells were installed during July 1996. Initial readings were taken using a hand-held Geokon readout box, prior to connection to the DCS. The load cells each contain three strain gages, and the total load acting on the cell is calculated by averaging the measurements from all three.

Posttest evaluation of bolt/grout interface was limited to the rockbolt pull test test because overcoring across these interfaces was unsuccessful.

The locations of the rock bolts instrumented with rock bolt load cells (RBLCs) are shown in Figures 9-1 and 9-2. Four RBLCs were installed on the heated side of the west face of the SHT block (RB-1, RB-2, RB-3, and RB-4), and four were installed on the opposite ambient side of the Thermomechanical Alcove (RB-5, RB-6, RB-7, and RB-8). The gage locations for rock bolts are given in Appendix G. The RBLC data are presented in Figures 9-28 through 9-35. The data are presented as load (lb) versus time from the start of heating (day zero). The data are also given in tabular form in Table 9-7.

Table 9-7. Rock Bolt Load Cells, Load Versus Time

TMA RBLC	Days after Start of Heating									
Gage	0	14	28	42	56	70	84	98	112	126
RB-LC-1-AVG	22662	22262 8	22158	21732.3	21537.1	21444.1	21407.5	21380.8	21340.3	21308.5
RB-LC-2-AVG	14859.4	14739.7	14708.6	14680.1	14643.7	14597	14559.8	14522 5	14496.5	14449.6
RB-LC-3-AVG	22428	22402 2	22378.7	22348.4	22317.5	22281	22262.3	22243.2	22231	22224 1
RB-LC-4-AVG	16663.9	16602 8	16580 3	16558.8	16522.1	16496.6	16467.4	16446.3	16424.2	16407 5
RB-LC-5-AVG	25971.9	25928.5	25887	25856.6	25829 3	25802.6	25783.4	25765 5	25748 7	25738 1
RB-LC-6-AVG	14642.7	14633.2	14632.7	14627.3	14619.4	14609.5	14601.2	14595 9	14589 2	14573 7
RB-LC-7-AVG	4932.6	4921 1	4919.7	4911.8	4904.3	4893.6	4890.9	4883.8	4877 5	4873
RB-LC-8-AVG	16862.8	16818.5	16783 6	16758.7	16738.7	16605	16592 7	16575 4	16566	16561.5

Table 9-7. Rock Bolt Load Cells, Load Versus Time (Continued)

TMA RBLC	Days after Start of Heating									
Gage	140	154	168	182	196	210	224	238	252	266
RB-LC-1-AVG	21279.7	21254.3	21206.3	21176.9	21161.2	21145.9	21127.1	21112.2	21100.9	21102.1
RB-LC-2-AVG	14422.7	14405.6	14389.9	14378.6	14369.9	14365.5	14353.4	14349	14342	14341.1
RB-LC-3-AVG	22214.2	22206.8	22201.1	22194.3	22189.6	22183.4	22176.4	22171.7	22165.3	22158.4
RB-LC-4-AVG	16394.3	16377.4	16361.5	16350.8	16340.4	16331	16320.2	16316.8	16312.1	16310.9
RB-LC-5-AVG	25728.1	25722.2	25714.1	25705.1	25698.3	25692.7	25683.1	25676	25665.6	25652
RB-LC-6-AVG	14567.1	14563.5	14562.3	14557.4	14553.9	14551.2	14549.3	14543.8	14543.4	14538.9
RB-LC-7-AVG	4866.9	4866.7	4867.2	4866.6	4866.2	4865.2	4863.2	4863.9	4864.1	4867.1
RB-LC-8-AVG	16552.8	16544.8	16538	16533.3	16528.6	16522.3	16516.4	16514	16503.2	16501.5
TMA RBLC	Days after Start of Heating									
Gage		280	294	308	322	336	350	364	378	392
RB-LC-1-AVG		21090.8	21092.2	21097.1	21090.6	21081.3	21076.5	21066.3	21073.0	21072.7
RB-LC-2-AVG		14354.1	14380.2	14391.6	14396.8	14404.6	14409	14412.4	14416.8	14421.9
RB-LC-3-AVG		22160.3	22171.6	22179.8	22180.8	22182.1	22179.1	22180.2	22177.4	22179.1
RB-LC-4-AVG		16315.9	16332.3	16338.5	16340.7	16346.6	16348.2	16350.4	16354.0	16358.0
RB-LC-5-AVG		25641.1	25617.7	25604.4	25589.9	25581.9	25573.6	25571.5	25561.4	25555.1
RB-LC-6-AVG		14538.6	14538.2	14536.1	14534.8	14531.9	14531.1	14529.5	14528.5	14530.7
RB-LC-7-AVG		4865	4858.2	4857.6	4856.9	4851	4850.2	4850.1	4852.8	4853.3
RB-LC-8-AVG		16497.8	16491.7	16491.7	16489.4	16487	16484.6	16477.2	16480.8	16475.8
TMA RBLC	Days after Start of Heating									
Gage		406	420	434	448	462	476	490	504	518
RB-LC-1-AVG		21080.6	21074.6	21058.0	21019.0	20999.9	20964.1	20943.1	20933.8	20928.1
RB-LC-2-AVG		14439.3	14435.0	14432.4	14419.5	14391.8	14352.8	14338.9	14347.6	14346.7
RB-LC-3-AVG		22183.0	22179.8	22177.4	22168.4	22150.2	22111.5	22097.6	22099.3	22096.8
RB-LC-4-AVG		16366.6	16360.9	16354.1	16345.6	16330.8	16282.0	16234.2	16268.8	16278.5
RB-LC-5-AVG		25548.7	25535.6	25525.3	25515.4	25496.9	25457.7	25444.7	25445.6	25445.2
RB-LC-6-AVG		14534.1	14533.1	14532.5	14528.0	14521.6	14503.0	14493.0	14492.2	14490.9
RB-LC-7-AVG		4856.6	4860.1	4858.9	4854.8	4842.0	4808.4	4796.1	4795.0	4680.1
RB-LC-8-AVG		16476.1	16468.7	16462.1	16454.2	16079.7	16060.3	16052.3	16056.2	16058.1

NOTE: Load cell data are for average load and are given in lbs.

The load cells are actually washers that fit over the rock bolts and are held in place by flat steel plates on either end and loaded with a nut. Each load cell includes three strain gages whose outputs must be averaged. Each RBLC was torqued to an initial load. Also, each of the three strain gages in each RBLC was monitored during torquing to maintain relatively uniform loading. If the loading was nonuniform, the wedge washers were adjusted and the nut retorqued. The important consideration in evaluating the rock bolt performance is the change in load from day zero, as well as the difference between the response of the heated versus the ambient rock bolts.

The data shown in Figures 9-28 through 9-35 show a general decline in load measured in all the RBLCs through the end of heating. Three of the four heated rock bolts (RB-2, RB-3, and RB-4) show an increase in load after the heater is turned off and RB-1 exhibits a stabilization of the previously observed load decrease. This increase amounts of only up to 100 lb, or 0.7 percent of the load measured in the bolt. The load increase is likely due to thermal contraction effects in the bolt itself, which likely has a higher thermal expansion/contraction coefficient than the rock mass surrounding it. The ambient rock bolts continue to experience a decrease in load throughout the reporting period. Table 9-8 presents the RBLC data expressed as a percent change from day zero

(heater startup) through the end of heating. Although measurable, the decreases are all less than about 7 percent of the initial load, including load changes after heater turnoff. Interestingly, the average percent decrease for the ambient RBLCs is 1.56 percent, whereas the average decrease for the heated RBLCs is 3.26 percent, although this decrease is most influenced by the decrease observed in RB-LC-1. Also, the two largest decreases are seen in the RBLCs that are nearest the heater (RB-1 and RB-2) and are therefore the hottest.

Table 9-8. Change in Rock Bolt Load Cell Readings During Heating

Location	Hot Side				Ambient Side			
Gage	RBLC-1	RBLC-2	RBLC-3	RBLC-4	RBLC-5	RBLC-6	RBLC-7	RBLC-8
%Change	7.05	3.00	1.11	1.68	1.56	0.81	1.60	2.27
Average % Change	Hot Side average change =3.26%				Ambient Side average change = 1.56%			

Loads were measured in rock bolts installed on both the heated side of the SHT block and on the opposite ambient rib of the Thermomechanical Alcove. The rock bolts were installed to evaluate the longer-term effects of elevated temperature on this type of rock anchorage. Preliminary results show that loads are decreasing in all load cells; however, the decrease is greatest in those rock bolts on the heated side of the SHT. In particular, two bolts predicted to be at the highest temperature experienced the greatest load decreases during heating (up to about 6.6 percent) from their initial pre-load values. The higher load decreases seen in the higher temperature rock bolts could result from several sources. For instance, the thermal expansion coefficient of carbon steel is about 10 to 11×10^{-6}/°C (Popov et al. 1976, p. 570). Thus the thermal expansion of the steel is likely greater than the rock mass expansion surrounding it. Alternatively, there could also be some load loss due to creep of the anchorage, which is composed of the steel bolt and mechanical anchor, the surrounding grout, and the rock itself.

The fact that load decreases were about 1 percent to 2 percent for all rock bolts, except RB-1 and RB-2, which decreased about 7 percent and 4 percent respectively, appears to indicate: (a) the influence of anchorage creep on all the bolts and (b) the effect of temperature on the creep of the bolts, because bolts with the highest temperatures had the most load decrease.

9.4 MISCELLANEOUS INSTRUMENTATION

Miscellaneous instrumentation and equipment include

- power, current, and voltage monitors
- air temperature (ambient) monitors in the Thermomechanical Alcove Extension, Thermomechanical Alcove, and Observation Drift
- insulation and vapor barrier installed on the three free surfaces of the SHT block.

Power, current, and voltage were monitored continuously using a Magtrol power monitor. The temperatures of the ambient air within the testing facility were measured using Type-K thermocouples. The ambient temperatures, heater power, heater current, and heater voltage were

recorded on the DCS. In addition, two 7.6-cm thick layers of insulation were installed on the three vertical surfaces of the SHT block. This insulation is aluminum foil-backed fiberglass insulation on the inner layer (which serves as the vapor barrier), and vinyl-backed fiberglass insulation for the outer layer. The insulation was attached to the rock surface using short copper "nails" at approximately regular intervals using high-temperature adhesive.

9.5 THERMAL-MECHANICAL ANALYSIS OF THE SHT AND ESTIMATES OF PERMEABILITY CHANGES

A thermal-mechanical analysis of the SHT aimed at assessing the potential of stresses due to heating to cause shear slip on fractures has been carried out in the rock mass during the SHT.

An earlier thermal-mechanical analysis (Wang et al. 1998) concluded that thermal stresses in the DST would be likely to induce shear slip and enhance permeability on pre-existing fracture sets in the test. In this earlier analysis, stresses were calculated using the 2D thermal-mechanical model, Fast Lagrangian Analysis of Continua (FLAC), Version 3.3, by Itasca Consulting Group in conjunction with the Mohr-Coulomb criterion. This section presents results obtained by applying this same methodology to the SHT. Estimates of regions of shear-slip and implications for permeability changes are presented.

Mechanical data collected in the SHT included MPBX measurements, drift convergence measurements, Goodman Jack measurements described in Section 5 of the *Single-Heater Test Status Report* (CRWMS M&O 1997b). None of these measurements was designed to monitor the shear stress or displacement in the regions below and to the heated sides of the drifts; thus, these measurements could not be compared with results reported here. The ratio of shear stress to frictional resistance is so small that it is unlikely to result in any measureable shear movement.

9.5.1 FLAC Model of the Single Heater Test

The thermal-mechanical analysis is based on the 2D Version of the geomechanical code FLAC Version 3.22 (Itasca Consulting Group, Inc. 1996). The code FLAC Version 3.22 represents an uncoupled thermal-mechanical model. The stress field depends on the temperature field, but the temperature field is independent of the stress field. Therefore, the thermal conduction problem can be solved independently of the mechanical equilibrium problem. The FLAC Version 3.22 code is not a qualified software. The QA status of the calculations performed by the software FLAC Version 3.22 is to be verified (TBV-3570). The thermal-mechanical values used in the FLAC modeling are given in Table 9-9.

Table 9-9. FLAC Properties and Sources

Property	Value	Source
Bulk Modulus	13 GPa	Computed from Young's modulus and Poisson's ratio; values of uncertainty of approximately ± 3 to 4 GPa
Young's Modulus	31 GPa	Bodvarsson and Bandurraga 1996, pp. 1 to 607; Bodvarsson et al. 1997, pp. 1 to 738
Shear Modulus	14 GPa	Computed from Young's modulus and Poisson's ratio; values of uncertainty of approximately ± 3 to 4 GPa

Table 9-9. FLAC Properties and Sources (Continued)

Property	Value	Source
Bulk Density	2300 kg/m^3	Bodvarsson and Bandurraga 1996, pp. 1 to 607; Bodvarsson et al. 1997, pp. 1 to 738
Thermal Conductivity	2.1 w/(m·K)	Large Block Test Modeling (Lee 1995, p. 6)
Specific Heat	840 J/(kg·K)	Large Block Test Modeling (Lee 1995, p. 6)
Thermal Expansion Coefficient	9.1 x 10^{-6} K^{-1}	Bodvarsson and Bandurraga 1996, pp. 1 to 607; Bodvarsson et al. 1997, pp. 1 to 738

A cross section through the SHT was simulated. The model grid for this simulation consisted of 35 zones in the horizontal x-direction and 40 zones in the vertical y-direction (Figure 9-36). The smallest zones for the heater cross section were about 0.1 m x 0.1 m, and the largest zones at the far corners of the model were 20 m x 6 m. This model was also symmetrical, with the heater cross section placed at the edge of the FLAC model and the 5-m-wide tunnel cross section placed 5 m away, closer to the center of the model. The edge of the FLAC model that represented the axis of symmetry was fixed in the direction perpendicular to that edge, while the other far edges of the model were fixed in both directions. The tunnels were assumed to have rounded corners because large stress concentrations otherwise occur near the corners.

The heater was represented by an interior source at the origin with a power density of 7000 W/m^3. This source strength was chosen to be equivalent to the heater in the thermal-hydrological model of Buscheck and Nitao (1995, pp. 32 to 34). The heater was modeled as a constant-power source, producing heat for a period of 200 days. Because FLAC requires that the heater power be specified in watts per square meter per meter in the third dimension, the heater in this model was a slice through an infinite rod. In this model, the smallest grid zone dimension was somewhat larger than the actual heater borehole diameter in the SHT; this contributed to the difficulty in converting FLAC heater values to actual heater wattages. For the purposes of the FLAC modeling, heat sources in the grid zones used to represent the heater were set to values that would allow nearby zones to reach temperatures of approximately 200°C in 200 days of heating. This may be approximately equivalent to a 10-m-long heater producing about 500 watts, but 3D modeling would be required to calibrate the modeled heater.

The mechanical boundary conditions were chosen to be σ_{xx} (horizontal) = -5.0 MPa and σ_{yy} (vertical) = -10.0 MPa (where compression is negative). The center of the heater and the far edges of model were taken to be symmetry (zero displacement) boundaries. The thermal-mechanical simulation was performed in several stages:

1. The mechanical model containing the heated drift and access drift excavations was run until force equilibrium was achieved.

2. The observation and tunnel alcove extensions were excavated, and the mechanical model was again run to achieve force equilibrium.

3. FLAC's mechanical mode was switched off, and the thermal option was switched on. The initial temperature was set to 20°C throughout the models. The tunnel walls and the edges of the models were assumed to be adiabatic boundaries. In the thermal modeling, the FLAC-explicit solution used a thermal time step of approximately 1 step per 3100 s. Therefore, 200 days of heating required approximately 5500 thermal time steps. The thermal conduction solution was saved at 100 days and at 200 days. The temperature fields for these two times are shown in Figure 9-37 and Figure 9-38. The temperatures are in general agreement with those in the thermal-hydrological model of Buscheck and Nitao (1995). Figure 9-38 shows that, after 200 days of heating, the highest temperature attained was approximately 200°C. The temperature in the zone closest to the heater reached maximum values of about 130°C after 10 days of heating, about 190°C after 100 days, and about 210°C after 200 days of heating. After 200 days of heating, temperatures remain within a few degrees of the initial 20°C value for all the model regions that lay more than about 10 m away from the heater.

4. Finally, the thermal option was switched off, and the mechanical mode was switched on to calculate the thermally coupled stress field at each of the five times at which the temperature field was saved. The thermal-mechanical solution was then saved at 100 days and at 200 days. The stress fields for before heating and for these two times after heating are shown in Figure 9-39, Figure 9-40, and Figure 9-41. The thermal stresses cause the maximum principal stress to turn in toward the heater in the direction of the thermal gradient.

After 200 days of heating, the horizontal stress in the cross-sectional model exceeded 30 MPa in compression in the region within a few cm of the heater. The horizontal stress was compressional everywhere in the model and remained near the original 5 MPa value everywhere except the area between the heater and the tunnel wall. There the stress varied from about 5 MPa right by the tunnel wall to more than 30 MPa of compression as it neared the heater. The top and bottom walls of the tunnel also showed stress concentrations of as much as 15 to 20 MPa of compression, probably because the grid was too coarse to smoothly model the tunnel walls. After 200 days of heating, the vertical stress in the cross-sectional model reached a maximum value of approximately 40 MPa of compression within a few cm of the heater. Vertical stress was compressional everywhere in the cross-sectional model. The vertical stress near the tunnel wall 5 m from the heater reached values of approximately 15 to 20 MPa of compression after 200 days of heating. These values were also found in the regions about 3 to 5 m above and below the heater. The tunnel walls showed some small areas of stress concentrations because of the grid coarseness. Vertical stresses remained near the original 10 MPa value elsewhere in the model. After 200 days of heating, shear stresses of as much as approximately 8 MPa developed in the cross-sectional model in the region between the heater and the tunnel wall 5 m away.

This model shows high values for the horizontal stress near the heater, 20 to 30 MPa of compression, and a large gradient for the horizontal stress between the heater and the tunnel wall 5 m away. Stress concentrations of approximately 10 to 20 MPa were also shown where the grid was too coarse to model smooth tunnel corners. After 200 days of heating, shear stress values of as much as about 8 MPa are shown in the region between the heater and the tunnel wall 5 m away.

9.5.2 Shear Slip Model

Barton, C.A. et al. (1997) presented convincing evidence that hydraulically conductive fractures in the Dixie Valley geothermal field are critically stressed, potentially active, normal faults based on the Mohr-Coulomb frictional slip criterion. This criterion was applied to the stress field calculated from the thermal-mechanical model to determine if permeability changes due to heating were likely to occur.

In broad terms, three fracture sets have been identified in the ESF (Albin et al. 1997, p. 1):

1. A steeply dipping set striking east-west
2. A steeply dipping set striking north-south
3. A subhorizontal set striking east-west

The axis of the single heater is oriented east-west; hence, set #1 and set #3 have their strike perpendicular to the plane of the FLAC model. The planes are defined by the angle θ of their normals to the x-axis. Therefore, an angle of zero degrees corresponds to a vertical plane (set #1) and an angle of 90° corresponds to a horizontal plane (set #3). The Mohr-Coulomb criterion is

$$|\tau| \geq c + fS_n \qquad (9\text{-}4)$$

where c is the cohesion, f is the coefficient of friction, τ is the shear stress, and S_n is the compressive normal stress. The maximum potential for frictional slip occurs for a cohesion value of zero (i.e., shear offset occurs when the ratio $|\tau|/(fS_n) \geq 1$). This ratio is contoured for the two pre-existing fracture sets after 100 and 200 days of heating for the vertical fracture set (Figure 9-42 and Figure 9-43, respectively) and similarly for the horizontal fracture set (Figure 9-44 and Figure 9-45, respectively). (The vertical fracture results are the FLAC variable EX_1, and the horizontal fracture results are the variable EX_4.)

The regions of frictional slip for planes of different orientation correlated with the principal stresses plotted in Figure 9-39, Figure 9-40, and Figure 9-41. For example, vertical fractures were expected to be favorably oriented for slip when they are approximately 30° to the maximum principal stress direction. The effect of heating is to create thermal gradients that are approximately radial toward the heat source. These gradients are equivalent to body forces and superpose with the isothermal stress field. The thermal gradients for the SHT were not as large as those predicted for several years of heating in the larger-scale DST. Thus, the region in which the thermal stresses are large enough to induce shear slip on pre-existing fracture planes is small. Additionally, the ratio of shear-to-normal stresses was not as large. The region of induced shear slip decreased between 100 and 200 days of heating. The exact shape was also affected by the approximation of the tunnel drift by a circle and the treatment of the tunnel boundary as an adiabatic boundary.

It is important to note that the thermal gradients generated in the SHT are much smaller than those expected, after many years of heating, in the potential repository. Thus, although the region of slip

induced here was small, this effect must also be considered specifically in relation to the potential repository.

9.5.3 Discussion

A critical link in the methodology linking the thermal-mechanical analysis to permeability is the concept that permeability is enhanced results from shear offset due to Mohr-Coulomb slip on pre-existing fracture sets. Previous use of the Brown (1995, pp. 5941 to 5952) and Brown and Bruhn (1997) model suggested that slip might lead to increasing permeability by a factor of two. The largest zone of enhanced permeability occurred at approximately 100 days for the vertical east-west fracture set. Using ERT (see Chapter 8.5 of this report), water was observed collected in a U-shaped region between the heater and the two drifts (Figure 9-46). This saturation pattern might be related to enhanced vertical permeability in the region shown in Figure 9-46 conducting water into the region of unenhanced permeability where it collects.

9.6 SUMMARY

Movements in the rock were measured with multi-point, wire, and tape extensometers. Results indicate good overall agreement between calculated and measured deformations, although some anomalous measurements were observed. Erratic measurements could come from failures in the gage, rod, or anchor, but, in some instances, reflect actual rock behavior such as slippage. The multi-point extensometers with LVDTs were found to be more reliable than those based on the vibrating wire system. The coefficient of thermal expansion in the rock mass was approximately 50 percent less than measured in the laboratory. This behavior is consistent with deformational response in a fractured rock media subjected to heating. Results from borehole jack testing show the rock mass modulus varies from 3 to 23 Gpa. The highest value corresponds to the measurement closest to the heater at 143°C. Rock bolt load cell measurements show an overall decrease with time in loading but less than 7 percent in all cases. The average percent decrease for the ambient and heated load cells was 1.6 percent and 3.3 percent, respectively. The two largest decreases for individual loadcells corresponded to highest temperature locations. Also, thermal-mechanical simulations suggest correlation of enhanced permeability with rock slippage in a localized region of the test block.

INTENTIONALLY LEFT BLANK

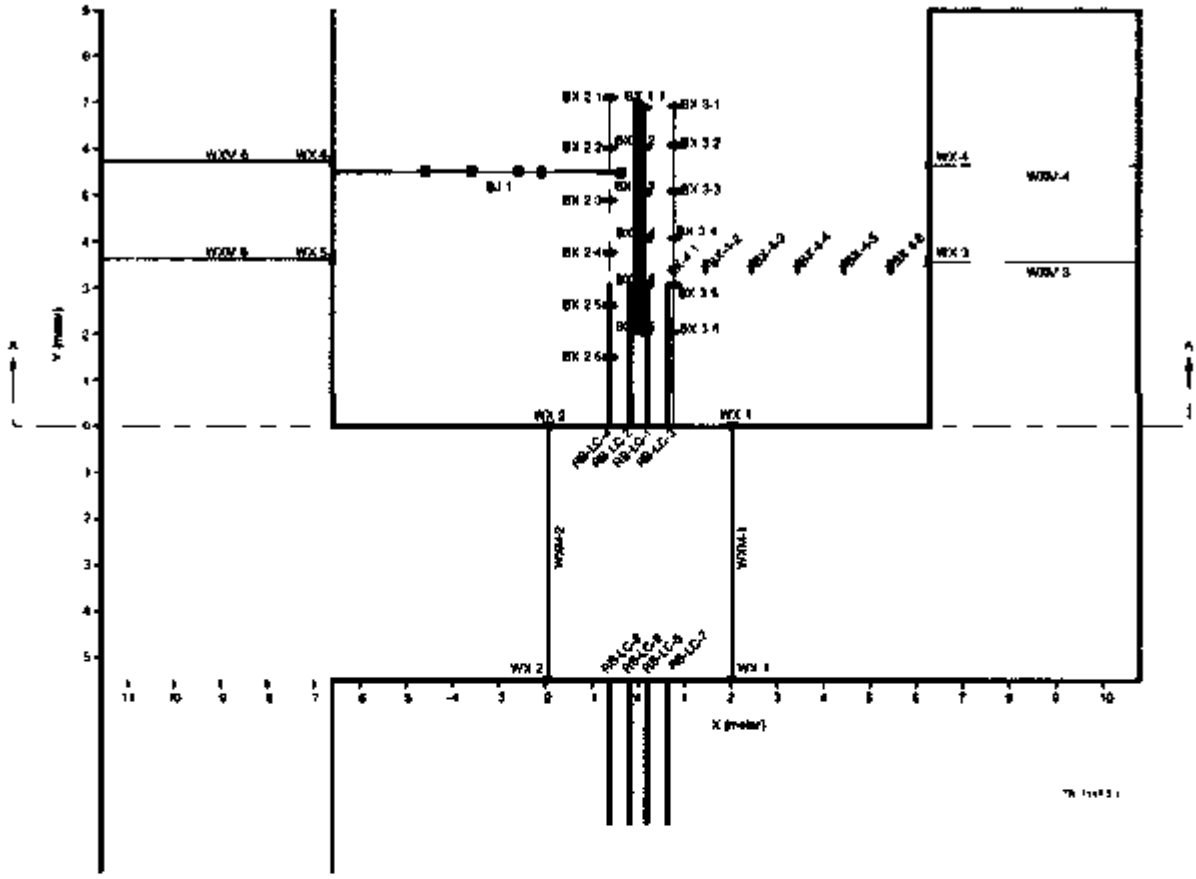

Figure 9-1 Plan View Showing Locations of the Original Mechanical Boreholes, MPBX Anchors, Wire Extensometers, Rock Bolt Load Cells, Borehole Jack, and Tape Extensometers in the SHT Block

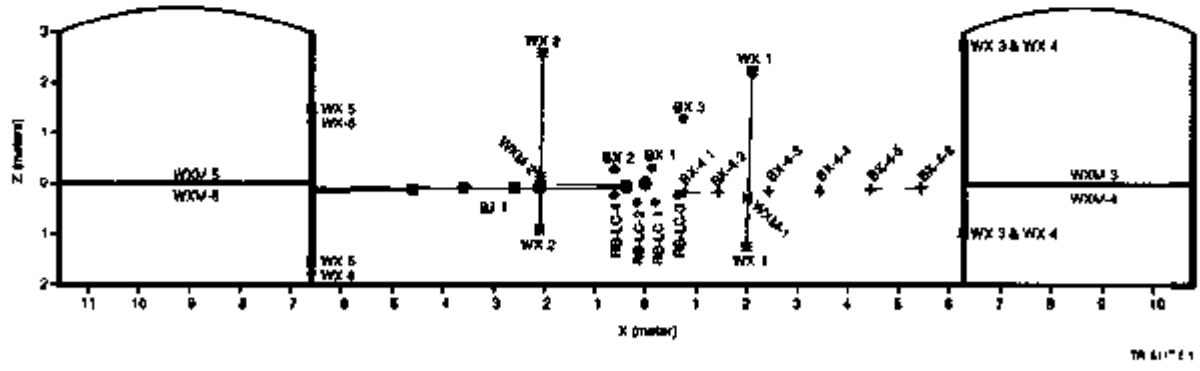

Figure 9-2 Cross-Section Showing Locations of the Original Boreholes, MPBX Anchors, Wire Extensometers, Rock Bolt Load Cells, Borehole Jack, and Tape Extensometers in the SHT Block

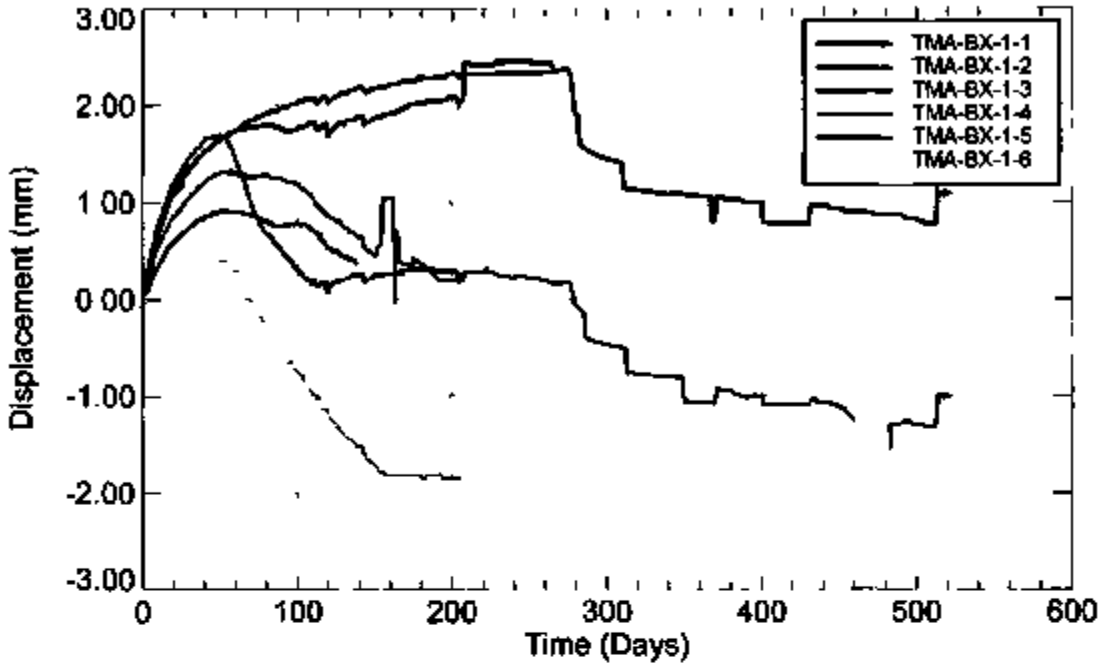

NOTE Corrected for rod thermal expansion, extension positive

Figure 9-3 Displacement History for ESF-TMA-MPBX-1

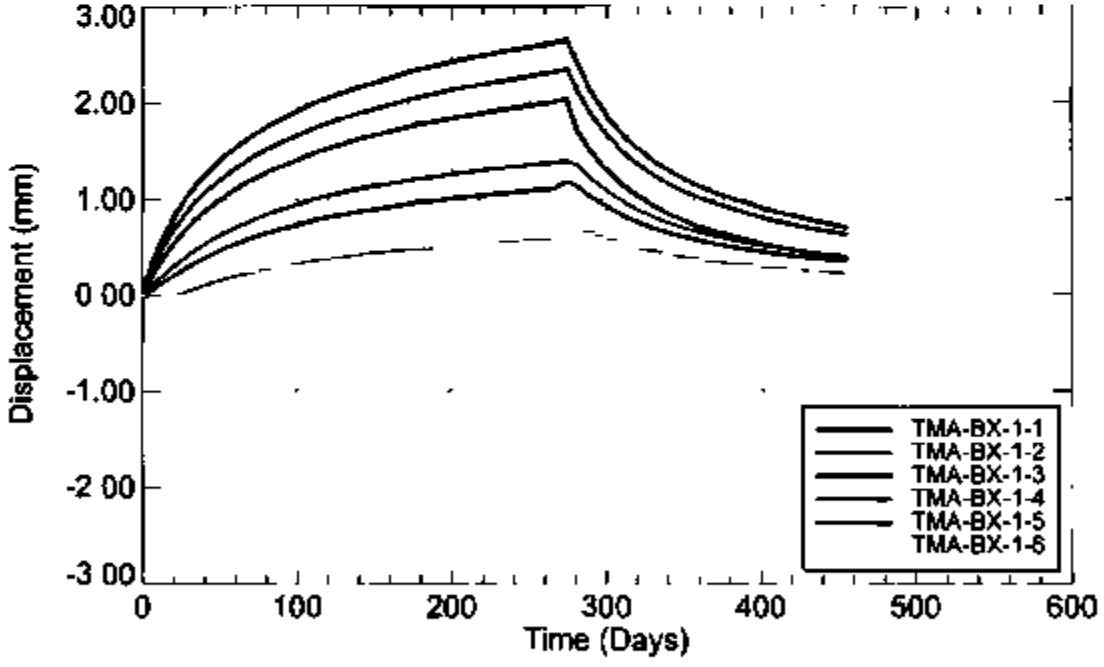

Source Sobolik, Francis, and Finley 1996

Figure 9-4 Pretest Predicted MPBX-1 Displacement History Relative to the Borehole Collar

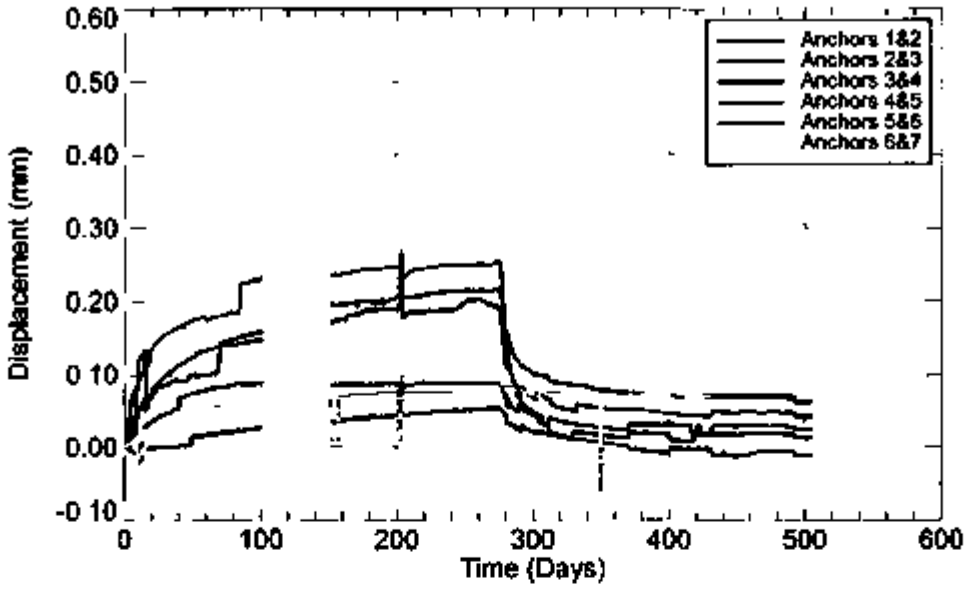

NOTE Corrected for rod thermal expansion, extension positive No data were collected from about Day 100 to about Day 150 due to a blown fuse in the signal conditioner for the LVDTs

Figure 9-5 Displacement History for ESF-TMA-MPBX-2

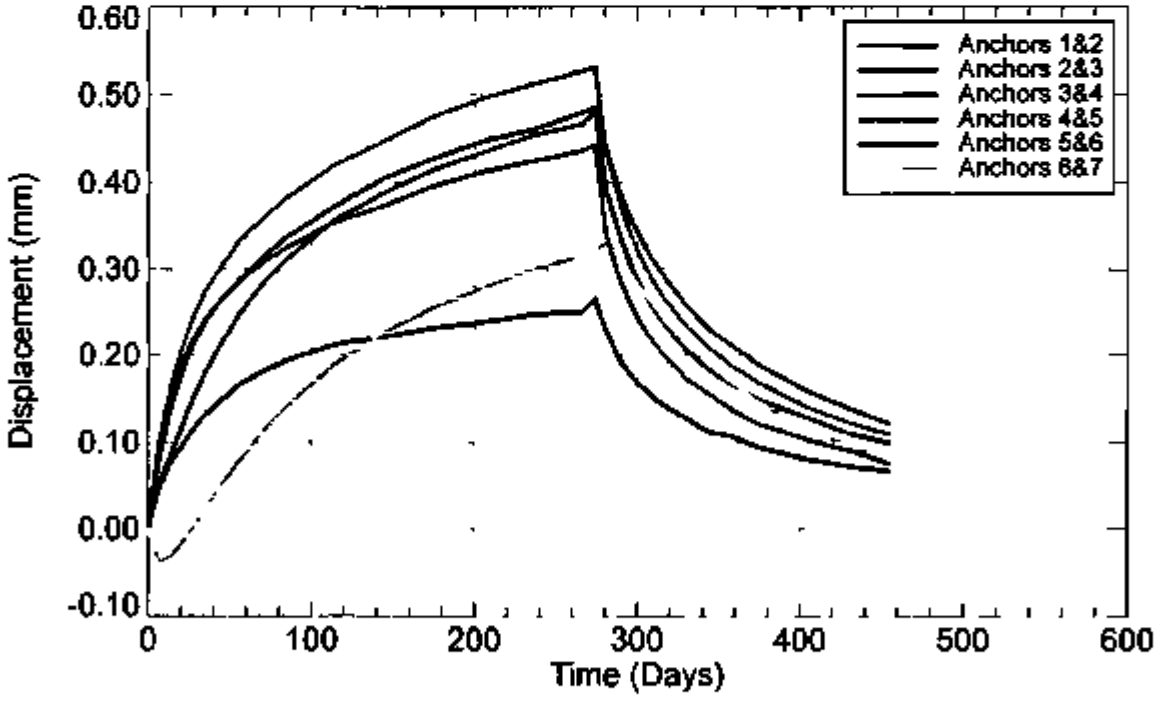

Source Sobolik, Francis, and Finley 1996

Figure 9-6 Pretest Predicted MPBX-2 Anchor-to-Anchor Displacement History Relative to the Borehole Collar

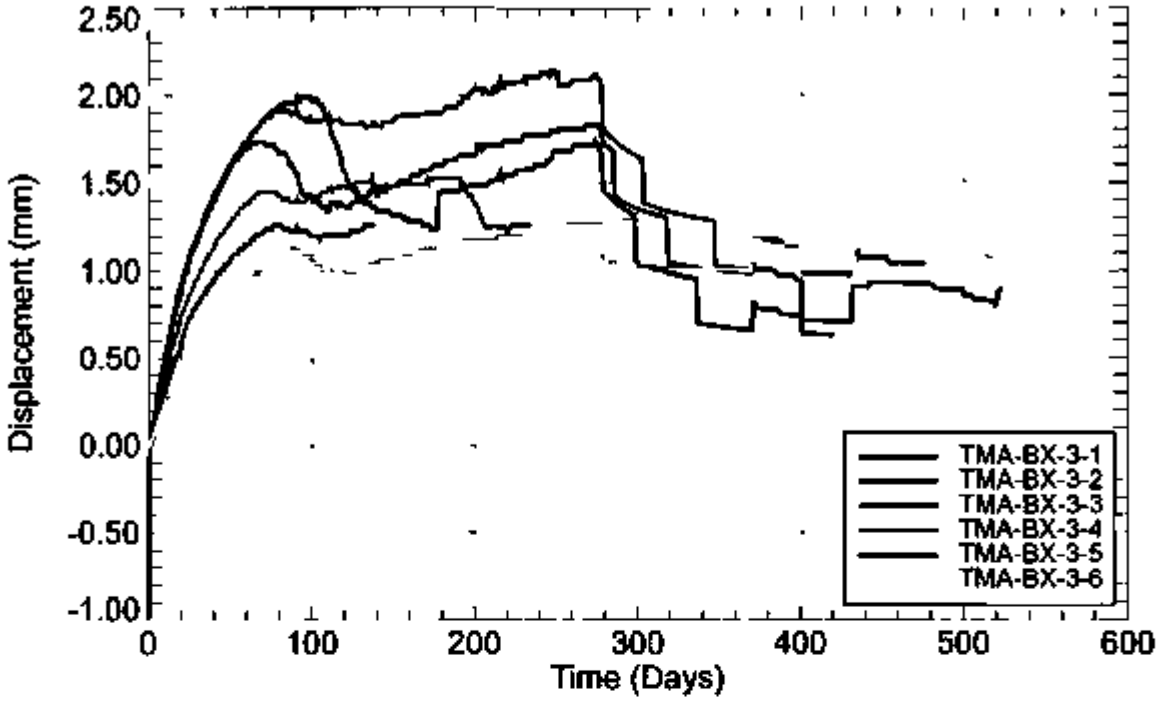

NOTE Corrected for rod thermal expansion, extension positive

Figure 9-7 Displacement History for ESF-TMA-MPBX-3

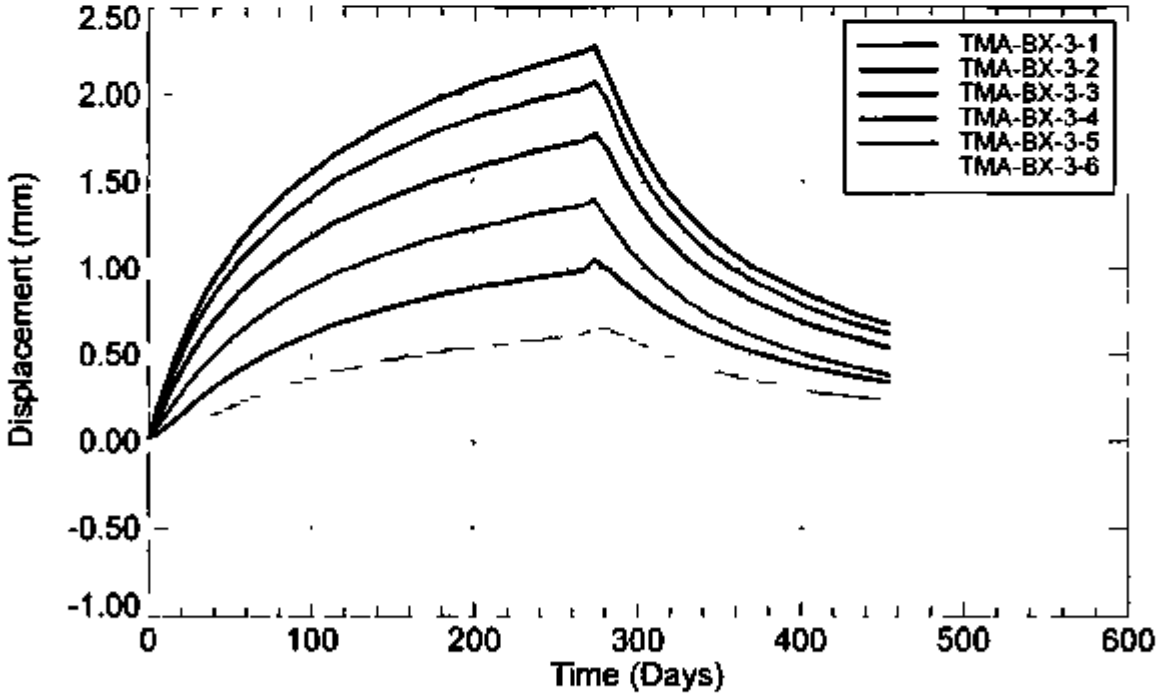

SOURCE Sobolik, Francis, and Finley 1996

Figure 9-8 Pretest Predicted MPBX-3 Displacement History Relative to the Borehole Collar

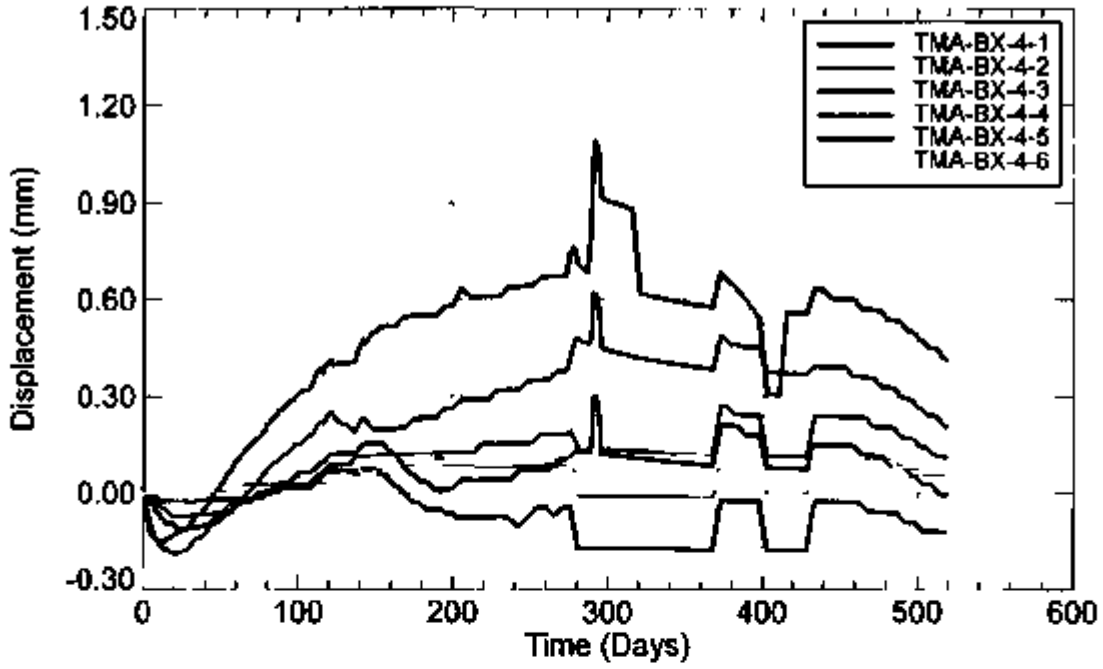

NOTE Corrected for rod thermal expansion, extension positive

Figure 9-9 Displacement History for ESF-TMA-MPBX-4

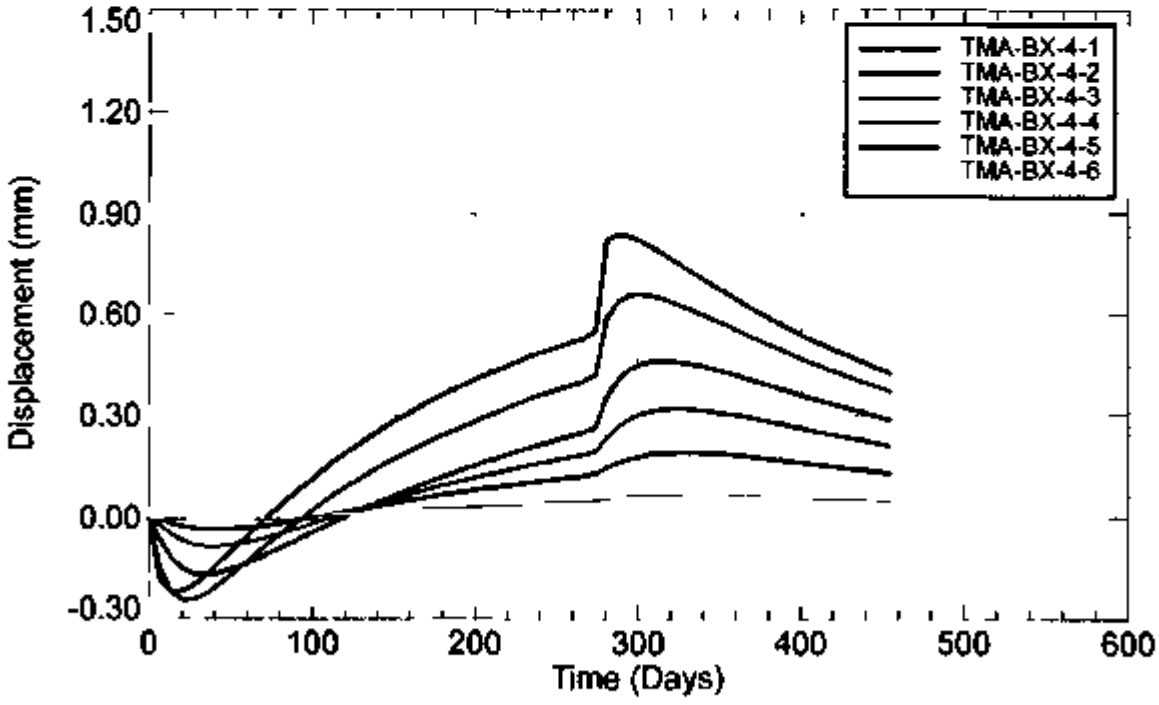

SOURCE Sobolik, Francis, and Finley 1996

Figure 9-10 Pretest Predicted MPBX-4 Displacement History Relative to the Borehole Collar

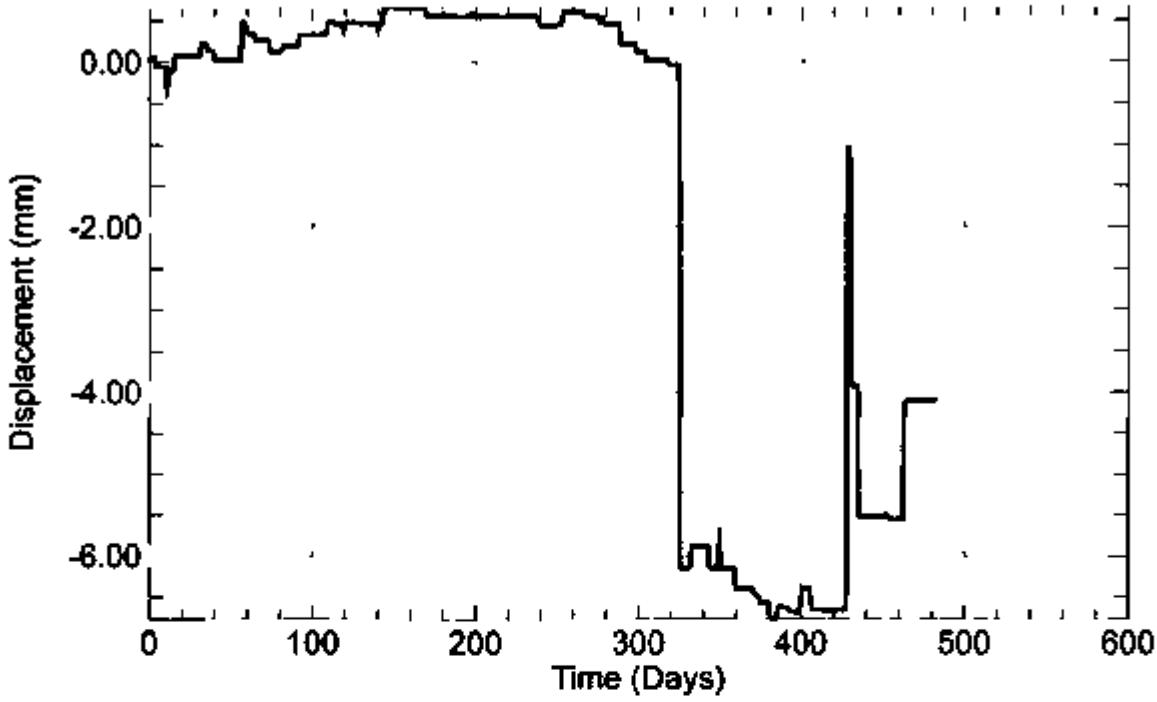

NOTE Extension positive

Figure 9-11 Displacement History for Wire Extensometer ESF-TMA-WX-1

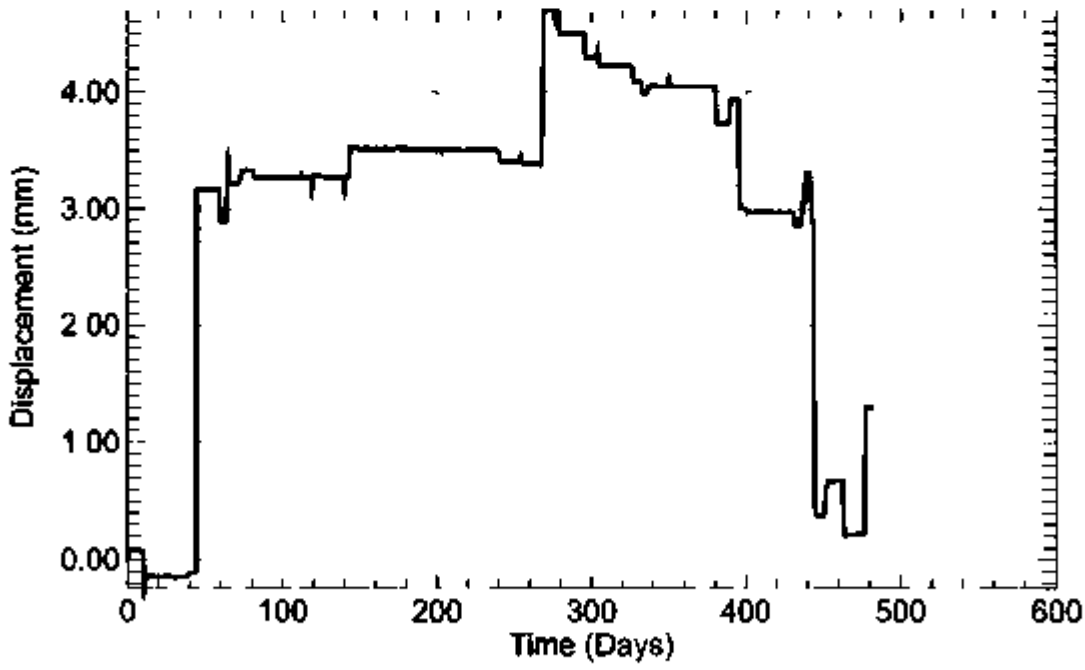

NOTE Extension positive

Figure 9-12 Displacement History for Wire Extensometer ESF-TMA-WX-2

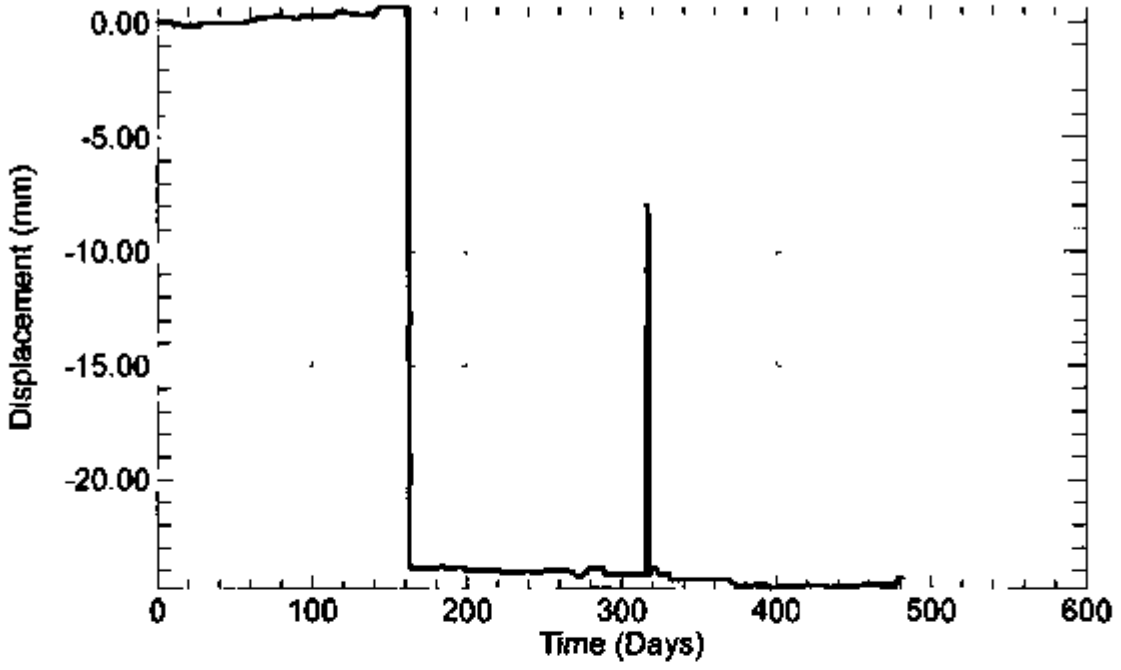

NOTE Extension positive

Figure 9-13 Displacement History for Wire Extensometer ESF-TMA-WX-3

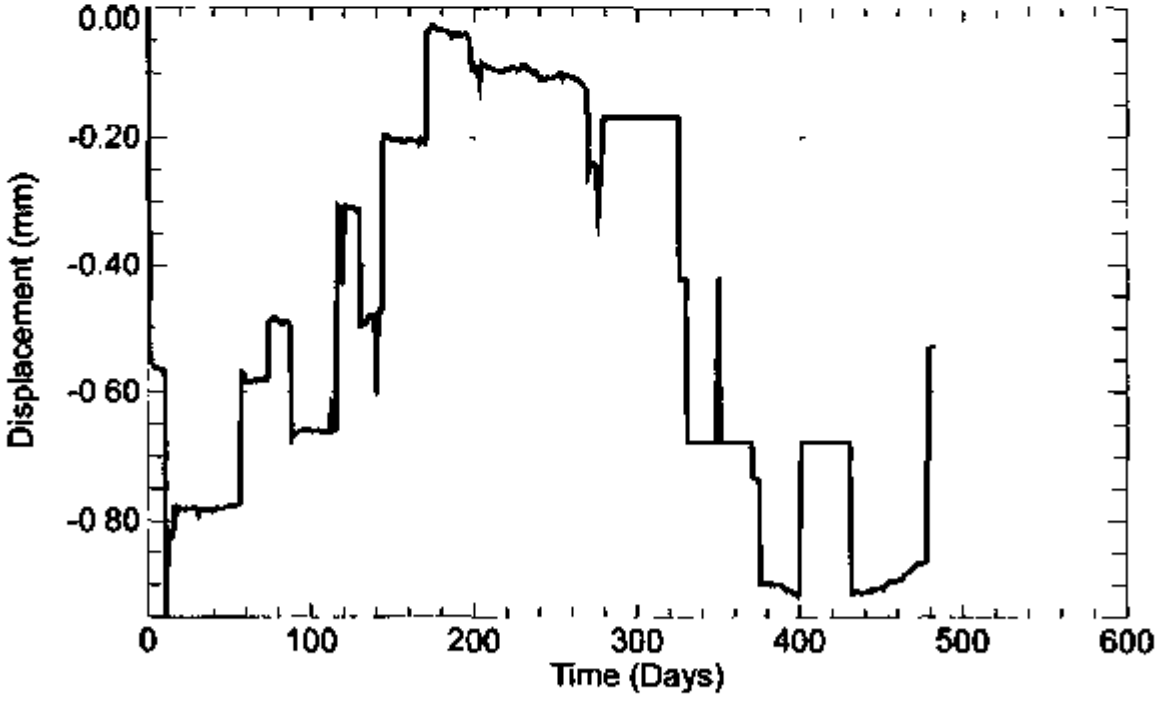

NOTE Extension positive

Figure 9-14 Displacement History for Wire Extensometer ESF-TMA-WX-4

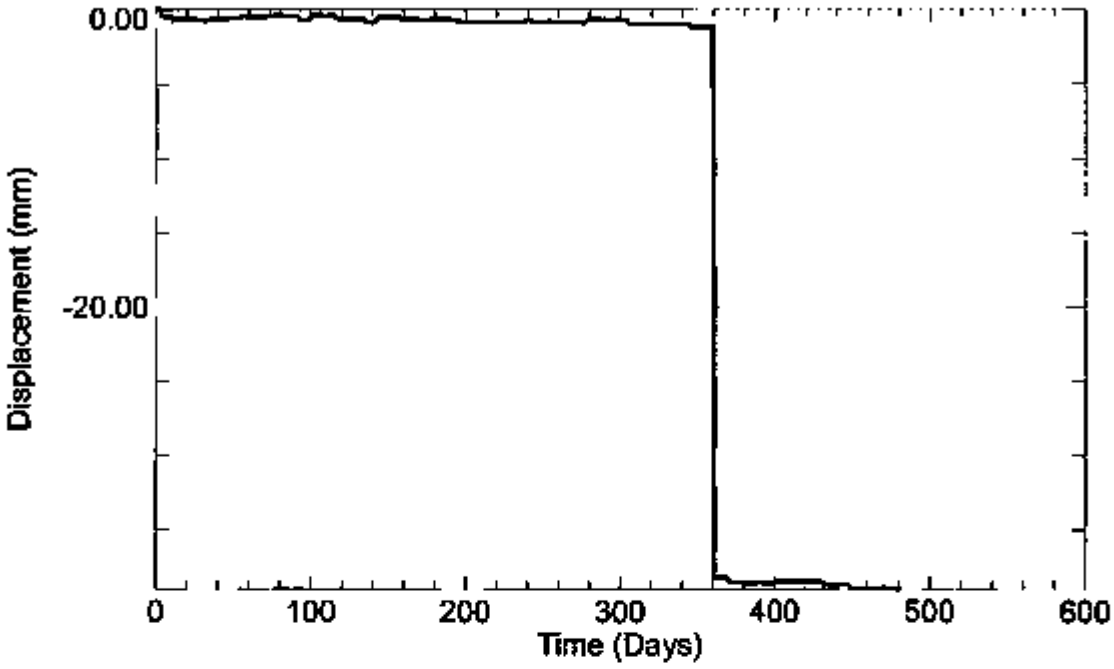

NOTE Extension positive

Figure 9-15 Displacement History for Wire Extensometer ESF-TMA-WX-5

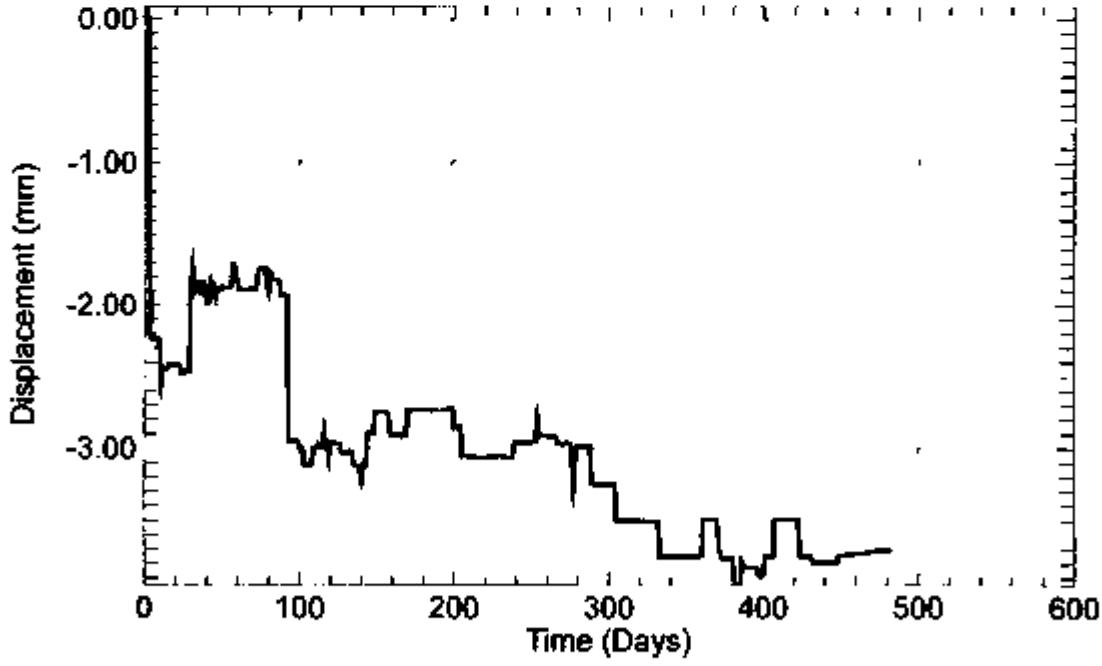

NOTE Extension positive

Figure 9-16 Displacement History for Wire Extensometer ESF-TMA-WX-6

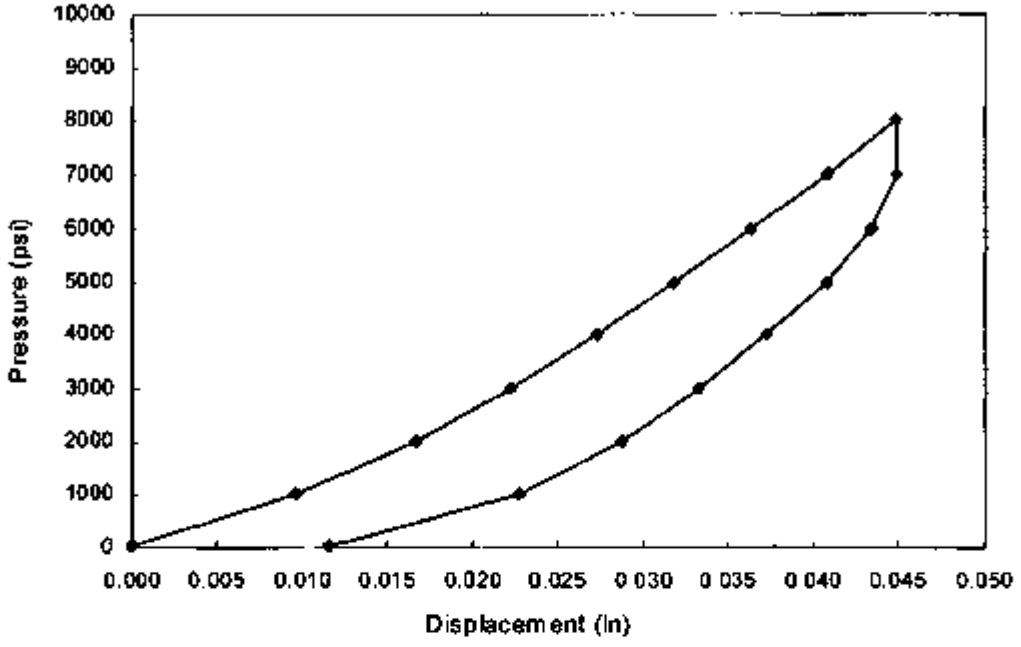

Figure 9-17. Goodman Jack Pressure-Displacement Plot at 2.0 m Depth on January 29, 1998

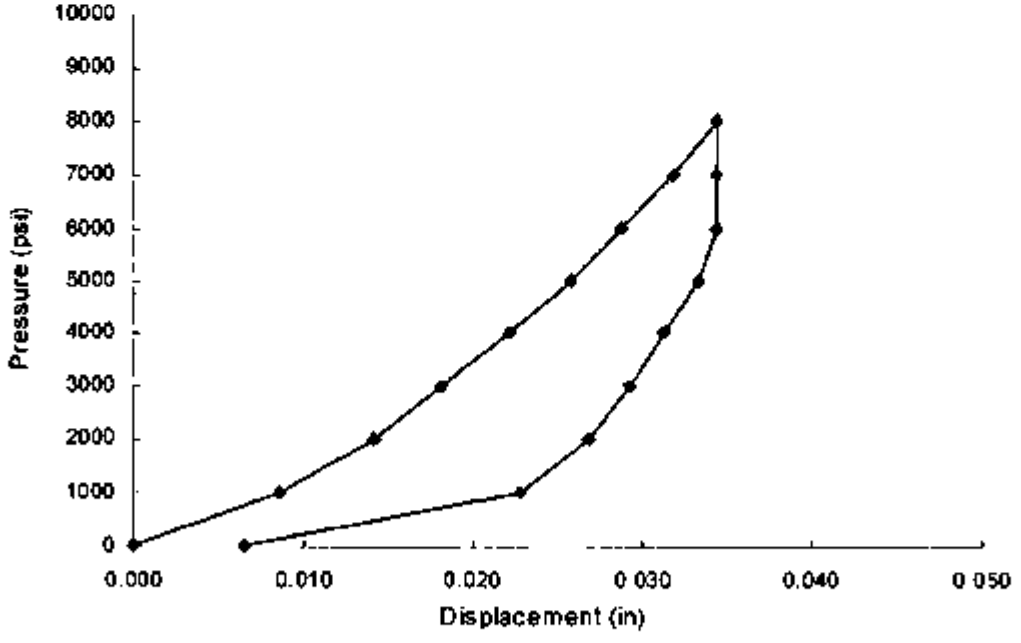

Figure 9-18. Goodman Jack Pressure-Displacement Plot at 3.0 m Depth on January 29, 1998

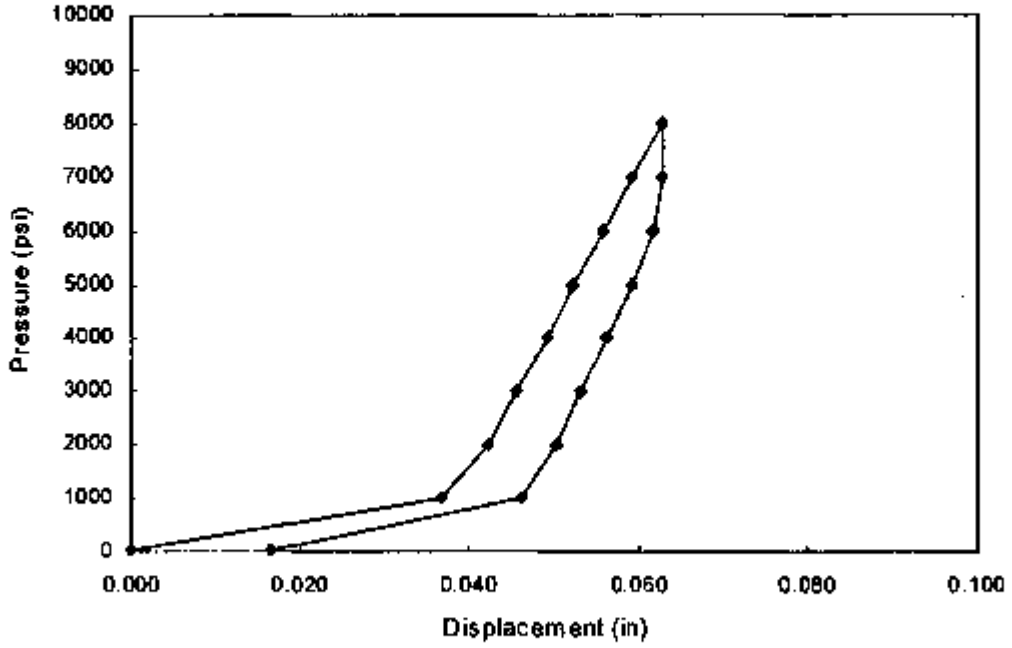

Figure 9-19. Goodman Jack Pressure-Displacement Plot at 4.0 m Depth on January 29, 1998

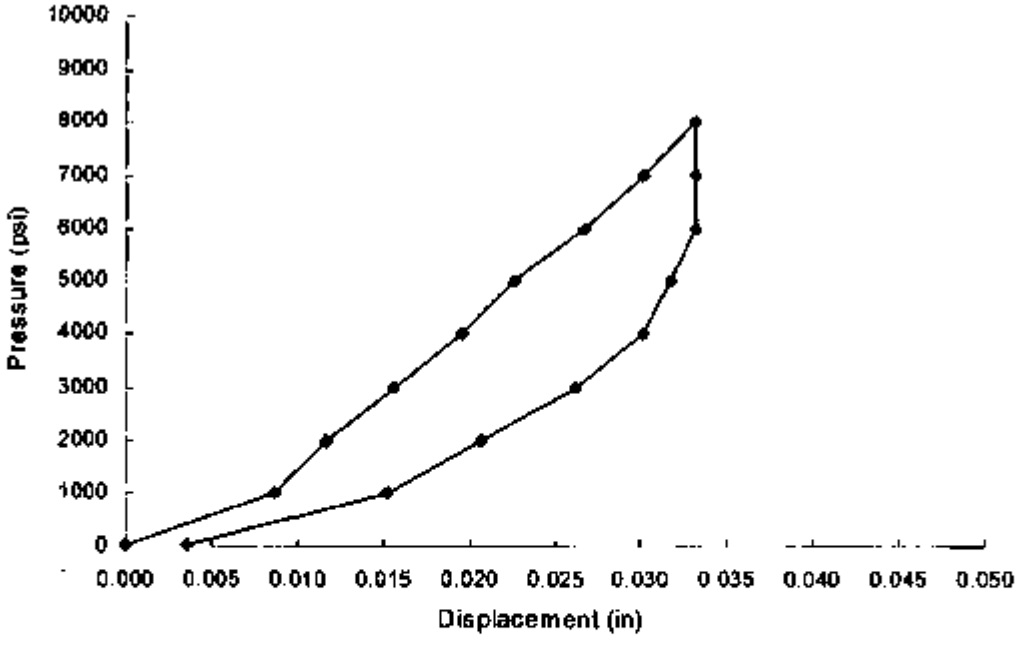

Figure 9-20. Goodman Jack Pressure-Displacement Plot at 4.5 m Depth on January 29, 1998

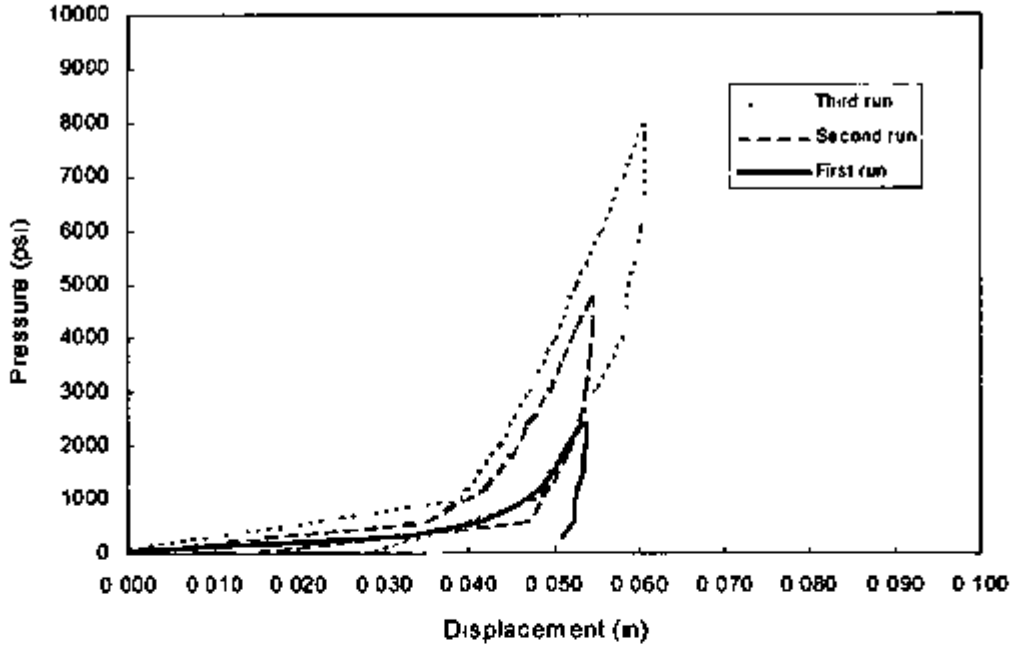

Figure 9-21 Goodman Jack Pressure-Displacement Plot at 6 2 m Depth on January 29, 1998

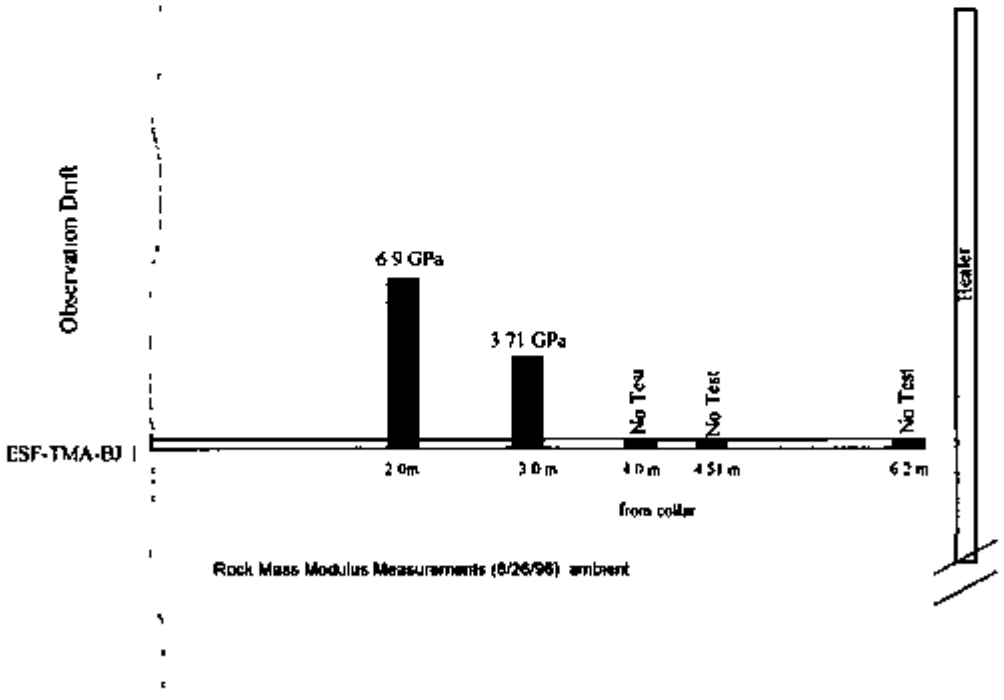

Figure 9-22 Results of Borehole Jack Tests Conducted on August 26, 1996

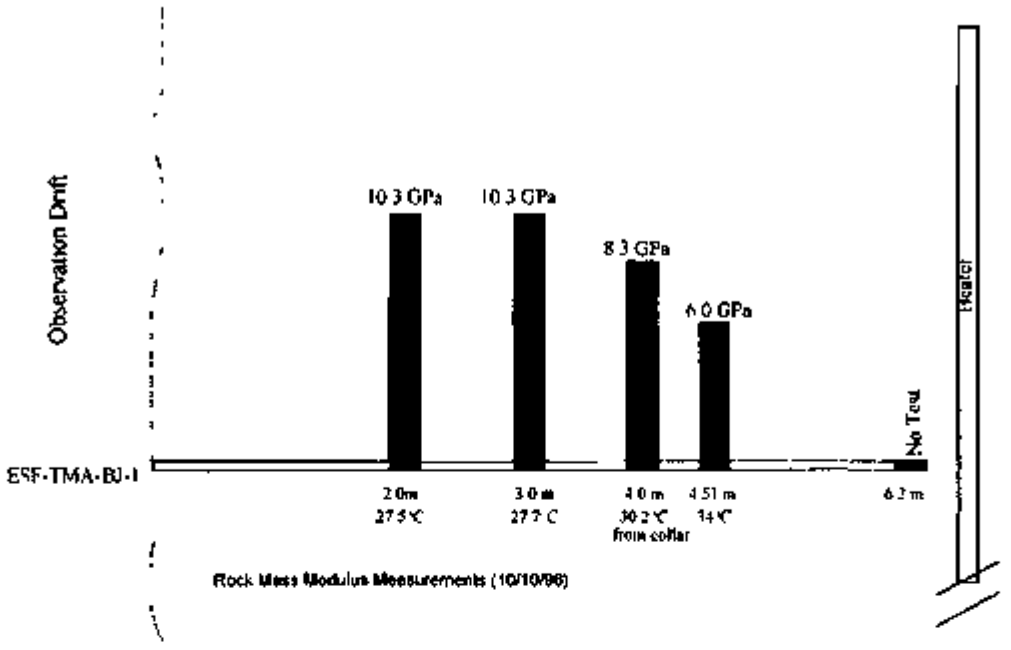

Figure 9-23 Results of Borehole Jack Tests Conducted on October 10, 1996

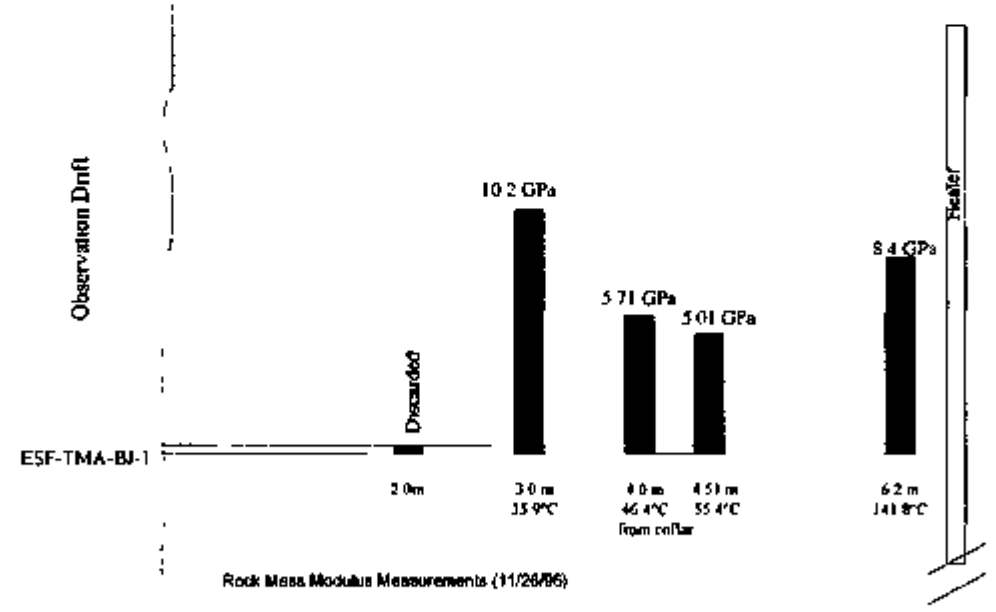

Figure 9-24 Results of Borehole Jack Tests Conducted on November 26, 1996

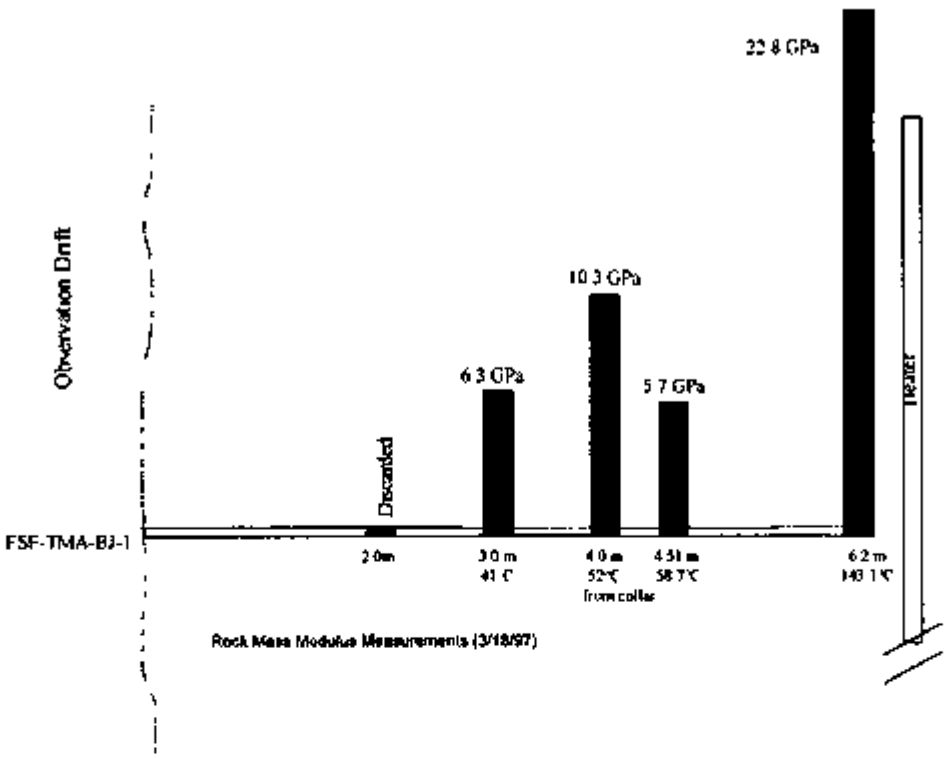

Figure 9-25 Results of Borehole Jack Tests Conducted on March 18, 1997

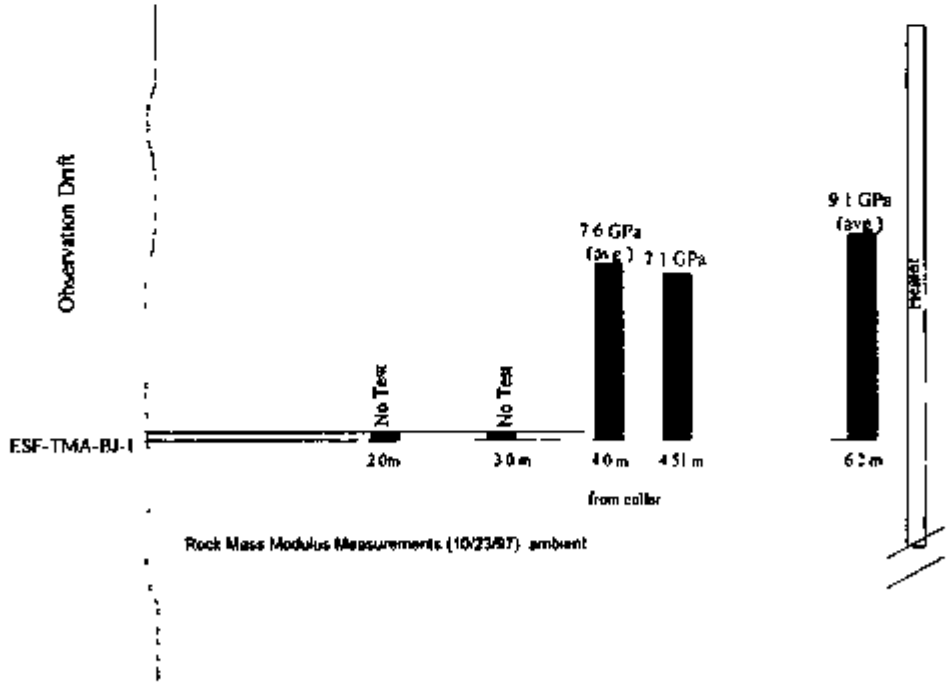

Figure 9-26 Results of Borehole Jack Tests Conducted on October 23, 1997

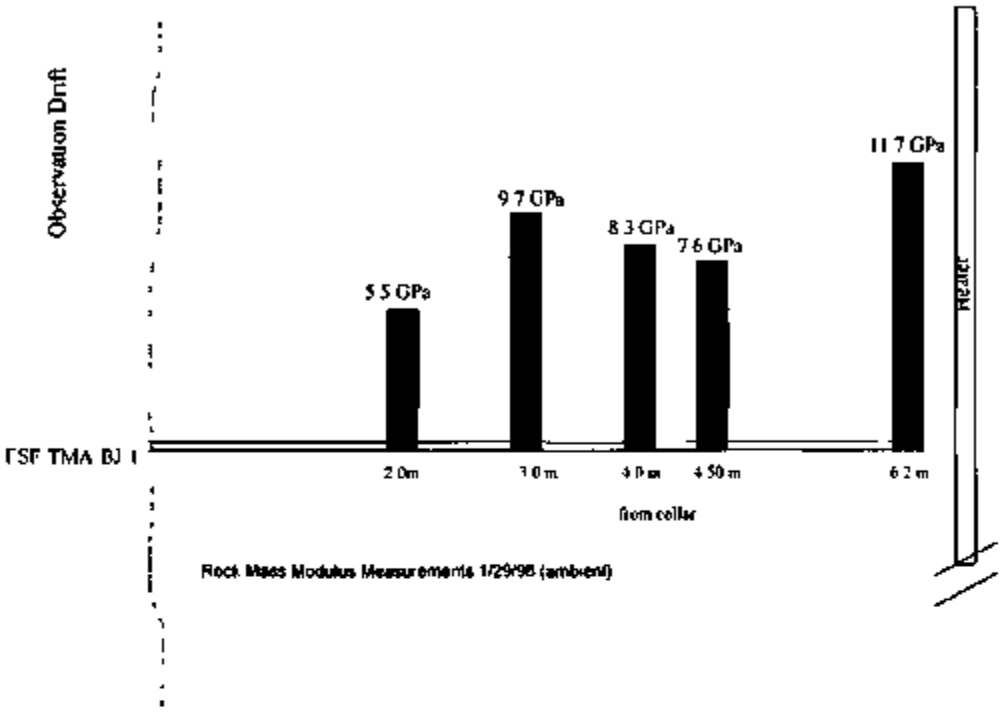

Figure 9-27 Results of Borehole Jack Tests Conducted on January 29, 1998 (Ambient)

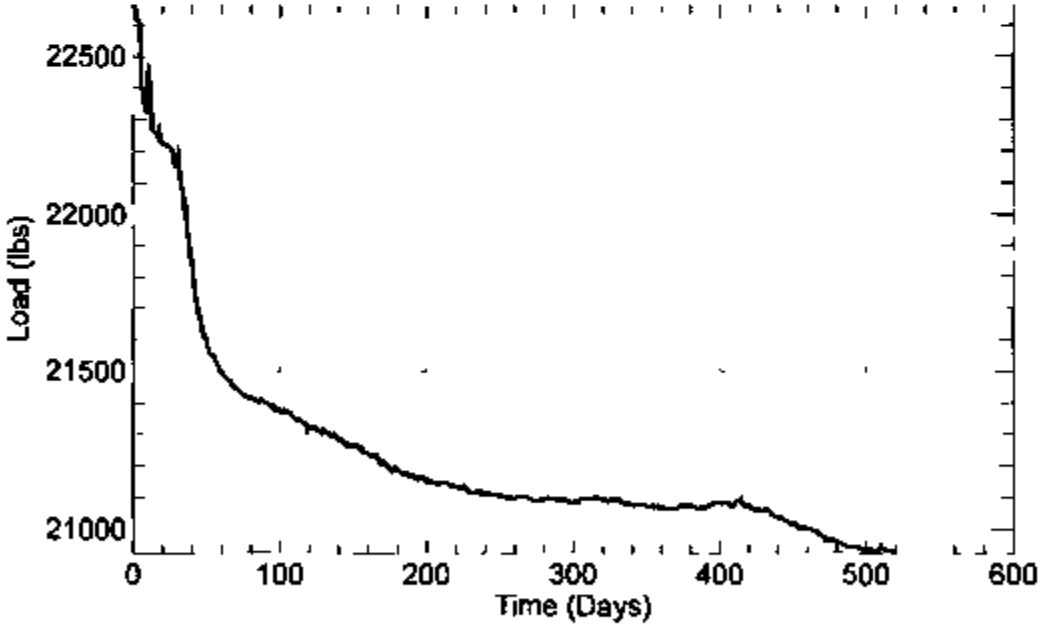

Figure 9-28 Rock Bolt Load History for TMA-RB-LC-1 (Average)

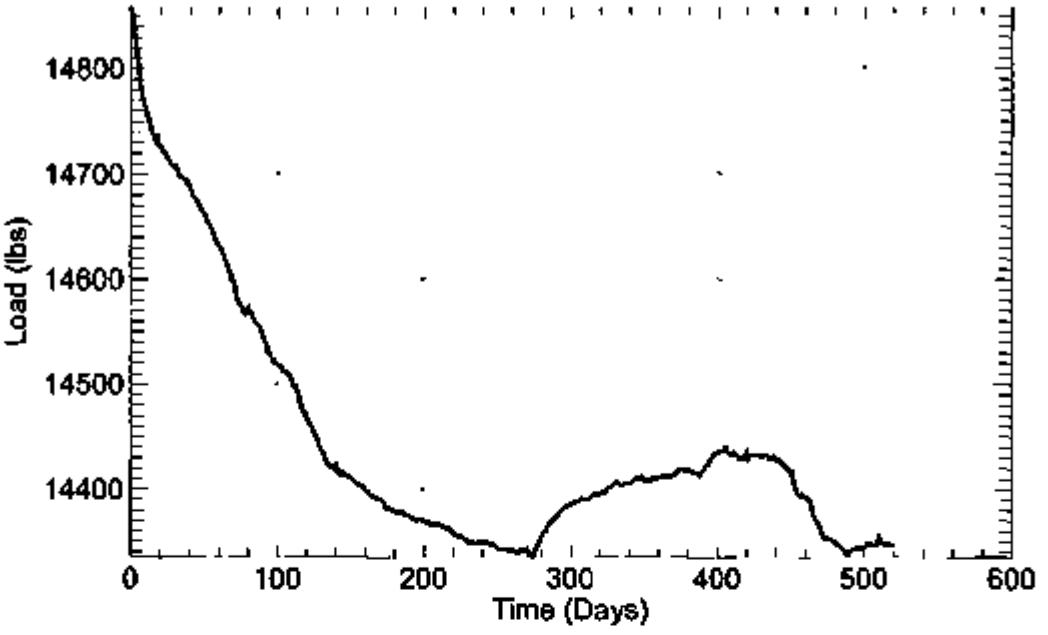

Figure 9-29 Rock Bolt Load History for TMA-RB-LC-2 (Average)

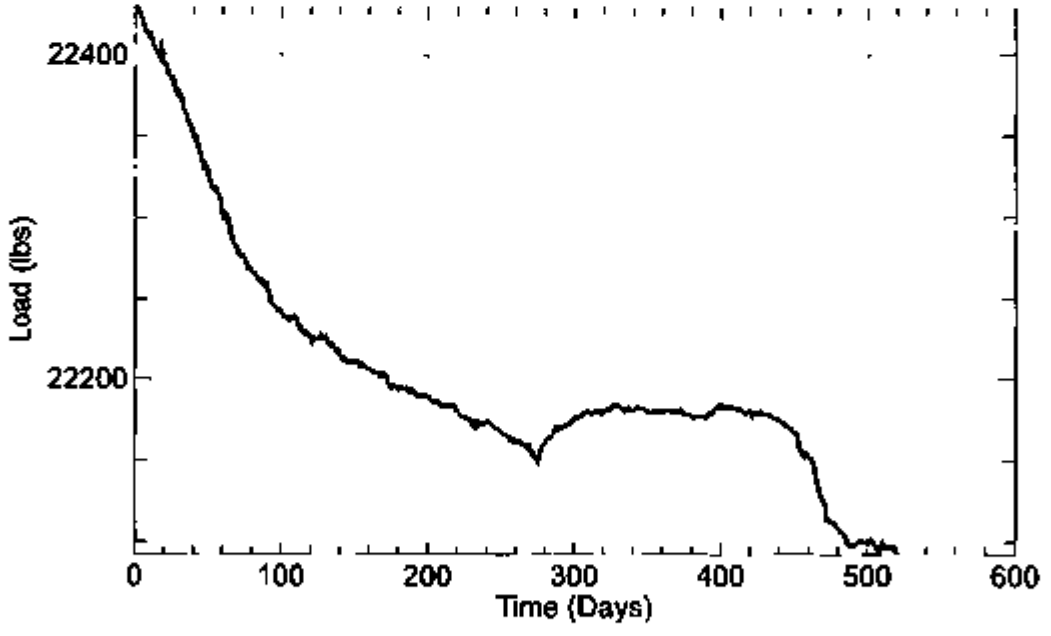

Figure 9-30 Rock Bolt Load History for TMA-RB-LC-3 (Average)

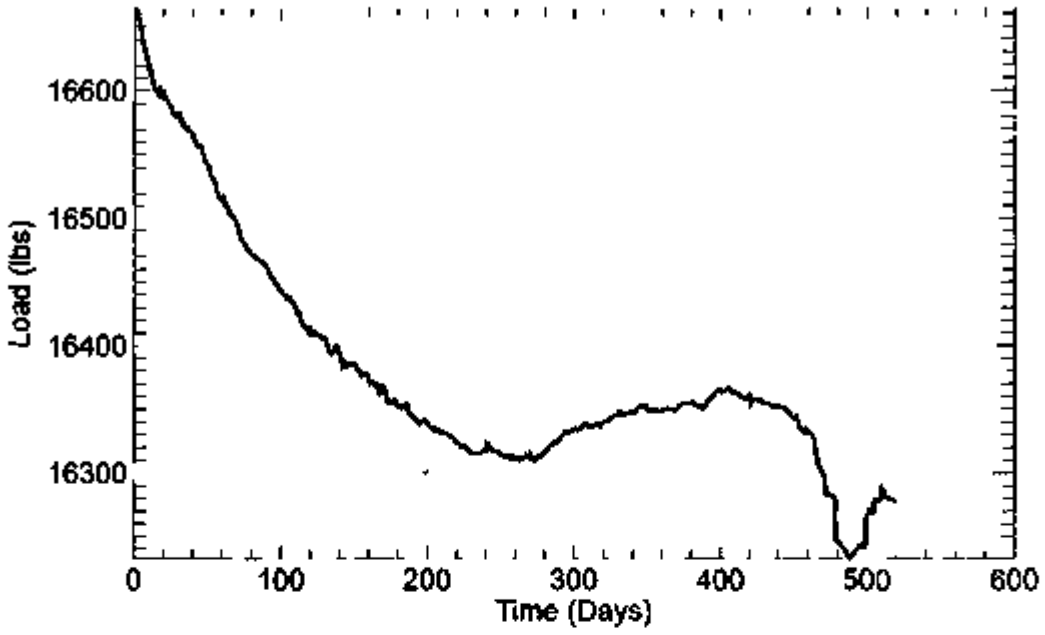

Figure 9-31 Rock Bolt Load History for TMA-RB-LC-4 (Average)

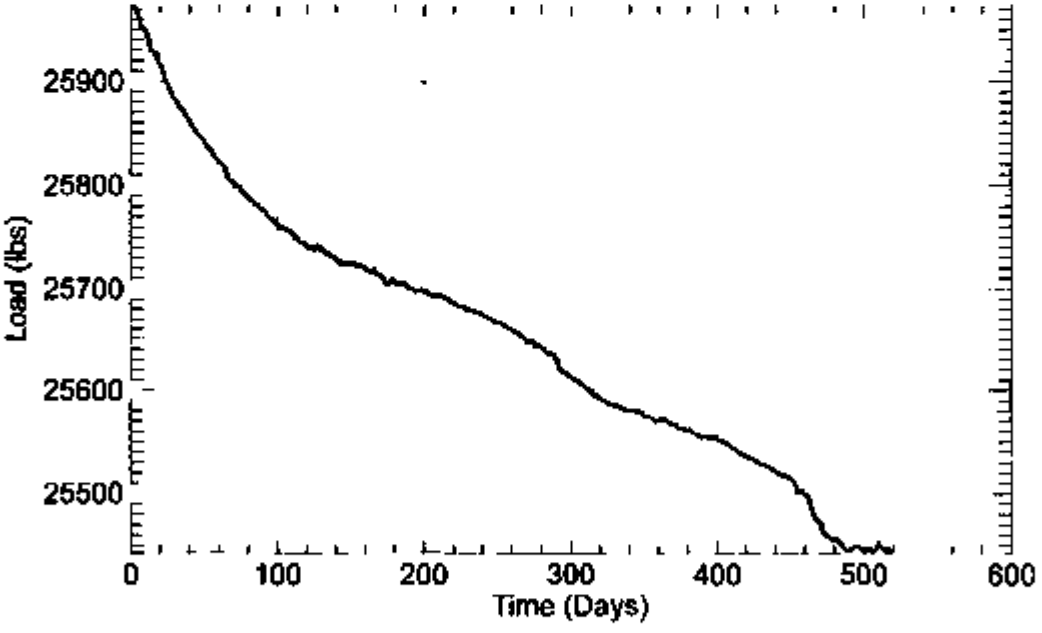

Figure 9-32 Rock Bolt Load History for TMA-RB-LC-5 (Average)

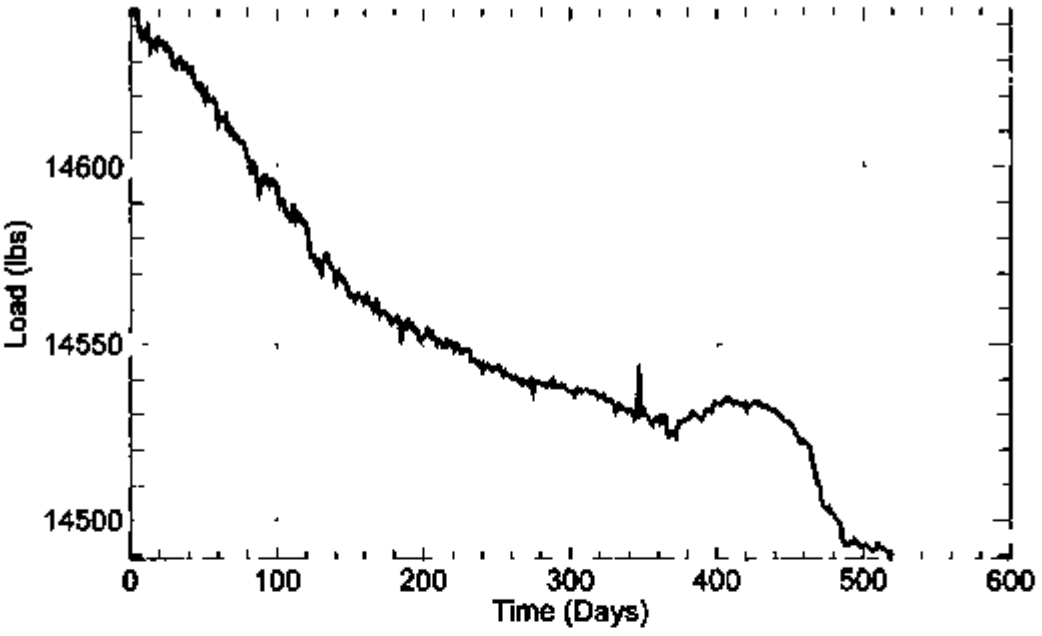

Figure 9-33 Rock Bolt Load History for TMA-RB-LC-6 (Average)

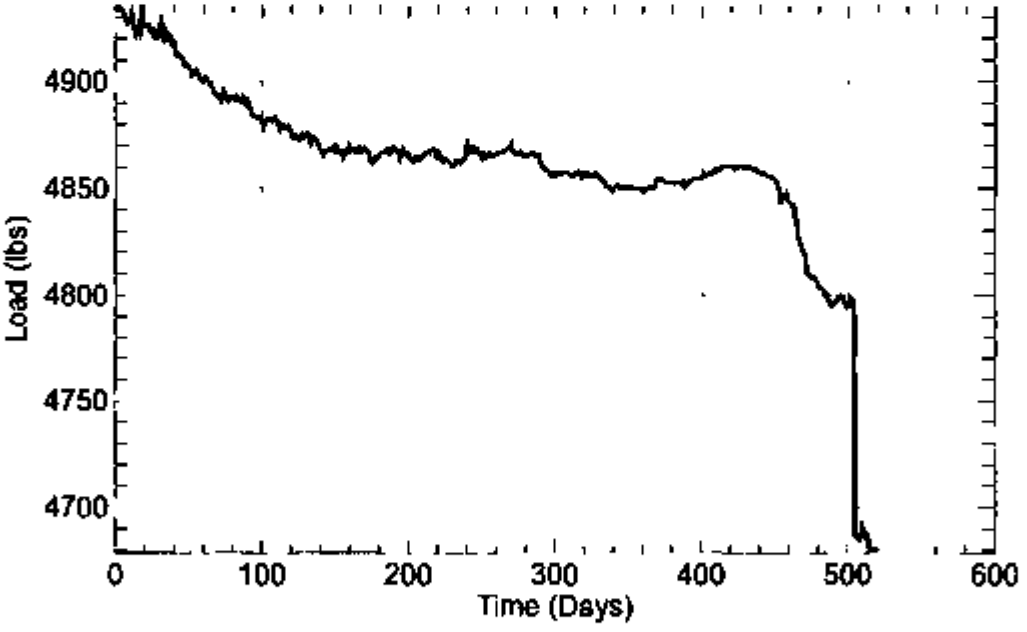

Figure 9-34 Rock Bolt Load History for TMA-RB-LC-7 (Average)

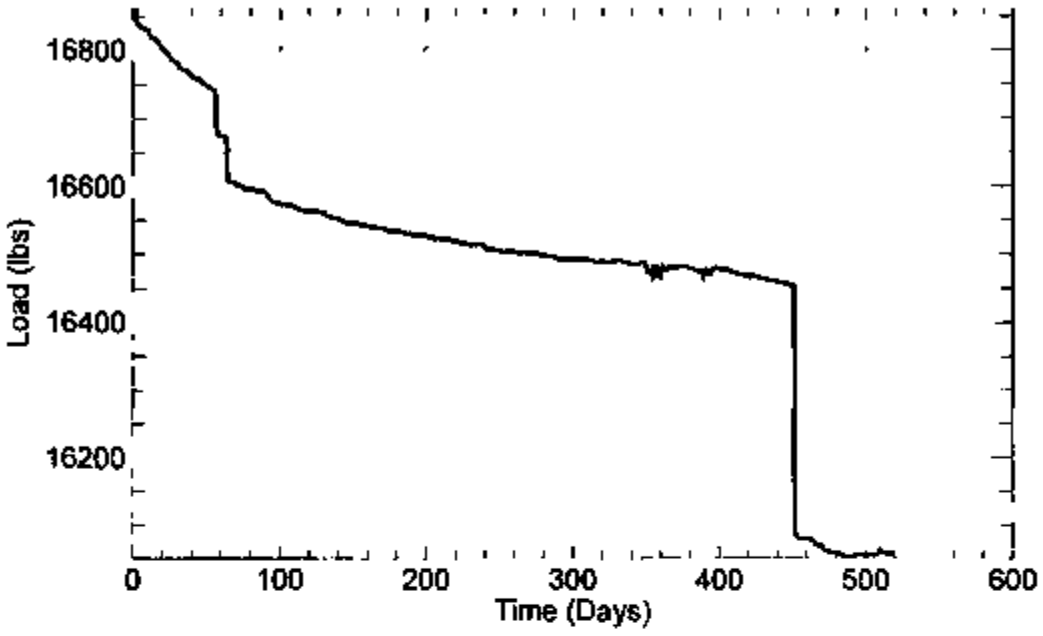

Figure 9-35 Rock Bolt Load History for TMA-RB-LC-8 (Average)

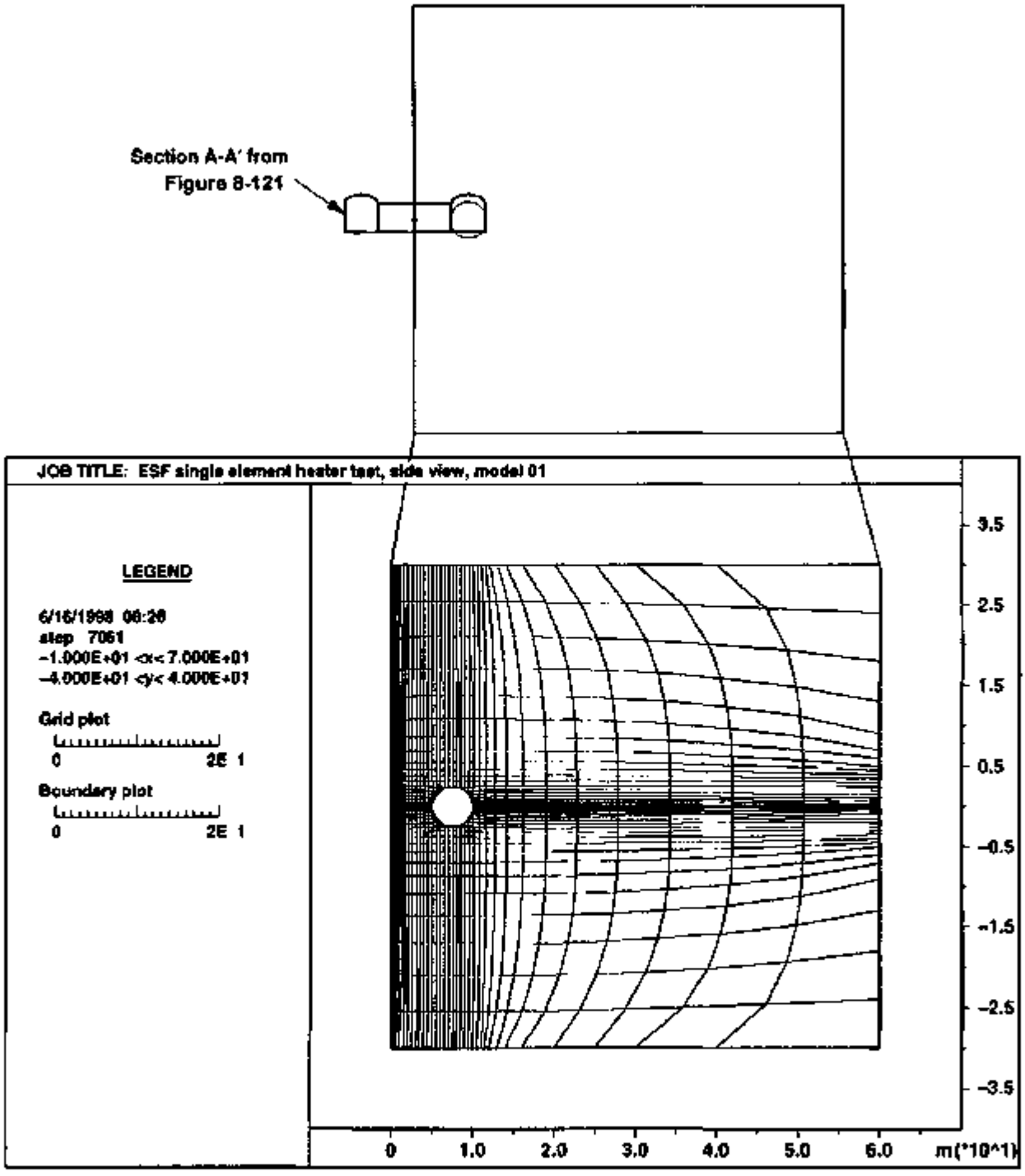

NOTE: Heater is at the center of the left edge of the model. The thermomechanical alcove extension and the observation drift are located symmetrically at about $x = 0$. All x and y coordinates are in meters x 10^1.

Figure 9-36. FLAC Grid

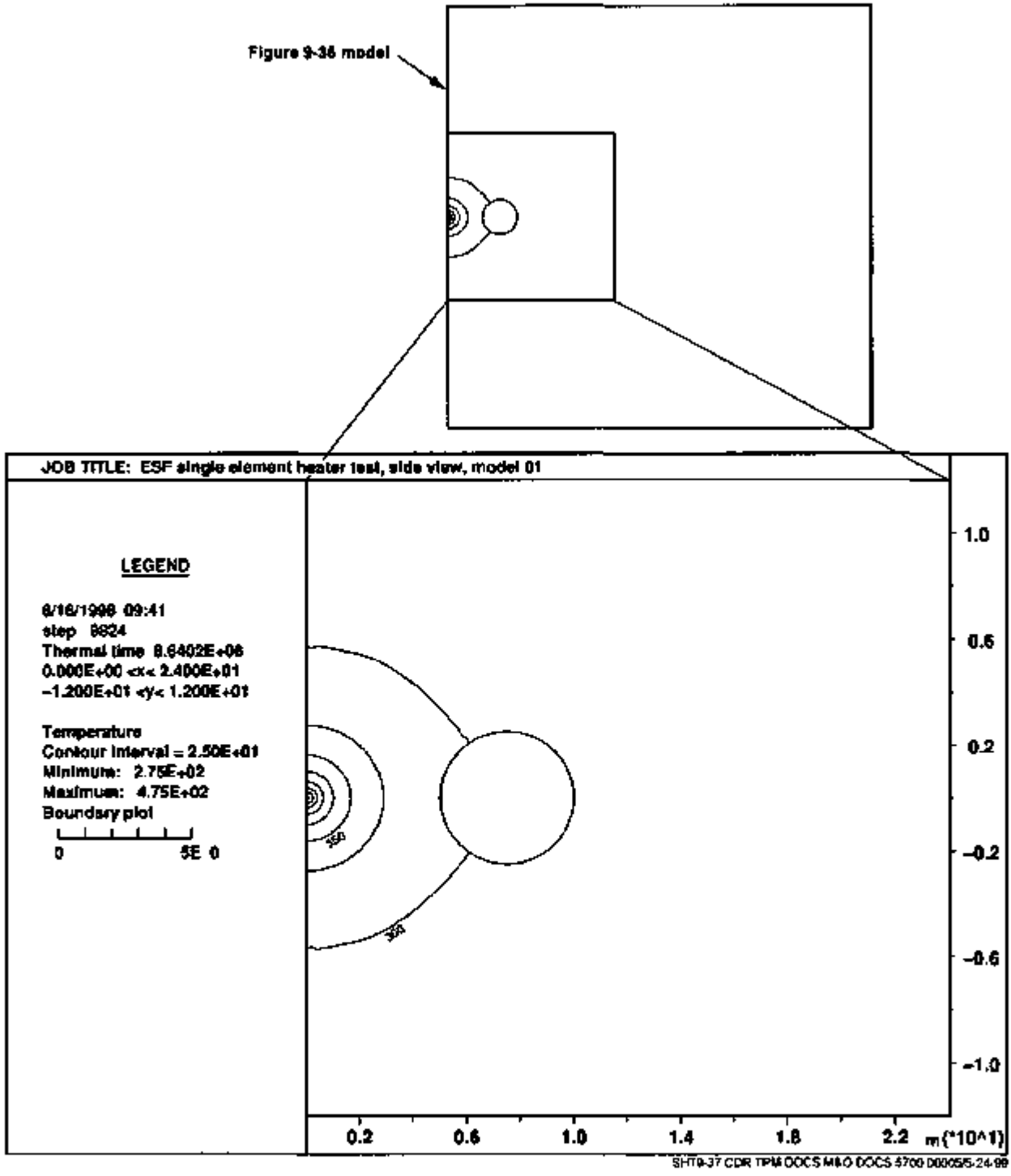

Figure 9-37. Temperature Field in °K near the Single Heater at 100 Days

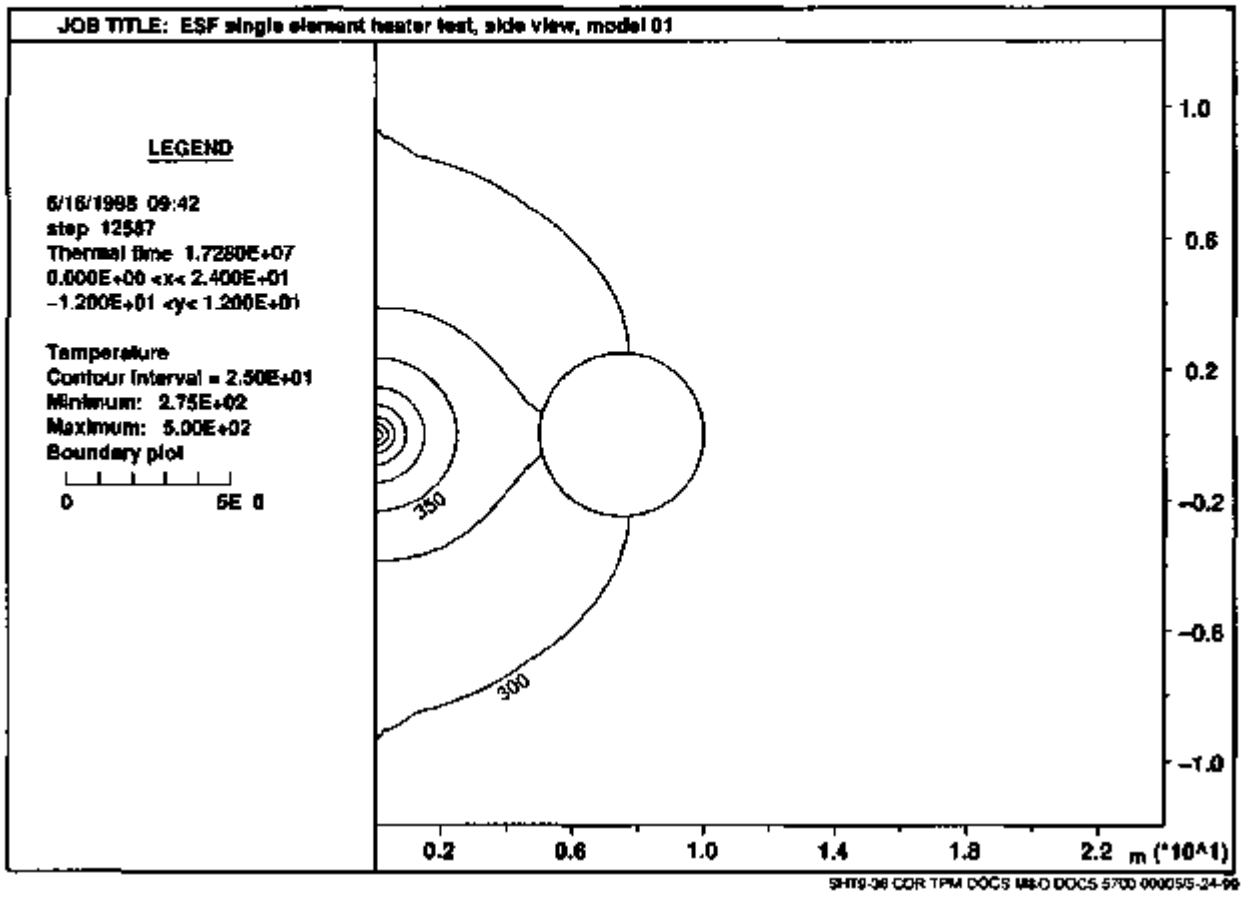

Figure 9-38. Temperature Field in °K near the Heater at 200 Days

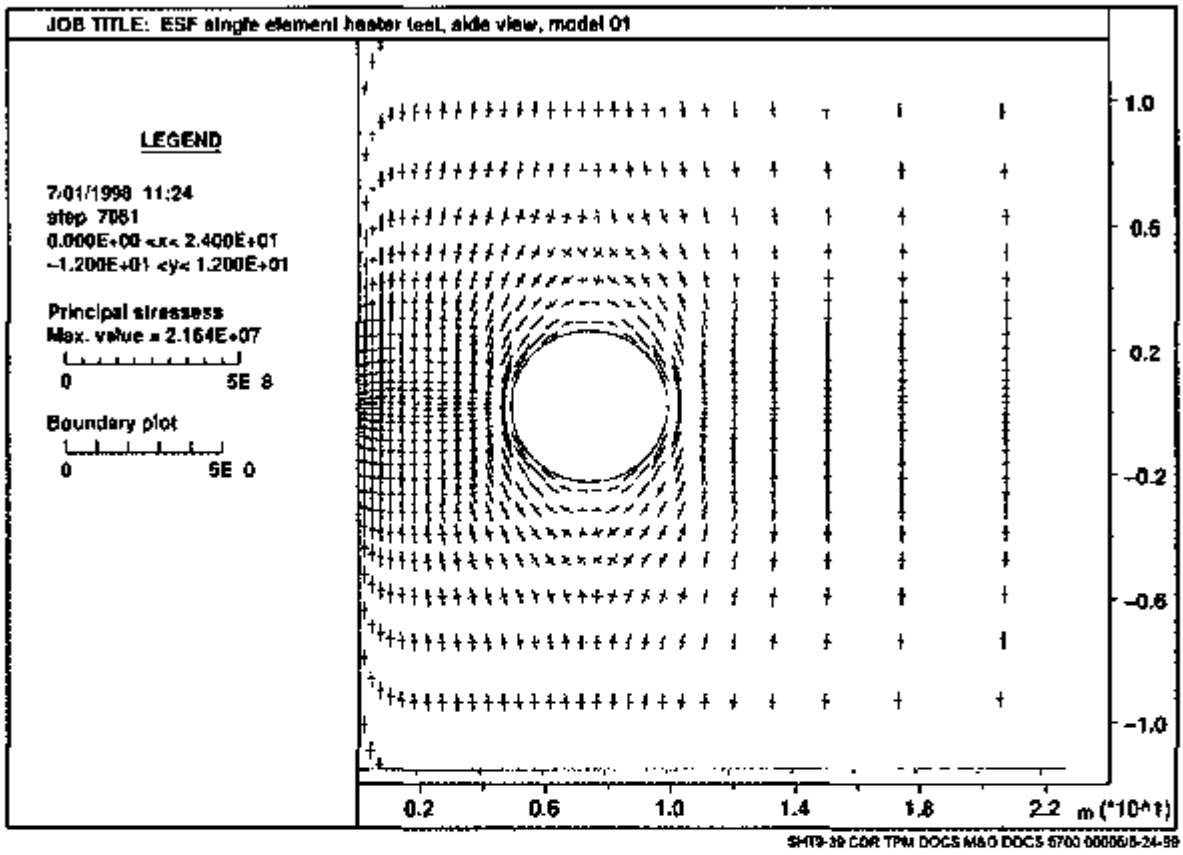

Figure 9-39. Principal Stresses in Pa near the Heater, before Heating

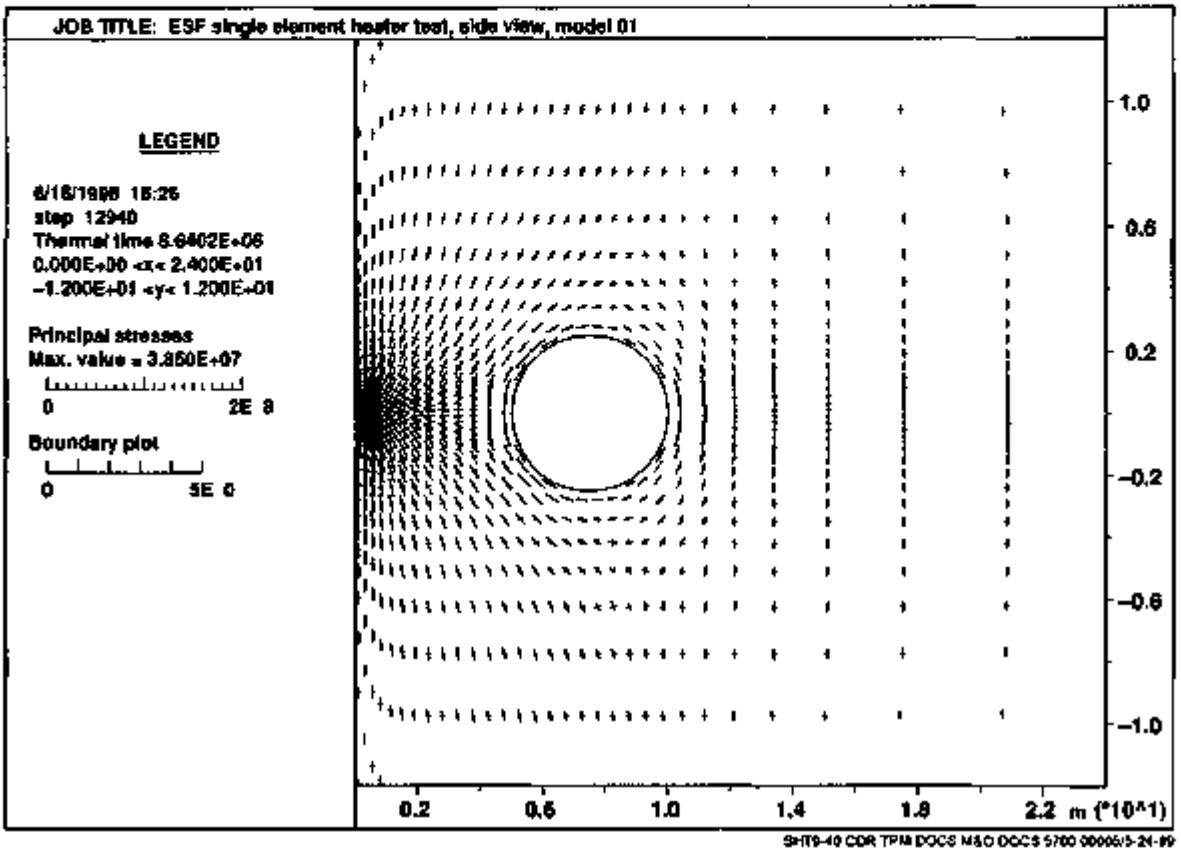

Figure 9-40. Principal Stresses in Pa near the Heater at 100 Days

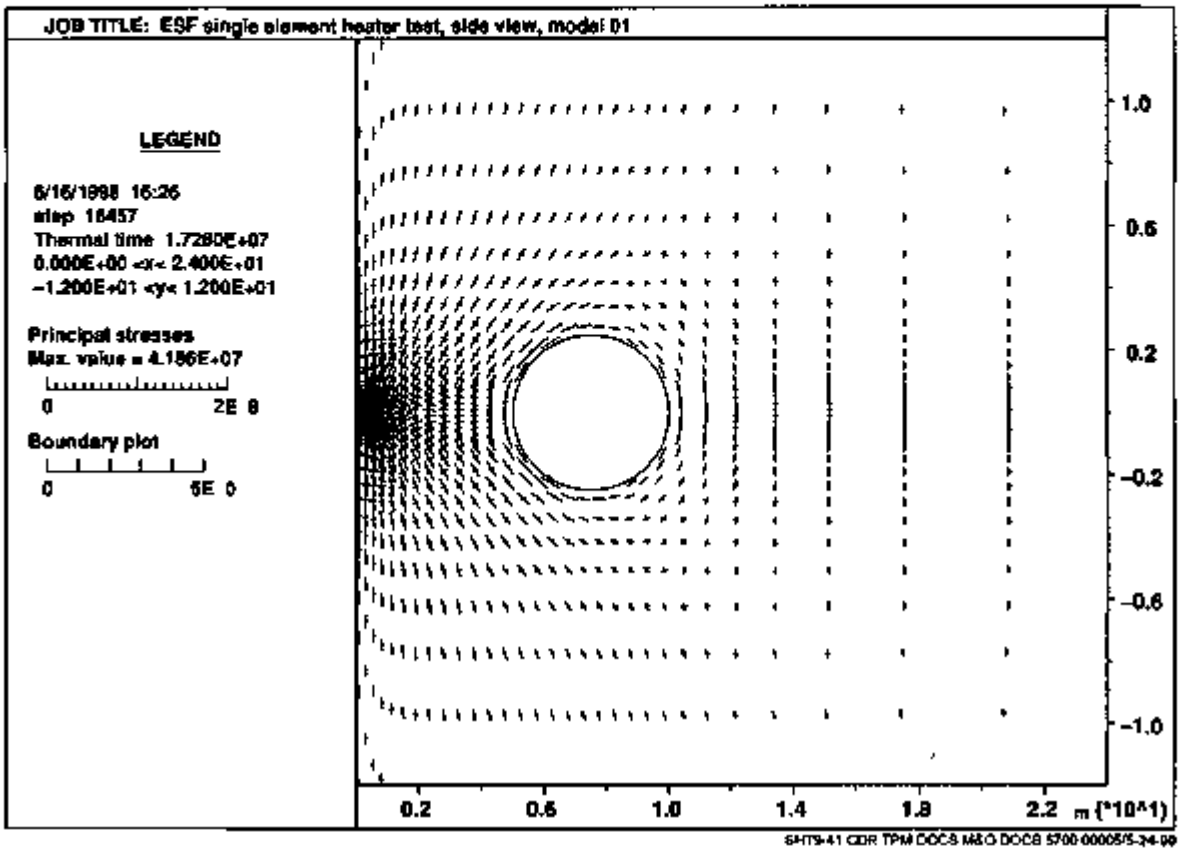

Figure 9-41. Principal Stresses in Pa near the Heater at 200 Days

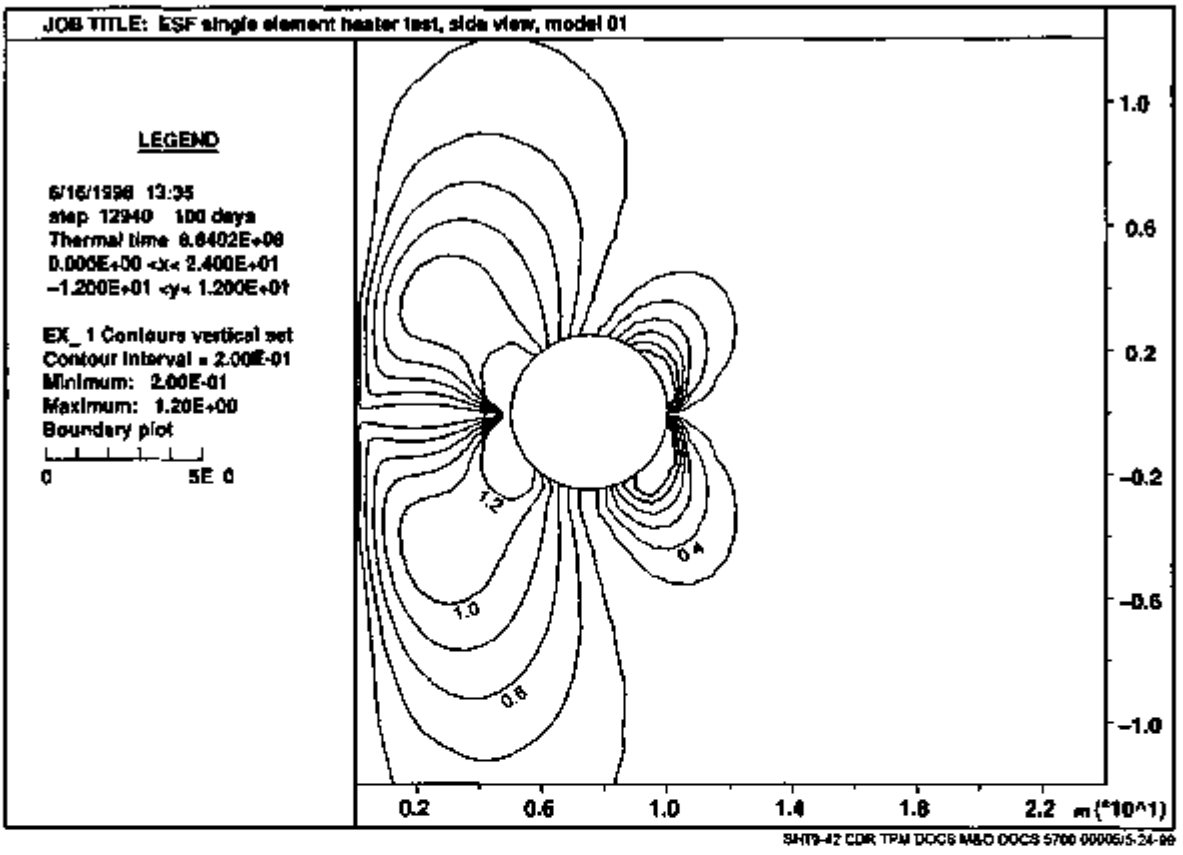

NOTE: Shear slip is expected where the ratio exceeds 1 (areas shown in gray regions).

Figure 9-42. Ratio of Shear Stresses to Frictional Resistance for Vertical Planes at 100 Days

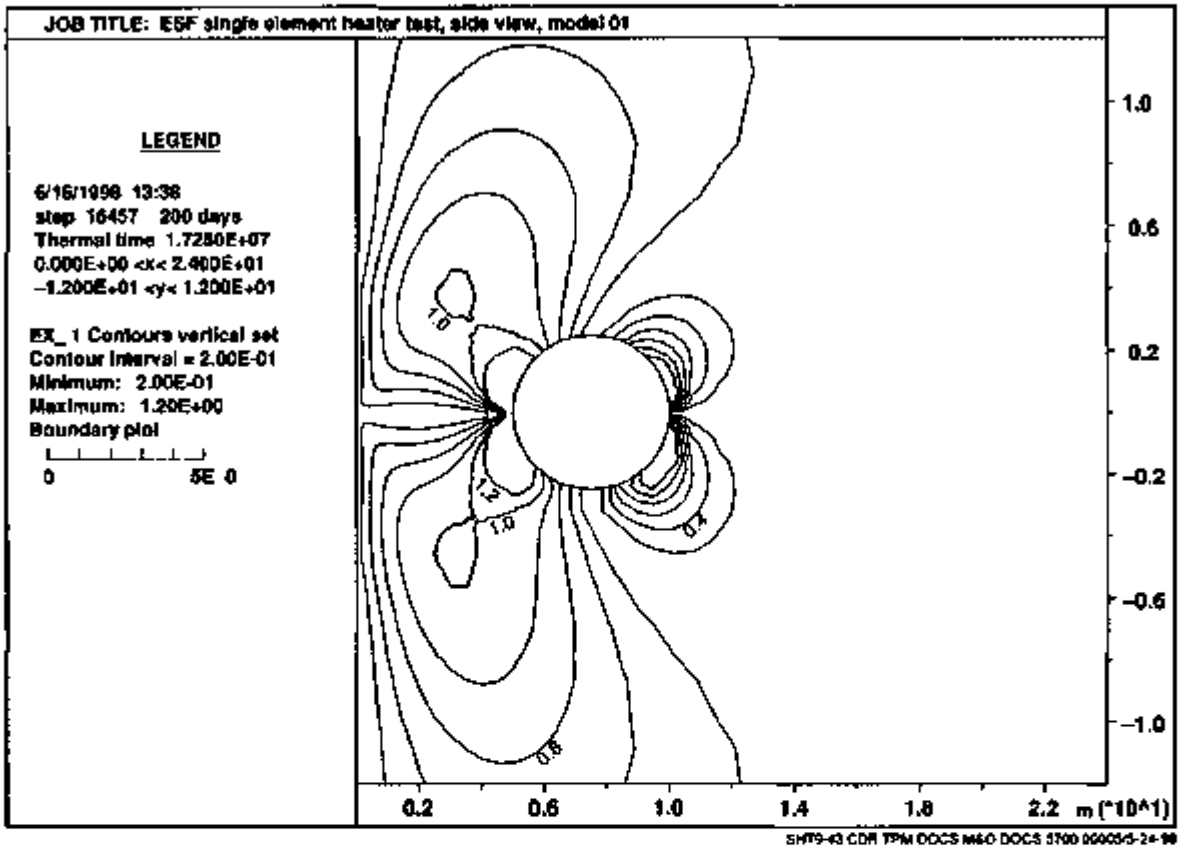

NOTE: Shear slip is expected where the ratio exceeds 1 (areas shown in gray regions).

Figure 9-43. Ratio of Shear Stresses to Frictional Resistance for Vertical Planes at 200 Days

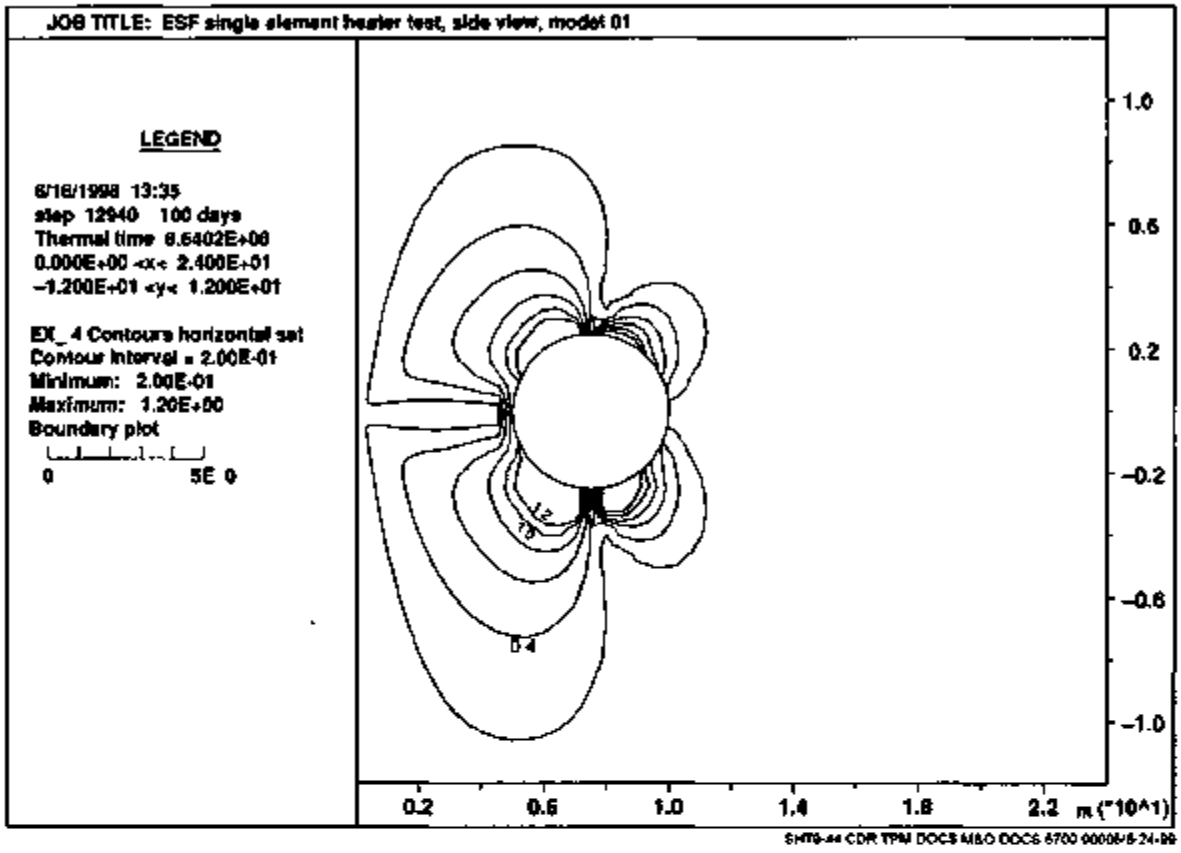

NOTE: Shear slip is expected where the ratio exceeds 1 (areas shown in gray regions).

Figure 9-44. Ratio of Shear Stresses to Frictional Resistance for Horizontal Planes at 100 Days

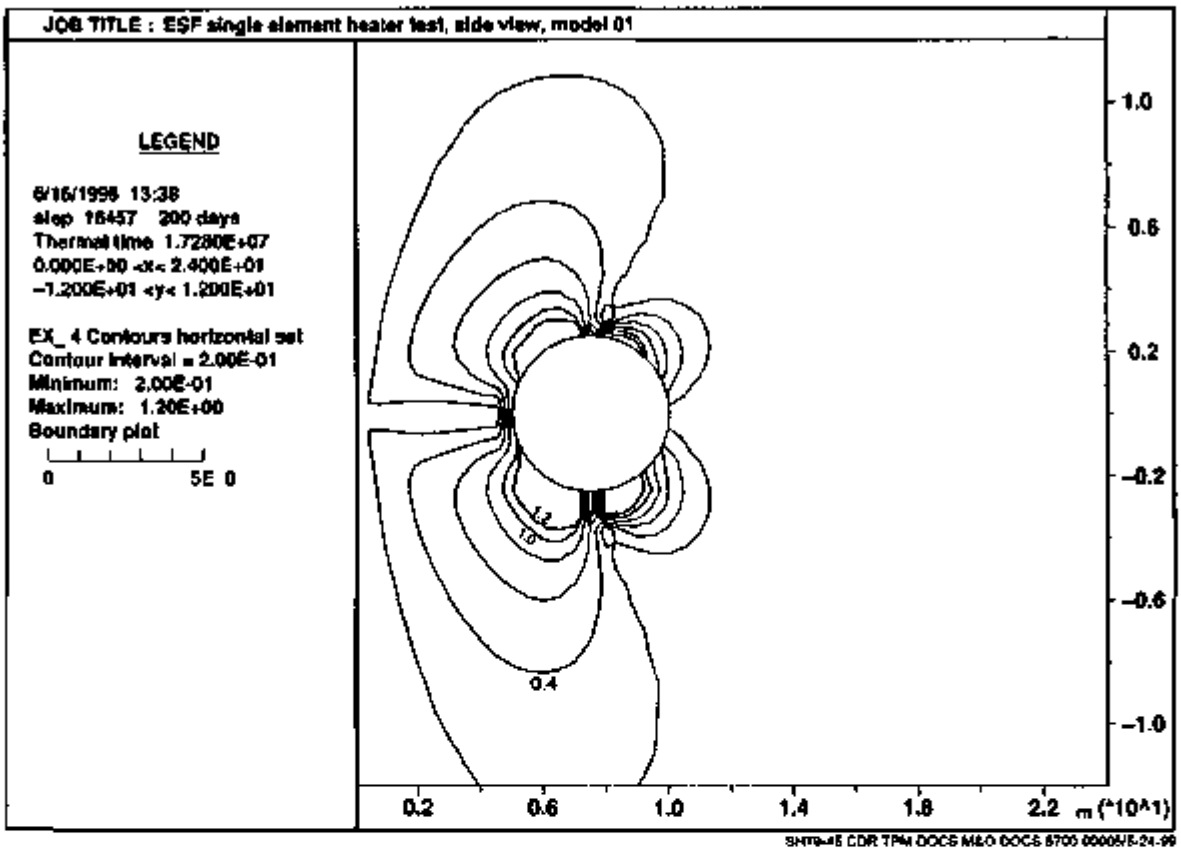

NOTE: Shear slip is expected where the ratio exceeds 1 (areas shown in gray regions).

Figure 9-45. Ratio of Shear Stresses to Frictional Resistance for Horizontal Planes at 200 Days

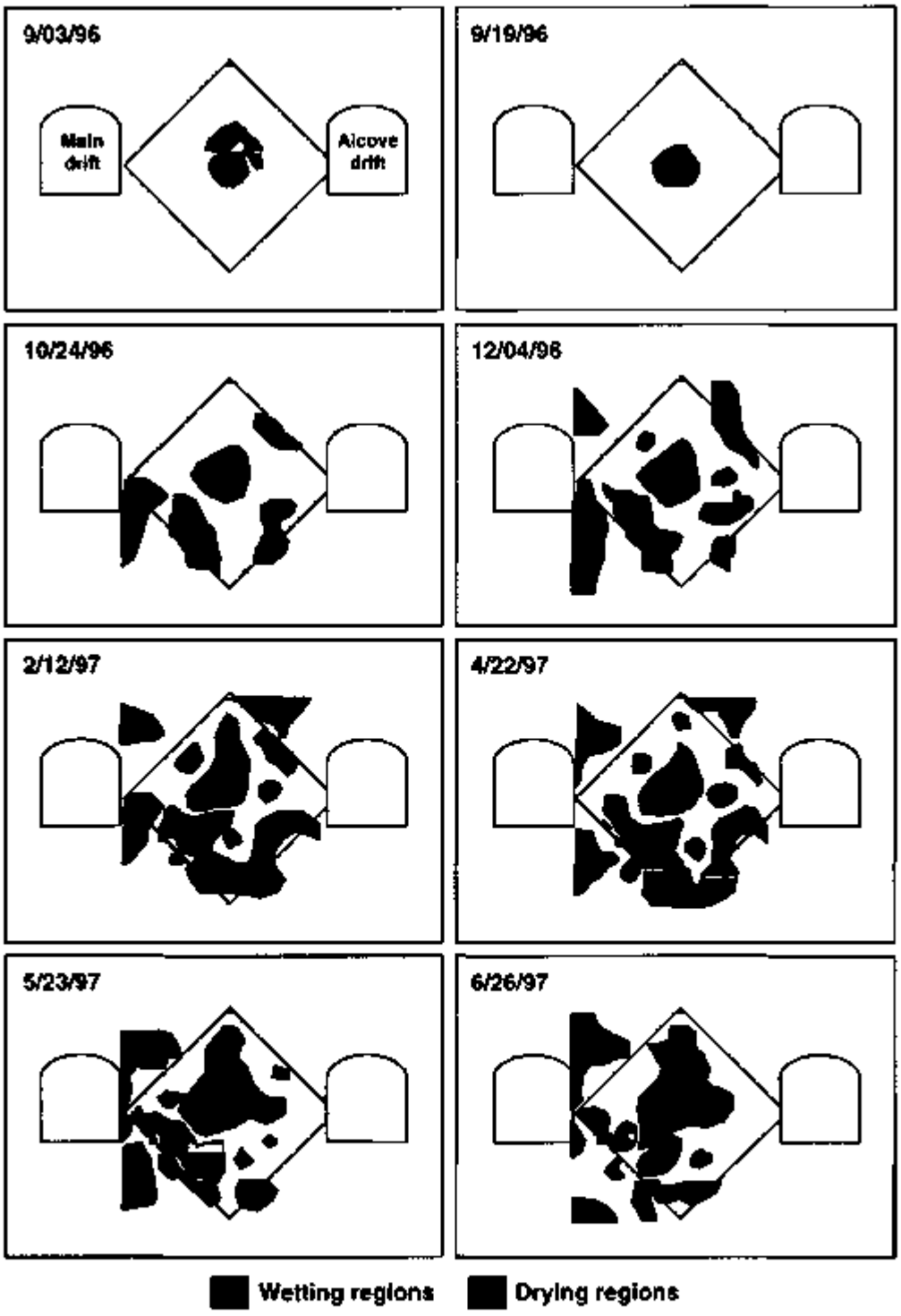

NOTE: The December 4, 1996, tomograph is approximately 100 days after the heater was turned on, and the April 22, 1997, tomograph is approximately 200 days after the heater was turned on. The drying zone is approximately circular and centered around the axis of the heater. The wetting zone extends between the heater and drifts in a U-shaped pattern.

Figure 9-46. ERT Tomographs Showing Drying and Wetting Regions in Cross-Sections of the Test Block

INTENTIONALLY LEFT BLANK

10. CHEMICAL MEASUREMENTS AND ANALYSES

This section focuses on modeling the thermal-chemical processes in the SHT and on interpreting the geochemical data collected during the test. This analysis is performed on the basis of thermal-hydrologic data discussed in Section 8 of this report, previous geochemical studies, and a conceptual model of thermal-hydrological-chemical processes developed from previous modeling efforts.

The geochemical data available from the SHT are limited to two sets of analyses of water samples collected in borehole 16 and mineralogical data from rock samples from overcoring borehole 16 and borehole 2 during the post-cooling period of the test. The interpretive analysis presented here is therefore limited and will be supplemented by more extensive geochemical data from the DST as these become available. For the present time, the results of simulations discussed in this section will be useful in supplementing previous studies of borehole 16 water and in further understanding of thermal-hydrological-chemical processes that may have implications for the assessment of repository performance and waste package design. By comparing field geochemical data with results of numerical simulations, the goal was also to determine whether the quantitative methods and input data used in current thermal-hydrological-chemical models are adequate to provide reliable long-term predictions of repository performance.

10.1 BACKGROUND AND PREVIOUS STUDIES

The SHT was primarily designed to collect thermal, mechanical, and hydrological data. The test was not designed to collect water samples, nor to provide extensive posttest mineralogical data. Ninety chemical sensors were installed for the SHT, but all either failed or could not be used because of calibration problems (CRWMS M&O 1997b, p. 5-53). Several existing boreholes (e.g., 2 and 16) were overcored during posttest characterization to provide mineralogical data on the test alteration products. Mineralogical effects of the SHT were concentrated only on overcores of boreholes that were not originally filled with grout. Analyses of overcores from originally grouted boreholes were not completed because the interaction of the grout with surrounding rock makes the identification of SHT water/rock interaction products essentially impossible.

A detailed analysis of posttest alteration products is presented in Section 6.4. That analysis was based on SEM and XRD analyses of overdrilled cores ESF-TMA-PTC-MPBX-1 (drilled over borehole 2) and ESF-TMA-PTC-NEU-2 (drilled over borehole 16) and identified several mineral phases deposited during the test (Section 10.3).

During air-permeability testing on November 25, 1996, fluid was observed in injection line 16-4 of borehole 16 and subsequently sampled for chemical analysis. Additional samples were also collected from the same location on February 4, 1997, providing a second set of water analyses (Section 10.3). An interpretation of these analytical data was completed by Glassley (1997b) and Glassley and DeLoach (1997). These authors carried out geochemical simulations as part of their evaluation and concluded the water consisted of steam condensate which underwent some, although minimal, chemical interaction with surrounding rock. Analyses of gas samples to help constrain the water chemistry and further evaluate the origin of water in borehole 16 were not conducted because gas analyses were not part of the SHT project scope. Therefore, the two sets of

water samples from borehole 16 constitute the only data providing direct insight into the chemistry of pore/fracture water during the SHT.

10.2 QA STATUS OF WORK

The work completed for this study was performed under the Yucca Mountain Project (YMP) QA program procedures. It is documented in appropriate YMP Scientific Notebooks. The input and output data for computer simulations presented here, as well as the computer program used for these simulations, were submitted to the technical database (DTN: LB980901123142.005).

Specifics on the QA status of data and computer programs used specifically in this section are presented in Subsection 10.2.1. These supplement the general QA status of data and computer programs stated in Section 2 of this report.

10.2.1 QA Status of Data

The data used as input to modeling in this report come from a variety of qualified and unqualified sources. Supporting data for some calculations were drawn from scientific literature cited in the reference section. The QA status of specific analytical data is provided in Table 10-1. Other data were used as follows:

1. Hydrologic parameters and other specifications of the SHT were taken from Section 8 of this report (with QA status further described in Section 2 of this report), and from Birkholzer and Tsang (1996).

2. Kinetic data were adapted from sources discussed in Section 10.5.4.4. These data are unqualified.

3. The thermodynamic database was developed as part of a previous study (Sonnenthal, Spycher, Apps, and Simmons 1998, pp. 23 to 28) with addition of new data in Section 10.5.4.3. It is considered preliminary.

4. The porewater chemistry data were taken from Sonnenthal, Spycher, Apps, and Simmons (1998, p. 63). These data are also preliminary.

All model output data are considered to be the results of exploratory calculations that are semi-quantitative at best because of the large uncertainty of input data

10.2.2 QA Status of Computer Programs

TOUGHREACT Version 1.0 (Section 10.5.1) is the computer program used for all numerical simulations presented in this section. The software tracking number of this version is 10067-1.0-00 and it is a qualified code. Several benchmark tests have been performed to verify the overall behavior of the geochemical reaction and transport modules of this numerical model (Sonnenthal, Spycher, Apps, and Simmons 1998, pp. 40 to 45; Xu, Pruess et al. 1998, pp. 10 to 14).

Version 1.0 of SUPCRT87 which is non-qualified was used for computing solubility products of zeolites (Section 10.5.4). This calculation will be redone with SUPCRT92 Version 1.0 (Johnson, Oelkers et al. 1992). The software tracking number of SUPCRT92 Version 1.0 is 10058-1.0-00, and it is a qualified software. The QA status of the calculations performed by SUPCRT87 Version 1.0 is to be verified (TBV-3568).

Table 10-1. Analytical Data Sources

Data Type, Organization, and Principal Investigator	DTN/ACCN (if available)
XRD Mineralogy, LLNL, Roberts and Viani (1997)	DTN: LL980106404244.050
SEM-EDX, XRD Mineralogy, LANL, Levy (Section 6.4 of this document)	DTN: LASL831151AQ98.001
Mineralogy, USGS, Paces, Marshall, Whelan, Neymark, and Peterman (1996)	MOL. 19970324.0052
UZ Porewater Analyses, USGS, (a) Yang, Rattray, et al (1996) (b) Yang, Yu, et al. (1998)	(a) MOL.19970715.0408 (b) DTN: GS970208312271.002
Borehole-16 Water Analyses, LLNL, (a) Glassley (1997b) (b) Glassley and DeLoach (1997)	(a) DTN: LL970703904244.034 (b) DTN: LL970409604244.030
Gas CO_2 Analyses, LBNL, Conrad (1998)	DTN: LB980715123142.003

10.3 GEOCHEMICAL DATA FROM THE SHT

Mineralogical and water chemistry data collected during the SHT are summarized here to provide a basis for input data to numerical simulations (Section 10.5) and to provide a context for interpretation of simulation results (Section 10.6).

10.3.1 Mineralogical Data

Mineralogical analysis of pre-DST core samples by bulk x-ray diffraction were conducted by Roberts and Viani (1997, p. 9) and provide the basis for mineral volume fractions input in simulations. The most common minerals, in order of decreasing abundance, are K-feldspar, plagioclase, cristobalite and quartz, with minor amounts of zeolites. Calcite was found almost exclusively in fractures (Paces, Marshall, Whelan, Neymark, and Peterman 1996). Estimated volume fractions of these minerals in both matrix and fractures are given in Section 10.5.4.2.

Six- to ten-inch diameter overcore of boreholes 2 and 16, recovered during posttest characterization, were examined using XRD, SEM and EDX methods as described in Section 6.4. In the course of this examination, they identified stellerite, a calcium-rich zeolite, as the predominant zeolitic phase. This zeolite was found to line fractures, and was also observed dispersed in the highly porous matrix adjacent to lithophysae. In both these occurrences, stellerite

was interpreted as a primary mineral (pretest). SEM images indicated that the stellerite was intergrown with, and/or overgrown by K-rich alkali feldspar crystals mostly ±10 mm across, accompanied by smectite and silica. Although the stellerite paragenesis is not certain, it probably formed at a late stage of hydrothermal activity during the terminal phase of deuteric alteration of the Topopah Spring welded tuffs (TSw), and quite possibly at temperatures less than 100°C. $^{87}Sr/^{86}Sr$ ratios of strontium substituting for calcium in the stellerite would probably aid in determining whether the source of the calcium was from the tuff itself or of later pedogenic provenance. The stellerite probably shares similar genetic affinities with heulandite and mordenite, other calcium-rich zeolites observed sparingly and lining fractures within the TSw (e.g., Carlos 1985, 1989, 1993; Levy and O'Neil 1989; Carlos, Bish, and Chipera 1991; Carlos, Chipera, and Bish 1995; Carlos, Chipera, and Snow 1995).

From the above observations, it was assumed for simulations presented later that stellerite is present in fractures (25 percent by volume), but not in the matrix. Other zeolites were assumed absent from the initial pretest mineral assemblage but were included in simulations as possible reaction products (Section 10.5.4.2).

Gypsum, amorphous silica, and calcite were also identified as test alteration products as indicated in Section 6.4 and discussed further in Section 10.6. These minerals were included as possible reaction products in computer simulations (Section 10.5.4.2).

10.3.2 Water Analyses

Two water samples were collected from borehole 16, one on November 25, 1996, and another on February 4, 1997. Both samples were collected from injection line 16-4 of this borehole (zone 3 in Figure 8-3 of this report). The water was considered to be a condensate that had drained through fractures into the borehole (Glassley and DeLoach 1997, p. 6). Chemical analyses of the waters are documented in the *Single Heater Test Status Report* (CRWMS M&O 1997b, Table 5-19, p. 5-49). Analyses of the waters, as described in the latter report, are reproduced here in Table 10-2.

Table 10-2 Analyses of Water Samples from the Single Heater Test

	Suite 1 (November 25, 1996)			Suite 2 (February 3, 1997)	
	SHT Borehole 16			SHT Borehole 16	
	LLNL Data	LANL Data	USGS Analyses	LLNL Data	LBNL Data
Na (mg/l)	16			13 9	
Si (mg/l)	16 8			17 4	
Ca (mg/l)	13			9 76	
K (mg/l)	2 5			2 5	
Mg (mg/l)	1 63			1 16	
pH	6 2			6 9	
HCO_3 (mg/l)	188 *				
F (mg/l)	0 44			0 12	
Cl (mg/l)	2 54	2 1		1 45	
S (mg/l)	0 71				

Table 10-2. Analyses of Water Samples from the Single Heater Test (Continued)

	Suite 1 (November 25, 1996)			Suite 2 (February 3, 1997)	
	SHT Borehole 16			SHT Borehole 16	
	LLNL Data	LANL Data	USGS Analyses	LLNL Data	LBNL Data
SO_4 (mg/l)	1.83	1.5		0.42	
PO^{3-}_4 (mg/l)	<0.03			<0.4	
Nitrate (mg/l)	<0.01			0.15	
NO_3 (mg/l)	1.1			<0.4	
Li (mg/l)	<0.03			<0.03	
B (mg/l)	0.37			0.74	
Al (mg/l)	<0.06			<0.06	
Fe (mg/l)	0.74			0.13	
Sr (mg/l)	0.2		0.22	0.14	
Rb (mg/l)					
Br (mg/l)	<0.2	0.008		<0.4	
del D	-101.7		-93.1	-99.6	-94
del ^{18}O	-12.8		-13.1	-12.9	-13.1
Tritium	0.44+0.19 TU	<0.3 TU			
$^{87}Sr/^{86}Sr$			0.71240		
U (mg/l)			0.0001013		
$^{234}U/^{238}U$			8.03200		

NOTE: Data taken from Table 5-19 of the *Single Heater Test Status Report* (CRWMS M&O 1997b, p. 5-49)

*From charge balance

On the basis of geochemical simulations using v.7.2a of EQ3/6 (Wolery 1992), Glassley and DeLoach (1997, p. 3 to 6) and Glassley (1997b, p. 3) concluded that the waters showed interaction with calcite and some dissolution of feldspars. The waters showed much more dilute concentrations than other waters collected at Yucca Mountain, suggesting their origin as condensates that had undergone only limited water-rock interaction. Glassley and DeLoach noted an inconsistency between the higher than expected sodium concentration in the collected samples relative to their model results and attributed this to uncertainties in the dissolution kinetics for plagioclase. Potassium concentrations, however, were well-described by dissolution of K-feldspar. The calcium concentrations were thought to reflect the interaction of calcite with water where pH is controlled externally, probably by elevated CO_2 partial pressures (P_{CO2}) near the boiling zone (Glassley 1997b, p. 3; CRWMS M&O 1997b, p. 5-52). It was pointed out in the latter reference that the CO_2 could have been derived from carbonate minerals, boiling of water, or movement of CO_2-rich pore gases.

Strontium isotopic ratios ($^{87}Sr/^{86}Sr$) in borehole-16 waters (CRWMS M&O 1997b, p. 5-49) were also similar to those observed in calcite at Yucca Mountain (Paces, Neymark, Marshall, Whelan, and Peterman 1996), indicate that very little reaction with the tuff matrix took place, which would have shifted the waters to higher ratios. Strontium concentrations in the water are also consistent with significant calcite interaction, because they are much higher than would be expected by dilution (Sonnenthal 1997).

Oxygen and deuterium isotopic ratios plotted near the meteoric water line indicating that the water was likely formed by near complete boiling and subsequent condensation of water (Sonnenthal 1997). Another possibility may be that the condensate waters were originally lighter in isotopic composition, and subsequently reequilibrated with matrix porewaters before collection.

The results of strontium and uranium analyses are shown in Table 10-3 below and plotted in Figure 10-1. USGS procedure GCP-03, R3-M2 was used for uranium analysis, and USGS procedure GCP-12, R4 was used for strontium analysis. Although the SHT water is, in general, depleted in major ions compared to typical porewater, the concentrations of strontium and uranium are not unreasonable for porewater (there are limited data on porewater uranium contents). The data are considered representative of the collected water with the exception of the February 4, 1997 sample with bar code number SPC00521246. This sample was collected in glass and not acidified, which evidently resulted in low uranium concentration; therefore it is not plotted in the figure although its other measured parameters agree with the second February 4, 1997 sample.

Table 10-3 Results of Strontium and Uranium Analysis of SHT Waters

Sample Management Facility Bar Code	Date Collected	Delta ^{87}Sr	[Sr] (ppm)	$^{234}U/^{238}U$	[U] (ppb)
SPC00520853	Nov. 25, 1996	4 53	0 198	8.03	0 101
SPC00521246	Feb 04, 1997	4 43	0 147	4 69	0 035
SPC00521248	Feb 04, 1997	4,43	0 147	4.56	0 078
SPC00522242	May 22, 1997	4 61	0 098	4.13	0 033

The decreases in strontium and uranium concentrations with time mimic those of the major cations, although the decreases are greater for strontium and uranium. The ratio $^{87}Sr/^{86}Sr$, expressed as $\delta^{87}Sr$, remains essentially constant and is within the range measured on porewater from these strata, which is also the same as the strontium isotope composition of latest fracture-lining calcite. In contrast, the uranium isotope composition changes from a $^{234}U/^{238}U$ activity ratio of about 8 in the earliest sample to 4.1 in the latest sample. This change is well outside the typical analytical error of about 0.1 (2σ).

These data indicate that the SHT water has three probable components: 1) very dilute water condensed from vapor (to explain the low concentrations of major constituents), 2) porewater (because the Sr and later U isotopic data are consistent with porewater), and 3) fracture-flow water along a previously dry path (in order to get the high $^{234}U/^{238}U$ from accumulation of ^{234}U on fracture surfaces). In addition, some dissolution of calcite is probable since the SHT water has similar alkalinity to porewaters that are essentially saturated with respect to calcite. Calcite dissolution alone (compared with some inherited or added porewater) is unlikely to explain the later $^{234}U/^{238}U$ ratio of about 4, because increased dissolution of older calcite (or other minerals) would lead to $^{234}U/^{238}U$ closer to the secular equilibrium value of 1. The decrease in concentration with time suggests a lesser contribution from calcite dissolution and/or a greater contribution from dilute condensate with time.

10.4 CONCEPTUAL MODEL OF THERMAL-HYDROLOGICAL-CHEMICAL PROCESSES AFFECTING THE SINGLE HEATER TEST

The thermal, hydrological, and chemical processes resulting from heating the host-rock during the SHT are briefly reviewed in this section, with a particular emphasis on water-gas-rock interaction processes that govern the behavior of the chemical system in the test area. The thermal-hydrological-chemical processes that may occur during thermal tests have been previously investigated by Glassley and DeLoach (1997) and Glassley (1997b) for the SHT, and by Sonnenthal, Spycher, Apps, and Simmons (1998, pp. 46 to 72) and Sonnenthal, Spycher, and Apps (1998, pp. 3-1 to 3-12) for the DST. Additional studies of thermal-hydrological-chemical processes at repository scale for the Yucca Mountain project have been presented in *Near Field/Altered Zone Models* (Hardin 1998), in Sections 5.3 to 5.7. The investigations of these authors are used to develop a conceptual model that can be used as a basic framework for interpretive analyses presented in Sections 10.5 and 10.6. The thermal-hydrological-chemical processes accompanying the SHT and other thermal tests are similar to those anticipated to affect the proposed repository at Yucca Mountain and, therefore, are important for the assessment of long-term repository design and performance.

The evolution of the chemical regime in the unsaturated zone surrounding the SHT is closely related to the hydrologic regime driven by the heating and cooling stages of the test. The main thermal-hydrological-chemical processes affecting the SHT (and, by analogy on a larger scale, the proposed repository) are schematically illustrated in Figure 10-2. Several zones are identified. The dryout zone extends immediately around the heat source, surrounded by a boiling zone, then by a condensation zone. Within the zones of boiling and condensation may lie an isothermal region where reflux is important, termed the "heat pipe" region. A drainage zone extends at some distance beneath the heat source, where water accumulates from drainage of steam condensate into fractures. In addition, recent simulations of the DST (which is essentially a longer version of the SHT) seem to indicate the formation of a CO_2 halo expanding away from the heat source as CO_2 is volatilized from pore and fracture waters in hot areas (Sonnenthal, Spycher, Apps, and Simmons 1998, p. 64; Sonnenthal, Spycher, and Apps 1998, p. 3-8; Conrad 1998, p. 3-6).

Each zone of the conceptual model is associated with typical chemical processes, as discussed in separate sections below. It is important to realize that in a natural setting such as the environment of the SHT, rock fracture and matrix heterogeneities are likely to result in more irregular zoning patterns than those shown on Figure 10-2 or resulting from the simulations presented in Section 10.5. Therefore, at a given time in a real system, the transition from dryout to boiling, condensation, or drainage zones could occur closer to the heat source in some areas than in others.

10.4.1 The Dryout Zone

During the heating stage of the test, rocks are heated significantly above the water boiling point, and evaporation and boiling of porewaters takes place. Areas close to the heat source eventually dry out, precipitating all salts previously in solution. This zone is currently not of primary interest in the study of thermal-hydrological-chemical processes because it is absent of aqueous geochemical processes. However, upon rewetting during cool-down, the dissolution of salts

precipitated previously in this zone is likely to affect the chemical behavior of fluids imbibed in this zone.

10.4.2 The Boiling Zone

The boiling zone comprises the area between the dryout zone and the condensation zone, where porewater is boiling but dryout conditions are not reached. If the boiling zone becomes significant in size, it can develop into a "heat-pipe" zone, which is essentially a zone of nearly constant temperature where porewater is continuously boiled, driven away as steam, condensed and refluxed back towards the heat source. Water saturation in fractures and matrix typically decrease from the outer edge of the boiling zone (or if present, heat-pipe zone) towards the dryout zone. CO_2 volatilization generally results in a pH increase of boiling waters (Sonnenthal, Spycher, Apps, and Simmons 1998, p. 55) from the reaction

$$HCO_3 + H^+ \rightarrow CO_{2(gas)} + H_2O \qquad (10\text{-}1)$$

although the development of heat-pipe effects may result in pH remaining nearly constant or increasing only slightly in the heat-pipe zone (Sonnenthal, Spycher, and Apps 1998, p. 3-48). The pH increase, together with the higher temperature, generally results in the precipitation of calcite and dissolution of silica phases in the boiling zone. Along with extreme evaporation and boiling, saturation with respect to calcium and magnesium sulfates and hydrated silicates may also occur.

Within a dual permeability framework (fractures and matrix), the salt concentration of solutions in fractures in the boiling zone can greatly increase due to evaporative concentration, even though the liquid saturation in those fractures may not decrease significantly. This is caused by an inflow of matrix water into fractures and subsequent boiling of this water in the fractures, with constant replenishment of water from the matrix keeping the saturation from decreasing. This phenomenon was reproduced in the numerical simulations presented in Section 10.5 and can produce very high salt loads where the boiling zone meets the dryout zone (typically a very thin zone, in the order of a few centimeters in the SIIT simulations).

10.4.3 Condensation Zone

A condensation zone occurs beyond the volume of rock in which boiling takes place. Although the boiling point of water at Yucca Mountain is near 95°C, the condensation boundary temperature may be modified by capillary action and dissolved salts. The main chemical processes affecting the condensation zone include dilution of porewaters with condensate, pH decrease due to uptake of CO_2 from the vapor phase (reverse of reaction 10-1), enhanced dissolution of calcite, and precipitation of silica phases at declining temperatures in places where the aqueous liquid drains toward cooler regions. The condensation zone would technically include the outer edge of a heat-pipe region. However, it typically extends much farther than the latter, and may occur from the condensation of H_2O vapor resulting from evaporation alone, without boiling.

10.4.4 Drainage Zone

The current conceptual model of the SHT includes a drainage zone mostly beneath the heat source (Figure 10-2). This zone results from steam condensation in fractures surrounding the heat source followed by gravity-driven downward flow, which causes the water saturation in fractures below the heat source to increase more than elsewhere around the heated area (see also Section 8.7 of this report). Because the water draining in fractures originates from steam condensation, its pH is typically lower than in matrix water because of CO_2 uptake from the vapor phase upon condensation. As a result, more dissolution of calcite and other pH-dependent mineral phases is expected to occur in the drainage zone than elsewhere in the test area. However, drainage below the heat source occurs towards cooler areas and is expected to induce the precipitation of silicates in this zone. Therefore, the net effect on overall porosity changes in the drainage zone may vary depending on the amounts of minerals precipitating by cooling versus those dissolved by the lower-pH draining water.

10.4.5 CO_2 Halo

Simulations of the DST presented by Sonnenthal, Spycher, Apps, and Simmons (1998, p. 64) and Sonnenthal, Spycher and Apps (1998, p. 3-8) indicate the formation of a CO_2 halo expanding away from the heat source with time, as CO_2 volatilized from matrix water is transported in fractures (mainly by advection) away from the hot areas. Data collected from the DST indicate that this halo is present (Conrad 1998). In a natural setting, it is likely that CO_2 and steam flow along preferential fracture pathways result in localized areas of increased CO_2 partial pressures without necessarily creating a complete halo around the heat source. The zones of increased CO_2 partial pressures typically correspond to zones of decreased pH, and therefore increased calcite dissolution.

10.4.6 Zoning During Cooling Phase

During the cooling phase of the test, the boiling and condensation zones retreat towards the location of the initial heat source. As the boiling front retreats, a coating of mineral precipitates may be deposited along fractures and perhaps to some degree into the rock matrix. Above the location of the initial heat source, the downward-retreating front may induce redissolution of previously precipitated salts, and concentration of the salt load at the migrating front.

During cool-down, the water composition is dominated by condensate and its actual composition depends on the extent of rock-water interaction. Waters of this more evolved nature are most likely to interact with repository materials.

10.5 QUANTITATIVE ANALYSIS OF THERMAL-HYDROLOGICAL-CHEMICAL PROCESSES

The following investigations were documented in accordance with LBNL procedure YMP-LBNL-QIP.SIII.0 (c), *Scientific Investigation.*

Numerical simulations of coupled thermal-hydrological-chemical processes affecting the SHT are presented in this section. These simulations follow the development of the conceptual and numerical models for thermal-hydrological-chemical processes presented for the DST (Sonnenthal, Spycher, Apps, and Simmons 1998, pp. 57 to 63; and Sonnenthal, Spycher, and

Apps 1998, pp. 3-5 to 3-11). In addition, limited water sampling and posttest mineralogical studies have provided data (Section 10.3) for which comparisons to the simulations can be made to assess the reliability of the model and its input data.

The basis of the thermal-hydrologic model used here is the two-dimensional dual-permeability mesh and thermal-hydrological parameters described in Birkholzer and Tsang (1996, pp. 8 to 12, 15 to 20, and p. 28) and further discussed in Section 8.7 of this report. A conceptual model for treating the rate-limited reactions of minerals, gas, and water coupled to the thermal-hydrologic calculations is presented in Sonnenthal, Spycher, Apps, and Simmons (1998, pp. 37 to 40). Details on numerical methods can be found in Xu and Pruess (1998) and references therein.

10.5.1 Numerical Model and Processes Considered

The numerical model used for this study is Version 1.0 of TOUGHREACT (Xu and Pruess 1998; Xu, Gerard et al. 1997; and Xu, Pruess et al. 1998). The software tracking number of this version is 10067-1.0-00 and it is a qualified code. TOUGHREACT considers heterogeneous chemical systems including an arbitrary number of primary chemical species and minerals. The precipitation and dissolution of minerals is computed under equilibrium and/or kinetic (i.e., nonequilibrium) constraints. Also considered is the transport of an arbitrary number of gases (such as CO_2) in an air/vapor phase at equilibrium with the aqueous solution. Within the dual-permeability framework considered here (fractures and matrix), gases in each medium are in equilibrium with the fluid in that medium.

An important aspect of TOUGHREACT is that its core structure is the TOUGH2 code (Section 8.7 of this report), enabling it to treat various geochemical processes in the framework of dual permeability/porosity, multiple-interacting continua, and equivalent continuum formalisms for fractured porous media, along with the transport of water, air, and heat. The full equations for heat, water, and gas flow are solved simultaneously, followed by the transport (advection-diffusion) of primary aqueous and gaseous chemical species in a sequential fashion, and then by the solution of the chemical system at each gridblock. Thus, the full multiphase thermal-hydrologic system is solved as in the modeling presented in Section 8.7 of this report, along with solving the rate-limited precipitation and dissolution of solid phases and the speciation of aqueous and gaseous species.

The geochemical and transport calculation methods incorporated in TOUGHREACT have been enhanced as part of this study to deal with boiling conditions and rock matrix-fracture interactions such as those arising from the Yucca Mountain thermal tests. Coupled processes included in the simulations include:

- Reactive advection-diffusion of CO_2 in the vapor phase
- Reactive advection-diffusion of aqueous species (up to 10 primary components and over 30 derived aqueous species for the present case)
- The precipitation and dissolution of minerals under kinetic and/or equilibrium constraints (up to 18 minerals for the present case)

- Coupled flow, transport, and chemical reaction within a dual permeability framework (matrix/fractures) where differing mineralogies in matrix and fractures (and in respective subdomains as necessary) are specified

- Full interaction between chemical processes in matrix and fractures (e.g., CO_2 volatilization from the matrix water and condensation/dissolution into fracture water; differing mineral precipitation and dissolution patterns in fractures and matrix, depending on the hydrochemical interactions between these two media)

- All thermal and hydrological processes discussed in Section 8.7 of this report, with the minor difference that no vapor pressure lowering due to capillary pressure was considered for the simulations presented here (i.e., the TOUGH2 module EOS3 was used while simulations in Section 8.7 of this report were carried out with module EOS4).

The effect of porosity change (from mineral precipitation/dissolution) on matrix and fracture permeability is not currently considered in the model. For the simulations presented here (which cover a short time frame), the amount of mineral precipitation and dissolution is very small compared to the matrix and fracture porosities, so that the mineral precipitation or dissolution effects on permeability can be assumed negligible.

Before reaching complete dryout conditions, chemical interactions stop being computed when the liquid saturation drops below 10^{-4} and/or the ionic strength of the solution exceeds 2. This is because chemical reactions cannot be computed without an aqueous phase present, and calculation methods are not suitable for elevated ionic strengths.

10.5.2 Grid and Boundary Conditions

The numerical results presented in this report are based on the two-dimensional dual-permeability grid, thermal-hydrologic parameters, and boundary conditions for the SHT developed by Birkholzer and Tsang (1996, pp. 15 to 20, 28) and as improved and further discussed in Section 8.7 of this report. The computational mesh is shown in Figure 10-3.

10.5.3 Thermal, Hydrological, and Transport Input Parameters

Details on the heating schedule, thermal-hydrologic parameters and grid generation can be found in Section 8.7 and in Birkholzer and Tsang (1996). Briefly, the base case model considers heating at approximately 94 percent full power for the first nine months of the test (3.758 kW), followed by eight months of cooling without heat input. Maximum temperatures in the dryout zone reached over 300°C during the test. The cooling phase of SHT ended approximately seven months after the heat source was turned off. The model was run for an eighth month of cooling to provide final results that coincide approximately with the time when boreholes 2 and 16 were overcored.

Although the rock properties and lithologic units vary over the area of influence of the SHT, they are assumed to be uniform for the simulations, and equivalent to the properties of the Tptpmn lithologic unit of the Topopah Spring Tuff (Birkholzer and Tsang 1996, pp. 8 to 12). For the simulations presented in this report it is assumed that there is no percolation flux at the top of the

model boundary for the entire period of the SHT. This assumption is considered appropriate because the percolation flux is very small (in the range of a few millimeters per year) compared to the duration of the test simulations (seventeen months). The bottom boundary and all drifts are considered to have a constant pressure and temperature, and therefore they are also assumed to have a constant chemical composition.

The diffusion coefficient of aqueous species was estimated to be 10^{-9} m^2/sec from data in Weast (1985, p. F-45). The coupled flow-transport-reaction calculation methods assume that the diffusion coefficient is the same for all aqueous species (e.g. Steefel and Lasaga 1994, p. 537). The diffusion coefficient of CO_2 in the vapor phase was estimated to be 2×10^{-5} m^2/sec from data at 0°C in Weast (1985, p. F-45) extrapolated to an average temperature of 50°C using methods in Lyman et al. (1990, Equations 17-11 and 17-16, and references therein). The tortuosity was assumed to be 0.2 in fractures and matrix. This parameter cannot be exactly determined, and a value of 0.2 is within a typical range of values (e.g., Bear 1972).

10.5.4 Chemical Input Parameters

Model input parameters for chemical processes considered in the coupled thermal-hydrological-chemical simulations include starting water and gas compositions, initial fracture and matrix mineralogies, other secondary mineral phases that may form as the result of thermal-hydrological-chemical processes, and thermodynamic and kinetic data for all considered reactive minerals, gases, and aqueous species. Except for mineral reactive surface areas and new thermodynamic data as discussed in the following subsections, these chemical input parameters were the same as those employed in thermal-hydrological-chemical simulations presented in Sonnenthal, Spycher, Apps, and Simmons (1998, pp. 58 to 63) for the DST. These data are summarized below. The modeled chemical system is assumed to be initially homogeneous with respect to mineral proportions, porewater chemistry, and all other geochemical parameters.

The Thermomechanical Alcove Extension and the Observation Drift were treated as zones without mineral reactions, but with a constant CO_2 partial pressure fixed at the value shown in Table 10-4 (approximately 1430 ppmV). This value is somewhat elevated compared to ambient concentrations (around 450 ppmV) measured by Conrad (1998, pp. 3-2 and 3-3) in the Observation Drift of the DST. This may result in predicted CO_2 partial pressures that are somewhat overestimated near the alcoves. However, in the proximity of the heater, the effect of the alcove boundary on calculated P_{CO2} is not believed to be significant.

Table 10-4. Initial Matrix and Fracture Water Composition for TOUGHREACT Simulations

	Average (mg/L)
Ca	27
Mg	5
Na	91
HCO_3^-	191 (219*)
Cl^-	41
NO_3^-	13
SO_4^{2-}	40

Table 10-4 Initial Matrix and Fracture Water Composition for TOUGHREACT Simulations (Continued)

Average (mg/L)	
SiO_2	60
Al	$1 \times 10^{-6**}$
K	4**
pH	8.2
P_{CO2} (bars)	1.43×10^{-3} (calculated at 25°C)

Source: Sonnenthal, Spycher, Apps, and Simmons 1998, p. 63

NOTE: A subset of these concentrations was used for some of the simulations as described in the text

*Adjusted
**Estimated

10.5.4.1 Initial Water and Gas Compositions

The starting matrix and fracture water compositions were assumed to be identical. The starting water composition (Table 10-4) was averaged from analyses of samples collected in boreholes UZ-16, SD-9, and SD-12 derived from Yang, Rattray et al. (1996, pp. 14 to 16) and Yang, Yu et al. (1998, Table 4, pp. 12 and 13). Detailed discussions of these porewater compositions can be found in these references and in Apps (1997); a discussion of the averaging technique and rationale for it can be found in Sonnenthal, Spycher, Apps, and Simmons (1998, pp. 62 to 63).

For consistency with the starting water composition, the initial CO_2 concentration in fractures and matrix pores was calculated to reflect the partial pressure at equilibrium with the porewater (Table 10-4) at 25°C and atmospheric pressure of 1 bar, corresponding to a concentration of approximately 1430 ppmV.

10.5.4.2 Mineralogy

Initial matrix and fracture mineralogies are shown in Table 10-5. The primary distinction between fractures and matrix is the presence of stellerite (a zeolite observed to amount up to 25 percent volume in fractures) and small amounts of calcite and illite in fractures, and absence of these minerals in the matrix.

The volume fractions of minerals in matrix were estimated from bulk mineral abundances reported by Roberts and Viani (1997, p. 9) and those given in Section 6.4 of this document and an assumed effective mineral reactive volume fraction of 0.85. The abundances of mineral end members albite and anorthite were recalculated based on the An content of albite given by Johnson, Knauss, Glassley et al. (1998, Table 6, p. 98).

Systematic analyses of fracture mineralogies in the Topopah Spring welded tuff have not been reported. For this reason, the volume fractions of minerals in fractures were assumed the same as those in the matrix, but normalized to include 2 percent (volume) calcite based on a range of observations by Paces, Neymark, Marshall, Whelan, and Peterman (1996), and an estimated 5 percent (volume) illite (arbitrary) to account for clay minerals. The volume fractions were then

renormalized to include an additional 25 percent (volume) stellerite estimated from a range of values reported in Section 6.4.

Table 10-5. Initial Mineral Volume Fractions Assumed in TOUGHREACT Simulations

Minerals	Vf (matrix)	Vf (fractures)
Quartz	0.0967	0.0746
Cristobalite-α	0.2179	0.1681
Am SiO_2	0.0	0.0
Calcite	0.0	0.015
Microcline	0.2860	0.2201
Albite-low	0.2374	0.1831
Anorthite	0.0079	0.0065
Kaolinite	0.0	0.0
Illite	0.0	0.0038
Sepiolite	0.0	0.0
Smectite-Na	0.0	0.0
Smectite-K	0.0	0.0
Smectite-Ca	0.0	0.0
Smectite-Mg	0.0	0.0
Stellerite	0.0	0.25
Heulandite	0.0	0.0
Mordenite	0.0	0.0
Gypsum	0.0	0.0

NOTE: Minerals with zero volume fractions are included in the simulations as possible reaction products not initially present at the start of simulations.

10.5.4.3 Thermodynamic Data

Solubility products of albite, k-feldspar (microcline), illite, smectites, kaolinite, sepiolite, calcite, quartz and cristobalite were identical to those recomputed in Sonnenthal, Spycher, Apps, and Simmons (1998, p. 28 and references therein). Solubility products of zeolites were computed as part of the present study as described below. Data for other minerals and aqueous phases were taken from the database of Version 7.2b of EQ3/6 (Wolery 1992), which consists mostly of data from SUPCRT92 (Johnson, Oelkers et al. 1992) and from Pokrovskii and Helgeson (1995). The software tracking number of Version 7.2b of EQ3/6 is 10075-7.2bLV-00, and it is a qualified software.

In modeling the thermal-hydrological-chemical evolution of the SHT, it is desirable to incorporate any phases that might participate either as reactants or products (precipitates) during the course of the test. As mentioned in Section 10.3.1, the zeolite minerals heulandite, mordenite and stellerite were identified in core samples from the SHT area. The inclusion of these minerals in the thermodynamic database of the TOUGHREACT code is therefore appropriate, as any one could participate in modifying the chemical evolution of the system. Fortunately, the $\Delta G^\circ_{f,298}$, $\Delta G^\circ_{f,298}$, $S^\circ_{f,298}$ and V° of these zeolites have been calculated (CRWMS M&O 1999), affording a basis for calculating their solubility products as a function of temperature. The reference CRWMS M&O 1999 is a input transmittal to a design input request for data on the thermodynamic properties of

zeolitic minerals, and submission of this data to the Technical Data Management System (TDMS) is to be verified (TBV-3572). The calculations were conducted as follows:

1. The Maier and Kelley (1932) heat capacity function for each zeolite was calculated according to the procedures recommended by Helgeson et al. (1978).

2. $\Delta G^{\circ}_{f,298}$, $\Delta G^{\circ}_{f,298}$, $S^{\circ}_{f,298}$, V° and the Maier-Kelley heat capacity function terms for each zeolite was entered in the SPRONS96.DAT database of SUPCRT92 (Johnson, Oelkers et al. 1992).

3. The dissolution reaction product constants with respect to each zeolite were calculated with respect to the aqueous species and quartz as a reaction product calculated along the saturation curve for water at 0°, 25°, 60°, 100°, and 150°C.

4. The final solubility products at the above-indicated temperatures were calculated by addition of the quartz solubility products calculated from the equation by Rimstidt (1997, p. 2,557). In this way, the application of erroneous data for SiO_2(aq), presently in the SPRONS96.DAT database could be conveniently circumvented.

A summary of the thermodynamic properties of heulandite, mordenite and stellerite used to calculate their solubility products is given in Table 10-6.

Table 10-6. Summary of Thermodynamic Properties of Calcium-Rich Zeolites

Mineral Name	Chemical Formula [1]	$G^{o}_{f,298}$ [2] (kcal.mol^{-1})	$\Delta H^{o}_{f,298}$ [2] (kcal.mol^{-1})	S^{o}_{298} [2] (kcal.mol^{-1}.K^{-1})	V^{o} [2] (cm^{3}.mol^{-1})	Maier-Kelley Coefficients [3]		
						a (cal.mol^{-1})	b x 10^{3} (cal.mol^{-1}.K^{-2})	c x 10^{-6} (cal.mol^{-1}.K)
Heulandite	$(K_{0.4}Na_{1.0}Ca_{3.3})Al_{8.0}Si_{28.0}O_{72}$·$26H_2O$	-9440.15	-10251.20	743.28	1266.4	784.66	281.56	103.83
Mordenite	$(K_{0.9}Na_{2.1}Ca_{1.5})Al_{5.0}Si_{30.0}O_{72}$·$22H_2O$	-9055.23	-9814.05	708.05	1273.5	697.62	289.84	102.86
Stellerite	$(Ca_{3.9}Na_{0.1})Al_{7.9}Si_{28.1}O_{72}$·$28H_2O$	-9550.69	-10389.20	770.63	1331.0	766.78	278.58	103.28

[1] From Broxton et al. (1986) for heulandite and mordenite. From Carlos, Chipera, and Bish (1995, p. 57) for stellerite.

[2] CRWMS M&O 1999

[3] $C^{o}_{P_r} = a + bT - cT^{-2}$ (Maier and Kelley 1932, p. 3244). Coefficients from oxide compounds and zeolitic water according to the method prescribed by Helgeson et al. (1978).

A tabulation of the calculated solubility product constants for the three zeolites is given in Table 10-7 for the following reactions:

Heulandite: $(K_{0.4}Na_{1.0}Ca_{3.3})Al_8Si_{28}O_{72} \cdot 26H_2O + 32H^+ =$

$$0.4K^+ + Na^+ + 3.3Ca^{2+} + 8Al^{3+} + 28SiO_2(aq) + 42H_2O \quad (10\text{-}2)$$

Mordenite: $(K_{0.9}Na_{2.1}Ca_{1.5})Al_6Si_{30}O_{72} \cdot 22H_2O + 24H^+ =$

$$0.9K^+ + 2.1Na^+ + 1.5Ca^{2+} + 6Al^{3+} + 30SiO_2(aq) + 34H_2O \quad (10\text{-}3)$$

Stellerite: $(Ca_{3.9}Na_{0.1})Al_{7.9}Si_{28.1}O_{72} \cdot 28H_2O + 31.6H^+ =$

$$3.9Ca^{2+} + 0.1Na^+ + 7.9Al^{3+} + 28.1SiO_2(aq) + 43.8H_2O \quad (10\text{-}4)$$

Table 10-7. Solubility Products, K_s, of Calcium-Rich Zeolites

Mineral Name	$\log K_s(T_{°C})$				
	0	25	60	100	150
Heulandite	-2.359	-10.134	-18.927	-26.742	-34.237
Mordenite	-35.232	-37.805	-40.592	-42.866	-44.881
Stellerite	-5.397	13.261	-22.147	-30.036	-37.598

To illustrate the procedure adopted with respect to steps 3 and 4 above, stellerite is used as an example. The equation to describe the solubility of stellerite with respect to quartz and aqueous species is:

$$(Ca_{3.9}Na_{0.1})Al_{7.9}Si_{28.1}O_{72} \cdot 28H_2O + 31.6H^+ =$$

$$3.9Ca^{2+} + 0.1Na^+ + 7.9Al^{3+} + 28.1SiO_2(s) + 43.8H_2O \quad (10\text{-}5)$$
$$\text{(quartz)}$$

The dissolution reaction constants for this reaction were calculated as described above. To these constants, corresponding solubility product constants for the reaction:

$$28.1SiO_2(s) = 28.1SiO_2(aq) \quad (10\text{-}6)$$
$$\text{(quartz)}$$

were added to yield solubility product constants for the stellerite dissolution (reaction 10-4). Similar procedures were adopted for heulandite and mordenite.

10.5.4.4 Kinetic Data

Kinetic data and references are shown in Table 10-8. For each mineral, surface areas used in calculating reaction rates were multiplied by the volume fraction of the mineral in the starting fracture and matrix mineral assemblages. Minerals absent from the starting assemblages had their

surface areas divided by 100. This is a departure from the simulations presented in Sonnenthal, Spycher, Apps, and Simmons (1998, pp. 63 to 70) and Sonnenthal, Spycher, and Apps (1998, pp. 3-7 to 3-12) in which larger surface areas (Table 10-8) were used, and which seemed to result in overestimated mineral reaction rates.

Table 10-8. Dissolution and Precipitation Rate Law Parameters and Reactive Surface Areas for Minerals

Minerals	k_o (mol/m^{2}s)	Ea (kJ/mol)	S (m^2/kg H_2O)	Original Reference
Quartz	1.2589e-14	87.5	71.07	Tester et al. (1994), Johnson, Knauss, and Glassley et al. (1998)
Cristobalite-α	3.1623e-13	69.08	71.07	Rimstidt and Barnes (1980), Johnson, Knauss, and Glassley et al. (1998)
Am. SiO_2	7.944e-13	62.8	142.14	Rimstidt and Barnes (1980), S estimated
Calcite	1.0e-11	41.87	71.07	Hardin (1998, Section 5.7), S estimated
Gypsum	equilibrium	equil.	equil.	
Microcline	1.0e-12	57.78	142.4	Hardin (1998, Section 5.4), S estimated from Johnson, Knauss, and Glassley et al. (1998)
Albite-low	1.0e-12	67.83	104.2	Hardin (1998, Section 5.4)
Anorthite	1.0e-12	67.83	124.6	Hardin (1998, Section 5.4)
Kaolinite	1.0e-13	62.80	142.4	Hardin (1998, Section 5.4), S estimated
Illite	1.0e-14	58.62	142.4	assumed equal to muscovite as given in Johnson, Knauss, and Glassley et al. (1998), S estimated
Sepiolite	1.0e-14	58.62	142.4	assumed equal to illite
Smectite-Na	1.0e-14	58.62	142.4	assumed equal to illite
Smectite-K	1.0e-14	58.62	142.4	assumed equal to illite
Smectite-Ca	1.0e-14	58.62	142.4	assumed equal to illite
Smectite-Mg	1.0e-14	58.62	142.4	assumed equal to illite
Heulandite	1.99e-12	62.802	124.6	Ragnarsdottir (1993) from Hardin (1998, Section 5.4), S assumed to be the same as anorthite
Stellerite	1.99e-12	62.802	124.6	assumed equal to heulandite
Mordenite	1.99e-12	62.802	124.6	assumed equal to heulandite

NOTE: Data from Hardin (1998, p. 5-42) and from Table 3 of Johnson, Knauss, and Glassley et al. (1998) and references therein as shown.

For amorphous silica, precipitation rate law from Rimstidt and Barnes (1980, p. 1690): log k = -7.07 - 2598/T_K, and reactive surface area set twice that of the other silica phases. Dissolution and precipitation rate law for other minerals: $k = k_0 \exp[-E_a/R(1/T_K - 1/298.15)]$. All other kinetic minerals were given the same rate law for precipitation as dissolution, except quartz and cristobalite, for which precipitation was suppressed.

10.5.5 Numerical Simulations

Two simulations are presented that are likely to bound the range of geochemical behavior expected for the SHT. The primary difference between them is that the first simulation (KIN05) does not consider aluminosilicate minerals, while the second one (KIN04) considers several of these minerals, including feldspars, various clay minerals, and zeolites. These minerals can have a substantial effect on pH and water chemistry, and because their thermodynamic and kinetic

properties are subject to much uncertainty due to their inherent great compositional and structural variability, morphology, and solid solution behavior, their importance in the evolution of condensate water chemistry will require further refinement through modeling and data collection from the ongoing DST.

The simulations were carried out over a simulated time period of 521 days (nine months of heating followed by eight months of cooling). Each simulation is discussed separately below.

10.5.5.1 Calcite-Silica-Gypsum System

This simulation considered the following chemical system:

- Aqueous components: H^+, H_2O, Na^+, Cl^-, HCO_3^-, Ca^{++}, $SiO_{2(aq)}$ and SO_4^{--} and their derived species
- Minerals: calcite, gypsum, amorphous silica, quartz, and alpha-cristobalite
- Gases (in H_2O vapor): CO_2

Simulation results are shown for fractures as vertical 2D cross sections on Figures 10-4 through 10-13. These results are discussed below and further compared with measured data in Section 10.6.

For this simulation, results for the matrix are not presented because fluids flow essentially in fractures where the most relevant and interesting hydrochemical processes take place. However, the inclusion of matrix-fracture interactions in the simulations is very important because the matrix acts as a source of vapor, CO_2, and other components in fractures. Computed aqueous phase compositions and mineral precipitation/dissolution trends in the matrix and fractures are presented for the second simulation (Section 10.5.5.2).

Distributions of temperature and liquid saturation in fractures are shown at 91 days after the initiation of heating (Figure 10-4), coinciding with the date of the first water sample collection from borehole 16. The projected location of this borehole traverses a range of elevated liquid saturations, which is consistent with observations of water drainage into the borehole. The computed CO_2 partial pressure (P_{CO2}) is also elevated through much of the length of the borehole (Figure 10-5), because of strong degassing of CO_2 in the rock closer to the heater. The strong degassing of CO_2 and subsequent redissolution into condensate waters farther from the borehole leads to a large drainage region of lower pH waters below the heater, and a small region above it (Figure 10-6). Along borehole 16, the computed pH varies from the ambient value of about 8.2 at the alcove to about 7 at the end of the borehole (closest to the heater). Condensate waters around and below the heater have pHs mostly below 7, down to a minimum of 6.55. Calcite dissolution in fractures (Figure 10-7) is most pronounced in this same region of low pH, with a larger amount of precipitation in the boiling and dryout regions, as a consequence of its decreased solubility at higher temperatures and higher pH in these regions.

At the time of the second water sample collection, 161 days after initiation of heating, the computed distributions of temperature and fracture liquid saturations are similar but expanded outward from the previous snapshot in time (Figure 10-8). The region of decreased P_{CO2} at the boiling front has moved outward to the end of borehole 16 (Figure 10-9), although most of the borehole still traverses the outer region of higher P_{CO2}. The drainage region below and partially around the heater exhibits the lowest pH values (to a minimum of about 6.6), as at 91 days, and this region has progressed well into the part of borehole 16 closest to the heater (Figure 10-10). The computed extent of calcite dissolution (Figure 10-11) increased significantly since the time of 91 days (when the first water sample was collected), with the last 2 m of borehole 16 in the main region of dissolution.

At 521 days, eight months after the heat source was turned off (coinciding with the time when overcoring took place) the mineral distributions are basically stabilized because temperatures have decreased substantially, thus retarding reaction rates. Changes in computed calcite amounts at 521 days (Figure 10-12) indicate the strongest dissolution occurs in a symmetric pattern around the heater with comparatively lesser but more extended dissolution in the drainage region below the heater. About the same magnitude of precipitation is concentrated about 1.5 m above the heater, just touching the end of borehole 16. Cristobalite dissolution is also predominant in a narrow region around the heater (Figure 10-13). In the drainage region, it shows a much more restricted extent of dissolution than calcite. The difference in the pattern of calcite and cristobalite dissolution in the drainage region is due to the increased solubility of calcite at lower-temperatures and lower pH. Water draining from the heater has a lower pH, and also equilibrates thermally with the lower temperature rock as it flows downward. Cristobalite solubility and reaction rates decrease with decreasing temperature and are little affected by pH (in near neutral waters), and therefore the drainage waters dissolve very little cristobalite once they leave the high temperature region.

Gypsum and amorphous silica were predicted to precipitate at a few grid nodes directly adjacent to the dryout zone, at near-zero liquid saturations. Contour plots of these restricted occurrences are not presented. Gypsum forms in the model by evaporative concentration of calcium and sulfate upon boiling at an elevated temperature. As discussed later (Section 10.6), the observed deposition of gypsum in the vicinity of the SHT is more widespread than predicted by the model, and probably resulted from evaporation at low temperature.

10.5.5.2 Calcite-Silica-Gypsum-Aluminosilicates System

This simulation considered the following chemical system:

- Aqueous components: H^+, H_2O, Na^+, Cl^-, HCO_3^-, Ca^{++}, $SiO_{2(aq)}$, SO_4^{--}, K^+, Mg^{++} and AlO_2^- as well as their derived species
- Minerals: calcite, gypsum, amorphous silica, quartz, alpha-cristobalite, low albite, K-feldspar (microcline), illite, kaolinite, smectites (Ca, Na, Mg, and K phases), and zeolites (stellerite, heulandite, and mordenite)
- Gases (in H_2O vapor): CO_2

Simulation results are shown as vertical 2D cross sections (Figures 10-14 through 10-28), a vertical profile through the heater at a time of 161 days (Figures 10-29 through 10-31), and time profiles for a point in the vicinity of borehole 16, zone 16-4 (Figures 10-32 though 10-36). These results are discussed below and further compared with measured data in Section 10.6.

In this simulation the thermal-hydrological conditions are identical to those shown previously. In the considered geochemical system, chloride is a nonreactive (conservative) species and it is therefore a useful indicator of the extent of dilution by condensate waters, the extent of evaporation, and the equilibration of matrix and fracture porewaters. Figure 10-14 shows the computed distribution of chloride concentrations at 91 days, showing the very strong dilution around the heater borehole and in the condensate waters draining below the heater. Concentrations of chloride in fracture porewaters are initially about 40 mg/l (Table 10-4) and are computed to decrease to much less than 1 mg/l in the most dilute waters (Figure 10-14). In areas where the liquid saturations reach the minimum allowable value for chemical calculations (10^{-4}), computed chloride concentrations are as high as 16,000 mg/l. These areas are, of course, very limited in extent.

The computed increase in P_{CO2} away from the heat source in fractures is much less than in the previous simulation, due to increased consumption of aqueous carbonate species and hydrogen ion by mineral reactions such as feldspar dissolution and increased calcite precipitation from anorthite breakdown (Figure 10-15). A region of decreased P_{CO2} around the heater is due to degassing. In the dryout zone, there is a large increase in P_{CO2}. However, the large P_{CO2} is calculated as the value reflecting equilibrium with the last residual water phase, and may be subject to greater numerical errors than in areas of less extreme hydrochemical changes. As discussed later, the P_{CO2} increase just before dryout may reflect an influx of CO_2 from the matrix into fractures that is greater than the rate of CO_2 consumption and advection in fractures.

The CO_2 dissolution in condensates leads to lower pH waters that drain below the heater (Figure 10-16). The lowest pH values attained are about 7.1 compared to 6.55 in the previous model that did not consider aluminosilicate minerals. The pH is also lower than initial values in a thin condensation zone above the heater (Figure 10-16). However, further above the heater, the pH becomes slightly higher than initial values due to evaporative loss of CO_2.

After 161 days the region of highly dilute condensate waters has increased (Figure 10-17) and encompassed the last 1 to 1.5 m of borehole 16. A large region of dilute waters has also drained several meters into the fractures underlying the heater. Areas of increased P_{CO2} are evident several meters above and below the heater, with the regions near the alcoves remaining near starting P_{CO2} due to buffering with the gas phase in the alcoves (Figure 10-18). Lower pH water has drained to the base of the model domain (about 12 m below the heater), and the area of slightly increased pH above the heater has enlarged (Figure 10-19).

Distributions of some of the more abundant mineral phases are shown in Figures 10-20 to 10-28 for the final simulation time of 521 days. Absolute volume percentage change in cristobalite (Figure 10-20) is similar to that seen in the first simulation, although the region of dissolution extends further from the heater in the case with aluminosilicate minerals. It is likely that the precipitation of other silica-bearing minerals (notably zeolites) tends to lower silica

concentrations further from the heater and therefore result in an increased dissolution rate for cristobalite. Calcite dissolution is also slightly greater (Figure 10-21) than in the first simulation. This was unexpected because the pH is higher in the condensation and drainage zones in this second simulation. However, it can be explained by the depletion of calcium in solution to form calcium zeolites.

Dissolution of feldspar minerals (microcline and albite) occurs dominantly within the narrow reflux zone near the heater (Figures 10-22 and 10-23) with some increased dissolution in the drainage zone below the heater. Precipitation of albite and microcline is predicted in the dryout region, however, slow nucleation and growth kinetics may limit the actual precipitation in the SHT. Clay mineral precipitation is directly related to the dissolution of feldspars, as seen in the plot of kaolinite (Figure 10-24), with the most precipitation in the combined condensation-drainage zones below the heater due to generally lower pH within this region. Ca-smectite (Figure 10-25) shows a larger region of precipitation (yet volumetrically much less) owing to the pH and temperature dependences of reactions involving calcium (the major calcium bearing minerals are calcite, anorthite, and stellerite).

Stellerite, which is an abundant calcium zeolite mineral coating fractures in the SHT shows precipitation over a large region away from the heater (Figure 10-26), unlike other minerals. This could be caused by CO_2 transport, as zones of increased P_{CO_2} away from the heater display a decreased pH, thus an increased solubility of calcite and a resulting increase in available calcium in solution to form stellerite. This mineral is predicted to undergo dissolution very close to the heater in the highest temperature regions. Another zeolite that may be more abundant in other areas of Yucca Mountain is heulandite. The total volumes of heulandite precipitated in the model simulations are very small, yet the distribution is quite unique (Figure 10-27). As one moves away from the heater, it varies from nearly zero precipitation, to a greater amount of crystallization, and then a zone of nearly zero crystallization, followed again by another large zone of greater precipitation. Such patterns of mineral precipitation, both in time and space, are characteristic of complex chemical systems that cannot be predicted by thermal stability alone.

Other minerals that are found at the edge and in the dryout zone are gypsum and amorphous silica. These phases are too localized in abundance to be shown in a contour plot, but they are seen to form where increased concentrations of sulfate and silica, respectively, eventually lead to precipitation as liquid saturations decrease during the motion outward of the boiling isotherm.

In addition to understanding the coupled chemical system accompanying the SHT, one of the important aspects of long-term repository behavior is the change in porosity and permeability over time. Although the SHT was very short in duration, it can yield some information on the effective rates of reaction under thermal-hydrologic conditions and the possible distribution of porosity changes around a heated drift over a short period of time. The total porosity change (sum of all the mineral changes) for the fracture medium is shown in Figure 10-28. As would be expected from the distribution of the minerals shown in the previous figures, the greatest porosity increase takes place in the condensation-reflux zone in a narrow band about 2 m away from the heater. Porosity decreases near the heater in the dryout zone, and most significantly in a broad region below the heater, where a combination of increased drainage through this region and

moderate temperatures lead to greater precipitation of phases such as clays and zeolites, relative to the dissolution of feldspars, silica phases, and calcite.

To further examine the geochemical system around the heater, computed profiles of temperature, liquid saturation, aqueous species concentrations and mineral abundances in fractures are shown on Figures 10-29 through 10-31 for a simulated time of 161 days. This time corresponds to the time after which the second set of water samples was collected in borehole 16. The location of the vertical profile is shown on Figure 10-4. Graphs are presented with the distance from the heater plotted as the X axis. Therefore, the X axis of these plots needs to be aligned with the profile in Figure 10-4 for true spatial representation (i.e., approximately 90-degree rotation).

Most of the previously discussed observations are relayed in the profiles. At the time considered (161 days), the dryout zone extends to approximately 1 m away from the heater. Around the dryout zone, a narrow heat-pipe zone of approximately 0.5 m in width has developed (Figure 10-29a). Accordingly, the liquid saturation drops quickly to zero within this narrow area (Figure 10-29b). Chemical reactions are computed only for zones above a liquid saturation of 10^{-4} (and/or ionic strength below 2), and for this reason no aqueous chemistry and mineral data are shown in the profiles in the zone where the liquid saturations are below this limit.

As mentioned earlier, the chloride concentration profile (Figure 10-30) is a useful indicator of dilution in the condensation zone, and evaporative concentration in the narrow boiling (heat pipe) zone closer to the heater. The concentrations of other species follow profiles that differ more or less from the chloride trend depending on the degree of water-rock interaction affecting these species. Calcium becomes strongly depleted in solution near the heater. This is not reflected in concentrations measured in water from borehole 16 (Section 10.6). This could be due to a too-low calcite dissolution rate and/or too high precipitation rates of calcium zeolites. By comparing calcium concentrations computed with and without aluminosilicate minerals (see also Section 10.6) and concentrations from simulations assuming calcite at equilibrium (not presented here), it appears that, in the case of these simulations, the calcium depletion is primarily due to overestimating the precipitation rates of zeolites. This could have resulted from overestimating the reactive surface areas of these minerals.

The pH is lower below the heater (negative X values on Figure 10-30b) than above it, due to increased drainage of less alkaline condensed water in this zone. The pH trend reflects some increase towards the heater due to evaporative loss of CO_2 with temperature (reaction 10-1), followed by a sharp decrease at the front of the condensation zone (where dilution is maximum), then a steep increase in the boiling zone from intense CO_2 volatilization. Away from the boiling zone, the P_{CO2} displays a trend which is inverse that of pH, as would be expected from reaction 10-1. Closer to the heater, the trends of pH and P_{CO2} become similar. The sharp P_{CO2} increase upon near dryout is likely to be caused by a strong influx of CO_2 from the matrix that cannot dissipate (through advection and/or diffusion) or be consumed by mineral reactions in fractures faster than the rate of boiling. However, the magnitude of the calculated P_{CO2} at this location may be unrealistic because assumptions for computing the system chemistry very near the dryout zone may no longer hold.

Computed mineral abundances along the profile show the dissolution of feldspars and precipitation of kaolinite and stellerite (Figure 10-31a) in a zone extending from approximately one to four meters away from the heater. An example of feldspar dissolution reaction can be written as:

$$2NaAlSi_3O_8 + H_2O + 2H^+ \rightarrow Al_2Si_2O_5(OH)_4 + 4SiO_2(aq) + 2Na^+ \qquad (10\text{-}7)$$
(albite) (kaolinite)

Reaction 10-7 is favored by lower pH and dilution, which is consistent with the greater amount of kaolinite computed below the heater (where the pH is lower and dilution greater) than above it. Stellerite may also form from feldspar dissolution according to the following reaction, which is not pH dependent:

$$2NaAlSi_3O_8 + SiO_2(aq) + Ca^{++} + 7H_2O \Diamond CaAl_2Si_7O_{18} \bullet 7H_2O + 2Na^+ \qquad (10\text{-}8)$$
(albite) (stellerite)

However, lower pH and dilution favor its dissolution to form kaolinite below the heater:

$$CaAl_2Si_7O_{18} \bullet 7H_2O + 2H^+ \rightarrow Al_2Si_2O_5(OH)_4 + 5SiO_2(aq) + Ca^{++} + 6H_2O \qquad (10\text{-}9)$$
(stellerite) (kaolinite)

Calcite and cristobalite dissolve to a lesser extent than feldspars close to the heater (Figure 10-31a). As mentioned earlier, stellerite precipitation rates may have been overestimated because calculated calcium concentrations are much lower than those observed in water samples from borehole 16 (Section 10.6). Other minerals dissolve (quartz) or precipitate (clays, zeolites other than stellerite) in very small quantities (Figure 10-31b). Reactions such as 10-7 or 10-9 appear to be primarily driven by reaction rates and dilution (as opposed to pH) and result in the solution pH being generally higher (by consuming hydrogen ion) than in the previous simulation, which did not consider aluminum silicates.

To illustrate the simulated chemical processes through time, profiles similar to those discussed above were plotted as a function of time, for a point location shown on Figure 10-4. This location was chosen in the vicinity of borehole 16, zone 16-4. Dryout conditions were never reached at this point during the length of the simulated test. Results are presented in Figures 10-32 through 10-36 for fractures and matrix and show that fracture and matrix waters exhibit significantly different aqueous chemistries.

The observations and reactions described above for the spatial profiles of fracture waters (Figures 10-28 through 10-31) can be applied to the time profiles as well. Dilution in fractures increases with time as the system heats up and steam condenses in fractures. This is shown by computed increasing liquid saturations (Figure 10-32b) and decreasing chloride concentrations (Figure 10-33a) in fractures with time until the heat source is turned off at approximately 275 days. At this time, fractures drain resulting in a steep decrease in their liquid saturation because no more steam is being generated. Accordingly, the concentrations of chloride and other

unreactive species quickly rise (Figure 10-33a) by equilibration with matrix water closer in composition to the initial water.

The computed water chemistry trends in the matrix are significantly different than in fractures because condensation and dilution effects are not as important in the matrix. The permeability of the matrix is also quite low, and thus the rates of liquid flow are much less than in fractures. Consequently, the matrix water chemistry exhibits trends more similar to those that would be predicted by simple heating (i.e., geochemical mass-transfer without fluid flow). At the start of the simulated test, the pH decreases with time as water dissociates and calcite precipitates with increasing temperature, until the volatilization of CO_2 becomes significant enough to reverse these trends and increase the pH (reaction 10-1). Accordingly, the computed P_{CO2} trend in the matrix is inversely related to the pH trend (Figure 10-34b). The pH increases with time, and somewhat more so after the heat is turned off because the system remains warm and CO_2 keeps volatilizing into fractures that now have a higher gas saturation (CO_2 advected faster away from the system).

The higher pH in the matrix water results in different computed mineral abundances in matrix (Figure 10-36) compared to those in fractures (Figure 10-35). Notably, there is proportionally more heulandite, mordenite, and sepiolite precipitation, less feldspar dissolution, and more quartz and cristobalite dissolution in the matrix than in fractures. In all cases, as discussed previously, the computed mineral volume changes are too small (over the length of the test) to have any significant effect on either the fracture or matrix permeability.

Results of simulations are further discussed with respect to the composition of water from borehole 16 in the next section.

10.6 INTERPRETATION AND DISCUSSION

Calcite, gypsum, and amorphous silica were found in posttest mineralogical analyses of ESF-TMA-PTC-NEU-2 (overcore of borehole 16) (see Section 6.4) and attributed to reactions that occurred during the SHT. Two possibilities for the origin of these evaporite minerals have been identified: (1) formation during water-rock interaction at elevated temperatures, and (2) precipitation during posttest evaporation. The distribution and textural attribute of these minerals suggest they formed through evaporation of the remaining waters during the posttest cool-down period. For this reason, a direct comparison of these precipitates cannot be made to the modeled mineral precipitates unless it can be shown that they crystallized at high temperatures.

Some comparison can be made of the last minerals predicted to form in the dryout zone at small liquid saturations (but at boiling temperatures) to those found in overcores of boreholes 2 and 16, as some of the phases are likely to be the same as those formed by evaporation at temperatures below boiling. At the boiling front, precipitated minerals in the model simulations include calcite, gypsum, minor amorphous silica, and minor quantities of clay minerals and zeolites. As mentioned above, calcite, gypsum, and amorphous silica were found in posttest mineralogical analyses. The other phases are also expected to form under evaporative conditions or dryout during boiling. However, borehole 16 was outside the dryout region and therefore never experienced the final dryout due to boiling. These phases were not calculated to form at the

location of borehole 16 because computed liquid saturations were too high (and concentrations too small) for amorphous silica and gypsum to precipitate, and the pH of condensate waters was too low for calcite precipitation at these locations. This is corroborated by the compositions of the waters collected in borehole 16, which were relatively dilute, and strongly undersaturated with respect to gypsum, calcite, and amorphous silica. Therefore, it is concluded that the phases observed in the posttest mineralogical studies most likely formed through evaporation of the remaining waters in the borehole, sometime after the test was completed.

Comparisons can be made directly between the compositions of collected waters in borehole 16 and those of fracture waters in the model simulations. These are shown on Tables 10-9 and 10-10 for three locations within the model, as indicated on Figure 10-37. Zone A and zone B include grid points along the simulated location of borehole 16, as well as within approximately 0.2 m on either side of this borehole. Zone C corresponds to grid nodes below the heater where the computed pH is the lowest, due to increased drainage of steam condensate at this location. The tabulated data are represented graphically as Shoeller-type diagrams on Figures 10-38 and 10-39, respectively, to facilitate comparing the general character of these waters.

Table 10-9. Comparison of Water Compositions Measured in Borehole 16 to Concentrations Computed in Model Zones A, B, and C (Simulation KIN04)

		Calculated - 91 days						Measured 11/25/96
		Zone A		Zone B		Zone C		Borehole 16
Temperature	deg.C	88 - 73		66 - 58		80 - 68		
Liquid Saturation		0.66 - 0.49		0.47 - 0.40		0.61 - 0.63		
pH		7.7 - 8.2		8.1 - 8.1		7.3 - 7.4		6.2
Ca	mg/l	0.19 - 0.00		0.00 - 0.72		0.21 - 0.18		13
Mg	mg/l	0.00 - 0 77		1 5 - 3.7		0.00 - 0.06		1.63
Na	mg/l	2.8 - 57		65 - 92		4.7 - 9.3		16
Cl	mg/l	0.64 - 17		20 - 33		1.2 - 2.6		2.54
Si	mg/l	4.0 - 7.8		7.1 - 5.1		3.3 - 3.4		16.8
HCO3	mg/l	4.2 - 99		115 - 172		9.6 - 19		188*
SO4	mg/l	0.63 - 17		20 - 32		1.2 - 2.6		1.83
K	mg/l	0.88 - 2.0		2.4 - 8.8		0.68 - 0.76		2.5
Al	mg/l	0.85 - 0.26		0.15 - 0 01		0.38 - 0.16		< 0.06
		Calculated - 161 days						Measured 2/3/97
		Zone A		Zone B		Zone C		Borehole16
Temperature	deg.C	96 - 90		83 - 72		95 - 83		
Liquid Saturation		0.34 - 0.63		0.57 - 0 46		0.42 - 0.60		
pH		7.8 - 7.7		8.1 - 8.3		7.6 - 7.6		6.9
Ca	mg/l	0.21 - 0.23		0.01 - 0.00		0.25 - 0.16		9.76
Mg	mg/l	0.00 - 0.00		0.00 - 0 12		0.00 - 0.00		1.16
Na	mg/l	3.3 - 4.0		23 - 81		1.7 - 5.0		13.9
Cl	mg/l	0.75 - 0.97		6.2 - 23		0 3 - 1.2		1.45
Si	mg/l	4.6 - 3.8		5.9 - 10		3.7 - 3.6		17.4
HCO3	mg/l	3.2 - 5.9		37 - 135		1.7 - 9.2		

Table 10-9. Comparison of Water Compositions Measured in Borehole 16 to Concentrations Computed in Model Zones A, B, and C (Simulation KIN04) (Continued)

		Calculated - 161 days									Measured 2/3/97
		Zone A			Zone B			Zone C			Borehole16
SO4	mg/l	0.73	-	0.95	6.0	-	22	0.32	-	1.2	0.42
K	mg/l	0.85	-	0.69	1.4	-	1.7	0.60	-	0.80	2.5
Al	mg/l	1.2	-	0.87	0.87	-	0.18	0.92	-	0.60	< 0.06

NOTE: Zones as shown in Figure 10-37. Simulation with aluminosilicate minerals (KIN04). Concentrations are listed in order of decreasing temperature within each zone, and correspond to the data shown graphically on Figure 10-38.
* calculated from charge balance

Table 10-10. Comparison of Water Compositions Measured in Borehole 16 to Concentrations Computed in Model Zones A, B, and C (Simulation KIN05)

		Calculated - 91 days									Measured 11/25/96
		Zone A			Zone B			Zone C			Borehole16
Temperature	deg.C	88	-	73	68	-	58	80	-	68	
Liquid Saturation		0.66	-	0.49	0.47	-	0.40	0.61	-	0.63	
pH		7.0	-	7.6	7.6	-	7.7	6.6	-	6.6	6.2
Ca	mg/l	0.19	-	4.27	6.02	-	14	0.31	-	0.88	13
Mg	mg/l		-			-			-		1.63
Na	mg/l	1.4	-	38	45	-	73	2.7	-	5.8	16
Cl	mg/l	0.64	-	17	20	-	33	1.2	-	2.6	2.54
Si	mg/l	0.8	-	13.0	14.6	-	23	1.2	-	2.3	16.8
HCO3	mg/l	3.1	-	73	89	-	157	7.7	-	16.3	188 *
SO4	mg/l	0.62	-	17	20	-	32	1.2	-	2.6	1.83
K	mg/l		-			-			-		2.5
Al	mg/l		-			-			-		< 0.06
		Calculated - 161 days									Measured 2/3/97
		Zone A			Zone B			Zone C			Borehole16
Temperature	deg.C	96	-	90	83	-	72	95	-	83	
Liquid Saturation		0.34	-	0.63	0.57	-	0.46	0.42	-	0.60	
pH		7.7	-	7.2	7.5	-	7.7	7.3	-	6.7	6.9
Ca	mg/l	0.22	-	0.21	0.80	-	4.28	0.11	-	0.27	9.76
Mg	mg/l		-			-			-		1.16
Na	mg/l	1.7	-	2.1	14	-	51	0.7	-	2.7	13.9
Cl	mg/l	0.75	-	0.96	6.2	-	23	0.3	-	1.2	1.45
Si	mg/l	1.3	-	1.3	6.2	-	18	0.6	-	1.6	17.4
HCO3	mg/l	1.8	-	3.9	24	-	92	1.0	-	6.8	
SO4	mg/l	0.73	-	0.94	6.0	-	22	0.33	-	1.2	0.42
K	mg/l		-			-			-		2.5
Al	mg/l		-			-			-		< 0.06

NOTE: Zones as shown in Figure 10-37. Simulation without aluminosilicate minerals (KIN05). Concentrations are listed in order of decreasing temperature within each zone, and correspond to the data shown graphically on Figure 10-39.
*calculated from charge balance

Computed and observed concentrations generally depict similar trends, with the exception of magnesium and calcium for the simulation with aluminosilicates. In most cases the computed pH is higher than measured values, although reasonably good agreement (lowest values) is obtained with the simulation without aluminosilicates. As mentioned earlier, inclusion of these minerals in the geochemical system results in higher computed pH than in the case of simulations without them.

Rapidly changing hydrochemical conditions in fractures around the heater in space and time make it difficult to exactly match borehole 16 water with simulated results. Refinement of the reaction rates for calcite, calcium zeolites, and magnesium smectite would likely result in closer agreement between measured and calculated calcium and magnesium concentrations. Nevertheless, the simulations appear to correctly represent the processes leading to the formation of waters of the type found in borehole 16, which essentially result from steam condensation followed by mild reaction with surrounding rock. This corroborates the conclusions of Glassley and DeLoach (1997, p. 6) and Glassley (1997b, p. 3) regarding the origin of borehole 16 water. It was noted in the *Single Heater Test Status Report* (CRWMS M&O 1997b, p. 5-52) that the source of CO_2 leading to the mild acidification of the water was uncertain. From the simulations presented here, it appears that volatilization of dissolved CO_2 from matrix water alone could account for the mild acidification of steam condensate.

The simulated water compositions that best match borehole 16 water are not near the simulated location of borehole 16 but below the heater in the zone of increased drainage. This would indicate that the water in borehole 16 originated from a zone with increased drainage compared to its surroundings. This would be expected in a preferential fluid pathway. The air-injection and gas-tracer data discussed in Section 8 of this report suggest a preferential pathway between the heat source and this borehole, which would be consistent with the modeling results.

10.7 EFFECT ON WASTE PACKAGE MATERIAL COUPONS

As mentioned in Section 3.3.4, coupons or test specimens of carbon steel were placed in sections of boreholes 16 and 18 to observe the effect of heating and cooling on them. The temperature, relative humidity, and air pressure were monitored during the test. Temperatures in these sections of the boreholes rose during heating and the highest measured temperatures ranged between 36°C and 52°C. The relative humidity in these sections of boreholes 16 and 18 ranged between 85 percent and 100 percent. Also, zone 4 in borehole 16 was filled with water at different times during the heating phase of the test. Some of the metal coupons in 16-4 were thus submerged in water from time to time.

After the end of the cooling period and after the completion of post-cooling pneumatic measurements in these two boreholes, the packer systems in them along with the metal coupons were withdrawn and sent to the laboratory for analyses.

All the metal coupons retrieved from boreholes 16 and 18 had undergone various degrees of corrosion. The corrosion products were identified by x-ray diffraction and Raman spectroscopy. Goethite (α-$Fe^{+3}O(OH)$) and magnetite (Fe_3O_4) were identified on all the specimens that were analyzed. In addition, the chloride containing mineral akaganeite (β-$Fe^{+3}O(OH,Cl)$) was

identified on a specimen that had been exposed to liquid water. The corrosion product on most specimens did not cover the entire surface and was somewhat adherent. The corrosion products on the specimens that were exposed to liquid water covered the entire surface, were voluminous, and were not adherent.

10.8 CONCLUSIONS

Reaction-transport simulations of the SHT were completed to provide insight into thermal-hydrological-chemical processes accompanying this test and to further understanding of these processes. The simulations were also useful for interpreting the chemical composition of water collected in borehole 16, and yield results that are consistent with conclusions reached previously by other authors. The borehole 16 water resulted from steam condensation in fractures, and its mildly acidic character reflects the dissolution of gaseous CO_2 at the time of steam condensation.

The simulations indicate that dissolved carbonate species in matrix water alone provide a sufficient source of CO_2 gas, upon heating, to drive the pH of condensates down to a mildly acidic range (pH 6 to 7). When including the reaction of aluminosilicate minerals, however, the simulations of the SHT overestimate the pH of condensates in fractures (computed pH 7 to 8 as opposed to pH between 6 and 7 in borehole 16 water). This may be related to overestimated mineral reaction rates. An overestimated pH of the initial matrix and fracture water could not be ruled out either.

Calcite, gypsum, and amorphous silica were found in posttest mineralogical analyses and attributed to reactions accompanying the SHT. Calcite and gypsum were predicted by the simulations to precipitate in some areas of the model at elevated temperature upon boiling. However, these three minerals appear to have formed during the SHT by evaporation at low temperature, most likely sometime after the heater was turned off.

In any case, the thermal-hydrological-chemical simulations presented here are encouraging, as they appear to reproduce fairly well the chemical processes affecting the SHT. The results underline the importance of considering a dual-permeability framework (fracture/matrix) when simulating water-gas-rock interactions in the test area, as the water chemistries in fractures and matrix differ significantly from each other and are directly affected by the hydrochemical interaction between these two media. However, the complexity of these processes and their interaction within a dual-permeability context, together with the uncertainty of input data, warrants that some caution be applied when interpreting modeling results. This is particularly true when extrapolating results of the SHT to the larger-scale proposed repository at Yucca Mountain. More work remains ahead to improve the reliability of input data and to enhance computational methods so that mountain-scale models of the repository can be implemented with efficiency and accuracy.

INTENTIONALLY LEFT BLANK

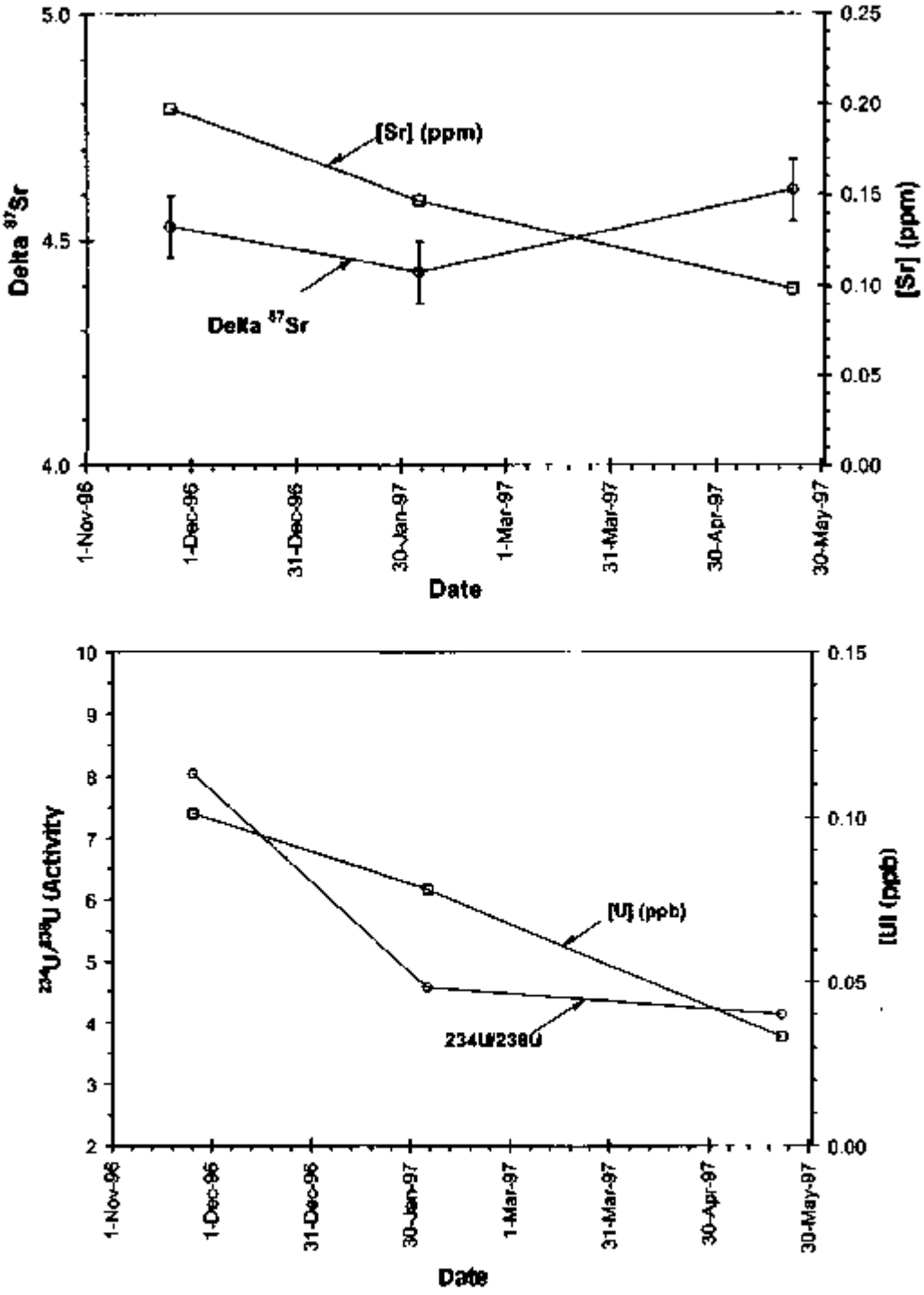

NOTE: Error bars (2σ) shown only where they exceed the size of the symbols. One sample was analyzed but not plotted due to probable lack of preservation. See text for discussion.

Figure 10-1. Plots Showing the Isotopic Composition and the Concentration of Strontium (Upper) and Uranium (Lower) in Water Samples Collected from Borehole 16, Zone 4

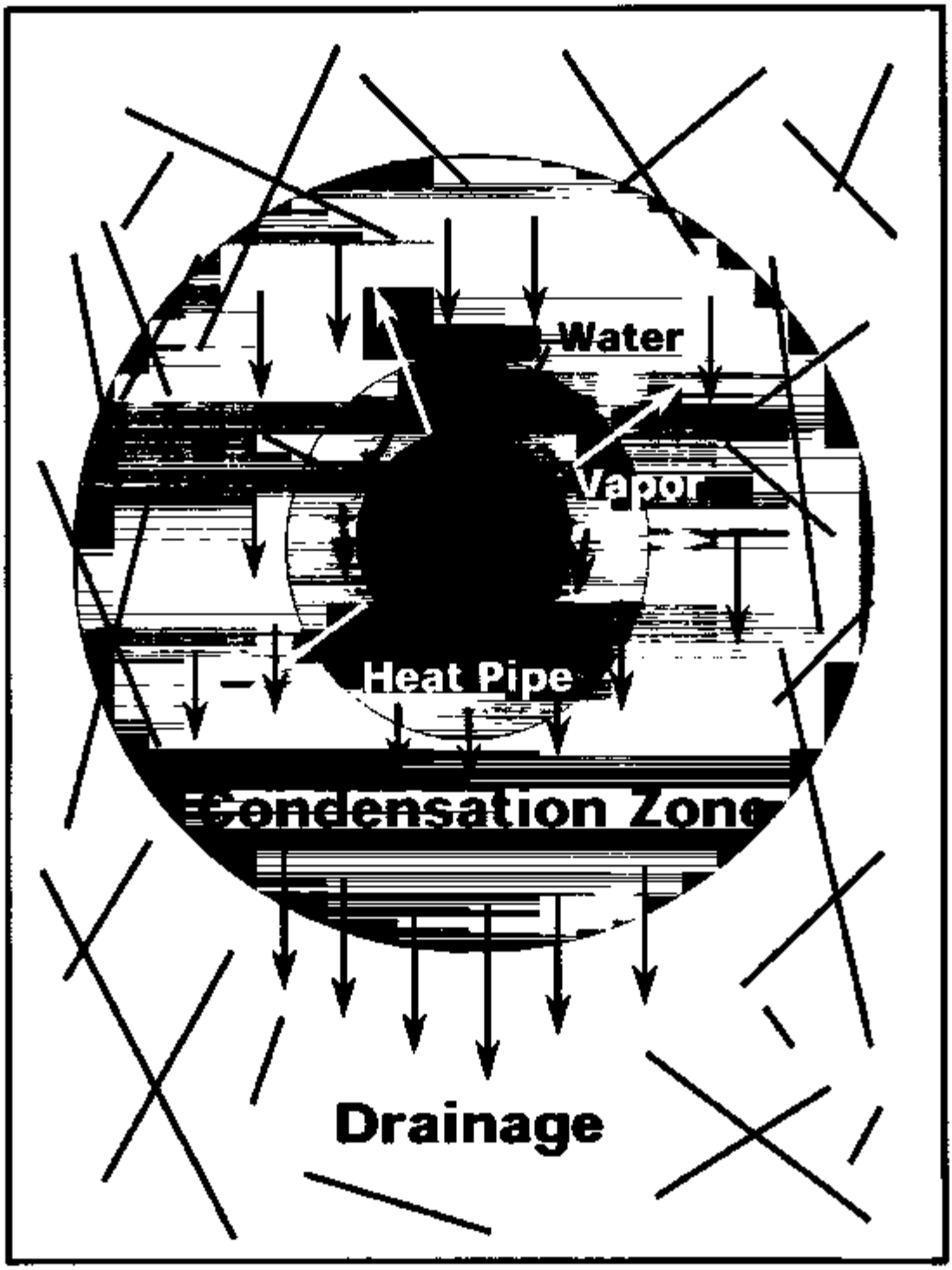

Figure 10-2. Conceptual Model of Thermal-Hydrological Processes for the SHT that are Important in the Evolution of the Geochemistry of Waters, Gases, and Minerals

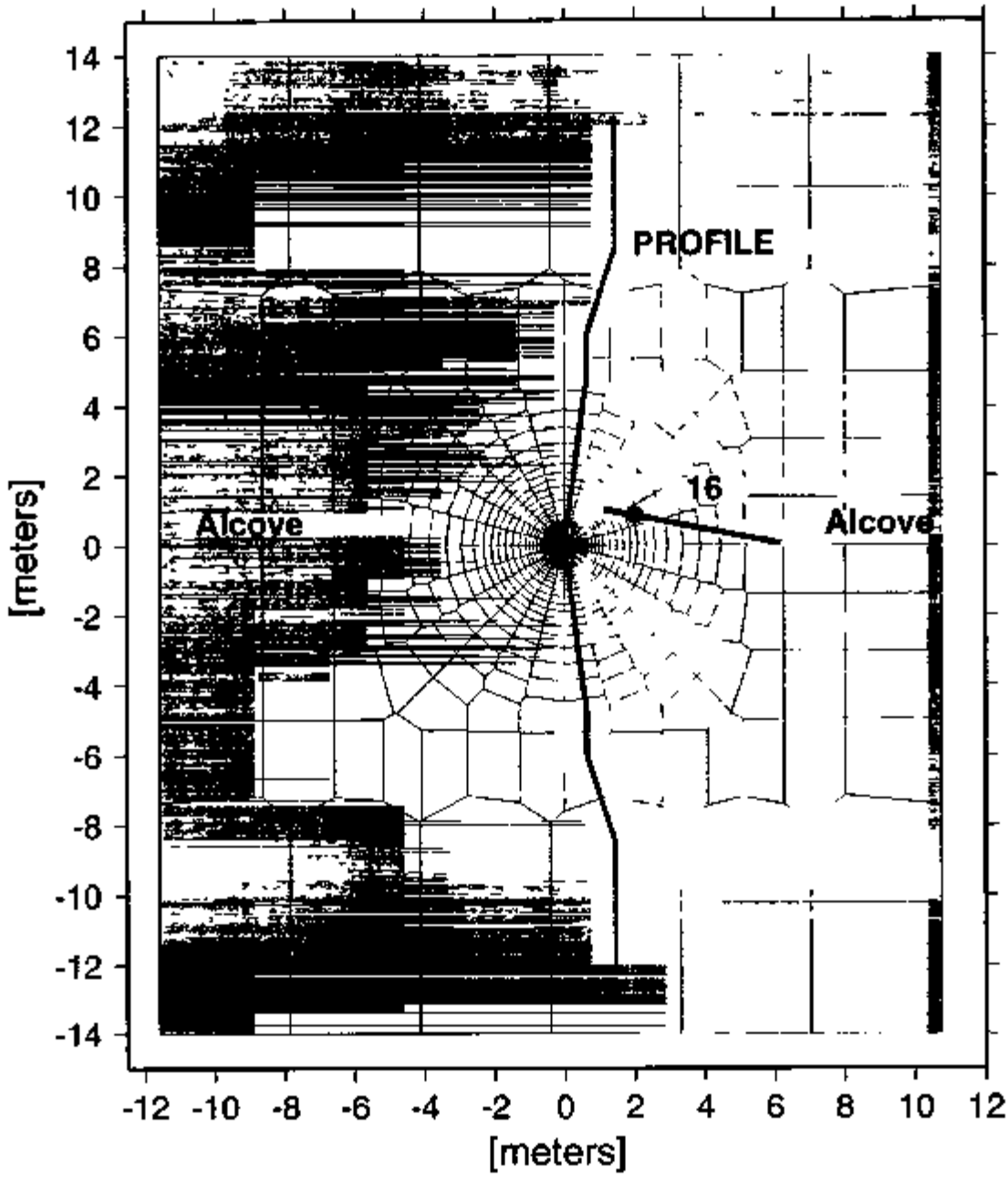

SOURCE Adapted from Birkholzer and Tsang (1996, p. 28)

NOTE The mesh represents a vertical cross section perpendicular to the axis of the heater borehole. The blue line through the heater coincides with the horizontal axis for profiles shown on Figures 10-29 to 10-31. The blue point plotted on the projection of borehole 16 shows the location of the grid node for which time profiles are displayed on Figures 10-32 and 10-36.

Figure 10-3 Two-Dimensional Computational Mesh for the Dual-Permeability Simulations of the Single Heater Test

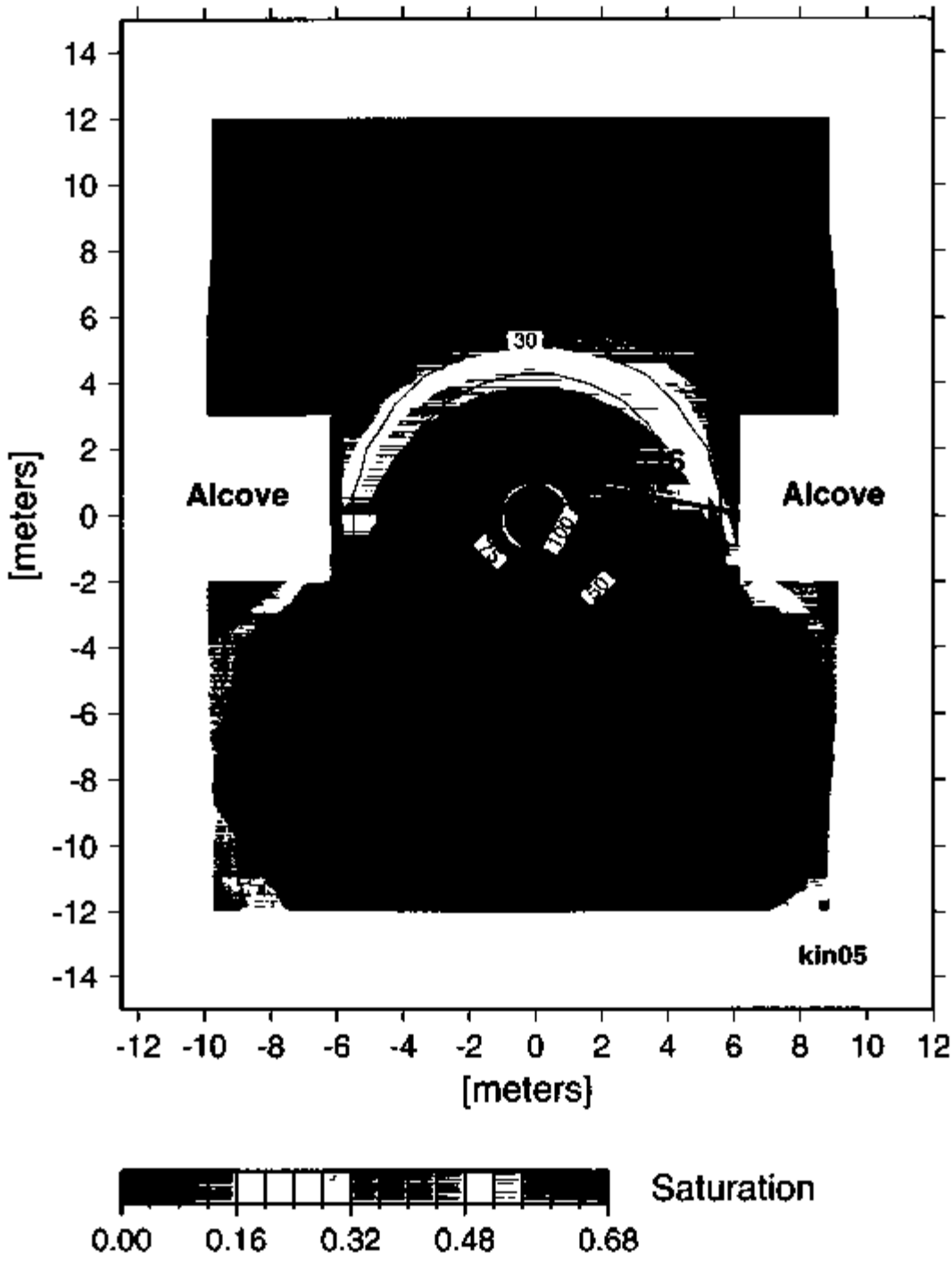

NOTE Corresponding to the sampling time of the first water sample collected from borehole 16 (Simulation KIN05)

Figure 10-4 Calculated Fracture Liquid Saturation and Temperature 91 Days after the Initiation of Heating

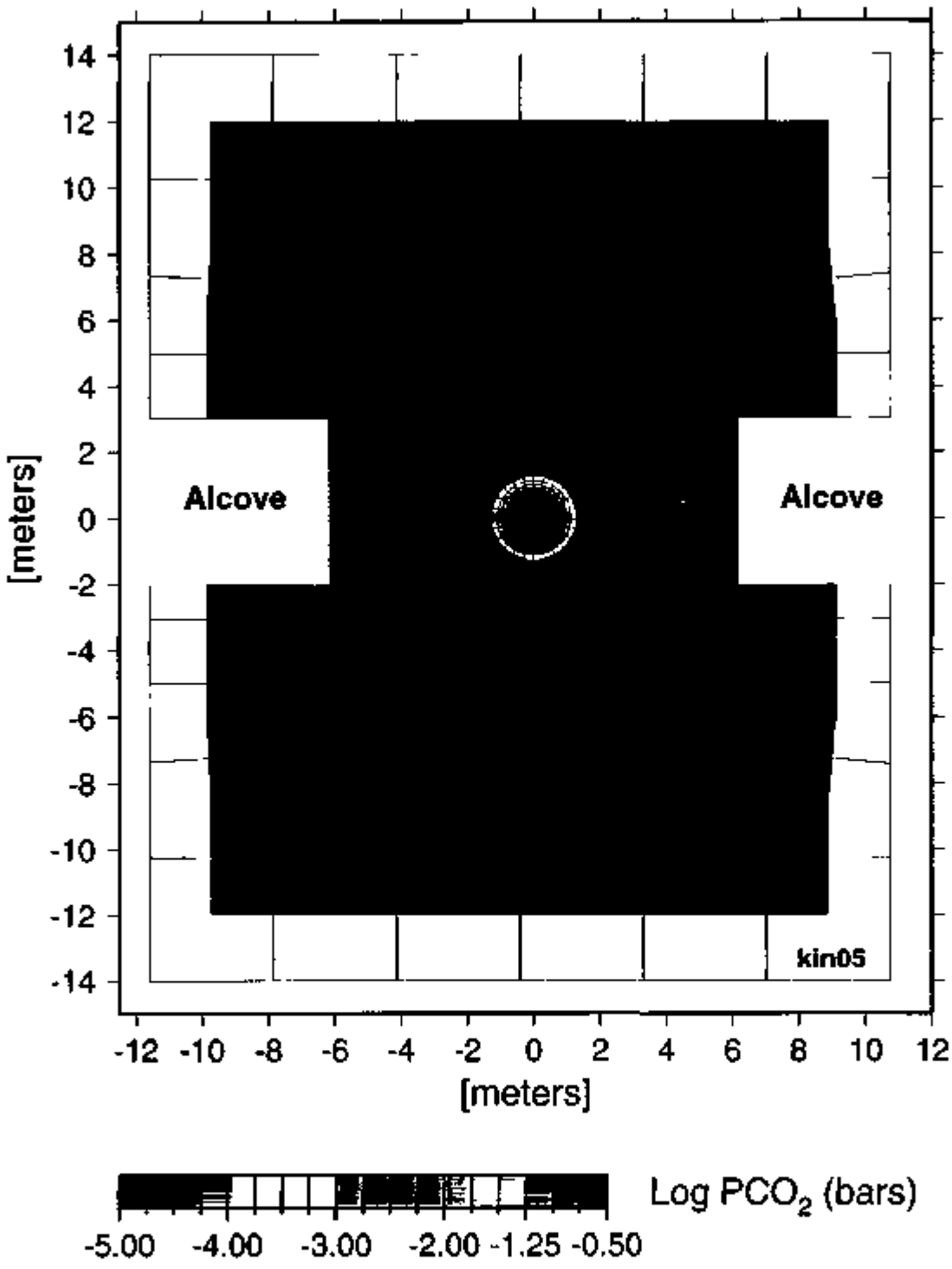

NOTE: Simulation KIN05

Figure 10-5. Calculated Partial Pressure of CO_2 in Equilibrium with Water in Fractures after 91 Days

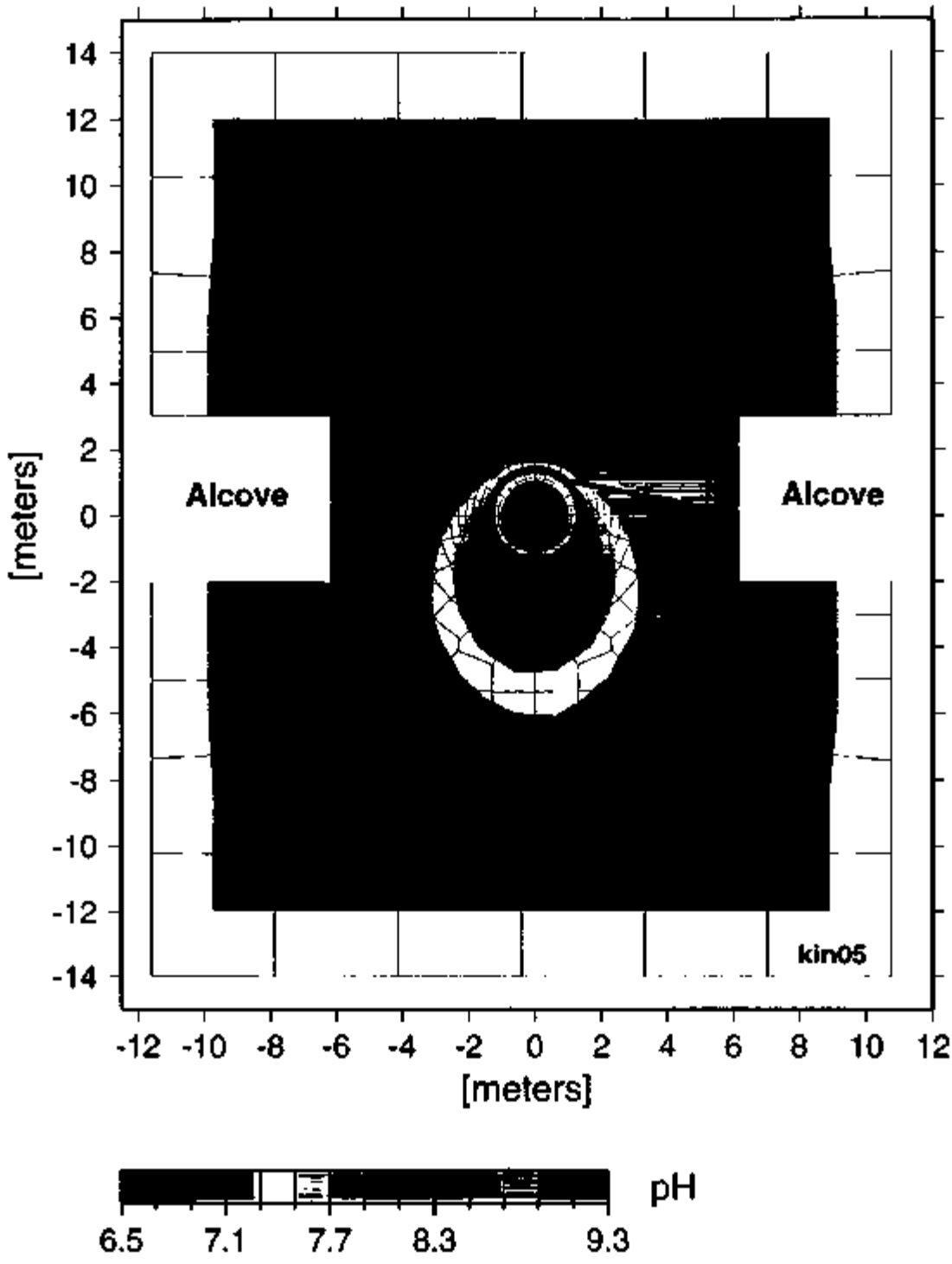

NOTE: Simulation KIN05

Figure 10-6. Calculated pH in Fracture Porewaters after 91 Days

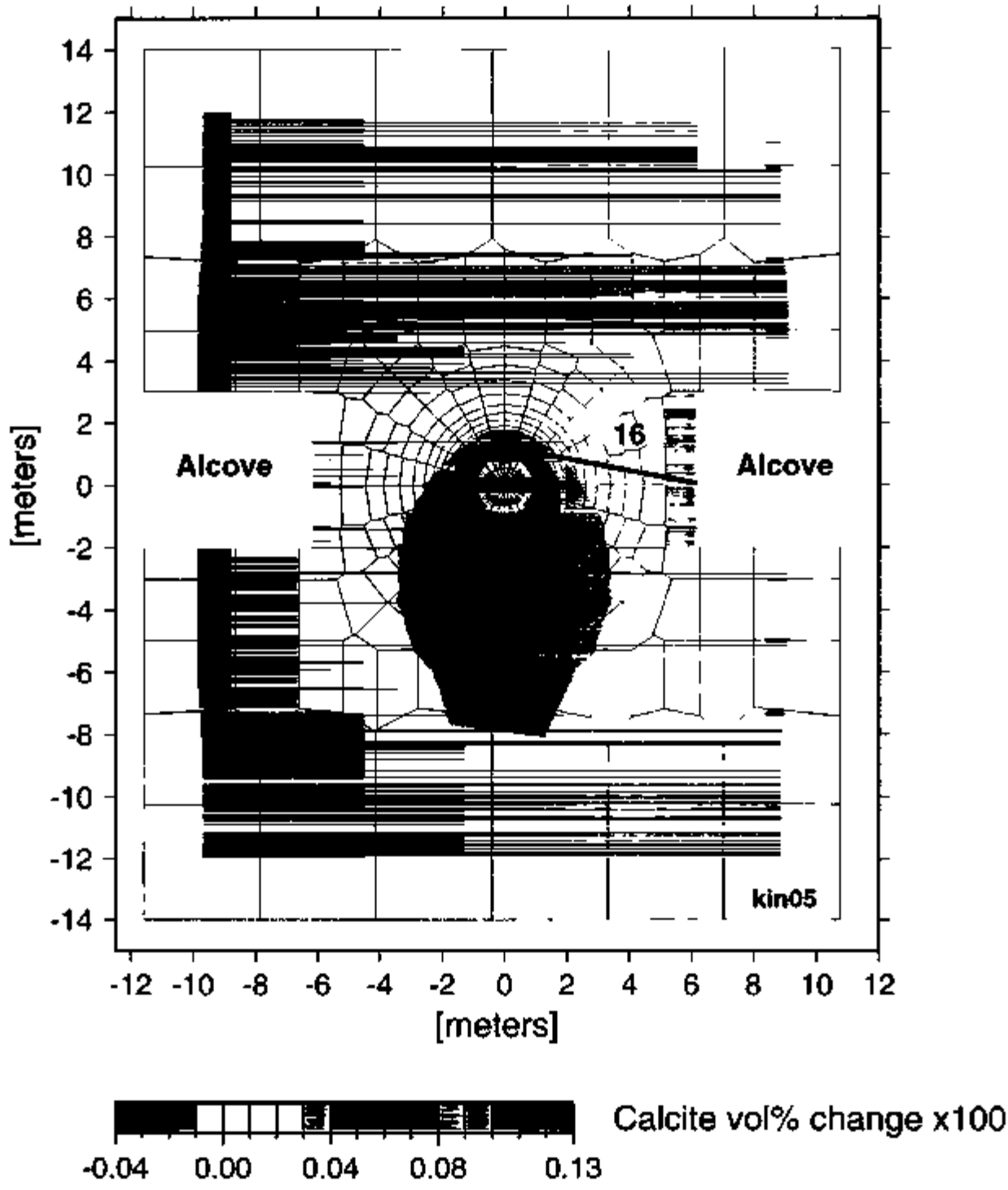

NOTE Simulation KIN05

Figure 10-7 Change in Calcite Volume Percent in Fractures after 91 Days

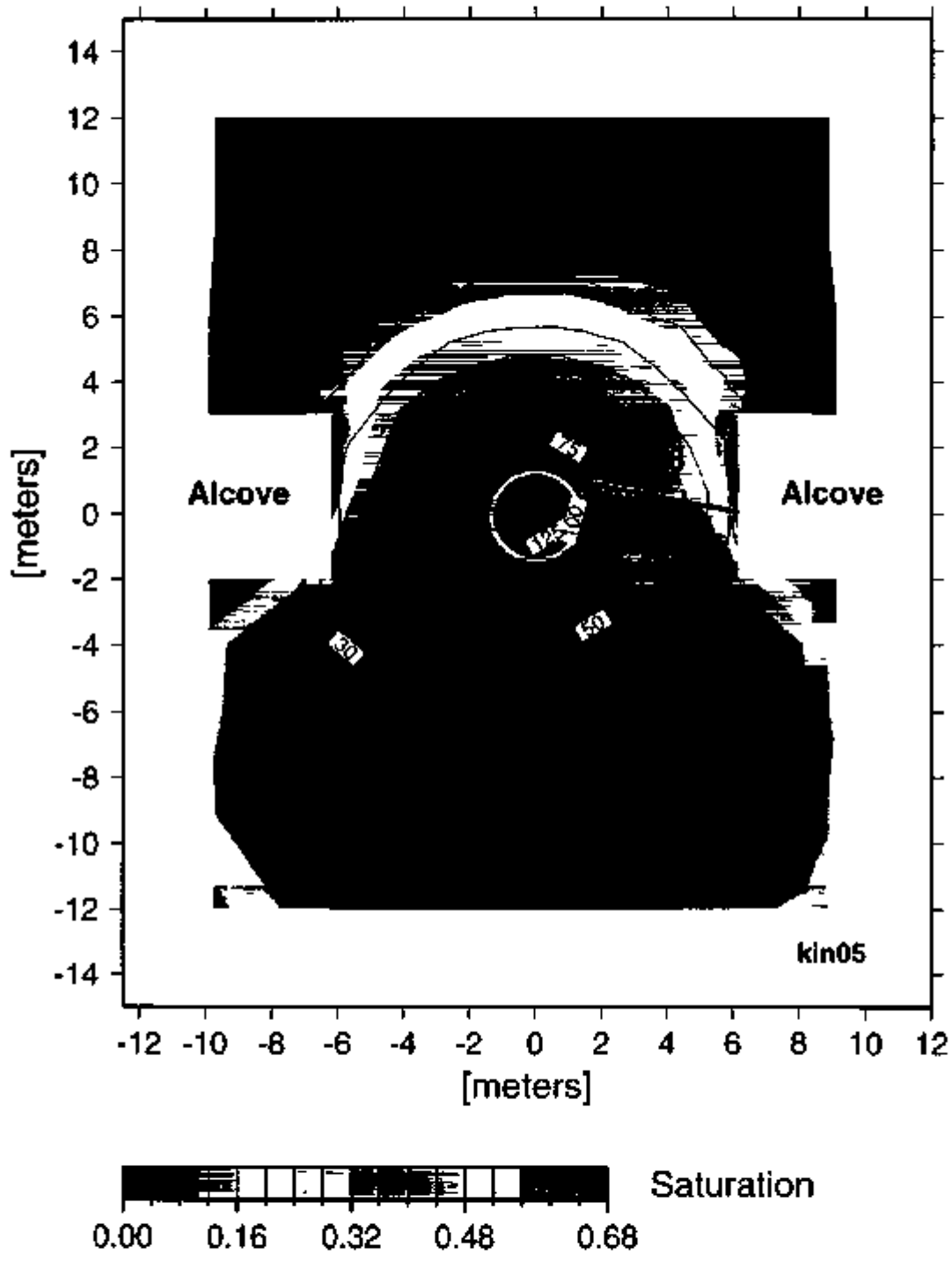

NOTE Corresponding to the sampling time of the second water sample collected from borehole 16 (Simulation KIN05)

Figure 10-8. Calculated Fracture Liquid Saturation and Temperature 161 Days after the Initiation of Heating

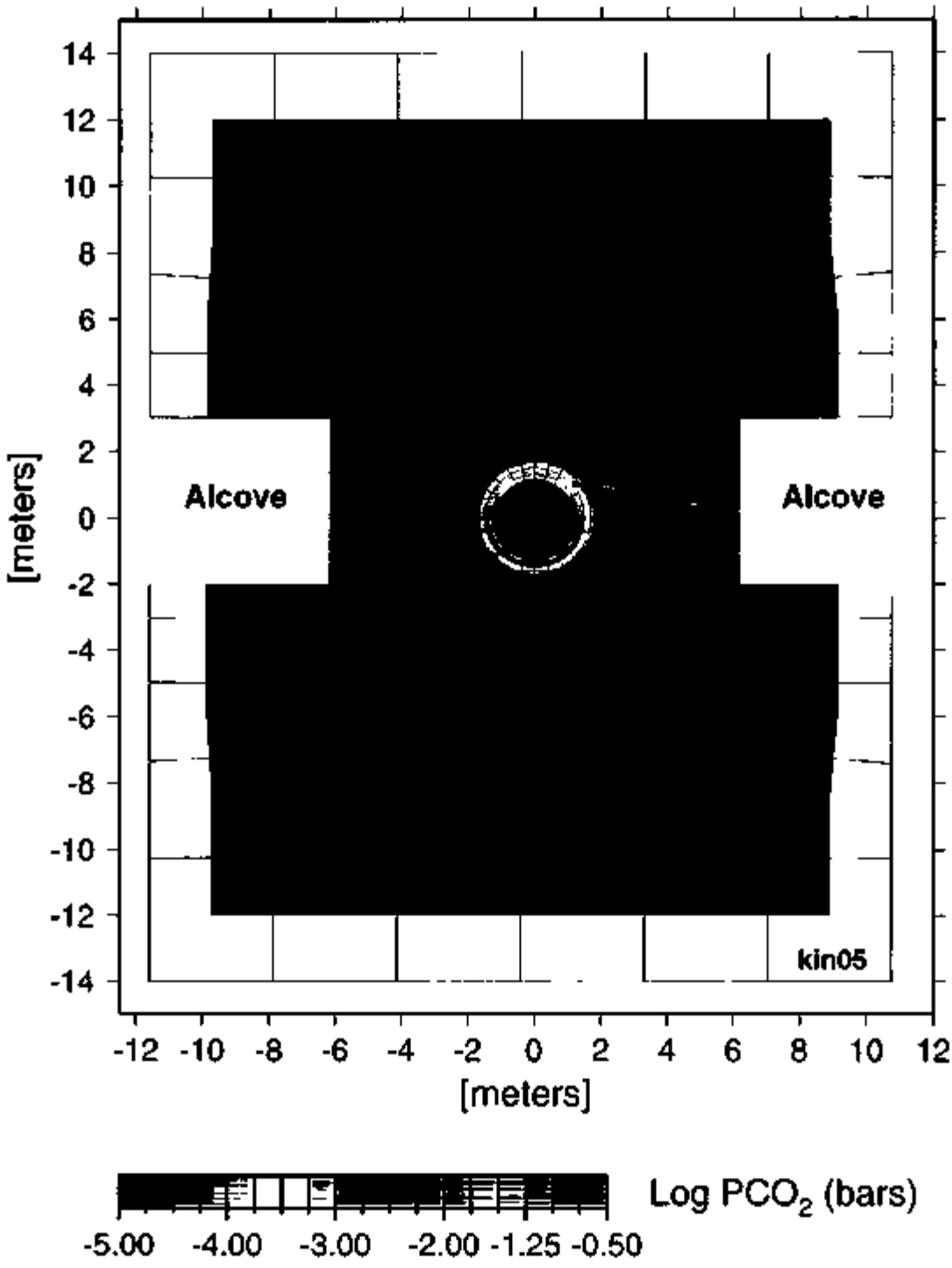

NOTE Simulation KIN05

Figure 10-9. Calculated Partial Pressure of CO_2 in Equilibrium with Water in Fractures after 161 Days

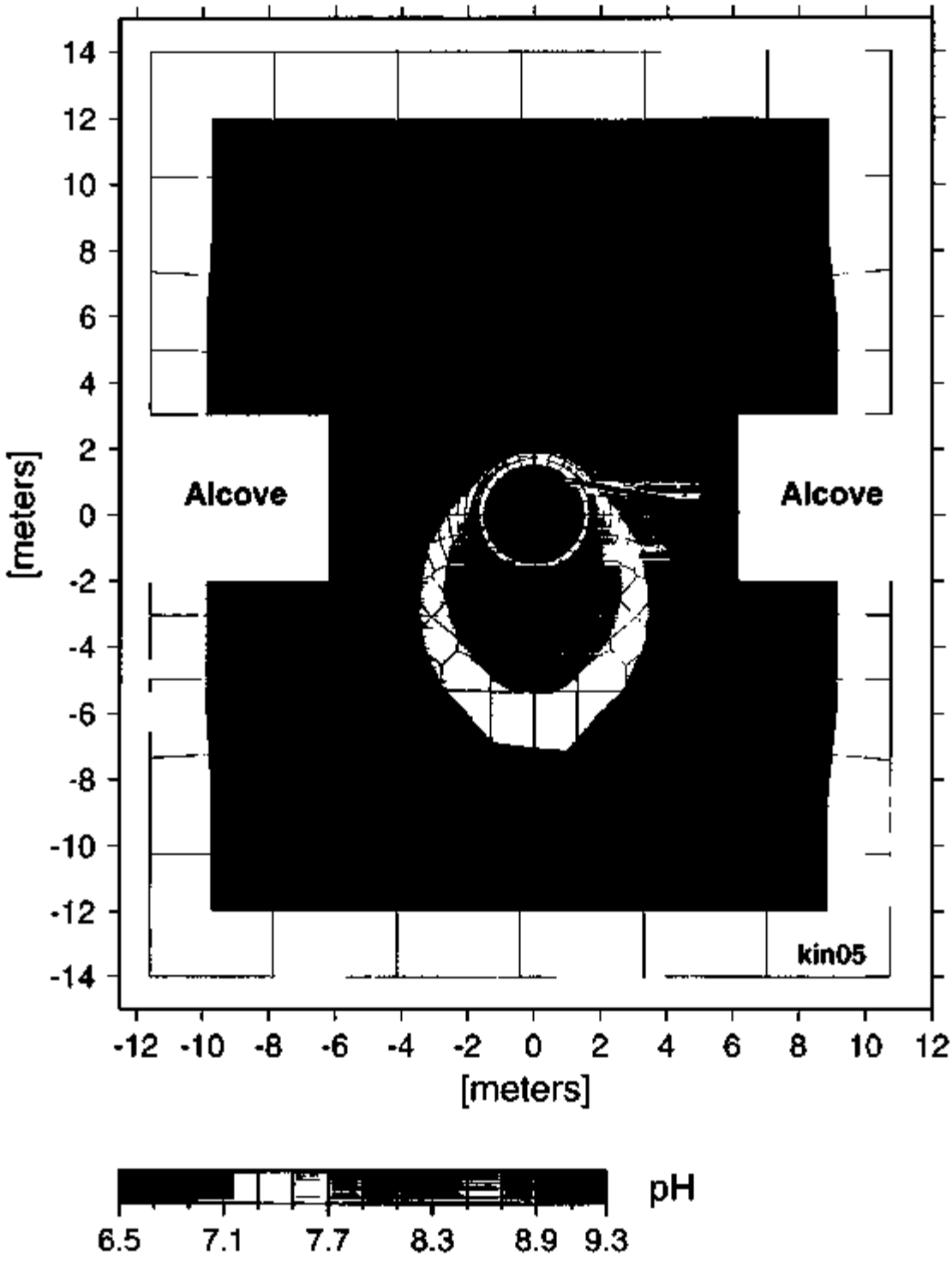

NOTE Simulation KIN05

Figure 10-10 Calculated pH in Fracture Porewaters after 161 Days

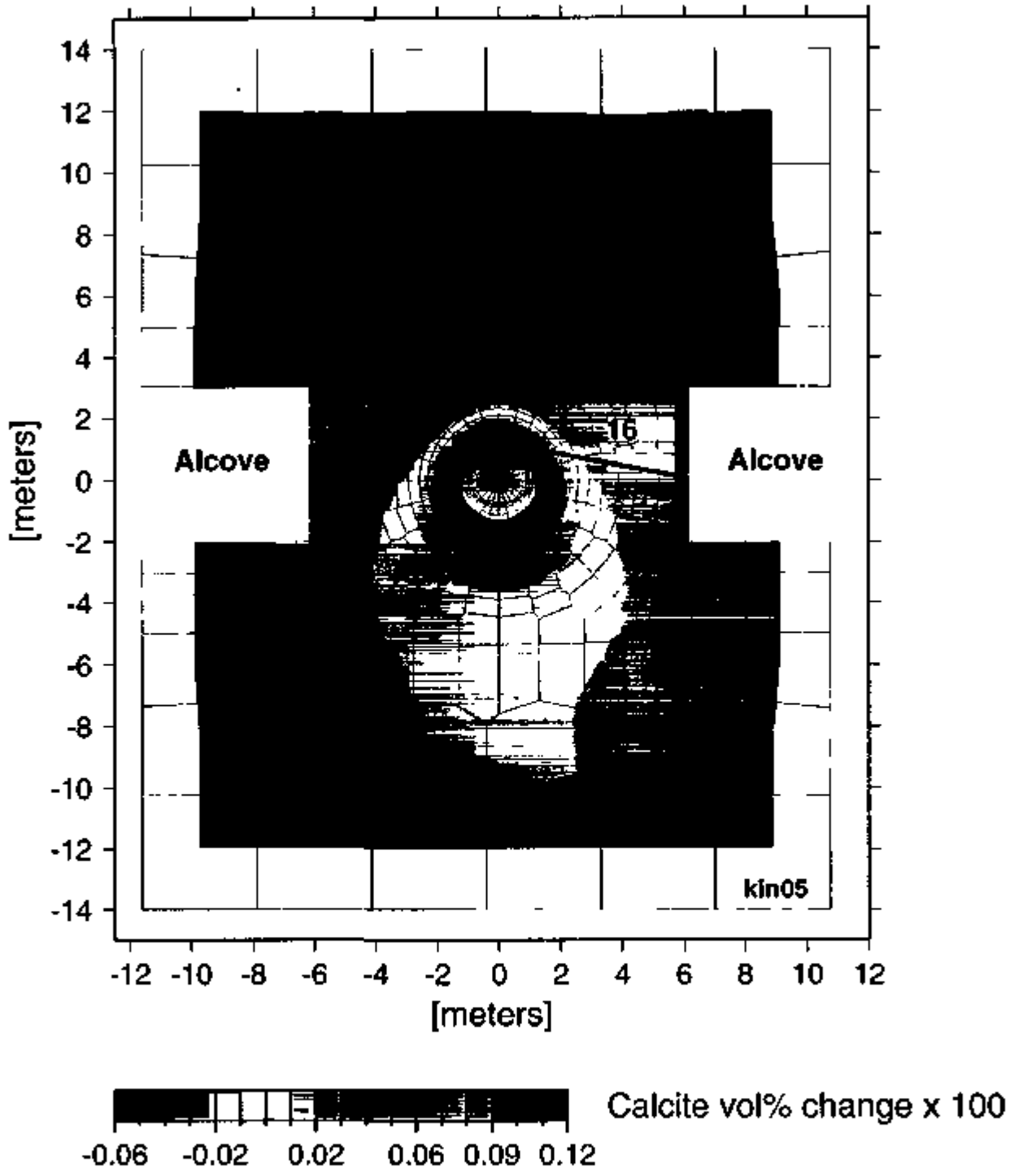

NOTE Simulation KIN05

Figure 10-11 Change in Calcite Volume Percent in Fractures after 161 Days

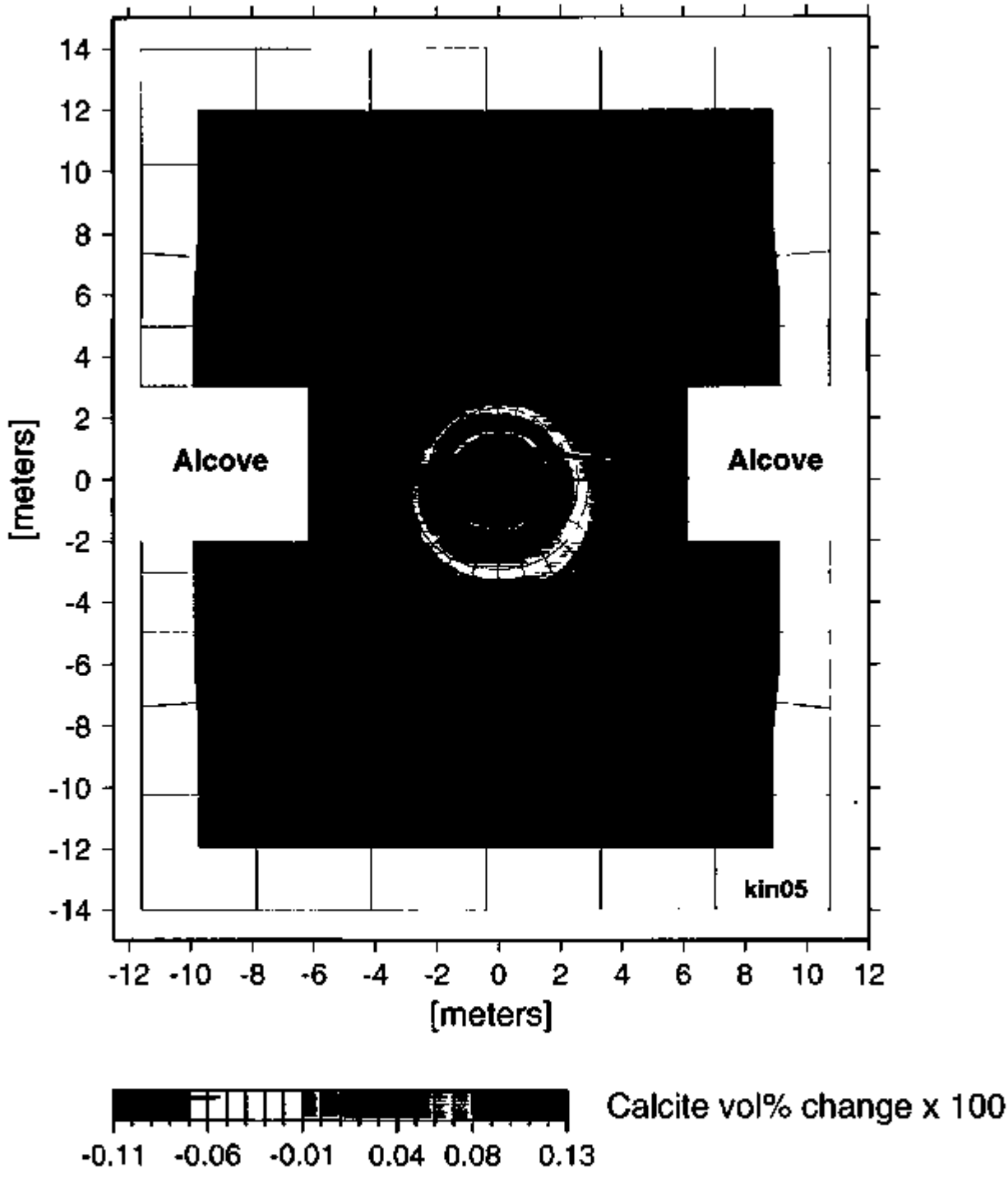

NOTE Simulation KIN05

Figure 10-12. Change in Calcite Volume Percent in Fractures after 521 Days, Approximately Eight Months after the Termination of Heating

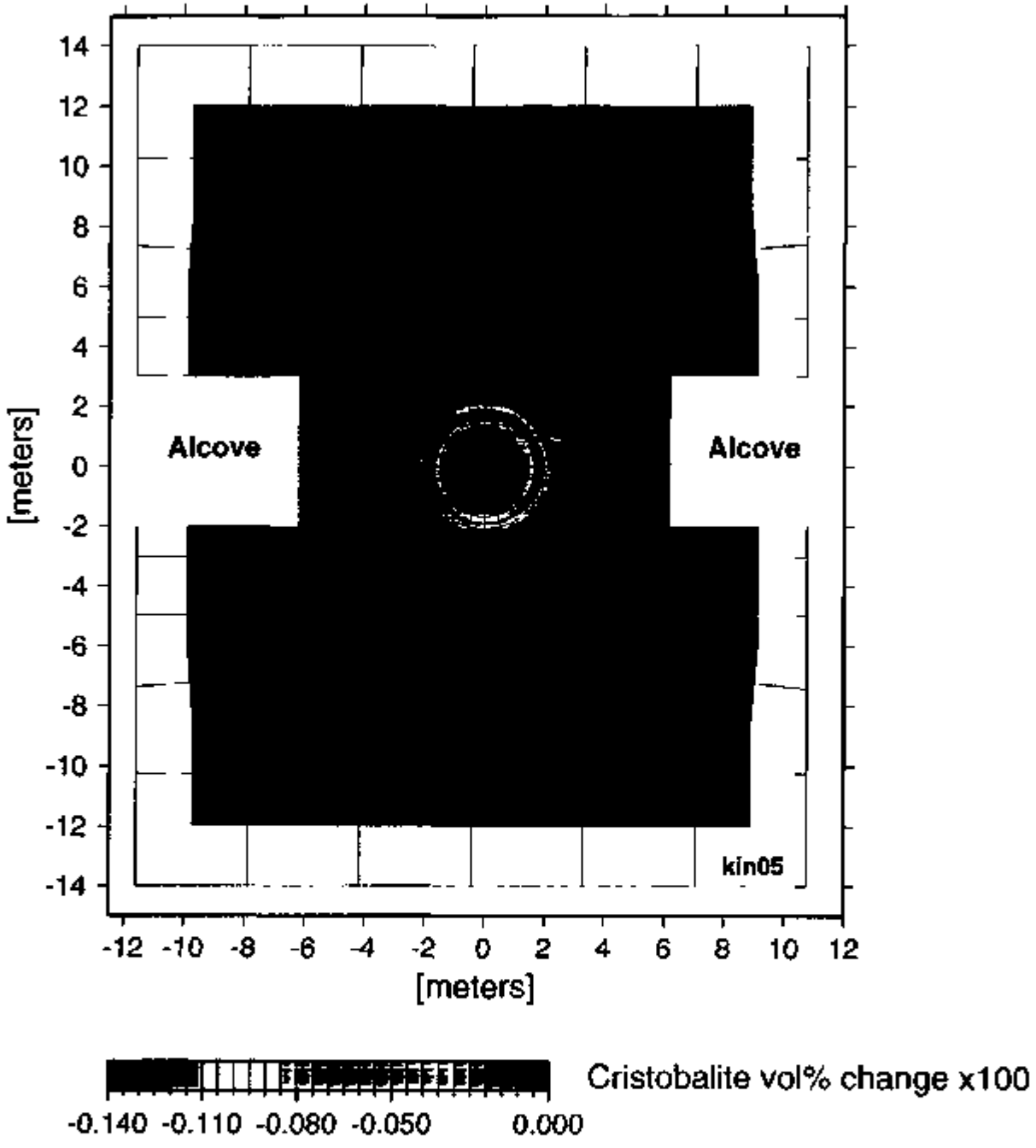

NOTE Simulation KIN05

Figure 10-13. Change in Cristobalite Volume Percent in Fractures after 521 Days

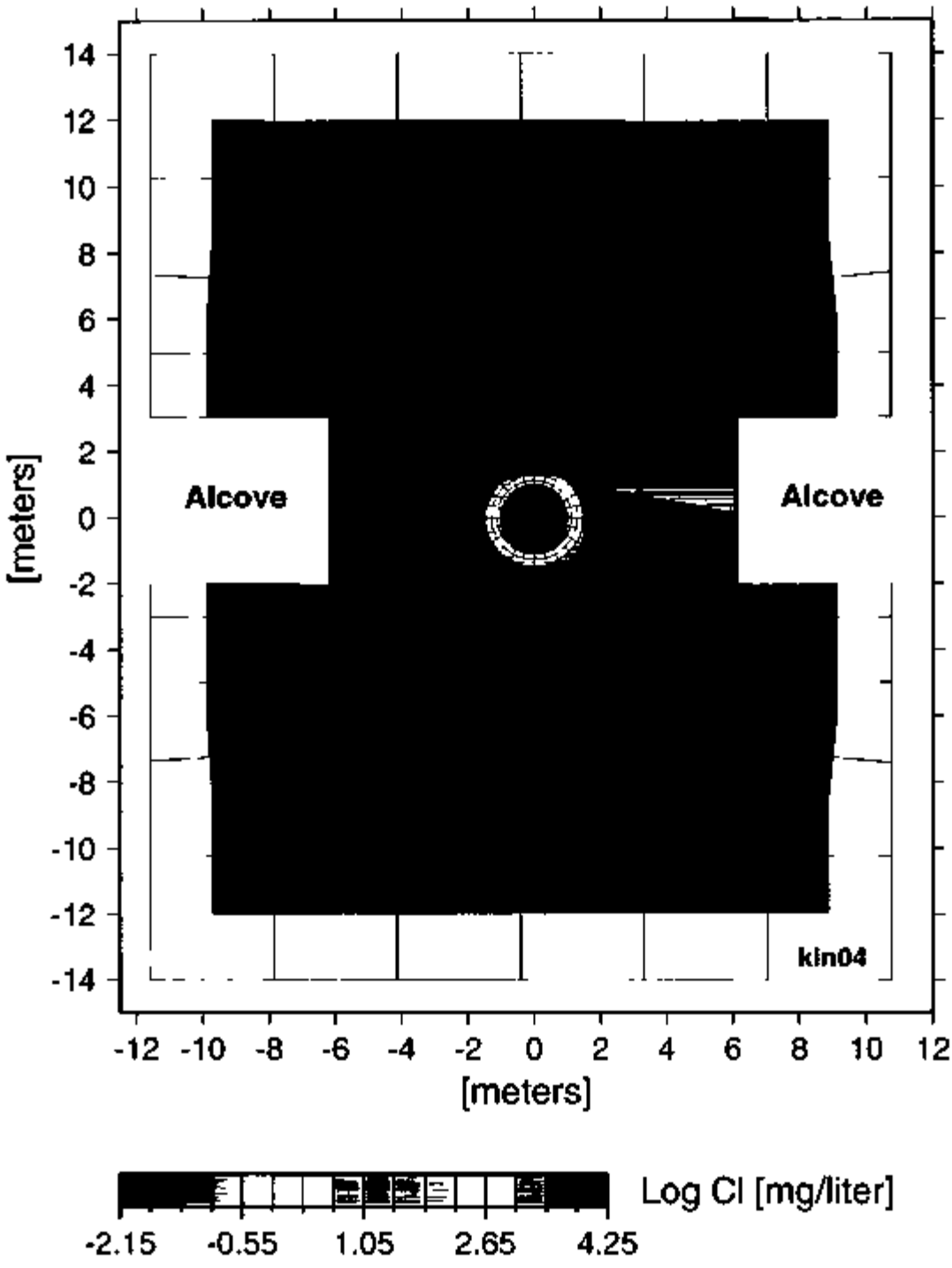

NOTE: Simulation KIN04

Figure 10-14. Calculated Chloride Concentration in Fracture Porewaters after 91 Days

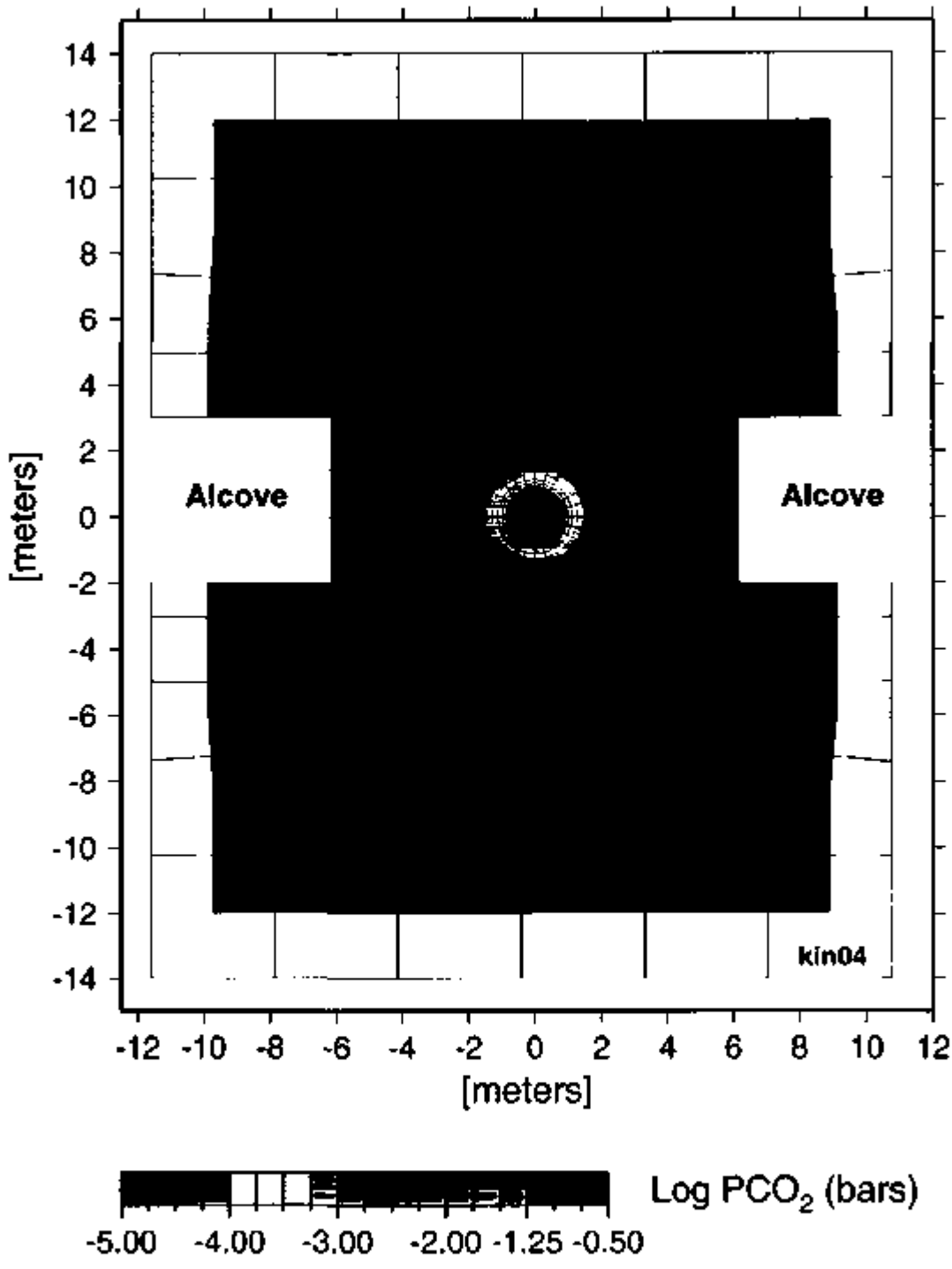

NOTE: Simulation KIN04

Figure 10-15. Calculated Partial Pressure of CO_2 in Equilibrium with Water in Fractures after 91 Days

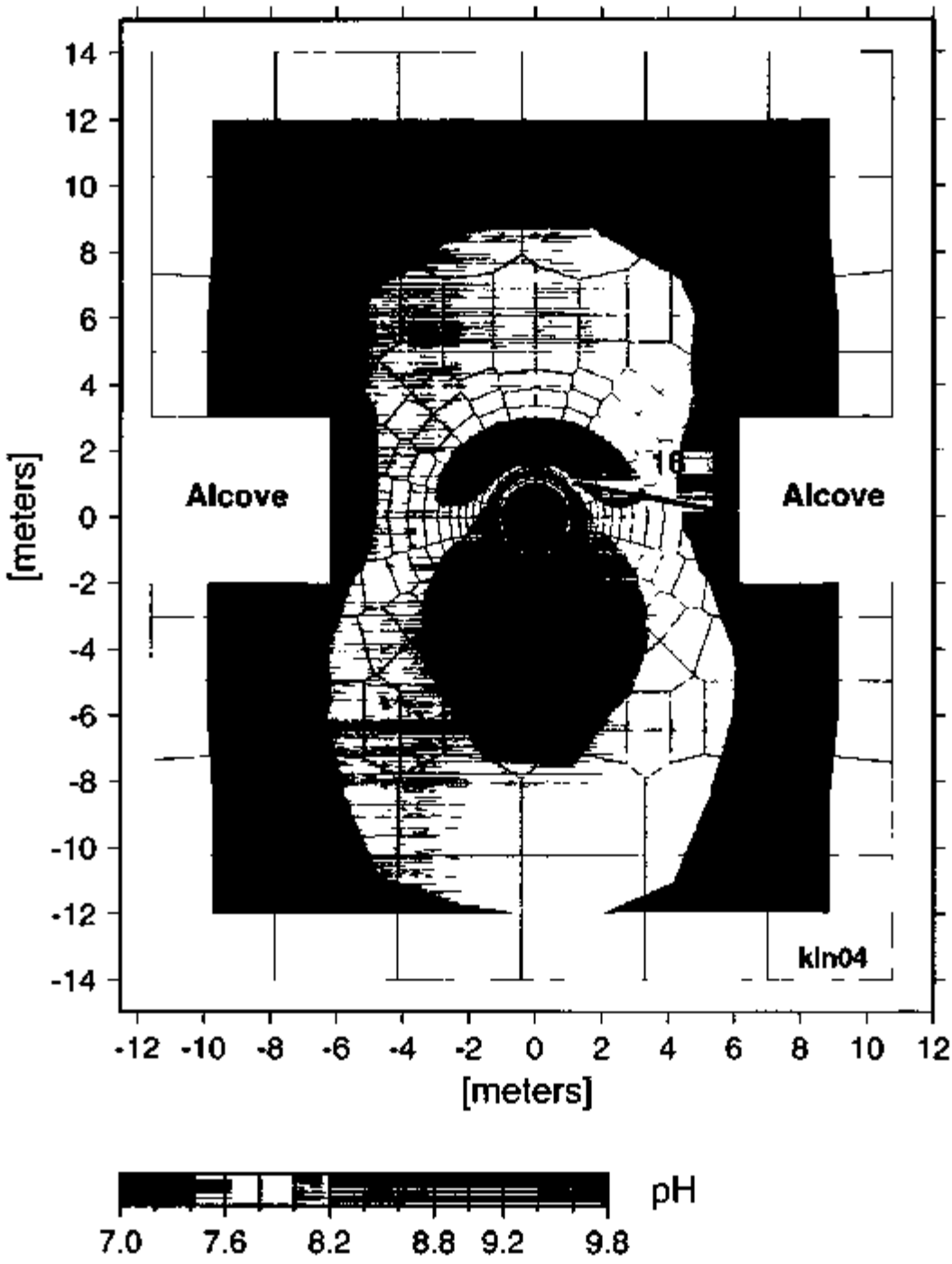

NOTE Simulation KIN04

Figure 10-16 Calculated pH in Fracture Porewaters after 91 Days

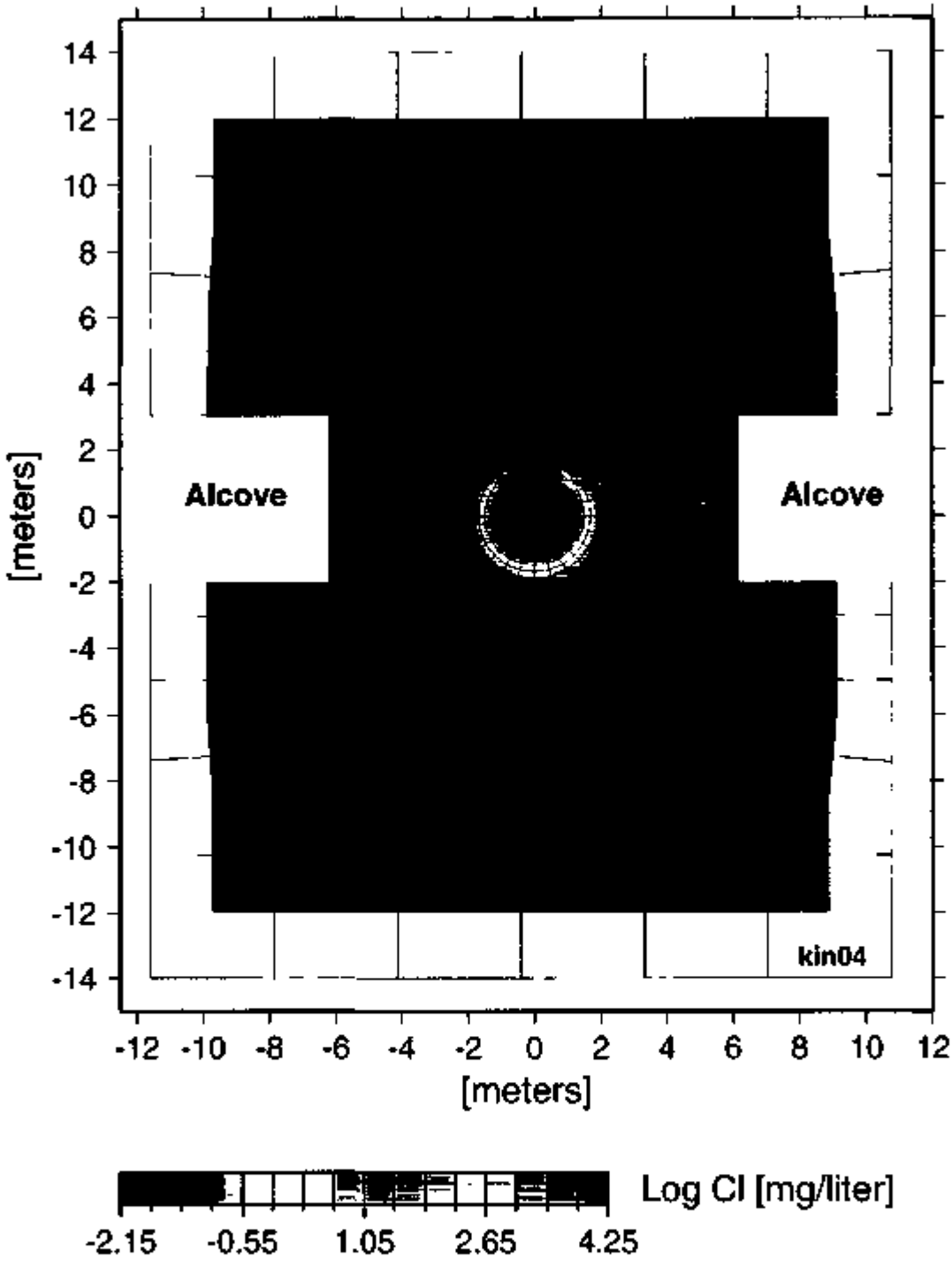

NOTE Simulation KIN04

Figure 10-17. Calculated Chloride Concentration in Fracture Porewaters after 161 Days

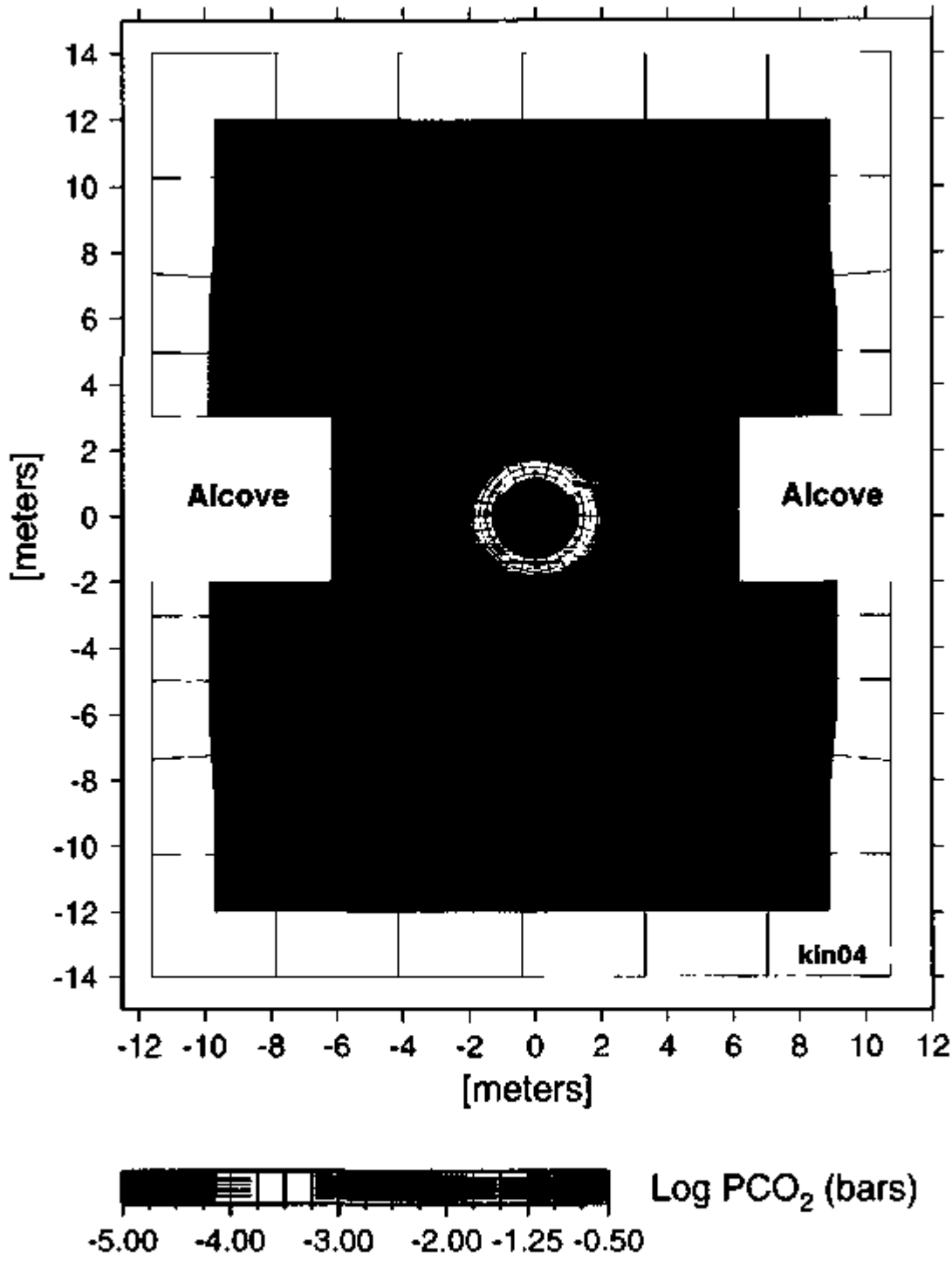

NOTE: Simulation KIN04

Figure 10-18. Calculated Partial Pressure of CO_2 in Equilibrium With Water in Fractures after 161 Days

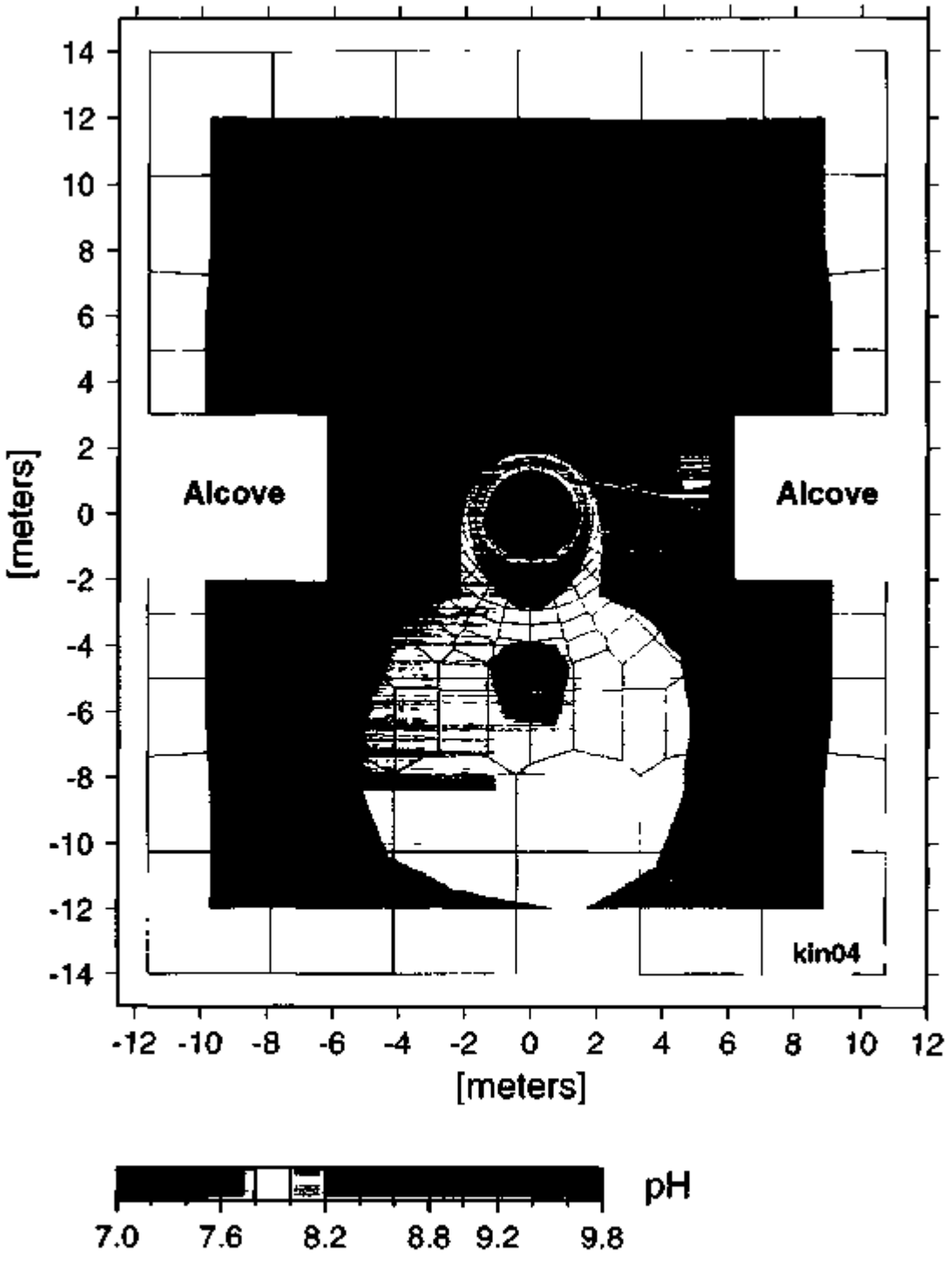

NOTE Simulation KIN04

Figure 10-19. Calculated pH in Fracture Porewaters after 161 Days

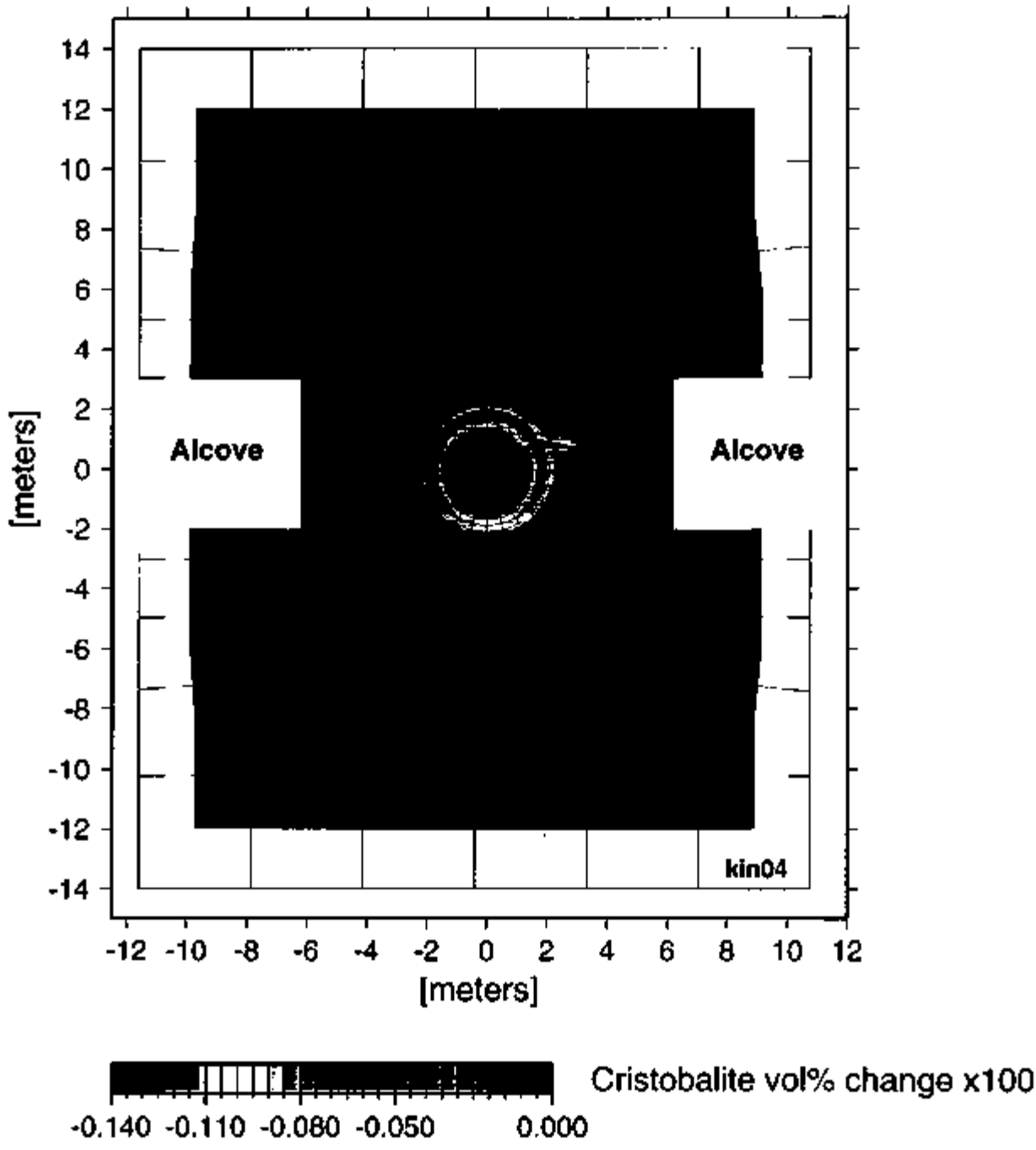

NOTE: Simulation KIN04

Figure 10-20. Change in Cristobalite Volume Percent in Fractures after 521 Days, Approximately Seven Months after the Termination of Heating

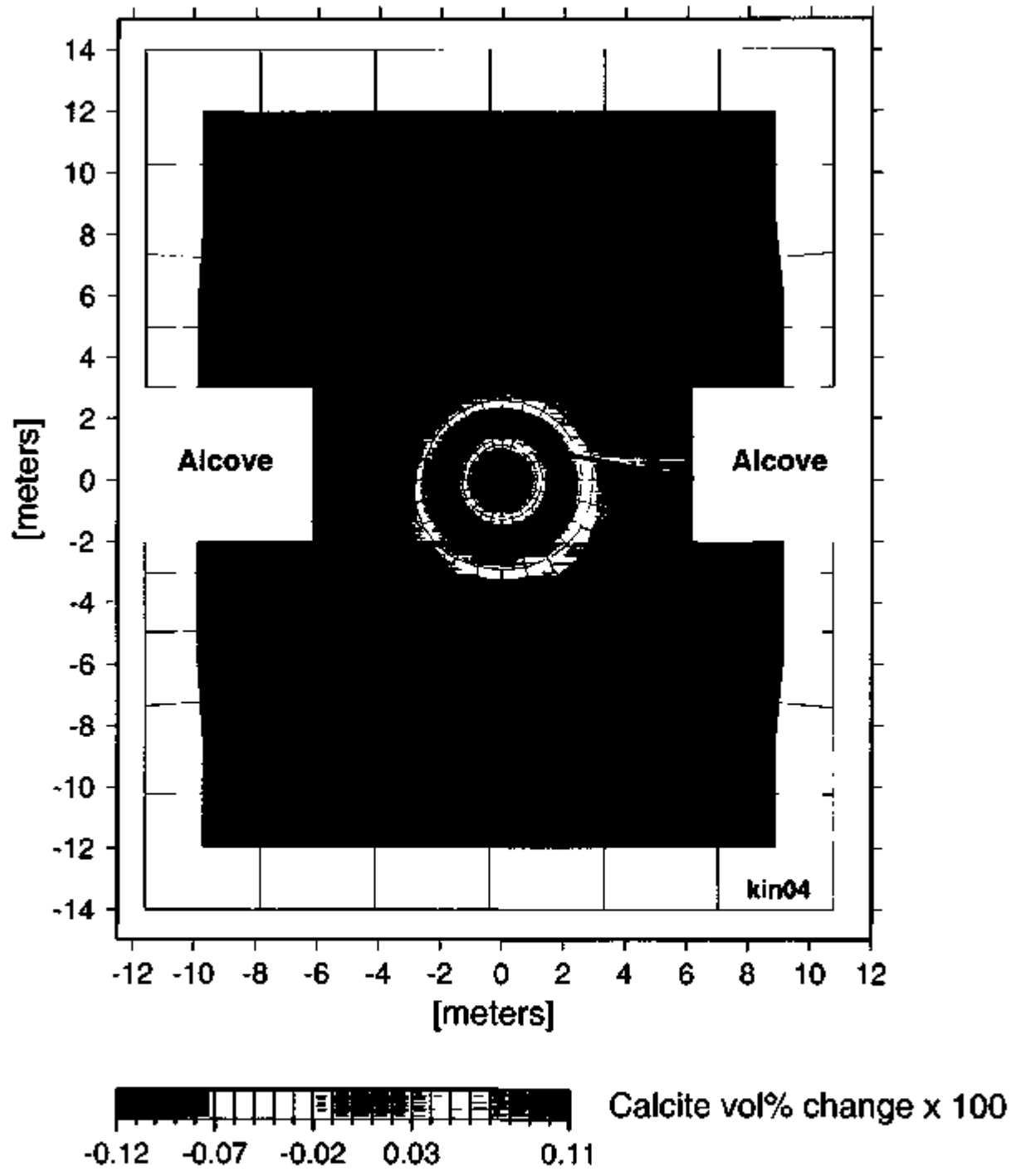

NOTE Simulation KIN04

Figure 10-21 Change in Calcite Volume Percent in Fractures after 521 Days

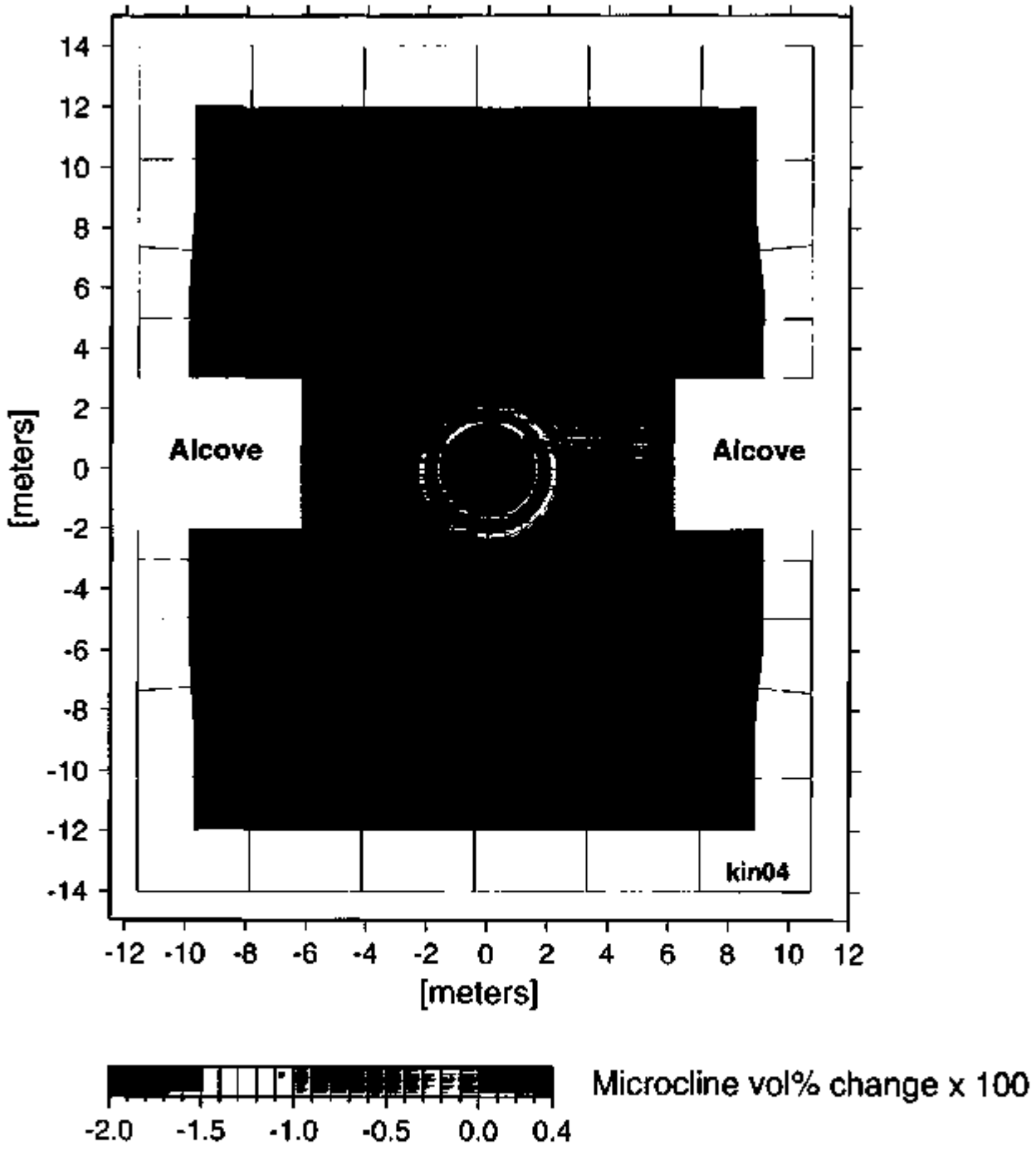

NOTE: Simulation KIN04

Figure 10-22. Change in Microcline (K-Feldspar) Volume Percent in Fractures after 521 Days

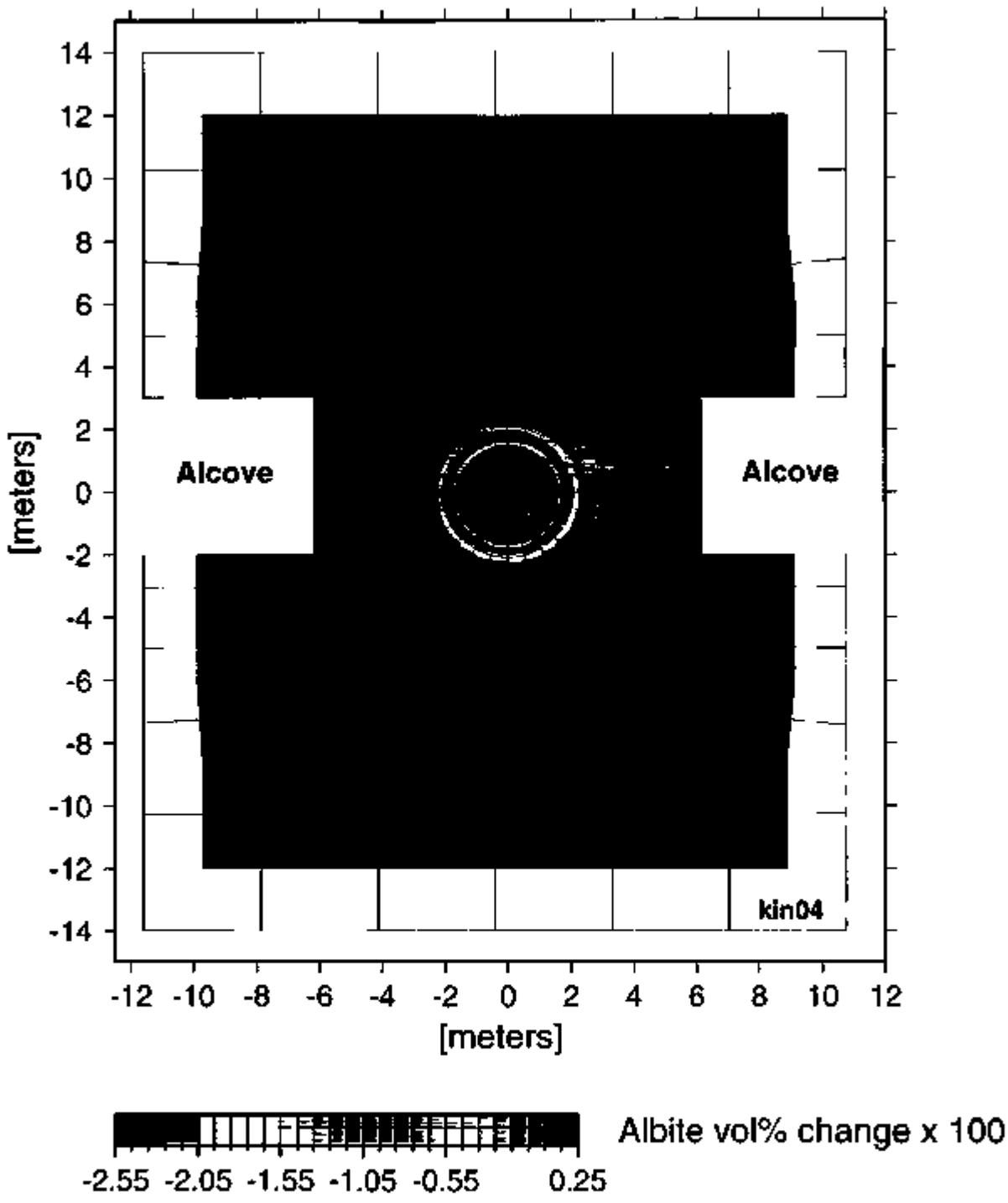

NOTE: Simulation KIN04

Figure 10-23. Change in Albite (Na-Feldspar) Volume Percent in Fractures after 521 Days

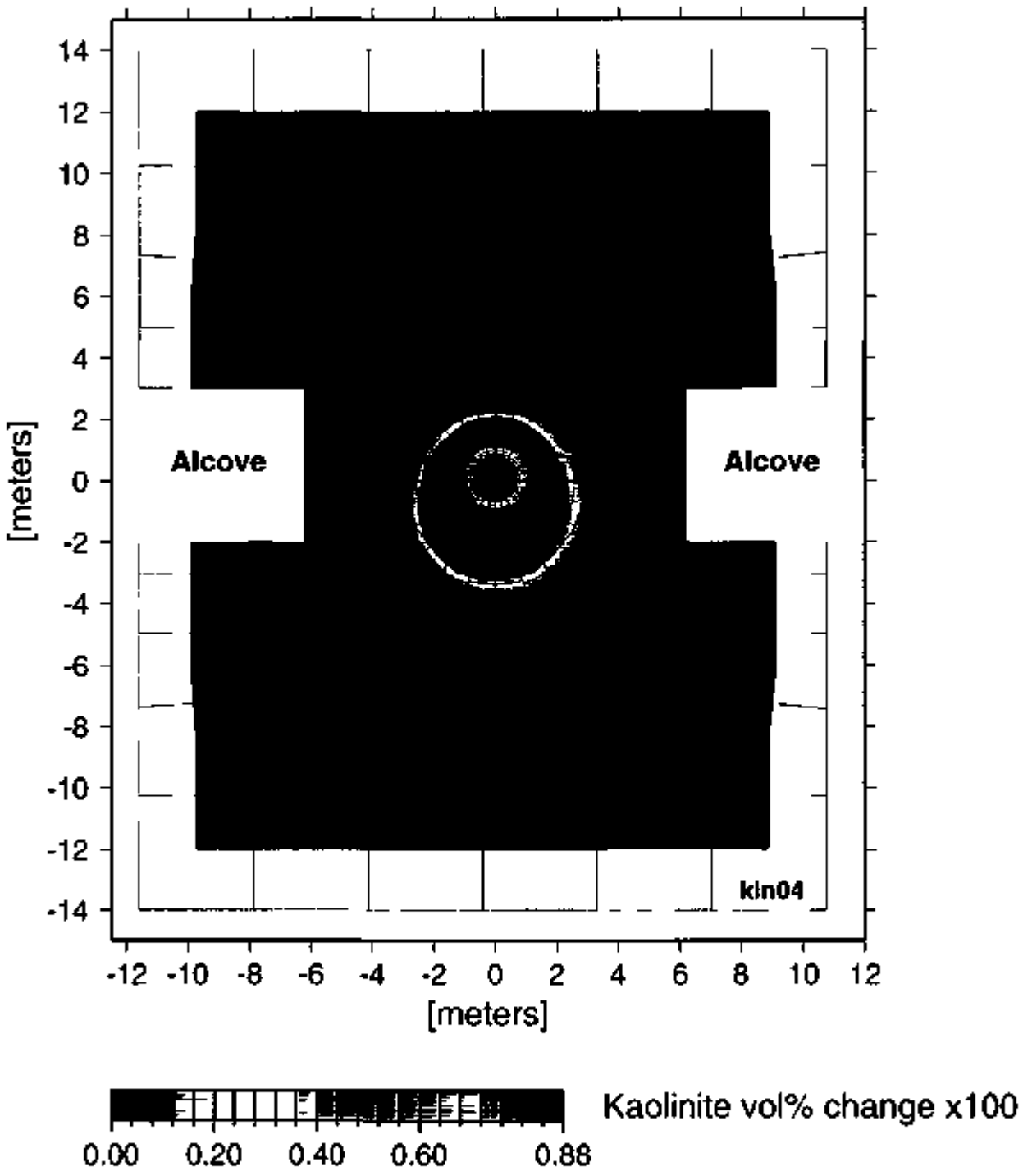

NOTE Simulation KIN04

Figure 10-24 Change in Kaolinite Volume Percent in Fractures after 521 Days

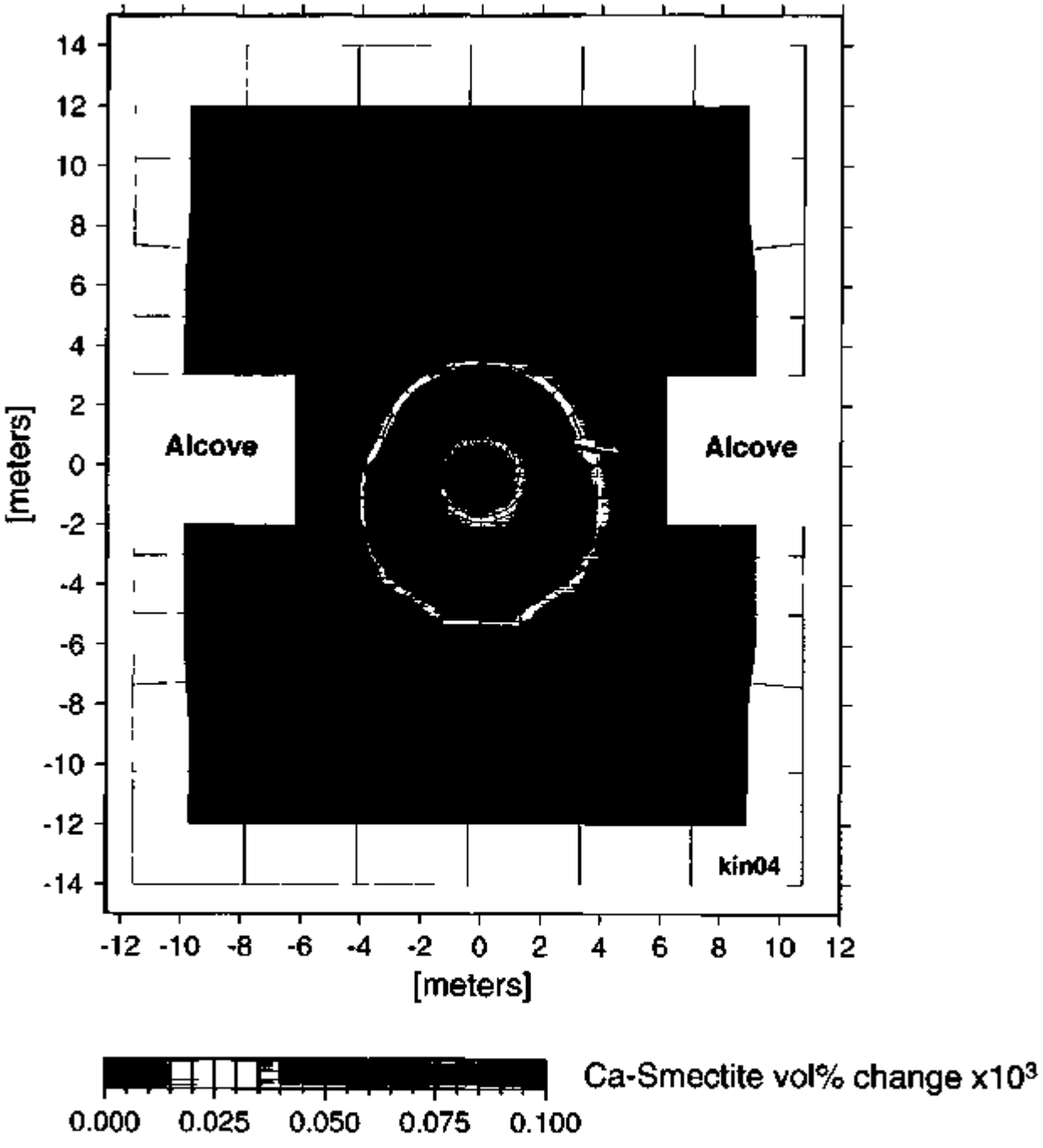

NOTE Simulation KIN04

Figure 10-25 Change in Ca-Smectite Volume Percent in Fractures after 521 Days

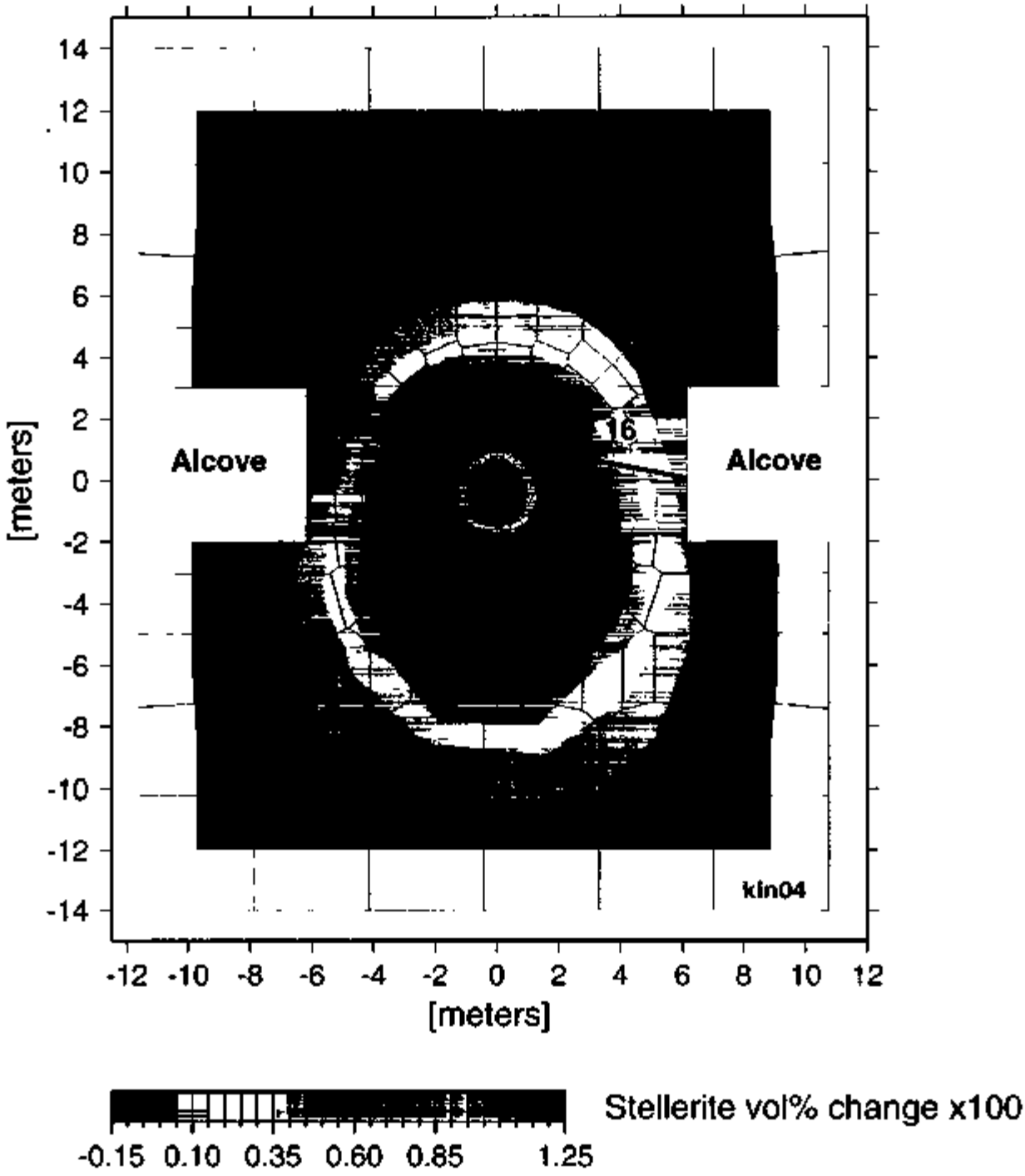

NOTE Simulation KIN04

Figure 10-26. Change in Stellerite (Zeolite) Volume Percent in Fractures after 521 Days

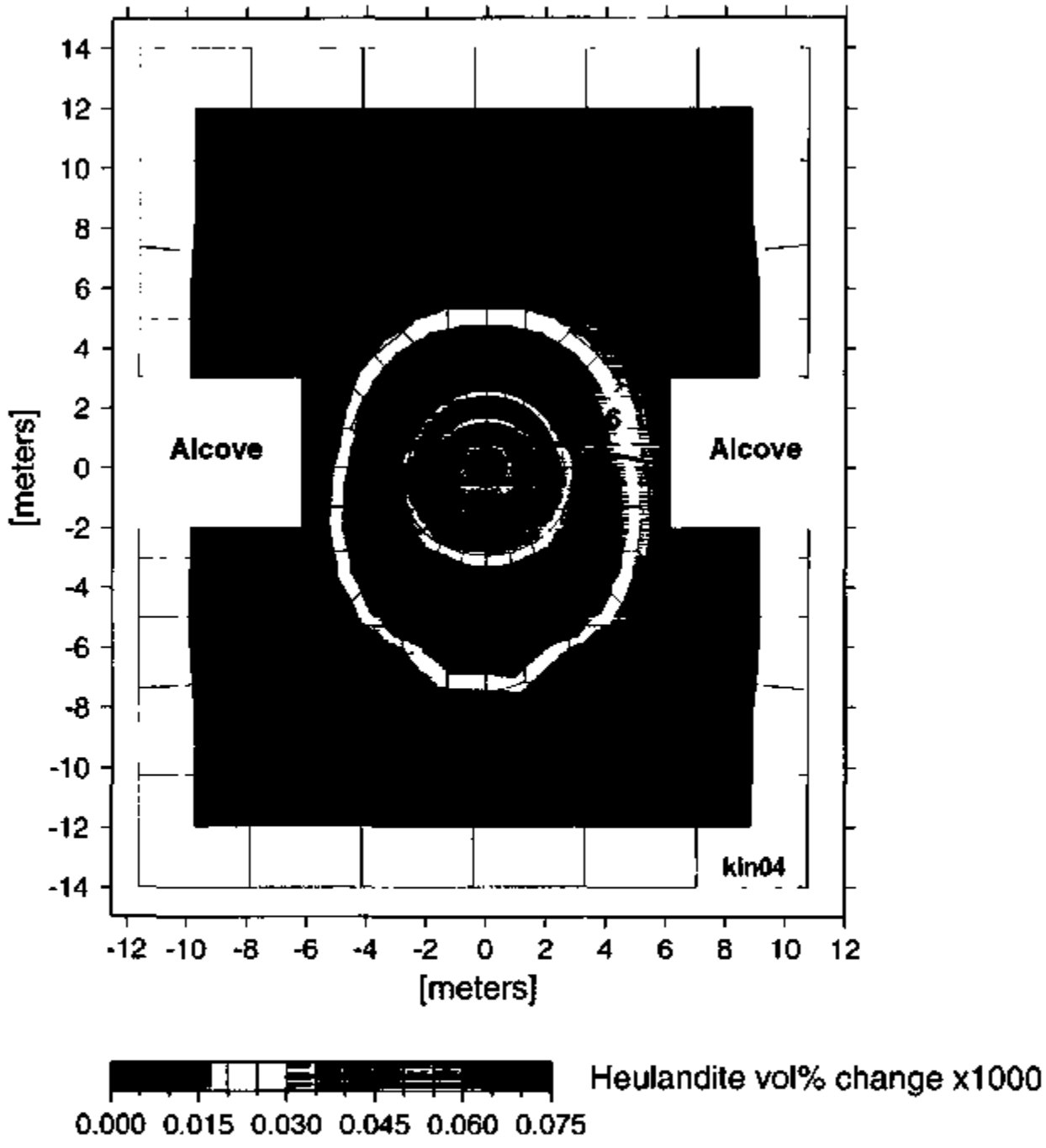

NOTE: Simulation KIN04

Figure 10-27. Change in Heulandite (Zeolite) Volume Percent in Fractures after 521 Days

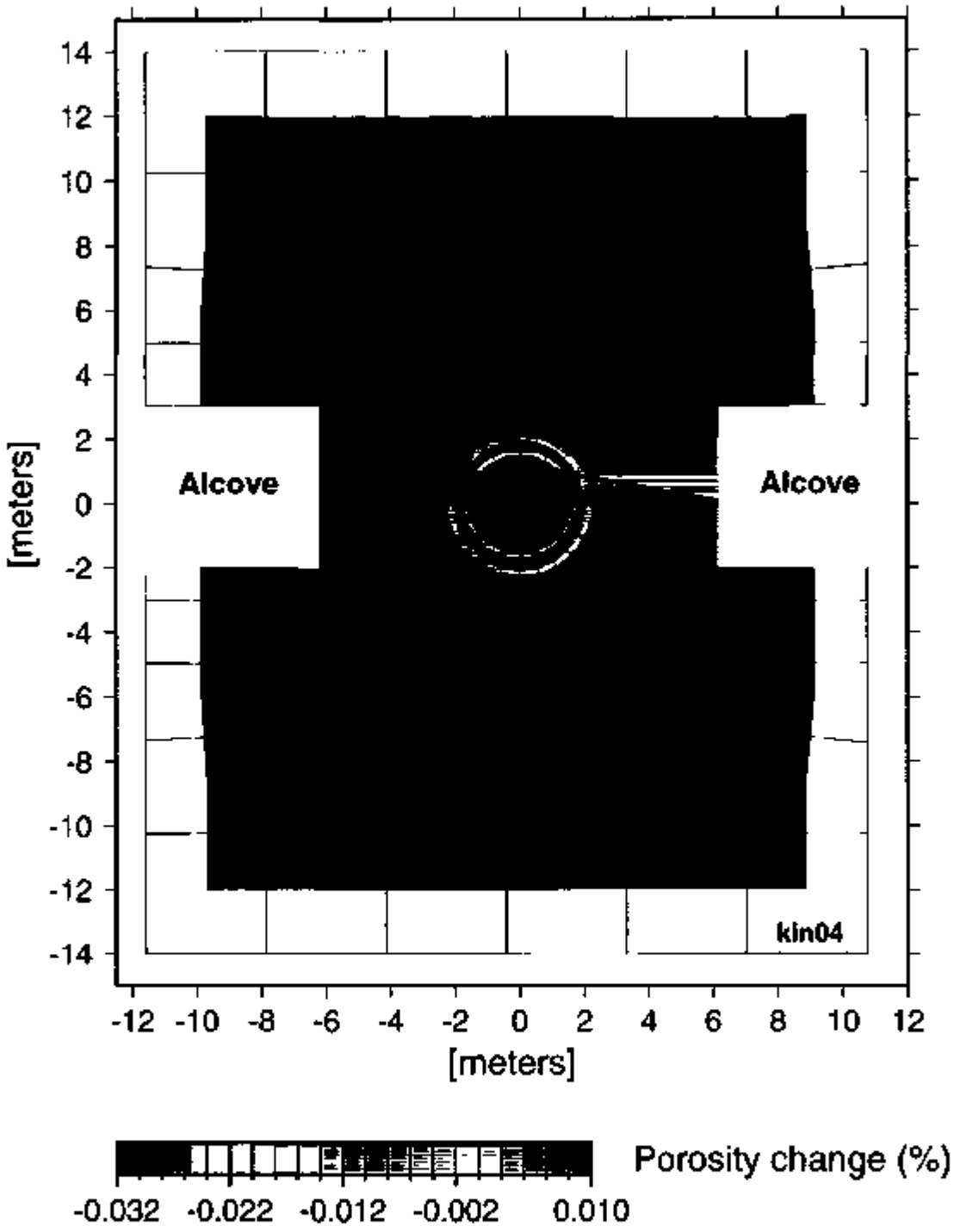

NOTE: Simulation KIN04

Figure 10-28. Change in Fracture Porosity (Percent) after 521 Days

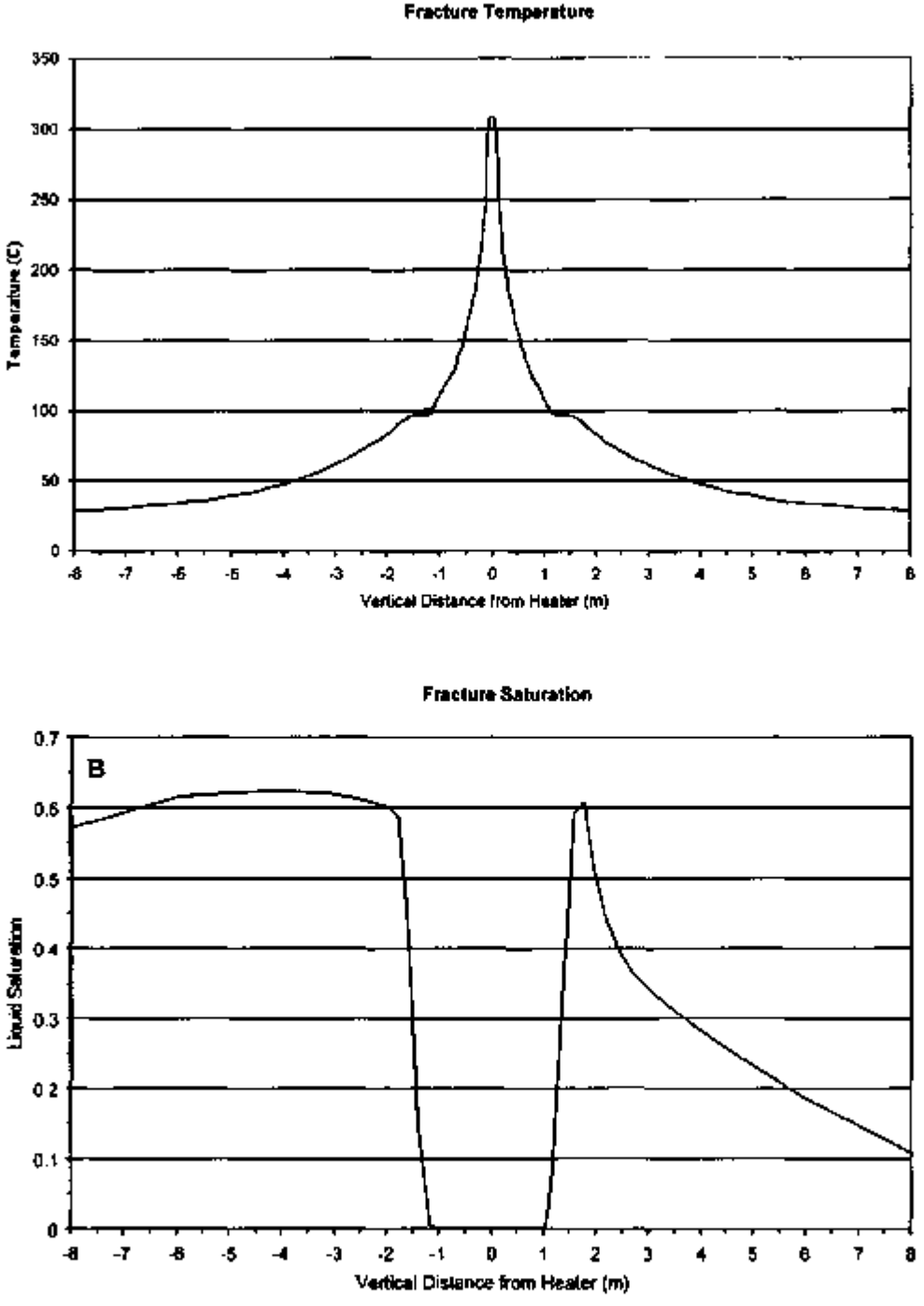

NOTE: Computed profiles through the heater at the location shown on Figure 10-3. Simulation with aluminosilicates (KIN04).

Figure 10-29. Temperature in Fractures, and Liquid Saturation in Fractures at 161 Days

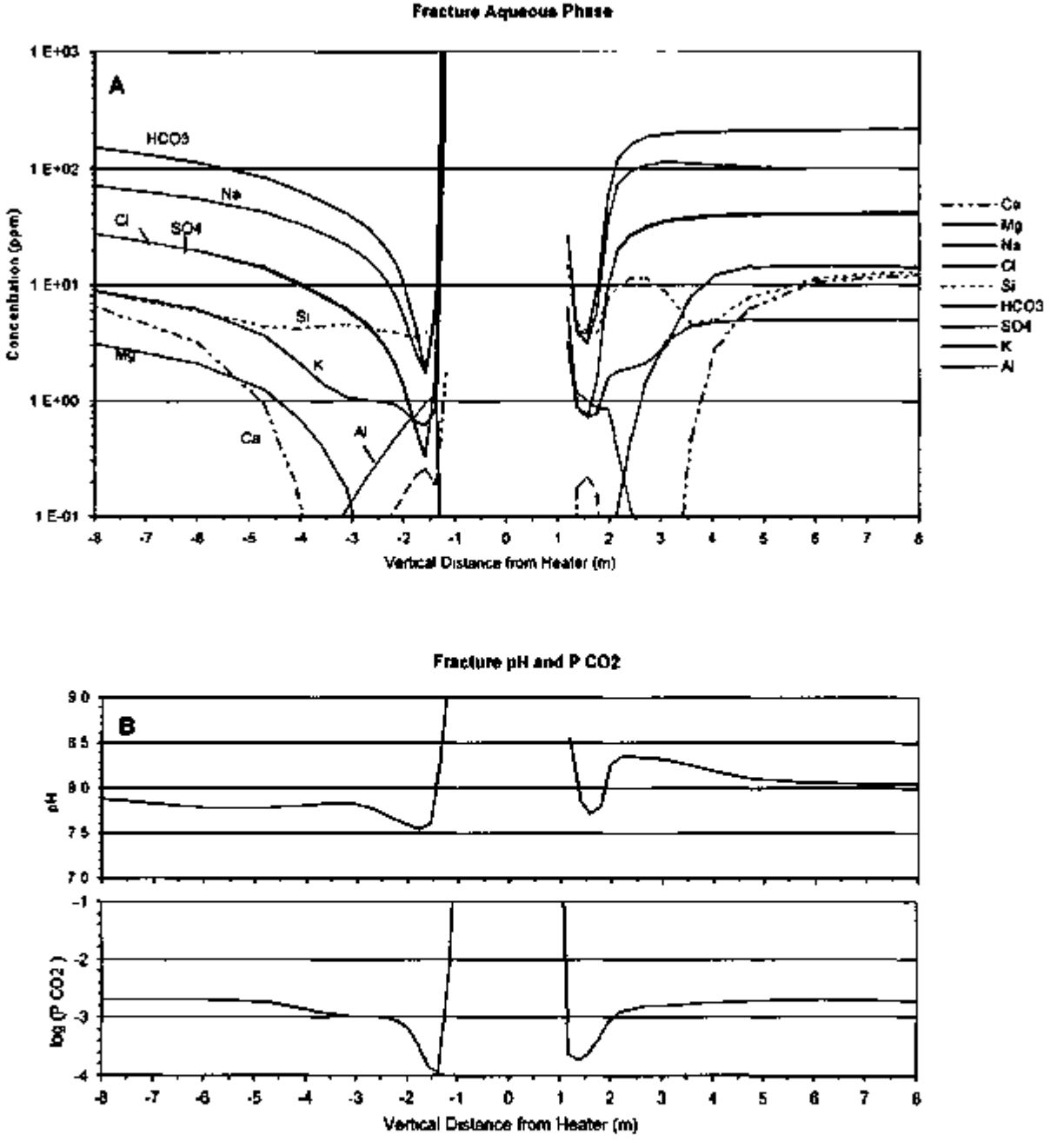

NOTE: Computed profiles through the heater at the location shown on Figure 10-3. Simulation with aluminosilicates (KIN04).

Figure 10-30. (a) Concentrations of Aqueous Species and (b) pH and CO_2 Partial Pressure (Bars) in Fractures at 161 Days

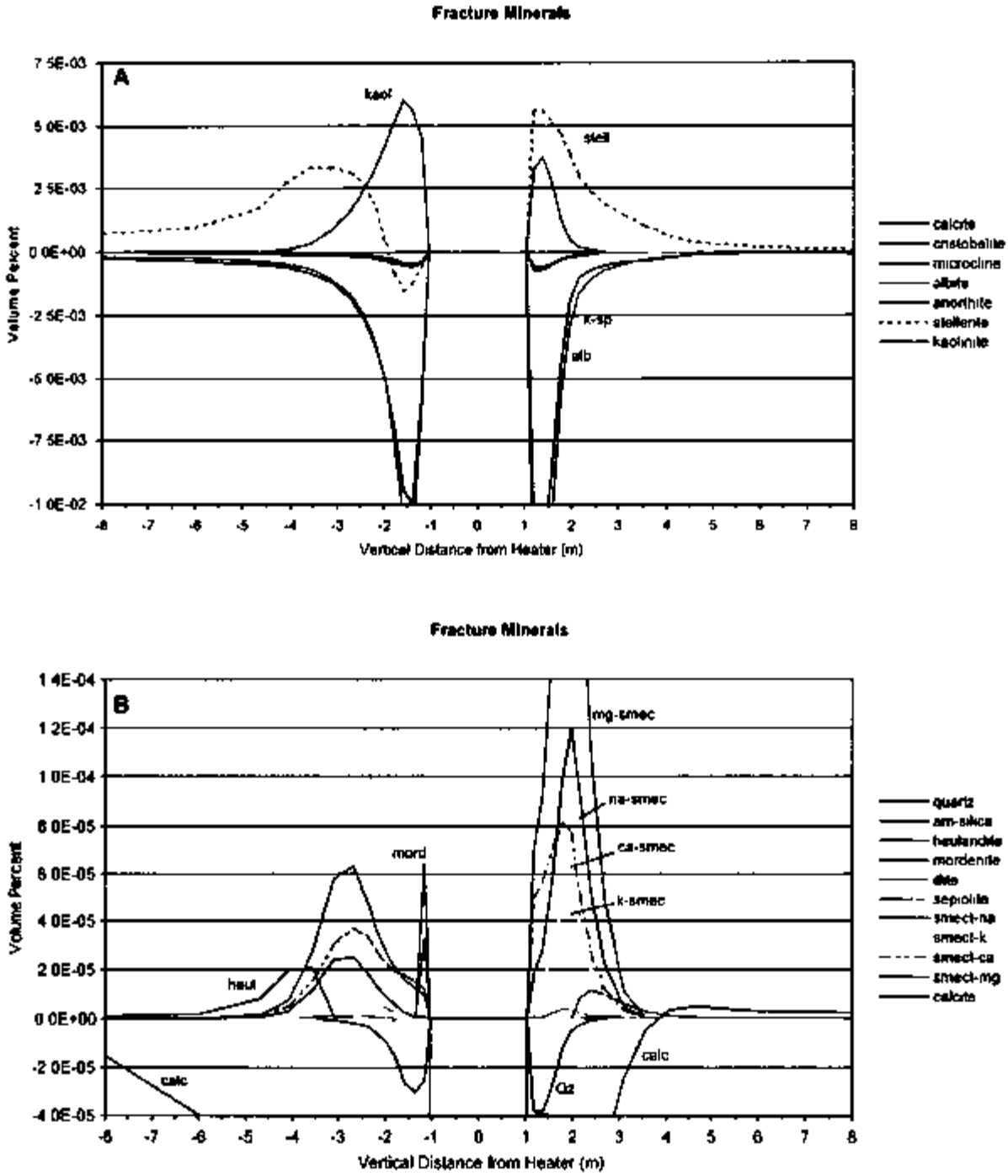

NOTE Computed profiles through the heater at the location shown on Figure 10-3 Simulation with aluminosilicates (KIN04)

Figure 10-31. Change in Mineral Volume Percent in Fractures, at 161 Days

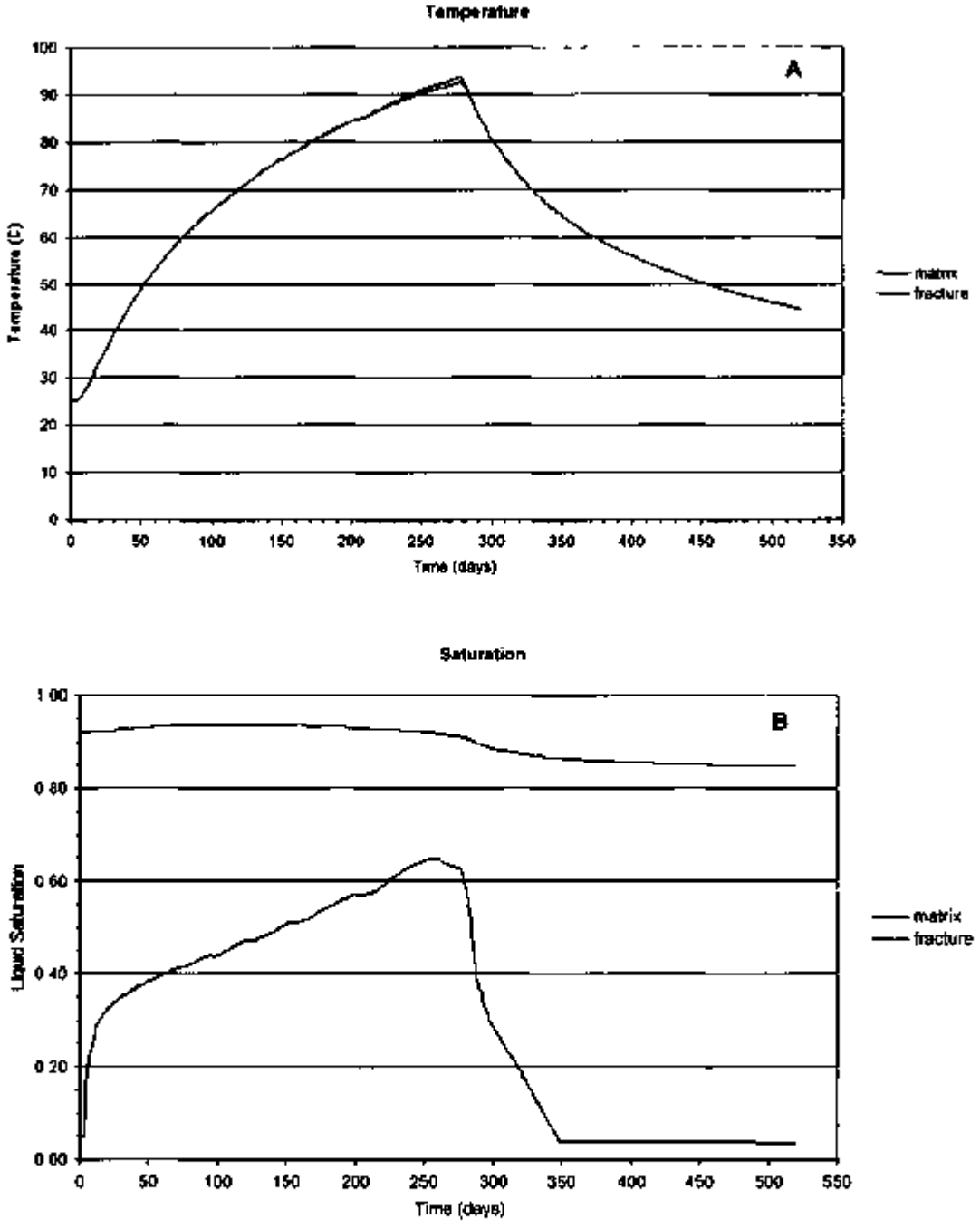

NOTE. Computed at a point shown on Figure 10-3. Simulation with aluminosilicates (KIN04).

Figure 10-32. Time Profiles of (a) Temperature and (b) Liquid Saturation in Fractures and Matrix

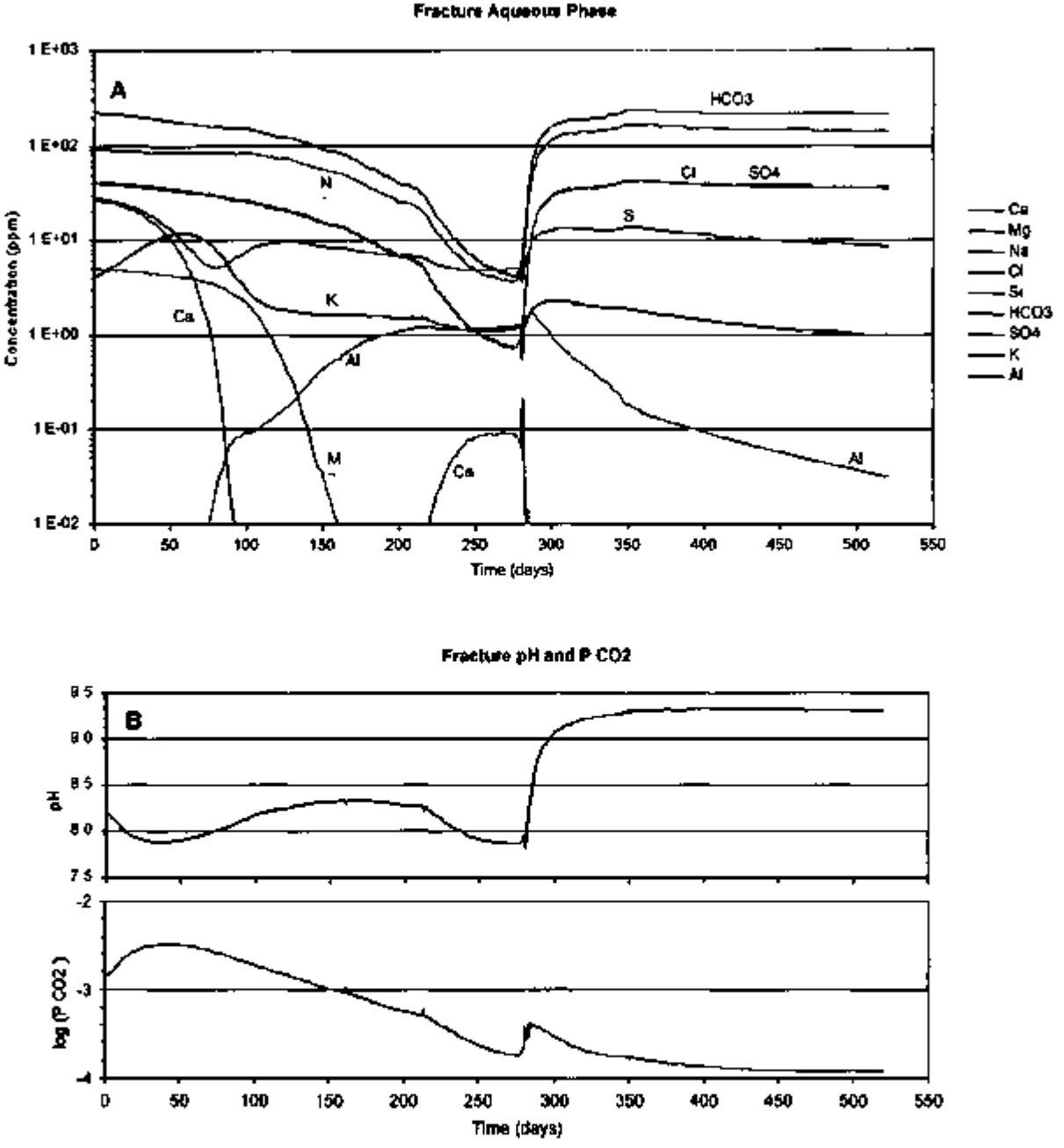

NOTE: Computed at a point shown on Figure 10-3. Simulation with aluminosilicates (KIN04).

Figure 10-33. Time Profiles of (a) Aqueous Species Concentrations and (b) pH and CO_2 Partial Pressure (Bars) in Fractures

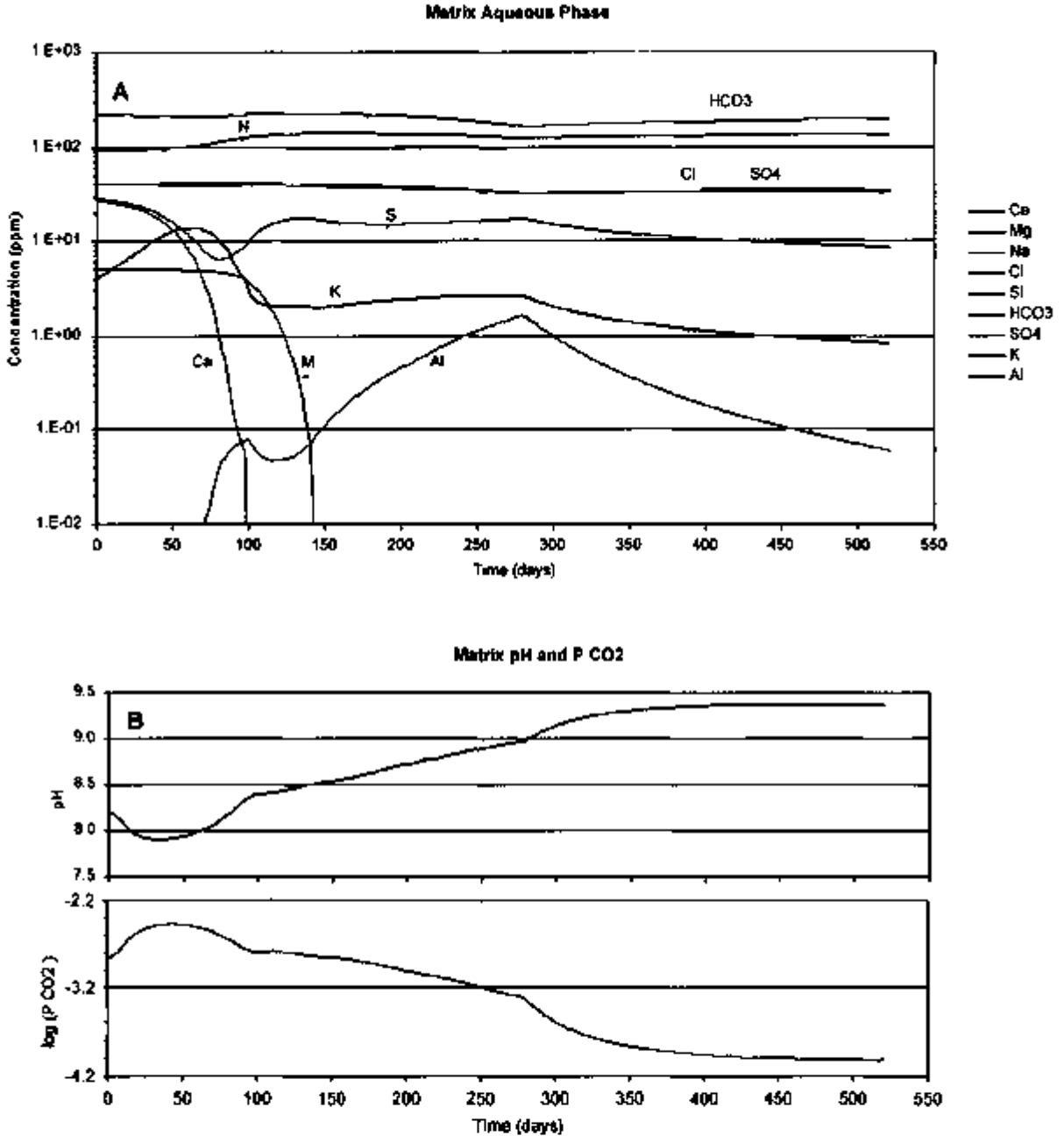

NOTE: Computed at a grid point shown on Figure 10-3. Simulation with aluminosilicates (KIN04).

Figure 10-34. Time Profiles of (a) Aqueous Species Concentrations and (b) pH and CO_2 Partial Pressure (Bars) in the Matrix

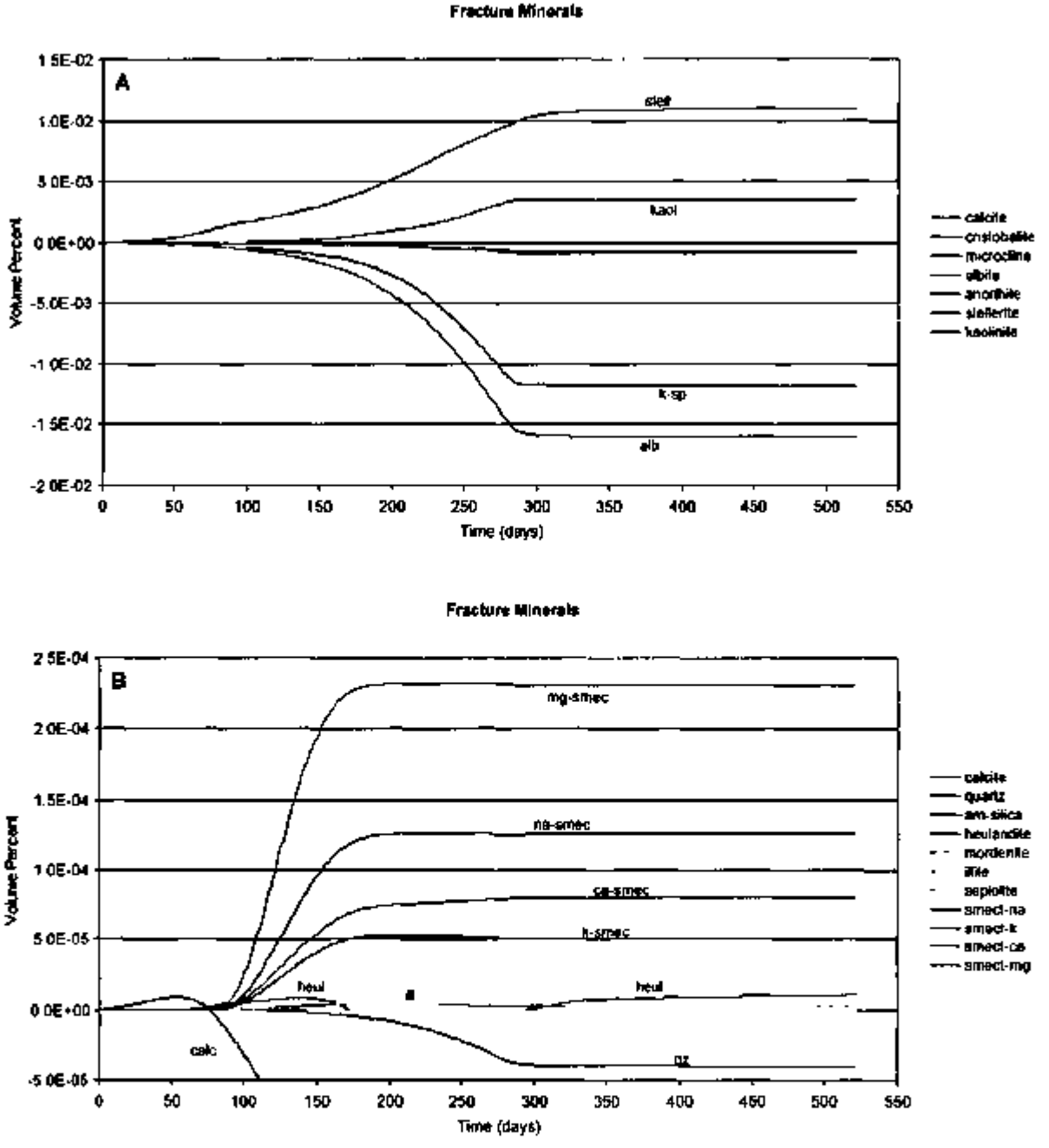

NOTE: Computed at a grid point shown on Figure 10-3. Simulation with aluminosilicates (KIN04).

Figure 10-35. Time Profiles of Mineral Volume Percent Changes in Fractures

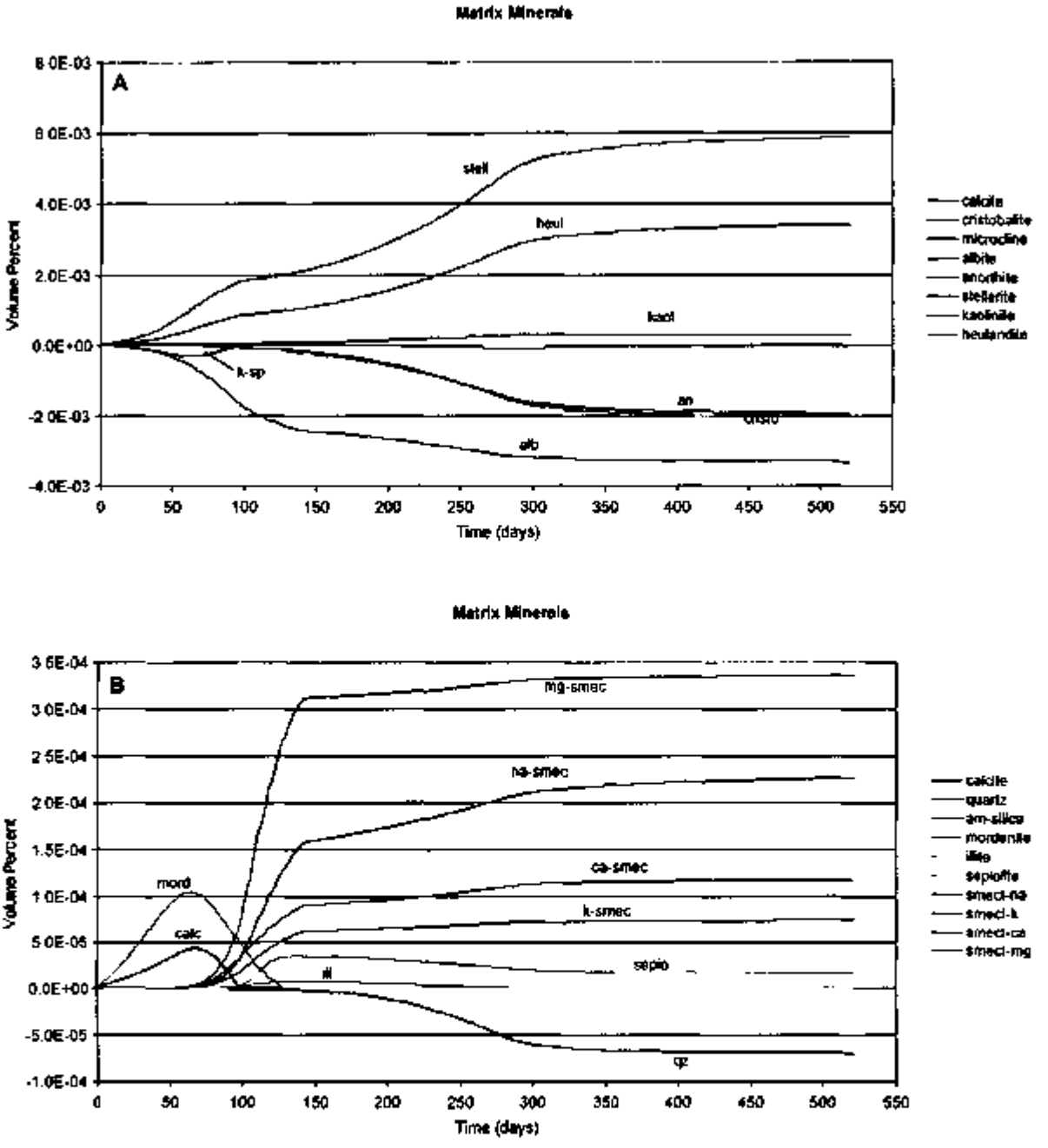

NOTE; Computed at a grid point shown on Figure 10-3. Simulation with aluminosilicates (KIN04).

Figure 10-36. Time Profiles of Mineral Volume Percent Changes in the Matrix

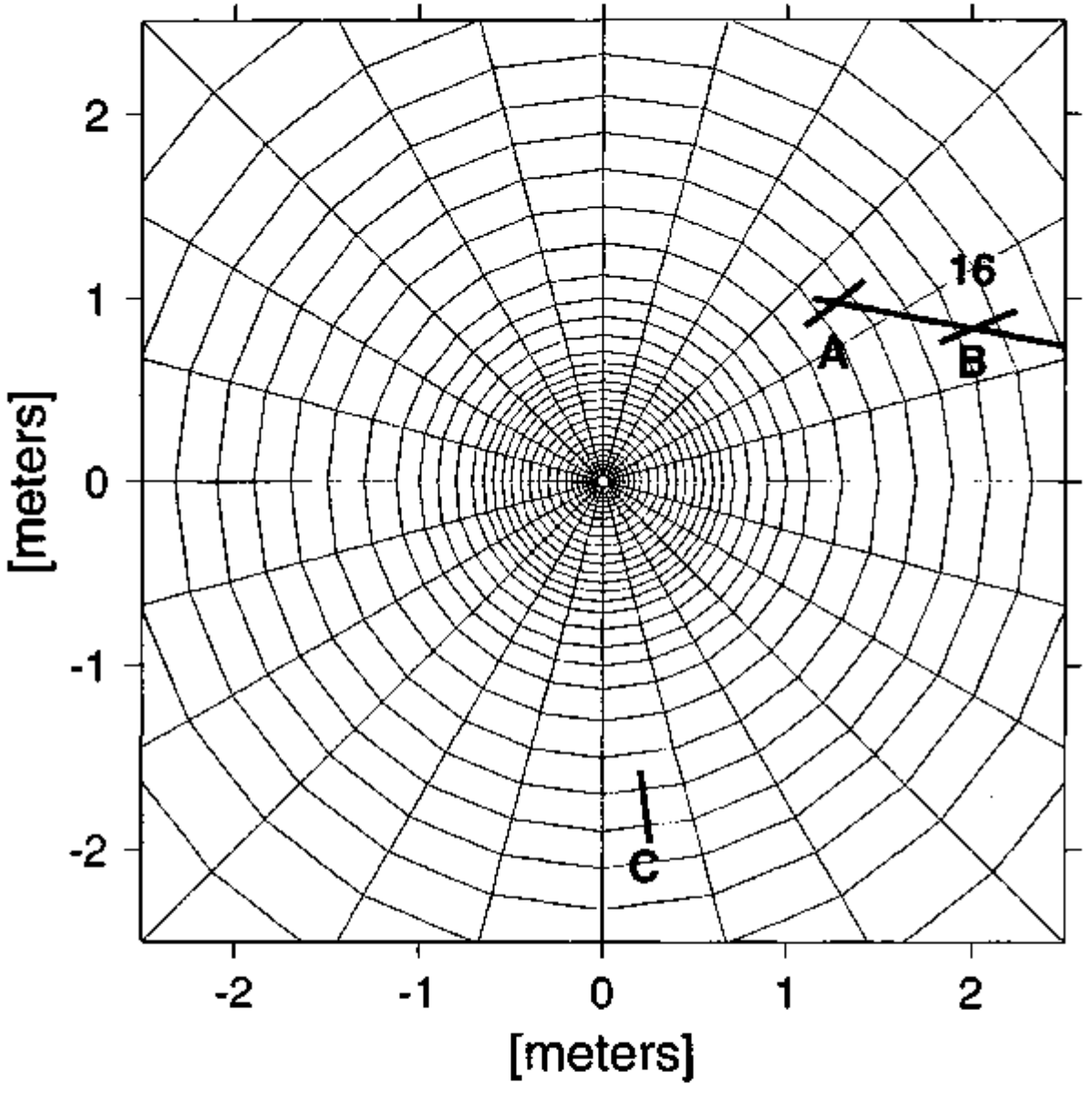

NOTE: Measured and calculated data shown on Tables 10-9 and 10-10 and Figures 10-38 and 10-39.

Figure 10-37. Location of Zones A, B, and C Used for Comparison of Measured and Calculated Data

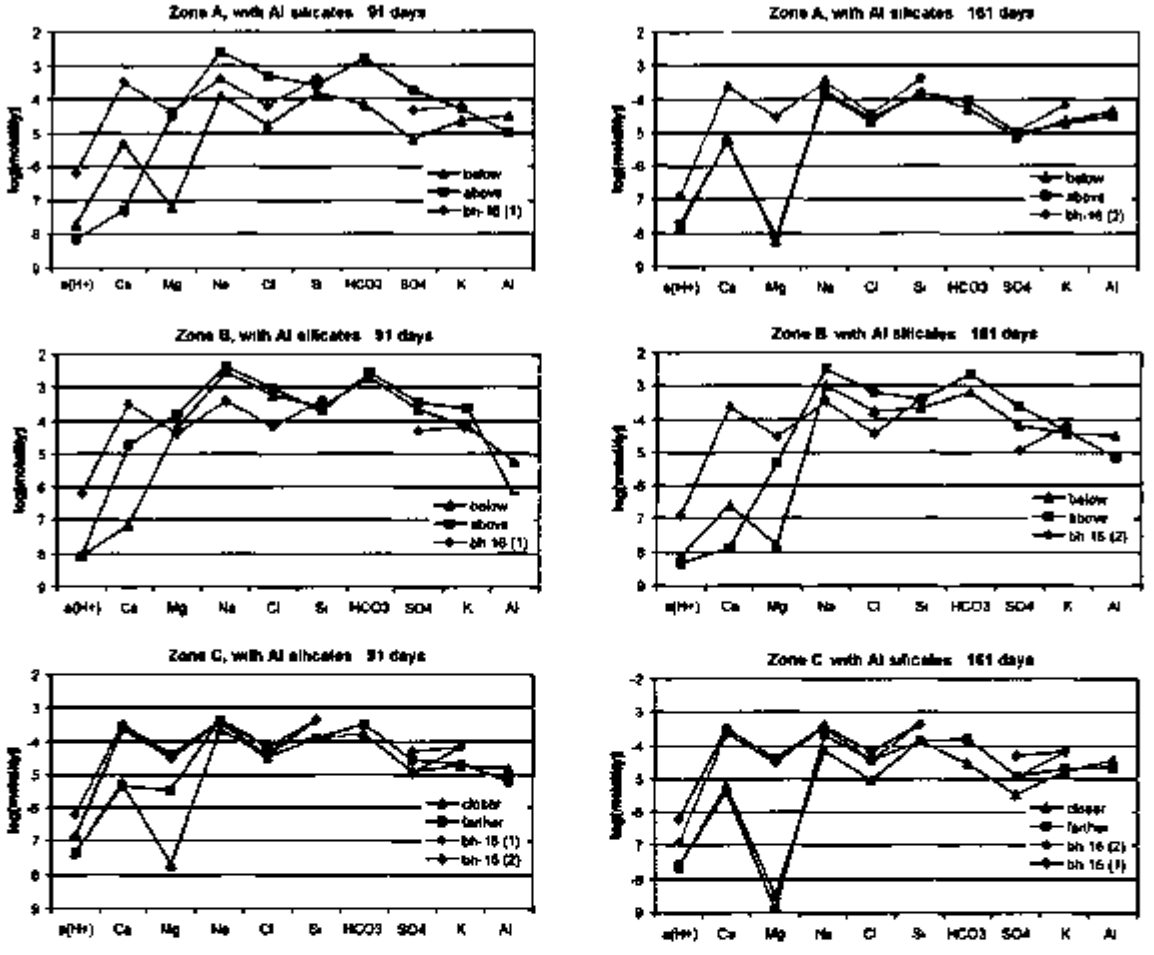

NOTE Concentrations of aqueous species measured in water collected from borehole 16 on November 25, 1996 [bh-16 (1)] and February 4, 1997 [bh-16 (2)] Compared with computed concentrations in zones A, B, and C shown on Figure 10-37 Simulation with aluminosilicates (KIN04) Computed concentrations are for locations either "below" or "above" the projected location of borehole 16 (zone A and B) and "closer" or "farther" from the heater (zone C) Molalities shown correspond to concentrations in mg/l in Table 10-9 $a(H^+)$ is the activity of hydrogen ion (10^{-pH})

Figure 10-38 Measured Concentrations of Aqueous Species Compared with Concentrations Computed with KIN04

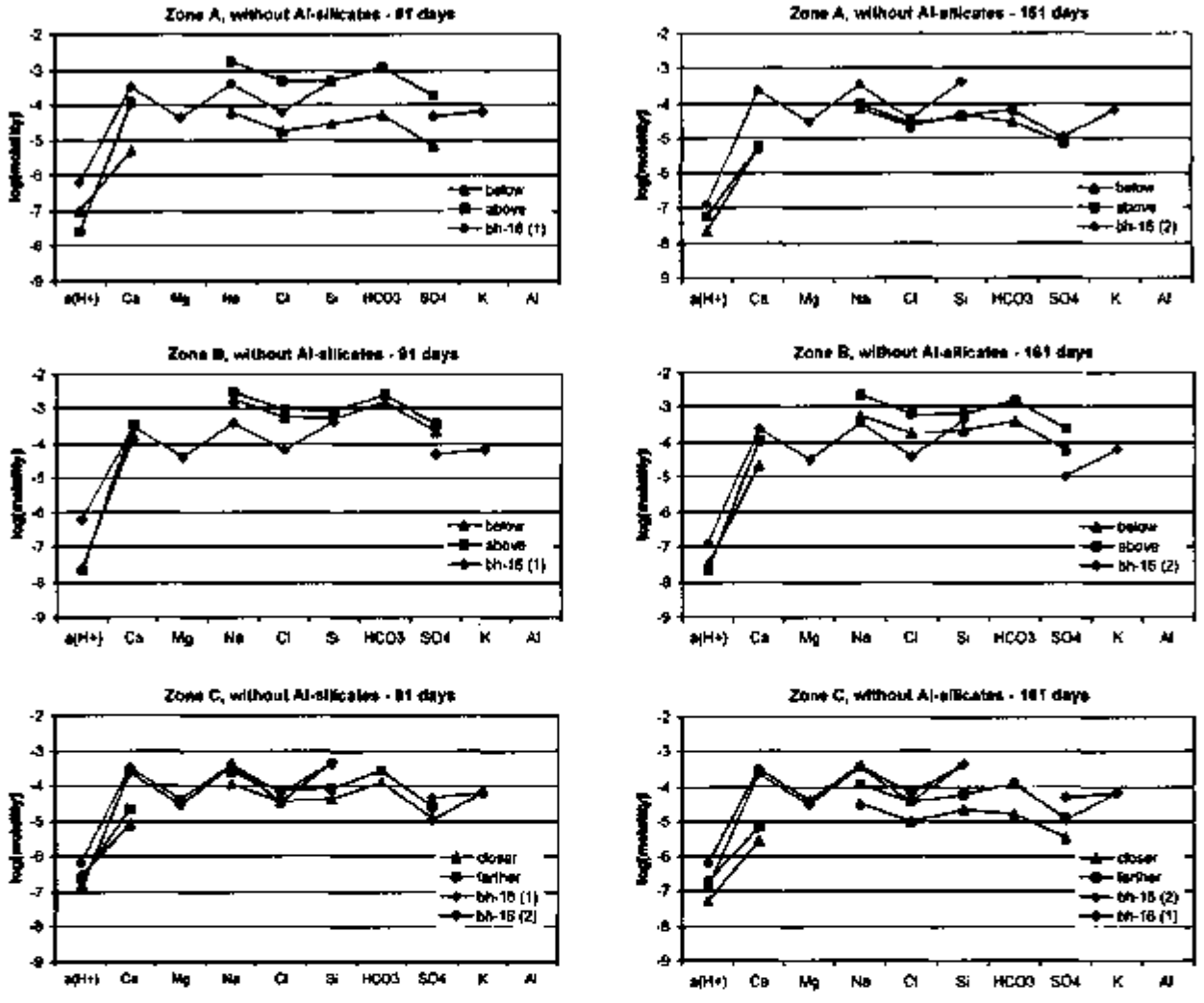

NOTE: Concentrations of aqueous species measured in water collected from borehole 16 on November 25, 1996 [bh-16 (1)] and February 4, 1997 [bh-16 (2)] Compared with computed concentrations in zones A, B, and C shown on Figure 10-36. Simulation without aluminosilicates (KIN05). Computed concentrations are for locations either "below" or "above" the projected location of borehole 16 (zone A and B) and "close" or "farther" from the heater (zone C). Molalities shown correspond to concentrations in mg/l in Table 10-9. $a(H^+)$ is the activity of hydrogen ion (10^{-pH}).

Figure 10-39. Measured Concentrations of Aqueous Species Compared with Concentrations Computed with KIN05

INTENTIONALLY LEFT BLANK

11. PERFORMANCE OF MEASURING SYSTEMS

One of the objectives of the SHT was to try out, in actual field conditions, the various measuring systems to evaluate their performance and reliability for future long-term field thermal tests. A number of items in the SHT were prototypes being tried in the field for the first time. The measuring systems are evaluated below by types.

11.1 THERMAL

The heater, heater controller, and the various types of temperature sensors are covered in this category. The heater consisted of two independently wired heating elements, capable of replacing each other, enclosed in a protective tubing made of copper. The heater controller was a Magtrol power monitor which recorded voltage, current, and heater power. The Magtrol was capable of switching to the other heating element whenever a pre-set threshold of current or power was reached.

The heater was de-energized on May 28, 1997 and removed from the test block on July 17, 1997. No sign of any structural or chemical damage to the copper tubing was visible. The heater and the controller functioned well during the SHT. Neither of the heating elements failed, although they were switched back and forth several times during the operation.

Table 7-1 in Section 7 summarizes the performance of the temperature sensors. Overall, the performance of all three types of temperature sensors were satisfactory. While there were no failure with thermistors, most of the failures were with the Type-K thermocouples, probably because there were more thermocouples than RTDs.

11.2 MECHANICAL

The instruments of various types to measure rock displacements, the borehole jack used to measure the modulus of deformation, and the rockbolt load cells, are covered in this category.

As previously discussed, three of the four MPBXs used vibrating wire displacement transducers located at the borehole collar. The other MPBXs used high-temperature LVDTs located within the borehole itself at elevated temperature. From a reliability perspective, the vibrating wire transducers did not perform well, with the majority failing during the course of the SHT. On the other hand, the high-temperature LVDTs performed exceptionally well, suffering no failures and providing smooth displacement data throughout the SHT. It is likely that the vibrating wire transducers, purportedly hermetically sealed and able to withstand the temperatures encountered at the MPBX head, were adversely affected by the warm humid air that likely moved within these unsealed boreholes. The temperature measurements exhibited in the unsealed MPBX boreholes (see Section 3) are suggestive of vapor-phase transport along the borehole and condensation of the water vapor at the cooler area at the borehole collar. Furthermore, qualitative inspection of some of the gages after testing showed that the vibrating wire had broken, possibly because of the presence of water. The high-temperature LVDTs were removed from the borehole (MPBX-2) after completion of the SHT and the gage calibrations were checked. All the high temperature LVDTs were within the calibration standards. This result is reassuring for the DST because the

MPBX gages installed in the heated drift itself were similar high-temperature LVDTs. The connecting rods and anchors from each of the MPBXs were inspected after the completion of the SHT and show no signs of deterioration.

All the rock bolt load cells measured reliably throughout the SHT. These load cells are vibrating wire transducers and were installed between fixed plates in the ambient Thermomechanical Alcove (see Section 9.2). The load cells have a maximum capacity of 60,000 lbs. and were originally loaded to up to about 26,000 lbs. All load cells continued to record valid data throughout the SHT, during both heating and cooldown. Each of the rock bolts was pull-tested to 10,000 lbs after cooldown using the designer's underground procedure.

The wire extensometers installed on the three free surfaces of the SHT block appear to have functioned properly, although the data are of limited value because of the likely effect of surface block movements. The data clearly exhibit jumps, both extensional and compressional, which are likely the result of loosening or rotation of the blocks of rock into which the mounting pins were grouted. It may have been more appropriate to monitor the movement of each pin (two for each wire extensometer) along each of the three axes of possible movement. This would have required an additional thirty gages. Additionally, the assumption of no movement of the reference pins must be made, which may or may not be accurate.

The NX borehole jack (Goodman jack) was used in a single borehole intermittently during both the heating and cooling phases of the SHT. The jacking results are presented in Section 9.2. The data give relatively low estimates of the rock mass deformation modulus as compared to other measurements from the DST Plate Loading Niche (CRWMS M&O 1998c). However, the results are fairly consistent for each of the measurement depths, with the exception of the deepest (6.2 m), the results from which are discussed in Section 9.2. It may also be appropriate to reevaluate the calculation sequence suggested in ASTM D4971-89 and Heuze and Amadei (1985) and suggest a YMP alternative that more closely compares with plate loading tests, estimates from rock mass quality surveys, and comparisons to numerical modeling results from other large-scale tests.

Posttest calibrations were performed on the wire extensometers and high-temperature LVDTs. All these instruments were found to be in calibration following the SHT cooldown.

11.3 OPTICAL MPBX

A multiple point borehole extensometer in which distance is measured using a modulated laser beam was developed by LLNL, and a prototype system was installed in two different instrument boreholes, 6 and 7, in the SHT. The Optical MPBX is described in Blair et al. 1997. While the system performed as expected, the measurements were not comparable, in terms of resolution and precision, to those by other systems such as mechanical MPBXs.

11.4 HYDROLOGICAL

The passive monitoring (of pressure, temperature, and relative humidity) and active testing in the two hydrology boreholes, 16 and 18 and the three different types of geophysical measurements, to

track the movement of moisture, are covered in this section. The geophysical measurements are neutron logging, ERT, and GPR.

The sensors used both for active testing and passive monitoring in the boreholes 16 and 18, namely, the pressure transducers, the RTDs, and the Humicaps (for relative humidity) performed satisfactorily during the SHT.

The GPR measurements in the SHT were for demonstration purposes only, and only a limited number of measurements were made. The ability of this technique in terms of tracking the growth of a dry-out zone was good. The ability to identify areas of increased saturation was only qualitative. Areas of dry-out and of increased saturation identified by the GPR technique generally coincided with such areas identified by the ERT method, thereby lending credence to each other.

Neutron logging, as applied in the SHT, was to measure the moisture content of the rock. Neutron logging is used to measure the moisture content of the formation; however, the depth of measurement or penetration is only few inches from the borehole wall. In the SHT, the logging was done in a Teflon™ tube which was grouted to the borehole. This required the logging tool to be calibrated in a known identical situation. In general, neutron logging in the SHT correctly identified the zones of drying.

ERT is a method of estimating the moisture content of a formation by measuring the changes in the dielectric constant of the material due to changes in the moisture content. The SHT was the first time ERT was employed to track the moisture content of this type of welded volcanic tuff. In general, the performance of ERT in the SHT was within expectation. The ability of this method to track the changes in saturation while it increased was found to be limited, especially in terms of the resolution of the measurements. The two techniques of ERT and GPR, both of which aimed at making bulk measurements, are considered to support each other's findings.

11.5 CHEMICAL

In the SHT, two boreholes, 20 and 21 were equipped with SEAMIST flexible liner systems. Each borehole had two liners. One of the liners carried several clusters of electronic sensors meant to measure a number of chemical parameters such as pH, Eh, and other elemental concentration. The other liner carried absorbing pads which were expected to absorb water, if any. The pads could be withdrawn from time to time for the water to be extracted from the pad and analyzed for its chemical characteristics.

In the SHT, the chemical sensors in the two chemistry boreholes did not function at all, primarily because they are not meant to work in an unsaturated environment. The ability to extract water samples from the pads was successful a couple of times. However, analysis and interpretation of the chemistry of the water was hindered because unused pads from the same manufacturing batch had not been saved for comparative purposes.

INTENTIONALLY LEFT BLANK

12. SINGLE HEATER TEST FINDINGS

Based on the results of the SHT and the analyses and interpretations thereof, described in the preceding pages, the following points can be presented as findings of the test.

- Conduction is the dominant heat transfer mechanism in the SHT block, although the pore water in the rock plays a role via the convection mode, both in the liquid and gas phases. It is important to take this into account in modeling, to correctly predict the effects of heating the rock, such as the distribution of temperature increase and movement of water.

- Based on locations of increased and decreased saturations as monitored in the test by ERT, neutron logging and GPR and such locations predicted by the models, as well as comparisons of the predicted and measured temperatures, the dual permeability model (DKM) is considered to be more effective than the equivalent continuum model (ECM) in simulating the thermal-hydrologic processes in the SHT block.

- ERT and GPR measurements in the SHT tend to suggest, as does DKM modeling, that rock moisture mobilized by heating drains, on condensation, by gravity via fractures to below the heated region rather than stay perched above it. This is an important finding with respect to a hot repository, and various observations in the DST so far are bearing this out.

- Pneumatic measurements in the SHT indicate that air-permeability in certain regions of the test block some distance away from the heater, decreased by a factor of 2 to 5 during the heating phase due to filling of fractures by the condensation of mobilized moisture. Permeability recovered when the heating stopped, as the supply of mobilized moisture ended and liquid water drained down the fractures by gravity.

- ERT and neutron logging measurements show good agreement with each other in tracking the growth of the drying regions. The transition from drying to wetting regions observed by neutron logs in boreholes 22 and 23 matches well with the drying/wetting transition derived from ERT measurements.

- Temperature measurements in the neutron boreholes indicate that drying of the rock begins to occur well before the boiling temperature of 96°C is reached probably as early as 60°C. Figure 12-2 shows the ERT tomographs of day 270 overlaid on temperature contours calculated for day 275. This figure shows drying in regions where the temperature is 60°C or more.

- The coefficient of thermal expansion of the rock mass below 200°C, as derived from measured displacements and temperatures in the SHT, is as much as 50 percent less than that measured in the laboratory using small hand samples. This lowering of the coefficient of thermal expansion in the larger scale is considered to be caused by fractures which tend to accommodate a large part of the expansion of the rock due to heating.

- Based on comparative analyses of various sets of predicted temperatures and the measured temperatures, the SHT indicates that the thermal conductivity of the in situ rock is substantially higher than that of dried rock, because of the moisture in the rock which has a higher thermal conductivity. This difference needs to be taken into account in simulating the thermal-hydrologic process to yield more accurate temperature predictions.

- Chemical analysis of samples of water mobilized by heat in the SHT and subsequent modeling to recreate the characteristics of this water demonstrated that gas-phase reactions play an important role in the thermal-chemical response of the rock. The slightly depressed pH of the water samples indicates that CO_2 partial pressure in the SHT have been as much as two orders of magnitude higher than that in ambient atmosphere.

- Interpretive analysis of the chemical compositions of the samples of water from borehole 16 in the context of reaction-transport simulations of the chemical processes in the SHT, leads to the conclusion that the borehole 16 water resulted from steam condensation in fractures. The mildly acidic character of the water reflects the dissolution of gaseous CO_2 at the time of condensation. The simulations indicate that dissolved carbonate species in matrix water alone is a sufficient source of CO_2 gas to drive the pH down to a mildly acidic range.

- Calcium, gypsum, and amorphous silica were found in the posttest mineralogic analyses of the samples from the overcoring of borehole 16. The distribution and textural attribute of these minerals suggest that they formed through evaporation of residual water during the post-heating (i.e., cooling phase of the test).

- Strontium and uranium analyses of the borehole 16 water samples indicate that the concentrations of these cations are not unreasonable compared to that of pore water from these strata, although data on the uranium content of pore water are limited. The $^{87}Sr/^{86}Sr$ ratio of all the borehole 16 water samples remain essentially constant at ~ 4.5 which is well within the range measured on pore water from these strata.

- Post-cooling air-permeability measurements show an increase in permeability ranging from 20 percent to a factor of 3.5 compared to the pre-heating values. Since air-permeability measurements are made over meters of length of borehole and the fluid always seeks the path of least resistance, this increase in permeability is considered to be resulting from the opening of fractures due to heating and/or cooling.

- All the test specimens or coupons of carbon steel left in the two hydrology boreholes before the start of heating underwent various degrees of corrosion. The corrosion products were generally goethite (α-$Fe^{+3}O(OH)$) and magnetite (Fe_3O_4). The chloride containing mineral akaganeite (β-$Fe^{+3}O(OH,Cl)$) was identified in one coupon.

- The copper tubing protecting the heating elements was found to be covered with oxidation products upon withdrawal after heating and cooling. The oxidation mineralization included tenorite, cuprite, paratacamite and atacomite.

- The performance of the temperature sensors was within expectation; approximately 5 percent of them failed. A small fraction of both thermocouples and RTDs failed. None of the thermistors failed.

- The chemical sensors installed in SEAMIST liners and designed to measure various chemical parameters did not function at all because of the unsaturated environment they were in.

- The performance of MPBXs with high temperature LVDTs was superior to the ones with vibrating wire gages; posttest examination and calibration checks indicated that all the high temperature LVDTs were within calibration standards.

- The optical MPBXs performed as expected; however, the measurements were inferior, in terms of resolution and precision, to those from other systems such as mechanical MPBXs.

- The GPR technique of monitoring the saturation of the rock was found to work as expected. The ability of GPR to identify areas of drying was good, while that to identify areas of increased saturation was qualitative. The results of GPR and ERT measurements generally coincided, thereby lending credence to each other.

- The infrared imaging conducted next to the SHT block failed to detect any heat-mobilized moisture escaping via fractures.

- Last, but not the least, the experiment of having numerous organizational entities work together in a short period of time and in limited space in fielding the SHT proved to be effective and successful. The experience made the fielding of the much larger and more complex DST to be completed smoothly the following year.

RECOMMENDATIONS

A number of the findings of the Single Heater Test listed above are also borne by the other thermal tests, namely, the Large Block Test and the early results of the Drift Scale Test. The following recommendations are, therefore, appropriate for taking into account in future total system performance assessments and the various analyses supporting them:

- The dual permeability model (DKM) should be the preferred conceptual model over the equivalent continuum model for simulating the thermal-hydrological responses of the near-field rock mass in the drift scale. The DKM should also be the preferred model for simulating the thermal-hydrological-mechanical responses.

- All three thermal tests indicate that the rock porewater mobilized by the heat tends to drain by gravity, via the fractures, to below the heated region rather than stay perched above it. This means that condensate refluxing or episodic seepage into the emplacement drifts are unlikely to occur during the postclosure period.

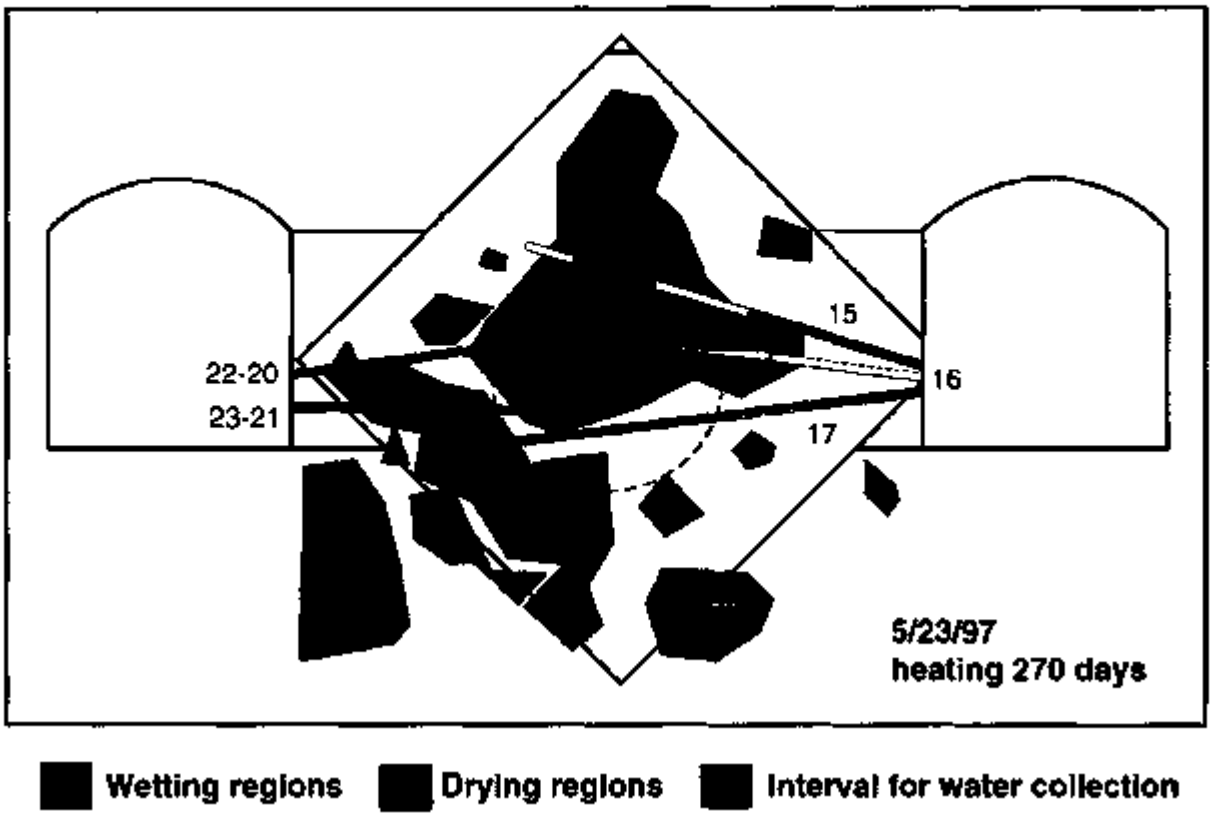

NOTE: Sampling interval for water samples is also shown.

Figure 12-1. Synthesis of ERT and Neutron Measurements for SHT Near the End of the Heating Phase

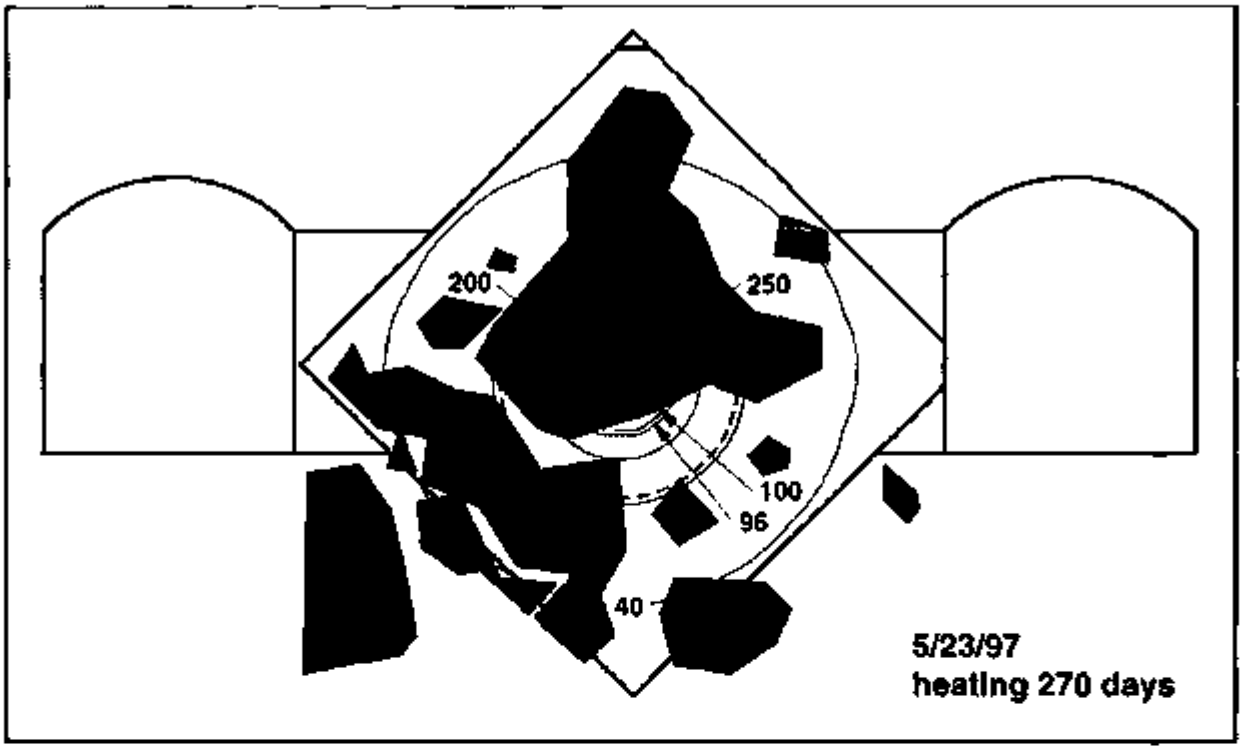

NOTE: Concentric circles indicate predicted temperatures in °C; note that drying is indicated for areas with temperatures greater than 60°C.

Figure 12-2. Synthesis of ERT Measurements and Predicted Temperatures Near the End of the Heating Phase

13. REFERENCES

13.1 DOCUMENTS CITED

Albin, A.L.; Singleton, W.L.; Moyer, T.C.; Lee, A.C.; Lung, R.C.; Eatman, G.L.W.; and Barr, D.L. 1997. *Geology of the Main Drift–Station 28+00 to 55+00, Exploratory Studies Facility, Yucca Mountain Project, Yucca Mountain, Nevada.* Denver, Colorado: Bureau of Reclamation and U.S. Geological Survey. ACC: MOL.19970625.0096.

Apps, J.A. 1997. "Hydrochemical Analysis." Chapter 14 in *The Site-Scale Unsaturated Zone Model of Yucca Mountain, Nevada, for the Viability Assessment*, Bodvarsson, G.S.; Bandurraga, T.M.; and Wu, Y.S. eds. Milestone SP24UFM4. LBNL-40376, UC-814. Berkeley, California: Lawrence Berkeley National Laboratory. ACC: MOL.19971014.0232.

Barton, C.A.; Hickman, S.; Morin, R.; Zoback, M.D.; Finkbeiner, T.; Sass, J.; and Benoit, D. 1997. "Fracture Permeability and its Relationship to In-Situ Stress in the Dixie Valley, Nevada, Geothermal Reservoir." *Proceedings: Twenty-Second Workshop on Geothermal Reservoir Engineering*, 210-215. Stanford, California: Stanford Geothermal Program. TIC: 237673.

Barton, N.R.; Lien, R.; and Lunde, J. 1974. "Engineering Classification of Rock Masses for the Design of Tunnel Support." *Rock Mechanics and Engineering, 6*, 4, 189-236. New York, New York: Springer-Verlag. TIC: 219995.

Bear, J. 1972. *Dynamics of Fluids in Porous Media.* New York, New York: Dover Publications. TIC: 217568.

Bieniawski, Z.T. 1974. "Geomechanics Classification of Rock Masses and its Application in Tunneling." *Proceedings of the Third International Congress on Rock Mechanics, IIA*, 27-32. Washington, D.C.: National Academy of Sciences. TIC: 217640.

Birkholzer, J.T. and Tsang, Y.W. 1996. *Forecast of Thermal-Hydrological Conditions and Air Injection Test Results of the Single Heater Test.* Milestone SP918M4. Berkeley, California: Lawrence Berkeley National Laboratory. ACC: MOL.19971124.0089.

Birkholzer, J.T. and Tsang, Y.W. 1997. *Pretest Analysis of the Thermal-Hydrological Conditions of the ESF Drift Scale Test.* Milestone SP9322M4. Berkeley, California: Lawrence Berkeley National Laboratory. ACC: MOL.19971201.0810.

Birkholzer, J.T. and Tsang, Y.W. 1998. *Numerical Analysis of Thermal-Hydrological Conditions in the Single Heater Test at Yucca Mountain.* Berkeley, California: Lawrence Berkeley National Laboratory. ACC: MOL.19980715.0257.

Bish, D.L. 1996. "Dust Sampling in the ESF, March 7, 1996." Bish (LANL) memorandum to Parker, C.W. (CRWMS M&O), March 15, 1996. ACC: MOL.19990303.0327.

Bish, D.L. and Howard, S.A. 1988. "Quantitative Phase Analysis Using the Rietveld Method." *Journal of Applied Crystallography, 21*, 86-91. Copenhagen, Denmark: Munksgaard International Publishers. TIC: 223712.

Bish, D.L. and Reynolds, R.C., Jr. 1989. "Sample Preparation for X-ray Diffraction." *Modern Powder Diffraction, Reviews in Mineralogy, 20*, 73-99. Washington, D.C.: Mineralogical Society of America. TIC: 237913.

Blair, S.C.; Sweider, D.; Trettenero, S.; and Boro, C. 1997. *A New Reflective Optical Extensometer (ROX) System for Geomechanical Deformation Measurements.* UCRL-JC-125628. Livermore, California: Lawrence Livermore National Laboratory. ACC: MOL.19980421.0102.

Boadu, F.K. 1997. "Rock Properties and Seismic Attenuation: Neural Network Analysis." *Pure and Applied Geophysics, 149*, 507-524. Basel, Switzerland: Birkhauser Verlag AG. TIC: 239532.

Bodvarsson, G.S. and Bandurraga, T.M. 1996. *Development and Calibration of the Three-Dimensional Site-Scale Unsaturated Zone Model of Yucca Mountain, Nevada.* LBNL-39315. Berkeley, California: Lawrence Berkeley National Laboratory. ACC: MOL.19970701.0692.

Bodvarsson, G.S.; Bandurraga, T.M.; and Wu, Y.S. 1997. *The Site-Scale Unsaturated Zone Model of Yucca Mountain, Nevada, for the Viability Assessment.* Milestone Report SP24UFM4. LBNL-40376, UC-814. Berkeley, California: Lawrence Berkeley National Laboratory. ACC: MOL.19971014.0232.

Boyd, P.J.; Noel, J.S.; Hill, T.N.; and Martin, R.J. 1996. *Unconfined Compression Tests on Specimens from the Single Heater Test Area in the Thermal Facility at Yucca Mountain, Nevada.* White River Junction, Vermont: New England Research, Inc. ACC: MOL.19961209.0198.

Brodsky, N.S. 1996. *Thermal Properties of Test Specimens from the Single Heater Test Area in the Thermal Testing Facility at Yucca Mountain, Nevada.* Albuquerque, New Mexico: Sandia National Laboratories. ACC: MOL.19961029.0115.

Brodsky, N.S. 1997. *Thermal Expansion of Carbon Fiber and Invar Rods.* Letter Report. Albuquerque, New Mexico: Sandia National Laboratories. ACC: MOL.19980210.0198.

Brodsky, N.S.; Riggins, M.; Connolly, J.; and Ricci, P. 1997. *Thermal Expansion, Thermal Conductivity, and Heat Capacity Measurements for Boreholes UE25 NRG-4, UE25 NRG-5, USW NRG-6, and USW NRG-7/7A.* SAND95-1955, UC-814. Albuquerque, New Mexico: Sandia National Laboratories. ACC: MOL.19980311.0316.

Brown, S.R. 1995. "Simple Mathematical Model of a Rough Fracture." *Journal of Geophysical Research, 100*, 5941-5952. Washington, D.C.: American Geophysical Union. TIC: 237570.

Brown, S.R. and Bruhn, R.L. 1997. *Fluid Permeability of Deformable Fracture Networks.* SAND97-0159. Albuquerque, New Mexico: Sandia National Laboratories. TIC: 236686.

Broxton, D.E.; Warren, R.G.; Hagan, R.C.; and Luedemann, G. 1986. *Chemistry of Diagenetically Altered Tuffs at the Potential Nuclear Waste Repository, Yucca Mountain, Nye County, Nevada.* LA-10802-MS, UC-70. Los Alamos, New Mexico: Los Alamos National Laboratory. ACC: MOL.19980527.0202.

Buesch, D.C. and Spengler, R.W. 1998. "Character of the Middle Nonlithophysal Zone of the Topopah Spring Tuff at Yucca Mountain." *High Level Radioactive Waste Management, Proceedings of the Eighth Annual International Conference, Las Vegas, Nevada, May 11-14, 1998,* 16-23. La Grange Park, Illinois: American Nuclear Society. TIC: 239266.

Buscheck, T.A. 1996. "Hydrothermal Modeling." Chapter 1 of *Near-Field and Altered-Zone Environment Report (Volume II).* Wilder, D.G., ed. UCRL-LR-124998. Livermore, California: Lawrence Livermore National Laboratory. ACC: MOL.19961212.0121.

Buscheck, T.A. and Nitao, J.J. 1995. *Thermal-Hydrological Analysis of Large-Scale Thermal Tests in the Exploratory Studies Facility at Yucca Mountain.* UCRL-ID-121791. Livermore, California: Lawrence Livermore National Laboratory. ACC: MOL.19960501.0392.

Buscheck, T.A.; Nitao, J.J.; and Chesnut, D.A. 1991. "The Impact of Episodic Nonequilibrium Fracture-Matrix Flow on Geological Repository Performance." *Proceedings of the Topical Meeting on Nuclear Waste Packaging: Focus '91, September 29-October 2, 1991, Las Vegas, Nevada.* La Grange Park, Illinois: American Nuclear Society. TIC: 231173.

Buscheck, T.A.; Nitao, J.J.; and Ramspott, L.D. 1997. "Near-Field Thermal-Hydrological Behavior for Alternative Repository Designs at Yucca Mountain." *Scientific Basis for Nuclear Waste Management XX: Symposium Held December 2-6, 1996, Boston, Massachusetts, U.S.A.* Materials Research Society Symposium Proceedings Volume 465, pp. 1029-1036. Pittsburgh, Pennsylvania: Materials Research Society. TIC: 238849.

Buscheck, T.A.; Shaffer, R.J.; Lee, K.H.; and Nitao, J.J. 1997. *Analysis of Thermal-Hydrological Behavior During the Heating Phase of the Single-Heater Test at Yucca Mountain.* Milestone SP9266M4. Livermore, California: Lawrence Livermore National Laboratory. ACC: MOL.19980109.0241.

Buscheck, T.A.; Shaffer, R.J.; and Nitao, J.J. 1997. *Pretest Thermal-Hydrological Analysis of the Drift-Scale Thermal Test at Yucca Mountain.* Livermore, California: Lawrence Livermore National Laboratory. ACC: MOL.19980507.0359.

Byers, F.M., Jr. 1985. *Petrochemical Variation of Topopah Spring Tuff Matrix with Depth (Stratigraphic Level), Drill Hole USW G-4, Yucca Mountain, Nevada.* LA-10561-MS. Los Alamos, New Mexico: Los Alamos National Laboratory. TIC: 202363.

Byers, F.M., Jr. and Moore, L.M. 1987. *Petrographic Variation of the Topopah Spring Tuff Matrix within and between Cored Drill Holes, Yucca Mountain, Nevada.* LA-10901-MS, UC-70. Los Alamos, New Mexico: Los Alamos National Laboratory. ACC: NNA.19900510.0144.

Carlos, B.A. 1985. *Minerals in Fractures of the Unsaturated Zone from Drill Core USW G-4, Yucca Mountain, Nye County, Nevada.* LA-10415-MS. Los Alamos, New Mexico: Los Alamos National Laboratory. TIC: 202360.

Carlos, B.A. 1987. *Minerals in Fractures of the Saturated Zone from Drill Core USW G-4, Yucca Mountain, Nye County, Nevada.* LA-10927-MS, UC-70. Los Alamos, New Mexico: Los Alamos National Laboratory. ACC: NNA.19900222.0149.

Carlos, B.A. 1989. *Fracture-Coating Minerals in the Topopah Spring Member and Upper Tuff of Calico Hills from Drill Hole J-13.* LA-11504-MS. Los Alamos, New Mexico: Los Alamos National Laboratory. TIC: 202383.

Carlos, B.A. 1993. *Appendix I: Fracture-Lining Minerals in Drill Core UE25 UZ-#16.* Milestone 4013. Los Alamos, New Mexico: Los Alamos National Laboratory. ACC: MOL.19950728.0196.

Carlos, B.A.; Bish, D.L.; and Chipera, S.J. 1991. "Fracture-Lining Minerals in the Lower Topopah Spring Tuff at Yucca Mountain." *High Level Radioactive Waste Management, Proceedings of the Second Annual International Conference, Las Vegas, Nevada, April 28-May 3, 1991, 1,* 486-493. La Grange Park, Illinois: American Nuclear Society. TIC: 234965.

Carlos, B.A.; Chipera, S.J.; and Bish, D.L. 1995. *Distribution and Chemistry of Fracture-Lining Minerals at Yucca Mountain, Nevada.* LA-12977-MS, UC-814. Los Alamos, New Mexico: Los Alamos National Laboratory. ACC: MOL.19960306.0564.

Carlos, B.A.; Chipera, S.J.; and Snow, M. 1995. *Multiple Episodes of Zeolite Deposition in Fractured Silicic Tuff.* Milestone 4079. Los Alamos, New Mexico: Los Alamos National Laboratory. ACC: MOL.19960514.0209.

Chipera, S.J. and Bish, D.L. 1995. "Multi-Reflection RIR and Intensity Normalizations for Quantitative Analyses: Applications to Feldspars and Zeolites." *Powder Diffraction, 10,* (1), 47-55. Swarthmore, Pennsylvania: Joint Committee for Powder Diffraction Standards, International Centre for Diffraction Data. TIC: 222001.

Chung, F.H. 1974a. "Quantitative Interpretation of X-Ray Diffraction Patterns of Mixtures. I. Matrix-Flushing Method for Quantitative Multicomponent Analysis." *Journal of Applied Crystallography, 7,* 519-525. Copenhagen, Denmark: Munksgaard International Publishers. TIC: 224051.

Chung, F.H. 1974b. "Quantitative Interpretation of X-Ray Diffraction Patterns of Mixtures. II. Adiabatic Principle of X-Ray Diffraction Analysis of Mixtures." *Journal of Applied Crystallography*, 7, 526-531. Copenhagen, Denmark: Munksgaard International Publishers. TIC: 237568.

Compton, R.R. 1962. *Manual of Field Geology*. New York, New York: John Wiley & Sons, Inc. TIC: 209518.

Conrad, M.E. 1998. "Isotope Analyses of Samples from the Drift Scale Test Hydrology Holes." Chapter 3 in *Second Quarter TDIF Submission for the Drift Scale Test (Hydrological, Radar, Microseismic)*. Milestone SP2790M4. Berkeley, California: Lawrence Berkeley National Laboratory. ACC: MOL.19980812.0240.

Cook, P. 1997. *Fourth Quarter FY 1997 Results of Infrared Mapping in the Single Heater Test Area*. Milestone SP1080M4. Berkeley, California: Lawrence Berkeley National Laboratory. ACC: MOL.19971208.0356.

Cook, P. 1998. *First Quarter FY 1998 Results of Infrared Mapping in the Single Heater Test Area*. Milestone SPY1160M4. Berkeley, California: Lawrence Berkeley National Laboratory. ACC: MOL.19980508.0044.

Cook, P. and Wang, J. 1997a. *Infrared Imaging in the Single Heater Test Area*. Milestone SP9230M4. Berkeley, California: Lawrence Berkeley National Laboratory. ACC: MOL.19971121.0882.

Cook, P. and Wang, J. 1997b. *Infrared Imaging in the Single Heater Test Area*. Milestone SP9237M4. Berkeley, California: Lawrence Berkeley National Laboratory. ACC: MOL.19971201.0842.

Cook, P. and Wang, J. 1997c. *Third Quarter Results of Infrared Mapping of the Single Heater Test Block*. Milestone SP9291M4. Berkeley, California: Lawrence Berkeley National Laboratory. ACC: MOL.19971204.0439.

CRWMS M&O (Civilian Radioactive Waste Management System Management and Operating Contractor) 1996a. *Test Design, Plans and Layout Report for the ESF Thermal Test*. BAB000000-01717-4600-00025 REV 01. Las Vegas, Nevada: CRWMS M&O. ACC: MOL.19970303.0107.

CRWMS M&O 1996b. *Characterization of the ESF Thermal Test Area*. B00000000-01717-5705-00047 REV 01. Las Vegas, Nevada: CRWMS M&O. ACC: MOL.19970116.0187.

CRWMS M&O 1996c. *Yucca Mountain Site Geotechnical Report*. BAAA00000-01717-4600-00065 REV 00. Las Vegas, Nevada: CRWMS M&O. ACC: MOL.19970425.0062.

CRWMS M&O 1997a. *Updated In-Situ Thermal Testing Program Strategy.* B00000000-01717-5705-00065 REV 01. Las Vegas, Nevada: CRWMS M&O. ACC: MOL.19990526.0296.

CRWMS M&O 1997b. *Single Heater Test Status Report.* BAB000000-01717-5700-00002 REV 01. Las Vegas, Nevada: CRWMS M&O. ACC: MOL.19980904.0202.

CRWMS M&O 1997c. *Single Heater Test Interim Report.* BABEAF000-01717-6900-00001 REV 00. Las Vegas, Nevada: CRWMS M&O. ACC: MOL.19990215.0396.

CRWMS M&O 1997d. *Ambient Characterization of the Drift Scale Test Block.* BADD00000-01717-5705-00001 REV 01. Las Vegas, Nevada: CRWMS M&O. ACC: MOL.19980425.0151.

CRWMS M&O 1998a. *Drift Scale Test As-Built Report.* BAB000000-01717-5700-00003 REV 01. Las Vegas, Nevada: CRWMS M&O. ACC: MOL.19990107.0223.

CRWMS M&O 1998b. *Total System Performance Assessment–Viability Assessment (TSPA-VA) Technical Basis Document. Chapter 3, Thermal Hydrology.* B00000000-01717-4301-00003 REV 01. Las Vegas, Nevada: CRWMS M&O. ACC: MOL.19981008.0003.

CRWMS M&O 1998c. *Drift Scale Test Progress Report No. 1.* BAB000000-01717-5700-00004 REV 01. Las Vegas, Nevada: CRWMS M&O. ACC: MOL.19990209.0240.

CRWMS M&O 1999. *Input Data for Thermal-Hydrological-Chemical Analysis of the Single Heater Test Results by the TOUGHREACT Code.* Design Input Request NEP-NEP-99213.R. ACC: MOL.19990527.0239.

Daily, W. and Ramirez, A. 1989. "Evaluation of Electromagnetic Tomography to Map In Situ Water in Heated Welded Tuff." *Water Resources Research, 25,* 1083-1096. Washington, D.C.: American Geophysical Union. TIC: 226913.

DOE (U.S. Department of Energy) 1988. *Site Characterization Plan: Yucca Mountain Site, Nevada Research and Development Area.* DOE/RW-0199. Washington, D.C.: Office of Civilian Radioactive Waste Management. ACC: HQO.19881201.0002.

DOE 1994. *Civilian Radioactive Waste Management Program Plan.* DOE/RW-0458. 3 volumes. Washington, D.C.: Office of Civilian Radioactive Waste Management. ACC: HQO.19941222.0001; HQO.19941222.0002; HQO.19941222.0003.

DOE 1995. *In-Situ Thermal Testing Program Strategy.* Las Vegas, Nevada: Office of Civilian Radioactive Waste Management. ACC: MOL.19960124.0233.

DOE 1998. *Quality Assurance Requirements and Description.* DOE/RW-0333P, Rev. 8. Washington, D.C.: Office of Civilian Radioactive Waste Management. ACC: MOL.19980601.0022.

Fabryka-Martin, J.T.; Flint, A.L.; Sweetkind, D.S.; Wolfsberg, A.V.; Levy, S.S.; Roemer, G.J.C.; Roach, J.L.; Wolfsberg, L.E.; and Duff, M.C. 1997. *Evaluation of Flow and Transport Models of Yucca Mountain, Based on Chlorine-36 Studies for FY97.* LA-CST-TIP-97-010. Milestone SP2224M3. Los Alamos, New Mexico: Los Alamos National Laboratory. ACC: MOL.19980204.0916.

Feynman, R.P.; Leighton, R.B.; and Sands, M. 1964. *The Feynman Lectures on Physics.* Volume II, 12-2. Reading, Massachusetts: Addison-Wesley Publishing Company. TIC: 238953.

Finley, R.E.; Ballard, S.; Brodsky, N.S.; Francis, N.D.; George, J.T.; and Sobolik, S.R. 1998. *Single Heater Test Final Report.* Draft 00B, Report for Milestones SP1430M4 and SPY148M4. Albuquerque, New Mexico: Sandia National Laboratories. ACC: MOL.19981030.0113. (Note: this record, TBV-1163, is used only to provide data traceability to the data indicated in Tables 2-2 and 2-3, which are not yet available in the technical database under DTN: SNF35110690001.010.)

Flint, L.E. 1998. *Characterization of Hydrogeologic Units Using Matrix Properties, Yucca Mountain, Nevada.* Milestone 3GUP603M. Water-Resources Investigations Report 97-4243. Denver, Colorado: U.S. Geological Survey. ACC: MOL.19980429.0512.

Francis, N.D. 1997. "The Base-Case Thermal Properties for TSPA-VA Modeling" Francis (SNL) memorandum to distribution (various organizations), April 16, 1997. ACC: MOL.19980518.0229.

Freifeld, B. 1997. *Letter Report on Fourth Quarter Results of Measurements in the Hydrology Holes in the Single Heater Test Area in the ESF.* Milestone SP1080M4. Berkeley, California: Lawrence Berkeley National Laboratory. ACC: MOL.19971208.0352.

Freifeld, B. 1998a. *Letter Report on First Quarter Results of Measurements in Hydrology Holes in the Single Heater Test Area in the ESF Area, FY 1998.* Milestone SPY1160M4. Berkeley, California: Lawrence Berkeley National Laboratory. ACC: MOL.19980508.0045.

Freifeld, B. 1998b. "Active Hydrological Testing." Chapter 2 of *Second Quarter TDIF Submission for the Drift Scale Test (Hydrological, Radar, Microseismic).* Milestone Report SP2790M4. Berkeley, California: Lawrence Berkeley National Laboratory. ACC: MOL.19980812.0240.

Freifeld, B. and Tsang, Y. 1997a. *Letter Report on First Quarter Results of Measurements in Hydrology Holes in the Single Heater Test Area in the ESF.* Milestone SP9263M4. Berkeley, California: Lawrence Berkeley National Laboratory. ACC: MOL.19970711.0192.

Freifeld, B. and Tsang, Y. 1997b. *Letter Report on Second Quarter Results of Measurements in Hydrology Holes in the Single Heater Test Area.* Milestone SP9216M4. Berkeley, California: Lawrence Berkeley National Laboratory. ACC: MOL.19980826.0160.

Freifeld, B. and Tsang, Y. 1997c. *Letter Report on Third Quarter Results of Measurements in the Hydrology Holes in the Single Heater Test Area.* Milestone SP9252M4. Berkeley, California: Lawrence Berkeley National Laboratory. ACC: MOL.19971204.0428.

Glassley, W.E. 1997a. *Thermochemical Analysis of the Single Heater Test.* Milestone SP912M4. Livermore, California: Lawrence Livermore National Laboratory. ACC: MOL.19970528.0073.

Glassley, W.E. 1997b. *Third Quarter Report, Chemical Analyses of Waters Collected from the Single Heater Test.* Milestone SP9281M4. Livermore, California: Lawrence Livermore National Laboratory. ACC: MOL.19980105.0625.

Glassley, W.E. and DeLoach, L. 1997. *Second Quarter Results of Chemical Measurements in the Single Heater Test.* Milestone SP9240M4. Livermore, California: Lawrence Livermore National Laboratory. ACC: MOL.19971218.0917.

Guzman, A.G.; Geddis, A.M.; Henrich, M.J.; Lohrstorfer, C.F.; and Neuman, S.P. 1996. *Summary of Air Permeability Data from Single-Hole Injection Tests in Unsaturated Fractured Tuffs at the Apache Leap Research Site: Results of Steady-State Test Interpretation.* U.S. Nuclear Regulatory Commission Report NUREG/CR-6360. Washington, D.C.: U.S. Nuclear Regulatory Commission. TIC: 234385.

Hardin, E.L. 1998. *Near-Field/Altered-Zone Models Report.* Milestone SP3100M3. UCRL-ID-129179. Livermore, California: Lawrence Livermore National Laboratory. ACC: MOL.19980630.0560.

Helgeson, H.C.; Delany, J.M.; Nesbitt, H.W.; and Bird, D.K. 1978. "Summary and Critique of the Thermodynamic Properties of Rock Forming Minerals." *American Journal of Science, 278A,* 229. New Haven, Connecticut: Kline Geology Laboratory, Yale University. TIC: 220013.

Heuze, F.E. and Amadei, B. 1985. "The NX-Borehole Jack: a Lesson in Trials and Errors." *International Journal of Rock Mechanics and Mining Sciences & Geomechanics Abstracts, 22,* (2), 105-112. Oxford/New York: Pergamon Press. TIC: 218975.

Hill, R.J. and Howard, C.J. 1987. "Quantitative Phase Analysis from Neutron Powder Diffraction Data Using the Rietveld Method." *Journal of Applied Crystallography, 20,* 467-474. Copenhagen, Denmark: Munksgaard International Publishers. TIC: 237039.

Ho, C.K. 1997. "Models of Fracture-Matrix Interactions during Multiphase Heat and Mass Flow in Unsaturated Fractured Porous Media." *Proceedings of the ASME Fluids Engineering Division.* FED-Vol. 244, 401-412. New York, New York: American Society of Mechanical Engineers. TIC: 234839.

Ho, C.K. and Francis, N.D. 1997. "Correction to Base-Case Thermal Properties for TSPA-VA Modeling." Ho (SNL) and Francis (SNL) memorandum to distribution (various organizations), August 7, 1997. ACC: MOL.19980518.0230.

Holcomb, D.J. and McNamee, M.J. 1984. *Displacement Gage for the Rock Mechanics Laboratory*. SAND84-0651. Albuquerque, New Mexico: Sandia National Laboratories. TIC: 226780.

Hubbard, C.R.; Evans, E.H.; and Smith, D.K. 1976. "The Reference Intensity Ratio, I/Ic, for Computer Simulated Powder Patterns." *Journal of Applied Crystallography, 9*, 169-174. Copenhagen, Denmark: Munksgaard International Publishers. TIC: 237040.

Hvorslev, M.J. 1951. *Time Lag and Soil Permeability in Ground-Water Observations*. AEWES Bulletin No. 36. Vicksburg, Mississippi: U.S. Army Corps of Engineers, Waterways Experiment Station. TIC: 238956.

Itasca Consulting Group, Inc. 1996. *FLAC–Fast Lagrangian Analysis of Continua, Version 3.3, Vol. I: User's Manual*. Minneapolis, Minnesota: Itasca Consulting Group, Inc. TIC: 236418.

JCPDS (Joint Committee for Powder Diffraction Standards) 1986. *Mineral Powder Diffraction File Data Book*, 16-20, 28, 122, 172, 241, 269, 455, 456, 481, 491, 492, 535-537, 770, 771, 787-789, 792, 843, 861, 862, 966, 1025-1027, 1030-1032, 1038, 1039, 1107, 1193, 1194. Swarthmore, Pennsylvania: Joint Committee for Powder Diffraction Standards, International Centre for Diffraction Data. TIC: 243579.

Johnson, J.W.; Knauss, K.G.; Glassley, W.E.; DeLoach, L.D.; and Thomson, A.F.B. 1998. "Reactive Transport Modeling of Plug-Flow Reactor Experiments: Quartz and Tuff Dissolution at 240°C." *Journal of Hydrology, 209*, 81-111. Amsterdam, Netherlands: Elsevier Science B.V. TIC: 240986.

Johnson, J.W; Oelkers, E.H.; and Helgeson, H.C. 1992. "SUPCRT92: A Software Package for Calculating the Standard Molal Thermodynamic Properties of Minerals, Gases, Aqueous Species, and Reactions from 1 to 5000 Bar and 0 to 1000°C." *Computers and Geosciences, 18*, 899-947. Oxford/New York: Pergamon Press. TIC: 234273.

Klavetter, E.A. and Peters, R.R. 1986. *Estimation of Hydrologic Properties of an Unsaturated, Fractured Rock Mass*. SAND-84-2642. Albuquerque, New Mexico: Sandia National Laboratories. TIC: 202727.

Klug, H.P. and Alexander, L.E. 1974. *X-ray Diffraction Procedures for Polycrystalline and Amorphous Materials*. Second edition. New York, New York: John Wiley & Sons, Inc. TIC: 243393.

LeCain, G.D. 1995. *Pneumatic Testing in 45-Degree-Inclined Boreholes in Ash-Flow Tuff near Superior, Arizona*. Water-Resources Investigations Report 95-4073. Denver, Colorado: U.S. Geological Survey. TIC: 221220.

LeCain, G.D. 1997. *Air-Injection Testing in Vertical Boreholes in Welded and Nonwelded Tuff, Yucca Mountain, Nevada*. Water-Resources Investigations Report 96-4262. Denver, Colorado: U.S. Geological Survey. ACC: MOL.19980310.0148.

Lee, K.H. 1995. *Progress Report on Pre-Test Calculations for the Large Block Test.* UCRL-ID-118699. Livermore, California: Lawrence Livermore National Laboratory. ACC: MOL.19950314.0178.

Levy, S.S. 1984. *Petrology of Samples from Drill Holes USW H-3, H-4, and H-5, Yucca Mountain, Nevada.* LA-9706-MS, UC-70. Los Alamos, New Mexico: Los Alamos National Laboratory. ACC: MOL.19970729.0322.

Levy, S.S. and Chipera, S.J. 1997. *Updated Mineralogic and Hydrologic Analysis of the PTn Hydrogeologic Unit, Yucca Mountain, Nevada, as a Barrier to Flow.* Milestone SP321DM4. Los Alamos, New Mexico: Los Alamos National Laboratory. ACC: MOL.19980520.0150.

Levy, S.S. and O'Neil, J.R. 1989. "Moderate Temperature Zeolitic Alteration in a Cooling Pyroclastic Deposit." *Chemical Geology, 76,* 321-326. Amsterdam, Netherlands: Elsevier Science Publishers. TIC: 221911.

Llera, F.J.; Sato, M.; Nakatsuka, K.; and Yokoyama, H. 1990. "Temperature Dependence of the Electrical Resistivity of Water-Saturated Rocks." *Geophysics, 55,* (5), 576-585. Tulsa, Oklahoma: Society of Exploration Geophysicists. TIC: 243329.

Lyman, W.J.; Reehl, W.F.; and Rosenblatt, D.H. 1990. *Handbook of Chemical Property Estimation Methods: Environmental Behavior of Organic Compounds.* Washington D.C.: American Chemical Society. TIC: 242823.

Maier, C.G. and Kelley, K.K. 1932. "An Equation for the Representation of High Temperature Heat Content Data." *Journal of the American Chemical Society, 54,* 3243-3246. Washington, D.C.: American Chemical Society. TIC: 239023.

Morelli, G., and LaBrecque, D. 1996. "Robust Scheme for ERT Inverse Modeling." *Proceedings of the Symposium on the Application of Geophysics to Engineering and Environmental Problems.* April 28–May 2, 1996, 629-638. Keystone, Colorado: Environmental and Engineering Geophysical Society. TIC: 236229.

Nitao, J.J. 1989. *VTOUGH–An Enhanced Version of the TOUGH Code for the Thermal and Hydrologic Simulation of Large-Scale Problems in Nuclear Waste Isolation.* UCID-21954. Livermore, California: Lawrence Livermore National Laboratory. ACC: NNA.19900508.0040.

Nitao, J.J. 1998a. *Reference Manual for the NUFT Flow and Transport Code, Version 2.0.* UCRL-MA-130651. Livermore, California: Lawrence Livermore National Laboratory. ACC: MOL.19980810.0391.

Nitao, J.J. and Buscheck, T.A. 1995. "Discrete-Fracture Modeling of Thermal-Hydrological Processes at Yucca Mountain and the LLNL G-Tunnel Heater Test." *Scientific Basis for Nuclear Waste Management XIX: Symposium held November 27-December 1, 1995, Boston, Massachusetts.* Materials Research Society Symposium Proceedings Volume 412, 747-758. Pittsburgh, Pennsylvania: Materials Research Society. TIC: 237788.

Nitao, J.J.; Buscheck, T.A.; and Chesnut, D.A. 1993. "Implications of Episodic Nonequilibrium Fracture-Matrix Flow on Repository Performance." *Nuclear Technology, 104,* 385-402. Hinsdale, Illinois: American Nuclear Society. TIC: 226953.

Paces, J.B.; Marshall, B.D.; Whelan, J.F.; and Neymark, L.A. 1997. *Progress Report on Unsaturated Zone Stable and Radiogenic Isotope Studies.* Milestone Report SPC23FM4. Denver, Colorado: U.S. Geological Survey. ACC: MOL.19990107.0150.

Paces, J.B.; Neymark, L.A.; Marshall, B.D.; Whelan, J.F.; and Peterman, Z.E. 1996. *Ages and Origins of Subsurface Secondary Minerals in the Exploratory Studies Facility (ESF).* Milestone Report 3GQH450M. Denver, Colorado: U.S. Geological Survey. ACC: MOL.19970324.0052.

Paterson, M.S. 1978. *Experimental Rock Deformation—The Brittle Field.* p. 36. New York, New York: Springer-Verlag. TIC: 217476.

Peterson, J.E. 1986. *The Application of Algebraic Reconstruction Techniques to Geophysical Problems.* LBL-21498. Berkeley, California: Lawrence Berkeley National Laboratory. TIC: 239765.

Peterson, J.E. and Williams, K.H. 1997. *To Assess the Effectiveness of the Ground Penetrating Radar Method in Measuring Moisture Content in the Single Heater Test.* Milestone SP9241M4. Berkeley, California: Lawrence Berkeley National Laboratory. ACC: MOL.19971119.0542.

Pokrovskii, V.A. and Helgeson, H.C. 1995. "Thermodynamic Properties of Aqueous Species and the Solubilities of Minerals at High Pressures and Temperatures: The System Al_2O^3-H_2O-NaCl." *American Journal of Science, 295,* 1255-1342. New Haven, Connecticut: Kline Geology Laboratory, Yale University. TIC: 236803.

Popov, E.P.; Nagarajan, S.; and Lu, Z.A. 1976. *Mechanics of Materials.* Second edition, p. 570. Englewood Cliffs, New Jersey: Prentice-Hall. TIC: 243814.

Pruess, K. 1991. *TOUGH2—A General-Purpose Numerical Simulator for Multiphase Fluid and Heat Flow.* LBL-29400. Berkeley, California: Lawrence Berkeley National Laboratory. ACC: NNA.19940202.0088.

Pruess, K. and Narasimhan, T.N. 1985. "A Practical Method for Modeling Fluid and Heat Flow in Fractured Porous Media." *Society of Petroleum Engineers Journal, 25* (1), 14-26. Dallas, Texas: Society of Petroleum Engineers. TIC: 221917.

Pruess, K.; Simmons, A.; Wu, Y.S.; and Moridis, G.J. 1996. *TOUGH2 Software Qualification.* LBL-38383, UC-814. Berkeley, California: Lawrence Berkeley National Laboratory. ACC: MOL.19960602.0274.

Pruess, K. and Tsang, Y. 1994. *Thermal Modeling for a Potential High-Level Nuclear Waste Repository at Yucca Mountain, Nevada.* LBL-35381, UC-600. Berkeley, California: Lawrence Berkeley National Laboratory. ACC: NNA.19940427.0248.

Pruess, K.; Wang, J.S.Y.; and Tsang, Y.W. 1990. "On the Thermohydrologic Conditions near High-Level Nuclear Wastes Emplaced in Partially Saturated Fractured Tuff, Part 2. Effective Continuum Approximation." *Water Resources Research, 26* (6), 1249-1261. Washington, D.C.: American Geophysical Union. TIC: 224854.

Ragnarsdottir, K.V. 1993. "Dissolution Kinetics of Heulandite at pH 2-12 and 25°C." *Geochimica et Cosmochimica Acta, 57,* 2439-2449. New York, New York: Pergamon Press. TIC: 243920.

Ramirez, A. 1997. *Deliverable SP9215M4 (LLYMP9705055) and SP9251M4 (LLYMP9707038).* Data Submittal. Livermore, California: Lawrence Livermore National Laboratory. ACC: MOL.19980108.0538.

Ramirez, A. and Daily, W. 1998. *Electrical Resistivity Monitoring of the Single Heater Test in Yucca Mountain, FY 98 - 1st Quarter Results.* Livermore, California: Lawrence Livermore National Laboratory. ACC: MOL.19980203.0217.

Rimstidt, J.D. 1997. "Quartz Solubility at Low Temperatures." *Geochimica et Cosmochimica Acta, 61* (13), 2553-2558. New York, New York: Pergamon Press. TIC: 239020.

Rimstidt, J.D. and Barnes, H.L. 1980. "The Kinetics of Silica-Water Reactions." *Geochimica et Cosmochimica Acta, 44,* 1683-1699. New York, New York: Pergamon Press. TIC: 219975.

Roberts, J.J. and Carlberg, E. 1998. *Electrical Properties of Tuff from the Exploratory Studies Facility as a Function of Water Saturation and Temperature.* Livermore, California: Lawrence Livermore National Laboratory. ACC: MOL.19980512.0055.

Roberts, J.J. and Lin, W. 1997. "Electrical Properties of Partially Saturated Topopah Spring Tuff: Water Distribution as a Function of Saturation." *Water Resources Research, 33* (4), 577-587. Washington, D.C.: American Geophysical Union. TIC: 239736.

Roberts, S.K. and Viani, B.E. 1996. *Determination of Mineral Abundances in Core Samples from the Exploratory Studies Facility Using X-ray Diffraction.* Milestone SPY195M4. Livermore, California: Lawrence Livermore National Laboratory. ACC: MOL.19961022.0030.

Roberts, S.K. and Viani, B.E. 1997. *Mineral Abundances for Samples from Six Chemistry (SEAMIST) Holes in the Drift Scale Test Area (DST) of the ESF.* Milestone SP9510M4. Livermore, California: Lawrence Livermore National Laboratory. ACC: MOL.19970507.0186.

Serafim, J.L. and Periera, J.P. 1983. "Considerations on the Geomechanical Classification of Bieniawski." *Proceedings of the International Symposium on Engineering Geology and Underground Construction, Lisbon, Portugal, 1983,* II.33 through II.44. Lisbon, Portugal: Laboratorio Nacional de Engenharia Civil. TIC: 226267.

Smith, D.K.; Johnson, G.G.; Scheible, A.; Wims, A.M.; Johnson, J.L.; and Ullmann, G. 1987. "Quantitative X-Ray Powder Diffraction Method Using the Full Diffraction Pattern." *Powder Diffraction, 2,* (2), 73-77. College Park, Maryland: American Institute of Physics. TIC: 237068.

Smith, D.K.; Nichols, M.C.; and Zolensky, M.E. 1983. *POWD10, a FORTRAN IV Program for Calculating X-Ray Powder Diffraction Patterns – Version 10.* University Park, Pennsylvania: Pennsylvania State University, College of Earth and Mineral Sciences. TIC: 236983.

SNL (Sandia National Laboratories) 1996. *Single Heater Test: SNL As-Built Gage Table.* Albuquerque, New Mexico: Sandia National Laboratories. ACC: MOL.19970618.0501.

SNL 1997a. *Unconfined Compression Tests on Specimens from the Drift Scale Test Area of the Exploratory Studies Facility at Yucca Mountain, Nevada.* Albuquerque, New Mexico: Sandia National Laboratories. ACC: MOL.19971120.0014.

SNL 1997b. *Laboratory Measurements of Thermal Expansion and Thermal Conductivity for Specimens from Alcoves 5 and 7 of the Exploratory Studies Facility and from SD Drillholes at Yucca Mountain, Nevada.* Albuquerque, New Mexico: Sandia National Laboratories. ACC: MOL.19980209.0406.

SNL 1997c. *Evaluation of Single Heater Test Thermal and Thermomechanical Data: Second Quarter Results (8/26/96 through 2/28/97).* Albuquerque, New Mexico: Sandia National Laboratories. ACC: MOL.19971111.0187.

SNL 1997d. *Evaluation and Comparative Analysis of Single Heater Test Thermal and Thermomechanical Data: Third Quarter Results.* Albuquerque, New Mexico: Sandia National Laboratories. ACC: MOL.19980209.0374.

SNL 1997e. *Thermal Expansion and Thermal Conductivity of Test Specimens from the Drift Scale Test Area of the Exploratory Studies Facility at Yucca Mountain, Nevada.* Albuquerque, New Mexico: Sandia National Laboratories. ACC: MOL.19971120.0018.

SNL 1998. *Laboratory Measurements of Thermal Conductivity as a Function of Saturation State for Welded and Nonwelded Tuff Specimens.* Albuquerque, New Mexico: Sandia National Laboratories. ACC: MOL.19980901.0177.

Sobolik, S.R.; Francis, N.D.; and Finley, R.E. 1996. *Pre-Experiment Thermal-Hydrological-Mechanical Analyses for the ESF Single Heater Test - Phase 2.* SLTR96-0005. Albuquerque, New Mexico: Sandia National Laboratories. ACC: MOL.19970224.0065.

Sobolik, S.R.; Francis, N.D.; and Pott, J. 1996. *Pre-Experiment Thermo-Hydrological-Mechanical Analyses for the ESF Single Heater Test.* SLTR96-0004. Albuquerque, New Mexico: Sandia National Laboratories. ACC: MOL.19971030.0006.

Sonnenthal, E.L. 1997. "Discussion of Water Chemistry from the Heater Test." Sonnenthal (LBNL) memorandum to Bodvarsson, G.S. (LBNL), January 20, 1997. ACC: MOL.19980825.0287.

Sonnenthal, E.L.; Ahlers, C.F.; and Bodvarsson, G.S. 1997. "Fracture and Fault Properties for the UZ Site-Scale Flow Model." Chapter 7 of *The Site-Scale Unsaturated Zone Model of Yucca Mountain, Nevada, for the Viability Assessment*. Milestone SP24UFM4. LBNL-40376, UC-814. Berkeley, California: Lawrence Berkeley National Laboratory. ACC: MOL.19971014.0232.

Sonnenthal, E.; Spycher, N.; and Apps, J. 1998. *Interpretative Analysis of the Thermo-Hydro-Chemical Processes of the Drift-Scale Test.* Milestone SP2930M4. Berkeley, California: Lawrence Berkeley National Laboratory. ACC: MOL.19980825.0268.

Sonnenthal, E.; Spycher, N.; Apps, J.; and Simmons, A. 1998. *Thermo-Hydro-Chemical Predictive Analysis for the Drift-Scale Heater Test.* Milestone SPY289M4. Berkeley, California: Lawrence Berkeley National Laboratory. ACC: MOL.19980812.0268.

Steefel, C.I. and Lasaga, A.C. 1994. "A Coupled Model for Transport of Multiple Chemical Species and Kinetic Precipitation/Dissolution Reactions with Application to Reactive Flow in Single Phase Hydrothermal Systems." *American Journal of Science, 294*, 529-592. New Haven, Connecticut: Kline Geology Laboratory, Yale University. TIC: 235372.

Tester, J.W.; Worley, G.W.; Robison, B.A.; Grigsby, C.O.; and Feerer, J.L. 1994. "Correlating Quartz Dissolution Kinetics in Pure Water from 25° to 625°C." *Geochimica et Cosmochimica Acta, 58* (11), 2407-2420. New York, New York: Pergamon Press. TIC: 236776.

Tsang, Y.W. and Birkholzer, J.T. 1997. *Interpreting the Thermal-Hydrological Response of the ESF Single Heater Test.* Milestone SP9267M4. Berkeley, California: Lawrence Berkeley National Laboratory. ACC: MOL.19971204.0759.

Tsang, Y.W. and Tsang, C.F. 1987. "Channel Model of Flow Through Fractured Media." *Water Resources Research, 23*, 467-479. Washington, D.C.: American Geophysical Union. TIC: 238954.

Tsang, Y.W.; Wang, J.; Freifeld, B.; Cook, P.; Suarez-Rivera, R.; and Tokunaga, T. 1996. *Letter Report on Hydrological Characterization of the Single Heater Test Area in the ESF.* Berkeley, California: Lawrence Berkeley National Laboratory. ACC: MOL.19971119.0549.

van Genuchten, M.T. 1980. "A Closed-Form Equation for Predicting the Hydraulic Conductivity of Unsaturated Soil." *Soil Science Society of America Journal, 44* (4), 892-898. Madison, Wisconsin: Soil Science Society of America Special Publication Series. TIC: 217327.

Wang, H.F.; Blair, S.C.; and Berge, P.A. 1998. "Estimating Changes in Rock Permeability Due to Thermal-Mechanical Effects." *High Level Radioactive Waste Management, Proceedings of the Eighth International Conference, Las Vegas, Nevada, May 11-14, 1998*, 108-110. La Grange Park, Illinois: American Nuclear Society. TIC: 242489.

Wang, J. and Suarez-Rivera, R. 1997. *Laboratory Test Results of Hydrological Properties from Dry Drilled and Wet Drilled Cores in the Drift Scale Test Area and in the Single Heater Test Area of the Thermal Test Facility.* Milestone SP5130M4. Berkeley, California: Lawrence Berkeley National Laboratory. ACC: MOL.19971224.0056.

Waxman, M.H. and Thomas, E.C. 1974. "Electrical Conductivities in Shaly Sands–I. The Relation between Hydrocarbon Saturation and Resistivity Index; II. The Temperature Coefficient of Electrical Conductivity." *Journal of Petroleum Technology, 26*, 213-225. Dallas, Texas: Society of Petroleum Engineers. TIC: 239699.

Weast, R.C., ed. 1985. *CRC Handbook of Chemistry and Physics*. 66th Edition. Boca Raton, Florida: CRC Press. TIC: 216054.

Wolery, T.J. 1992. *EQ3/6, A Software Package for Geochemical Modeling of Aqueous Systems: Package Overview and Installation Guide (Version 7.0).* UCRL-MA-110662, Pt. I. Livermore, California: Lawrence Livermore National Laboratory. ACC: NNA.19921023.0028.

Wu, Y.S.; Ahlers, C.F.; Fraser, P.; Simmons, A.; and Pruess, K. 1996. *Software Qualification of Selected TOUGH2 Modules*. LBL-39490, UC-800. Berkeley, California: Lawrence Berkeley National Laboratory. ACC: MOL.19970219.0104.

Xu, T.; Gerard, F.; Pruess, K.; and Brimhall, G. 1997. *Modeling Non-Isothermal Multiphase Multi-Species Reactive Chemical Transport in Geologic Media.* LBNL-40504, UC-400. Berkeley, California: Lawrence Berkeley National Laboratory. TIC: 238918.

Xu, T. and Pruess, K. 1998. *Coupled Modeling of Non-Isothermal Multi-Phase Flow, Solute Transport and Reactive Chemistry in Porous and Fractured Media: 1. Model Development and Validation.* LBNL-42050. Berkeley, California: Lawrence Berkeley National Laboratory. TIC: 243735.

Xu, T.; Pruess, K.; and Brimhall, G. 1998. *An Improved Equilibrium-Kinetics Speciation Algorithm for Redox Reactions in Variably Saturated Subsurface Flow Systems.* LBNL-41789. Berkeley, California: Lawrence Berkeley National Laboratory. TIC: 240019.

Yang, I.C.; Rattray, G.W.; and Yu, P. 1996. *Interpretation of Chemical and Isotopic Data from Boreholes in the Unsaturated Zone at Yucca Mountain.* Water-Resources Investigation Report 96-4058. Denver, Colorado: U.S. Geological Survey. TIC: 236260.

Yang, I.C.; Yu, P.; Rattray, G.W.; Ferarese. J.S.; and Ryan, J.N. 1998. *Hydrochemical Investigations in Characterizing the Unsaturated Zone at Yucca Mountain, Nevada.* Water-Resouces Investigations Report 98-4132. Denver, Colorado: U.S. Geological Survey. ACC: MOL.19981012.0790.

YMP (Yucca Mountain Site Characterization Project) 1997. *YMP Reference Information Base.* YMP/93-02, Rev. 4. Las Vegas, Nevada: Yucca Mountain Site Characterization Office. TIC: 236604.

Zimmerman, R.M. and Finley, R.E. 1987. *Summary of Geomechanical Measurements Taken In and Around the G-Tunnel Underground Facility, NTS.* SAND86-1015, UC-70. Albuquerque, New Mexico: Sandia National Laboratories. ACC: NNA.19870526.0015.

13.2 CODES AND STANDARDS

ASTM D4535-85. 1985. *Standard Test Methods for Measurement of Thermal Expansion of Rock Using a Dilatometer.* Philadelphia, Pennsylvania: American Society for Testing and Materials. TIC: 236774.

ASTM D4971-89. 1989. *Standard Test Method for Determining the In Situ Modulus of Deformation of Rock Using the Diametrically Loaded 76-mm (3-in.) Borehole Jack.* West Conshohocken, Pennsylvania: American Society for Testing and Materials. TIC: 238036.

ASTM E228-85. 1985. *Standard Test Method for Linear Thermal Expansion of Solid Materials with a Vitreous Silica Dilatometer.* Philadelphia, Pennsylvania: American Society for Testing and Materials. TIC: 244463.

ASTM F433-77. 1977 (Reapproved 1993). *Standard Practice for Evaluating Thermal Conductivity of Gasket Materials.* Philadelphia, Pennsylvania: American Society for Testing and Materials. TIC: 243152.

13.3 PROCEDURES

CRWMS M&O Procedures

QAP-2-0. *Conduct of Activities.* Rev. 5. Las Vegas, Nevada: CRWMS M&O. ACC: MOL.19980826.0209.

LANL Procedures

LANL-EES-DP-03, R5. *Petrography Procedure.* Albuquerque, New Mexico: Los Alamos National Laboratory. ACC: MOL.19971009.0544.

LANL-EES-DP-16, R5. *Siemens X-ray Diffraction Procedure.* Albuquerque, New Mexico: Los Alamos National Laboratory. ACC: NNA.19920430.0206.

LANL-EES-DP-56, R4. *Brinkmann Automated Grinder Procedure*. Albuquerque, New Mexico: Los Alamos National Laboratory. ACC: MOL.19980626.0230.

LANL-EES-DP-101, R3. *Sample/Specimen Collection, Identification, and Control for Mineralogy-Petrology Studies*. Albuquerque, New Mexico: Los Alamos National Laboratory. ACC: MOL.19980213.0024.

LANL-YMP-QP-03.5, R8. *Documenting Scientific Investigations*. Albuquerque, New Mexico: Los Alamos National Laboratory. ACC: MOL.19971029.0005.

LBNL Procedure

YMP-LBNL-QIP-SIII.0 (c). *Scientific Investigation*. Berkeley, California: Lawrence Berkeley National Laboratory. MOL.19970625.0190.

LLNL Procedure

LLNL QP 3.4. *Scientific Notebooks*. Livermore, California: Lawrence Livermore National Laboratory. MOL.19980114.0131.

SNL Procedures

SNL QAIP 20-3, Rev. 02. *Sample Control*. Albuquerque, New Mexico: Sandia National Laboratories. ACC: MOL.19980908.0428.

SNL TP-51, Rev. 01. *Preparing Cylindrical Samples, Including Inspection of Dimensional and Shape Tolerances*. Albuquerque, New Mexico: Sandia National Laboratories. ACC: MOL.19971121.0240.

SNL TP-065. *Drying Geologic Samples to Constant Weight*. Rev. B. Albuquerque, New Mexico: Sandia National Laboratories. ACC: NNA.19900614.0359.

SNL TP-200, Rev. 01. *Inspection of Samples Used in Thermal Properties Measurements*. Albuquerque, New Mexico: Sandia National Laboratories. ACC: MOL.19980218.0156.

SNL TP-202, Rev. 00. *Measurement of Thermal Conductivity of Geologic Samples by the Guarded-Heat-Flow-Meter Method*. Albuquerque, New Mexico: Sandia National Laboratories. ACC: NNA.19910724.0006.

SNL TP-203, Rev. 01, ICN 1. *Measurement of Thermal Expansion of Geologic Samples Using a Push Rod Dilatometer*. Albuquerque, New Mexico: Sandia National Laboratories. ACC: MOL.19971121.0264; MOL.19971121.0267.

SNL TP-215, Rev. 00. *Calibration of Lawson Board Systems*. Logbook #1001. Albuquerque, New Mexico: Sandia National Laboratories. ACC: MOL.19961101.0023.

USGS Procedures

GCP-03, R3-M2. *Uranium-Thorium Disequilibrium Studies*. Denver, Colorado: United States Geologic Survey. MOL.19980203.0400.

GCP-12, R4. *Rb-Sr Isotope Geochemistry*. Denver, Colorado: United States Geologic Survey. NNA.19940321.0057.

YMP Procedure

YAP-SIII.3Q. *Processing of Technical Data on the Yucca Mountain Site Characterization Project*. Rev. 2, ICN 2. Las Vegas, Nevada: Yucca Mountain Site Characterization Office. ACC: MOL.19990323.0455.

13.4 SOURCE DATA, LISTED BY DATA TRACKING NUMBER

GS970208312271.002. Unsaturated Zone Hydrochemistry Data, 10-1-96 to 1-31-97, Including Chemical Composition and Carbon, Oxygen, and Hydrogen Isotopic Composition. Submittal date: 02/21/97.

GS980908312272.003. Strontium Isotope Ratios and Strontium Concentrations in Waters from the Single Heater Test in ESF-TMA-NE U2, February, 1997 and May, 1997. Submittal date: 09/25/98.

GS980908312322.009. Uranium Concentrations and $^{234}U/^{238}U$ Ratios from Spring, Well, Runoff, and Rain Waters Collected from the Nevada Test Site and Death Valley Vicinities and Analyzed between 01/15/98 and 08/15/98. Submittal date: 09/23/98.

LASL831151AQ98.001. Mineralogic Characterization of the ESF Single Heater Test Block. Submittal date: 08/31/98.

LB960500834244.001. Letter Report on Hydrological Characterization of the Single Heater Test Area in ESF by Y.W. Tsang, J. Wang, B. Freifeld, P. Cook, R. Suarez-Rivera, and T. Tokunaga. Submittal date: 08/23/96.

LB971000123142.001. Air Injections in Boreholes #16 and #18 in the Single Heater Test Area. Submittal date: 10/17/97.

LB980120123142.002. Air Injections in Boreholes #16 and #18 in the Single Heater Test Area, 1st Quarter FY98 Results. Submittal date: 01/20/98.

LB980901123142.001. Active Hydrology Testing Data in Boreholes 16 and 18; Air Injection Tests and Gas Tracer Tests for the Final TDIF Submittal for the Single Heater Test. Submittal date: 08/26/98.

LB980901123142.002. Passive Monitoring Data (Temperature, Relative Humidity, and Gauge Pressure) for the Final TDIF Submittal for the Single Heater Test. Submittal date: 08/26/98.

LB980901123142.003. Ground Penetrating Radar Data for Final TDIF Submittal for the Single Heater Test. Submittal date: 08/26/98.

LB980901123142.006. Laboratory Test Results of Hydrological Properties from Post-Test Dry-Drilled Cores in the Single Heater Test Area for the Final TDIF Submittal for the Single Heater Test. Submittal date: 08/31/98.

LL970703904244.034. Third Quarter Results of Chemical Measurements in the Single Heater Test. VA Supporting Data. Submittal date: 07/15/97.

LL971004604244.045. Fourth Quarter Results of the Neutron Logging Report. Data on Moisture Content in Boreholes 15, 17, 22 and 23 of the Single Heater Test (SHT). VA Supporting Data. Submittal date: 10/16/97.

LL980106404244.050. Three Tables of Mineral Abundances for Samples Used for Thermal Testing (Boreholes in the Drift Scale Test (DST) Area of the ESF). (These Data Supersede DTNS LL970206704244.029, LL970600304244.032, and LL960810704244.017 and Show Data that have been Reanalyzed). VA Supporting Data. Submittal date: 01/15/98.

LL980106904244.051. First Quarter FY98 Results of the Neutron Logging Report. Data on Moisture Content in Boreholes 15, 17, 22 and 23 of the Single Heater Test (SHT). VA Supporting Data. Submittal date: 01/16/98.

LL980810804242.050. Seven Figures and One Table of Data Associated With Milestone Report #SPY1320M4, URL-ID-131491 Entitled "Single-Heater Test, Final Report." Submittal date: 09/23/98.

LL981109904242.072. Drift-Scale Report, "Electrical Properties of Tuff from the ESF as a Function of Water Saturation and Temperature," One Table and Ten Figures. VA Supporting Data. Associated with UCRL-ID-129594, SPY195M4, DST4Q97. Submittal date: 11/19/98.

SNF35110695001.008. Evaluation and Comparative Analysis of Single Heater Test, Thermal and Thermomechanical Data: First Quarter FY98 Results (8/26/96 through 11/30/97) (This Data Supersedes Data Previously Identified by DTN: SNF35110695001.007). Submittal date: 01/06/98.

SNF35110695001.009. Thermal and Thermomechanical Data for the Single Heater Test Final Report. This Submittal is for the next Increment of Measurements Performed since the 1st Quarter FY98 Submittal under DTN: SNF35110695001.008. Submittal date: 08/24/98.

SNL22080196001.001. Thermal Properties of Test Specimens from the Single Heater Test Area in the Thermal Testing Facility at Yucca Mountain, Nevada. VA Supporting Data. Submittal date: 08/15/96.

SNL22080196001.003. Posttest Laboratory Thermal and Mechanical Characterization for Single Heater Test (SHT) Block. Submittal date: 08/26/98.

INTENTIONALLY LEFT BLANK

APPENDIX A

THERMAL EXPANSION DATA: SUMMARY SHEET FOR EACH TEST CYCLE

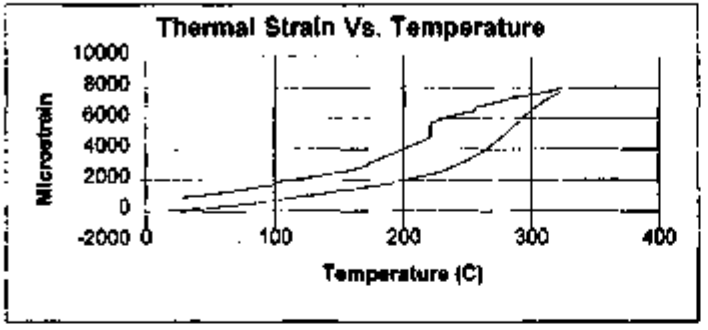

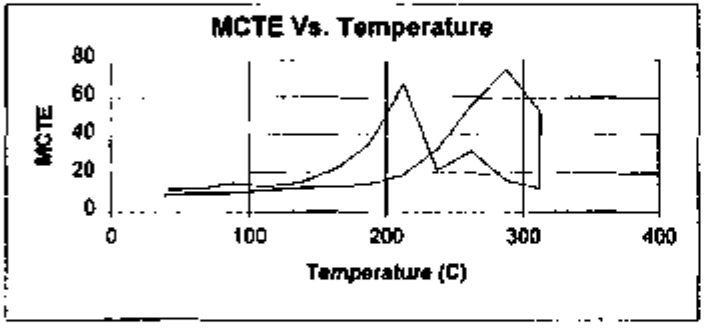

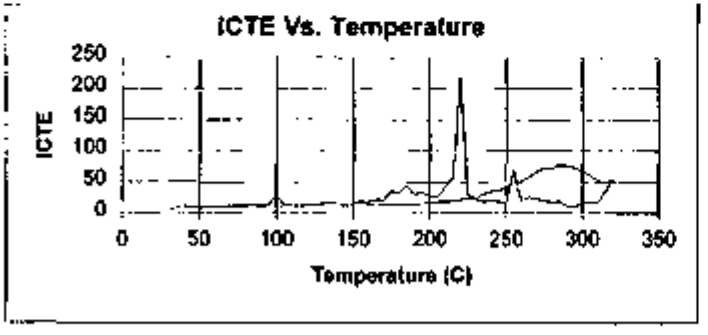

Specimen ID:	PTC1-A 2.9-B Cycle 1
Date of Test Completion:	31-07-98
Thermal/Mechanical Unit:	TSw2
Lithostratigraphic Unit:	Tptpmn
Original Location:	ESF; Alcove 5,Thermal Drift Scale Test Area Collected after Completion of Single Heater Test
Initial Moisture Content	Air-dried (As-is)
Nominal Dimensions:	50 8 mm (L) 25 4 mm (D)

Specimen Data:	Length (mm)	Mass (g)
Pre-test:	50.77	55.572
Post-test:	50.77	55.03
Change:	0	0.542

Temp Range (C)			Mean Temp (C)	Mean CTE (10^{-6}/C)
25	-	50	37.5	8.7
50	-	75	62.5	9.6
75	-	100	87.5	9.8
100	-	125	112.5	11.2
125	-	150	137.5	12.3
150	-	175	162.5	13.1
175	-	200	187.5	14.6
200	-	225	212.5	19.4
225	-	250	237.5	32.7
250	-	275	262.5	56.3
275	-	300	287.5	75.0
300	-	325	312.5	52.3
325	-	300	312.5	12.2
300	-	275	287.5	16.5
275	-	250	262.5	31.8
250	-	225	237.5	21.6
225	-	200	212.5	67.2
200	-	175	187.5	35.4
175	-	150	162.5	22.1
150	-	125	137.5	15.2
125	-	100	112.5	13.2
100	-	75	87.5	15.0
75	-	50	62.5	11.6
50	-	30	40	11.4

Temp Range (C)			Mean Temp (C)	Instant. CTE (10^{-6}/C)
27.5	-	32.5	30	7.7
47.5	-	52.5	50	9.0
72.5	-	77.5	75	9.8
97.5	-	102.5	100	10.7
122.5	-	127.5	125	12.4
147.5	-	152.5	150	12.1
172.5	-	177.5	175	14.4
197.5	-	202.5	200	16.7
222.5	-	227.5	225	22.8
247.5	-	252.5	250	42.1
272.5	-	277.5	275	71.8
297.5	-	302.5	300	67.7
302.5	-	297.5	300	16.3
277.5	-	272.5	275	20.6
252.5	-	247.5	250	18.0
227.5	-	222.5	225	28.0
202.5	-	197.5	200	28.8
177.5	-	172.5	175	36.4
152.5	-	147.5	150	15.7
127.5	-	122.5	125	13.4
102.5	-	97.5	100	29.6
77.5	-	72.5	75	12.9
52.5	-	47.5	50	11.6

Figure A-1. Thermal Testing Data for Specimen PCT1-A 2.9-B, Cycle 1

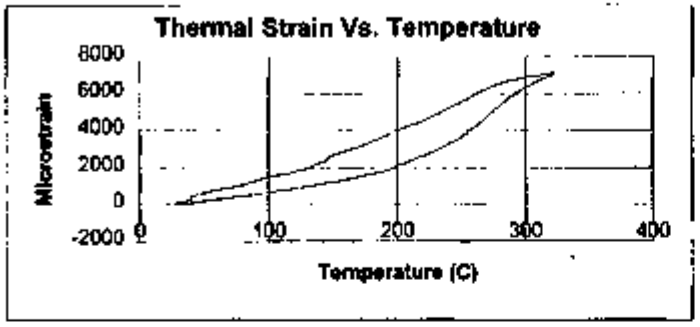

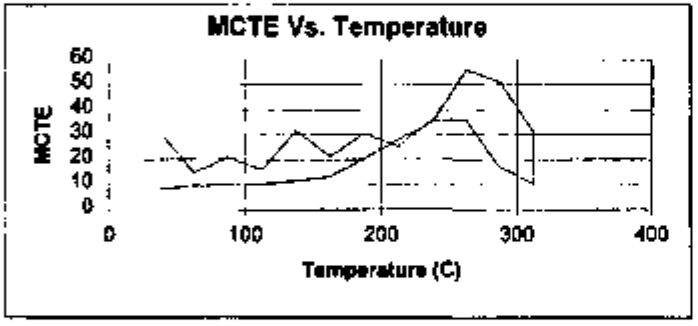

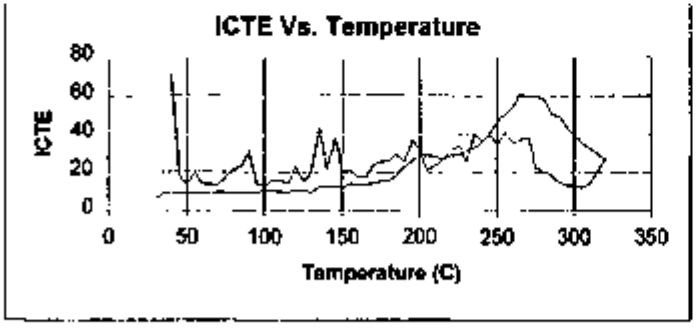

Specimen ID:	PTC1-A 2.9-B Cycle 2
Date of Test Completion:	04-08-98
Thermal/Mechanical Unit:	TSw2
Lithostratigraphic Unit:	Tplpmn
Original Location:	ESF; Alcove 5;Thermal Drift Scale Test Area
	Collected after Completion of Single Heater Test
Initial Moisture Content	Air-dried (As-is)
Nominal Dimensions:	50.8 mm (L) 25.4 mm (D)

Specimen Data:	Length (mm)	Mass (g)
Pre-test:	50.8	55.17
Post-test:	50.82	54.975
Change:	-0.02	0.195

Temp Range (C)		(C)	Mean Temp (C)	Mean CTE (10^{-6}/C)
25	- 50	37.5	8.2	
50	- 75	62.5	9.4	
75	- 100	87.5	9.6	
100	- 125	112.5	10.5	
125	- 150	137.5	11.7	
150	- 175	162.5	13.3	
175	- 200	187.5	20.5	
200	- 225	212.5	28.1	
225	- 250	237.5	35.0	
250	- 275	262.5	56.2	
275	- 300	287.5	51.1	
300	- 325	312.5	31.2	
325	- 300	312.5	10.6	
300	- 275	287.5	17.1	
275	- 250	262.5	36.2	
250	- 225	237.5	36.1	
225	- 200	212.5	25.5	
200	- 175	187.5	30.7	
175	- 150	162.5	21.6	
150	- 125	137.5	32.0	
125	- 100	112.5	16.2	
100	- 75	87.5	21.0	
75	- 50	62.5	14.8	
50	- 30	40	29.6	

Temp Range (C)		(C)	Mean Temp (C)	Instant. CTE (10^{-6}/C)
27.5	- 32.5	30	6.0	
47.5	- 52.5	50	9.0	
72.5	- 77.5	75	9.6	
97.5	- 102.5	100	10.9	
122.5	- 127.5	125	10.7	
147.5	- 152.5	150	12.0	
172.5	- 177.5	175	15.4	
197.5	- 202.5	200	28.8	
222.5	- 227.5	225	29.1	
247.5	- 252.5	250	47.1	
272.5	- 277.5	275	59.8	
297.5	- 302.5	300	39.4	
302.5	- 297.5	300	12.8	
277.5	- 272.5	275	22.5	
252.5	- 247.5	250	35.0	
227.5	- 222.5	225	34.2	
202.5	- 197.5	200	31.5	
177.5	- 172.5	175	25.8	
152.5	- 147.5	150	20.8	
127.5	- 122.5	125	15.3	
102.5	- 97.5	100	13.0	
77.5	- 72.5	75	18.0	
52.5	- 47.5	50	13.5	

Figure A-2. Thermal Testing Data for Specimen PCT1-A 2.9B, Cycle 2

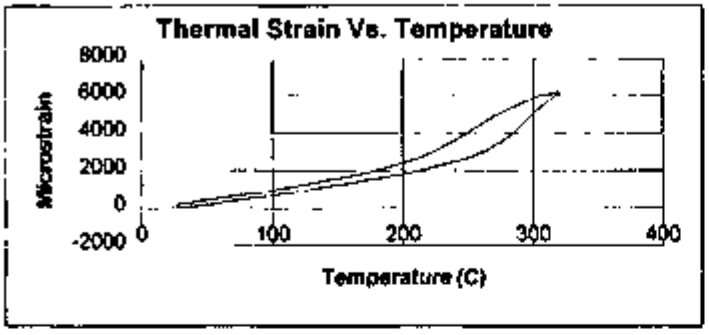

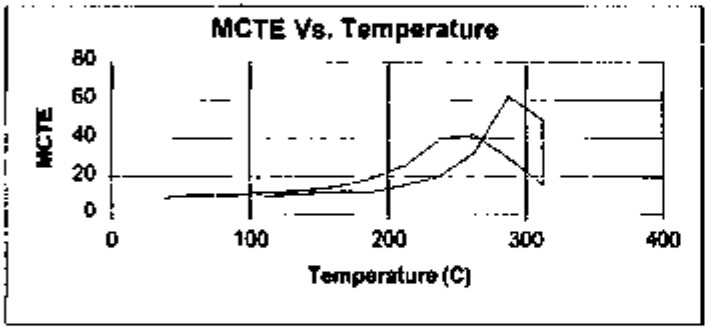

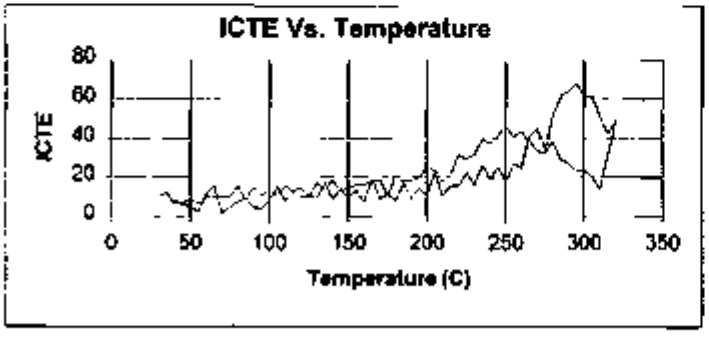

Specimen ID:	PTC1-A 16.8-B Cycle 1
Date of Test Completion:	29-06-98
Thermal/Mechanical Unit:	TSw2
Lithostratigraphic Unit:	Tptpmn
Original Location:	ESF; Alcove 5; Single Heater Test Area Collected after Completion of Single Heater Test
Initial Moisture Content	Air-dried (As-is)
Nominal Dimensions:	50.8 mm (L) 25.4 mm (D)

Specimen Data	Length (mm)	Mass (g)
Pre-test:	50.77	58.087
Post-test	50.76	57.343
Change	-0.01	0.744

Temp Range (C)		(C)	Mean Temp (C)	Mean CTE (10^{-6}/C)
25	-	50	37.5	9.07302
50	-	75	62.5	10.9926
75	-	100	87.5	9.64112
100	-	125	112.5	10.4474
125	-	150	137.5	11.305
150	-	175	162.5	12.4635
175	-	200	187.5	12.3409
200	-	225	212.5	15.7772
225	-	250	237.5	20.2915
250	-	275	262.5	33.1766
275	-	300	287.5	62.1499
300	-	325	312.5	49.7925
325	-	300	312.5	16.0814
300	-	275	287.5	30.1611
275	-	250	262.5	42.0959
250	-	225	237.5	39.4593
225	-	200	212.5	26.2917
200	-	175	187.5	19.1543
175	-	150	162.5	15.0987
150	-	125	137.5	12.8823
125	-	100	112.5	12.0769
100	-	75	87.5	10.6606
75	-	50	62.5	10.2433
50	-	30	40	9.69996

Temp Range (C)		(C)	Mean Temp (C)	Instant. CTE (10^{-6}/C)
27.5	-	32.5	30	10.4465
47.5	-	52.5	50	4.9849
72.5	-	77.5	75	4.75617
97.5	-	102.5	100	8.62277
122.5	-	127.5	125	11.3326
147.5	-	152.5	150	9.74703
172.5	-	177.5	175	11.4707
197.5	-	202.5	200	11.0549
222.5	-	227.5	225	22.6726
247.5	-	252.5	250	17.9493
272.5	-	277.5	275	34.7826
297.5	-	302.5	300	61.1508
302.5	-	297.5	300	24.0435
277.5	-	272.5	275	32.6691
252.5	-	247.5	250	46.3329
227.5	-	222.5	225	29.7836
202.5	-	197.5	200	26.2726
177.5	-	172.5	175	10.9147
152.5	-	147.5	150	14.5163
127.5	-	122.5	125	10.0095
102.5	-	97.5	100	13.447
77.5	-	72.5	75	10.453
52.5	-	47.5	50	8.87783

Figure A-3. Thermal Testing Data for Specimen PCT1-A 16.8-B, Cycle 1

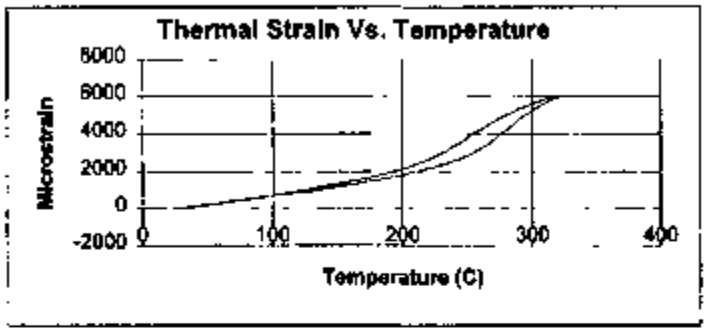

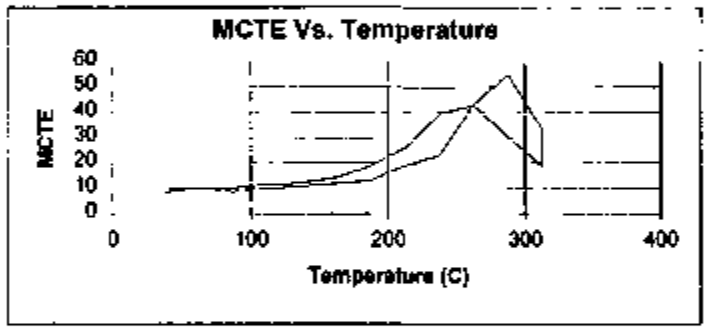

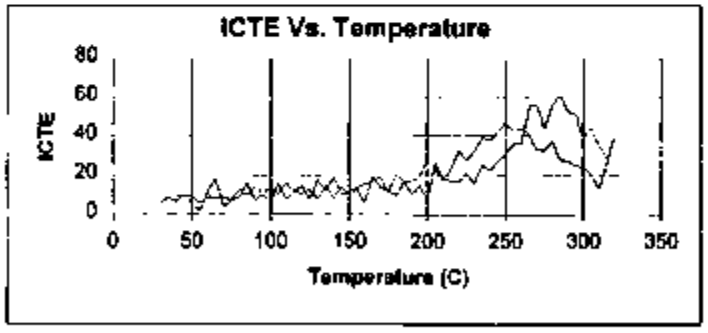

Specimen ID:	PTC1-A 16.8-B Cycle 2
Date of Test Completion:	14-07-98
Thermal/Mechanical Unit:	TSw2
Lithostratigraphic Unit:	Tptpmn
Original Location:	ESF; Alcove 5; Thermal Drift Scale Test Area
	Collected after Completion of Single Heater Test
Initial Moisture Content	Air-dried (As-is)
Nominal Dimensions:	50.8 mm (L) 25.4 mm (D)

Specimen Data	Length (mm)	Mass (g)
Pre-test:	50.8	57.493
Post-test:	50.8	57.363
Change:	0	0.13

Temp Range (C)		(C)	Mean Temp (C)	Mean CTE (10^{-6}/C)
25	-	50	37.5	8.80272
50	-	75	62.5	10.2929
75	-	100	87.5	9.0263
100	-	125	112.5	10.3335
125	-	150	137.5	11.1329
150	-	175	162.5	12.3517
175	-	200	187.5	13.3963
200	-	225	212.5	19.1934
225	-	250	237.5	23.1668
250	-	275	262.5	43.4436
275	-	300	287.5	54.9749
300	-	325	312.5	33.5369
325	-	300	312.5	18.9021
300	-	275	287.5	30.7335
275	-	250	262.5	42.7888
250	-	225	237.5	39.6108
225	-	200	212.5	26.3281
200	-	175	187.5	18.8772
175	-	150	162.5	14.6838
150	-	125	137.5	12.5129
125	-	100	112.5	11.8018
100	-	75	87.5	10.5502
75	-	50	62.5	9.9857
50	-	30	40	9.74457

Temp Range (C)		(C)	Mean Temp (C)	Instant CTE (10^{-6}/C)
27.5	-	32.5	30	6.07525
47.5	-	52.5	50	6.14253
72.5	-	77.5	75	7.38601
97.5	-	102.5	100	7.15085
122.5	-	127.5	125	13.012
147.5	-	152.5	150	9.863
172.5	-	177.5	175	12.2758
197.5	-	202.5	200	8.30421
222.5	-	227.5	225	21.409
247.5	-	252.5	250	30.9564
272.5	-	277.5	275	43.9137
297.5	-	302.5	300	39.4686
302.5	-	297.5	300	24.5705
277.5	-	272.5	275	32.7554
252.5	-	247.5	250	47.1752
227.5	-	222.5	225	28.215
202.5	-	197.5	200	27.9099
177.5	-	172.5	175	11.153
152.5	-	147.5	150	11.828
127.5	-	122.5	125	7.71265
102.5	-	97.5	100	14.1733
77.5	-	72.5	75	7.74322
52.5	-	47.5	50	9.27225

Figure A-4. Thermal Testing Data for Specimen PTC1-A 16.8-B, Cycle 2

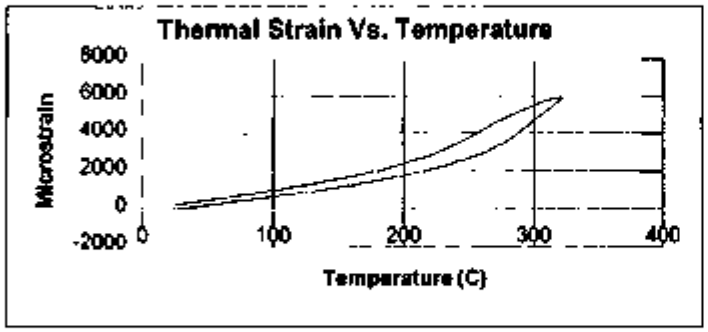

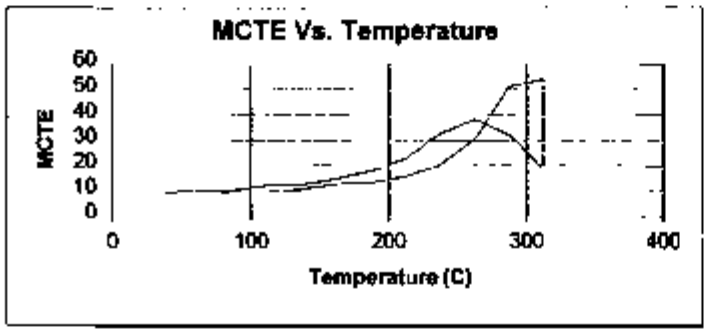

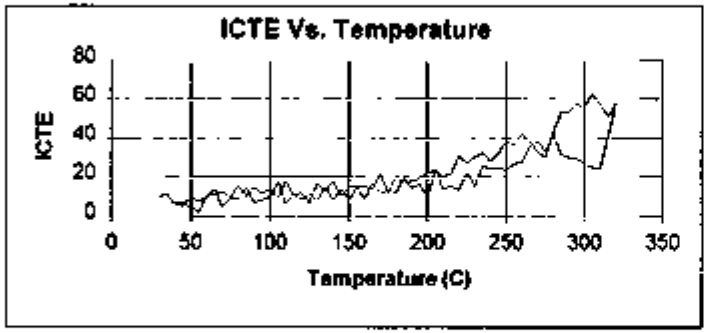

Specimen ID:	PTC1-B 19.0-B Cycle 1
Date of Test Completion:	31-07-98
Thermal/Mechanical Unit.	TSw2
Lithostratigraphic Unit.	Tptpmn
Original Location:	ESF, Alcove 5;Thermal Drift Scale Test Area Collected after Completion of Single Heater Test
Initial Moisture Content	Air-dried (As-Is)
Nominal Dimensions:	50.8 mm (L) 25.4 mm (D)

Specimen Data:	Length (mm)	Mass (g)
Pre-test:	50.8	59.009
Post-test:	50.8	58.181
Change:	0	0.828

Temp Range (C)		(C)	Mean Temp (C)	Mean CTE (10^{-6}/C)
25	-	50	37.5	9.0
50	-	75	62.5	10.1
75	-	100	87.5	8.9
100	-	125	112.5	9.4
125	-	150	137.5	10.6
150	-	175	162.5	12.9
175	-	200	187.5	13.5
200	-	225	212.5	16.0
225	-	250	237.5	20.4
250	-	275	262.5	30.6
275	-	300	287.5	51.4
300	-	325	312.5	54.0
325	-	300	312.5	18.8
300	-	275	287.5	32.2
275	-	250	262.5	38.3
250	-	225	237.5	32.9
225	-	200	212.5	22.9
200	-	175	187.5	18.0
175	-	150	162.5	15.0
150	-	125	137.5	12.7
125	-	100	112.5	12.3
100	-	75	87.5	10.3
75	-	50	62.5	10.2
50	-	30	40	9.1

Temp Range (C)		(C)	Mean Temp (C)	Instant CTE (10^{-6}/C)
27.5	-	32.5	30	10.3
47.5	-	52.5	50	4.5
72.5	-	77.5	75	9.6
97.5	-	102.5	100	9.8
122.5	-	127.5	125	11.3
147.5	-	152.5	150	8.3
172.5	-	177.5	175	12.8
197.5	-	202.5	200	9.5
222.5	-	227.5	225	22.6
247.5	-	252.5	250	23.6
272.5	-	277.5	275	32.9
297.5	-	302.5	300	55.7
302.5	-	297.5	300	27.3
277.5	-	272.5	275	30.4
252.5	-	247.5	250	38.5
227.5	-	222.5	225	27.3
202.5	-	197.5	200	22.2
177.5	-	172.5	175	12.3
152.5	-	147.5	150	15.2
127.5	-	122.5	125	7.1
102.5	-	97.5	100	13.9
77.5	-	72.5	75	10.0
52.5	-	47.5	50	10.0

Figure A-5. Thermal Testing Data for Specimen PTC1-B 19.0-B, Cycle 1

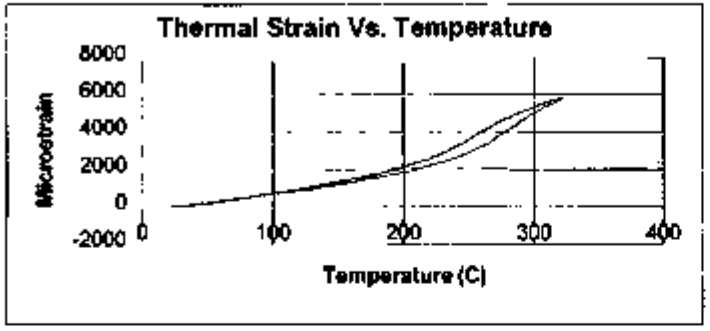

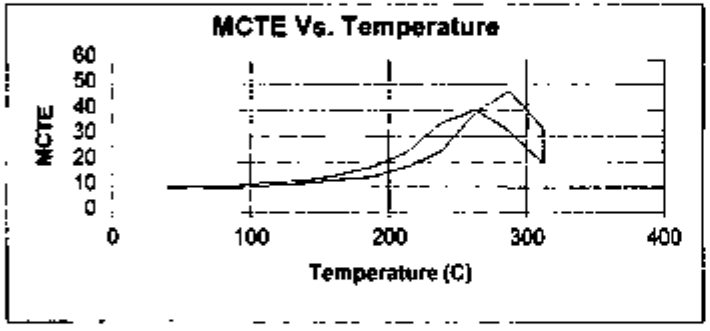

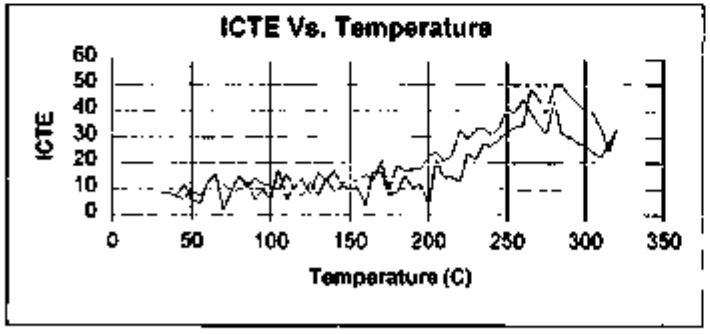

Specimen ID:	PTC1-B 19.0-B Cycle 2
Date of Test Completion:	04-08-98
Thermal/Mechanical Unit:	TSw2
Lithostratigraphic Unit:	Tptpmn
Original Location.	ESF; Alcove 5;Thermal Drift Scale Test Area Collected after Completion of Single Heater Test
Initial Moisture Content	Air-dried (As-is)
Nominal Dimensions:	50 8 mm (L) 25.4 mm (D)

Specimen Data.	Length (mm)	Mass (g)
Pre-test.	50 8	58.242
Post-test:	50.8	58.154
Change:	0	0.088

Temp Range (C)		(C)	Mean Temp (C)	Mean CTE (10^{-6}/C)
25	-	50	37.5	9 0
50	-	75	62.5	10.0
75	-	100	87.5	9.5
100	-	125	112.5	10.7
125	-	150	137.5	11.5
150	-	175	162.5	13.1
175	-	200	187.5	14 2
200	-	225	212.5	18 0
225	-	250	237.5	23.9
250	-	275	262.5	39.2
275	-	300	287.5	47 9
300	-	325	312.5	32.5
325	-	300	312.5	19.5
300	-	275	287.5	32.1
275	-	250	262.5	40.2
250	-	225	237.5	35.0
225	-	200	212.5	23.8
200	-	175	187.5	18 0
175	-	150	162.5	14.7
150	-	125	137.5	12.6
125	-	100	112.5	11.9
100	-	75	87.5	10.4
75	-	50	62.5	10.1
50	-	30	40	9.6

Temp Range (C)		(C)	Mean Temp (C)	Instant. CTE (10^{-6}/C)
27 5	-	32 5	30	8 0
47.5	-	52.5	50	6.1
72.5	-	77.5	75	9 2
97.5	-	102.5	100	5.5
122.5	-	127 5	125	12.9
147.5	-	152 5	150	10.5
172.5	-	177 5	175	8.1
197.5	-	202.5	200	4.1
222.5	-	227 5	225	23.9
247.5	-	252 5	250	31.8
272.5	-	277.5	275	39.1
297 5	-	302.5	300	40.5
302.5	-	297 5	300	26.8
277.5	-	272.5	275	31.4
252 5	-	247.5	250	41.6
227.5	-	222.5	225	29.3
202.5	-	197.5	200	22.7
177.5	-	172.5	175	10.3
152.5	-	147.5	150	14.1
127.5	-	122.5	125	8.6
102.5	-	97.5	100	11.9
77.5	-	72.5	75	9.7
52.5	-	47.5	50	9.2

Figure A-6. Thermal Testing Data for Specimen PTC1-B 19.0-B, Cycle 2

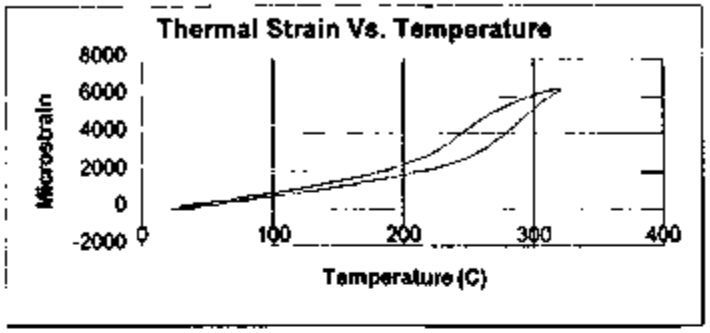

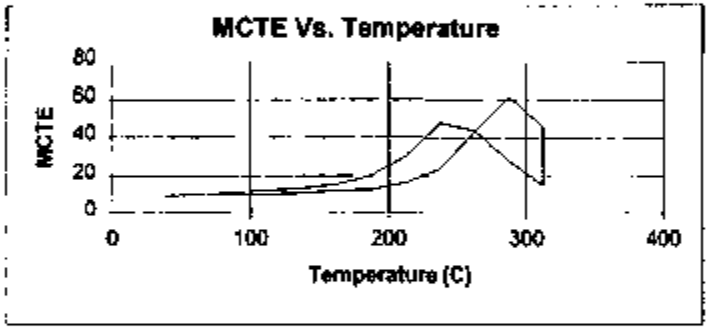

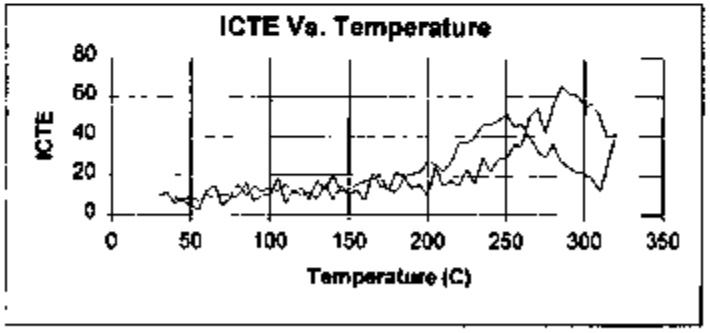

Specimen ID:	PTC2-B 4 1-B Cycle 1
Date of Test Completion:	01-07-98
Thermal/Mechanical Unit	TSw2
Lithostratigraphic Unit.	Tptpmn
Original Location:	ESF; Alcove 5;Thermal Drift Scale Test Area Collected after Completion of Single Heater Test
Initial Moisture Content	Air-dried (As-is)
Nominal Dimensions:	50.8 mm (L) 25.4 mm (D)

Specimen Data:	Length (mm)	Mass (g)
Pre-test:	50.78	57.615
Post-test:	50.8	57.109
Change:	-0.02	0.506

Temp Range (C)		(C)	Mean Temp (C)	Mean CTE (10^{-6}/C)
25	-	50	37.5	9.18535
50	-	75	62.5	10.4532
75	-	100	87.5	9.90015
100	-	125	112.5	10.3211
125	-	150	137.5	11.0607
150	-	175	162.5	12.3241
175	-	200	187.5	12.7682
200	-	225	212.5	16.4068
225	-	250	237.5	23.8304
250	-	275	262.5	43.0531
275	-	300	287.5	61.3781
300	-	325	312.5	45.625
325	-	300	312.5	14.8564
300	-	275	287.5	27.815
275	-	250	262.5	43.7519
250	-	225	237.5	47.9506
225	-	200	212.5	30.0925
200	-	175	187.5	20.3721
175	-	150	162.5	15.6121
150	-	125	137.5	13.2712
125	-	100	112.5	12.2593
100	-	75	87.5	10.8025
75	-	50	62.5	10.1758
50	-	30	40	9.56604

Temp Range (C)		(C)	Mean Temp (C)	Instant. CTE (10^{-6}/C)
27.5	-	32.5	30	10.197
47.5	-	52.5	50	4.87661
72.5	-	77.5	75	9.31032
97.5	-	102.5	100	10.1059
122.5	-	127.5	125	11.4169
147.5	-	152.5	150	10.4948
172.5	-	177.5	175	13.0623
197.5	-	202.5	200	10.6307
222.5	-	227.5	225	23.8126
247.5	-	252.5	250	28.4801
272.5	-	277.5	275	42.1274
297.5	-	302.5	300	54.8154
302.5	-	297.5	300	21.1346
277.5	-	272.5	275	29.3839
252.5	-	247.5	250	51.6126
227.5	-	222.5	225	36.6521
202.5	-	197.5	200	27.7316
177.5	-	172.5	175	12.651
152.5	-	147.5	150	13.1162
127.5	-	122.5	125	8.14735
102.5	-	97.5	100	14.3385
77.5	-	72.5	75	9.74374
52.5	-	47.5	50	9.08148

Figure A-7. Thermal Testing Data for Specimen PTC2-B 4.1-B, Cycle 1

Thermal Testing Data for

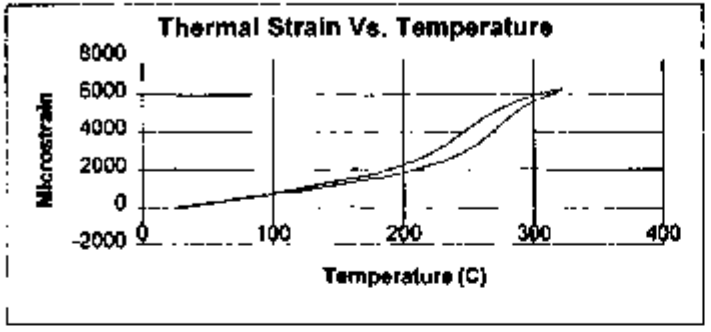

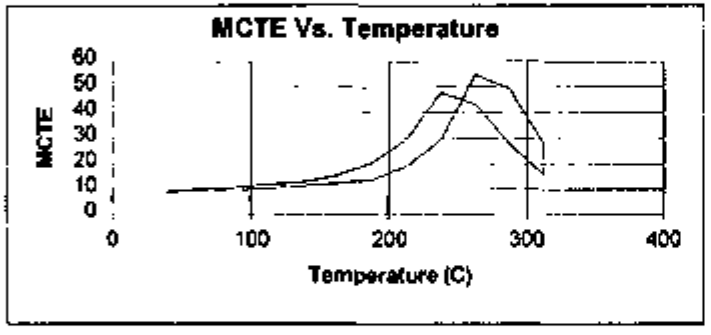

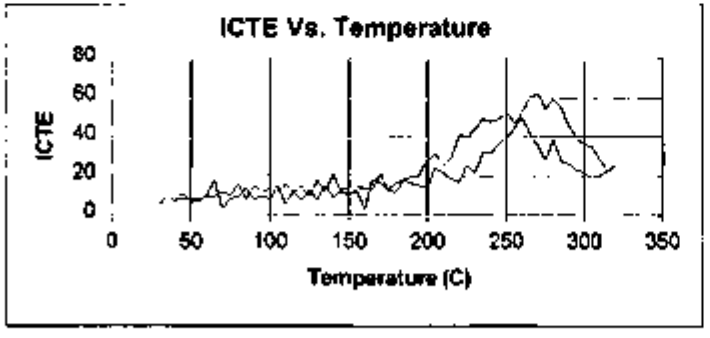

Specimen ID:	PTC2-B 4.1-B Cycle 2
Date of Test Completion:	15-07-98
Thermal/Mechanical Unit	TSw2
Lithostratigraphic Unit:	Tptpmn
Original Location:	ESF, Alcove 5;Thermal Drift Scale Test Area Collected after Completion of Single Heater Test
Initial Moisture Content	Air-dried (As-is)
Nominal Dimensions:	50.8 mm (L) 25.4 mm (D)

Specimen Data:	Length (mm)	Mass (g)
Pre-test:	50.77	57.232
Post-test:	50.78	57.098
Change:	-0.01	0.134

Temp Range (C)		(C)	Mean Temp (C)	Mean CTE (10^{-6}/C)
25	-	50	37.5	8.65595
50	-	75	62.5	10.3778
75	-	100	87.5	9.30685
100	-	125	112.5	10.5675
125	-	150	137.5	11.4294
150	-	175	162.5	12.4058
175	-	200	187.5	13.91
200	-	225	212.5	19.35
225	-	250	237.5	29.4718
250	-	275	262.5	54.8437
275	-	300	287.5	49.4218
300	-	325	312.5	27.6557
325	-	300	312.5	15.5689
300	-	275	287.5	27.7842
275	-	250	262.5	43.5198
250	-	225	237.5	47.9337
225	-	200	212.5	29.8987
200	-	175	187.5	20.6478
175	-	150	162.5	15.4373
150	-	125	137.5	13.0653
125	-	100	112.5	12.0795
100	-	75	87.5	10.8125
75	-	50	62.5	9.91686
50	-	30	40	9.649

Temp Range (C)		(C)	Mean Temp (C)	Instant. CTE (10^{-6}/C)
27.5	-	32.5	30	4.08362
47.5	-	52.5	50	7.04833
72.5	-	77.5	75	8.65265
97.5	-	102.5	100	7.7872
122.5	-	127.5	125	12.824
147.5	-	152.5	150	10.0526
172.5	-	177.5	175	12.9955
197.5	-	202.5	200	13.7108
222.5	-	227.5	225	25.8292
247.5	-	252.5	250	39.8682
272.5	-	277.5	275	54.787
297.5	-	302.5	300	36.0946
302.5	-	297.5	300	22.2088
277.5	-	272.5	275	28.1869
252.5	-	247.5	250	52.676
227.5	-	222.5	225	39.4547
202.5	-	197.5	200	28.4311
177.5	-	172.5	175	13.2465
152.5	-	147.5	150	14.7933
127.5	-	122.5	125	9.64705
102.5	-	97.5	100	13.6052
77.5	-	72.5	75	10.5958
52.5	-	47.5	50	9.04538

Figure A-8. Thermal Testing Data for Specimen PTC2-B 4.1-B, Cycle 2

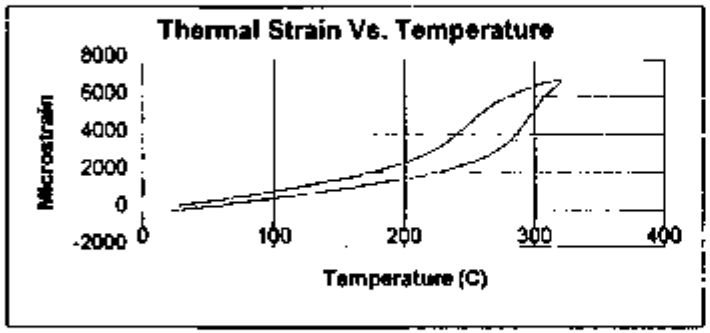

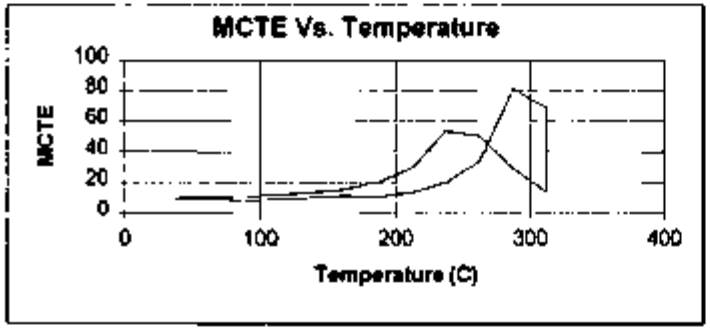

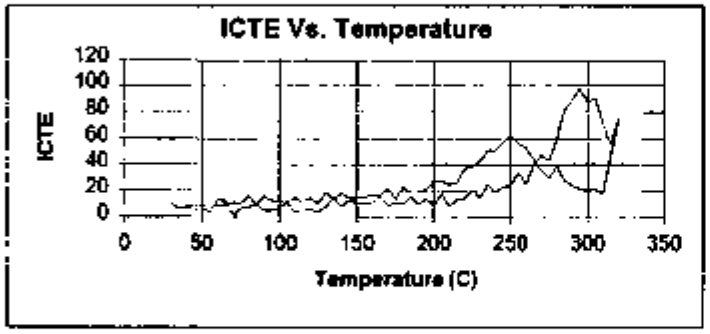

Specimen ID:	PTC4-A-4.6-B Cycle 1
Date of Test Completion:	07-07-98
Thermal/Mechanical Unit:	TSw2
Lithostratigraphic Unit:	Tptpmn
Original Location:	ESF; Alcove 5;Thermal Drift Scale Test Area Collected after Completion of Single Heater Test
Initial Moisture Content	Air-dried (As-is)
Nominal Dimensions:	50.8 mm (L) 25.4 mm (D)

Specimen Data:	Length (mm)	Mass (g)
Pre-test:	50.8	56.468
Post-test	50.82	55.71
Change:	-0.02	0.758

Temp Range (C)		(C)	Mean Temp (C)	Mean CTE (10^{-6}/C)
25	-	50	37.5	8.81403
50	-	75	62.5	10.0334
75	-	100	87.5	8.3162
100	-	125	112.5	9.48603
125	-	150	137.5	10.457
150	-	175	162.5	11.922
175	-	200	187.5	11.2359
200	-	225	212.5	13.8673
225	-	250	237.5	20.1414
250	-	275	262.5	34.1076
275	-	300	287.5	81.3867
300	-	325	312.5	69.0376
325	-	300	312.5	14.2097
300	-	275	287.5	29.3156
275	-	250	262.5	50.6752
250	-	225	237.5	53.8414
225	-	200	212.5	29.5529
200	-	175	187.5	20.6946
175	-	150	162.5	15.7591
150	-	125	137.5	13.7252
125	-	100	112.5	12.5905
100	-	75	87.5	11.4523
75	-	50	62.5	10.3967
50	-	30	40	10.424

Temp Range (C)		(C)	Mean Temp (C)	Instant. CTE (10^{-6}/C)
27.5	-	32.5	30	10.2182
47.5	-	52.5	50	6.81182
72.5	-	77.5	75	6.81051
97.5	-	102.5	100	7.03344
122.5	-	127.5	125	3.34267
147.5	-	152.5	150	10.6208
172.5	-	177.5	175	10.9756
197.5	-	202.5	200	8.72443
222.5	-	227.5	225	20.9229
247.5	-	252.5	250	23.9083
272.5	-	277.5	275	43.8735
297.5	-	302.5	300	87.3953
302.5	-	297.5	300	20.5192
277.5	-	272.5	275	30.0906
252.5	-	247.5	250	62.4729
227.5	-	222.5	225	38.3641
202.5	-	197.5	200	27.65
177.5	-	172.5	175	13.4825
152.5	-	147.5	150	14.2841
127.5	-	122.5	125	10.3779
102.5	-	97.5	100	11.9234
77.5	-	72.5	75	10.4857
52.5	-	47.5	50	8.81938

Figure A-9. Thermal Testing Data for Specimen PTC4-A 4.6-B, Cycle 1

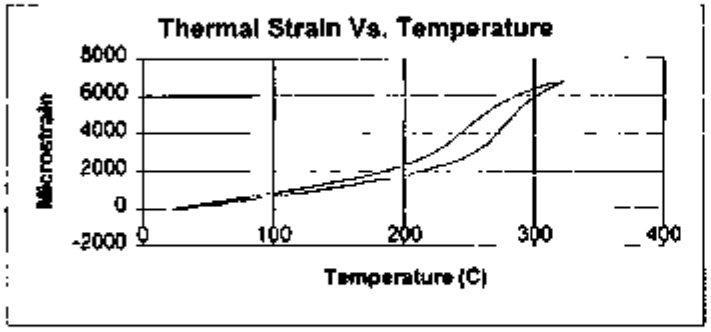

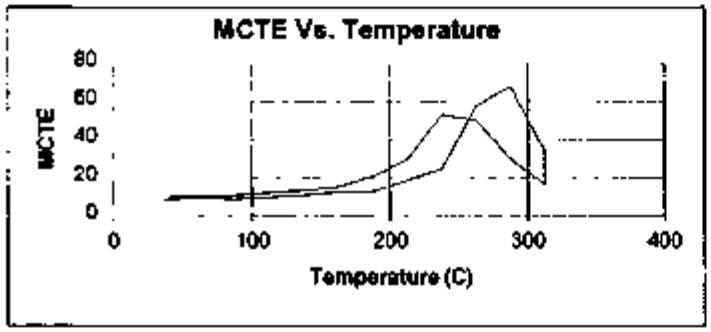

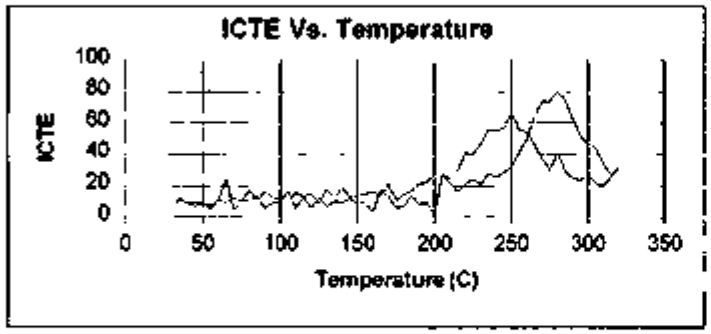

Specimen ID:	PTC4-A 4.6-B Cycle 2
Date of Test Completion:	16-07-98
Thermal/Mechanical Unit.	TSw2
Lithostratigraphic Unit	Tptpmn
Original Location:	ESF; Alcove 5,Thermal Drift Scale Test Area Collected after Completion of Single Heater Test
Initial Moisture Content	Air-dried (As-Is)
Nominal Dimensions:	50 8 mm (L) 25 4 mm (D)

Specimen Data:	Length (mm)	Mass (g)
Pre-test:	50.81	55.835
Post-test:	50.82	55.686
Change:	-0 01	0.149

Temp Range (C)		(C)	Mean Temp (C)	Mean CTE (10^{-6}/C)
25	-	50	37.5	8.68658
50	-	75	62.5	9.91441
75	-	100	87.5	8.99806
100	-	125	112 5	9.93796
125	-	150	137.5	10.999
150	-	175	162 5	12.5613
175	-	200	187 5	13.0047
200	-	225	212.5	18 6167
225	-	250	237.5	24.6748
250	-	275	262.5	57.8571
275	-	300	287.5	67.6979
300	-	325	312.5	33.7705
325	-	300	312.5	16.4494
300	-	275	287.5	29 8941
275	-	250	262.5	50 1492
250	-	225	237 5	53.1448
225	-	200	212 5	29.696
200	-	175	187.5	20.6279
175	-	150	162.5	15.4106
150	-	125	137.5	13 4089
125	-	100	112 5	12.2334
100	-	75	87 5	11.0166
75	-	50	62.5	10.5392
50	-	30	40	10 111

Temp Range (C)		(C)	Mean Temp (C)	Instant. CTE (10^{-6}/C)
27.5	-	32.5	30	6.26873
47.5	-	52.5	50	8.71708
72.5	-	77.5	75	11 5425
97.5	-	102 5	100	10.5921
122.5	-	127.5	125	12 5759
147.5	-	152 5	150	8.94895
172 5	-	177.5	175	6.33879
197 5	-	202 5	200	1.23066
222 5	-	227.5	225	24.0382
247.5	-	252.5	250	31.7559
272.5	-	277.5	275	73.3733
297 5	-	302 5	300	46.6579
302.5	-	297.5	300	27.0053
277.5	-	272.5	275	30.225
252.5	-	247.5	250	66 236
227 5	-	222.5	225	40.1315
202.5	-	197.5	200	28.3521
177 5	-	172.5	175	11 2726
152 5	-	147 5	150	13 7936
127 5	-	122.5	125	9 05819
102 5	-	97 5	100	12 3304
77 5	-	72 5	75	9.90002
52.5	-	47.5	50	9.42403

Figure A-10. Thermal Testing Data for Specimen PTC4-A 4.6-B, Cycle 2

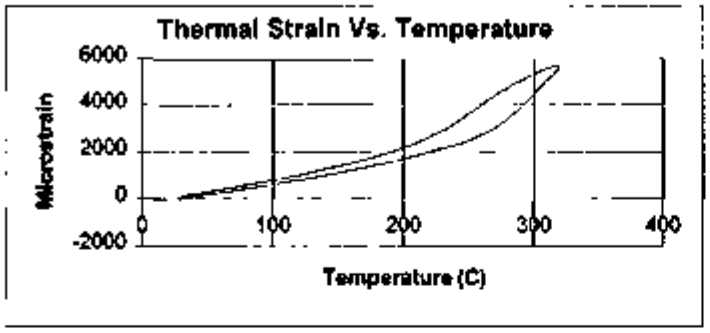

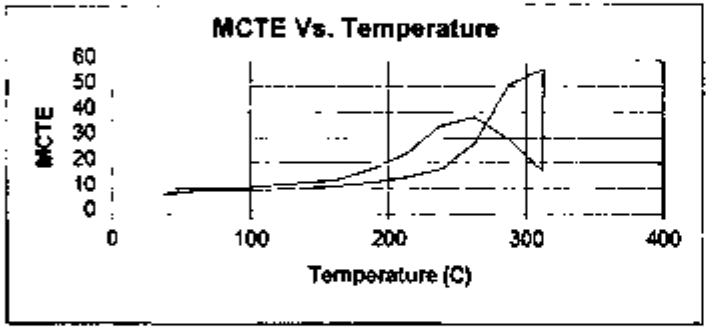

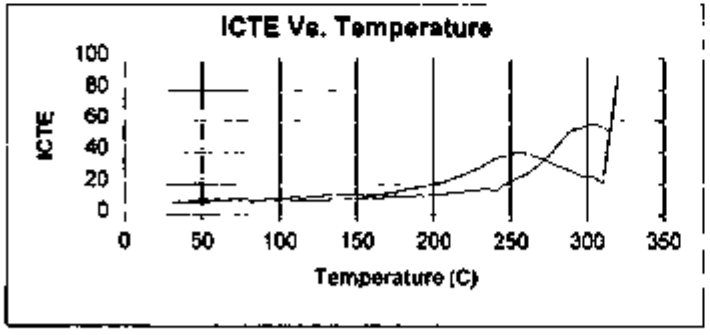

Specimen ID:	PTC4-A 19 0 Cycle 1
Date of Test Completion:	17-07-98
Thermal/Mechanical Unit:	TSw2
Lithostratigraphic Unit:	Tptpmn
Original Location:	ESF, Alcove 5,Thermal Drift Scale Test Area Collected after Completion of Single Heater Test
Initial Moisture Content	Air-dried (As-is)
Nominal Dimensions:	50 8 mm (L) 25.4 mm (D)

Specimen Data:	Length (mm)	Mass (g)
Pre-test:	50.78	57.985
Post-test:	50.78	57 305
Change:	0	0 68

Temp Range (C)		(C)	Mean Temp (C)	Mean CTE (10^{-6}/C)
25	-	50	37.5	8.06256
50	-	75	62.5	8 86125
75	-	100	87 5	8 9452
100	-	125	112 5	9.18362
125	-	150	137.5	10 0974
150	-	175	162.5	11.0683
175	-	200	187 5	12.3772
200	-	225	212.5	14.4934
225	-	250	237.5	17.4714
250	-	275	262.5	27.953
275	-	300	287.5	50.9568
300	-	325	312.5	56.8625
325	-	300	312 5	16.9094
300	-	275	287.5	29.2127
275	-	250	262.5	38.2546
250	-	225	237.5	34.5695
225	-	200	212.5	23.3683
200	-	175	187.5	17.5351
175	-	150	162 5	13.6673
150	-	125	137.5	12.3245
125	-	100	112 5	11.1663
100	-	75	87 5	9.67649
75	-	50	62.5	9.71758
50	-	30	40	10.0151

Temp Range (C)		(C)	Mean Temp (C)	Instant CTE (10^{-6}/C)
27.5	-	32.5	30	7.53855
47.5	-	52.5	50	8.43528
72.5	-	77.5	75	9.40929
97.5	-	102 5	100	9.14027
122 5	-	127 5	125	9 40504
147 5	-	152 5	150	10.1115
172 5	-	177.5	175	12.3073
197.5	-	202 5	200	12.9395
222 5	-	227.5	225	15.7357
247.5	-	252 5	250	21.838
272.5	-	277.5	275	38.0759
297.5	-	302.5	300	57.7721
302 5	-	297 5	300	24.5817
277.5	-	272.5	275	34.1633
252.5	-	247.5	250	39.1934
227.5	-	222 5	225	28.998
202.5	-	197.5	200	20 2619
177 5	-	172.5	175	14.5397
152 5	-	147.5	150	13.6656
127 5	-	122.5	125	12.079
102.5	-	97.5	100	10.9303
77 5	-	72 5	75	10 2711
52.5	-	47.5	50	10 1688

Figure A-11. Thermal Testing Data for Specimen PTC4-A 19.0, Cycle 1

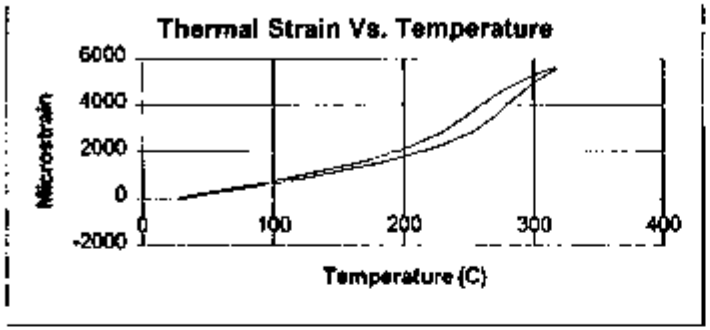

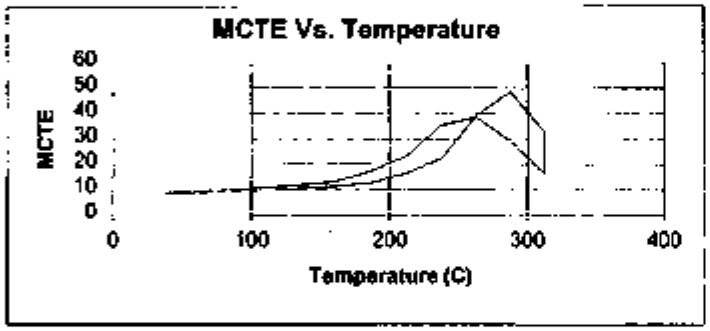

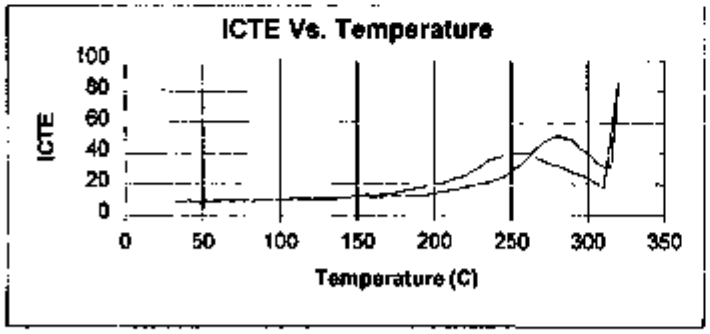

Specimen ID:	PTC4-A 19 0-B Cycle 2
Date of Test Completion:	21-07-98
Thermal/Mechanical Unit:	TSw2
Lithostratigraphic Unit:	Tptpmn
Original Location:	ESF; Alcove 5;Thermal Drift Scale Test Area Collected after Completion of Single Heater Test
Initial Moisture Content	Air-dried (As-is)
Nominal Dimensions:	50.8 mm (L) 25.4 mm (D)

Specimen Data:	Length (mm)	Mass (g)
Pre-test:	50.78	57.38
Post-test:	50.8	57.305
Change:	-0.02	0.075

Temp Range (C)		(C)	Mean Temp (C)	Mean CTE (10^{-6}/C)
25	-	50	37.5	8.4
50	-	75	62.5	8.9
75	-	100	87.5	9.1
100	-	125	112.5	9.8
125	-	150	137.5	10.9
150	-	175	162.5	11.6
175	-	200	187.5	13.0
200	-	225	212.5	16.7
225	-	250	237.5	22.4
250	-	275	262.5	39.1
275	-	300	287.5	48.5
300	-	325	312.5	33.1
325	-	300	312.5	16.4
300	-	275	287.5	29.3
275	-	250	262.5	38.6
250	-	225	237.5	35.6
225	-	200	212.5	23.5
200	-	175	187.5	17.7
175	-	150	162.5	13.6
150	-	125	137.5	12.1
125	-	100	112.5	11.0
100	-	75	87.5	10.1
75	-	50	62.5	9.4
50	-	30	40	9.3

Temp Range (C)		(C)	Mean Temp (C)	Instant. CTE (10^{-6}/C)
27.5	-	32.5	30	7.9
47.5	-	52.5	50	7.9
72.5	-	77.5	75	9.5
97.5	-	102.5	100	9.8
122.5	-	127.5	125	10.4
147.5	-	152.5	150	11.6
172.5	-	177.5	175	12.7
197.5	-	202.5	200	14.3
222.5	-	227.5	225	18.6
247.5	-	252.5	250	28.5
272.5	-	277.5	275	49.8
297.5	-	302.5	300	40.3
302.5	-	297.5	300	24.5
277.5	-	272.5	275	33.6
252.5	-	247.5	250	39.1
227.5	-	222.5	225	28.8
202.5	-	197.5	200	20.4
177.5	-	172.5	175	14.6
152.5	-	147.5	150	12.7
127.5	-	122.5	125	11.0
102.5	-	97.5	100	10.2
77.5	-	72.5	75	9.8
52.5	-	47.5	50	9.4

Figure A-12. Thermal Testing Data for Specimen PTC4-A 19.0-B, Cycle 2

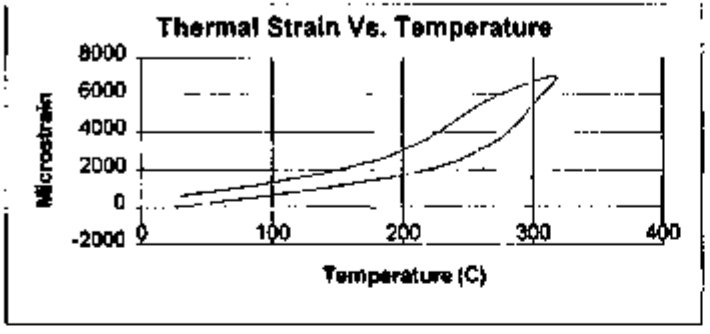

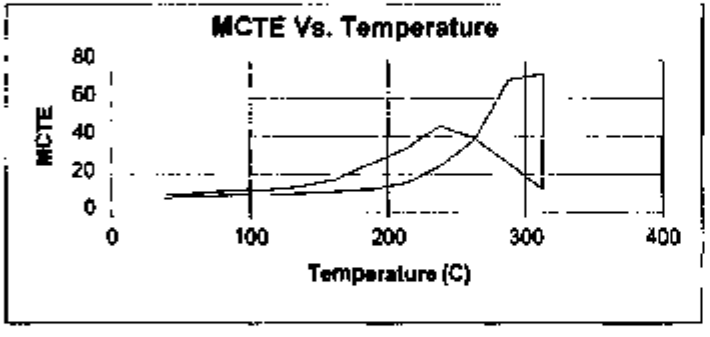

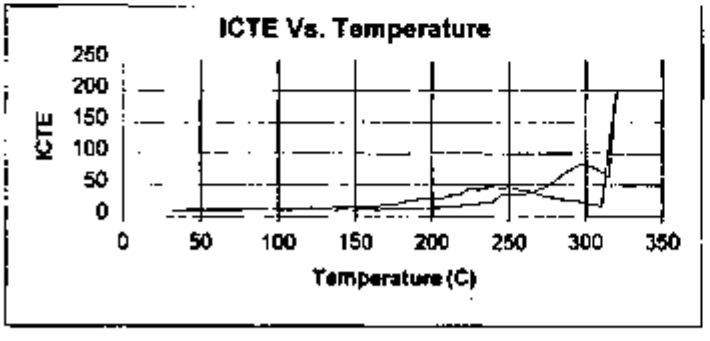

Specimen ID:	PTC4-B 6.8-B Cycle 1
Date of Test Completion:	10-07-98
Thermal/Mechanical Unit:	TSw2
Lithostratigraphic Unit.	Tptpmn
Original Location:	ESF; Alcove 5;Thermal Drift Scale Test Area Collected after Completion of Single Heater Test
Initial Moisture Content	Air-dried (As-is)
Nominal Dimensions:	50.8 mm (L) 25.4 mm (D)

Specimen Data:	Length (mm)	Mass (g)
Pre-test:	50.8	57.915
Post-test:	50.82	57.309
Change:	-0.02	0.606

Temp Range (C)		(C)	Mean Temp (C)	Mean CTE (10^{-6}/C)
25	-	50	37.5	7.86
50	-	75	62.5	8.81
75	-	100	87.5	9.10
100	-	125	112.5	9.40
125	-	150	137.5	10.47
150	-	175	162.5	11.10
175	-	200	187.5	12.40
200	-	225	212.5	15.41
225	-	250	237.5	24.35
250	-	275	262.5	37.98
275	-	300	287.5	70.25
300	-	325	312.5	73.02
325	-	300	312.5	12.23
300	-	275	287.5	26.60
275	-	250	262.5	38.99
250	-	225	237.5	45.78
225	-	200	212.5	33.53
200	-	175	187.5	26.00
175	-	150	162.5	17.51
150	-	125	137.5	14.00
125	-	100	112.5	12.17
100	-	75	87.5	11.87
75	-	50	62.5	10.39
50	-	30	40	9.79

Temp Range (C)		(C)	Mean Temp (C)	Instant. CTE (10^{-6}/C)
27.5	-	32.5	30	6.95
47.5	-	52.5	50	8.22
72.5	-	77.5	75	9.07
97.5	-	102.5	100	9.31
122.5	-	127.5	125	9.99
147.5	-	152.5	150	9.75
172.5	-	177.5	175	11.90
197.5	-	202.5	200	13.04
222.5	-	227.5	225	18.00
247.5	-	252.5	250	36.59
272.5	-	277.5	275	49.02
297.5	-	302.5	300	82.17
302.5	-	297.5	300	20.75
277.5	-	272.5	275	31.66
252.5	-	247.5	250	48.67
227.5	-	222.5	225	46.06
202.5	-	197.5	200	30.18
177.5	-	172.5	175	19.55
152.5	-	147.5	150	15.47
127.5	-	122.5	125	12.46
102.5	-	97.5	100	11.53
77.5	-	72.5	75	11.70
52.5	-	47.5	50	9.90

Figure A-13. Thermal Testing Data for Specimen PTC4-B 6.8-B, Cycle 1

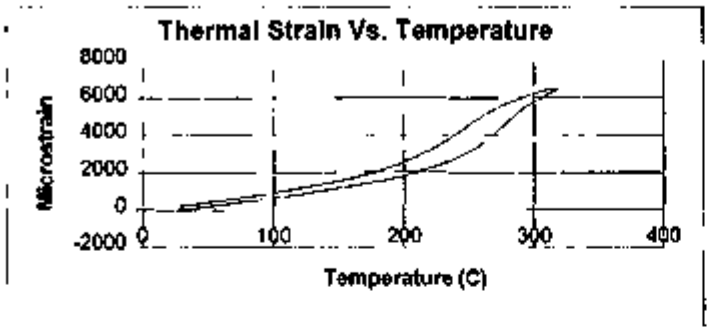

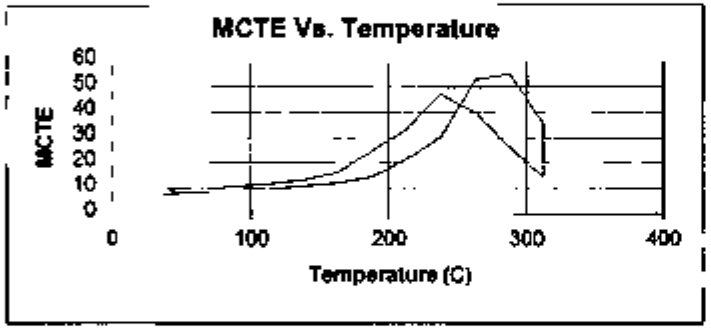

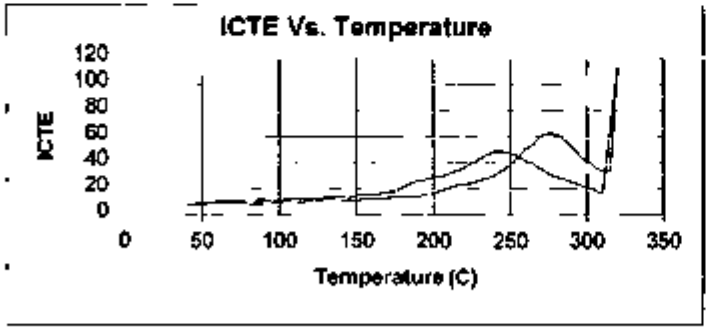

Specimen ID	PTC4-B 6 8-B Cycle 2
Date of Test Completion	16-07-98
Thermal/Mechanical Unit	TSw2
Lithostratigraphic Unit	Tptpmn
Original Location	ESF, Alcove 5 Thermal Drift Scale Test Area Collected after Completion of Single Heater Test
Initial Moisture Content	Air-dried (As-is)
Nominal Dimensions	50 8 mm (L) 25 4 mm (D)

Specimen Data	Length (mm)	Mass (g)
Pre-test	50 82	57 392
Post-test	50 82	57 293
Change	0	0 099

Temp Range (C)		(C)	Mean Temp (C)	Mean CTE (10^{-6}/C)
25	-	50	37 5	8 0
50	-	75	62 5	9 0
75	-	100	87 5	9 3
100	-	125	112 5	10 0
125	-	150	137 5	11 1
150	-	175	162 5	12 1
175	-	200	187 5	14 5
200	-	225	212 5	21 5
225	-	250	237 5	29 9
250	-	275	262 5	52 8
275	-	300	287 5	55 3
300	-	325	312 5	36 0
325	-	300	312 5	14 7
300	-	275	287 5	26 6
275	-	250	262 5	40 3
250	-	225	237 5	47 3
225	-	200	212 5	33 1
200	-	175	187 5	24 9
175	-	150	162 5	16 3
150	-	125	137 5	13 4
125	-	100	112 5	11 8
100	-	75	87 5	10 8
75	-	50	62 5	10 0
50	-	30	40	9 7

Temp Range (C)		(C)	Mean Temp (C)	Instant CTE (10^{-6}/C)
27 5	-	32 5	30	7 1
47 5	-	52 5	50	8 3
72 5	-	77 5	75	9 6
97 5	-	102 5	100	9 9
122 5	-	127 5	125	10 7
147 5	-	152 5	150	10 9
172 5	-	177 5	175	13 9
197 5	-	202 5	200	16 9
222 5	-	227 5	225	24 6
247 5	-	252 5	250	39 4
272 5	-	277 5	275	62 6
297 5	-	302 5	300	41 5
302 5	-	297 5	300	21 1
277 5	-	272 5	275	32 0
252 5	-	247 5	250	47 4
227 5	-	222 5	225	39 8
202 5	-	197 5	200	28 8
177 5	-	172 5	175	18 1
152 5	-	147 5	150	14 8
127 5	-	122 5	125	12 4
102 5	-	97 5	100	11 0
77 5	-	72 5	75	10 5
52 5	-	47 5	50	9 7

Figure A-14 Thermal Testing Data for Specimen PTC4-B 6 8-B, Cycle 2

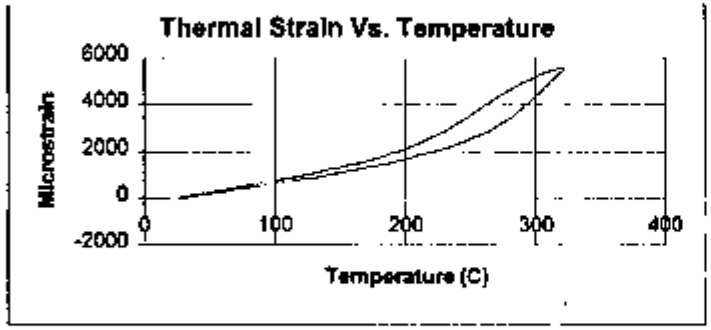

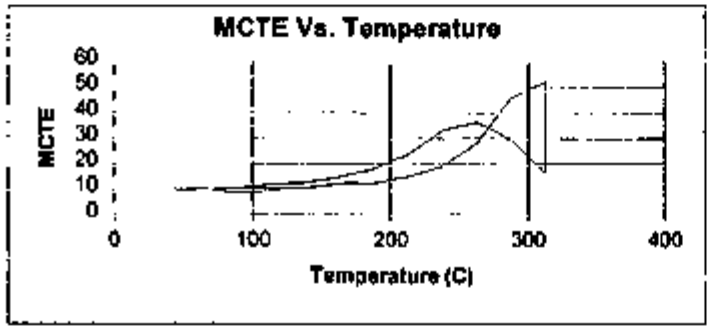

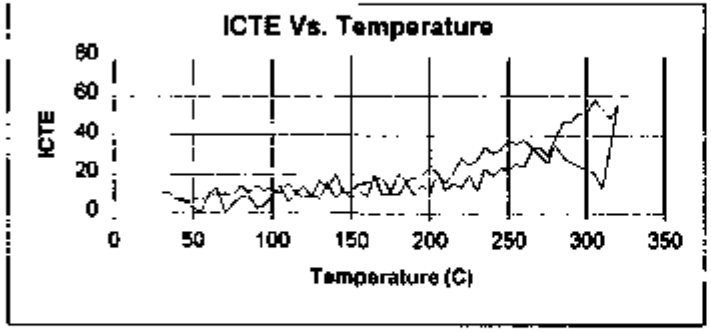

Specimen ID:	PTC4-B 14.8-B Cycle 1
Date of Test Completion:	10-07-98
Thermal/Mechanical Unit:	TSw2
Lithostratigraphic Unit:	Tplpmn
Original Location:	ESF; Alcove 5;Thermal Drift Scale Test Area Collected after Completion of Single Heater Test
Initial Moisture Content	Air-dried (As-is)
Nominal Dimensions:	50.8 mm (L) 25.4 mm (D)

Specimen Data:	Length (mm)	Mass (g)
Pre-test:	50.8	57.604
Post-test:	50.8	56.85
Change:	0	0.754

Temp Range (C)		(C)	Mean Temp (C)	Mean CTE (10^{-6}/C)
25	-	50	37.5	9.0294
50	-	75	62.5	10.2726
75	-	100	87.5	8.84828
100	-	125	112.5	9.29544
125	-	150	137.5	10.4496
150	-	175	162.5	12.0036
175	-	200	187.5	12.4104
200	-	225	212.5	14.9962
225	-	250	237.5	19.1916
250	-	275	262.5	26.1249
275	-	300	287.5	45.7849
300	-	325	312.5	52.1521
325	-	300	312.5	16.5396
300	-	275	287.5	29.4501
275	-	250	262.5	36.4929
250	-	225	237.5	33.1216
225	-	200	212.5	23.6839
200	-	175	187.5	18.1444
175	-	150	162.5	14.6397
150	-	125	137.5	12.5292
125	-	100	112.5	11.7762
100	-	75	87.5	10.3849
75	-	50	62.5	9.88835
50	-	30	40	9.29002

Temp Range (C)		(C)	Mean Temp (C)	Instant. CTE (10^{-6}/C)
27.5	-	32.5	30	11.3288
47.5	-	52.5	50	2.94832
72.5	-	77.5	75	4.92955
97.5	-	102.5	100	9.44916
122.5	-	127.5	125	9.6703
147.5	-	152.5	150	7.52864
172.5	-	177.5	175	10.496
197.5	-	202.5	200	11.0013
222.5	-	227.5	225	20.1663
247.5	-	252.5	250	22.7383
272.5	-	277.5	275	29.5827
297.5	-	302.5	300	51.3661
302.5	-	297.5	300	22.8478
277.5	-	272.5	275	26.1941
252.5	-	247.5	250	37.9429
227.5	-	222.5	225	24.9999
202.5	-	197.5	200	24.6438
177.5	-	172.5	175	10.8389
152.5	-	147.5	150	11.7511
127.5	-	122.5	125	8.3951
102.5	-	97.5	100	13.5564
77.5	-	72.5	75	9.6041
52.5	-	47.5	50	7.56783

Figure A-15. Thermal Testing Data for Specimen PTC4-B 14.8-B, Cycle 1

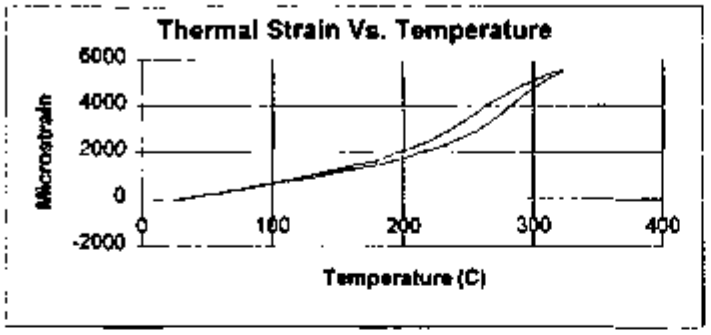

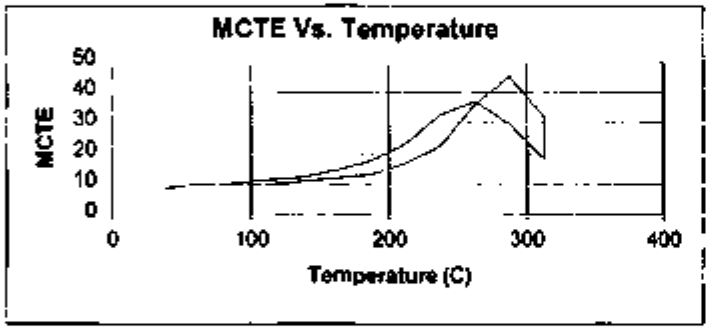

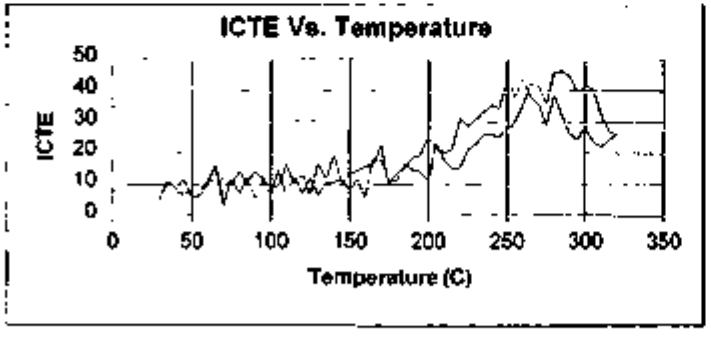

Specimen ID:	PTC4-B 14.8-B Cycle 2
Date of Test Completion:	22-07-98
Thermal/Mechanical Unit:	TSw2
Lithostratigraphic Unit:	Tptpmn
Original Location:	ESF, Alcove 5;Thermal Drift Scale Test Area Collected after Completion of Single Heater Test
Initial Moisture Content	Air-dried (As-is)
Nominal Dimensions:	50 8 mm (L) 25 4 mm (D)

Specimen Data	Length (mm)	Mass (g)
Pre-test:	50 8	56.955
Post-test:	50.8	56 827
Change:	0	0.128

Temp Range (C)		(C)	Mean Temp (C)	Mean CTE (10^{-6}/C)
25	-	50	37.5	8.7
50	-	75	62.5	9.9
75	-	100	87.5	9.3
100	-	125	112.5	10.2
125	-	150	137.5	11.1
150	-	175	162.5	12.1
175	-	200	187.5	13.4
200	-	225	212.5	17 2
225	-	250	237.5	22.7
250	-	275	262.5	36.1
275	-	300	287.5	45 2
300	-	325	312.5	32.2
325	-	300	312.5	18.5
300	-	275	287.5	29.7
275	-	250	262 5	37.1
250	-	225	237.5	32.8
225	-	200	212.5	23.5
200	-	175	187 5	18.0
175	-	150	162 5	14.7
150	-	125	137 5	12.4
125	-	100	112 5	11.6
100	-	75	87.5	10.4
75	-	50	62.5	9.8
50	-	30	40	9.2

Temp Range (C)		(C)	Mean Temp (C)	Instant CTE (10^{-6}/C)
27.5	-	32.5	30	5.3
47.5	-	52.5	50	6.2
72.5	-	77.5	75	11.6
97.5	-	102 5	100	6.8
122 5	-	127.5	125	11.9
147 5	-	152.5	150	8 1
172.5	-	177.5	175	11.2
197.5	-	202.5	200	11.1
222 5	-	227.5	225	20 9
247 5	-	252.5	250	27.6
272 5	-	277.5	275	35 6
297.5	-	302.5	300	41 6
302.5	-	297.5	300	28 2
277.5	-	272.5	275	28 8
252 5	-	247 5	250	43 2
227.5	-	222.5	225	28 6
202 5	-	197.5	200	25 3
177.5	-	172 5	175	10 1
152 5	-	147 5	150	12 9
127.5	-	122 5	125	6 7
102.5	-	97.5	100	9.1
77 5	-	72.5	75	9.3
52 5	-	47.5	50	8.4

Figure A-16. Thermal Testing Data for Specimen PTC4-B 14.8-B, Cycle 2

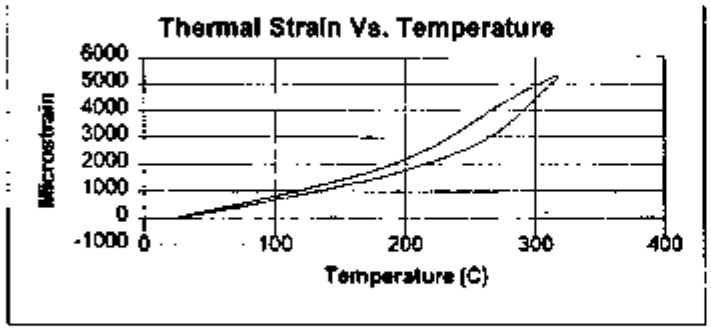

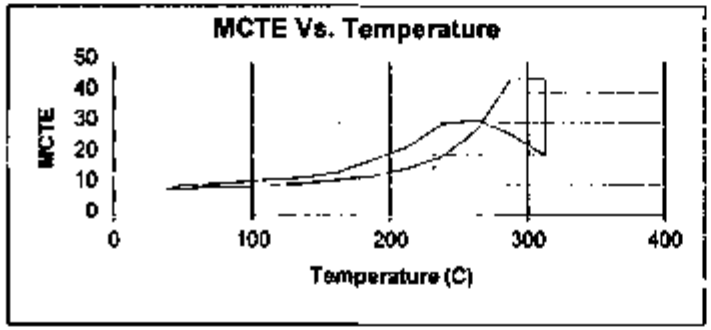

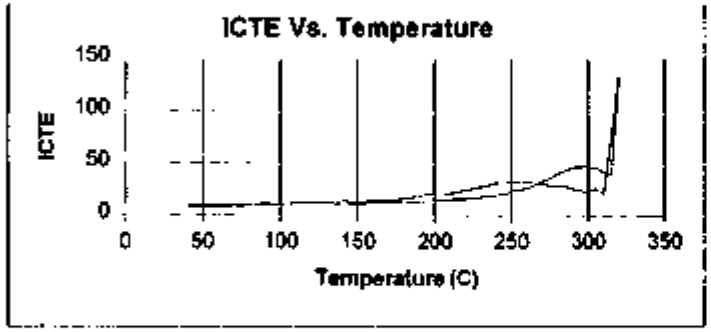

Specimen ID:	PTC4-B 19.8-B Cycle 1
Date of Test Completion:	14-07-98
Thermal/Mechanical Unit:	TSw2
Lithostratigraphic Unit:	Tptpmn
Original Location:	ESF; Alcove 5;Thermal Drift Scale Test Area Collected after Completion of Single Heater Test
Initial Moisture Content	Air-dried (As-is)
Nominal Dimensions:	50.8 mm (L) 25.4 mm (D)

Specimen Data:	Length (mm)	Mass (g)
Pre-test:	50.8	59.107
Post-test:	50.8	58.276
Change:	0	0.831

Temp Range (C)		(C)	Mean Temp (C)	Mean CTE (10^{-6}/C)
25	-	50	37.5	8.3607
50	-	75	62.5	9.06611
75	-	100	87.5	9.39238
100	-	125	112.5	9.75249
125	-	150	137.5	10.5855
150	-	175	162.5	11.5021
175	-	200	187.5	12.8987
200	-	225	212.5	15.4487
225	-	250	237.5	19.1754
250	-	275	262.5	27.758
275	-	300	287.5	44.2243
300	-	325	312.5	44.3508
325	-	300	312.5	19.769
300	-	275	287.5	26.6348
275	-	250	262.5	31.1524
250	-	225	237.5	29.8347
225	-	200	212.5	22.5079
200	-	175	187.5	18.2317
175	-	150	162.5	14.0467
150	-	125	137.5	12.2738
125	-	100	112.5	11.4411
100	-	75	87.5	10.7735
75	-	50	62.5	10.0309
50	-	30	40	9.36067

Temp Range (C)		(C)	Mean Temp (C)	Instant CTE (10^{-6}/C)
27.5	-	32.5	30	8.39893
47.5	-	52.5	50	8.4007
72.5	-	77.5	75	8.97551
97.5	-	102.5	100	9.73205
122.5	-	127.5	125	10.1353
147.5	-	152.5	150	10.5687
172.5	-	177.5	175	12.6044
197.5	-	202.5	200	14.136
222.5	-	227.5	225	17.0151
247.5	-	252.5	250	23.4463
272.5	-	277.5	275	35.9616
297.5	-	302.5	300	47.3543
302.5	-	297.5	300	22.9487
277.5	-	272.5	275	28.8668
252.5	-	247.5	250	32.0831
227.5	-	222.5	225	25.8735
202.5	-	197.5	200	20.1386
177.5	-	172.5	175	14.9924
152.5	-	147.5	150	12.6493
127.5	-	122.5	125	11.8907
102.5	-	97.5	100	10.4689
77.5	-	72.5	75	10.3971
52.5	-	47.5	50	9.28553

Figure A-17. Thermal Testing Data for Specimen PTC4-B 19.8-B, Cycle 1

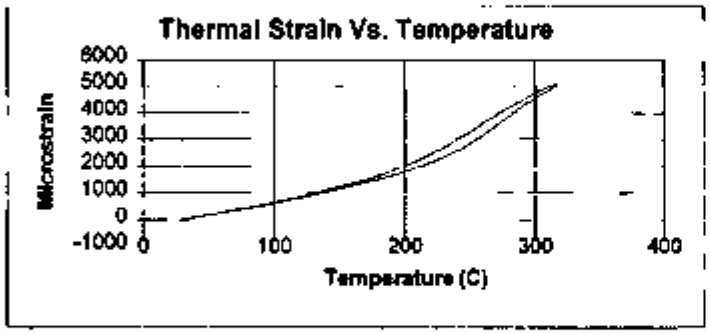

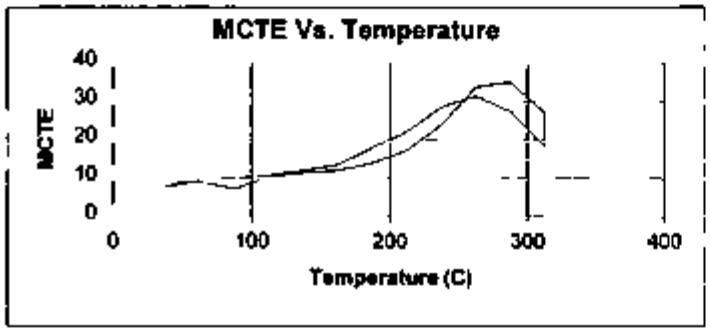

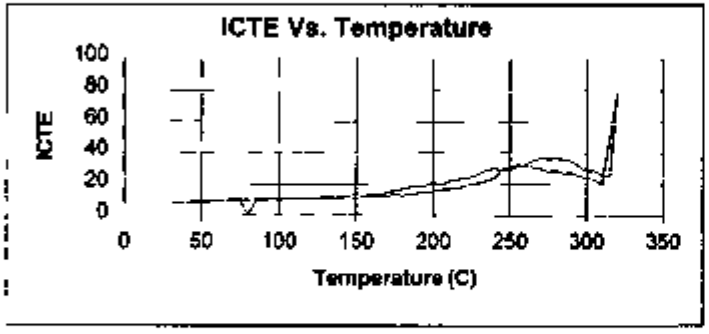

Specimen ID	PTC4-B 19 8-B Cycle 2
Date of Test Completion	15-07-98
Thermal/Mechanical Unit	TSw2
Lithostratigraphic Unit	Tptpmn
Original Location	ESF, Alcove 5,Thermal Drift Scale Test Area Collected after Completion of Single Heater Test
Initial Moisture Content	Air-dried (As-is)
Nominal Dimensions	50 8 mm (L) 25 4 mm (D)

Specimen Data	Length (mm)	Mass (g)
Pre-test	50 8	58 276
Post-test	50 8	58 265
Change	0	0 011

Temp Range (C)		(C)	Mean Temp (C)	Mean CTE (10^{-6}/C)
25	-	50	37 5	7 91903
50	-	75	62 5	9 19648
75	-	100	87 5	7 3626
100	-	125	112 5	10 3282
125	-	150	137 5	11 4688
150	-	175	162 5	12 2197
175	-	200	187 5	14 0033
200	-	225	212 5	17 3675
225	-	250	237 5	23 9691
250	-	275	262 5	33 7619
275	-	300	287 5	35 0111
300	-	325	312 5	27 175
325	-	300	312 5	18 3368
300	-	275	287 5	27 4458
275	-	250	262 5	31 2708
250	-	225	237 5	28 5806
225	-	200	212 5	22 147
200	-	175	187 5	18 0298
175	-	150	162 5	13 6115
150	-	125	137 5	12 0586
125	-	100	112 5	10 8337
100	-	75	87 5	9 93354
75	-	50	62 5	9 37959
50	-	30	40	8 87047

Temp Range (C)		(C)	Mean Temp (C)	Instant CTE (10^{-6}/C)
27 5	-	32 5	30	7 16135
47 5	-	52 5	50	8 46104
72 5	-	77 5	75	9 42418
97 5	-	102 5	100	9 67398
122 5	-	127 5	125	10 9131
147 5	-	152 5	150	11 1197
172 5	-	177 5	175	13 357
197 5	-	202 5	200	15 6653
222 5	-	227 5	225	19 6934
247 5	-	252 5	250	29 5162
272 5	-	277 5	275	36 45
297 5	-	302 5	300	28 3635
302 5	-	297 5	300	24 3752
277 5	-	272 5	275	28 1713
252 5	-	247 5	250	31 2998
227 5	-	222 5	225	24 9777
202 5	-	197 5	200	21 1125
177 5	-	172 5	175	15 7086
152 5	-	147 5	150	12 9434
127 5	-	122 5	125	10 7775
102 5	-	97 5	100	10 0875
77 5	-	72 5	75	9 76747
52 5	-	47 5	50	9 30163

Figure A-18 Thermal Testing Data for Specimen PTC4-B 19 8-B, Cycle 2

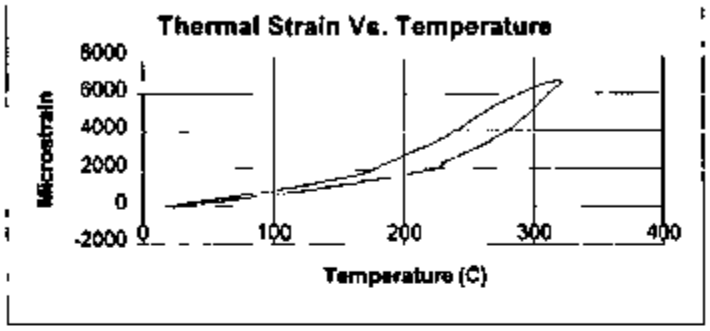

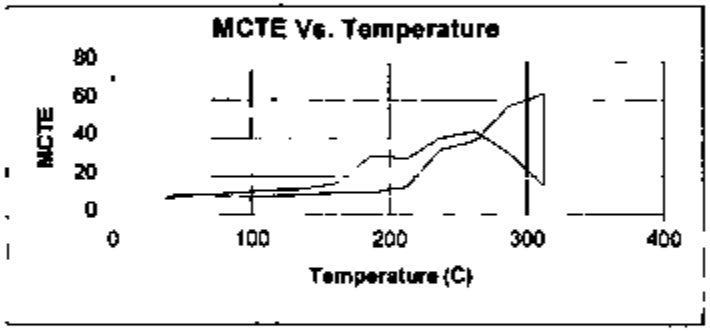

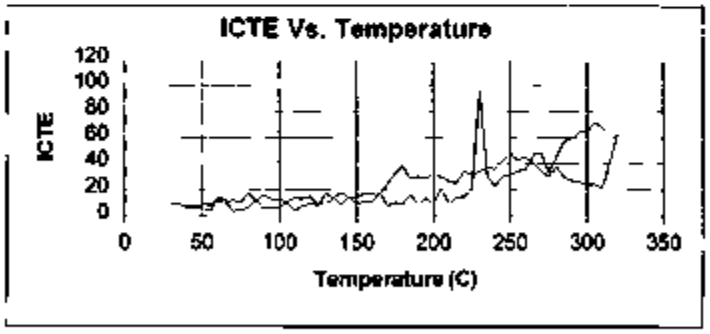

Specimen ID	PTC5-B 4 1-B Cycle 1
Date of Test Completion	09-07-98
Thermal/Mechanical Unit	TSw2
Lithostratigraphic Unit	Tptpmn
Original Location	ESF Alcove 5 Thermal Drift Scale Test Area Collected after Completion of Single Heater Test
Initial Moisture Content	Air-dried (As-is)
Nominal Dimensions	50 8 mm (L) 25 4 mm (D)

Specimen Data	Length (mm)	Mass (g)
Pre-test	50 78	57 386
Post-test	50 8	56 779
Change	0 02	0 607

Temp Range (C)		(C)	Mean Temp (C)	Mean CTE (10^{-6}/C)
25	-	50	37 5	8 7
50	-	75	62 5	10 4
75	-	100	87 5	8 9
100	-	125	112 5	9 6
125	-	150	137 5	10 6
150	-	175	162 5	11 6
175	-	200	187 5	11 7
200	-	225	212 5	14 5
225	-	250	237 5	34 2
250	-	275	262 5	38 5
275	-	300	287 5	57 0
300	-	325	312 5	63 1
325	-	300	312 5	15 1
300	-	275	287 5	31 8
275	-	250	262 5	43 4
250	-	225	237 5	40 4
225	-	200	212 5	29 2
200	-	175	187 5	31 2
175	-	150	162 5	17 1
150	-	125	137 5	13 5
125	-	100	112 5	12 7
100	-	75	87 5	11 2
75	-	50	62 5	10 4
50	-	30	40	9 9

Temp Range (C)		(C)	Mean Temp (C)	Instant CTE (10^{-6}/C)
27 5	-	32 5	30	9 0
47 5	-	52 5	50	6 3
72 5	-	77 5	75	4 7
97 5	-	102 5	100	7 3
122 5	-	127 5	125	10 4
147 5	-	152 5	150	9 0
172 5	-	177 5	175	10 5
197 5	-	202 5	200	9 6
222 5	-	227 5	225	22 0
247 5	-	252 5	250	32 0
272 5	-	277 5	275	33 0
297 5	-	302 5	300	64 7
302 5	-	297 5	300	23 8
277 5	-	272 5	275	30 3
252 5	-	247 5	250	47 1
227 5	-	222 5	225	31 4
202 5	-	197 5	200	32 3
177 5	-	172 5	175	32 6
152 5	-	147 5	150	14 0
127 5	-	122 5	125	7 7
102 5	-	97 5	100	12 5
77 5	-	72 5	75	10 4
52 5	-	47 5	50	8 9

Figure A-19 Thermal Testing Data for Specimen PTC5-B 4 1-B, Cycle 1

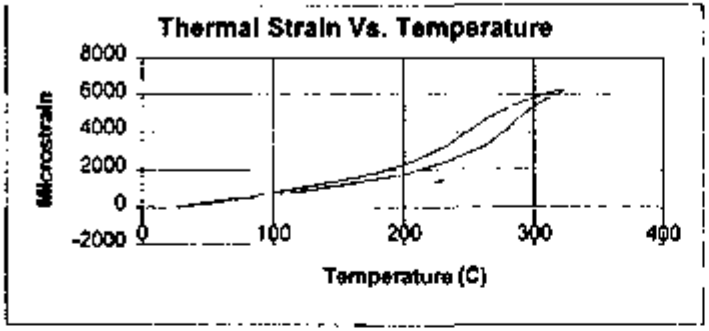

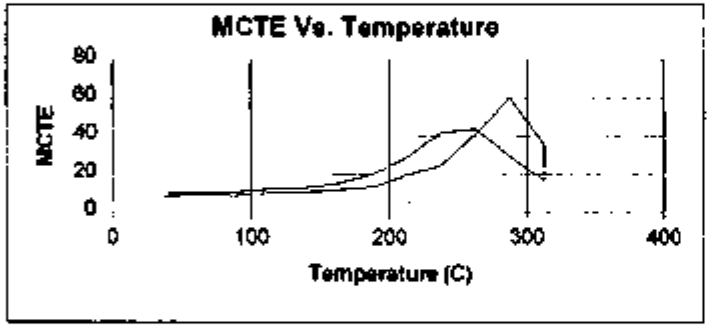

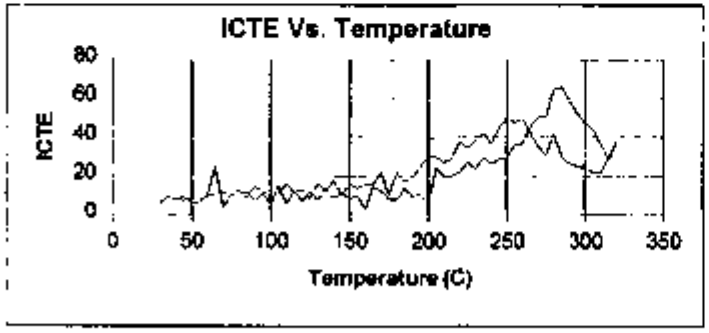

Specimen ID:	PTC5-B 4.1-B Cycle 2
Date of Test Completion:	17-07-98
Thermal/Mechanical Unit:	TSw2
Lithostratigraphic Unit.	Tptpmn
Original Location:	ESF; Alcove 5;Thermal Drift Scale Test Area Collected after Completion of Single Heater Test
Initial Moisture Content	Air-dried (As-is)
Nominal Dimensions:	50.8 mm (L) 25.4 mm (D)

Specimen Data:	Length (mm)	Mass (g)
Pre-test:	50.8	56.88
Post-test:	50.8	56.755
Change:	0	0.125

Temp Range (C)		(C)	Mean Temp (C)	Mean CTE (10^{-6}/C)
25	-	50	37.5	8.4
50	-	75	62.5	9.9
75	-	100	87.5	9.0
100	-	125	112.5	10.2
125	-	150	137.5	10.7
150	-	175	162.5	11.9
175	-	200	187.5	13.5
200	-	225	212.5	20.0
225	-	250	237.5	25.3
250	-	275	262.5	41.2
275	-	300	287.5	60.3
300	-	325	312.5	35.6
325	-	300	312.5	17.3
300	-	275	287.5	29.6
275	-	250	262.5	43.6
250	-	225	237.5	42.5
225	-	200	212.5	29.2
200	-	175	187.5	20.3
175	-	150	162.5	15.3
150	-	125	137.5	13.0
125	-	100	112.5	12.2
100	-	75	87.5	10.8
75	-	50	62.5	10.3
50	-	30	40	10.1

Temp Range (C)		(C)	Mean Temp (C)	Instant. CTE (10^{-6}/C)
27.5	-	32.5	30	6.3
47.5	-	52.5	50	6.6
72.5	-	77.5	75	10.4
97.5	-	102.5	100	5.7
122.5	-	127.5	125	12.2
147.5	-	152.5	150	6.8
172.5	-	177.5	175	8.7
197.5	-	202.5	200	6.8
222.5	-	227.5	225	27.5
247.5	-	252.5	250	29.6
272.5	-	277.5	275	51.0
297.5	-	302.5	300	47.6
302.5	-	297.5	300	24.5
277.5	-	272.5	275	30.8
252.5	-	247.5	250	50.4
227.5	-	222.5	225	34.5
202.5	-	197.5	200	30.7
177.5	-	172.5	175	10.5
152.5	-	147.5	150	16.2
127.5	-	122.5	125	8.8
102.5	-	97.5	100	12.7
77.5	-	72.5	75	10.6
52.5	-	47.5	50	9.3

Figure A-20. Thermal Testing Data for Specimen PTC5-B 4.1-B, Cycle 2

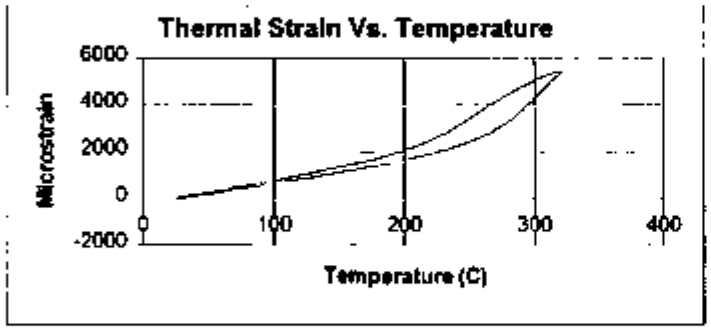

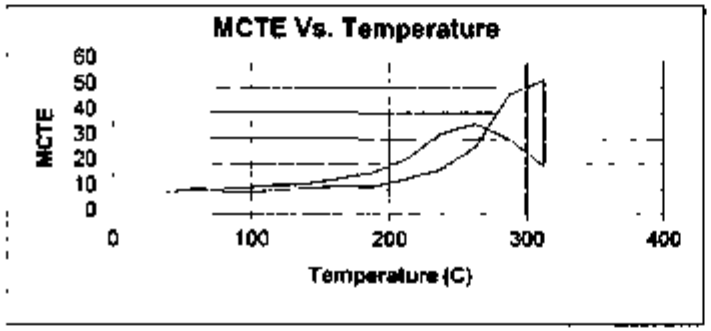

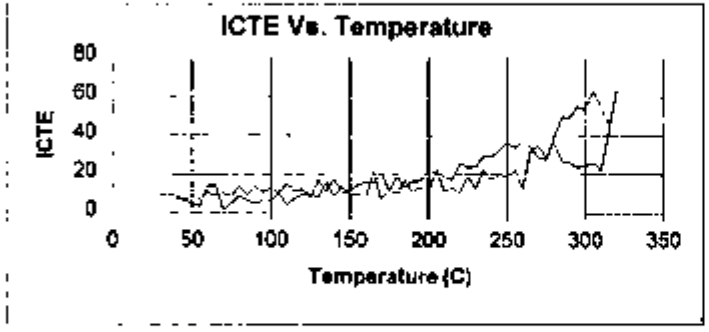

Specimen ID:	PTC5B 24 4-B Cycle 1
Date of Test Completion:	08-07-98
Thermal/Mechanical Unit:	TSw2
Lithostratigraphic Unit:	Tptpmn
Original Location:	ESF, Alcove 5;Thermal Drift Scale Test Area
	Collected after Completion of Single Heater Test
Initial Moisture Content	Air-dried (As-is)
Nominal Dimensions:	50 8 mm (L) 25.4 mm (D)

Specimen Data:	Length (mm)	Mass (g)
Pre-test:	50.81	58.853
Post-test:	50.81	58.029
Change:	0	0.824

Temp Range (C)		(C)	Mean Temp (C)	Mean CTE (10^{-6}/C)
25	-	50	37.5	8.9
50	-	75	62.5	10.5
75	-	100	87.5	8.6
100	-	125	112 5	9.4
125	-	150	137 5	10.2
150	-	175	162.5	11.2
175	-	200	187.5	11.1
200	-	225	212.5	14.1
225	-	250	237.5	17.9
250	-	275	262 5	26.7
275	-	300	287.5	47.5
300	-	325	312.5	52 9
325	-	300	312.5	19.1
300	-	275	287.5	29 9
275	-	250	262.5	35 9
250	-	225	237.5	32.0
225	-	200	212.5	21 9
200	-	175	187.5	16.6
175	-	150	162.5	14 0
150	-	125	137.5	11.9
125	-	100	112.5	11.5
100	-	75	87.5	10 2
75	-	50	62 5	9.7
50	-	30	40	9.1

Temp Range (C)		(C)	Mean Temp (C)	Instant. CTE (10^{-6}/C)
27 5	-	32.5	30	9.4
47 5	-	52 5	50	5.3
72.5	-	77.5	75	5 5
97.5	-	102.5	100	6.6
122.5	-	127.5	125	10.1
147.5	-	152.5	150	9.0
172.5	-	177.5	175	12.7
197.5	-	202.5	200	11.1
222.5	-	227.5	225	19.4
247.5	-	252.5	250	18.7
272.5	-	277.5	275	28.9
297.5	-	302.5	300	53.4
302.5	-	297.5	300	24 5
277.5	-	272.5	275	28 1
252 5	-	247.5	250	37 0
227 5	-	222 5	225	23 9
202 5	-	197 5	200	22 2
177.5	-	172.5	175	11.9
152.5	-	147.5	150	11.9
127.5	-	122.5	125	8 1
102.5	-	97.5	100	12 9
77 5	-	72 5	75	8 9
52.5	-	47.5	50	9.0

Figure A-21. Thermal Testing Data for Specimen PTC5-B 24.4-B, Cycle 1

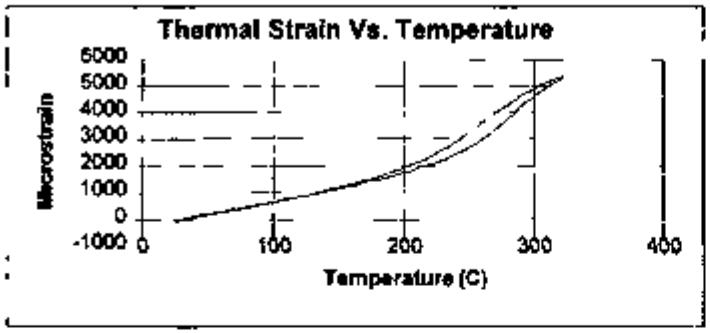

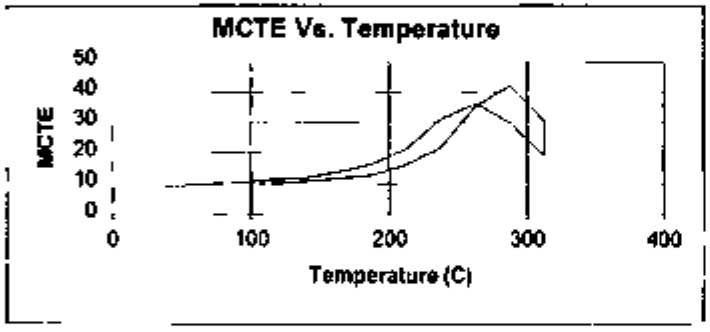

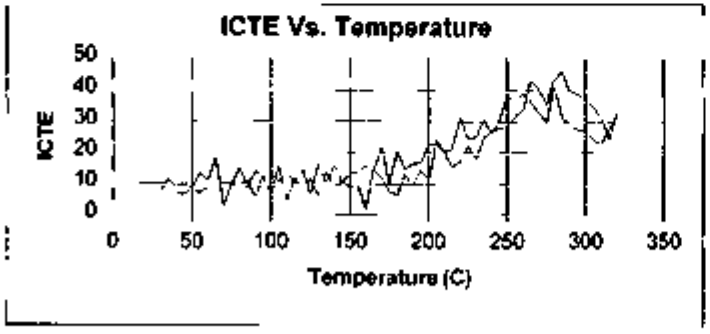

Specimen ID	PTC5-B 24 4-B Cycle 2
Date of Test Completion	21-07-98
Thermal/Mechanical Unit	TSw2
Lithostratigraphic Unit	Tptpmn
Original Location	ESF, Alcove 5 Thermal Drift Scale Test Area Collected after Completion of Single Heater Test
Initial Moisture Content	Air-dried (As-is)
Nominal Dimensions	50 8 mm (L) 25 4 mm (D)

Specimen Data	Length (mm)	Mass (g)
Pre-test	50 8	58 2
Post-test	50 8	58 027
Change	0	0 173

Temp Range (C)		(C)	Mean Temp (C)	Mean CTE (10^{-6}/C)
25	-	50	37 5	8 9
50	-	75	62 5	10 0
75	-	100	87 5	8 9
100	-	125	112 5	10 1
125	-	150	137 5	10 8
150	-	175	162 5	11 8
175	-	200	187 5	12 9
200	-	225	212 5	16 5
225	-	250	237 5	22 1
250	-	275	262 5	35 5
275	-	300	287 5	42 2
300	-	325	312 5	30 8
325	-	300	312 5	19 1
300	-	275	287 5	30 4
275	-	250	262 5	36 4
250	-	225	237 5	31 3
225	-	200	212 5	21 6
200	-	175	187 5	16 6
175	-	150	162 5	13 9
150	-	125	137 5	11 9
125	-	100	112 5	11 3
100	-	75	87 5	10 1
75	-	50	62 5	9 6
50	-	30	40	9 1

Temp Range (C)		(C)	Mean Temp (C)	Instant CTE (10^{-6}/C)
27 5	-	32 5	30	7 5
47 5	-	52 5	50	8 8
72 5	-	77 5	75	10 0
97 5	-	102 5	100	6 7
122 5	-	127 5	125	11 6
147 5	-	152 5	150	9 0
172 5	-	177 5	175	7 7
197 5	-	202 5	200	11 0
222 5	-	227 5	225	22 4
247 5	-	252 5	250	28 6
272 5	-	277 5	275	35 3
297 5	-	302 5	300	37 2
302 5	-	297 5	300	27 0
277 5	-	272 5	275	29 6
252 5	-	247 5	250	38 0
227 5	-	222 5	225	24 5
202 5	-	197 5	200	22 8
177 5	-	172 5	175	9 9
152 5	-	147 5	150	13 1
127 5	-	122 5	125	6 5
102 5	-	97 5	100	12 9
77 5	-	72 5	75	9 5
52 5	-	47 5	50	9 0

Figure A-22 Thermal Testing Data for Specimen PTC5-B 24 4-B, Cycle 2

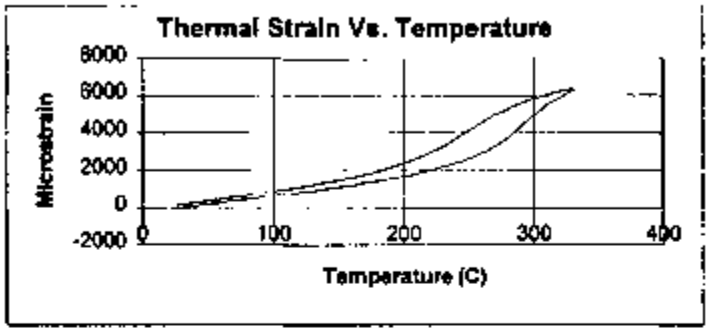

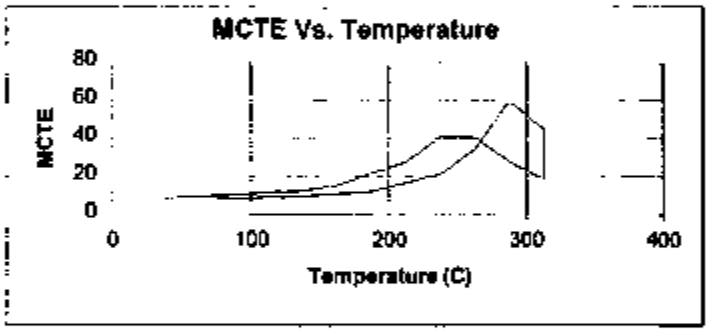

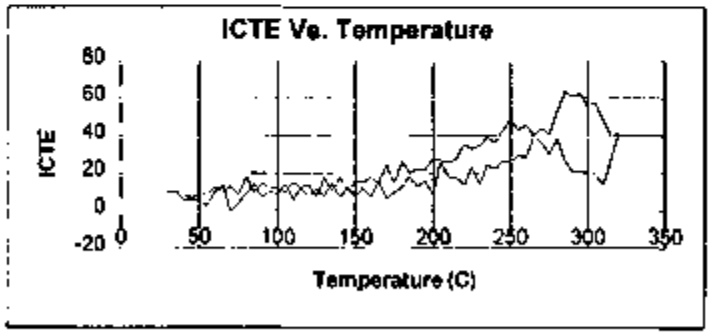

Specimen ID:	PTC5-B 24 4 - C Cycle 1
Date of Test Completion:	05-08-98
Thermal/Mechanical Unit:	TSw2
Lithostratigraphic Unit:	Tptpmn
Original Location:	ESF; Alcove 5,Thermal Drift Scale Test Area Collected after Completion of Single Heater Test
Initial Moisture Content	Air-dried (As-is)
Nominal Dimensions:	50.8 mm (L) 25 4 mm (D)

Specimen Data:	Length (mm)	Mass (g)
Pre-test:	49.32	56.029
Post-test:	49.33	55.065
Change:	-0.01	0.964

Temp Range (C)		(C)	Mean Temp (C)	Mean CTE (10^{-6}/C)
25	-	50	37.5	8.8
50	-	75	62.5	9.9
75	-	100	87.5	8.5
100	-	125	112.5	9.3
125	-	150	137.5	10.2
150	-	175	162.5	11.4
175	-	200	187.5	12.6
200	-	225	212.5	17.2
225	-	250	237.5	21.5
250	-	275	262.5	34.5
275	-	300	287.5	59.9
300	-	325	312.5	45.1
325	-	300	312.5	18.6
300	-	275	287.5	28.1
275	-	250	262.5	40.9
250	-	225	237.5	41.1
225	-	200	212.5	27.8
200	-	175	187.5	22.1
175	-	150	162.5	15.8
150	-	125	137.5	12.9
125	-	100	112.5	11.9
100	-	75	87.5	10.5
75	-	50	62.5	9.8
50	-	30	40	9.2

Temp Range (C)		(C)	Mean Temp (C)	Instant. CTE (10^{-6}/C)
27.5	-	32.5	30	10.5
47.5	-	52.5	50	5.1
72.5	-	77.5	75	3.9
97.5	-	102.5	100	9.0
122.5	-	127.5	125	11.7
147.5	-	152.5	150	7.1
172.5	-	177.5	175	10.0
197.5	-	202.5	200	8.8
222.5	-	227.5	225	23.2
247.5	-	252.5	250	26.4
272.5	-	277.5	275	41.1
297.5	-	302.5	300	55.8
302.5	-	297.5	300	20.4
277.5	-	272.5	275	30.2
252.5	-	247.5	250	48.6
227.5	-	222.5	225	32.9
202.5	-	197.5	200	27.8
177.5	-	172.5	175	14.6
152.5	-	147.5	150	15.1
127.5	-	122.5	125	8.1
102.5	-	97.5	100	12.0
77.5	-	72.5	75	9.0
52.5	-	47.5	50	9.2

Figure A-23. Thermal Testing Data for Specimen PTC5-B 24.4-C, Cycle 1

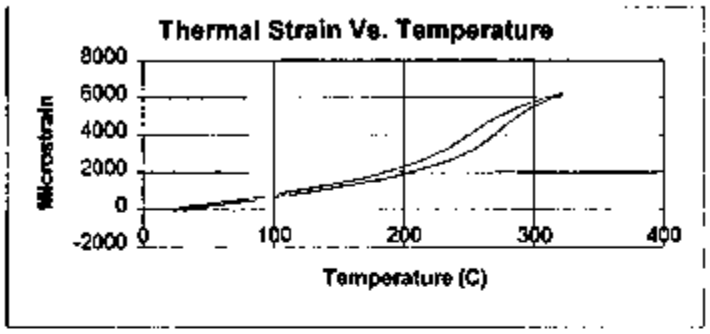

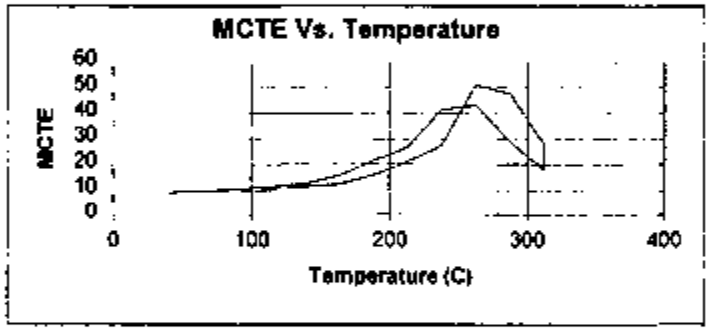

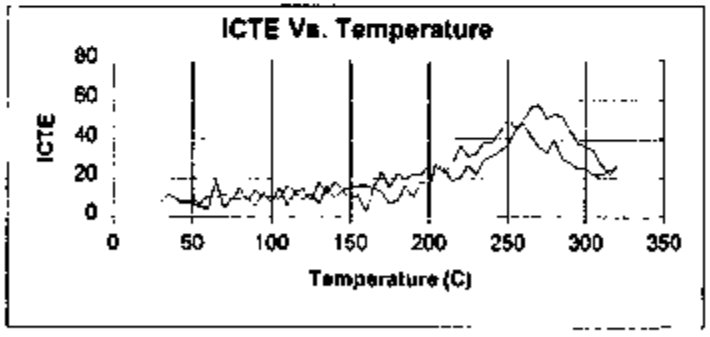

Specimen ID:	PTC5-B 24.4 - C Cycle 2
Date of Test Completion:	06-08-98
Thermal/Mechanical Unit:	TSw2
Lithostratigraphic Unit:	Tplpmn
Original Location:	ESF; Alcove 5;Thermal Drift Scale Test Area Collected after Completion of Single Heater Test
Initial Moisture Content	Air-dried (As-is)
Nominal Dimensions:	50.8 mm (L) 25.4 mm (D)

Specimen Data:	Length (mm)	Mass (g)
Pre-test:	49.33	55.065
Post-test:	49.33	55.049
Change:	0	0.016

Temp Range (C)		(C)	Mean Temp (C)	Mean CTE (10^{-6}/C)
25	-	50	37.5	9.1
50	-	75	62.5	10.0
75	-	100	87.5	9.4
100	-	125	112.5	10.5
125	-	150	137.5	11.6
150	-	175	162.5	12.5
175	-	200	187.5	15.8
200	-	225	212.5	21.1
225	-	250	237.5	27.5
250	-	275	262.5	51.1
275	-	300	287.5	47.9
300	-	325	312.5	27.8
325	-	300	312.5	17.9
300	-	275	287.5	28.7
275	-	250	262.5	43.3
250	-	225	237.5	41.3
225	-	200	212.5	26.6
200	-	175	187.5	21.5
175	-	150	162.5	15.7
150	-	125	137.5	12.5
125	-	100	112.5	11.6
100	-	75	87.5	10.6
75	-	50	62.5	9.7
50	-	30	40	9.1

Temp Range (C)		(C)	Mean Temp (C)	Instant. CTE (10^{-6}/C)
27.5	-	32.5	30	7.7
47.5	-	52.5	50	7.7
72.5	-	77.5	75	9.6
97.5	-	102.5	100	7.6
122.5	-	127.5	125	12.3
147.5	-	152.5	150	9.4
172.5	-	177.5	175	6.9
197.5	-	202.5	200	15.7
222.5	-	227.5	225	26.6
247.5	-	252.5	250	36.9
272.5	-	277.5	275	50.5
297.5	-	302.5	300	36.5
302.5	-	297.5	300	25.2
277.5	-	272.5	275	32.7
252.5	-	247.5	250	50.5
227.5	-	222.5	225	31.1
202.5	-	197.5	200	27.7
177.5	-	172.5	175	14.6
152.5	-	147.5	150	14.8
127.5	-	122.5	125	8.4
102.5	-	97.5	100	10.7
77.5	-	72.5	75	9.3
52.5	-	47.5	50	9.5

Figure A-24. Thermal Testing Data for Specimen PTC5-B 24.4-C, Cycle 2

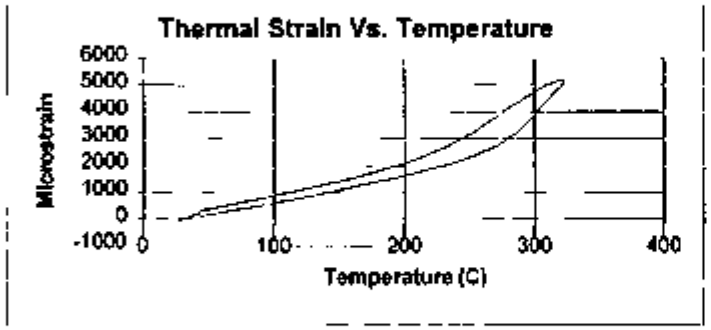

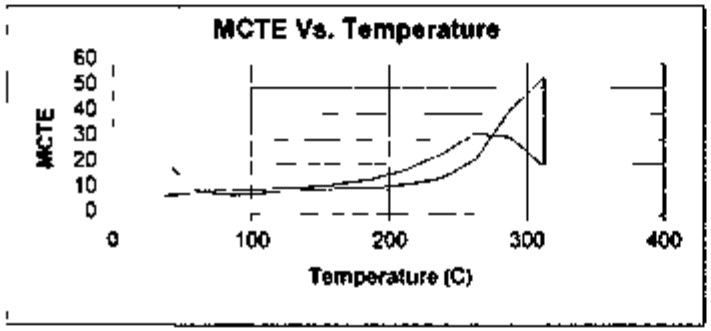

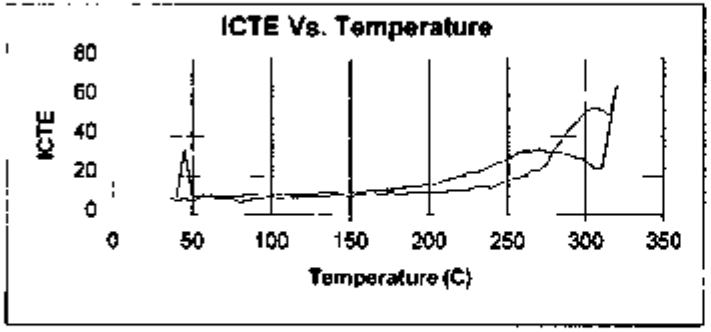

Specimen ID	PTC H1-A 15 6-BCycle 1
Date of Test Completion	27-07-98
Thermal/Mechanical Unit	TSw2
Lithostratigraphic Unit	Tptpmn
Original Location	ESF, Alcove 5 Thermal Drift Scale Test Area Collected after Completion of Single Heater Test
Initial Moisture Content	Air-dried (As-is)
Nominal Dimensions	50 8 mm (L) 25 4 mm (D)

Specimen Data	Length (mm)	Mass (g)
Pre-test	50 44	57 576
Post-test	50 44	57 182
Change	0	0 394

Temp Range (C)		(C)	Mean Temp (C)	Mean CTE (10^{-6}/C)
25	-	50	37 5	7 7
50	-	75	62 5	9 5
75	-	100	87 5	8 2
100	-	125	112 5	9 1
125	-	150	137 5	10 2
150	-	175	162 5	10 7
175	-	200	187 5	11 0
200	-	225	212 5	12 3
225	-	250	237 5	14 6
250	-	275	262 5	22 0
275	-	300	287 5	41 4
300	-	325	312 5	54 2
325	-	300	312 5	19 3
300	-	275	287 5	30 9
275	-	250	262 5	32 3
250	-	225	237 5	24 1
225	-	200	212 5	18 1
200	-	175	187 5	14 4
175	-	150	162 5	12 6
150	-	125	137 5	11 2
125	-	100	112 5	10 6
100	-	75	87 5	10 0
75	-	50	62 5	9 3
50	-	30	40	20 2

Temp Range (C)		(C)	Mean Temp (C)	Instant CTE (10^{-6}/C)
27 5	-	32 5	30	7 2
47 5	-	52 5	50	7 3
72 5	-	77 5	75	8 8
97 5	-	102 5	100	9 6
122 5	-	127 5	125	9 5
147 5	-	152 5	150	9 4
172 5	-	177 5	175	11 6
197 5	-	202 5	200	11 3
222 5	-	227 5	225	12 8
247 5	-	252 5	250	17 6
272 5	-	277 5	275	26 0
297 5	-	302 5	300	53 2
302 5	-	297 5	300	28 2
277 5	-	272 5	275	32 4
262 5	-	247 5	250	28 4
227 5	-	222 5	225	21 8
202 5	-	197 5	200	16 4
177 5	-	172 5	175	12 9
152 5	-	147 5	150	11 9
127 5	-	122 5	125	10 3
102 5	-	97 5	100	10 0
77 5	-	72 5	75	9 5
52 5	-	47 5	50	9 5

Figure A-25 Thermal Testing Data for Specimen PTC H1-A 15 6-B, Cycle 1

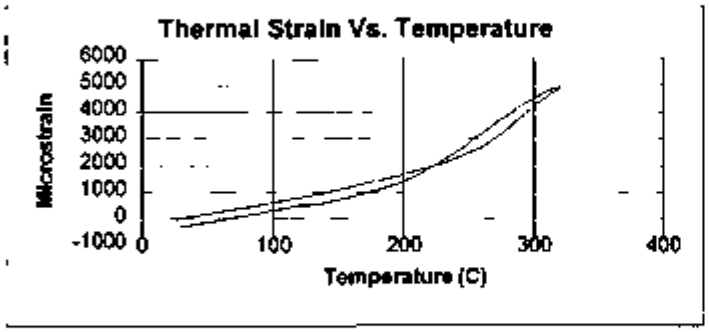

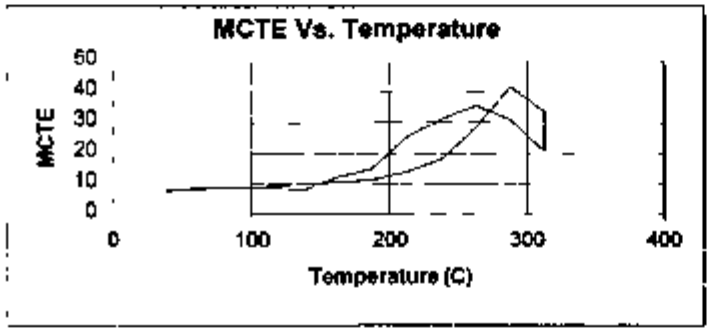

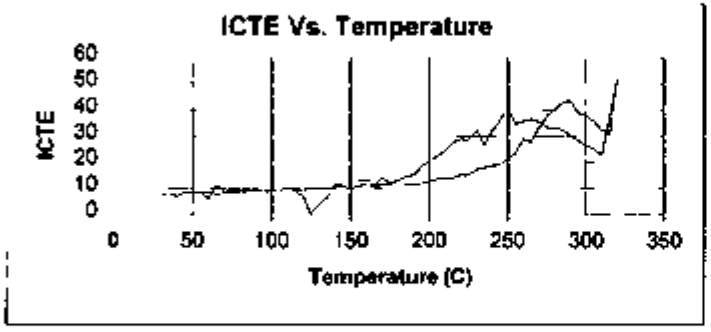

Specimen ID	PTC H1-A 15 6-B Cycle 2
Date of Test Completion	30-07-98
Thermal/Mechanical Unit	TSw2
Lithostratigraphic Unit	Tptpmn
Original Location	ESF, Alcove 5,Thermal Drift Scale Test Area Collected after Completion of Single Heater Test
Initial Moisture Content	Air-dried (As-is)
Nominal Dimensions	50 8 mm (L) 25 4 mm (D)

Specimen Data	Length (mm)	Mass (g)
Pre-test	50 44	57 182
Post-test	50 45	57 113
Change	-0 01	0 069

Temp Range (C)		(C)	Mean Temp (C)	Mean CTE (10^{-6}/C)
25	-	50	37 5	7 8
50	-	75	62 5	8 6
75	-	100	87 5	8 9
100	-	125	112 5	9 5
125	-	150	137 5	10 3
150	-	175	162 5	10 8
175	-	200	187 5	11 3
200	-	225	212 5	14 1
225	-	250	237 5	18 0
250	-	275	262 5	28 5
275	-	300	287 5	41 9
300	-	325	312 5	33 7
325	-	300	312 5	20 8
300	-	275	287 5	31 1
275	-	250	262 5	35 8
250	-	225	237 5	31 1
225	-	200	212 5	25 5
200	-	175	187 5	15 1
175	-	150	162 5	12 5
150	-	125	137 5	8 3
125	-	100	112 5	9 1
100	-	75	87 5	9 4
75	-	50	62 5	8 6
50	-	30	40	8 4

Temp Range (C)		(C)	Mean Temp (C)	Instant CTE (10^{-6}/C)
27 5	-	32 5	30	7 7
47 5	-	52 5	50	8 4
72 5	-	77 5	75	8 8
97 5	-	102 5	100	9 1
122 5	-	127 5	125	10 2
147 5	-	152 5	150	10 2
172 5	-	177 5	175	12 0
197 5	-	202 5	200	12 2
222 5	-	227 5	225	15 2
247 5	-	252 5	250	21 2
272 5	-	277 5	275	37 6
297 5	-	302 5	300	37 9
302 5	-	297 5	300	26 5
277 5	-	272 5	275	33 4
252 5	-	247 5	250	40 7
227 5	-	222 5	225	28 3
202 5	-	197 5	200	20 4
177 5	-	172 5	175	12 2
152 5	-	147 5	150	12 1
127 5	-	122 5	125	0 3
102 5	-	97 5	100	9 0
77 5	-	72 5	75	9 1
52 5	-	47 5	50	8 9

Figure A-26 Thermal Testing Data for Specimen PTC H1-A 15 6-B, Cycle 2

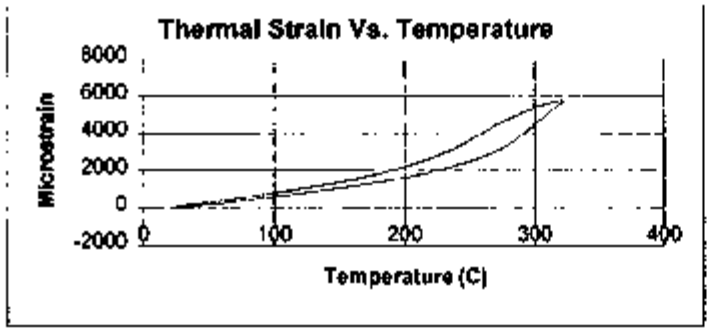

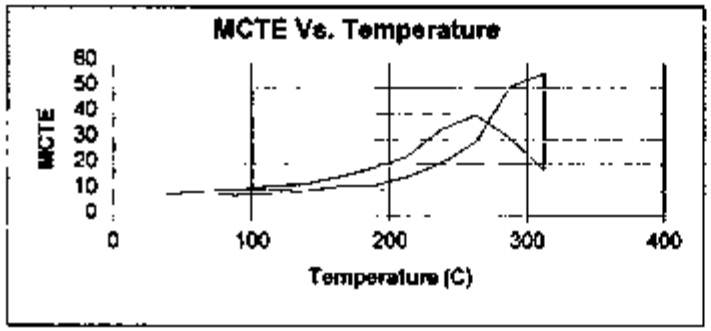

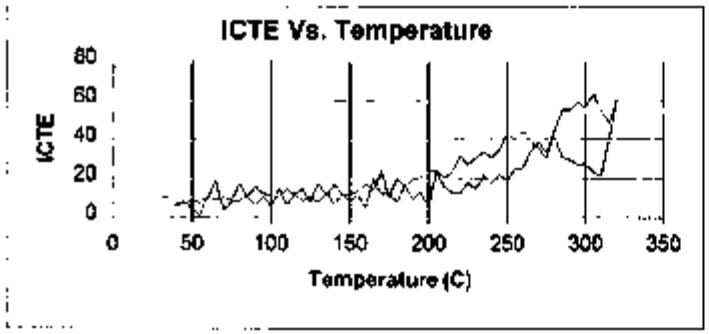

Specimen ID:	PTC MPBX1 14.2-B Cycle 1
Date of Test Completion:	28-07-98
Thermal/Mechanical Unit:	TSw2
Lithostratigraphic Unit:	Tptpmn
Original Location:	ESF; Alcove 5;Thermal Drift Scale Test Area
	Collected after Completion of Single Heater Test
Initial Moisture Content	Air-dried (As-is)
Nominal Dimensions:	50.8 mm (L) 25.4 mm (D)

Specimen Data:	Length (mm)	Mass (g)
Pre-test:	50.77	57.82
Post-test:	50.77	57.242
Change:	0	0.578

Temp Range (C)		(C)	Mean Temp (C)	Mean CTE (10^{-6}/C)
25	-	50	37.5	8.5
50	-	75	62.5	9.6
75	-	100	87.5	8.5
100	-	125	112.5	9.0
125	-	150	137.5	9.9
150	-	175	162.5	11.5
175	-	200	187.5	11.8
200	-	225	212.5	15.3
225	-	250	237.5	20.7
250	-	275	262.5	29.0
275	-	300	287.5	50.5
300	-	325	312.5	55.9
325	-	300	312.5	17.9
300	-	275	287.5	30.7
275	-	250	262.5	39.4
250	-	225	237.5	33.9
225	-	200	212.5	23.3
200	-	175	187.5	18.8
175	-	150	162.5	15.1
150	-	125	137.5	12.4
125	-	100	112.5	11.6
100	-	75	87.5	10.3
75	-	50	62.5	9.8
50	-	30	40	9.0

Temp Range (C)		(C)	Mean Temp (C)	Instant. CTE (10^{-6}/C)
27.5	-	32.5	30	10.0
47.5	-	52.5	50	4.5
72.5	-	77.5	75	7.7
97.5	-	102.5	100	5.8
122.5	-	127.5	125	10.8
147.5	-	152.5	150	7.6
172.5	-	177.5	175	12.4
197.5	-	202.5	200	5.3
222.5	-	227.5	225	17.9
247.5	-	252.5	250	19.0
272.5	-	277.5	275	33.1
297.5	-	302.5	300	56.6
302.5	-	297.5	300	27.8
277.5	-	272.5	275	30.4
252.5	-	247.5	250	42.7
227.5	-	222.5	225	27.2
202.5	-	197.5	200	24.3
177.5	-	172.5	175	10.4
152.5	-	147.5	150	11.9
127.5	-	122.5	125	7.8
102.5	-	97.5	100	11.7
77.5	-	72.5	75	8.8
52.5	-	47.5	50	8.5

Figure A-27. Thermal Testing Data for Specimen PTC MPBX1 14.2-B, Cycle 1

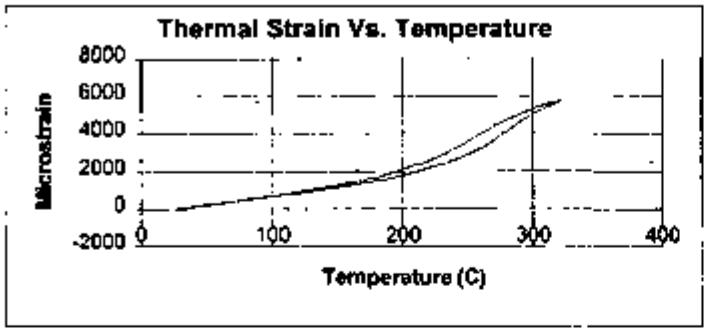

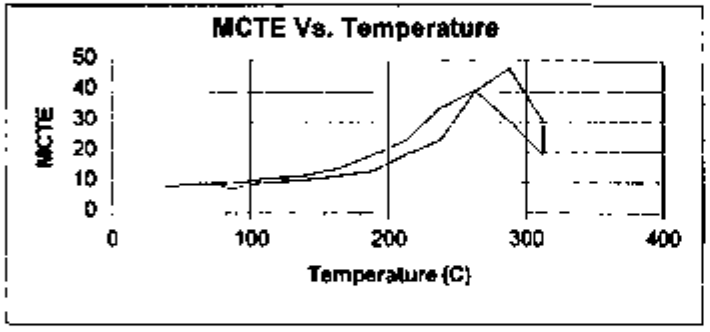

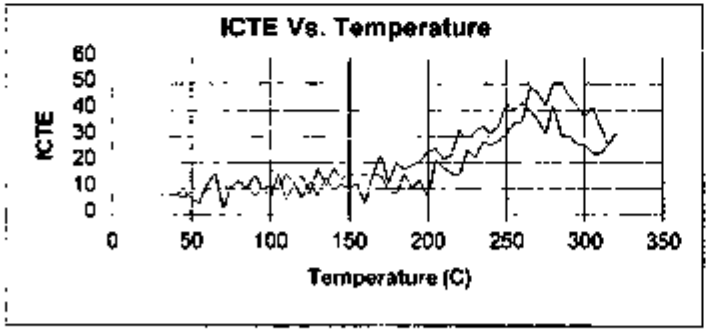

Specimen ID	PTC MPBX1 14 2-B Cycle 2
Date of Test Completion:	30-07-98
Thermal/Mechanical Unit:	TSw2
Lithostratigraphic Unit:	Tplpmn
Original Location:	ESF; Alcove 5,Thermal Drift Scale Test Area Collected after Completion of Single Heater Test
Initial Moisture Content	Air-dried (As-is)
Nominal Dimensions:	50.8 mm (L) 25 4 mm (D)

Specimen Data:	Length (mm)	Mass (g)
Pre-test:	50.77	57 242
Post-test:	50 77	57 166
Change:	0	0.076

Temp Range (C)		(C)	Mean Temp (C)	Mean CTE (10^{-6}/C)
25	-	50	37.5	8 8
50	-	75	62 5	9.9
75	-	100	87.5	8.4
100	-	125	112.5	10.3
125	-	150	137.5	11.1
150	-	175	162.5	12.4
175	-	200	187.5	14.0
200	-	225	212.5	19.4
225	-	250	237.5	24.2
250	-	275	262.5	40.1
275	-	300	287.5	47.6
300	-	325	312.5	30.3
325	-	300	312.5	19 3
300	-	275	287.5	30 6
275	-	250	262 5	40.4
250	-	225	237.5	34.8
225	-	200	212.5	24.1
200	-	175	187.5	19.1
175	-	150	162.5	14.9
150	-	125	137.5	12.4
125	-	100	112.5	11.7
100	-	75	87 5	10.0
75	-	50	62.5	9.7
50	-	30	40	9 3

Temp Range (C)		(C)	Mean Temp (C)	Instant CTE (10^{-6}/C)
27.5	-	32.5	30	6.0
47.5	-	52.5	50	6 0
72 5	-	77.5	75	11.0
97.5	-	102.5	100	6.2
122.5	-	127.5	125	13 3
147 5	-	152.5	150	10.3
172.5	-	177.5	175	9.7
197.5	-	202.5	200	6 6
222 5	-	227.5	225	24.9
247.5	-	252.5	250	31.0
272 5	-	277.5	275	41 8
297 5	-	302.5	300	37 6
302 5	-	297.5	300	26 6
277 5	-	272.5	275	31 1
252 5	-	247.5	250	42 3
227 5	-	222.5	225	28.7
202 5	-	197.5	200	24 2
177.5	-	172.5	175	12 0
152.5	-	147.5	150	15.3
127.5	-	122.5	125	7.8
102.5	-	97.5	100	11.2
77.5	-	72.5	75	10.3
52 5	-	47.5	50	8.6

Figure A-28. Thermal Testing Data for Specimen PTC MPBX1 14.2-B, Cycle 2

APPENDIX B

PLOTS OF THERMAL CONDUCTIVITY VERSUS TEMPERATURE FOR EACH SPECIMEN

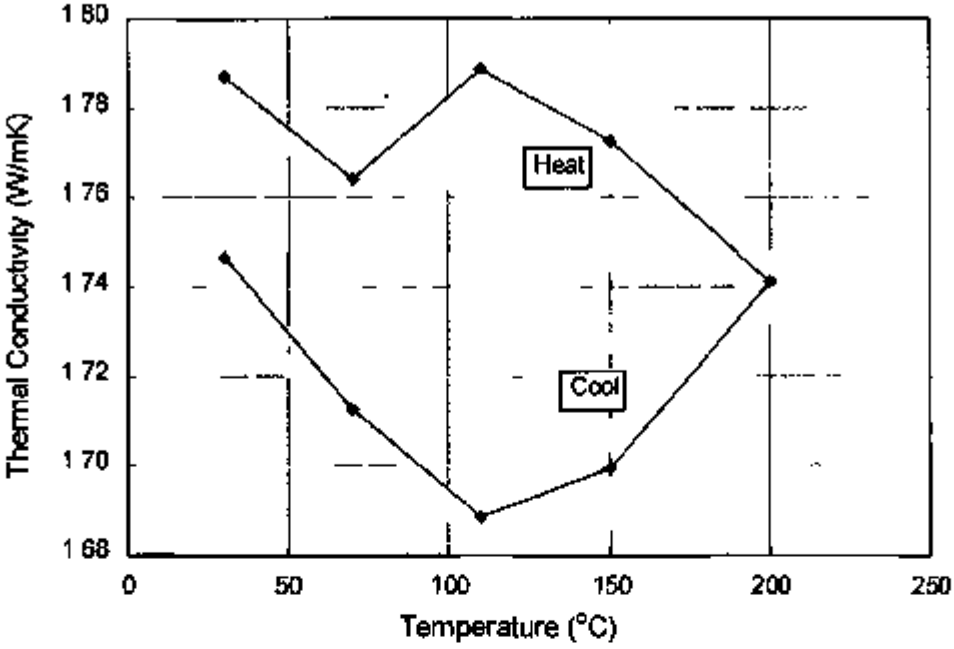

Figure B-1 Thermal Conductivity vs Temperature for the Complete Thermal Cycle on Specimen PTC1-A 15 7

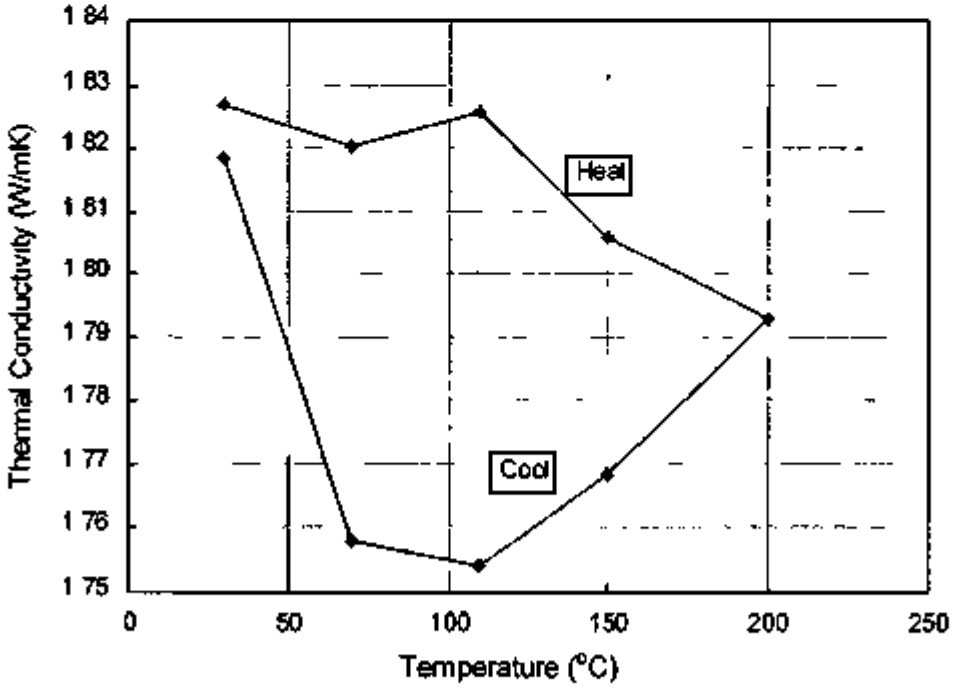

Figure B-2 Thermal Conductivity vs Temperature for the Complete Thermal Cycle on Specimen PTC1-A 19 0

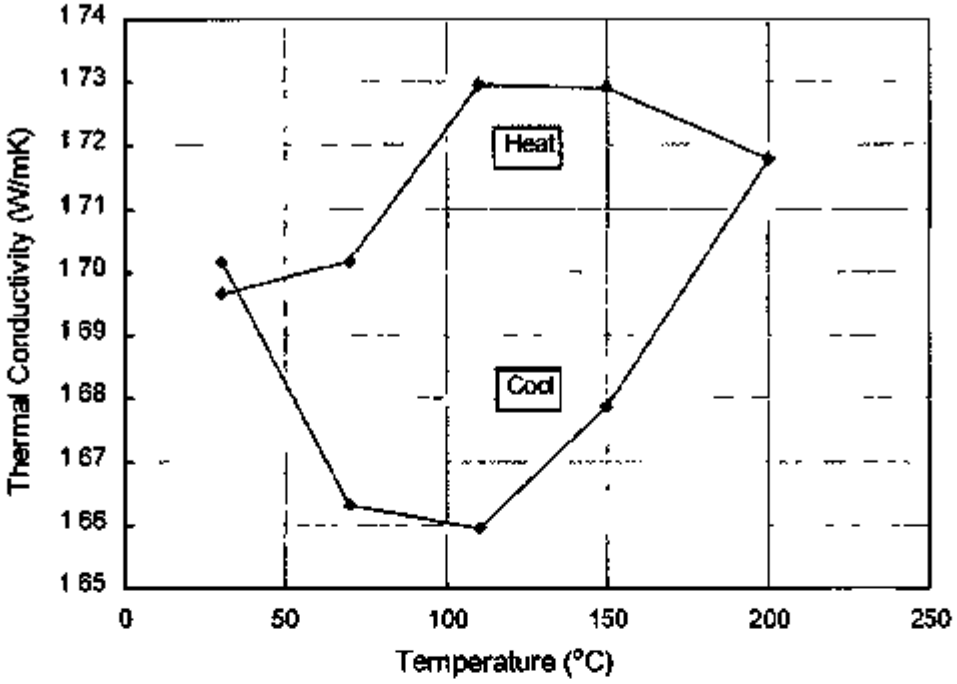

Figure B-3 Thermal Conductivity vs Temperature for the Complete Thermal Cycle on Specimen PTC2-A 4 1

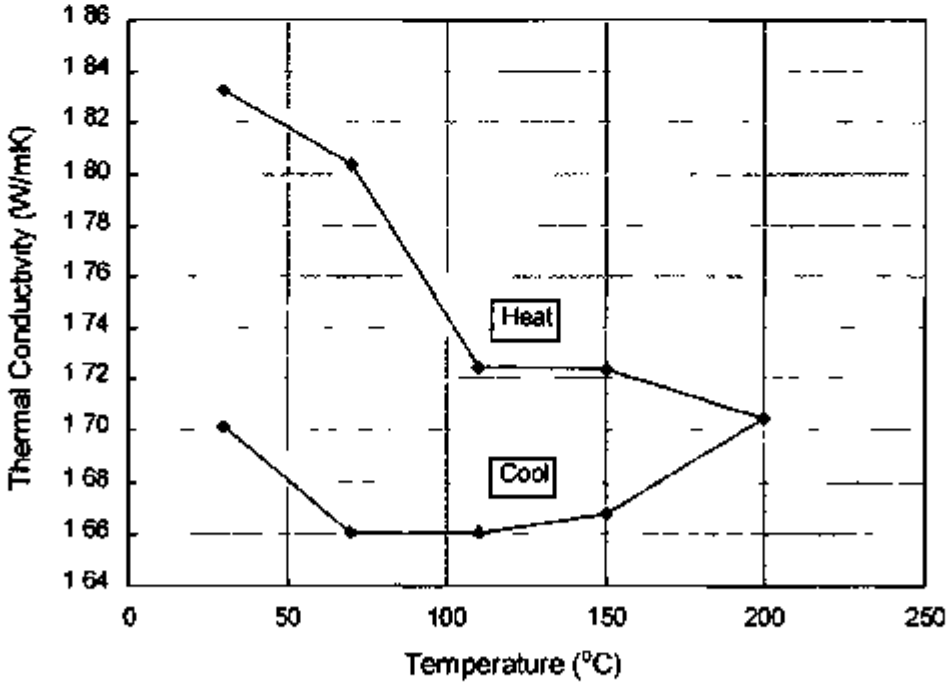

Figure B-4 Thermal Conductivity vs Temperature for the Complete Thermal Cycle on Specimen PTC2-A 10 8

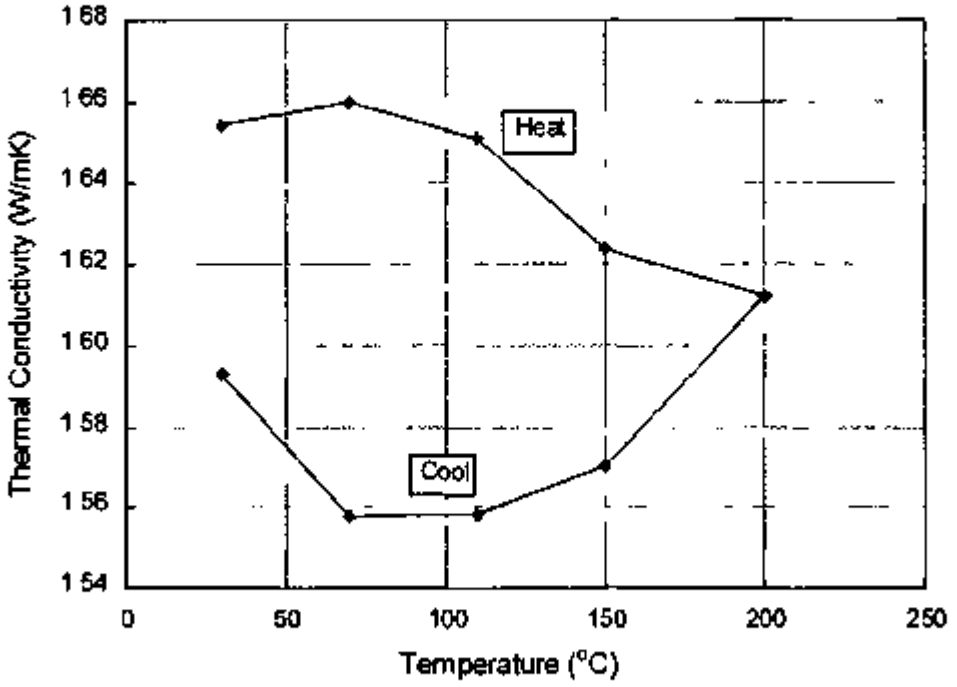

Figure B-5 Thermal Conductivity vs Temperature for the Complete Thermal Cycle on Specimen PTC2-A 14 1

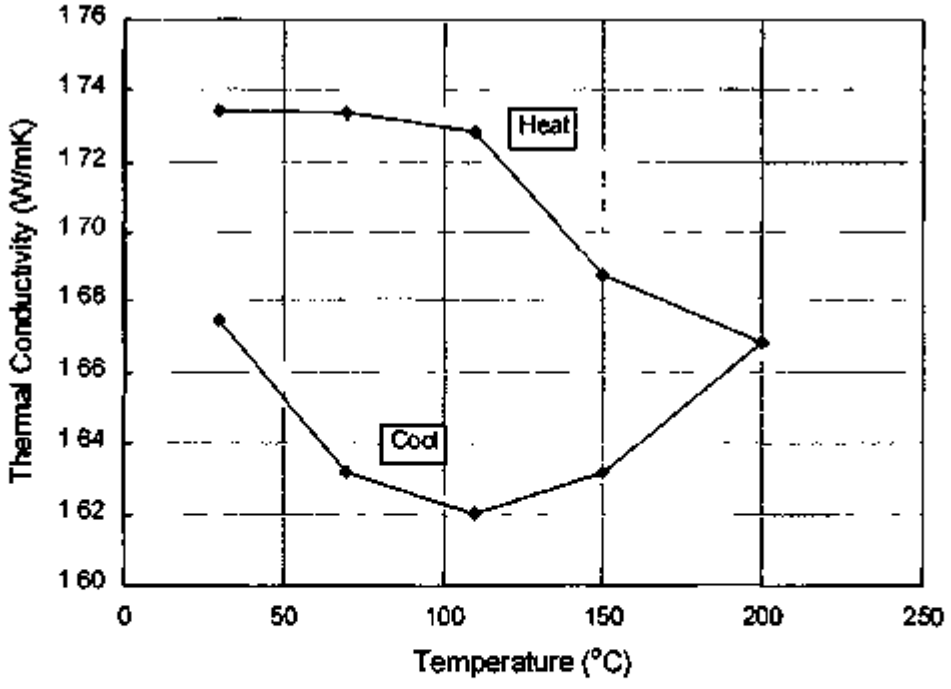

Figure B-6 Thermal Conductivity vs Temperature for the Complete Thermal Cycle on Specimen PTC4-A 4 3

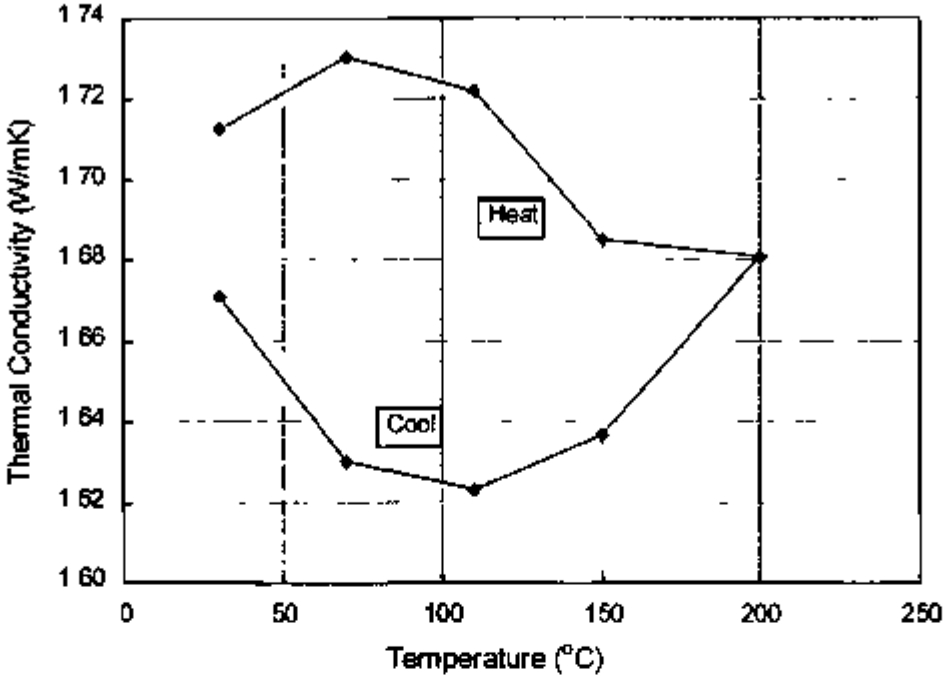

Figure B-7 Thermal Conductivity vs Temperature for the Complete Thermal Cycle on Specimen PTC4-A 6 6

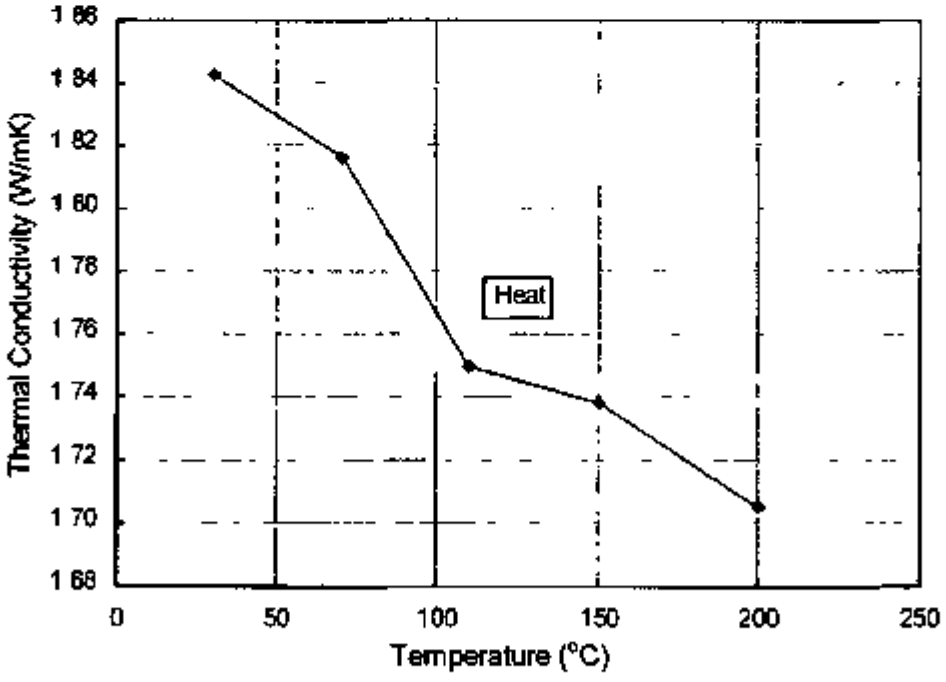

Figure B-8 Thermal Conductivity vs Temperature for the Complete Thermal Cycle on Specimen PTC4-A 9 2

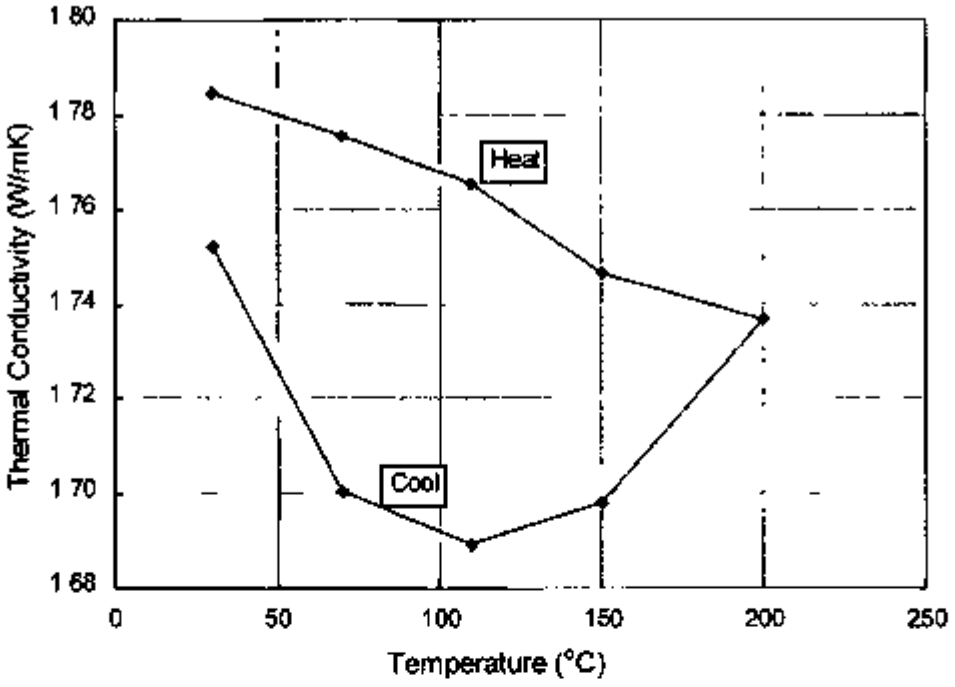

Figure B-9 Thermal Conductivity vs Temperature for the Complete Thermal Cycle on Specimen PTC4–A 14 8

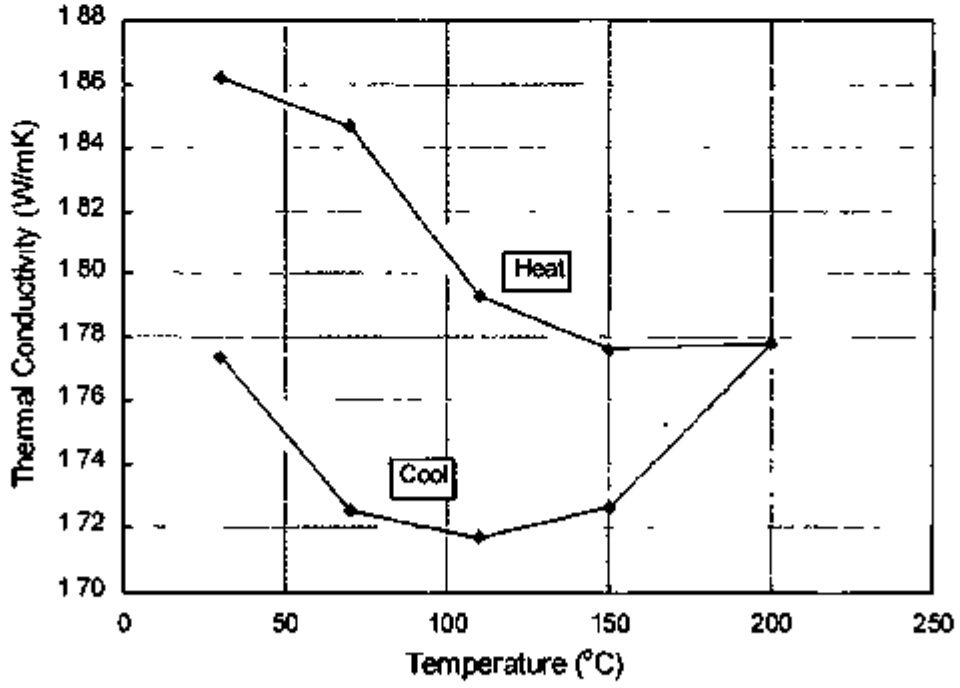

Figure B-10 Thermal Conductivity vs Temperature for the Complete Thermal Cycle on Specimen PTC4–A 19 8

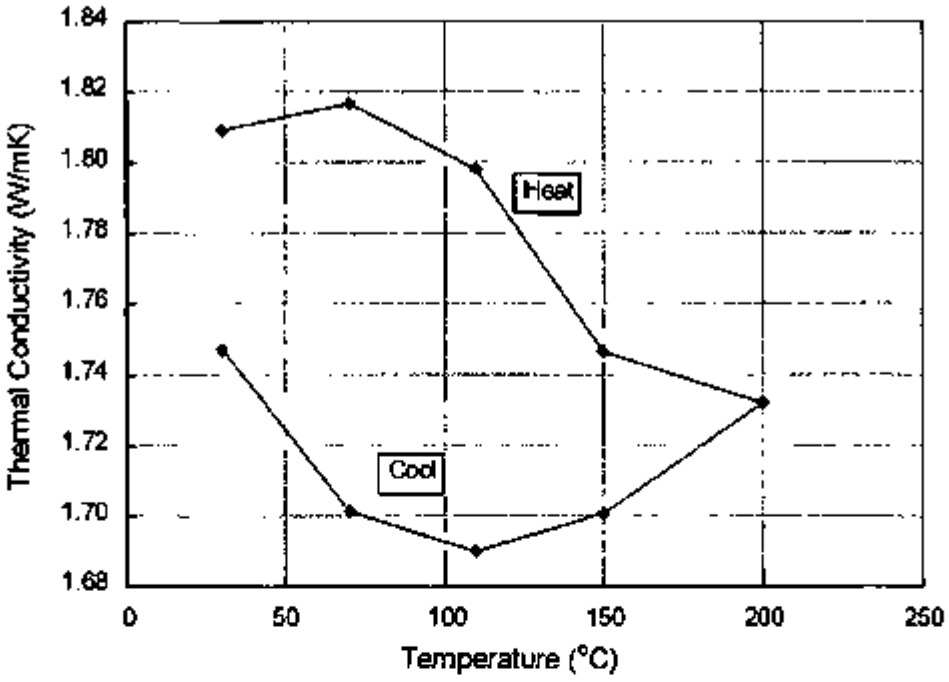

Figure B-11. Thermal Conductivity vs. Temperature for the Complete Thermal Cycle on Specimen PTC4–A 26.0

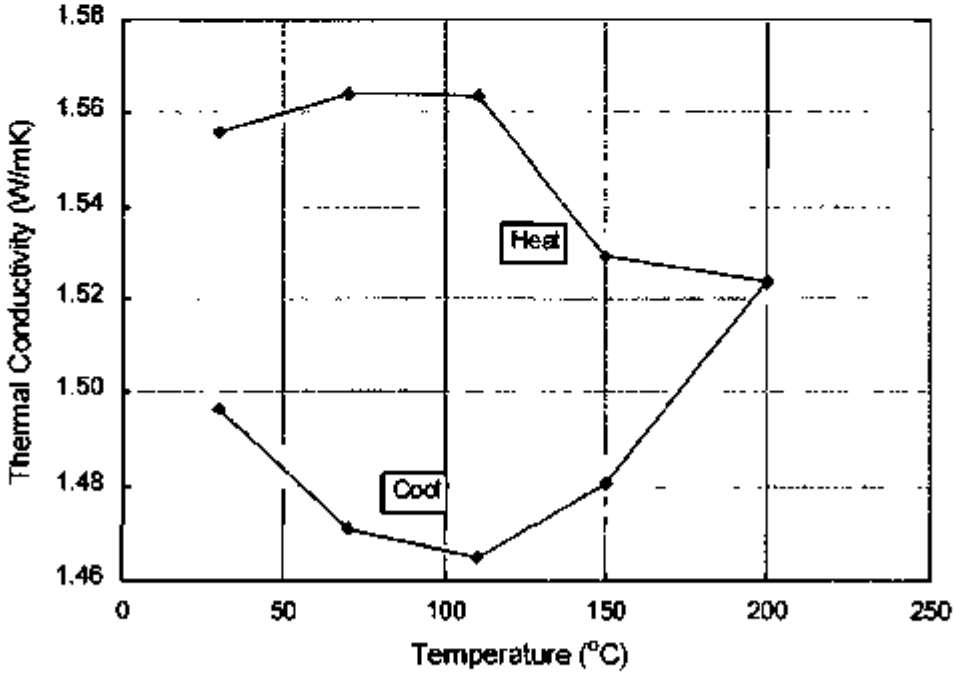

Figure B-12. Thermal Conductivity vs. Temperature for the Complete Thermal Cycle on Specimen PTC5–A 4.1

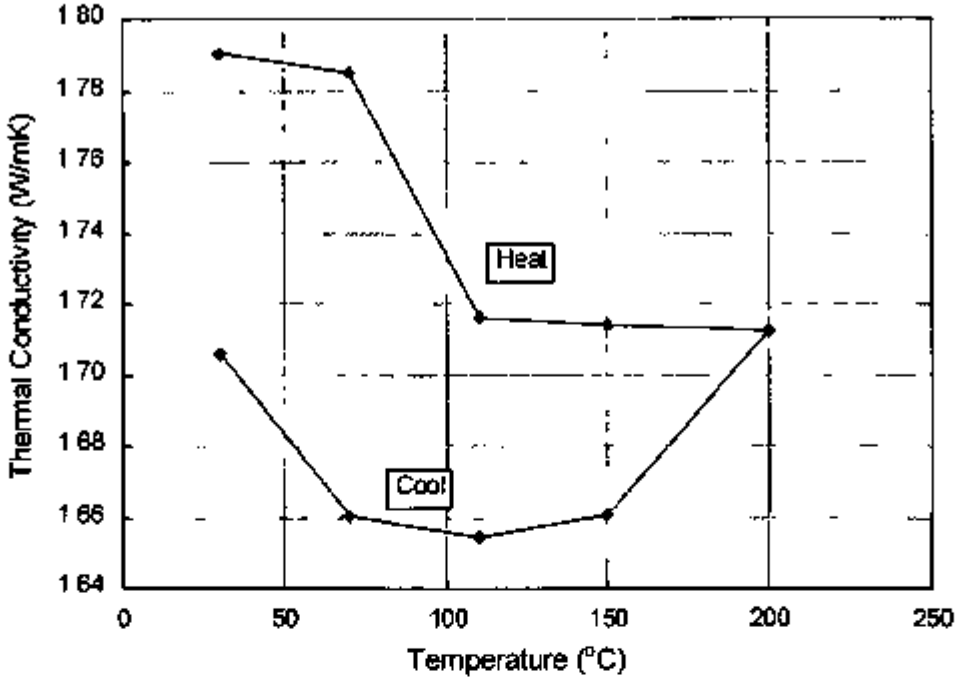

Figure B-13 Thermal Conductivity vs Temperature for the Complete Thermal Cycle on Specimen PTC5–A 14 9

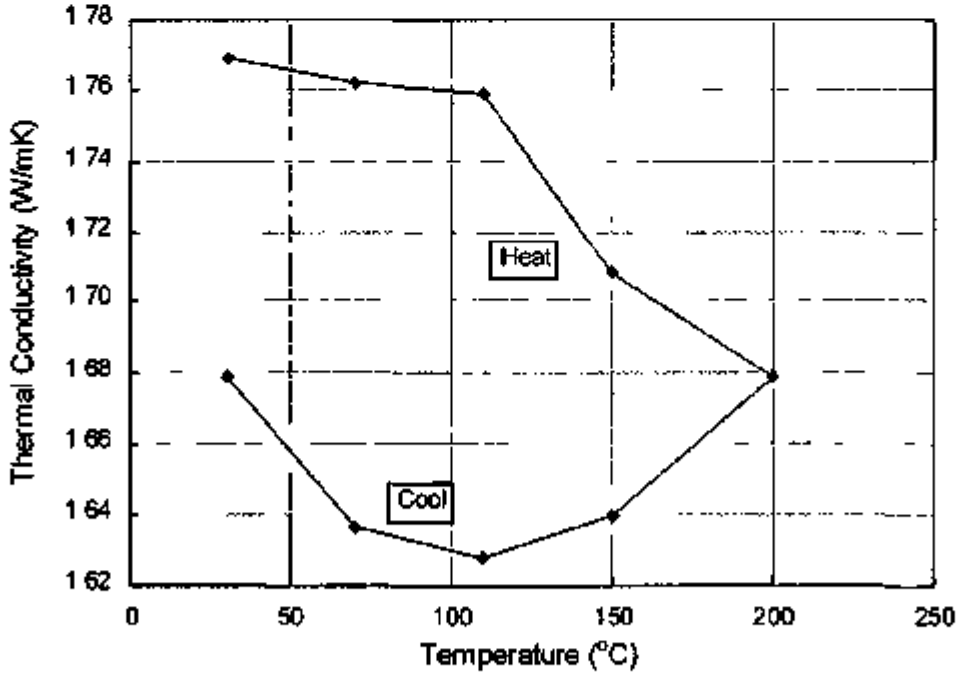

Figure B-14 Thermal Conductivity vs Temperature for the Complete Thermal Cycle on Specimen PTC5–A 25 4

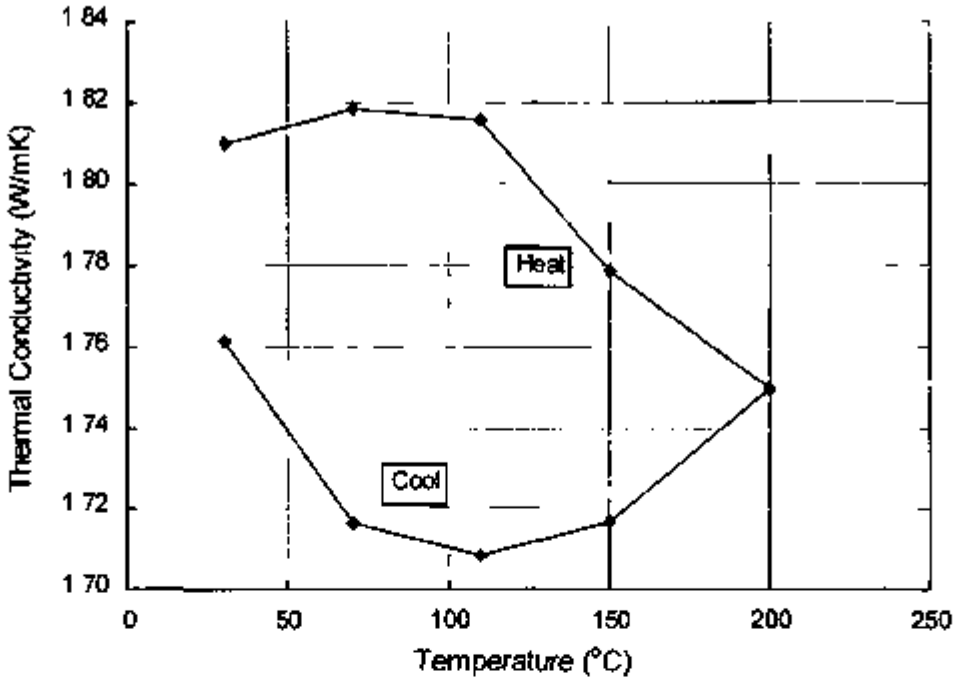

Figure B-15 Thermal Conductivity vs Temperature for the Complete Thermal Cycle on Specimen PTCH1–A 8 6

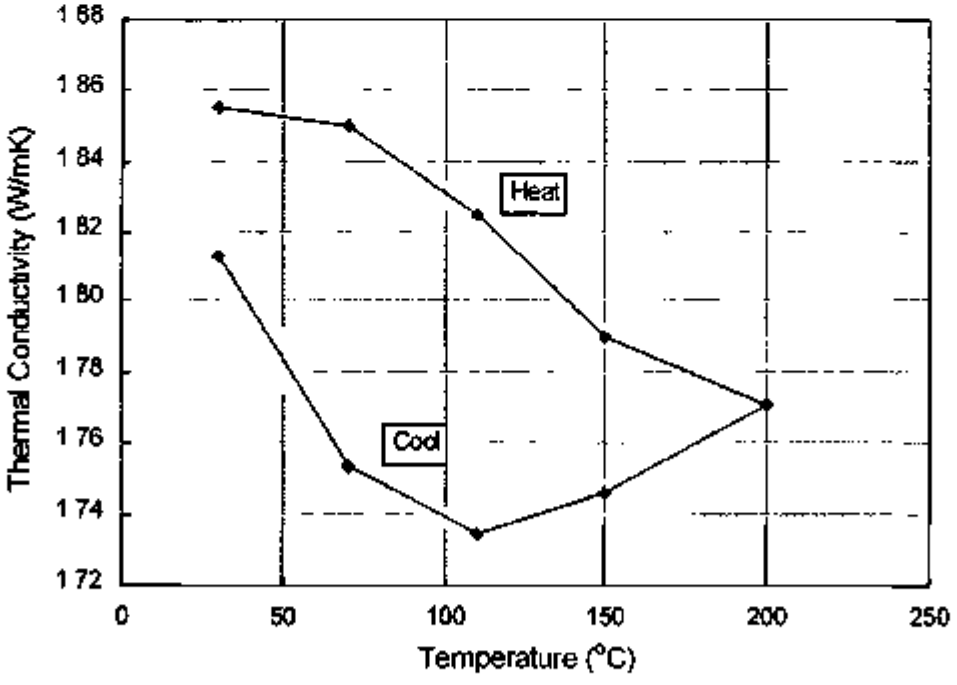

Figure B-16 Thermal Conductivity vs Temperature for the Complete Thermal Cycle on Specimen PTC MPBX1–A 14 4

APPENDIX C

THERMAL EXPANSION PLOTS FOR MULTIPLE THERMAL CYCLES

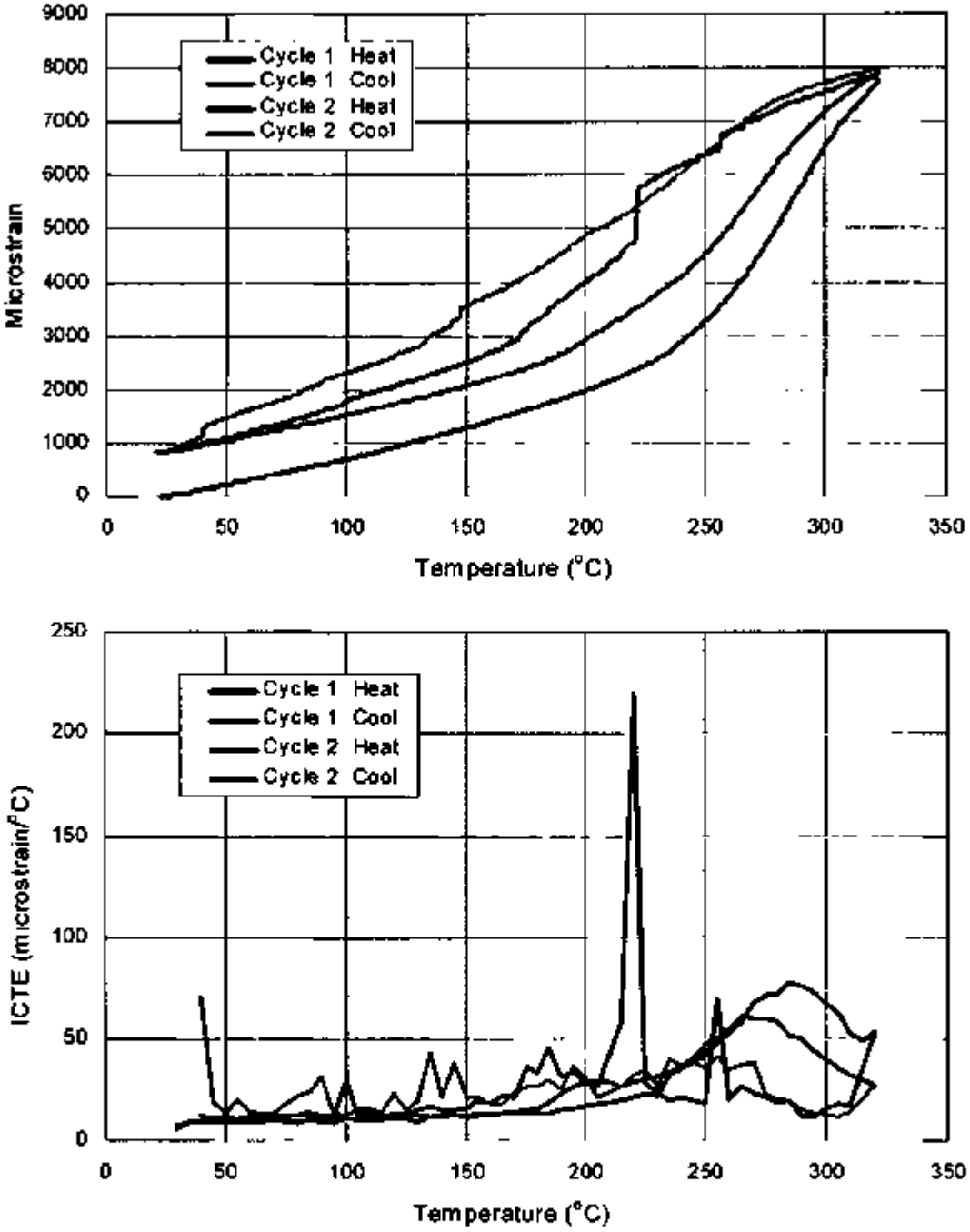

Figure C-1. Thermal Strain vs. Temperature (Top) and ICTE vs. Temperature (Bottom) for All Thermal Cycles Run on Specimen PTC1-A 2.9-B

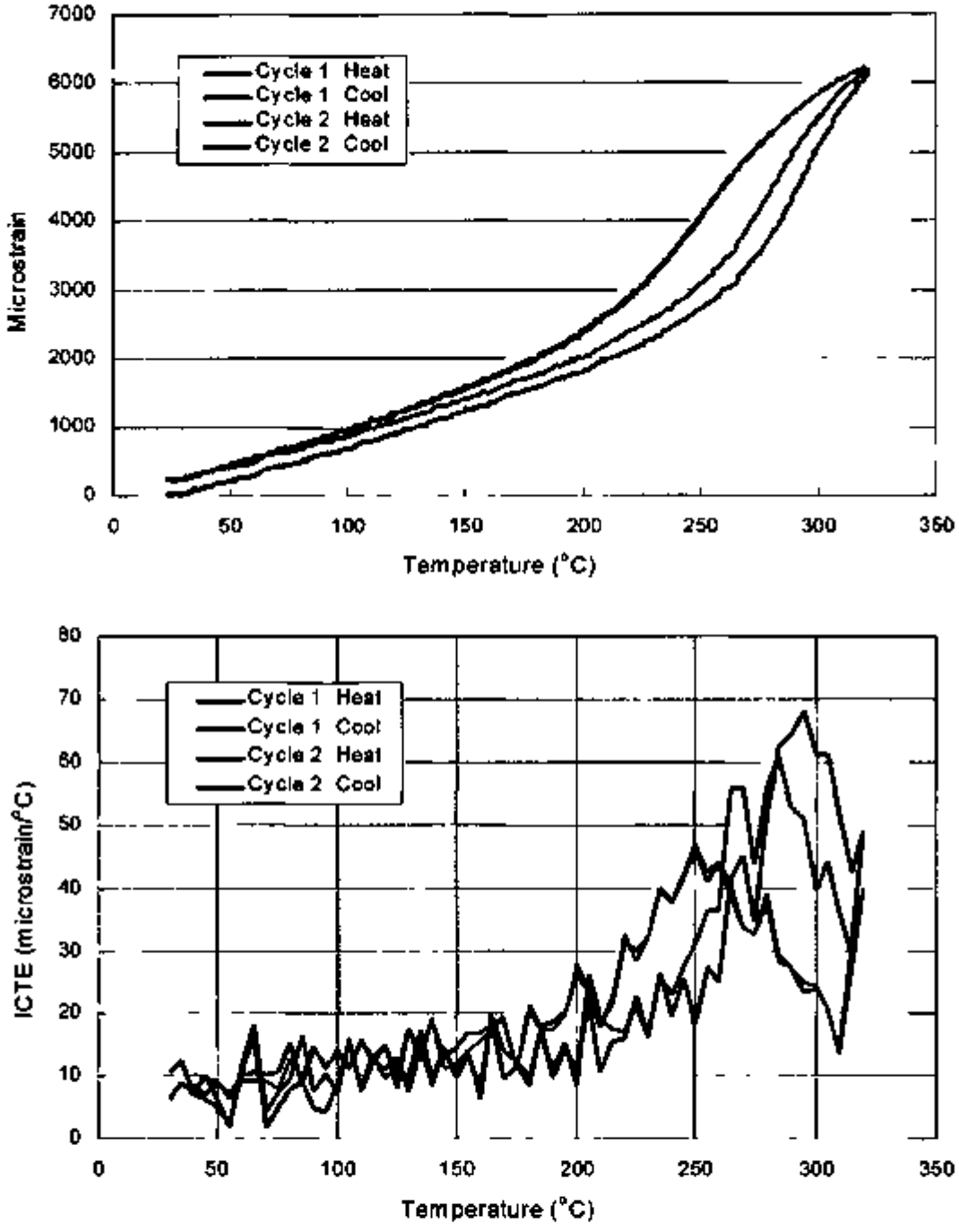

Figure C-2 Thermal Strain vs. Temperature (Top) and ICTE vs. Temperature (Bottom) for All Thermal Cycles Run on Specimen PTC1-A 16 8-B

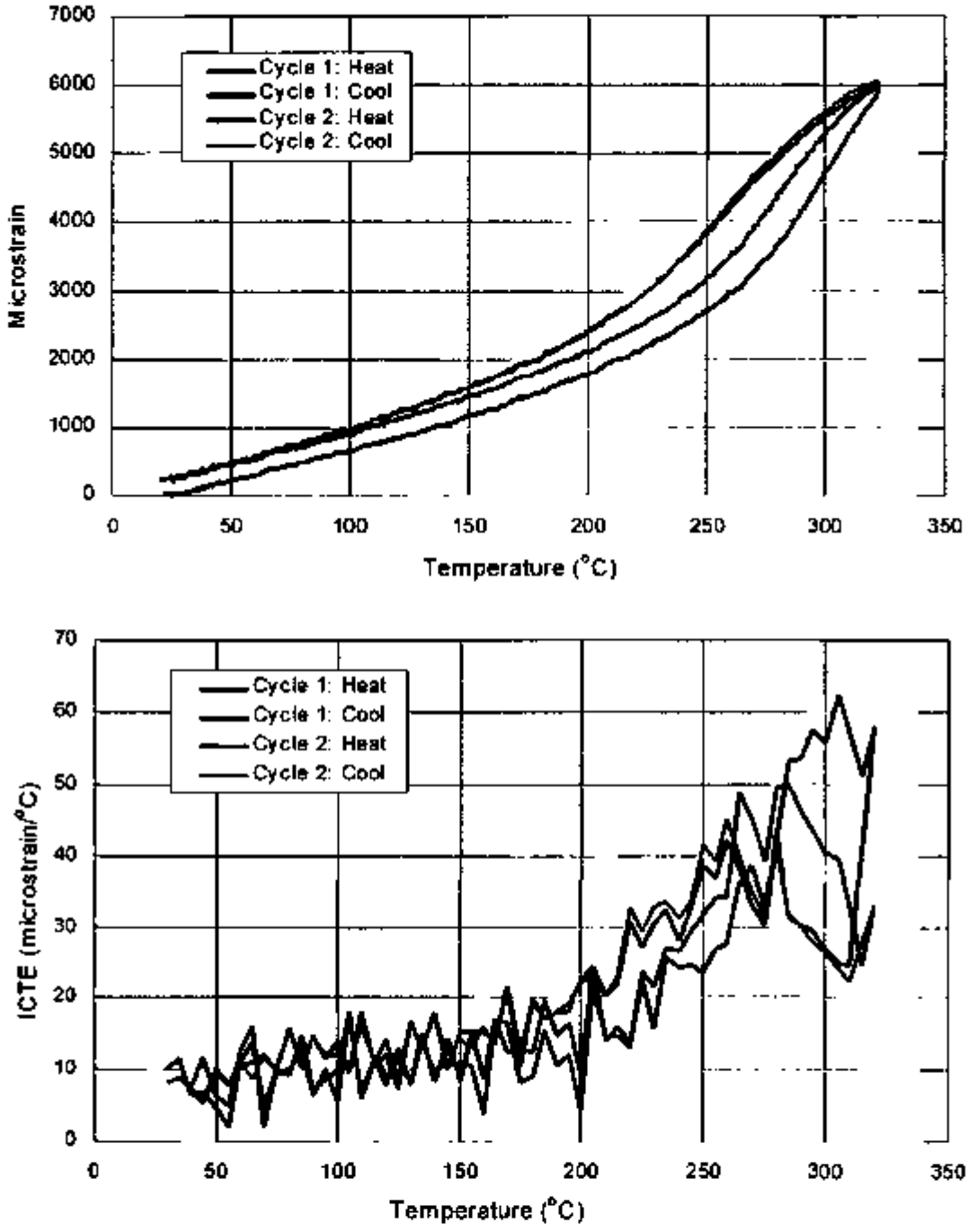

Figure C-3. Thermal Strain vs. Temperature (Top) and vs. Temperature (Bottom) for All Thermal Cycles Run on Specimen PTC1-B 19.0-B

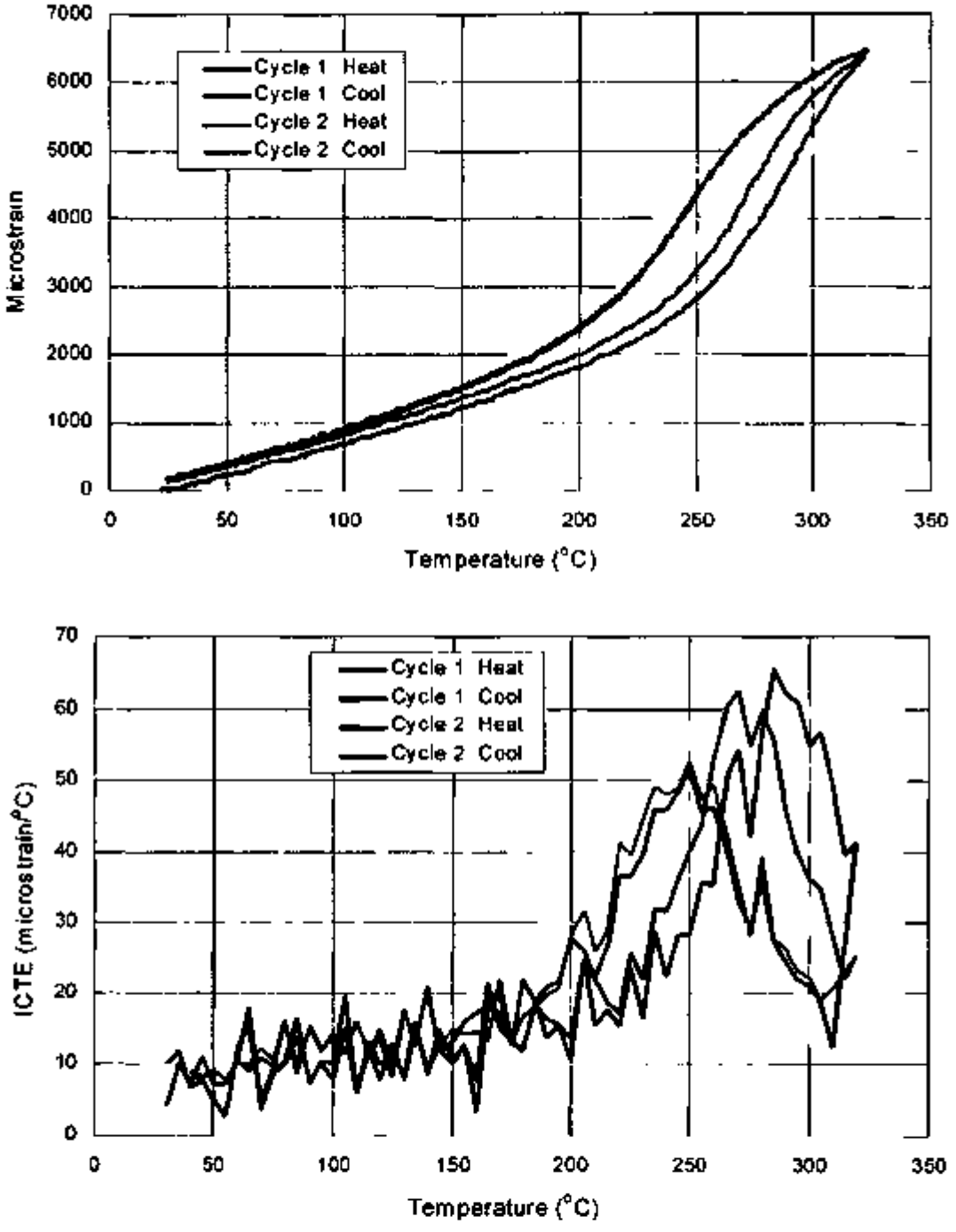

Figure C-4. Thermal Strain vs. Temperature (Top) and vs. Temperature (Bottom) for All Thermal Cycles Run on Specimen PTC2-B 4.1

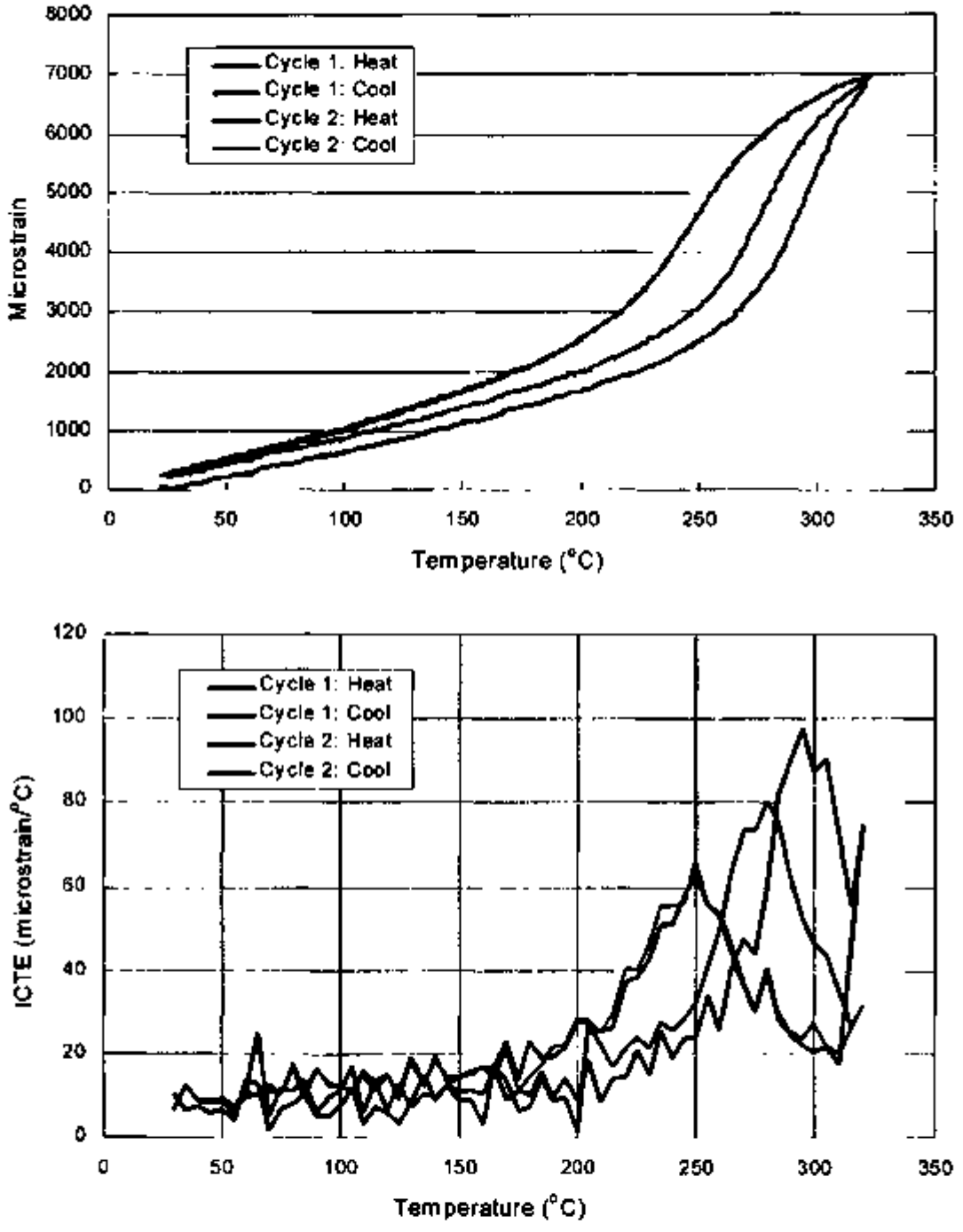

Figure C-5. Thermal Strain vs. Temperature (Top) and ICTE vs. Temperature (Bottom) for All Thermal Cycles Run on Specimen PTC4-A 4.6-B

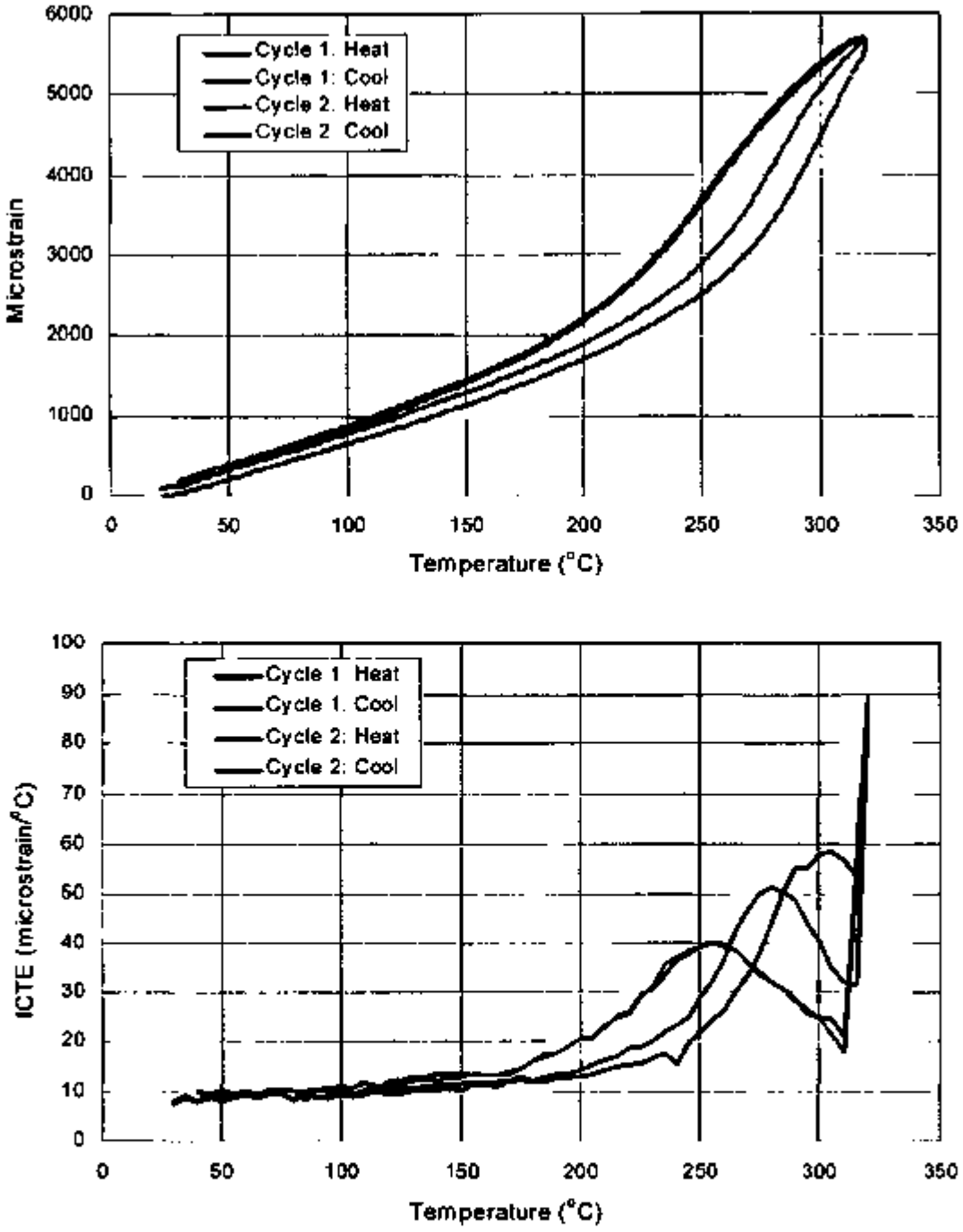

Figure C-6. Thermal Strain vs. Temperature (Top) and ICTE vs. Temperature (Bottom) for All Thermal Cycles Run on Specimen PTC4-A 19.0

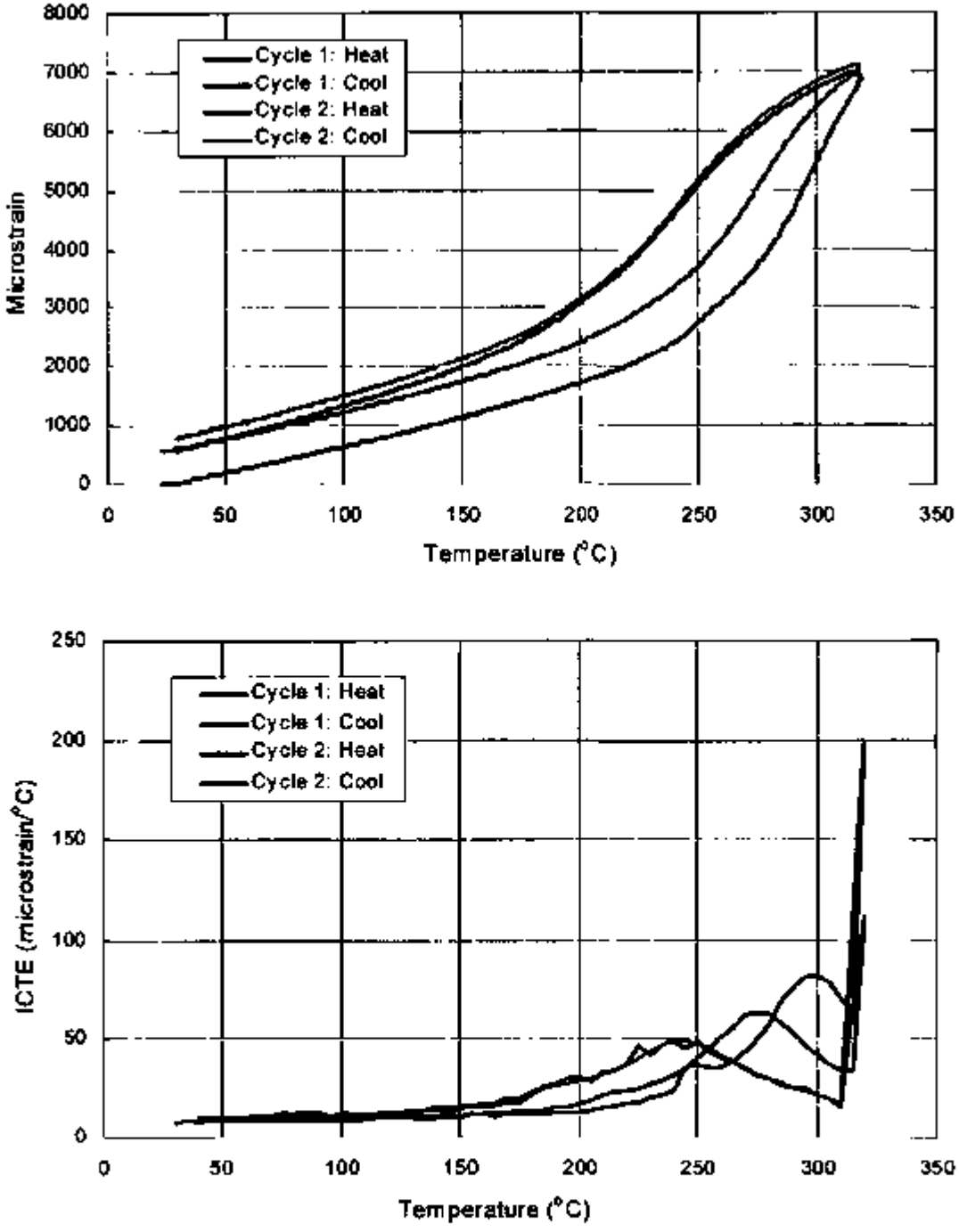

Figure C-7. Thermal Strain vs. Temperature (Top) and ICTE vs. Temperature (Bottom) for All Thermal Cycles Run on Specimen PTC4-B 6.8-B

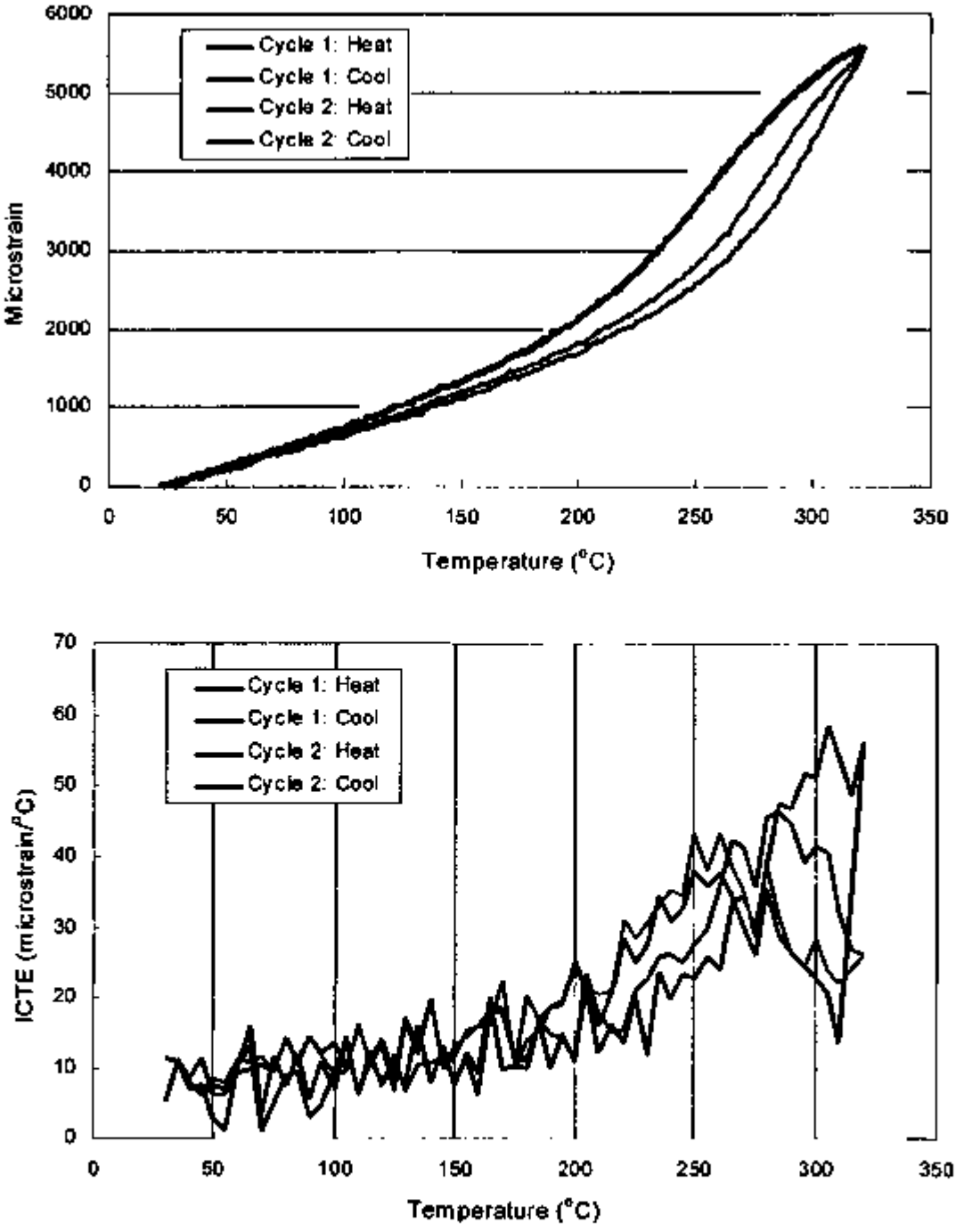

Figure C-8. Thermal Strain vs. Temperature (Top) and ICTE vs. Temperature (Bottom) for All Thermal Cycles Run on Specimen PTC4-B 14.8-B

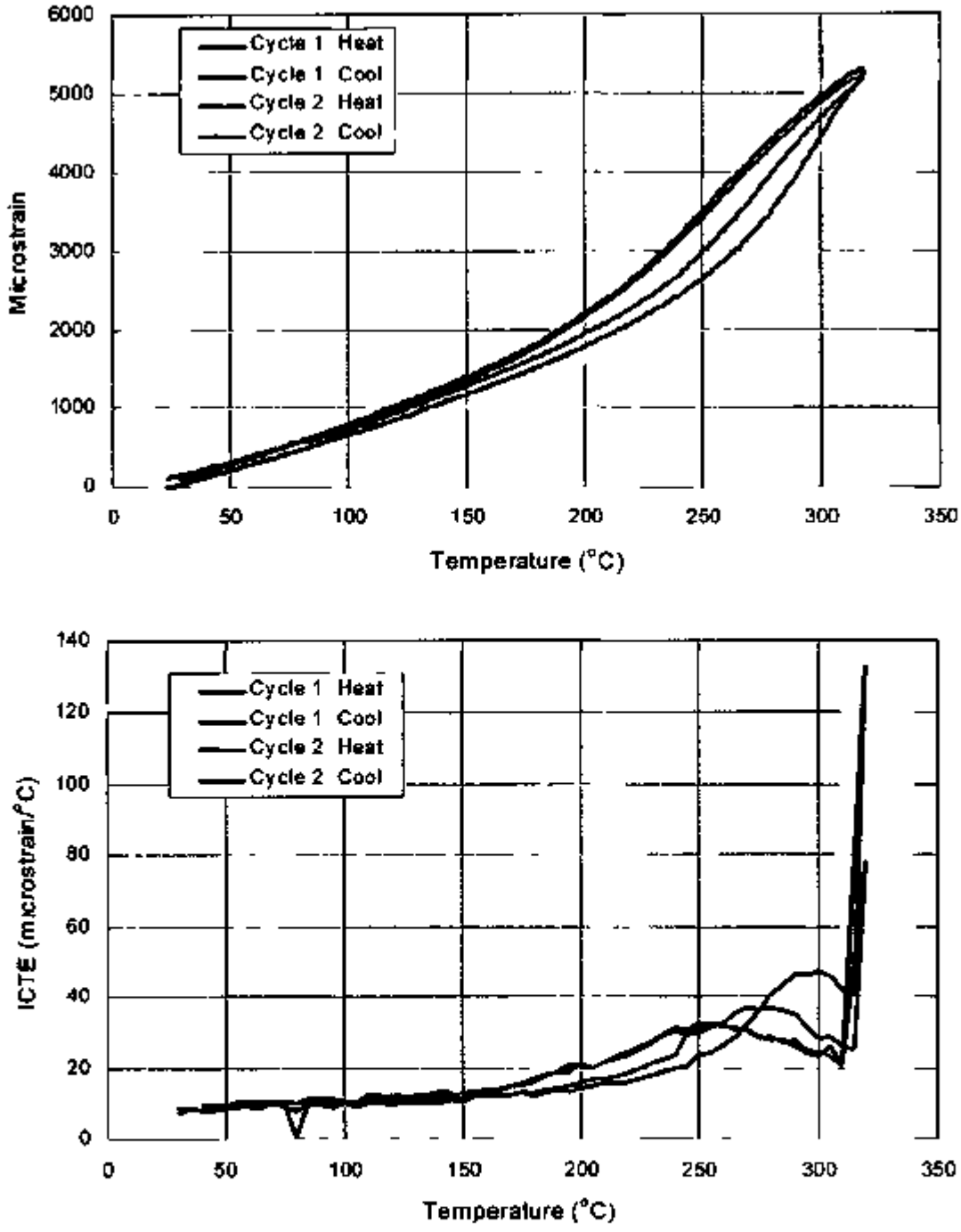

Figure C-9 Thermal Strain vs. Temperature (Top) and ICTE vs Temperature (Bottom) for All Thermal Cycles Run on Specimen PTC4-B 19 8-B

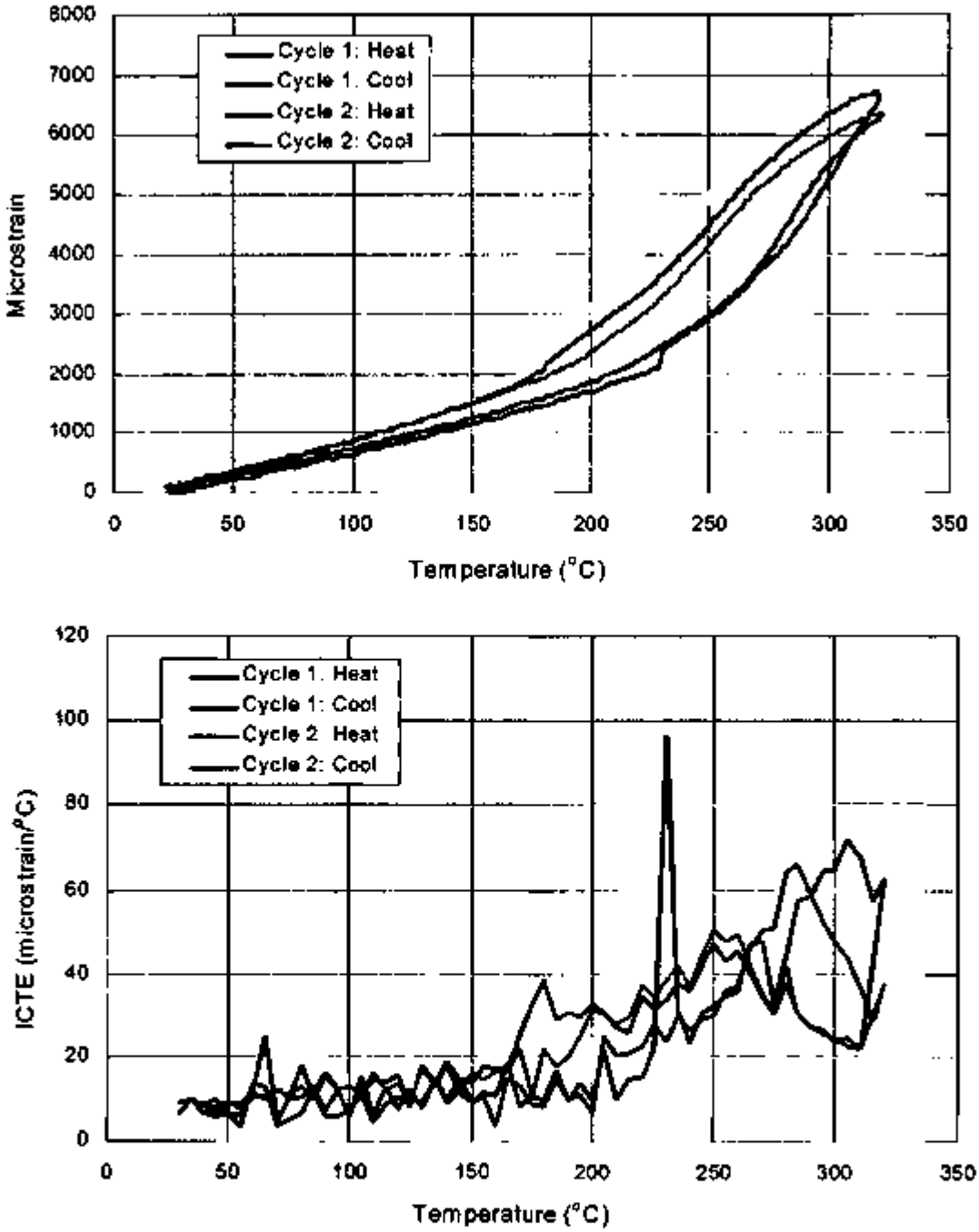

Figure C-10. Thermal Strain vs. Temperature (Top) and ICTE vs. Temperature (Bottom) for All Thermal Cycles Run on Specimen PTC5-B 4.1-B

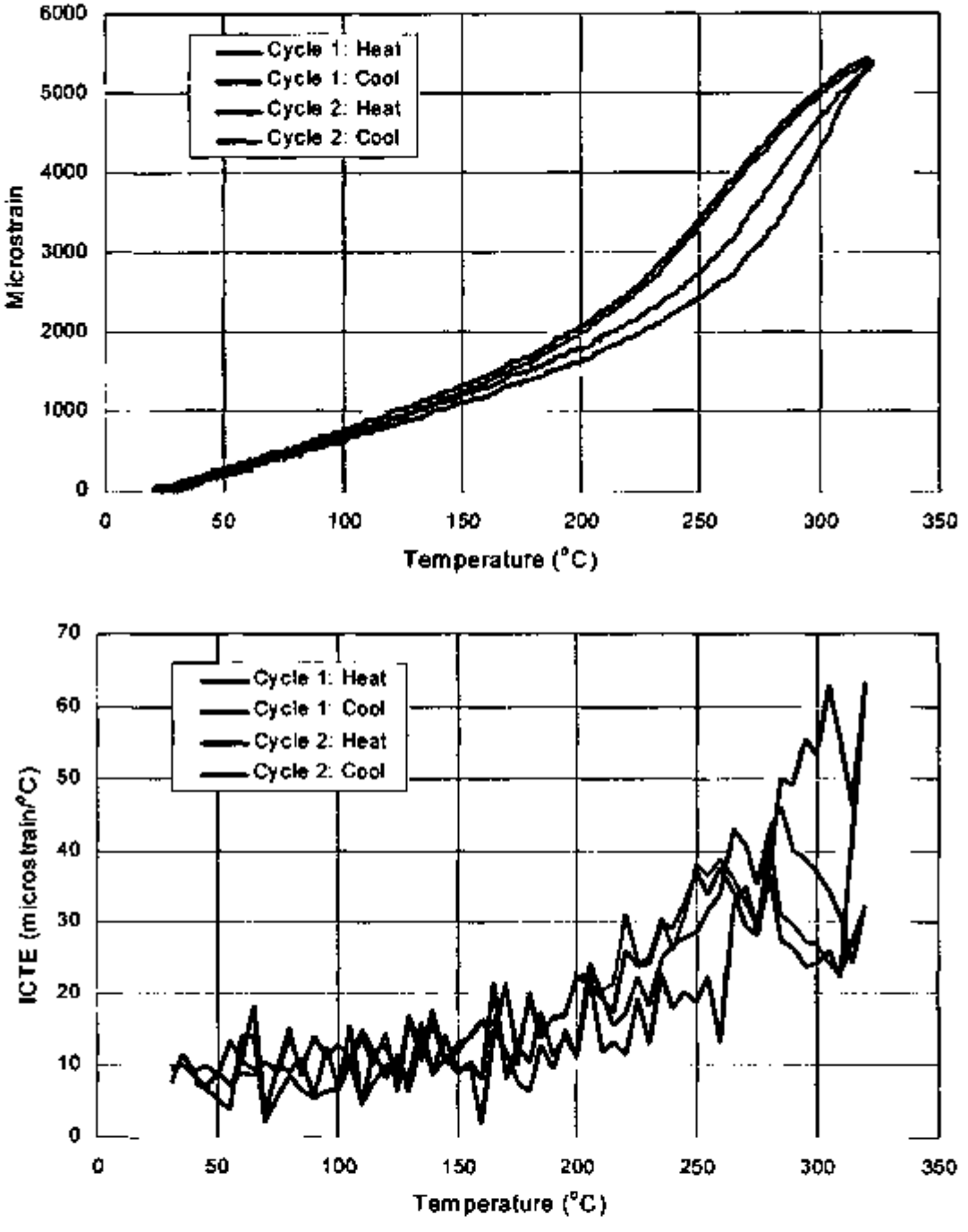

Figure C-11. Thermal Strain vs. Temperature (Top) and ICTE vs. Temperature (Bottom) for All Thermal Cycles Run on Specimen PTC5-B 24.4-B

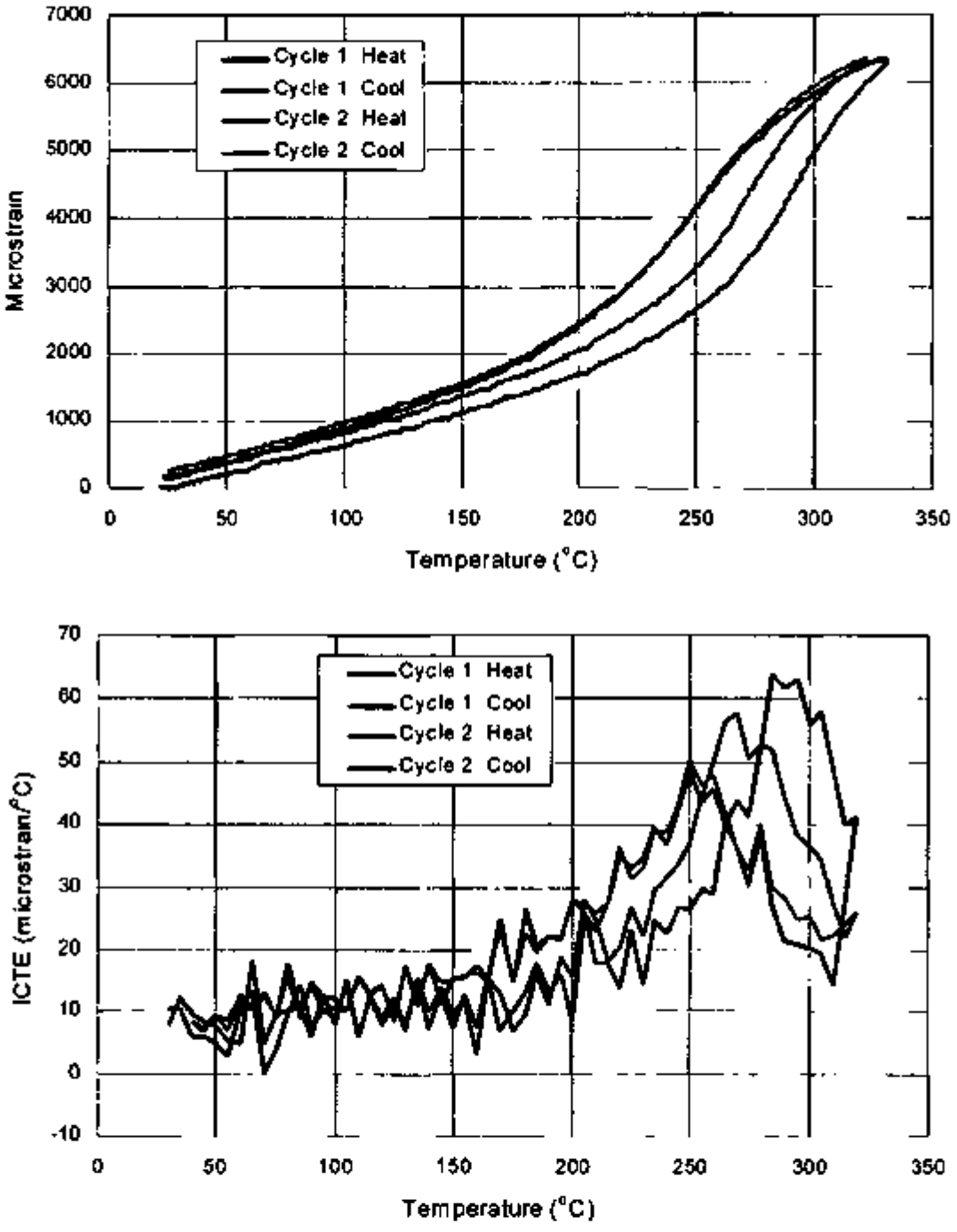

Figure C-12. Thermal Strain vs. Temperature (Top) and ICTE vs. Temperature (Bottom) for All Thermal Cycles Run on Specimen PTC5-B 24.4-C

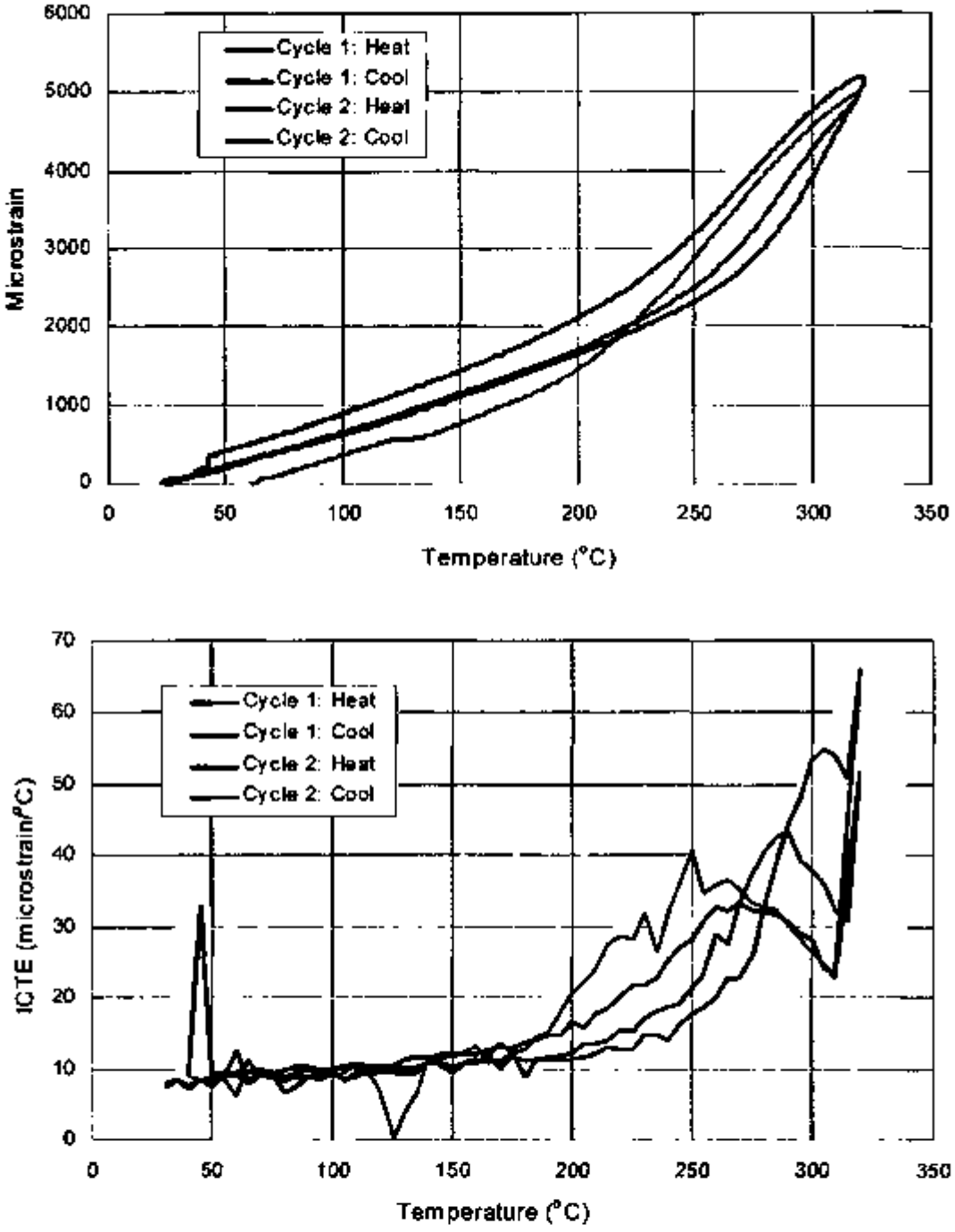

Figure C-13. Thermal Strain vs. Temperature (Top) and ICTE vs. Temperature (Bottom) for All Thermal Cycles Run on Specimen PTC H1-A 15.6-B

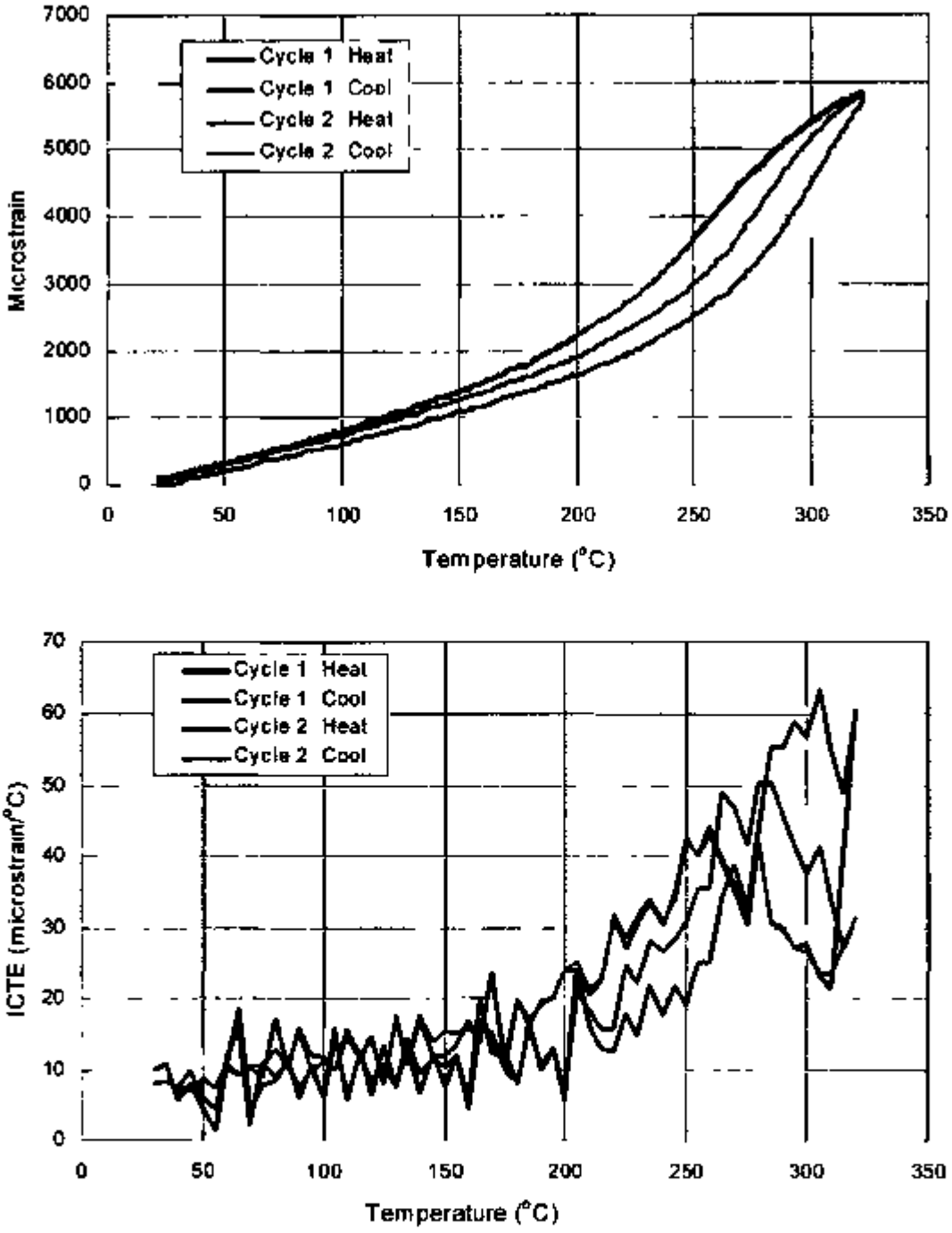

Figure C-14. Thermal Strain vs. Temperature (Top) and ICTE vs. Temperature (Bottom) for All Thermal Cycles Run on Specimen PTC MPBX1 14.2-B

APPENDIX D

PLOTS OF THERMAL EXPANSION COEFFICIENTS FOR TEST SUITE FOR FIRST COOLING, SECOND HEATING, AND SECOND COOLING

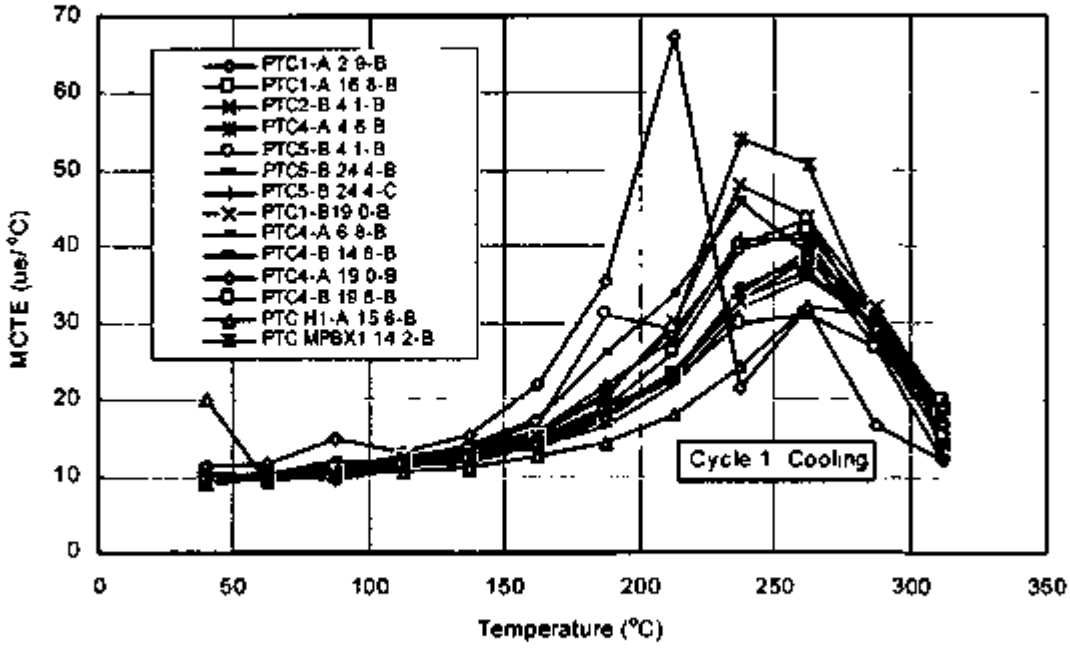

Figure D-1. MCTEs vs Temperature during First Cooling, Specimens Plotted Individually

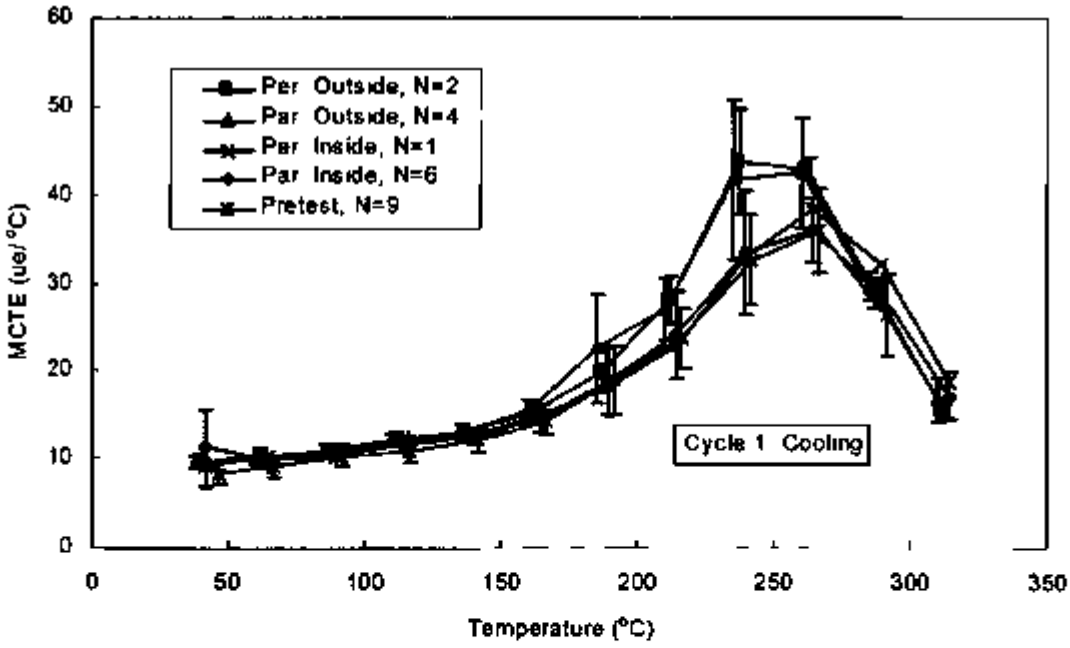

NOTE Pretest characterization data are also given Legend provides the number of specimens tested Error bars represent ± one standard deviation

Figure D-2 MCTEs vs. Temperature during First Cooling Grouped According to Orientation and Location with Respect to the 100°C Isotherm

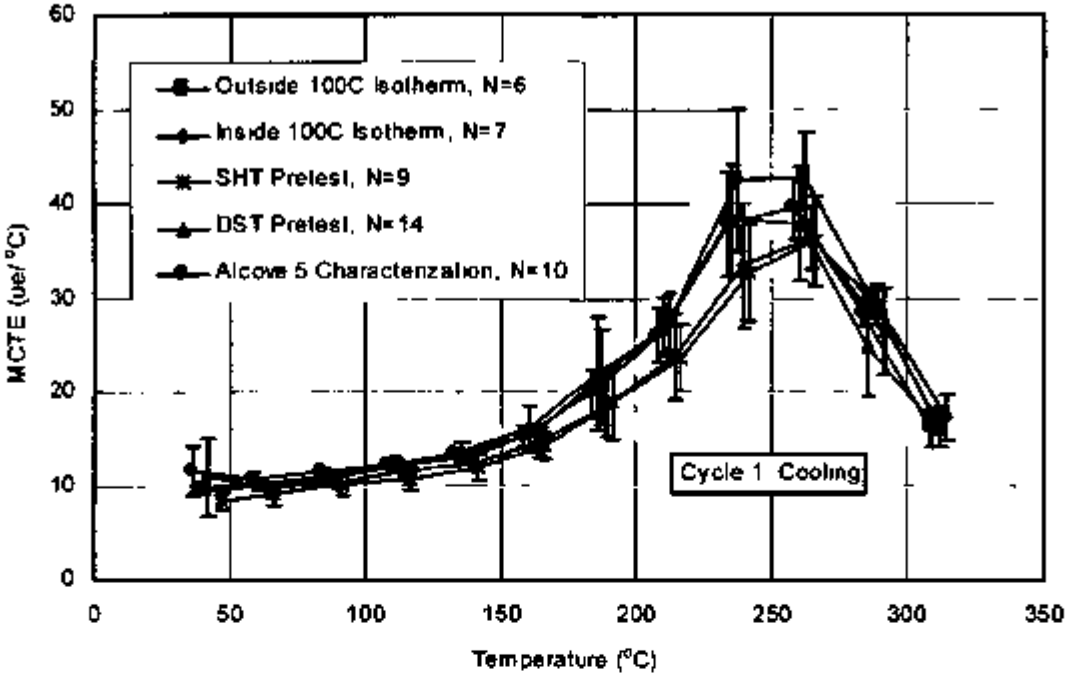

NOTE Legend provides the number of specimens tested Error bars represent ± one standard deviation

Figure D-3 MCTEs vs Temperature during First Cooling for All Alcove 5 Data Sets

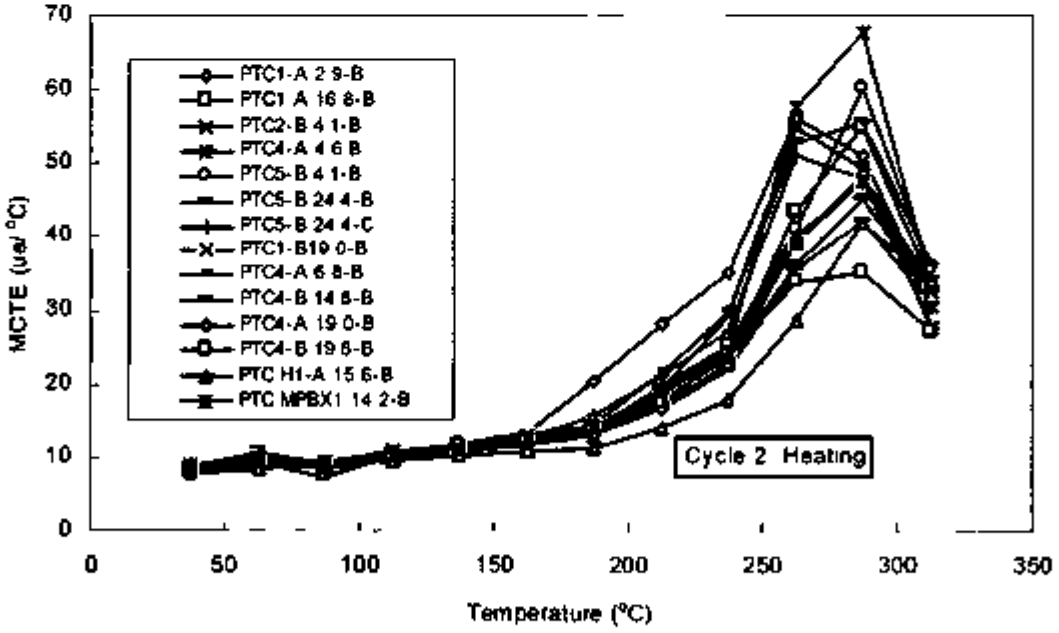

Figure D-4 MCTEs vs Temperature during Second Heating, Specimens Plotted Individually

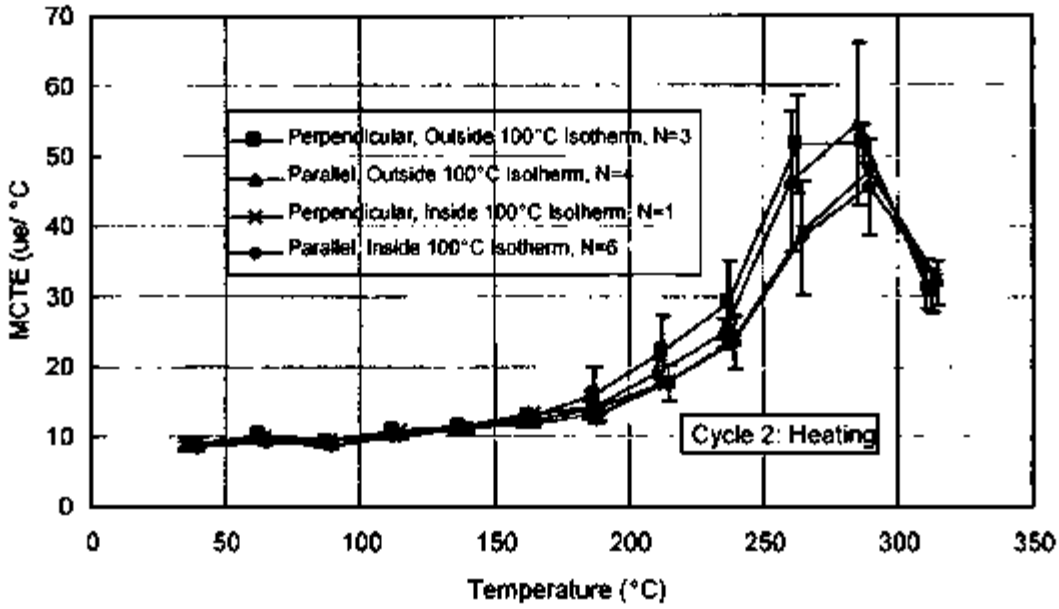

NOTE: Pretest characterization data are also given. Legend provides the number of specimens tested. Error bars represent ± one standard deviation.

Figure D-5. MCTEs vs. Temperature during Second Heating, Grouped According to Orientation and Location with Respect to the 100°C Isotherm

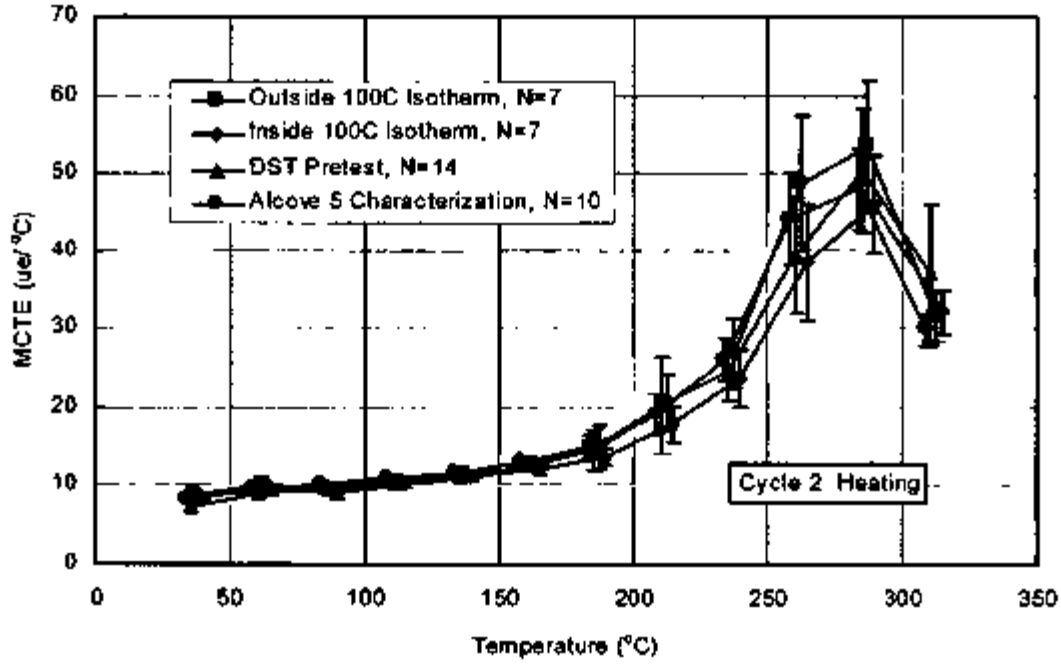

NOTE: Legend provides the number of specimens tested. Error bars represent ± one standard deviation.

Figure D-6. MCTEs vs. Temperature during Second Heating for All Alcove 5 Data Sets

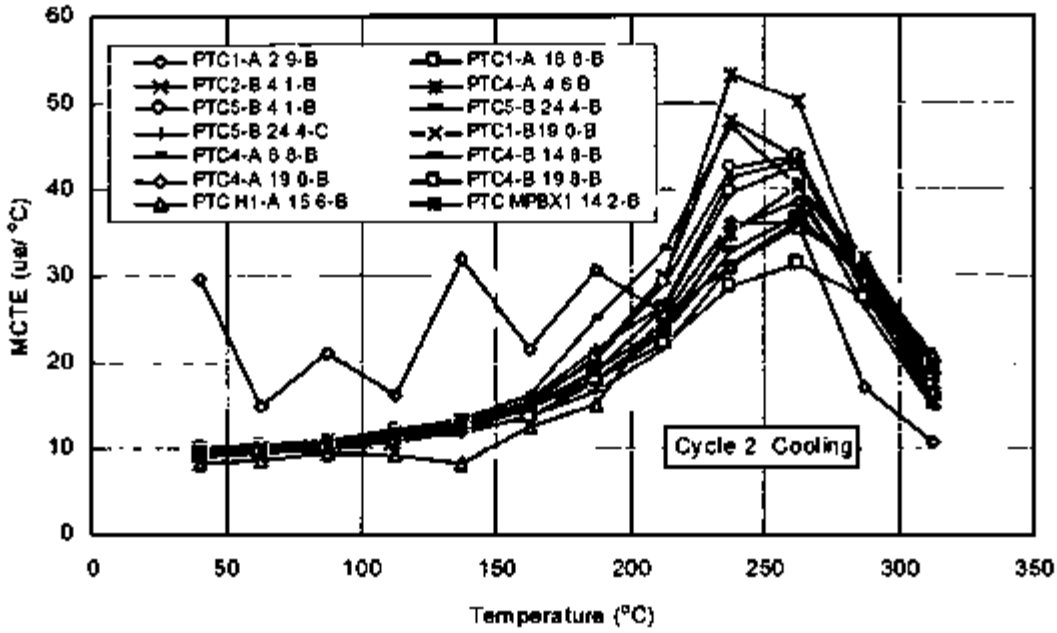

Figure D-7. MCTEs vs. Temperature during Second Cooling, Specimens Plotted Individually

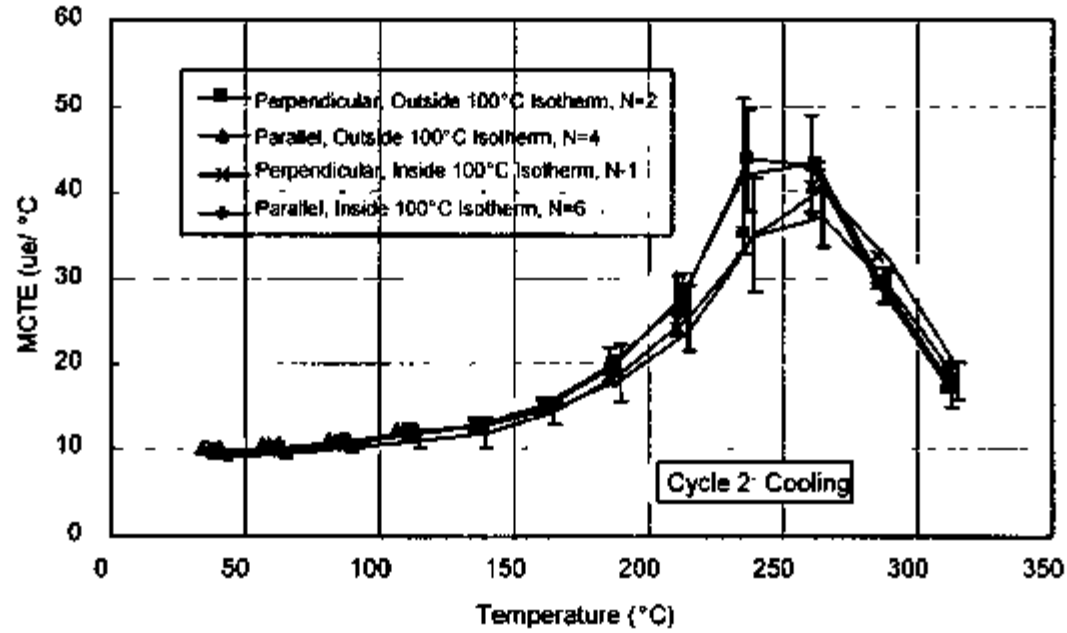

NOTE: Pretest characterization data are also given. Legend provides the number of specimens tested. Error bars represent ± one standard deviation.

Figure D-8. MCTEs vs. Temperature during Second Cooling, Grouped According to Orientation and Location with Respect to the 100°C Isotherm

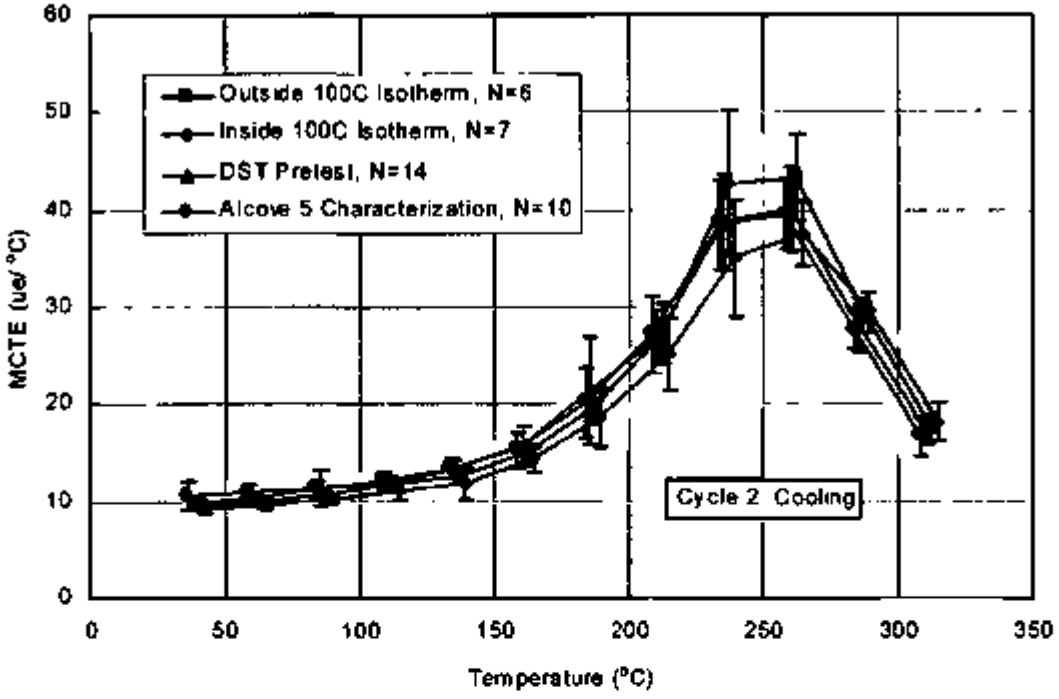

NOTE Legend provides the number of specimens tested Error bars represent ± one standard deviation.

Figure D-9. MCTEs vs. Temperature during Second Cooling for All Alcove 5 Data Sets

INTENTIONALLY LEFT BLANK

APPENDIX E

STRESS-STRAIN CURVES FOR ALL UNCONFINED COMPRESSION TESTS

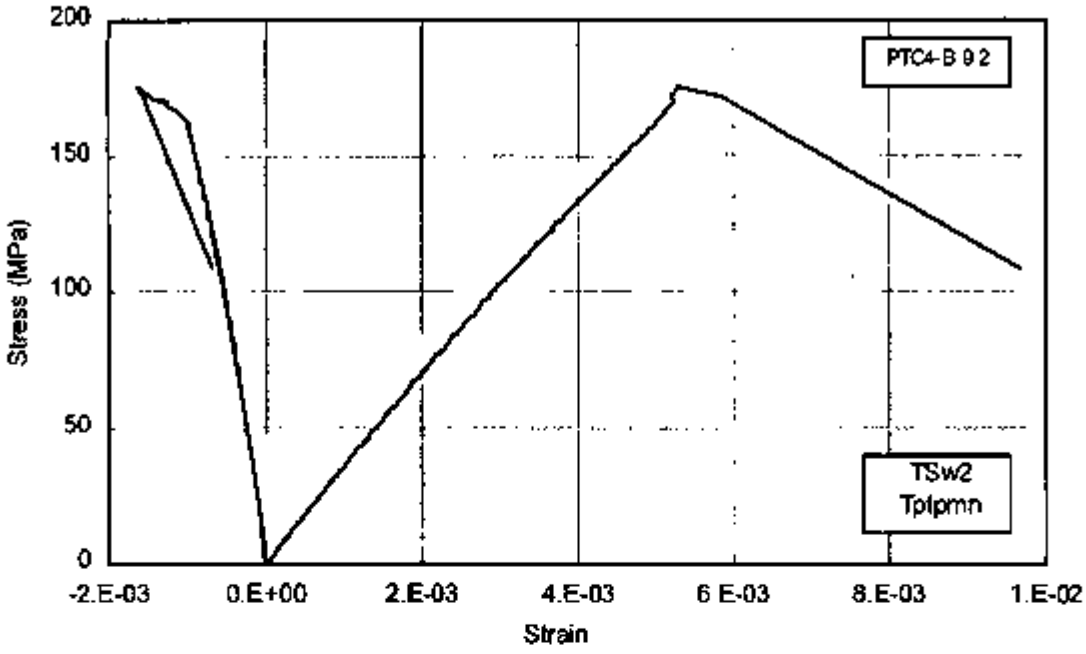

NOTE: Compressional strains (axial) are positive; extensional strains (lateral) are negative. Specimen is from TSw2 thermomechanical unit and Tptpmn lithostratigraphic unit.

Figure E-1. Stress-Strain Curves for Test SHTUC02 on Specimen PTC4-B 9.2

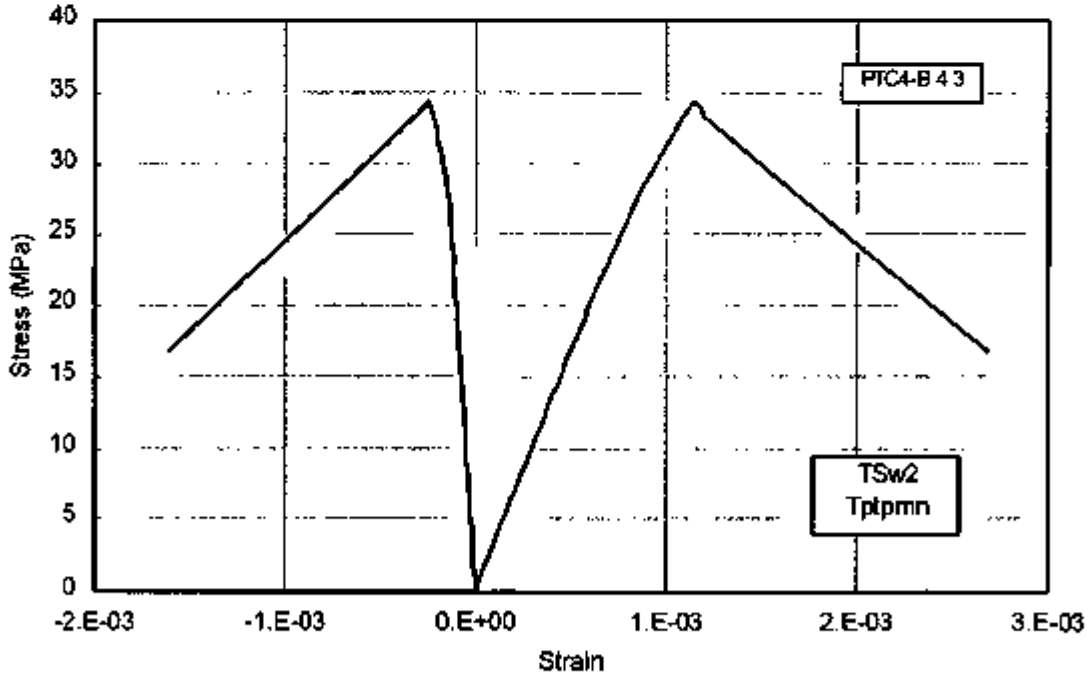

NOTE: Compressional strains (axial) are positive; extensional strains (lateral) are negative. Specimen is from TSw2 thermomechanical unit and Tptpmn lithostratigraphic unit.

Figure E-2. Stress-Strain Curves for Test SHTUC03 on Specimen PTC4-B 4.3

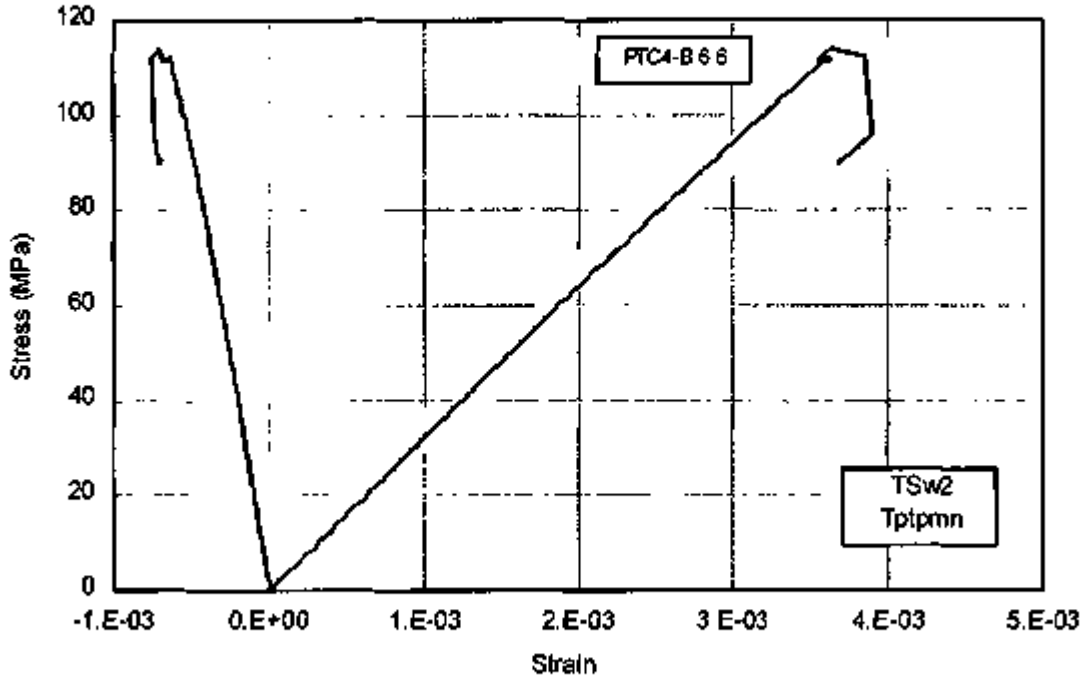

NOTE: Compressional strains (axial) are positive; extensional strains (lateral) are negative. Specimen is from TSw2 thermomechanical unit and Tptpmn lithostratigraphic unit.

Figure E-3. Stress-Strain Curves for Test SHTUC04 on Specimen PTC4-B 6.6

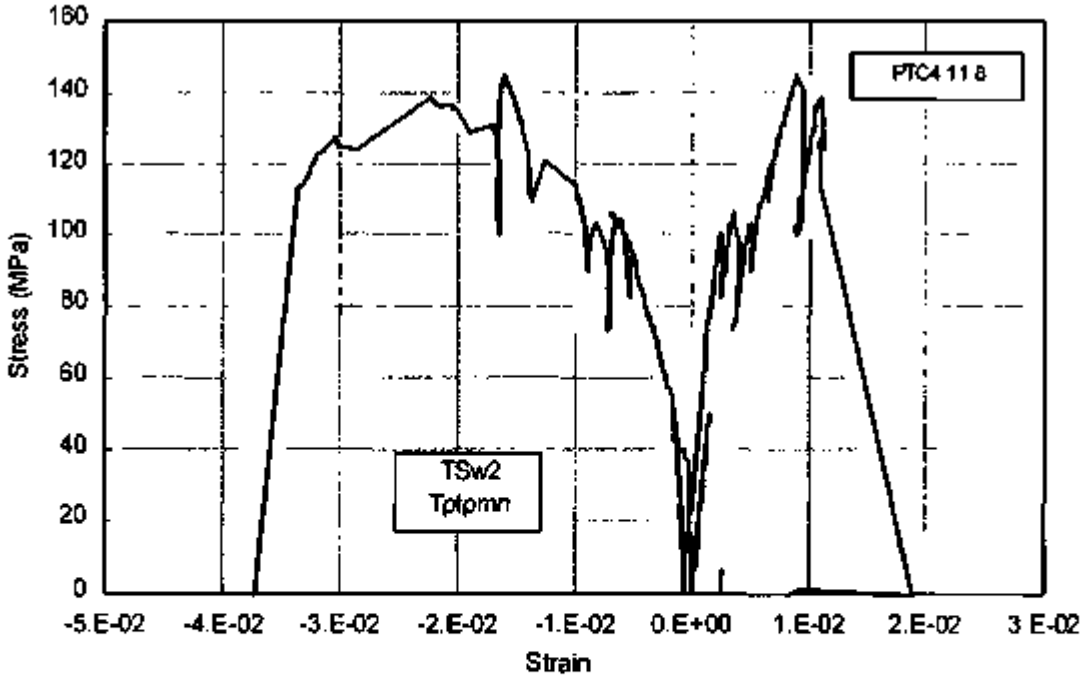

NOTE: Compressional strains (axial) are positive; extensional strains (lateral) are negative Specimen is from TSw2 thermomechanical unit and Tptpmn lithostratigraphic unit.

Figure E-4. Stress-Strain Curves for Test SHTUC05 on Specimen PTC4-B 11 8

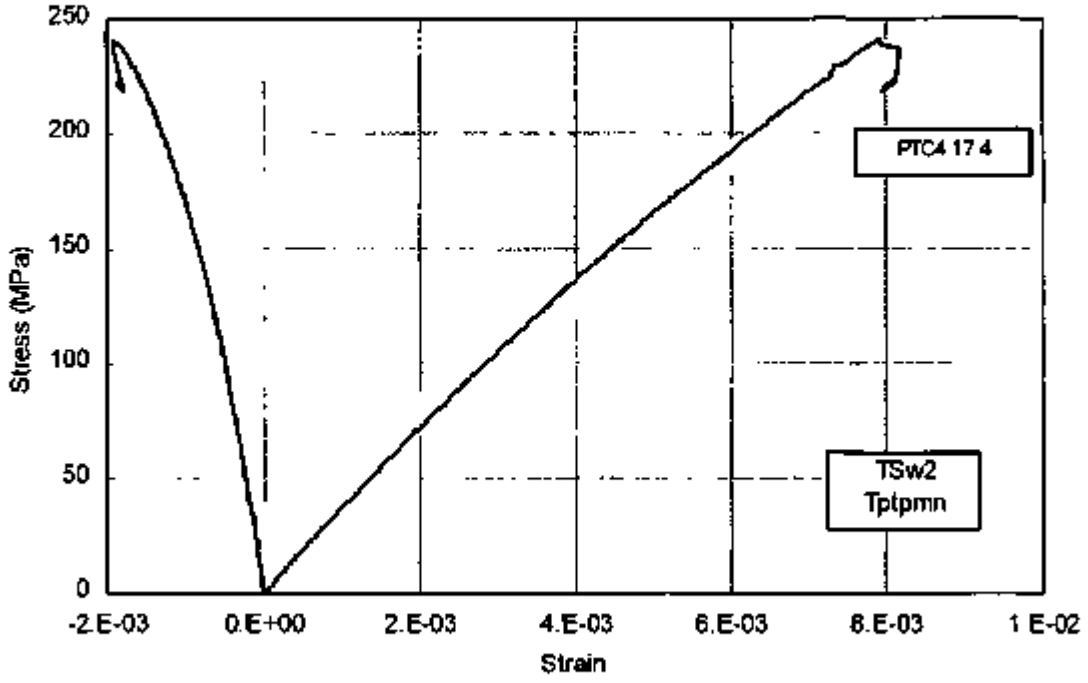

NOTE: Compressional strains (axial) are positive; extensional strains (lateral) are negative. Specimen is from TSw2 thermomechanical unit and Tptpmn lithostratigraphic unit.

Figure E-5. Stress-Strain Curves for Test SHTUC06 on Specimen PTC4-B 17.4

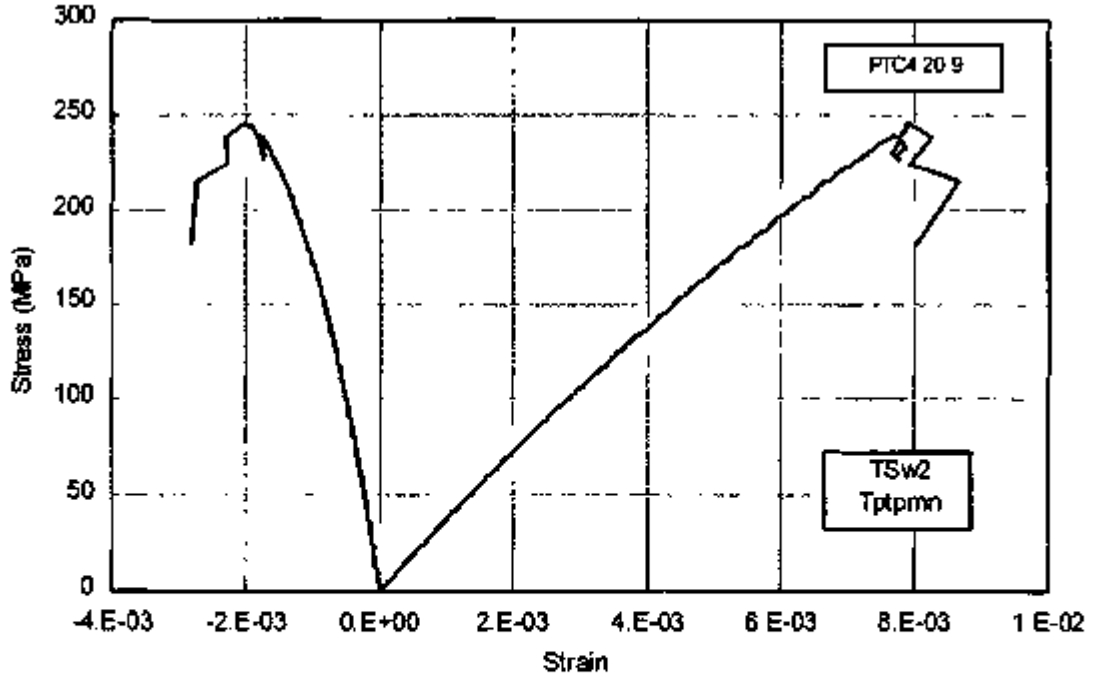

NOTE: Compressional strains (axial) are positive; extensional strains (lateral) are negative. Specimen is from TSw2 thermomechanical unit and Tptpmn lithostratigraphic unit

Figure E-6. Stress-Strain Curves for Test SHTUC07 on Specimen PTC4-B 20.9

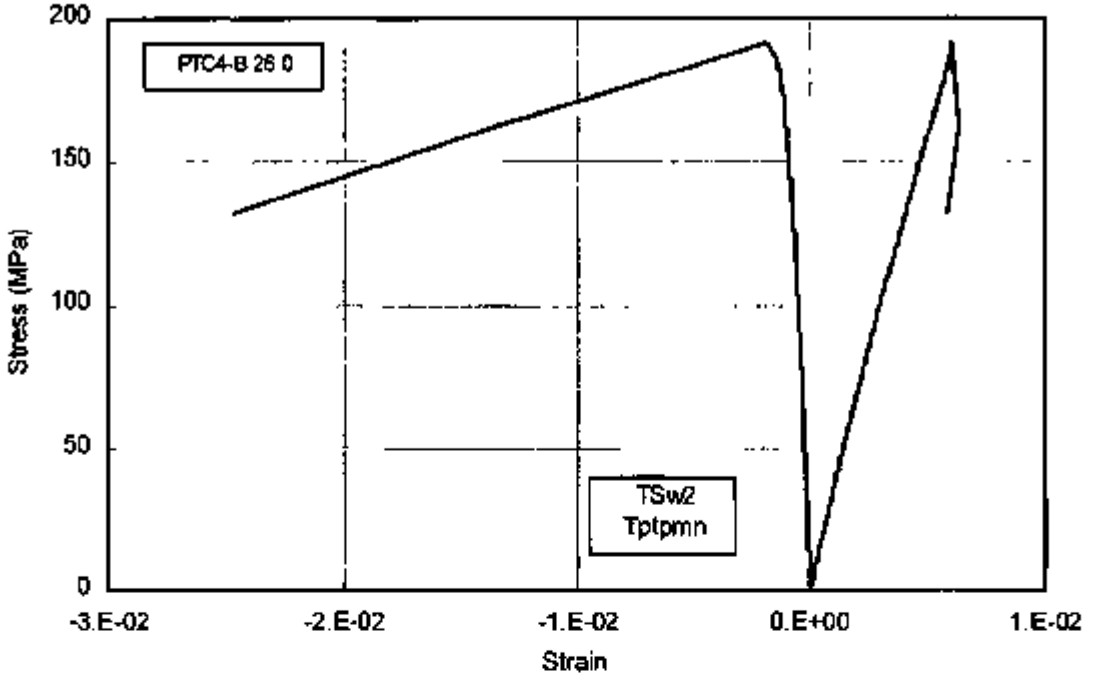

NOTE: Compressional strains (axial) are positive; extensional strains (lateral) are negative. Specimen is from TSw2 thermomechanical unit and Tptpmn lithostratigraphic unit.

Figure E-7. Stress-Strain Curves for Test SHTUC08 on Specimen PTC4-B 26.0

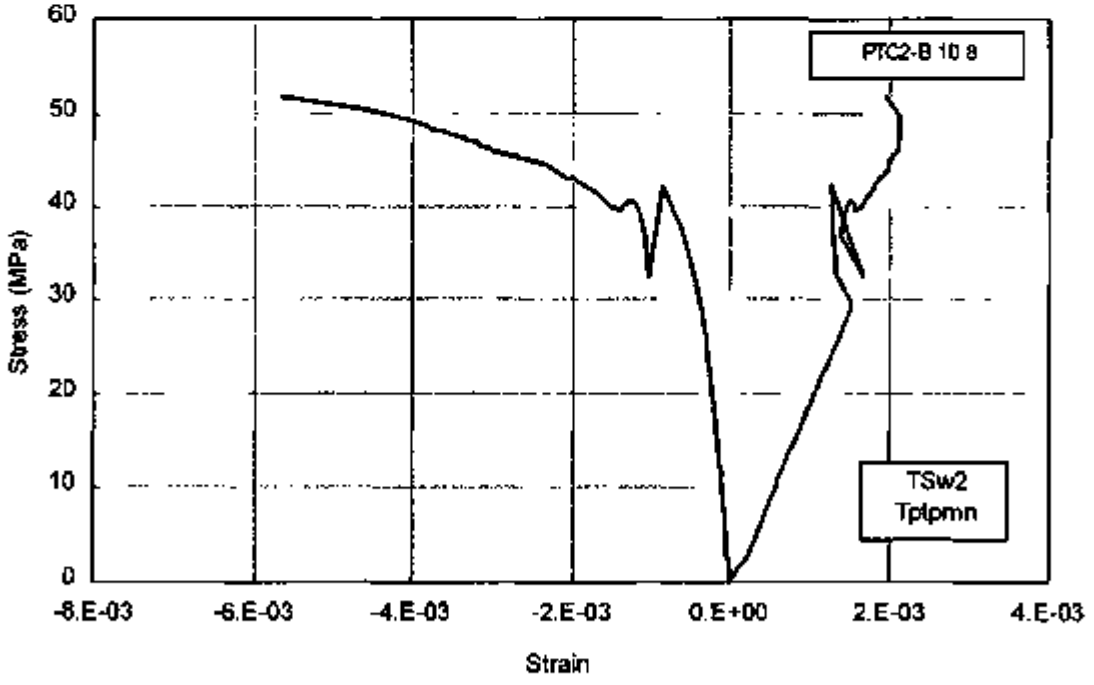

NOTE: Compressional strains (axial) are positive; extensional strains (lateral) are negative. Specimen is from TSw2 thermomechanical unit and Tptpmn lithostratigraphic unit.

Figure E-8. Stress-Strain Curves for Test SHTUC09 on Specimen PTC2-B 10.8

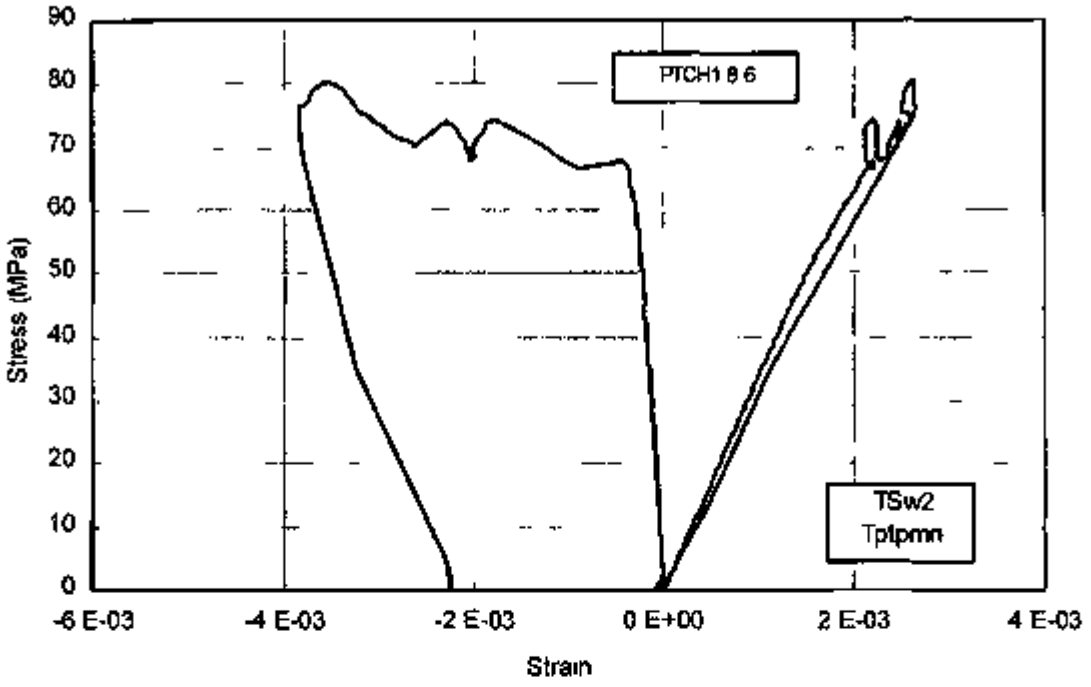

NOTE Compressional strains (axial) are positive, extensional strains (lateral) are negative Specimen is from TSw2 thermomechanical unit and Tptpmn lithostratigraphic unit

Figure E-9 Stress-Strain Curves for Test SHTUC10 on Specimen PTCH1 8 6

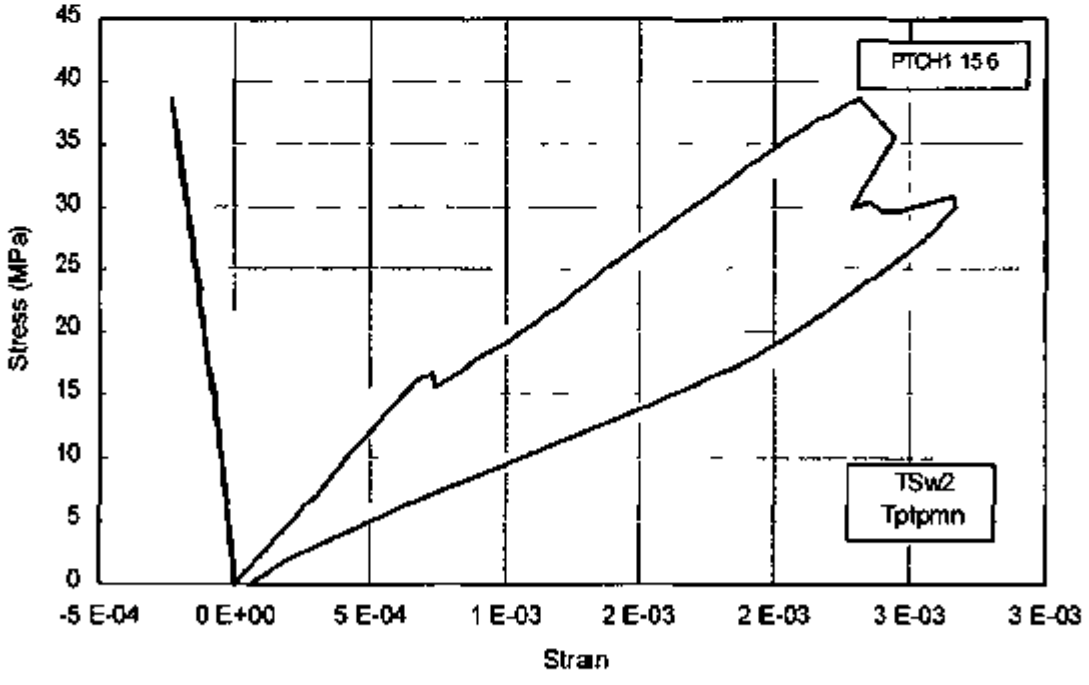

NOTE Compressional strains (axial) are positive, extensional strains (lateral) are negative Specimen is from TSw2 thermomechanical unit and Tptpmn lithostratigraphic unit

Figure E-10 Stress-Strain Curves for Test SHTUC11 on Specimen PTCH1 15 6

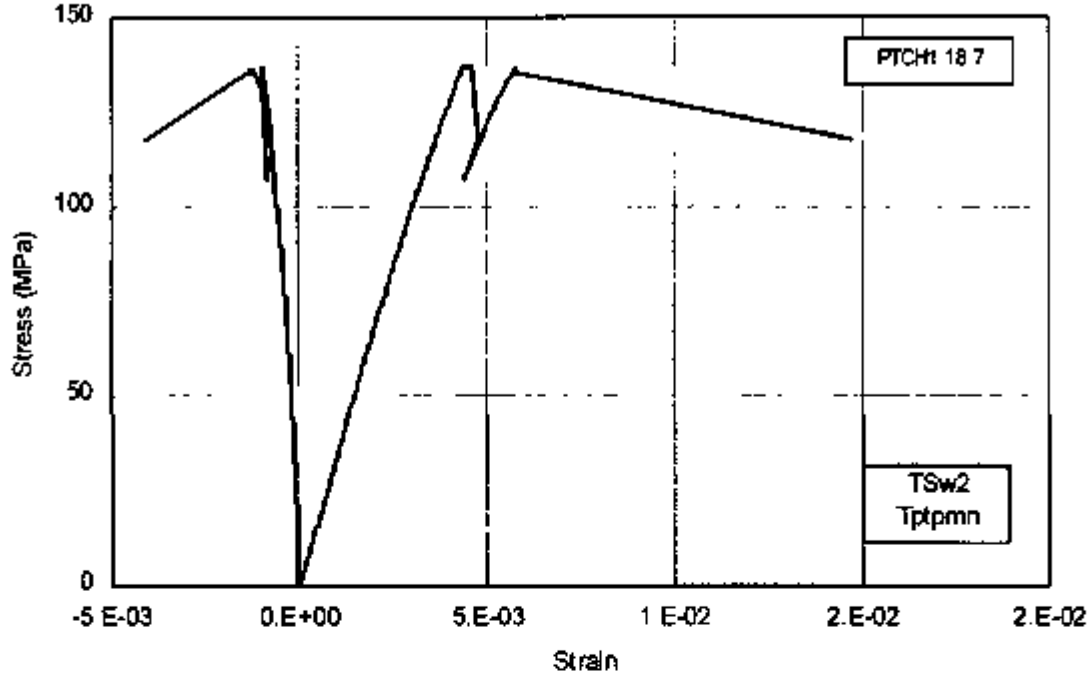

NOTE: Compressional strains (axial) are positive; extensional strains (lateral) are negative. Specimen is from TSw2 thermomechanical unit and Tptpmn lithostratigraphic unit.

Figure E-11. Stress-Strain Curves for Test SHTUC13 on Specimen PTCH1 18.7

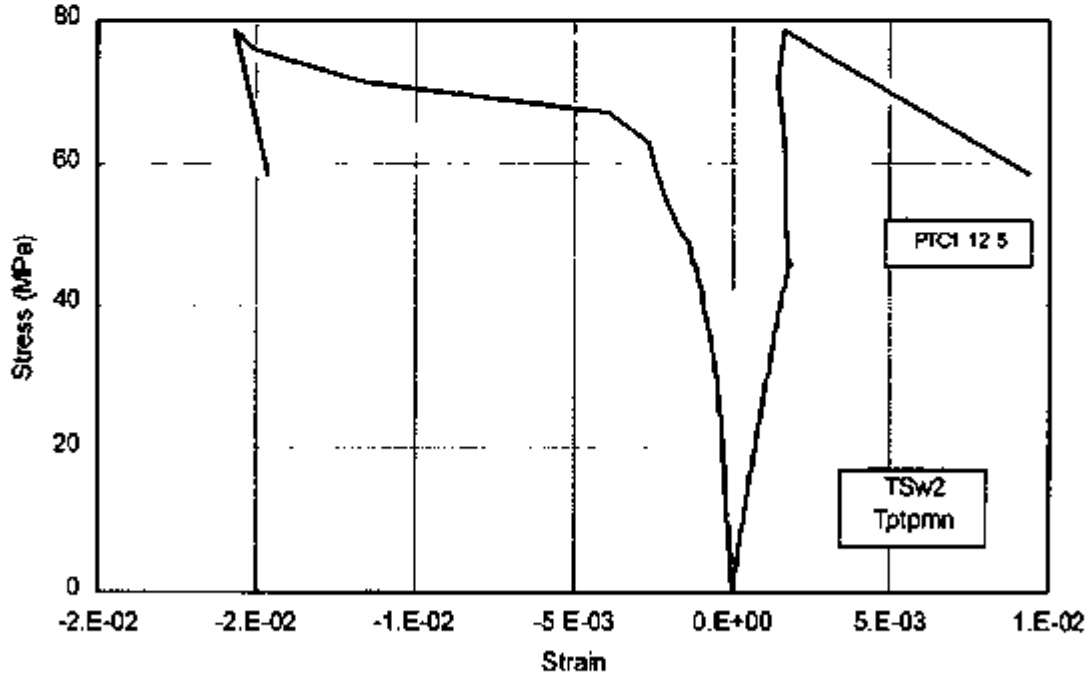

NOTE: Compressional strains (axial) are positive; extensional strains (lateral) are negative. Specimen is from TSw2 thermomechanical unit and Tptpmn lithostratigraphic unit.

Figure E-12. Stress-Strain Curves for Test SHTUC14 on Specimen PTC1 12.5

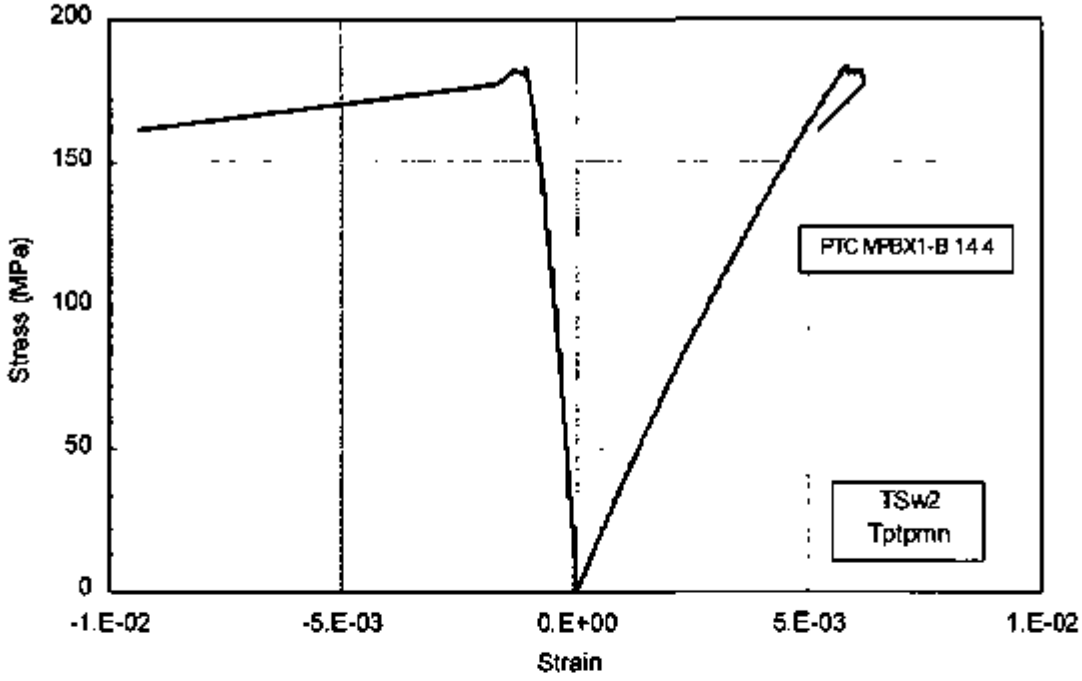

NOTE. Compressional strains (axial) are positive; extensional strains (lateral) are negative. Specimen is from TSw2 thermomechanical unit and Tptpmn lithostratigraphic unit.

Figure E-13. Stress-Strain Curves for Test SHTUC15 on Specimen PTC MPBX1-B 14.4

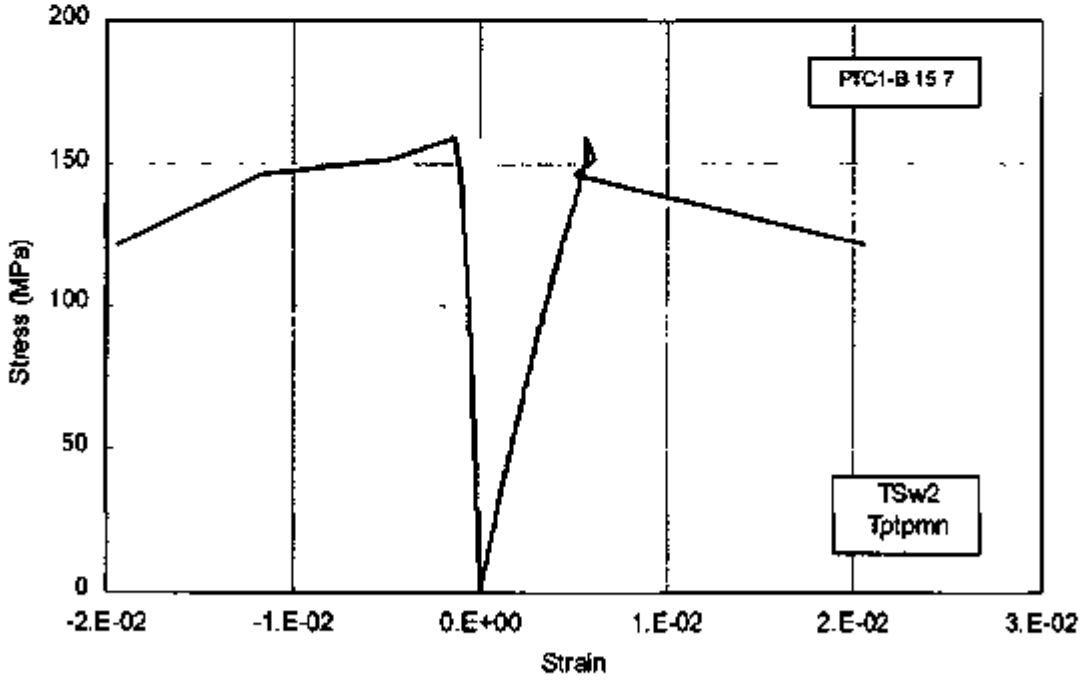

NOTE: Compressional strains (axial) are positive; extensional strains (lateral) are negative Specimen is from TSw2 thermomechanical unit and Tptpmn lithostratigraphic unit.

Figure E-14. Stress-Strain Curves for Test SHTUC16 on Specimen PTC1-B 15 7

INTENTIONALLY LEFT BLANK

APPENDIX F

THERMAL-MECHANICAL GAGE SPECIFICATIONS FOR THE SHT

Table F-1. Summary of SNL-Installed Measurement System Specifications

Measurement System	Manufacturer	Gage Accuracy, Range & Precision	Comments
Type-K Thermocouples	STI (probes) Omega	±2.2°C max 1260°C	Chromel-Alumel
Vibrating Wire Displacement Transducers	Geokon	1 in. full range Resolution: .02%	
High-Temp LVDT	RDP	±0.5% of full range = ±19 mm @200°C	
Wire Extensometer	Houston Scientific, Inc.	0.1% resolution 2-in. range	
Vibrating Wire Load Cell	Geokon	60,000 lb max ±0.5% full range	
Tape Extensometer	Geokon	±0.127 mm	
Goodman Jack -Readout Box -Near LVDT -Far LVDT -Pressure Gage -Enerpak Pump	Sinco	0–10,000 psi -0.25 to +0.25 in. displacement	
Power Monitor	Magtrol	Volts (0.2% of reading +0.2% of range) 0–600 volts Amps (0.22% of reading +0.25% of range) 0–50 amps watts (0.2% of reading +0.3% of range)	
Thermistors	Omega	±0.2°C 100°C range	

Note: Additional gage information can be found in the SNL Scientific Notebook covering this work.

INTENTIONALLY LEFT BLANK

APPENDIX G

AS-BUILT GAGE LOCATIONS AND SELECTED DATA

As-built Gage Locations and Data Selected

The gage locations presented in this appendix are identified by a unique designation based on borehole (if used), gage type, and gage location along the hole. In all cases the gage identification for the SHT begins with "TMA," which stands for Thermomechanical Alcove (the location of the SHT). This is followed by the borehole ID and number as follows:

H-1	=	Heater borehole
TC-1 through TC-7	=	Thermocouple borehole
BX-1 through BX-4	=	MPBX borehole
WX-1 through WX-6	=	Wire extensometer station pins
WXM-1 through WXM-6	=	Wire extensometer manual pins (tape extensometer)
RBLC-1 through RBLC-8	=	Rock bolt boreholes
STC	=	Surface Thermocouple (on rock surface)
IN-THRM	=	Insulation Thermistor
TEMP	=	Temperature data from hydrology boreholes in which RTDs were used to measure temperature
TCT	=	Thermocouple top (of heater)
TCS	=	Thermocouple side (of heater)
TCB	=	Thermocouple bottom (of heater)
RTD	=	Resistance Temperature Device

The gage numbers follow at the end of the designation. Exceptions are the RTD and Temp gages in which the gage type precedes the LANL-TCO borehole number and are of the form TMA-RTD-15-1, where RTD is the gage type, 15 is the borehole number, and 1 is the unique gage number.

The "as-built" gage locations (x, y, z coordinates) for all gages presented in Appendix G have been submitted as QA records in TDIF 305721 (DTN: SNF35110695001.001) (SNL 1996) *with the exception of RTD and TEMP gages*. RTD and TEMP gage locations are the responsibility of LLNL.

Table G-1. Selected Heater Power in Watts Obtained from the Heater Power Gage

Gage	Location				Days After Startup		
	x	y	z	r	0	275	490
TMA-HEATER-POWER	0	0	0	0	16.88	3725.75	0

Table G-2. Selected Temperature Data Obtained from the SHT Block

Gage	Location				Temperature, °C		
	x	y	z	r	0	275	490
TMA-H-1-TCT-1	-0.008	6.970	0.048	0.049	24.11	299.98	NA
TMA-H-1-TCT-2	-0.007	6.470	0.046	0.047	24.33	346.70	NA
TMA-H-1-TCT-3	-0.007	5.970	0.045	0.046	24.08	362.93	NA
TMA-H-1-TCT-4	-0.006	5.470	0.043	0.043	23.69	384.53	NA
TMA-H-1-TCT-5	-0.005	4.470	0.040	0.040	23.64	390.64	NA
TMA-H-1-TCT-6	-0.004	3.470	0.037	0.037	23.56	364.79	NA
TMA-H-1-TCT-7	-0.003	2.970	0.035	0.035	23.66	368.71	NA
TMA-H-1-TCT-8	-0.003	2.470	0.033	0.033	23.81	336.41	NA
TMA-H-1-TCT-9	-0.002	1.970	0.032	0.032	23.79	217.58	NA
TMA-H-1-TCS-1	-0.041	6.970	0.002	0.041	23.34	299.01	NA
TMA-H-1-TCS-2	-0.040	6.470	0.000	0.040	23.76	338.18	NA
TMA-H-1-TCS-3	-0.040	5.970	-0.001	0.040	23.86	367.10	NA
TMA-H-1-TCS-4	-0.039	5.470	-0.003	0.039	23.79	375.17	NA
TMA-H-1-TCS-5	-0.038	4.470	-0.006	0.038	23.66	385.36	NA
TMA-H-1-TCS-6	-0.037	3.470	-0.009	0.038	23.79	363.00	NA
TMA-H-1-TCS-7	-0.036	2.970	-0.011	0.038	23.76	361.98	NA
TMA-H-1-TCS-8	-0.036	2.470	-0.013	0.038	23.79	333.09	NA
TMA-H-1-TCS-9	-0.035	1.970	-0.014	0.038	23.79	203.17	NA
TMA-H-1-TCB-1	-0.008	6.970	-0.019	0.021	23.76	297.75	NA
TMA-H-1-TCB-2	-0.007	6.470	-0.021	0.022	23.84	345.07	NA
TMA-H-1-TCB-3	-0.007	5.970	-0.022	0.023	24.28	361.38	NA
TMA-H-1-TCB-4*	-0.006	5.470	-0.024	0.025	24.11	NA	NA
TMA-H-1-TCB-5	-0.005	4.470	-0.027	0.027	23.56	382.56	NA
TMA-H-1-TCB-6	-0.004	3.470	-0.030	0.030	23.76	367.31	NA
TMA-H-1-TCB-7	-0.003	2.970	-0.032	0.032	23.71	362.07	NA
TMA-H-1-TCB-8	-0.003	2.470	-0.034	0.034	23.69	343.04	NA
TMA-H-1-TCB-9	-0.002	1.970	-0.035	0.035	23.76	207.19	NA
TMA-TC-1A-1	-0.275	7.977	0.367	0.459	23.81	65.00	32.77
TMA-TC-1A-2	-0.269	7.477	0.364	0.453	25.27	82.49	33.09
TMA-TC-1A-3	-0.264	6.977	0.360	0.446	24.26	106.36	32.40
TMA-TC-1A-4	-0.259	6.477	0.356	0.440	23.96	130.39	32.55
TMA-TC-1A-5	-0.253	5.978	0.353	0.434	23.91	146.62	31.76
TMA-TC-1A-6	-0.248	5.478	0.349	0.428	23.64	156.37	31.54
TMA-TC-1A-7	-0.237	4.478	0.342	0.416	23.74	160.07	31.57
TMA-TC-1A-8	-0.226	3.478	0.335	0.404	23.51	148.66	31.13
TMA-TC-1A-9	-0.221	2.978	0.331	0.398	23.84	139.73	30.91
TMA-TC-1A-10	-0.215	2.478	0.328	0.392	24.06	127.91	30.61
TMA-TC-1B-1	-0.213	2.218	0.326	0.389	24.13	126.23	30.59
TMA-TC-1B-2	-0.207	1.718	0.322	0.383	24.28	97.71	30.15
TMA-TC-1B-3	-0.202	1.218	0.319	0.378	24.31	75.91	29.41
TMA-TC-1B-4	-0.196	0.718	0.315	0.371	24.38	60.31	28.45
TMA-TC-1B-5	-0.191	0.218	0.312	0.366	24.65	48.39	26.45
TMA-TC-2A-1	0.609	8.136	0.283	0.672	24.58	58.36	33.46
TMA-TC-2A-2	0.610	7.636	0.280	0.671	24.63	67.03	33.58
TMA-TC-2A-3	0.610	7.136	0.277	0.670	24.03	81.16	33.55

Table G-2. Selected Temperature Data Obtained from the SHT Block (Continued)

Gage	Location				Temperature, °C		
	x	y	z	r	0	275	490
TMA-TC-2A-4*	0.611	6.636	0.274	0.670	24.08	97.49	33.01
TMA-TC-2A-5	0.611	6.136	0.272	0.669	23.76	111.24	32.57
TMA-TC-2A-6	0.612	5.636	0.269	0.669	23.84	119.76	32.13
TMA-TC-2A-7	0.613	4.636	0.263	0.667	23.61	125.03	31.74
TMA-TC-2A-8	0.614	3.636	0.257	0.666	23.51	119.44	31.27
TMA-TC-2A-9	0.615	3.136	0.254	0.665	23.42	114.15	31.05
TMA-TC-2A-10	0.615	2.636	0.251	0.664	23.61	105.63	30.78
TMA-TC-2B-1	0.616	2.126	0.248	0.664	23.99	94.37	30.54
TMA-TC-2B-2	0.616	1.626	0.245	0.663	24.38	78.53	30.02
TMA-TC-2B-3	0.617	1.126	0.242	0.663	24.55	65.29	29.43
TMA-TC-2B-4	0.617	0.626	0.239	0.662	24.73	55.89	28.57
TMA-TC-2B-5	0.618	0.126	0.237	0.662	24.83	47.49	26.90
TMA-TC-3A-1	-0.719	8.268	1.342	1.522	24.80	52.90	33.19
TMA-TC-3A-2	-0.721	7.768	1.338	1.520	24.46	54.69	32.89
TMA-TC-3A-3	-0.723	7.268	1.335	1.518	25.49	60.41	33.04
TMA-TC-3A-4	-0.725	6.768	1.332	1.517	24.75	65.92	32.94
TMA-TC-3A-5	-0.728	6.268	1.328	1.514	27.27	73.51	33.01
TMA-TC-3A-6	-0.730	5.768	1.325	1.513	24.23	76.06	33.09
TMA-TC-3A-7	-0.734	4.768	1.318	1.509	23.29	78.65	31.86
TMA-TC-3A-8	-0.738	3.768	1.312	1.505	23.22	77.74	31.45
TMA-TC-3A-9	-0.741	3.268	1.308	1.503	23.07	74.88	31.20
TMA-TC-3A-10	-0.743	2.768	1.305	1.502	23.22	71.66	31.00
TMA-TC-3B-1	-0.745	2.298	1.302	1.500	23.64	67.95	30.76
TMA-TC-3B-2	-0.747	1.798	1.299	1.498	24.06	62.27	30.44
TMA-TC-3B-3	-0.749	1.298	1.295	1.496	24.23	56.33	29.85
TMA-TC-3B-4	-0.751	0.798	1.292	1.494	24.48	51.43	29.14
TMA-TC-3B-5	-0.754	0.298	1.289	1.493	24.50	47.07	28.15
TMA-TC-4A-1*	-0.117	6.888	-0.759	0.768	23.07	79.06	31.25
TMA-TC-4A-2	-0.111	6.388	-0.752	0.760	23.69	91.18	31.30
TMA-TC-4A-3	-0.104	5.888	-0.745	0.752	23.64	98.33	31.25
TMA-TC-4A-4	-0.097	5.388	-0.738	0.744	23.44	108.18	31.13
TMA-TC-4A-5	-0.090	4.888	-0.731	0.737	23.24	112.91	31.15
TMA-TC-4A-6	-0.083	4.388	-0.724	0.729	23.37	115.90	30.98
TMA-TC-4A-7	-0.070	3.388	-0.709	0.712	23.17	111.85	30.47
TMA-TC-4A-8	-0.056	2.389	-0.695	0.697	23.14	96.55	30.27
TMA-TC-4B-1	-0.052	2.099	-0.691	0.693	23.71	89.40	30.39
TMA-TC-4A-9	-0.050	1.889	-0.688	0.690	23.34	83.21	30.00
TMA-TC-4B-2	-0.046	1.599	-0.684	0.686	23.81	74.81	29.83
TMA-TC-4A-10	-0.043	1.389	-0.681	0.682	23.44	68.77	29.46
TMA-TC-4B-3	-0.039	1.099	-0.677	0.678	23.94	62.13	29.16
TMA-TC-4B-4	-0.032	0.599	-0.670	0.671	23.91	52.08	28.05
TMA-TC-4B-5	-0.025	0.099	-0.662	0.662	23.94	43.20	26.31
TMA-TC-5A-1	-0.059	8.145	0.712	0.714	29.24	57.66	33.75
TMA-TC-5A-2	-0.056	7.645	0.710	0.712	27.17	67.22	32.75
TMA-TC-5A-3	-0.053	7.145	0.708	0.710	23.49	77.14	31.42
TMA-TC-5A-4	-0.050	6.645	0.706	0.708	24.06	92.49	32.08

Table G-2. Selected Temperature Data Obtained from the SHT Block (Continued)

Gage	Location				Temperature, °C		
	x	y	z	r	0	275	490
TMA-TC-5A-5	-0.047	6.145	0.705	0.707	24.03	101.43	32 18
TMA-TC-5A-6	-0.044	5 645	0.703	0.704	23.71	112.86	31.74
TMA-TC-5A-7	-0.038	4.645	0.699	0 700	23.34	123.17	31 57
TMA-TC-5A-8	-0.032	3.645	0 696	0.697	23.09	118.93	31.20
TMA-TC-5A-9	-0.029	3.145	0.894	0.695	23.19	113.11	31.08
TMA-TC-5A-10	-0.025	2.645	0.692	0.692	23.27	105.22	30.78
TMA-TC-5B-1	-0.023	2.225	0.691	0.691	23 59	94.35	30.61
TMA-TC-5B-2	-0.020	1.725	0.689	0.689	23.79	80.39	30 20
TMA-TC-5B-3	-0.017	1.225	0.687	0.687	24.16	67.08	29 61
TMA-TC-5B-4	-0.014	0.725	0.685	0.685	24.18	57.25	28.69
TMA-TC-5B-5	-0.011	0.225	0.683	0.683	24.55	49.46	27.27
TMA-TC-6-1	0.617	5.417	-0.016	0.617	23.04	124.85	30.98
TMA-TC-6-2	0.757	5.418	-0.015	0.757	23.17	111.82	30.96
TMA-TC-6-3	0.917	5.419	-0.014	0.917	22.95	99.81	31 00
TMA-TC-6-4*	1.257	5.421	-0.012	1.257	23.56	85.36	31.00
TMA-TC-6-5	1.507	5.423	-0.011	1.507	23.02	76.39	30.93
TMA-TC-6-6	1.737	5.424	-0.010	1.737	23 34	70.07	30.96
TMA-TC-6-7	2.257	5.428	-0.007	2.257	22.90	59.78	30 91
TMA-TC-6-8	3.257	5.434	-0.001	3.257	22.87	47.49	30.71
TMA-TC-6-9	4.257	5.441	0.005	4.257	23.37	40.22	30.29
TMA-TC-6-10	5.257	5.447	0.010	5.257	23.94	35.71	29.43
TMA-TC-7-1	-0.960	3.400	0.007	0.960	23.19	100.75	30 83
TMA-TC-7-2	-1.100	3.401	0.008	1.100	23.17	94.64	30.83
TMA-TC-7-3	-1.260	3.402	0.008	1.260	23.29	87.57	30.64
TMA-TC-7-4	-1.600	3.403	0.009	1.600	22.92	76.37	30.78
TMA-TC-7-5	-1.850	3.404	0.010	1.850	23.32	69.37	30.78
TMA-TC-7-6	-2.080	3.406	0.010	2.080	23.19	64.30	30.71
TMA-TC-7-7	-2 600	3.408	0.011	2.600	23.19	55.36	30.59
TMA-TC-7-8	-3.600	3.413	0.014	3.600	23.34	44.44	30.34
TMA-TC-7-9	-4.600	3.418	0.016	4.600	23.66	37.87	29.85
TMA-TC-7-10	-5.600	3.423	0.019	5.600	23.74	33.90	29.01
TMA-BX-1-TC-1	0.131	6.863	0.310	0.337	24.03	48.27	30.71
TMA-BX-1-TC-2	0.136	6.023	0.309	0.338	22.80	147.64	31.05
TMA-BX-1-TC-3	0.142	5.023	0.307	0.338	23.00	165.82	31.23
TMA-BX-1-TC-4	0.148	4.023	0.306	0.340	23.29	166.20	31.32
TMA-BX-1-TC-5	0.154	3.023	0.304	0.341	23.34	154.35	31.15
TMA-BX-1-TC-6	0.161	2.023	0.303	0.343	23.69	125.91	30.64
TMA-BX-1-TC-7	0.164	1.543	0.302	0.344	23.76	92.13	30.02
TMA-BX-1-TC-8	0.167	1.043	0.301	0.344	23.86	71.25	29.31
TMA-BX-1-TC-9*	0.170	0.543	0.301	0.346	24.18	NA	NA
TMA-BX-2-TC-1	-0.631	7.093	0.281	0.691	22.62	86.30	30.59
TMA-BX-2-TC-2	-0.630	6.543	0.278	0.689	22.87	92.58	30.78
TMA-BX-2-TC-3	-0.630	6.023	0.274	0.687	22.65	99.03	30.96
TMA-BX-2-TC-4	-0.629	5.473	0.271	0.685	22.80	116.61	31.13
TMA-BX-2-TC-5	-0.628	4.883	0.267	0.682	22.95	120.44	31.10
TMA-BX-2-TC-6	-0.628	4.333	0.263	0.681	23.09	121.98	31.08

Table G-2. Selected Temperature Data Obtained from the SHT Block (Continued)

Gage	Location				Temperature, °C		
	x	y	z	r	0	275	490
TMA-BX-2-TC-7	-0.627	3.773	0.259	0.678	22.57	119.29	30.42
TMA-BX-2-TC-8	-0.626	3.223	0.256	0.676	23.04	114.08	30.91
TMA-BX-2-TC-9	-0.626	2.623	0.252	0.675	23.49	107.04	30.74
TMA-BX-2-TC-10	-0.625	2.073	0.248	0.672	23.27	90.99	30.34
TMA-BX-2-TC-11	-0.625	1.513	0.245	0.671	23.37	77.28	29.75
TMA-BX-2-TC-12	-0.624	0.963	0.241	0.669	23.59	63.43	28.69
TMA-BX-2-TC-13	-0.623	0.390	0.237	0.667	23.69	53.12	27.54
TMA-BX-3-TC-1*	0.768	6.887	1.314	1.522	22.75	NA	NA
TMA-BX-3-TC-2*	0.765	6.047	1.309	1.516	22.67	NA	NA
TMA-BX-3-TC-3	0.762	5.047	1.302	1.509	22.75	76.92	30.96
TMA-BX-3-TC-4	0.759	4.047	1.295	1.501	22.95	79.04	31.05
TMA-BX-3-TC-5	0.756	3.047	1.288	1.493	23.02	75.65	30.91
TMA-BX-3-TC-6	0.753	2.047	1.281	1.486	23.66	67.68	30.49
TMA-BX-3-TC-7*	0.752	1.567	1.277	1.482	23.79	NA	NA
TMA-BX-3-TC-8	0.750	1.087	1.274	1.478	24.06	55.65	29.53
TMA-BX-3-TC-9*	0.749	0.567	1.270	1.474	24.01	NA	NA
TMA-BX-4-TC-1	0.788	3.460	-0.176	0.807	24.88	103.29	31.00
TMA-BX-4-TC-2	1.108	3.460	-0.171	1.121	24.43	98.12	31.03
TMA-BX-4-TC-3*	1.448	3.460	-0.165	1.457	NA	NA	NA
TMA-BX-4-TC-4	1.928	3.461	-0.156	1.934	24.06	67.85	31.05
TMA-BX-4-TC-5	2.448	3.461	-0.147	2.452	23.94	62.08	30.98
TMA-BX-4-TC-6	2.928	3.461	-0.139	2.931	23.89	52.37	30.93
TMA-BX-4-TC-7	3.447	3.461	-0.130	3.449	24.03	48.02	30.86
TMA-BX-4-TC-8*	3.927	3.461	-0.122	3.929	24.06	43.11	NA
TMA-BX-4-TC-9	4.447	3.461	-0.112	4.448	23.96	40.29	30.42
TMA-BX-4-TC-10*	4.927	3.462	-0.104	4.928	23.84	NA	NA
TMA-BX-4-TC-11	5.447	3.462	-0.095	5.448	24.46	32.52	27.73
TMA-BX-4-TC-12	5.927	3.462	-0.087	5.928	24.03	32.55	27.73
TMA-RTD-15-1	-1.592	4.245	2.768	3.193	23.97	49.48	30.52
TMA-RTD-15-2	-1.309	4.246	2.679	2.982	23.81	50.94	30.64
TMA-RTD-15-3	-1.022	4.246	2.589	2.783	24.38	53.39	30.52
TMA-RTD-15-4	-0.738	4.247	2.500	2.607	23.92	55.57	30.75
TMA-RTD-15-5	-0.452	4.247	2.411	2.453	23.87	57.79	30.82
TMA-RTD-15-6	-0.165	4.248	2.321	2.327	23.66	59.69	30.62
TMA-RTD-15-7	0.120	4.248	2.231	2.234	23.76	61.38	30.34
TMA-RTD-15-8	0.409	4.249	2.141	2.160	23.79	61.85	30.85
TMA-RTD-15-9	0.694	4.249	2.052	2.166	23.74	60.55	29.69
TMA-RTD-15-10	0.983	4.250	1.961	2.194	23.89	61.85	31.01
TMA-RTD-15-11	1.268	4.250	1.872	2.261	23.79	60.70	30.85
TMA-RTD-15-12	1.552	4.251	1.783	2.364	23.84	59.24	30.95
TMA-RTD-15-13	1.841	4.251	1.692	2.500	23.92	57.01	30.98
TMA-RTD-15-14	2.129	4.252	1.602	2.664	24.20	54.82	31.03
TMA-RTD-15-15	2.416	4.252	1.512	2.850	23.92	52.19	30.82
TMA-RTD-15-16	2.700	4.253	1.423	3.052	24.46	50.23	30.95
TMA-RTD-15-17	2.984	4.253	1.334	3.269	24.10	48.08	30.80
TMA-RTD-15-18	3.269	4.254	1.245	3.498	24.54	45.85	30.77

Table G-2. Selected Temperature Data Obtained from the SHT Block (Continued)

Gage	Location				Temperature, °C		
	x	y	z	r	0	275	490
TMA-RTD-15-19	3.558	4.254	1.154	3.740	24.43	43.96	30.70
TMA-RTD-15-20*	3.844	4.255	1.065	3.989	24.36	48.16	32.99
TMA-RTD-15-21	4.125	4.255	0.977	4.239	24.43	40.60	30.34
TMA-RTD-15-22	4.412	4.256	0.887	4.500	24.56	39.07	30.13
TMA-RTD-15-23*	4.699	4.256	0.797	4.766	24.85	21.39	20.77
TMA-RTD-15-24	4.985	4.257	0.707	5.035	24.85	36.68	29.66
TMA-RTD-15-25	5.267	4.258	0.619	5.303	25.21	35.78	29.46
TMA-RTD-15-26	5.555	4.258	0.529	5.580	25.13	34.79	28.97
TMA-RTD-15-27	5.842	4.259	0.439	5.858	25.31	34.15	28.74
TMA-TEMP-16-1	5.258	4.271	0.187	5.261	24.90	36.74	29.79
TMA-TEMP-16-2	4.565	4.274	0.280	4.574	24.29	39.61	30.25
TMA-TEMP-16-3	3.873	4.277	0.372	3.891	24.22	44.19	30.74
TMA-TEMP-16-4	3.181	4.280	0.464	3.215	24.13	50.05	47.96
TMA-RTD-17-1	-1.767	4.275	-1.438	2.278	23.76	59.82	29.56
TMA-RTD-17-2	-1.475	4.275	-1.401	2.034	24.18	66.20	31.11
TMA-RTD-17-3	-1.184	4.274	-1.364	1.806	23.84	70.94	30.41
TMA-RTD-17-4	-0.879	4.274	-1.325	1.590	23.58	76.65	30.46
TMA-RTD-17-5	-0.521	4.273	-1.279	1.381	23.63	83.01	30.46
TMA-RTD-17-6	-0.284	4.273	-1.249	1.281	23.56	86.50	30.49
TMA-RTD-17-7	0.017	4.273	-1.210	1.210	23.69	88.95	30.70
TMA-RTD-17-8	0.316	4.272	-1.172	1.214	24.43	88.82	30.54
TMA-RTD-17-9	0.613	4.272	-1.134	1.269	23.89	85.45	30.59
TMA-RTD-17-10	0.904	4.271	-1.096	1.421	23.81	80.97	30.64
TMA-RTD-17-11	1.207	4.271	-1.058	1.605	23.81	76.49	30.80
TMA-RTD-17-12	1.499	4.270	-1.020	1.813	23.79	70.47	30.64
TMA-RTD-17-13	1.796	4.270	-0.982	2.047	23.56	65.10	30.54
TMA-RTD-17-14	2.097	4.270	-0.943	2.299	23.56	60.47	30.54
TMA-RTD-17-15	2.390	4.269	-0.906	2.556	23.61	56.48	30.54
TMA-RTD-17-16	2.689	4.269	-0.869	2.826	23.63	52.94	30.54
TMA-RTD-17-17	2.992	4.268	-0.829	3.105	24.18	49.90	30.49
TMA-RTD-17-18	3.290	4.268	-0.791	3.384	24.07	46.89	30.34
TMA-RTD-17-19	3.582	4.268	-0.753	3.660	24.30	44.53	30.34
TMA-RTD-17-20	3.885	4.267	-0.715	3.950	24.38	42.41	30.31
TMA-RTD-17-21	4.173	4.267	-0.678	4.228	24.51	40.70	30.18
TMA-RTD-17-22	4.469	4.266	-0.640	4.515	25.21	39.04	30.03
TMA-RTD-17-23	4.771	4.266	-0.601	4.809	26.96	37.49	29.59
TMA-RTD-17-24	5.072	4.265	-0.562	5.103	25.21	36.27	29.33
TMA-RTD-17-25	5.367	4.265	-0.525	5.393	25.13	35.08	28.89
TMA-RTD-17-26*	0.000	0.000	0.000	0.000	75.79	329.89	35.00
TMA-RTD-17-27	5.953	4.264	-0.450	5.970	25.39	33.07	27.37
TMA-RTD-17-28	6.255	4.264	-0.411	6.268	26.13	29.54	22.68
TMA-RTD-17-29	6.545	4.263	-0.374	6.556	26.24	29.05	22.22
TMA-TEMP-18-1	5.120	4.255	-0.205	5.124	24.55	36.78	29.64
TMA-TEMP-18-2	4.422	4.254	-0.215	4.427	24.25	40.22	30.28
TMA-TEMP-18-3	3.723	4.252	-0.224	3.730	24.02	45.03	30.63
TMA-TEMP-18-4	3.025	4.250	-0.234	3.034	23.99	51.54	31.00

Table G-2. Selected Temperature Data Obtained from the SHT Block (Continued)

Gage	Location				Temperature, °C		
	x	y	z	r	0	275	490
TMA-RTD-22-1	-1.584	4.358	-0.711	1.736	23.40	72.91	30.49
TMA-RTD-22-2	-1.879	4.360	-0.706	2.007	23.66	66.31	30.57
TMA-RTD-22-3	-2.179	4.362	-0.701	2.289	23.84	60.91	30.62
TMA-RTD-22-4	-2.479	4.364	-0.696	2.575	23.97	55.89	30.41
TMA-RTD-22-5	-2.777	4.366	-0.691	2.862	23.99	52.55	30.67
TMA-RTD-22-6	-3.081	4.368	-0.686	3.156	23.89	48.52	30.31
TMA-RTD-22-7	-3.377	4.370	-0.681	3.445	23.61	45.93	30.23
TMA-RTD-22-8	-3.680	4.372	-0.676	3.742	23.97	43.24	30.00
TMA-RTD-22-9	-3.980	4.374	-0.671	4.036	24.41	41.11	29.95
TMA-RTD-22-10	-4.280	4.376	-0.666	4.332	24.18	39.46	29.87
TMA-RTD-22-11	-4.578	4.378	-0.661	4.625	23.81	37.67	29.56
TMA-RTD-22-12	-4.876	4.380	-0.657	4.920	24.33	36.17	29.23
TMA-RTD-22-13	-5.175	4.382	-0.652	5.216	24.46	35.03	29.05
TMA-RTD-22-14	-5.480	4.384	-0.647	5.518	24.28	33.99	28.76
TMA-RTD-22-15	-5.775	4.386	-0.642	5.811	30.44	32.96	28.30
TMA-RTD-22-16	-6.078	4.388	-0.637	6.111	24.41	32.09	27.68
TMA-RTD-22-17	-6.386	4.390	-0.632	6.417	24.46	31.44	26.98
TMA-RTD-23-1	-1.404	4.350	0.694	1.566	23.97	85.58	30.95
TMA-RTD-23-2	-1.682	4.352	0.659	1.806	24.33	77.75	31.01
TMA-RTD-23-3	-1.967	4.355	0.622	2.063	24.07	70.64	30.85
TMA-RTD-23-4	-2.247	4.357	0.586	2.322	24.25	64.69	30.52
TMA-RTD-23-5	-2.530	4.359	0.549	2.589	23.66	59.48	30.62
TMA-RTD-23-6	-2.813	4.362	0.513	2.859	25.03	55.34	30.72
TMA-RTD-23-7	-3.092	4.364	0.477	3.129	23.84	51.43	30.46
TMA-RTD-23-8	-3.376	4.366	0.440	3.405	23.79	48.06	30.34
TMA-RTD-23-9	-3.656	4.369	0.404	3.678	23.99	45.47	30.41
TMA-RTD-23-10	-3.938	4.371	0.368	3.955	24.36	43.19	30.28
TMA-RTD-23-11*	-4.224	4.373	0.331	4.237	24.23	40.26	21.73
TMA-RTD-23-12	-4.501	4.376	0.296	4.511	24.59	39.12	29.87
TMA-RTD-23-13	-4.783	4.378	0.259	4.790	24.36	37.88	29.77
TMA-RTD-23-14	-5.067	4.380	0.223	5.072	24.51	36.27	29.46
TMA-RTD-23-15	-5.342	4.383	0.187	5.345	24.64	34.97	29.10
TMA-RTD-23-16	-5.624	4.385	0.151	5.626	25.05	34.07	28.87
TMA-RTD-23-17	-5.906	4.387	0.115	5.907	24.51	33.09	28.35
TMA-RTD-23-18	-6.193	4.390	0.078	6.193	25.00	32.35	27.71
TMA-RTD-23-19*	-6.474	4.392	0.042	6.474	21.55	-58.09	22.35
TMA-STC-1	1.000	0.000	2.000	2.236	24.21	42.94	28.28
TMA-STC-2	1.000	0.000	0.000	1.000	24.03	45.49	26.97
TMA-STC-3	0.500	0.000	-1.000	1.118	23.56	39.44	26.43
TMA-STC-4	0.500	0.000	1.000	1.118	24.50	47.15	27.68
TMA-STC-5	-1.000	0.000	0.000	1.000	23.86	46.71	27.34
TMA-STC-6	3.000	0.000	0.750	3.092	24.13	38.65	28.60
TMA-STC-19	0.000	0.000	1.250	1.250	24.21	48.46	27.86
TMA-STC-20	4.000	0.000	0.000	4.000	24.28	34.61	28.10
TMA-STC-21	3.000	0.000	-0.750	3.092	23.86	35.25	27.49
TMA-STC-22	-3.000	0.000	0.750	3.092	24.03	37.06	28.00

Table G-2. Selected Temperature Data Obtained from the SHT Block (Continued)

Gage	Location				Temperature, °C		
	x	y	z	r	0	275	490
TMA-STC-23	-4.000	0.000	0.000	4.000	23.94	33.11	27.36
TMA-STC-24	0.000	0.000	-1.250	1.250	23.24	34.58	25.25
TMA-STC-13	-6.593	3.463	0.493	6.611	24.11	31.67	27.68
TMA-STC-14	-6.593	3.463	-0.007	6.593	23.96	31.45	27.27
TMA-STC-15	-6.593	3.463	-1.007	6.669	23.81	30.59	27.00
TMA-STC-16	-6.593	5.463	0.993	6.667	24.01	31.05	27.44
TMA-STC-17	-6.593	5.463	-0.007	6.593	23.66	31.08	26.97
TMA-STC-18	-6.593	5.463	-0.507	6.612	23.69	31.00	22.72
TMA-STC-25	-6.593	1.963	1.993	6.888	26.26	30.29	28.00
TMA-STC-26	-6.593	1.963	-0.007	6.593	24.26	30.81	27.32
TMA-STC-27	-6.593	1.963	1.493	6.760	24.78	30.71	27.32
TMA-STC-34	-6.593	4.463	-0.007	6.593	23.71	31.50	25.81
TMA-STC-35	-6.593	6.963	-0.007	6.593	23.74	30.32	27.34
TMA-STC-36	-6.593	6.963	1.493	6.760	23.99	28.79	24.90
TMA-STC-7	6.264	3.489	0.488	6.283	24.38	32.84	27.91
TMA-STC-8	6.264	3.489	-0.012	6.264	24.43	32.43	27.59
TMA-STC-9	6.264	3.489	-0.488	6.283	24.13	31.89	27.24
TMA-STC-10	6.264	5.489	0.988	6.341	24.26	33.50	28.40
TMA-STC-11	6.264	5.489	-0.012	6.264	24.13	33.21	28.05
TMA-STC-12	6.264	5.489	-1.012	6.345	23.84	32.03	27.59
TMA-STC-28	6.264	1.989	1.988	6.572	24.90	31.91	28.03
TMA-STC-29	6.264	1.989	-0.012	6.264	24.46	31.96	27.98
TMA-STC-30	6.264	1.989	1.488	6.438	24.70	32.16	28.20
TMA-STC-31	6.264	4.489	-0.012	6.264	24.41	33.31	27.83
TMA-STC-32	6.264	6.989	-0.012	6.264	23.91	32.38	28.05
TMA-STC-33	6.264	6.989	1.488	6.438	23.94	32.30	28.40
TMA-IN-THRM-1	1.000	-0.076	2.000	2.236	25.53	33.70	24.41
TMA-IN-THRM-2	-3.000	-0.076	1.500	3.354	25.31	32.54	24.81
TMA-IN-THRM-3	0.500	-0.076	-1.000	1.118	24.93	34.02	24.31
TMA-IN-THRM-4	4.000	-0.076	0.000	4.000	25.32	31.34	25.02
TMA-IN-THRM-5	-1.000	-0.076	0.000	1.000	24.56	38.36	24.58
TMA-IN-THRM-11	-6.670	2.000	2.000	6.963	25.87	29.75	25.30
TMA-IN-THRM-12	-6.670	3.500	0.500	6.689	25.12	30.05	24.85
TMA-IN-THRM-13	-6.670	4.500	0.000	6.670	24.67	29.85	23.61
TMA-IN-THRM-14	-6.670	5.500	-0.500	6.689	24.79	29.67	24.46
TMA-IN-THRM-15	-6.670	3.500	-1.000	6.745	24.68	29.80	25.17
TMA-IN-THRM-6	6.340	5.500	1.000	6.418	25.19	31.55	25.90
TMA-IN-THRM-7	6.340	4.500	0.000	6.340	25.26	31.28	25.17
TMA-IN-THRM-8	6.340	3.500	-0.500	6.360	25.19	30.70	25.13
TMA-IN-THRM-9	6.340	5.500	-1.000	6.418	24.94	30.90	25.50
TMA-IN-THRM-10	6.340	7.000	-2.000	6.648	25.18	30.93	25.98
TMA-BX-1-1-THRM	0.173	0.043	0.300	0.346	25.82	29.93	21.63
TMA-BX-3-1-THRM	0.747	0.067	1.267	1.471	26.01	30.53	22.47
TMA-BX-4-1-THRM	6.427	3.462	-0.078	6.427	25.43	29.45	23.31

NOTE: x, y, z are coordinates in meters, r is radial distance from heater in meters.

* Suspected failed gages. NA = Not available.

Table G-3. Selected Multiple Point Borehole Extensometer Displacement Data Obtained from the SHT Block, Uncorrected for Thermal Expansion of Rods (Extension Positive)

Gage	Location (m)			Days After Startup		
	x	y	z	0	280	490
TMA-BX-1-1*	0.130	6.883	0.310	-0.0903	NA	NA
TMA-BX-1-2*	0.136	6.043	0.309	-0.0797	NA	NA
TMA-BX-1-3	0.142	5.043	0.307	-0.0808	1.9027	0.8576
TMA-BX-1-4	0.148	4.043	0.306	-0.0582	-0.0686	-1.2908
TMA-BX-1-5*	0.154	3.043	0.304	-0.0373	NA	NA
TMA-BX-1-6*	0.161	2.043	0.303	-0.0176	NA	NA
TMA-BX-2-1	-0.631	7.093	0.281	-0.0003	0.0458	0.0166
TMA-BX-2-2	-0.630	6.023	0.274	0.0013	0.1527	0.0673
TMA-BX-2-3	-0.628	4.883	0.267	-0.0009	0.1131	0.0484
TMA-BX-2-4	-0.627	3.773	0.259	0.0023	0.1442	-0.0065
TMA-BX-2-5	-0.626	2.623	0.252	-0.0013	0.0760	0.0283
TMA-BX-2-6	-0.625	1.513	0.245	0.0006	0.0794	0.0725
TMA-BX-3-1	0.768	6.907	1.315	0.0006	1.4418	NA
TMA-BX-3-2	0.765	6.067	1.309	-0.0248	1.7894	NA
TMA-BX-3-3	0.762	5.067	1.302	-0.0250	1.7131	NA
TMA-BX-3-4*	0.759	4.067	1.295	-0.0250	NA	NA
TMA-BX-3-5*	0.756	3.067	1.288	-2.4889	NA	NA
TMA-BX-3-6	0.753	2.067	1.281	-0.0252	1.0589	NA
TMA-BX-4-1	0.768	3.460	-0.177	0.0256	0.7109	0.5325
TMA-BX-4-2	1.428	3.460	-0.165	0.0006	0.4766	0.2973
TMA-BX-4-3	2.428	3.461	-0.148	0.0259	0.1291	0.0833
TMA-BX-4-4	3.427	3.461	-0.130	0.0005	0.1359	0.1743
TMA-BX-4-5	4.427	3.461	-0.113	0.0004	-0.1726	-0.0895
TMA-BX-4-6	5.427	3.462	-0.095	0.0003	-0.0131	0.0812

* Suspected failed gages.
Displacement data given in mm.

Table G-4. Selected Rock Bolt Load Cell Data Obtained from the SHT Block

Gage	Location (m)			Days After Startup		
	x	y	z	0	280	490
TMA-RB-LC-1-AVG	0.180	-0.300	-0.370	22662.0	21090.8	20943.1
TMA-RB-LC-2-AVG	0.180	-0.300	-0.370	14859.4	14354.1	14338.9
TMA-RB-LC-3-AVG	0.620	-0.300	-0.210	22428.0	22160.3	22097.6
TMA-RB-LC-4-AVG	0.620	-0.300	-0.210	16663.9	16315.9	16234.2
TMA-RB-LC-5-AVG	-0.180	-4.700	-0.370	25971.9	25641.1	25444.7
TMA-RB-LC-6-AVG	-0.180	-4.700	-0.370	14642.7	14538.6	14493.0
TMA-RB-LC-7-AVG	0.620	-4.700	-0.290	4932.6	4865.0	4796.1
TMA-RB-LC-8-AVG	0.620	-4.700	-0.290	16862.8	16497.8	16052.3

Load cell data given in lbs.

Table G-5. Selected Wire Extensometer Data Obtained from the SHT Block

Gage	Location (m)			Days After Startup		
	x	y	z	0	280	490
TMA-WX-1 (top)	2.098	0.000	2.230	0	0.46	-2.31
TMA-WX-1 (bottom)	1.983	0.000	-1.240			
TMA-WX-2 (top)	-2.040	0.000	2.591	0	4.49	-21.04
TMA-WX-2 (bottom)	-2.085	0.000	-0.914			
TMA-WX-3 (top)	6.264	3.612	2.752	0	-23.91	1.19
TMA-WX-3 (bottom)	6.264	3.582	-0.978			
TMA-WX-4 (top)	6.264	5.633	2.759	0	-0.17	-53.45
TMA-WX-4 (bottom)	6.264	5.613	-1.041			
TMA-WX-5 (top)	-6.593	3.622	1.477	0	-0.69	1.72
TMA-WX-5 (bottom)	-6.593	3.712	-1.558			
TMA-WX-6 (top)	-6.593	5.735	1.216	0	-2.99	-3.6
TMA-WX-6 (bottom)	-6.593	5.735	-1.784			

Table G-6. Tape Extensometer Measurements for the SHT (Extension Positive)

Tape Extensometer Gage	Location (m)			Initial Reading (m)	Displ. 9/24/96 (mm)	Displ. 10/21/96 (mm)	Displ. 12/19/96 (mm)	Displ. 1/7/97 (mm)
	x	y	z					
TMA-WXM-1	2.008	0.000	-0.295	5.40439	-0.48	-0.78	-0.86	-0.76
TMA-WXM-2	-1.960	0.000	0.121	5.08585	-3.2	-3.2	-1.17	-3.71
TMA-WXM-3	6.264	3.702	0.012		4.67249	0.33	erroneous	0.08
TMA-WXM-4	6.264	5.603	-0.056	4.33635	-0.46	-0.21	-0.56	-0.64
TMA-WXM-5	-6.593	3.722	0.012	5.87639	-0.04	-0.32	-0.49	-0.57
TMA-WXM-6	-6.593	5.735	-0.019	5.83158	-0.29	-0.129	-0.17	-0.39
Tape Extensometer Gage	Location (m)			Displ. 2/11/97 (mm)	Displ. 3/10/97 (mm)	Displ. 4/21/97 (mm)	Displ. 5/6/97 (mm)	Displ. 6/25/97 (mm)
	x	y	z					
TMA-WXM-1	2.008	0.000	-0.295	-1.14	-1.19	-1.27	-0.86	-1.39
TMA-WXM-2	-1.960	0.000	0.121	-3.71	-3.71	erroneous	-4.39	-4.21
TMA-WXM-3	6.264	3.702	0.012	-1.93	2.24	0.26	0.31	-0.17
TMA-WXM-4	6.264	5.603	-0.056	-0.84	erroneous	-0.36	-0.18	-1.17
TMA-WXM-5	-6.593	3.722	0.012	-0.37	-0.82	-0.72	-0.79	-0.88
TMA-WXM-6	-6.593	5.735	-0.019	-0.72	-0.8	-0.64	-0.31	-1.15
Tape Extensometer Gage	Location (m)					Displ. 7/24/97 (mm)	Displ. 8/20/97 (mm)	Displ. 7/15/97 (mm)
	x	y	z					
TMA-WXM-1	2.008	0.000	-0.295			-1.52	-1.34	-1.16
TMA-WXM-2	-1.960	0.000	0.121			-4.21	-4.21	-3.71
TMA-WXM-3	6.264	3.702	0.012			2.29	-0.07	0.26
TMA-WXM-4	6.264	5.603	-0.056			-1.22	-1.2	-1.5
TMA-WXM-5	-6.593	3.722	0.012			-0.95	-0.62	-0.6
TMA-WXM-6	-6.593	5.735	-0.019			-0.95	-0.21	-0.64

*Note: WXM-3 initial reading suspect. Change in displacement from 9/24/96
This table includes corrected data not included in previous reports.

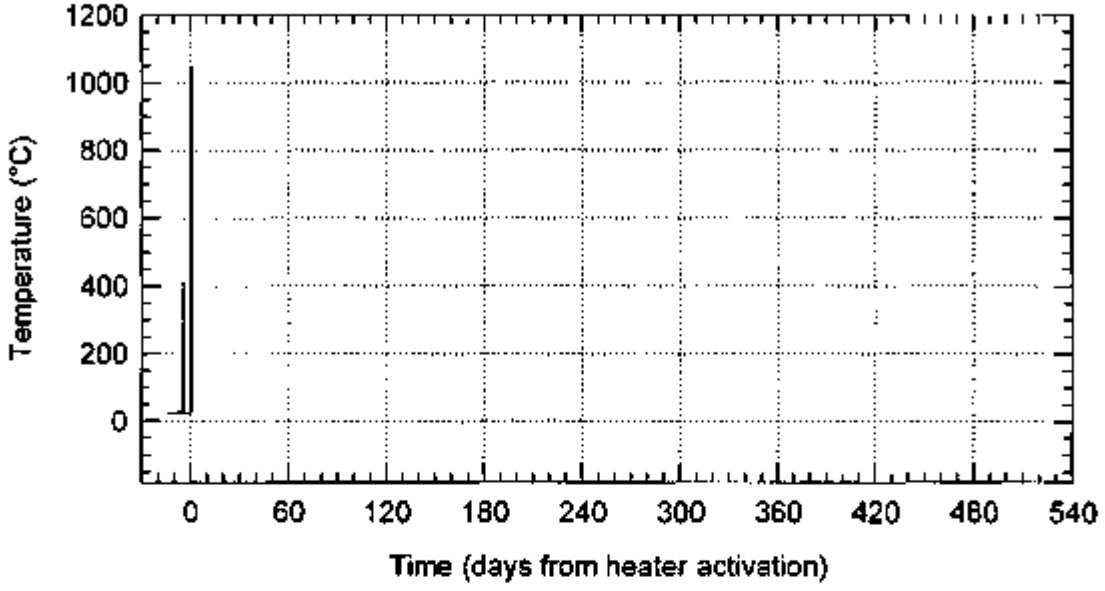

Figure G-1. Data from Failed Gage TMA-H-1-TCB-4

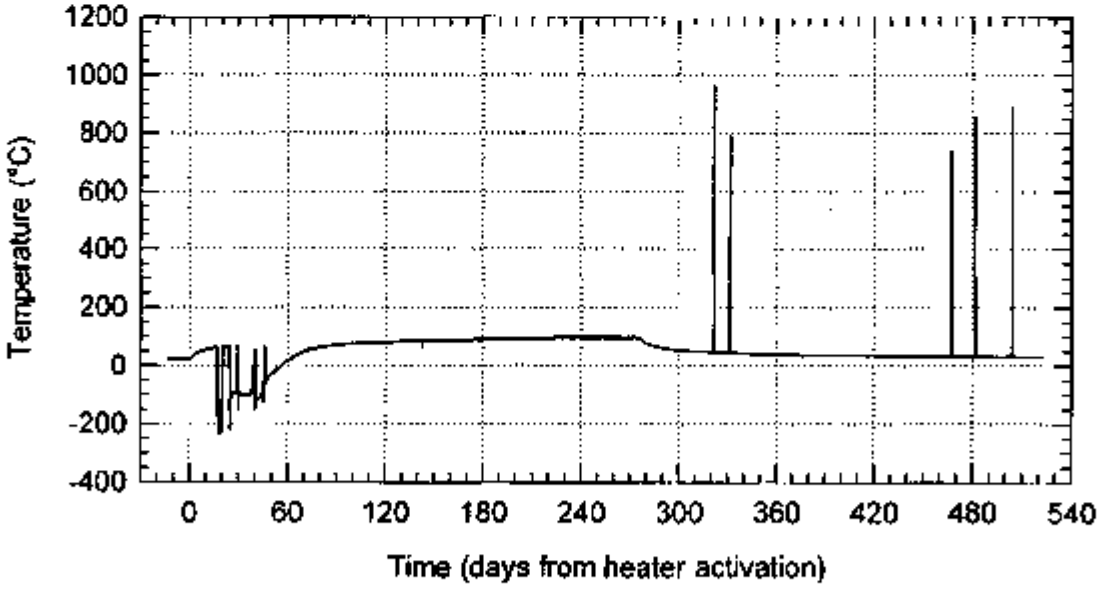

Figure G-2. Data from Failed Gage TMA-RC-2A-4

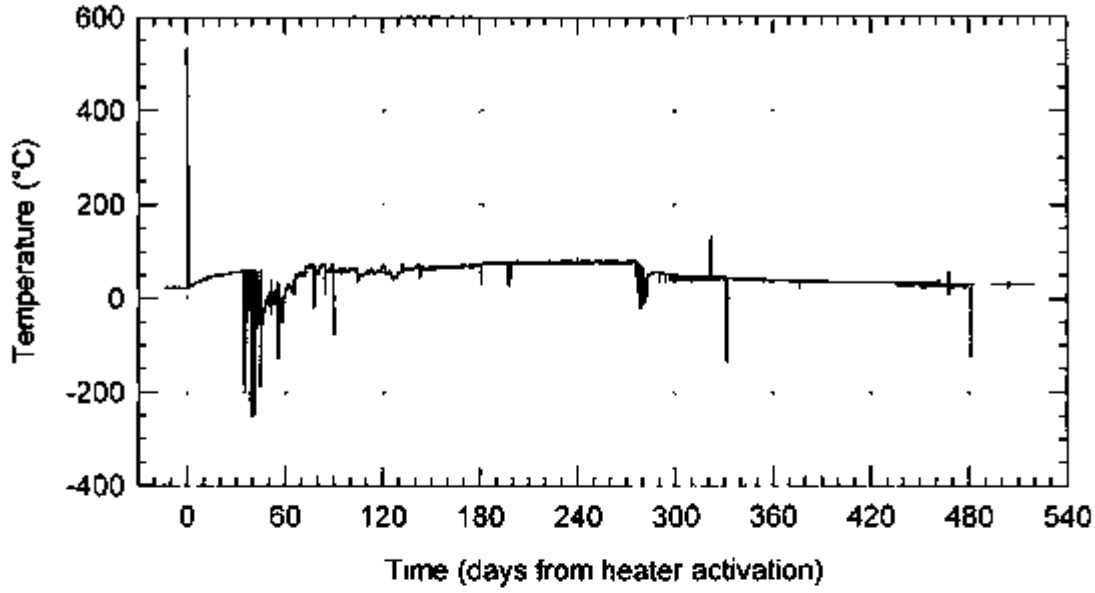

Figure G-3 Data from Failed Gage TMA-TC-4A-1

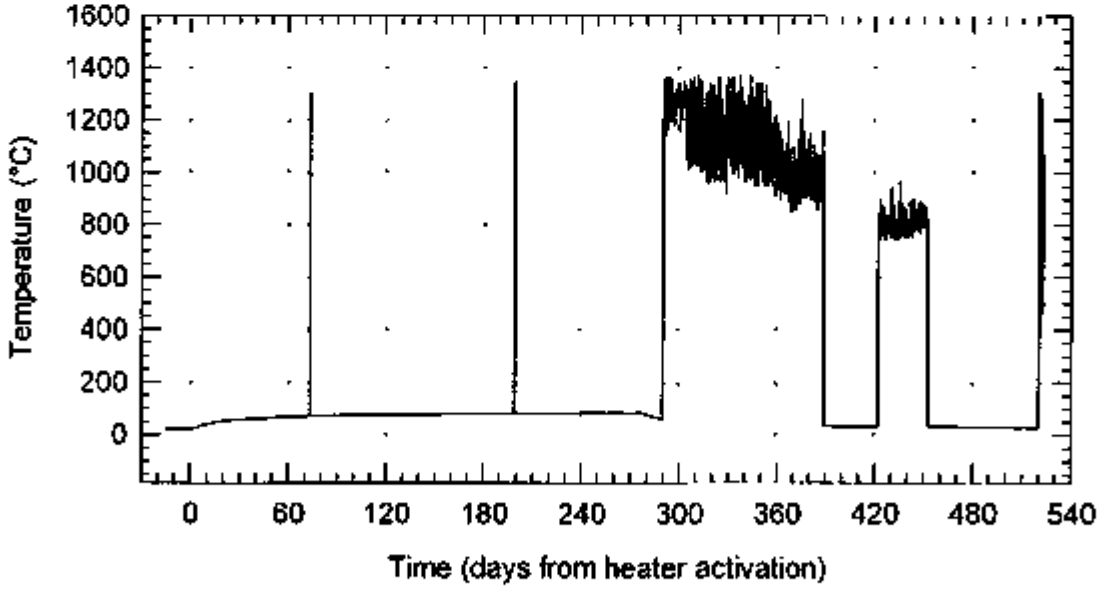

Figure G-4 Data from Failed Gage TMA-TC-6-4

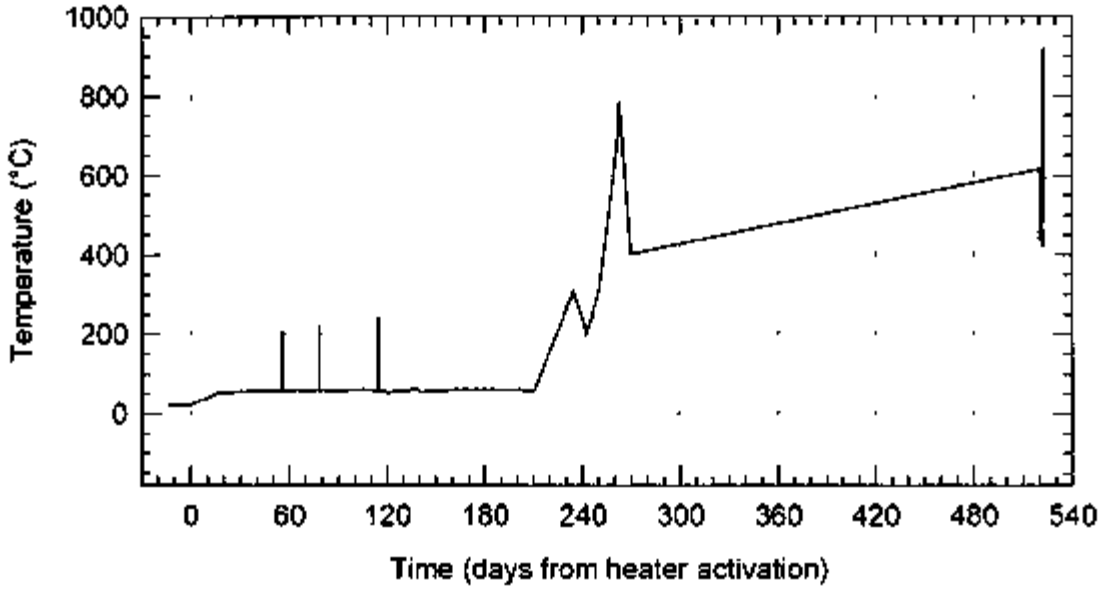

Figure G-5 Data from Failed Gage TMA-BX-1-TC-9

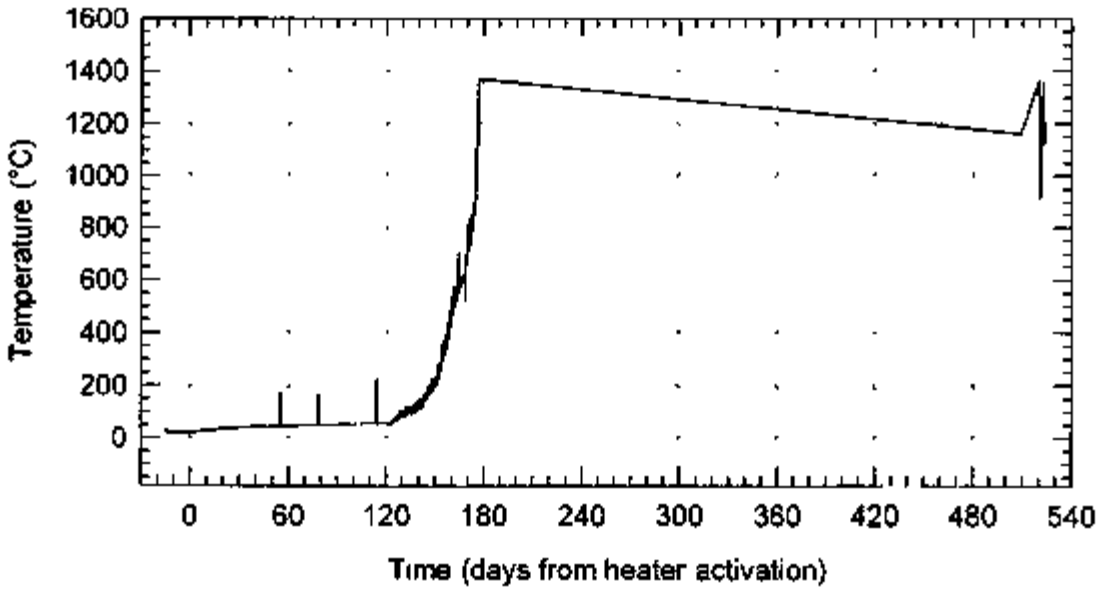

Figure G-6 Data from Failed Gage TMA-BX-3-TC-1

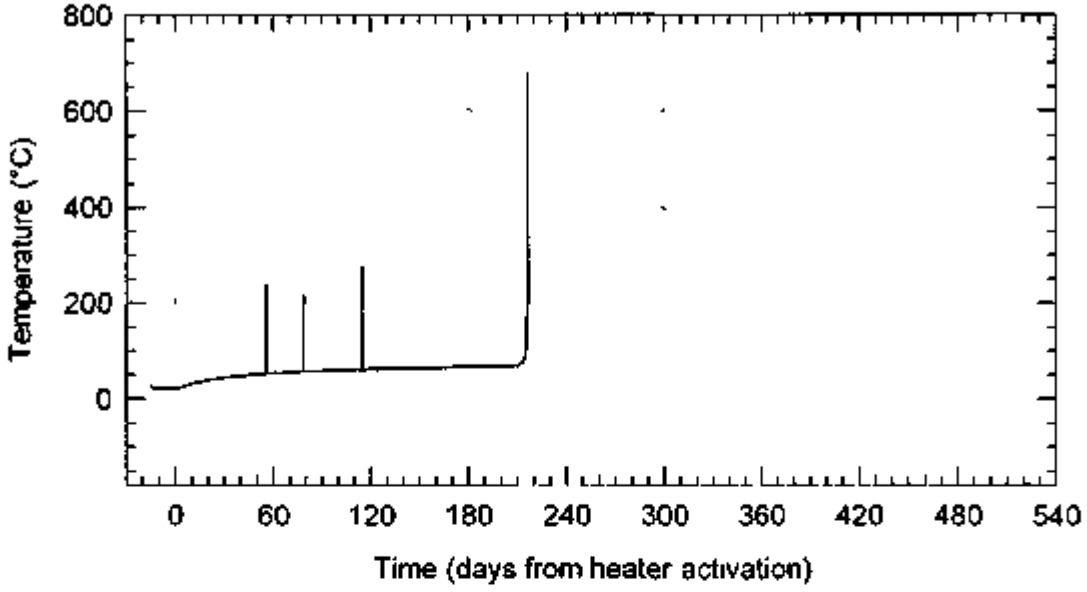

Figure G-7 Data from Failed Gage TMA-BX-3-TC-2

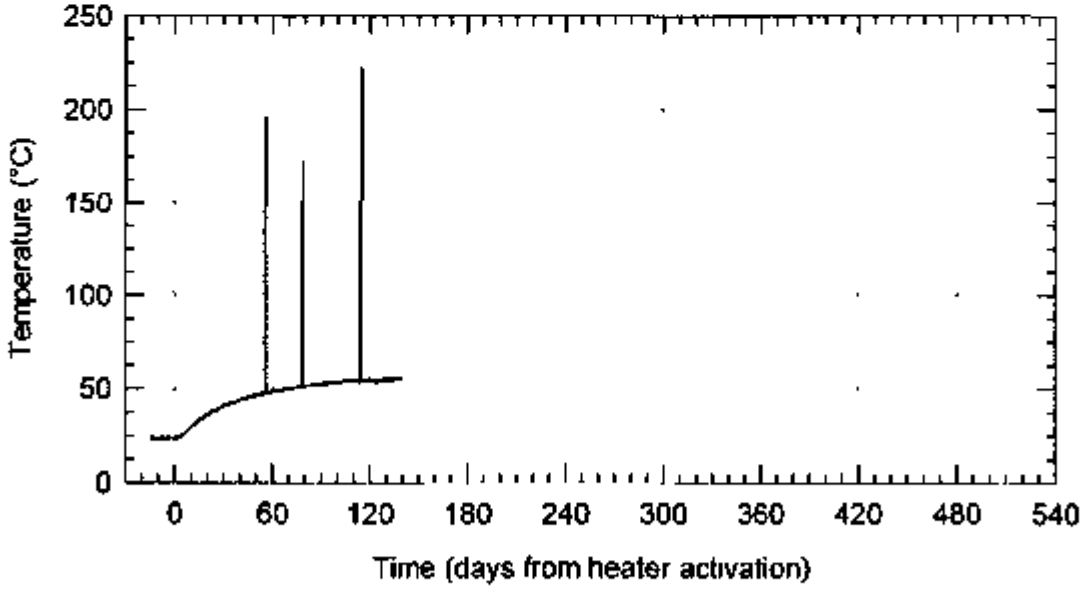

Figure G-8 Data from Failed Gage TMA-BX-3-TC-7

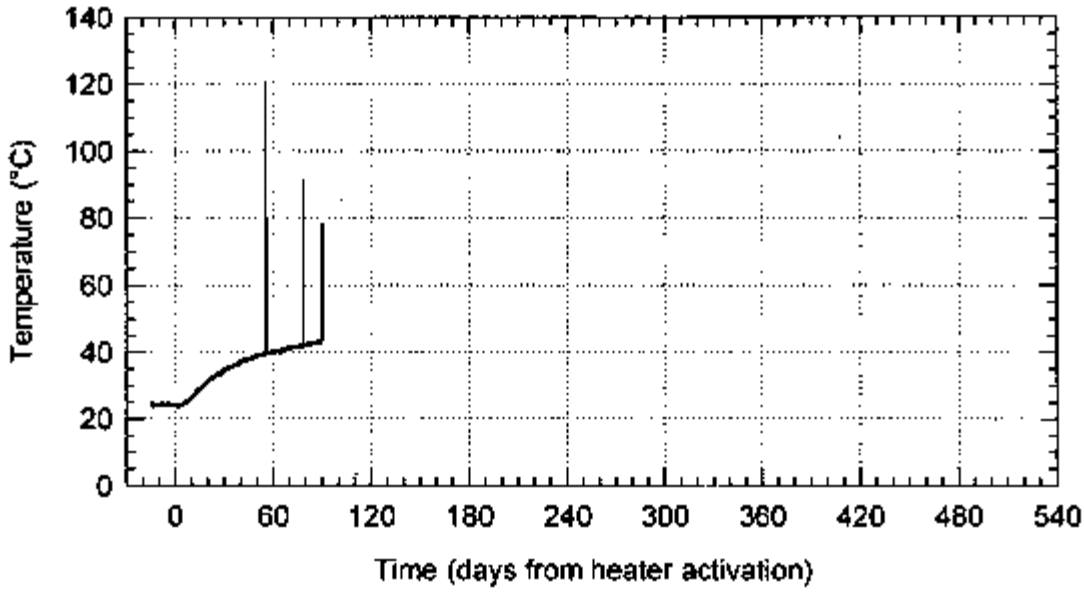

Figure G-9. Data from Failed Gage TMA-BX-3-TC-9

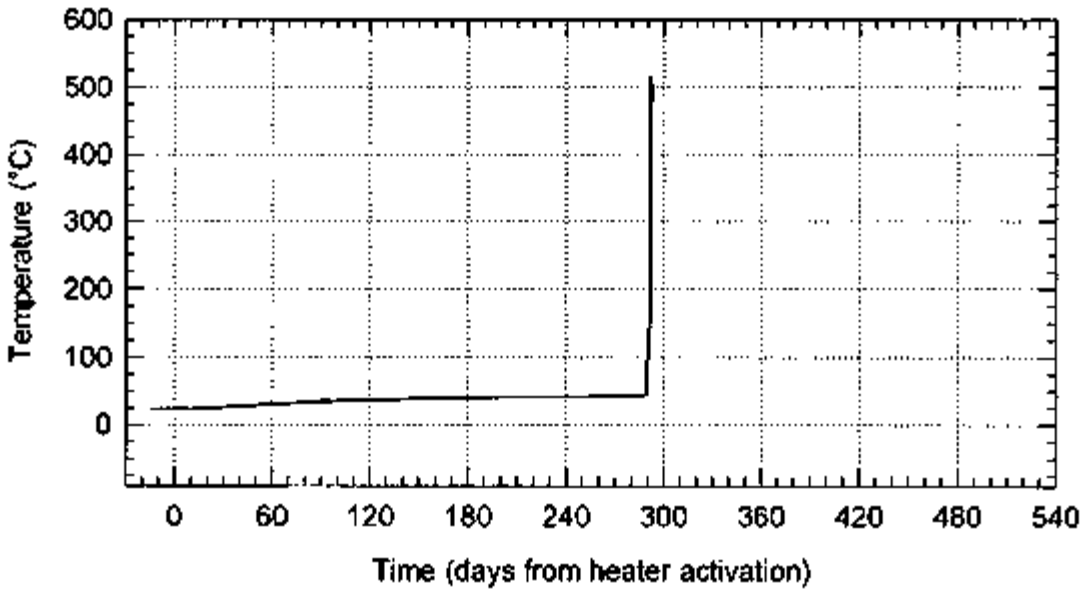

Figure G-10. Data from Failed Gage TMA-BX-4-TC-8

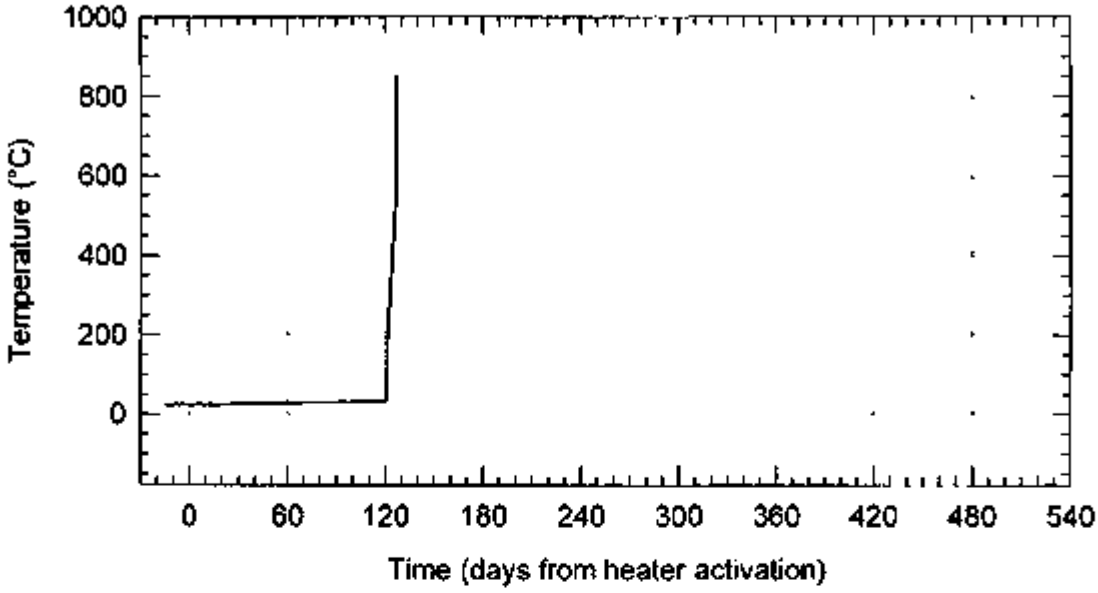

Figure G-11 Data from Failed Gage TMA-BX-4-TC-10

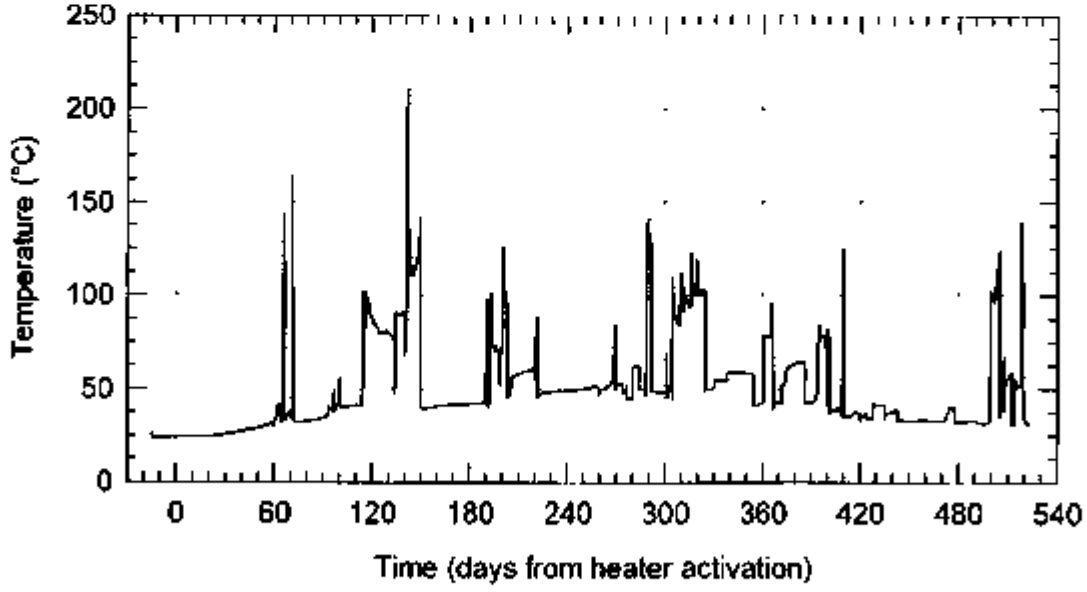

Figure G-12 Data from Failed Gage TMA-RTD-15-20

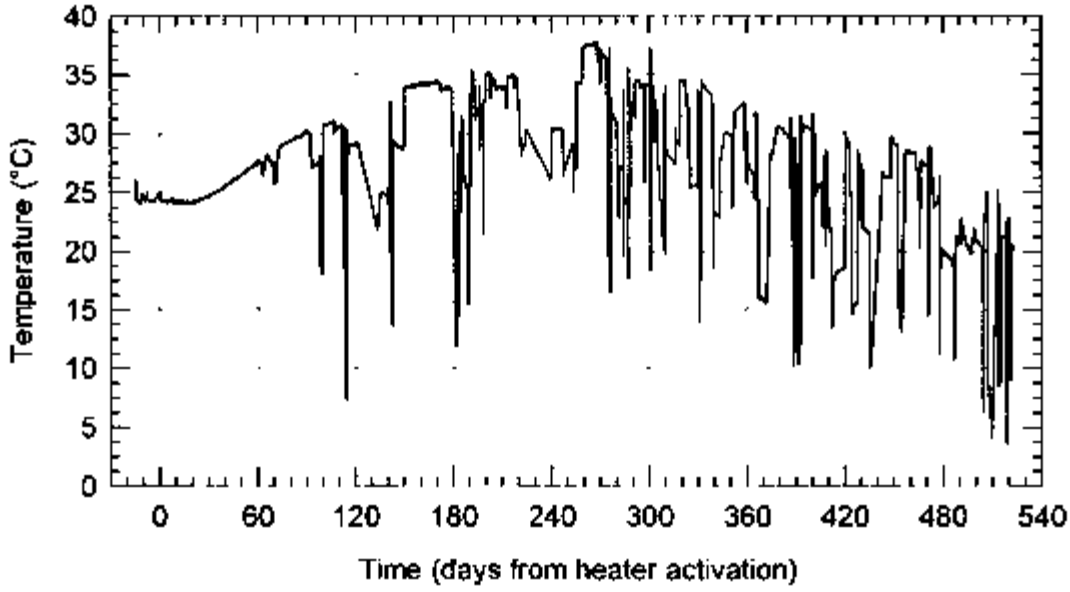

Figure G-13 Data from Failed Gage TMA-RTD-15-23

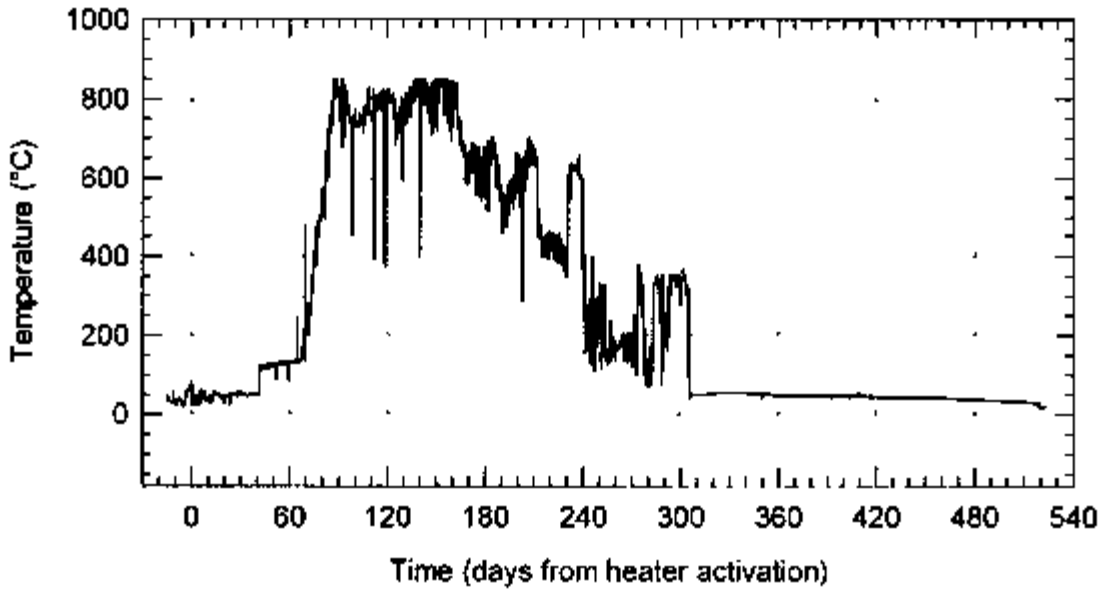

Figure G-14 Data from Failed Gage TMA-RTD-15-26

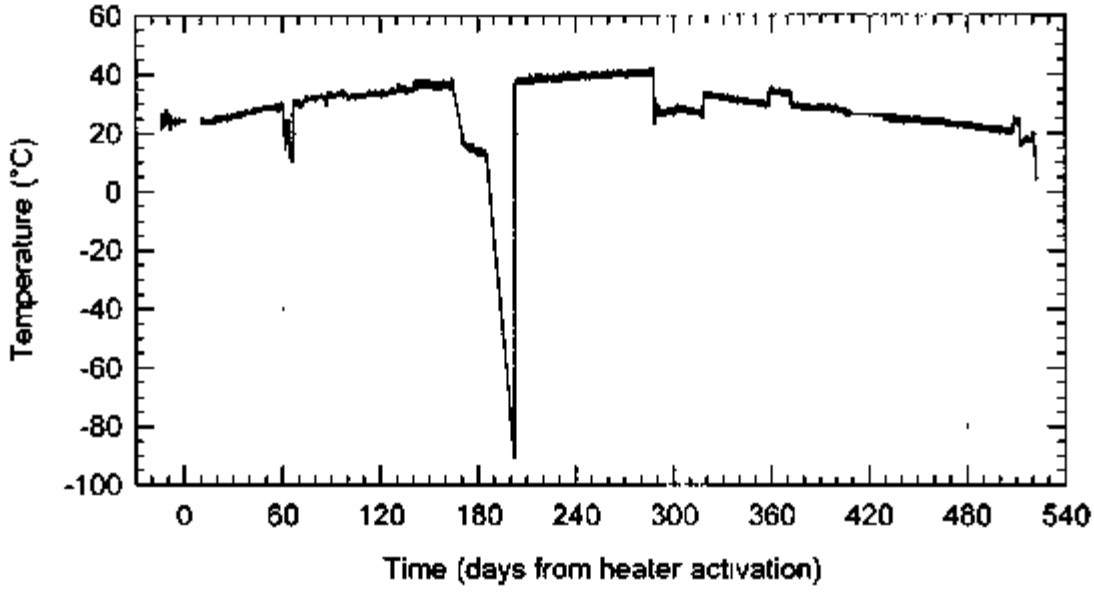

Figure G-15 Data from Failed Gage TMA-RTD-23-11

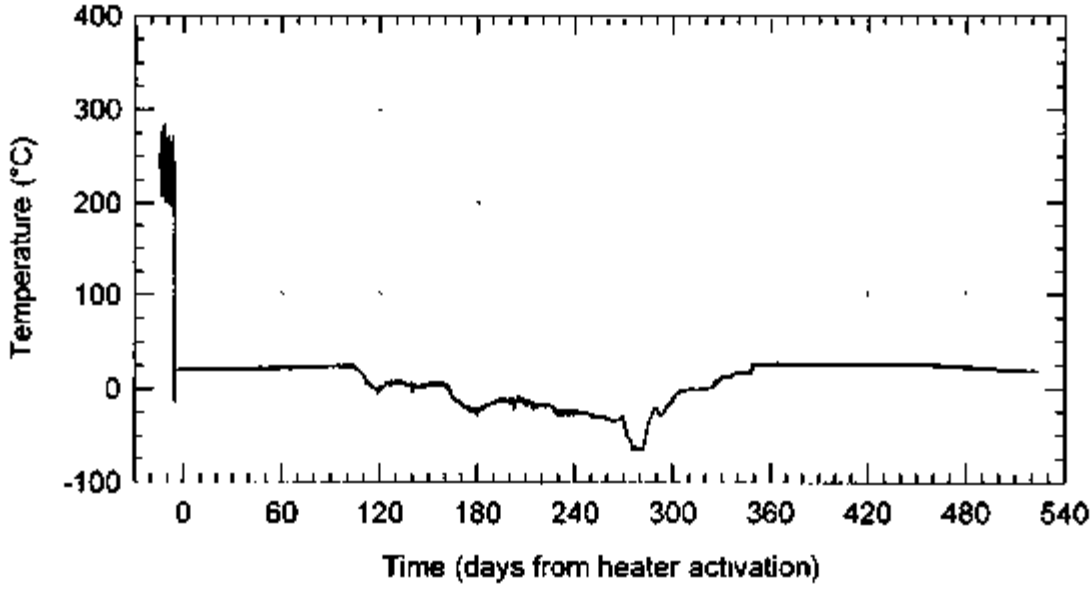

Figure G-16 Data from Failed Gage TMA-RTD-23-19

APPENDIX H

BOREHOLE JACK DATA

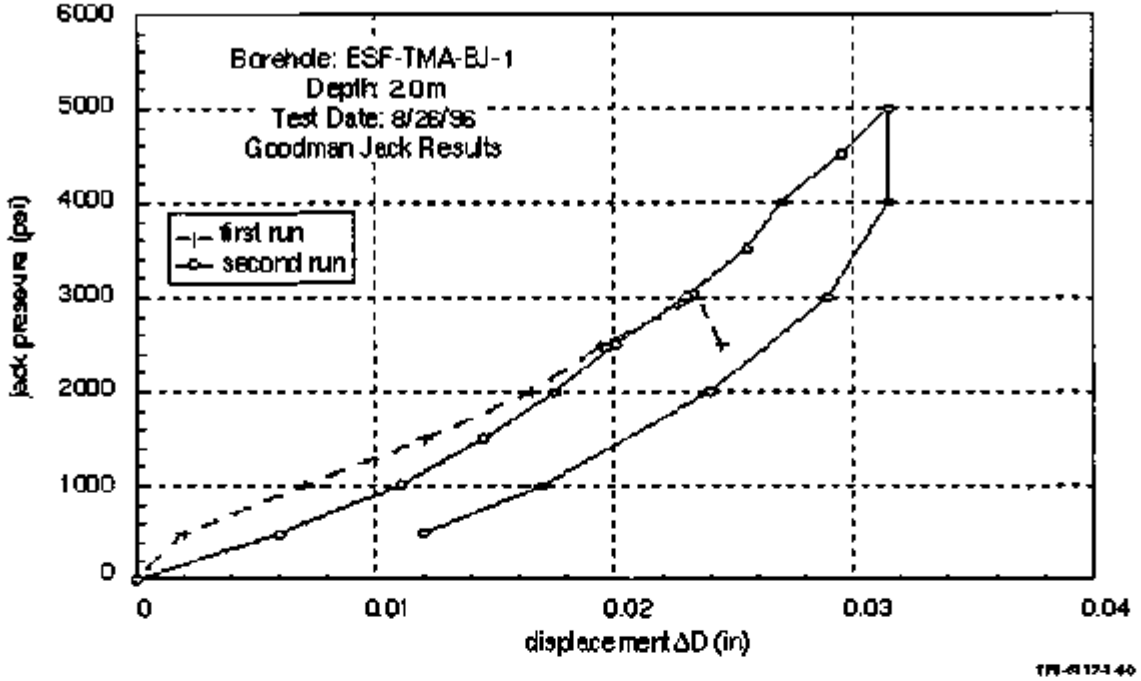

Figure H-1. Pressure/Displacement History for Goodman Jack Test Date August 26, 1996, 2.0 m from Collar

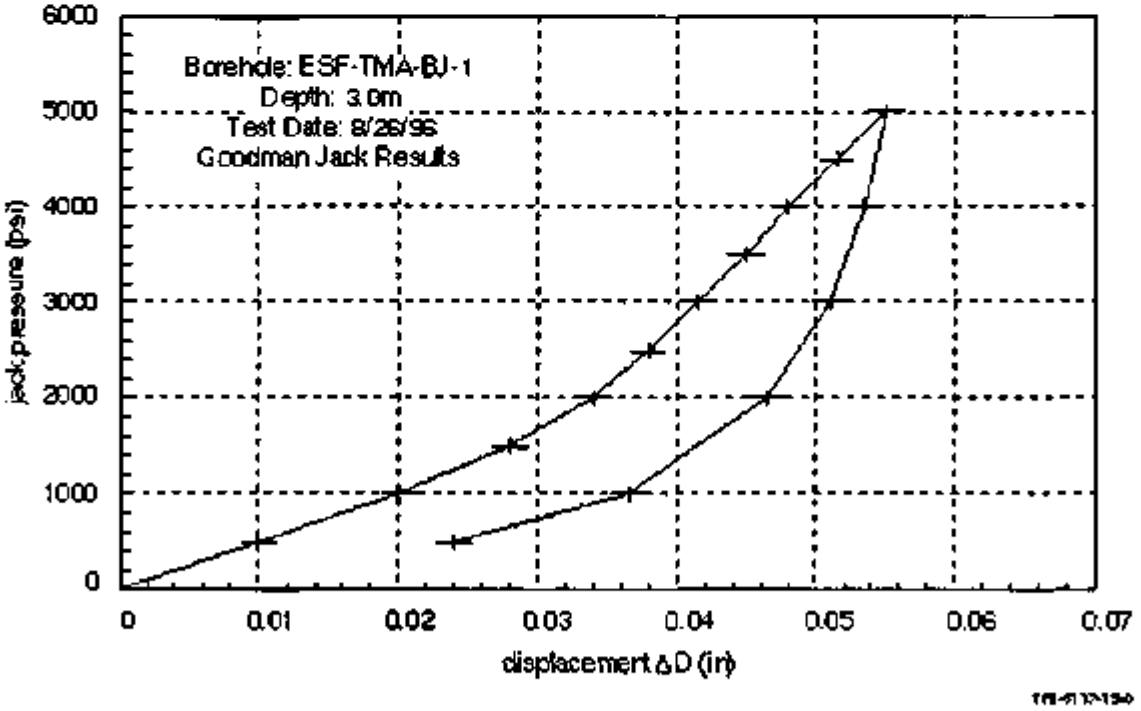

Figure H-2. Pressure/Displacement History for Goodman Jack Test Date August 26, 1996, 3.0 m from Collar

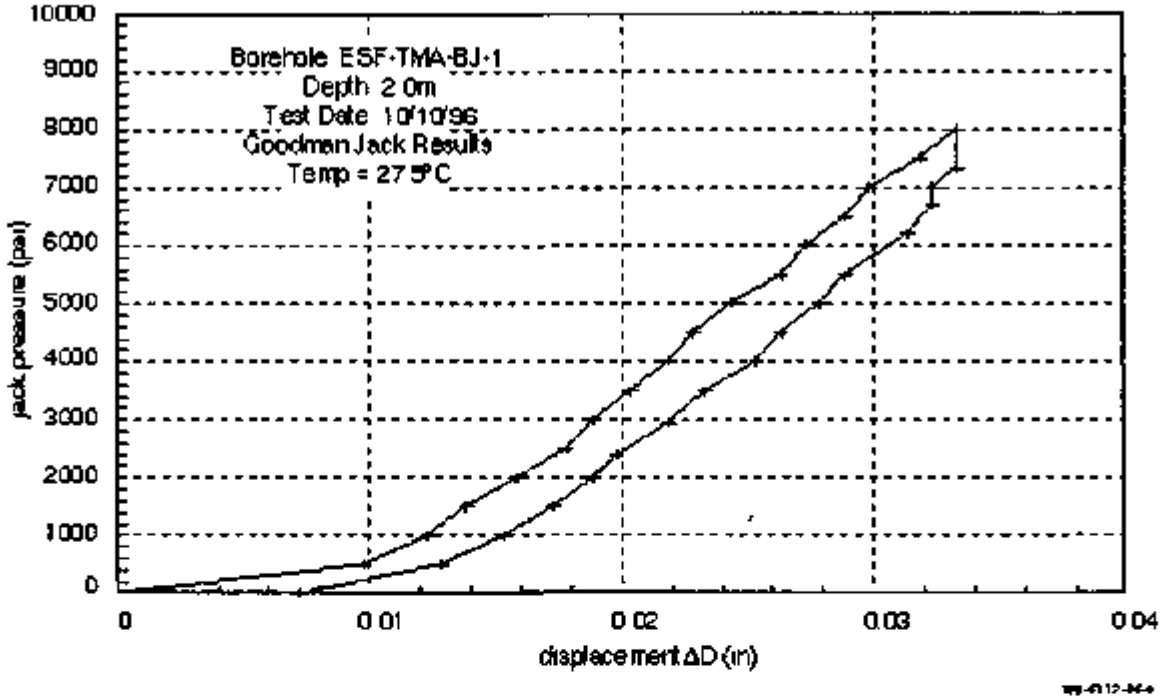

Figure H-3 Pressure/Displacement History for Goodman Jack Test Date October 10, 1996, 2 0 m from Collar

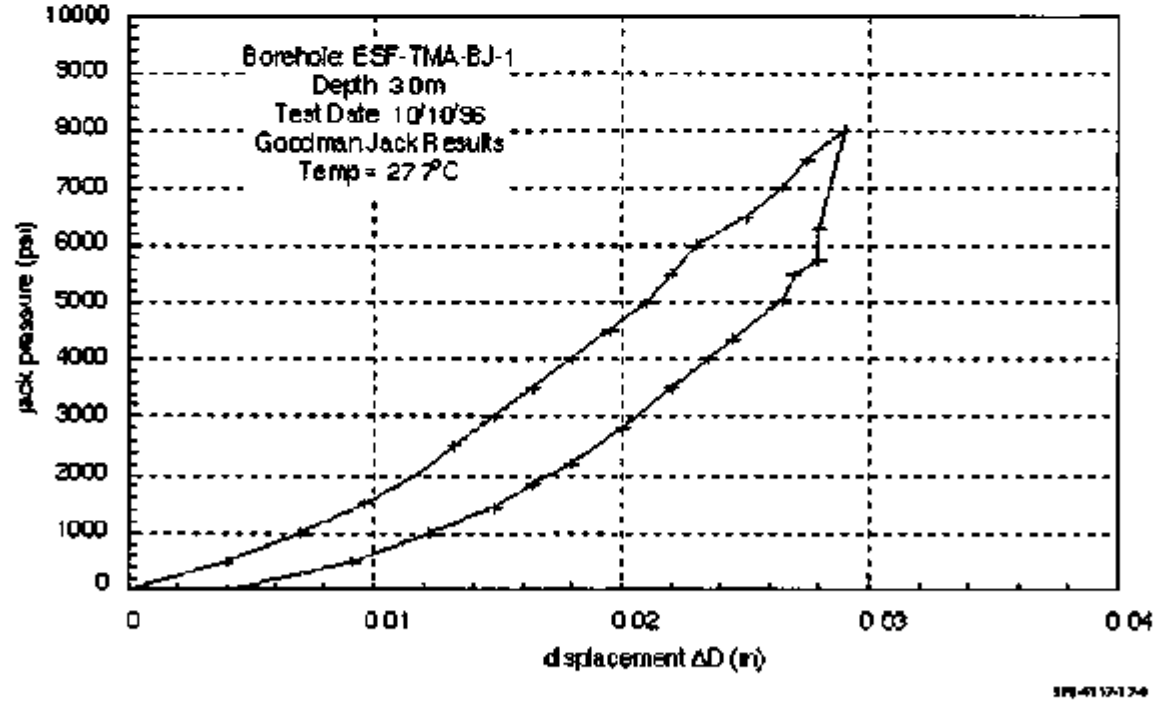

Figure H-4 Pressure/Displacement History for Goodman Jack Test Date October 10, 1996, 3 0 m from Collar

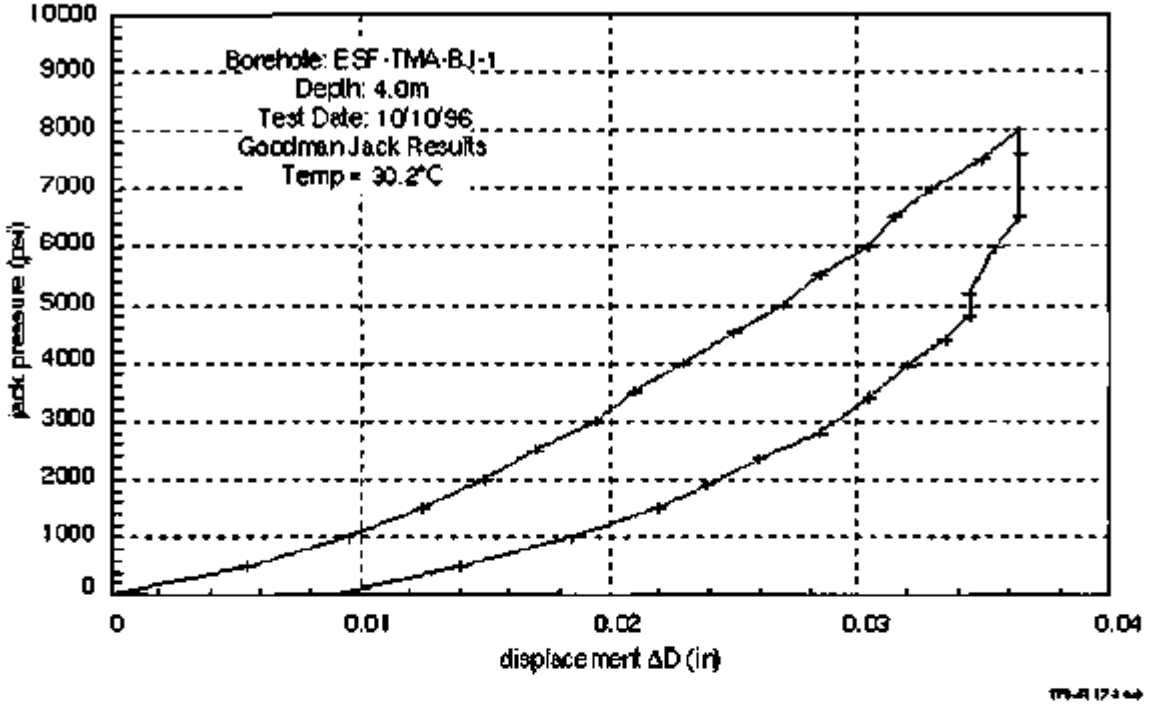

Figure H-5. Pressure/Displacement History for Goodman Jack Test Date October 10, 1996, 4.0 m from Collar

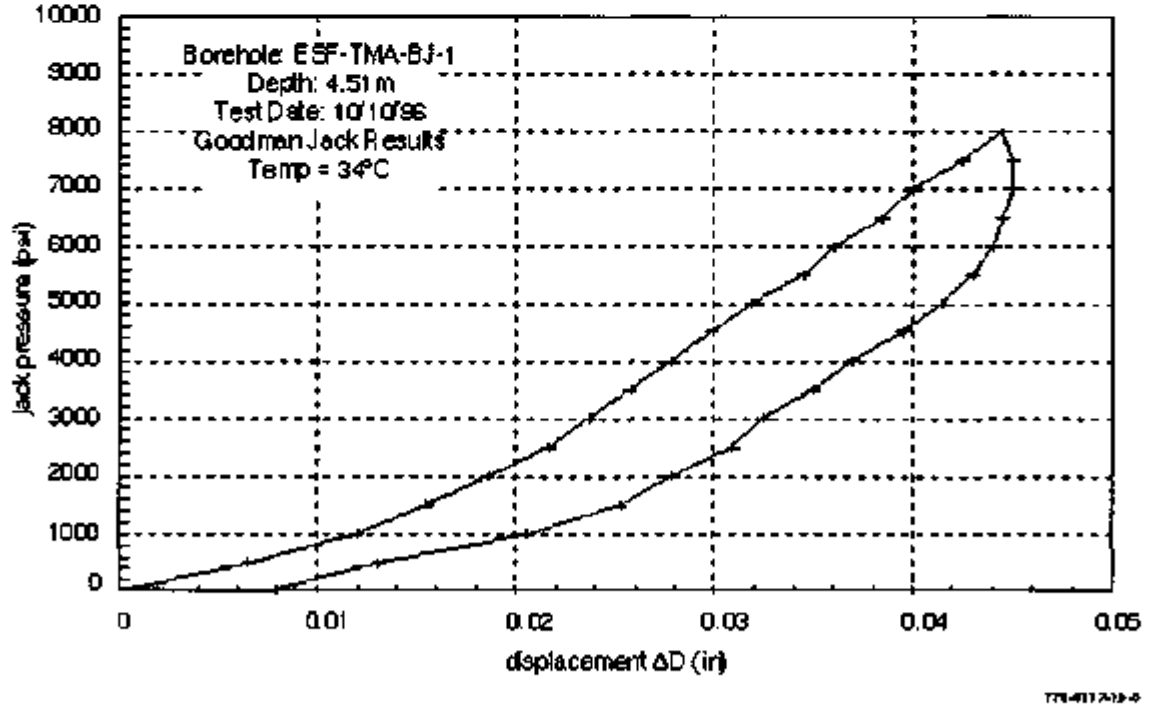

Figure H-6. Pressure/Displacement History for Goodman Jack Test Date October 10, 1996, 4.51 m from Collar

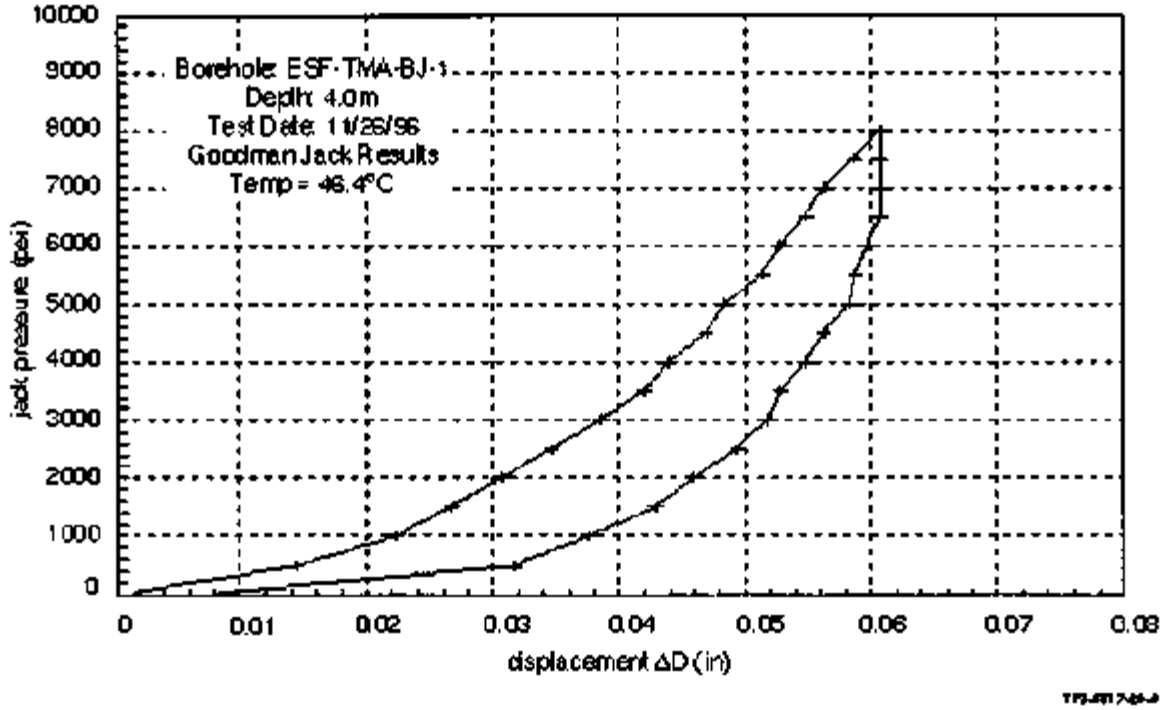

Figure H-7. Pressure/Displacement History for Goodman Jack Test Date November 26, 1996, 3.0 m from Collar

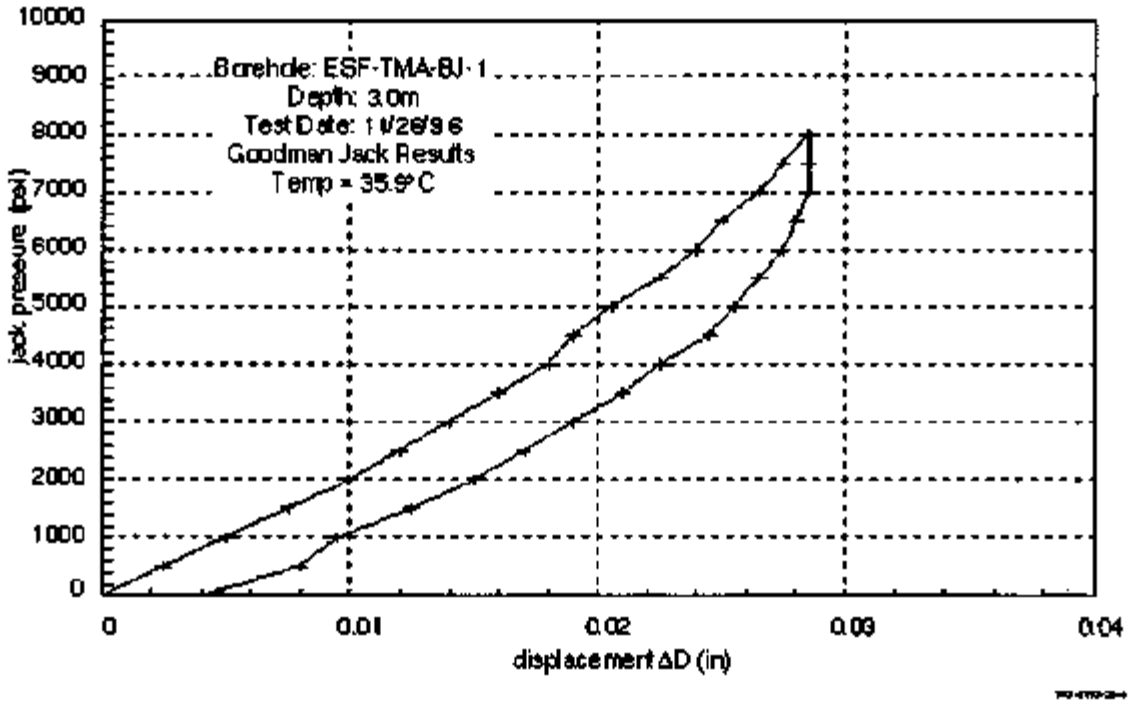

Figure H-8. Pressure/Displacement History for Goodman Jack Test Date November 26, 1996, 4.0 *m* from Collar

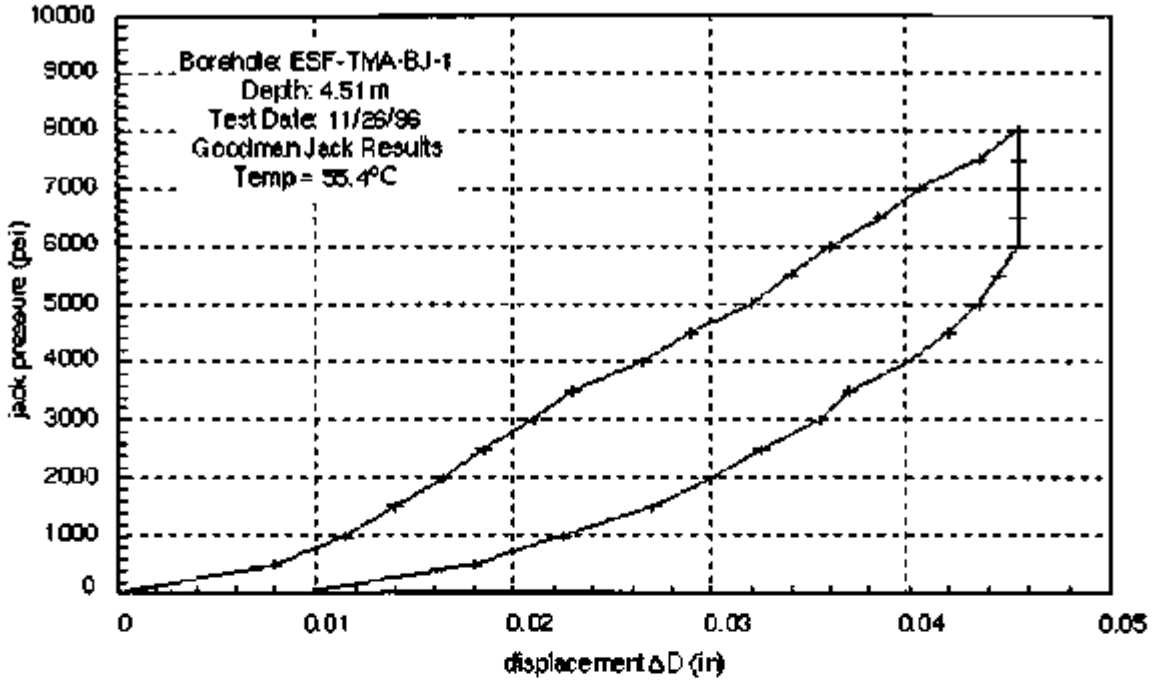

Figure H-9. Pressure/Displacement History for Goodman Jack Test Date November 26, 1996, 4.51 m from Collar

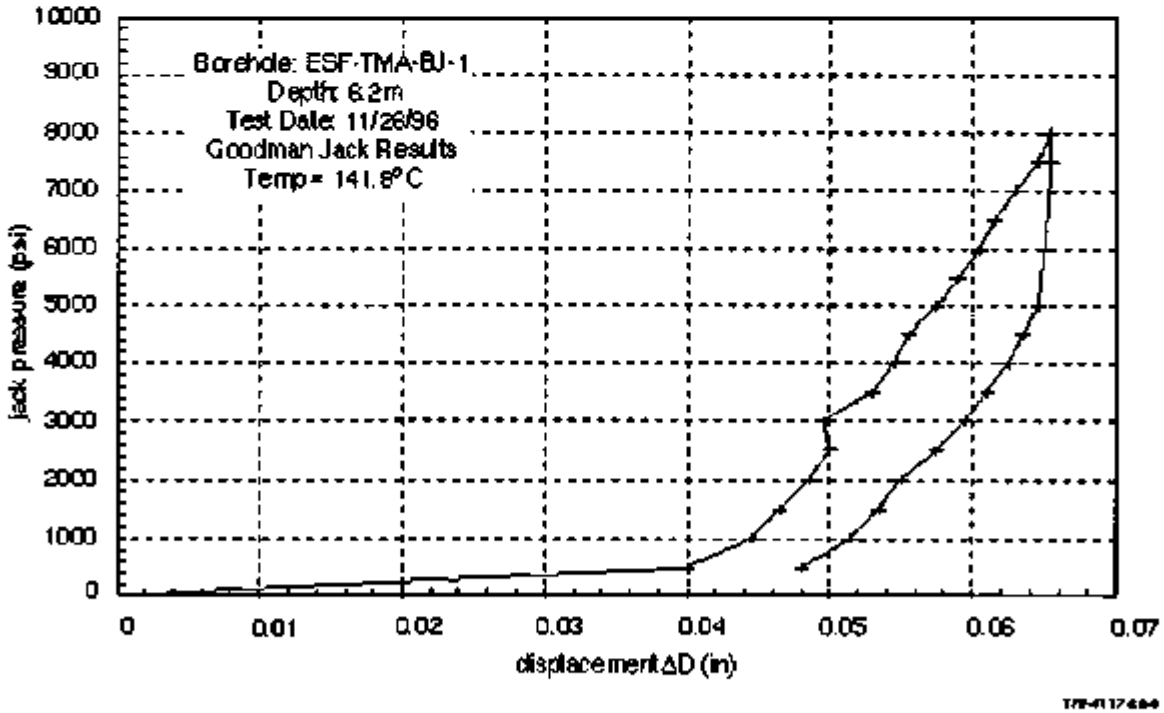

Figure H-10. Pressure/Displacement History for Goodman Jack Test Date November 26, 1996, 6.2 m from Collar

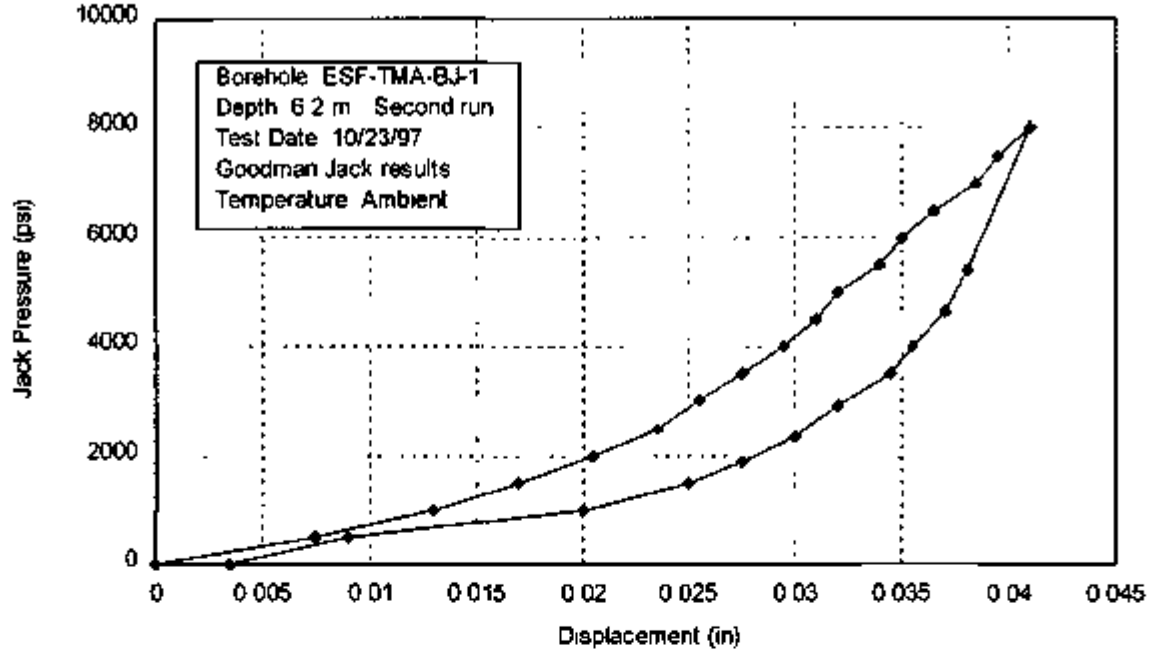

Figure H-11. Pressure/Displacement History for Borehole Jack Test Date March 18, 1997, 2 0 m from Collar

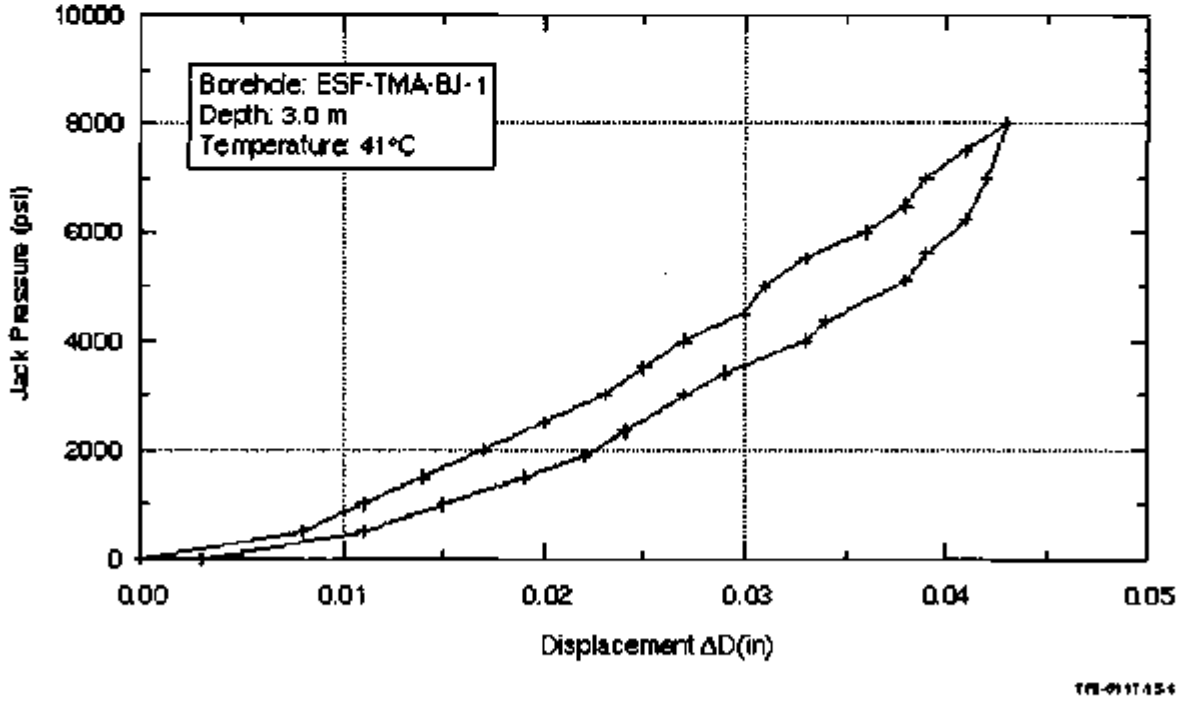

Figure H-12. Pressure/Displacement History for Borehole Jack Test Date March 18, 1997, 3 0 m from Collar

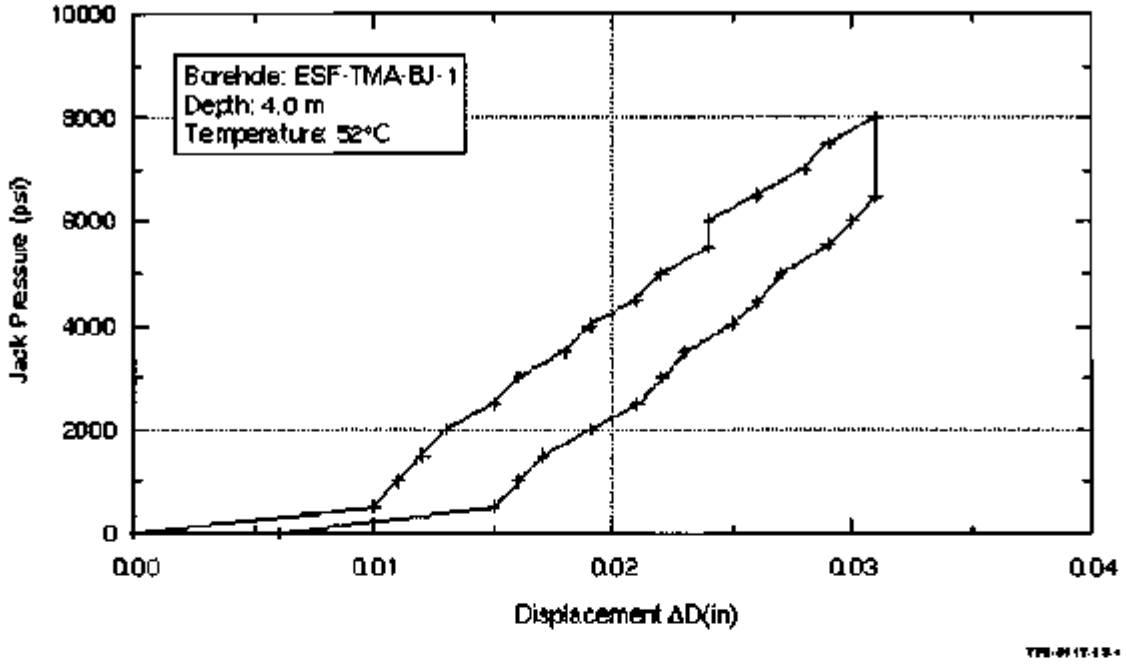

Figure H-13. Pressure/Displacement History for Borehole Jack Test Date March 18, 1997, 4.0 m from Collar

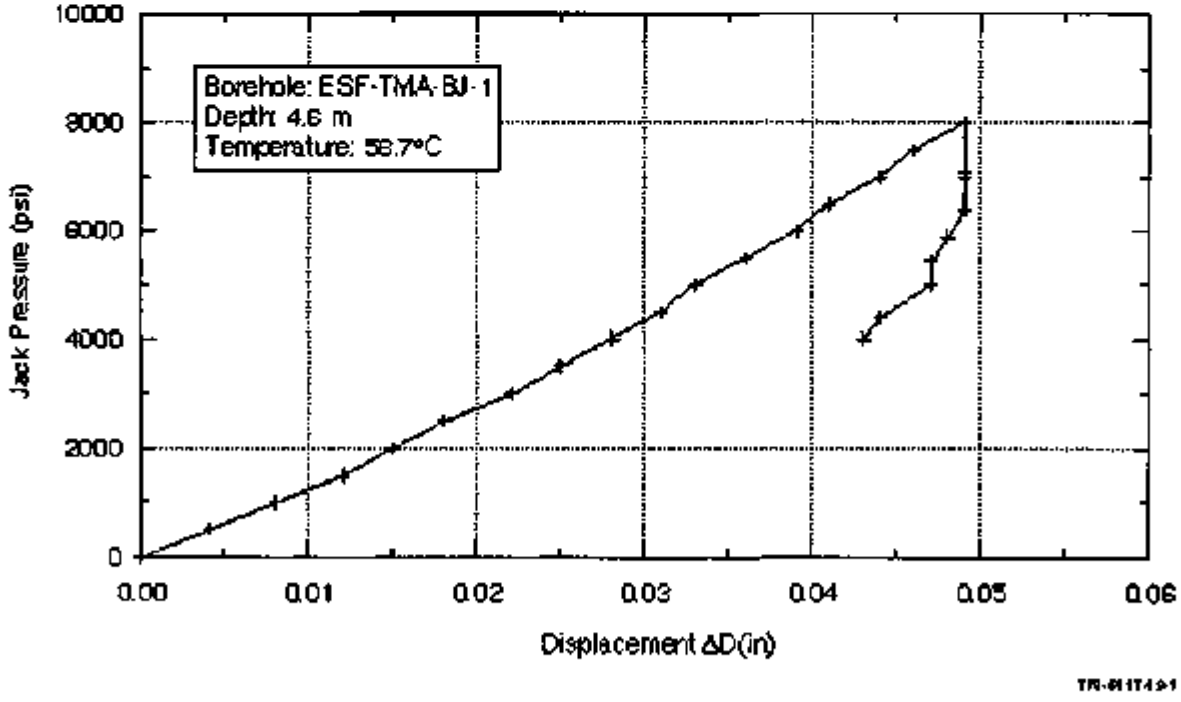

Figure H-14. Pressure/Displacement History for Borehole Jack Test Date March 18, 1997, 4.6 m from Collar

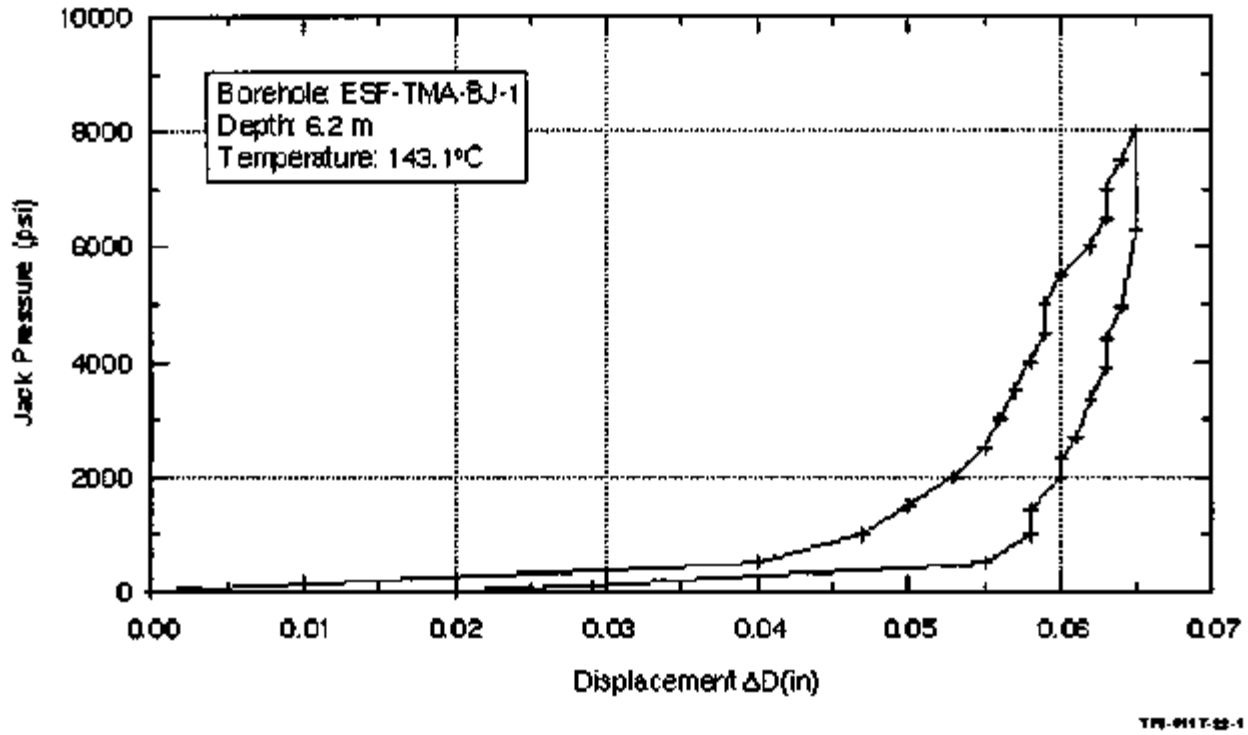

Figure H-15. Pressure/Displacement History for Borehole Jack Test Date March 18, 1997, 6.2 m from Collar

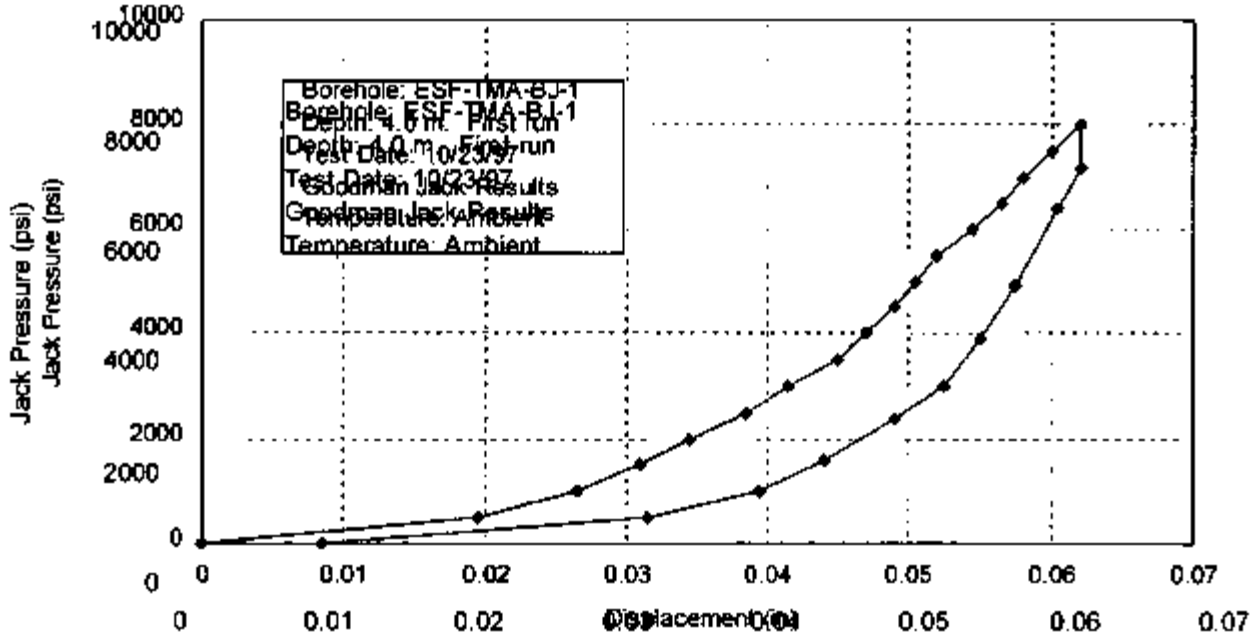

Figure H-16. Pressure/Displacement History for Borehole Jack Test Date October 23, 1997, 4.0 m from Collar, First Load Cycle

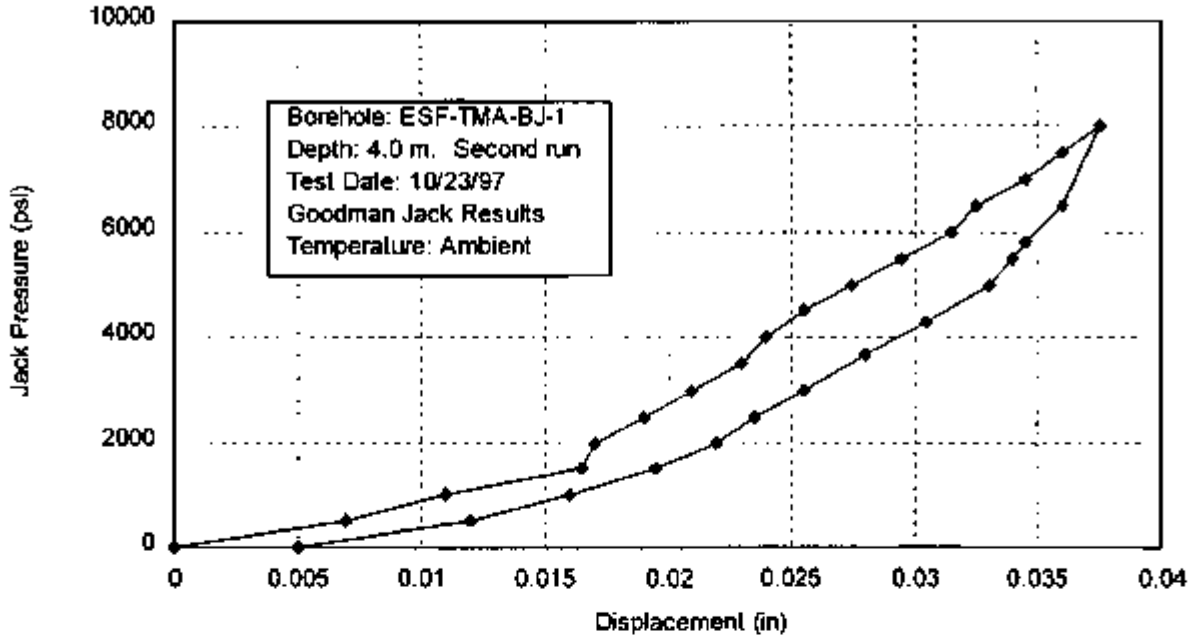

Figure H-17. Pressure/Displacement History for Borehole Jack Test Date October 23, 1997, 4.0 m from Collar, Second Load Cycle

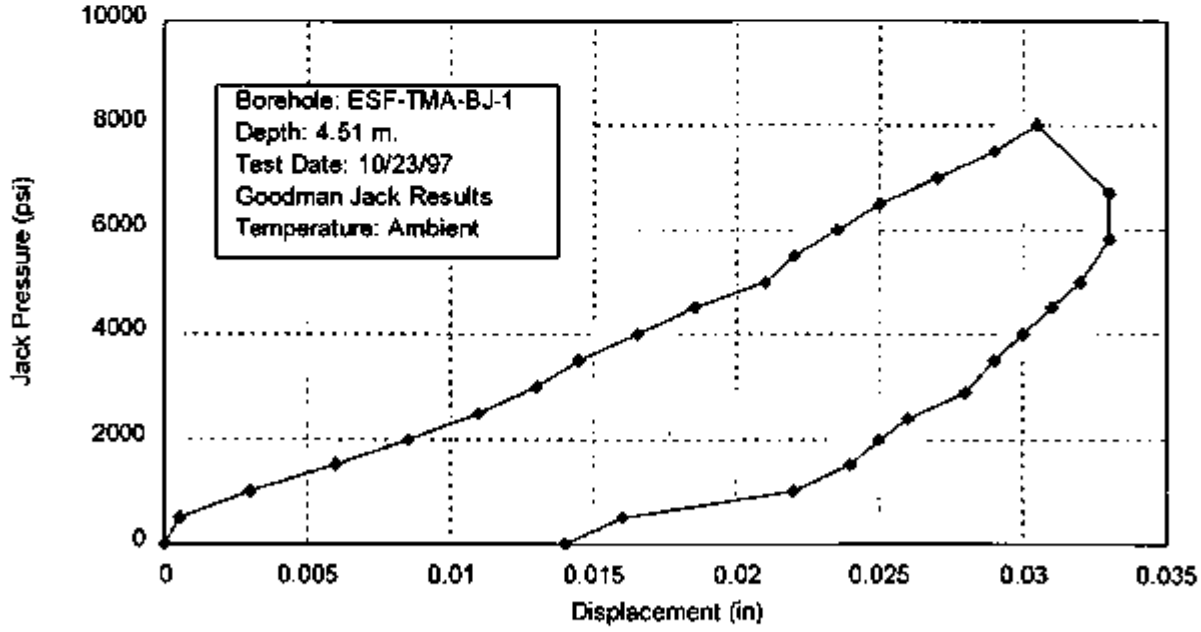

Figure H-18. Pressure/Displacement History for Borehole Jack Test Date October 23, 1997, 4.51 m from Collar

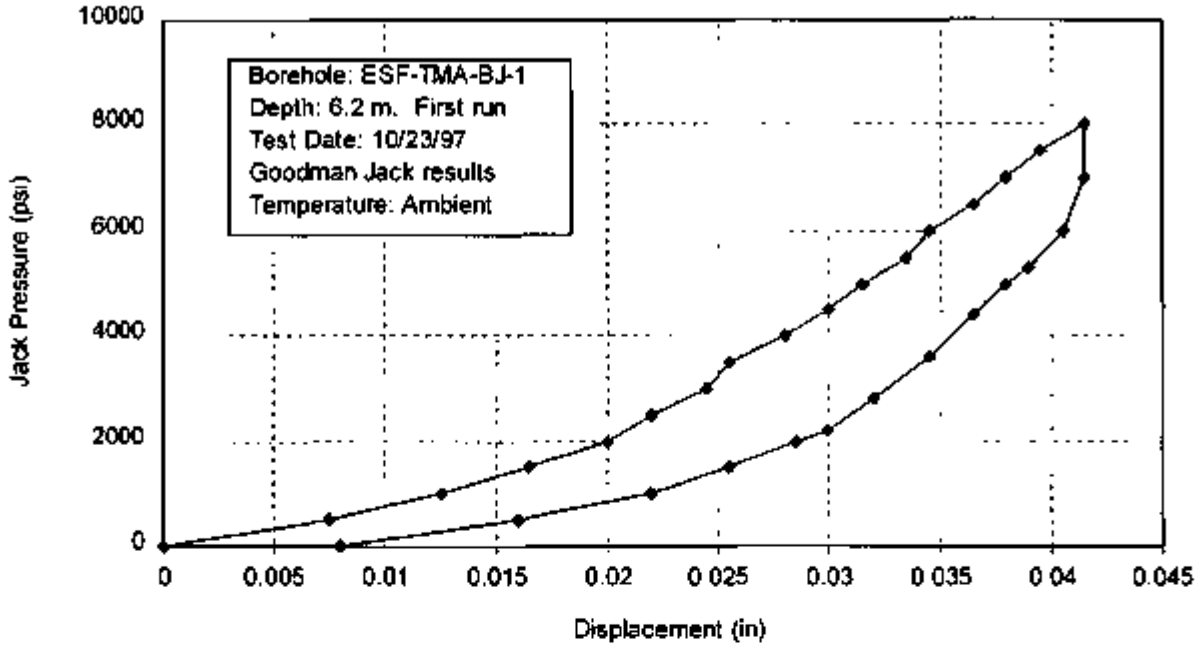

Figure H-19. Pressure/Displacement History for Borehole Jack Test Date October 23, 1997, 6 2 m from Collar, First Load Cycle

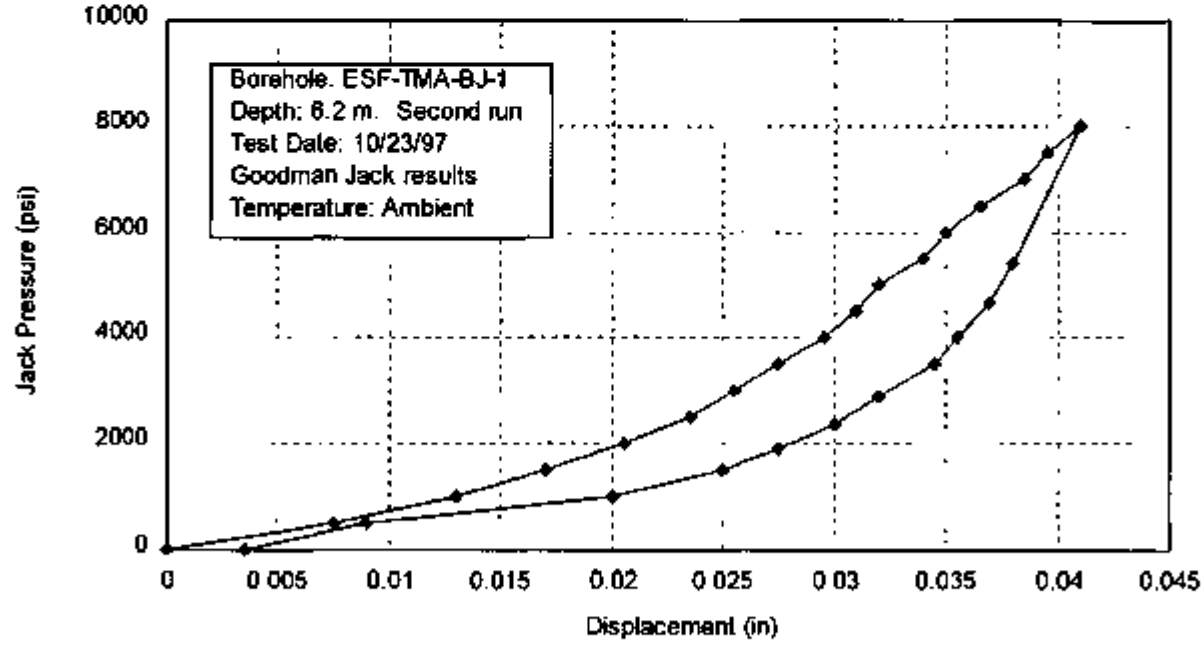

Figure H-20. Pressure/Displacement History for Borehole Jack Test Date October 23, 1997, 6.2 m from Collar, Second Load Cycle

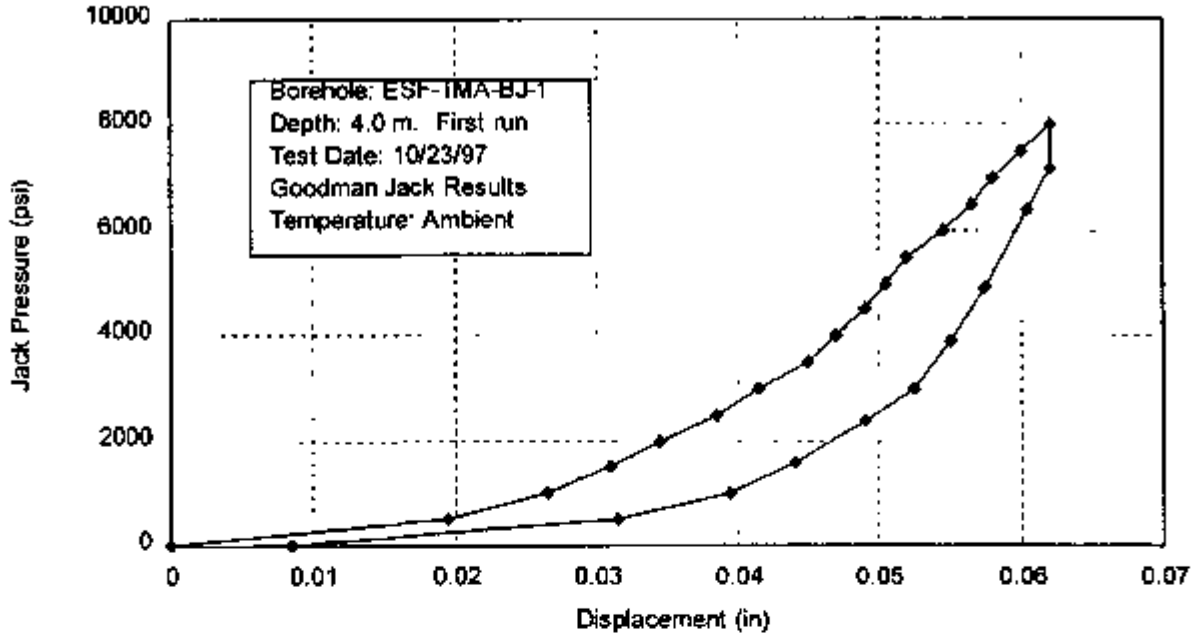

Figure H-21. First Load Cycle for Jack Tests Conducted at 4 0 m Depth on October 23, 1997

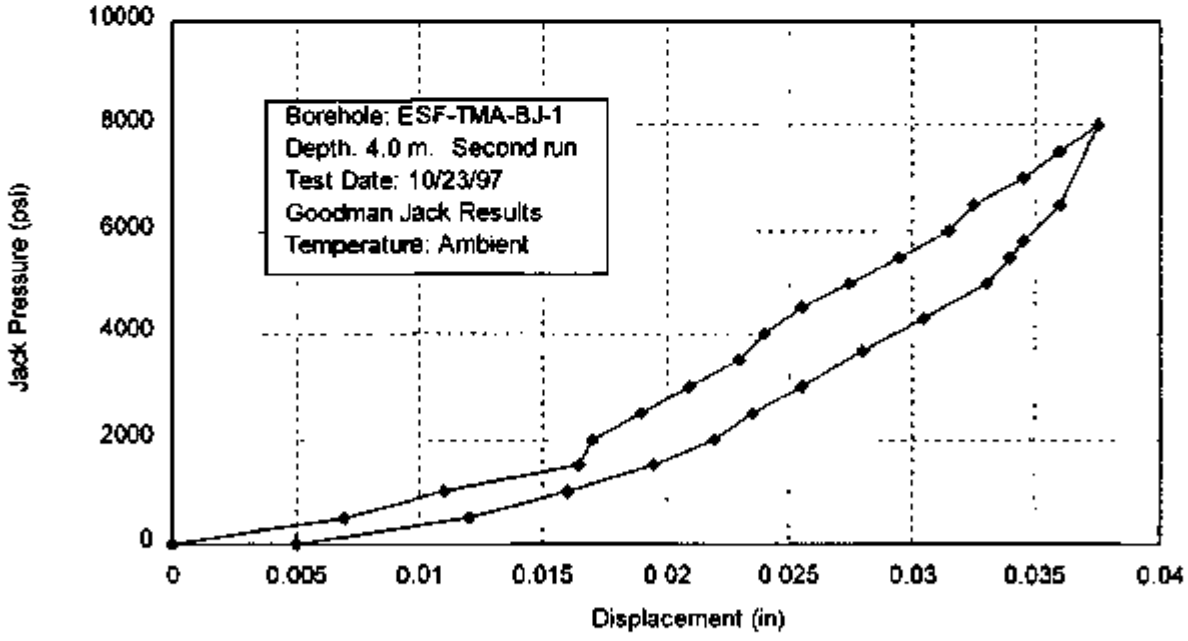

Figure H-22. Second Load Cycle for Jack Tests Conducted at 4 0 m Depth on October 23, 1997

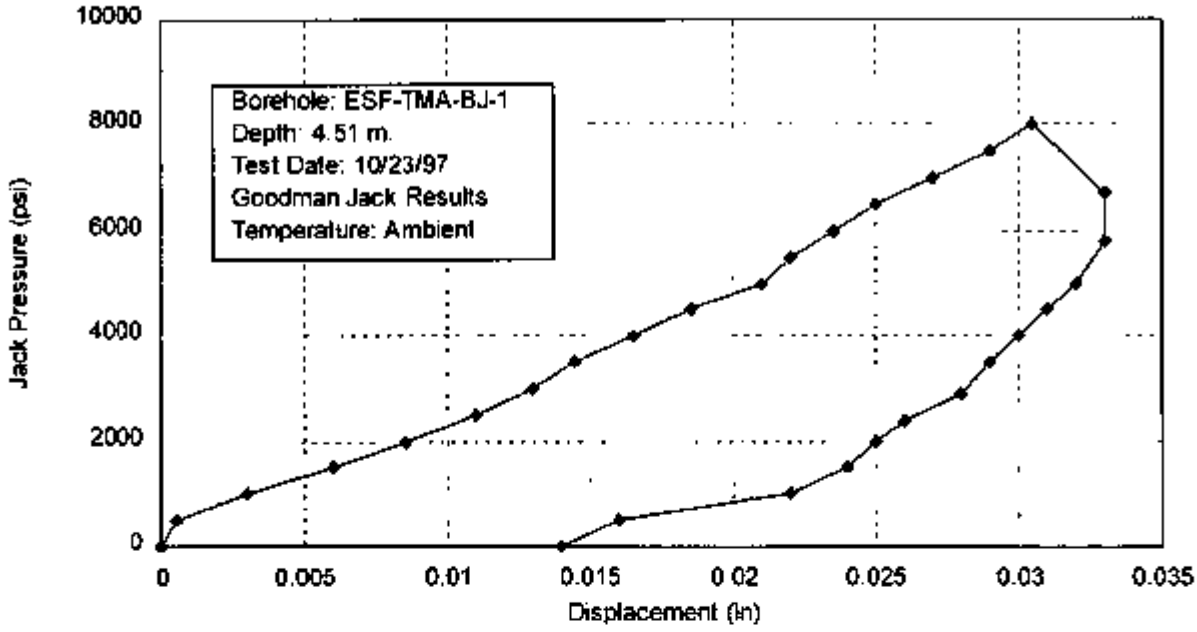

Figure H-23. Load Cycle for Jack Tests Conducted at 4.51 m Depth on October 23, 1997

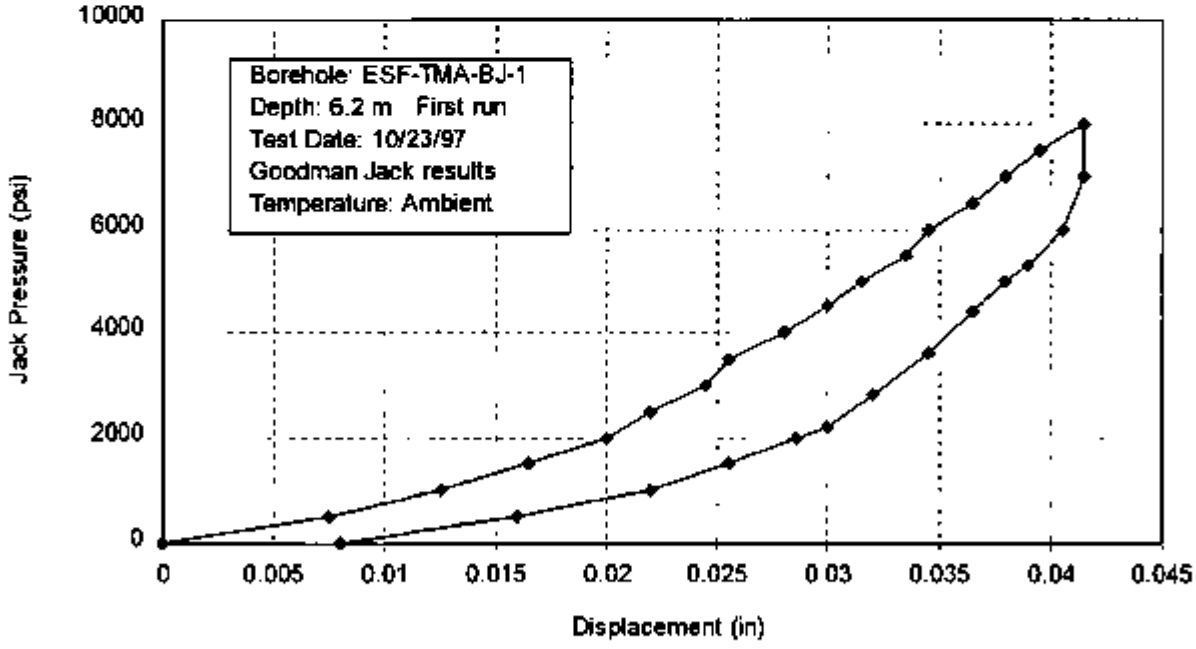

Figure H-24 First Load Cycle for Jack Tests Conducted at 6.2 m Depth on October 23, 1997

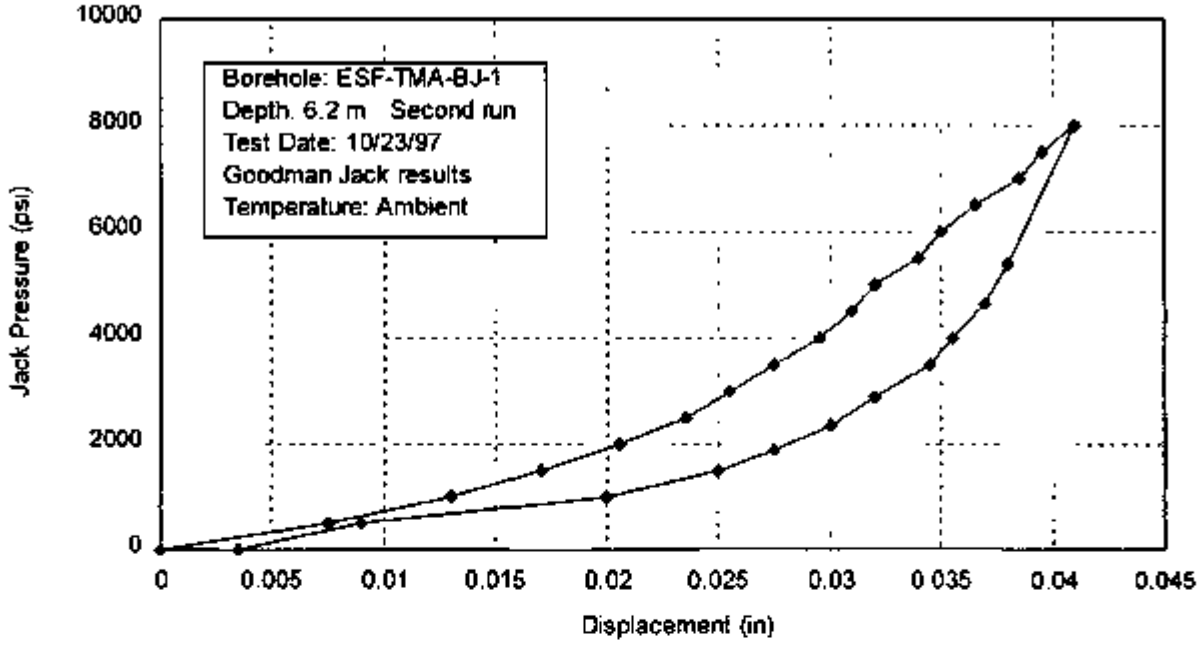

Figure H-25. Second Load Cycle for Jack Tests Conducted at 6.2 m Depth on October 23, 1997

INTENTIONALLY LEFT BLANK

APPENDIX I

TECHNICAL DATA INFORMATION FORMS FOR DATA SUBMITTED TO THE TECHNICAL DATA MANAGEMENT SYSTEM

August 31, 1998

From: Suzanne Lahr - Technical Data Coordinator

Subject: Cover Letters for SP1190M4

Three different cover letters exist for this report. The reason for this is as follows:

I originally submitted three data sets for Level 4 Milestone Report SP1190M4 on August 26, 1998, these are identified by DTN: LB980901123142.001, DTN: LB980901123142.002, and DTN: LB980901123142.003 (TDIF Numbers 307117, 307118, and 307119, respectively). The cover letter that was originally submitted reflects these three data sets.

On August 31, 1998 Yvonne Tsang had another data set that she wished to submit; this data set is identified by DTN: LB980901123142.006 (TDIF Number 307129). I submitted that data set alone on a 3.5" diskette to the YMP TDB. This cover letter reflects this later data set only.

The cover letter that will be submitted to Larry Hayes with the actual report includes all TDIF Numbers and DTNs that are submitted for Milestone SP1190M4.

All data sets (DTNs: LB980901123142.001, .002, .003, and .006) are now burned onto three CD-ROM disks, two of which will be submitted to the RPC, and one which will remain in the LBNL NWP QA records room.

Earth Sciences Division

August 26, 1998

QA:N/A

Phill Jones
M&O TRW
Technical Data Management
MS 423/127
1180 Town Center Drive
Las Vegas, NV 89134

WBS: 1.2.3.14.2

SUBJECT: Yucca Mountain Site Characterization Project (YMP) Technical Data Base (TDB) data transmittal letter for the submittal of technical data associated with the Level 4 Milestone SP1120M4: "Single Heater Test Final TDIF Submittal," Y.W. Tsang, P.I.

DTN: LB980901123142.001	**TDIF: 307117**	(Active Hydrology Testing)
DTN: LB980901123142.002	**TDIF: 307118**	(Passive Monitoring Data)
DTN: LB980901123142.003	**TDIF: 307119**	(Ground Penetrating Radar Data)
DTN: LB980901123142.006	**TDIF: 307129**	(Lab Measurements of Cores)

The Subject Data Transmittal Package is submitted to the YMP TDB in accordance with YMP Administrative Procedure YAP-SIII.3Q, REV. 2, ICN 0. All technical reviews of the data have been completed as required. The following items are included in this submittal:

1. Technical Data Information (TDIF) Forms;
2. An electronic copy of the data submitted on CD-ROM;
3. A list of data files;
4. A hardcopy of the data;
5. Annotated example sheets of the data; and
6. Supplemental data sheets explaining the data.

If you have any questions, please contact me at (510) 495-2641.

Sincerely,

Suzanne M. Link

Suzanne M. Link
Technical Data Coordinator

cc. G.S. Bodvarsson
Y.W. Tsang
File

Earth Sciences Division

August 26, 1998 QA:N A

Phil Jones
M&O TRW
Technical Data Management
MS 423/127
1180 Town Center Drive
Las Vegas, NV 89134

WBS 1.2.3.14.2

SUBJECT Yucca Mountain Site Characterization Project (YMP) Technical Data Base (TDB) data transmittal letter for the submittal of technical data associated with the Level 4 Milestone SP1198M4: "Single Heater Test Final TDIF Submittal" Y.W. Tsang, P.I.

DTN: LB980901123142.001	**TDIF: 307115**	(Active Hydrology Testing)
DTN: LB980901123142.002	**TDIF: 307116**	(Passive Monitoring Data)
DTN: LB980901123142.003	**TDIF: 307119**	(Ground Penetrating Radar Data)

The Subject Data Transmittal Package is submitted to the YMP TDB in accordance with YMP Administrative Procedure YAP SIII.3Q REV 1, ICN 0. All technical reviews of the data have been completed as required. The following items are included in this submittal:

1. Technical Data Information (TDIF) Forms,
2. An electronic copy of the data submitted on CD-ROM;
3. A list of data files;
4. A hardcopy of the data,
5. Annotated example sheets of the data, and
6. Supplemental data sheets explaining the data

If you have any questions, please contact me at (510) 495-2841.

Sincerely,

Signature of Link

Suzanne M. Link
Technical Data Coordinator

cc: G.S. Bodvarsson
Y.W. Tsang
File

Ernest Orlando Lawrence Berkeley National Laboratory
One Cyclotron Road • Berkeley, California 94720 Tel: 510 486 7041 • Fax: 510 486 5686

Earth Sciences Division

August 31, 1999 QA: N/A

Phil Jones
M&O/TRW
Technical Data Management
MS 423/127
1180 Town Center Drive
Las Vegas, NV 89134

WBS: 1.2.3.2.4.2

SUBJECT: Yucca Mountain Site Characterization Project (YMP) Technical Data Base (TDB) data transmittal letter for the submittal of technical data associated with the Level 4 Milestone SP1290M4: "Single Heater Test Final TDIF Submittal," Y.W. Tsang, P.I.

DTN: LB980901123142.006 TDIF: 307139 (Lab Measurements of Cores)

The Subject Data Transmittal Package is submitted to the YMP TDB in accordance with YMP Administrative Procedure YAP-SIII.3Q REV. 2, ICN 0. All technical reviews of the data have been completed as required. The following items are included in this submittal:

1. Technical Data Information (TDIF) Forms;
2. An electronic copy of the data submitted on diskette.
3. A list of data files,
4. A hardcopy of the data; and
5. An annotated example sheets of the data

If you have any questions, please contact me at (510) 495-2841.

Sincerely,

Suzanne M. Tink
Technical Data Coordinator

cc: G.S. Bodvarsson
Y.W. Tsang
File

Ernest Orlando Lawrence Berkeley National Laboratory
One Cyclotron Road , Berkeley, California 94720 , Tel 510.485.7671 , Fax 510.486.5686

YMP 025 R4
05/06/96

YUCCA MOUNTAIN SITE CHARACTERIZATION PROJECT
TECHNICAL DATA INFORMATION

Page 1 of ...

(Check one) ☒ ACQUIRED DATA *(complete Parts I and II)*
Data Tracking Number (DTN): [illegible]

☐ DEVELOPED DATA *(complete Parts I and III)*
Data Tracking Number (DTN): _____

PART I Identification of Data

Title/Description of Data: AC INJ. TRACER DETAIL DATA IN BOREHOLES UE-25 NRP #1, AIR INJECTION TESTS AND GAS TRACER TESTS FOR THE FINAL TOP SUBINTERVAL FOR THE SINGLE HEATER TEST

Principal Investigator (PI): [illegible] T. N.
(Last Name) (First and Middle Initials)

PI Organization: LAWRENCE BERKELEY NATIONAL LABORATORY

Are Data Qualified? ☒ Yes ☐ No Governing Plan: TSPA

SCPB Activity Number(s): _____

WBS Number(s): 1.2.3.14.2

PART II Data Acquisition/Development Information

Method: [illegible] AIR INJECTION TESTS AND GAS TRACER TESTS USING SULFUR HEXAFLUORIDE (SF6)

Location(s): ESF TCOVE 5 - SINGLE HEATER TEST BLOCK

Period(s): 3/30/98 to 3/28/98
(Start - M/D/YYYY) (End - M/D/YYYY)

Sample ID Number(s): _____

PART III Source Data DTN(s)

_____ _____ _____

_____ _____ _____

_____ _____ _____

Comments

IT IS IMPERATIVE FOR THE USER OF THE DATA TO READ CHAPTER 2, SECTION 2.3.3 OF THIS REPORT BEFORE USING THE DATA

Checked by: [signature] (Signature) August 26, 1998 (Date)

YAP SIII 3Q 1

YMP-623-R4
05/05 96

YUCCA MOUNTAIN SITE CHARACTERIZATION PROJECT
TECHNICAL DATA INFORMATION

Page 1 of 1

(Check one) [X] ACQUIRED DATA (Complete Parts I and II)
Data Tracking Number (DTN): [illegible]

[ ] DEVELOPED DATA (Complete Parts I, II and III)
Data Tracking Number (DTN): _____

PART I Identification of Data

Title/Description of Data: PASSIVE MONITORING DATA (TEMPERATURE, RELATIVE HUMIDITY AND GAUGE PRESSURE) FOR THE FINAL DRIFT SUBMITTAL FOR THE SINGLE HEATER TEST

Principal Investigator (PI): [illegible] Y. N
Last Name First and Middle Initials

PI Organization: LAWRENCE BERKELEY NATIONAL LABORATORY

Are Data Qualified? [X] Yes [ ] No Governing Plan: PMP

SCPB Activity Number(s): _____

WBS Number(s): 1.2.3.14.2

PART II Data Acquisition/Development Information

Method: PASSIVE MONITORING IN THE ESF DRIFT OF THE DATA LOGGER UNDER MANAGEMENT OF THERMAL TEST DATA MANAGER FRED HOKETT

Location(s): ESF ALCOVE 5 - SINGLE HEATER TEST ROOM

Period(s): 8/1/96 to 12/31/97
From: MM/DD/YY To: MM/DD/YY

Sample ID Number(s): _____

PART III Source Data DTN(s)

_____ _____ _____
_____ _____ _____
_____ _____ _____

Comments

IT IS IMPERATIVE FOR THE USER OF THE DATA TO READ CHAPTER 2, SECTION 2.2 OF THIS REPORT BEFORE USING THE DATA.

Checked by: [signature] [illegible] August 26, 1998
Signature Date

YAP-SIII.3Q.1

307119

YMP-023-R4
05/06/96

YUCCA MOUNTAIN SITE CHARACTERIZATION PROJECT
TECHNICAL DATA INFORMATION

Page 1 of 1

(Check one): [X] ACQUIRED DATA *(complete Parts I and II)*
Data Tracking Number (DTN): LB990901123142.003

[ ] DEVELOPED DATA *(complete Parts I, II and III)*
Data Tracking Number (DTN): _____

PART I Identification of Data

Title/Description of Data: GROUND PENETRATING RADAR DATA FOR FINAL TDIF SUBMITTAL FOR THE SINGLE HEATER TEST.

Principal Investigator (PI): TSANG, Y W
Last Name First and Middle Initials

PI Organization: LAWRENCE BERKELEY NATIONAL LABORATORY

Are Data Qualified?: [X] Yes [ ] No Governing Plan: PMP

SCPB Activity Number(s): _____

WBS Number(s): 1.2.3.16.2

PART II Data Acquisition/Development Information

Method: GROUND PENETRATING RADAR (GPR) DATA ARE RECORDED AND REVIEWED USING SENSORS AND SOFTWARE INC. PULSE EKKO SOFTWARE INTERFACING A PC COMPUTER.

Location(s): RSF ALCOVE 5 - BOREHOLES 17 AND 25

Period(s): 1/2/98 to 8-18/98
From: MM/DD/YY To: MM/DD/YY

Sample ID Number(s): _____

PART III Source Data DTN(s)

Comments

IT IS IMPERATIVE FOR THE USER OF THE DATA TO READ THE QPA SECTION OF THIS REPORT BEFORE USING THE DATA.

Checked by: Stephanie M. Link August 26, 1998
Signature Date

YAP-SIII.3Q.1

YMP 023 R4
05/06/98

YUCCA MOUNTAIN SITE CHARACTERIZATION PROJECT
TECHNICAL DATA INFORMATION

(Check one): [X] ACQUIRED DATA *(complete Parts I and II)*
Data Tracking Number (DTN): LB980901123142.036

[ ] DEVELOPED DATA *(complete Parts I, II and III)*
Data Tracking Number (DTN): _____

PART I Identification of Data

Title/Description of Data: LABORATORY TEST RESULTS OF HYDROLOGICAL PROPERTIES FROM POST-TEST DRY-DRILLED CORES IN THE SINGLE HEATER TEST AREA FOR THE FINAL TDIF SUBMITTAL FOR THE SINGLE HEATER TEST.

Principal Investigator (PI): TSANG, Y. W.
Last Name First and Middle Initials

PI Organization: LAWRENCE BERKELEY NATIONAL LABORATORY

Are Data Qualified?: [X] Yes [ ] No Governing Plan: PAMP

SCPB Activity Number(s): _____

WBS Number(s): 1.2.3.16.2

PART II Data Acquisition/Development Information

Method: LAB MEASUREMENTS OF CORES.

Location(s): ESF - SINGLE HEATER TEST AREA

Period(s): 7/1/96 to 8/12/96
From: MM/DD/YY To: MM/DD/YY

Sample ID Number(s): _____

PART III Source Data DTN(s)

_____ _____ _____
_____ _____ _____
_____ _____ _____

Comments

IT IS IMPERATIVE FOR THE USER OF THE DATA TO READ SECTION 2.5 OF THIS REPORT BEFORE USING THE DATA.

Checked by: Suzanne M. Linck August 31, 1998
Signature Date

YAP-SIII.3Q.1

MOL 19980429 0943

SAIC

Science Applications International Corporation
An Employee-Owned Company

February 10, 1998
WBS 1 2 3 14 2
QA L

Joanna Wiggins
TRW/M&O, MS 423/SU-127
1241 Town Center Drive
Las Vegas, NV 89134

Dear Joanna

Subject: Sandia National Laboratories Transfer of Data to the Technical Database GENISES for Data in the Report "Evaluation and Comparative Analysis of Single Heater Test, Thermal and Thermomechanical Data First Quarter FY98 Results (8/26/96 through 11/30/97)" (WBS 1 2 3 14 2) (SCP B 3 1 15 1 6)

Enclosed is a copy of the TDIF (Technical Data Information Form) for Data Tracking Number, DTN SNF35110695001 008, TDIF #306549, for your information, for the transfer of data to GENISES for the Single Heater Test, First Quarter FY98 Results , as listed above All technical reviews of this data have been performed The Data Transmittal Package will be submitted to the Yucca Mountain Project Records Processing Center under the Data Tracking Number and TDIF number listed

This data supersedes data previously identified by DTN SNF35110695001 007 The data on the disk enclosed includes the data for the previous quarters, as well as the current quarter, therefore superseding the previous data I have attached a hard copy of the data with the Parameters and Attributes which are applicable to this data labeled, as well as one 3 1/2" disk with the electronic files

If you have questions or concerns, please call me at 505-842-7789 The Principal Investigator is Ray Finley, and he can be reached at 505-844-4462

Sincerely yours,

Eloise M James

Eloise M James
SNL Technical Data Records

Enclosures: As stated
Copy to (w/o encl)
SNL 6117 R E Finley
YMP/1 2 3 14 2/TD QA 55/F35-11/06/95
SNL 6850 S A Orrell
SNL 6117 L S Costin
YMP RPC (TDIF not included-Information Only, Original Submitted Separately, Disk Included)

2108 Air Park Road S E , Albuquerque, New Mexico 87106 (505) 247-8787
Other SAIC Offices: Boston, Colorado Springs, Dayton, Huntsville, Las Vegas, Los Angeles, McLean, Oak Ridge, Orlando, Palo Alto, San Diego, Seattle and Tucson

MOL.19980429.0936

306549

YMP-023-R4
05/06/96

YUCCA MOUNTAIN SITE CHARACTERIZATION PROJECT
TECHNICAL DATA INFORMATION

(Check one): [X] ACQUIRED DATA *(complete Parts I and II)*
Data Tracking Number (DTN): SNF35110695001.008

[ ] DEVELOPED DATA *(complete Parts I, II and III)*
Data Tracking Number (DTN): _____

PART I Identification of Data

Title/Description of Data: EVALUATION AND COMPARATIVE ANALYSIS OF SINGLE HEATER TEST, THERMAL AND THERMOMECHANICAL DATA: FIRST QUARTER FY98 RESULTS (8/26/96 THROUGH 11/30/97) (THIS DATA SUPERSEDES DATA PREVIOUSLY IDENTIFIED BY DTN: SNF35110695001.007)

Principal Investigator (PI): FINLEY, R E
Last Name First and Middle Initials

PI Organization: SANDIA NATIONAL LABORATORIES

Are Data Qualified?: [ ] Yes [X] No Governing Plan: SCP

SCPB Activity Number(s): 8.3.1.15.1.6

WBS Number(s): 1.2.3.84.2

PART II Data Acquisition/Development Information

Method: INSTRUMENTS WERE INSTALLED IN BOREHOLES AND ON THE ROCK SURFACE TO MEASURE THERMOMECHANICAL/HYDROLOGIC RESPONSE TO THE ROCK MASS TO HEATING.

Location(s): THERMAL TESTING FACILITY IN THE EXPLORATORY STUDIES FACILITY, YUCCA MTN.

Period(s): 8/26/96 to 11/30/97
From: MM/DD/YY To: MM/DD/YY

Sample ID Number(s): N/A

PART III Source Data DTN(s)

_____ _____ _____
_____ _____ _____
_____ _____ _____

Comments

SNL DATASET ID: SS/F3S-11/06/95 (NOTE: THE DATA PRESENTED IN THIS REPORT SHOULD BE CONSIDERED INDETERMINATE UNTIL THE PROCUREMENT/CALIBRATIONS ISSUES RELATED TO YMP DEVIATION REPORT YM-97-D-025

Checked by: R Lois Jones 11/6/98
Signature Date

YAP-SIII.3Q.1

306549

YMP-023-R4
08/31/95

YUCCA MOUNTAIN SITE CHARACTERIZATION PROJECT
TECHNICAL DATA INFORMATION
CONTINUATION SHEET

Page 2 of 2

Comments (continued)

HAVE BEEN RESOLVED.) DATA WAS SUPERSEDED BECAUSE ADDITIONAL DATA WAS INCLUDED.

YAP-SIII.3Q 1

MOL.19981030.0111

Science Applications International Corporation
An Employee-Owned Company

October 8, 1998
WBS: 1.2.3.14.2
QA: L

Phill Jones
TRW/M&O, MS 423
1261 Town Center Drive
Las Vegas, NV 89134

Dear Phill:

Subject: Sandia National Laboratories Transfer to the Technical Database of the Thermal and Thermomechanical Data, and the Posttest Laboratory Thermal and Mechanical Characterization Data in the "Single Heater Test Final Report"

Enclosed are copies of the TDIFs (Technical Data Information Forms) for Data Tracking Number (DTN): SNF35110695001.009, TDIF #307112, and DTN: SNL22080196001.003, TDIF #307123, for your information. This is for the transfer of data from the Single Heater Test Final Report, as listed above, to the Technical Database. A technical review of these data was performed and the data will be submitted to the YMP Records Processing Center under the Data Tracking numbers and TDIF numbers noted.

I have attached a hard copy of the data with the Parameters and Attributes labeled which are applicable to these data, as well as two 3 ½" disks with the electronic files for the data.

If you have questions or concerns, please call me at 505-842-7789. The Principal Investigators are Ray Finley, (505-844-4462) and Nancy Brodsky (505-844-3408).

Sincerely yours,

Eloise M. James

Eloise M. James
SNL Technical Data Records

Enclosures: As stated
Copy to (w/o encl.):

SNL 6117	R. E. Finley	SNL 6117	L. S. Costin
SNL 6850	S. A. Orrell	SNL 6117	N. S. Brodsky

YMP:1.2.3.14.2:TD:QA:55/F35-11/06/95
YMP:1.2.3.14.2:TD:QA:51/L22-08/01/96
YMP:1.2.3.14.2:WP:QA:WP123E2270M3:DEL:SPY148M4
YMP:1.2.3.14.2:WP:QA:WP123E2270M1:DEL:SP1430M4
YMP RPC (Encl: TDIFs and Disks - Submitted in Data Transmittal Packages)- Under DTNs: SNF35110695001.009 and SNL22080196001.003 dtd 10/12/98

2109 Air Park Road S.E., Albuquerque, New Mexico 87106 (505) 247-0707
Other SAIC Offices: Denver, Colorado Springs, Dayton, Huntsville, Las Vegas, Los Angeles, McLean, San Diego, Orlando, Palo Alto, San Diego, Seattle, and Tucson

MOL.19981030.0108 QA:L

307112

YMP-023-R4
05/06/96

YUCCA MOUNTAIN SITE CHARACTERIZATION PROJECT
TECHNICAL DATA INFORMATION

(Check one): [X] ACQUIRED DATA *(complete Parts I and II)*
Data Tracking Number (DTN): SNF35110695001.009

[ ] DEVELOPED DATA *(complete Parts I, II and III)*
Data Tracking Number (DTN): _____

PART I Identification of Data

Title/Description of Data: THERMAL AND THERMOMECHANICAL DATA FOR THE SINGLE HEATER TEST FINAL REPORT. THIS SUBMITTAL IS FOR THE NEXT INCREMENT OF MEASUREMENTS PERFORMED SINCE THE 1ST QUARTER FY98 SUBMITTAL UNDER DTN: SNF35110695001.008. (THE POSTTEST LABORATORY THERMAL AND MECHANICAL CHARACTERIZATION DATA IN SECTION 5.3 IS UNDER DTN: SNL22080196001.003)

Principal Investigator (PI): FINLEY, R E
Last Name — First and Middle Initials

PI Organization: SANDIA NATIONAL LABORATORIES

Are Data Qualified?: [ ] Yes [X] No Governing Plan: SCP

SCPB Activity Number(s): 8.3.1.15.1.6

WBS Number(s): 1.2.3.14.2

PART II Data Acquisition/Development Information

Method: INSTRUMENTS WERE INSTALLED IN BOREHOLES AND ON THE ROCK SURFACE TO MEASURE THERMOMECHANICAL/HYDROLOGIC REPONSE TO THE ROCK MASS TO HEATING.

Location(s): THERMAL TESTING FACILITY IN THE EXPLORATORY STUDIES FACILITY, YUCCA MTN.

Period(s): 12/1/97 to 1/31/98
From: MM/DD/YY — To: MM/DD/YY

Sample ID Number(s): N/A

PART III Source Data DTN(s)

Comments

SNL DATASET ID: 55/F35-11/06/95 (NOTE: THE DATA PRESENTED IN THIS REPORT SHOULD BE CONSIDERED INDETERMINATE UNTIL THE PROCUREMENT/CALIBRATIONS ISSUES RELATED TO THP CORRECTIVE ACTION REPORT

Checked by: Eloise James 8/27/98

307112

YMP-023-R4
08/31/95

YUCCA MOUNTAIN SITE CHARACTERIZATION PROJECT
TECHNICAL DATA INFORMATION
CONTINUATION SHEET

Page 2 of 2

Comments (continued)

YM-97-C-004 HAVE BEEN RESOLVED. PENDING RESOLUTION OF THESE ISSUES, THESE DATA HAVE BEEN CLASSIFIED AS UNQUALIFIED)

YAP-SIII.3Q.1

Earth Sciences Division

May 9, 1997

Joanna L. Wiggins
M&O/TRW
Technical Data Management Dept.
1180 Town Center Drive
Las Vegas, NV 89134

QA:N/A

WBS: 1.2.3.14.2

SUBJECT: Yucca Mountain Site Characterization Project (YMP) Technical Data Base (TDB) Data transmittal for Level 4 Milestone SP9263M4 "Letter Report on First Quarter Results of Measurements in Hydrology holes in Single Heater Test area in the ESF"
by B. Freifeld and Y. Tsang.
DTN: LB970100123142.001,
TDIF: 305939.

The Subject Data Transmittal Package is been submitted to the YMP TDB in accordance with YMP Administrative Procedure YAP-SIII.3Q, Revision 1, ICN 0. The following items are included in this submittal:

1. Technical Data Information, TDIF 305939.
2. The data set is submitted in ASCII format in a PC disk.
3. A table identifying the data parameters, and units

If You have any questions, please contact me at (510) 486-5610.

Sincerely,

V. Fissekidou

Y. Tsang
RPC

Ernest Orlando Lawrence Berkeley National Laboratory
One Cyclotron Road • Berkeley, California 94720 • Tel: 510.486.7071 • Fax: 510.486.5686

LBA010D123142.00

Earth Sciences Division

March 6, 1998 QA:N/A

Jemma Wiggins
M&O/TRW
Technical Data Management
MS 423/127
1180 Town Center Drive
Las Vegas, NV 89134

SUBJECT: **RESUBMITTAL OF:**
Yucca Mountain Site Characterization Project (YMP) Technical Data Base (TDB) data transmittal letter for the submittal of technical data.

Enclosed are the two PC disks you have been expecting containing the data that was previously submitted on disks originally formated on a Mac computer.

The Subject Data Transmittal Package is submitted to the YMP TDB in accordance with YMP Administrative Procedure YAP-SIII.3Q, REV. 1, ICN 0. All technical reviews of the data have been completed as required. Because you are currently processing this package, we are only submitting the disks you requested and no other additional paperwork in this submittal.

If you have any questions, please contact me at (510) 486-4323.

Sincerely,

Colleen O'Shea
Technical Data Coordinator

cc: G.S. Bodvarsson
Larry Hayes
J. Wang
File

Ernest Orlando Lawrence Berkeley National Laboratory
One Cyclotron Road • Berkeley, California 94720 • Tel: 510.486.7071 • Fax: 510.486.5686

LB970700123142.001

Earth Sciences Division

NUCLEAR WASTE DEPARTMENT
YMP-LBNL RECORDS PROCESSING CENTER
TEL 510.486.4323/ FAX 510.486.6115

August 21, 1997

Phill Jones
M&O/TRW/RFC
Technical Data Management Dept.
1180 Town Center Drive
Las Vegas, Nevada 89134

Dear Mr. Jones:

SUBJECT: Yucca Mountain Site Characterization Project (YMP) Technical Data Base (TDB) Data transmittal letter for Level 4 Milestone SP9252M4- "Letter Report on Third Quarter Results of Measurements in Hydrology Holes in the Single Heater Test Area," by Y.W. Tsang and B. Friefeld.

DTN: LB970700123142.001 TDIF: 806187

The Subject Data Transmittal Package is submitted to the YMP TDB in accordance with YMP Administrative Procedure YAP-SIII.3Q, Revision 1, ENC 0. All technical reviews of the data have been completed as required. The following items are included in this submittal:

1. Technical Data Information (TDIF).
2. An example of the data. This one example applies to the two files of data.
3. Hard Copy of each data file : The hard copy consists of the first and last page of the first columns of data and the first and last page of the last columns of data for verification purposes.
4. The data set on floppy disk.

If you have any questions, please contact me at (510) 486-4323.

Thank you.

Sincerely,

Colleen O'Shea

Colleen O'Shea
Records Coordinator

cc: File, QA Library, LBNL
G.S. Bodvarsson, LBNL

LB970700123142.001

Earth Sciences Division

March 18, 1998

QA:N/A

Joanna Wiggins
M&O/TRW
Technical Data Management
MS 423/127
1180 Town Center Drive
Las Vegas, NV 89134

SUBJECT: Yucca Mountain Site Characterization Project (YMP) Technical Data Base (TDB) data transmittal letter for TDIFs 306187 and 306375.

Vince and Joanna-
Enclosed is a partial hardcopy of the data from the submittals with the above TDIF Nos. Also enclosed is a memo to serve as the footnote for the omitted data files from both data submittals. I believe you have held onto the media which the data was transmitted to you. However, I am sending you another floppy containing the data with TDIF No. 306187. I believe this disk was formatted on a Mac computer, so I am re-sending a disk that has been formatted for a PC.

If you have any questions, please contact me at (510) 486-4323.

Sincerely,
Colleen O'Shea

Colleen O'Shea
Technical Data Coordinator

cc: G.S. Bodvarsson
File

Ernest Orlando Lawrence Berkeley National Laboratory
One Cyclotron Road • Berkeley, California 94720 • Tel: 510.486.7071 Fax: 510.486.5686

LB971000123142.001

Earth Sciences Division

October 20, 1997

Phill Jones
M&O/TRW/RPC
Technical Data Management Dept.
1180 Town Center Drive
Las Vegas, Nevada 89134

Dear Mr. Jones:

SUBJECT: Yucca Mountain Site Characterization Project (YMP) Technical Data Base (TDB) Data transmittal letter for Level 4 Milestone SP1080M4- "Letter Report on Fourth Quarter Results of Measurements in Hydrology Holes in the Single Heater Test Area" by B. Freifeld.

DTN: LB971000123142.001 TDIF: 306440

The Subject Data Transmittal Package is submitted to the YMP TDB in accordance with YMP Administrative Procedure YAP-SIII3Q, Revision 1, INC 0. All technical reviews of this data have been completed as required. The following items are included in this submittal.

1. Technical Data Information (TDIF).
2. Due to the size of the file, only the first six pages and last six pages of all columns of data have been included as hardcopy.
3. An example of the data.
4. The data set submitted on floppy disk formatted for PC.

As previously discussed with you, at the present time, the TDB in Las Vegas cannot accept any imaging data such as the data included in part of this Milestone SP1080M4- "Fourth Quarter FY 1997 Results of Infrared Mapping in the Single Heater Test Area" by P. Cook under DTN: LB971000123142.002; TDIF#: 306441. It is our understanding that the TDB does not have the software to read this type of data and incorporate it into their present database. Therefore, the imaging data from this milestone has not been submitted to the TDB at this time. However, this data has been submitted to the Records Center on CD-Rom and is available by contacting the RPC in Las Vegas.

If you have any questions, please contact me at (510) 486-4323.

Thank you.
Sincerely,

Colleen O'Shea

Colleen O'Shea
Records Coordinator

cc: File, QA Library, LBNL

Ernest Orlando Lawrence Berkeley National Laboratory
One Cyclotron Road • Berkeley, California 94720 • Tel: 510.486.7071 • Fax: 510.486.5686

MOL.19971208.0344 QA:C 306440

YMP-023-R4
05/06/98

YUCCA MOUNTAIN SITE CHARACTERIZATION PROJECT
TECHNICAL DATA INFORMATION

(Check one): [X] ACQUIRED DATA *(complete Parts I and II)*
Data Tracking Number (DTN): LB971000123142.001

[ ] DEVELOPED DATA *(complete Parts I, II and III)*
Data Tracking Number (DTN):

PART I Identification of Data

Title/Description of Data: AIR INJECTIONS IN BOREHOLES #16 AND #18 IN THE SINGLE HEATER TEST AREA

Principal Investigator (PI): TSANG, Y W
Last Name First and Middle Initials

PI Organization: LAWRENCE BERKELEY NATIONAL LABORATORY

Are Data Qualified?: [X] Yes [ ] No Governing Plan: SCP

SCPB Activity Number(s): 8.3.4.2.4.4.2

WBS Number(s): 1.2.3.14.2

PART II Data Acquisition/Development Information

Method: CONSTANT RATE AIR INJECTION USING PNEUMATIC PACKERS IN BOREHOLES

Location(s): THERMAL ALCOVE SINGLE HEATER TEST AREA IN THE ESF

Period(s): 9/10/97 6/6/97 to 9/5/97 10/8/97
From: MM/DD/YY To: MM/DD/YY

Sample ID Number(s): N/A

PART III Source Data DTN(s)

Comments

N/A

Checked by: [signature] 10/15/97
Signature Date

YAP-SIII.3Q.1

Earth Sciences Division

MOL.19980508.0043

March 30, 1998

QA:NA

Joanna Wiggins
M&O/TRW
Technical Data Management
MS 423/127
1180 Town Center Drive
Las Vegas, NV 89134

WBS: 1.2.3.14.2

SUBJECT: Yucca Mountain Site Characterization Project (YMP) Technical Data Base (TDB) data transmittal letter for the submittal of technical data associated with the **Level 4 Milestone SPY1160M4**:

"Letter Report on First Quarter Results of Measurements in Hydrology Holes in the Single Heater Test Area, FY 1998" by B. Freifeld
DTN: LB980120123142.002 **TDIF: 306569**
and
First Quarter FY 1998 Results of Infrared Mapping in the Single Heater Test Area" by P. Cook
DTN: LB980120123142.001 **TDIF: 306567**

The Subject Data Transmittal Package is submitted to the YMP TDB in accordance with YMP Administrative Procedure YAP-SIII.3Q, REV. 1, ICN 0. All technical reviews of the data have been completed as required. The following items are included in this submittal for data identified by **TDIF No. 306569**:

1. Technical Data Information (TDIF) Form;
2. A hard-copy of the tabular data files;
3. A marked up example of the data; and
4. The data set submitted on CD-Rom.

The data identified by **TDIF No. 306567** is imaging data. This data is readable by the PowerPoint program. Two files of imaging data are included as part of this submittal: SHT Front and SHTSID. It is unclear at this time whether or not the TDB has the program capabilities to read and incorporate technical data in this format into the existing database. However, the files are being submitted to either be archived or incorporated into the database. The following items are included in this data submittal:

1. Technical Data Information (TDIF) Form; and
2. A hard-copy of the tabular data files; and
3. The data set submitted on CD-Rom.

Ernest Orlando Lawrence Berkeley National Laboratory
One Cyclotron Road • Berkeley, California 94720 • Tel: 510.486.7071 • Fax: 510.486.5686

If you have any questions, please contact me at (510) 486-4323.

Sincerely,

Colleen O'Shea

Colleen O'Shea
Technical Data Coordinator

cc: G.S. Bodvarsson
Larry Hayes
J. Wang
File

306569

YMP 023 R4
05/06/96

YUCCA MOUNTAIN SITE CHARACTERIZATION PROJECT
TECHNICAL DATA INFORMATION

Page 1 of 1

(Check one) [X] ACQUIRED DATA *(complete Parts I and II)*
Data Tracking Number (DTN): LV980170123142.002

[ ] DEVELOPED DATA *(complete Parts I, II and III)*
Data Tracking Number (DTN):

PART I Identification of Data

Title/Description of Data: AIR INJECTIONS IN BOREHOLES NIC AND NIB IN THE SINGLE HEATER TEST AREA 1ST QUARTER FY98 RESULTS

Principal Investigator (PI): PSANG, T M
Last Name / First and Middle Initials

PI Organization: LAWRENCE BERKELEY NATIONAL LABORATORY

Are Data Qualified? [X] Yes [ ] No Governing Plan: AMR

SCPB Activity Number(s):

WBS Number(s): 1.2.3.14.2

PART II Data Acquisition/Development Information

Method: CONSTANT RATE AIR INJECTION TESTS USING PNEUMATIC PACKERS IN BOREHOLES

Location(s): THERMAL ALCOVE SINGLE HEATER TEST AREA IN THE ESF

Period(s): 9/6/97 to 11/30/97
From MM/DD/YY To MM/DD/YY

Sample ID Number(s):

PART III Source Data DTN(s)

Comments

N/A

Checked by: [signature] 1/16/1997

MOL.19981105.0172

Earth Sciences Division

August 14, 1998 QA:N/A

Phill Jones
M&O/TRW
Technical Data Management
MS 423/127
1180 Town Center Drive
Las Vegas, NV 89134

WBS: 1.2.3.14.2

SUBJECT: Yucca Mountain Site Characterization Project (YMP) Technical Data Base (TDB) data transmittal letter for the submittal of technical data associated with the Level 4 Milestone SPY1160M4: "First Quarter FY 1998 Results of Infrared Mapping in the Single Heater Test Area," by P.J. Cook.

DTN: LB980120133143.001 TDIF: 206567 (Infrared Images of the SHT Area)

The Subject Data Transmittal Package is submitted to the YMP TDB in accordance with YMP Administrative Procedure YAP-SIII.3Q, REV. 2, ICN 0. All technical reviews of the data have been completed as required. The following items are included in this submittal:

1. Technical Data Information (TDIF) Form;
2. An electronic copy of the data submitted on CD-ROM; and — not an enclosure for the RPC. MC 11/2/98
3. A list of data files.

If you have any questions, please contact me at (510) 495-2841.

Sincerely,

Suzanne M. Link

Suzanne M. Link
Technical Data Coordinator

cc: G.S. Bodvarsson
Y.W. Tsang
File

Ernest Orlando Lawrence Berkeley National Laboratory
One Cyclotron Road • Berkeley, California 94720 • Tel: 510.486.7071 • Fax: 510.486.5686

MOL.19981105.0173

205567

YMP-023-R4
05/06/96

YUCCA MOUNTAIN SITE CHARACTERIZATION PROJECT
TECHNICAL DATA INFORMATION

Page 1 of 1

(Check one): [X] ACQUIRED DATA *(complete Parts I and II)*
Data Tracking Number (DTN): LB980120123142.001

[ ] DEVELOPED DATA *(complete Parts I, II and III)*
Data Tracking Number (DTN): _____

PART I Identification of Data

Title/Description of Data: FIRST QUARTER FY98 IR PICTURES OF THE SINGLE HEATER TEST AREA

Principal Investigator (PI): TSANG, Y W
Last Name First and Middle Initials

PI Organization: LAWRENCE BERKELEY NATIONAL LABORATORY

Are Data Qualified?: [X] Yes [ ] No Governing Plan: TWP

SCPB Activity Number(s): _____

WBS Number(s): 1.2.3.14.2

PART II Data Acquisition/Development Information

Method: PICTURES ACQUIRED USING INFRARED CAMERA

Location(s): SINGLE HEATER TEST AREA IN THE ESF THERMAL ALCOVE 5

Period(s): 3/6/97 to 12/19/97
From: MM/DD/YY To: MM/DD/YY

Sample ID Number(s): _____

PART III Source Data DTN(s)

_____ _____ _____

_____ _____ _____

_____ _____ _____

Comments
SET OF INFRARED (COOLED) THERMAL PICTURES

Checked by: Suzanne M. Link August 14, 1998
Signature Date

YAP-SIII.3Q.1

LLYMP9804032 (A)

Lawrence Livermore National Laboratory

MOL.19980508.0742

LLYMP9803046
March 23, 1998
25 QA 3/25/98

QA: N

Joanne Wiggins, GENISES Administrator
Yucca Mountain Site Characterization
Project Office
1180 Town Centre Drive
Las Vegas, NV 89134

SUBJECT: Fourth Quarter FY'97 and First Quarter FY'98 Results of Neutron Logging for Technical Data Base Submittal Associated with DTN LL980106904244.051 from Deliverable SP1270M4 and DTN LL971004604244.045 from Deliverable SP1090M4 (WBS 1.2.3.14.2)

Enclosed are hardcopies of the subject results. Also enclosed are a disk with the data in tab delimited form in excel and a copy of the TDIFs.

The data review package will be sent to the RPC in accordance with procedures. These data have been technically reviewed in accordance with 033-YMP-QP 3.6, "Collection, Review, and Submittal of Technical Data."

If there are any questions, please contact the custodian of the data, Wunan Lin at (925) 422-7162.

James Blink
(Acting) CRWMS LLNL Manager

JB/BB/bb

cc (w/o enc):
C. Newbury, DOE/YMP

An Equal Opportunity Employer • University of California • P.O. Box 808 Livermore, California 94551-9900 • Telephone (510) 422-1100 • Twx 910-386-8289 UCLL LVMR
Yucca Mountain Project, P.O. Box 5514, L-617, Livermore, California 94551-9900 • Fax (510) 422-3540 or FTS 532-3540

LLYMP9804032 C

386443

YMP-023-R4
05/08/96

YUCCA MOUNTAIN SITE CHARACTERIZATION PROJECT
TECHNICAL DATA INFORMATION

(Check one): [X] ACQUIRED DATA *(complete Parts I and II)*
Data Tracking Number (DTN): LL971004684244.045

[ ] DEVELOPED DATA *(complete Parts I, II and III)*
Data Tracking Number (DTN): _____

MOL.19980508.0744

PART I Identification of Data

Title/Description of Data: FOURTH QUARTER RESULTS OF THE NEUTRON LOGGING REPORT. DATA ON MOISTURE CONTENT IN BOREHOLES 15, 17, 22 AND 23 OF THE SINGLE HEATER TEST (SHT).

Principal Investigator (PI): LIN, M
Last Name First and Middle Initials

PI Organization: LAWRENCE LIVERMORE NATIONAL LABORATORY

Are Data Qualified?: [X] Yes [ ] No Governing Plan: SCP

SCPB Activity Number(s): 8.3.4.2.4.4.2

WBS Number(s): 1.2.3.14.2

PART II Data Acquisition/Development Information

Method: THE 1.5 INCH DIAMETER PROBE AND A COUNTING TIME OF 16 SECONDS WAS USED TO COLLECT NEUTRON DATA DURING THE SHT. STANDARD COUNTS WERE MEASURED AND RECORDED IMMEDIATELY PRIOR TO, AND SUBSEQUENT TO PERFORMING MEASUREMENTS. THE NEUTRON PROBE WAS PLACED IN A BOREHOLE AT A SPECIFIC LOCATION AND THE NEUTRON COUNT RECORDED IN A SCIENTIFIC NOTEBOOK, AS WELL AS ELECTRONICALLY IN THE DEVICE MEMORY. UPON

Location(s): SHT SHT

Period(s): 7/23/97 to 9/23/97
From: MM/DD/YY To: MM/DD/YY

Sample ID Number(s): _____

PART III Source Data DTN(s)

Comments
DELIVERABLE SP1990M4

Checked by: M. Jeanne Palmer 10/16/97
Signature Date

YAP-SIII.3Q.1

YMP-023-R4
08/31/95

YUCCA MOUNTAIN SITE CHARACTERIZATION PROJECT
TECHNICAL DATA INFORMATION
CONTINUATION SHEET

Method (continued)

COMPLETION OF THE TEST, DATA WAS DOWNLOADED TO A COMPUTER AND THE DATA VALUES CHECKED AGAINST THE HAND-RECORDED VALUES. DATA WAS RECORDED AT DEPTH INTERVALS OF 10 CM IN EACH BOREHOLE.

YAP-SIII.3Q.1

LLYM971104532 (B)

196593

YMP-623-R4
05/06/96

YUCCA MOUNTAIN SITE CHARACTERIZATION PROJECT
TECHNICAL DATA INFORMATION

(Check one): [X] ACQUIRED DATA (complete Parts I and II) Data Tracking Number (DTN): LLS980106994244.951

[ ] DEVELOPED DATA (complete Parts I, II and III) Data Tracking Number (DTN): _____ MOL.19980508.0763

PART I Identification of Data

Title/Description of Data: FIRST QUARTER FY98 RESULTS OF THE NEUTRON LOGGING REPORT. DATA ON MOISTURE CONTENT IN BOREHOLES 15, 17, 22 AND 23 OF THE SINGLE HEATER TEST (SHT).

Principal Investigator (PI): LIN, M (Last Name / First and Middle Initials)

PI Organization: LAWRENCE LIVERMORE NATIONAL LABORATORY

Are Data Qualified?: [X] Yes [ ] No Governing Plan: SCP

SCPB Activity Number(s): 8.3.4.2.4.4.2

WBS Number(s): 1.2.3.14.2

PART II Data Acquisition/Development Information

Method: THE 1.5 INCH DIAMETER PROBE AND COUNTING TIME OF 16 SECONDS WAS USED TO COLLECT NEUTRON DATA DURING THE SINGLE HEATER TEST. STANDARD COUNTS WERE MEASURED AND RECORDED IMMEDIATELY PRIOR TO, AND SUBSEQUENT TO PERFORMING MEASUREMENTS. THE NEUTRON PROBE WAS PLACED IN A BOREHOLE AT A SPECIFIC LOCATION AND THE NEUTRON COUNT RECORDED IN A SCIENTIFIC NOTEBOOK, AS WELL AS ELECTRONICALLY IN THE

Location(s): EXP SHT

Period(s): 9/25/97 to 12/17/97 (From: MM/DD/YY / To: MM/DD/YY)

Sample ID Number(s): _____

PART III Source Data DTN(s)

_____ _____ _____

_____ _____ _____

_____ _____ _____

Comments

MILESTONE SP12T6M4.

Checked by: M. Jeanne Palmer (Signature) 1/16/98 (Date)

YAP-6IILSQ.1

YMP-023-R4
08/31/95

YUCCA MOUNTAIN SITE CHARACTERIZATION PROJECT
TECHNICAL DATA INFORMATION
CONTINUATION SHEET

Method (continued)

DEVICE MEMORY. UPON COMPLETION OF THE TEST, DATA WAS DOWNLOADED TO A COMPUTER AND THE DATA VALUES CHECKED AGAINST THE HAND-RECORDED VALUES. DATA WAS RECORDED AT DEPTH INTERVALS OF 10 CM IN EACH BOREHOLE.

YAP-SIII.3Q.1

MOL.19990113.0111

Record Package for: LASL831151AQ98.001
Designator/Date: LASL831151AQ98.001 12/10/98
QAL Author/Organization: Young/LANL

Los Alamos National Laboratory

EES-13 Integrated Geosciences
P.O. Box 1663, Mail Stop J521
Los Alamos, New Mexico 87545
505-667-9768 / FAX 505-667-1934

December 10, 1998

EES-13-12-98-248

Mr. Phil Jones
Technical Database Administrator
TRW Environmental Safety Systems, Incorporated
1261 Town Center Drive
M/S 423
Las Vegas, NV 89134

Dear Mr. Jones:

Technical Database Re-Submission for "Mineralogic Characterization of the ESF Single Heater Test Block," DTN LASL831151AQ98.001

Enclosed is a Corrected Data Transmittal Package (DTP) for the subject data. All data have been technically reviewed as required.

Please make corrections to the data tables as annotated on the attached page.

If you have any questions regarding this transmittal or require additional information, please call Jim Young at 505-667-9286 or Dan Stone at 505/667-4054

Sincerely,

J. E. Young
Technical Data Coordinator

JEY:ar

cy w/o enc:

T. Hirons, EES-13, J521
C. Harrington, EES-13, J521
S. Klein, EES-13, J521
C. Newbury, DOE/YMP, Las Vegas, NV
R. Patterson, DOE/YMP, Las Vegas, NV
S. Bodner, M&O, Las Vegas, NV
J. Friend, EES-13, MS J521
S. S. Levy, EES-1, MS D469
EES-13 File, MS J52

307131

YMP-023-R4
05/06/98

YUCCA MOUNTAIN SITE CHARACTERIZATION PROJECT
TECHNICAL DATA INFORMATION

Record Package for: [illegible]
Designer/Date: [illegible]
QAP Author/Organization: [illegible]

(Check one): [X] ACQUIRED DATA *(complete Parts I and II)*
Data Tracking Number (DTN): LASL831151AQ98.001

[ ] DEVELOPED DATA *(complete Parts I, II and III)*
Data Tracking Number (DTN): _____

PART I Identification of Data

Title/Description of Data: MINERALOGIC CHARACTERIZATION OF THE ESF SINGLE HEATER TEST BLOCK

Principal Investigator (PI): LEVY, S S
Last Name First and Middle Initials

PI Organization: LOS ALAMOS NATIONAL LABORATORY

Are Data Qualified?: [X] Yes [ ] No Governing Plan: SCP

SCPB Activity Number(s): 8.3.1.15.1.6

WBS Number(s): 1.2.3.14.2

PART II Data Acquisition/Development Information

Method: PETROGRAPHIC EXAMINATION, X-RAY DIFFRACTION

Location(s): LANL

Period(s): 2/4/98 to 8/21/98
From: MM/DD/YY To: MM/DD/YY

Sample ID Number(s): (SEE DATA RECORDS PACKAGE)

PART III Source Data DTN(s)

Comments:
MILESTONE SP1410M4

Checked by: J.E. Young 8/31/98
Signature Date

YAP-SII.3Q.1

LLYMP9710100 A.

Lawrence Livermore National Laboratory

MOL.19980115.0111

LLYMP9710047
October 20, 1997

QA: N

Phillip Jones, GENISES Administrator
Yucca Mountain Site Characterization
Project Office
1180 Town Centre Drive
Las Vegas, NV 89134

SUBJECT: One Table of Third Quarter Results of Chemical Measurements for Technical Data Base Submittal Associated with DTN LL970703904244.034 from Deliverable SP9281M4 (WBS 1.2.3.14.2)

Enclosed is a hardcopy of the subject table. Also enclosed are a disk with the data in tab delimited form and a copy of the TDIF from the milestone.

The data review package will be sent to the RPC in accordance with procedures. These data have been technically reviewed in accordance with 033-YMP-QP 3.6, "Collection, Review, and Submittal of Technical Data."

If there are any questions, please contact the author of the report, William Glassley at (510) 422-6499.

W. L. Clarke

Willis L. Clarke
CRWMS LLNL Manager

WC/BB/bb

cc (w/o enc):
C. Newbury, DOE/YMP
R. Lewis, TRW

Disk not included. Data in hardcopy is in this package.

An Equal Opportunity Employer • University of California • P.O. Box 808, Livermore, California 94551-9900 • Telephone (510) 422-1100 • Fax 510 386 8339 UCLL / WMR
Yucca Mountain Project P.O. Box 5514, L-217, Livermore, California 94551-9900 • Fax (510) 423-0540 or FTS 532-0540

LL970710106 B

306201

YMP-023-R4
05/06/98

YUCCA MOUNTAIN SITE CHARACTERIZATION PROJECT
TECHNICAL DATA INFORMATION

(Check one): [X] ACQUIRED DATA (complete Parts I and II)
Data Tracking Number (DTN): LL970703904244.034

[ ] DEVELOPED DATA (complete Parts I, II and III)
Data Tracking Number (DTN): MOL.19980115.0112

PART I Identification of Data

Title/Description of Data: THIRD QUARTER RESULTS OF CHEMICAL MEASUREMENTS IN THE SINGLE HEATER TEST.

Principal Investigator (PI): GLASSLEY, W E
Last Name First and Middle Initials

PI Organization: LAWRENCE LIVERMORE NATIONAL LABORATORY

Are Data Qualified?: [X] Yes [ ] No Governing Plan: SCP

SCPB Activity Number(s): 8.3.4.2.4.1

WBS Number(s): 1.2.3.14.2

PART II Data Acquisition/Development Information

Method: UNDER LLNL STUDY PLAN 8.3.4.2.4.4 INDUCTIVELY COUPLED PLASMA SPECTROMETRY.

Location(s): THERMAL ALCOVE SINGLE HEATER TEST AREA IN THE ESF.

Period(s): 3/8/97 to 7/18/97
From: MM/DD/YY To: MM/DD/YY

Sample ID Number(s):

PART III Source Data DTN(s)

Comments

LLNL MILESTONE SP9281M4

Checked by: Barbara Bryan 7-17-97
Signature Date

YAP-SII.3Q.1

LB9705001231 42.003

Earth Sciences Division

August 25, 1997

Phill Jones
M&O/TRW/RPC
Technical Data Management Dept
1180 Town Center Drive
Las Vegas, Nevada 89134

Dear Mr Jones:

SUBJECT: Yucca Mountain Site Characterization Project (YMP) Technical Data Base (TDB) Data transmittal letter for Level 4 Milestone SP5130M4 "Laboratory Test Results of Hydrological Properties from Dry Drilled and Wet Drilled Cores in the Drift Scale Test Area and in the Single Heater Test Area of the Thermal Test Facility," by J Wang and R Suarez-Rivera
DTN: LB9705001231 42.003 TDIF: 306139

The Subject Data Transmittal Package is submitted to the YMP TDB in accordance with YMP Administrative Procedure YAP-SIII.3Q, Revision 1, INC 0. All technical reviews of the data have been completed as required. The following items are included in this submittal.

1. Technical Data Information (TDIF)
2. An example of the data. This one example applies to all of data represented in Tables 1-4.
3. Hard Copy of data.
4. The data set on floppy disk.

If you have any questions, please contact me at (510) 486-4523.

Thank you.

Sincerely,

Colleen O'Shea

Colleen O'Shea
Records Coordinator

cc: File, QA Library, LBNL
GS Bodvarsson, LBNL

Ernest O Iando Lawrence Berkeley National Laboratory
One Cyclotron Road • Berkeley, California 94720 Tel. 510.486 7071 • Fax: 510.486.5686

MOL.19981020.0116

Science Applications International Corporation
An Employee-Owned Company

October 8, 1998
WBS: 1.2.3.14.2
QA: L

Phill Jones
TRW/M&O, MS 423
1261 Town Center Drive
Las Vegas, NV 89134

Dear Phill:

Subject: Sandia National Laboratories Transfer to the Technical Database of the Thermal and Thermomechanical Data, and the Posttest Laboratory Thermal and Mechanical Characterization Data in the "Single Heater Test Final Report"

Enclosed are copies of the TDIFs (Technical Data Information Forms) for Data Tracking Number (DTN): SNF35110695001.009, TDIF #307112, and DTN: SNL22080196001.003, TDIF #307123, for your information. This is for the transfer of data from the Single Heater Test Final Report, as listed above, to the Technical Database. A technical review of these data was performed and the data will be submitted to the YMP Records Processing Center under the Data Tracking numbers and TDIF numbers noted.

I have attached a hard copy of the data with the Parameters and Attributes labeled which are applicable to these data, as well as two 3 ½" disks with the electronic files for the data.

If you have questions or concerns, please call me at 505-842-7789. The Principal Investigators are Ray Finley, (505-844-4462) and Nancy Brodsky (505-844-3408).

Sincerely yours,

Eloise M. James

Eloise M. James
SNL Technical Data Records

Enclosures: As stated
Copy to (w/o encl.):

SNL 6117	R. E. Finley	SNL 6117	L. S. Costin
SNL 6850	S. A. Orrell	SNL 6117	N. S. Brodsky

YMP:1.2.3.14.2:TD:QA:55/F35-11/06/95
YMP:1.2.3.14.2:TD:QA:51/L22-08/01/96
YMP:1.2.3.14.2:WP:QA:WP123E2270M3:DEL:SPY148M4
YMP:1.2.3.14.2:WP:QA:WP123E2270M1:DEL:SP1430M4
YMP RPC (Encl: TDIFs and Disks - Submitted in Data Transmittal Packages)

2109 Air Park Road S.E., Albuquerque, New Mexico 87106 (505) 247-8787
Other SAIC Offices: Denver, Colorado Springs, Boston, Monterey, Las Vegas, Los Angeles, Oakland, San Diego, Orlando, Palo Alto, San Diego, Seattle, and Tucson

MOL.19981030.0115 QA:L

207123

YMP-023-R4
05/06/98

YUCCA MOUNTAIN SITE CHARACTERIZATION PROJECT
TECHNICAL DATA INFORMATION

(Check one): [X] ACQUIRED DATA (complete Parts I and II)
Data Tracking Number (DTN): SNL22080196001.003

[ ] DEVELOPED DATA (complete Parts I, II and III)
Data Tracking Number (DTN): _____

PART I Identification of Data

Title/Description of Data: POSTTEST LABORATORY THERMAL AND MECHANICAL CHARACTERIZATION FOR SINGLE HEATER TEST (SHT) BLOCK (THESE DATA APPEAR IN SECTION 5.1 OF THE SINGLE HEATER TEST (SHT) FINAL REPORT,

SUBMITTED UNDER DTN: SNF35110695001.003)

Principal Investigator (PI): BRODSKY, N S
Last Name First and Middle Initials

PI Organization: SANDIA NATIONAL LABORATORIES

Are Data Qualified?: [X] Yes [ ] No Governing Plan: SCP

SCPB Activity Number(s): 8.3.1.15.1.1.3

WBS Number(s): 1.2.3.14.2

PART II Data Acquisition/Development Information

Method: USED SNL TDP TECHNICAL PROCEDURE TP-202, 'MEASUREMENT OF THERMAL CONDUCTIVITY OF GEOLOGIC SPECIMENS USING THE GUARDED HEAT-FLOW METER METHOD'; TP-203, 'MEASUREMENT OF THERMAL EXPANSION OF GEOLOGIC SAMPLES USING A FUSED SIO DILATOMETER', AND TP-215, 'UNCONFINED COMPRESSION EXPERIMENTS AT AMBIENT CONDITIONS AND CONSTANT STRAIN RATE'; AND ASTM F433-77, ASTM D4535-85, ASTM E228-85, ASTM

Location(s): SANDIA NATIONAL LABORATORIES, ALBUQUERQUE, NEW MEXICO

Period(s): 6/1/98 to 8/25/98
From: MM/DD/YY To: MM/DD/YY

Sample ID Number(s): PTC-MPRI-14.2-B

PART III Source Data DTN(s)

_____ _____ _____

_____ _____ _____

_____ _____ _____

Comments

SNL DATASET ID: 51/132-08/01/96

Checked by: Eloise James 10/12/98
Signature Date

YAP-SIII.3Q.1

YMP-023-R4
08/31/95

YUCCA MOUNTAIN SITE CHARACTERIZATION PROJECT
TECHNICAL DATA INFORMATION
CONTINUATION SHEET

SCPB Activity Number(s) (continued)

8.3.1.15.1.2.1
8.3.1.2.4.4

WBS Number(s) (continued)

1.2.3.2.7.1.1
1.2.3.2.7.1.2

Method (continued)

02938-86, ASTM D3148-93 TO OBTAIN THERMAL CONDUCTIVITY COEFFICIENTS OF THERMAL EXPANSION AND MECHANICAL PROPERTIES IN UNCONFINED COMPRESSION

Sample ID Number(s) (continued)

PTC-KMEX1-A-14.4
PTC-KMEX1-B-14.4
PTC1-12.5
PTC1-A-15.7
PTC1-A-16.8-B
PTC1-A-19.0
PTC1-A-2.9-B
PTC1-B-15.7
PTC1-B-19.0-B
PTC2-A-10.8
PTC2-A-14.1
PTC2-A-4.1
PTC2-B-10.8
PTC2-B-4.1
PTC4-11.8
PTC4-17.4
PTC4-20.9
PTC4-A-14.8
PTC4-A-15.8
PTC4-A-15.8
PTC4-A-26.0
PTC4-A-4.3
PTC4-A-4.6-B
PTC4-A-6.6
PTC4-A-9.2
PTC4-B-14.8-B
PTC4-B-19.8-B
PTC4-B-26.0
PTC4-B-4.3
PTC4-B-6.6
PTC4-B-6.8-B
PTC4-B-9.2
PTC5-A-18.9
PTC5-A-25.4
PTC5-A-4.1
PTC5-B-24.4-B
PTC5-B-24.4-C
PTC5-B-4.1-B

YAP-SIII.3Q.1

YMP-023-R4
08/31/95

YUCCA MOUNTAIN SITE CHARACTERIZATION PROJECT
TECHNICAL DATA INFORMATION
CONTINUATION SHEET

Page 1 of 1

Sample ID Number(s) (continued)

PTCH1-15.6
PTCH1-19.7
PTCH1-8.6
PTCH1-A-15.6-B
PTCH1-A-8.6

YAP-SIII.3Q.1

MOL.19971001.0378

306045

YMP-023-R4
05/06/96

YUCCA MOUNTAIN SITE CHARACTERIZATION PROJECT
TECHNICAL DATA INFORMATION

(Check one): [X] ACQUIRED DATA (complete Parts I and II)
Data Tracking Number (DTN): GS970208312271.002

[ ] DEVELOPED DATA (complete Parts I, II and III)
Data Tracking Number (DTN): _____

PART I Identification of Data

Title/Description of Data: UNSATURATED ZONE HYDROCHEMISTRY DATA, 10-1-96 TO 1-31-97, INCLUDING CHEMICAL COMPOSITION AND CARBON, OXYGEN AND HYDROGEN ISOTOPIC COMPOSITION

Principal Investigator (PI): YANG, I C
Last Name First and Middle Initials

PI Organization: U.S. GEOLOGICAL SURVEY

Are Data Qualified?: [X] Yes [ ] No Governing Plan: SCP

SCPB Activity Number(s): 8.3.1.2.2.7.1

WBS Number(s): 1.2.3.1.1.2.7

PART II Data Acquisition/Development Information

Method: DATA WERE ACQUIRED BY THE UZ HYDROCHEMISTRY LABORATORY IN ACCORDANCE WITH MP-204, RD-H2, LIQUID SCINTILLATION SPECTROMETRY METHOD FOR TRITIUM MEASUREMENT OF WATER SAMPLES, AND BY YMP-USGS APPROVED SUPPLIERS - HUFFMAN LABORATORY, CU-BOULDER/INSTAAR, AND BETA ANALYTIC [CONTRACTS 1434-95-SA-01372 & 1434-DR-96-00517). AMS PERFORMED BY LLNL. AUTHORIZATION FOR USE OF BETA AND LLNL

Location(s): BETA ANALYTIC, MIAMI, FL

Period(s): 10/1/96 to 1/31/97
From MM/DD/YY To: MM/DD/YY

Sample ID Number(s): SPC00022055

PART III Source Data DTN(s)

_____ _____ _____

_____ _____ _____

_____ _____ _____

Comments

SUBJECT TO REVISION. NCR-USGS-97-003 WAS WRITTEN TO THIS DATA PACKAGE FOR AN OVERDUE BALANCE CALIBRATION. USGS-96-0003, CONCERNING PROCUREMENT OF LABORATORY SERVICES, ALSO APPLIES TO DATA IN THIS

Checked by: Gordon Rattray 3-11-97
Signature Date

YAP-SIII.3Q.1

YMP-023-R4
08/31/96

YUCCA MOUNTAIN SITE CHARACTERIZATION PROJECT
TECHNICAL DATA INFORMATION
CONTINUATION SHEET

Method (continued)

IS DOCUMENTED IN DOE YMQAD LETTER DATED 7-8-96 FROM R.E. SPENCE TO R.W. CRAIG.

Location(s) (continued)

HUFFMAN LAB, GOLDEN, CO
INSTAAR, UNIVERSITY OF COLORADO, BOULDER
LLNL, LIVERMORE, CA
USGS, DENVER, CO

Sample ID Number(s) (continued)

SPC00022160
SPC00029412
SPC00029415
SPC00029416
SPC00029559
SPC00029647
SPC00029671
SPC00029702
SPC00029936
SPC00029981
SPC00029992
SPC00030021
SPC00030131
SPC00030174
SPC00030192
SPC00030242
SPC00030296
SPC00031178
SPC00031650
SPC00031653
SPC00031940
SPC00031944
SPC00032064
SPC00032166
SPC00032175
SPC00032345
SPC00032349
SPC00032364
SPC00033765
SPC00033873
SPC00033892
SPC00033893
SPC00034151
SPC00034356
SPC00034376
SPC00034666
SPC00034663
SPC00035239
SPC00035298
SPC00035303
SPC00035753

YAP-SIII.3Q.1

YMP-023-R4
08/31/95

YUCCA MOUNTAIN SITE CHARACTERIZATION PROJECT
TECHNICAL DATA INFORMATION
CONTINUATION SHEET

Page 1 of 1

Sample ID Number(s) (continued)

SPC00035755
SPC00035810
SPC00035812
SPC00035823
SPC00035825
SPC00035849
SPC00035851
SPC00035932
SPC00036128
SPC00036193
SPC00036216
SPC00036392
SPC00036417
SPC00036484
SPC00036647
SPC00036706
SPC00036878
SPC00036879
SPC00037045
SPC00037193
SPC00037249
SPC00037250
SPC00037342
SPC00037467
SPC00037664
SPC00037762
SPC00037808
SPC00039969
SPC00040032
SPC00040038
SPC00040615
SPC00040620
SPC00040646
SPC00041014
SPC00041136
SPC00041438
SPC00041490
SPC00041559
SPC00041598
SPC00041617
SPC00041736
SPC00041930
SPC00041996
SPC00042023
SPC00044336
SPC00044339
SPC00044376
SPC00044377
SPC00045984
SPC00045985

YAP-SIII.3Q.1

YMP-023-R4
08/31/95

YUCCA MOUNTAIN SITE CHARACTERIZATION PROJECT
TECHNICAL DATA INFORMATION
CONTINUATION SHEET

Sample ID Number(s) (continued)

SPC00045988
SPC00045995
SPC00045999
SPC00046002
SPC00046003
SPC00046272
SPC00046274
SPC00046275
SPC00046285
SPC00047436
SPC00047437
SPC00047438
SPC00047441
SPC00047442
SPC00047444
SPC01000445
SPC01000447
SPC01000450

Comments (continued)

PRC. NEITHER HAD AN ADVERSE IMPACT ON DATA QUALITY.

YAP-SIII.3Q.1

MOL.19990602.0121

307306

YMP-023-R4
05/06/98

YUCCA MOUNTAIN SITE CHARACTERIZATION PROJECT
TECHNICAL DATA INFORMATION

(Check one): [X] ACQUIRED DATA (complete Parts I and II)
Data Tracking Number (DTN): GS980908312272.003

[ ] DEVELOPED DATA (complete Parts I, II and III)
Data Tracking Number (DTN):

PART I Identification of Data

Title/Description of Data: STRONTIUM ISOTOPE RATIOS AND STRONTIUM CONCENTRATIONS IN WATERS FROM THE SINGLE HEATER TEST IN ESF-THM-NEU2, FEBRUARY, 1997 AND MAY, 1997

Principal Investigator (PI): PETERMAN, Z E
Last Name First and Middle Initials

PI Organization: U.S. GEOLOGICAL SURVEY

Are Data Qualified?: [X] Yes [ ] No Governing Plan: SCP

SCPB Activity Number(s): 8.3.1.2.2.7.2

WBS Number(s): 1.2.3.1.1.2.7

PART II Data Acquisition/Development Information

Method: DATA WERE COLLECTED IN ACCORDANCE WITH YMP-USGS GCP-12,R4, RB-SR ISOTOPE GEOCHEMISTRY

Location(s): USGS, DENVER, CO

Period(s): 6/15/98 to 8/24/98
From: MM/DD/YY To: MM/DD/YY

Sample ID Number(s): SPC00521246

PART III Source Data DTN(s)

Comments

SUBJECT TO REVISION

Checked by: J.A. Luiszer for S.K. Dasovich 9/24/98
Signature Date

YAP-SIII.3Q.1

307306

YMP-023-R4
08/31/95

YUCCA MOUNTAIN SITE CHARACTERIZATION PROJECT
TECHNICAL DATA INFORMATION
CONTINUATION SHEET

Page 2 of 2

Sample ID Number(s) (continued)

SPC00521248
SPC00522242

YAP-SIII.3Q.1

MOL.19990602.0134

307279

YMP-023-R6
04/99

YUCCA MOUNTAIN SITE CHARACTERIZATION PROJECT
TECHNICAL DATA INFORMATION FORM

(Check one): [X] ACQUIRED DATA *(complete Parts I and II)*
Data Tracking Number (DTN): GS980908312322.009

[ ] DEVELOPED DATA *(complete Parts I, II and III)*
Data Tracking Number (DTN):

PART I Identification of Data

Title of Data: SEE DESCRIPTION OF DATA

Description of Data: URANIUM CONCENTRATIONS AND 234U/238U RATIOS FROM SPRING, WELL, RUNOFF AND RAIN WATERS COLLECTED FROM THE NEVADA TEST SITE AND DEATH VALLEY VICINITIES AND ANALYZED BETWEEN

Data Originator/Preparer: PACES, J B
Last Name First and Middle Initials

Data Originator/Preparer Organization: U.S. GEOLOGICAL SURVEY

Qualification Status: [X] Q [ ] Non-Q [ ] Accepted Governing Plan: SCP

SCP Activity Number(s): 8.3.1.2.3.2.2

WBS Number(s): 1.2.3.3.1.3.2

PART II Data Acquisition/Development Information

Method: DATA WERE COLLECTED USING NWM USGS TECHNICAL PROCEDURE GCP-01,R3-M2, URANIUM-THORIUM DISEQUILIBRIUM STUDIES.

Location(s): USGS, DENVER, CO

Period(s): 1/15/1998 to 8/15/1998
From: MM/DD/YY To: MM/DD/YY

Sample ID Number(s): SPC00100159

PART III Source Data DTN(s)

Comments
TDIF CORRECTED 8/7/99

Checked by: Patricia A. Shaffer 5/20/99
Signature Date

AP-SIII.3Q

307279

YMP-023-R6
04/99

YUCCA MOUNTAIN SITE CHARACTERIZATION PROJECT
TECHNICAL DATA INFORMATION
CONTINUATION SHEET

Page 2 of 2

Description of Data [continued]

01/15/98 AND 08/15/98

Sample ID Number(s) (continued)

SPC00510179
SPC00512072
SPC00516842
SPC00516865
SPC00516969 - SPC00516988
SPC00521246
SPC00521248
SPC00522242
SPC00529310
SPC00529335
SPC00529419
SPC00529435
SPC00529478
SPC00529907
SPC00529917
SPC00529927
SPC00531110
SPC00531118
SPC00532653
SPC00532679

AP-SIII.3Q

MOL.19971119 0555

305605

YMP-023-R4
05/06/96

YUCCA MOUNTAIN SITE CHARACTERIZATION PROJECT
TECHNICAL DATA INFORMATION

Page 1 of 1

(Check one): [X] ACQUIRED DATA *(complete Parts I and II)*
Data Tracking Number (DTN): LB960500834244.001

[ ] DEVELOPED DATA *(complete Parts I, II and III)*
Data Tracking Number (DTN): _____

PART I Identification of Data

Title/Description of Data: LETTER REPORT ON HYDROLOGICAL CHARACTERIZATION OF THE SINGLE HEATER TEST AREA IN ESF BY Y.W. TSANG, J. WANG, B. FREIFELD, P COOK, R SUAREZ-RIVERA, AND T. TOKUNAGA.

Principal Investigator (PI): TSANG, Y W
Last Name First and Middle Initials

PI Organization: LAWRENCE BERKELEY NATIONAL LABORATORY

Are Data Qualified?: [X] Yes [ ] No Governing Plan: SCPB

SCPB Activity Number(s): 8.3.4.2.4.4

WBS Number(s): 1.2.3.14.2

PART II Data Acquisition/Development Information

Method: PNEUMATIC TESTING. AIR INJECTION TESTS.

Location(s): THERMAL TEST FACILITY

Period(s): 5/21/96 to 5/31/96
From MM/DD/YY To MM/DD/YY

Sample ID Number(s): _____

PART III Source Data DTN(s)

_____ _____ _____

_____ _____ _____

_____ _____ _____

Comments

N/A

Checked by: _____ 6/23/96
Signature Date

YAP-SIII.3Q.1

ATTACHMENT 2
KEY TECHNICAL DATA TRACEABILITY

PROCEDURE ID: YMP-LBNL-QIP-SIII.3 | REV. 1 MOD. 0 | EFFECTIVE: ~~xx/xx/96~~ 7/31/96 VF 8/1/96

Date: 8/23/96 Data Tracking Number: LB960500834244.001

Prepared By: Y. TSANG

Title/Subject:
LETTER REPORT ON HYDROLOGICAL CHARACTERIZATION OF THE SINGLE HEATER TEST AREA IN THE ESF

The following contain supporting documentation for the attached data submittal. These documents have been, or shall be submitted to YMP-LBNL Records Processing Center.

Notebooks:	YMP-LBNL-YWT-1.2	4 - 22	
	YMP-LBNL-YWT-1.3	11 - 26	
Photos:			
Maps:			
Computer Files:			
Other:			
	ID#	Page Numbers	
	ID (if possible)	ID (if possible)	
	Filename	Filename	

YVONNE TSANG	Yvonne Tsang	8/23/1996
Principal Investigator's Name	Signature	Date
V. FISSEKIDOU		8/23/96
Technical Data Coordinator's Name	Signature	Date

LLYM0990212O A

NOL.19980409.0244

306578

YMP-023-R4
05/06/96

YUCCA MOUNTAIN SITE CHARACTERIZATION PROJECT
TECHNICAL DATA INFORMATION

(Check one): [X] ACQUIRED DATA (complete Parts I and II)
Data Tracking Number (DTN): LL980106404244.058

[ ] DEVELOPED DATA (complete Parts I, II and III)
Data Tracking Number (DTN):

PART I Identification of Data

Title/Description of Data: THREE TABLES OF MINERAL ABUNDANCES FOR SAMPLES USED FOR THERMAL TESTING (BOREHOLES IN THE DRIFT SCALE TEST (DST) AREA OF THE ESF). (THESE DATA SUPERSEDE DTNS LL970206704244.029 AND LL970600304244.032 AND SHOW DATA THAT HAS BEEN REANALIZED.)

Principal Investigator (PI): VIANI, B E
Last Name First and Middle Initials

PI Organization: LAWRENCE LIVERMORE NATIONAL LABORATORY

Are Data Qualified?: [X] Yes [ ] No Governing Plan: SCP

SCPB Activity Number(s): 8.3.4.2.4.4.1

WBS Number(s): 1.2.3.14.2

PART II Data Acquisition/Development Information

Method: X-RAY DIFFRACTION AND WHOLE PATTERN FITTING (RIETVELD ANALYSIS) WAS USED TO ESTIMATE MINERAL ABUNDANCES IN CRUSHED AND GROUND TOPOPAH SPRING TUFF SAMPLES FROM THE DRIFT SCALE TEST AREA OF THE EXPLORATORY STUDIES FACILITY. X-RAY PATTERNS WERE CORRECTED FOR INSTRUMENTAL ERROR PRIOR TO RIETVELD ANALYSIS CALIBRATION USING X-RAY SPACING STANDARDS. CORUNDUM WAS ADDED TO EACH SAMPLE IN A KNOWN AMOUNT

Location(s): LAWRENCE LIVERMORE NATIONAL LABORATORY

Period(s): 1/2/97 to 12/30/97
From: MM/DD/YY To: MM/DD/YY

Sample ID Number(s): AOD-HD6861-48.5-D

PART III Source Data DTN(s)

Comments

ASSOCIATED WITH DELIVERABLE SPY1B5M4. THESE DATA SUPERCEDE DTNS LL970206704244.029 AND LL970600304244.032.

Checked by: M. Jeanne Palmer 1/20/98
Signature Date

YAP-SIII.3Q.1

YMP-023-R4
08/31/95

YUCCA MOUNTAIN SITE CHARACTERIZATION PROJECT
TECHNICAL DATA INFORMATION
CONTINUATION SHEET

Method (continued)

TO ASSESS THE ACCURACY OF THE METHOD.

Sample ID Number(s) (continued)

ADD-HDFR#1-68 6-D
ADD-HDFR#1-9 0-D
ADD-HDFR#1-98 0-D
BJ-1-1 0-B
BJ-1-10 0-B
BJ-1-18 0-B
CHE-1, 122 6-123 2
CHE-1, 32 0-32 8
CHE-1, 53 4-54 2
CHE-1, 66 6-67 3
CHE-1, 76 7-77 6
CHE-1, 85 7-86 6
CHE-10, 100 1-101 0
CHE-10, 27 3-28 0
CHE-10, 75 6-76 3
CHE-10, 80 7-81 6
CHE-10, 85 0-85 7
CHE-2, 114 0-114 7
CHE-2, 128 9-129 6
CHE-2, 18.6-19 1
CHE-2, 50 3-51 0
CHE-2, 65 0-65 7
CHE-2, 76 7-77 4
CHE-2, 89 0-89 7
CHE-2, 97 0-97 7
CHE-5, 5.2-6.0
CHE-5, 50 0-50 7
CHE-5, 74 2-74.9
CHE-5, 82.8-83.5
CHE-5, 99.0-99.6
CHE-6, 105.0-105.5
CHE-6, 118 6-119 3
CHE-6, 29 0-29.7
CHE-6, 63 9-64 6
CHE-6, 74 8-75 5
CHE-6, 91.3-92.0
CHE-6, 99 7-100 4
CHE-7, 101 0-101 7
CHE-7, 80 0-80 7
CHE-7, 95 6-96 3
H1-0 6-C
H1-11 3-C
H1-11.6-C
H1-22.2-B
MPBX-2-8.6-D
MPBX-3-12 5-B
MPBX-4-5.0-B

YAP-SIII.3Q.1

YMP-023-R4
08/31/95

YUCCA MOUNTAIN SITE CHARACTERIZATION PROJECT
TECHNICAL DATA INFORMATION
CONTINUATION SHEET

Page 1 of 1

Sample ID Number(s) (continued)

SDH-MPBX1-1 0-1 2-D
SDH-MPBX1-21 0-21 2-D
SDH-MPBX1-31 9-32 1-D
SDH-MPBX1-40 4-40 6-D
SDH-MPBX1-62 0-D
SDH-MPBX1-80 7-80 9-D
SDH-MPBX2-29 0-29 2-D
SDH-MPBX2-48 6-D
SDH-MPBX2-72 0-D
SDH-MPBX2 85 0 D
SDH-MPBX3-17 5-17 7-D
SDH-MPBX3-38 5-38 7-D
SDH-MPBX3-85 6-D

YAP-SIII.3Q.1

LLYM990404A4 A

MOL.19990428.0184

307270

YMP/023-R4
05/06/98

YUCCA MOUNTAIN SITE CHARACTERIZATION PROJECT
TECHNICAL DATA INFORMATION

(Check one): [X] ACQUIRED DATA *(complete Parts I and II)*
Data Tracking Number (DTN): LL980810804242.050

[ ] DEVELOPED DATA *(complete Parts I, II and III)*
Data Tracking Number (DTN): ____

PART I Identification of Data

Title/Description of Data: SEVEN FIGURES AND ONE TABLE OF DATA ASSOCIATED WITH MILESTONE REPORT
SPY132000, URL-ID-131491 ENTITLED "SINGLE-HEATER TEST, FINAL REPORT"

Principal Investigator (PI): BUSCHECK, T A
Last Name First and Middle Initials

PI Organization: LAWRENCE LIVERMORE NATIONAL LABORATORY

Are Data Qualified?: [X] Yes [ ] No Governing Plan: SCP

SCPB Activity Number(s): 8.3.4.2.4.2.4

WBS Number(s): 1.2.3.12.2

PART II Data Acquisition/Development Information

Method: PROGRESS REPORT FOR THE SINGLE HEATER TEST

Location(s): LAWRENCE LIVERMORE NATIONAL LABORATORY

Period(s): 6/1/97 to 8/17/98
From: MM/DD/YY To: MM/DD/YY

Sample ID Number(s): ____

PART III Source Data DTN(s)

Comments

Checked by: [signature] 10/30/98
Signature Date

YAP-SIII.3Q.1

LLNL990629133 A

MOL.19990629.0254

307505

YMP-023-FH
05/06/96

YUCCA MOUNTAIN SITE CHARACTERIZATION PROJECT
TECHNICAL DATA INFORMATION

(Check one): [X] ACQUIRED DATA *(complete Parts I and II)*
Data Tracking Number (DTN): LL981109904242 072

[ ] DEVELOPED DATA *(complete Parts I, II and III)*
Data Tracking Number (DTN):

PART I Identification of Data

Title/Description of Data: DRIFT-SCALE REPORT, "ELECTRICAL PROPERTIES OF TUFF FROM THE ESF AS A FUNCTION OF WATER SATURATION AND TEMPERATURE," ONE TABLE AND TEN FIGURES VA SUPPORTING DATA. ASSOCIATED WITH UCRL-ID-129594. SPY195M4. DST4097

Principal Investigator (PI): ROBERTS, J
Last Name First and Middle Initials

PI Organization: LAWRENCE LIVERMORE NATIONAL LABORATORY

Are Data Qualified?: [X] Yes [ ] No Governing Plan: SCP

SCPB Activity Number(s): 8 3.4 2.4.3.1

WBS Number(s): 1.2 3.12.3

PART II Data Acquisition/Development Information

Method: ELECTRICAL RESISTIVITY AND DIELECTRIC PERMITTIVITY WERE MEASURED AS A FUNCTION OF FREQUENCY. THE MEASUREMENTS WERE MADE OVER A WIDE RANGE OF FREQUENCY TO VERIFY MEASUREMENTS MADE AT A SINGLE FREQUENCY AND TO PROVIDE ADDITIONAL INFORMATION ABOUT CONDUCTION MECHAISMS AND MICROSTRUCTURAL PARAMETERS RESISTIVITY MEASUREMENTS WERE REPORTED AT 1KHZ, DIELECTRIC PERMITTIVITY WAS REPORTED AT 1

Location(s): LLNL

Period(s): 10/1/97 to 12/31/97
From: MM/DD/YY To: MM/DD/YY

Sample ID Number(s):

PART III Source Data DTN(s)

Comments

UCRL-ID-129594. SPY195M4. DST4097.

Checked by: Signature 12/4/98 Date

YAP-SIII.3Q.1

YMP-023.R4
08/31/95

YUCCA MOUNTAIN SITE CHARACTERIZATION PROJECT
TECHNICAL DATA INFORMATION
CONTINUATION SHEET

Method (continued)

XRD. SAMPLES WERE PREPARED FROM BOREHOLES CHE-6,7,10. SAMPLES WERE HEATED TO 35, 50 AND 70 DEGREES CELSIUS.

YAP-SIII.3Q.t

MOL.19961029.0113

305593

YMP-023-R4
05/06/96

YUCCA MOUNTAIN SITE CHARACTERIZATION PROJECT
TECHNICAL DATA INFORMATION

(Check one): [X] ACQUIRED DATA (complete Parts I and II) Data Tracking Number (DTN): SNL22080196001.001

[ ] DEVELOPED DATA (complete Parts I, II and III) Data Tracking Number (DTN): _____

PART I Identification of Data

Title/Description of Data: THERMAL PROPERTIES OF TEST SPECIMENS FROM THE SINGLE HEATER TEST AREA IN THE THERMAL TESTING FACILITY AT YUCCA MOUNTAIN, NEVADA.

Principal Investigator (PI): BRODSKY, N S (Last Name / First and Middle Initials)

PI Organization: SANDIA NATIONAL LABORATORIES

Are Data Qualified?: [X] Yes [ ] No Governing Plan: SCPB

SCPB Activity Number(s): 8.3.1.15.1.1.3

WBS Number(s): 1.2.3.16.2

PART II Data Acquisition/Development Information

Method: TESTED THERMAL CONDUCTIVITY ACCORDING TO SNL TECHNICAL PROCEDURE, TP-202, 'MEASUREMENT OF THERMAL CONDUCTIVITY OF GEOLOGIC SAMPLES BY THE GUARDED-HEAT-FLOW-METER METHOD;' AND TESTED THERMAL EXPANSION ACCORDING TO SNL TECHNICAL PROCEDURE, TP-203, 'MEASUREMENT OF THERMAL EXPANSION OF GEOLOGIC SAMPLES USING A PUSH ROD DILATOMETER'.

Location(s): HOLOMETRIX, BEDFORD, MA

Period(s): 6/1/96 to 8/9/96 (From: MM/DD/YY / To: MM/DD/YY)

Sample ID Number(s): ESF-33-1-1.0-A

PART III Source Data DTN(s)

Comments

SNL DATASET ID: S1/L22-08/01/96.

Checked by: Mary J Brodsky (Signature) 8-20-96 (Date)

YAP-SIII3Q.1

305593

YMP-023-R4
08/31/95

YUCCA MOUNTAIN SITE CHARACTERIZATION PROJECT
TECHNICAL DATA INFORMATION
CONTINUATION SHEET

Page 2 of 2

SCPB Activity Number(s) (continued)

8.3.1.15.1.2.1

Sample ID Number(s) (continued)

ESF-BJ-1-10.0-A
ESF-H1-0.6-A
ESF-H1-0.6-B
ESF-H1-11.3-A
ESF-H1-11.3-B
ESF-H1-11.6-A
ESF-H1-11.6-B
ESF-H1-19.9-B
ESF-H1-22.2-A
ESF-HPBX-1-12.5-A
ESF-HPBX-4-10.3-A
ESF-HPBX-4-5.0-A

YAP-SIII.3Q.1

INTENTIONALLY LEFT BLANK